

Eighth Symposium

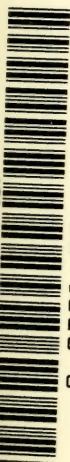
**NAVAL
HYDRODYNAMICS**

**HYDRODYNAMICS IN THE
OCEAN ENVIRONMENT**

ARC-179

**Office of Naval Research
Department of the Navy**

MBL/WHOI

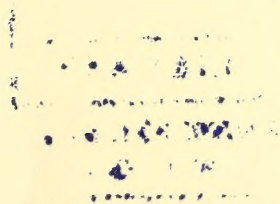


0 0301 0047199 1

John H. Thomson

Feb 1923 -

Lynn, Mass.



1792

Eighth Symposium

VM
156
S87
8th

NAVAL HYDRODYNAMICS

HYDRODYNAMICS IN THE OCEAN ENVIRONMENT

sponsored by the

OFFICE OF NAVAL RESEARCH

the

NAVAL UNDERSEA RESEARCH AND DEVELOPMENT CENTER

and the

CALIFORNIA INSTITUTE OF TECHNOLOGY

August 24-28, 1970

Rome, Italy

MILTON S. PLESSET

T. YAO-TSU WU

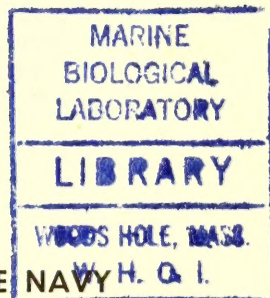
STANLEY W. DOROFF

Editors



WOODS HOLE O.I. Pt

OFFICE OF NAVAL RESEARCH—DEPARTMENT OF THE NAVY
Arlington, Va.



PREVIOUS BOOKS IN THE NAVAL HYDRODYNAMICS SERIES

"First Symposium on Naval Hydrodynamics," National Academy of Sciences—National Research Council, Publication 515, 1957, Washington, D.C.; PB133732, paper copy \$6.00, 35-mm microfilm 95¢.

"Second Symposium on Naval Hydrodynamics: Hydrodynamic Noise and Cavity Flow," Office of Naval Research, Department of the Navy, ACR-38, 1958; PB157668, paper copy \$10.00, 35-mm microfilm 95¢.

"Third Symposium on Naval Hydrodynamics: High-Performance Ships," Office of Naval Research, Department of the Navy, ACR-65, 1960; AD430729, paper copy \$6.00, 35-mm microfilm 95¢.

"Fourth Symposium on Naval Hydrodynamics: Propulsion and Hydroelasticity," Office of Naval Research, Department of the Navy, ACR-92, 1962; AD447732, paper copy \$9.00, 35-mm microfilm 95¢.

"The Collected Papers of Sir Thomas Havelock on Hydrodynamics," Office of Naval Research, Department of the Navy, ACR-103, 1963; AD623589, paper copy \$6.00, microfiche 95¢.

"Fifth Symposium on Naval Hydrodynamics: Ship Motions and Drag Reduction," Office of Naval Research, Department of the Navy, ACR-112, 1964; AD640539, paper copy \$15.00, microfiche 95¢.

"Sixth Symposium on Naval Hydrodynamics: Physics of Fluids, Maneuverability and Ocean Platforms, Ocean Waves, and Ship-Generated Waves and Wave Resistance," Office of Naval Research, Department of the Navy, ACR-136, 1966; AD676079, paper copy \$6.00, microfiche 95¢.

"Seventh Symposium on Naval Hydrodynamics: Unsteady Propeller Forces, Fundamental Hydrodynamics, Unconventional Propulsion," Office of Naval Research, Department of the Navy, DR-148, 1968; AD721180; Available from Superintendent of Documents, U.S. Government Printing Office, Washington, D.C. 20402, Clothbound, 1690 pages, illustrated (Catalog No. D 210.15:DR-148; Stock No. 0851-0049); \$13.00.

NOTE: The above books, except for the last, are available from the National Technical Information Service, U.S. Department of Commerce, Springfield, Virginia 22151. The catalog number and the price for paper copy and for microform copy are shown for each book.

Statements and opinions contained herein are those of the authors and are not to be construed as official or reflecting the views of the Navy Department or of the naval service at large.

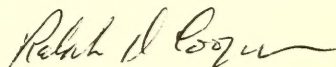
For sale by the Superintendent of Documents, U.S. Government Printing Office
Washington, D.C. 20402 - Price \$10
Stock Number 0851 0056

PREFACE

Continuing in an uninterrupted manner since 1956, the biennial symposia on naval hydrodynamics convened for its Eighth Symposium, August 24-28, 1970 at Pasadena, California. This conference was jointly sponsored by the Office of Naval Research, the Naval Undersea Research and Development Center, and the California Institute of Technology.

The technical program in this series is traditionally structured about a limited number of topics of current interest in naval hydrodynamics. In the case of the Eighth Symposium, "Hydrodynamics in the Ocean Environment" was selected as the focal theme not only because of the present widespread research interest and activity in this subject but also in recognition of 1970 as the inaugural year of the "International Decade of Ocean Exploration." This motif for the Eighth Symposium was also aptly reflected in the banquet address to the participants by Rear Admiral O.D. Waters, USN, then Oceanographer of the Navy.

The organization and management of a meeting of this magnitude requires the attention and energy of a large number of people over a long period of time. To Dr. Harold Brown, President of the California Institute of Technology, to Captain Charles Bishop, Commander, Naval Undersea Research and Development Center, and to all the various members of their organizations who contributed in many different ways to the success of the Eighth Symposium, the Office of Naval Research is deeply indebted, and to them we extend our heartfelt gratitude and appreciation for a job well done. It is particularly appropriate, however, to acknowledge the specific roles of Professor Milton S. Plesset and Professor T.Y. Wu of the California Institute of Technology and Dr. J. Hoyt of the Naval Undersea Research and Development Center who as a group carried the lion's share of the responsibility for the detailed planning and day-to-day management of the Eighth Symposium. We take special pleasure in acknowledging the invaluable assistance of Mrs. Barbara Hawk, secretary to Professor Plesset, who in a most gracious and efficient manner carried out a multitude of important tasks in support of the Symposium. In addition, Mrs. Hawk, together with Mrs. Alrae Tingley, were responsible for the preparation of the typescript which was used in the publication of these proceedings. Mr. Stanley Doroff of the Office of Naval Research played his usual critical role, participating actively in every aspect of the planning and execution of the arrangements for the Eighth Symposium.



RALPH D. COOPER
Director,
Fluid Dynamics Program
Office of Naval Research

CONTENTS

	Page
Preface	iii
Address of Welcome	xi
Rear Admiral C. O. Holmquist, Chief of Naval Research and Assistant Oceanographer for Ocean Science	
Address at the Symposium Banquet	xiv
Rear Admiral O. D. Waters, Jr., Oceanographer of the Navy	
HYDRODYNAMICS IN THE OCEAN ENVIRONMENT	
TSUNAMIS	3
G. F. Carrier, Harvard University, Cambridge, Massachusetts	
LABORATORY INVESTIGATIONS ON AIR-SEA INTERACTIONS	11
E. Y. Hsu and H. Y. Yu, Stanford University, Stanford, California	
AIR-SEA INTERACTIONS; RESEARCH PROGRAM AND FACILITIES AT IMST	37
M. Coantic and A. Favre, IMST, Marseille, France	
EXPLOSION-GENERATED WATER WAVES	71
Bernard LeMéhauté, Tetra Tech, Inc., Pasadena, California	
RESONANT RESPONSE OF HARBORS (THE HARBOR PARADOX REVISITED)	95
John W. Miles, University of California, San Diego, California	
UNSTEADY, FREE SURFACE FLOWS: SOLUTIONS EMPLOYING THE LAGRANGIAN DESCRIPTION OF THE MOTION	117
C. Brennen and A. K. Whitney, California Institute of Technology, Pasadena, California	

	Page
TWO METHODS FOR THE COMPUTATION OF THE MOTION OF LONG WATER WAVES - A REVIEW AND APPLICATIONS	147
Robert L. Street and Robert K. C. Chan, Stanford University, Stanford, California and Jacob E. Fromm, IBM Corporation, San Jose, California	
AN UNSTEADY CAVITY FLOW	189
D. P. Wang, The Catholic University of America, Washington, D.C.	
DEEP-SEA TIDES.	217
Walter H. Munk, University of California, San Diego, California	
STABILITY OF AND WAVES IN STRATIFIED FLOWS. .	219
Chia-Shun Yih, University of Michigan, Ann Arbor, Michigan	
DISCUSSION	235
L. van Wijngaarden, Twente Institute of Technology, Enschede, The Netherlands	
REPLY TO DISCUSSION	236
Chia-Shun Yih, University of Michigan, Ann Arbor, Michigan	
ON THE PREDICTION OF IMPULSIVELY GENERATED WAVES PROPAGATING INTO SHALLOW WATER . .	239
Paul R. Van Mater, Jr., United States Naval Academy, Annapolis, Maryland, and Eddie Neal, Naval Ship Research and Development Center, Washington, D.C.	
THREE DIMENSIONAL INSTABILITIES AND VORTICES BETWEEN TWO ROTATING SPHERES	275
J. Zierep and O. Sawatski, Universitat Karlsruhe, Karlsruhe, West Germany	
DISCUSSION	287
L. van Wijngaarden, Twente Institute of Technology, Enschede, The Netherlands	
REPLY TO DISCUSSION	288
J. Zierep, Universitat Karlsruhe, Karlsruhe, West Germany	

	Page
ON THE TRANSITION TO TURBULENT CONVECTION. .	289
Ruby Krishnamurti, Florida State University, Tallahassee, Florida	
TURBULENT DIFFUSION OF TEMPERATURE AND SALINITY: - AN EXPERIMENTAL STUDY	311
Allen H. Schooley, U.S. Naval Research Laboratory, Washington, D.C.	
SELF-CONVECTING FLOWS	321
Marshall P. Tulin, Hydronautics, Incorporated, Laurel, Maryland, and Josef Schwartz, Hydronautics-Israel, Ltd. and Israel Institute of Technology	
RADAR BACK-SCATTER FROM THE SEA SURFACE . .	361
K. Hasselmann and M. Schieler, Institut für Geophysik, University of Hamburg	
INTERACTION BETWEEN GRAVITY WAVES AND FINITE TURBULENT FLOW FIELDS	389
Daniel Savitsky, Stevens Institute of Technology, Hoboken, New Jersey	
DISCUSSION	446
Dr. N. Hogben, National Physical Laboratory, Ship Division, Feltham, Middlesex, England	
REPLY TO DISCUSSION.	447
Daniel Savitsky, Stevens Institute of Technology, Hoboken, New Jersey	
CHARACTERISTICS OF SHIP BOUNDARY LAYERS . . .	449
L. Landweber, University of Iowa, Iowa City, Iowa	
DISCUSSION	473
Dr. N. Hogben, National Physical Laboratory, Ship Division, Feltham, Middlesex, England	
DISCUSSION	474
H. Lackenby, The British Ship Research Association, Northumberland, England	
REPLY TO DISCUSSION	475
L. Landweber, University of Iowa, Iowa City, Iowa	

	Page
STUDY OF THE RESPONSE OF A VIBRATING PLATE IMMERSED IN A FLUID	477
L. Maestrello, NASA Langley Research Center, Hampton, Virginia, and T. L. J. Linden, European Space Operations Center, Darmstadt, Germany	
RECENT RESEARCH ON SHIP WAVES	519 -
J. N. Newman, Massachusetts Institute of Technology, Cambridge, Massachusetts	
DISCUSSION	540
N. Hogben, National Physical Laboratory, Ship Division, Feltham, Middlesex, England	
VARIATIONAL APPROACHES TO STEADY SHIP WAVE PROBLEMS	547
Masatoshi Bessho, The Defense Academy, Yokosuka, Japan	
WAVEMAKING RESISTANCE OF SHIPS WITH TRANSOM STERN.	573
B. Yim, Naval Ship Research and Development Center, Washington, D. C.	
DISCUSSION	599
Georg P. Weinblum, Institut für Schiffbau, Hamburg, Germany	
DISCUSSION	601
S. D. Sharma and L. J. Doctors, University of Michigan, Ann Arbor, Michigan	
REPLY TO DISCUSSION	604
B. Yim, Naval Ship Research and Development Center, Washington, D.C.	
REPLY TO DISCUSSION	604
B. Yim, Naval Ship Research and Development Center, Washington, D.C.	
BOW WAVES BEFORE BLUNT SHIPS AND OTHER NON-LINEAR SHIP WAVE PROBLEMS	607
Gedeon Dagan, Technion-Israel Institute of Technology, Haifa, Israel and Marshall P. Tulin, Hydronautics, Inc., Laurel, Maryland	
DISCUSSION	622
L. van Wijngaarden, Twente Institute of Technology, Enschede, The Netherlands	

	Page
DISCUSSION	624
Prof. Hajime Maruo, Yokohama National University, Yokohama, Japan	
REPLY TO DISCUSSION	625
Gedeon Dagan, Technion-Israel Institute of Technology, Haifa, Israel	
REPLY TO DISCUSSION	626
M. P. Tulin, Hydronautics, Inc., Laurel, Maryland	
SHALLOW WAVE PROBLEMS IN SHIP HYDRODYNAMICS	627
E. O. Tuck and P. J. Taylor, University of Adelaide, Adelaide, South Australia	
DISCUSSION	658
Prof. Hajime Maruo, Yokohama National University, Yokohama, Japan	
REPLY TO DISCUSSION	659
E. O. Tuck and P. J. Taylor, University of Adelaide, Adelaide, South Australia	
SINGULAR PERTURBATION PROBLEMS IN SHIP HYDRODYNAMICS	663
T. Francis Ogilvie, University of Michigan, Ann Arbor, Michigan	
THEORY AND OBSERVATIONS ON THE USE OF A MATHEMATICAL MODEL FOR SHIP MANEUVERING IN DEEP AND CONFINED WATERS	807
Nils H. Norrbin, Statens Skeppsprovsningsanstalt, Sweden	
THE SECOND-ORDER THEORY FOR NONSINUSOIDAL OSCILLATIONS OF A CYLINDER IN A FREE SURFACE	905
Choung Mook Lee, Naval Ship Research and Development Center, Washington, D.C.	
DISCUSSION	951
Edwin C. James, California Institute of Technology, Pasadena, California	
REPLY TO DISCUSSION	951
Choung Mook Lee, Naval Ship Research and Development Center, Washington D.C.	

	Page
THE DRIFTING FORCE ON A FLOATING BODY IN IRREGULAR WAVES	955
J. H. G. Verhagen, Netherlands Ship Model Basin, The Netherlands	
DYNAMICS OF SUBMERGED TOWED CYLINDERS . . .	981
M. P. Paidoussis, McGill University, Montreal, P.Q., Canada	
HYDRODYNAMIC ANALYSES APPLIED TO A MOORING AND POSITIONING OF VEHICLES AND SYSTEMS IN A SEAWAY	1017
Paul Kaplan, Oceanics, Inc., Plainview, New York	
WAVE INDUCED FORCES AND MOTIONS OF TUBULAR STRUCTURES	1083
J. R. Paulling, University of California, Berkeley, California	
SIMULATION OF THE ENVIRONMENT AND OF THE VEHICLE DYNAMICS ASSOCIATED WITH SUBMARINE RESCUE	1111
H. G. Schreiber, Jr., J. Bentkowsky and K. P. Kerr, Lockheed Missiles and Space Co., Sunnyvale, California	
AUTHORS INDEX	1185

ADDRESS OF WELCOME

Rear Admiral C. O. Holmquist
*Chief of Naval Research and Assistant
Oceanographer for Ocean Science*

I am pleased to welcome you to the Eighth International Symposium in Naval Hydrodynamics. This is a symposium sponsored every other year by the Office of Naval Research, with the objective of bringing together the leading investigators in the field of hydrodynamics research throughout the world.

ONR has held many international meetings during the nearly quarter-century of its existence. This is in line with its charter issued by Congress, which includes the responsibility to disseminate information on world-wide trends in research and development. It is for this reason, for example, that we have a branch office in London.

This series of meetings, however, has a unique characteristic. Every other meeting is held outside the United States. Two years ago we met in Rome, and two years from now we plan to hold this symposium in another country. This stimulates attendance by non-U.S. participants.

This year we welcome to the United States a number of distinguished researchers in the field of hydrodynamics. As you have noted in your program, you will hear papers read by scientists from institutions as far away as Australia. The information made available through this international meeting will not only provide the U.S. Navy with new ideas for significantly improving its ship designs but also a pool of knowledge that will stimulate international cooperation in science. The Navy has already received important benefits from an exchange of research data with other countries.

In regard to this symposium, ONR owes a great deal both to the Naval Undersea Research and Development Center and the California Institute of Technology, who have joined together to serve as hosts. We appreciate very much their efforts in arranging this meeting and providing the excellent facilities.

I might add as a personal note that I am delighted to have this opportunity to return to the Cal Tech campus, where I studied for my doctorate in the early 1950's. Since my field is aeronautics, I

cannot pose as an expert in hydrodynamics, although I am sure you recognize that the two fields have similar and related problems. In fact, in ONR we label our program Fluid Dynamics, with part of this program dealing with hydrodynamics and part with aerodynamics.

Aside from serving as co-hosts, both Cal Tech and NURDC have made major contributions to the work in hydrodynamics, some under ONR sponsorship. For some time Cal Tech has been studying a problem of critical concern to the Navy. This is the damage caused to propellers and other vital components by cavitation. Theoretical and experimental investigations on basic problems in fluid mechanics conducted here are assisting naval engineers in solving cavitation damage problems. At the same time, this work is adding to our knowledge of the phenomenon known as supercavitation, which has led to the development of supercavitating propellers and hydrofoils resulting in increased speed of specialized naval vehicles.

A major program at NURDC sponsorship promises not only to reduce drastically drag resistance during turbulent flow but also to reduce the flow noise which frequently interferes with sonar operations. I am referring to the use of polymer additives which when injected into the boundary layer of water promises to give naval vehicles the capability of burst speed.

At present NURDC is engaged in achieving a complete understanding of the mechanism of the drag and noise reduction properties of dilute solutions of polymer additives. This will give us a firm technical basis for predicting what extent we can achieve drag reduction and flow-noise suppression on Navy vehicles.

Research in hydrodynamics is carried out under contract to ONR at a variety of academic and at industrial organizations and at naval laboratories and field stations. Typical of the universities participating in the program are Stevens Institute, the Massachusetts Institute of Technology, Stanford, University of California, Harvard, Florida State, and Michigan in addition to Cal Tech. Industrial organizations include Hydronautics, Inc., and LTV Research Center and the Ampex Corp. Our in-house work in addition to NURDC is performed at the Naval Ship Research and Development Center, the Naval Research Laboratory, the Naval Ordnance Laboratory and the Naval Postgraduate School in Monterey, California.

Each of these three elements -- the university, industry and the Navy laboratory -- have a unique contribution not only to the Navy's fluid dynamics program but to Navy research and development in general. Universities provide us with the more fundamental data on which all good technology is based. Industry has special know-how in producing test beds and experimental hardware needed to prove our theories. The Navy laboratory provides in one location theoretical scientists working with naval engineers and naval officers

who have an intimate understanding of the Navy's operational problems.

As an example of what this combination can produce, we have developed computer programs to predict the coupled motions of heave and pitch for surface ships operating in a seaway. The input information that is used consists of ship geometry, forward speed, and a stochastic description of the sea state. Another computer program simulates the launch perturbations of a torpedo leaving a moving submarine. This provides a relatively inexpensive method for determining the operational limitations during launch, an insight into how launch problems can be solved, and tool for the design of future submarine weapon systems.

The research process is continuous and complex, and it is rarely, if ever possible, to label a new discovery as the product of one individual or even one institution. Research has to be cooperative, and we can achieve the most by cooperating on an international scale. As this meeting indicates, ONR and the Navy subscribes to that objective. I am sure that all of us are faced with the problem of producing the maximum amount of significant research results with a minimum of funds and manpower, so that we should all benefit from a mutual sharing of our knowledge.

ADDRESS AT THE SYMPOSIUM BANQUET

Rear Admiral O. D. Waters, Jr.
Oceanographer of the Navy

Mr. Chairman, distinguished foreign guests, geniuses in residence, Ladies and Gentlemen:

It is both an honor and a pleasure to be given an opportunity to speak here tonight to the delegates to the 8th Symposium on Naval Hydrodynamics.

It is obviously an honor for a mere sailor to be invited to talk to so erudite an audience and under such distinguished sponsorship as the California Institute of Technology, the Office of Naval Research and the Naval Undersea Research and Development Center.

It is a particular pleasure since it is not often the wheel of fortune stops right on your number and you get invited to speak just fifty miles from the birthplace of a brand new grandchild.

I believe it's customary about here for a visiting speaker to tell a condescending joke about California smog but since most of you read the newspapers you know that we on the East Coast are now living in a glass house where that subject is concerned. After all, when it gets to the point where you can no longer see the National Capital from the top of the Washington Monument you can't pass it off any longer as a morning haze.

In any case I arrived here by way of Alaska where most of the country's current supply of fresh air seems to be stockpiled so my lungs are back in pretty good condition.

This subject of smog and pollution in general reminds me that an acquaintance recently told me of an opinion poll he claimed had been taken among American Indians. Only 12% of them, he said, felt we should get out of Vietnam, but 88% thought we should get out of North America.

I originally intended to say a few kind words about the sponsors of this annual event but changed my mind. Anything about the valuable work that has been done in oceanography and many related fields by the Office of Naval Research and the Naval Undersea Research and

Development Center (our chief semanticist had us remove the nasty word warfare from their title) would come under the heading of bragging about a relative. And after bringing myself up-to-date on the history of the California Institute of Technology I felt there was just nothing I could say. Even an amateur of science who walks across a campus where such men as Millikan and Michaelson once tarried to think, feels as an art lover must feel when he walks on a stone bridge across the Arno where Leonardo once set his mighty sandal. The debt the nation and the Navy owe this Institute is beyond all calculation.

The point was adroitly made, I thought in a booklet about Cal Tech that Dr. Plesset was kind enough to send me. The booklet contained a picture of a man on a bicycle as an illustration of the Institutes recreational opportunities. The man on the bicycle who was unidentified in the caption, was Einstein.

Dr. Plesset also provided me with a program of Symposium events and I ran through it looking for a possible clue as to what I should choose as a topic. Several arresting items caught my eye. Listed was a paper on "The Second-Order Theory for Nonsinusoidal Oscillations of a Cylinder in a Free Surface." Another was on "Three Dimensional Instabilities and Vortices between two Rotating Spheres," and another on "Interaction between Gravity Waves and Finite Turbulent Flow Fields."

Well, I know when I'm out of my league so I decided to just make a few First Order remarks on the mission of Navy Oceanography and how it is organized.

First a definition. Hydrodynamics is not generally considered to be oceanography but then neither specifically is anything else. Oceanography as we use it is just an omnibus word for any scientific or engineering discipline as it applies to the oceans.

It is nothing new. In the American Navy it goes back at least to our pre-civil war patron saint, Lieutenant Matthew Fontaine Maury, who used his knowledge of winds and currents to help the clipper ships set their famous world speed records. In Great Britain it goes back to the famous voyage of the HMS CHALLENGER. Benjamin Franklin took a lively interest in it and so did Aristotle.

But modern oceanography in the Navy dates from the christening of the NAUTILUS and the nuclear missile submarines that followed it. Warfare had suddenly become truly three-dimensional. The new mission of Navy oceanography was to see to it that the Fleet was given the information it had to have to insure its ability to operate efficiently in this new and deadly area of underseas warfare.

Before I tell you how we went about this let me say a few

words about the broader aspects of oceanography. In the Navy we consider it as our field of special competence and we are entrusted with close to half the Federal budget -- or about 210 million dollars in this current year of fiscal austerity.

Work in the entire field however is carried on at three levels.

First there is the National effort. This involves industries like the oil business -- 15% of our oil already comes from under-water -- and the fishing industry where our annual catch can be greatly increased with a better understanding of the ocean currents and temperatures, which influence the distribution of fish -- and the growing aquatic recreation field where beach erosion, the character of marine life, the most efficient design of boat hulls and other oceanographic factors are most important.

The next area is the Federal effort. There are close to thirty major Federal agencies concerned with oceanography to some degree. The Department of the Interior in fisheries. The Food and Drug Administration in medicine from the sea. And the Coast Guard with a variety of oceanographic interests -- to mention just a few. This Federal effort is now being examined from an organizational standpoint. The President has recommended and the Congress is considering a broad new plan to streamline this effort under unified executive direction.

This brings me to the third area of oceanography, the military aspects, for which the Navy, quite logically, is the Defense Department agent.

Our job of controlling the seas for defense requires that Navy have the broadest program in scope in the Federal Government.

To avoid duplication of effort and give us a clear-cut chain of command we put all of our efforts under the technical direction of the Oceanographer of the Navy.

For organizational efficiency the program was set up in four divisions. These divisions are Ocean Engineering and Development, Ocean Science; Operations, and Environmental Prediction Services.

Our newest and fastest developing area is Ocean Engineering and Development. Seven major efforts are included here: undersea search and location; submarine rescue and escape; salvage and recovery; diving; instruments for survey and environmental prediction; and underwater construction. We have allocated 57 million dollars for these programs this year.

Our first rescue vessel, the DSRV-I, which can be equipped also for survey work was launched recently at San Diego. Our first nuclear deep submersible, the NR-I, has already completed its

early tests, and is currently undergoing some changes including improvements to its main propulsion system. The DSRV-II will be ready soon for launching. Our goal with these vehicles and their attendant systems is a capability of rescuing personnel down to submarine crush depth. They will be made available on request to other governments and some are already making the necessary modifications required for utilizing their services.

Our first nuclear propelled deep sea vehicle the NR-I, has done some bathymetric work during her sea trials and is undergoing continuing tests to determine the limits of her capabilities.

We are working on a Large Object Salvage System (LOSS). The goal is to develop a capability of bringing up a submarine intact down to a depth of 850 feet.

An extension of the engineering effort is our Deep Ocean Technology or DOT program designed to anticipate the multiplying requirements of the pioneering technology.

For instance we are well past the blue print stage on our proposed Deep Submergence Search Vehicle (DSSV) designed to operate to a depth of 20,000 feet -- a depth that accounts for 98% of the ocean floor.

An immediate concern is with new power packs. The old style batteries just can't give us either the speed, power or endurance now required. We need electrical systems that will operate in salt water and we are working on thermochemical power sources. We are currently sponsoring a design competition between two firms in this area. It is a long range item that already shows promise.

Our new machines with all of the improvements we are achieving are no better than the skills of the men who operate them. To make the point by hyperbole, if I had only a dollar to spend I would spend 95 cents on training and equipping men and 5 cents on the hardware. So the whole engineering effort is concerned with extensive bio-medical work, particularly in relation to deep saturation diving.

We are already working deeper than 600 feet in the open sea and 1,000 feet experimentally. We are hoping to go to 2,000 feet, perhaps 3,000 feet before we are through.

This means we need more and more bio-medical data for equipment design and for shaping the selection, training, operational use and health care of our aquanauts and undersea vehicle pilots.

We are taking the field of underwater medicine from its rather narrow corner as an occupational sub-specialty, for its scope transcends its size in at least three important ways. First, it has forced us to study the effects of pressure on living systems,

a study neglected in biology as compared with other fields of science and one which promises to advance the understanding of normal processes. Second, it is an important confluence of the rapidly mixing disciplines of biology and engineering. And finally, it is the keystone to safe and effective utilization of a growing number of underwater systems.

Our second field, first really in long-range importance, is science.

The primary objective is to provide the basic knowledge needed in all our programs. About 75% of this effort is directed toward anti-submarine warfare particularly in studies of the behavior of sound underwater, as sound is our only practical method of detecting a potential underwater enemy. Much of this work is done under contract with academic and non-profit institutions such as Cal Tech where we can pick the brains of hundreds of the nations top scientists. Engineering, of course, comes in here to provide and equip the platforms that our research scientists need to work from -- ships, deep submersibles, flip type vessels that can stand on their head, surface and subsurface buoys, airplanes, satellites, even a floating ice island.

Next our Operations effort. It functions in direct support of the Fleet. In addition to much else, including various world-wide surveys, it carries out duties imposed on us long ago by law to prepare and disseminate charts and publications necessary for navigational safety both for Navy ships and for the Merchant Marine.

In support of this program is our Environmental Prediction section which operates as an undersea weather bureau to forecast those changes within the waters of the ocean that affect our operations. In this field we work very closely with the Fleet Numerical Weather Center.

Despite our concentration on our primary defense mission, the Navy program is necessarily a broad one -- the broadest in the Federal program -- for the seas are our domain -- and we must know and understand everything we can about them -- the animal life that abounds in them, the nature of the ocean waters, their circulation, the character of the bottom, and much else.

Thus many of the things we must learn and study are of interest to others, in the government, including foreign governments, in the academic world, in industry. I am proud to report that the Navy takes part in many cooperative programs in such fields as fisheries, oil and minerals from the sea, wave predictions, and others. We strongly support this phase of our program because as taxpayers it gives us a feeling of accomplishment to see federal tax dollars doing double duty. I will give just two examples.

A friendly neighbor, Iceland, asked for help when they realized that herring, which make up 90% of their export products, were going to be difficult to find this last season. The herring migrate from Norway and stop off at the East Coast of Iceland when they reach the cold edge of the Greenland current. When this current meanders or changes its location, as these ocean currents are likely to do, it may divert the fish away from their normal grounds near Iceland, as happened recently. We diverted an ice patrol plane with a heat measuring sensor long enough to find the cold wall of the current. And sure enough there were the herring. We are planning now to help Iceland develop its own capability for this kind of work.

We are also providing technical help in harbor improvement programs for several South American countries, and we are running annual courses on oceanography and hydrography for foreign students.

We opened our files on ice reconnaissance and trained some people and also provided an on-board oceanographer to the owners of the great new tanker the MANHATTAN, which has recently successfully navigated the Northwest Passage. Free passage of this once impassable channel should prove to be an invaluable national asset both from an industrial and a strategic viewpoint.

Recognition of the importance of oceanography and hydrography to present day and future naval operations, coupled with a concern for the availability of technically competent naval officers within these areas, has caused us to establish a new Special Duty Officer category. It will consist of approximately 140 officers of ranks Ensign through Captain. Promotion opportunities are equal to that of an Unrestricted Line Officer.

Inputs to the specialty at the Ensign level will come from the Naval Officer Candidate School at Newport, R. I., and the Naval Reserve Officer Training Corps Contract Units. Applicants must have a degree in oceanography, or in another field of earth science, physical science, marine science or engineering (with emphasis on survey engineering for hydrography or ocean engineering for oceanography); must have completed mathematics through calculus plus one year of college physics and chemistry; and should have a B average or better in mathematics, physical science and engineering courses. Graduates of the U. S. Naval Academy and the Naval Reserve Officer Training Corps Units (regular students) may apply after approximately three years active duty.

The first three years of commissioned service will consist of a tour of sea duty on an oceanographic or hydrographic survey vessel and a shore duty tour at a naval facility involving application of oceanographic information to naval operations. Subsequent tours may include management of research and development projects, oceanographic forecasting, mapping, charting and geodesy, instructor

duty, and administration of various areas of the Navy's Oceanographic program.

Turning to the Federal scene, the big push now would seem to be with the war on pollution and, certainly we need to fight it. Oceanography of course is involved here, particularly in the coastal zones, estuaries and lakes.

Thousands of words are being written on the pollution of our environment and the new "in" word is ecology. My daughter heard it and read it so often she decided to look it up. The dictionary told her it meant "the relationship between living organisms and their environment." "Here," she said, "I was wondering what it was and I've been right in the middle of it all the time."

Our new consciousness of our total ecology and the drive against pollution are going to lead to some complex conflicts -- such as between the off-shore oil interests and the conservationists -- the real estate developers and the fishing industry. When you drain a salt marsh, for instance, you interfere with the food chain that supports the fish we need for human food. Involved also is the huge and growing water recreation industry.

In solving our problems we have to be sure not to throw out the baby with the polluted bath water.

Has oceanography got an assured future? Yes of course. We are going to have to turn more and more to the inexhaustible seas for the food and the minerals we will need for the worlds exploding population.

But I don't see that future going up in a near vertical line as it did, for instance, in the space business. In the first place there are none of those big hunks of development money lying around these days.

But I do see it going up steadily in a much more gently rising curve.

But go up it will and as it goes we will need more and more sophisticated equipment and techniques to gather and evaluate information and ever smarter and better educated men to program and run them.

HYDRODYNAMICS IN THE OCEAN ENVIRONMENT

Monday, August 24, 1970

Morning Session

Chairman: F. H. Clauser
California Institute of Technology

	Page
Tsunamis G. F. Carrier, Harvard University	3
Laboratory Investigations on Air-Sea Interactions E. Y. Hsu, H. Y. Yu, Stanford University	11
Air-Sea Interactions; Research Program and Facilities at IMST A. Favre, M. Coantic, IMST Marseille, France Presented by: A. Ramamonjiarisoa	37
Explosion-Generated Water Waves B. Le Méhauté, Tetra Tech, Inc.	71

TSUNAMIS

G. F. Carrier
Harvard University
Cambridge, Massachusetts

I. INTRODUCTION

An understanding of the coastal inundation caused by Tsunamis requires the piecing together of several studies. Among the potentially important characterizing features of the phenomenon are: the temporal and spatial distribution of the ground motion which initiates the Tsunami, the distance from the source to the target area in question, the bottom topography of the intervening ocean, and the topography of the coastal area itself. These are all discussed in some detail in [1], a manuscript which was prepared in conjunction with a longer series of lectures than this one. In order to avoid excessive duplication of publication, we content ourselves here with a brief summary of that material. As will be evident, many details remain to be explored; unfortunately, there is no evidence to suggest that even a more comprehensive understanding of the phenomena will suggest procedures for alleviating the intensity of Tsunami inundation.

II. INITIATION AND DEEP WATER PROPAGATION

The wave generated by a submarine earthquake is large enough in lateral extent and small enough in amplitude so that a linear theory is completely adequate for an analysis of the propagation over deep water. However, the propagation path is so long that dispersion and its attendant changes in wave shape cannot be ignored. Accordingly one can adopt either the classical linear theory of gravity waves or the Boussinesque formalism to study the early stages of the wave propagation. When either is done, for a basin of constant depth, H , it is convenient to present the results in terms of a particular family of initial ground motions. We discuss here the waves which result when the ground motion is given by

$$F_0(x,t) = (\pi L^2)^{-1/2} \exp \left[-x^2/L^2 \right] \delta(t).$$

When the half width, L , of the disturbed region is "small," the wave which arrives at a distance x_0 will have been greatly affected by dispersion; when the width of the generating ground motion is

longer, smaller distortions of the wave will be apparent at x_0 . Figures 1a, 1b, and 1c illustrate the quantitative aspects of the foregoing statement. In the notation of those figures,

$$L^2 = 4\alpha H^2.$$

When the depth of the water is 3 miles and $x_0 = 3000$ miles, the three cases shown represent ground motions whose half widths are 0, 19 and 33 miles. Figure 1d indicates the wave which ensues when the ground displacement is given by

$$F = F_b(x, t) - F_0(x + 20, t)$$

with $\alpha = 10$. That is, the ground motion has a dipole character rather than a general subsidence or elevation. The persistent lore that the second or third crest of the Tsunami penetrates more than the first makes it interesting to speculate (in view of Figs. 1) that many initiating ground motions may be of dipole form.

III. RUN-UP ON A PLANE BEACH

When the wave encounters a sloping shelf along which the water depth generally goes to zero, the wave steepens and becomes greater in amplitude. Accordingly one no longer can rely on a linear theory. However, the shelves of real interest are such that the distance along the wave trajectory above such a shelf is short enough so that dispersion in this region is not of any real importance.

There is a non-linear, non-dispersive shallow water theory which leads to tractable problems when the depth of the basin is linear in one horizontal coordinate and when the entire phenomenon is independent of the other. Thus, we can regard the results referred to in Section 2 as the input information for a study in which we ask how such waves climb up a sloping shelf. The analysis which accompanies such a study involves only the solution of a linear equation whose interpretation in the non-linear context is explicit and accurate.

The result of interest is the ratio of the run-up, η_0 , (the vertical distance above sea level to which water encroaches) to the wave height, η_1 , at the edge of the shelf. One interesting result is this:

For $\alpha = 0$

$$\frac{\eta_0}{\eta_1} \simeq A\theta^{-1/2}(x_0/H)^{-1/6}$$

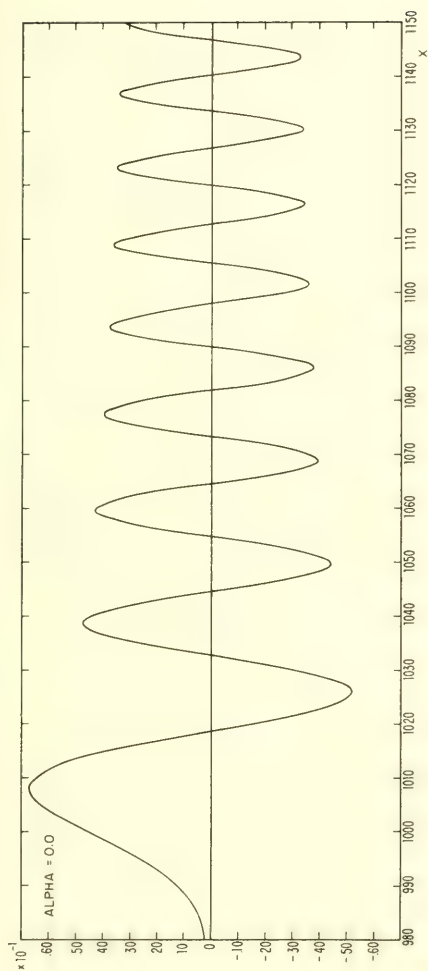


Fig. 1a

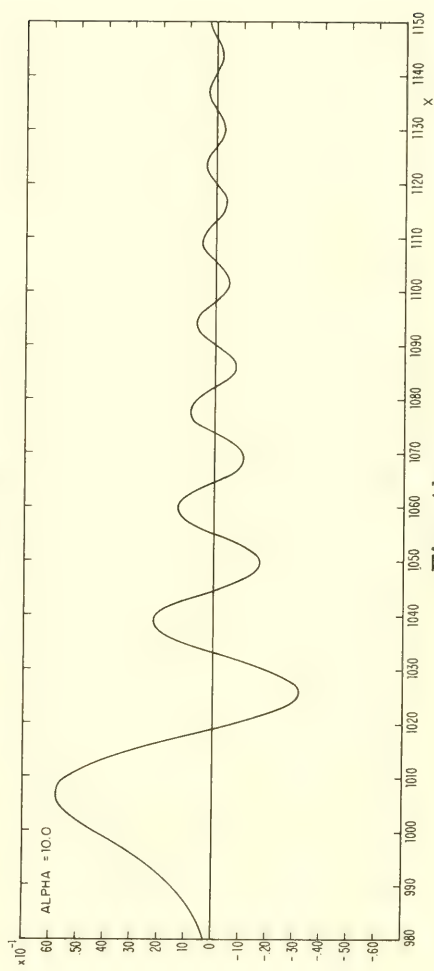


Fig. 1b

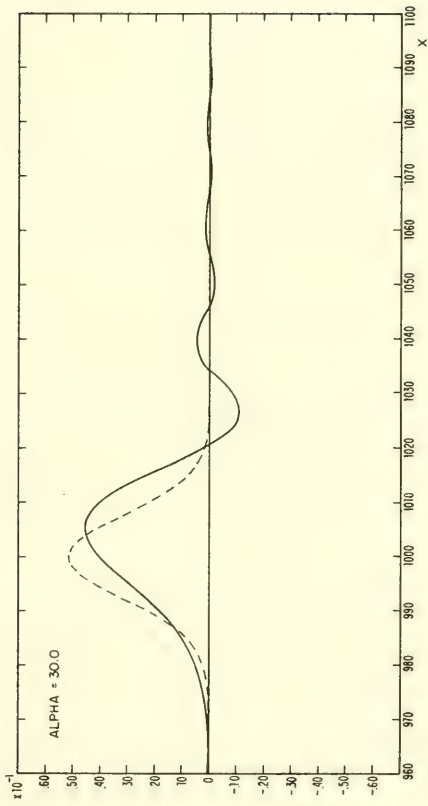


Fig. 1c

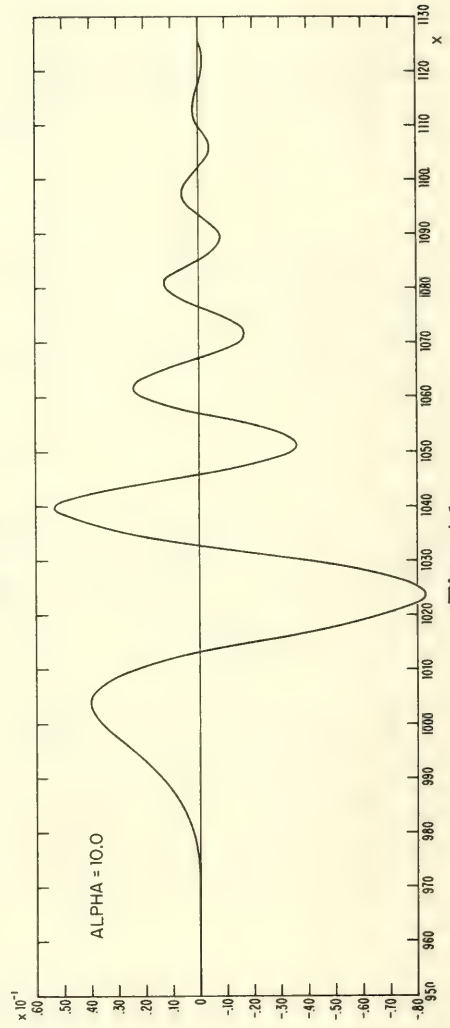


Fig. 1d

where $A = 4.2$ if the ground motion is upward or $A = 5.6$ if it is downward. The corresponding results for other values of L can easily be found (the calculation requires only the use of the method of stationary phase). The dependence on the shelf slope, θ , is that which would be found for monochromatic waves whereas the dependence on x is a consequence of the dispersion during the deep water propagation.

IV. DEEP OCEAN TOPOGRAPHY

If there were systematic variations in the water depth between, say, the Aleutians and the equatorial Pacific, one might expect that the relative intensities of the Tsunamis (with Aleutian source) which were incident on different Pacific islands might differ because of mid-ocean refractive effects. Exhaustive studies of this effect have certainly not been completed but the indications are that this is not a major reason for the different response at (for example) Wake and Hawaii. One might also anticipate that the irregular deep ocean topographical variations could seriously modify the wave which propagates across the ocean. This possibility has been analyzed treating each event as a member of an ensemble of phenomena each of which take place over a topography which is itself a member of a stochastically described collection of random topographies. This is motivated loosely by the fact that the one-dimensional topography between any given source and any given target differ from that associated with any other source-target pair, and the fact that the topographies are so poorly known that little else can be done. The result of this study indicates that the ratio of intensity at x_0 of the wave over the irregular bottom to that over constant depth is characterized by

$$1 - \frac{e^{\epsilon^2 L} - 1}{e^{\epsilon^2 L} + 1}$$

where ϵ is the ratio of the average irregularity height to the average depth and $L = 2\pi N$ where N is the number of wave lengths of the monochromatic wave whose scattering is being studied. For wave lengths in the spectral region of major interest, the effect of this facet of the wave propagation seems to be of relatively small importance too.

V. ISLAND TOPOGRAPHY

When the wave encounters an island, the lateral scale of that island has the same order of magnitude as much of the important part of the wave length spectrum. Thus, the pretense that the wave climbs a plane shelf must be corrected. The refractive effects so

implied cannot be estimated readily by geometric optics methods at such wave lengths and one must resort to numerical procedures. The results of such studies are depicted in Figs. 2 and 3, taken from Lauterbacher [2]. Figure 2 indicates the variations of intensity with position on a given island and Fig. 3 indicates the extent of this effect for different ratios of wave length to island size.

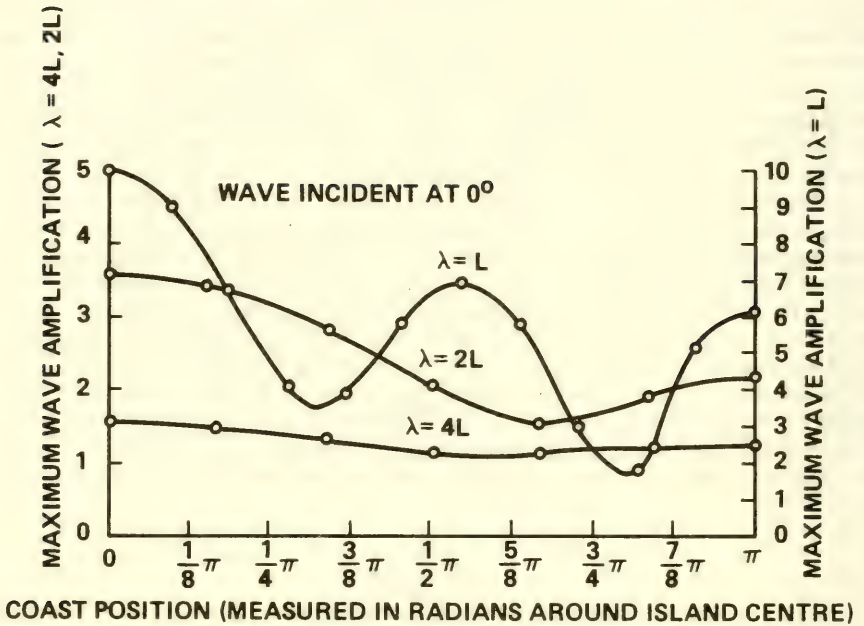


Fig. 2. Maximum wave amplification at coast (OAHU)

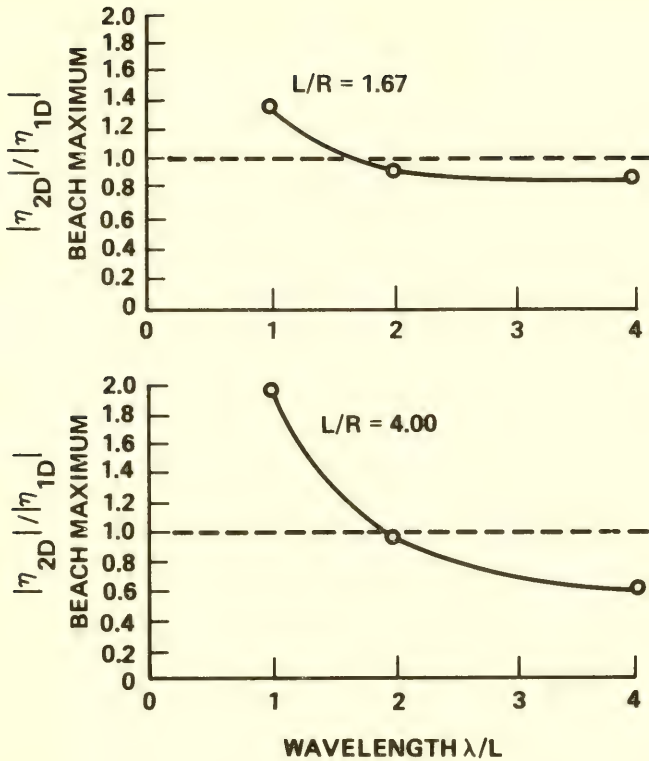


Fig. 3. Ratio of two-dimensional to one-dimensional maximum wave amplitude on beach. L , island diameter at ocean floor; R , island diameter at beach.

ACKNOWLEDGMENT

This work was supported in part by the Office of Naval Research under contract N00014-67-0298-0002 and in part by the Division of Engineering and Applied Physics, Harvard University.

REFERENCES

1. Carrier, G. F., "The Dynamics of Tsunamis," to appear in the Proceedings of the Summer Symposium on Mathematic Problems in Geophysics, 1970.
2. Lauterbacher, C. C., "Gravity Wave Refraction by Islands," J. Fluid Mechs., Vol. 41, Part 3, pp. 655-672, April 1970.

LABORATORY INVESTIGATIONS ON AIR-SEA INTERACTIONS

E. Y. Hsu and H. Y. Yu
Stanford University
Stanford, California

I. INTRODUCTION

Since the comprehensive review on wind wave generation by Ursell [1956], there have been renewed, intensive studies, theoretical as well as experimental, on the subject. Although significant contributions have been made by many investigators, the final goal of achieving a basic understanding of the fundamental mechanism of energy transfer between a turbulent air stream and the ocean has not been realized. A unified, comprehensive theory of wind wave generation must provide adequate explanation of the energy transfer between the two media at all stages of wave growth from capillary waves to sea swell. In the absence of such a unified theory, a convenient classification of various flow regimes in wind-wave generation may be made by use of the ratio of water wave celerity C and the air shear velocity u^* at the interface. When $C \approx u^*$, the dominant mechanism of energy transfer between air and water is the "viscous mechanism," characterized by the critical layer being within the laminar sublayer and treated by Miles [1962]. When $C \approx 10 u^*$, the critical layer is outside the laminar sublayer and the dominant mechanism of energy transfer is the "inviscid mechanism" (Miles [1957, 1967] and Benjamin [1959]) with transfer arising from the normal pressure acting on the interface and the necessary phase angle between the pressure distribution and the progressive wave. As pointed out by Longuet-Higgins [1969], neither of the above theories accounts for two well-established features of wave generation: (1) the existence of some wave energy in a frequency range corresponding to waves traveling faster than the mean free-stream velocity and (2) the damping of a swell by an adverse wind.

The experimental investigations of Sutherland [1967], Hires [1968], and Chang [1968] and many others are limited to the viscous range. Because of the high Reynolds number in a typical wind blowing over the ocean surface, the viscous mechanism can be safely neglected as irrelevant to full-scale wave energy transfer. Hence, Miles' inviscid model has received most attention and been widely employed in comparisons with experimental data obtained in full scale (ocean) and laboratory simulations.

The dearth of systematic measurements taken under controlled conditions closely comparable to those of Miles' model was a motivation for our research program at Stanford University. In order to examine the applicability of Miles' inviscid theory, experiments were designed for measuring the wave induced perturbation pressure or inviscid Reynolds stress under steady-state and unsteady-state conditions. Other experiments were also devised for measuring the growth of mechanically generated waves subjected to wind action. From these measured wave growths, the growth factor of Miles was calculated. The objectives of this paper are to present a summary of our experimental data in the inviscid range, to compare our data and other existing data to the theory and the ocean observations, and to suggest specific and fruitful avenues for further study.

II. A BRIEF REVIEW OF THE THEORY

To facilitate presentation and discussion of the experimental data, a brief outline of the assumptions, key equations and results of Miles' inviscid, shear-flow theory are presented below.

The deep-water, wave profile is assumed to be a progressive, sinusoidal wave, expressed as

$$\eta = a \exp [ik(x - Ct)], \quad ka \ll 1 \quad (1)$$

where a is the amplitude, $k = 2\pi/L$ is the wave number, L is the wave length, and C is the wave celerity. The assumptions of irrotational, incompressible water motion lead to the existence of velocity potential. By substituting the velocity potential in the linearized Bernoulli equation and evaluating the result at the free surface, one obtains the equation of motion governing the propagation of a small amplitude, surface wave

$$\rho_w g \eta + \frac{\rho_w}{k} \frac{\partial^2 \eta}{\partial t^2} = -p_a \quad (2)$$

where g is the acceleration caused by gravity, ρ_w is the mass density of water, and p_a is the aerodynamic pressure caused by the wind stream.

Miles [1957] assumed the aerodynamic pressure p_a has the form

$$p_a = (\alpha + i\beta) \rho_a U_1^2 k \eta \quad (3)$$

where ρ_a is the mass density of the air, U_1 is a reference speed for the air, and α and β are, respectively, the in-phase and

out-of-phase non-dimensional-pressure-coefficients. The phase angle φ is

$$\varphi = \tan^{-1} \left(\frac{\beta}{\alpha} \right) \quad (4)$$

The constants α and β were determined by solving an inviscid Orr-Sommerfeld equation which represents the perturbations (caused by the water wave at the interface) to a wind shear-flow described by an assumed logarithmic, mean velocity distribution

$$U(y) = U_1 \ln \frac{y}{y_0} \quad (5)$$

where y is the vertical distance from the mean water surface and y_0 is the roughness height.

The effect of the impressed aerodynamic pressure P_a on the surface wave can be evaluated by solving Eq. (2). It follows that the complex wave celerity

$$C = C_0 \left[1 + \frac{1}{2} \frac{\rho_a}{\rho_w} (\alpha + i\beta) \left(\frac{U_1}{C_0} \right)^2 \right] \quad (6)$$

where $C_0 = (g/k)^{1/2}$. Substituting Eq. (6) into Eq. (1) yields

$$a = a_0 \exp \left[\frac{1}{2} k C_0 \frac{\rho_a}{\rho_w} \left(\frac{U_1}{C_0} \right)^2 \beta t \right] \quad (7)$$

where a_0 is the amplitude at $t = 0$.

It is convenient to measure the growth of wave amplitude as a function of fetch x in a wind-wave channel. The dynamic equivalence, valid for $x \gg L$, is given by Phillips [1958] as

$$x = \frac{C_0}{2} t, \quad x \gg L$$

where $C_0/2$ is the group velocity of a deep-water wave. Consequently, the fetch-dependent amplitude growth a is

$$a = a_0 \exp \left[\frac{\rho_a}{\rho_w} \frac{k^2}{g} U_1^2 \beta x \right] \quad (8)$$

where a_0 is now the wave amplitude that would exist without wind

action or at $x = 0$.

The total energy per unit of surface area E of a small-amplitude, sinusoidal, progressive wave is

$$E = \frac{1}{2} \rho_w g a^2$$

If the energy corresponding to a_0 is E_0 , Eq. (8) may be rewritten as

$$E = E_0 \exp \left[\frac{2}{g} \frac{\rho_a}{\rho_w} k^2 U_1^2 \beta x \right] \quad (9)$$

The out-of-phase pressure component β is responsible for the energy transfer from the air stream to the wave. Experimental results are presented in the non-dimensional form

$$\log_{10} \frac{E(F)}{E(0)} = AF \quad (10)$$

where F is a non-dimensional fetch

$$F = \frac{k^2}{g} U_1 \beta x$$

and

$$A = \left(2 \frac{\rho_a}{\rho_w} \right) \log_{10} e = 1.03 \times 10^{-3}$$

for $\rho_w = 1 \text{ gm/cm}^3$ and $\rho_a = 0.00118 \text{ gm/cm}^3$.

III. LABORATORY INVESTIGATIONS

3.1. Techniques of Simulation

3.1.1. Moving wavy-boundary (steady-state)

In attempts to verify Jeffreys' sheltering hypothesis, Stanton, et al. [1932], Motzfeld [1937], Thijssen [1951], and Larras and Claris [1960] measured pressure distributions over stationary, solid, and two-dimensional sinusoidal boundaries in either a wind tunnel or a water channel. In the light of the critical-layer mechanism proposed by Miles, these stationary wavy-boundary experiments

cannot be regarded as an adequate, steady-state simulation of the wind-generated wave problem, because the critical layer in the experiments is of zero thickness and, hence, the critical level lies on the stationary boundary. All of the above experiments, with the exception of Thijsse's indicated a smaller sheltering coefficient than that anticipated by Jeffreys, who expected the pressure distribution to be out-of-phase with the wave (in accordance with Miles' inviscid theory). The resulting small sheltering coefficient may be attributed to either viscous or finite wave-amplitude effects.

For a more realistic steady-state simulation of wind-generated waves and demonstration of the importance of the critical-layer mechanism of energy transfer, the wavy boundary must be moving with a speed equal to the wave celerity and opposite to the direction of mean free-stream. An important advantage in this simulation is that the flow field is steady. Consequently, measuring techniques are greatly simplified.

The first successful moving, wavy boundary experiment and its resultant presentation of the normal pressure distribution on the boundary were reported by Zagustin, et al. [1966, 1968]. Subsequently, Ott, et al. [1968] extended the Zagustin investigation and used refined experimental procedures to achieve better experimental accuracy. Small amplitude waves with a length of 3 ft and amplitude of 0.65 in. were used. Because of the limited capability of the experimental facility, C/U_{∞} was limited to approximately 0.75 (U_{∞} is the air velocity at the edge of the boundary layer).

3.1.2. Flexible wall with progressive waves (unsteady-state)

Kendall [1970] described a series of experiments on wind-wave simulation in a low turbulence wind tunnel. The wavy wall was the floor of the constant pressure test section of the tunnel. The surface of the wavy wall was composed of neoprene rubber sheet which was constrained to form a series of sinusoidal waves (length = 4 in. and height = 0.25 in.). The rubber sheet was supported from beneath by a series of ribs which were connected to individual circular eccentric cams. Each cam was positioned with proper phase difference on a common cam shaft expending the length of test section. Rotation of the cam shaft caused each rib to execute a reciprocating vertical motion and thus a progressive wave form was produced. Reversing the direction of rotation of the cam shaft produced waves traveling in the opposite direction, giving $-0.5 < C/U_{\infty} < 0.5$.

The boundary conditions for the two methods of wind-generated wave simulation described above deviate slightly from those of a true air-water interface. If the fluid particle velocity in a wave motion is small compared to the wave celerity (true for small amplitude waves), the moving wavy boundary simulation approximately satisfied the boundary conditions. In the flexible wall experiment the surface

particle motion resulting from the flexure of the rubber sheet was a backward-rotating 3:1 ellipse as compared with the forward-rotating circle of deep water waves. Again, the boundary condition was approximately satisfied for small amplitude waves.

3.1.3. Wind-wave research channel (unsteady-state, true air-water interface)

The physical features of the Stanford facility were reported by Hsu [1965]. The channel is approximately 6 ft high and 3 ft wide and has a usable test section length of 75 ft. At the downwind end, there are a beach to absorb wave energy and a centrifugal fan to produce the wind in the channel. At the other end, the air is drawn vertically through a system of filters and then carried horizontally on to the water surface at the beginning of the test section by a converging elbow. A hydraulically-driven, horizontal-displacement, wave-generating plate is located 17 ft upstream of the test section. This distance is sufficient to allow generated waves to become fully established prior to being subjected to wind action. Sinusoidal waves, ranging in frequency from 0.2 to 4 cps, can be generated. The maximum wind speed is approximately 70 fps with a nominal water depth of 3 ft in the channel. A limitation of the present facility is that the wind and the propagating waves move in the same direction.

3.2. Measurements of Wave-Induced Perturbation Pressures

Because the flow field was steady in the moving wavy-boundary experiment (Sec. 3.1.1), two conventional, but small (1/32 in. O.D.), pitot-static probes were used for all the velocity and pressure measurements. The reference probe was located in the free-stream while the other probe could be moved to any distance from the moving boundary by a traversing mechanism. Realizing that the traversing probe must be aligned with the local flow direction, we mounted this probe in a special rotating device. These probes were connected to a Pace P-90 differential pressure transducer through a manifold system which provided selective readings of dynamic pressure or pressure differential between the two probes.

The pressure measurements in the flexible wall experiments (Sec. 3.1.2) were made through static holes in the flexible surface. Essentially, a length of metal tubing in the form of a loop was used to connect the static hole and the pressure transducer. The loop served to cancel the unwanted pressure gradient generated by the motion of the tubing.

Because the thickness of critical layer was small in the wind-wave channel experiment (Sec. 3.1.3), the measurements of perturbation pressure were obtained by use of a specially-designed wave following system. Again, the perturbation pressure is the difference between the pressure at the air-water interface and that in the free

stream and was monitored by two identical pressure sensors, one at the interface and the other in the free stream, through a Pace P-90 differential pressure transducer. The whole system was allowed to follow the wave motion so that the lower pressure sensor was kept a fixed distance from the instantaneous air-water interface and inside the critical layer. The unwanted pressure signal caused by the motion of the system was determined by calibration tests and removed in the final data reduction.

3.3. Measurement of Wave Growth

A series of experiments was run to measure wave growth rate in the Stanford wind-wave channel. Small-amplitude, deep-water waves with frequencies varying from 0.9 to 1.4 cps were used with the maximum wind speed ranging from 12 to 44 fps (fan speed of 100-300 rpm). Time records of wave profiles were obtained with capacitance-wire sensors at seven locations spaced at 10 ft intervals along the centerline of the test section. Air velocity distributions were taken at six intermediate locations with a conventional pitot-static probe.

Although the mechanically-generated waves were initially of small amplitude and closely sinusoidal, they become steep and somewhat non-sinusoidal with increasing fetch in response to the wind action. The true wave profile could be viewed as a superposition of a mean wave and a spectrum of ripples. Therefore, a phase averaging procedure was adopted to determine the mean wave profile at each fetch and fan speed. The mean wave profile at each phase angle was the result of averaging 35 waves in the time series. The stream function fitting technique introduced by Dean [1965] and outlined for this application by Bole and Hsu [1967] was used for evaluating the kinetic and potential energy of each mean wave profile. Finally, the total wave energy at each location of the test section was adjusted for wave energy dissipation due to viscous action. The dissipation was determined experimentally for conditions without wind.

Along with the mean wave profile, the ripple variance of the water surface about the mean wave profile at each phase angle of the wave and the mean ripple variance and standard deviation for all the phase angles were calculated. The ripple variance is, of course, proportional to the potential energy contained in the ripple.

IV. RESULTS AND DISCUSSION

4.1. Water Surface Roughness (Unsteady-State, True Air-Water Interface)

When mechanically generated waves were subjected to wind action, ripples were always present and were superposed on the waves. Thus, the water surface can no longer be regarded as smooth

and its roughness can be described by the ripple standard deviation σ of the water surface elevation about the mean-wave profile. It was observed that σ increased with wind speed at the same fetch. In general, σ increased as $y_0 u^* / \nu$ increased. The values of σ are listed in Table 1 and vary from about 0.001 to 0.039 ft.

From a least-square fit of the velocity profile Eq. (5) to the measured data, values of U_1 and y_0 can be obtained and hence the values of y_c , ky_c , and β (see Sec. 2). The values of y_c are compiled in Table 2 and vary from 0.004 to 0.011 ft. The values in Table 1 and Table 2 show that the ripple standard deviation is larger than the critical layer thickness in all cases. It seems that the surface roughness or ripples should destroy the organized actions of vorticity which Lighthill [1962] presented as the physical explanation of Miles' instability mechanism. Thus, Miles' interpretation of the energy transfer mechanism (adopted from Lin [1955]) as the perturbation Reynolds stress working against the mean velocity profile at the critical layer is severely strained by the existence of a ripple layer large enough to obliterate the critical layer.

The potential energies of wind-generated ripples with and without mechanically generated waves are presented in Table 3. The presence of the generated waves decreases ripple energy significantly. Although there are many irregularities, ripple energy generally decreases as wave frequency increases. Exceptions occur at 300 rpm and 60 ft fetch where the 1.2 and 1.4 cps waves are breaking and ripple energy is sharply decreased. Sample power spectra of the ripples superposed on a 1.1 cps wave were obtained by subtracting the mean 1.1 cps wave profile from the original water surface elevation time series. The remaining time series, which contains only ripple variation, was then spectral analyzed. The resulting power spectra of wind-generated ripple with and without mechanically generated waves is exhibited in Fig. 1. Spectral peaks for the two cases appear at about the same frequency, but spectral density is drastically reduced when waves are present.

The two possible reasons for ripple attenuation in the presence of waves are

- a. sheltering effects retard ripple generation by the wind,
- b. non-linear wave-wave interactions cause ripple energy to be dissipated and to be transferred to the waves as suggested by Longuet-Higgins [1969] (see later discussion on wave energy).

4.2. Mean Wave Profiles

Mean wave profiles were determined by phase-averaging over records of 35 waves. A sample of corresponding pairs of mean wave profiles and their corresponding original recordings for

TABLE 1. RIPPLE SPECTRUM STANDARD DEVIATION

$$\sigma \times 10^3 \text{ (ft)}$$

RPM	Fetch (ft)	0 (no wave)	Mechanical Wave Frequency (cps)					
			0.9	1.0	1.1	1.2	1.3	1.4
100	10	1			1	1	1	1
	20	3			2	2	1	2
	30	5			3	3	4	4
	40	6			5	5	5	5
	50	8			6	7	6	6
	60	9			7	7	7	7
150	10	4	2	2	3	2	3	3
	20	9	5	5	6	5	5	5
	30	13	7	8	6	8	8	7
	40	17	7	9	8	9	9	9
	50	18	10	11	8	8	10	8
	60	19	9	12	8	9	12	11
200	10	9	4	5	6	6	6	6
	20	15	9	9	8	9	11	9
	30	21	10	12	8	11	10	10
	40	22	10	14	9	13	14	12
	50	32	10	12	13	16	15	12
	60	34	12	14	12	16	16	14
250	10	14	8	8	8	8	9	8
	20	19	12	12	13	12	14	15
	30	28	12	18	13	13	17	15
	40	35	10	23	20	17	16	15
	50	41	16	27	25	18	17	19
	60	43	27	27	27	20	18	18
300	10	18	10	13	11	14	13	12
	20	26	17	17	15	19	20	17
	30	38	19	25	20	19	22	17
	40	44	22	21	19	19	17	20
	50	53	32	24	21	20	16	26*
	60	57	30	23	23	21	20*	39*

* Waves breaking.

TABLE 2. CRITICAL LAYER THICKNESS

$$y_c \times 10^3 \text{ (ft)}$$

RPM	Fetch (ft)	Mechanical Wave Frequency (cps)					
		0.9	1.0	1.1	1.2	1.3	1.4
100	10			1.0	0.6	0.5	0.4
	20			2.9	2.2	1.8	1.5
	30			2.9	2.1	1.7	1.4
	40			4.8	3.4	2.7	2.2
	50			5.1	3.7	3.0	2.5
	60			8.5	6.4	5.2	4.4
150	10	1.0	0.8	0.6	0.5	0.4	0.4
	20	1.3	1.0	0.8	0.6	0.5	0.5
	30	2.5	2.0	1.6	1.3	1.1	1.0
	40	2.4	1.9	1.5	1.3	1.1	1.0
	50	2.7	2.2	1.7	1.4	1.2	1.1
	60	2.8	2.2	1.8	1.5	1.3	1.2
200	10	0.8	0.7	0.6	0.5	0.5	0.4
	20	0.7	0.6	0.5	0.4	0.4	0.3
	30	0.7	0.6	0.5	0.4	0.4	0.3
	40	0.4	0.3	0.3	0.2	0.2	0.2
	50	0.6	0.5	0.4	0.4	0.3	0.3
	60	0.5	0.4	0.3	0.3	0.2	0.2
250	10	1.2	1.0	0.9	0.8	0.8	0.7
	20	1.6	1.4	1.2	1.1	1.1	1.0
	30	2.5	2.3	2.1	1.9	1.8	1.7
	40	2.6	2.4	2.1	1.9	1.8	1.7
	50	2.3	2.1	1.9	1.7	1.6	1.5
	60	1.7	1.5	1.4	1.2	1.2	1.1
300	10	0.4	0.4	0.3	0.3	0.3	0.3
	20	1.4	1.3	1.2	1.1	1.0	1.0
	30	2.8	2.6	2.4	2.2	2.1	2.0
	40	4.9	4.5	4.2	3.9	3.7	3.6
	50	6.7	6.2	5.8	5.5	5.3	5.1
	60	11.4	10.7	10.1	9.6	9.3	9.0

TABLE 3. RIPPLE SPECTRUM POTENTIAL ENERGY

Values $\times 10^3$ (ft-lb/ft²)

RPM	Fetch (ft)	0 (no wave)	Mechanical Wave Frequency (cps)					
			0.9	1.0	1.1	1.2	1.3	1.4
100	10	0.04			0.04	0.07	0.05	0.08
	20	0.25			0.22	0.28	0.30	0.30
	30	0.83			0.53	0.49	0.65	0.61
	40	1.30			1.10	1.12	0.92	1.19
	50	2.10			1.64	1.76	1.70	1.45
	60	2.80			2.10	2.00	2.06	1.96
150	10	0.57	0.37	0.28	0.33	0.35	0.40	0.51
	20	2.56	1.32	1.57	1.33	1.12	1.27	1.22
	30	5.31	2.67	2.80	1.44	2.45	2.46	1.99
	40	9.06	2.70	3.38	2.37	2.87	2.87	2.98
	50	10.30	4.26	4.94	2.45	2.34	3.66	2.45
	60	11.77	3.86	5.89	2.49	3.20	5.32	4.67
200	10	2.58	1.18	1.17	1.57	1.48	1.57	1.33
	20	7.29	3.59	3.67	2.63	2.98	4.13	3.09
	30	13.28	4.41	6.33	2.60	4.48	3.88	3.78
	40	14.82	4.56	7.63	3.11	6.17	6.79	5.63
	50	31.17	4.22	6.24	5.64	8.51	7.60	5.58
	60	36.92	5.68	7.74	5.35	8.97	9.08	7.01
250	10	5.99	2.92	2.94	2.58	2.70	3.23	2.37
	20	11.74	5.82	5.90	6.21	5.43	7.42	7.56
	30	24.73	6.22	12.90	5.92	6.18	9.88	7.94
	40	37.71	4.56	20.11	14.03	9.55	9.40	7.82
	50	53.44	10.25	26.18	20.85	10.83	10.17	11.82
	60	58.84	25.46	26.92	24.28	13.38	11.34	11.32
300	10	9.59	4.65	7.17	4.68	6.57	6.34	5.37
	20	21.75	11.17	10.67	8.06	13.03	14.35	10.19
	30	44.11	13.51	22.97	13.69	12.22	16.94	10.32
	40	60.64	17.49	16.18	12.33	12.58	10.59	13.27
	50	86.66	36.87	21.55	15.11	14.21	9.24	22.43*
	60	102.62	32.63	19.20	17.89	14.48	14.18*	50.10*

* Waves breaking.

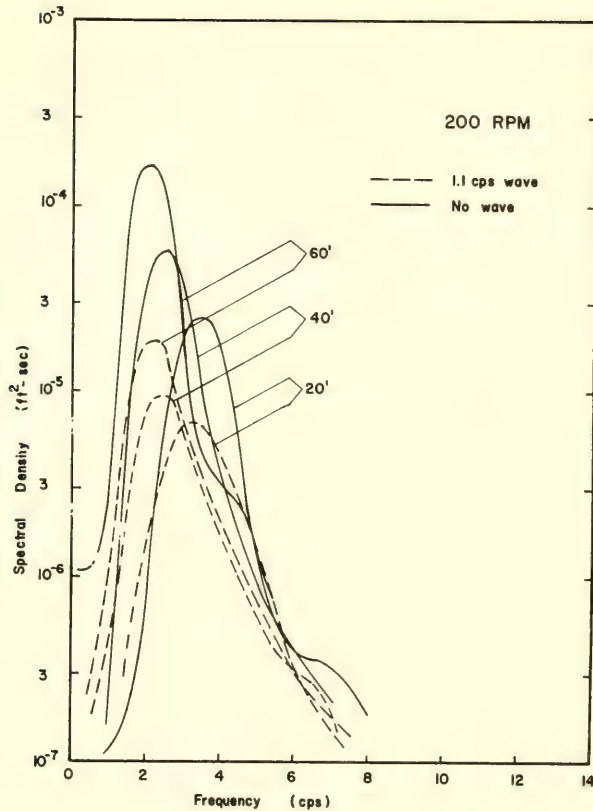


Fig. 1. Influence of 1.1-cps wave on 200-rpm ripple spectra

1 cps and 1.3 cps waves at 300 rpm is given in Figs. 2 to 5. A close examination of these figures (wave motion is toward the left and the usual Sanborn attenuation scales are marked) reveals that the positions assumed by the ripples influence the mean wave profile. For example, ripple superposition in the 1.0 cps wave caused the mean wave crest to become flattened. However, ripple superposition on the 1.3 cps wave did not cause mean wave profile distortion. Many of the records show ripples superposed in such a way that the crest was sharply peaked. The existence of such conditions may enhance separation of the air flow over the wave surface.

A source of error arises from the fact that mean wave profiles were distorted, and yet their energy was compared with that of Miles' pure sinusoids. An expression consisting of a cosine and sine plus their two higher harmonics was least-square fitted to each of the mean wave profiles (see below). Results indicated that the total

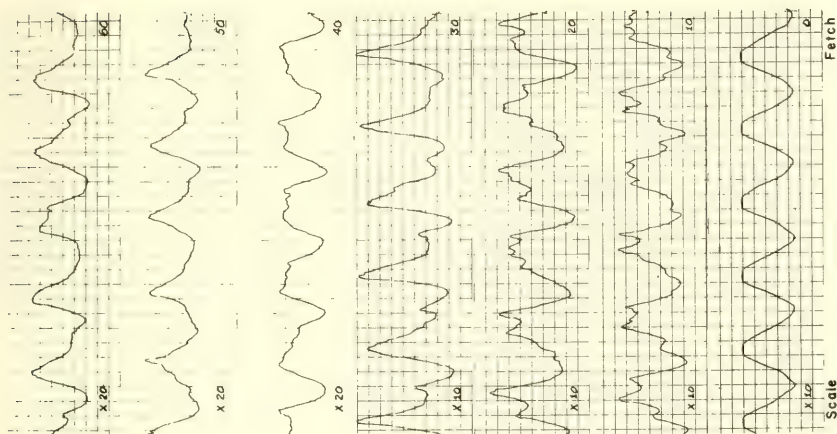


Fig. 3. 1.0-cps Sanborn recordings at 300 rpm (1 horizontal division = 0.2 sec)

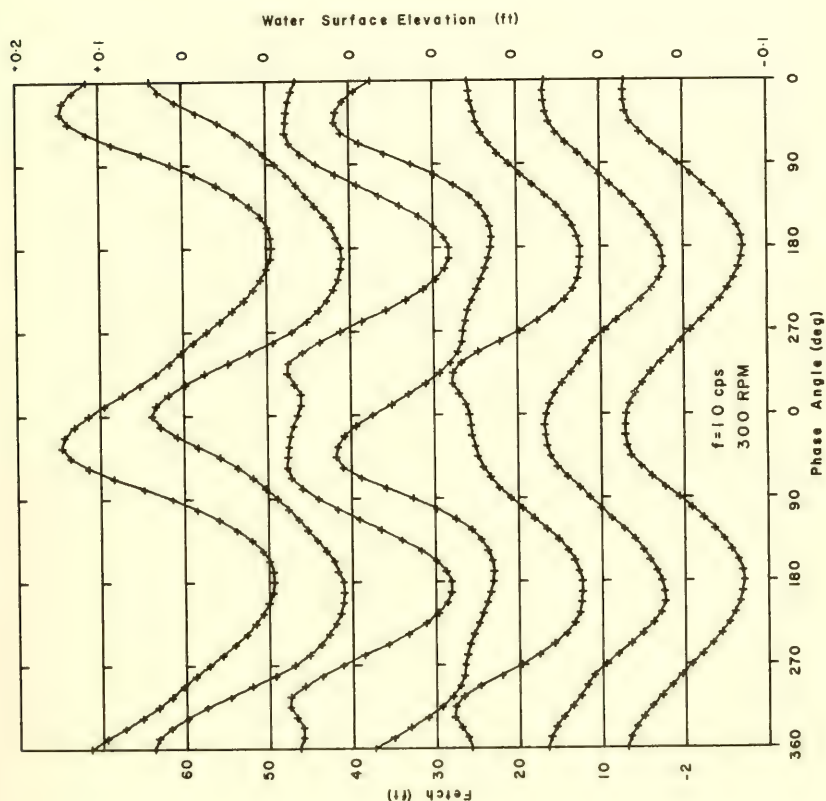
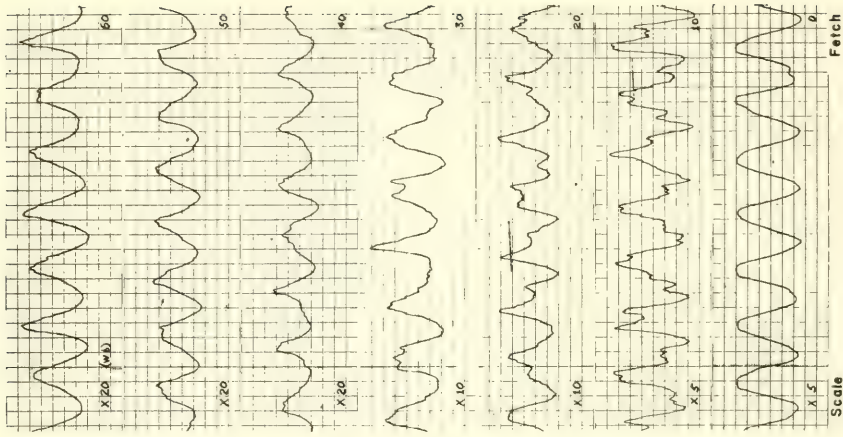
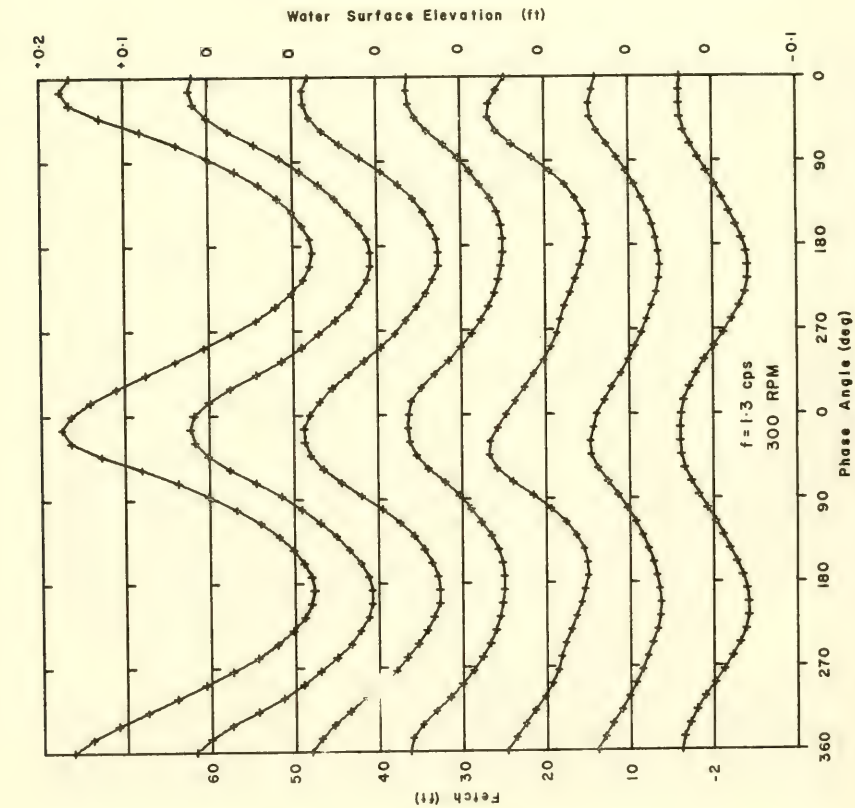


Fig. 2. 1.0-cps mean wave profiles at 300 rpm



error introduced by representing the mean wave by these five terms was not greater than 5 per cent in any case.

4.3. Wave Energy

The total wave energy (potential plus kinetic) was calculated by the method developed by Dean [1965] through least-square-fitting an analytic stream function to the mean measured wave profiles. Details of the procedure were presented by Bole and Hsu [1967]. In order to compare the measured wave energy with Miles' prediction, wave dissipation in the channel, determined experimentally under the condition of no wind, as a function of fetch was added to the measured wave energy. Figure 6 shows the energy ratio $E(x)/E(0)$, as a function of downstream distance for a 1.4 cps wave subjected to various wind speeds, while the results in Fig. 7 are for a constant wind speed (300 rpm) acting on waves of various frequencies. The data was then reduced to the non-dimensional fetch F defined in Eq. (10). The final results, compared with Miles' inviscid theory,

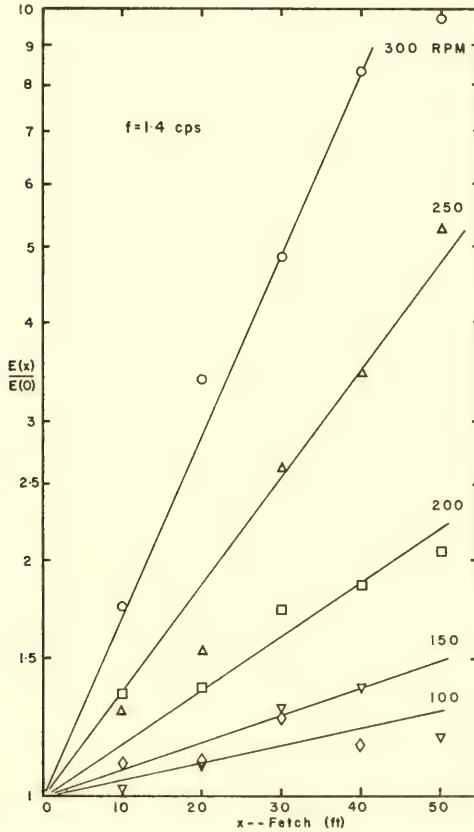


Fig. 6. 1.4-cps wave growth vs. x

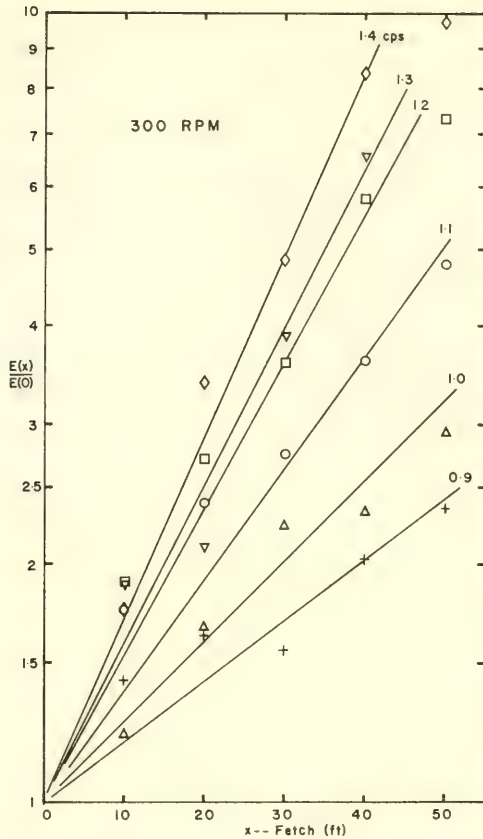


Fig. 7. 300-rpm_wave growth vs. x

are exhibited in Figs. 8 and 9. In nearly every case, experimental values fall well above the theoretical line. By assuming the growth to be totally dependent on F in the form of Eq. (9), we calculated a ratio of the experimental and theoretical β values and present the results in Table 4. The β -ratios vary from about 1 to 10. The mean ratio for all frequencies and rpm's is about 3.

The total spectral energy of the ripples in most of the experimental cases was no more than about 20 per cent of the mechanically-generated wave energy. Phillips [1966] argued that non-linear interactions between waves should be weak. Hence, our procedure of measuring the growth of a single wave within a spectrum should be a valid means of evaluating the parameters necessary for comparisons with Miles' theory.

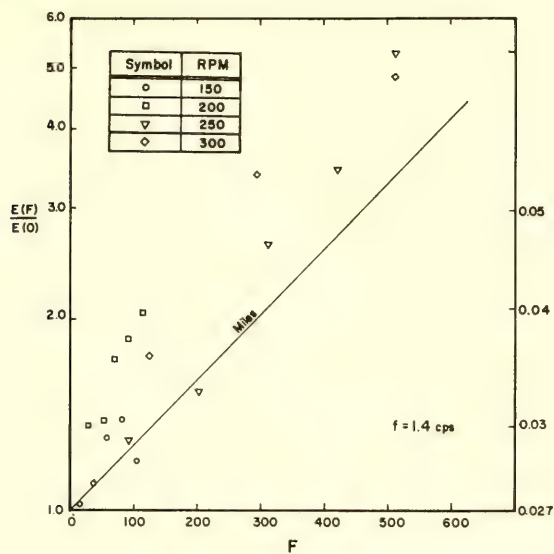


Fig. 8. 1.4-cps wave growth vs. F

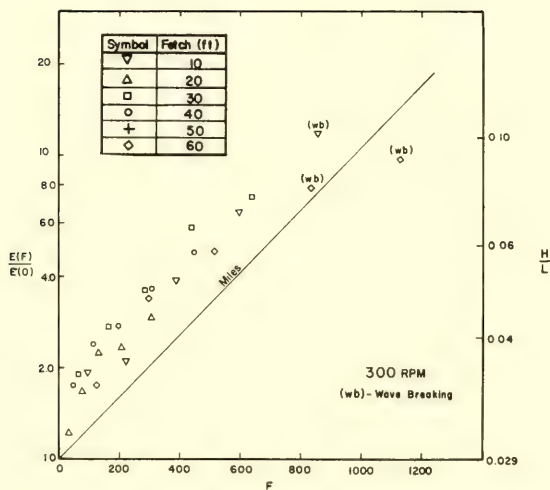


Fig. 9. 300-rpm wave growth vs. F

TABLE 4. RATIO OF EXPERIMENTAL TO THEORETICAL β

RPM	Fetch (ft)	Mechanical Wave Frequency (cps)					
		0.9	1.0	1.1	1.2	1.3	1.4
100	10			4.8	4.7	5.4	4.2
	20			2.2	(-0.4)	11.0	2.4
	30			1.1	3.1	7.4	3.7
	40			2.1	2.4	4.4	1.8
	50			1.8	1.4	6.1	(-0.6)
150	10	7.2	3.1	2.8	1.5	1.5	0.6
	20	2.9	3.2	3.5	1.9	3.8	1.1
	30	1.9	1.3	2.2	3.3	3.7	1.9
	40	3.8	1.3	2.9	2.3	3.9	1.7
	50	3.3	1.3	3.2	2.7	3.5	0.7
200	10	7.2	7.4	9.2	4.0	0.4	4.5
	20	7.3	4.7	7.2	2.2	4.7	2.5
	30	7.7	3.8	7.3	3.6	2.6	3.3
	40	4.8	3.8	5.9	3.5	3.2	2.8
	50	6.1	5.9	5.2	3.6	4.6	2.6
250	10	3.8	2.2	2.9	2.5	1.5	1.1
	20	3.4	2.3	2.4	2.1	1.0	0.9
	30	2.5	2.0	1.9	1.6	0.6	1.3
	40	3.5	1.6	1.9	1.5	1.3	1.2
	50	2.6	1.9	2.0	1.5	1.3	1.4
300	10	7.2	2.7	5.0	4.0	2.8	1.9
	20	4.1	2.9	3.3	2.6	1.4	1.7
	30	2.1	2.6	2.2	1.9	1.5	1.3
	40	2.1	1.7	1.8	1.7	1.3	1.1*
	50	1.8	1.5	1.5	1.3	1.2*	0.9*

* Waves breaking.

On the other hand, our experimental evidence indicated that the wind-generated ripples riding on the mechanically-generated waves had a tendency to break on the crests rather than in the troughs. Longuet-Higgins [1969] showed that, in breaking, the ripples may impart a significant portion of their momentum to the longer waves in a strong non-linear interaction. Mollo-Christensen's [1970] field observations showed that there were relatively high peaks of energy in a high frequency band located near the crest of the main wave. It is difficult to conclude that Mollo-Christensen's data, taken in a confused sea, whether these high frequency peaks are produced as a result of the breaking waves, caused by wave

groups of different frequency overtaking one another, or partly by the generation of high frequency waves on the wave crest. To fully investigate the non-linear, wave-wave interactions and to establish the role of ripples in the transfer process, measurements similar to those of Mollo-Christensen and additional detail measurements of the velocity field below the air-water interface should be carried out under the controlled conditions of a laboratory simulation.

The incompatibilities of the Miles' mathematical model with the natural wave-growth environment, as discussed in the previous section, were anticipated by Miles. He stated in this 1957 paper that "our model cannot be expected to have more than qualitative significance for rough flow." It would appear that a more realistic model and an improved theory of energy transfer cannot be formulated until detailed studies of the structure of air flow near the air-water interface are carried out.

4.4. Non-dimensional Pressure Coefficients

The non-dimensional pressure coefficients α and β obtained from the various techniques of laboratory simulation are exhibited in Figs. 10 and 11 as functions of ky_c . Comparison between the measured values of the in-phase pressure coefficient α (steady-state, moving-wavy-boundary; unsteady-state, wind-wave channel) and the Miles' theory is shown in Fig. 10. The experimental values of the out-of-phase pressure coefficient β , evaluated from wave growth measurements, are shown in Fig. 11. Although there is considerable scatter in the experimental data, the deviation from the inviscid theory is clearly evident and is consistent with the results of the wave growth measurements. Because of the limited capability of the experimental facility in the steady-state, moving-wavy-boundary experiment, experimental values were limited to $ky_c = 0.1$.

The experimentally determined phase angle ϕ obtained from the three different methods of laboratory simulation -- moving-wavy-boundary, flexible boundary with progressive waves, and wind-wave channel -- is shown in Fig. 12 as a function of C/u^* . In view of the uncertainties among investigators in determining u^* values, the experimental phase angle as a function of C/U_∞ and their corresponding theoretical values are shown in Fig. 13. The JPL-data includes negative values of C . Because the measured velocity profiles varied to some extent with U_∞ and C as discussed by Kendall [1970], theoretical values of ϕ for the case in which $U_\infty = 5.5$ in./sec and $C = 0$ were calculated.

In an attempt to detect flow separation in the region near the air-water interface in the wind-wave channel experiments, pressure measurements over waves of various amplitudes with constant frequency were made. The measured phase angles for two wave frequencies, 0.6 and 0.78 cps, are shown in Fig. 13. The scatter

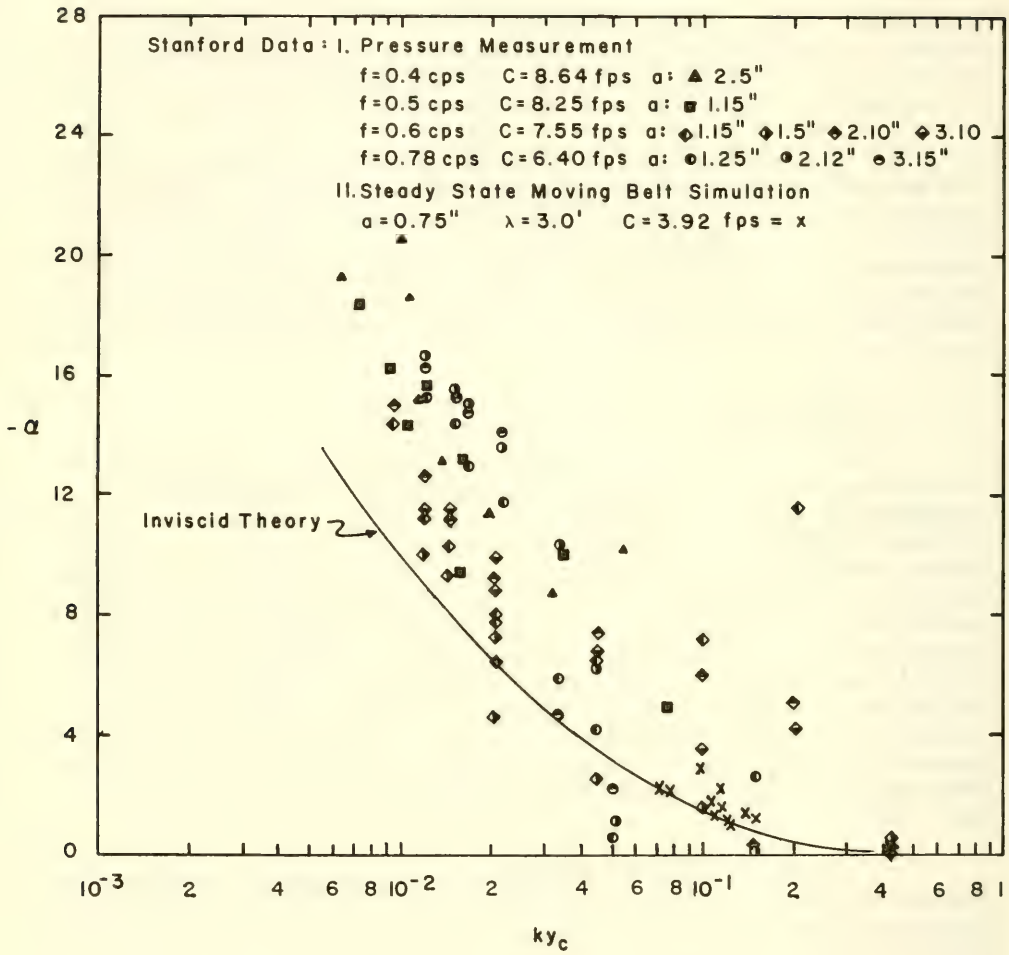


Fig. 10. Comparison between measured and theoretical values of α vs. ky_c

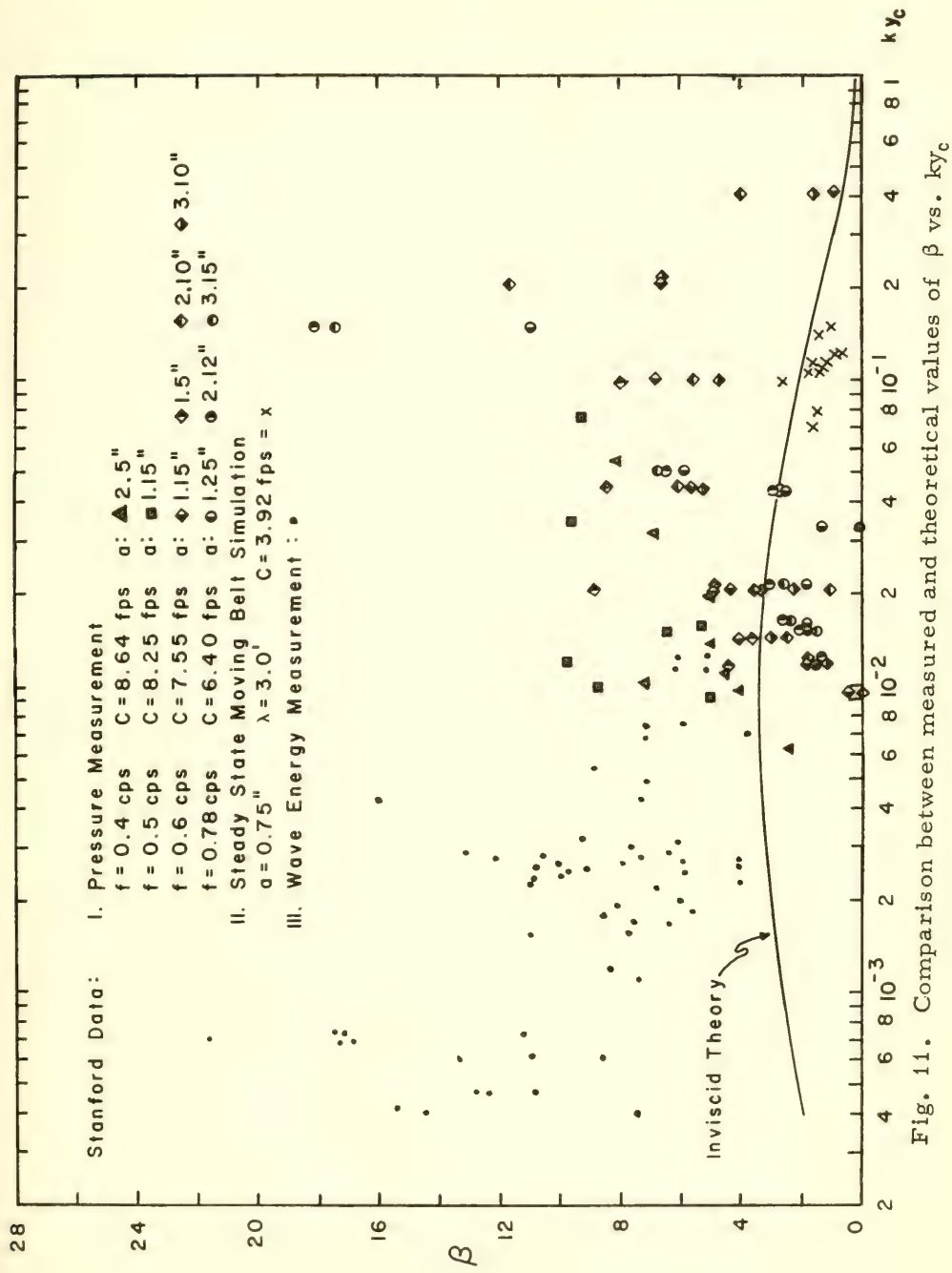


Fig. 11. Comparison between measured and theoretical values of β vs. $k y_c$

JPL Data: \circ 5.5 m/sec Δ 10.6 m/sec

Stanford Data: I. Pressure Measurement

$f = 0.4$ cps $C = 8.64$ fps $a : \Delta$ 2.5"
 $f = 0.5$ cps $C = 8.25$ fps $a : \square$ 1.15"
 $f = 0.6$ cps $C = 7.55$ fps $a : \diamond$ 1.15" \diamond 1.5" \diamond 2.10" \diamond 3.10"
 $f = 0.78$ cps $C = 6.40$ fps $a : \circ$ 1.25" \circ 2.12" \circ 3.15"

II. Steady State Moving Belt Simulation

$a = 0.75"$ $\lambda = 3.0'$ $C = 3.92$ fps = x

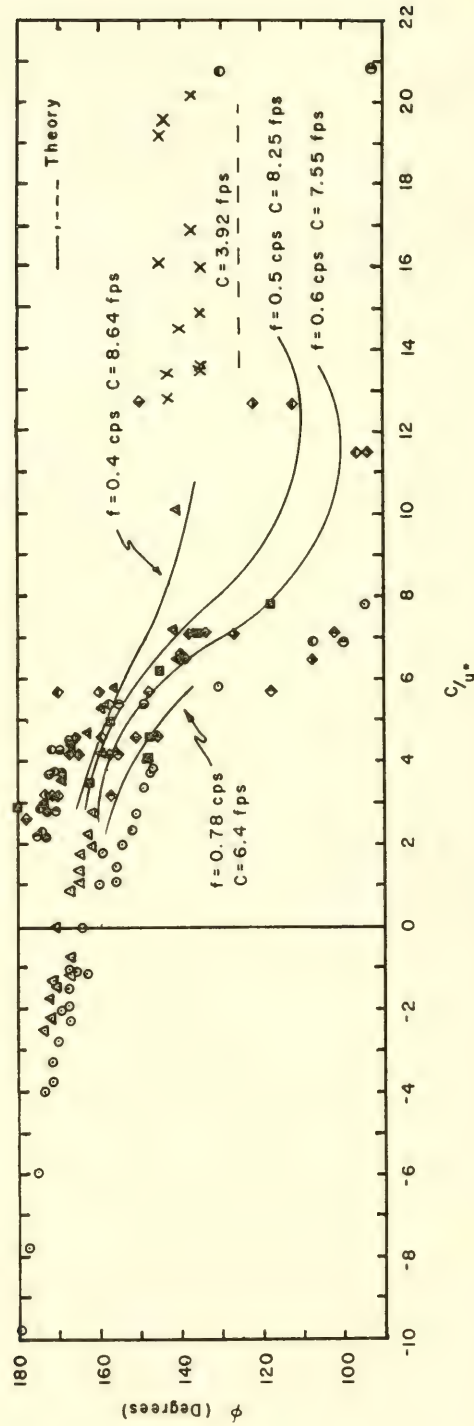


Fig. 12. Comparison between measured and theoretical values of ϕ vs. C/u_o^*

JPL Data: $a=0.125''$ $\lambda=4.0''$ U_∞ : $\diamond 3.2$ m/sec. $\nabla 4.4$ m/sec. $\circ 5.5$ m/sec. $\triangle 10.6$ m/sec.
 $\square 13.2$ m/sec. $\Lambda 16.0$ m/sec.

Stanford Data:

I. Pressure Measurement

- $f = 0.4$ cps $C = 8.64$ fps a : $\blacktriangle 2.5''$
- $f = 0.5$ cps $C = 8.25$ fps a : $\blacksquare 1.15''$
- $f = 0.6$ cps $C = 7.55$ fps a : $\blacklozenge 1.15''$ $\blacklozenge 1.5''$ $\blacklozenge 2.10''$ $\blacklozenge 3.10''$
- $f = 0.78$ cps $C = 6.40$ fps a : $\circ 1.25''$ $\circ 2.12''$ $\circ 3.15''$

II. Steady State Moving Belt Simulation
 $a = 0.75''$ $\lambda = 3.0'$ $C = 3.92$ fps $\alpha = x$

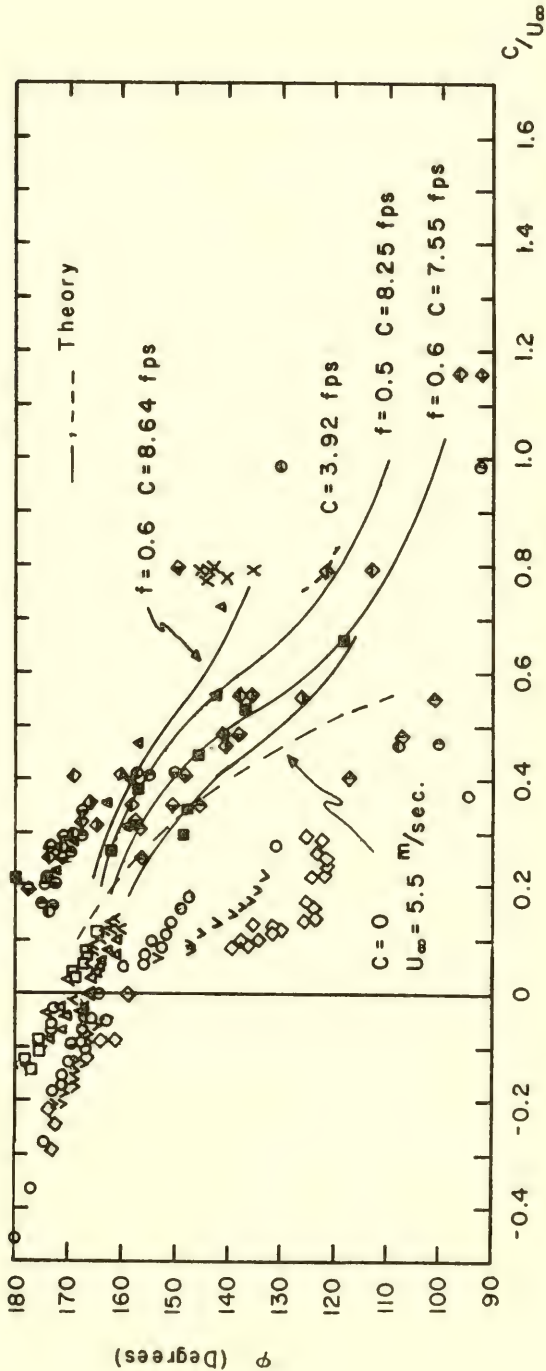


Fig. 13. Comparison between measured and theoretical values of ϕ vs. C/U_∞

of the experimental data precludes any definite conclusion about possible flow separation. Although a unified theory is needed to describe the relationship between the phase angle ϕ and $\pm C/U_\infty$, the experimentally determined phase angles in the inviscid range do indicate a correct trend compared with Miles' theory.

V. CONCLUSIONS

The accumulated laboratory experimental evidence obtained at Stanford and elsewhere indicates general support for Miles' inviscid theory of energy transfer between air stream and progressive waves through the phase shift of the aerodynamic pressure at the interface. However, the experimental growth rate is considerably in excess of Miles' prediction, being approximately three times larger. The most fruitful avenue for further study would appear to be to reexamine the necessary simplifying assumptions in the Miles' inviscid model. The incompatibilities near the air-water interface suggest that detailed experimental investigations of this region are essential before an understanding of the energy transfer mechanisms and the conditions under which they occur can be fully established. The effects of turbulence, possible flow separation, ripple superposition and boundary layer development are complex, but could be modelled and fruitfully studied in laboratory simulations.

REFERENCES

- Benjamin, T. B., "Shearing Flow over a Wavy Boundary," *J. Fluid Mech.*, 6, 161-205, 1959.
- Bole, J. B. and Hsu, E. Y., "Response of Gravity Water Waves to Wind Excitation," Stanford Univ. Dept. of Civil Engineering Tech. Rep. No. 79, 1967.
- Chang, P. C., "Laboratory Measurements of Air Flow over Wind Waves Following the Moving Water Surface," CER-8-69PcC18, Colorado State Univ., 1968.
- Dean, R. G., "Stream Function Representation of Non-Linear Ocean Waves," *J. Geophys. Res.*, 70, (18), 4651-72, 1965.
- Hires, R. I., "An Experimental Study of Wind Wave Interactions," Tech. Rep. No. 37, Chesapeake Bay Inst., Johns Hopkins Univ., 1968.
- Hsu, E. Y., "A Wind, Water-Wave Research Facility," Stanford Univ., Dept. of Civil Engineering Tech. Rep. No. 57, 1965.
- Kendall, J. M. Jr., "The Turbulent Boundary Layer Over a Wall With Progressing Surface Waves," *J. Fluid Mech.*, 41, Pt. 2, 13 April 1970, pp. 259-282.

- Larras, H. and Claria, W., "Recherches en Souffleries sur L'Action Relative de la Houle et du Vent," *La Houille Blanche*, 6, 647-677, 1960.
- Lighthill, M. J., "Physical Interpretation of the Mathematical Theory of Wave Generation by Wind," *J. Fluid Mech.*, 14, 385-398, 1962.
- Lin, C. C., *The Theory of Hydrodynamic Stability*, Cambridge Univ. Press, London, 1955.
- Longuet-Higgins, M. S., "A Non-Linear Mechanism for Generation of Sea Waves," *Proc. Roy. Soc. A*, 1969.
- Miles, J. W., "On the Generation of Surface Waves by Shear Flow," *J. Fluid Mech.*, 3, 185-204, 1957.
- Miles, J. W., "On the Generation of Surface Waves by Shear Flow, Part 4," *J. Fluid Mech.*, 13, 433-477, 1962.
- Miles, J. W., "On the Generation of Surface Waves by Shear Flow, Part 5," *J. Fluid Mech.*, 30, 163-175, 1967.
- Mollo-Christensen, E., "Observations and Speculations on Mechanisms of Wave Generation by Wind," Dept. of Meteorology, MIT, 1970.
- Motzfeld, H., "Die Turbulent Strömung an Welligen Wänden," *Z. Angew. Math. Mech.*, 17, 193-212, 1937.
- Ott, R., Hsu, E. Y. and Street, R. L., "A Steady-State Simulation of Small Amplitude Wind-Generated Waves," Stanford Univ. Dept. of Civil Engineering Tech. Rep. No. 94, 1968.
- Phillips, O. M., "Wave Generation by Turbulent Wind Over a Finite Fetch," *Proc. 3rd Natl. Congr. Appl. Mech.*, pp. 785-789, 1958.
- Phillips, O. M., *The Dynamics of the Upper Ocean*, Cambridge Univ. Press, New York, 1966.
- Stanton, T. E., Marshall, D., and Houghton, R., "The Growth of Waves on Water Due to the Action of Wind," *Proc. Roy. Soc., Ser. A*, 137, pp. 283-293, 1932.
- Sutherland, A. S., "Spectral Measurements and Growth Rates of Wind-Generated Water Waves," Stanford Univ. Dept. of Civil Engineering Tech. Rep. No. 84, 1967.

- Thijsse, J. T., "Growth of Wind-Generated Waves and Energy Transfer," National Bureau of Standards, Washington, D.C., Circular No. 512, 281-287, 1951.
- Ursell, F., "Wave Generation by Wind," Survey in Mechanics, Cambridge Univ. Press, 1956.
- Zagustin, K., Hsu, E. Y., Street, R. L., "Turbulent Flow Over Moving Boundary," J. of the Waterways and Harbor Div., Proc. ASCE, 397-414, 1968.
- Zagustin, K., Hsu, E. Y., Street, R. L., and Perry, B., "Flow over a Moving Boundary in Relation to Wind-Generated Waves," Stanford Univ. Dept. of Civil Engineering Tech. Rep. No. 60, 1966.

AIR-SEA INTERACTIONS: RESEARCH PROGRAM AND FACILITIES AT IMST

M. Coantic and A. Favre
IMST
Marseille, France

ABSTRACT

This research concerns the small-scale physical processes responsible for mass, momentum and energy exchanges between the atmospheric surface layer and the oceans.

Their theoretical study has been undertaken. It outlines the importance of turbulence and the influence of reciprocal interactions between the various transfer processes. It has led to the design of an experiment where the natural phenomena shall be partially simulated, in a large laboratory facility.

This one combines a micrometeorological wind tunnel with a 40 meters long wave tank, under controlled temperature and humidity conditions. It has been extensively tested with a one-fifth scale model. It is presently under construction, and will be operative by 1971.

Instrumental studies have also been undertaken, and results obtained in the measurement of turbulence in water flows.

I. INTRODUCTION

The knowledge of energy exchange processes between atmosphere and oceans appears of major interest for oceanography as well as for meteorology. These two media have indeed to be considered as elements of a single system, for the dynamical and thermodynamical evolution of each of them largely depends on interactions through their common boundary.

One of the essential steps in the solution of the air-sea interaction problem lies in the understanding of small-scale processes in the air and water layers adjacent to the interface, where the various forms of energy are either transferred or converted, while going from one medium to the other. The experimental study of these phenomena involves a detailed and delicate exploration of a region whose thickness is of the order of the wave height. Now, experiments performed at sea are subjected to such environmental constraints that the accuracy and repeatability of measurements seems necessarily limited. It has therefore appeared useful to complement field studies by laboratory experiments, where an extensive investigation is feasible under exactly repeatable conditions and with the possibility to control independently each of the governing parameters.

This is the program which has been undertaken at I. M. S. T. , and which is described in the present paper. The preliminary steps of this program have included: collection of information about current research; attempt of a critical survey of existing knowledge, in order to find out definite research objectives; and a first theoretical study of the physical mechanisms of air-sea interactions, and of their governing parameters. These studies have led to the conclusion that it would be feasible to obtain, in the laboratory, a partial simulation of the atmospheric-oceanic energy exchange processes, provided that a sufficiently large facility could be realized.

The following steps of the program have then comprised: the preliminary design of this facility, combining a micrometeorological wind tunnel with a 40 meters long wave tank; the realization of a one-fifth scale model, and its use for various preliminary tests and experiments; the detailed design and the building of the large wind-wave facility; and, last but not least, the development of various theoretical and instrumental researches.

The purpose of the present paper is to introduce the various objectives and results of our research program, and to describe the facilities which have been, or are being, realized. Due to space limitation, that presentation will be limited to a rather short account referring to previous publications for more details, when possible. The plan adopted is logical rather than chronological:

- Theoretical studies;
- Setting up the characteristics and design of the large air-sea facility;
- Model tests;
- Building of the air-sea facility;
- Studies of measuring instruments and methods.

At last, we shall try to draw some preliminary conclusions about this program, the prospects it opens, and its possible applications. We shall also have the pleasure to express our thanks to the many individuals and organizations who have contributed to its realization.

II. THEORETICAL STUDIES

1. The Physical Mechanisms of the Ocean-Atmosphere Interaction

As it is well known, the small-scale transfer of energy between atmosphere and oceans occurs following four various mechanisms, sketched by Fig. 1:

- a) Radiation, including: i) short-wave radiation from the sun on the sea surface, which is partially reflected and absorbed over a more or less large depth under the interface; ii) long-wave radiation coming from the atmosphere and from the sea, and involving a radiative transfer process between the interface itself and the atmospheric layers (see II.3).
- b) Evaporation (or condensation), and turbulent convection of water vapor, which, due to the very high latent heat of vaporization of water, leads to a turbulent latent enthalpy transfer from the sea surface to the atmosphere.
- c) Turbulent convection of sensible enthalpy, resulting from temperature differences between adjoining points of the system.

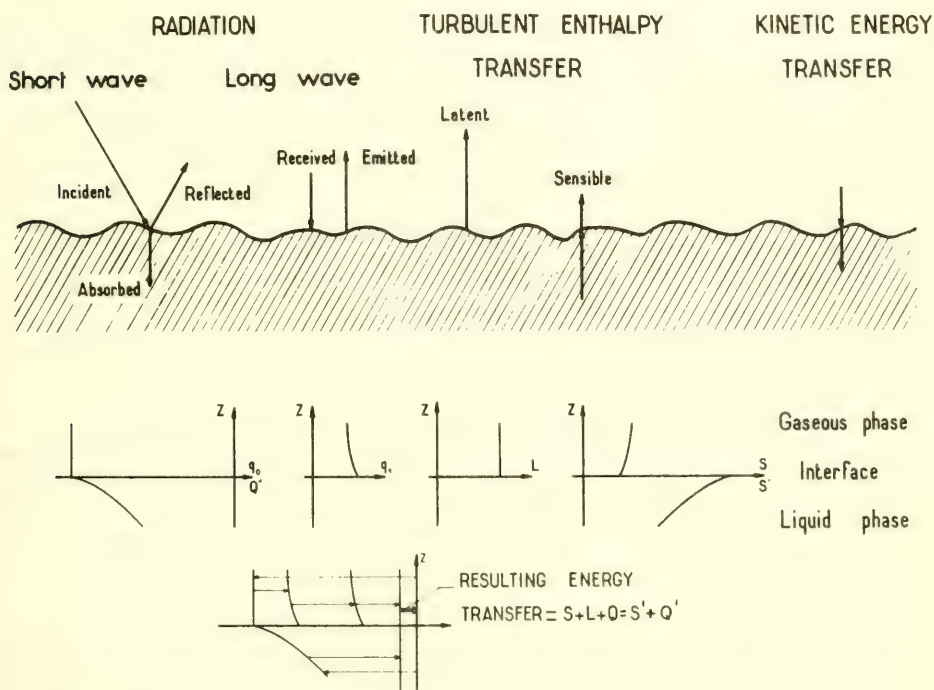


Fig. 1. Schematic display of energy transfers in the vicinity of the ocean-atmosphere interface.

- d) Transfer of kinetic energy across the turbulent boundary layers on both sides of the interface, of which the most obvious effect is the generation of waves.

Information on these mechanisms can be gathered in many books, ranging from meteorology (e.g. Brunt [1939], Haltiner and Martin [1967], Roll [1965]) to oceanography (e.g. Lacombe [1965], Phillips [1966], Sverdrup [1957]), or devoted to atmospheric turbulence (e.g. Lumley and Panofsky [1964], Monin and Yaglom [1966], Priestley [1959]). One of the first steps of our program has been to attempt to review the physical laws and equations governing the ensemble of these phenomena (see Coantic [1968]).

The main conclusion that can be reached is that, although the above types of transfer have been analyzed and listed separately, they are not independent, and the key of the problem lies in their reciprocal interactions. For instance, processes a) and b) set in action very large amounts of energy, whereas c) and chiefly d) are responsible for much smaller exchanges. However, the kinetic energy transfer, which enters as the smallest term in the energy balance, strongly influences the turbulent evaporation and convection processes. In fact, except for certain radiation effects, air-sea interactions are essentially governed by turbulence.

This is only one aspect of the aforementioned reciprocal interactions. Other ones will appear, for instance, when considering the boundary conditions for the various variables at the interface, or when expressing the conservation of the different energy fluxes, as schematized on the lower part of Fig. 1. Furthermore, two most important peculiarities are displayed when comparing the present case to the more classical problem of simultaneous heat, mass and momentum exchange between a fluid flow and a more or less rough surface. In the latter case, the turbulent convective processes, if not completely understood, are sufficiently well known to allow a good estimate of the various transfer rates. However, the methods of computation therein developed are not applicable here for two main reasons:

- On one hand, because the boundary is no longer static, and possesses "dynamic rugosities" capable of yielding and absorbing momentum with large variations of the ratio of the tangential shear stresses to the normal pressure forces. This fact will have consequences difficult to ascertain, not only upon the dynamical exchange mechanism but also upon the degree of "Reynolds analogy" between this process and those concerning exchange of scalar variables.
- On the other hand, because, due to the well known stratification effects in the atmosphere, heat and humidity can no longer be considered as "passive scalar containments." This means that the turbulent structure of the boundary layer, and the transfer rates themselves, are strongly modified by the direction and intensity of the vertical heat and humidity gradients.

As discussed in our previous publications (Coantic [1968], Coantic et al. [1969]), and in Part III of the present paper, the preceeding considerations have been the basis for the settling of our research program and the design of our simulation facility. Some aspects of the problem are already being the subject of theoretical investigations, which we shall now mention shortly.

2. Wave and Current Generation by Wind

The transfer of mechanical energy from air to sea has two main consequences: the development of currents and turbulence in the upper ocean, and the generation and amplification of waves. This latter process can be broadly described as follows: the turbulent atmospheric boundary layer exerts on the water surface normal and tangential stresses, with steady, periodic and random components. As a consequence of these stresses and of the gravity and capillarity restoring forces, motions of a wavy character are generated at the interface. As soon as their amplitude becomes appreciable, non-linear effects are developed, which result in a modification of the airflow structure and, hence, of the applied stresses, the existence of a continuous wave spectrum and the production of turbulent energy in the sea. The wave amplitude is then limited by the dissipative action of turbulence and viscosity.

As mentioned earlier, the understanding of this complex mechanism is essential to elucidate, not only the dynamical, but also the thermodynamical aspects of air-sea interactions. A careful study has, accordingly, been undertaken (Ramamonjiarisoa [1969, 1970]), first of existing theories (based on models proposed by Miles and Phillips) and later on of more recent developments in the researches of Stewart, Mollo-Christensen, Longuet-Higgins, Hasselmann and Reynolds, among others. This helped us in identifying some points that have to be subjected to experimental study, namely: the existence of separation after the wave crests, the phase shift between surface pressure and elevation, the spatial and temporal variations of Reynolds stresses, and of the turbulent structure of the flow in general. Our future measurement program has been established in consequence, taking advantage of the possible use of the space-time correlation technique, and of numerical data processing methods to separate the "mean," the "phase average" and the "turbulent" parts of each variable.

3. Interaction of Turbulent and Radiative Transfers

Another typical example of reciprocal interactions between the various modes of energy transfer near the air-sea interface is the simultaneous transport of sensible enthalpy by turbulent convection, and by infrared radiation. The turbulent heat flux is usually assumed constant with height in the atmospheric surface layer. However, the validity of this hypothesis is known to be questionable, due to a possible vertical variation of the infrared

radiative flux (see e.g. Munn [1967]).

This problem has been approached theoretically, using semi-empirical expressions fitted to the emissivity curves, and assuming logarithmic temperature and humidity profiles. A first approximation of the radiative heat flux divergence is thus obtained analytically, as a function of the surface layer parameters (Coantic and Seguin [1970]). Numerical values of the infrared flux gradient, dq_1/dz , in the first ten meters of the marine atmosphere are shown in Fig. 2, for two different wind velocities (A: $U_{10} = 3$ m/s; B: $U_{10} = 9$ m/s); two sea surface temperatures (cases 1,2: $\theta_0 = +5^\circ\text{C}$; cases 3,4: $\theta_0 = +20^\circ\text{C}$); and two temperature differences (cases 1,3: $\theta_{10} - \theta_0 = -5^\circ\text{C}$; cases 2,4: $\theta_{10} - \theta_0 = +1^\circ\text{C}$). The resulting vertical variations of the turbulent heat flux, shown by Fig. 3, are seen to attain unexpectedly large values, of the order of 30 to 40%, when wind velocity is low and humidity is high.

These results are considered as preliminary. If confirmed, they could lead to a reinterpretation of some experimental data, and should appeal to an extension of turbulent transfer theories to the case of a variable heat flux.

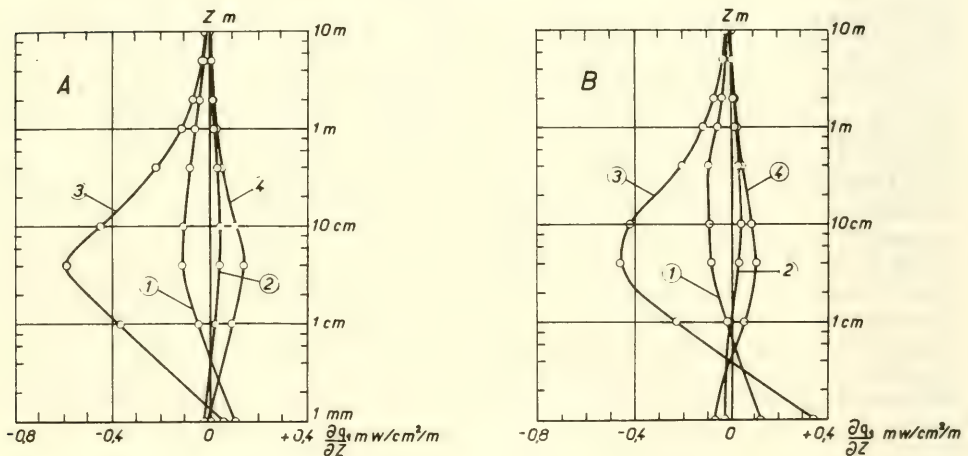


Fig. 2. Computed vertical variations of radiative flux divergence for various atmospheric situations

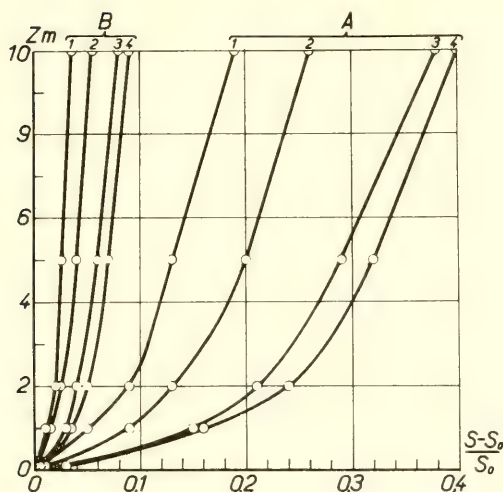


Fig. 3. Relative vertical variation of the turbulent heat flux, for various atmospheric situations

4. Water Vapor Turbulence and Its Measurement

The turbulent transfer of humidity in the lowest atmospheric layers is, as mentioned earlier, one of the principal mechanisms for the exchange of energy between air and sea. In addition, this process governs the mean distribution and turbulent structure of specific humidity in the lower levels, and thus exerts an essential influence on electromagnetic wave propagation. Therefore, the contemplated studies require the measurement of humidity fluctuations, whose levels and scales have to be estimated to delineate suitable measuring devices.

This estimation has been obtained by: a) studying the equations governing the mean distributions, turbulent fluxes and levels of fluctuations of humidity b) examining the known experimental data; and c) predicting the form of the spectrum from the Kolmogorov-Obukhov theory (Coantic and Leducq [1969]). Figure 4 compares the predicted spectral behavior of turbulent humidity fluctuations (after some shift towards lower frequencies), and recent measurements by Miyake and McBean [1970]. Considering the experimental under-estimation of the high frequency part of the spectrum, the overall agreement is not too bad.

Once the estimate is made, it is then possible to define specifications for devices measuring humidity turbulence, for use either in the field or in the laboratory (see VI.3).

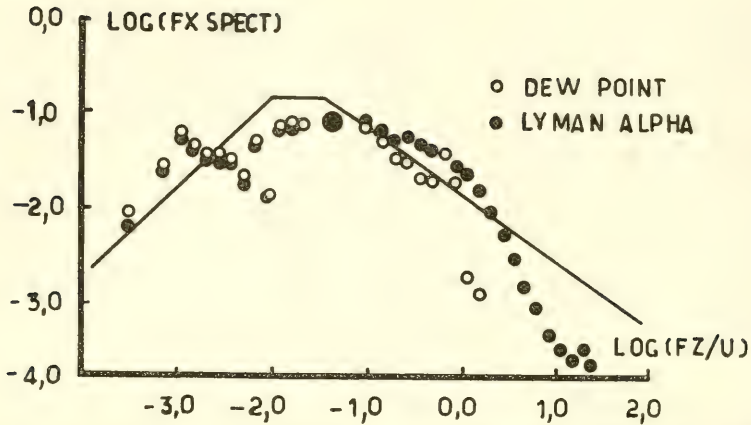


Fig. 4. Comparison between predicted spectral behavior of turbulent humidity fluctuations, and measurements by Miyake and Mc Bean [1970]

5. Two-Phase Processes in the Vicinity of Air-Sea Interface

The equations governing the mean properties of air-sea interactions are usually written in an earth fixed Eulerian frame of reference, and different sets of equations have to be used in the gaseous and in the liquid phase. Due to the unsteady random character of the interface, this means that an appreciable part of the system has, strictly speaking, to be treated as a two-phase flow.

If one wants to take into account the obviously important effects of sea spray in the lower atmosphere, and of air bubbles in the upper ocean, the necessity of considering two-phase effects is still more clear. Prompted by chemical and nuclear engineering problems, notable progress has been gained these last years in the analytical and empirical description of such processes. We plan to apply the methods therein developed to the study of the two-phase portion of the ocean-atmosphere system.

III. STUDY OF CHARACTERISTICS AND DESIGN OF THE SIMULATING FACILITY

1. Conditions for Modelling Small-Scale Air-Sea Interactions

In consequence of the physical mechanisms of air-sea energy exchanges, the planned laboratory experiments will concern the structure of turbulent velocity, temperature and humidity boundary

layers obtained at the interface between an airflow and a water mass. The three basic processes of momentum, heat and mass transfer will be effectively realized by controlling air velocity, temperature and humidity, and water velocity and temperature. Furthermore, appropriate heating or cooling will provide an approximate representation of the most important radiation effects.

However, such experiments will be really useful in modelling the atmospheric-oceanic phenomenon, only if the three aforementioned specific features: turbulent atmospheric structure, stratification effects, and interface motion, are at least partially reproduced. This seems feasible, provided that a sufficiently large facility can be realized.

2. Simulation of the Atmospheric Dynamical Structure

It is well known that the atmospheric surface layer motions can be simulated in the laboratory, in so-called "micrometeorological wind-tunnels" (see e.g. Pocock [1960], Cermak et al. [1966], McVehil et al. [1967], Mery [1968]). In short, these motions are characterized, on one hand by extremely high values of Reynolds number, and on the other hand, by stratification effects corresponding to appreciable values of Richardson number. For a good modelling, these dimensionless numbers have to keep significant values in the laboratory flow. For the latter, this implies rather large temperature differences, and low wind velocities. In consequence, to preserve sufficiently high Reynolds numbers while observing cumulative stratification effects, it is necessary to build large facilities. Similar conclusions are reached if one considers the problem of maintaining the ratio between the roughness height at the surface and the boundary layer thickness or the Monin-Obukhov length, or if one requires the reproduction of an appreciable Kolmogorov inertial range.

For these reasons, the test section length of micrometeorological wind tunnels reaches several tens of meters and the velocity range is of the order of a few meters per second, while provision is made for creating temperature differences of several tens of degrees centigrade. The main characteristics of our project are as follows:

- Length of the water surface forming the interface in the test section: 40 meters.
- Air velocity range: 0.5 to 14 meters per second.
- Maximum temperature and specific humidity differences: 30 °C, and $25 \cdot 10^{-3}$ Kg water by Kg air.

The estimated performance of the facility is sketched by Fig. 5, which shows the rather wide range of dimensionless parameters that should be covered. The general scheme of the tunnel is given in Fig. 6. It is a closed-circuit wind-tunnel, with several rather

unusual dispositions, dictated by specific requirements. For instance, to obtain stable functioning at the lowest velocities, the return circuit's area has been purposely reduced; the total head loss has been increased by tightly finned heat exchangers acting as flow equalizers just upstream the settling chamber; and the diffusers have been fitted with vortex generators and stabilizing vanes. The test section's area is 3.20 by 1.45 meter, and the overall size of the facility 61 by 7.50 meters. The wind velocity can be continuously varied from 0.5 to 14 meters per second, with a relative accuracy of $2 \cdot 10^{-3}$, using a helicoidal fan driven by a variable speed D.C. motor with electronic regulation.

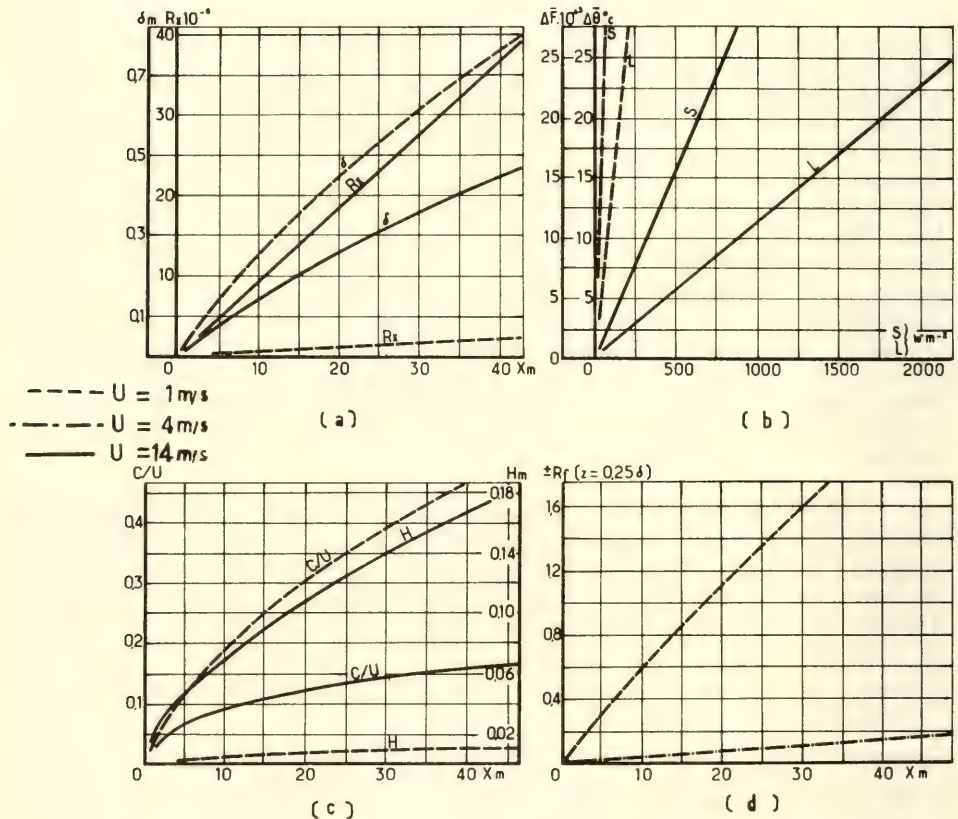


Fig. 5. Estimated performance of the facility: a) Reynolds number, and boundary layer thickness; b) Sensible and latent enthalpy fluxes; c) Wind-Waves' age and significant height; d) Richardson number.

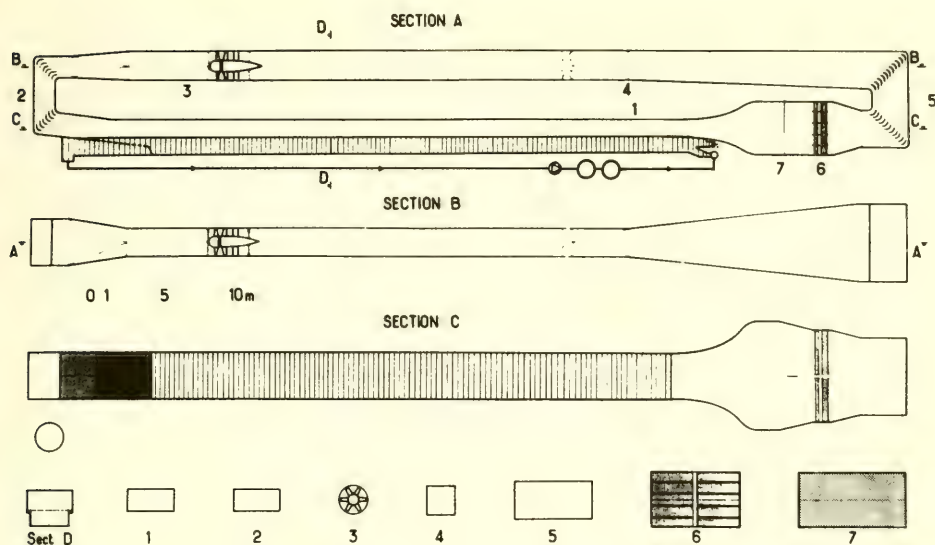


Fig. 6. General scheme of the wind-water tunnel

3. Reproduction of Heat and Mass Transfer Processes

Supposing a convenient flow structure has been obtained, the existence of nonzero temperature and partial water vapor pressure differences between the water surface and the incoming air flow will be sufficient to cause turbulent convective processes of mass and sensible and latent enthalpy similar to those encountered in the atmospheric boundary layer.

The equations governing these transfers being linear with respect to temperature and humidity, these last variables can be fixed on grounds of experimental convenience, as long as stratification effects do not arise. The estimated values of flux Richardson number, computed at one-quarter boundary layer thickness and for a temperature difference amounting to 25 °C, are displayed in Fig. 2(d) as a function of longitudinal abscissa and velocity. At the highest velocities, Richardson number is clearly negligible, and temperature and humidity differences will be chosen, to improve experimental accuracy, at the highest levels authorized by the equipment's capabilities (see Fig. 2(b), and below). On the other hand, at the lowest velocities, temperature and humidity can no longer be considered as scalar passive contaminants, and their differences will be chosen in order to obtain a given Richardson number, i.e. a given effect on the dynamical structure.

A first approximation representation of radiative heat exchanges seems also to be feasible in the laboratory. At the small scale we are interested in, the main effect of short wave solar radiation is a global elevation of the oceanic temperature, that can be reproduced by heating the water mass. Due to the radiative transfer process mentioned in II.3, the reproduction of infrared heat exchange is more delicate, but its primary effect yet remains the cooling (or occasionally heating) of the interface itself. This localized heat sink shall be simulated, either by increasing the cooling produced at the same place by evaporation, or by lowering the temperature of the ceiling of the test section, and thus controlling the radiative heat exchange between this wall and the water surface.

The designed facility will allow independent control of air and water temperatures in the $5^{\circ}\text{C} - 35^{\circ}\text{C}$ range, with an accuracy of the order of 0.1°C . The relative humidity of air entering the test section will be varied from 60% to 100%. Fig. 7 schematizes the main components of temperature and humidity control system: cooling and drying (by condensing) coils, heating coils and vapor injectors in the air circuit; cooling and heating heat exchangers in the water circuit; heat generator, frigorific unit with cooling tower, steam boiler, regulating system. The working principle is represented using the temperature-mixing ratio diagram.

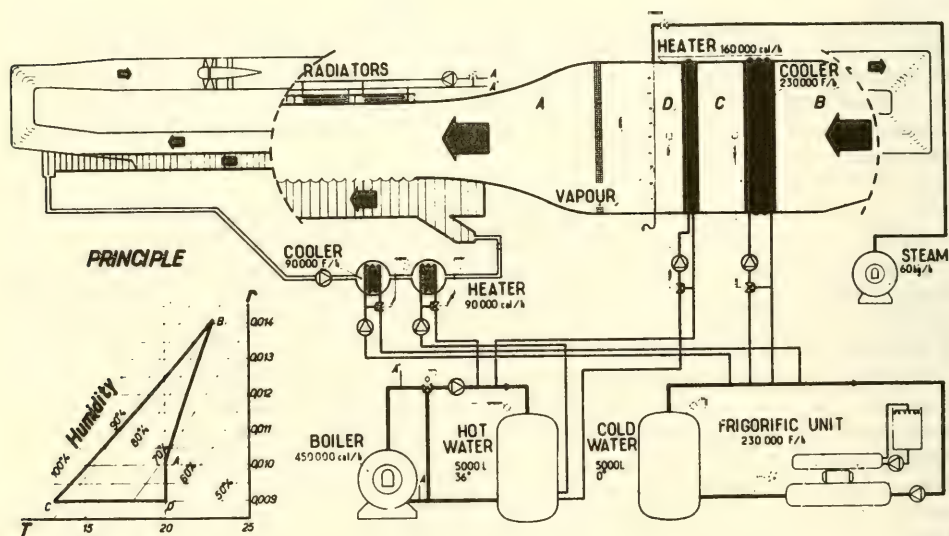


Fig. 7. Schematic diagram of temperature and humidity control systems

4. Reproduction of Interfacial Motions

The problem of obtaining laboratory waves statistically similar to those encountered over the oceans has been thoroughly studied these last years, with the view, either to perform more realistic structural tests, or to experimentally investigate the mechanism of wave generation by wind. The works of Veras [1963], Hidy and Plate [1965], Hsu [1965], Gupta [1966], and of the Waterloopkundig Laboratorium [1966a,b] can be cited among many others. The unsymmetrical, randomly varying and three-dimensional waves existing in nature can be simulated only at the cost of building large laboratory facilities. The so-called "wind-wave tunnels" reach one hundred meters in length and several meters in width, with smooth and parallel side walls and an efficient absorbing beach at the end.

The main characteristics of waves naturally generated by wind along our 40 meters long tank have been forecast from the preceding references and are shown by Fig. 2(c). It is clearly possible to generate gravity waves of appreciable amplitude, and thus to cover a nonnegligible range of Froude numbers. However, the "wave age," i.e. the ratio of the celerity of propagation, C , of dominant waves to the wind velocity, U , remains low, especially at the highest velocities. The same is true of the ratio C/U^{\pm} (where U^{\pm} is the friction velocity in the boundary layer), which is known as an important parameter in the wave generation process. As a matter of fact, these two ratios control the relative magnitude of normal and tangential stresses exerted by wind on water, with important consequences upon the various energy exchange mechanisms (see II.1). It is therefore necessary to have the possibility to act on these parameters, by controlling the wave height and celerity independently of wind velocity. This will be done by means of a wavemaker set at the beginning of the water channel and conveniently randomly actuated. It is known that the combined action of such a device and of wind blowing will result, after some distance, in a satisfying wave pattern.

The details of that part of the equipment are sketched by Fig. 8. A new type of wavemaker, comprising a fully submerged wave plate connected to the tank by means of bellows, has been imagined.* This arrangement allows to realize a fairly smooth joining of air and water flows, even in the presence of waves. The end of the channel will be equipped with an absorbing beach made from parallel tubes with a 7° slope. A slight water movement (between 0.1 and 0.01 m/s) necessary for cleaning and temperature controlling purposes, will be insured by a recirculating 35 HP helicoidal pump.

*By A. Ramamonjiarisoa.

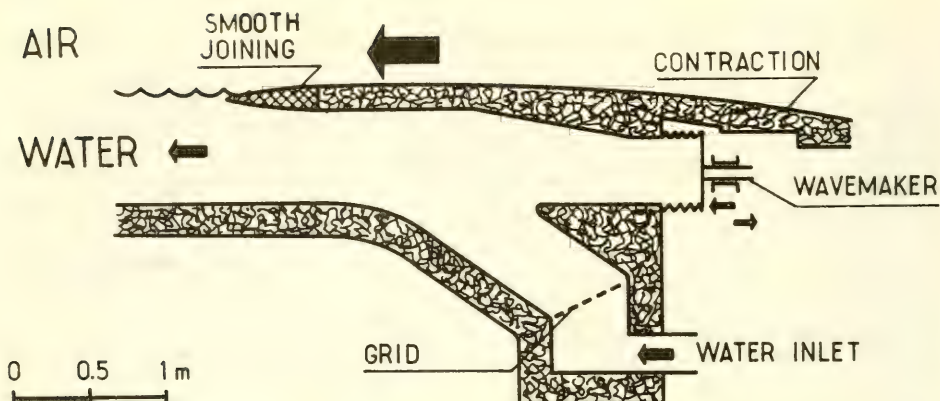


Fig. 8. Details of junction between air and water flows, and arrangement of the submerged wavemaker.

5. Further Details and Conclusions

At each step in the design of the facility, we endeavored to improve the simulation of the natural phenomenon and some of the arrangements taken to this end have just been described. A peculiar problem was set by the parasitic boundary layers which unavoidably originate along the side walls and ceiling of an elongated working section, and which are known to result in cumbersome secondary motions. The dispositions adopted to reduce these effects, thereby improving the representation of the unlimited atmospheric-oceanic system, are represented by Fig. 9. The cross sectional shape of the working section (see Fig. 9(a)) has been designed with a height/width ratio of 1 to 2.2, and furthermore fitted, like in the Waterloopkundig Laboratorium [1966a,b] design, with vertical plates restricting the span of the useful water surface to 2.62 meters. The lateral quays thus realized will limit the parasitic dynamical as well as thermodynamical effects in the central part of the working section, where the measurements will be performed. To further improve the two-dimensionality of the flow, and to prevent the interaction of the studied boundary layer with that one developing on the working section's ceiling, boundary layer control devices will be used. As shown by Fig. 9 (b), they combine boundary layer suction (by means of slots or porous walls) and blowing (through slots), taking advantage of the possibilities of tangential blowers.

At last, it will be necessary, specially at the lowest wind velocities, to artificially trigger transition, and eventually to increase the boundary layer thickness, by means of devices similar to those studied by Counihan [1969] or Campbell and Staden [1969].

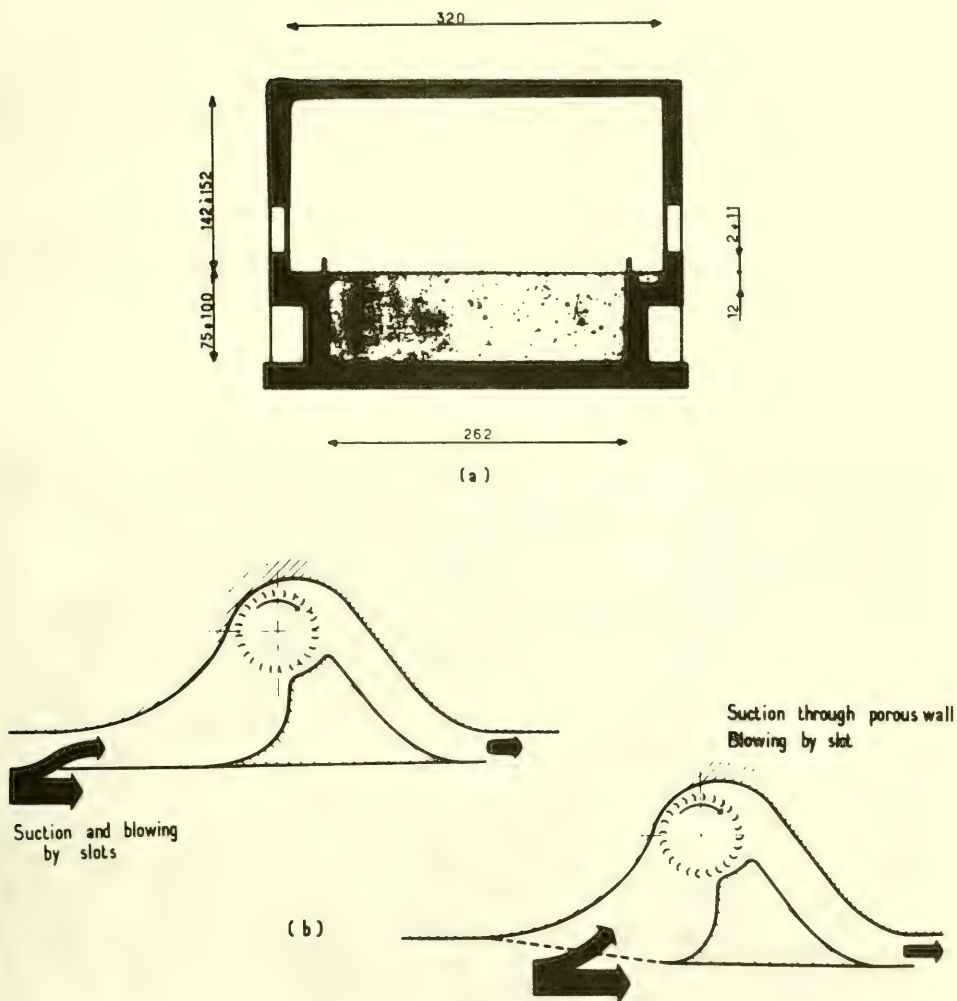


Fig. 9. Details of test section: a) Section view, showing the lateral quays; b) Boundary layer control devices.

All the foregoing will make clear that we have tried to insure an acceptable simulation of the main aspects of air-sea interactions. Entire modelling, with full similarity, cannot, of course, be attained. We believe, however, that experiments where the various physical mechanisms are effectively put in action, and where basic parameters possess significant values, will realize a partial simulation of natural exchanges, thus affording the possibility of interesting investigations.

IV. PRELIMINARY ONE-FIFTH SCALE MODEL TESTS

A one-fifth scale model of the large air-sea interaction facility has been built. The primary object was to check and improve various design characteristics; altogether it was also planned to perform instrumental studies, and to execute preliminary small-scale scientific experiments.

This scale model is a detailed reproduction of all parts of the large facility, including not only the aerodynamic and hydraulic elements, but also the equipment controlling heat and humidity exchanges. A view of the wind-water tunnel, and of the control console, is given in Fig. 10.

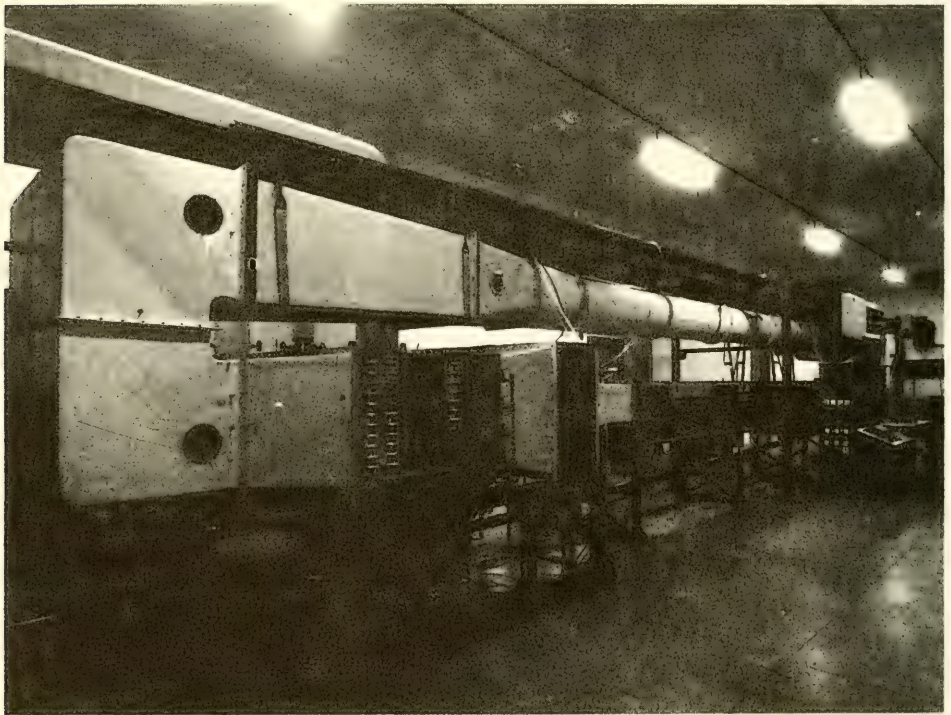


Fig. 10. General picture of the model

1. Overall Aerodynamic Tests

The first use of the model has been to test the global aerodynamic performance of the facility. The initial design, represented by the upper part of Fig. 11, suffered from several imperfections resulting in a low power factor and in an inadequate working stability. Detailed flow explorations have led to successive amendments in the geometry of the model (see Pouchain [1970] and Coantic et al. [1969]). The final design, shown in the lower part of Fig. 11, offers satisfactory performance, and has therefore been adopted in the later building of the large facility, the aerodynamic characteristics of which have been predicted from the model tests.

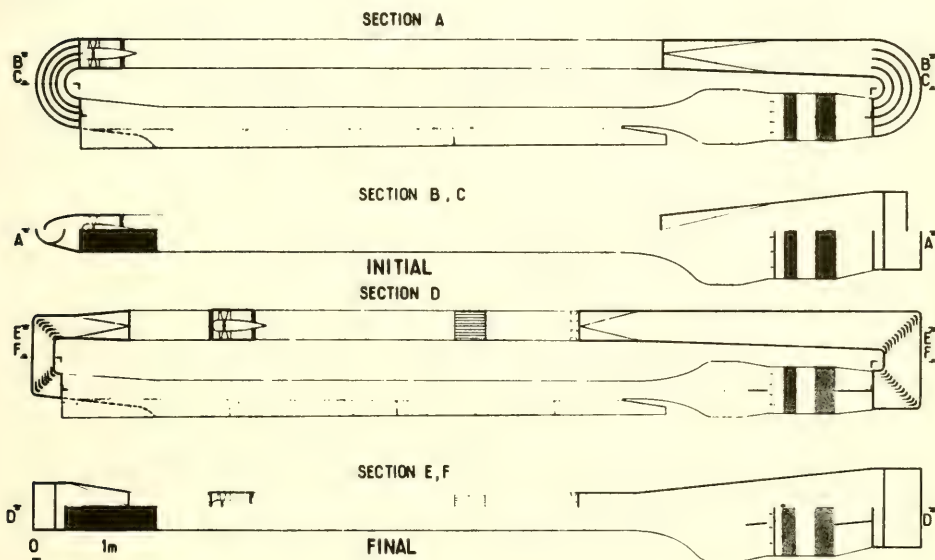
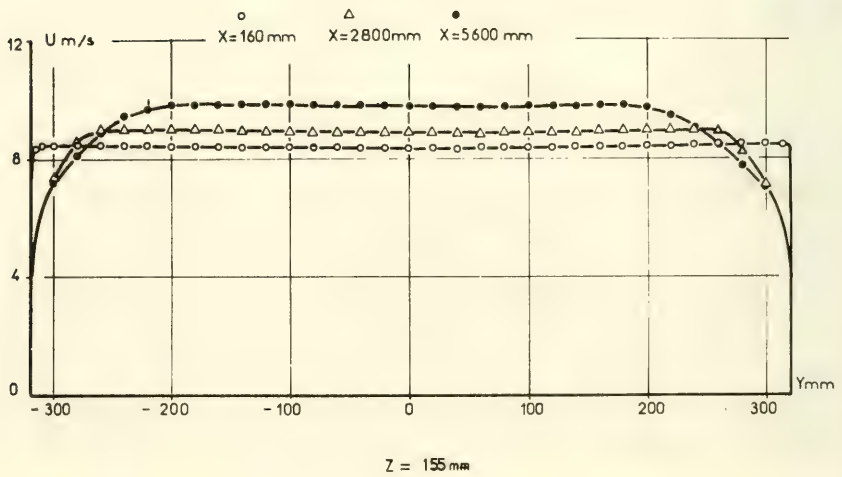
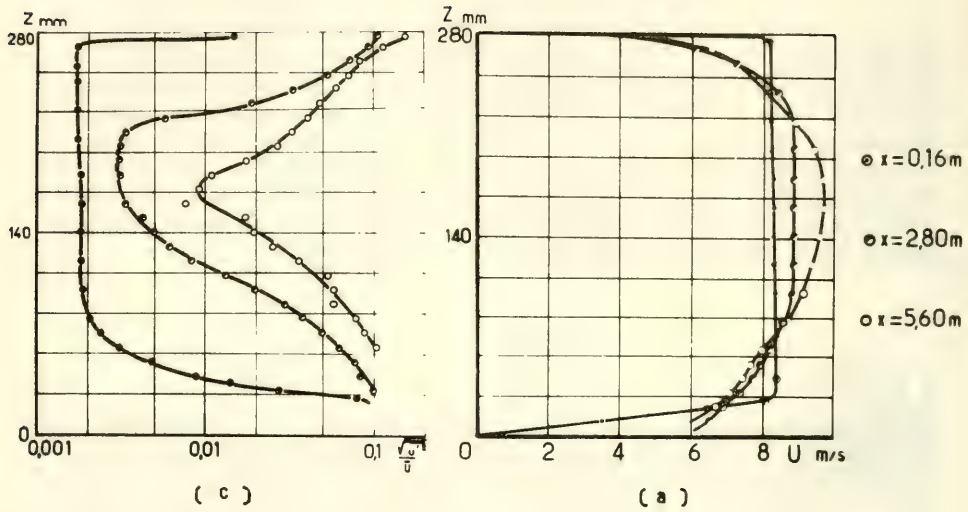


Fig. 11. Improvements in aerodynamic design of the model

2. Flow Exploration and Improvement in the Working Section

A deeper flow study of the working section has then been performed, of which typical results, obtained for a wind velocity of 8.3 m/s, are displayed by Fig. 12. It can be seen that the situation is good in the entrance section, with a very flat velocity profile, and a turbulence intensity below 0.002 (the effects that can be discerned near the water surface are the consequence of artificial boundary layer thickening in the final part of the contraction). The further growth of the various boundary layers, and the fact that they



$Z = 155$ mm

(b)

Fig. 12. Flow characteristics in the test section: a) Vertical velocity profiles; b) Horizontal velocity profiles; c) Vertical distributions of turbulence intensity.

begin to join together towards the end of the working section, leading to a fully developed channel flow, are also apparent.

As already mentioned (see III.5), it is therefore necessary to take steps to restrict the development of the lateral and upper boundary layers. Tests performed under different conditions have proven that the contemplated control method was efficient in this respect (Pouchain [1970]). Fig. 13 illustrates typical results obtained for various blowing rates (i.e. ratios of jet velocity to mean flow velocity), while sucking through a porous wall and blowing across a 15 millimeters height slot. The improvement in velocity distribution is clear. As shown by Fig. 14, the turbulent intensity distribution is also ameliorated. Some problems related to pressure perturbations still have to be solved, but, on the whole, the method appears as promising.

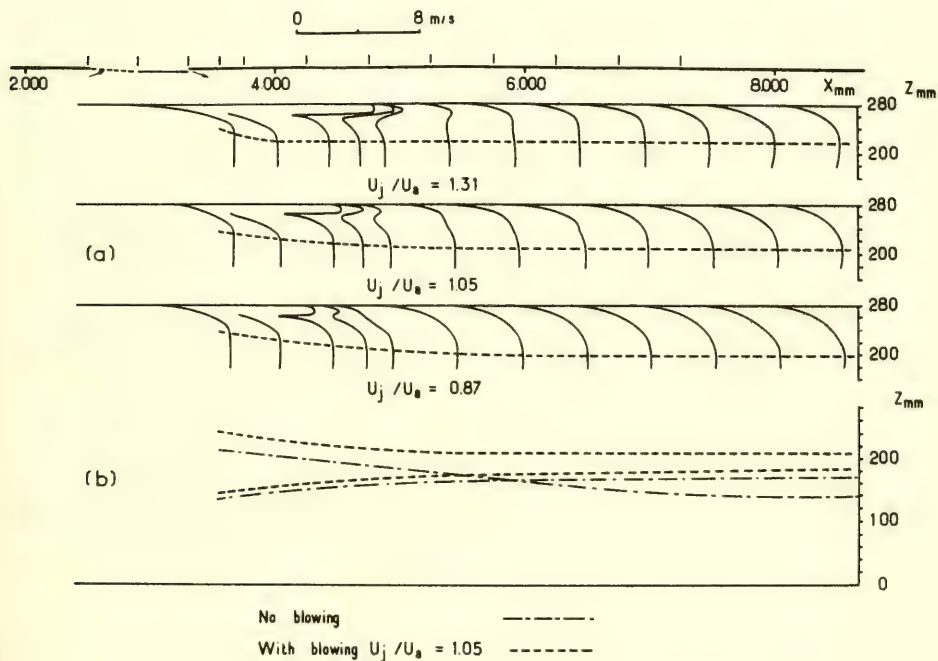


Fig. 13. Improvement in test section's flow by means of boundary layer control: a) Flow configurations for three rates of blowing; b) Variation of boundary layers' thickness.

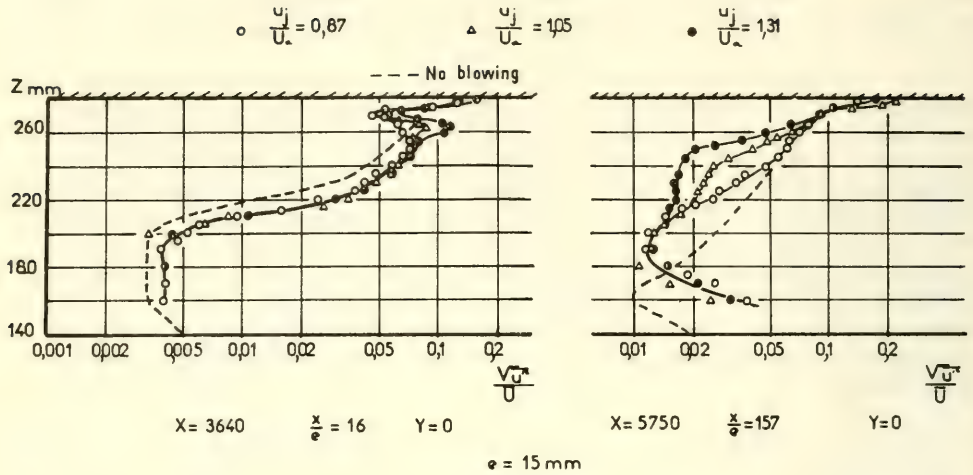


Fig. 14. Effects of blowing on turbulence intensity distributions.

3. Hydraulic Tests

The hydraulic performance of the facility has also been subjected to various tests. The functioning of the water recirculating circuit has been controlled. The working of the new submerged wavemaker, and of the absorbing beach, has also been found satisfactory.

Observations of waves generated by wind in the model tank, such as those shown by Fig. 15, suggests they qualitatively possess the three-dimensional random structure typical of oceanic wind waves. Measurements of wave spectrum at different fetches along the working section have just been done, and the results displayed in Fig. 16 compare favorably with those of previous studies (see the references in III.4). The spectral shape and evolution strongly suggests the existence of nonlinear effects transferring energy from higher to smaller frequencies, as recently postulated by Longuet-Higgins and Mollo-Christensen.

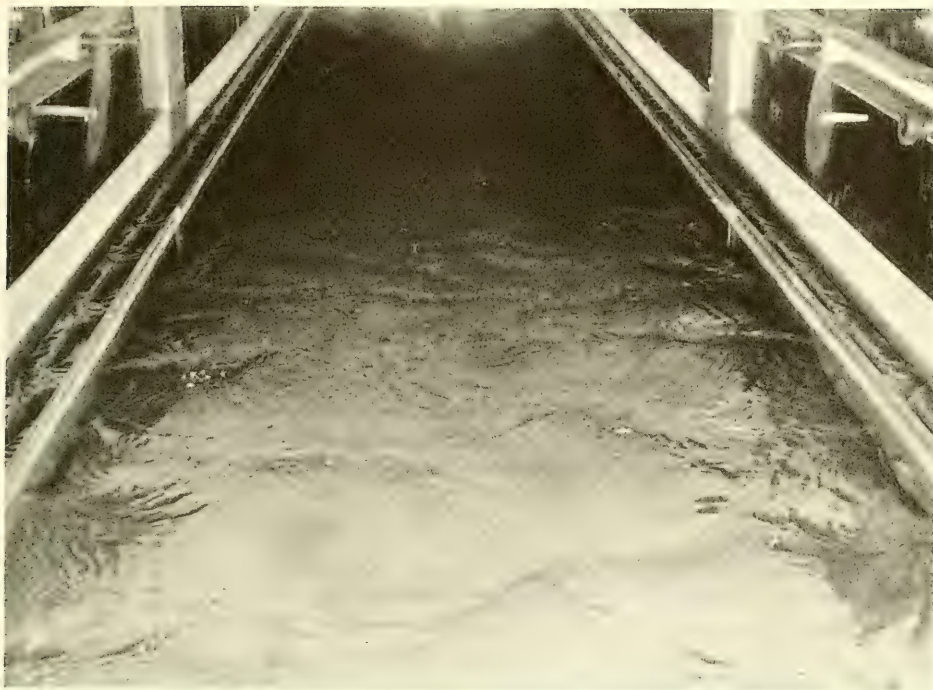


Fig. 15. Sample view of wind-waves obtained for a 4 m/s velocity and a 4 m fetch.

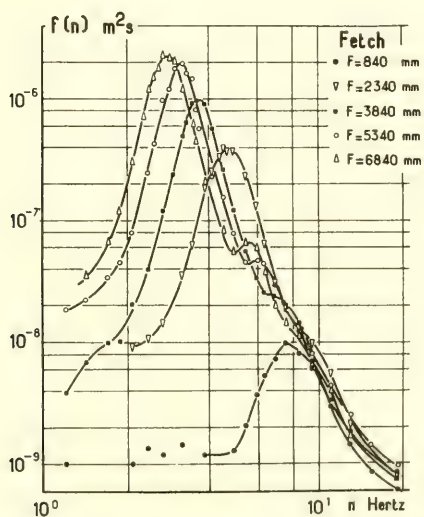


Fig. 16. Evolution of wind-waves' spectra as a function of fetch along the model's test section.

4. Tests of Temperature and Humidity Control Systems

Various working tests of that part of the equipment have been executed. The validity of the previously chosen control methods has been checked, the obtainable temperature and humidity range has been controlled, and the stability of regulating loops has been tested. After some improvements, the overall thermodynamic performance of the model has been correct.

A further study of temperature repartitions upstream and inside the working section has then been undertaken, for different flow and thermal conditions. Typical results are shown by Fig. 17, where an initially isothermal airflow, and the development of thermal boundary layers can be observed. The temperature distribution in the entrance section is usually good, except in extreme cases of large heating and velocities of the order of one meter per second, where parasitic stratification effects appear.

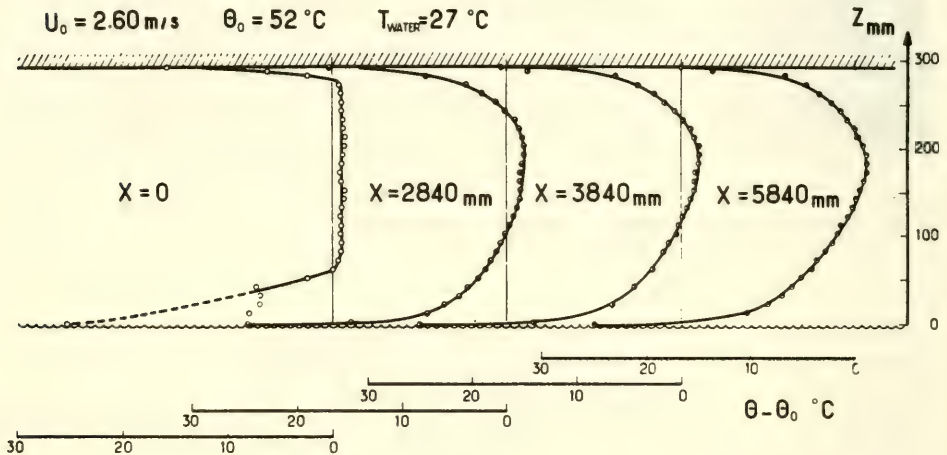


Fig. 17. Temperature Distribution in the Model's Test Section

V. CONSTRUCTION OF THE LARGE AIR-SEA INTERACTION FACILITY

In view of the rather considerable size of the designed wind-wave tunnel, its erection was not possible inside I. M. S. T.'s main building. It was therefore decided to build a new laboratory, including the large air-sea facility, its auxiliary equipments and a group of offices, workshops and laboratories, and located in the new Marseille-Luminy Campus. Its floor plan is shown by Fig. 18.

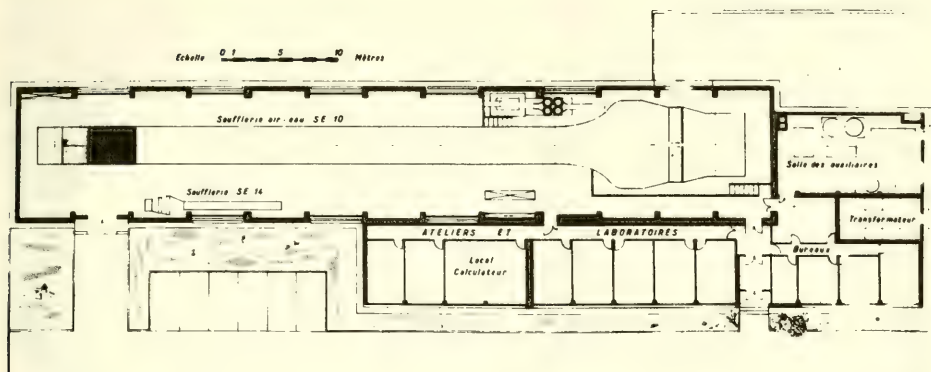


Fig. 18. Air-Sea Interactions Laboratory Floor Plan

The preliminary design of the facility has been determined by I.M.S.T., and its detail drawings set up with the aid of architect and engineering offices. The construction works have been planned in three stages: a) Erection of buildings, concrete structural parts of the tunnel, electric equipments, temperature and humidity control systems; b) Fitting up of the main elements of air and water circuits, including static parts (tunnel walls etc.) as well as pump and fan; c) Completion and equipment of the facility, placing control apparatus and such parts as wave-maker and boundary layer control devices in position.

Works have been started in January 1969, and step a) is fully completed from several months (see Fig. 19). Step b) is now nearly achieved, and the first run of the wind-water tunnel is planned for the end of the present year.* Our program forecasts about one more year for the execution of step c), and the beginning of strictly scientific experiments by the end of 1971. These experiments will concern: first the dynamic exchange process alone; then, the heat and mass transfer processes; and later on the effects of stratification upon these three mechanisms. The execution of this program will clearly take several years.

VI. RESEARCHES RELATED TO INSTRUMENTATION PROBLEMS

Some of the anticipated experiments obviously necessitate, either the development of new measuring instruments and methods, or the adaptation of existing ones. Corresponding researches have been undertaken since the early stages of our program.

*Note added in proof: this has been achieved by November 1970.

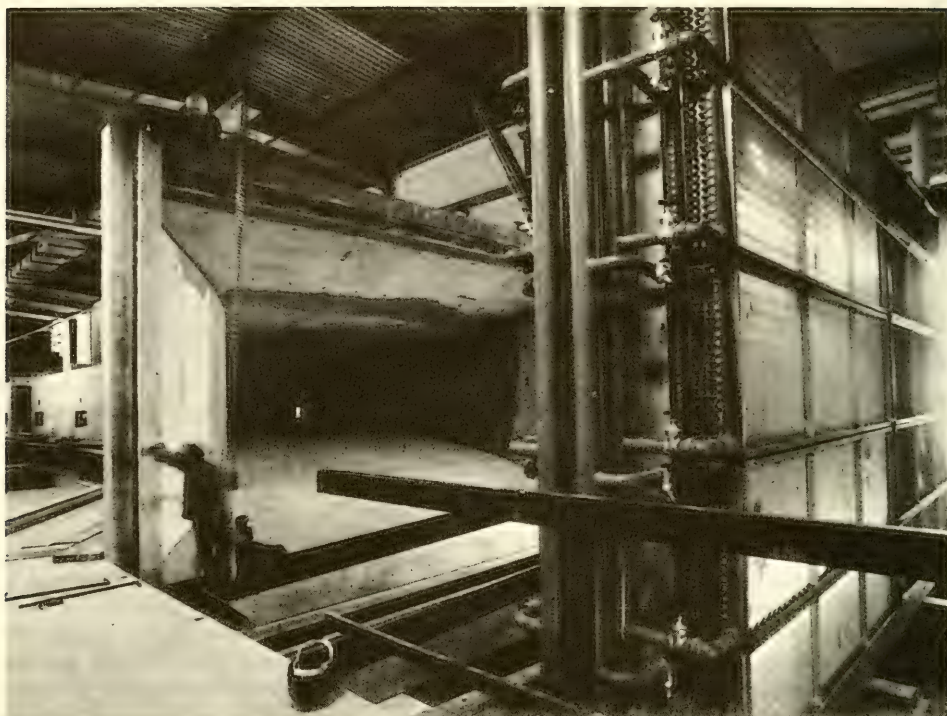
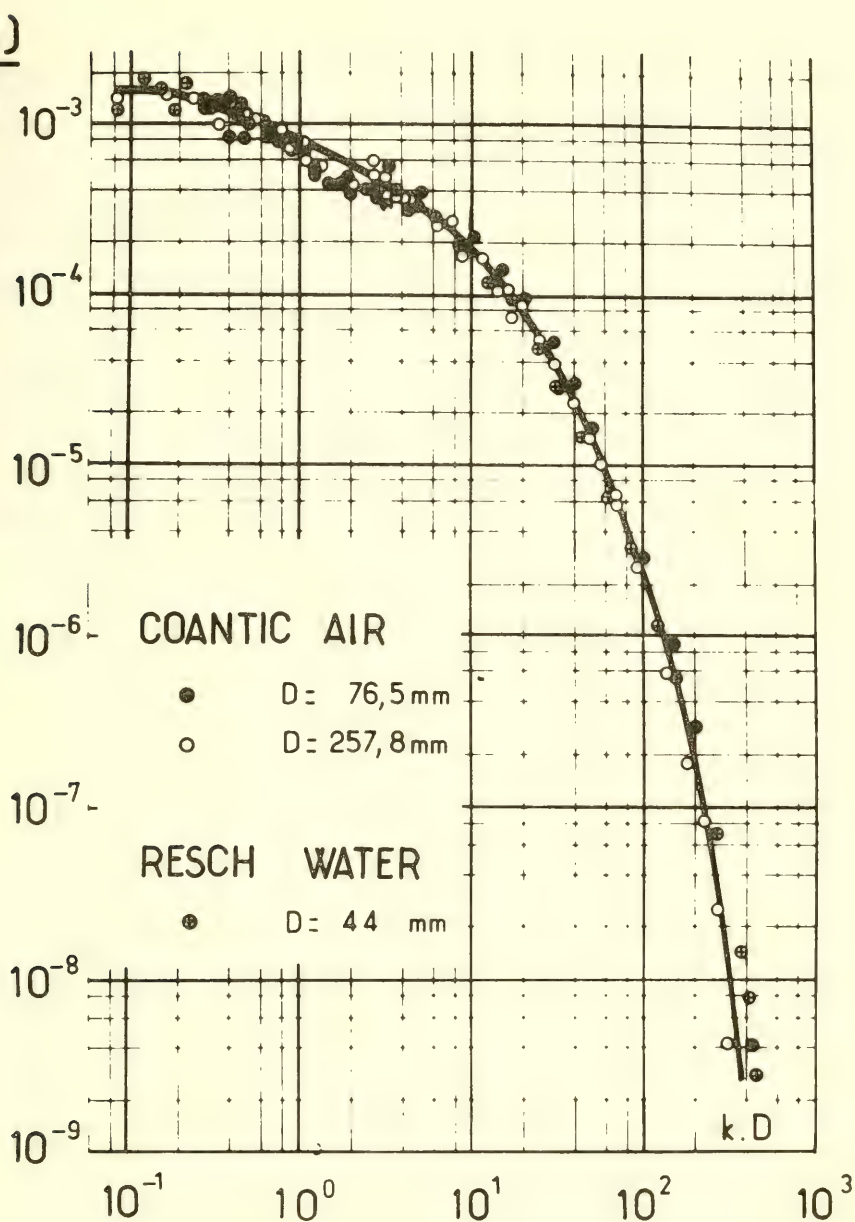


Fig. 19. Constructions' progress by May 1970: view of refrigerating coils, and of concrete contraction and test section.

1. Turbulence Measurements in Water Flows

A first work has been devoted to the measurement of velocity and temperature mean and fluctuating values in water flows, and of the associated turbulent momentum and heat fluxes. The adaptation to this problem of the well known hot-wire technique has been studied experimentally. An apparatus including a tubular water channel was constructed to that end, and hot-wire sensors were manufactured. The theoretical and experimental study of the performance of various types of wires and films has resolved satisfactory methods of calibration and measurement, particularly for commercially manufactured conical hot films for which dimensionless cooling laws have been proposed, and for slanting wedge-shaped films. The intensity and the spectrum of turbulence, and the Reynolds stresses themselves, have been determined inside a circular conduit, with a comparable degree of accuracy to that attainable in air flows (see Fig. 20). Later on, the effects of water temperature variations upon the hot-film response



(a)

Fig. 20. Turbulence measurements in water flows: a) Comparison of turbulence spectra measured in dynamically similar air and water flows.

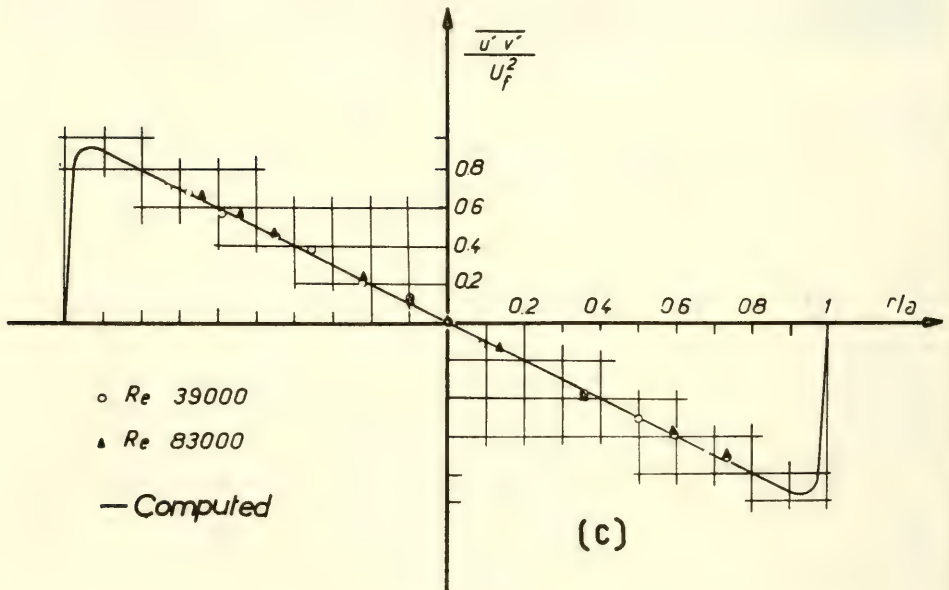
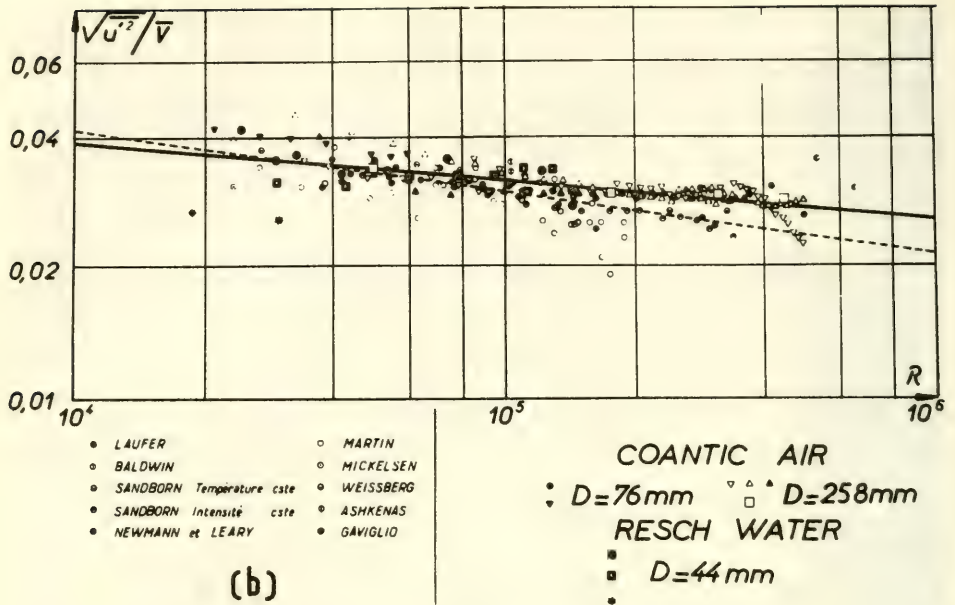


Fig. 20. Turbulence measurements in water flows: b) Comparison of turbulence intensities measured in dynamically similar air and water flows; c) accuracy checking of measured shear stresses.

have been thoroughly studied (see Fig. 21), and measurements of the intensity of temperature turbulence have been executed.

These results are given in a number of publications: Resch [1968, 1970], Resch and Coantic [1969], Ezraty and Coantic [1970], Ezraty [1970]. They show conclusively that, subject to some precautions, turbulence measurements can be quite accurately performed in water flows, using hot-film anemothermometers.

2. Measurements of Turbulent Fluctuations of Humidity

After the theoretical study reported in II.4, the development of a water vapor turbulence measuring technique has been undertaken. Various methods have been considered: psychrometry, dew-point measurement, use of hot-wire, absorption of Lyman alpha or infrared

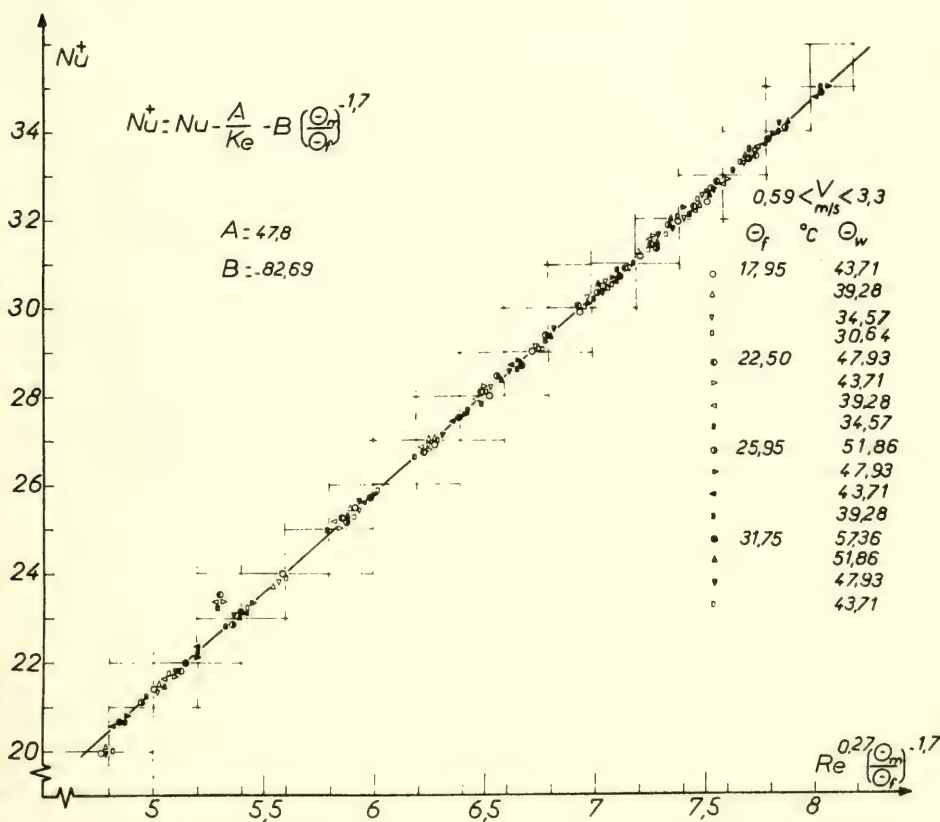


Fig. 21. Dimensionless Cooling Law for a Conical Hot-Film.

radiation, measurement of refractive index, use of the ionic probe. These techniques which depend on the thermodynamic properties of moist air present advantages from the point of view of miniaturization, whereas those based on electromagnetic properties are advantageous from the point of view of bandwidth. Psychrometry and Lyman alpha absorption seem to be the most promising ones, the latter appearing to have the best chance for adaptation to particularly difficult measuring conditions (Coantic and Leducq [1969]).

For practical reasons, psychrometry has been chosen for a first deeper investigation. A small calibrating tunnel has been built and various types of miniaturized small time constant psychrometers have been manufactured and tested. A prototype psychrometer is used with wet and dry balsa fibers, of which surface temperature is measured by platinum resistors (5 microns in diameter), the resulting electrical signals being fed into a small analogue computer, whose output is directly proportional to specific humidity fluctuations. The physical size of the sensing head is a few millimeters and the bandwidth several cycles per second (Leducq [1970]). These results are only preliminary, and further studies are now being undertaken.

3. Data Processing

Considering on one hand the volume of measurements to be taken, and on the other hand the necessity, mentioned in II.2, to separate any variable in its "mean," "phase average" and "turbulent" parts, the use of digital data acquisition and processing methods seem unavoidable.

Preliminary studies have been done of a small data acquisition system for continuous digitizing and numerical tape recording of turbulent variables. The recorded data could be later, pre-processed on the system itself and eventually transferred to a large computer for a comprehensive treatment. This data acquisition system could also be useful for control process of the tunnel and of the measuring equipments, thereby largely increasing the efficiency of the facility.

VII. CONCLUSIONS AND PROSPECTS

The research program which has just been introduced is obviously a long-term one. It is therefore too soon to state any definitive conclusion, and we can only try to survey some preliminary results, and to think about the probable prospects of the research we have undertaken.

The main result of the work performed till now is the detailed definition of a scientific experiment which, although done in the laboratory, seems capable to give results applicable to the natural processes occurring near the ocean-atmosphere interface. The

interest of this original approach is clear, but its success will be ascertainable only after fulfillment of the anticipated experimental program. Indeed, in spite of the growing evidence in favor of the laboratory simulation of such geophysical phenomena, it is only by direct comparison with field data that the exact degree of similarity achieved with the natural process will be known. It is, however, reasonable to expect, at worst, a partial success of this approach, namely the elucidation of some among the many unsolved aspects of small scale air-sea interactions.

Besides this main point, a few results have been, to date, obtained in various related domains. We shall quote: some progress in the understanding of effects of water vapor transfer and long-wave radiation upon turbulent heat transfer in the atmospheric surface layer; some improvements in the technique of micrometeorological and wind-wave facilities; results on the measurement of turbulent processes in water flows, with the aid of hot-film anemothermometers.

It is clear that much work still remains to be done, when the present program is necessarily limited in scope. On the other hand, the described facilities will offer possibilities that will not be fully exploited by only one scientific group. Therefore, it should be possible in the future to consider some cooperation with other groups, in order to take full advantage of the capabilities of that tunnel.

The researches that can be performed with such an equipment have multiple fields of application. The results of the present program could obviously be useful for oceanography and naval hydrodynamics (wave forecasting, shiprouting, fishing, pollution, oceanographic methods, etc.), as well as for meteorology (long range forecasting, air pollution, future climatic control, etc.), and seem also to be applicable in other domains: chemical engineering, air conditioning, heliotechnique, and even biological and agricultural micrometeorology. Furthermore, new experiments could be planned in the fields of acoustic wave propagation, light transmission or reflexion, electromagnetic propagation, structural mechanics, and so on. In short, this facility ought to be a kind of "pocket ocean-atmosphere interface," where basic as well as applied experiments could be done more easily and economically than in the field.

VIII. ACKNOWLEDGMENTS

This research program would have never been undertaken without the insight of a number of scientists who have encouraged us to make a start in such an enterprise. In the first place, we have to cite the name of President Maurice Roy who, after the IUGG-IUTAM Symposium on Turbulence in Geophysics, held at IMST in September 1961, advised us to engage ourselves in some kind of laboratory experiments related to air-sea turbulent interactions. Then, the Presidents and the members of the "Comité de Recherches

"Atmosphériques de la Délégation Générale à la Recherche Scientifique et Technique" induced us to go further in that way, and secured the financial support necessary to start the program. We are happy to specially mention here the name of Professor H. Lacombe, who has been, from the very beginning, the adviser and ardent supporter of the project. We have also received much interest and helpful advice from Ingénieur Général R. Legendre, Professor L. Malavard, and from numerous French and foreign scientists whose names cannot, for lack of space, be mentioned here.

The program is being supported by several French governmental Agencies, to which we are happy to have here an opportunity to give due acknowledgments. We already mentioned the primary intervention of the "Délégation Générale à la Recherche Scientifique et Technique" which supported the preliminary research program, and granted the major part of funds necessary for the building of the large air-sea interaction facility. The "Direction des Enseignements Supérieurs du Ministère de l'Education Nationale," through the "Université d'Aix-Marseille," has provided the building site and financed the construction of offices and laboratories. The operational cost of the research is presently supported by the "Centre National pour l'Exploitation des Océans." The program also benefits of the direct or indirect aid of several other Agencies, chiefly the "Centre National de la Recherche Scientifique," the "Direction des Recherches et Moyens d'Essais," and the "Office National d'Etudes et Recherches Aéronautiques."

The results presented in this paper are the consequence of the cooperative work of many individuals. The scientific and technical team in charge of the program includes a number of research workers, doctoral students and technicians, to each of whom a definite part has been attributed in the project management. We shall mention: Dr. P. Bonmarin (Engineer in charge), Dr. A. Ramamonjariisoa (Study of dynamical interactions), Dr. F. Resch (Turbulence measurements in water flows), Mr. B. Pouchain (Model tests), Mr. D. Leducq (Humidity measurements), Mr. R. Ezraty (Measurement of turbulent fluxes in water), Mr. B. Seguin (Turbulent and radiative transfer computations), Mr. J. Quaccia (Designer), Mrs. F. Laugier, and MM. P. Chambaud, B. Bacuez, M. Bourguet, B. Zucchini and A. Laurence (Technical assistants having contributed to the program). Last, but not least, we should like to acknowledge the cooperation of the various contractors who have been, or still are, contributing materially to the construction of the large wind-wave facility, and of the associated equipments.

REFERENCES

- Brunt, D., Physical and dynamical meteorology, Cambridge University Press, Cambridge, 1939.
- Campbell, G. S. and Standen, M. M., "Progress report II on simulation of earth's surface winds by artificially thickened wind tunnel boundary layers," Laboratory Technical Report LA-37, National Aeronautical Establishment, National Research Council of Canada, 1969.
- Cermak, J. E., Sandborn, V. A., Plate, E. J., Binder, G. K., Chuang, K., Meroney, R. N., and Ito, S., "Simulation of atmospheric motion by wind tunnel flows," Technical Report Colorado State University, A.D. 633 584, 1966.
- Coantic, M., "Les interactions atmosphère-océans, les processus physiques et les équations qui les gouvernent," I.M.S.T. Report, Cahiers Oceanographiques Vol. XXI, N° 1 pp. 17-46; N° 2 pp. 105-143; N° 3, pp. 223-249, 1969.
- Coantic, M., Bonmarin, P., Pouchain, B., and Favre, A., "Etude d'une soufflerie pour recherches sur les échanges atmosphère-océans," A.G.A.R.D. Conference Proceedings N° 48, 1969.
- Coantic, M. and Leducq, D., "Turbulent fluctuations of humidity and their measurement," Radio-science, Vol. 4, N° 12, pp. 1169-1174, 1969.
- Coantic, M. and Seguin, B., "On the interaction of turbulent and radiative transfers in the surface layer," IUGG-IAMAP-AMS Conference on Planetary Boundary Layers, Boundary Layer Meteorology, Vol. 1, pp. 245-263, 1971.
- Counihan, J., "An improved method of simulating an atmospheric boundary layer in a wind tunnel, Atmospheric Environment, Vol. 3, pp. 197-214, Pergamon Press, 1969.
- Ezraty, R. and Coantic, M., "Sur la mesure des tensions de frottement turbulent dans un écoulement d'eau," C. R. Académie des Sc. Paris, T., 270, pp. 613-616, 1970.
- Ezraty, R., "Sur la mesure des caractéristiques turbulentes dans de écoulement d'eau," Thèse Doct. Eng. Marseille, 1970.
- Gupta, A. K., "An experimental investigation of the generation of water waves by air shear flows," ASRL TR 116-3, Dept. of Aeronautics and Astronautics, Massachusetts Institute of Technology, 1966.

- Haltiner, C. J., and Martin, F. L. Dynamical and physical meteorology, McGraw Hill, New York, 1967.
- Hidy, G. M. and Plate, E. J., "Wind action on water standing in a laboratory channel, Report P.M. 135- NCAR, Boulder, Colorado, 1965.
- Hsu, E. Y., "A wind, water-wave research facility," Dept. of Civil Eng. Tech. Report 57, Stanford University, 1965.
- Lacombe, H., Cours d'Océanographie Physique, Gauthier-Villars-Paris, 1965.
- Leducq, D., "Recherches sur un hygromètre adapté à la mesure des fluctuations turbulentes," Thèse Doct. Ing. Marseille, 1970.
- Lumley, J. L. and Panofsky, H. A., The structure of atmospheric turbulence, Interscience, New York, 1964.
- Mc Vehil, G. E., Ludwig, G. R., and Sundaram, T. R., "On the feasibility of modeling small-scale atmospheric motions," Cornell Aeronautical Laboratory Report N° Z B -2328-P-1, 1967.
- Mery, P., "Reproduction en similitude de la diffusion dans la couche limite atmosphérique," Communication Comité Technique N° 86, Sté Hydrotechnique de France, Paris, 1968.
- Miyake, M. and Mc Bean, C., "On the measurement of vertical humidity transport over land," Boundary Layer Meteorology, Vol. 1, N° 1, pp. 88-101, 1970.
- Monin, A. S. and Yaglom, A. M., Statistical Hydromechanics, Nauka, Moscou (English translation J.P.R.S. 37, 763), 1966.
- Munn, R. E., Descriptive micrometeorology, Academic Press, New York, 1966.
- Phillips, O. M., The dynamics of the upper ocean, Cambridge University Press, Cambridge, 1966.
- Pocock, P. J., "Non-aeronautical applications of low-speed wind tunnel techniques," AGARD Report 313, 1960.
- Pouchain, B., "Contribution à l'étude sur maquette d'une soufflerie de simulation des interactions océans-atmosphère," Thèse Doct. Ing. Marseille, 1970.
- Priestley, C. H. B., Turbulent transfer in the lower atmosphere, University of Chicago Press, Chicago, 1959.

- Ramamonjariisoa, A., "Théories modernes de la génération des vagues par le vent," I.M.S.T. Report (unpublished), 1969.
- Ramamonjariisoa, A., "Rapport sur les missions d'études au Canada et aux Etats Unis en 1969," I.M.S.T. Report (unpublished), 1970.
- Resch, F., "Etudies sur le fil chaud et le film chaud dans l'eau," Thèse Doct. Ing. Marseille, 1968.
- Resch, F., and Coantic, M., "Etudie sur le fil chaud et le film chaud dans l'eau," *Le Houille Blanche*, N° 2, pp. 151-161, 1969.
- Resch, F., "Hot-film turbulence measurements in water flow," J. Hydr. Div. Proceedings ASCE, pp. 787-800, 1970.
- Roll, H. U., Physics of the marine atmosphere, Academic Press, New York, 1965.
- Sverdrup, H. U., Oceanography, Handbuch der Physik, vol. XLVIII, Springer, Verlag, Berlin, 1957.
- Veras, M. S. Jr., "Etude expérimentale de la houle dans un canal," Thèse Doct. d'Université, Paris (Division d'Etudes Maritimes duCREC), 1963.
- Waterloopknndic Laboratorium, Delft, a Windgoot van het Laboratorium "de Voorst" Detailmeting aan de Luchterstroming S. 72-I, 1966; Varmegeving Luchtcirculatie-system windgoot, S. 72-II, 1966b.



EXPLOSION-GENERATED WATER WAVES

Bernard LeMéhauté
Tetra Tech, Inc.
Pasadena, California

I. INTRODUCTION: A review of the state of the art

This paper reviews recent developments concerning water waves generated by underwater explosions, with particular emphasis on the wave generation mechanism. Analytic models for predicting water waves from explosions in deep water are presented together with methods for improving our understanding of the wave generation mechanism.

A submerged detonation almost instantaneously produces hot gas or plasma within a limited volume. High temperatures and pressures result in two disturbances of the ambient fluid: emission of a shock wave traveling outward, which vaporizes a mass of water; and radial motion of the fluid, so that the "bubble," consisting of explosive debris and water vapor, begins to expand. At the same time, if undisturbed by bounding surfaces, it begins to rise due to its buoyancy.

During the expansion phase, pressure within the bubble falls considerably below the ambient hydrostatic pressure, owing to its outward momentum acquired by the water. The motion then reverses; the bubble contracts under hydrostatic pressure, [acquiring inward momentum and adiabatically compressing the central gas volume to a second -- but lower -- pressure.] Upon reaching its minimum diameter, several phenomena may occur: energy is radiated by the emission of a second shock wave; if near the free surface, the contracted bubble will not be spherical but may evert, the bottom rushing up and passing through the top; lastly, the surface of the contracting bubble is extremely unstable -- it may break up irregularly, forming a spray within the bubble.

The bubble may lose enough energy through repetitive expansions and contractions so that it collapses entirely, leaving a mass of turbulent warm water and explosion debris, and no waves of consequence will be generated. This case is typical for large, deeply submerged detonations, and will not be further discussed here.

For shallower explosions, the nature of ensuing surface

motions depends upon the phase with which the bubble reaches the surface. Depending upon the depth of the burst, these may include a well-formed hollow column, a very high, narrow jet, or a low, turbulent mound, followed by development of a prominent base surge. The duration of this "initial" disturbance may be quite great, starting from the first appearance of a mound as the bubble nears the free surface, to the collapse, under gravity, of the water thrown upwards. Base surge of plumes are not related to shock interaction. These phenomena are ultimately manifested by a system of water waves radiating from the location of the explosion.

If the water is of uniform depth, the wave system will have circular symmetry. Most of the energy of the explosion goes into the shock wave and local turbulence; only a small amount (10% at the most) actually appears in the ensuing water wave system.

As a result of its complicated origin, the initial disturbance comprises a broad, irregular spectrum. Since deep water is a dispersive medium, as the waves travel outwards, they will become sorted according to frequency; the longer waves running ahead, and the shorter waves trailing behind. A curve of wave period versus time at any distant location, therefore, will monotonically decrease.

In general, the energy distribution among the frequencies generated will not be uniform; the spectrum will be peaked near a frequency corresponding to a wave length which is a small multiple of the radius of the central disturbance.

At a fixed distance r from the explosion, if one measures the maximum amplitude η_{\max} of the envelope of the water waves generated by a given yield W as a function of burst depth, curves having the general shape shown in Fig. 1 will be obtained. These curves have two characteristic peaks.

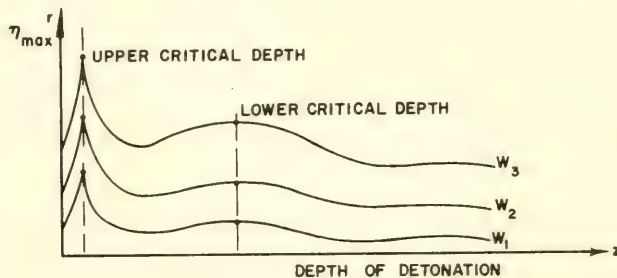


Fig. 1 A schematic illustration of the relationship between wave amplitude, range, depth-of-burst, and yield

The first peak is called upper critical depth (u.c.d.); the second one is the lower critical depth (l.c.d.). While there is so far no adequate theoretical explanation for the u.c.d., the l.c.d. is clearly analogous to the influence of burst depth on crater dimensions in solid materials, and is related to the balance between explosion energy going into cratering and that vented to the atmosphere.

Another interesting feature which has been experimentally observed is a change of phase between corresponding waves of trains generated by explosions above and below the upper critical depth. Such a change, in fact, is predicted between theoretical models of wave trains generated by an initial impulse acting on the surface and an initial surface elevation, respectively, suggesting that the impulse model may be more appropriate for explosions above the upper critical depth. The u.c.d. is a rather puzzling aspect of explosive wave generation. Abundant experimental data with HE charges within the range 0.5 - 300 lbs exhibit a large scatter under presumably identical conditions, η_{\max} varying between 0.5 - 2 times that at the l.c.d. Moreover, the scaled wave frequency at η_{\max} is uniformly higher, indicating a smaller effective source radius. Lastly, the existence of the u.c.d. is still somewhat in question for large explosions, since several attempts to reproduce it with 10,000 lb HE charges have been unsuccessful. It has been suggested (Kriebel [1968]) that the upper critical depth effect is obtained from interference between the direct incident shock wave and its reflected waves, resulting in more effective containment and greater cavity expansion than from deeper or shallower charges. As the detonation depth increases, the pressure impulse on the free surface has less and less effect on the cavity formation and ultimately becomes negligible. This undoubtedly influences the shape of a theoretical cavity, which produces an equivalent system of water waves, since the dimension of this cavity is closely related to both frequency and amplitude of the first envelope. Nevertheless, it appears that the large data scatter obtained under fixed experimental conditions at the upper critical depth are largely due to Taylor instability of the collapsing cavity.

The mathematical model described later can be adjusted to produce practically any type of wave train desired, by assuming various shapes for the initial cavity.

II. INPUT CONDITION

The theoretical formulation of an overall mathematical model for simulating the time history resulting from an underwater detonation is an extremely complicated task. However, keeping in mind the main objective of our problem -- the generation process of water waves -- many detailed phenomena, chemical or nuclear, can be ignored, retaining only the kinematic and dynamic features.

For example, one can consider only the following phases,

both of which are mathematically tractable.

The Compressible Hydrodynamic Phase The Incompressible Phase

The first is arrived at by defining the conditions which prevail at the location of the explosion and in its immediate neighborhood. The second makes use of this input as an initial condition to calculate the water waves at a distance far from the explosion.

2.1 The Compressible Hydrodynamic Phase

The compressible phase of an underwater detonation lasts for a relatively short time. Initially, upon detonation, there is immediate vaporization of water around the weapon due to intense radiation. This takes place in a time scale of microseconds. As the shock wave propagates outward, the bubble front initially coincides with the shock front (Fig. 2). Only the initial phase of the formation of the bubble need be considered compressible. Bubble migration, expansion, and collapse can be treated as incompressible,

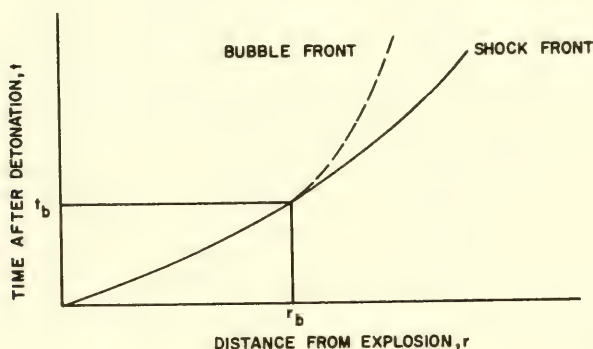


Fig. 2 Qualitative relationship between shock front and bubble front

or, perhaps more correctly, as quasi-incompressible, since subsequent shock waves are emitted at each minimum of the bubble history. It is obvious that, from the point of view of wave generation, the only problems of importance during the compressible phase concern the fluid motions generated in the vicinity of the bubble and the effect of reflected shocks. The early, compressible phase of bubble (cavity) expansion can be treated by the particle-in-cell technique, which has been successfully employed in many similar cases of compressible flow, both in fluids and in solids (Mader [1967]).

Again, it should be emphasized that the objective is to obtain an input condition for wave generation rather than to solve the many associated problems of bubble dynamics, shock propagation, and radioactive debris distribution. However, these problems cannot be ignored, inasmuch as they affect the wave generation process. Extensive work has been performed on bubble dynamics of both conventional and nuclear explosives (Snay [1966]). The energy partitioning between radioactive potential energy, thermal energy to heated and vaporized water, shock energy, and kinetic and potential bubble energy has been investigated by a number of authors (see, for example, DASIAC Special Report 104 - Secret). Detailed studies of shock propagation and pressure fields have been performed by many investigators. Some of these studies neglect the effect of gravity; others make gross assumptions about the thermodynamic properties of the bubble. But all of these effects should be included in an effective model for analyzing the wave generation process, unless it can be shown that they can be neglected because they do not affect the wave characteristics.

2.2 The Incompressible Phase

The input condition being defined by the compressible phase, the subsequent cavity behavior may be treated as incompressible flow. It is tentatively proposed to analyze the wave generation process through a numerical solution to the time-dependent, viscous, incompressible flow of a fluid with a free surface. Figure 3 is an experimental example of near-burst free surface history. The most

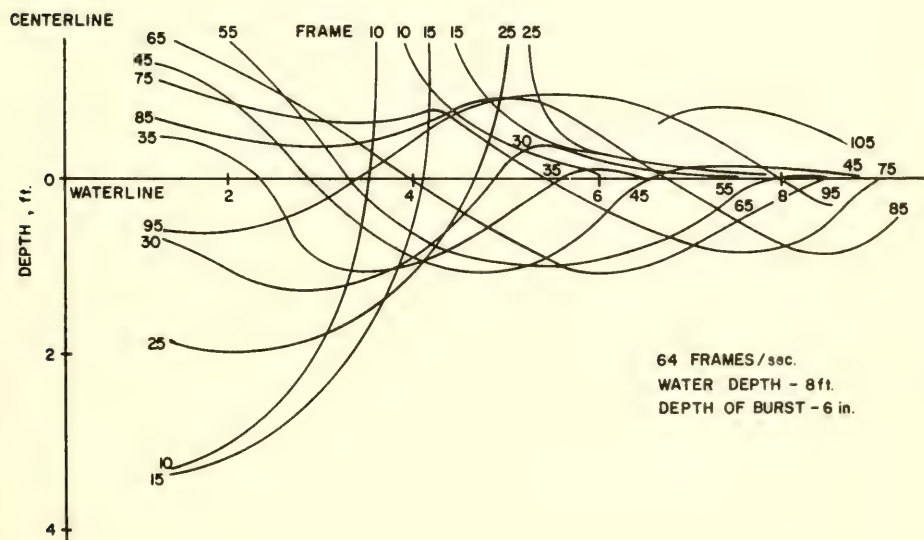


Fig. 3 Cavity shape versus time - shot 11 (Courtesy of URS)

promising method applicable to this problem seems to be the MAC Method developed by Harlow and his group at the Los Alamos Scientific Laboratory. Further study to improve both accuracy and efficiency (with respect to computer time) has led to development of other techniques, such as SUMMAC (Chan, et al. [1969]). Despite the degree of sophistication that has been achieved for treating free surface flow problems by numerical techniques, problems still remain which require some approximation. These are related to the amount of energy dissipated by viscous turbulence associated with the plume and base-surge radiating from the explosion. Energy dissipated by the radiating surge is similar to that in a tidal bore, except for the difference in water depth. The choice of a suitable viscosity coefficient that realistically accounts for turbulent dissipation can only be made empirically, and will be related to the mesh size of the numerical model. This choice is also subject to the constraint of numerical stability.

III. WATER WAVE FORMULATION

3.1 General Analytical Generation Model

Using the initial conditions obtained by the above methods, one can determine the water waves generated by such disturbance analytically.

The problem of surface waves generated by an arbitrary -- but localized -- disturbance of the free surface has been investigated by Kajiura [1963], who has derived very general solutions incorporating the effects of initial displacement, velocity, pressure, and bottom motion. Kranzer and Keller [1959] present a simplified approach through the assumption of radial symmetry. The two solutions are equivalent under appropriate conditions, but, because the former permits utilization of the previous methods in the form of a time-dependent input condition, the approach of Kajiura [1963] will be adopted here.

The problem may be formulated as follows. In water of constant depth D , the coordinate system is established with x^* and y^* in the horizontal plane of the undisturbed surface and z^* taken vertically upward; t^* is the time, $\eta^*(x^*, y^*, t^*)$ the surface elevation, $v^*(x^*, y^*, z^*, t^*)$ the particle velocity, and $p^*(x^*, y^*, z^*, t^*)$ the pressure. The motion is assumed irrotational, implying the existence of a potential function $\Phi(x^*, y^*, z^*, t^*)$. Dimensionless quantities are introduced as follows:

$$\begin{aligned} x &= x^*/D & y &= y^*/D & z &= z^*/D \\ t &= t^*\sqrt{g/D} & \eta &= \eta^*/D & v &= v^*/\sqrt{g/D} \\ \Phi &= \Phi^*/(D\sqrt{gD}) & p &= p^*/\rho g D \end{aligned}$$

where g is the gravitational acceleration.

Making use of Green's formula, Kajiura [1963] gives a solution of $\nabla^2 \Phi = 0$ satisfying bottom conditions ($\Phi_z = 0$, $z = -1$) and the linear free surface condition:

$$\begin{aligned} \Phi_\tau(x, y, z; \tau) = & 1/4\pi \iint_S \left(G \Phi_{\tau z_0} - \Phi_\tau G_{z_0} \right)_{z_0=0} dS_0 \\ & - 1/4\pi \iint_S \left(G \Phi_{\tau z_0} - \Phi_\tau G_{z_0} \right)_{z_0=-1} dS_0 \end{aligned} \quad (1)$$

where S denotes the source region, initial conditions are denoted by subscript zero and G is the appropriate Green's function; τ is a time associated with the generation period. The Green's function is:

$$\begin{aligned} G(x_0, y_0, z_0; \tau | x, y, z; t) = & \int_0^\infty \frac{J_0(k\bar{r})}{\cosh k} \left[\sinh k \left\{ 1 - |z - z_0| \right\} \right. \\ & - \sinh k \left\{ 1 + (z + z_0) \right\} \\ & \left. + \frac{2}{\omega^2} \left\{ 1 - \cos \omega(t - \tau) \right\} \frac{k}{\cosh k} \cosh k(1 + z) \cosh k(1 + z_0) \right] dk \end{aligned} \quad (2)$$

where \bar{r} is the horizontal distance between the source point (x_0, y_0) and the point under consideration (x, y) i.e.,

$$\bar{r}^2 = (x - x_0)^2 + (y - y_0)^2 \quad (3)$$

and

$$\omega^2 = k \tanh k. \quad (4)$$

Clearly, G is symmetric with respect to t and τ , and with respect to source and field points. The quantities ω and k are dimensionless frequency and wave number, respectively.

Applying the given boundary conditions and integrating Eq. (1) with $0 < \tau < t$ gives, after some calculation

$$\eta + p = \frac{1}{4\pi} \iint_S (F_1 + F_2) dS_0 \quad (5)$$

where

$$F_1 = (G_t \Phi_{z_0} - G_{\tau t} \eta)_{\tau=0} \quad z_0 = z = 0 \quad (6)$$

and

$$\begin{aligned} F_2 &= \int_0^t p G_{\tau \tau t} d\tau + (p G_{\tau \tau})_{\tau=t} \\ &= - \int_0^t p_{\tau} G_{\tau t} d\tau + (p G_{\tau t})_{\tau=0} \quad z_0 = z = 0 \end{aligned} \quad (7)$$

It can be seen that F_1 contains the contribution to η from the initial velocity and surface deformation of the source while F_2 represents the influence of initial pressure. Therefore, the model is very general; in fact, Kajiura [1963] gives an additional term representing the contribution from an arbitrary bottom disturbance, which is ignored here. It has been found, however, that such generality is not necessary in order to make practical predictions of water wave production. Instead, it is possible, for example, to absorb the effects of initial velocity and pressure into a fictitious initial surface deformation, chosen in such a way that the predicted waves are essentially the same as would be found using actual velocity, deformation and pressure.

3.2 Simplified Approach

The advantage of this approach in practical work will be apparent later in discussing the correlation between theory and experiment. The essential point, however, is that, instead of needing to predict the complicated phenomena leading to initial deformation, velocity and pressure, it may be sufficient to utilize easily measurable quantities to calibrate a simplified source model.

With this in mind, we rewrite Eq. (5) as a Green's function of time only:

$$\eta = \frac{1}{4\pi} \iint_S (-G_{\tau t} \eta)_{\tau=0} dS_0 \quad z_0 = z = 0 \quad (8)$$

Furthermore, it is reasonable to assume that, for a single explosion in water of constant depth, the problem is symmetric about the z -axis passing through the source. When the appropriate operations [in Eq. (8)] are performed, and the transformation to cylindrical coordinates (r, θ) is made, one obtains the time-and-space dependent surface elevation:

$$\eta(r, t) = \frac{1}{2\pi} \int_0^\infty k \cos \omega t \left\{ \int_0^{2\pi} \int_0^\infty \eta_0(r_0) J_0(kr) r_0 dr_0 d\theta_0 \right\} dk \quad (9)$$

where $\eta_0(r_0)$ is the initial deformation. Noting that

$$\bar{r}^2 = r^2 + r_0^2 - 2rr_0 \cos(\theta_0 - \theta) \quad (10)$$

the Bessel function $J_0(k\bar{r})$ may be rewritten according to Graf's addition theorem as

$$J_0(k\bar{r}) = J_0(kr)J_0(kr_0) + 2 \sum_{n \geq 1} J_n(kr)J_n(kr_0) \cos n(\theta_0 - \theta). \quad (11)$$

Integration with respect to θ_0 from zero to 2π deletes the summation so that

$$\eta(r, t) = \int_0^\infty k \cos \omega t J_0(kr) \left\{ \int_0^\infty \eta_0(r_0) J_0(kr_0) r_0 dr_0 \right\} dk. \quad (12)$$

The same result was obtained previously by Kranzer and Keller [1959] using integral transforms; in the literature dealing with radial dispersive waves, Eq. (12) is generally referred to as the Kranzer-Keller solution.

Equation (12) is a double integral solution that can be considerably simplified by additional approximations. In particular, for large r and t , $J_0(kr)$ may be replaced by an asymptotic cosine function, and the resulting integral approximated by the method of stationary phase (Stoker [1965]), to obtain

$$\eta(r, t) \approx \frac{1}{r} \sqrt{\frac{kV(k)}{-V'(k)}} \bigg|_{k=\lambda} \bar{\eta}(\lambda) \cos(\lambda r - t\sqrt{\lambda \tanh \lambda}) \quad (13)$$

where

$$\bar{\eta} = \int_0^\infty \eta_0(r_0) J_0(kr_0) r_0 dr_0 \quad (14)$$

is the zero-order Hankel transform of the initial elevation $\eta_0(r_0)$ and

$$V(k) = \frac{1}{2k} \sqrt{k \tanh k} + \frac{k}{2 \cosh^2 k} \frac{1}{\sqrt{k \tanh k}} \quad (15)$$

is the wave group velocity, and λ is the particular value of k for a given r and t found from:

$$V = r/t. \quad (16)$$

The problem now is to choose $\eta_0(r_0)$ in such a way, depending on water depth and explosion characteristics, that Eq. (13) best fits an observed wave train.

3.3 Time-Dependent Free Surface Deformation

Another possible mathematical model includes the kinetic and potential energy transmitted to the water by both the atmospheric overpressure and the gaseous expansion of the bubble. The initial conditions are now time-dependent, and at least one additional parameter (time) is added to the initial conditions.

While Eq. (13) gives the total energy partitioned to water waves as a function of detonation depth, as well as the distribution of energy amongst frequencies, the introduction of time-dependence, if properly used, permits a better fit to observations, not only for the first maximum of the wave envelope η_{\max} (and its corresponding wave number k_{\max}^*), but also to the whole shape of the wave envelope.

As an example of a time-dependent input condition, consider for example,

$$\eta_0(r_0, \tau) = \eta_0(r_0) \sin \frac{\pi}{2} \frac{\tau}{\tau_*} \quad (17)$$

where τ_* can be considered as the dimensionless period of first expansion of the crater cavity from an explosion (Whalin [1965]).

The initial surface velocity at time $\tau = 0$ is

$$\varphi_{z_0} \left| \begin{array}{l} z_0 = 0 \\ z = 0 \\ \tau = t = 0 \end{array} \right. = \frac{d\eta_0}{d\tau} \bigg|_{\tau=0} = \frac{\pi}{2\tau_*} \eta_0(r_0) \quad (18)$$

and the resulting wave train is given by

$$\eta(r, t) = \frac{\pi}{2\tau_*} \frac{\bar{\eta}(\lambda)}{r\sqrt{\tanh \lambda}} \sqrt{\frac{kV(k)}{-V'(k)}}_{k=\lambda} \sin (\lambda r - t\sqrt{\lambda \tanh \lambda}). \quad (19)$$

It is interesting to note that $\eta(r, t)$ is independent of real-time history of the free surface deformation and depends only upon its time derivative at time $\tau = 0$.

3.4 Main Features of the Mathematical Models

[Based on Eqs. (13) and (14)], typical examples of various models for initial surface deformations $\eta_0(r_0)$ are given in Table I. The first case, a parabolic water crater, is that proposed by Kranzer and Keller [1959].

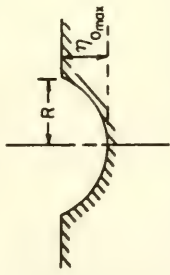
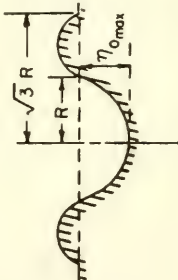
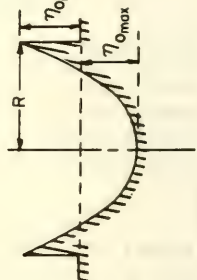
The general features of traveling wave trains given by the equations presented in Table I are:

- a. The waves travel radially from the explosion.
- b. The leading free surface disturbance or leading wave travels at velocity \sqrt{gD} .
- c. At a given location, the frequency of individual waves increases monotonically.
- d. The amplitudes of individual waves (cosine function in Eq. (12)) are modulated into groups of successively smaller amplitude by the slowly varying Bessel function $J_0(kr_0)$ in Eq. (14).
- e. The number of waves in a given group increases with time or distance traveled.
- f. The length of a group increases linearly with time or distance traveled.
- g. The frequency associated with a specific crest decreases with time or distance traveled (equivalently, a given crest moves forward within a group).
- h. The frequency associated with the maximum amplitude of a given group is constant.
- i. The maximum height of a given group decreases as the inverse of time or distance traveled.
- j. The maximum height of successive groups passing a given point decreases with time.

These features are partly illustrated in Fig. 4, which shows a computed wave train at three different locations. The general decay of wave height with distance is the result of both radial dispersion and circular spreading. This radial dispersion is characterized by a general increase in the wave length of individual waves with distance.

Wave crests occur when $\cos(\omega t - kr) = 1$ (Eq. (13)), and crest order numbers are given by $\omega t - kr = \pi(2n - 1)$ where n is an integer. It is also interesting to note that in the case of deep water, the trajectories of individual waves in the $r - t$ plane are defined by parabolae: $\pi(2n - 1) = gt^2/4r$, whose consecutive arrival times at any point r will be in the ratios $t:t/\sqrt{3}:t/\sqrt{5}$, etc. Similarly, at any instant of time t , the consecutive crest radii will have the ratios $r:r/3:r/5$, etc.

TABLE 1
WAVE FORMULATION AS FUNCTION OF INITIAL SURFACE DEFORMATION

Initial Surface Deformation		Resulting Wave Amplitude (Dimensionless)
Illustration	Functional Expression	
	$\eta_0(r_0) = \begin{cases} \eta_{0\max} \left[\left(\frac{r_0}{R} \right)^2 - 1 \right] & r_0 \leq R \\ 0 & r_0 > R \end{cases}$ <p>Parabolic Non-zero Net Volume Displacement</p>	$\eta(r, t) = A_1 \cos(kr - t\sqrt{k \tanh k})$ $A_1 = \frac{2\eta_{0\max}}{rk^2} J_2(kR) \left(\frac{kV(k)}{-dV/dk} \right)^{1/2}$
	$\eta_0(r_0) = \begin{cases} \eta_{0\max} \left[\frac{4}{3} \left(\frac{r_0}{R} \right)^2 - \frac{1}{3} \left(\frac{r_0}{R} \right)^4 \right] & r_0 \leq \sqrt{3} R \\ 0 & r_0 > \sqrt{3} R \end{cases}$ <p>Fourth-Degree with Lip Zero Net Volume Displacement</p>	$\eta(r, t) = A_2 \cos(kr - t\sqrt{k \tanh k})$ $A_2 = \frac{4\eta_{0\max}}{rk^2} J_4(\sqrt{3}kR) \left(\frac{kV(k)}{-dV/dk} \right)^{1/2}$
	$\eta_0(r_0) = \begin{cases} \eta_{0\max} \left[2 \left(\frac{r_0}{R} \right)^2 - 1 \right] & r_0 \leq R \\ 0 & r_0 > R \end{cases}$ <p>Parabolic with Lip Zero Net Volume Displacement</p>	$\eta(r, t) = A_3 \cos(kr - t\sqrt{k \tanh k})$ $A_3 = \frac{-\eta_{0\max} R}{rk} J_3(kR) \left(\frac{kV(k)}{-dV/dk} \right)^{1/2}$

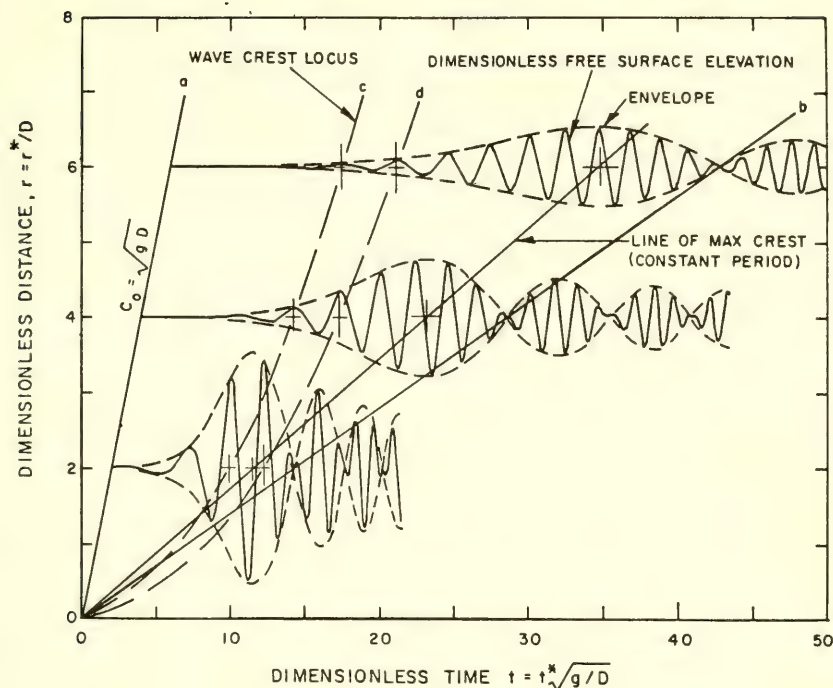


Fig. 4 Schematic drawing of wave trains as function of time at three different locations (Van Dorn, personal communication)

Based on this formulation, an equivalent crater size defined by its maximum depth $\eta_{0\max}$ and radius R can be empirically related to yield W and detonation depth as shown in the following.

However, the present formulation is oversimplified. The cavity shape (and not only its overall dimension) is a function of submergence depth and charge weight, and the phenomena of the upper critical depth is very sensitive to the manner in which the cavity is formed.

IV. CORRELATION WITH EXPERIMENTS

4.1 Practical Formulation

In Eq. (13) the cosine term represents the individual waves, while the remainder of the expression gives their varying amplitude or envelope which we shall call A :

$$A = \frac{\bar{\eta}}{r} \sqrt{\frac{kV(k)}{-V'(k)}} \quad (20)$$

in which it is understood that k is the root of Eq. (16)

It can be seen from Eq. (20) that for any fixed value of r , the least nonzero value of k for which $dA/dk = 0$ is independent of r ; this means that the maximum of the first wave envelope (where $dA/dk = 0$) is associated with a constant value of k (and, therefore, wavelength and period) throughout its propagation. This constant value of k at the first envelope maximum, k_{\max} depends only on the nature of the source disturbance $\eta_0(r_0)$ through the factor $\bar{\eta}(k)$.

Evaluating A at k_{\max} , we can write

$$A_{\max r} = \left\{ \bar{\eta}(k) \left(\frac{kV(k)}{-dV/dk} \right)^{1/2} \right\} \Big|_{k=k_{\max}} = \text{Constant} \quad (21)$$

for a particular source deformation $\eta_0(r_0)$, which means that the amplitude of the maximum waves is inversely proportional to r .

Before we can proceed with the quantification of the theoretical model, we must select an appropriate form of $\eta_0(r_0)$. The two constraints on this choice are, first, that the resulting wave envelope shape be sufficiently similar to observed shapes that some manipulation of numerical coefficients will give an accurate fit; and, second, that the Hankel transform of $\eta_0(r_0)$ be within our power to obtain in a closed form.

In addition, it would be nice -- although it is not really necessary -- to have $\eta_0(r_0)$ intuitively resemble the effective surface deformation due to an explosion. For all these reasons, we are led to try simple polynomials in r_0 for $\eta_0(r_0)$ with crater-like shapes.

Of the three forms which have been used in practical work (Table I), the last has been tentatively established as most suitable:

$$\eta_0(r_0) = \eta_{0\max} \left[2 \left(\frac{r_0}{R} \right)^2 - 1 \right] r_0 \leq R$$

$$0 \quad r_0 > R$$

where $\eta_{0\max}$ is a coefficient which, for the sake of simplicity, will be written as η_0 in the following.

The wave amplitude is then given by

$$\eta(r, t) = \frac{-\eta_0 R}{r} \left(\frac{V/k}{-dV/dk} \right)^{1/2} J_3(kR) \cos(kr - t\sqrt{k \tanh k}), \quad (22)$$

the two "cavity parameters" η_0 and R being embodied within our previous expression for the envelope amplitude, A . It is through empirical determination of these two parameters that we hope to correlate theory and experiment.

4.2 Experimental Correlation

While η_0 and R cannot be experimentally measured, they can be determined indirectly from k_{\max} and $\eta_{\max} r$, which are characteristic of the source disturbance, and also measurable. Hence, we seek to relate k_{\max} and $\eta_{\max} r$ to the characteristics of the explosion by experiment, and η_0 and R to k_{\max} and $\eta_{\max} r$ by theory. The expression giving k_{\max} in terms of η_0 and R is

$$\frac{dA}{dk} = 0 \quad (23)$$

since this expression defines the maxima of the wave envelope; the least non-zero value of k for which the above expression holds is k_{\max} .

For $k_{\max} > 3$ (relatively deep water), $\frac{V/k}{-dV/dk} = \sqrt{2} = \text{const}$,
and

$$A \approx \frac{\sqrt{2} \eta_0 R}{r} J_3(kR). \quad (24)$$

Therefore, k_{\max} can be determined from the first turning value of the Bessel function $J_3(kR)$; viz for

$$k_{\max} R = 4.20. \quad (25)$$

Our other measurable, $\eta_{\max} r$, may now be related to η_0 and R by evaluating A_{\max} (or η_{\max}) at $k = k_{\max}$. When this is done and the resulting expression is simplified, we have

$$\eta_0 R = 1.63 \eta_{\max} r. \quad (26)$$

All that remains now is to relate $\eta_{\max} r$ and k_{\max} to the characteristics of the explosion; these are W , explosive yield in pounds of TNT, Z , detonation depth in feet, and D , the water depth

in feet. A large volume of experimental data (with small chemical changes in relatively deep water) has been obtained at the Waterways Experimental Station, Vicksburg, Mississippi, from which the following empirical relations were deduced:

$$\text{u. c. d.} \quad \left[\begin{array}{l} \eta_{\max}^* r = 18 W^{0.54} \\ k_{\max}^* = 0.44 W^{-0.3} \end{array} \right] \quad 0 > \frac{Z}{W^{0.3}} \geq -0.25 \quad (27a)$$

$$\text{l. c. d.} \quad \left[\begin{array}{l} \eta_{\max}^* r \approx 10 W^{0.54} \\ k_{\max}^* = 0.39 W^{-0.3} \end{array} \right] \quad -0.25 \geq \frac{Z}{W^{0.3}} \geq -7.5 \quad (27b)$$

$$\text{Insufficient Data} \quad \frac{Z}{W^{0.3}} < -7.5 \quad (27c)$$

The products $\eta_{\max}^* r^*$ given above were determined from the empirical data of Fig. 5. Corresponding data for shallow water explosions and other aspects of explosion-generated waves in shallow water are beyond the scope of this presentation, and the reader is referred to LeMéhauté [1971].

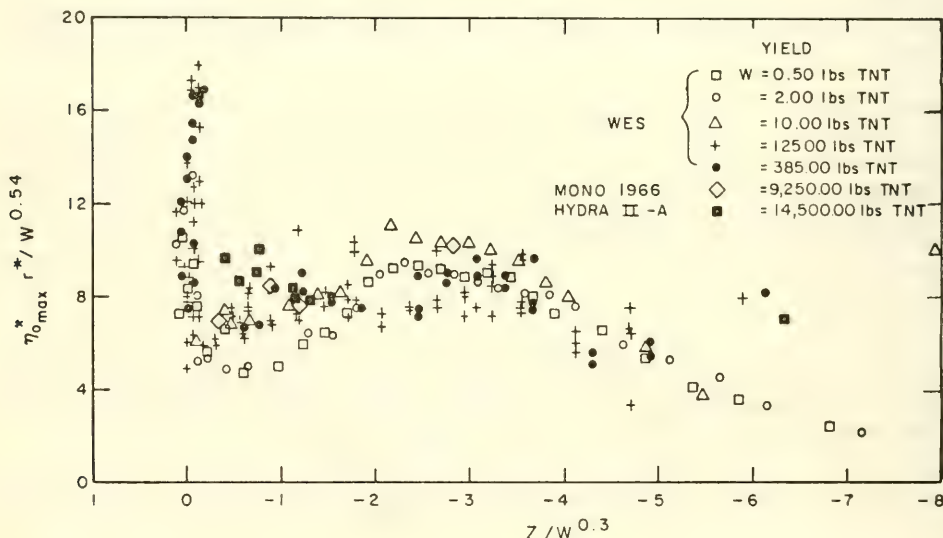


Fig. 5 An empirical scaling fit relating the maximum wave height η_{\max}^* with distance from explosion r^* , yield and depth of explosion (data provided by Waterways Experimental Station)

Figure 6 presents examples of the matching between theoretical wave envelope and wave records due to a 9,620 lb TNT explosion. The slight irregularities in the symmetry of the recorded wave trains are attributed to partial shoreline reflection interfering with the radiating wave trains (Hwang et al. [1969]). But, in general, the computed wave envelopes agree fairly closely with the observed amplitudes.

4.3 Limitations of the Model Due to Scale Effects

An examination of Fig. 5 reveals that the bulk of data upon which predictions are based are restricted to yields from one-half to a few hundred pounds of TNT. One wonders then just how reliable extrapolation to very large yield (say, 10^{10} pounds of TNT) would be. The limited data available from nuclear explosions is insufficient to resolve this problem. Comparison between crater data in soft materials for both nuclear and TNT explosions suggest that the laws of similitude may be applied to contained explosions but may not apply over a large yield range for venting detonations. In particular, the shock wave from a nuclear explosion travels much faster in air than in water, which is not the case for a TNT explosion.

We may infer several things, however, just from the nature of the scaling parameters given by Eq. (27). Consider, for example, the groups $\eta_{\max}^* r^* / W^{0.54}$ and $Z / W^{0.3}$. In each, the exponent of W was chosen to best compress the data of Fig. 5 into a single curve, since W represents an energy, dimensional analysis suggests that $\eta_{\max} r / (W/\rho g)^{1/2}$ and $Z / (W/\rho g)^{1/4}$ are appropriate scaling parameters, although similar conditions also require that other parameters, such as atmospheric pressure and sonic velocity in water, should also be scaled with yield. These conditions are never satisfied experimentally, and it is therefore not surprising that exponential scaling alone is not satisfactory. Moreover, the fact that the parametric coefficients vary with Z means that the phenomena are not simply scalable (Pace et al. [1969]). Lastly, the lack of evidence for an u.c.d. at large yields suggests that the generation process is fundamentally different.

For small yields (and subsequent small depth at burst) hydrostatic pressure is small compared to atmospheric pressure; for large yields the reverse is true. In the former extreme, dimensional analysis suggests $1/3$ power scaling; in the latter, $1/4$ power scaling. In an analogous review of earth crater scaling, (Chabai [1965]) has proposed an "overburden scaling law" in which the scaling exponent varies between these two extremes, but without convincing improvement in agreement to the experimental data.

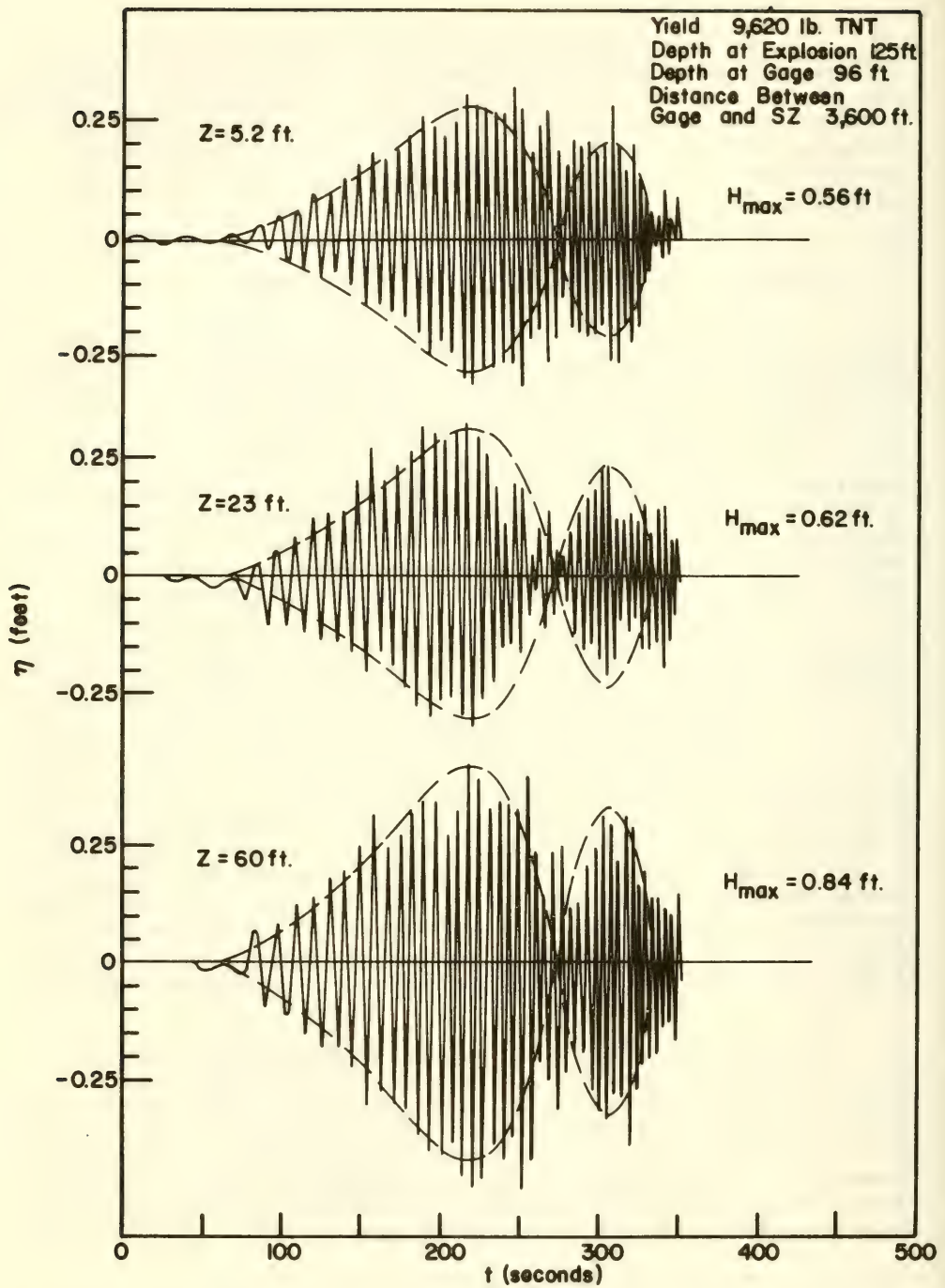


Fig. 6 Comparison of OSI 1966 Mono Lake experiments with theory

4.4 Energy Coupling

The deficiencies of simple exponential scaling are more apparent when considering the efficiency of energy coupling into water waves. The analytic source models discussed above are linear, and thus the total wave energy is equal to the potential energy of the source model; i.e., proportional to $\eta_0^2 R^2$. But, in view of Eq. (26), the empirical relations given in Eq. (27) imply that $\eta_0^2 R^2 \sim W^{1.08}$, which obviously cannot be true for all yields, since it states that wave energy increases faster than explosion energy under geometrically similar conditions. It is also pertinent to recall that the calculating of energy based on the theoretical source model may lead to a significant error; since only the first wave train has been watched with experiments, it may happen that the following wave train contains less energy than the theoretical model, as due the dissipative mechanism which influences the high frequency waves. Keeping in mind these reservations, it is found that the energy in the wave train is

$$E_W = 126 (\eta_{\max} r)^2 \text{ ft-lb.}$$

Then, inserting the value of $\eta_{\max} r$ in terms of yield and water depth, it is found that at lower critical depth, the efficiency e is

$$e = 0.0074 W^{0.07} \approx 1\% \quad (W \text{ is in pounds}).$$

At upper critical depth, the increase of efficiency with yield within the range of available experiments is even more pronounced. For example, e which is 1% in the case of 0.5 lbs of TNT has been found to be 6% in the case of an explosion of 375 pounds, which implies that $\eta r \approx W^{0.61}$ at upper critical depth. Such results cannot, of course, be extrapolated to atomic yield.

Since the fraction of yield energy appearing as waves is only a few per cent for the largest tests so far conducted, we are faced with the problem of trying to distinguish very small energy differences in normalizing analytic models to actual experiments. While the present models provide adequate predictions for the largest waves over an impressive range of yields (0.5 - 64,000,000 lbs TNT equivalent), it is recognized that important phenomenological factors, such as atmospheric pressure, shock interaction, and cavity stability have been neglected, each of which can reasonably be expected to influence wave formation to some extent. What is really surprising is that such simple models work as well as they do, considering the great complexity of the process of explosive wave generation.

ACKNOWLEDGMENT

The writer has had the opportunity of collaborating with a number of researchers who have deeply contributed to establishing the present state of the art. The original contributions of Dr. Li-San Hwang, Manager of the Hydrodynamics Group at Tetra Tech, Inc. and Mr. David Divoky have been of invaluable assistance in assembling and editing this material and verifying formulation and notation. Dr. William Van Dorn of Scripps Institution of Oceanography and Mr. Robert Whalin of the Waterways Experiment Station have also significantly contributed to the contents. Dr. Van Dorn revised this manuscript and made many most pertinent suggestions. Mr. John Strange provided the writer with the set of experimental data on wave generation obtained by the Waterways Experiment Station. This study was sponsored by the Office of Naval Research, Contract No. N00014-68-C-0227, under the technical management of Mr. Jacob L. Warner.

REFERENCES

- Chabai, A. J., "On scaling dimensions of craters produced by buried explosives," *J. Geophys. Res.*, vol. 70, no. 20, pp. 5075-5098, 1965.
- Chan, R. K. C., Street, R. L. and Strelkoff, T., "Computer studies of finite amplitude water waves," *Tech. Report No. 104*, Stanford University, ONR Contract No. Non 255(71)NR-62-320, June, 1969.
- Hwang, L.-S., Fersht, S. and Le Méhauté, B., "Transformation and run-up of tsunami type wave trains on a sloping beach," *Proc. 13th Congress I.A.H.R.*, vol. 3, pp. 131-140, 1969.
- Kajiura, K., "The leading waves of tsunami," *Bull. of Earthquake Res. Inst.*, vol. 41, pp. 535-571, 1963.
- Kranzer, H. C. and Keller, J. B., "Water waves produced by explosions," *J. App. Physics*, vol. 30, no. 3, 1959.
- Kreibel, A. R., "Cavities and waves from explosions in shallow water," *URS Research Co., Report No. URS-679-5*, DASA Contract No. N0014-67-C-045, 1968.
- Mader, C. L., "Fortran BKW: a code for computing the detonation properties of explosives," *Los Alamos Scientific Laboratory of the University of California Report No. LA-3704* under Atomic Energy Commission Contract No. W-7405-ENG. 36, 1967.

- Le Méhauté, B., "Explosion-generated water waves," *Advances in Hydrosiences*, Academic Press, New York (publication pending), 1971.
- Pace, C. E., Whalin, R. W., Sakurai, A. and Strange, J. N., "Surface waves resulting from explosions in deep water," Report No. 4, Waterways Experiment Station, Vicksburg, Mississippi, 1969.
- Snay, H. G., "Hydrodynamic concepts selected topics for underwater nuclear explosions," NOL TR 65-52, DASA-1240-1(2) U.S. Naval Ordnance Laboratory, September 15 (AD-803-113), 1966.
- Stoker, J. J., "Water waves," Interscience Publishers, Inc., New York, New York, 1957.
- Whalin, R. W., "Contributions to the Mono Lake Experiments," NESCO Report S 256-2, ONR Contract No. Nonr-5006(00), 1965.
- Whalin, R. W., "Research on the generation and propagation of water waves produced by underwater explosions (U)," National Marine Consultants Report NMC-ONR-64, Part II: A Prediction method (CONFIDENTIAL), 1965.

HYDRODYNAMICS IN THE OCEAN ENVIRONMENT

Monday, August 24, 1970

Afternoon Session

Chairman: J. Wehausen
University of California, Berkeley

	Page
Resonant Response of Harbors (The Harbor Paradox Revisited) J. W. Miles, University of California, San Diego	95
Unsteady, Free Surface Flows; Solutions Employing the Lagrangian Description of the Motion C. Brennen, A. K. Whitney, California Institute of Technology	117
Two Methods for the Computation of the Motion of Long Water Waves -- A Review and Applications R. L. Street, R. K. C. Chan, Stanford University, and J. E. Fromm, IBM Corporation	147
An Unsteady Cavity Flow D. P. Wang, The Catholic University of America	189

RESONANT RESPONSE OF HARBORS (THE HARBOR PARADOX REVISITED)

John W. Miles
*University of California
San Diego, California*

I. INTRODUCTION

We consider the surface-wave response of a harbor to a prescribed, incident wave in an exterior half-space on the hypothesis of linearized, shallow-water theory, an ideal fluid, and a narrow mouth, invoking the equivalent-circuit techniques that have proved so efficient in attacking analogous problems in acoustics and electromagnetic theory. These techniques offer significant advantages in practice: (i) the sub-problems of external radiation, channel coupling, and internal resonance may be attacked separately; (ii) the equivalent-circuit parameters may be expressed as homogeneous, quadratic forms that may be simply approximated without solving the complete boundary-value problem; (iii) observed values (including those from model experiments) of dominant parameters, such as resonant frequencies, may be incorporated in preference to, or in place of, theoretical values; (iv) empirically determined dissipation parameters (resistances) may be incorporated; (v) analog computation, both conceptual and electrical, may be invoked to expedite understanding of the resonant response.

Referring to Fig. 1, we consider a harbor H that opens to the sea through a narrow mouth M in a straight coastline, $x = 0$. Let

$$\zeta_i(x, y) = \frac{1}{2} V_i \exp \{-jk(x \cos \theta_i + y \sin \theta_i)\} \quad (1.1)$$

and

$$\zeta_r \equiv \zeta_i(-x, y) \quad (1.2)$$

be the complex amplitudes of the incident and specularly reflected

[†] A more detailed version of this work has been published elsewhere [Miles, 1971].

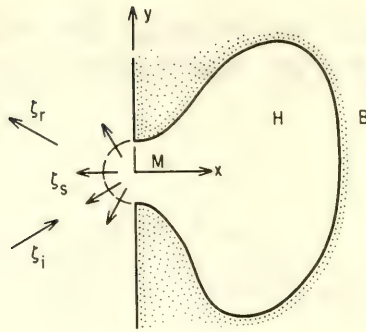


Fig. 1. Schematic diagram of harbor opening on straight coast line; ζ_i , ζ_r and ζ_s are, respectively, the incident, specularly reflected, and scattered waves

(from $x = 0$) waves on the hypothesis of the monochromatic time dependence $\exp(j\omega t)$, where ζ denotes free-surface displacement (we omit the modifier complex amplitude of throughout the subsequent development), k is the wave number, and $V_i \equiv 2\zeta_i(0,0)$ is a measure of the excitation of the harbor through M . By narrow, we imply

$$a/R \ll 1 \quad \text{and} \quad ka \ll 1, \quad (1.3a,b)$$

where a is the width of M , and R is a characteristic dimension of H . These restrictions imply that the motion within H is small, and that the energy of the motion induced by V_i (or, more precisely, by the pressure $\rho g V_i$) is dominantly kinetic and concentrated near M (the narrowness of which implies locally high velocities), except in the spectral neighborhoods of the resonant frequencies of the harbor. An appropriate measure of this dominant motion is the flow through M , say I , which, by hypothesis (linearized theory), must be simply proportional to V_i . We regard V_i and I as the voltage and current at the input terminals of an equivalent circuit and seek a description of the resonant response of the harbor in terms of the voltages induced in this equivalent circuit.

The input impedance, $Z_i \equiv V_i/I$, for the configuration of Fig. 1 may be resolved (see Fig. 2a) into a series combination of a radiation impedance, $Z_M \equiv R_M + jX_M$, and a harbor impedance, $Z_H \equiv jX_H$, where $R_M |I|^2$, $X_M |I|^2/\omega$, and $X_H |I|^2/\omega$ are respectively proportional to the power radiated from H through M (in the form

of a scattered wave, ζ_s), the non-radiated energy stored in the exterior half-space, and the energy stored in the harbor (we also could incorporate an empirical, resistive component in Z_H , say R_H , to account for an energy dissipation proportional to $R_H|I|^2$). We infer from the solution of the corresponding acoustical radiation problem [Miles 1948; §3 below] that both R_M and X_M are bounded, positive-definite functions of ω , by virtue of which we may regard them as single resistive and inductive elements, respectively (although neither R_M nor X_M has the same frequency dependence as its elementary, electrical counterpart). We infer from the analogy with the corresponding acoustical resonator [Morse 1948, §23] that Z_H comprises an infinite sequence of parallel combinations of inductance L_n and capacitance C_n , which bear a one-to-one correspondence to the natural modes of the closed harbor and resonate at the corresponding frequencies, $\omega_n \equiv (L_n C_n)^{1/2}$, together with a single capacitor C_0 , which corresponds to the degenerate mode of uniform displacement, for which $\omega_0 \equiv 0$. The solution within H may be expanded in this infinite set of modes, with the root-mean-square displacement and the kinetic and potential energies in the n 'th mode being proportional to the voltage across C_n and the energies stored in L_n and C_n , respectively. The arguments of the preceding paragraph suggest that the individual modal impedances are important only in the neighborhoods of their respective resonant frequencies, and hence that Z_H may be approximated in the neighborhood of $\omega = \omega_n$ by a lumped inductance, say L_H , in series with either C_0 or the single, parallel combination of L_n and C_n , such that the energy in all modes but the n 'th is proportional to $L_H|I|^2$. The corresponding equivalent circuit is shown in Fig. 2b (we give a quantitative derivation of this equivalent circuit in §§2 and 3).

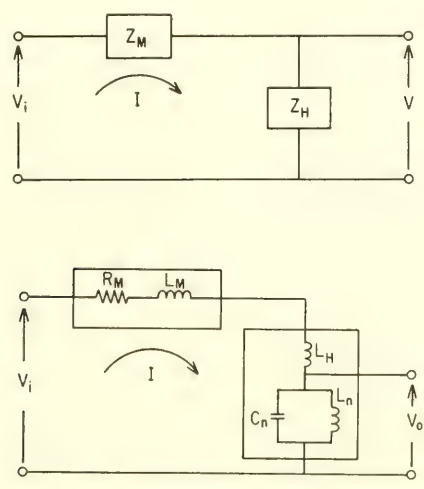


Fig. 2. Equivalent circuit for harbor opening directly at coastline: (a) implied by (3.2); (b) implied by (3.2) and (4.6).

The voltage-amplification ratio, $Q_n \propto |V_n/V_i|$, provides a measure of the resonant response in the neighborhood of $\omega = \omega_n$. The zero'th mode, in which the harbor acts like a Helmholtz resonator, is unique in that the equivalent circuit reduces to a series combination of R_M , $L_M + L_H$, and C_0 and exhibits a simple, series-resonant behavior with a resonant frequency, say $\tilde{\omega}_0$, that is determined by a balance between the potential energy stored in H , $\frac{1}{2} C_0 |V_0|^2$, and the kinetic energy stored in the vicinity of M , $\frac{1}{2} (L_M + L_H |I|^2)$. The results for the rectangular harbor [Miles and Munk 1961] suggest that the sharpness of the Helmholtz resonance is measured by

$$\delta = \{\log (R/a)\}^{-1} \quad (1.4)$$

and that

$$\tilde{\omega}_0 = O(\delta^{1/2}), \quad \tilde{Q}_0 = O(1/\delta), \quad \text{and} \quad Q_0 = O(1/\delta) \quad (1.5a, b, c)$$

as $a/R \rightarrow 0$, where \tilde{Q}_n is the peak value of Q_n , and Q_n is the ratio of the resonant frequency to the half-power bandwidth of the resonance curve for the n 'th mode.

The resonant response of the harbor in the higher modes is strikingly different than that of a simple, series-resonant circuit in consequence of the proximity of the parallel-resonant frequency, ω_n , at which $Z_1 = \infty$, and the series-resonant frequency, $\tilde{\omega}_n$, at which $|Z_1|$ has a minimum and $Q_n = \tilde{Q}_n \gg 1$. We show in §4 that

$$\tilde{\omega}_n = \omega_n + O(\delta), \quad \tilde{Q}_n = O(1/\delta), \quad \text{and} \quad Q_n = O(1/\delta^2) \quad (n \neq 0) \quad (1.6a, b, c)$$

It follows from (1.5) and (1.6) that narrowing the harbor mouth does not affect the mean-square response to a random excitation in the spectral neighborhood of $\omega = \omega_n$ (which response is proportional to $\tilde{\omega}_n \tilde{Q}_n^2 / Q_n$ if the bandwidth of the random input is large compared with $\delta \omega_n$) except in the Helmholtz mode, but that the response in that mode increases inversely as $\delta^{1/2}$. Miles and Munk [1961] overlooked the proximity of parallel and series resonance in the higher modes and arrived at the erroneous conclusion that narrowing the harbor mouth would increase $\tilde{\omega}_n \tilde{Q}_n^2 / Q_n$ for all modes, rather than only the Helmholtz mode, and designated the phenomenon as "the harbor paradox." In fact, as pointed out by Garrett [1970], this qualitative conclusion is inconsistent with their quantitative results, which actually imply (1.6) for the higher modes in a narrow rectangular harbor. Garrett also showed that $\tilde{\omega}_n \tilde{Q}_n^2 / Q_n$ is similarly invariant for excitation of a circular harbor through an open bottom and correctly conjectured that the result holds generally for the higher modes in any harbor. In brief, the harbor paradox originally stated by Miles and Munk

holds only for the Helmholtz mode and otherwise must be replaced by the weaker paradox that narrowing the harbor mouth has no effect on the mean-square response of the higher modes to a random input in the absence of friction (narrowing the mouth increases friction, thereby decreasing the response, in a real harbor). It follows that the higher modes are not likely to be strongly excited, but that the Helmholtz mode may dominate the response of a harbor to an exterior disturbance that has significant energy in the spectral neighborhood of ω_0 .

Carrier, Shaw and Miyata [1970] consider a harbor that communicates with the coast through a narrow canal and find that both \tilde{Q}_0 and Q_0 are significantly increased (as might be inferred from the analogy with the classical Helmholtz resonator; cf. Rayleigh [1945], §307). We show in §5 that such a canal is analogous to an electrical transmission line and may be replaced by a symmetrical, four-terminal network for the calculation of V_n (see Fig. 3). The analogy with the transmission line rests on the hypothesis that only plane waves are excited in the canal. An examination of the effects of higher modes shows that the elements of the four-terminal network may be appropriately generalized, but that the plane-wave approximation is likely to be adequate if the breadth of the channel is less than a half-wavelength.

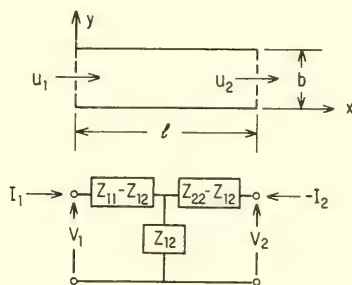


Fig. 3. Canal and equivalent circuit for the plane-wave approximation. The impedances $Z_{11} = Z_{22}$ and Z_{12} are given by (5.4)

The precise determination of Z_M and Z_H requires the solution of an integral equation for the normal velocity in M (or, in the case of an intervening canal, a pair of integral equations for the normal velocities across the terminal sections of the canal). The formulation of §§2 and 3 yields variational approximations to Z_M and Z_H that are invariant under a scale transformation (i.e. a

change in the mean value) of the velocity in M and stationary with respect to first-order variations of this velocity about the true solution to the integral equation (cf. Miles and Munk [1961] and Miles [1946, 1948, 1967]; we omit the explicit formulation of the integral equation and further discussion of the variational principle in the present development). The resulting representation of Z_M is relatively insensitive to the geometry of H and yields a simple, explicit approximation that depends essentially only on ka . The corresponding representation of Z_H requires Green's function (subject to a Neumann boundary condition) for the closed harbor, the explicit, analytical construction of which is possible only for those boundaries (rectangular, circular or circular-sector, and elliptic or elliptic-hyperbolic sector) that permit separation of variables; however, we may infer the matrix representation of this Green's function for a polygonal approximation to an arbitrarily shaped harbor from Lee's [1971] collocation solution of the general problem. We give explicit results for a circular harbor in §6 with special emphasis on the Helmholtz mode. It appears from these results that a large harbor with a short entrance or a small harbor with an entry canal of length comparable with R may resonate in the Helmholtz mode under tsunami excitation.

II. HARBOR IMPEDANCE

Let x and y be the Cartesian coordinates in the free surface, t the time, ω the angular frequency, h the depth,

$$c = (gh)^{1/2} \quad \text{and} \quad k = \omega/c \quad (2.1a, b)$$

the wave speed and wave number, $\hat{\zeta}$ the free-surface displacement, \hat{u} the x -component of the particle velocity, ζ and u the corresponding complex amplitudes, such that

$$\{\hat{\zeta}(x, y, t), \hat{u}(x, y, t)\} = \Re[\{\zeta(x, y), u(x, y)\} e^{j\omega t}], \quad (2.2)$$

where \Re implies the real part of and $j \equiv \sqrt{-1}$,

$$I = \int_M u \, dS \quad (dS = h \, dy) \quad (2.3)$$

the flow through M ,

$$V = \left(\int_M u^* \, dy \right)^{-1} \int_M \zeta u^* \, dy \quad (2.4)$$

a weighted measure of the displacement in M , where u^* is the

complex conjugate of u ,

$$Z_H \equiv V/I = h^{-1} \left| \int_M u \, dy \right|^2 \int_M \zeta u^* \, dy \quad (2.5)$$

the harbor impedance, and

$$P = \frac{1}{2} R \{ \rho g h \int_M \zeta u^* \, dy \} = \frac{1}{2} \rho g R (VI^*) \quad (2.6)$$

the rate at which energy flows through M . We may regard αV , βI , $(\alpha/\beta)Z_H$, and $\alpha\beta R(VI^*)$ as the voltage, current, impedance, and power in an equivalent electrical circuit, where the constants of proportionality, α and β , may be chosen to obtain convenient electrical units. The choice $\alpha = \beta = 1$ is implicit in the discussion in §1, but not in what follows except as noted.

Solving the shallow-water equations (Lamb [1932], §189) for an assumed velocity in M , subject to the boundary condition that the normal derivative of ζ , $\underline{n} \cdot \nabla \zeta$, vanish on B , the lateral boundary of the free surface in H , we obtain

$$\zeta(x, y) = (j\omega/g) \int_M G(x, y; 0, \eta) u(0, \eta) \, d\eta \quad (2.7)$$

where

$$G(x, y; \xi, \eta) = \sum_n (k_n^2 - k^2)^{-1} \psi_n(x, y) \psi_n(\xi, \eta), \quad (2.8)$$

is the point-source Green's function for H , the ψ_n are the normalized eigenfunctions for the closed harbor, and the summation is over the complete set of these functions. The ψ_n are real and satisfy

$$(\nabla^2 + k_n^2) \psi_n = 0 \quad (x, y \text{ in } H), \quad (2.9a)$$

$$(\underline{n} \cdot \nabla) \psi_n = 0 \quad \text{on } B, \quad (2.9b)$$

and

$$\int_H \psi_m \psi_n \, dA = \delta_{mn}, \quad (2.9c)$$

where k_n are the eigenvalues (resonant wave numbers), and δ_{mn} is the Kronecker delta. We designate the degenerate (but non-trivial)

solution corresponding to $\psi = \text{const.}$ by $n = 0$:

$$k_0 = 0, \quad \psi_0 = A^{-1/2}, \quad (2.10)$$

where A is the area of H . We also note that more explicit results may require the use of two indices to count off the individual modes.

The exact determination of the assumed velocity $u(0, y)$ requires u and ζ to be matched across M to the corresponding solution of the exterior boundary-value problem (see §3 below). This matching condition yields an integral equation for $u(0, y)$, the exact solution of which in finite terms does not appear to be possible; however, simple approximations to $u(0, y)$ are capable of yielding excellent approximations to Z_M and Z_H by virtue of the associated variational principle (cf. Miles [1946, 1948, 1967] and Miles and Munk [1961]). We proceed directly to such approximations by introducing the normalized trial function $f(y)$, such that

$$u(0, y) = (I/h)f(y), \quad \int_M f(y) dy = 1, \quad (2.11a, b)$$

In the subsequent development, we neglect the dependence of $f(y)$ on k and assume that it depends only on the geometry of M . The validity of this approximation, which also implies that $f(y)$ is real, depends essentially on the antecedent approximation $ka \ll 1$.

Substituting (2.11) into (2.4) and (2.7), combining the results in (2.5), and invoking (2.8), we obtain

$$V = \int_M \zeta f^* dy \quad (2.12)$$

and

$$Z_H = \sum_n Z_n, \quad (2.13)$$

where

$$Z_n = \left(\frac{j\omega}{\omega_n^2 - \omega^2} \right) \left| \int_M \psi_n f dy \right|^2 \equiv \left(\frac{j\omega}{\omega_n^2 - \omega^2} \right) \left(\frac{\mu_n}{A} \right) \quad (2.14)$$

is the modal impedance, and μ_n is a dimensionless measure of the excitation of the n 'th mode through M (note that $\mu_0 \equiv 1$ and $Z_0 = 1/j\omega A$). The Z_n in the equivalent circuit appear in series, Z_0 as a capacitor, and each of the remaining Z_n as a parallel combina-

tion of an inductor and capacitor, $L_n = \mu_n/(\omega_n^2 A)$ and $C_n = A/\mu_n$. The dominant terms in Z_H as $\omega \rightarrow 0$ are Z_0 and the sum of the inductive reactances obtained by neglecting ω^2 relative to ω_n^2 in the remaining Z_n .

III. RADIATION IMPEDANCE

The solution of the shallow-water equations in the exterior half-space ($x < 0$) for a prescribed incident wave, say $\zeta_i(x,y)$, and the assumed velocity $u(0,y)$ in the harbor mouth is given by [Miles and Munk 1961]

$$\zeta(x,y) = \zeta_i(x,y) + \zeta_i(-x,y) + \zeta_s(x,y), \tag{3.1a}$$

where

$$\zeta_s(x,y) = -\frac{1}{2}(\omega/g) \int_M H_0^{(2)}[k(x^2 + |y-\eta|^2)^{1/2}] u(0,\eta) d\eta \quad (x \leq 0), \tag{3.1b}$$

$H_0^{(2)}$ is a Hankel function, the first two terms on the right-hand side of (3.1a) give the solution for total reflection from the plane $x = 0$ (as would occur if M were closed), and ζ_s is the scattered wave. Substituting u into (3.1) from (2.11), setting $x = 0$, and then substituting the result into (2.12), we obtain

$$V = V_i - Z_M I, \tag{3.2}$$

where

$$V_i = 2 \int_M \zeta_i f^* dy \tag{3.3a}$$

$$\doteq 2\zeta_i(0,0) \quad (ka \ll 1) \tag{3.3b}^\dagger$$

is the equivalent exciting voltage of the incident wave, and

$$Z_M = \frac{1}{2}(\omega/c^2) \int_M \int_M H_0^{(2)}(k|y-\eta|) f^*(y) f(\eta) d\eta dy \tag{3.4}$$

[†]The definition of V_i implicit in (1.1) corresponds to the approximation (3.3b).

is the radiation impedance of the harbor mouth. The equivalent circuit corresponding to (3.2) is sketched in Fig. 2a.

The velocity distribution in M for $ka \ll 1$ corresponds to that for potential flow. Normalizing this distribution according to (2.11b), we obtain

$$f(y) = \pi^{-1} [(\frac{1}{2}a)^2 - y^2]^{-1/2} \quad (|y| < a). \quad (3.5)$$

Substituting (3.5) into (3.4) and invoking $ka \ll 1$, we obtain

$$Z_M = (\omega/c^2) [\frac{1}{2} + j\Lambda_M(ka)] \quad (ka \ll 1), \quad (3.6)$$

where

$$\pi\Lambda_M = \ln [8/(\gamma ka)], \quad (3.7)$$

and $\ln \gamma = 0.577\dots$ is Euler's constant.

IV. RESONANT RESPONSE

An appropriate measure of the response of the harbor to a prescribed incident wave is the mean-square elevation, say σ^2 , as determined by averaging over both space and time (the temporal average of ζ^2 is $\frac{1}{2}|\zeta|^2$):

$$\sigma^2 = \frac{1}{2} A^{-1} \int_H |\zeta|^2 dA. \quad (4.1)$$

Substituting ζ into (4.1) from (2.7), invoking (2.8) for G and (2.11) for u , carrying out the integration over A with the aid of (2.9c), and invoking (2.14) for $Z_n = V_n/I$, where V_n is the voltage induced across Z_n by I , we obtain

$$\sigma^2 = \frac{1}{2} \sum_n \mu_n^{-1} |V_n|^2 \equiv \frac{1}{2} |V_i|^2 \sum_n G_n^2(\kappa), \quad (4.2)$$

where

$$G_n(\kappa) \equiv \mu_n^{-1/2} |V_n/V_i| = \mu_n^{-1/2} |Z_n/(Z_M + Z_H)| \quad (4.3)$$

is the amplification factor for the n 'th mode, and

$$\kappa \equiv k^2 A = \omega^2 (A/gh) \quad (4.4)$$

is a dimensionless measure of (the square of) the frequency (similarly, $\kappa_n \equiv k_n^2 A$). Invoking (3.3b) on the hypothesis $a^2/A \ll 1$, we obtain $\sigma_i^2 = \frac{1}{2} |V_i|^2$ for the (temporal) mean-square elevation of $2\zeta_i$, by virtue of which (4.2) reduces to

$$\sigma^2 = \sigma_i^2 \sum_n Q_n^2(\kappa). \quad (4.5)$$

The hypotheses (1.3a,b) imply $|Z_n| \ll |Z_M + Z_H|$ for each of the modal impedances in the summation of (2.13) except in the neighborhood of $\kappa = \kappa_n$, where the sum may be approximated by

$$Z_H \doteq (j\omega/c^2) [\Lambda + \mu_n(\kappa_n - \kappa)^{-1}], \quad (4.6a)$$

where

$$\Lambda_H = \sum_m \mu_m \kappa_m, \quad (4.6b)$$

$m = 0$ being excluded from the summation. Invoking (2.14), (3.6), and (4.6) in (4.3), we obtain

$$Q_0(\kappa) = \left\{ \frac{1}{4} \kappa^2 + [\kappa \Lambda_0(\kappa) - 1]^2 \right\}^{-1/2} \quad (4.7a)$$

and

$$Q_n(\kappa) = \mu_n^{1/2} \left\{ \frac{1}{4} (\kappa - \kappa_n)^2 + [(\kappa - \kappa_n) \Lambda_n - \mu_n]^2 \right\}^{-1/2}, \quad (4.7b)$$

where

$$\Lambda_0(\kappa) = \Lambda_H + \Lambda_M(\kappa a), \quad (4.8a)$$

$$\Lambda_n = \Lambda_H + \Lambda_M(\kappa_n a) \quad (n \neq 0). \quad (4.8b)$$

The peak values of Q_n are given by

$$Q_0 = 2\tilde{\kappa}_0^{-1} \quad \text{and} \quad Q_n = 2\mu_n^{-1/2} \Lambda_n \quad (n \neq 0), \quad (4.9a,b)$$

where $\kappa = \tilde{\kappa}_n$ is the series-resonant point determined by

$$\tilde{\kappa}_0 \Lambda(\tilde{\kappa}_0) = 1 \quad \text{and} \quad \tilde{\kappa}_n = \kappa_n + \mu_n \Lambda_n^{-1} \quad (n \neq 1). \quad (4.10a,b)$$

The amplification factor drops off sharply on both sides of $\kappa = \tilde{\kappa}_n$

and is $O(1/\Lambda_n)$ for $|\kappa - \kappa_n| \gg 1/\Lambda_n$. The point $\kappa = \kappa_n$ corresponds to parallel resonance ($Z_n = \infty$), for which the total flow through M vanishes ($I = 0$) whilst σ^2 remains of the same order as σ_1^2 . We define the Q of the resonant response near $\kappa = \tilde{\kappa}_n$ as the ratio of the resonant frequency to the half-power bandwidth, such that [the frequencies at the half-power points are proportional to $\tilde{\kappa}_n^{1/2}(1 \pm \frac{1}{2} Q_n^{-1})$]

$$G[\kappa_n(1 \pm Q_n^{-1})] = 2^{-1/2} \tilde{G}_n. \quad (4.11)$$

Substituting (4.7) into (4.11) and invoking (4.10), we obtain the first approximations

$$Q_0 = 2\tilde{\kappa}_0^{-1} = \tilde{G}_0 \quad (4.12a)$$

and

$$Q_n = 2\mu_n^{-1} \kappa_n \Lambda_n^2 = \frac{1}{2} \tilde{\kappa}_n \tilde{G}_n^2. \quad (4.12b)$$

Now suppose that the incident wave is random with the power spectral density $S_i(f)$, such that

$$\sigma_1^2 = \int_0^\infty S_i(f) df \quad (\omega = 2\pi f), \quad (4.13)$$

where f is the frequency. Generalizing (4.5), we obtain

$$\sigma^2 = \sum_n \int_0^\infty S_i(f) |G_n(\kappa)|^2 df \quad (4.14)$$

for the power spectral density in the harbor. Substituting (4.7) into (4.14), invoking $\omega = c\kappa/\sqrt{A}$, and calculating the contribution of the resonant peaks at $\omega = \omega_n$ on the hypothesis that their bandwidths are small compared with those of $S_i(f)$, we obtain

$$\sigma^2 = (gh/A)^{1/2} \sum_n P_n S_i(\tilde{f}_n), \quad (4.15)$$

where

$$P_n = (4\pi)^{-1} \tilde{\kappa}_n^{-1/2} \tilde{G}_n^2 \int_0^\infty [1 + (Q_n/\tilde{\kappa}_n)^2 (\kappa - \tilde{\kappa}_n)^2]^{-1} d\kappa \quad (4.16a)$$

$$\sim \frac{1}{4} \tilde{\kappa}_n^{-1/2} Q_n^{-1} \tilde{G}_n^2 \quad (Q_n/\tilde{\kappa}_n \rightarrow \infty) \quad (4.16b)$$

is the power-spectrum-amplification factor for the n 'th mode. Substituting (4.9), (4.10) and (4.12) into (4.16b), we obtain

$$\mathcal{P}_n = \frac{1}{2} K_n^{-1/2}, \quad (4.17)$$

from which we infer that narrowing the harbor mouth does not affect the mean response to a random input except in the Helmholtz mode, but that it does increase significantly the response in that mode [this conclusion ignores the increase in viscous dissipation that would be associated with narrowing the mouth].

V. EQUIVALENT CIRCUIT FOR CANAL

We now interpose a canal[†] of breadth b and length ℓ between the harbor and the coast, as shown in Fig. 3, and obtain the equivalent circuit on the assumption that only plane waves need be considered in the canal. This approximation is strictly valid only for $kb \ll 1$, but a more complete analysis shows that the effects of the cross-waves (y -dependent modes) are not likely to be significant for $kb < \pi$.

Invoking the plane-wave approximation, $u = u(x)$ and $\zeta = \zeta(x)$, in (2.3) and (2.4), we obtain

$$I(x) = bhu(x) \quad \text{and} \quad V(x) = \zeta(x). \quad (5.1 \text{ a, b})$$

Assuming $I(0) = I_1$ and $I(\ell) = I_2$, we obtain the transmission-line solution

$$I(x) = \csc k\ell [I_1 \sin k(\ell - x) + I_2 \sin kx] \quad (5.2a)$$

and

$$V(x) = (jbc \sin k\ell)^{-1} [I_1 \cos k(\ell - x) - I_2 \cos kx]. \quad (5.2b)$$

Setting $V(0) = V_1$ and $V(\ell) = V_2$ in (5.2b), we obtain the matrix equation

$$\begin{Bmatrix} V_1 \\ V_2 \end{Bmatrix} = \begin{Bmatrix} Z_{11} & Z_{12} \\ Z_{12} & Z_{22} \end{Bmatrix} \begin{Bmatrix} I_1 \\ -I_2 \end{Bmatrix}, \quad (5.3)$$

[†]We use canal in the same sense as Lamb [1932, §169ff]. Some might regard the synonym channel as more appropriate in the present context.

where

$$Z_{11} = Z_{22} = - (j/bc) \cot k\ell, \quad Z_{12} = - (j/bc) \csc k\ell,$$

and

(5.4)

$$Z_{11} - Z_{12} = Z_{22} - Z_{12} = (j/bc) \tan \frac{1}{2} k\ell.$$

The four-terminal network implied by (5.3) and (5.4) is sketched in Fig. 3, wherein the arms $(Z_{11} - Z_{12})$ and pillar (Z_{12}) are inductive and capacitive, respectively, for $k\ell < \pi$ (ℓ less than a half-wave-length).

The preceding results remain valid for a canal of arbitrary (but constant) cross section S if $h \equiv S/b$, where b is the breadth of the canal of variable depth in the sense that the effects of the cross waves (y -dependent modes) that are generated by a change in depth are negligible in the shallow-water approximation (see Lamb, §176 for a qualitative argument and Bartholomeusz [1958] for a proof).

Inserting the equivalent circuit for the canal between the equivalent circuits for the harbor mouth (at $x = 0$) and the harbor (at $x = \ell$), we obtain the equivalent circuit shown in Fig. 4a. Calculating I_2 and the corresponding voltage drop across Z_n and invoking (4.3a) for the modal amplification factor, we obtain

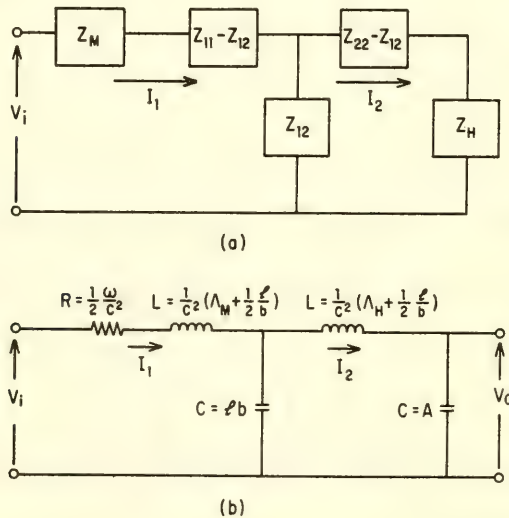


Fig. 4. Equivalent circuit for harbor connected to coast through canal: (a) general case; (b) Helmholtz mode ($k^2 A \ll 1$, $k\ell \ll 1$).

$$\begin{aligned}
 \mu_n^{1/2} Q_n(\kappa) &= |V_i|^{-1} |Z_n I_2| \\
 &= |(Z_M + Z_{11})(Z_H + Z_{22}) - Z_{12}^2|^{-1} |Z_n Z_{12}| \\
 &= |(Z_M + Z_H) \cos \kappa \ell + j\{(bc)^{-1} + bc Z_M Z_H\} \sin \kappa \ell|^{-1} |Z_n|,
 \end{aligned}
 \tag{5.5c}$$

where (5.5c) follows from (5.5b) through (5.4). The frequency dependence of $Q_n(\kappa)$ is qualitatively similar to that established in §4, but $\tilde{\kappa}_n - \kappa_n$ may not be small. The values of \tilde{Q}_n and Q_n may be substantially larger than those given by (4.9) and (4.12); however, (4.17) remains valid for $n \neq 0$, and the results therefore are of limited interest. There also exist modes that correspond to resonance of the canal itself, for which $x = \ell$ is approximately a node and the motion excited in H is small, but these, too, are governed by (4.17) in the sense that decreasing the channel width does not affect the mean response of the canal to a random input except in the Helmholtz mode.

We consider further the special case of Helmholtz resonance, assuming $\kappa \ell \ll 1$ as well as $\kappa^2 A \ll 1$. The equivalent circuit then reduces to that of Fig. 4b. Calculating $|V_o/V_i|$ in this circuit and neglecting terms of $O(\kappa^2 b \ell)$ relative to unity, we obtain

$$Q_o(\kappa) = \left\{ \frac{1}{4} (1 + \alpha)^2 \kappa^2 + [\kappa \Lambda(\kappa) - 1]^2 \right\}^{-1/2}, \tag{5.6}$$

where

$$\alpha = b \ell / A \tag{5.7}$$

is the ratio of the canal and harbor areas, and

$$\Lambda(\kappa) = \Lambda_H + (1 + \alpha) \Lambda_M(\kappa a) + (1 + \frac{1}{2} \alpha) (\ell / b). \tag{5.8}$$

Resonance is determined by $\tilde{\kappa}_0 \Lambda(\tilde{\kappa}_0) = 1$ and yields

$$\tilde{Q}_0 = Q_0 = 2(1 + \alpha)^{-1} \tilde{\kappa}_0^{-1} \tag{5.9}$$

and

$$P_0 = \frac{1}{2} (1 + \alpha)^{-1} \tilde{\kappa}_0^{-1/2} \tag{5.10}$$

in place of (4.9a), (4.12a), and (4.17).

VI. CIRCULAR HARBOR

The eigenfunctions determined by (2.9) for a circular harbor of radius R are given by

$$\psi_{0s}(r, \theta) = A^{-1/2} [J_0(j'_{0s})]^{-1} J_0(j'_{0s}r/R) \quad (m = 0), \quad (6.1a)$$

$$\psi_{ms}(r, \theta) = \left(\frac{2}{A}\right)^{1/2} \left[1 - \left(\frac{m}{j'_{ms}}\right)^2\right]^{-1/2} \frac{J_m(j'_{ms}r/R)}{J_m(j'_{ms})} \begin{cases} \cos m\theta \\ \sin m\theta \end{cases} \quad (m \geq 1), \quad (6.1b)$$

and

$$J'_m(j_{ms}) = 0 \quad (m = 0, 1, 2, \dots; \quad s = 0, 1, 2, \dots), \quad (6.1c)$$

where r is the polar radius measured from the center of the harbor, θ is the polar angle measured from the midplane of the mouth, we write $\psi_{ms}(r, \theta)$ in place of $\psi_n(x, y)$, the indices m (the number of azimuthal nodes) and s (the number of radial nodes) jointly replace the single index n in §2, and the eigenfunctions obtained by choosing the alternatives $\cos m\theta$ and $\sin m\theta$ are distinct. The eigenvalues are given by

$$\kappa_{ms} = \pi(j'_{ms})^2. \quad (6.2)$$

The zero'th mode of (2.10) corresponds to $m = s = 0$, for which $j'_{00} \equiv 0$.

We specify M by $R = 1$ and $-\frac{1}{2}\theta_M < \theta < \frac{1}{2}\theta_M$, where

$$\theta_M \equiv a/R \ll 1, \quad (6.3)$$

by virtue of which we may neglect the curvature of the harbor boundary over its intersection with the straight coastline. The essential approximation is $\sin \frac{1}{2}\theta_M \doteq \frac{1}{2}\theta_M$, which is in error by less than 5% for $a/R < 1$. Carrying out the calculation of μ_n , (2.15), and Λ_H , (4.6), on the basis of the approximations (6.3) and (3.5), we obtain

$$\mu_{ms} = (2 - \delta_{0m}) [1 - (m/j'_{ms})^2]^{-1} [1 + O(m^2 \theta_M^2)] \quad (6.4)$$

for the $\cos m\theta$ modes and $\mu_{ms} = 0$ for the $\sin m\theta$ modes [the approximation (6.4) is not uniformly valid as $m \rightarrow \infty$, but it suffices for all but the calculation of Λ_H] and

$$\pi\Lambda_H = \frac{1}{8} + \ln(4R/a) \quad (\theta_M \ll 1). \quad (6.5)$$

Combining (3.7) and (6.5) in (4.8), we obtain

$$\pi\Lambda_{ms} = 3.0135 + 2\ell \ln(R/a) - \ell \ln(kR), \quad (6.6)$$

wherein $k = k_{ms}$ for $n \neq 0$.

The resonant wavelength, $\lambda_0 = 2\pi/\tilde{k}_0$, $\tilde{Q}_0 = Q_0$, and \tilde{P}_0 for the Helmholtz mode, as determined by (4.9a), (4.10a), (4.12a), and (4.17) in conjunction with (6.6) are given by the lowest curves in each of Figs. 5 - 7. The higher curves in Figs. 5 - 7 are based on (5.8) - (5.10) and illustrate the striking effects of an intervening canal on Helmholtz resonance. Q_{ms} , as determined by (4.12), is plotted in Fig. 8 for the first five modes. The remarkable sharpness of the higher modes, vis-a-vis the Helmholtz mode, is borne out by Lee's [1971] experiments.

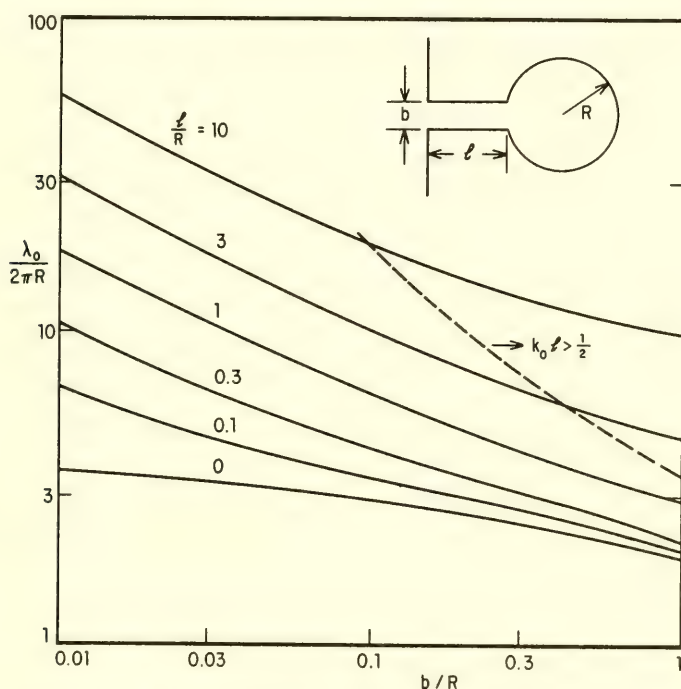


Fig. 5. Wavelength for Helmholtz resonance of circular harbor plus canal ($b \equiv a$ for $\ell = 0$). The results are strictly valid only for $b/R \ll 1$ and $k_0\ell \ll 1$, but the corresponding errors are not likely to exceed 5 - 10% for $b/R < 1$ and $k_0\ell < \frac{1}{2}$.

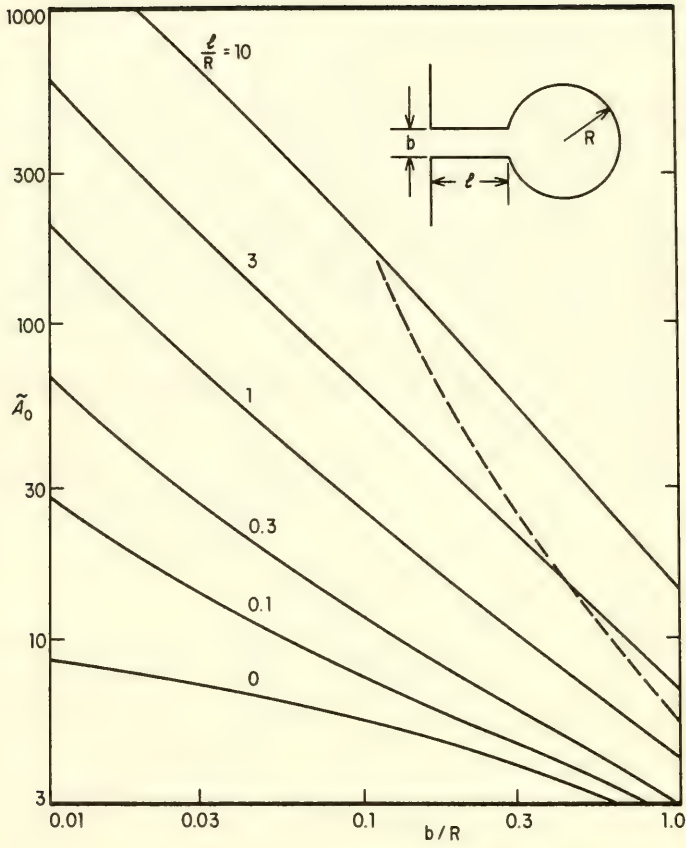


Fig. 6. Resonant amplification factor, $\tilde{A}_0 = Q_0$, for Helmholtz mode in circular harbor. $k_0 \ell > \frac{1}{2}$ to the right of the dashed line.

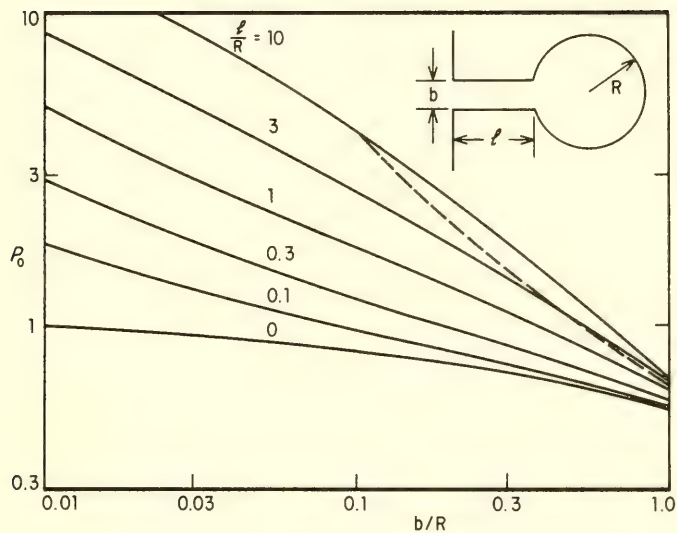


Fig. 7. Power-spectrum-amplification factor for Helmholtz mode in circular harbor. $k_0 \ell > \frac{1}{2}$ to the right of the dashed line.

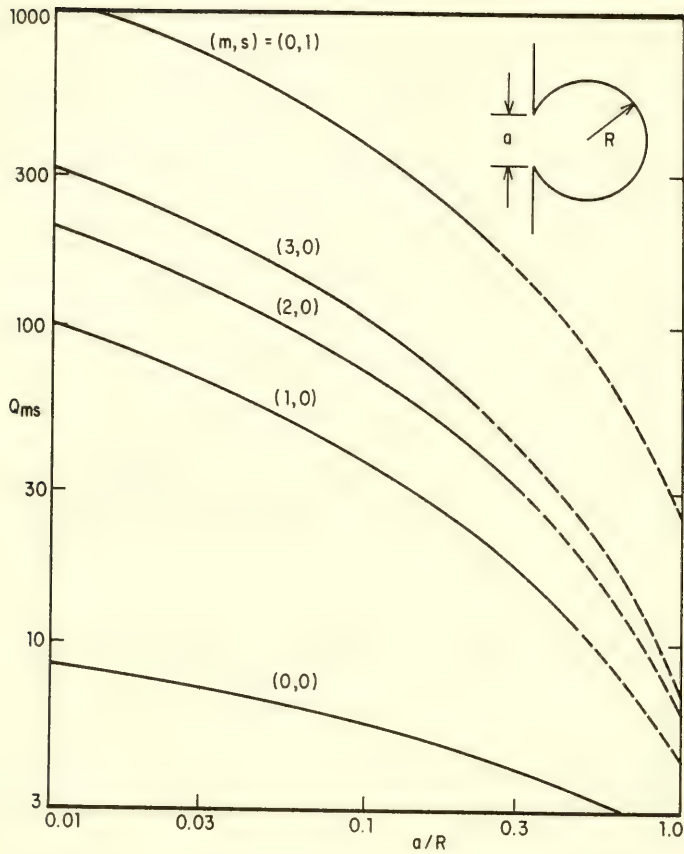


Fig. 8. Q_{ms} for the first five modes in a circular harbor. The dashed portions of the curves correspond to $ka > 1$

The period for the Helmholtz mode is given by

$$T_0 = \lambda_0/c = 2\pi(A/gh)^{1/2} \sim K_0^{1/2}. \quad (6.7)$$

Choosing $R = 1000'$ and $h = 20'$, we obtain $T_0 = 2\lambda_0/\pi R$ minutes, which approximates typical tsunami periods (20 - 40 minutes) for $\lambda_0/2\pi R$ in the range of 5 - 10 (see Fig. 5). We infer that a large harbor with a short entrance ($l/R \ll 1$) or a small harbor with a canal ($l/R \sim 0.3 - 3$) may act as a Helmholtz resonator under tsunami excitation.

REFERENCES

- Bartholomeusz, E. F., "The reflexion of long waves at a step," *Proc. Camb. Phil. Soc.*, 54, 106-18, 1958.
- Carrier, G. F., Shaw, R. P. and Miyata, M., "The response of narrow mouthed harbors in a straight coastline to periodic incident waves," *J. Appl. Mech.* (in press), 1970.
- Garrett, C. J. R., "Bottomless harbors," *J. Fluid Mech.*, 43, 443-49, 1970.
- Lamb, H., Hydrodynamics, Cambridge University Press, 1932.
- Lee, J. J., "Wave induced oscillations in harbors of arbitrary shape," *J. Fluid Mech.*, 45, 375-93, 1971.
- Miles, J. W., "The analysis of plane discontinuities in cylindrical tubes," Parts I and II. *J. Acoust. Soc. Am.*, 17, 259-71, 272-84, 1946.
- Miles, J. W., "The coupling of a cylindrical tube to a half-infinite space," *J. Acoust. Soc. Am.*, 20, 652-64, 1948.
- Miles, J. W., "Surface-wave scattering matrix for a shelf," *J. Fluid Mech.*, 23, 755-67, 1967.
- Miles, J. W., "Resonant response of harbors: an equivalent-circuit analysis," *J. Fluid Mech.*, 46, 241-65, 1971.
- Miles, J. W. and Munk, W. H., "Harbor paradox," *J. Waterways Harb. Div., Am. Soc. Civ. Engrs*, 87, 111-30, 1961.
- Morse, P. M., Vibration and Sound, New York: McGraw-Hill, 1948.
- Rayleigh, Lord, Theory of Sound, New York: Dover, 1945.

UNSTEADY, FREE SURFACE FLOWS; SOLUTIONS EMPLOYING THE LAGRANGIAN DESCRIPTION OF THE MOTION

Christopher Brennen, Arthur K. Whitney
California Institute of Technology
Pasadena, California

ABSTRACT

Numerical techniques for the solution of unsteady free surface flows are briefly reviewed and consideration is given to the feasibility of methods involving parametric planes where the position and shape of the free surface are known in advance. A method for inviscid flows which uses the Lagrangian description of the motion is developed. This exploits the flexibility in the choice of Lagrangian reference coordinates and is readily adapted to include terms due to inhomogeneity of the fluid. Numerical results are compared in two cases of irrotational flow of a homogeneous fluid for which Lagrangian linearized solutions can be constructed. Some examples of wave run-up on a beach and a shelf are then computed.

I. INTRODUCTION

There are many instances of unsteady flows in which analytic solutions, even approximate ones, are not available. This is particularly true of free surface flows when, for example, non-linear waves or even slightly complicated boundaries are involved. Though analytical methods are progressing, especially through the use of variational principles (Whitham [1965]) and, in some cases, the non-linear shallow water wave equations yield important results (Carrier and Greenspan [1958]) there is still a need for numerical methods. Indeed, numerical "experiments" can be used to complement actual experiments.

Until very recently numerical solutions in two dimensions

invariably seemed to employ the Eulerian description of the motion though the Lagrangian concept has been used for some time in the much simpler one-dimensional case (e.g., Heitner [1969], Brode [1969]) and to make small time expansions (Pohle [1952]). Perhaps the best known of these Eulerian methods is the Marker-and-Cell technique (MAC) begun by Fromm and Harlow [1963] and further refined by Welch, *et al.* [1966], Hirt [1968], Amsden and Harlow [1970], Chan, Street and Strelkoff [1969] and others. The most difficult problem arises in attempting to reconcile the initially unknown shape and position of a free surface with a finite difference scheme and the necessity of determining derivatives at that surface. In the same way, few solutions exist with curved or irregular solid boundaries. In steady flows, mapping techniques have been employed to transform the free surface to a known position (e.g., Brennen [1969]). It would therefore seem useful to examine the use of parametric planes for unsteady flows. The Lagrangian description in its most general form (Lamb [1932]) involves such a plane and by suitable choice of the reference coordinates, the free surface can be reduced to a known and fixed straight line. However a discussion of other parametric planes and mapping techniques is included in Section 3.

The major part of this paper is devoted to the development of a numerical method for the solution of the Lagrangian equations of motion in which full use is made of the flexibility allowed in the choice of reference coordinates. For the moment, we have restricted ourselves to cases of inviscid flow. Very recently, Hirt, Cook and Butler [1970] published details of a method which employs a Lagrangian tagging space but is otherwise similar to the MAC technique. This is further discussed in Section 4B.

II. LAGRANGIAN EQUATIONS OF MOTION

The general inviscid dynamical equations of motion in Lagrangian form are (Lamb [1932]):

$$(X_{tt} - F) \begin{Bmatrix} X_a \\ X_b \\ X_c \end{Bmatrix} + (Y_{tt} - G) \begin{Bmatrix} Y_a \\ Y_b \\ Y_c \end{Bmatrix} + (Z_{tt} - H) \begin{Bmatrix} Z_a \\ Z_b \\ Z_c \end{Bmatrix} + \frac{1}{\rho} \begin{Bmatrix} P_a \\ P_b \\ P_c \end{Bmatrix} = 0 \quad (1)$$

where X, Y, Z are the Cartesian coordinates of a fluid particle at time t , F, G, H are the components of extraneous force acting upon it, P is the pressure, ρ the density and a, b, c are any three quantities which serve to identify the particle and which vary continuously from one particle to the next. For ease of reference (X, Y, Z) are termed Eulerian coordinates, (a, b, c) Lagrangian coordinates. Suffices a, b, c, t denote differentiation.

If X_0, Y_0, Z_0 is the position of a particle at some reference time t_0 (when the density is ρ_0) then the equation of continuity is simply

$$\rho \frac{\partial(X, Y, Z)}{\partial(a, b, c)} = \rho_0 \frac{\partial(X_0, Y_0, Z_0)}{\partial(a, b, c)}. \quad (2)$$

Frequently it is convenient to define a, b, c as identical to X_0, Y_0, Z_0 , thus reducing the R.H.S. of (2) to ρ_0 ; however it will be seen in the following sections that flexibility in the definition of a, b, c is of considerable value when designing numerical methods of solution.

If the extraneous forces, F, G, H , have a potential Ω and ρ , if not uniform, is a function only of P then, eliminating $\Omega + P/\rho$ from (1):

$$\begin{aligned} \frac{\partial}{\partial t} (U_b X_c - U_c X_b + V_b Y_c - V_c Y_b + W_b Z_c - W_c Z_b) &= \frac{\partial \Gamma_1}{\partial t} = 0 \\ \frac{\partial}{\partial t} (U_c X_a - U_a X_c + V_c Y_a - V_a Y_c + W_a Z_c - U_a Z_c) &= \frac{\partial \Gamma_2}{\partial t} = 0 \\ \frac{\partial}{\partial t} (U_a X_b - U_b X_a + V_a Y_b - V_b Y_a + W_a Z_b - W_b Z_a) &= \frac{\partial \Gamma_3}{\partial t} = 0 \end{aligned} \quad (3)$$

where, for convenience, the velocities X_t, Y_t, Z_t are denoted by U, V, W . The quantities $\Gamma_1, \Gamma_2, \Gamma_3$ are related to the Eulerian vorticity components, $\zeta_1, \zeta_2, \zeta_3$ by

$$\begin{aligned} \Gamma_1 &= \zeta_1(Y_b Z_c - Y_c Z_b) + \zeta_2(Z_b X_c - Z_c X_b) + \zeta_3(X_b Y_c - X_c Y_b) \\ \Gamma_2 &= \zeta_1(Y_c Z_a - Y_a Z_c) + \zeta_2(Z_c X_a - Z_a X_c) + \zeta_3(X_c Y_a - X_a Y_c) \\ \Gamma_3 &= \zeta_1(Y_a Z_b - Y_b Z_a) + \zeta_2(Z_a X_b - Z_b X_a) + \zeta_3(X_a Y_b - X_b Y_a) \end{aligned} \quad (4)$$

(Thus, of course, vorticity changes with time are due solely to changes in the coefficients of the L.H.S. of (4) which, in turn, represents stretching and twisting of the vortex line.) Given the vorticity distribution $\zeta(X, Y, Z)$ at some initial time, t_0 , $\Gamma(a, b, c)$ (which is independent of time) may be obtained through Eqs. (4) and used in the final form of the dynamical equations of motion, namely Eqs. (3) integrated with respect to time.

For incompressible, planar flow the equations reduce to

Continuity: $X_a Y_b - Y_a X_b = F(a, b)$ (5)

(or differentiated w.r.t. t):

$$U_b Y_a - U_a Y_b + V_a X_b - V_b X_a = 0$$
 (6)

Motion: $U_b X_a - U_a X_b + V_b Y_a - V_a Y_b = -\Gamma(a, b).$ (7)

By introducing the vectors $Z = X + iY$ and $W = U - iV$, (6) and (7) conveniently combine to:

$$Z_a W_b - Z_b W_a = -\Gamma(a, b).$$
 (8)

Other types of flow have also been investigated. For example, in the case of a heterogeneous, or non-dispersive stratified liquid in which ρ is a function of (a, b) , Eq. (8) becomes:

$$Z_a W_b - Z_b W_a = -[\Gamma(a, b)]_{t=t_0} - \frac{1}{\rho} \int_{t_0}^t (X_{tt} - F)(\rho_b X_a - \rho_a X_b) + (Y_{tt} - G)(\rho_b Y_a - \rho_a Y_b) dt. \quad (9)$$

The integral term therefore manufactures vorticity. The methods developed for a homogeneous fluid in Sections 4A to D are modified in Section 4E to include such effects.

III. OTHER PARAMETRIC PLANES

It may be of interest to digress at this point to consider other parametric planes (a, b) , which are not necessarily Lagrangian. That is to say the restrictions $X_t(a, b, t) = U$, $Y_t(a, b, t) = V$ are abandoned so that U, V are no longer either Eulerian or Lagrangian velocities. Provided $J = \partial(X, Y)/\partial(a, b) \neq 0$, or ∞ , the equation for incompressible and irrotational planar flow remains

$$Z_a W_b - Z_b W_a = 0. \quad (10)$$

To incorporate one of the advantages of the Lagrangian system, it is required that the free surface be fixed and known, say on a line of constant b . Then the kinematic and dynamic free surface conditions are respectively

$$(U - X_t)Y_a - (V - Y_t)X_a = 0 \quad (11)$$

$$(U_t + F)X_a + (V_t + G)Y_a + (U - X_t)U_a - (V - Y_t)V_a = 0. \quad (12)$$

Now a useful choice concerning the (a,b) plane would be to require the mapping from (X,Y) to be conformal. Then, of course, (10) simply reduces to the Cauchy-Riemann conditions $U_a = -V_b$, $U_b = V_a$ so that $W = U - iV$ is an analytic function of $c = a + ib$ or of Z .

In this way, John [1953] has constructed some special, exact analytic solutions. The kinematic condition, (11), has the particular solution $W(a,t) = \overline{Z_t(a,t)}$ on the free surface, which implies $W(c,t) = \overline{Z_t(\bar{c},t)}$ by analytic continuation. If, in addition,

$$Z_{tt} + (F + iG) = iZ_c K(c,t) \quad (13)$$

where K is real on the free surface, then the dynamic condition thereon is also satisfied. John discusses several examples for various choices of the function K .

The potential of such methods may not have been fully realized either analytically or numerically. In the latter case, however, the conformality of the (X,Y) to (a,b) mapping is not necessarily a great advantage, whereas a fixed and known free surface position most certainly is.

The digression ends here and the following sections develop a Lagrangian numerical method from the equations of Section 2.

IV. A NUMERICAL METHOD EMPLOYING LAGRANGIAN COORDINATES

A method for the numerical solution of incompressible, planar flows is now described. It attempts to take full advantage of the flexibility in the choice of Lagrangian coordinates.

A. Time Variant Part

The method uses an implicit scheme with central differencing over time, t . Thus $Z^p(a,b)$ is determined at a series of stations in time, distinguished by the integer, p . Knowledge of velocity values, $Z_t^{p+1/2}$, at a midway station $p + \frac{1}{2}$ enables $Z^{p+1}(a,b)$ to be found from Z^p through the numerical approximation

$$Z^{p+1} = Z^p + \tau Z_t^{p+1/2} \quad (\text{error order } \tau^3 Z_{ttt}) \quad (14)$$

where τ is the time interval. Acceleration values, $Z_{\uparrow\uparrow}^p$, needed in the free surface condition (Section 4C) are approximated by $(Z_{\uparrow}^{p+1/2} - Z_{\uparrow}^{p-1/2})/\tau$ (error order $\tau^4 Z_{\uparrow\uparrow\uparrow\uparrow}$). Thus the main part of the solution involves finding $P_{\uparrow}^{p+1/2}$ knowing Z^p , $Z_{\uparrow}^{p-1/2}$ and their previous values.

The first time step (from $p = 0$ to $p = 1$) requires a little special attention. Clearly $Z^0(a,b)$ is chosen to fit the required initial conditions. But further information is required on a free surface which will enable the accelerations in that condition to be found (see Section 4C).

B. Spatial Solution

A method of the present type is restricted to a finite body of fluid, S . However, S , could be part of a larger or infinite mass of fluid if an "outer" approximate solution of sufficient accuracy was available to provide the necessary matching boundary conditions at the interface. The region, S , need not be fixed in time. It would indeed be desirable, for example, to "follow" a bore.

In a great number of cases of widely different physical geometry including all the examples of Section 6, it is convenient to choose S to be rectangular in the (a,b) plane. This rectangle (ABCD, Fig. 1) is then divided into a set of elemental rectangles. The motion of each of these cells of fluid is to be followed by determining the Z values at all the nodes.

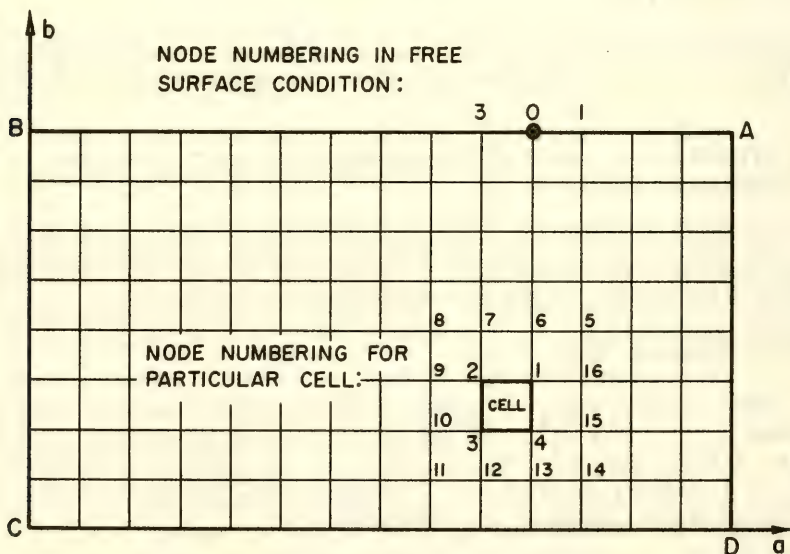


Fig. 1. The Rectangular Lagrangian Space, S , Showing the Numbering Conventions Used

Making the assumption of straight sides the actual area of a cell in the physical plane is

$$A = \frac{1}{2}[(X_1 - X_3)(Y_2 - Y_4) - (X_2 - X_4)(Y_1 - Y_3)] \quad (15)$$

Number suffices refer to the four vertices, numbered anticlockwise; other node numbering conventions are shown in Fig. 1. If this area is to remain unaltered after proceeding in time from station p to $p + 1$ through Eq. (14) then

$$\begin{aligned} & \text{Imag} \{ (Z_2 - Z_4)^p (W_1 - W_3)^{p+1/2} - (Z_1 - Z_3)^p (W_2 - W_4)^{p+1/2} \} \\ & + \tau \{ (U_1 - U_3)(V_2 - V_4) - (U_2 - U_4)(V_1 - V_3) \}^{p+1/2} + \frac{2(A^p - A^0)}{\tau} \\ & = 0 = R_c \end{aligned} \quad (16)$$

where the terms on the L.H.S., second line are numerical corrections required to preserve continuity more exactly and prevent accumulation of error over a large number of time steps. The numerical value of the L.H.S. at some point in the iterative solution is termed the continuity residual, R_c .

Assuming linear variation in velocity along each side of the cell, evaluating the circulation around 1234 and setting this equal to the known, initial circulation, Γ_c , yields (in the case of a homogeneous fluid):

$$\text{Real} \{ (Z_2 - Z_4)(W_1 - W_3) - (Z_1 - Z_3)(W_2 - W_4) \} - 2\Gamma_c = 0 = R_I \quad (17)$$

Slight hesitation is required here since, for validity, the Z and W values in this equation should relate to the same station in time. But by choosing to apply it at the midway stations and substituting $Z^{p+1/2} = Z^p + (\tau/2)Z_1^{p+1/2}$ the τ terms are found to cancel and (17) persists when the values referred to are Z^p and $W^{p+1/2}$. R_I is the circulation residual. The modification of (17) in the case of a heterogeneous fluid is delayed until section 4E.

Combining (16) and (17) produces the cell equation:

$$\begin{aligned} & (Z_2 - Z_4)(W_1 - W_3) - (Z_1 - Z_3)(W_2 - W_4) && \text{Main Part} \\ & + i\tau \{ (U_1 - U_3)(V_2 - V_4) - (U_2 - U_4)(V_1 - V_3) \} + \frac{2(A^p - A^0)i}{\tau} && \text{Continuity} \\ & - 2\Gamma_c && \text{Permanent Cell Circulation Term} \end{aligned}$$

$$\begin{aligned}
 & + \frac{1}{12} \{ (W_{16} + W_9 - W_1 - W_2)(Z_1 - Z_2) && \text{Higher} \\
 & - (W_{15} + W_{10} - W_3 - W_4)(Z_4 - Z_3) && \text{Order} \\
 & + (W_7 + W_{12} - W_2 - W_3)(Z_2 - Z_3) && \text{Correction} \\
 & - (W_6 + W_{13} - W_1 - W_4)(Z_1 - Z_4) \} && \text{if required} \\
 & = 0 = R_I + iR_C = R, \text{ the cell residual.} && (18)
 \end{aligned}$$

The higher order correction, included for completeness, allows the shape of the cell sides and the variations in velocity along them to be of cubic form. Without it the neglected terms are of order $Z_0 W_{bbb}$, $Z_{ab} W_{ab}$, etc., with it they are of order $Z_0 W_{bbbb}$, etc. Values referred to are Z^p and $W^{p+1/2}$, $U^{p+1/2}$, $V^{p+1/2}$.

Though this derivation of the cell equation is instructive, it can be obtained more directly (except for the continuity correction) by integration of (8) over the area of the cell in the (a,b) plane (using Taylor expansions about the center of the cell).

The cell equations must now be solved for $W^{p+1/2} = (U - iV)$, Z^p being known, in order to proceed in time.

In a recently published paper, Hirt, Cook and Butler [1970] take a rather different approach in which the (a,b) plane is employed merely as a tagging space. The equations are written in essentially Eulerian terms, no derivatives with respect to a,b appearing. The numerical method (LINC) is similar to that of the MAC technique (Fromm and Harlow [1963], Welch, et al. [1966], Chan, Street and Strelkoff [1969], etc.) and involves solving for the pressure at the center of a cell as well as for the vertex velocities. Advantages of the method described in the present paper are: the pressure has been eliminated (though this may be disadvantageous in compressible flows); no special treatment is required for cells adjacent to boundaries; inhomogeneous density terms are relatively easily included. However, since the LINC system is based on the Eulerian equations of motion, the inclusion of viscous terms is more easily accomplished than in the present method where such an attempt leads to horrendous difficulties.

C. Boundary Conditions

To complete the specifications, a condition upon $W^{p+1/2}$ is required at each of the boundary nodes. This usually takes the form of an expression connecting $U^{p+1/2}$ and $V^{p+1/2}$. For example, solid boundaries, whether fixed or moving in time, may be prescribed by a function, $F(X,Y,t) = 0$. Then the required relation is

$$F(X^p + \tau U^{p+1/2}, Y^p + \tau V^{p+1/2}, t) = 0 \quad (19)$$

Dynamic free surface conditions are simply constructed from Eqs. (1). If, for example, the only extraneous force is that due to gravity, g , in the negative Y direction, the condition on a free surface such as AB , Fig. 1, is

$$X_{\eta\eta}X_a + (Y_{\eta\eta} + g)Y_a = \frac{T}{\rho} \frac{\partial}{\partial a} \left(\frac{Y_{aa}X_a - X_{aa}Y_a}{(X_a^2 + Y_a^2)^{3/2}} \right) \quad (20)$$

where T is the surface tension if this is required.

Unlike the field Eqs. (8) or (18) these boundary conditions may not be homogeneous in all the variables. In a given problem only the boundary conditions are altered by different choices of typical length, h (perhaps an initial water depth), and typical time, say $\sqrt{h/g}$ in the above example. Then, using the same letters for the dimensionless variables, g and T/ρ in Eq. (20) would be replaced by 1 and $S = T/\rho gh^2$. The numerical form of that condition used at a free surface node such as 0 (Fig. 1) is:

$$\begin{aligned} (X_1 - X_3)^p (U_0^{p+1/2} - U_0^{p-1/2}) + (Y_1 - Y_3)^p (V_0^{p+1/2} - V_0^{p-1/2} + \tau) \\ = \tau S (P_1^p - P_3^p) \end{aligned} \quad (21)$$

where P is assessed at each node as

$$P_0 = \frac{[(X_1 - X_3)(Y_1 + Y_3 - 2Y_0) - (Y_1 - Y_3)(X_1 + X_3 - 2X_0)]}{[(X_1 - X_3)^2 + (Y_1 - Y_3)^2]^{3/2}}$$

and the accelerations have been replaced by the expressions given in Section 4A. Again, Eq. (21) relates $U_0^{p+1/2}$ to $V_0^{p+1/2}$ since all other quantities are known.

If the liquid starts from rest at $t = 0$ (as in the examples of Section 6) then difficulties at the singular point $t = 0$ can be avoided by choosing to apply the condition at $t = \tau/4$ rather than $t = 0$. Using $Z_{\eta\eta} = 2Z_1^{1/2}/\tau$ and $Z = Z^0 + (\tau/4)Z_1^{1/2}$ at that station the special boundary condition becomes

$$U_0^{1/2} \{ (X_1 - X_3)^0 + \frac{\tau}{4} (U_1 - U_3)^{1/2} \} + \frac{\tau}{4} (V_1 - V_3)^{1/2} (V_0^{1/2} + \tau g/2) = 0 \quad (22)$$

in the case of zero surface tension.

D. Method of Solution

It remains to discuss how the equations may be solved to find $W^{p+1/2}$ at every node. Due to the non-linear terms in (18) and some boundary conditions as well as to the fact that a good estimate of $W^{p+1/2}$ can be made from values at previous time stations, a simple iterative or relaxation scheme was employed. Such a method involves visiting each cell in turn and adjusting the W values at its vertices in such a way that repetition of the process reduces the cell residuals, R , to negligible proportions. But, on arrival at a particular cell, there are an infinite number of ways in which its four vertex values can be altered in order to dissipate the single cell residual. However, experience demonstrated that a procedure based on the following changes ($\Delta W_{1,2,3 \text{ and } 4}$) was superior in convergence and stability to any of the others tested:

$$\begin{aligned}\Delta W_1 &= -\Delta W_3 = \omega i R (\overline{Z_1 - Z_3}) / 8A \\ \Delta W_2 &= -\Delta W_4 = \omega i R (\overline{Z_2 - Z_4}) / 8A\end{aligned}\tag{23}$$

Here ω is an overrelaxation factor and A is the area of the cell, which is unchanged with time and given by the expression (15). These incremental changes have a simple and meaningful physical interpretation. As can be seen from Fig. 2, they are a combination of two changes, one representing pure stretching and the other pure rotation, which dissipate respectively the continuity and circulation components of the residual.

Having visited each and every cell, the boundary conditions were then imposed. Where these were given in the form $A \cdot U^{p+1/2} + B \cdot V^{p+1/2} + C = 0 = R_B$, A, B, C being constants and R_B the residual, the following changes were made, the choice being based upon experience:

$$\begin{Bmatrix} \Delta U^{p+1/2} \\ \Delta V^{p+1/2} \end{Bmatrix} = - \begin{Bmatrix} A \\ B \end{Bmatrix} \frac{R_B}{(A^2 + B^2)}\tag{24}$$

The whole process was then repeated to convergence.

E. Inhomogeneous Fluid

In a non-dispersive, inhomogeneous fluid, $\rho(a,b)$, which is independent of time, will be prescribed through the initial choice of $Z^0(a,b)$. Indeed in many cases it will be convenient to choose Z^0 in

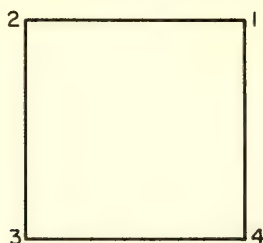


Fig. 2(a). The Cell in the Reference Plane (a,b)

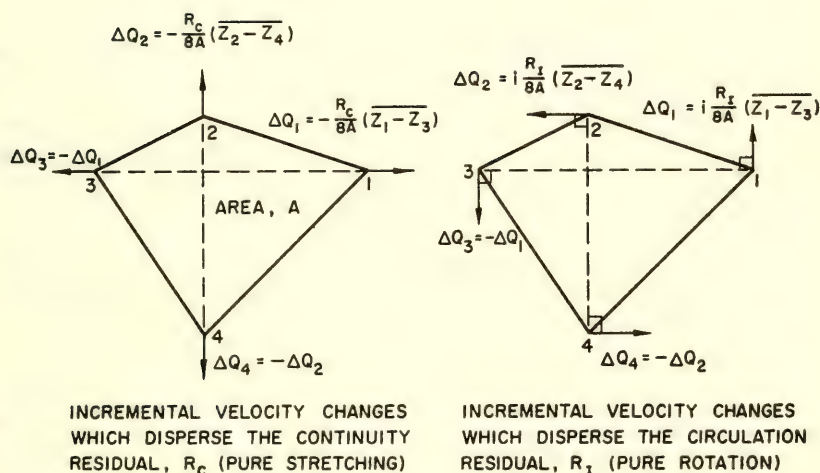


Fig. 2(b). The Cell in the Physical Plane (X,Y)

such a way that ρ is some simple analytic function of (a,b). This is particularly desirable because by substituting for ρ , ρ_a , ρ_b in Eq. (9), this can then be integrated over a cell area (as in Section 4B) to produce a convenient additional term, $\theta^{p+1/2}$, on the L.H.S. of the cell Eq. (18). Since the expression for $\theta^{p+1/2}$ will depend upon that choice of $\rho(a,b)$ an example will illustrate this.

If ρ is to be constant along the free surface, AB, Fig. 1, and along the bed, CD, it may be possible to choose Z^0 such that ρ is a linear function of b , say $\rho = \rho_{CD} (1 + \gamma b)$ where $\gamma = \rho_{AB}/\rho_{CD} - 1$ and $b = 1$ on AB. Then,

$$\theta_{1234}^{p+1/2} - \theta_{1234}^{p-1/2}$$

$$\begin{aligned} \approx & -\frac{1}{4} \ln(1 - \mu) \left[\{(U_1 + U_2 + U_3 + U_4)^{p+1/2} - (U_1 + U_2 + U_3 + U_4)^{p-1/2}\} \right. \\ & \times \{X_1 - X_2 - X_3 + X_4\}^p \\ & + \{V_1 + V_2 + V_3 + V_4\}^{p+1/2} - \{(V_1 + V_2 + V_3 + V_4)^{p-1/2} + 4\pi g\} \{Y_1 - Y_2 - Y_3 + Y_4\}^p \Big] \\ & + \left\{1 + \frac{1}{\mu} - \frac{1}{2} \ln(1 - \mu)\right\} \left[(X_1 - X_2)^p \{(U_1 + U_2)^{p+1/2} - (U_1 + U_2)^{p-1/2}\} \right. \\ & - (X_4 - X_3)^p \{(U_3 + U_4)^{p+1/2} - (U_3 + U_4)^{p-1/2}\} \\ & + (Y_1 - Y_2)^p \{(V_1 + V_2)^{p+1/2} - (V_1 - V_2)^{p-1/2} + 2\pi g\} \\ & \left. - (Y_4 - Y_3)^p \{(V_3 + V_4)^{p+1/2} - (V_3 + V_4)^{p-1/2} + 2\pi g\} \right] \end{aligned}$$

where $\mu = \gamma \Delta b / (1 + \gamma b_{34})$, b_{34} being the b value on side 34 of the cell and Δb the difference across each and every cell. The first term is of order μ , the second order μ^2 . The boundary conditions are usually identical to the homogeneous case.

V. ACCURACY, STABILITY, CONVERGENCE AND SINGULARITIES

A. Accuracy

If the cell equation, (18), is used without the higher order spatial correction, an indication of the errors due to neglected higher order spatial derivatives can be obtained by assessing the value of that correction and inferring its effect upon the final values of W . Unfortunately, the mesh distribution and mesh size required for a solution of given accuracy will not be known a priori and can only be arrived at either by trial and error or by using some technique of rezoning. The latter method in which cells are subdivided where and when the violence of the motion demands it, can be difficult to program satisfactorily and has not been attempted thus far.

Errors due to higher order temporal derivatives are most easily regulated by ensuring that, for each cell, both $\tau |W_1 - W_3| / |Z_1 - Z_3|$ and $\tau |W_2 - W_4| / |Z_2 - Z_4|$ are comfortably less than unity. A workable rule of thumb can be devised in which a suitable τ for a particular time step is determined from the W and Z values of the preceding step.

B. Stability of Cell Relaxation

Suppose the central member, cell A, of the group of cells shown in Fig. 3 contained a residual R_A which was then dissipated according to the relations (23). Transfer functions, D_{AB} , D_{AC} , etc., will describe the residual changes, ΔR_B , etc., in the surrounding cells where

$$\Delta R_B = \omega D_{AB} R_A, \text{ etc.} \quad (24)$$

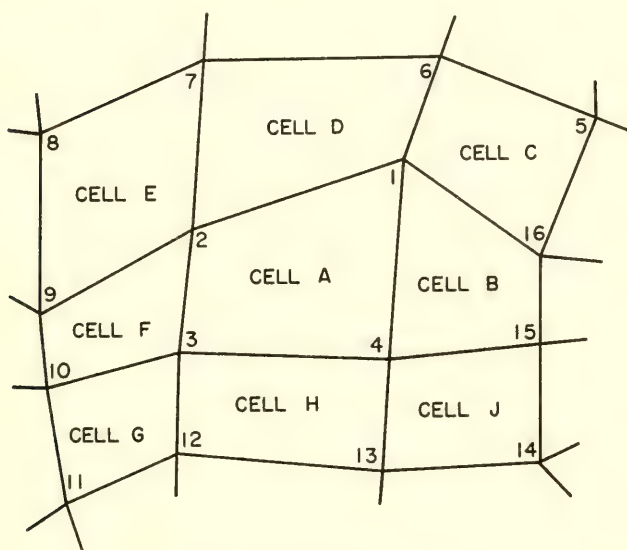


Fig. 3. Z-Plane

For example

$$D_{AB} = \{(Z_1 - Z_{15})(Z_2 - Z_4) - (Z_{16} - Z_4)(Z_1 - Z_3)\}i/8A_A$$

where A_A is the area of cell A. For convergence of the relaxation method it is clearly necessary that the ω for each cell be chosen so that all $\omega|D|$ are significantly less than unity. It is instructive to inspect the case in which all the cells are roughly geometrically similar in the Z plane. Then

$$|D_{AB}| = |D_{AD}| = |D_{AF}| = |D_{AH}| \approx \frac{|d_1^2 - d_2^2|}{8A_A} = \gamma_1$$

$$|D_{AC}| = |D_{AE}| = |D_{AG}| = |D_{AJ}| \approx \frac{d_1 d_2}{8A_A} = \frac{1}{4} + \gamma_2$$

where d_1, d_2 are the lengths of the cell diagonals. For square cells, $\gamma_1 = \gamma_2 = 0$ and the situation is stable. However difficulties may arise when the cells are very skewed or elongated and it is in such situations, in general, that care has to be taken with the relaxation technique.

C. Observation on the Cell Equation

One feature of the basic cell equation, (18), itself demands attention. Note that without the higher order spatial correction, the residuals, R in all of the cells (of Fig. 3) remain unaltered when the W or Z values at alternating points (say the odd numbered points of Fig. 3) are changed by the same amount. Such alternating "errors" must be suppressed. Some damping is provided by the higher order spatial correction since it is not insensitive to these changes. But experience showed this to be insufficient unless all the boundary conditions also inhibited such alternating "errors." Solid boundaries usually provide adequate damping. For instance, in Fig. 4(a) fluctuations in U on BC, DA and in V on BC are obviously barred. But the free surface provides little or no such suppression and as will be seen in the next section this can lead to difficulties. It is of interest to note that some of the solutions of Hirt, Cook and Butler [1970] exhibit the same kind of alternating errors.

In the MAC technique, neglected higher order derivatives of the diffusion type and with negative coefficients (a "numerical" viscosity) can lead to a numerical instability if not counteracted by the introduction of sufficient real viscosity. In the present method, as with that of Hirt, Cook and Butler [1970], the convection terms which cause that problem are not present. The higher order spatial correction does contain terms of diffusion order, but it cannot be directly correlated with a viscosity since viscous terms are of a different form (i.e., like $\int \nu \nabla_{xy}^2 \Gamma dt$). Also, the higher order spatial correction has a beneficial rather than a destabilizing effect.

D. The Free Surface

By including previously neglected derivatives, the numerical free surface condition (without surface tension) is found to correspond more precisely to:

$$\begin{aligned} \{X_a X_{tt} + Y_a(Y_{tt} + 1)\} + \frac{(\Delta a)^2}{6} \{X_{aaa} X_{tt} + Y_{aaa}(Y_{tt} + 1)\} \\ + \frac{\tau^2}{24} \{X_a X_{tttt} + Y_a Y_{tttt}\} = 0 \end{aligned} \quad (26)$$

where Δa is the a difference across a cell and the second and third terms constitute truncation errors. Inspect this in the light of a linearized standing wave solution (see Section 6A), i.e.,

$$X = a - M \cos \sqrt{k} t \sin ka e^{kb}$$

$$Y = b + M \cos \sqrt{k} t \cos ka e^{kb}$$

where the variables are non-dimensionalized as in Section 4C and k is the non-dimensional wave number in the a, b plane. Then, the second and third terms of Eq. (26) will be insignificant provided

$$\frac{k^2(\Delta a)^2}{6} \ll 1 \quad \text{and} \quad \frac{\tau^2 k}{24} \ll 1$$

respectively. Or, in terms of a wavelength, $\lambda = 2\pi/k$:

$$\frac{\lambda}{\Delta a} \gg 2 \quad \text{and} \quad \tau \ll 4 \frac{\lambda}{\Delta a} \Delta X \quad (27)$$

since $\Delta a \approx \Delta X$, the X difference between points on the free surface. The first condition states the inevitable; namely, that the solution will be hopelessly inaccurate for (a, b) plane wavelengths comparable with the mesh-length Δa . Given that the first condition holds then the second says that $\tau \ll 8\Delta X$. For a travelling wave system the same condition states that τ should be less than the time taken for a wave to travel one mesh length. This constitutes a restriction on τ which is usually more stringent than that of Section 5A. If, for example, the depth of the fluid is divided into N intervals and the X difference across each cell is of the same order as the Y difference then τ should be less than $8/N$.

A more difficult problem arises when the first condition is considered alongside the fact, ascertained in the previous section, that the field equation provides little or no resistance to disturbances whose wavelength is equal to Δa . The only resort would seem to be to some artificial damping technique which would eliminate or suppress these small wavelengths. The technique used in the examples to follow was to relax the W values on the free surface such that $W = \beta W^{FSC} + (1 - \beta)W^*$ where W^{FSC} was the value indicated by the free surface condition, W^* the value which would make the numerical equivalent of W_{quad} be zero at that point and β was slightly less than one half.

E. Singularities

Successful numerical treatments of singularities depend upon the availability of analytic solutions to the flow in the neighborhood of that point. For example, at a corner between solid walls the velocity varies as the $(\pi - \beta)/\beta$ power of distance from that junction where β is the included angle. If this is $\pi/2$ (as at points C or D, Fig. 4(a)) the variation is linear and thus the numerical estimate of the circulation around the cell (see Section 4) in such a corner is a good one. Where the angle is not $\pi/2$ (D, Fig. 4(c)) errors will occur due to the non-linear variation of velocity, but corrective procedures are easily devised.

A great deal less is known about the singularities at a junction of a free surface and a solid boundary. If the wall is static and vertical (A, Fig. 4(a)) so that $X_{tt} = X_b = X_{bt} = 0$, etc., it follows from the equation of motion that if $Y_a = 0$ at $t = 0$ then it is always zero for irrotational flow; the tangent to the free surface at the wall is always horizontal. Thus the free surface condition without surface tension is automatically satisfied at such a junction and only weak singular behavior is expected. But a similar analysis of the case when the wall begins to move at $t = 0$ (remaining vertical) indicates that Y_{tt} must be infinite at the junction (B, Fig. 4(a)) at $t = 0$, the singularity being logarithmic in space. An extension to $t \neq 0$ has not so far been obtained. One approach might be a Fourier analysis of the step in X_{tt} so that the steadily oscillating solutions of Fontanet [1961] could be used. These suggest that Y_{tt} becomes finite for $t > 0$.

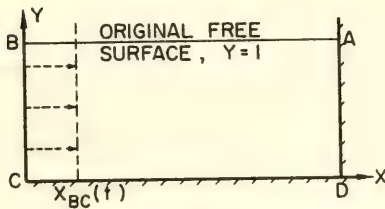


FIG. 4(a)

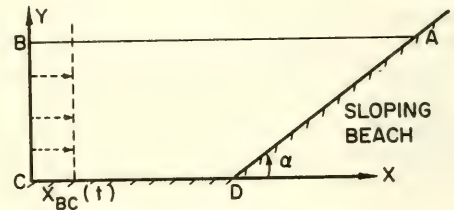


FIG. 4(c)

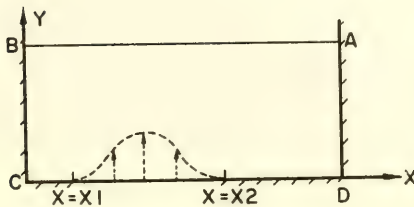


FIG. 4(b)

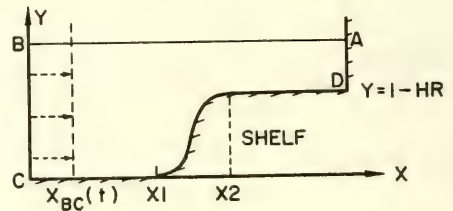


FIG. 4(d)

In the examples to follow (see Figs. 4(a) to (d)) satisfactory numerical solutions could be obtained by ignoring all but one of the singularities. The exception was the shoreline, point A, Fig. 4(c). If β is the angle between the tangent to the free surface at A and the horizontal then correlating the two boundary conditions yields:

$$(Z_{tt})_A = -e^{ia}/(\cot \beta \cos \alpha + \sin \alpha) \quad (28)$$

Thus the sign of β determines the direction of the acceleration up or down the beach. If the fluid starts from rest at $t = 0$, $\beta = 0$, then $(Z_{tt})_{t=0} = 0$ and successive differentiation of the basic equation (8) and the boundary conditions yields (for irrotational motion):

$$\text{At A, } t = 0 \quad (\alpha \neq \frac{\pi}{2}) \quad Z_{tt}, Z_{ttt} = 0$$

$$Z_{tttt}, Z_{attt}, Z_{bttt}, Z_{ttttt} = 0 \text{ or } \infty, \text{ unless } \alpha = \frac{\pi}{4} \quad (29)$$

$$Z_{ttttt}, Z_{atttt}, Z_{btttt} = 0 \text{ or } \infty, \text{ unless } \alpha = \frac{\pi}{4} \text{ or } \frac{\pi}{6}$$

These relations suggest a behavior which is logarithmically singular in time at $t = 0$ unless $\alpha = \pi/2n$, n integer. Roseau [1958] found similar logarithmic singularities in periodic solutions for the general case which excluded $\alpha = \pi/2n$ and another set of particular angles (see also Lewy [1946]). But a systematic analysis of the singular behavior (especially for $t \neq 0$) has not as yet been completed. Rather, since the relations (29) no longer necessarily hold if the condition of irrotationality near that point is relaxed, the problem was circumvented numerically by replacing the circulation condition on the single cell in that corner by the condition (28) at the point A and the time $t = 0$ was avoided by applying (28) at $t = \tau/4$ just as was done with the general free surface condition (Section 4C).

Note that strong singularities could be introduced by unsuitable mapping to the (a,b) plane.

VI. SOME RESULTS INCLUDING COMPARISONS WITH LINEAR SOLUTIONS

A. Lagrangian Linearized Solutions

Linearized solutions to the Lagrangian equations are obtained by substituting $X = a + \xi$, $Y = B + \eta$ into the equations of continuity and motion and neglecting all multiples of derivatives of ξ and η . For incompressible and irrotational planar flow the Cauchy-Riemann conditions $\xi_a = -\eta_b$, $\xi_b = \eta_a$ result so that $\xi + i\eta$, and therefore $Z - c$ (where $c = a + ib$) is an analytic function of \bar{c} . In the absence

of surface tension the free surface condition reduces to

$$\xi_{\eta\eta} + g\eta_a = 0 \quad (g = 1 \text{ in the dimensionless variables}) \quad (30)$$

only when the additional assumption that $\eta_{\eta\eta} \ll g$ is made. In this way harmonic solutions can be obtained for some simple problems.

In passing, it may be of interest to compare Lagrangian linearization with the more common Eulerian type, at least in some simple cases. For travelling waves on an infinite ocean the first order Lagrangian terms are precisely those of Gerstner's waves. The Eulerian solution must be taken to the third order to achieve this waveform. On the other hand, while the Eulerian solution is always irrotational the Lagrangian only approaches it. Thus the comparative accuracy of the two methods depends upon what particular feature of the flow is under scrutiny. A comparison of the works of Zen'kovich [1947] and Penney and Price [1952] for standing waves on an infinite ocean demonstrates the same features.

B. Example One, Figs. 4(a), 5, 6, 7, 8, 9, and 10

In the example of Fig. 4(a), the liquid is initially at rest in the rectangular vessel BCDA; between $t = 0$ and $t = T$ the side BC moves inward according to

$$\begin{aligned} X_{BC}(t) &= M \sin^2 \pi t / 2T \quad \text{for} \quad 0 < t < T \\ &= M \quad \text{for} \quad t > T \end{aligned}$$

With a suitable choice of M and T this creates a wave which travels along the box, builds up on and is reflected by the opposite wall, AD. The linearized solution (which requires a Fourier analysis of the free surface boundary condition) is

$$Z - c = X_{BC}(t) \left[1 - \frac{\bar{c}}{l} \right] + \sum_{k=1}^{\infty} R_k B_k(t) \sin \left(\frac{k\pi \bar{c}}{l} \right) \quad (31)$$

where

$$\begin{aligned} R_k &= M / \pi k \left(\frac{\nu k^2 T^2}{\pi^2} - 1 \right) \cosh \left(\frac{\pi k}{l} \right) \\ B_k(t) &= \cos \nu_k t - \cos \frac{\pi t}{T}, \quad 0 < t < T \\ &= \cos \nu_k t + \cos \nu_k (t - T), \quad t > T \\ \nu_k &= \left[\frac{k\pi}{l} \tanh \frac{k\pi}{l} \right]^{\frac{1}{2}} \end{aligned}$$

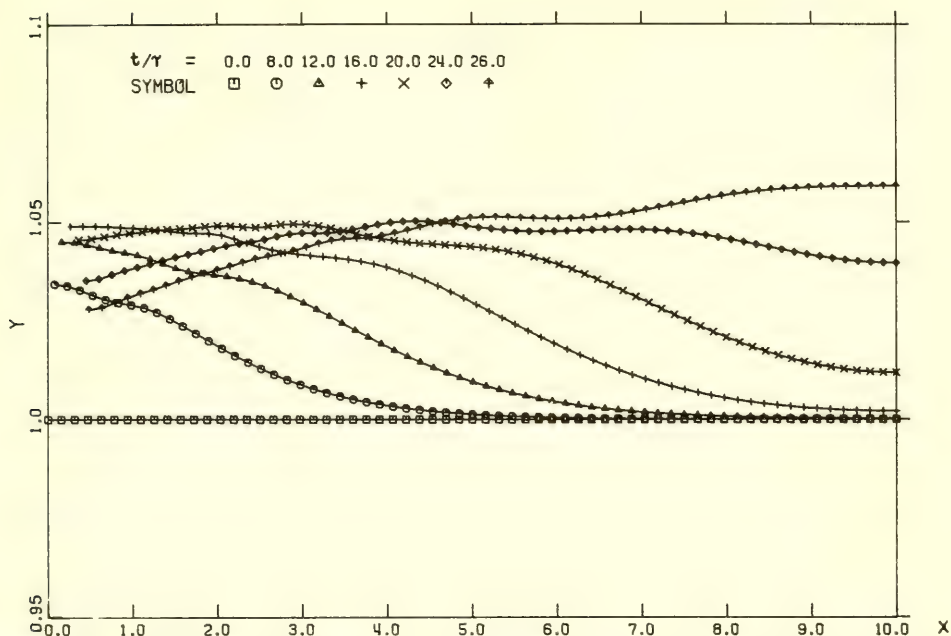


Fig. 5. Linearized solution to example 1: $M=0.53$, $T=32\tau$, $\tau=0.53$, showing free surface position at a selection of times, t .

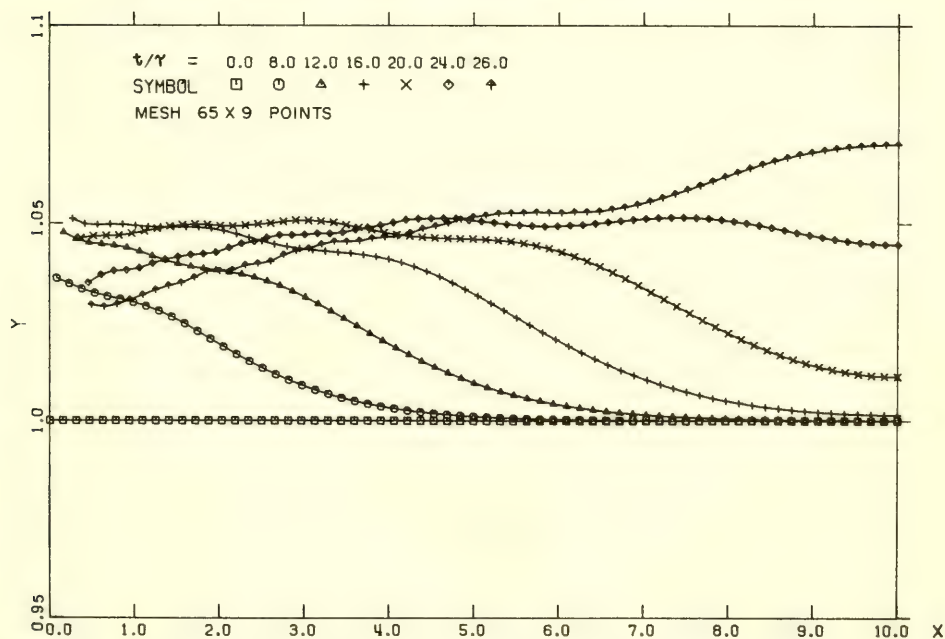


Fig. 6. Numerical solution to example 1: $M=0.53$, $T=32\tau$, $\tau=0.53$, showing free surface position at a selection of times, t .

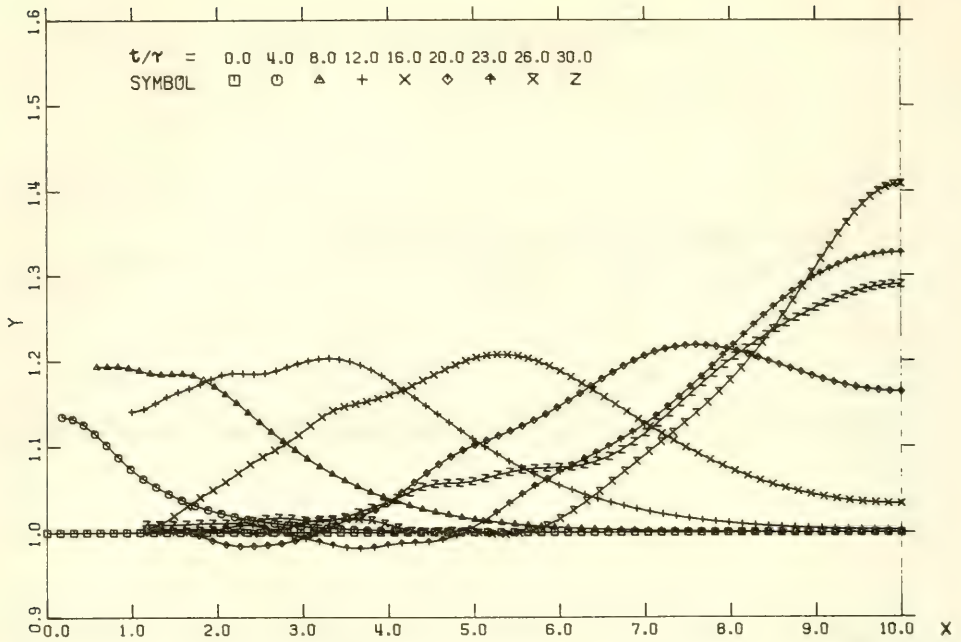


Fig. 7. Linearized solution to example 1: $M = 1.16$, $T = 16\tau$, $\tau = 0.60$, showing free surface position at a selection of times, t

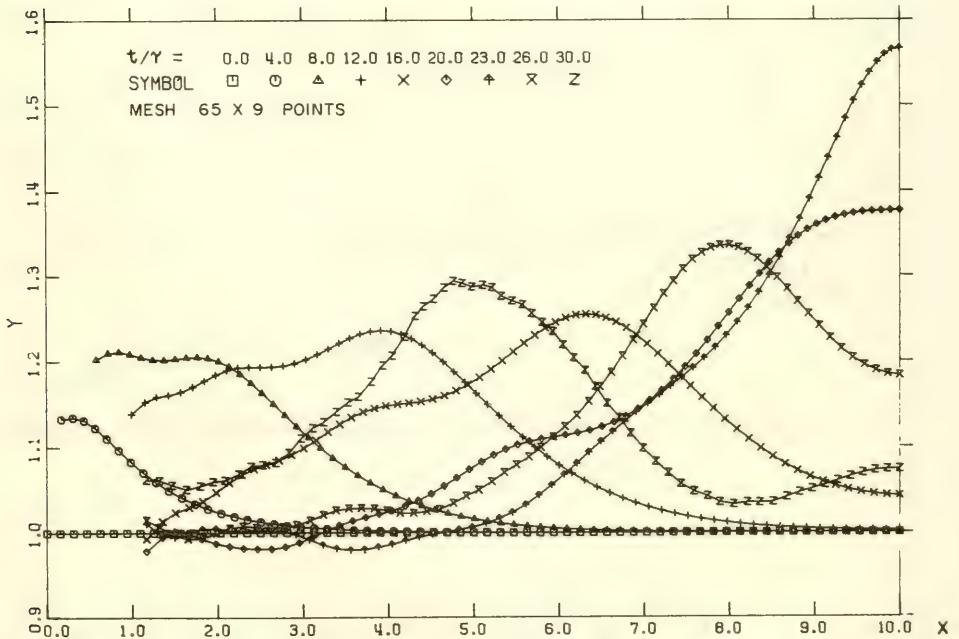


Fig. 8. Numerical solution to example 1: $M = 1.16$, $T = 16\tau$, $\tau = 0.60$, showing free surface position at a selection of times, t

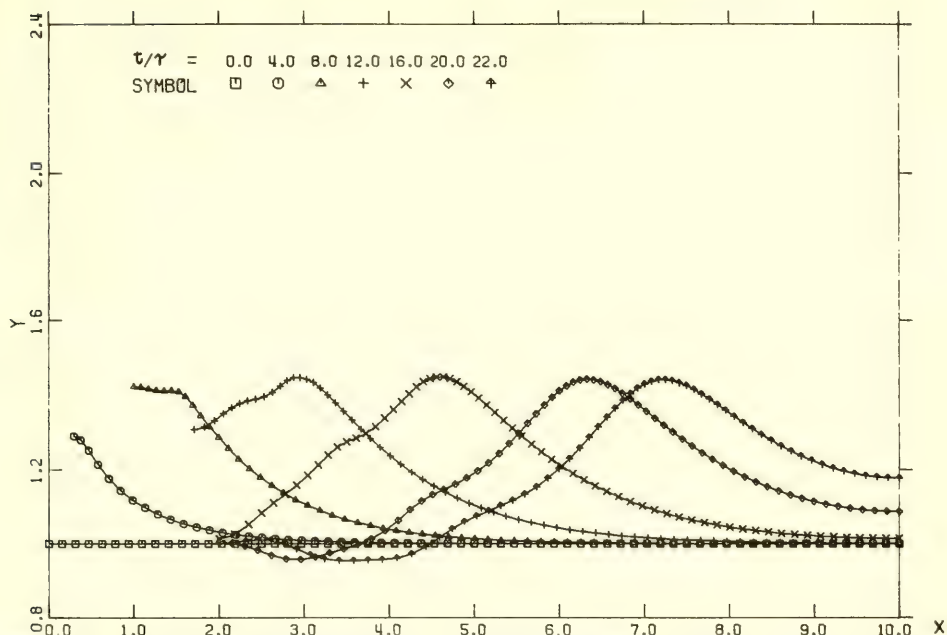


Fig. 9. Linearized solution to example 1: $M = 2.00$, $T = 16\tau$, $\tau = 0.48$, showing free surface position at a selection of times, t

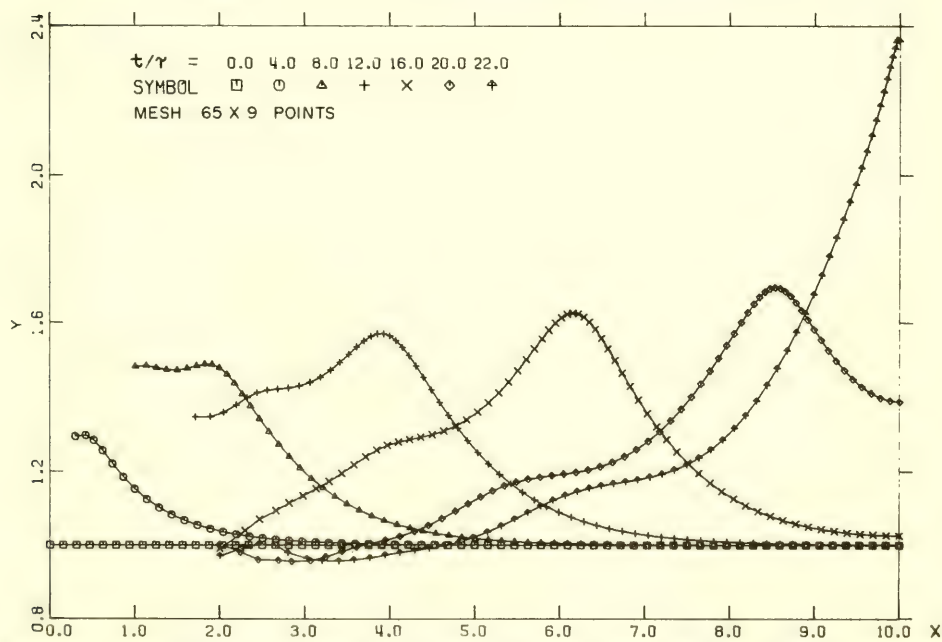


Fig. 10. Numerical solution to example 1: $M = 2.00$, $T = 16\tau$, $\tau = 0.48$, showing free surface position at a selection of times, t

and ℓ is the difference between the walls AD and BC. In Figs. 5 and 6, 7 and 8, 9 and 10 the numerical and linearized free surface shapes are compared for three cases of increasing wave amplitude. As the amplitude increases the similarity between the two diverges; both the wave velocity and the build up on the wall become progressively greater in the numerical solution. Note also that, especially in Fig. 10, the peak of the wave is much sharper than in the linearized solution. For amplitudes less than that of Figs. 5 and 6 the results were almost identical.

C. Example Two, Figs. 4(b), 11, and 12

The second example, Fig. 4(b), introduces moving and curved solid boundaries; the liquid is disturbed from rest by a bed uplift of the form:

$$\begin{aligned} \text{For } X_1 < X < X_2, \quad Y_{CD} &= M \sin^2 \left[\frac{\pi t}{2T} \right] \sin^2 \left[\frac{\pi(X - X_1)}{(X_2 - X_1)} \right] & \text{for } 0 < t < T \\ &= M \sin^2 \left[\frac{\pi(X - X_1)}{(X_2 - X_1)} \right] & \text{for } t > T \end{aligned}$$

$$\text{For } X < X_1, X > X_2, \quad Y_{CD} = 0 \quad \text{all } t$$

Within certain extreme limits on M and T this causes a surface wave immediately above the bed disturbance which then spreads out to each side and is followed by a depression wave over the bed uplift. The linearized solution is

$$\begin{aligned} Z - c &= \frac{iM}{4} \cdot \frac{(X_2 - X_1)}{\ell} \cdot A(t) + \sum_{k=1}^{\infty} R_k \left[i \tanh \left(\frac{\pi k}{\ell} \right) A(t) \cos \left(\frac{k\pi c}{\ell} \right) \right. \\ &\quad \left. + B_k(t) \sin \left(\frac{k\pi c}{\ell} \right) \right] \end{aligned} \quad (32)$$

where

$$R_k = M \left\{ \sin \left(\frac{k\pi X_2}{\ell} \right) - \sin \left(\frac{k\pi X_1}{\ell} \right) \right\} / 2\ell \nu_k^2 \left\{ 1 - \left(\frac{k(X_2 - X_1)}{2\ell} \right)^2 \right\}$$

$$\nu_k = \left[\frac{k\pi}{\ell} \tanh \frac{k\pi}{\ell} \right]^{\frac{1}{2}}$$

$$A(K) = 2 \sin^2 \frac{\pi t}{T} \quad \text{for } 0 < t < T, \quad = 2 \quad \text{for } t > T$$

$$B_k(t) = \sigma_k \cos \nu_k t + 1 - (1 + \sigma_k) \cos \frac{\pi t}{T} \quad \text{for } 0 < t < T$$

$$= 2 + \sigma_k (\cos \nu_k t + \cos \nu_k (t - T)) \quad \text{for } t > T$$

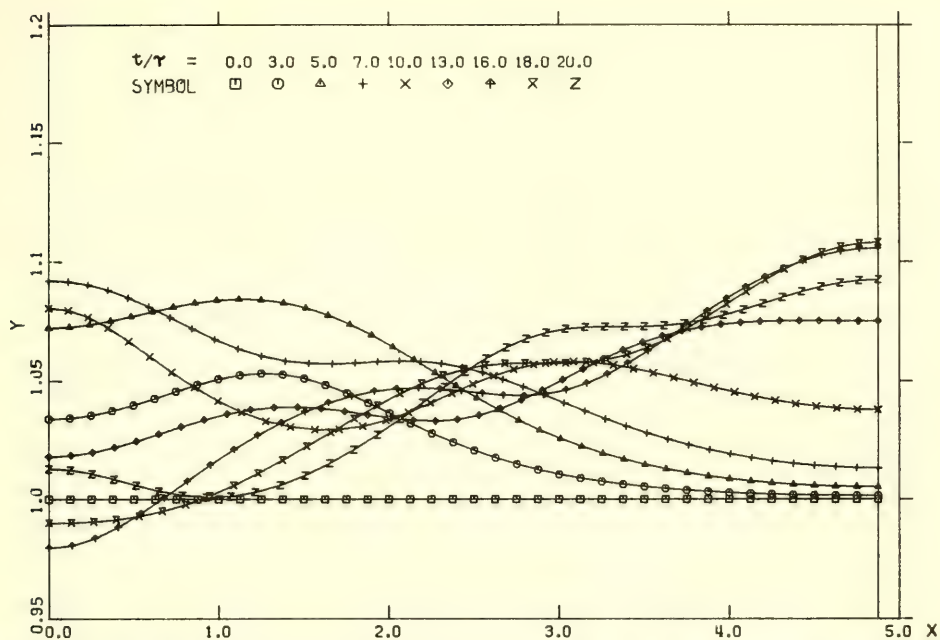


Fig. 11. Linearized solution to example 2: $M = 0.344$, $X_1 = 0.75$, $X_2 = 2.12$, $T = 6\tau$, $\tau = 0.35$, free surface positions at selection of times, t

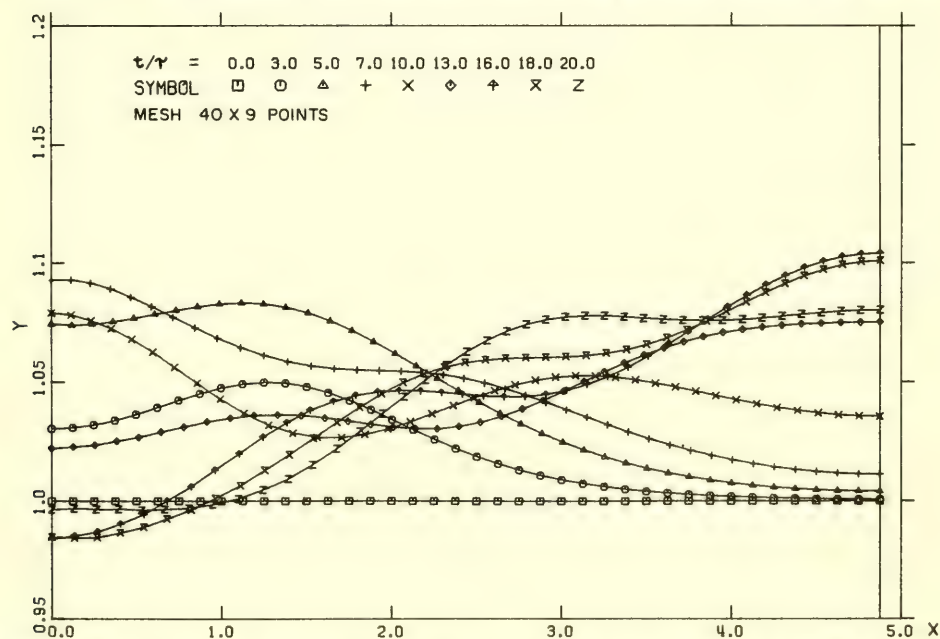


Fig. 12. Numerical solution to example 2: $M = 0.344$, $X_1 = 0.75$, $X_2 = 2.12$, $T = 6\tau$, $\tau = 0.35$, free surface positions at selection of times, t

$$\sigma_k = \operatorname{sech}^2 \left(\frac{\pi k}{l} \right) / \left[\frac{T^2 v_k^2}{\pi^2} - 1 \right]$$

and l is the a difference between the vertical walls. For T of the order of 2 or 3 and for values of M up to 0.3, at least, there was virtually no difference between the numerical and linearized solutions. Figures 10 and 11 in which $M = 0.344$ demonstrate this.

D. Example Three, Figs. 4(c), 13, 14, 15. A Sloping Beach

By altering the condition on the boundary AB of example one and employing the shoreline treatment of Section 5E, the interaction of the waves with a sloping beach could be studied. In Fig. 13 a small wave approaches a 27° beach. As the horizontal inclination of the tangent to the free surface at the shoreline (β) decreases, the shoreline (A) accelerates up the beach until β becomes positive. The acceleration then reverses (as in Eq. (28)) and the wave reaches maximum run up. The backwash is extremely rapid and positions $t/\tau = 21, 22$ suggest that this causes the small wave which is following the main one to break. By this time the cells have become very distorted and the mesh points excessively widely spaced to allow further progress. A similar succession of events takes place with the larger wave and smaller beach angle (18°) of Fig. 14. Note in this case the large run-up to wave-height ratio. In neither of these cases does there appear to be any tendency for the main wave to break on its approach run. Indeed the reaction with the beach is similar to the behavior predicted by Carrier and Greenspan [1958] in their non-linear shallow water wave analysis. The wave amplitude was further increased and the beach slope decreased to 9° in an attempt to produce breaking on the approach run. A preliminary result is shown in Fig. 15. Variations in the application of the free surface condition and in the shoreline treatment have, as yet, failed to remove the irregularities in that solution. A stronger shoreline singularity coupled with an insufficiently rigorous treatment of it may be to blame. An optimistic viewer might detect a breaking tendency.

E. Example Four, Figs. 4(d), 16. A Shelf

One final example is shown in Figs. 4(d) and 16 where the wave travels up a shelf, created by changing the boundary condition on CD, Fig. 1. Excessive vertical elongation of the cells on top of the shelf caused this computation to be stopped at the last time shown. (At this point the wave height/water depth ratio on the shelf is of the order of 2.) However, one can detect a splitting of the wave into two waves as might be expected from the theory of Lax [1968].

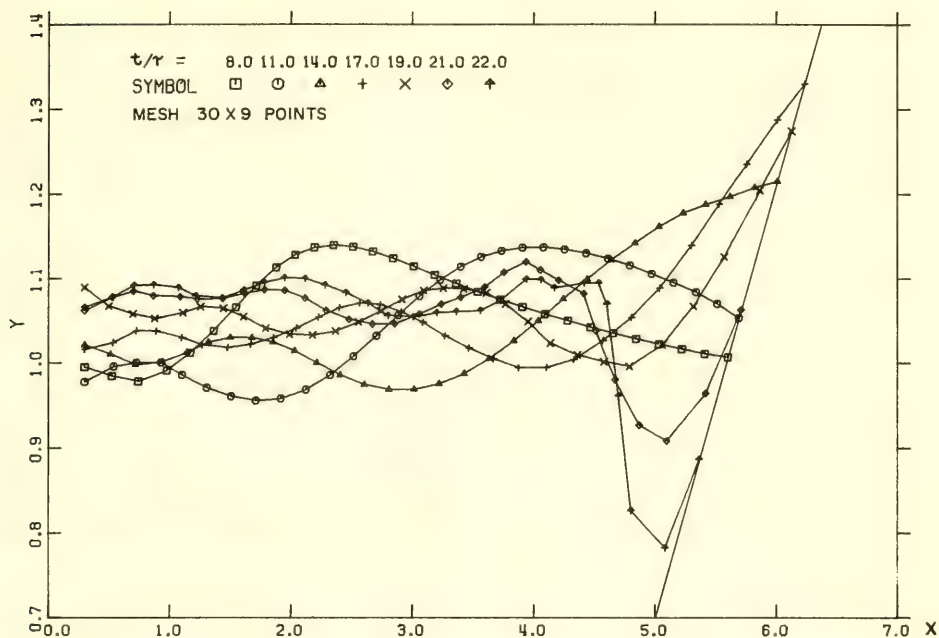


Fig. 13. Example 3 with $M=0.30$ and $T=6\tau$, $\tau=0.571$. The beach slope is 27° . Free surface positions at selection of times, t

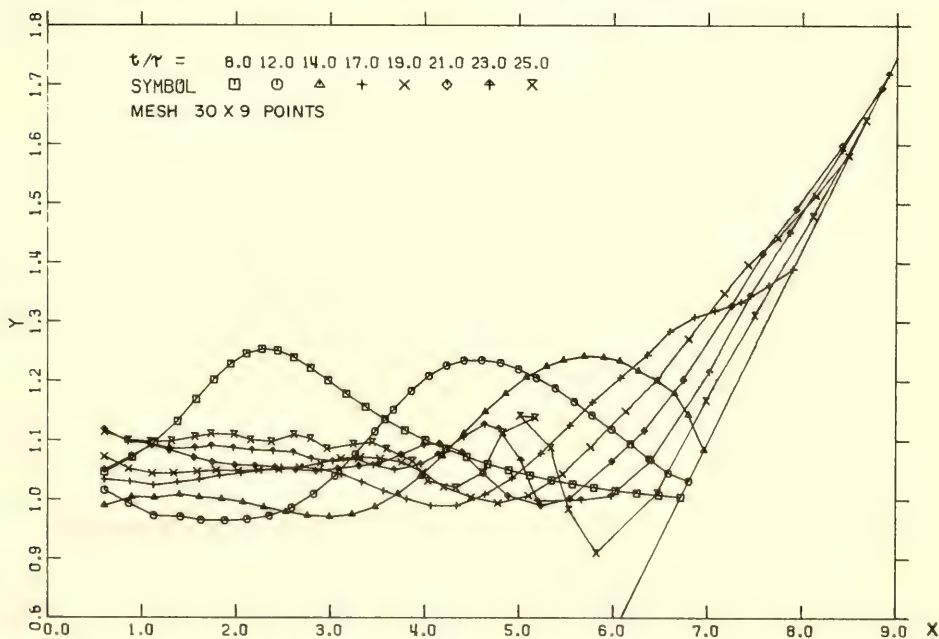


Fig. 14. Example 3 with $M=0.60$ and $T=8\tau$, $\tau=0.571$. The beach slope is 18° . Free surface positions at selection of times, t

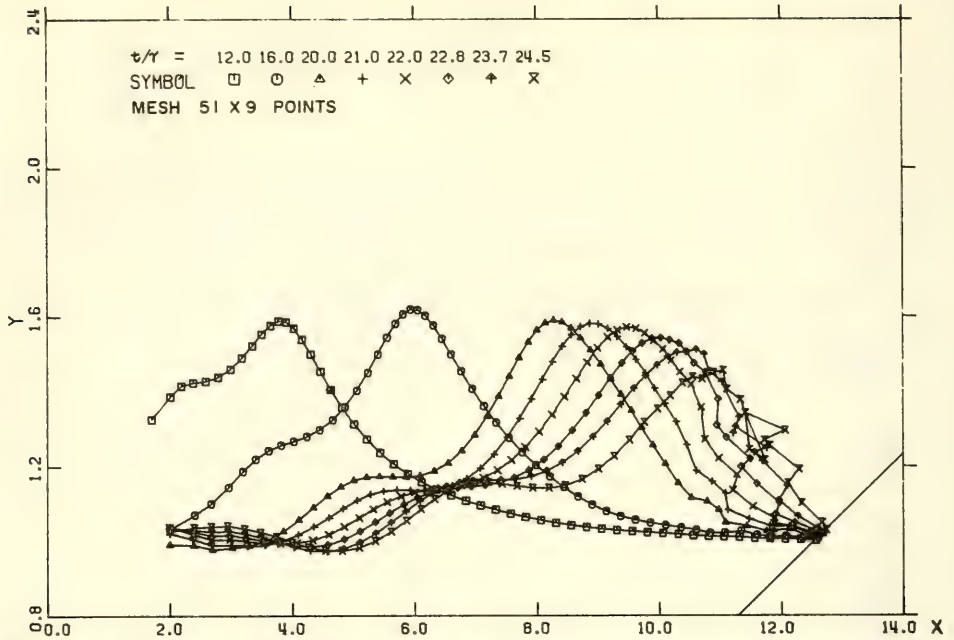


Fig. 15. Example 3 with $M=2.00$, $T=16\tau$, $\tau=0.481$. The beach slope is 9° . Free surface positions at selection of times, t

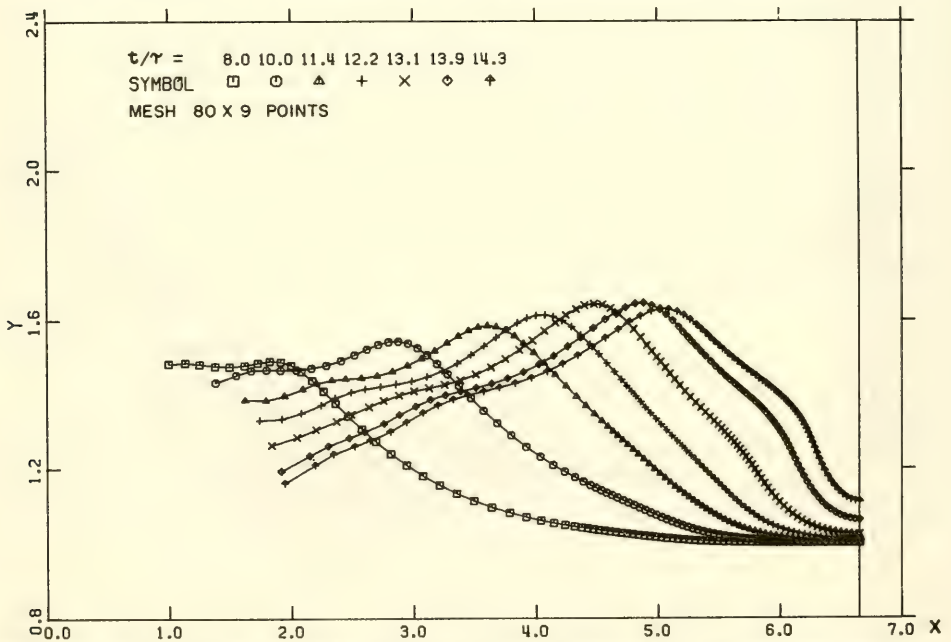


Fig. 16. Example 4 with $M = 2.00$, $T = 16\tau$, $\tau = 0.481$. Shelf defined by $X_1 = 4.41$, $X_2 = 5.16$, $HR = 0.3$. Free surface positions at selection of times, t

VII. CONCLUDING REMARKS

Rather severe examples were taken in order to test the limiting characteristics of the method developed. Provided the various interval limitations were adhered to only two problems arose which could prematurely conclude a computation. First, excessive elongation of the cells in regions of the most violent motion could cause the mesh points to be excessively widely spaced; rezoning could, however, make it possible to continue. Secondly, it would appear that a more detailed knowledge and treatment of some singularities is required. Work on this, and especially on the shoreline singularity of example three, is in progress at the moment.

Other types of examples which have been only briefly investigated thus far are: the matching with a semi-infinite region in which some analytic solution is used; the inclusion of surface tension; the extension of the method to three dimensions; examples in which the fluid is inhomogeneous. It is hoped to present such results in the near future.

The authors are deeply appreciative of the kind and considerate help given by Professor T. Y. Wu.

This work was partially sponsored by the National Science Foundation under grant GK 2370 and by the Office of Naval Research under contract N00014-67-A-0094-0012.

REFERENCES

- Amsden, A. A. and Harlow, F. H., The S.MAC method: A numerical technique for calculating incompressible fluid flows, Los Alamos Scientific Laboratory Report LA-4370, 1970.
- Biesel, F., "Study of wave propagation in water of gradually varying depth," in Gravity Waves, U.S. National Bureau of Standards NBS Circular 521, 1952.
- Brennen, C., "A numerical solution of axisymmetric cavity flows," J. Fluid Mech., 37, 4, 1969.
- Brode, H. L., "Gas dynamic motion with radiation: a general numerical method," Astronautica Acta, 14, 1969.
- Carrier, G. F. and Greenspan, H. P., "Water waves of finite amplitude on a sloping beach," J. Fluid Mech., 4, 1958.

- Chan, R. K-C., Street, R. L. and Strelkoff, T., Computer studies of finite amplitude water waves, Stanford University Civil Engineering Technical Report No. 104, 1969.
- Fontanet, P., Théorie de la génération de la houle cylindrique par un bateau plan, Thesis, University of Grenoble, 1961.
- Fromm, J. E. and Harlow, F. H., "Numerical solution of the problem of vortex street development," Physics of Fluids, 6, 1963.
- Heitner, K. L., A mathematical model for the calculation of the run-up of tsunamis, Thesis, California Institute of Technology, 1969.
- Hirt, C. W., The numerical simulation of viscous incompressible fluid flows, Proceedings of the 7th ONR Symposium, Rome, 1968.
- Hirt, C. W., Cook, J. L. and Butler, T. D., "A Lagrangian method for calculating the dynamics of an incompressible fluid with free surface," J. of Computational Physics, 5, 1970.
- John, F., "Two-dimensional potential flows with free boundaries," Communs. Pure and Appl. Math., 6, 1953.
- Lamb, H., Hydrodynamics (6th Ed.), Cambridge University Press, 1932.
- Lax, P. D., "Integrals of non-linear equations of evolution and solitary waves," Communs. Pure and Appl. Math., 21, 1968.
- Lewy, H., "Water waves on sloping beaches," Bull. Amer. Math. Soc., 52, 1946.
- Penney, W. G. and Price, A. T., "Finite periodic stationary gravity waves in a perfect liquid," Phil. Trans. Roy. Soc., A, 244, 1952.
- Pohle, F., "Motions of water due to breaking of a dam, and related problems," in Gravity Waves, U.S. National Bureau of Standards Circular 521, 1952.
- Roseau, M., "Short waves parallel to the shore over a sloping beach," Communs. Pure and Appl. Math., 11, 1958.
- Sekerz-Zen'kovich, Ya. I., "On the theory of standing waves of finite amplitude on the surface of a heavy fluid," (R) Dokl. Akad. Nauk. SSSR, (N. S.), 58, 1947.

Wehausen, J. V. and Laitone, E. V., "Surface Waves," Handbuch der Physik, Vol. IX, Fluid Dynamics III, 1960.

Welch, J. E., Harlow, F. H., Shannon, J. P. and Daly, B. J.
The MAC method, Los Alamos Scientific Laboratory Report
No. LA-3425, 1966.

Whitham, G. B., "A general approach to linear and non-linear dispersive waves using a Lagrangian," J. Fluid Mech., 22, 2, 1965.

TWO METHODS FOR THE COMPUTATION OF THE MOTION OF LONG WATER WAVES — A REVIEW AND APPLICATIONS

Robert L. Street
Robert K. C. Chan
Stanford University
Stanford, California
and
Jacob E. Fromm
IBM Corporation
San Jose, California

I. INTRODUCTION

The continuing evolution in speed and capacity of digital computers has encouraged the development of many computationally oriented methods for analysis of the movement of waves over the surface of the ocean and onto the shore. Carrier [1966] gave analytical techniques requiring numerical evaluation for the propagation of tsunamis over the deep ocean and for the run-up on a sloping beach of periodic waves that do not break. He noted that linear theory is valid in the deep ocean and over much of the sloping shelf; thus, nonlinear theory is needed only in specific regions where the nonlinear contributions to the dynamics are important. However, his nonlinear, approximate theory was developed only for the plane flows. An extension and application of Carrier was made by Hwang, et al. [1969]. They studied the transformation of non-periodic wave trains on a uniformly sloping beach using the nonlinear shallow water wave equation and the Carrier-Greenspan transform. This transform fixes the moving, instantaneous shoreline of the physical plane to a single point in the transformed plane. Although the analysis deals only with plane flows and does not handle breaking waves, it does predict wave run-up and reveals a significant beat phenomenon.

To study nonlinear effects and/or to account more completely for the waves' reaction to arbitrary ocean topography and boundaries, it is natural to turn to numerical methods and their accompanying computer codes. The simplest of the numerical methods are represented by the refraction techniques of Keulegan and Harrison [1970]

and Mogel, et al. [1970]. These methods, based on linear, geometric-optics theory, are applicable to arbitrary bottom topography but can predict neither breaking nor run-up. They also neglect reflection and diffraction effects. The computer code is very simple, requiring step-by-step solution of Snell's law and a wave intensity equation over a grid of bottom depths.

Vastano and Reid [1967] described a procedure employing a numerical integration of the linearized long wave equation to study tsunami response at islands. They concluded, by comparison with analytic solutions for special cases, that their numerical model gave an adequate representation of the solution to the linearized equations. Their paper indicated that the work was a lead-in to a more general treatment of arbitrary bottom topography. At the island they used a vertical cylinder that penetrates the surface and thereby restricts the movement of the instantaneous shoreline. No run-up can be calculated in the usual sense.

In another approach, Lautenbacher [1970] used linear, shallow water theory to study run-up and refraction of oscillating waves of tsunami-like character on islands. His method allows for the moving, instantaneous shoreline and, of course, for superposition of individual results from monochromatic waves. Working from an integral equation formulation and employing a Hankel function representation of the far-field radiation condition similar to that used by Vastano and Reid [1967], Lautenbacher used a grid of discrete points to numerically integrate the integral equation of his model. Combining his work with Carrier [1966], Lautenbacher was able to estimate total tsunami run-up from a distant source. He also emphasized the importance of refractive focusing effects.

The numerical methods aimed specifically at modelling nonlinear effects take three forms:

- a. Approximate, plane-flow models for arbitrary or sloping beaches and based on approximate equations.
- b. Exact plane-flow models.
- c. Quasi-three-dimensional models.

The approximate, plane-flow models are represented by the work of Freeman and LeMéhauté [1964], Peregrine [1967], Heitner [1969], Street, et al. [1969], Camfield and Street [1969], and Madsen and Mei [1969a, 1969b]. With the exception of Heitner [1969], the authors used Eulerian coordinates. Freeman and LeMéhauté [1964] applied the method of characteristics to the nonlinear, shallow water wave equations for plane flow. They described a method for computing the shoaling of a limit-height solitary wave on a plane beach, predicting the point of breaking inception by the crossing of characteristic lines and computing the subsequent bore development and run-up at the shoreline. A term was added to the equations to correct the

assumed hydrostatic pressure distribution beneath the wave, the assumption not being valid for finite amplitude waves. Camfield and Street [1969] used a refined correction term, but the results were not entirely satisfactory in either case.

Peregrine [1967] and Madsen and Mei [1969a] derived approximate, nonlinear, governing equations for the propagation of long waves over slowly varying bottom topography. In these equations the vertical component of motion is integrated out of the computation so a single-space-dimension problem is all that remains. Madsen and Mei [1969a] showed that, while they and Peregrine used different approaches and solution methods, the equations are the same when presented in the same variables. Furthermore, Madsen and Mei [1969a] explained that these nonlinear equations, obtained under assumptions similar to those leading to cnoidal waves in the case of horizontal bottoms, give a uniformly valid description of long wave problems as long as breaking does not occur. In particular, their equations were derived under the condition that the Ursell parameter

$$U_* = \frac{\eta_0 L_0^2}{d_0^3} = O(1) \quad (1)$$

where η_0 is a measure of wave amplitude, L_0 is a characteristic wave length and d_0 is the water depth. Thus, the nonlinear, governing equations are of the Korteweg-deVries type (KdV) that have permanent solutions, e.g., cnoidal waves, for the case of horizontal bottoms. Madsen and Mei [1969a] demonstrated that, although the equations pertinent to each of the three groups of long waves (Airy where $U_* \gg 1$, KdV where $U_* = O(1)$ and Linear where $U_* \ll 1$) have different mathematical solutions, the features characterizing each group are all contained in the equations derived under the assumption of waves of the KdV type.

The method of characteristics was applied by Madsen and Mei [1969a, 1969b] to solve their equations for initial, boundary value problems involving solitary waves and periodic waves on plane slopes and a shelf; their equations, like those of Peregrine [1967], are applicable to general, uneven bottoms. Street, et al. [1969] presented a numerical model APPSIM and results based on the Peregrine [1967] method, but employing initial and boundary conditions similar to those of Madsen and Mei [1969b]. These methods reproduced the nonlinear breakdown on a shelf of a solitary wave, the breakdown having previously been observed only in experiments [Street, et al., 1968]. Furthermore, comparison shows quantitative agreement amongst these methods and relevant experiments. Run-up cannot be calculated with these models which employ the vertical beach (or island) face that was used by Vastano and Reid [1967]. However, Peregrine's [1967] derivation included the two horizontal space dimensions, while Madsen and Mei [1969a] did not. Accordingly, as an extension of APPSIM, a quasi-three-dimensional model

APPSIM2 is based on Peregrine's equations and is described in detail in Section III below.

Heitner [1969] presented a nonlinear method based on Lagrangian coordinates and a finite element representation of the fluids. His theory retains terms representing the kinetic energy of the vertical motion; thus, like the methods described just above, Heitner's approximate method permits permanent waves to propagate. Unlike those methods, Heitner's formulation gives a representation of wave breaking inception, bore formation and run-up on a linear beach for plane flows.

The exact, plane-flow models are represented by the work of Brennen [1970], Hirt, et al. [1970], and Chan and Street [1970]. All are based on the exact equations of motion; however, Chan and Street [1970] work in Eulerian coordinates, Brennen [1970] uses Lagrangian coordinates and equations, and Hirt, et al. [1970] employ Lagrangian coordinates but retain the Eulerian form of the governing equations. Based on the Marker-and-Cell (MAC) method [Welch, et al., 1966], Chan and Street's model for water waves is called SUMMAC and is discussed in Section IV of this paper. Brennen has applied his technique to tsunami generation by ocean floor movements and to run-up on a beach. Hirt, et al., made applications to wave sloshing in a tank by way of verification of their method, called LINC, which has wide application in ocean wave analyses as well. All the exact, plane-flow methods mentioned employ some form of finite-difference or cell representation of a discrete grid of points.

Finally, the quasi-three-dimensional methods are represented by the work of Pritchett [1970] and Leendertse [1967] and by the extension to two horizontal dimensions of the APPSIM program of Street, et al. [1969] discussed above. Pritchett presents a code for solving incompressible, two-dimensional, axisymmetric, time-dependent, viscous fluid flow problems involving up to two free surfaces. The basic equations are exact; heuristic models for turbulence simulation are used. Scalar quantities such as heat and solute concentration can be traced, and the fluid may be slightly non-homogeneous. Most of the variables, their placement in the computational mesh, and the free surface treatment are those used in MAC [Welch, et al., 1966].

Leendertse [1967] developed a computational model for the calculation of long-period water waves in which the effects of bottom topography, bottom roughness and the earth's rotation were included. The equations of motion are vertically integrated so only the two horizontal space-dimensions remain (much in the manner of Peregrine, [1967]), but while Peregrine [1967], Madsen and Mei [1969a, 1969b] and Street et al. [1969] retain terms to account for the vertical accelerations of the fluid, Leendertse [1967] does not. His equations become the usual nonlinear shallow water wave equations with added terms to account for the bottom roughness and earth's rotation. He

focuses his attention on the modelling of long waves such as tsunamis in areas with irregular bottom topography and complicated ocean boundaries. His computation uses a space-staggered scheme (where velocities, water levels, and depth are described at different grid points) and a double time step operation in which the time integral is considered over two successive operations in a manner designed to make effective use of the space-staggered scheme. Among the papers mentioned in this Introduction, only Leendertse [1967], Welch, et al. [1966] and Chan and Street used computer graphic display for output of results. The value of graphic display is illustrated in the results presented in the remainder of this work.

II. THE PRESENT WORK

Street, et al. [1969] gave a progress report on the development of computer programs for two numerical, finite-difference models for the study of long water waves. These models and their accompanying programs were, as noted above, given the acronyms APPSIM and SUMMAC. Both were based on representation of the motion of inviscid, incompressible fluids in terms of the Euler equations of motion in Eulerian coordinates. Flow boundary conditions were derived from physical requirements and the governing equations at the boundaries. The mathematical models thus obtained were then transformed to numerical, finite difference models for the purposes of computation. In 1969 the study had been confined to plane flows, but the numerical results had been verified by comparison with experiments and the work of others. The models were to provide detailed flow field data in the portion of the wave shoaling process where nonlinear effects are significant, but breaking has not occurred.

Our approximate simulation (APPSIM) is based on the method of Peregrine [1967] and supplemented by the work of Madsen and Mei [1969a, 1969b]. APPSIM was implemented for quasi-two-dimensional, plane flows (vertical motion integrated out). For the purpose of implementing, testing, and verifying the program and method, we simulated the propagation of solitary waves on a stepped slope which represents the configuration of the continental slope and shelf, i.e., we examined long waves in moderately shallow water. The key criteria to be satisfied were

- a. Solitary waves propagate stably on a horizontal bottom.
- b. Solitary waves decompose into undular bores when the waves propagate onto a stepped slope [Street, et al., 1968].
- c. Wave heights must be in good quantitative agreement with available experimental data.

As reported by Street, et al. [1969] APPSIM met these criteria.

The successful application of APPSIM to examples of plane motion of long waves indicated that the method could be applied to a quasi-three dimensional simulation (two horizontal space dimensions with vertical effects represented in once integrated equations) of the motion of waves over arbitrary bottom topography. We have extended APPSIM to handle general bottom topography and both solitary and oscillatory wave inputs. The new method is called APPSIM2 and presented in Section III below.

An objective of our exact simulation was to provide detailed information about wave processes near the shore and at the ocean-structures interface. The Stanford-University-Modified Marker-and-Cell (SUMMAC) method computes time-dependent, inviscid, incompressible fluid flows with a free surface; the method is suitable for analyzing two-dimensional flows. Initially, we simulated the propagation of solitary waves in a horizontal channel filled with fluid to unit depth and with vertical end walls. The solitary wave propagation problem possessed several key features:

- a. The theories for the wave motion against the wall were not in agreement with experiments.
- b. The solitary wave should propagate stably (without change of form) in zones not near the channel walls.
- c. Perfect reflection from the walls should occur.

We undertook a significant modification of the MAC method to create a numerical scheme suitable for water wave simulation. As reported in 1969, the resulting SUMMAC simulation met the criteria of stable propagation and perfect reflection of solitary waves and resolved the disagreement between theory and experiment for motion against a vertical wall.

The successful application of SUMMAC to the initial example indicated the possibility of employing a modification of the same technique to attack a variety of other problems. We have subsequently studied the generation of water waves by a periodic pressure pulse and the shoaling and run-up of solitary waves on a stepped slope and on plane beaches. A summary of the presently implemented SUMMAC method and results for the periodic pressure pulse problem are presented in Section IV of this paper. An evaluation of the numerical qualities of SUMMAC and a report of the shoaling and run-up studies are given in Chan, et al. [1970] and Chan and Street [1970b].

III. APPSIM2

3.1. The Governing Equations and Auxiliary Conditions

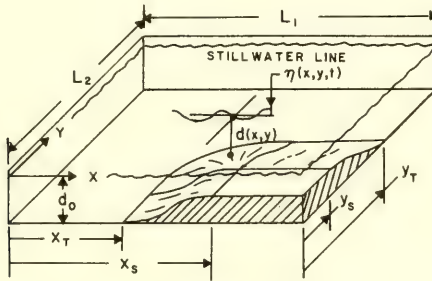
Dimensionless variables are defined below and in Fig. 1 where the physical domains considered are also illustrated. The variables are

$$(x, y, \eta, d) = (x^*, y^*, \eta^*, d^*) d_0^{-1}$$

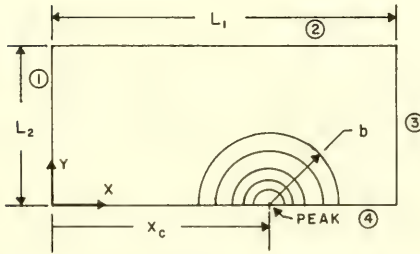
$$t = t^* (g/d_0)^{1/2}$$

$$(u, v) = (u^*, v^*) (g d_0)^{-1/2}$$

where those on the left-hand sides are dimensionless and d_0 is the depth in the deepest part of the simulated wave tank. Here, x and y are fixed, Cartesian coordinates in the horizontal plane; $u(x, y, t)$ and $v(x, y, t)$ are the corresponding mean (vertically-averaged) horizontal fluid velocities; $\eta(x, y, t)$ is the free surface shape, measured from the still or undisturbed water line in the tank, and $d(x, y)$ is the depth of the still water.



a. Shelf (Perspective View)



b. Submerged Seamount (Plan View)

Fig. 1. Definition of symbols and simulated wave tanks for APPSIM2

If For waves of the KdV type that we wish to study, $U_* = O(1)$.

$$\epsilon = \eta_0/d_0 \quad (2)$$

and

$$\sigma = d_0/L_0 \ll 1 \quad (3)$$

for long waves, then from Eq. (1), $U_* = \epsilon/\sigma^2 = 1$ and $\epsilon = \sigma^2$. This is the relation on which Peregrine [1967] based his expansion-in-a-parameter analysis. He pointed out also that $d(x,y) = O(1)$ and the derivatives of d equal $O(\sigma)$ are necessary restrictions; otherwise, the variations in the depth of water are shorter than the incident waves and tend to generate shorter waves, thus upsetting the scheme of the approximations.

Under the above conditions Peregrine [1967] obtained the momentum equations

$$u_t + uu_x + vu_y + \eta_x = \frac{1}{2} d[(du)_{xx} + (dv)_{xy}]_t - \frac{1}{6} d^2[u_{xx} + v_{xy}]_t \quad (4)$$

$$0 < x < L_1, \quad 0 < y < L_2, \quad 0 < t$$

$$v_t + uv_x + vv_y + \eta_y = \frac{1}{2} d[(du)_{xy} + (dv)_{yy}]_t - \frac{1}{6} d^2[u_{xy} + v_{yy}]_t \quad (5)$$

$$0 < x < L_1, \quad 0 < y < L_2, \quad 0 < t$$

and the continuity equation

$$\eta_t + [(d + \eta)u]_x + [(d + \eta)v]_y = 0 \quad (6)$$

$$0 < x < L_1, \quad 0 < y < L_2, \quad 0 < t$$

These equations and the appropriate auxiliary conditions described below are solved numerically by a straightforward finite difference scheme that is presented in Section 3.2.

The auxiliary conditions are the boundary and initial conditions appropriate to Eqs. (4-6) for motion in a vertical-walled tank (Fig. 1). For solid, vertical walls the velocity perpendicular to the wall is zero at the wall and non-breaking waves reflect perfectly from the wall. If n is the normal coordinate and U and V are

typical normal and tangential fluid velocities at the wall, then in inviscid flow

$$\eta_n = 0 \quad (7)$$

$$U = 0 \quad (8)$$

$$V_n = 0 \quad (9)$$

$$U_{nn} = 0 \quad (10)$$

Accordingly, for Wall 1 shown in Fig. 1 we have for $0 < y < L_2$, $0 < t$:

$$\eta_x(0, y, t) = 0, \quad v_x(0, y, t) = 0, \quad u(0, y, t) = 0, \quad u_{xx}(0, y, t) = 0$$

Similar conditions hold on the other walls.

If we choose to prescribe $\eta = \eta(t)$ along Wall 1 where $x = 0$, then a special set of conditions must be derived (cf., Madsen and Mei [1969a] who point out that this prescription corresponds physically to the situation of having measured the incoming wave height at a particular station). Peregrine [1967] gave the irrotationality condition

$$\begin{aligned} u_y - v_x &= \frac{1}{2} d_y[\nabla \cdot (d\vec{u})]_x - \frac{1}{2} d_x[\nabla \cdot (d\vec{u})]_y \\ &\quad - \frac{1}{3} dd_y[\nabla \cdot \vec{u}] + \frac{1}{3} dd_x[\nabla \cdot \vec{u}]_y \end{aligned} \quad (11)$$

where $\vec{u} = (u, v)$ and $\nabla = (\partial/\partial x, \partial/\partial y)$. If the bottom is flat in the neighborhood of Wall 1, $d_x \equiv d_y \equiv 0$ and Eq. (11) becomes

$$u_y = v_x \quad (12)$$

But, if $\eta(0, y, t) = \eta(t)$, then until some reflection from a shoal or beach in the tank returns to $x = 0$,

$$u_y(0, y, t) = 0 \quad (13)$$

and, hence,

$$v_x(0, y, t) = 0 \quad (14)$$

Given $\eta(0, y, t) = \eta(t)$ and Eqs. (13) and (14) and using Eqs. (4-6) at Wall 1, one can uniquely determine u , v and η there for the case of a prescribed incoming wave. The conditions at the remaining walls are, of course, not changed.

The appropriate initial conditions for Eqs. (4-6) are the initial values of the dependent variables, viz.,

$$\eta(x, y, 0) = \eta_i(x, y); \quad u(x, y, 0) = u_i(x, y); \quad v(x, y, 0) = v_i(x, y) \quad (15)$$

3.2. The Difference Representation and Computation Scheme

For numerical computation the region $0 \leq x \leq L_1$, $0 \leq y \leq L_2$ is covered by a grid of discrete mesh points with a spacing $\Delta x = \Delta y = \Delta$ and calculations are carried forth with time steps Δt . To allow for proper representation of the boundary conditions the grid indices (i, j) run over the intervals $(1, M)$ and $(1, N)$ respectively and points $(1, j)$, (M, j) , $(i, 1)$ and (i, N) lie outside the tank walls, e.g., $x = 0$ is equivalent to $(2, j)$, etc. Consequently, $L_1 = (M-2)\Delta$ and $L_2 = (N-2)\Delta$ (see Fig. 1).

In the finite difference representation of the differential equations and auxiliary conditions, central space-differences are always used; both forward and time-splitting schemes are used for time-differences. The differential equations of motion, eqs. (4-6), lead to a highly nonlinear and coupled set of difference equations. These are solved iteratively, using a predictor-corrector method. If u , v and η are known at all the grid points at the n^{th} time level, the following scheme leads to calculation of u , v and η at the $n+1^{\text{th}}$ level.

First, u , v and η are predicted at the $n+1^{\text{th}}$ level by use of the nonlinear, shallow water wave equations (Eqs. (4-6) with their right-hand sides set to zero). With the superscript P indicating the predicted value, the difference equations are, after rearrangement for computation,

$$u_{ij}^P = u_{ij} - \frac{\Delta t}{2\Delta} (u_{ij}(u_{i+1j} - u_{i-1j}) + v_{ij}(u_{ij+1} - u_{ij-1}) + \eta_{i+1j} - \eta_{i-1j}) \quad (16)$$

$$v_{ij}^P = v_{ij} - \frac{\Delta t}{2\Delta} (u_{ij}(v_{i+1j} - v_{i-1j}) + v_{ij}(v_{ij+1} - v_{ij-1}) + \eta_{ij+1} - \eta_{ij-1}) \quad (17)$$

$$\eta_{ij}^P = \eta_{ij} - \frac{\Delta t}{2\Delta} (u_{ij}(d_{i+1j} + \eta_{i+1j} - d_{i-1j} - \eta_{i-1j}) + (d_{ij} + \eta_{ij})(u_{i+1j} - u_{i-1j} + v_{ij+1} - v_{ij-1}) + v_{ij}(d_{ij+1} + \eta_{ij+1} - d_{ij-1} - \eta_{ij-1})) \quad (18)$$

where variables without superscript are known at the n^{th} time level.

Second, the x-momentum Eq. (4) is used to obtain a difference equation for u values at the $n+1^{\text{th}}$ level. Central space-differences and time-splitting are used about the point $(i, j, n + \frac{1}{2})$; this leads to a difference equation that is implicit. Now we gather the u^{n+1} terms from the j^{th} row on the left-hand side of the equation and all other terms on the right-hand side. The heart of our procedure is to use u^p , v^p and η^p values in lieu of the u^{n+1} , v^{n+1} and η^{n+1} terms which appear on the right-hand side of the equation, these terms being mostly in the $j-1$ and $j+1$ rows. The result, when rearranged for computation is, for each j ,

$$A u_{i-lj}^{n+1} + B_{ij}^{n+1} + C u_{i+l j}^{n+1} = E, \quad i = 3, 4, \dots, M-2 \quad (19)$$

where

$$A = -\frac{\Delta t}{4\Delta} u_{ij} + \frac{1}{2\Delta^2} \left(\frac{d_{ij}^2}{3} - d_{ij} d_{i-lj} \right)$$

$$B = 1 + \frac{2d_{ij}^2}{3\Delta^2}$$

$$C = \frac{\Delta t}{4\Delta} u_{ij} + \frac{1}{2\Delta^2} \left(\frac{d_{ij}^2}{3} - d_{ij} d_{i+l j} \right)$$

$$\begin{aligned} E = & u_{ij} - \frac{\Delta t}{4\Delta} u_{ij} (u_{i+l j} - u_{i-l j}) \\ & - \frac{\Delta t}{4\Delta} v_{ij} (u_{i j+l} - u_{i j-l} + u_{i j+l}^p - u_{i j-l}^p) \\ & - \frac{\Delta t}{4\Delta} (\eta_{i+l j} - \eta_{i-l j} + \eta_{i+l j}^p - \eta_{i-l j}^p) \\ & + \frac{d_{ij}}{2\Delta^2} \left(-d_{i+l j} u_{i+l j} + 2d_{ij} u_{ij} - d_{i-l j} u_{i-l j} \right. \\ & + \frac{1}{4} (d_{i+l j+l} v_{i+l j+l}^p - d_{i-l j+l} v_{i-l j+l}^p - d_{i+l j-l} v_{i+l j-l}^p \\ & + d_{i-l j-l} v_{i-l j-l}^p - d_{i+l j+l} v_{i+l j+l} + d_{i-l j+l} v_{i-l j+l} \\ & \left. + d_{i+l j-l} v_{i+l j-l} - d_{i-l j-l} v_{i-l j-l}) \right) - \end{aligned}$$

$$\begin{aligned}
 & - \frac{d_{ij}^2}{6\Delta^2} \left(-u_{i+j} + 2u_{ij} - u_{i-j} \right. \\
 & + \frac{1}{4} (v_{i+j+1}^P - v_{i-j+1}^P - v_{i+j-1}^P + v_{i-j-1}^P \\
 & \left. - v_{i+j+1} + v_{i-j+1} + v_{i+j-1} - v_{i-j-1}) \right)
 \end{aligned}$$

Equation (19) must be solved for all i simultaneously for a given j . The matrix of coefficients of the unknowns in Eq. (19) is tridiagonal and is quickly and easily solved by a tridigonal-matrix equation solver employing Gaussian Elimination. The process is repeated for each j until the u_{ij}^{n+1} are known. Appropriate boundary conditions are introduced at the ends of the j^{th} row in each computation.

Third, the y -momentum Eq. (5) is used to obtain a difference equation for the v values at the $n+1^{\text{th}}$ level. The result is entirely equivalent to that for the u values, viz., the third-order terms on the right-hand side create a naturally implicit system so time-splitting is used. Now, however, we use v^P and η^P values for all $i-1$ and $i+1$ points along a given column of implicit equations ($i = \text{constant}$, $3 \leq j \leq N-2$) and we use the u^{n+1} values just computed. The result, when rearranged for computation, is

$$\tilde{A}v_{ij-1}^{n+1} + \tilde{B}v_{ij}^{n+1} + \tilde{C}v_{ij+1}^{n+1} = \tilde{E}, \quad j = 3, 4, \dots, N-2 \quad (20)$$

where

$$\tilde{A} = -\frac{\Delta t}{4\Delta} v_{ij} + \frac{1}{2\Delta^2} \left(\frac{d_{ij}^2}{3} - d_{ij}d_{ij-1} \right)$$

$$\tilde{B} = 1 + \frac{2d_{ij}^2}{3\Delta^2}$$

$$\tilde{C} = \frac{\Delta t}{4\Delta} v_{ij} + \frac{1}{2\Delta^2} \left(\frac{d_{ij}^2}{3} - d_{ij}d_{ij+1} \right)$$

$$\begin{aligned}
 \tilde{E} = & v_{ij} - \frac{\Delta t}{4\Delta} u_{ij} (v_{i+j} - v_{i-j} + v_{i+j}^P - v_{i-j}^P) \\
 & - \frac{\Delta t}{4\Delta} v_{ij} (v_{ij+1} - v_{ij-1}) \\
 & - \frac{\Delta t}{4\Delta} (\eta_{ij+1} - \eta_{ij-1} + \eta_{ij+1}^P - \eta_{ij-1}^P) +
 \end{aligned}$$

$$\begin{aligned}
 & + \frac{d_{ij}}{2\Delta^2} \left(\frac{1}{4} (d_{i+j+1} u_{i+j+1}^{n+1} - d_{i-j+1} u_{i-j+1}^{n+1} - d_{i+j-1} u_{i+j-1}^{n+1} \right. \\
 & + d_{i-j-1} u_{i-j-1}^{n+1} - d_{i+j+1} u_{i+j+1} + d_{i-j+1} u_{i-j+1} \\
 & + d_{i+j-1} u_{i+j-1} - d_{i-j-1} u_{i-j-1}) - d_{ij+1} v_{ij+1} \\
 & + 2d_{ij} v_{ij} - d_{ij-1} v_{ij-1} \Big) \\
 & - \frac{d_{ij}^2}{6\Delta^2} \left(\frac{1}{4} (u_{i+j+1}^{n+1} - u_{i-j+1}^{n+1} - u_{i+j-1}^{n+1} + u_{i-j-1}^{n+1} \right. \\
 & - u_{i+j+1} + u_{i-j+1} + u_{i+j-1} - u_{i-j-1}) \\
 & \left. - v_{ij+1} + 2v_{ij} - v_{ij-1} \right)
 \end{aligned}$$

Now, Eq. (20) must be solved for all j simultaneously for a given i . Again we use the tridiagonal-matrix equation solver. The process is repeated for each i until the v_{ij}^{n+1} are known.

Fourth, the continuity Eq. (6) is used to obtain a difference equation for the η values at the $n+1^{\text{th}}$ level. The u^{n+1} and v^{n+1} values are used in an equation that, as suggested by Peregrine [1967], uses an average for u and v values, but forward differences for η values. The result, rearranged for computation, is the explicit equation

$$\begin{aligned}
 \eta_{ij}^{n+1} = \eta_{ij} - \frac{\Delta t}{2\Delta} \left(\frac{u_{ij}^{n+1} + u_{ij}}{2} (d_{i+j} + \eta_{i+j} - d_{i-j} - \eta_{i-j}) \right. \\
 + \frac{1}{2} (d_{ij} + \eta_{ij})(u_{i+j} + u_{i+j}^{n+1} - u_{i-j} - u_{i-j}^{n+1} \\
 + v_{ij+1} + v_{ij+1}^{n+1} - v_{ij-1} - v_{ij-1}^{n+1}) \\
 \left. + \frac{v_{ij}^{n+1} + v_{ij}}{2} (d_{ij+1} + \eta_{ij+1} - d_{ij-1} - \eta_{ij-1}) \right) \quad (21)
 \end{aligned}$$

This equation is used to compute η_{ij}^{n+1} for $2 \leq i \leq M-1$, $2 \leq j \leq N-1$, and then the first iteration, the predictor iteration, at the n^{th} time level is complete.

If now the second through fourth steps above are repeated with

P values replaced by the $n+1^{th}$ values just calculated, the accuracy of the solution is increased; this is the corrector iteration. Numerical tests showed that the computations remained stable if at least two iterations were used (one predictor, one corrector). The u^{n+1} , v^{n+1} and η^{n+1} values obtained in the second and the third iteration agreed to at least four significant figures after several hundred Δt steps in simulation of solitary wave motion onto a shelf (Fig. 1a).

Boundary conditions in difference form were derived from Eqs. (7-10) in the case of solitary wave simulation. The wave was started well inside the tank walls which were held rigid. For example, for Wall 1 in Fig. 1 we have from Eqs. (7-10) at any time level $\eta_{1j} = \eta_{3j}$, $v_{1j} = v_{3j}$, $u_{2j} = 0$, and $u_{1j} = -u_{3j}$. Other walls have similar conditions.

For input of an oscillatory wave propagating in the positive x-direction at $x = 0$ we prescribe

$$\eta_{2j}^{n+1} = \eta_0 \sin \left[-\frac{2\pi C_0}{L_0} \cdot \Delta t \cdot (n+1) \right] \quad (22)$$

where η_0 is the amplitude (usually small) and L_0 is the wave length. The celerity C_0 is taken to be unity in nondimensional terms. From Eq. (14) we have $v_{1j} = v_{3j}$. Because η_{3j}^{n+1} and η_{4j}^{n+1} are computed explicitly in the tank region, η_{1j}^{n+1} is obtained by polynomial interpolation according to the second-order formula

$$\eta_{1j}^{n+1} = \eta_{4j}^{n+1} - 3\eta_{3j}^{n+1} + 3\eta_{2j}^{n+1} \quad (23)$$

Finally, the continuity difference Eq. (21) is used for points (2j) where it has not been previously employed to relate u_{1j}^{n+1} to the values in the interior, $j \geq 2$. With u_{1j} known as a function of u_{2j} , u_{3j} , etc., Eq. (19) can be used in $2 \leq i \leq M-2$ and the u_{ij}^{n+1} found; v_{ij}^{n+1} values are replaced by v_{ij}^p values in the first iteration.

Figure 2 is a flow chart for the APPSIM2 computations. These were performed on an IBM 360/91 system. For a typical computation with $\Delta = 0.25$, $\Delta t = 0.22$, $M = 154$, $N = 54$ and 126 time steps the program required about 360K bytes (90K words) of core storage and 4 minutes of CPU time (about 1/30 minute per time step). The stability of the method is discussed in Sec. 3.4 after presentation of computational results.

3.3. Results and Discussion

To illustrate the focusing effect of wave refraction and the reaction of waves to a shelf geometry, solitary and oscillatory waves were shoaled over the bottom topography shown in Fig. 1a. The water depth in the tank was 1.0 while the depth of the shelf was 0.4.

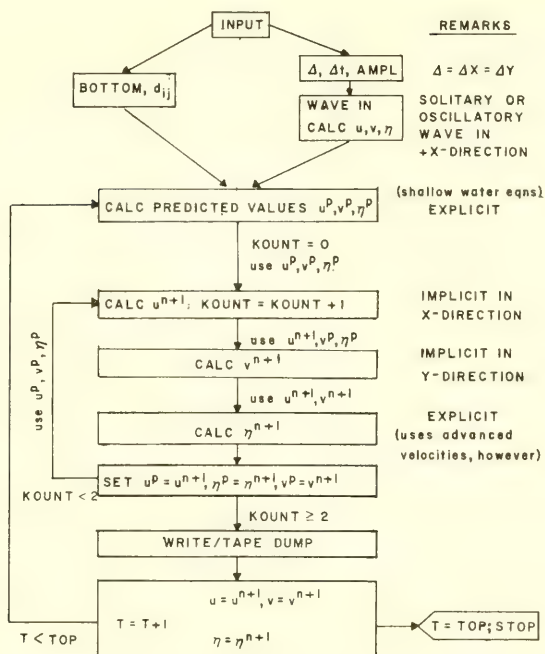


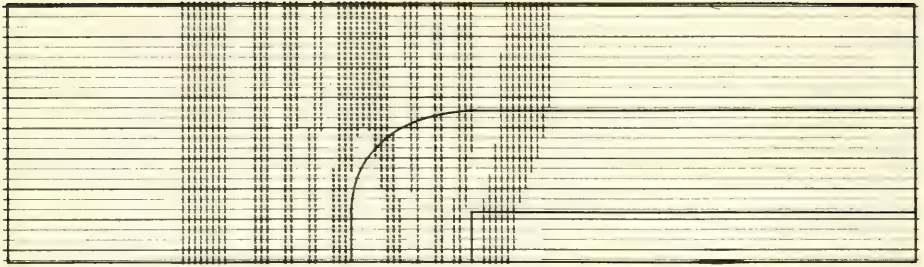
Fig. 2. APPSIM2 flow chart

The deep and shallow portions are connected smoothly by a cosine curve.

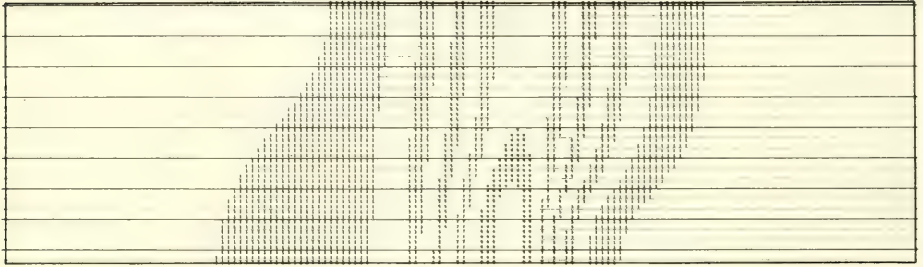
For the solitary wave simulation, the pertinent parameters were $L_1 = 38$, $L_2 = 13$, $x_T = 14.5$, $x_S = 19.5$, $y_T = 7.75$, $y_S = 2.75$, $\Delta = 0.25$, $\Delta t = 0.2165$, and $\eta_0 = 0.1$. The wave was started with its crest lying along $x_0 = 8.0$ and propagated in the positive x-direction toward the shelf. Chan and Street [1970a] showed that the effective half-length of a solitary wave of amplitude $\eta_0 = 0.1$ is about 11 so it is necessary to correct the initial Boussinesq [Wiegel, 1964] wave profile for the influence of the wall at $x = 0$; however, it was unnecessary to correct the leading portion of the wave for the bottom influence. The initial u-velocity distribution was calculated from Eq. (6) under the assumptions that $v \equiv 0$, $\eta = \eta(x, t)$ and the wave is moving at a constant speed $C_0 = 1 + 0.5 \eta_0$ [Wiegel, 1964] with constant form. In addition Δt was selected in accordance with the Courant-type condition

$$\Delta t \leq \frac{\Delta}{C_0}$$

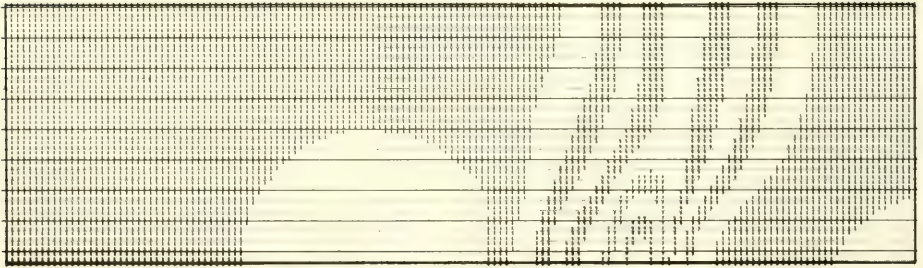
Results of the solitary wave computation are shown in Figs. 3-5.



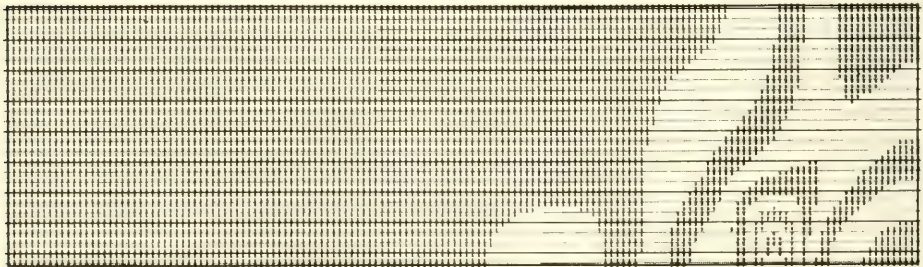
T = 6.5



T = 13.0



T = 19.5



T = 26.0

Fig. 3. Free surface maps for a solitary wave on the shelf

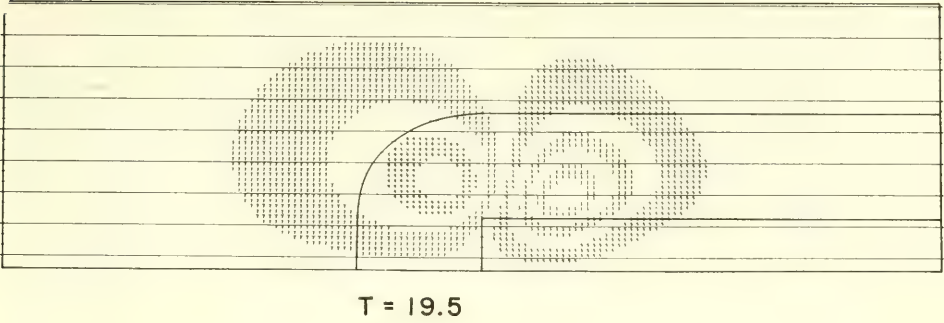


Fig. 4. Velocity map (v) for $t = 19.5$

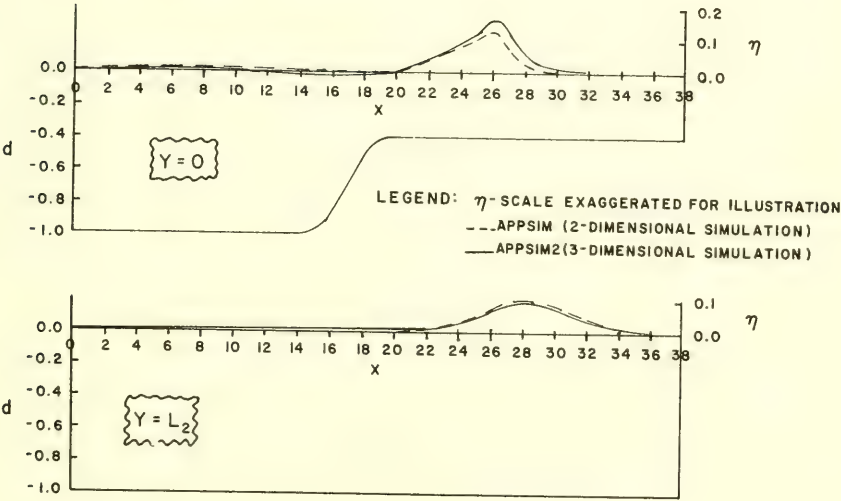


Fig. 5. Wave profiles for two- and three-dimensional propagation

The evolution of the free surface is illustrated by free surface maps in Fig. 3, while Fig. 4 shows a v -velocity map for $t = 19.5$. The maps are printed during program execution by a subroutine that scales the variable values on a range running from a minimum of zero to a maximum of ten. Only odd numbers are printed at their corresponding node points. These maps are extremely useful for initial interpretation of the data. Later, quantitative studies of results can be made because the u, v, η fields are stored on tape after every five time steps and maps are made after every 20 to 40 steps. Thus Fig. 5 illustrates a quantitative comparison between the two-dimensional results and the three-dimensional simulation at $t = 19.5$ for $y = 0$ and $y = L_2$. Both the effect of wave refraction and the nonlinear response of the flow are evident.

As another example, Fig. 6 contains pictures of the development of the η, u , and v fields for oscillatory waves shoaling on a shelf. The pertinent parameters were $L_1 = 66, L_2 = 41, x_T = 25.5, x_S = 45.5, y_T = 25.5, y_S = 15.5, \Delta = 0.5, \Delta t = 0.5$, and $2\eta_0 = H_0 = 0.05$. The input wave at Wall 1 (Fig. 1) had assumed length $L_0 = 20$ and speed $C_0 = 1.0$ so the period $T_0 = 20$. The actual computed length was essentially 20 also. In this case we sought to simulate a large region so Δ was large; even so 458K bytes of core storage were required for the program. In spite of the rather coarse grid the computed properties of the waves were smooth and well behaved.

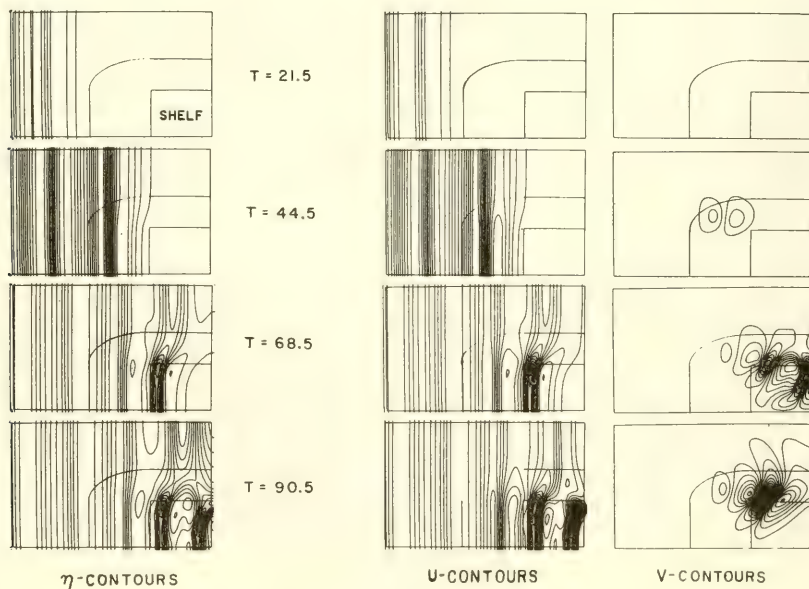


Fig. 6. Shoaling on a shelf (oscillatory waves)

The contour lines in Fig. 6 were computed by a plotting program developed by Schreiber [1968]. The facility used was an IBM 2250 graphic display unit in which the computed contour lines are projected on a TV screen. The contour plots were recorded by photographing the surface of the screen. Several motion pictures have also been made with this apparatus.

Two 2250 units are used when films are made. First, as noted above the computed field values are stored on tape during the APPSIM2 computer run. Later, a special program calls up the tapes and transforms the field data to contour lines. These are transmitted to the 2250 units. One is used as a control console to monitor picture quality and to set the movie camera speed. The second unit has a 16 mm movie camera mounted on it and focused on the screen. The camera operation is synchronized with the succession of contour plots flashed on the TV screen. Titles are also constructed on the screen and filmed. Judicious editing transforms the 16 mm film into a useful and interesting movie. As the sequence of Fig. 6 shows, the evolution of the flow fields is particularly instructive. Because all the pertinent parameters are usually shown simultaneously on the screen with the contour plots, quantitative interpretations of the contour information can be made directly from the graphic display. For example, at $t = 68.5$ the maximum wave height along the line $y = 0$ is about 0.06, while along $y = L_2$, the height is 0.05 (i.e., the wave is unaffected by the shelf at this time). In Fig. 6, the η -plot increment for $t = 68.5$ is 0.01, the maximum value is $\eta = 0.064$ and the minimum is $\eta = -0.026$. For oscillatory waves it is necessary to have some detailed printout in addition to the graphic display for quantitative analyses because the contours are not marked with their contour level values.

Finally, we simulated long wave amplification by a circular submarine seamount and compared our results with the experimental values of Williams and Kartha [1966]. The following pertinent parameters exactly match one of their experimental runs for a half-seamount (Fig. 1b) with non-dimensional parameter $X = 2\pi b/L_0 = 3.0$: $x_c = 56.7$ is the distance from the wave generator to the peak of the island; $b = 7.73$ is the radius of the base of the seamount, $T = 16.6$ is the wave period, $\eta_0 = 0.0082$, $d = 1.0$ beyond the seamount base, $\epsilon = 0.116$ is the submergence of the seamount at its peak and $L_2 = 23.2$. The tank length $L_1 = 116$ was selected to prevent reflections from reaching the seamount. The amplification ratio $H_i/H_0 = A_f$ was calculated where $H_0 = 2\eta_0$ and H_i is the trough-to-crest distance on waves at the island peak where $d = \epsilon$.

The experimental $A_f = 2.42$, while $A_f = 2.46$ according to the refraction theory of Mogel, et al. [1970] and $A_f = 2.70$ according to APPSIM2 for a seamount whose shape was given by

$$d(x, y) = (1.0 - \epsilon) \left(\frac{r}{b} \right)^q + \epsilon$$

with

$$r(x,y) = [(x - x_c)^2 + y^2]^{1/2}$$

and $q = 1.0$ (the shape factor). This was a linear seamount with a sharp peak where the first derivative of $d(x,y)$ is discontinuous and the higher derivatives are undefined (cf., Sec. 3.1). Unfortunately, the difficulty of resolution of the island features near the peak was compounded by the fact that to simulate the experimental conditions within our nominal core allotment of 500K bytes we had to use $\Delta = 0.5$ where $\Delta = 0.25$ would have been preferable. As a consequence, we believe, of the coarse grid the short waves generated by the island wave response are not properly resolved, being of the order of one or two grid divisions. The solution, therefore, while not unbounded, appears unstable.

On the other hand, Williams and Kartha [1966] did not report on the sea-state near the islands and our results might be physically reasonable. A test using $q = 2.0$ which gives a dome-like island produced an $A_f = 4.65$ for $X = 2\pi b/L_0 = 3.0$ which is slightly beyond the range of the experiment. However, this A_f value lies, as does our result for $q = 1.0$, within the uncertainty band of results presented by Williams and Kartha.

3.4. Stability Analysis

Initial calculations with APPSIM2 and no iteration, viz., operating with only a single predictor/corrector step produced somewhat ragged results after several tens of time steps. Accordingly, a linear stability analysis was made to examine the amplitude properties of the computational scheme.

For the stability analysis we set $d_{ij} \equiv 1$ and defined the constant parameters

$$\begin{aligned}\alpha &= \Delta t \cdot u_{ij} / \Delta \\ \beta &= \Delta t \cdot v_{ij} / \Delta \\ \gamma &= \Delta t \cdot \eta_{ij} / \Delta \\ R &= \Delta t / \Delta\end{aligned}\tag{24}$$

The equations defining the computational scheme were linearized by considering only difference quantities as variables and treating the remaining terms as the constants of Eq. (24). Thus, the prediction Eqs. (16-18) become

$$u_{ij}^P = u_{ij} - \frac{1}{2} \alpha(u_{i+1j} - u_{i-1j}) - \frac{1}{2} \beta(u_{ij+1} - u_{ij-1}) - \frac{1}{2} R(\eta_{i+1j} - \eta_{i-1j}) \quad (25)$$

$$v_{ij}^P = v_{ij} - \frac{1}{2} \alpha(v_{i+1j} - v_{i-1j}) - \frac{1}{2} \beta(v_{ij+1} - v_{ij-1}) - \frac{1}{2} R(\eta_{ij+1} - \eta_{ij-1}) \quad (26)$$

$$\eta_{ij}^P = \eta_{ij} - \frac{1}{2} \alpha(\eta_{i+1j} - \eta_{i-1j}) - \frac{1}{2} \beta(\eta_{ij+1} - \eta_{ij-1}) - \frac{1}{2} (\gamma+R)(u_{i+1j} - u_{i-1j}) - \frac{1}{2} (\gamma+R)(v_{ij+1} - v_{ij-1}) \quad (27)$$

The remaining Eqs. (19-21) of the corrector step were treated in a similar manner; where P values appeared, the values from Eqs. (25-27) were introduced. To test the resulting linearized form of Eqs. (19-21) we introduced the Fourier component solution (or error)

$$\vec{W} = \vec{W}^* e^{i(\sigma_1 x + \sigma_2 y)} \cdot e^{i\omega t}$$

where we seek to determine if ω values, either real or complex, exist such that W is a solution of the difference equation and where

$$\vec{W}^* = \begin{pmatrix} u^* \\ v^* \\ \eta^* \end{pmatrix} = \text{constant}$$

$$\sigma_1 = 2\pi/\lambda_1$$

$$\sigma_2 = 2\pi/\lambda_2$$

for representative wave lengths λ_1 and λ_2 in the x - and y -directions respectively. Now, let $\mu = e^{i\omega\Delta t}$ so

$$\vec{W} = \vec{W}^* \mu^n e^{i(\sigma_1 x + \sigma_2 y)} \quad (28)$$

at any point in time and space. Thus, we insert Eq. (28) in the linearized u , v , η equations and obtain

$$[A] \vec{W}^* = \begin{bmatrix} a_{11} & a_{12} & a_{13} \\ a_{21} & a_{22} & a_{23} \\ a_{31} & a_{32} & a_{33} \end{bmatrix} \begin{bmatrix} u^* \\ v^* \\ \eta^* \end{bmatrix} = 0 \quad (29)$$

where the $a_{ij} = a_{ij}(\alpha, \beta, \gamma, R, \Delta, \sigma_1, \sigma_2, \mu)$. Because $\vec{W}^* \neq 0$ in general, a Fourier component solution can exist and Eq. (29) can be satisfied only if $|A| = 0$, viz., only if a set of eigenvalues exists for the matrix A . The condition $|A| = 0$ leads to a determination of μ ; linear stability depends on the amplitude of μ . If $|\mu| \leq 1$ the solution by Eqs. (16-21) would be termed linearly stable.

Analysis of the coefficient matrix A in Eq. (29) is complex and is not reproduced here, but the key results are as follows. First, if $\theta_1 = 2\pi\Delta/\lambda_1$ and $\theta_2 = 2\pi\Delta/\lambda_2$, then for finite Δt , λ_1 and λ_2 ,

$$\lim_{\Delta \rightarrow 0} |\mu| = 1$$

Similarly, for finite Δ , λ_1 and λ_2 ,

$$\lim_{\Delta t \rightarrow 0} |\mu| = 1$$

The solution scheme is stable in these limit cases.

Second, the case $\theta_2 = 0$, namely, $\lambda_2 = \infty$, was investigated. Then,

$$|\mu| = f(\alpha, \gamma, \theta_1)$$

for assumed Δ and R . This approach leads to a complex, cubic equation with a possible root

$$|\mu_1| = 1 + O(\alpha^4) \quad (30)$$

and a possible root pair with maximum modulus equal to or slightly exceeding unity, i.e.,

$$|\mu_{2,3}|_{\max} \geq 1 \quad (31)$$

Specifically, in a solitary wave computation with $\Delta = 0.5$ and $\Delta t = 0.25$, we have for $\eta = 0.1$, $\gamma = 0.05$, $\alpha \leq 0.05$, $\beta = 0$, $R = 0.5$,

and

$$|\mu_1| \approx 1 + 7 \times 10^{-7} < 1 + o(\alpha)$$

$$|\mu_{2,3}|_{\max} \approx 1.005 < 1 + O(\alpha)$$

for $\lambda_1 > 2\Delta$. For $\lambda_1 = 2\Delta$, $|\mu| = 1$ exactly. Forsythe and Wasow [1960] suggest that the errors may be controllable and lead to a stable computation when

$$|\mu| \leq 1 + O(\Delta t) \quad (32)$$

In the present case $\alpha < \Delta t$ because $\alpha = u\Delta t/\Delta$ and $u/\Delta < 1$; accordingly, the condition (32) can be written as $|\mu| \leq 1 + O(\alpha)$. Our computational experience with APPSIM which has $\theta_2 = 0$ always and does not use iteration also suggests that the computation is stable, at least for several hundred time steps. APPSIM2, however, because of its coupled (u, v, η) equations and the propagation of error from the u -field where $|u_{ij}|$ is relatively large compared to the v -field and η -field, does require at least one iteration (which tends to make the computation more like an implicit scheme) to retain a smoothly varying solution on a smoothly varying bottom topography.

3.5. Prognosis

The computational results indicate that APPSIM2 is a useful means of studying the evolution of flow fields in wave shoaling over smoothly varying bottom topography. However, the method requires considerable computer storage and moderate execution time. Thus, APPSIM2, which models nonlinear processes in nonbreaking waves, should be used only when nonlinear effects are expected to be significant, other methods (cf., Section I) being appropriate otherwise. As Madsen and Mei [1969a] indicate, the equations of KdV type used in APPSIM2 should make the method applicable to a wide range of long wave problems.

Two further steps should be made in the development of the method. First, the linear stability property could be improved by introduction of a second-order central difference method for the convective terms in Eqs. (18) and (21). This central difference [Fromm, 1968] leads to a modification of Eq. (31) such that

$$|\mu_{2,3}|_{\max} \leq 1$$

for most components of interest. Alternatively, Eq. (21) can be made an entirely implicit equation for η_{ij}^{n+1} [cf., Eq. (19)]; this will eliminate the growing contribution represented by Eq. (31) and

caused by the explicit nature of the η_{ij}^{n+1} equation. Second, a series of simulations of specific hydraulic models should be made to determine the grid size Δ required to resolve the smallest significant feature of a problem and to determine the sensitivity of the simulation to discontinuous bottom topography.

IV. SUMMAC

Chan and Street [1970a] proposed the SUMMAC computing technique as a tool for analyzing two-dimensional finite-amplitude water waves under transient conditions. The method is, as noted above, a modified version of MAC which was developed by Welch, *et al.* [1966]. The essence of the initial modifications consisted of a rigorous application of the pressure boundary condition at the free surface and extrapolation of velocity components from the fluid interior so that inaccuracy in shifting the surface boundary is kept at a minimum.

The objective of this section is to provide a summary of the SUMMAC method, of its application to water wave problems and of a number of new improvements added to SUMMAC since Chan and Street [1970a] was written.

4.1. Summary of the Method

The fluid is regarded as incompressible and the effect of viscosity on the macroscopic behavior of flow is considered to be negligible. The entire flow field is covered with a rectangular mesh of cells, each of dimensions δx and δy . The center of each cell is numbered by the indices i and j , with i counting the columns in the x -direction and j counting the rows in the y -direction of a fixed Cartesian coordinate system (Fig. 7). The field-variable values describing the flow are directly associated with these cells [Welch, *et al.* 1966]. The fluid velocity components u and v and the pressure p are the dependent variables while the independent variables are x , y and the time variable t .

In addition to the cell system which represents the flow field by a finite number of data points, there is a line of marker particles whose sole purpose is to indicate where the free surface is located. These hypothetical particles may or may not represent the actual fluid particles at the free surface, depending on whether one chooses the Lagrangian or the Eulerian point of view to calculate the motion of free surface.

The marker-and-cell system provides an instantaneous representation of the flow field for any particular time. When an initial set of conditions is given, the entire fluid configuration can be advanced through a small but finite increment of time δt . First, the pressure for each cell is obtained by solving a finite-difference

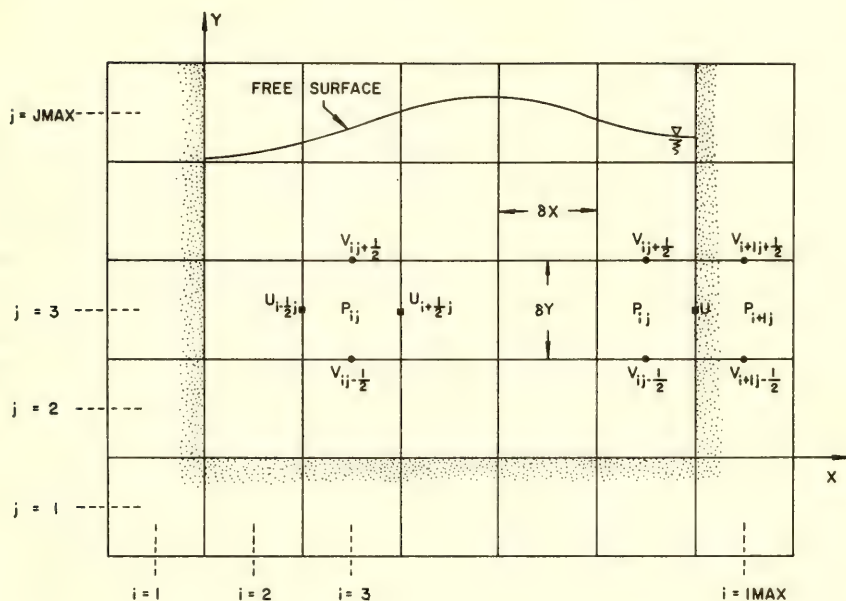


Fig. 7. Cell setup and position of variables

Poisson's equation, whose source term is a function of the velocities. This equation was derived subject to the requirement that the resulting finite-difference momentum equations should produce a new velocity field that satisfies the continuity equation (conservation of mass). The finite-difference equations of motion are then used to compute the new velocities throughout the mesh. Finally, the marker particles are moved to their new positions, their velocities being interpolated from the nearby cells. The new flow configuration now serves as the initial condition for the next time step and the foregoing procedure is repeated as many times as necessary for the investigation. With proper choice of δx , δy and δt , the SUMMAC algorithm is capable of yielding solutions that are computationally stable and also reasonably faithful in simulating the physical phenomena.

Dimensionless variables are used throughout (cf., Sec. 3.1). The governing equations for an incompressible, inviscid fluid are

$$\frac{\partial u}{\partial t} + u \frac{\partial u}{\partial x} + v \frac{\partial u}{\partial y} = - \frac{\partial p}{\partial x} + g_x \quad (33)$$

$$\frac{\partial v}{\partial t} + u \frac{\partial v}{\partial x} + v \frac{\partial v}{\partial y} = - \frac{\partial p}{\partial y} + g_y \quad (34)$$

and

$$\frac{\partial u}{\partial x} + \frac{\partial v}{\partial y} = 0 \quad (35)$$

Here, p is the pressure; g_x and g_y are the x and y components of the gravity acceleration whose absolute value is g and t is the time variable. Also, if the direction of gravity is the same as the $-y$ direction, then $g_x = 0$ and $g_y = -1$.

Boundary conditions are easily derived for the fluid motion at the solid walls of the tank (cf., Chan and Street [1970a]). For incompressible fluids with very low viscosity, such as water, it is sufficiently accurate to use at the free surface the single condition

$$p = p_0(x, t) \quad (36)$$

where p_0 is the externally applied pressure at the free surface. Under usual circumstances $p_0 = 0$, but it can also be prescribed as a function of x and t for some problems.

As shown in Fig. 7 the computation region is divided into a number of rectangular cells. The fluid pressure p is evaluated at the cell centers, while u is defined at the mid-point of the right-hand and left-hand sides of the cell and v is defined at the mid-point of the upper and lower sides. Then, for the cell (i, j) the following set of equations are derived from Eqs. (33) and (34):

$$u_{i+\frac{1}{2},j}^{n+1} = u_{i+\frac{1}{2},j}^* + \delta t g_x + \frac{\partial t}{\partial x} (p_{ij} - p_{i+\frac{1}{2},j}) \quad (37a)$$

$$u_{i-\frac{1}{2},j}^{n+1} = u_{i-\frac{1}{2},j}^* + \delta t g_x + \frac{\partial t}{\partial x} (p_{i-1,j} - p_{ij}) \quad (37b)$$

$$v_{ij,\frac{1}{2}}^{n+1} = v_{ij,\frac{1}{2}}^* + \delta t g_y + \frac{\partial t}{\partial y} (p_{ij} - p_{ij+1}) \quad (37c)$$

$$v_{ij,-\frac{1}{2}}^{n+1} = v_{ij,-\frac{1}{2}}^* + \delta t g_y + \frac{\partial t}{\partial y} (p_{ij-1} - p_{ij}) \quad (37d)$$

In the above equations, variables with the superscript $n+1$ are related to the $n+1^{\text{th}}$ time step. Variables lacking a superscript are evaluated at the n^{th} step. Thus, Eqs. (37) are suitable for updating the values of u and v about the cell (i, j) . The "convective contributions" u^* and v^* are

$$u_{i+\frac{1}{2}j}^* = u_{i+\frac{1}{2}j} + \delta t \left\langle -u \frac{\partial u}{\partial x} - v \frac{\partial u}{\partial y} \right\rangle_{i+\frac{1}{2}j} \quad (38)$$

$$v_{ij+\frac{1}{2}}^* = v_{ij+\frac{1}{2}} + \delta t \left\langle -u \frac{\partial v}{\partial x} - v \frac{\partial v}{\partial y} \right\rangle_{ij+\frac{1}{2}} \quad (39)$$

where $u_{i+\frac{1}{2}j}^*$ and $v_{ij+\frac{1}{2}}^*$ contribute to $u_{i+\frac{1}{2}j}^{n+1}$ and $v_{ij+\frac{1}{2}}^{n+1}$, respectively, through the convection process and $\langle \rangle$ represents the as yet unspecified finite difference approximation of the enclosed terms.

Before Eqs. (37) can be employed to compute the new velocities, the p field must be obtained. Consider the finite-difference continuity equation [see Eq. (35)]

$$D_{ij}^{n+1} \equiv \frac{u_{i+\frac{1}{2}j}^{n+1} - u_{i-\frac{1}{2}j}^{n+1}}{\delta x} + \frac{v_{ij+\frac{1}{2}}^{n+1} - v_{ij-\frac{1}{2}}^{n+1}}{\delta y} = 0 \quad (40)$$

Substituting Eqs. (37) into Eq. (40) and requiring $D_{ij}^{n+1} = 0$ leads to the pressure equation

$$p_{ij} = \frac{1}{z} \left(\frac{p_{i+1j} + p_{i-1j}}{\delta x^2} + \frac{p_{ij+1} + p_{ij-1}}{\delta y^2} + R_{ij} \right) \quad (41)$$

Here

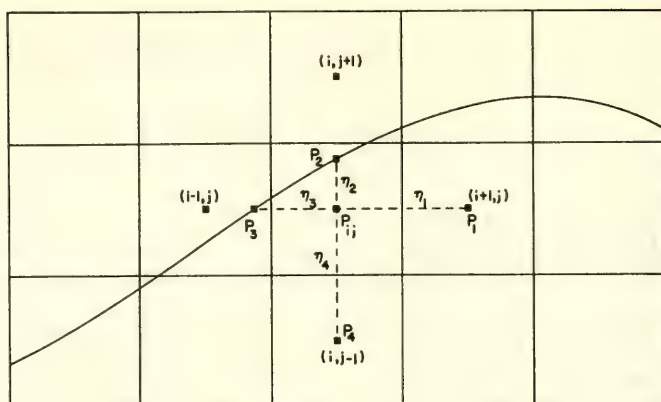
$$z \equiv 2 \left(\frac{1}{\delta x^2} + \frac{1}{\delta y^2} \right) \quad (42)$$

$$R_{ij} \equiv -\frac{1}{\delta t} \left[\frac{u_{i+\frac{1}{2}j}^* - u_{i-\frac{1}{2}j}^*}{\delta x} + \frac{v_{ij+\frac{1}{2}}^* - v_{ij-\frac{1}{2}}^*}{\delta y} \right] \quad (43)$$

Near the free surface "irregular stars" (Fig. 8) must be used to derive an appropriate pressure equation so that, in the discrete sense, the free surface condition $p = p_a$ is applied to the exact location. Let $\eta_1, \eta_2, \eta_3, \eta_4$ be the lengths of the four legs of the irregular star (Fig. 8) and p_1, p_2, p_3, p_4 be the value of p at the ends of these legs. Then, it can be shown the irregular-star pressure equation is

$$p_{ij} = \frac{\eta_1 \eta_2 \eta_3 \eta_4}{2(\eta_2 \eta_4 + \eta_1 \eta_3)} \left[\frac{\eta_3 p_1 + \eta_1 p_3}{\eta_1 \eta_3 \frac{\eta_1 + \eta_3}{2}} + \frac{\eta_4 p_2 + \eta_2 p_4}{\eta_2 \eta_4 \frac{\eta_2 + \eta_4}{2}} + R_{ij} \right] \quad (44)$$

Equation (44) reduces to Eq. (41) when Eq. (44) is applied to an interior cell.

Fig. 8. Irregular star for p calculations

The hypothetical particles that mark the free surface are moved to their new locations according to their locally interpolated values of u and v . For a given particle k we find the velocity component u_k for the particle by making a Taylor series expansion about the nearest data point of the u field. Similarly, a series expansion about the nearest data point of the v field gives v_k , the y -component of the particle velocity. With u_k and v_k available, each free surface marker particle is advanced by the following formulas:

$$\begin{aligned} x_k^{n+1} &= x_k^n + u_k^{n+1} \delta t \\ y_k^{n+1} &= y_k^n + v_k^{n+1} \delta t \end{aligned} \quad (45)$$

where x_k^n and y_k^n refer to the position of the k^{th} particle at the n^{th} time step. Also, the particle velocities are evaluated at the advanced, i.e., $n+1^{\text{th}}$, time step.

The quantities u and v are not defined outside the fluid domain, but they are needed to carry out the computations using Eqs. (37) and (43) and the particle velocities near the free surface. We calculate these undefined u and v values by a simple linear extrapolation from the fluid interior.

A complete set of initial data -- the u and v fields and the position of a line of particles depicting the free surface, are needed to start the computation. The initial pressure p needs to be known only approximately, such as a hydrostatic distribution, because the p field is solvable if u and v are given.

The evolution of fluid dynamics is calculated in "cycles," or time steps. At the start of each cycle the source term R_{ij} for each cell is evaluated by Eq. (43). The pressure p is computed only for those cells whose centers fall in the fluid region; either Eq. (41) or Eq. (44) is used as appropriate. The successive-over-relaxation method is used to solve the p field. The iteration is terminated when

$$\left| p_{ij}^{(m)} - p_{ij}^{(m-1)} \right| < \epsilon_p \quad (46)$$

for every cell, where (m) means the m^{th} iteration and ϵ_p is a predetermined small positive number. The accuracy in solving p_{ij} at the n^{th} time step has a direct bearing on the accuracy of satisfying the continuity equation $D_{ij}^{n+1} = 0$ [Eq. (41)] at the $n+1^{\text{th}}$ step. Smaller values of D_{ij}^{n+1} result when smaller ϵ_p are used. However, there is little improvement in reducing D_{ij}^{n+1} for $\epsilon_p < 10^{-6}$ because the round-off level of the computer has been reached.

Now Eqs. (37) yield the new velocities. Then each marker particle is advanced to its new position by Eqs. (45). Thus a cycle is completed and the next one can be started immediately.

The convective contributions given by Eqs. (38) and (39) can be approximated by a wide variety of finite difference formulas. Chan and Street [1970c] show that, while the original MAC and early SUMMAC equations used a first-order explicit method, second-order explicit methods are better. Of the two second-order explicit schemes studied, the so-called "upstream" difference alone rather than in a "phase-averaged" procedure yields better results in problems where free surface waves are present. In this upstream difference, if w_{lm}^* represents either $u_{i+\frac{1}{2}}^*$ or $v_{i+\frac{1}{2}}^*$, then for the case when $u_{lm}^n > 0$ and $v_{lm}^n > 0$

$$\begin{aligned} w_{lm}^* &= \tilde{w}_{lm}^* + \frac{\beta-1}{2} (\tilde{w}_{lm-2} - \tilde{w}_{lm}) \\ &+ \frac{(\beta-1)^2}{2} (\tilde{w}_{lm-2} - 2\tilde{w}_{lm-1} + \tilde{w}_{lm}) \end{aligned} \quad (47)$$

where

$$\begin{aligned} \tilde{w}_{lm} &= w_{l-1m}^n + \frac{\alpha-1}{2} (w_{l-2m}^n - w_{lm}^n) \\ &+ \frac{(\alpha-1)^2}{2} (w_{l-2m}^n - 2w_{l-1m}^n + w_{lm}^n) \end{aligned} \quad (48)$$

and

$$\alpha = \frac{\delta t u_{lm}^n}{\delta x}; \quad \beta = \frac{\delta t v_{lm}^n}{\delta y}$$

We examined the finite difference convection equations by the extended von Neumann method in which nonlinear equations are first linearized. The resulting criteria were

$$|\alpha| \leq 1; \quad |\beta| \leq 1 \quad (49)$$

A second criterion

$$\frac{\delta t}{\delta x} < \frac{1}{C} \quad (50)$$

where C = the surface wave celerity, was derived by considering the propagation of the free surface waves. These were simple linear analyses and can only be used as guidelines in choosing the time increment δt for given δx and δy . Because numerical dispersion is quite severe for short wave components, care must be exercised to provide adequate resolution for all the important features in the flow. As a rule of thumb, the smallest significant flow feature must be represented by at least ten cells.

In both the MAC and SUMMAC a line of particles was used to mark the free surface position. A pair of (x_k^n, y_k^n) values were associated with the k^{th} particle at the n^{th} time step. Then Eq. (45) was employed to calculate (x_k^{n+1}, y_k^{n+1}) . This procedure is really a Lagrangian method that tends to be unstable after a large number of time steps. The problem is not serious for simulating solitary waves [cf., Chan and Street, 1970a]. But, in calculating periodic waves a given particle is moved up and down as each wave passes. In the process a small number is systematically added to and then subtracted from x_k and y_k contributing to very large round-off errors. In addition, there is no restraint on the individual particle positions because each is calculated independently of the others.

To overcome the difficulty with moving particles, an alternative approach using the Eulerian point of view can be developed. The flow region is divided by a number of vertical lines with equal spacing Δ and η is now the height of the free surface measured from the reference level $y = 0$ at the channel bottom. The horizontal positions of these vertical lines are fixed and we only compute the change in η along each vertical line as time passes.

The kinematic condition at the free surface, from the Eulerian viewpoint is

$$\frac{\partial \eta}{\partial t} = v - u \frac{\partial \eta}{\partial x} \quad (51)$$

Many difference schemes may be developed to approximate Eq. (51). Our tests show that the forward implicit method with the difference equation

$$\frac{\eta_k^{n+1} - \eta_k^n}{\delta t} = v_k^{n+1} - u_k^{n+1} \left(\frac{\eta_{k+1}^{n+1} - \eta_{k-1}^{n+1}}{2\Delta} \right) \quad (52)$$

is one of the best. A stability analysis shows that Eq. (52) leads to a linearly stable computation with slight damping.

Numerical tests were carried out in the context of a simple physical problem whose exact solution was known, viz., a solitary wave in a horizontal channel. Among five alternative combinations of surface and correction term treatments tested, that using Eq. (52) and Eqs. (47) and (48) was the best.

Now consider δt . The maximum fluid speed in the above tests was $u_{\max} \approx 0.30$ and $\delta x = 0.5$ while $\delta y = 0.1$. According to Eq. (49)

$$\delta t < \frac{\delta x}{u_{\max}} = \frac{0.50}{0.30} = 1.67$$

The speed of the surface wave is $C = 1.18$. The Courant condition [Eq. (50)] would require

$$\delta t < \frac{\delta x}{C} = \frac{0.50}{1.18} = 0.424$$

But the Courant condition should also be observed in computing the free surface. Because we used the spacing $\Delta = 0.05$ at the free surface, the condition

$$\delta t < \frac{\Delta}{C} = \frac{0.05}{1.18} = 0.0424$$

must be satisfied. Therefore, the most restrictive condition is $\delta t < 0.0424$. In all the test examples, $\delta t = 0.05$ was used. This is slightly larger than the estimated maximum allowable δt , but no distortions or instabilities were noted. However, the result of seriously violating the Courant condition, i.e., using $\delta t = 0.10$, was large non-physical distortions that suggest one has to be careful about the choice of δt .

Experiments were also performed on the problem of generating periodic waves by pressure pulse (Sec. 4.2). Instability at the free surface became explosive after 600 time steps when the particle method was used. Using the forward implicit method, we were able to calculate up to more than 3000 steps and there were still no signs of instability.

The numerical tests described above indicated that it is advantageous to use the second-order upstream difference method to compute the convective contributions to $u_{i+\frac{1}{2}}^{n+1}$ and $v_{i+\frac{1}{2}}^{n+1}$. For the free surface calculations, the forward implicit scheme is best. However, the particle method of computing the free surface need not be dismissed altogether. The Eulerian method is restricted to waves in a channel whose two ends are vertical walls. If the water surface has an advancing front, such as a solitary wave climbing on a slope [Chan and Street, 1970b], the particle method is the only choice. When δt is small enough and the particle velocities are evaluated at the $n+1^{\text{th}}$ time step, the particle method does provide a stable solution. However, the particle method should not be used in the simulation of periodic waves over long periods of time.

4.2. Results and Discussion

As an example, periodic pressure pulses were used to generate a train of oscillatory waves in a channel of constant depth (Fig. 9). The fluid is entirely at rest at $t = 0$. Then, the pressure distribution

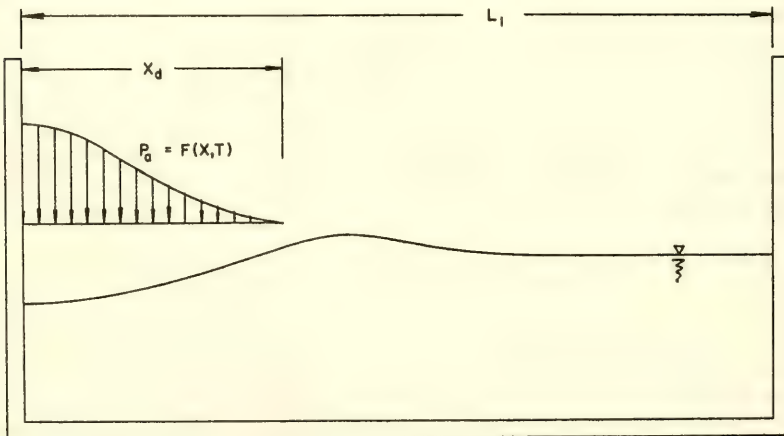


Fig. 9. Setup of pressure pulse problem

$$P_0 = \left\{ \begin{array}{ll} p_0 \sin \left(\frac{2\pi t}{T_p} \right) \cdot \left[\frac{1 + \cos (\pi x/x_d)}{2} \right] & \text{for } 0 \leq x \leq x_d \\ 0 & \text{for } x > x_d \end{array} \right\} \quad (53)$$

is applied to the free surface. Here p_0 is the amplitude of the pressure pulse, T_p is its period and x_d is the horizontal length of the surface subject to the prescribed pressure. Equation (53) was employed by Fangmeier [1967] in solving the same type of problems using time-dependent potential flow equations.

In the first case, a channel of the length $L_1 = 30.0$ was used. The computation domain consists of 80×24 cells, each with $\delta x = 0.30$ and $\delta y = 0.10$. We used $p_0 = 0.10$, $T_p = 7.6$ and $x_d = 4.0$ in Eq. (53) to generate the surface disturbances. The development of the u field is shown in Fig. 10. The plot increment is 0.025 per contour line with $u = 0.0125$ on the contours closest to the ends of the channel. At $t = 10.0$ the leading wave leaves the generating area and progresses to the right. At $t = 43.493$ the first wave runs up the right-hand wall and reflection begins to interfere with the on-coming waves. As a result, a standing wave pattern occurs when $t = 72.986$ to $t = 84.233$.

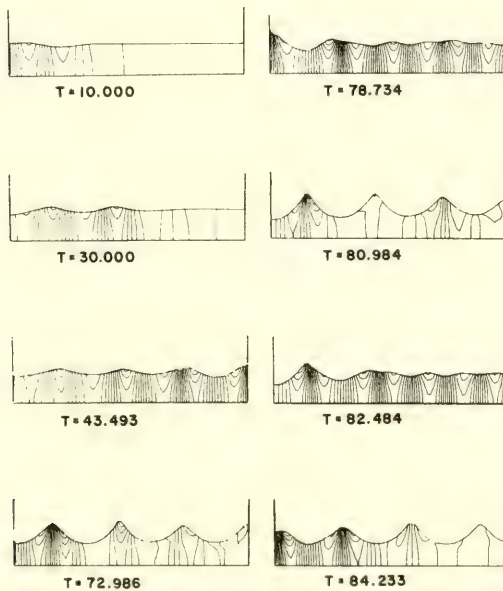
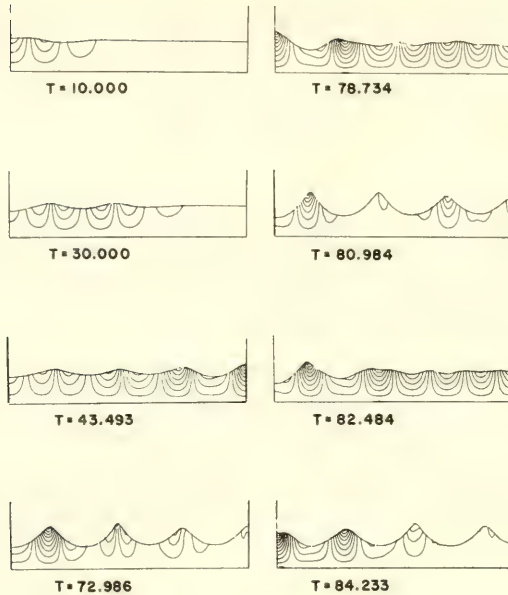


Fig. 10. Periodic waves (u contours)

Fig. 11. Periodic waves (v contours)

In Fig. 11, the time history of the v -field is shown. The plot increment for the contours is also 0.025 per line. On the channel floor, $v = 0.0$. The first contour above the floor has $v = +0.0125$ if it is in front of the wave crest, and $v = -0.0125$ if it is at the back. The sparse contours on the right-hand side of the channel at $t = 80.984$ and $t = 84.233$ indicate that when the standing waves reach their peaks the fluid velocity almost becomes zero temporarily. This phenomenon is caused by the interaction of the reflected and incident waves that tend to alternately enhance and cancel each other.

In Fig. 12 we used a long channel with $L_1 = 60.0$. Thus the "progressive" wave patterns can be analyzed before the reflection sets in. The wave train is composed of a group of dispersive waves. The amplitude increases from the leading wave to the third wave. It then decreases on the following waves. This observation suggests that the nonlinear response of the fluid system is somewhat out of phase with the forcing function at the surface. Therefore, it appears that pure nondispersive periodic waves cannot be generated by the disturbance described by Eq. (53) unless the amplitude p_0 is very small.

Because of its symmetrical profile, we selected the fourth wave in Fig. 12 and compare it in Fig. 13 with Stokes' second-order and third-order theories [Wiegel, 1964]. Good agreement with the

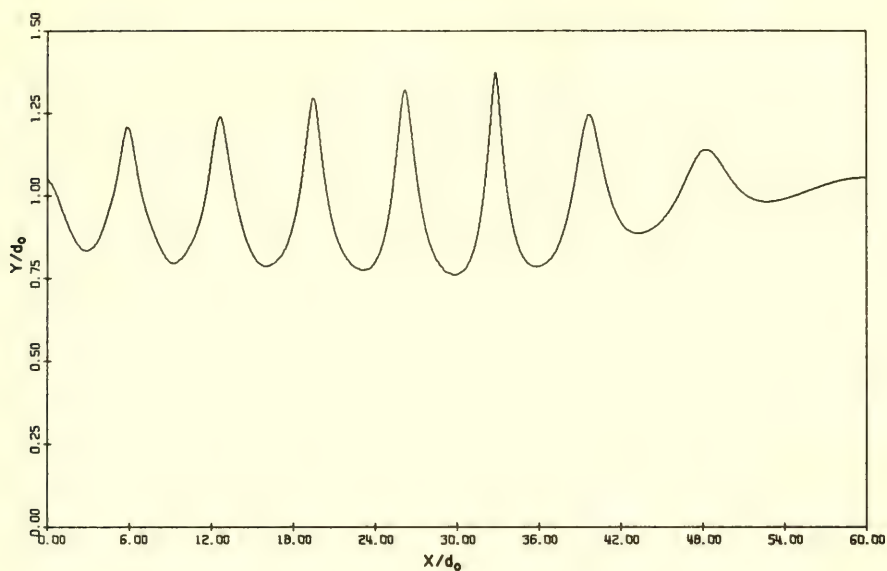


Fig. 12. A train of nearly periodic waves

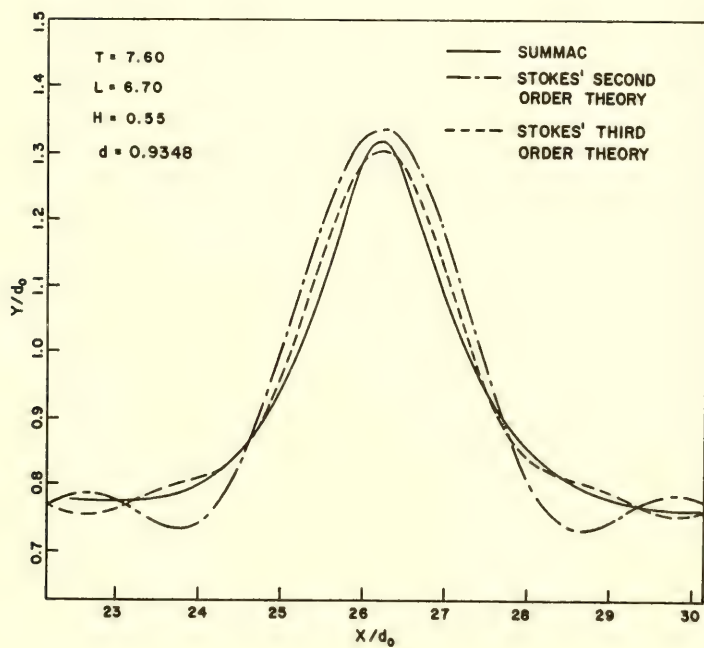


Fig. 13. Comparison of wave profiles

third-order theory is found.

To obtain a meaningful comparison with the profiles of the Stokes' waves, a Fourier analysis was performed on the profile computed by the SUMMAC method. The SUMMAC wave profile in Fig. 13 can be expanded in a Fourier series of the Stokes form [Wiegel, 1964]. The coefficients can be evaluated by the standard procedures in calculus. The first ten coefficients have been computed and compared with those for the Stokes' theories. From the trend of each coefficient, it appeared that as the order of approximation increases the Stokes' wave converges to our numerical solution. Also, in comparison of wave speeds we find good agreement with Stokes' third-order theory. The difference is within 0.4 per cent.

In Fig. 14 the distribution of u under the wave crest and the wave trough is compared with Stokes' theory. The SUMMAC method predicts a much lower u velocity under the crest than Stokes' solutions. This discrepancy is probably caused by the fact that the numerical simulation was made in a channel of finite length which is a closed system and the waves have not quite reached the steady state, while the Stokes' waves hold for an infinitely long channel. Nevertheless, the slope of the u -distribution (i. e., $\partial u / \partial y$) is very close to that of the third-order theory.

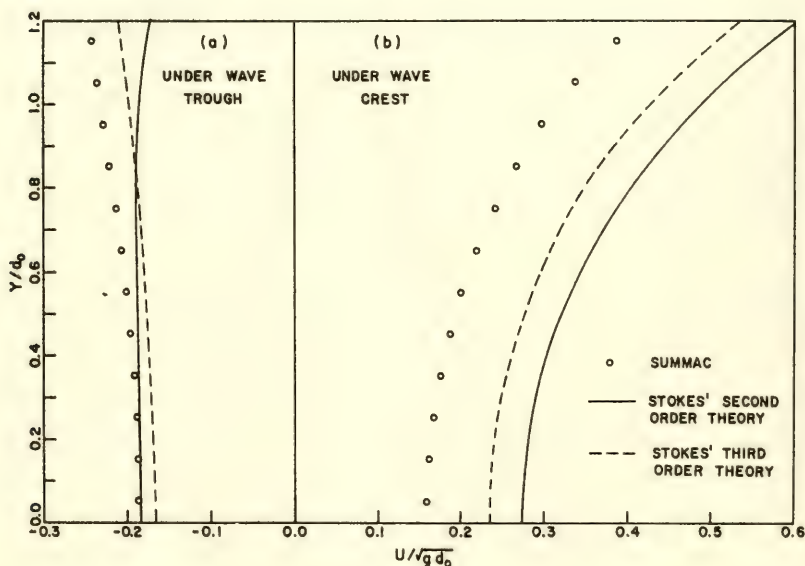


Fig. 14. Distribution of u under wave crest and trough

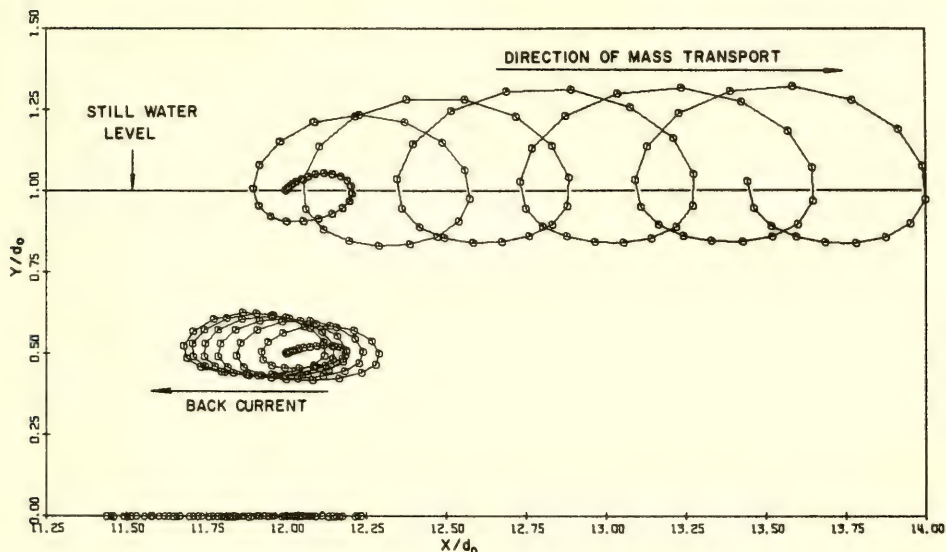


Fig. 15. Motion of fluid particles

The paths of the fluid particles are plotted in Fig. 15. We selected three fluid particles which lie on the vertical plane $x = 12.0$ at $t = 0.0$. Their initial vertical positions are $y = 0.0, 0.5$ and 1.0 , respectively. The instantaneous particle positions are plotted at every $5 \delta t$'s ($\delta t = 0.05$). Each particle moves in an oscillatory pattern which completely differs in nature from the translation motion in a solitary wave. The surface particle travels in a quasi-elliptic orbit but never returns to its original position. Thus, there is a net mass transport in the direction of wave propagation near the free surface. At half water depth the scale of the orbits is smaller and the current (mass transport) is opposite to the wave direction. On the channel bottom the particle merely goes back and forth horizontally and the "backward current" is also larger there. Because the wave channel in our simulation is a closed system, the fluid carried along by the surface waves must return in the opposite direction in the lower fluid layers.

Finally, a comparison was made with the numerical solutions of Fangmeier [1967]. The qualitative agreement was good, as was the agreement in the wave phase; however, the SUMMAC method gave a much better treatment of the free surface that markedly reduced the height of the largest of the waves as compared to Fangmeier's simulation.

4.3. Prognosis

The successful application of the SUMMAC technique to several physical problems indicates its usefulness as an engineering research tool for analyzing the dynamics of water waves in two space dimensions. It is capable of providing accurate quantitative results as well as qualitative descriptions [see, e.g., Chan and Street, 1970b]. In addition, rapid advance in the design of high-speed computing systems makes numerical modelling economically feasible.

While it is possible to employ the SUMMAC technique to attack a wide variety of water wave problems, some limitations inherent in the method must be noted. First, as a result of achieving a high degree of accuracy in applying the free surface pressure condition by using irregular stars, waves after breaking cannot be simulated. When breaking occurs, the computation must be terminated. Second, only non-turbulent flows are considered in our model. Although laminar viscous damping has little effect on large scale wave motions, energy dissipation due to the turbulence can be significant. However, a recent study by Pritchett [1970] shows that it is feasible to implement a heuristic simulation of turbulence in the MAC framework.

ACKNOWLEDGMENT

This research was supported in part by the Fluid Dynamics Branch, Office of Naval Research, through Contract Nonr 225(71), NR 062-320.

REFERENCES

- Brennen, C., "Some Numerical Solutions of Unsteady Free Surface Wave Problems Using Lagrangian Description of the Flow," 2nd International Conf. on Numer. Meth. in Fluid Dyn., Berkeley, Calif., Springer-Verlag, Pub., September, 1970.
- Camfield, F. E., and Street, R. L., "Shoaling of Solitary Waves on Small Slopes," J. Waterways and Harbors Division, ASCE, V. 95, No. WW1, Proc. Paper 6380, pp. 1-22, February, 1969.
- Carrier, G. F., "Gravity Waves on Water of Variable Depth," J. Fluid Mech., Vol. 24, Pt. 4, pp. 641-660, April 1966.
- Chan, R. K. C., and Street, R. L., "A Computer Study of Finite-Amplitude Water Waves," J. Comput. Physics, Vol. 6, No. 1, August 1970 [1970a].

- Chan, R. K. C., and Street, R. L., "Shoaling of Finite-Amplitude Waves on Plane Beaches." Proc. 12th Conf. on Coastal Engineering, Washington, D.C., ASCE, September 1970 [1970b].
- Chan, R. K. C., and Street, R. L., "SUMMAC -- A Numerical Model for Water Waves," Stanford C. E. Dept. T. R. No. 135, Stanford, Calif., August 1970 [1970c].
- Chan, R. K. C., Street, R. L., and From, J. E., "The Digital Simulation of Water Waves -- An Evaluation of SUMMAC," 2nd International Conf. on Numer. Meth. in Fluid Dyn., Berkeley, Calif., Springer-Verlag, Pub., September, 1970.
- Fangmeier, D. D., "Steady and Unsteady Potential Flow with Free Surface and Gravity," Ph.D. Dissertation to U.C. (Davis), Davis, Calif., 1967.
- Forsythe, G. E., and Wasow, W. R., Finite-Difference Methods for Partial Differential Equations, J. Wiley and Sons, Inc., 1960.
- Freeman, J. C. and LeMéhauté, B., "Wave Breakers on a Beach and Surges on a Dry Bed," J. Hydr. Div., ASCE, V. 90, No. HY2, pp. 187-216, March, 1964.
- Fromm, J. E., "Practical Investigation of Convective Difference Approximation of Reduced Dispersion," IBM Research Report, RJ531, IBM Res. Lab., San Jose, Calif., 1968.
- Heitner, K. L., "A Mathematical Model for Calculation of the Run-up of Tsunamis," Earthquake Engrg. Res. Lab. Report, Calif. Inst. Tech., Pasadena, Calif., May 1969.
- Hirt, C. W., Cook, J. L., and Butler, T. D., "A Lagrangian Method for Calculating the Dynamics of an Incompressible Fluid with Free Surface," J. Comput. Physics, V. 5, No. 1, April, 1970.
- Hwang, L. S., Fersht, S., and LeMéhauté, B., "Transformation and Run-up of Tsunami Type Wave Trains on a Sloping Beach," 13th Cong. of IAHR, Kyoto, Japan, 31 Aug. to 5 Sept. 1969.
- Keulegan, G. H., and Harrison, J., "Tsunami Refraction Diagrams by Digital Computer," J. Waterways and Harbors Div., ASCE, V. 96, No. WW2, Proc. Pap. 7261, pp. 219-233, May 1970.
- Lautenbacher, C. C., "Gravity Wave Refraction by Islands," J. Fluid Mech., V. 41, Pt. 3, pp. 655-672, 29 April, 1970.

- Leendertse, J. J., "Aspects of a Computational Model for Long-Period Water-Wave Propagation," RAND Memo RM-5294-PR, Santa Monica, Calif., May 1967.
- Madsen, O. S., and Mei, C. C., "Dispersive Long Waves of Finite Amplitude over an Uneven Bottom, MIT Hydro. Lab. Rep. No. 117, Dept. of Civil Engrg., Cambridge, Mass., November 1969 [1969a].
- Madsen, O. J., and Mei, C. C., "The Transformation of a Solitary Wave over an Uneven Bottom," J. Fluid Mech., V. 39, Pt. 4, pp. 781-792, 15 December, 1969 [1969b].
- Mogel, T. R., Street, R. L., and Perry, B., "Computation of Along-shore Energy and Transport," Proc. 12th Conf. on Coastal Engrg., Wash., D. C., ASCE, September 1970.
- Peregrine, D. H., "Long Waves on a Beach," J. Fluid Mech., V. 27, Pt. 4, pp. 815-827, 1967.
- Pritchett, J. W., "The MACYL6 Hydrodynamic Code," Info. Res. Assoc., IRA-TR-1-70, Berkeley, Calif., 15 May, 1970.
- Schreiber, D. E., "A Generalized Equipotential Plotting Routine for a Scalar Function of Two Variables," IBM Research Rep. RJ-499 (No. 10673), Computer Applications, New York, 24 May, 1968.
- Street, R. L., Burges, S. J., and Whitford, P. W., "The Behavior of Solitary Waves on a Stepped Slope," Stanford C. E. Dept. T.R. No. 93, Stanford, Calif., August 1968.
- Street, R. L., Chan, R. K. C., and Fromm, J. E., "The Numerical Simulation of Long Water Waves -- Progress on Two Fronts," Proc. Intl. Symposium on Tsunamis and Tsunami Res., East/West Center, Honolulu, Hawaii, October 1969.
- Vastano, A. C., and Reid, R. O., "Tsunami Response for Islands; Verification of a Numerical Procedure," J. Marine Res., V. 25, No. 2, pp. 129-139, 1967.
- Welch, J. E., Harlow, F. H., Shannon, J. P., and Daly, B. J., "The MAC Method -- A Computing Technique for Solving Viscous, Incompressible, Transient Fluid-Flow Problems Involving Free Surfaces," Los Alamos Sci. Lab. Rep. LA-3425, 1966.
- Wiegel, R. L., Oceanographical Engineering, Prentice Hall, Englewood Cliffs, New Jersey, 1964.

Williams, J. A., and Kartha, K. K., "Model Studies of Long Wave Amplification by Circular Islands and Submarine Seamounts," Hawaii Inst. of Geophys., Final Report (HIG-66-19), November, 1966.

AN UNSTEADY CAVITY FLOW

D. P. Wang

The Catholic University of America
Washington, D.C.

I. INTRODUCTION

A perturbation theory for two-dimensional unsteady cavity flows has been formulated by the present author and Wu [1965]*. In that formulation we regard the unsteady part of the motion as a small perturbation of a steady cavity flow already established. This already established steady cavity flow will be called as the basic flow. Our perturbation expansion is carried out in terms of a set of intrinsic coordinates (s, n) of the basic flow. The coordinate s is the arc length measured along a streamline in the direction of the basic flow, and n the distance measured normal to a streamline. An illustration is given in Fig. 1, where the solid lines represent the basic flow configuration, AB represents the wetted side of the solid body, AI and BI , the two branches of the cavity wall which is a free surface. Also shown in Fig. 1 is the unsteady perturbed flow configuration represented by dotted lines. The unsteady

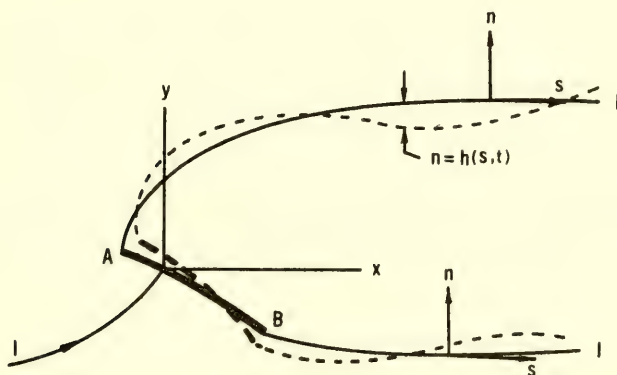


Fig. 1 Illustration of an unsteady perturbation flow

*This paper will henceforth be referred to as W.

displacement of the free surface and the solid body from their corresponding locations in the basic flow is denoted by $n = h(s, t)$. If the wetted side of the solid body and the free surface of the basic flow are taken to be $n = 0$, $h(s, t)$ is assumed to be a very small quantity. In W we have found that the linearized kinematic and dynamic boundary conditions on the free surface for the unsteady perturbation potential ϕ_1 are

$$\frac{\partial \phi_1}{\partial n} = \frac{\partial h}{\partial t} + q_c \frac{\partial h}{\partial s} \quad \text{on } n = 0 \quad (1)$$

and

$$\frac{\partial \phi_1}{\partial t} + q_c \frac{\partial \phi_1}{\partial s} = \pm \frac{q_c^2}{R} h \quad \text{on } n = 0, \quad (2)$$

and that the boundary condition on the solid body is

$$\frac{\partial \phi_1}{\partial n} = \frac{\partial h}{\partial t} + \frac{\partial}{\partial s} (q_0 h) \quad \text{on } n = 0. \quad (3)$$

In the above equations R and q_c are respectively the radius of curvature and the constant speed on the free surface of the basic flow, and q_0 is the speed of the basic flow. The $+$ (or $-$) sign on the right-hand side of (2) holds for the upper (or lower) branch of the cavity wall; these signs are necessary to make R a positive quantity. We should mention here that in obtaining (2) we have assumed that the cavity pressure remains unchanged during the unsteady perturbation.

If we regard q_c^2/R as an equivalent gravitational acceleration and the s -coordinate rectilinear, then (1) and (2) are in the same form as the linearized free surface boundary conditions in water wave problems. Thus we expect that the centrifugal acceleration q_c^2/R due to the curvature of the basic flow streamline should play the role of a restoring force in producing and propagating the surface waves along the curved cavity wall.

The purpose of the present paper is to use this perturbation theory to study some unsteady behavior of the Kirchhoff flow when the solid plate is in small harmonic oscillations.

II. THE BASIC FLOW

In this paper we consider the basic flow to be a flat plate held normal to an incoming uniform stream of infinite breadth, with a cavity formation of infinite length as shown in Fig. 2. This is the so-called Kirchhoff flow. Both the speed of the incoming stream and the length of the plate AB are taken to be unity. A set of Cartesian coordinates (x, y) with its origin at the stagnation point C is chosen as indicated in Fig. 2, where the point I denotes the point at infinity.

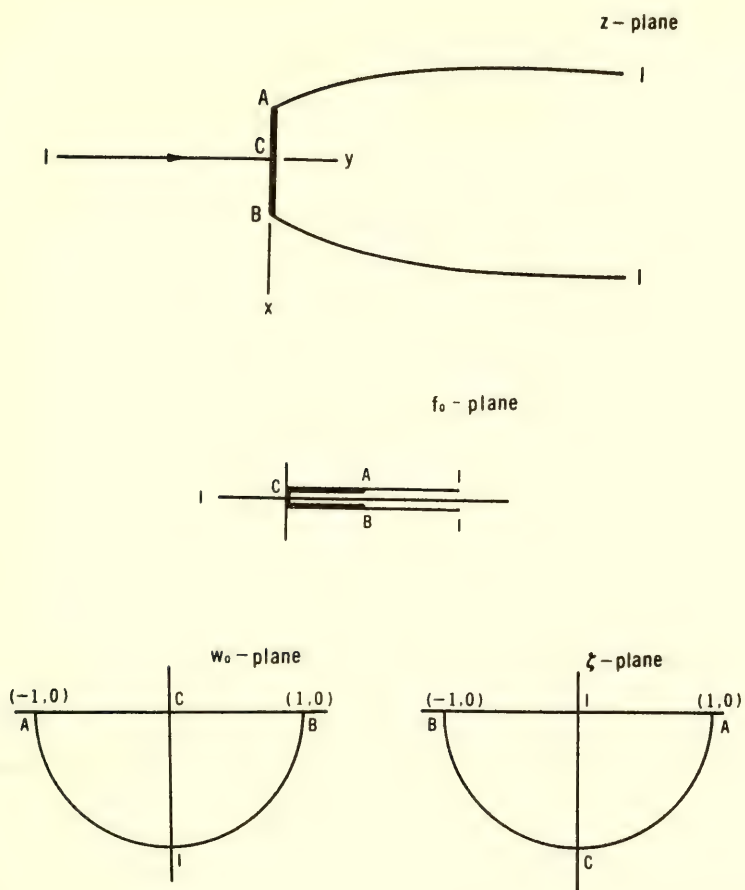


Fig. 2 The basic flow and its conformal mapping planes

The solution of this problem can be obtained by the Levi-Civita method in terms of a parametric variable ζ (Gilbarg [1960]), and we simply give it below for subsequent use. The complex potential f_0 , velocity w_0 and the complex variable $z = x + iy$ are

$$f_0 = \frac{K}{4} \left(\zeta + \frac{1}{\zeta} \right)^2, \quad (4)$$

$$w_0 = \frac{i\zeta - 1}{\zeta - i}, \quad (5)$$

and

$$z = \int_{-i}^{\zeta} \frac{1}{w_0} \frac{df_0}{d\zeta} d\zeta, \quad (6)$$

where

$$K = \frac{1}{4 + \pi}. \quad (7)$$

The flow region in various planes can also be found in Fig. 2. For points on the plate AB, we may deduce from (6)

$$x = \frac{K}{2} (\sin 2\theta - 4 \cos \theta - \pi - 2\theta), \quad (8)$$

where $\theta = \text{Arg } \zeta$, when ζ is on the circular arc ACB, and

$$-\pi \leq \theta \leq 0. \quad (9)$$

III. UNSTEADY PERTURBED FLOW

It is shown in W that by eliminating h between (1) and (2) and transforming (s, n) and R to the variables f_0 and w_0 a single free surface boundary condition in complex variable form can be obtained, which is

$$\text{Re} [L(f_1)] = 0, \quad (10)$$

where

$$f_1 = \phi_1 + i\psi_1 \quad (11)$$

is the complex perturbation potential, and the linear differential operator L is

$$L = \left(\frac{\partial}{\partial t} + \frac{\partial}{\partial f_0} \right)^2 - \left[\frac{d}{df_0} \ln \left(\frac{1}{w_0} \frac{dw_0}{df_0} \right) \right] \left(\frac{\partial}{\partial t} + \frac{\partial}{\partial f_0} \right) - \frac{1}{w_0} \frac{dw_0}{df_0} \frac{\partial}{\partial f_0}. \quad (12)$$

It is also shown in W that the boundary condition (3) on the solid body can be transformed into

$$\text{Im} \frac{\partial f_1}{\partial f_0} = - \frac{1}{q_0} \left[\frac{\partial h}{\partial t} + \frac{\partial}{\partial s} (q_0 h) \right], \quad (13)$$

where h is regarded as a given function of s and t . Since along the solid body $df_0 = q_0 ds$, which is purely real, (13) may be written as

$$\text{Im } f_1 = - \int_0^s \frac{\partial h}{\partial t} ds - q_0 h, \quad (14)$$

where we have set $\text{Im } f_1$ to zero at $s = 0$, the stagnation point of the basic flow. For the basic flow considered and from the definition adopted for the intrinsic coordinates (s, n) , we note that along CB

$$q_0 = w_0, \quad (s, n) = (x, y), \quad (15)$$

and along CA

$$q_0 = -w_0, \quad (s, n) = -(x, y). \quad (16)$$

If we denote the prescribed motion of AB as $y = \eta_1(x, t)$ instead of $n = h(s, t)$, with the aid of (15) and (16), (14) becomes

$$\text{Im } f_1 = - \int_0^x \frac{\partial \eta_1}{\partial t} dx - w_0 \eta_1. \quad (17)$$

Let us assume that the prescribed motion of AB is given by

$$\eta_1(x, t) = \epsilon \cos \omega t, \quad (18)$$

where ϵ is a very small constant quantity and ω is the frequency of oscillation. For convenience in the following analysis, let us introduce an imaginary unit $j = \sqrt{-1}$ which is regarded as different and non-interacting with the imaginary unit i used in defining the complex variable $z = x + iy$. If we agreed that only the real part with respect to j of a quantity is meaningful to us, we may write (18) as

$$\eta_1(x, t) = \epsilon e^{j\omega t}. \quad (19)$$

To avoid any confusion in the notation, from now on when we mention the real (or imaginary) part of a function \mathfrak{F} , denoted by $\text{Re } \mathfrak{F}$ (or $\text{Im } \mathfrak{F}$) as it has been used so far, we mean the real (or imaginary) part of \mathfrak{F} with respect to i , not with respect to j , even if \mathfrak{F} contains j . Only when the final result is obtained shall we take the real part with respect to j as our solution.

If we assume that the disturbance has already been applied for a long time so that the entire flow is in harmonic oscillation, we may write the complex velocity potential $f_1(z, t)$ as

$$f_1(z, t) = f(z)e^{j\omega t}. \quad (20)$$

If we substitute (20) into (10) we may write the free surface boundary condition as

$$\operatorname{Re} H = 0 \quad (21)$$

where

$$H = \frac{d^2 f}{df_0^2} + \left(2j\omega - \frac{d}{df_0} \ln \frac{dw_0}{df_0} \right) \frac{df}{df_0} - \left[\omega^2 + j\omega \frac{d}{df_0} \ln \left(\frac{1}{w_0} \frac{dw_0}{df_0} \right) \right] f, \quad (22)$$

which is an analytic function defined in the flow field. We may also write

$$\begin{aligned} H = & \frac{1}{w_0^2} \frac{d^2 f}{dz^2} + \frac{1}{w_0} \left[2j\omega - \frac{d}{df_0} \ln \left(w_0 \frac{dw_0}{df_0} \right) \right] \frac{df}{dz} \\ & - \left[\omega^2 + j\omega \frac{d}{df_0} \ln \left(\frac{1}{w_0} \frac{dw_0}{df_0} \right) \right] f. \end{aligned} \quad (23)$$

Since the differential operator L is purely real on the plate AB, the boundary condition (17) may be expressed in terms of the analytic function H . By a straightforward application of L on (17) and by the use of (19) and (20), the boundary condition on AB may be written as

$$\operatorname{Im} H = \gamma, \quad (24)$$

where

$$\begin{aligned} \gamma = \epsilon \left\{ \left[-\omega^2 x + j\omega \left(w_0 + \frac{1}{w_0} \right) \right] \frac{d}{df_0} \ln \frac{dw_0}{df_0} + \left[\omega^2 x \right. \right. \\ \left. \left. - j\omega \left(3w_0 - \frac{1}{w_0} \right) \right] \frac{d}{df_0} \ln w_0 + j\omega^3 x + \omega^2 \left(w_0 + \frac{2}{w_0} \right) \right\}. \end{aligned} \quad (25)$$

The boundary conditions expressed in the forms of (21) and (24) may be used to determine H for points in the interior of the flow field. However, to obtain a physically acceptable H , other boundary conditions have to be imposed on H .

We shall assume that the free surface displacement due to the unsteady disturbance of the plate AB has to be bounded everywhere. This condition can be satisfied if the free surface displacement is bounded at the separation points A, B and at the point at infinity.

It is shown in W that the curvature of the free surface of the basic flow is

$$\frac{1}{R} = \left| \frac{q_c}{w_0} \frac{dw_0}{df_0} \right|, \quad (26)$$

where $q_c = 1$ in our problem. From the local mapping behavior near $|z| = \infty$ between the w_0 -, f_0 - and z -planes shown in Fig. 2, we see that

$$w_0 + i \sim a_1 z^{-1/2}, \quad (27)$$

and

$$f_0 \sim -iz \quad \text{as} \quad |z| \rightarrow \infty, \quad (28)$$

where a_1 is a constant. In the following analysis we always use a_n to indicate some constant. The substitution of (27) and (28) into (26) gives us

$$\frac{1}{R} = O(|z|^{-3/2}) \quad (29)$$

on the free surface as $|z| \rightarrow \infty$. Since we assume that the free surface displacement near the point at infinity has to be bounded, then, from (2) and (29), we have, near the point at infinity,

$$\frac{\partial \phi_I}{\partial t} + \frac{\partial \phi_I}{\partial s} \sim 0. \quad (30)$$

For harmonic oscillations, (30) suggests that we may write

$$\phi_I = A(f_0) e^{j\omega(t-f_0)} \quad \text{as} \quad |z| \rightarrow \infty, \quad (31)$$

since along the free surface of the basic flow $\partial/\partial s = \partial/\partial f_0$. The substitution of (31) into (2) gives

$$h = \pm R \frac{dA}{df_0} e^{j\omega(t-f_0)} \quad \text{as} \quad |z| \rightarrow \infty. \quad (32)$$

In view of (29) and (28), (32) implies that along the free surface near the point at infinity $A = O(z^{-1/2})$, at most, in order that h be bounded there. With h being bounded at infinity and having a form shown

in (32), we can obtain, from (1), that on the free surface $\partial\phi_I/\partial n = o(z^{-1})$ as $|z| \rightarrow \infty$. These results indicate that along the free surface near the point at infinity both f and df/dz should vanish. Since the unsteady disturbance is mainly a surface phenomenon, it is not unreasonable for us to assume that f and df/dz also vanish in the interior of the flow field near the point at infinity. Therefore, we assume that

$$H \rightarrow 0 \quad \text{as} \quad |z| \rightarrow \infty. \quad (33)$$

This rules out the possibility that there is any induced circulation around the point at infinity. Based on the assumption that h is bounded at infinity and the result that on the free surface $\partial\phi_I/\partial n = o(z^{-1})$ as $|z| \rightarrow \infty$, an integration of (1) will show that if

$$\frac{\partial\phi_I}{\partial n} = O(r^{-1+\delta}) \quad \delta > 0 \quad (34)$$

in the neighborhood of the points A, B with r the distance from these points, h will be bounded at A, B . Condition (34) is also necessary in order that the pressure be integrable over the plate AB .

To facilitate the determination of H , let us introduce a transformation

$$\begin{aligned} \tau &= \frac{1}{2} \left(\zeta + \frac{1}{\zeta} \right) \\ \zeta &= \tau - (\tau^2 - 1)^{1/2} \end{aligned} \quad (35)$$

where the cut in the τ -plane is taken along the straight line between -1 and 1 , and $(\tau^2 - 1)^{1/2} \rightarrow \tau$ as $|\tau| \rightarrow \infty$, $-\pi < \text{Arg } \tau \leq \pi$. The mapping (35) maps the entire basic flow onto the upper-half τ -plane as shown in Fig. 3. In terms of the variable τ , the function γ becomes

$$\begin{aligned} \gamma &= \frac{\epsilon}{2k^2\tau^2(\tau^2-1)} \left\{ j(K\omega)^3 \tau^2(1-\tau^2) \left[2\tau(1-\tau^2)^{1/2} + 4\tau \right. \right. \\ &\quad \left. \left. + \pi + 2 \cos^{-1} \tau \right] + (K\omega)^2 \left[\tau(1-\tau^2)^{1/2} (4-5\tau^2) \right. \right. \\ &\quad \left. \left. - 12\tau^3 - \frac{3\pi}{2} \tau^2 + 10\tau + \pi + (2-3\tau^2) \cos^{-1} \tau \right] + 2jK\omega\tau \right\}, \end{aligned} \quad (36)$$

where

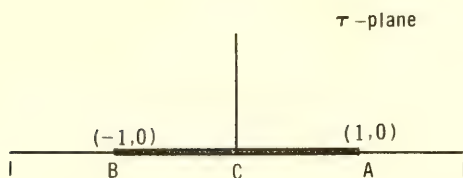


Fig. 3 A conformal mapping plane of the basic flow

$$-\pi \leq \cos^{-1} \tau \leq 0. \quad (37)$$

We note that γ , shown in (36), has simple poles at $\tau = 0$ and ± 1 , and therefore, it obviously does not satisfy the Hölder condition on AB, where $-1 \leq \tau \leq 1$. In order to find H , which is regarded as a function of τ now, let us continue it analytically into the lower-half τ -plane by

$$H(\bar{\tau}) = -\overline{H(\tau)}, \quad (38)$$

and let us define another analytic function $\Omega(\tau)$ by

$$\Omega(\tau) = \tau(\tau^2 - 1)^{1/2} H(\tau), \quad (39)$$

where the branch cut for $(\tau^2 - 1)^{1/2}$ has been defined after (35). If we denote the limiting values of Ω as $\text{Im } \tau \rightarrow \pm 0$ by Ω_{\pm} , then, from (39), (21) and (24),

$$\begin{aligned} \Omega_+ - \Omega_- &= 0 & \text{on} & \quad |\text{Re } \tau| > 1 \\ &= -2\tau(1 - \tau^2)^{1/2} \gamma & \text{on} & \quad |\text{Re } \tau| < 1. \end{aligned} \quad (40)$$

With $\Omega_+ - \Omega_-$ given by (40), the function $\Omega(\tau)$ may be determined (Muskhelishvili [1946])

$$\Omega(\tau) = \frac{i}{\pi} \left\{ \int_{-1}^1 \frac{\sigma(1-\sigma^2)^{1/2} \gamma(\sigma)}{\sigma - \tau} d\sigma + \sum_{n=0}^N b_n \tau^n \right\}, \quad (41)$$

where b_n are arbitrary constants and N is an arbitrary integer. From (39), $H(\tau)$ may be written as

$$H(\tau) = \frac{i}{\pi} \tau^{-1} (\tau^2 - 1)^{-1/2} \left\{ \int_{-1}^1 \frac{\sigma(1-\sigma^2)^{1/2} \gamma(\sigma)}{\sigma - \tau} d\sigma + \sum_{n=0}^N b_n \tau^n \right\}, \quad (42)$$

However, to satisfy (21), b_n have to be purely real. The condition (33) is equivalent to

$$H(\tau) \rightarrow 0 \quad \text{as} \quad |\tau| \rightarrow \infty, \quad (43)$$

since near $|z| = \infty$

$$\tau \sim a_2 z^{1/2}. \quad (44)$$

To satisfy (43),

$$b_n = 0 \quad \text{for} \quad n \geq 2. \quad (45)$$

Due to the symmetry of our problem, which implies

$$\text{Im } f = 0 \quad \text{on} \quad CI, \quad (46)$$

and due to the fact that the differential operator L is purely real on CI , we require that

$$b_0 = 0. \quad (47)$$

This leaves only the constant b_1 undetermined. After carrying out the integrations in (42), we may write

$$H(\tau) = \frac{\epsilon}{2\pi i K^2} \frac{1}{\tau^2(\tau^2 - 1)} \left[j(K\omega)^3 M_1(\tau) + (K\omega)^2 M_2(\tau) \right. \\ \left. - 2\pi j K \omega \tau + b_1 \tau^2 (\tau^2 - 1)^{1/2} \right], \quad (48)$$

where

$$M_1(\tau) = \pi \tau^2 (\tau^2 - 1) (4\tau + \pi) + \tau^2 (\tau^2 - 1)^{1/2} \left[2\pi - \frac{4}{3} - 4(1 + \pi)\tau^2 \right] \\ - 2\tau^3 (\tau^2 - 1)^{3/2} \ln \frac{\tau - 1}{\tau + 1} - 2\tau^2 (\tau^2 - 1)^{3/2} \mathfrak{B}(\tau), \quad (49)$$

$$M_2(\tau) = 2\pi\tau(6\tau^2-5) + \pi^2\left(\frac{3}{2}\tau^2-1\right) - 2(\tau^2-1)^{1/2} [4G + (5+6\pi)\tau^2] \\ + \tau(4-5\tau^2)(\tau^2-1)^{1/2} \ln \frac{\tau-1}{\tau+1} + (2-3\tau^2)(\tau^2-1)^{1/2} \mathfrak{L}(\tau), \quad (50)$$

$$G = \text{Catalan's constant} = 0.915965594, \quad (51)$$

and

$$\mathfrak{L}(\tau) = \int_{-1}^1 \frac{\cos^{-1} \sigma}{(1-\sigma^2)^{1/2}(\sigma-\tau)} d\sigma \quad -\pi \leq \cos^{-1} \sigma \leq 0, \quad (52)$$

which cannot be expressed in terms of elementary functions.

It is not difficult to see from (48) that as $|\tau| \rightarrow \infty$, the dominating term is the one containing b_1 , which is of the order $|\tau|^{-1}$. Since the remaining terms in (48) are obtained from the integral shown in (42), they are, therefore, of the order $|\tau|^{-3}$. This indicates that the b_1 term is the most important term for the flow field near the point at infinity.

With H given by (48), (22) may be regarded as a linear, second order, ordinary differential equation for f .

If we transform the independent variable from f_0 to ζ and make the following change of dependent variable

$$f = F(\zeta) \left(\frac{dw_0}{d\zeta} \right)^{1/2} e^{-j\omega f_0}. \quad (53)$$

The differential equation (22) is readily reduced to

$$\frac{d^2 F}{d\zeta^2} - ijK\omega \frac{\zeta^2-1}{\zeta^3} F = G(\zeta), \quad (54)$$

where

$$G(\zeta) = \left(\frac{df_0}{d\zeta} \right)^2 \left(\frac{dw_0}{d\zeta} \right)^{-1/2} e^{j\omega f_0} H, \quad (55)$$

f_0 and w_0 as functions of ζ are given by (4) and (5), and H is given by (48) with τ as a function of ζ given by (35). To help us to understand the properties of the Eq. (54), let us make the following change of variables

$$\begin{aligned}\zeta &= ie^{-2i\beta} \\ F &= i\tilde{F}e^{-i\beta},\end{aligned}\tag{56}$$

which transforms (54) into

$$\frac{d^2\tilde{F}}{d\beta^2} + (1 - 8jK\omega \cos 2\beta)\tilde{F} = -4iGe^{-3i\beta}.\tag{57}$$

This is Mathieu's differential equation. The flow region now occupies in the β -plane a semi-infinite strip shown in Fig. 4. In principle, a general solution of (57), or (54), can be obtained. If we denote the solutions of the homogeneous equation of (54) by $F_1(\zeta)$ and $F_2(\zeta)$, then a general solution of (54) is

$$F(\zeta) = \frac{1}{W(F_1, F_2)} \left\{ F_1(\zeta) \int_{a_3}^{\zeta} F_2(\lambda) G(\lambda) d\lambda - F_2(\zeta) \int_{a_4}^{\zeta} F_1(\lambda) G(\lambda) d\lambda \right\},\tag{58}$$

where

$$W(F_1, F_2) = \frac{dF_1}{d\zeta} F_2 - \frac{dF_2}{d\zeta} F_1\tag{59}$$

which is a constant.

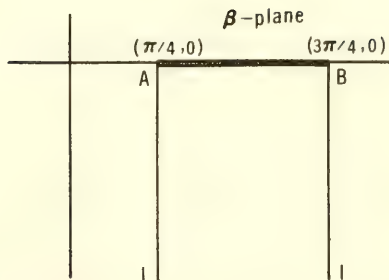


Fig. 4 A conformal mapping plane of the basic flow

To obtain F explicitly we must first obtain F_1 and F_2 . In this paper we are not going to obtain the exact forms of F_1 and F_2 , even though they can be expressed in terms of the solutions of the Mathieu equation given in (57). We shall, instead, obtain the asymptotic representations for F_1 and F_2 as $\omega \rightarrow \infty$. We should mention here that Langer [1934] has developed asymptotic representations for the solutions of the Mathieu equation with at least one parameter large; however, instead of modifying his asymptotic representations to cover the equation shown in (53) with j another imaginary unit, we shall derive the asymptotic representations for F_1 and F_2 below.

Let us denote

$$\chi(\zeta) = i \frac{\zeta^2 - 1}{\zeta^3}, \quad (60)$$

then, the homogeneous equation of (54) can be written as

$$\frac{d^2 F}{d\zeta^2} = jK\omega\chi(\zeta)F. \quad (61)$$

Due to the symmetric properties of our problem we need only consider half of the flow region, say the region bounded by ICAI, which in the ζ -plane is a quarter circle as shown in Fig. 2. In this region χ has a simple zero at $\zeta = 1$ and a pole of order 3 at $\zeta = 0$. If we make a typical change of the independent variable to ξ , defined by (Jeffreys [1962])

$$\frac{2}{3} \xi^{3/2} = \int_1^\zeta \chi^{1/2}(\zeta) d\zeta, \quad (62)$$

and put

$$F = \left(\frac{d\xi}{d\zeta} \right)^{-1/2} U, \quad (63)$$

the differential Eq. (61) becomes

$$\frac{d^2 U}{d\xi^2} = [jK\omega\xi + r(\xi)] U, \quad (64)$$

where

$$\begin{aligned}
 r(\xi) &= \left(\frac{d\zeta}{d\xi} \right)^{1/2} \frac{d^2}{d\xi^2} \left(\frac{d\zeta}{d\xi} \right)^{-1/2} \\
 &= \frac{1}{16} \left[\frac{\zeta}{\xi^2} - i\xi\zeta \frac{3\zeta^4 - 26\zeta^2 + 3}{(\zeta^2 - 1)^3} \right] .
 \end{aligned} \tag{65}$$

A straightforward expansion of (62) shows that

$$\xi = O(\zeta^{-1/3}) \quad \text{as} \quad \zeta \rightarrow 0, \tag{66}$$

and, of course,

$$r(\xi) = O(1) \quad \text{as} \quad \zeta \rightarrow 1. \tag{67}$$

Equation (66) indicates that the mapping (62) maps the point I to the point at infinity in the ξ -plane. The flow region ICA in the ξ -plane is shown in Fig. 5. From (65) and (66) we can see that

$$r(\xi) = O\left(\frac{1}{\xi^2}\right) \quad \text{as} \quad |\xi| \rightarrow \infty. \tag{68}$$

Olver [1954] has investigated an equation of the form

$$\frac{d^2 U}{d\xi^2} = [\mu^2 \xi + r(\xi)] U, \tag{69}$$

where μ^2 is a positive large parameter. He shows that for a domain D , if $r(\xi)$ is regular in D and $r(\xi) = O(|\xi|^{-1/2-\sigma})$ for some $\sigma > 0$

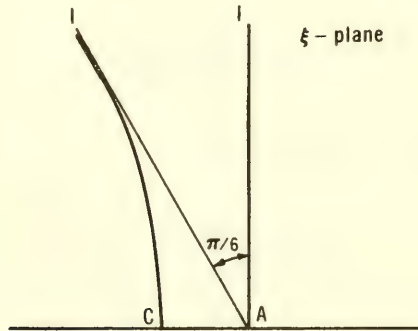


Fig. 5 A conformal mapping plane of the basic flow region bounded between ICA

as $|\xi| \rightarrow \infty$, and if the distance between the boundary lines of D does not tend to zero as $|\xi| \rightarrow \infty$ in any subdomain of D , then, a uniformly valid expansion of U in terms of Airy functions can be obtained. Olver [1957] later extends the result to the case when μ^2 is a large complex parameter. For our problem, all the above requirements for a uniformly valid expansion in terms of Airy functions are satisfied except that the parameter μ^2 in our case is $jK\omega$, where j is an imaginary unit independent of the imaginary unit i used in the complex variable ξ . Since i and j do not interact and j may be regarded as a real quantity so far as the imaginary unit of i is concerned, we assume that Olver's result is applicable here and write the two solutions of (64) as

$$U_1 = \text{Ai}[(jK\omega)^{1/3} \xi] [1 + O(\frac{1}{\omega})] \quad (70)$$

and

$$U_2 = \text{Ai}[(jK\omega)^{1/3} e^{-2\pi i/3} \xi] [1 + O(\frac{1}{\omega})] \quad \text{as } \omega \rightarrow \infty, \quad (71)$$

where $\text{Ai}(X)$ is the Airy function with argument X , which may be expressed either as the sum of two converging series or as an integral given in the following (Jeffreys & Jeffreys [1956])

$$\text{Ai}(x) = \frac{1}{2\pi i} \int_{\infty e^{-2\pi i/3}}^{\infty e^{2\pi i/3}} e^{xs - \frac{1}{3}s^3} ds. \quad (72)$$

Substituting $x = (jK\omega)^{1/3} \xi$ into (72) and manipulating the result, we can show that

$$\text{Ai}[(jK\omega)^{1/3} \xi] = \frac{1}{2} \{ (1-ij) \text{Ai}[(iK\omega)^{1/3} \xi] + (1+ij) \text{Ai}[-(iK\omega)^{1/3} \xi] \}, \quad (73)$$

where $(i)^{1/3}$ and $(-i)^{1/3}$ will be taken as $e^{\pi i/6}$ and $e^{-\pi i/6}$ respectively. Therefore, from (63)

$$\begin{aligned} F_1 &= \left(\frac{d\xi}{d\zeta} \right)^{-1/2} U_1 \\ &\sim \frac{1}{2} \left(\frac{d\xi}{d\zeta} \right)^{-1/2} \{ (1-ij) \text{Ai}[(iK\omega)^{1/3} \xi] + (1+ij) \text{Ai}[-(iK\omega)^{1/3} \xi] \}. \end{aligned} \quad (74)$$

Similarly,

$$F_2 = \left(\frac{d\xi}{d\zeta} \right)^{-1/2} U_2$$

$$\sim \frac{1}{2} \left(\frac{d\xi}{d\zeta} \right)^{-1/2} \{ (1-ij) \text{Ai}[(iK\omega)^{1/3} e^{-2\pi i/3} \xi] + (1+ij) \text{Ai}[-(iK\omega)^{1/3} e^{-2\pi i/3} \xi] \}.$$
(75)

In (74) and (75)

$$\left(\frac{d\xi}{d\zeta} \right)^{-1/2} = \left(\frac{\xi}{\chi} \right)^{1/4},$$
(76)

where ξ is given by (62) and χ given by (60). With F_1 and F_2 given in (74) and (75), we may find $W(F_1, F_2)$, which is

$$W(F_1, F_2) \sim -\frac{i}{2\pi} (K\omega)^{1/3} e^{j\pi/6 - i\pi/3},$$
(77)

or

$$\frac{1}{W(F_1, F_2)} \sim \frac{\pi i}{(K\omega)^{1/3}} [(1+ij)e^{\pi i/2} + (1-ij)e^{\pi i/6}].$$
(78)

Let us now express the solution F in terms of the τ variable. From (4), (5) and (35), we have

$$f_0 = K\tau^2,$$
(79)

$$\left(\frac{df_0}{d\zeta} \right)^2 = 4K^2\tau^2(\tau^2 - 1)[\tau + (\tau^2 - 1)^{1/2}]^2,$$
(80)

and

$$\left(\frac{dw_0}{d\zeta} \right)^{-1/2} = \frac{1}{\sqrt{2}} [\tau - (\tau^2 - 1)^{1/2} - i].$$
(81)

When we change the variable of integration in (58) from ζ to τ , we need the quantity $d\zeta/d\tau$, which may be obtained from (35) and is

$$\frac{d\zeta}{d\tau} = -[\tau - (\tau^2 - 1)^{1/2}](\tau^2 - 1)^{-1/2}.$$
(82)

If we denote $G(\zeta) d\zeta/d\tau$ by $g(\tau)e^{jk\omega\tau^2}$, then with the aid of (55), (48), (79), (80), (81) and (82)

$$g(\tau) = \frac{\sqrt{2} \epsilon}{\pi i} \frac{[i(\tau + \sqrt{\tau^2 - 1}) - 1]}{(\tau^2 - 1)^{1/2}} [j(K\omega)^3 M_1(\tau) + (K\omega)^2 M_2(\tau) - 2\pi j K \omega \tau + b_1 \tau^2 (\tau^2 - 1)^{1/2}]. \quad (83)$$

In (83) we note that although b_1 is purely real with respect to i , it may be complex with respect to j ; we also note that the term $2\pi j K \omega \tau$ is extremely small as compared to the term $j(K\omega)^3 M_1(\tau)$ as $\omega \rightarrow \infty$, and since both of them are dependent on j , so we may neglect $2\pi j K \omega \tau$ from (83) and write

$$g(\tau) \sim \frac{\sqrt{2} \epsilon}{\pi i} \frac{[i(\tau + \sqrt{\tau^2 - 1}) - 1]}{(\tau^2 - 1)^{1/2}} [j(K\omega)^3 M_1(\tau) + (K\omega)^2 M_2(\tau) + b_1 \tau^2 (\tau^2 - 1)^{1/2}]. \quad (84)$$

The asymptotic form of F can now be expressed as

$$F \sim \frac{1}{W(F_1, F_2)} \left\{ F_1[\zeta(\tau)] \int_{a_5}^{\tau} F_2[\zeta(\sigma)] e^{jK\omega\sigma^2} d\sigma - F_2[\zeta(\tau)] \int_{a_6}^{\tau} F_1[\zeta(\sigma)] g(\sigma) e^{jK\omega\sigma^2} d\sigma \right\}, \quad (85)$$

where σ is the integration variable in the τ -plane and $F_1(\zeta)$, $F_2(\zeta)$, $g(\tau)$ and $W(F_1, F_2)$ are given in (74), (75), (84) and (77).

Substituting all the necessary results obtained above into (20), noting the relations

$$\begin{aligned} (1 \pm ij)^2 &= 2(1 \pm ij) \\ (1 + ij)(1 - ij) &= 0 \end{aligned} \quad (86)$$

when we are taking the real part of (20) with respect to j , we obtain the complex velocity potential f_1 as

$$f_1 \sim \frac{2\epsilon}{(K\omega)^{1/3}} \frac{(\xi/\chi)^{1/4}}{(\tau - \sqrt{\tau^2 - 1} - i)} \times \left\{ \int_{\omega}^{\tau} e^{\frac{\pi i}{6} + i\omega(t - K\tau^2 + K\sigma^2)} \left\{ \text{Ai}[(iK\omega)^{1/3} \xi] \text{Ai}[(iK\omega)^{1/3} e^{-2\pi i/3} \tilde{\xi}] - \right. \right.$$

$$\begin{aligned}
& \text{Ai}[(iK\omega)^{1/3} e^{-2\pi i/3} \xi] \text{Ai}[(iK\omega)^{1/3} \tilde{\xi}] \left\{ (\tilde{\xi}/\chi)^{1/4} [g_1(\sigma) + B_1 g_3(\sigma)] d\sigma \right. \\
& + \int_{\omega e^{-\pi i/4}}^{\tau} e^{\frac{\pi i}{2} - i\omega(t - K\tau^2 + K\sigma^2)} \left\{ \text{Ai}[(-iK\omega)^{1/3} \xi] \text{Ai}[(-iK\omega)^{1/3} e^{-2\pi i/3} \tilde{\xi}] \right. \\
& - \text{Ai}[(-iK\omega)^{1/3} e^{-2\pi i/3} \xi] \text{Ai}[(-iK\omega)^{1/3} \tilde{\xi}] \left. \right\} (\tilde{\xi}/\chi)^{1/4} [g_2(\sigma) \\
& \left. + \bar{B}_1 g_3(\sigma)] d\sigma \right\} \quad (87)
\end{aligned}$$

where ξ and χ as functions of τ are given by

$$\frac{2}{3} \xi^{3/2} = \sqrt{2} e^{3\pi i/4} \int_1^{\tau} \frac{d\sigma}{(\sigma^2 - 1)^{1/4}}, \quad (88)$$

and

$$\chi = \left[i \left(\frac{2\tau^2 - 1}{\sqrt{\tau^2 - 1}} - \tau \right) \right]^{-1}, \quad (89)$$

$\tilde{\xi}$ and $\tilde{\chi}$ indicate the functional values of ξ and χ when the variable τ is replaced by the integration variable σ ,

$$g_1(\tau) = \frac{i(\tau + \sqrt{\tau^2 - 1}) - 1}{(\tau^2 - 1)^{1/2}} [i(K\omega)^3 M_1(\tau) + (K\omega)^2 M_2(\tau)], \quad (90)$$

$$g_2(\tau) = \frac{i(\tau + \sqrt{\tau^2 - 1}) - 1}{(\tau^2 - 1)^{1/2}} [-i(K\omega)^3 M_1(\tau) + (K\omega)^2 M_2(\tau)], \quad (91)$$

$$g_3(\tau) = \tau^2 [i(\tau + \sqrt{\tau^2 - 1}) - 1], \quad (92)$$

B_1 is an arbitrary complex constant which is derived from b_1 , and \bar{B}_1 is the complex conjugate of B_1 . The lower limits of integration shown in (87) are chosen for our convenience. Therefore, when necessary, homogeneous solutions of the form

$$\begin{aligned}
 A(\tau) e^{i\omega(t-\kappa\tau^2)} \text{Ai}[(iK\omega)^{1/3} \xi], \\
 A(\tau) e^{i\omega(t-\kappa\tau^2)} \text{Ai}[(iK\omega)^{1/3} e^{-2\pi i/3} \xi], \\
 A(\tau) e^{-i\omega(t-\kappa\tau^2)} \text{Ai}[(-iK\omega)^{1/3} \xi]
 \end{aligned} \tag{93}$$

and

$$A(\tau) e^{-i\omega(t-\kappa\tau^2)} \text{Ai}[(-iK\omega)^{1/3} e^{-2\pi i/3} \xi],$$

where

$$A(\tau) = \frac{(\xi/\chi)^{1/4}}{\tau - \sqrt{\tau^2 - 1} - i}, \tag{94}$$

may be added to (87).

We shall now study the behavior of the solution (87) for $|\tau| > R_1 \gg 1$, $0 \leq \text{Arg } \tau \leq \pi/2$. A circular arc of radius R_1 is drawn in the σ -plane as indicated in Fig. 6. Also shown in that figure is a hyperbola S representing the equation $\text{Re}[i(\sigma^2 - \tau^2)] = 0$.

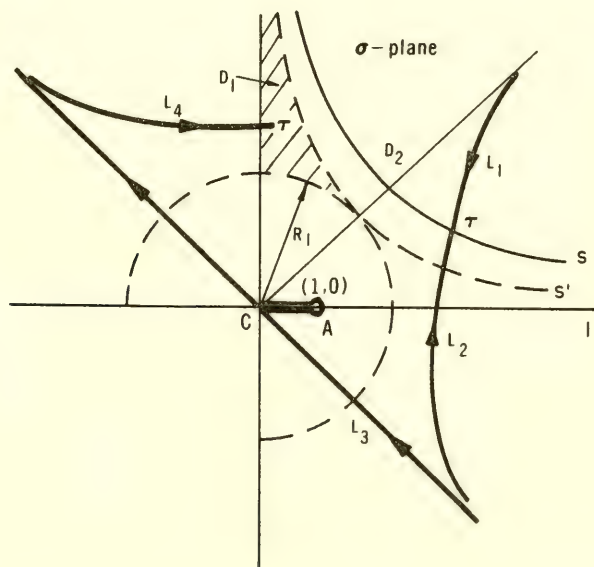


Fig. 6 Paths of integration for the solution given in Eq. (87) when τ is large

If we are travelling along S in the direction of increasing $\text{Im } \sigma$ and if we restrict ourselves to the first, second and fourth quadrants of the σ -plane only, then on the right-hand side of S $\text{Re}[i(\sigma^2 - \tau^2)] < 0$, and on the left-hand side $\text{Re}[i(\sigma^2 - \tau^2)] > 0$. When either $\text{Im } \tau$ or $\text{Re } \tau$ is zero, S degenerates into the positive real and imaginary σ -axes.

From (88), we note that

$$\xi \sim a_7 \tau^{1/3} \quad (95)$$

and

$$\text{Arg } \xi = \frac{1}{3} \text{Arg } \tau + \frac{\pi}{2} \quad \text{as} \quad |\tau| \rightarrow \infty \quad (96)$$

Therefore, for τ and ω large, the arguments of the Airy functions appearing in (87) are large. Their asymptotic representations are (cf. Jeffreys & Jeffreys [1956]),

$$\begin{aligned} \text{Ai}[(iK\omega)^{1/3} \xi] &\sim \frac{e^{-\frac{\pi i}{24} - \frac{2}{3} e^{\pi i/4} \sqrt{K\omega} \xi^{3/2}}}{2\sqrt{\pi} (K\omega)^{1/12} \xi^{1/4}} \\ &\quad \text{when } -\frac{7\pi}{6} < \text{Arg } \xi < \frac{5\pi}{6}, \\ \text{Ai}[(iK\omega)^{1/3} e^{-2\pi i/3} \xi] &\sim \frac{e^{\frac{\pi i}{8} + \frac{2}{3} e^{\pi i/4} \sqrt{K\omega} \xi^{3/2}}}{2\sqrt{\pi} (K\omega)^{1/12} \xi^{1/4}} \\ &\quad \text{when } -\frac{\pi}{2} < \text{Arg } \xi < \frac{3\pi}{2}, \\ \text{Ai}[-(iK\omega)^{1/3} \xi] &\sim \frac{e^{\frac{\pi i}{24} - \frac{2}{3} e^{-\pi i/4} \sqrt{K\omega} \xi^{3/2}}}{2\sqrt{\pi} (K\omega)^{1/12} \xi^{1/4}} \\ &\quad \text{when } -\frac{5\pi}{6} < \text{Arg } \xi < \frac{7\pi}{6}, \\ \text{Ai}[-(iK\omega)^{1/3} e^{-2\pi i/3} \xi] &\sim \frac{e^{\frac{5\pi i}{24} + \frac{2}{3} e^{-\pi i/4} \sqrt{K\omega} \xi^{3/2}}}{2\sqrt{\pi} (K\omega)^{1/12} \xi^{1/4}} \\ &\quad \text{when } -\frac{\pi}{6} < \text{Arg } \xi < \frac{11\pi}{6}. \end{aligned} \quad (97)$$

A straightforward expansion shows that, as $|\tau| > R_1$,

$$2\chi^{-1/4}(\tau - \sqrt{\tau^2 - 1 - i})^{-1} \sim 2^{1/4} i e^{\pi i/8} \tau^{-3/4}. \quad (98)$$

And it is easy to see, as some related explanation has been given in the paragraph after (52), that as $|\tau| > R_1$

$$\begin{aligned} \chi^{-1/4} [g_1(\tau) + B_1 g_3(\tau)] &\sim B_1 2^{1/4} i e^{\pi i/8} \tau^{9/4} \\ \chi^{-1/4} [g_2(\tau) + \bar{B}_1 g_3(\tau)] &\sim \bar{B}_1 2^{1/4} i e^{\pi i/8} \tau^{9/4}. \end{aligned} \quad (99)$$

Let us denote the part of the potential represented by the first integral in (87) by $f_1^{(e)}$,

$$\begin{aligned} f_1^{(e)} &= \frac{2\epsilon}{(K\omega)^{1/3}} \frac{(\xi/\chi)^{1/4}}{(\tau - \sqrt{\tau^2 - 1 - i})} \\ &\times \int_{\omega e^{\pi i/4}}^{\tau} e^{\frac{\pi i}{6} + i\omega(t - K\tau^2 + K\sigma^2)} \left\{ \text{Ai}[(iK\omega)^{1/3} \xi] \text{Ai}[(iK\omega)^{1/3} e^{-2\pi i/3} \xi] \right. \\ &\quad \left. - \text{Ai}[(iK\omega)^{1/3} e^{-2\pi i/3} \xi] \text{Ai}[(iK\omega)^{1/3} \xi] \right\} (\xi/\chi)^{1/4} [g_1(\sigma) + B_1 g_3(\sigma)] d\sigma. \end{aligned} \quad (100)$$

For any τ with $|\tau| > R_1$ and $0 \leq \text{Arg } \tau \leq \pi/2$, the path of integration in (100) can always be chosen to be L_1 , which is a path coming from $\omega e^{\pi i/4}$ to τ , lying completely on the right-hand side of the hyperbola S and outside the circular arc $|\sigma| = R_1$. A typical L_1 is shown in Fig. 6. Since along L_1 $|\sigma| > R_1$, we may substitute the expansion given in (97), (98) and (99) into (100) and obtain

$$f_1^{(e)} \sim \frac{\epsilon B_1 i}{\pi(2K\omega)^{1/2} \tau^{3/4}} \int_{L_1}^{\tau} e^{i\omega(t - K\tau^2 + K\sigma^2)} \sigma^{9/4} \sinh \Phi(\xi, \tilde{\xi}) d\sigma, \quad (101)$$

where

$$\Phi(\xi, \tilde{\xi}) = \frac{2}{3} e^{\pi i/4} \sqrt{K\omega} (\xi^{3/2} - \tilde{\xi}^{3/2}). \quad (102)$$

We note that along L_1 the hyperbolic sine function in (101) may become exponentially large, however, since L_1 lies on the right of S , the factor $\exp [iK\omega(\sigma^2 - \tau^2)]$ will be overwhelmingly small there. Let us now integrate (101) by parts once to get

$$f_1^{(e)} \sim \frac{\epsilon B_1 i}{\pi(2K\omega)^{1/2} \tau^{3/4}} \frac{1}{(2iK\omega)} \left\{ e^{i\omega(t - K\tau^2 + K\sigma^2)} \sigma^{5/4} \sinh \Phi(\xi, \tilde{\xi}) \right\} \Big|_{\infty e^{-\pi i/4}}^{\tau} \\ - \int_{\infty e^{-\pi i/4}}^{\tau} e^{i\omega(t - K\tau^2 + K\sigma^2)} \left[\frac{5}{4} \sigma^{1/4} \sinh \Phi(\xi, \tilde{\xi}) + \sigma^{5/4} \frac{d\Phi}{d\sigma} \cosh \Phi(\xi, \tilde{\xi}) \right] d\sigma \quad (103)$$

The integrated part in (103) is identically zero; when we evaluate it at the upper limit, $\sinh \Phi(\xi, \tilde{\xi}) = 0$, and at the lower limit, the factor $\exp(iK\omega\sigma^2)$ is overwhelmingly small. If we integrate the integral (103) successively by parts and note the relation that

$$\frac{d\Phi}{d\sigma} = -e^{\pi i/4} \sqrt{K\omega} \tilde{\xi}^{1/2} \frac{d\tilde{\xi}}{d\sigma} \sim \sqrt{2K\omega} \sigma^{-1/2} \quad (104)$$

where $\tilde{\xi}^{1/2} d\tilde{\xi}/d\sigma \sim \sqrt{2} e^{3\pi i/4} \sigma^{-1/2}$ is obtained from (88), we can show that

$$f_1^{(e)} \sim \frac{\epsilon B_1 i}{4\pi(K\omega)^2} e^{i\omega t} \tau^{-1} \quad (105)$$

Since $\tau = O(z^{1/2})$ as $|z| \rightarrow \infty$, from (104), we see that the contribution to the potential due to $f_1^{(e)}$ is of order $|z|^{-1/2}$ for $|z|$ large. This type of potential is acceptable. Now, let us denote the part of the potential represented by the second integral in (87) by $f_1^{(w)}$.

$$f_1^{(w)} = \frac{2\epsilon}{(K\omega)^{1/3}} \frac{(\xi/\chi)^{1/4}}{(\tau - \sqrt{\tau^2 - 1} - i)} \int_{\infty e^{-\pi i/4}}^{\tau} e^{\frac{\pi i}{2} - i\omega(t - K\tau^2 + K\sigma^2)} \\ \times \left\{ \text{Ai}[(-iK\omega)^{1/3} \xi] \text{Ai}[(-iK\omega)^{1/3} e^{-2\pi i/3} \tilde{\xi}] - \text{Ai}[(-iK\omega)^{1/3} e^{-2\pi i/3} \xi] \text{Ai}[(-iK\omega)^{1/3} \tilde{\xi}] \right\} (\xi/\chi)^{1/4} [g_2(\sigma) + \bar{B}_1 g_3(\sigma)] d\sigma \quad (106)$$

To investigate the behavior of $f_1^{(w)}$ for $|\tau| > R$, let us divide the region in the first quadrant of the σ -plane outside the circular arc $|\sigma| = R_1$ into two parts, D_1 and D_2 . D_1 , as shown by the shaded area in Fig. 6, is bounded by the circular arc $|\sigma| = R_1$, the imaginary σ -axis and the hyperbola S' representing the equation $\text{Re}[i(\sigma^2 - R_1^2 e^{\pi i/2})] = 0$. D_2 is bounded by the real σ -axis, $|\sigma| = R_1$ and S' . For τ in D_2 , we may choose the path of integration in (106) to be L_2 , which is similar to L_1 except now it lies on the left-hand side of S . A typical L_2 is shown in Fig. 6. Using a process similar to that used to obtain (105) from (100), we may obtain, from (106),

$$f_1^{(w)} \sim \frac{\epsilon \bar{B}_1 i}{4\pi(K\omega)^2} e^{-i\omega\tau} \tau^{-1}. \quad (107)$$

When τ is in D_1 , the hyperbola S will be extremely close to both positive axes of the σ -plane, S degenerates into the axes when τ lies on the imaginary σ -axis. For this case we have to deform the simple path L_2 into $L_3 + L_4$, as shown in Fig. 6, in order that the factor $\exp[-iK\omega(\sigma^2 - \tau^2)]$ will not become exponentially large along the path. L_3 is a path coming from $\infty e^{-\pi i/4}$ to 0 on the lower-half σ -plane, from there along the real σ -axis towards $\sigma = 1$, turning a small circle to the upper side of the real σ -axis and along it to 0 on the upper-half σ -plane, to circumscribe the cut in the σ -plane, and then leaving 0 to $\infty e^{3\pi i/4}$. Path L_4 comes from $\infty e^{3\pi i/4}$ to τ , lying completely on the left-hand side of the hyperbola S and outside the circular arc $|\sigma| = R_1$. The integration along L_3 is convergent; near both ends of the path the integral is exponentially small, near $\sigma = 0$ $M_1(\sigma)$ and $M_2(\sigma)$, which appear in $g_2(\sigma)$, are of order σ^2 and σ respectively and $g_3(\sigma)$ is of order σ^2 , near $\sigma = 1$ only $M_2(\sigma)$ contributes to $g_2(\sigma)$ a square-root type of singularity. The latter property of $M_2(\sigma)$ is the reason that $(K\omega)^2 M_2(\sigma)$ is being kept in the integrand together with the term $(K\omega)^3 M_3(\sigma)$. We may remark here that if we did not neglect the term $2\pi j K\omega \tau$ appearing in $g_2(\sigma)$ from $g(\tau)$ in (83), we would have a term of the form $2\pi i K\omega \sigma$. Since the presence of such a term would not affect the property of the integrand along L_3 near $\sigma = 0$ and 1, and since it is one order in ω smaller than the $(K\omega)^2 M_2(\sigma)$ term, its neglect is justified. Let us now denote the contribution to $f_1^{(w)}$ from the integration along L_3 by $Z(\tau)$,

$$Z(\tau) = \frac{2\epsilon}{(K\omega)^{1/3}} \frac{(\xi/\chi)^{1/4}}{(\tau - \sqrt{\tau^2 - 1} - i)} e^{\frac{\pi}{2} i - i\omega(t - K\tau^2)} \left\{ \text{Ai}[(-iK\omega)^{1/3} \xi] \right. \\ \left. \int_{L_3}^{\infty e^{3\pi i/4}} e^{-iK\omega\sigma^2} \text{Ai}[(-iK\omega)^{1/3} e^{-2\pi i/3} \xi] (\tilde{\xi}/\tilde{\chi})^{1/4} [g_2(\sigma) + \bar{B}_1 g_3(\sigma)] d\sigma - \right.$$

$$- \text{Ai}[(-iK\omega)^{1/3} e^{-2\pi i/3} \xi] \int_{L_3}^{\infty e^{3\pi i/4}} e^{-iK\omega\sigma^2} \text{Ai}[(-iK\omega)^{1/3} \tilde{\xi}] (\tilde{\xi}/\chi)^{1/4} \\ [g_2(\sigma) + \overline{B}_1 g_3(\sigma)] d\sigma \}. \quad (108)$$

We note that when τ is in D_1 the Airy function $\text{Ai}[(-iK\omega)^{1/3} \xi]$ is exponentially large and $\text{Ai}[(-iK\omega)^{1/3} e^{-2\pi i/3} \xi]$ is exponentially small. Therefore, in order that $f_1^{(w)}$ tend to zero as $|\tau| \rightarrow \infty$ in D_1 , we require that the coefficient $\text{Ai}[(-iK\omega)^{1/3} \xi]$ be zero. This determines the constant \overline{B}_1 , or B_1 ,

$$\overline{B}_1 = \int_{L_3} e^{-iK\omega\sigma^2} \text{Ai}[(-iK\omega)^{1/3} e^{-2\pi i/3} \xi] (\tilde{\xi}/\chi)^{1/4} g_2(\sigma) d\sigma / \\ \int_{L_3} e^{-iK\omega\sigma^2} \text{Ai}[(-iK\omega)^{1/3} e^{-2\pi i/3} \tilde{\xi}] (\tilde{\xi}/\chi)^{1/4} g_3(\sigma) d\sigma. \quad (109)$$

With \overline{B}_1 given by (109), $Z(\tau)$ becomes exponentially small when τ is in D_1 . We shall not attempt to evaluate \overline{B}_1 explicitly in this paper, however, in view of (91) and (92) we may conclude that

$$\overline{B}_1 = O[(K\omega)^3]. \quad (110)$$

Since L_4 is outside the circular arc $|\sigma| = R_1$, we may substitute the expansions given in (97), (98) and (99) into the integral along L_4 to obtain

$$f_1^{(w)} \sim Z(\tau) - \frac{\epsilon \overline{B}_1}{4\pi(K\omega)^2 \tau^{3/4}} \int_{L_4}^{\tau} e^{3\pi i/4} e^{-i\omega(t - K\tau^2 + K\sigma^2)} \\ \times \sigma^{9/4} \sinh \left[\frac{2}{3} e^{-\pi i/4} \sqrt{K\omega} (\xi^{3/2} - \tilde{\xi}^{3/2}) \right] d\sigma. \quad (111)$$

Now, if we apply the method of integration by parts to the integral along L_4 , we can show that for τ in D_1 , with $Z(\tau)$ being exponentially small,

$$f_1^{(w)} \sim \frac{\epsilon \overline{B}_1 i}{4\pi(K\omega)^2} e^{-i\omega\tau} \tau^{-1}. \quad (112)$$

Summing up all the results obtained in (105), (107) and (112), we

have

$$f_1 \sim \frac{\epsilon i}{4\pi(K\omega)^2} (B_1 e^{i\omega\tau} + \overline{B}_1 e^{-i\omega\tau}) \tau^{-1} \quad \text{as} \quad |\tau| \rightarrow \infty. \quad (113)$$

From (113) we may derive the following results: (i) From (110) we may conclude that $f_1 \propto \epsilon K\omega$. (ii) For τ lying on the real τ -axis, which corresponds to the cavity wall of the basic flow, f_1 is purely imaginary; this indicates that near the point at infinity the perturbation velocity $w_1 = \partial f_1 / \partial z$ is always perpendicular to the original cavity wall. (iii) If we recall that $\tau = O(z^{1/2})$ as $|z| \rightarrow \infty$, we can see that the perturbation velocity is of order $|z|^{-3/2}$ for large values of $|z|$; this, together with the result stated in (ii), implies that the unsteady free surface displacement tends to zero as $|z| \rightarrow \infty$. (iv) Along the imaginary τ -axis, which corresponds to the line of symmetry of the flow, f_1 is purely real; this means that there is no velocity component normal to the line of symmetry which, of course, is what we should expect.

It should be pointed out here that the order of magnitude and the direction of the perturbation velocity on the free surface near the point at infinity agree with the results obtained by Wang and Wu [1963] in the study of small-time behavior of unsteady cavity flows.

Finally, we shall investigate the behavior of the solution (87) near the separation point $\tau = 1$. From (4), (35) and (5), the perturbation velocity w_1 may be written as

$$w_1 = \frac{\partial f_1}{\partial z} = \frac{w_0}{2K\tau} \frac{\partial f_1}{\partial \tau}. \quad (114)$$

Equation (114) indicates that the singular behavior of w_1 near $\tau = 1$ can be studied from that of $\partial f / \partial \tau$ near $\tau = 1$. Let us now differentiate f_1 given by (87) with respect to τ . The differentiation of f_1 with respect to τ may be viewed as consisting of four parts; the differentiation of the τ appearing in the limits of integration, the differentiation of the factors $\exp(\pm iK\omega\tau^2)$, the differentiation of the Airy functions with respect to τ , and the differentiation of the factor in front of the curly brackets in (87). Only the latter two parts produce terms of the form $a_7(\tau^2 - 1)^{-1/2}$ near $\tau = 1$; all the other parts either give zero or a finite contribution to w_1 . Therefore, condition (34) and the condition that the pressure is integrable over the plate AB are satisfied.

Since the solution given by (87) behaves properly at infinity and at the separation point, we conclude that it is the solution of the problem; no additional solution of the homogeneous equation, as shown in (93) needs to be added.

ACKNOWLEDGMENTS

I wish to express my appreciation to Professor T. Y. Wu for useful discussions during this research. I am also indebted to my wife Yvonne for typing this manuscript.

REFERENCES

- Gilbarg, D., Jets and Cavities, Encyclopedia of Physics, IX, Berlin: Springer-Verlag, pp. 369-71, 1960.
- Jeffreys, H., Asymptotic Approximations, Cambridge University Press, pp. 52-9, 1962.
- Jeffreys, H. & Jeffreys, B. S., Methods of Mathematical Physics, 3rd Ed., Cambridge University Press, pp. 508-11, 1956.
- Langer, R. E., "The solution of the Mathieu equation with a complex variable and at least one parameter large," Am. Math. Soc., Trans. 36, pp. 637-95, 1934.
- Muskhelishvili, N. I., Singular Integral Equations, Groningen, Holland: P. Noordhoff Ltd., pp. 109-12, 1946.
- Olver, F. W. J., "The asymptotic solution of linear differential equations of the second order for large values of a parameter," Phil. Trans., Roy. Soc. London, 247A, pp. 307-68, 1954.
- Olver, F. W. J., "Uniform asymptotic expansions of solutions of linear second-order differential equations for large values of a parameter," Phil. Trans., Roy. Soc. London, 250A, pp. 479-517, 1958.
- Wang, D. P. & Wu, T. Y., "Small-time behavior of unsteady cavity flows," Arch. Rat. Mech. & Anal., 14, pp. 127-52, 1963.
- Wang, D. P. & Wu, T. Y., "General formulation of a perturbation theory for unsteady cavity flows," J. Basic Eng., ASME, Trans. D, 87, pp. 1006-10, 1965.

HYDRODYNAMICS IN THE OCEAN ENVIRONMENT

Tuesday, August 25, 1970

Morning Session

Chairman: J. K. Lunde
Skipsmodelltanken, Trondheim, Norway

	Page
Deep-Sea Tides W. H. Munk University of California, San Diego	217
Stability of and Waves in Stratified Flows C. Yih, University of Michigan	219
On the Prediction of Impulsively Generated Waves Propagating into Shallow Water P. van Mater, Jr., U.S. Naval Academy and E. Neal, Naval Ship Research and Development Center	239

DEEP-SEA TIDES

Walter H. Munk
University of California
San Diego, California

ABSTRACT

The classical Laplace tidal theory, when applied in numerical form to the world's ocean basins, does not yield results in good accord with observations. In part, this may be due to density stratification and internal tides (coupled to external tides); and in part to dissipation at the ocean boundaries. At a given port the spectrum of the observed tides shows a complicated line structure superimposed over a continuum. The continuum rises at the frequencies where the lines are clustered, probably as a result of internal tides.

Tide dissipation leads to an exchange of angular momentum between the spin of the earth and the orbit of the moon. As a result of this spin-orbital coupling, the length of day and month are both increasing. Observations of the moon since 1680, of Babylonian eclipses and of the structure of Devonian tropical coral (which give the number of Devonian days per year) confirm these calculations.

To untangle these problems, it is probably necessary to make observations in the deep sea, relatively removed from the scattering and absorbing boundaries. Such observations have now been made for the last three years, and they yield relatively clear pictures of the deep-sea tidal pattern. The tides in the northeast Pacific can be roughly accounted for by superposition of a northward-traveling Kelvin wave (trapped by rotation to the boundary) and a southward-traveling non-trapped Poincaré wave.

In order for the calculations to be realistic, they need take into account the tidal yielding of the sea floor.

STABILITY OF AND WAVES IN STRATIFIED FLOWS

Chia-Shun Yih
University of Michigan
Ann Arbor, Michigan

ABSTRACT

A theorem giving sufficient conditions for stability of stratified flows, which is a natural generalization of Rayleigh's theorem for shear flows of a homogeneous fluid, is given. Sufficient conditions for the existence of singular neutral modes, and consequently of unstable modes, are also presented, and in the development the possibility of multi-valued wave number for neutral stability of the same flow is explained. Finally, neutral waves with a wave velocity outside of the range of the velocity of flow (non-singular modes) are studied, and results concerning the possibility of these waves are given. In addition, Miles' theorem [1961] on the stability of stratified flows for which the Richardson number is nowhere less than $1/4$, and Howard's semi-circle theorem [1961] are extended to fluids with density discontinuities.

I. INTRODUCTION

The stability of stratified flows of an inviscid fluid has been studied in a general way, i.e., without specifying the actual density and velocity distributions, by Synge [1933], Yih [1957], Drazin [1958], Miles [1961, 1963], Howard [1961], and others. Of these, Miles has made particularly substantial contributions to the subject. However, many questions still remain open. Among these are the following:

- (i) Miles [1961] showed that if the Richardson number is nowhere less than $1/4$, the flow must be stable. This is a sufficient condition for stability. What can one say regarding the stability of the flow when the Richardson number is less than $1/4$ in part or all of the fluid? Are there then some sufficient conditions for stability not

covered by Miles' criterion? What, in fact, is the natural generalization of Rayleigh's theorem on the sufficient condition for stability of a homogeneous fluid in shear flow?

- (ii) Are there some sufficient conditions for instability?
- (iii) Miles [1963] has shown that the wave number at neutral stability can be multi-valued for the same flow, in an actual calculation for a special density distribution and a special velocity distribution. Is there an explanation for this, even if not completely general?
- (iv) Do internal waves with a wave velocity outside the range of the velocity of flow exist? How many modes are there? What is the character of each mode?

In this paper the questions posed above will be answered in as general a way as possible. By "general" I mean "without numerical computation." Although special calculations for special flows, involving the use of computers, are important because they often give us insight into and understanding of the subject, and sometimes are of practical interest, results obtained in a general way are often more useful. The question naturally arises: Can general results be continually improved and sharpened, albeit with increasing cost in labor, but without the use of computers? The answer to this question necessarily reveals the attitude of the respondent more than anything else. My answer to it is in the affirmative, and the results contained in this paper, aside from whatever interest or merit they may have for those cultivating the subject, are given to substantiate my faith.

In addition, some straightforward extensions of Miles' theorem mentioned in (i) above, and of Howard's semi-circle theorem [1961], are made to make these theorems applicable to fluids with discontinuities in addition to continuous stratification in density.

II. DIFFERENTIAL SYSTEM GOVERNING STABILITY

If U and $\bar{\rho}$ denote the velocity (in the x -direction) and the density, respectively, of the primary flow in the absence of disturbances, and u and v denote the components of the perturbation in velocity in the directions of increasing x and y , the linearized equations of motion are

$$\bar{\rho}(u_t + Uu_x + U'v) = -p_x, \quad (1)$$

$$\bar{\rho}(v_t + Uv_x) = -p_y - g\rho, \quad (2)$$

in which subscripts indicate partial differentiation, t denotes time,

p is the deviation of the pressure from the hydrostatic pressure in the primary flow, ρ is the density perturbation, g is the gravitational acceleration, and

$$U' = \frac{dU}{dy}.$$

The equation of continuity

$$u_x + v_y = 0$$

permits the use of a stream function ψ , in terms of which the velocity components can be expressed:

$$u = \psi_y, \quad v = -\psi_x. \quad (3)$$

The linearized form of the equation of incompressibility is

$$\rho_t + U\rho_x + v\bar{\rho}' = 0, \quad (4)$$

in which

$$\bar{\rho}' = \frac{d\bar{\rho}}{dy}.$$

If η is the vertical displacement of a line of constant density from its mean position, the kinematic relationship

$$\eta_t + U\eta_x = v = -\psi_x \quad (5)$$

holds. All perturbation quantities will be assumed to be periodic in x and have the exponential factor $\exp ik(x - ct)$, so that from (5) and (3) we have

$$\psi = -(U - c)\eta, \quad u = -[(U - c)\eta]', \quad v = ik(U - c)\eta. \quad (6)$$

Then (1) and (4) give

$$p = \bar{\rho}(U - c)^2\eta' \quad \text{and} \quad \rho = -\bar{\rho}'\eta. \quad (7)$$

Writing

$$\eta(x, y, t) = F(y)e^{ik(x - ct)} \quad (8)$$

and substituting (6) and (7) into (2), we have, with β denoting $-\bar{\rho}'/\bar{\rho}$,

$$[\bar{\rho}(U - c)^2 F']' + \bar{\rho}[\beta g - k^2(U - c)^2] F = 0, \quad (9)$$

which is the equation used by Miles [1961] and Howard [1961] to study the stability of stratified flows.

Miles [1961] assumed U to be monotonic and U and $\bar{\rho}$ to be analytic in his studies. Howard [1961] was able to prove Miles' theorem (on a sufficient condition for stability) and to obtain his own semi-circle theorem without these hypotheses. But both of them assumed $\bar{\rho}$ to be continuous, and considered the upper boundary to be fixed as well as the lower one. We shall now show that the theorems of Miles and Howard can be generalized to allow density discontinuities. The mean velocity U (though not necessarily U') will be assumed continuous.

Let there be n surfaces of density discontinuity, and let the free surface, if there is one, be the first of such surfaces. The densities above and below the i -th surface of density discontinuity will be denoted by $(\bar{\rho}_u)_i$ and $(\bar{\rho}_l)_i$, respectively, and we shall define $(\Delta\bar{\rho})_i$ by

$$(\Delta\bar{\rho})_i = (\bar{\rho}_l - \bar{\rho}_u)_i. \quad (10)$$

The interfacial condition can be obtained by integrating (9) in the Stieltjes sense in an arbitrarily small interval containing the discontinuity under consideration, and is, with the accent indicating differentiation with respect to y ,

$$[\bar{\rho}(U - c)^2 F']_u - [\bar{\rho}(U - c)^2 F']_l = -g\Delta\bar{\rho}F, \quad (11)$$

to be applied at any surface of discontinuity. At a free surface $\bar{\rho}_u$ vanishes, and (11) becomes

$$(U - c)^2 F' = gF, \quad (12)$$

which is the free-surface condition, to be applied at $y = d$, d being the depth. If the upper surface is fixed instead of free, the condition there is

$$F(d) = 0. \quad (12a)$$

The boundary condition at the bottom, where $y = 0$, is

$$F(0) = 0. \quad (13)$$

III. EXTENSION OF MILES' THEOREM

Following Howard [1961], we set

$$G = W^{1/2} F,$$

where $W = U - c$. Then (9) can be written as

$$(\bar{\rho} W G')' - [(\bar{\rho} U')'/2 + k^2 \bar{\rho} W + \bar{\rho} W^{-1} (U'^2/4 - g\beta)] G = 0. \quad (14)$$

The boundary condition at the bottom is

$$G(0) = 0. \quad (15)$$

The interfacial conditions (11) become

$$\bar{\rho}_\ell (W G' - U' G/2)_\ell - \bar{\rho}_u (W G' - U' G/2)_u = g \Delta \bar{\rho} W^{-1} G, \quad (16)$$

to be applied at the surfaces of density discontinuity, and in particular the upper-surface condition becomes

$$W G' - U' G/2 = g W^{-1} G, \quad \text{or} \quad G(d) = 0, \quad (17)$$

depending on whether the upper surface is free or fixed.

Multiplying (14) by G^* , where the asterisk indicates the complex conjugate, and integrating from the bottom to the first surface of density discontinuity and then from discontinuity to discontinuity throughout the fluid domain, and utilizing (15), (16), and (17), we have

$$\begin{aligned} & \int \bar{\rho} W [|G'|^2 + k^2 |G|^2] + \int (\bar{\rho} U')' |G|^2/2 + \int \bar{\rho} [U'^2/4 - g\beta] W^* |G/W|^2 \\ & - \sum_i g \Delta_i \bar{\rho} W^* |G/W|^2 - \sum_i [(\bar{\rho} U')_\ell - (\bar{\rho} U')_u] |G|^2/2 = 0, \end{aligned} \quad (18)$$

in which each of the integrals is over the entire fluid domain exclusive of the surfaces of density discontinuity (i.e., it is a summation of integrals over the layers of continuous density distributions), and the summation is over the discontinuities, including the free surface if there is one. If the flow is unstable, $c_i > 0$, and the imaginary part of (18) is

$$\int \bar{\rho} [|G'|^2 + k^2 |G|^2] + \int \bar{\rho} [g\beta - U'^2/4] |G/W|^2 + \sum_i g \Delta_i \bar{\rho} |G/W|^2 = 0, \quad (19)$$

from which it is again evident that if

$$g\beta \geq U'^2/4$$

everywhere in the fluid exclusive of the interfaces and the free surface (if there is one), the flow must be stable.

IV. EXTENSION OF HOWARD'S SEMI-CIRCLE THEOREM

Equation (9) can be written as

$$(\bar{\rho} W^2 F')' + \bar{\rho}(\beta g - k^2 W^2) F = 0.$$

Multiplying this equation by F^* , the complex conjugate of F , integrating throughout the fluid domain and using the boundary or interfacial conditions (11), (12), and (13), we have

$$\int \bar{\rho} W^2 [|F'|^2 + k^2 |F|^2] - \int \bar{\rho} g \beta |F|^2 - \sum_i g \Delta_i \bar{\rho} |F|^2 = 0, \quad (20)$$

in which the summation is over the surfaces of density discontinuity, and the integrals extend throughout the fluid exclusive of the surface of discontinuity in density. The real and imaginary parts of (20) are

$$\int \bar{\rho} [(U - c_r)^2 - c_i^2] [|F'|^2 + k^2 |F|^2] - \int \bar{\rho} g \beta |F|^2 - \sum_i g \Delta_i \bar{\rho} |F|^2 = 0, \quad (21)$$

$$2c_i \int \bar{\rho} (U - c_r) [|F'|^2 + k^2 |F|^2] = 0. \quad (22)$$

Writing

$$Q = \bar{\rho} [|F'|^2 + k^2 |F|^2],$$

we obtain from (22)

$$\int U Q = c_r \int Q, \quad (23)$$

then from this and from (21) we obtain

$$\int U^2 Q = (c_r^2 + c_i^2) \int Q + \int g \rho \beta |F|^2 + \sum_i g \Delta_i \bar{\rho} |F|^2. \quad (24)$$

If a and b are respectively the minimum and the maximum of U ,

so that $a \leq U \leq b$, we have

$$\begin{aligned} 0 &\geq \int (U - a)(U - b)Q = \int U^2 Q - (a + b) \int UQ + ab \int Q \\ &= [c_r^2 + c_i^2 - (a + b)c_r + ab] \int Q + \int g\bar{\rho}B|F|^2 + \sum_i g\Delta_i \bar{\rho}|F|^2, \end{aligned}$$

after using (23). This means that

$$[c_r - (a + b)/2]^2 + c_i^2 \leq [(b - a)/2]^2, \quad (25)$$

that is, the complex wave velocity c for any unstable mode must lie inside the semi-circle in the upper half-plane, which has the range of U for diameter. Thus Howard's semi-circle theorem is recovered.

From (19) and noting that $|W|^2 \leq c_i^{-2}$, we deduce that

$$k^2 c_i^2 \leq \max(U^2/4 - g\beta) \quad (26)$$

remains valid even if there are surfaces of discontinuity in density. In (26) we exclude these surfaces in the evaluation of β . It is easy to see that (26) contains Miles' theorem.

V. SUFFICIENT CONDITIONS FOR STABILITY

Miles' theorem gives a sufficient condition for stability. But it certainly does not guarantee instability if the local Richardson number $J(y)$ defined by

$$J(y) = \frac{g\beta}{U^2} \quad (27)$$

is less than $1/4$ in part of the fluid or even all of the fluid. We shall sharpen Miles' sufficient condition for stability by deriving two theorems which constitute, more than anything hitherto known, the natural generalization of Rayleigh's theorem for the stability of a homogeneous inviscid fluid.

For the discussion in this section it is more convenient to use the stream function

$$\psi = f(y)e^{ik(x-ct)}. \quad (28)$$

Comparison with (6) and (8) shows that

$$f(y) = (c - U)F(y). \quad (29)$$

In terms of $f(y)$, the governing equation (9) becomes

$$(\bar{\rho}f')' + \left[\frac{(\bar{\rho}U')'}{c - U} - k^2\bar{\rho} - \frac{g\bar{\rho}'}{(c - U)^2} \right] f = 0. \quad (30)$$

Equation (30) can be made dimensionless by the use of the new variables

$$\hat{f} = \frac{f}{V}, \quad \hat{\rho} = \frac{\bar{\rho}}{\rho_0}, \quad \hat{y} = \frac{y}{d}, \quad \hat{U} = \frac{U}{V}, \quad \hat{c} = \frac{c}{V}, \quad (31)$$

where ρ_0 is a reference density and V a reference velocity. Then (30) becomes, after the circumflexes are dropped,

$$(\bar{\rho}f')' + \left[\frac{(\bar{\rho}U')'}{c - U} - \alpha^2\bar{\rho} - \frac{N\bar{\rho}'}{(c - U)^2} \right] f = 0, \quad (32)$$

in which everything is now dimensionless, the accents indicate differentiation with respect to the dimensionless y ,

$$\alpha = kd \quad (33)$$

is the dimensionless wave number, and

$$N = gd/V^2 \quad (34)$$

is actually the reciprocal of the square of a Froude number. The appearance of N does not necessarily signify the importance of surface waves, since it appears even if the upper boundary is fixed. The fact that it is associated by multiplication to $\bar{\rho}'$ indicates that the entire term represents the effect of gravity in a stratified fluid in shear flow.

Henceforth in this paper we shall consider rigid boundaries only, for which the boundary conditions are

$$f(0) = 0 \quad \text{and} \quad f(1) = 0, \quad (35a,b)$$

to be imposed on the function f in (32).

It is then clear that the system consisting of (32) and (35a,b) gives, for a non-trivial solution, a relationship

$$F_1(\alpha, N, c) = 0. \quad (36)$$

Since c is complex, (36) has a real part and an imaginary part. When c_i is set to zero and c_r eliminated from the two component equations, a relationship

$$F_2(\alpha, N) = 0, \quad (37)$$

if one such exists, gives the neutral-stability curve. It is possible, however, that c is real for all values of α and N , in which case $c_i = 0$ in the entire $N - \alpha$ plane, and then of course there is no neutral-stability curve because one component equation of (36) is $c_i = 0$, and the other is simply (36) itself, with the c therein real.

In this section, we shall assume $\bar{\rho}$ and U to be continuous, analytic, and monotonic. Furthermore, we assume $\bar{\rho}' < 0$ throughout. We now recall the following known results:

- (i) If $J(y)$ is not less than $1/4$ for the entire fluid domain, then the flow is stable [Miles 1961],
- (ii) If $c_i \neq 0$ then c_r must be equal to U at some point in the flow, as a consequence of the semi-circle theorem of Howard [1961], and
- (iii) If an eigenfunction exists for (c_0, α_0, N_0) , then near that point c is a continuous function of α and N , [Miles 1963 and Lin 1945].

Under the assumptions we have made on $\bar{\rho}$ and U , and in view of the known results just cited, we conclude that the non-existence of any singular neutral mode, which is a mode with a real c equal to U at some point in the flow, implies the non-existence of unstable modes. The reason is as follows. In the $N - \alpha$ plane there is always a region of stability. For we can imagine g and hence $J(y)$ to increase indefinitely, until $J(y)$ is everywhere greater than $1/4$, which is attainable since β is nowhere zero. Thus there is a region of large N for which the flow is stable. If unstable modes exist there must then be a stability boundary dividing the region of stability from the region of instability, and hence a neutral-stability curve. As we approach that curve from the region of instability, c_r being within the range of U so long as $c_i \neq 0$ and continuous in α and N so long as c is an eigenvalue, according to (iii) above, in the limit, when $c_i = 0$, c_r must be within the range of U , i.e., the limiting mode must be a singular neutral mode. Hence the non-existence of a singular neutral mode implies the non-existence of unstable modes.

In fact even the existence of special singular neutral modes for which c equals the maximum or minimum of U does not imply the existence of contiguous unstable modes, as a consequence of the semi-circle theorem of Howard. Hence we need not be concerned with these special border cases. In demonstrating the non-existence of unstable modes it is sufficient to demonstrate the non-existence of singular neutral modes with $a < c < b$, where a is the minimum and b the maximum of U .

Miles [1961, p. 507] has shown that singular neutral modes are impossible for monotonic U if $J(y) > 1/4$ everywhere. In his demonstration he actually showed that a singular neutral mode with a $J(y_c) > 1/4$ at the place $y = y_c$ where $U = c$ is impossible. Hence we need only consider the case $J(y_c) \leq 1/4$ in our search for the non-existence of singular neutral modes. For $J(y_c) = 1/4$, one solution of (32) is

$$f_1 = (y - y_c)^{1/2} w_1 \quad (38)$$

where

$$w_1 = 1 + A(y - y_c) + \dots \quad (39)$$

with

$$A = \left[(1 + J) \frac{(\bar{\rho} U')'}{\bar{\rho} U'} - \frac{J \bar{\rho}''}{\bar{\rho}'} + \gamma (\ln \bar{\rho})' \right]_c, \quad (\gamma = \frac{1}{2}) \quad (40)$$

provided U' does not vanish at $y = y_c$. [We shall consider monotonic U only. Hence this restriction on U' does not affect our results in this paper.] The other solution is found by assuming it to be of the form $f_1 h$, substituting it into (32), and solving for h . The result, after division by a constant (which is $\bar{\rho}_c$ or ρ at y_c), is

$$f_2 = f_1 \ln (y - y_c) - [2A + (\ln \bar{\rho})'_c] (y - y_c)^{3/2} [1 + B(y - y_c) + \dots], \quad (41)$$

where B is a constant. Now the Reynolds stress defined by

$$\tau = - \bar{\rho} \overline{uv}, \quad (42)$$

where the bar over uv means time or space average, can be expressed in terms of f as

$$\tau = \frac{\rho_0 V^2}{2} \alpha (f' f^*)_i e^{2\alpha c_i t}, \quad (43)$$

in which the asterisk denotes the complex conjugate, and the t , now in terms of d/V , is dimensionless, as is f . Considering the singular neutral case, for which $c_i = 0$, it is easy to see from (40) and (41) that $f'f^*$ is real for $y > y_c$ and equal to $-\pi$ for $y < y_c$. Hence $(f'f^*)_i$ suffers a jump at y_c . Since $f'f^*$ is zero at both rigid boundaries, it cannot afford this jump. [If $\alpha \neq 0$, this jump corresponds to a jump in the Reynolds stress. But we do not have to consider the jump in τ , and can consider merely the jump in $(f'f^*)_i$.] Consequently a singular neutral mode with $J(y_c)$ equal to $1/4$ is impossible. And we can henceforth concentrate on the case $J(y_c) < 1/4$.

For $J(y_c) < 1/4$ Miles [1961] gave the solutions of (32):

$$f_{\pm}(y) = (y - y_c)^{(1 \pm \nu)/2} w_{\pm} \quad (44)$$

in which

$$w_{\pm} = 1 + A(y - y_c)/(1 \pm \nu) + \dots, \quad (45)$$

with A given by (40) [but with $\gamma = (1 \pm \nu)/2$ therein] and

$$\nu = (1 - 4J_c) \quad , \quad J_c = J(y_c). \quad (46)$$

We can use (44) and (45) with all terms therein considered dimensionless. Miles [1961, pp. 506-507] showed that for $J_c < 1/4$ the solution, if one exists, must be either f_+ or f_- . We can demonstrate our point by considering f_+ as the solution. The demonstration for the other case is strictly similar.

The study of the eigenvalue problem defined by (32) and (35a,b) naturally leads to a study of the zeros of f . Since f is given by (44), it leads to the study of the zeros of w_+ . This in turn leads us to consider the differential equation for w (from which the subscripts are removed for convenience). Denoting w_+ or w_- by w , we can easily obtain that equation:

$$(\bar{\rho} z^2 \gamma w')' + z^2 \gamma \left[-J_c \bar{\rho} z^{-2} + \bar{\gamma} \bar{\rho}' z^{-1} + \frac{(\bar{\rho} U')'}{c - U} - \alpha^2 \bar{\rho} - \frac{N \bar{\rho}'}{(c - U)^2} \right] w = 0, \quad (47)$$

with $z = y - y_c$, and $\gamma = (1 \pm \nu)/2$.

We are now in a position to present

Theorem 1. If $\bar{\rho}$ and U are continuous and analytic, with $\bar{\rho}' < 0$ and $U' > 0$, and if $(\bar{\rho} U')'$ and $(\ln \bar{\rho})''$ are positive throughout, then singular neutral modes are impossible.

Proof. We have shown that it is necessary only to consider the case $J(y_c) < 1/4$. We may consider f_+ only, since the proof for f_- is the same, and since the solution is either f_+ or f_- . Now at $y = y_c$ we have $f_+ = 0$. Near y_c we have

$$Q \equiv -\frac{N\bar{\rho}'}{(U-c)^2} - \frac{J_c \bar{\rho}}{z^2} = \frac{\bar{\rho}_c J_c}{z^2} \left[\left\{ \bar{\rho} (\ln \bar{\rho})'' / \bar{\rho}' - \frac{U''}{U'} \right\} z + \dots \right]. \quad (48)$$

Since $\bar{\rho}'$ is negative and U' and $(\bar{\rho}U')'$ are positive, U'' is positive. Thus $U-c$ is greater than $U'_c z$ for $z > 0$. On the other hand $-\bar{\rho}'/\bar{\rho}$ is less than $(-\bar{\rho}'/\bar{\rho})_c$ for $y > y_c$, since $(\ln \bar{\rho})''$ is positive. We know that for small positive z Q is negative, as can be seen from (48). Hence for any $z > 0$ the term

$$-\frac{N\bar{\rho}'}{(U-c)^2}$$

is less than $\bar{\rho}J_c/z^2$ and Q is negative. Equation (48) exhibits the behavior of Q near y_c . Let the bracket in (47) be denoted by $-G$. Then since Q is negative and $U-c$ is positive for $y > y_c$, and since $\bar{\rho}'$ is negative and $(\bar{\rho}U')'$ positive, G must be positive for $y > y_c$. Multiplying (47) by w and integrating between y_c and 1, we have

$$(\rho z^2 \gamma_{ww'})_1 - \int_{y_c}^1 z^2 \gamma (\bar{\rho} w'^2 + G w^2) dy = 0, \quad (49)$$

where the subscript 1 indicates that the parenthesis is evaluated at $y = 1$. Note that the integral in (49) is convergent in spite of the simple pole in two terms contained in G -- one of which in Q , as indicated by (48). Equation (49) clearly shows that $w(1)$ cannot be zero. Hence the theorem.

Another theorem is

Theorem 2. If $\bar{\rho}$ and U are continuous and analytic, with $\bar{\rho}'$ negative and U' positive, and if U'' and $(\ln \bar{\rho})''$ are negative throughout, then singular neutral modes are impossible.

The proof for this theorem is similar to that for Theorem 1. The only modification demanded for clarity is that instead of (44) we should write

$$f_{\pm}(y) = z^{(1 \pm \nu)/2} w_{\pm}(z)$$

with z now defined as $y_c - y$. The equation corresponding to (47) is now

$$\frac{d}{dz} \left[\bar{\rho} z^2 \gamma \frac{d}{dz} w \right] + z^2 \gamma \left[-J_c \bar{\rho} z^{-2} + \gamma \bar{\rho}' z^{-1} + \frac{(\bar{\rho} U')'}{c - U} - \alpha^2 \bar{\rho} - \frac{N \bar{\rho}'}{(c - U)^2} \right] w = 0, \quad (50)$$

in which, it must be emphasized, all accents indicate differentiation with respect to y , not z . The rest is strictly similar to the proof for Theorem 1, except the range of integration is between $z = 0$ and $z = y_c$ (or between $y = y_c$ and $y = 0$), and we want to show $w \neq 0$ at $y = 0$. Note also that $U'' < 0$ now guarantees $(\bar{\rho} U')' < 0$.

Since the non-existence of singular neutral modes implies the non-existence of unstable modes, we have also

Theorem 3. If $\bar{\rho}$ and U are continuous and analytic, with $\bar{\rho}'$ negative and U' positive, and if either $(\bar{\rho} U')'$ and $(\ln \bar{\rho})''$ are both positive throughout, or U'' and $(\ln \bar{\rho})''$ are negative throughout, the flow is stable.

This theorem is the natural generalization of Rayleigh's theorem for inviscid homogeneous fluids in shear flow. Previous attempts at this generalization [Synge 1933, Yih 1957, Drazin 1958] have produced the result that there must be stability if (in dimensional terms)

$$\frac{2\beta g(U - c_r)}{|U - c|^2} - \frac{(\bar{\rho} U')'}{\bar{\rho}}$$

does not change sign. This criterion is not useful because it involves not only c_r but also c_i .

VI. SUFFICIENT CONDITIONS FOR INSTABILITY

Sufficient conditions for instability have seldom been given in studies of hydrodynamic stability. In giving some such conditions, we shall also be able to explain why the α can be multi-valued for the same N , at neutral stability.

We assume that $\bar{\rho}$ and U are analytic, that $\bar{\rho}' \leq 0$, and that at a point where $\bar{\rho}' = 0$, U'' is also zero. The value of U at that point will be denoted by U_c , for we shall consider the possibility of having c equal to U at that point. We demand that at any other point where $U = U_c$, $\bar{\rho}' = 0 = U''$ must be satisfied. If U is monotonic, of course there is only one point at which $U = U_c$.

Under the assumptions made, $\bar{\rho}''$ must be zero at y_c , since $\bar{\rho}'$ is never positive, and near y_c

$$\bar{\rho}' = \bar{\rho}_c''(y - y_c).$$

If $\bar{\rho}_c''$ were not zero $\bar{\rho}'$ would be positive for y slightly larger than y_c . With this realization, it is immediately clear that the bracket in (32) has no singularity at y_c . Let us denote the bracket in (32) by the symbol B , which is a function of y , α , and N . Then if m is the minimum of $B/\bar{\rho}$ between two points y_1 and y_2 , with $0 \leq y_1 < y_2 \leq 1$, for $\alpha = 0$, and if

$$m \geq \frac{(n\pi)^2}{(y_2 - y_1)^2}, \quad n = \text{a positive integer}, \quad (51)$$

by the use of Sturm's first comparison theorem we know that there must be at least n zeros of f between y_1 and y_2 , whatever the value of $f(0)$ and $f'(0)$. (Note that the $\bar{\rho}$ in m or in (32) is dimensionless.) We can always choose $f(0) = 0$. If (51) is satisfied then there must be at least n internal zeros of f . We can increase α so that, again by Sturm's first comparison theorem

$$f(1) = 0$$

for

$$\alpha = \alpha_1, \alpha_2, \alpha_3, \dots, \alpha_n,$$

where

$$\alpha_1 < \alpha_2 < \alpha_3 < \dots < \alpha_n.$$

It is evident that for $\alpha = \alpha_i$ there are at least $n - i$ internal zeros.

Hence we have

Theorem 4. Under the assumptions stated in the second paragraph of this section, if (51) is satisfied there are at least n modes with $c = U_c$ and $\alpha = \alpha_i$ ($i = 1, 2, \dots, n$), and with α_i increasing with i . For the i -th mode there are at least $n - i$ internal zeros.

It is easy to show, by exactly the same approach used by Lin [1955, pp. 122-123], which we shall not repeat here, that by varying α^2 slightly (now not necessarily by decreasing it, as is in Lin's case), c will become complex. Hence we have

Theorem 5. Near the neutral modes stated in Theorem 4, there are contiguous unstable modes.

Theorem 4 explains why for the same N , given $\bar{\rho}$ and U , there can be many values for α on the neutral-stability curve (or curves), which has been observed by Miles [1963] for a special $\bar{\rho}$ and a special U .

We can sharpen Theorems 4 and 5 by defining M to be the maximum of $B/\bar{\rho}$ in (y_1, y_2) for $\alpha = 0$. Then if (51) holds and

$$M \leq \frac{(n+1)^2 \pi^2}{(y_2 - y_1)^2}, \quad (52)$$

the words "at least" in Theorem 4 can be replaced by the word "exactly."

We note that the analyticity of $\bar{\rho}$ and U is needed only near y_c , and that, as a consequence of Theorem 5, a layer of homogeneous fluid containing a point of zero U'' and adjoining a stratified layer with uniformly large $J(y)$ is always unstable.

VII. NON-SINGULAR MODES

It remains to study neutral waves with a (real) c outside of the range of U , whose minimum and maximum will continue to be denoted by a and b . We assume $\bar{\rho}$ and U to be continuous, and that their derivatives as appear in (32) exist. Then if m and M retain their definitions as given by (51) and (52), except that $c = a - \epsilon$, we have

Theorem 6. Under the assumptions on $\bar{\rho}$ and U stated above, if (51) holds there are at least n modes with $c = a - \epsilon$, $\alpha = \alpha_i$ ($i = 1, 2, \dots, n$), and α_i increasing with i . For the i -th mode there are at least $n - i$ internal zeros. If (52) holds in addition, then there are exactly n such modes, the i -th of which has exactly $n - i$ internal zeros. If $(\bar{\rho}U)'$ is negative, then n can only increase as the arbitrary positive constant ϵ decreases.

The proof of this theorem is by a straightforward application of the first comparison theorem of Sturm. Similarly, if m and M are defined by (51) and (52), except that $c = b + \epsilon$, where ϵ is an arbitrary positive constant, we have

Theorem 7. Under the assumptions on $\bar{\rho}$ and U stated above, if (51) holds there are at least n modes with $c = b + \epsilon$, $\alpha = \alpha_i$ ($i = 1, 2, \dots, n$), and α_i increasing with i . For the i -th mode there are at least $n - i$ internal zeros. If (52) holds in addition, then there are exactly n such modes, the i -th of which has exactly $n - i$ internal zeros. If $(\bar{\rho}U)'$ is negative, then n can only increase as ϵ decreases.

If for $c = a - \epsilon$ or $c = b + \epsilon$, and any $\epsilon \geq 0$, M is less than $\pi^2/(y_2 - y_1)^2$ for all y_1 and y_2 between zero and 1, then there can be no waves propagating with c equal to a or b , or outside of the range of U . On the other hand, if $U' = 0$ at the point of maximum or minimum U , and, a fortiori, if there is a region of constant U where $U = a$ or b , it can be easily shown that waves of any finite wave length and any finite number of internal zeros n can propagate with $c < a$ or $c > b$. All this is in contrast with waves propagating in a layer of homogeneous fluid with a free surface and in shear flow. In that case [Yih 1970], if U is monotonically increasing with y , waves of all wave lengths can propagate with c greater than b , and only sufficiently long waves can propagate with c less than b .

ACKNOWLEDGMENT

This work has been supported by the National Science Foundation.

REFERENCES

- Drazin, P. G., "On the Dynamics of a Fluid of Variable Density," Ph.D. Thesis, Cambridge University, 1958.
- Howard, L. N., "Note on a Paper of John W. Miles," J. Fluid Mech., Vol. 10, pp. 509-512, 1961.
- Lin, C. C., "On the Stability of Two-dimensional Parallel Flows, Part II," Quart. Appl. Math., pp. 218-234, 1945.
- Lin, C. C., The Theory of Hydrodynamic Stability, Cambridge University Press, 1955.
- Miles, J. W., "On the Stability of Heterogeneous Shear Flows," J. Fluid Mech., Vol. 10, pp. 496-508, 1961.
- Miles, J. W., "On the Stability of Heterogeneous Shear Flows, Part 2," J. Fluid Mech., Vol. 16, pp. 209-227, 1963.
- Synge, J. I., "The Stability of Heterogeneous Liquids," Trans. Roy. Soc. Can., Vol. 27, pp. 1-18, 1933.
- Yih, C.-S., "On Stratified Flows in a Gravitational Field," Tellus, Vol. 9, pp. 220-227, 1957.
- Yih, C.-S., "Surface Waves in Flowing Water," to be published in J. Fluid Mech. in 1971.

DISCUSSION

L. van Wijngaarden
Twente Institute of Technology
Enschede, The Netherlands

The flow with a free surface of a fluid, homogeneous in density, but with inhomogeneous velocity distribution, is a special case of your class of stratified fluids. Burns [1953] considered this case and I guess his results are comprised in yours. When viscosity is allowed for, the problem becomes much more complicated. It may be of interest to note that Velthuisen and I [1969a, 1969b] studied this problem taking viscosity into account. We obtained results essentially different from Burn's results, which is due to viscous effects.

At large Reynolds number the flow can be divided in an inviscid region and viscous regions at the critical layer and at the bottom. At the outer edge of the viscous layer at the wall the Reynolds stress cannot be put equal to zero a priori because a stress may build up in the wall layer.

REFERENCES

- Burns, J. C., "Long Waves in Running Waters," *Proc. Camb. Phil. Soc.* 49, 695, 1953.
- Velthuisen, H.G.M. and L. v. Wijngaarden, *J. Fluid Mech.* 39, 4, 817, 1969a.
- Velthuisen, H.G.M. and L. v. Wijngaarden, *IUTAM Symposium on Instability of Continuous Systems*, Herrenalb, Sept. 1969.

* * * * *

REPLY TO DISCUSSION

Chia-Shun Yih
University of Michigan
Ann Arbor, Michigan

It is well known that Rayleigh's sufficient condition for stability of inviscid fluids flowing between rigid boundaries is satisfied by a parabolic velocity profile, whereas plane Poiseuille flow, which has this profile, has been found by Heisenberg and Lin to be unstable at sufficiently large Reynolds numbers, when viscous effects are taken into account. Since the present paper is a study of the stability of inviscid fluids, and, in particular, Rayleigh's criterion for stability is generalized in it, Professor van Wijngaarden's position that the consideration of viscosity may force us to modify some of the conclusions in the paper is easily acceptable.

In considering viscous effects, however, it is not entirely self-consistent to assume a horizontal mean flow with a free surface, as Velthuisen and Professor van Wijngaarden have done [1969a,b], since such a flow obviously cannot be maintained, and must in time attenuate to a state of rest. This is not to say that any conclusion of instability reached by them is without significance, for instability of a transient nature may well occur, with the disturbances growing for a short duration of time. In this regard the results of Benjamin [1957] and Yih [1963] for surface waves in a fluid layer flowing down an inclined plane are relevant. They found that the speed c_r of long surface waves, be they unstable, neutral, or stable, exceeds the maximum speed of flow. The absence of long waves propagating upstream supports Professor van Wijngaarden's claim in connection with Burn's result, which is supported by a study [Yih 1971] of waves in a flowing inviscid liquid. But the nonexistence of a critical layer renders rather less cogent the argument given in Professor van Wijngaarden's discussion. On the other hand, this nonexistence substantiates the conclusion made in Yih [1971] (and similarly in this paper) regarding the nonexistence of singular neutral modes, since the velocity U in laminar flow of a viscous fluid down an inclined plane is parabolic, with a constant U'' .

We also recall that Tollmien's sufficient condition for instability [1935] of an inviscid fluid is not much affected by the consideration of viscosity, at least when the Reynolds number is large, and hope that the same is true with the sufficient conditions for instability presented in this paper.

REFERENCES

- Benjamin, T. B., "Wave formation in laminar flow down an inclined plane," *J. Fluid Mech.*, 2, pp. 554-574, 1957.
- Tollmien, W., "Ein allgemeines kriterium der instabilität laminarer geschwindigkeitsverteilungen," *Nachr. Ges. Wiss. Göttingen, Math. Phys. Kl., Fachgruppe 1*, 1, pp. 79-114, 1935.
- Yih, C.-S., "Stability of liquid flow down an inclined plane," *Phys. of Fluids*, 6, pp. 321-334, 1963.

(The other references are given either in the paper itself or in Professor van Wijngaarden's discussion.)

* * * * *

ON THE PREDICTION OF IMPULSIVELY GENERATED WAVES PROPAGATING INTO SHALLOW WATER

Paul R. Van Mater, Jr.
United States Naval Academy
Annapolis, Maryland

and
Eddie Neal
Naval Ship Research and Development Center
Washington, D.C.

ABSTRACT

This report treats the problem of the propagation of a dispersive wave system generated impulsively by a surface explosion in deep water into shoaling and shallow water regions. A topography consisting of an arbitrary bottom profile with parallel straight contour lines is assumed. The linear theory of impulsive wave generation for water of uniform depth is used as a basis for evaluating the spectral energy of the wave system at a point in deep water distant from the explosion. Conservation of energy is then invoked to extend the prediction to propagation over a bottom of variable depth. A cnoidal wave theory is introduced to describe the changes in form of the individual phase waves and the wave envelope as the system enters the shallow water regime. The effect of wave refraction at locations other than along an axis normal to the bottom contours is treated. Empirical criteria are incorporated to predict the occurrence of wave breaking, the decay of wave height after breaking, and the attainment of stability in the reforming wave. Attenuation of wave height due to dissipation of energy at the fluid boundaries is also considered. All of the above elements have been incorporated in a computer program. Details of the computational procedure are described in an appendix. Typical predictions made using this program are displayed for small, moderate, and large source strengths. The agreement of the predictions with experimental observations is discussed qualitatively, but no experimental data are included.

I. INTRODUCTION

The nature of wave systems generated impulsively by explosions at or below the water surface is of natural interest to researchers in the naval community because of the ship behavior which results from such an environment. When water-wave systems enter shallow water they undergo changes in form which may have an adverse effect on motions depending on the size of the waves relative to the ship or small craft. While the motivation of this work from our point of view is ultimately the prediction of ship behavior in a shallow-water explosion-generated wave environment, this paper is confined to the prediction of the forcing function -- the wave system. In itself this case presents an interesting means of studying the shoaling behavior of a dispersive wave system, an area which has received surprisingly little attention. Previous efforts in the direction of predicting impulsively-generated wave systems entering water of variable depth stem from the work of Dr. William Van Dorn (cf. Van Dorn and Montgomery [1963]) and have been confined to the prediction of wave envelopes. This paper should be viewed as a second generation of the Van Dorn model.

As a starting point we shall tabulate some of the rather complex effects which occur in shallow water. Not all of these will be considered in the present prediction scheme but the exclusions will be noted.

- (a) In deep water, phase and group velocities depend primarily on wave frequency giving rise to the well-known characteristic of the system known as frequency dispersion. As the system moves into water whose depth is small compared to the lengths of the waves in the system this frequency dependence weakens and dependence on water depth and wave height strengthens. Waves which in deep water moved through the group at phase velocities up to twice the group velocity now become nearly frozen in their position in the group.
- (b) The nearly sinusoidal form of the waves in deep water changes to one of sharp crests separated by long flat troughs. An asymmetry about the horizontal plane develops in which the crest height above the still water line is greater than the trough depth. The maximum slope of the waves increases. This last feature is of particular importance in ship motion prediction.
- (c) As wave height becomes significant with respect to the water depth and the wave nears the breaking point the leading face of the wave steepens and a wave slope asymmetry develops. As the slope of the face of the wave near the crest approaches the vertical the wave becomes

irreversibly unstable and breaking follows. In the final stage before breaking there is an abrupt increase in wave height known as "wave peak-up." Breaking may fall into one of three broad categories: plunging, spilling, or surging.

- (d) After breaking the wave continues as a spilling wave until it either runs up on the beach or reforms as a stable wave. Energy dissipation accompanying breaking reduces the wave height.
- (e) In the case of dispersive systems entering shallow water a low-frequency oscillation is superposed on the wave train. This "wave set-up and set-down" is caused by the transport of mass with the system, particularly when breaking or near breaking occurs, and the resulting counterflow.
- (f) When an element of a wave crest passes over a bottom contour line obliquely it is refracted so as to be more nearly aligned with the bottom contour line. If the bottom contours are not parallel straight lines a focusing of wave energy can occur at "caustic points" and considerable wave height enhancement can result.
- (g) The height of waves in shallow water is attenuated by energy losses due to bottom friction, bottom percolation, internal friction, and surface contamination.
- (h) Incoming waves which encounter steep offshore bars or beaches may be reflected seaward. Under the right conditions standing wave systems of surprising severity may be produced.
- (i) Non-linear instabilities in a shallow-water wave may cause it to decompose, or split into two or more component waves. The hazardous "double rollers" are often-times an example of this. A different type of decomposition may occur when a wave passes over an offshore bar and nearly breaks but then recovers. One or more smaller waves known as "solitons" may be shed from the back of the larger wave. Little is known about these waves at present.

All of these features can affect ship and small craft operations in shallow water and have been included to emphasize the complexity of the overall problem. Not all will be attempted in the prediction scheme presented in this paper. For our purposes we will consider a wave system resulting from an explosion in deep water of nearly uniform depth, which propagates into shallow water over a terrain represented by parallel straight line bottom contours. We will

include change of wave form with wave slope symmetry retained, wave asymmetry about the horizontal plane, wave peak-up, wave breaking, wave height attenuation after breaking, stability of the reforming waves, wave refraction along paths other than normal to the bottom contours, bottom friction, and surface contamination. Excluded are: wave slope asymmetry and change of wave form close to breaking, wave set-up and set-down, the presence of caustics, bottom percolation and internal friction, wave reflection, non-linear decomposition, and solitonic shedding. The system will not be carried all the way into the beach.

Specifically, a linear theory for impulsively-generated waves in water of uniform depth is invoked to describe the waves in deep water at a large distance from the source. From this point a different linear theory based on conservation of energy per unit frequency is employed to depict the system as it moves into a region of shoaling topography. The integral expressions in this theory are evaluated numerically using the conditions at each of a series of closely-spaced stations as input for evaluating conditions at the next station. As the system progresses into shallow water its frequency-dispersive nature gradually disappears and non-linear features dominate in the wave form and propagation velocities. A non-linear cnoidal wave theory is matched numerically to the previous solutions to carry the system in this region. The cnoidal theory is used to describe the profiles of the individual waves in the system and the asymmetry of the system about the horizontal plane. To treat wave breaking existing experimental evidence has been reexamined and an improved criterion for wave breaking is incorporated. From the same experimental source empirical formulations are developed to account for wave height attenuation after breaking and the attainment of stability in the reforming wave. The Van Dorn formula for bottom friction and surface contamination is used to account for these effects. The system is computed not only along an axis normal to the bottom contours but also along a series of rays which emanate radially from the source and change direction continuously due to refraction as the waves move inshore over the shoaling water.

All these features have been incorporated in a computer program. Results of this program for a specified bottom profile and for several source strengths are presented as figures. For the researcher working on similar type problems perhaps the most useful part of the paper will be the computational procedure which is discussed in some detail in an appendix.

II. WAVE GENERATION

Treatment of the subject of water waves produced by a local disturbance has a long history beginning with Cauchy [1815] and Poisson [1816] each of whom independently solved the classic two-dimensional wave problem which bears their names. In recent

years Kranzer and Keller [1959], Kajiura [1963], Whalin [1965a], and Whalin [1965b] have made significant contributions on the subject. The last cited is an extension of the Kajiura work and appears to be the most general treatment on the subject.

The theory as presented by Whalin relates an initial distribution of impulse, surface velocities, and surface deformations to the waves produced at some distance from the source in water of finite but uniform depth. To a certain extent the choice of a source model is arbitrary in that several models may give an adequate fit to experimental data with each having its own particular advantages and disadvantages. No physical reality is assigned to the source model in terms of the dynamics of the explosion; fortunately, however, the dimensions of the source model have been found scalable in terms of explosive yield so that useful predictions can be made.

A source model that has been found to give good agreement with experiment is a paraboloidal cavity given by:

$$\hat{\eta}(\hat{r}) = 2d_0 \left[\left(\frac{\hat{r}}{r_0} \right)^2 - \frac{1}{2} \right], \quad \hat{r} \leq r_0 \quad (1)$$

$$0 \quad \hat{r} > r_0$$

The collapse of this cavity at time $t = 0$ generates the wave system. In cases of large explosions where the dimensions of the cavity are not small compared to the water depth, this model yields a poor prediction and a different source model, perhaps utilizing an initial time dependency should be employed.

According to Whalin the surface elevation, (r, t) , for an axially symmetric surface deformation is:

$$\eta(r, t) = - \int_0^\infty \bar{\eta}(\sigma) \sigma \cos(\Omega t) J_0(\sigma r) d\sigma \quad (2)$$

where $\bar{\eta}(\sigma)$ is the Hankel transform of the initial surface deformation $\hat{\eta}(\hat{r})$:

$$\bar{\eta}(\sigma) = \int_0^\infty \hat{\eta}(\hat{r}) J_0(\sigma \hat{r}) \hat{r} d\hat{r}. \quad (3)$$

All unprimed quantities in these equations have been non-dimensionalized using the water depth, h . Primed variables indicate the corresponding dimensional quantities.

r_0, d_0 = dimensionless radius and height of initial surface deformation = $r_0'/h, d_0'/h$

r = dimensionless radius to field point = r'/h

η = dimensionless elevation of water surface = η'/h

h = water depth

σ = dimensionless wave number = κh

κ = wave number = root of equation: $\omega^2 = g\kappa \tanh \kappa h$

Ω = dimensionless frequency = $(\omega^2 h/g)^{1/2}$

ω = frequency, radians/sec

t = dimensionless time = $t'\sqrt{g/h}$

t' = time, sec.

The integral in (2) is evaluated using the method of stationary phase (cf. Stoker [1957]). After doing this and making the substitutions the result is:

$$\eta(r, t) = \frac{r_0 d_0}{r} \cdot \left[-\frac{\sigma v(\sigma)}{\sigma'(\sigma)} \right]^{1/2} \cdot J_3(\sigma r_0) \cdot \cos(\sigma r - \Omega t) \quad (4)$$

Here, v = group velocity = $\frac{1}{2}[(\theta/\kappa) \tanh \sigma]^{1/2} [1 + (2\sigma/\sinh 2\sigma)]$. Eq. (4) is valid at distances from the source that are large in comparison with the radius of the cavity and in water of uniform depth. A point is selected which satisfies these conditions and the spectral energies of the system evaluated as will be discussed in the next section.

III. WAVE PROPAGATION OVER A BOTTOM OF VARIABLE DEPTH

The extension of the solution to regions of variable depth is based on a conservation of energy approach originally presented by Van Dorn and Montgomery [1963]. The equation presented therein evaluated the spectral energy, that is the energy per unit frequency of the system, for the special case of propagation along a ray normal to parallel bottom contour lines. The derivation is presented here in a slightly different way to permit its extension to include refractive propagation. The topography considered is represented in Fig. 1 which also shows the coordinate system and a typical refracted wave ray.

The following assumptions apply:

- (a) wave frequency remains constant throughout the region of wave travel and is unaffected by refraction
- (b) energy is transported at group velocity in a direction normal to the wave crest
- (c) energy per unit frequency is conserved between adjacent wave orthogonals.

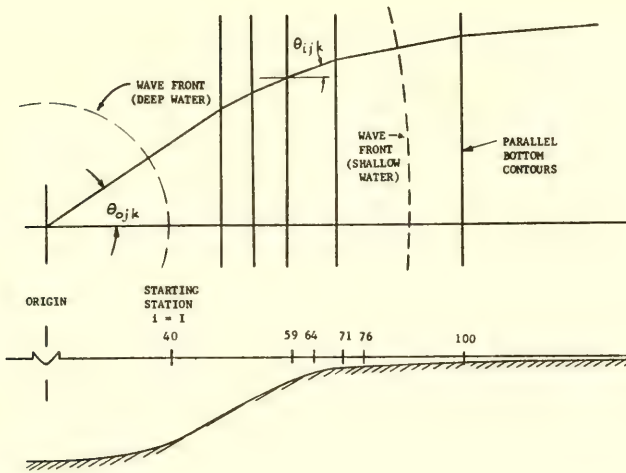


Fig. 1. Bottom topography and wave refraction

The approach will be to consider the energy patch between two adjacent wave rays, S_1 and S_2 , and between two adjacent frequencies, ω and $\omega + d\omega$, and to establish the dimensions of this patch as a function of path position. While the total energy of the patch remains constant the energy density changes with patch size and this, in turn, determines the local wave amplitude. Establish a rectilinear coordinate system, (x,y) , with x -axis normal to the parallel bottom contours and the beach. Orient the curvilinear coordinate system (s,n) shown in Fig. 2 to the median between rays. Since $\kappa = \kappa(\omega, h)$ only the magnitude of κ_1 , κ_2 , and κ will be the same but due to the curvature of the orthogonals the directions will be different. Let κ_1 have components (l_1, m_1) parallel to (s,n) . Since the patch $\delta\xi \delta\eta$, is small $l_1 \div l_2 \equiv l$ $m_1 \div m_2 \equiv m$.

It may be shown by application of Snell's Law that the head of the vector κ_1 will shift to the right along line AB in Fig. 3 maintaining a constant projection on the beach as the patch moves inshore. Then, from Fig. 3,

$$m_1 \cos \theta_1 = m \cos \theta = m_0 \cos \theta_0 . \quad (5)$$

and also,

$$m_0 = \kappa_0 \delta\theta_0 . \quad (6)$$

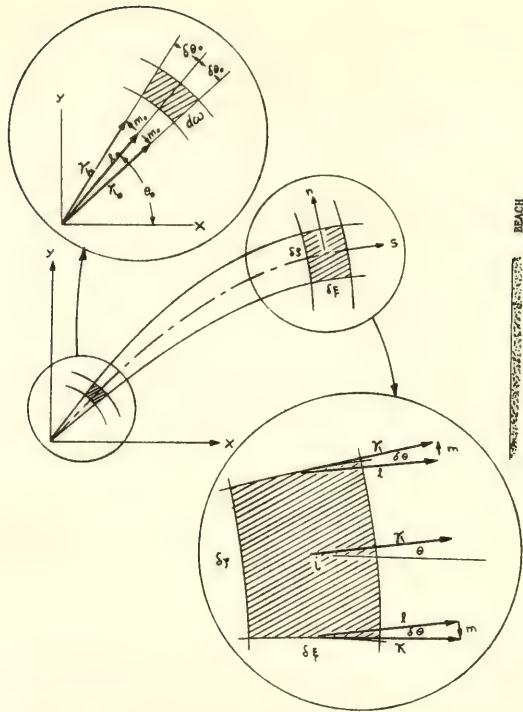


Fig. 2. Propagation of an energy patch over a variable-depth bottom

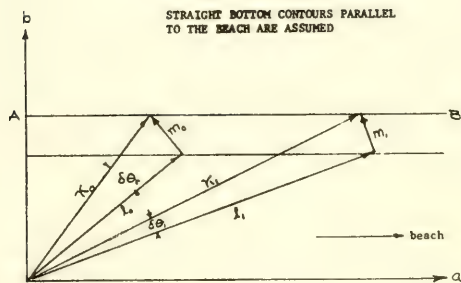


Fig. 3. Wave number vector diagram for a shoaling bottom

so that,

$$m = \frac{\cos \theta_0}{\cos \theta} \delta \theta_0. \quad (7)$$

Since $d\omega$ is small the frequency dependent change in the trajectory of the phase wave orthogonal may be neglected. The change in the patch width due to the geometric spreading of the rays as the patch moves through a distance, ds , will be

$$2 \frac{m}{l} ds.$$

The patch width will be

$$\begin{aligned} \delta \zeta &= 2 \int_{s=0}^{s=i} \frac{m}{l} ds \doteq 2 \int_0^i \frac{m}{K} ds \\ \delta \zeta &= 2\theta_0 \int_0^i \frac{K_0}{K} \cdot \frac{\cos \theta_0}{\cos \theta} ds. \end{aligned} \quad (8)$$

Next, consider the patch length, $\delta \xi$. If δt is the interval required for the patch to pass a given point, i , on s , then

$$\delta \xi \doteq v_i \delta t$$

where v_i is the group velocity at point i . The time interval, δt , may also be represented as follows

$$\begin{aligned} \delta t &= \frac{\delta t}{\delta \omega} d\omega \\ &\doteq d\omega \frac{\partial}{\partial \omega} \int_0^i \frac{ds}{v} = d\omega \int_0^i \frac{\partial}{\partial \omega} (1/v) ds \\ &= -d\omega \int_0^i \frac{1}{v^2} \frac{\partial v}{\partial \omega} ds = -d\omega \int_0^i \frac{1}{v^2} \frac{\partial v}{\partial K} \frac{\partial K}{\partial \omega} ds. \end{aligned}$$

Since $v = \partial \omega / \partial K$,

$$\delta t = -d\omega \int_0^i \frac{1}{v^3} \frac{\partial v}{\partial K} ds$$

or

$$\delta t = d\omega \int_0^i \frac{\partial}{\partial K} \left(\frac{1}{2v^2} \right) ds. \quad (9)$$

The patch length becomes,

$$\delta \xi = v_i d\omega \int_0^i \frac{\partial}{\partial K} \left(\frac{1}{2v^2} \right) ds. \quad (10)$$

If $E(\omega)$ is the energy per unit frequency of the source disturbance then the energy between orthogonals in a frequency band, $d\omega$, near the source will be

$$E(\omega) d\omega \frac{2\delta\theta_0}{2\pi}.$$

Since the energy of the patch has been assumed constant this will also be the value at the field point, i , and this in turn may be equated to the local wave energy:

$$E(\omega) d\omega \frac{2\delta\theta_0}{2\pi} = \frac{1}{2} \rho g \eta_i^2 \delta \zeta \delta \xi, \quad (11)$$

where η_i is the local wave amplitude. Substituting the expressions for $\delta \zeta$ and $\delta \xi$ from Eqs. (8) and (10) gives:

$$E(\omega) d\omega \frac{2\delta\theta_0}{2\pi} = \frac{1}{2} \rho g \eta_i^2 \left[2\delta\theta_0 \int_0^i \frac{\cos \theta_0}{\cos \theta} ds \right] \cdot \left[v_i d\omega \int_0^i \frac{\partial}{\partial K} \left(\frac{1}{2v^2} \right) ds \right].$$

The final result is,

$$\frac{E(\omega)}{\pi \rho g} = \underbrace{\eta_i^2 \left[\int_0^i \frac{\kappa_0}{K} \frac{\cos \theta_0}{\cos \theta} ds \right]}_{\alpha_i} \cdot \underbrace{\left[v_i \int_0^i \frac{\partial}{\partial K} \left(\frac{1}{2v^2} \right) ds \right]}_{\beta_i}. \quad (12)$$

The first bracketed factor, α_i , represents the effect of geometric spreading between rays while the second bracketed factor, β_i , represents the effect of the spatial stretching of energy between adjacent frequencies, or frequency separation.

Computationally, $E(\omega)$ will be evaluated using the results of the previous section, Eq. (4), at a point sufficiently removed from the source and over bottom depths nearly enough uniform to satisfy the conditions on application of that equation. From that point on inshore new α 's and β 's will be computed numerically for each

field point desired. Treating $E(\omega)$ as a constant a new $\eta_i = \eta(\omega)$ will be computed. Details will be discussed in the appendix on computational procedure.

The phase of the waves in water of variable depth requires attention. The phase function of Eq. (4), $\cos(\sigma r - \Omega t)$, for uniform depth may be rewritten as

$$\cos\left(\kappa - \frac{\omega}{v'}\right) r'$$

since $t' = r'/v'$. Now, however, in water of variable depth wave number and group velocity will depend on location as well as frequency. The argument must now be represented in integral form with the integration performed along the path, s . The phase term now becomes

$$\cos\left[\int_0^i \left(\kappa - \frac{\omega}{v'}\right) ds'\right] \quad (12)$$

where $\kappa = \kappa(h, \omega)$, $v' = v'(h, \omega)$, and $h = h(s')$.

The central assumptions involved throughout this development have been that the system is linear and conservative and that the energy per unit frequency remains constant. The assumptions are quite viable as long as the water is of deep to moderate depths, say one-half wave length or deeper. Inshore of this point the system becomes progressively more non-linear, non-conservative and the frequency assumption more vulnerable. An evaluation of the linear assumption will appear in the section.

IV. NON-LINEAR FEATURES OF THE SHALLOW WATER SYSTEM

The previous section carried the wave system from a region of uniform depth into a region of variable depth; however, the description of the system retained its linear character. We have described earlier the change in form of shallow-water waves from one of sinusoidal form to one of sharp crests separated by long flat troughs with an associated horizontal plane asymmetry. In this section a particular non-linear theory, the cnoidal wave theory of Keulegan and Patterson [1940], will be incorporated to modify the form of the waves and the wave envelope.

The first of the cnoidal family of wave theories was presented by Korteweg and de Vries [1895]. Because the wave elevation was given in terms of the Jacobian elliptic cn function they coined the work cnoidal to describe the resulting wave form. Subsequent contributions, in addition to the Keulegan and Patterson paper cited above,

have come from Keller [1948], Benjamin and Lighthill [1954], Laitone [1960], and Laitone [1962]. Masch [1964] has computed the shoaling characteristics of cnoidal waves assuming constant power. Iwagaki [1968] has simplified cnoidal wave equations to a form which he calls "hyperbolic waves." Masch and Wiegel [1961] have provided extremely useful tables of cnoidal wave functions.

A paper by Le Méhauté, Divoky, and Lin [1968] motivated, in part, the choice of the Keulegan and Patterson theory for incorporation in this prediction scheme. These authors reported shallow-water wave experiments and compared the results with twelve different wave theories. Their finding was that none of the theories was uniformly satisfactory but that the cnoidal theory of Keulegan and Patterson was the most generally satisfactory. For the shortest waves linear theory was the best but failed rapidly as the wave length was increased. Stokes' second order and Laitone's second order were consistently worst. Stokes' third and fifth order were better but not as good as linear theory. In terms of the wave profile the Keulegan and Patterson cnoidal profile gave the overall best agreement and was accurately placed with respect to the still water line. This latter finding has also been confirmed by Adeymo [1968].

The central equations adapted from Keulegan and Patterson for use here are:

$$\eta'(r', t') = -\eta_2' + H \operatorname{cn}^2 \left[\frac{K(k)}{\pi} (Kr' - \omega t'), k \right] \quad (14)$$

$$c_c = \sqrt{gh} \left[1 - \left(\frac{H}{h} \right) + \left(\frac{H}{h} \right) \left(\frac{1}{k^2} \right) \left(2 - 3 \frac{E(k)}{K(k)} \right) \right]^{1/2} \quad (15)$$

$$\frac{\eta_1'}{H} = \frac{K_2(k) - E(k)}{k^2 K(k)^2}; \quad \frac{\eta_2'}{H} = 1 - \frac{\eta_1'}{H} \quad (16)$$

$$\frac{L^2 H}{h^3} = \frac{16}{3} [k K(k)]^2 \quad (17)$$

$$\frac{\omega^2 h}{g} = \frac{3\pi^2}{4} \cdot \left[\frac{1}{k K(k)} \right]^2 \cdot \left[\left(\frac{H}{h} \right) - \left(\frac{H}{h} \right)^2 + \left(\frac{1}{k^2} \right) \left(2 - 3 \frac{E(k)}{K(k)} \right) \right] \quad (18)$$

(primes indicate that the variable is in the dimensional coordinate system.) The expression, $L^2 H/h^3$, may be recognized as the Ursell parameter, although, in fact, Stokes was the first to identify it. The parameter gives a measure of the linear or non-linear nature of the system. Linear theory is generally applicable for values less than 1 while cnoidal theory is most appropriate for values greater than 10.

The cn function displays a character that is particularly useful

for this application. When the modulus, k , assumes its minimum value, zero, cn reduces to cosine. When it assumes its maximum value, unity, it reduces to the hyperbolic secant, sech . Since \cos^2 reduces to \cos by the double angle formula and since the form of a solitary wave is given by a sech^2 function, the cn^2 function by appropriate choices of k describe the complete transition from sinusoidal waves to solitary waves. As the value of the modulus increases from zero toward unity the wave crests become more sharply peaked and the troughs longer and flatter; the height of the crest above the still water line increases and the depth of the trough decreases. The wave form is symmetrical about a vertical through the wave crest so that no wave slope asymmetry is reflected. Thus the cnoidal feature may be used to improve the realism of the phase waves in several ways:

- (a) to give the non-breaking waves a more realistic profile
- (b) to introduce asymmetry of the waves about the still water line
- (c) to increase the velocity of the waves in very shallow water. This feature has not been utilized in this application.

Computationally, the frequency, ω , and the water depth, h , are defined in the given frequency and spatial array. The wave height, H , is obtained from the linear theory of the previous section. The elliptic modulus, k , is computed from an iterative solution of Eq. (18). $K(k)$ and $E(k)$ are computed from a series expansion in terms of k . Further details appear in the appendix on computational procedure.

The application, then, involves the use of a theory developed by irrotational, periodic, non-dispersive waves of permanent form in water of uniform depth to represent a wave system which is dispersive and not periodic passing over a bottom of variable depth and in which vorticity due to bottom friction is present at least to some extent. The assumptions implicit in this extension are that the phase waves assume a form appropriate to their local frequency within the group and that this frequency content changes only slowly, and further that rotationality effects are small. The latter assumption appears to be the most vulnerable.

V. WAVE BREAKING AND ENERGY DISSIPATION

Despite abundant literature on the subject of wave breaking there does not exist today a fully-adequate mathematical description of the process, and, in fact, much of the experimental evidence is contradictory and subject to wide scatter bands. In the case of this analysis the need is for a criterion for wave breaking which relates the wave frequency, ω , the linearly computed wave height, H , and

the water depth, h . In addition expressions are needed which determine the wave height decay after breaking and the point at which spilling waves regain their stability. In the absence of an adequate theoretical base a purely empirical approach will be used.

Experimental evidence has been plentiful. Iverson [1952] and Morison and Crooke [1953] made classical contributions. Nakamura, Shiraishi, and Sasaki [1966] presented what is perhaps the broadest range of data on breaking and decay after breaking. A fairly complete bibliography of other works on the subject appears in Van Mater [1970].

No uniformly satisfactory criterion which predicts both the occurrence and the location of wave breaking has yet been developed. A commonly used but crude criterion is that a wave breaks when the wave height-to-water-depth ratio is equal to or greater than 0.78. The Nakamura et al. paper previously alluded to contains all this information covering a rather broad range of beach slopes and wave conditions, and on this basis it was selected to develop the criteria needed for this application. The paper is essentially a report of experimental data with no analytical comparisons or proposals. A comparison of the shoaling coefficients inferred from the Nakamura data shows lower values for the gentler bottom slopes than would be obtained by linear theory. This gives rise to suspicion of prominent frictional effects in the experiments. Although the wave height may have been attenuated by friction as the waves moved inshore it seems reasonable to assume that the characteristics, ω , H , and h , at the breaking point would not be severely affected. More vulnerable, perhaps, is the rate of decay after breaking and the length of the surf zone reported in the paper. Nevertheless, the scale of the experiments is approximately the size of those with which we are concerned. The following formulas are a result of reworking and fitting curves to the Nakamura data.

(a) Wave breaking occurs if:

$$\frac{h}{H} < \frac{5}{2\pi} \cdot \frac{\omega^2 h}{g} + \log_{10} \left(\frac{150}{S} \right)^{1/4} \quad (\omega^2 h/g \geq 0.13, \quad S \geq 0.01)$$

$$\frac{h}{H} < \left(10 \frac{\omega^2 h}{g} - 1.1 \right)^4 + \log_{10} \left(\frac{150}{S} \right)^{1/4} + 0.10 \quad (\omega^2 h/g < 0.13, \quad S \geq 0.01)$$

(19)

where S = tangent of the angle of bottom slope. A plot of this criteria for several bottom slopes is given in Fig. 4.

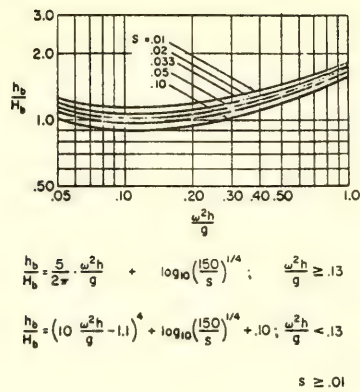


Fig. 4. Wave breaking criteria

(b) Decay of wave height after breaking is given by,

$$H_a = H_b \left(\frac{h_a}{h_b} \right)^{1.55-5S} \tag{20}$$

where,

H_a, h_a = wave height and water depth at a point after breaking
 H_b, h_b = wave height, water depth at breaking

The expression is for two-dimensional waves. In the explosion-generated wave case to account for geometric spreading the expression must be multiplied by the ratio α_b/α_a where α is obtained from Eq. (12).

(c) The equation for wave stability after breaking is:

$$\left(\frac{H}{h} \right)_{\text{Stable}} = \frac{H_b}{h_b} \left(0.85 - 0.40 \frac{\omega^2 h}{g} \right) \tag{21}$$

The wave heights in Eqs. (17) - (21) reflect experimentally-measured quantities; however the wave height information we have at hand is computed from the linear theory of Eq. (12). Linear theory is known to underpredict wave shoaling as the wave height becomes a substantial fraction of the water depth. In addition, in the final stages before breaking the wave front slows more rapidly than the back. Associated with this developing wave slope asymmetry

is a rapid increase in wave height known as "wave peak-up" which occurs just before breaking. The effect has been observed by Le Méhauté, Snow, and Webb [1966]. On the basis of the experiments reported in that source, Van Dorn, Le Méhauté, and Hwang [1968] state that the increase in wave height due to peak-up is 40% of the linearly computed value.

Computationally, the wave height computed on the basis of Eq. (12) is multiplied by a factor of 1.40 to account for peak up and tested against Eq. (19) for each point in the spatial and frequency array. If breaking occurs the increased wave height is retained as H_b for use in Eqs. (20) and (21). If no breaking occurs the linear value of wave height is retained.

The Van Dorn boundary dissipation equation for impermeable bottoms and modified for a wide basin is:

$$\frac{H_2}{H_1} = \exp \left\{ \frac{1}{S} \left(\frac{\nu}{2\omega} \right)^{1/2} \left[\left(\frac{\omega^2}{g} \right) (\kappa_2 h_2 - \kappa_1 h_1) - (\kappa_2 - \kappa_1) \right] \right\} \quad (22)$$

where, ν = kinematic viscosity of water and points 1 and 2 are successive points in the direction of propagation.

VI. RESULTS AND DISCUSSION

In this section the computer program predictions for three source strengths, corresponding to small, moderate, and large explosions, will be described and discussed. No experimental data are included but comments will be made on the agreement between the predictions and experiments which have been conducted.

The theory and the computational procedure outlined in the preceding sections are applicable to any arbitrary bottom profile with parallel straight contours and gentle slopes. However, to compare the theory with experiment a specific bottom profile, that of a test basin at the Waterways Experiment Station, Vicksburg, Miss., was introduced as an input to the computer program. Through the courtesy of that laboratory access was granted to data from a series of experiments conducted there. The data has not yet been formally published by WES at this time, so it cannot be reproduced here; however general comments on the agreement between predicted and experimental results will be made.

The computer results are non-dimensionalized on the basis of the water depth at the explosion, h_0 . Previous notation is used except that the water depth, h , is taken as the depth at the origin, h_0 .

Radial distance along axis:	$r = r'/h_0$
Distance along path:	$s = s'/h_0$
Wave elevation:	$\eta = \eta'/h_0$
Offset of path from axis:	$y = y'/h_0$
Source strength:	$W = Y^{0.3}/h_0$

In the last definition Y is the explosive yield in pounds of TNT, equivalent. For dimensional consistency the exponent should be $1/4$; however experiments have shown that exponents from 0.26 to 0.30 (depending on the submergence of the source) provide better scaling. The value 0.3 is taken here.

Results of time histories along the axis for three different source strengths are presented in Figs. 5 - 7:

- Figure 5, small explosion, $W = 0.139$
- Figure 6, moderate explosion, $W = 0.166$
- Figure 7, large explosion, $W = 0.224$.

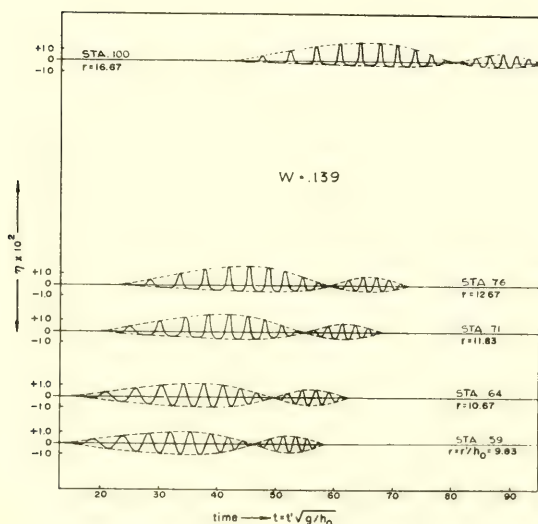


Fig. 5. Prediction of wave system on axis for small explosion

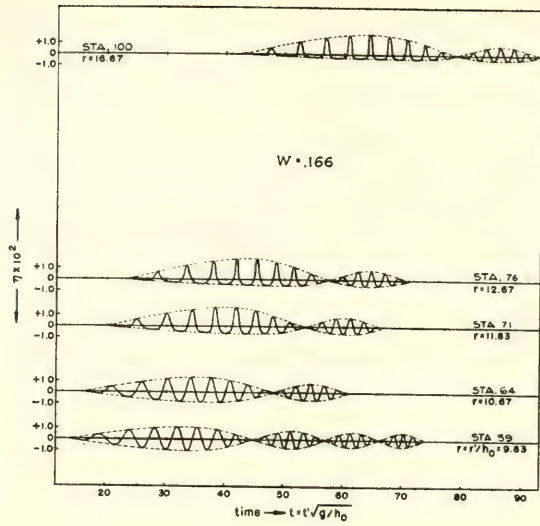


Fig. 6. Prediction of wave system on axis for moderate explosion

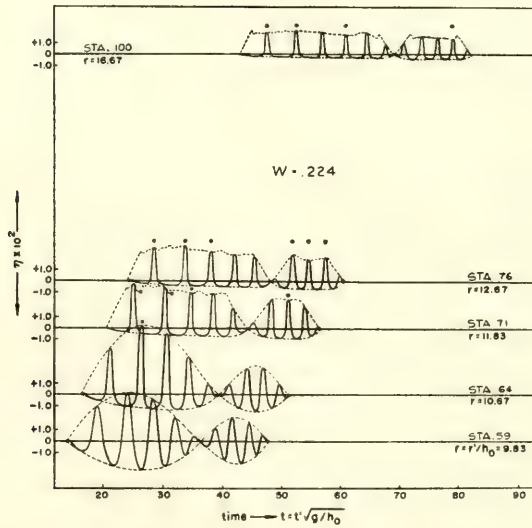


Fig. 7. Prediction of wave system on axis for large explosion

Predictions are displayed for the five stations, 59, 64, 71, 76, 100 shown in Fig. 1. The first station, station 59, may be considered to be in the transition range from deep to shallow water for the larger waves in these explosions. The remaining stations are all in progressively shallower water. A frequency range was chosen which would permit the computation of the first four wave groups. The full four groups are shown at station 59, Fig. 6; however since only the first two groups are of practical interest these are the only ones shown in the remaining displays.

Wave breaking occurred for the large explosion but not for the two smaller explosions. The individual phase waves which have either just started to break or are continuing to break are indicated by an asterisk in Fig. 11. The irregular shape of the envelope at stations 71, 76, and 100 is caused by the fact that breaking and wave (envelope) height decay after breaking have already occurred for these frequencies within the envelope. Typically, breaking will start within a small frequency band then spread to adjacent frequencies as the envelope moves inshore.

The effect of refraction is shown in Fig. 8 for the moderate explosion case only. The wave trains correspond to those along the ray families $\theta_0^* = 0^\circ$, 20° , and 40° . Mean offsets of the path from the axis are indicated. Three stations, 59, 76, and 100 are shown to give a representative effect.

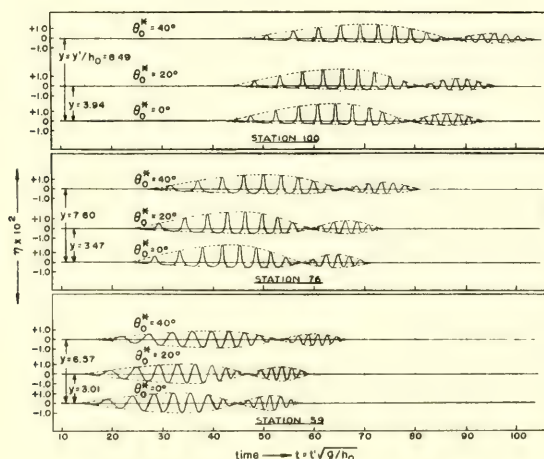


Fig. 8. Prediction of wave system along refracted rays for moderate explosion

Early runs on the computer used the cavity dimensions suggested in Van Dorn, Le Méhauté, and Hwang [1968] and the wave peak-up, wave breaking, decay, and stability criteria which have been outlined previously. To improve agreement between the theory and observation adjustments were made to some of these empirical coefficients. First, cavity dimensions were adjusted for the best fit with the results shown below.

$$r_0 = C_{r_0} \frac{y^{0.3}}{h}; \quad d_0 = C_{d_0} \frac{y^{0.24}}{h}$$

	C_{r_0}	C_{d_0}
small explosion	7.80	1.53
moderate explosion	7.82	1.33
large explosion	8.14	2.03
recommended by Van Dorn	9.60	2.80

For wave breaking the peak-up ratio was changed from 1.40 to 1.50, breaking and decay criteria were not changed. The criteria for stability after breaking was changed as follows

$$\left(\frac{H_a}{h_a} \right)_{\text{Stable}} = \frac{H_b}{h_b} \left(0.90 - 0.40 \frac{\omega^2 h_a}{g} \right)$$

where H_b is now taken as the height before peak-up.

The trajectory of an individual wave ray is dependent on the initial angle at the origin, θ_0 , bottom profile, and frequency. Consequently absolute convergence of a family of wave rays representing an array of frequencies is not possible. To give the best overall conformity over the spatial domain, θ_0 is adjusted with frequency, i.e. $\theta_0 = \theta_0(\omega)$. For the conditions assumed a simple linear variation in $\theta_0(\omega)$ was found to give a variation in path lengths which generally fell within a 1% band and a variation in offsets from the axis which fell within a 5% band. The control angle upon which $\theta_0(\omega)$ is based is designated θ_0^* .

With the background now established the following remarks may be made regarding the agreement between the predicted, or to put it more accurately, the hindcast wave system and the wave system observed in experiments.

(a) For the two smaller explosions, $W = 0.139$ and $W = 0.166$, agreement of the envelopes at stations 59 and 64 is very good. The envelopes of the first group are underpredicted at stations 71 and 76 but overpredicted at station 100. This infers that the linear theory underpredicts shoaling wave height enhancement in very

shallow water, and also that the boundary dissipation formula used in the program does not provide sufficient attenuation. The asymmetry of the envelopes show particularly good agreement and is one of the strong features of the program. The observed trough levels at stations 71 and 76 is slightly lower than predicted. This is attributed to wave set-down due to the presence of a counterflow, or backwash current.

(b) For these two smaller explosions the theory in general predicts the correct number of waves in the envelope. Agreement in phase is poor at station 59 but better at subsequent stations. There is also some grounds for suspicion of zero-set clock errors in the experimental data so that it is difficult to make definitive statements on this subject. The same suspicion makes it difficult to comment on the agreement of the phase velocity of the observed waves.

(c) The agreement in regard to the form of the waves in these smaller explosions is especially impressive. The change from sinusoidal form to cnoidal form quite accurately represents the observed waves.

(d) The observed waves were nearly fully attenuated by the middle of the second wave group. Stronger attenuation in the higher-frequency range is required in the boundary dissipation formula.

(e) Time of arrival (based on linear group velocity) of the wave groups is in very good agreement indicating that transporting energy at linear group velocity, even in the presence of noticeable viscous effects, remains valid into quite shallow water.

(f) The fit of the envelope for the large explosion, $W = 0.224$, at station 59 is only fair. The observed envelope of the first group reaches its maximum at a later time. It appears that for this source strength the explosion may no longer be considered to occur in deep water and that a different source model, perhaps one yielding a higher-order Bessel function, is indicated. In addition the observed troughs of the large waves were much lower than those predicted. Again the probable cause is the presence of an observed strong backwash current which would have the effect of depressing the trough level. The presence of backwash currents is not reflected by the theory.

(g) The agreement in phase is quite good at stations 59 and 64, but not perfect. After wave breaking sets in the phase agreement deteriorates. One of the observed waves in the vicinity of the first node decomposed into two component waves both of which eventually broke. Otherwise, the theory predicted the correct number of waves.

(h) For the large explosion breaking is predicted for the second wave at station 64. Actually, the third and fourth waves broke at this

location and the second wave did not break until a subsequent station. A different source model giving a later peak to the first envelope would probably also correct this discrepancy. The theory predicts about the right number of waves breaking at subsequent stations, although there is disagreement in some cases on which individual waves break. The decay rate after breaking appears to be about right for the envelope heights in the surf zone match quite well. As before there is still distortion of the envelope due to backwash effects. The stability criteria seems to give a surf zone of about the right length, but the data are inadequate to say conclusively. Comparison with a much larger number of experiments is needed to fine tune these empirical breaking relationships; however impulsively-generated wave system furnish an ideal vehicle for such studies.

(i) The form of the breaking waves and the near-breaking waves is very poorly predicted by this program. The wave slope asymmetries which develop near and at breaking are not reflected at all in the cnoidal wave form. For future generations of the program the incorporation of a theory developed by Biesel [1952] is under consideration.

(j) Despite the fact that the "correction factor" approach in accounting for wave peak-up is somewhat distasteful it appears useful at this evolutionary stage. At the minimum the peak-up correction factor should be refined to reflect the influence of ω , H/h , and bottom slope. Clearly what is needed is a computationally useable non-linear theory which predicts this phenomena.

(k) No comments can be made on the quality of predictions along the refracted rays. Such data were taken in the WES experiments but are not presently available for comparison.

In summary it may be said that for small and moderate size explosions the theoretical and empirical program presented gives good predictions of envelope shapes and asymmetry, wave form, and times of arrival of wave groups in shallow water. Wave height enhancement in very shallow water and viscous attenuation are somewhat under-predicted. The quality of the prediction of the phase of individual waves remains to be established. For large explosions the present source model gives only a fair prediction of envelope shape. Group times of arrival and form of non-breaking waves continues to be well predicted. Form of near-breaking waves is poorly predicted. Counterflow currents have a prominent influence when waves are very large, but the presence or effect of such currents is not predicted. The location, size, and extent of the surf zone appears satisfactory based on a limited comparison.

ACKNOWLEDGMENTS

The work described in this presentation was performed at the Naval Ship Research and Development Center, Washington, D. C. under the joint sponsorship of the Defense Atomic Support Agency and the Naval Ship Systems Command, Task Area SR 104 0301, Task 0583.

The authors wish to express their gratitude to the following persons for assistance and support in this project:

Dr. Ming-Shun Chang	Naval Ship Research and Development Center
Dr. Hun Chol Kim	Korean Institute of Science and Technology
Professor T. Francis Ogilvie	University of Michigan
Mr. John Strange	U.S.A.E. Waterways Experiment Station
Mr. Raymond Wermter	Naval Ship Research and Development Center
Miss Claire Wright	Naval Ship Research and Development Center

REFERENCES

- Abramowitz, M. and Stegun, I. A., Handbook of Mathematical Functions, U. S. Dept. of Commerce, Nat. Bureau of Stds., Appl. Math. Series 55, 1964.
- Adeyemo, M. D., "Effect of Beach Slope and Shoaling on Wave Asymmetry," Proc. 11th Conf. Coastal Engineering, ASCE, 1968.
- Benjamin, T. B. and Lighthill, M. J., "On Cnoidal Waves and Bores," Proc. Royal Soc., A., v. 224, 1954.
- Biesel, F., Gravity Waves, U. S. Dept. of Commerce, Nat. Bureau of Stds., Circular 521, 1952.
- Cauchy, A. L. de, Mem. de l'Acad. Roy. des Sciences (Memoir dated 1815), 1827.
- Iverson, H. W., Gravity Waves, U. S. Dept. of Commerce, Nat. Bureau of Stds., Circular 521, 1952.

- Iwagaki, Y., "Hyperbolic Waves and their Shoaling," Proc. 11th Conf. Coastal Engineering, ASCE, 1968.
- Keller, J. B., Comm. Appl. Math., v. 1, 1948.
- Keulegan, G. H. and Patterson, G. W., Jour. Res., Dept. of Commerce, Nat. Bureau of Stds., v. 24, 1940.
- Kajiwara, K., Bull. Earthquake Res. Inst., Japan, v. 41, 1963.
- Korteweg, D. J. and de Vries, G., "On the Change of Form of Long Waves Advancing in a Rectangular Canal, and on a New Type of Long Stationary Waves," Philo. Magazine (Br.), V Series, v. 39, 1895.
- Kranzer, H. C. and Keller, J. B., "Water Waves Produced by Explosions," Jour. Appl. Physics, v. 30, n. 3, 1959.
- Laitone, E. V., "The Second Approximation to Cnoidal and Solitary Waves," J. Fluid Mech., Vol. 9, 1960.
- Laitone, E. V., "Limiting Conditions for Cnoidal and Stokes Waves," J. Geophysical Res., v. 67, n. 4, 1962.
- Le Méhauté, B., Divoky, D. and Lin, A., "Shallow Water Waves: A Comparison of Theories and Experiments," Proc. 11th conf. Coastal Engineering, ASCE, 1968.
- Le Méhauté, B., Snow, G. F. and Webb, L. M., Nat. Engr. Science Co., Rpt. S245A, 1966.
- Masch, F. D., "Cnoidal Waves in Shallow Water," Proc. 9th Conf. Coastal Engineering, ASCE, 1964.
- Masch, F. D. and Wiegel, R. L., "Cnoidal Waves, Table of Functions," Council on Wave Research, The Engineering Foundation, Richmond, Calif., 1961.
- Morison, J. R. and Croke, R. C., U.S. Army Corps of Engineers, Beach Erosion Board, Tech. Memo. 40, 1953.
- Nakamura, M., Shiraishi, H. and Sasaki, Y., "Wave Decaying Due to Breaking," Proc. 10th Conf. Coastal Engineering, ASCE, 1966.
- Poisson, S. D., Mem. de l'Acad. Roy. des Sciences, 1816.
- Stoker, J. J., Water Waves, Interscience, Chap. 6, 1957.
- Van Dorn, W. G., Le Méhauté, B. and Hwang, L., Tetra-Tech, Inc. Rpt. TC-130, 1968.

Van Dorn, W. G. and Montgomery, W. S., Scripps Inst. Ocean.
Ref. 63-20, 1963.

Van Mater, P. R., Nav. Ship Res. and Dev. Ctr. Rpt. 3354, 1970.

Whalin, R. W., "Water Waves Produced by Underwater Explosions:
Propagation Theory for Regions Near the Explosion,"
Jour. Geophysical Res., v. 70, n. 22, 1965a.

Whalin, R. W., Nat. Engr. Science Co. Rpt. S 256-2, 1965b.

Wiegel, R. L., Oceanographical Engineering, Prentice Hall, 1964.

APPENDIX 1

COMPUTATIONAL PROCEDURE

This appendix discusses the details of implementing the theory outlined in the previous sections in a computer program which will predict the wave system in shallow water.

Initially, a monotonically decreasing bottom profile is assumed with parallel straight bottom contours as shown in Fig. 4. Actually, the specific profile used in this program was chosen to conform to that of a test basin at the U.S. Army Engineer Waterways Experiment Station, Vicksburg, Miss. in order to permit comparison of the analytical predictions with experiments performed there. A polar coordinate system is established with the origin at the point of the explosion and the axis taken normal to the bottom contours. The axis is divided into a number of closely spaced stations, indexed i , with $i = 0$ at the origin. The frequency range of interest is also divided into a number of closely spaced frequencies, indexed j . A number of rays, or orthogonals, indexed k , are established emanating from the origin. The local angle of the orthogonal with the normal to the bottom contours varies with the frequency, ω , and the water depth at a given location is identified as θ_{ijk} . Because of the frequency dependence absolute congruence of the trajectories of the orthogonals is not possible. To give the best overall conformity with respect to both location and path length the initial angle of the orthogonal at the origin, θ_{0jk} , is adjusted with frequency. Thus the index k identifies a family of orthogonals which have approximate but not precise spatial agreement, except, of course, on the axis. Throughout indexical notation is for array identification only and tensor convention is not implied.

A starting station, $i = I$, is selected in deep water sufficiently distant from the explosion for Eq. (4) to be valid. That theory strictly

is for water of uniform depth, but for practical purposes as long as the minimum depth (at $i = I$) is greater than half the length of the longest waves with significant energy results will be quite satisfactory. Accordingly the depth used in Eq. (4) is taken as the depth at $i = I$. Equation (4) may be rewritten in indexical notation as

$$B'_{ijk} = \frac{r'_0 d'_0}{s_{ijk} \sigma_{ij}} \cdot \left[- \frac{\sigma_{ij} v'_{ij}}{\left(\frac{dv'}{d\sigma} \right)_{ij}} \right]^{1/2} \cdot J_3(\kappa_{ij} r'_0) \quad (23)$$

$$\eta'_{ijk} = B'_{ijk} \cos (\kappa_{ij} s'_{ijk} - \omega_j t'_{ijk}) \quad (24)$$

where,

B'_{ijk} = envelope elevation function in dimensional system, (ft)

η'_{ijk} = wave elevation in dimensional system, (ft)

r'_0, d'_0 = radius and depth of cavity in dimensional system, (ft)

s'_{ijk} = path length to i^{th} station along k^{th} ray. Also indexed j since path varies with frequency

$\sigma_{ij} = \kappa_{ij} h_i$

v_{ij} = group velocity

$$= \sqrt{gh_i} \cdot \frac{1}{2} \left(\frac{\tanh \sigma_{ij}}{\sigma_{ij}} \right)^{1/2} \left(1 + \frac{2\sigma_{ij}}{\sinh 2\sigma_{ij}} \right) \quad (25)$$

J_3 = third-order Bessel function of the first kind

$$\left(\frac{dv'}{d\sigma} \right)_{ij} = \sqrt{gh_i} \cdot \left(\frac{\tanh \sigma_{ij}}{\sigma_{ij}} \right)^{1/2} \left(\frac{\sinh 2\sigma_{ij} - 2\sigma_{ij} \cosh 2\sigma_{ij} + \sigma_{ij}}{\sinh^2 2\sigma_{ij}} - \frac{1}{4\sigma_{ij}} \right) \quad (26)$$

The wave number, κ_{ij} , obtained from the equation

$$\omega_j^2 = g\kappa_{ij} \tanh \kappa_{ij} h_i \quad (27)$$

and may be approximated in closed form by

$$\kappa_{ij} = \frac{\omega_j^2}{g} \left(\coth \frac{\omega_j^2 h_i}{g} \right)^{1/2} . \quad (28)$$

The Bessel functions $J_0(z)$ and $J_1(z)$ are computed from series expansions given in Abramowitz and Stegun [1964] (eqs. 9.41-9.46). $J_2(z)$ and $J_3(z)$ are then computed from the recursion relation

$$J_{n-1}(z) + J_{n+1}(z) = (2n/z)J_n(z).$$

The time of arrival of each frequency at the starting station is computed from the relation

$$t_{ijk}^I = \frac{s_{ijk}^I}{v_{ijk}^I}. \tag{29}$$

It is now possible to compute the wave spectral energy at the starting station by applying Eq. (12). That equation, rewritten for numerical integration, is:

$$\frac{E_{ijk}}{\eta \rho g} = \eta_{ijk}^2 \alpha_{ijk} \beta_{ijk} \tag{30}$$

where

$$\alpha_{ijk} = \sum_{i=0}^I \frac{K_{0ijk}}{K_{ijk}} \cdot \frac{\cos \theta_{0ijk}}{\cos \theta_{ijk}} \cdot \frac{\Delta s^I}{\cos \theta_{i-1,j,k}} \tag{31}$$

$$\begin{aligned} \beta_{ijk} &= v_{ij}^I \sum_{i=0}^I \frac{\partial}{\partial K} \left(\frac{1}{2v_{ij}^2} \right) \cdot \frac{\Delta s^I}{\cos \theta_{i-1,j,k}} \\ &= v_{ij}^I \sum_{i=0}^I \left[\frac{8}{g \tanh \sigma_{ij}} \right] \cdot \left[\frac{\frac{1}{4} - \frac{\sigma_{ij}}{\sinh 2\sigma_{ij}} - \frac{\sigma_{ij}^2 (1 - 2 \cosh 2\sigma_{ij})}{\sinh^2 2\sigma}}{\left(1 + \frac{2\sigma_{ij}}{\sinh 2\sigma_{ij}} \right)^2} \right] \\ &\quad \cdot \frac{\Delta s^I}{\cos \theta_{i-1,j,k}} \end{aligned} \tag{32}$$

The last factor in Eqs. (31) and (32) represents the incremental distance along the path where Δs^I is the station spacing on the axis.

The energy may now be carried forward from station to station as:

$$E_{i+1,j,k} = E_{ijk}$$

or

$$\eta_{i+1,j,k}'^2 \alpha_{i+1,j,k} \beta_{i+1,j,k} = \eta_{ijk}'^2 \alpha_{ijk} \beta_{ijk}$$

Thus

$$\eta_{i+1,j,k}' = \eta_{ijk}' \left[\frac{\alpha_{ijk} \beta_{ijk}}{\alpha_{i+1,j,k} \beta_{i+1,j,k}} \right]^{1/2}. \quad (33)$$

Similarly,

$$\beta_{i+1,j,k}' = \beta_{ijk}' \left[\frac{\alpha_{ijk} \beta_{ijk}}{\alpha_{i+1,j,k} \beta_{i+1,j,k}} \right]^{1/2}. \quad (34)$$

In the computer program it is the wave system envelope, B' , that is carried forward to the next station and the new value at that station computed from Eq. (34). The phase term is then applied to obtain the wave elevation.

The envelope function $B'(\omega)$ is symmetrical about the SWL by definition. This corresponds well to the observed envelopes at the starting station in deep water, but as the system moves into shallow water the envelope and the phase waves develop asymmetries about the SWL which we seek to describe by the application of the cnoidal theory as previously discussed.

The first problem is to calculate the elliptic modulus, k , for once this parameter is known, all other cnoidal properties may be computed directly. Two difficulties are immediately realized in the determination of the elliptic modulus. First, Eq. (18) does not admit an explicit solution in k . Secondly, the form of cnoidal waves becomes quite sensitive to k as k approaches unity. For example, there is a noticeable difference between the form of the wave determined by $k^2 = 0.99990$ and that determined by $k^2 = 0.999990$. Further, explosion parameters of interest require the determination of modulus values as large as $k^2 = 1 - 10^{-40}$. Thus the following procedure was employed to efficiently and accurately determine k from Eq. (18).

Write Eq. (18) as

$$g(k) = \frac{\omega^2 h}{g} - \frac{3\pi^2}{4} \cdot \left[\frac{1}{kK(k)} \right]^2 \cdot \left[\left(\frac{H}{h} \right) \cdot \left(\frac{H}{h} \right)^2 + \left(\frac{1}{k^2} \right) \left(2 - 3 \frac{E(k)}{K(k)} \right) \right].$$

We then seek the roots of the equation

$$g(k) = 0 \quad (35)$$

Now, smaller roots of $g(k)$, say $0 < k^2 \leq 1 - 10^{-4}$, are readily obtained by iteratively searching for zeros of $g(k)$ in successively finer increments. Larger roots of $g(k)$, say $1 - 10^{-4} < k^2 \leq 1 - 10^{-40}$, are then obtained by iteratively searching for roots of $g(k)$ in half-power increments of 10^{-n} , where $k^2 = 1 - 10^{-n}$. Nearly exact solutions in terms of n are then obtained using the approximate interpolation relation

$$n = \alpha / \Omega^{0.575} + \beta \quad (36)$$

where α and β are interpolation constants and Ω is the dimensionless frequency. This approximation is based on a family of curves (n vs. t) in Wiegel [1964] (Fig. 2.24).

Computer computational difficulties are avoided in solving Eq. (18) for values of k near unity, since the modulus k and the complete elliptic integrals $K(k)$, $E(k)$ can be determined from the value of $10^{-n} = 1 - k^2$, using the approximations given in Abramowitz and Stegun [1964] (eqs. 17.3.33-17.3.36). Since only the largest real root of $g(k)$ is of interest, the computer program searches first for the largest real root. If no real root is found in the range $1 - 10^{-4} < k^2 < 1$, then the largest real root in the range $0 < k^2 \leq 1 - 10^{-4}$ is computed. The smaller roots or imaginary roots have no meaning. Whenever no real root is obtained in the range $0 < k < 1$, the modulus is set equal to zero. The computation is repeated for each frequency at each location. Note that the calculation is based on the double amplitude of the envelope and not on the phase wave elevation.

The distortion of the envelope to its asymmetrical form is achieved by applying Eq. (16). Denoting the elevation of the envelope above and below the SWL as H_1 and H_2 those equations become

$$\begin{aligned} H_{1ijk} &= H_{ijk} \left[\frac{K(k_{ijk}) - E(k_{ijk})}{k_{ijk}^2 K(k_{ijk})} \right] \\ H_{2ijk} &= H_{ijk} \left[1 - \frac{H_{1ijk}}{H_{ijk}} \right] \end{aligned} \quad (37)$$

The phase term for water of variable depth was given as Expression (13). Denoting the argument of the function as ψ and the field point on s as s_i

$$\psi = \int_0^{s_i} \left(\kappa - \frac{\omega}{v} \right) ds',$$

the expression may be written for numerical integration as follows:

$$\psi_{ijk} = \sum_{i=0}^i \kappa_{i-1,j,k} \cdot \frac{\Delta s'}{\cos \theta_{i-1,j,k}} + \omega_j t'_{ijk} \quad (38)$$

where

$$t'_{ijk} = \sum_{i=0}^i \frac{1}{v_{ij}} \cdot \frac{\Delta s'}{\cos \theta_{i-1,j,k}} \quad (39)$$

In Eq. (39) t'_{ijk} is the time of arrival of the j th frequency component at location (i,k) and is printed out for each frequency at each location.

Introducing the cnoidal phase term of Eq. (14) the wave elevation becomes

$$\eta_{ijk} = -H_{2ijk} + H_{ijk} \text{cn}^2 \left[\frac{K(k_{ijk})}{\pi} (\psi_{ijk}), k_{ijk} \right] \quad (40)$$

The Jacobian elliptic functions can all be expressed in terms of theta functions, and can be computed from the resulting infinite series. However, in this program the elliptic function cn in Eq. (40) is evaluated to any specified degree of accuracy using Landen's transformations.

Let $m = k^2$, $m_1 = \xi - m$. Then for m sufficiently small such that m^2 and higher powers are negligible, we have the following approximations for the Jacobian elliptic functions

$$\text{sn}(u, m) \doteq \sin u - 0.25 m (u - \sin u \cos u) \cos u \quad (41)$$

$$\text{cn}(u, m) \doteq \cos u + 0.25 m (u - \sin u \cos u) \sin u \quad (42)$$

$$\text{dn}(u, m) \doteq 1 - 0.50 m \sin u \quad (43)$$

For m sufficiently close to unity such that m_1^2 and higher powers are negligible, we have the approximations

$$\text{sn}(u, m) \doteq \tanh u + 0.25 m_1 (\sinh u \cosh u - u) \text{sech}^2 u \quad (44)$$

$$\text{cn}(u, m) \doteq \text{sech} u - 0.25 m_1 (\sinh u \cosh u - u) \tanh u \text{sech} u \quad (45)$$

$$\text{dn}(u, m) \doteq \text{sech} u + 0.25 m_1 (\sinh u \cosh u + u) \tanh u \text{sech} u \quad (46)$$

Using the following transformations, intermediate values of the parameter m are reduced or increased such that the above approximations are applicable.

To increase the parameter, let

$$p = \frac{4m^{1/2}}{(1 + m^{1/2})^2}, \quad p_1 = \left(\frac{1 - m^{1/2}}{1 + m^{1/2}} \right)^2$$

$$v = \frac{u}{1 + p_1^{1/2}}.$$

Then

$$\operatorname{sn}(u, m) = (1 + p_1^{1/2}) \frac{\operatorname{sn}(v, p) \operatorname{cn}(v, p)}{\operatorname{dn}(v, p)} \quad (47)$$

$$\operatorname{dn}(u, m) = (1 - (1 - p_1^{1/2})) \frac{\operatorname{sn}^2(v, p)}{\operatorname{dn}(v, p)} \quad (48)$$

$$\operatorname{cn}(u, m) = (1 - (1 - p_1^{1/2})) \frac{\operatorname{sn}^2(v, p)}{\operatorname{dn}(v, p)} \quad (49)$$

To decrease the parameter, let

$$p = \left(\frac{1 - m_1^{1/2}}{1 + m_1^{1/2}} \right), \quad v = \frac{u}{1 + p^{1/2}}.$$

Then

$$\operatorname{sn}(u, m) = (1 + p^{1/2}) \frac{\operatorname{sn}(v, p)}{1 + p^{1/2} \operatorname{sn}^2(v, p)} \quad (50)$$

$$\operatorname{dn}(u, m) = (1 - p^{1/2}) \frac{\operatorname{sn}(v, p)}{1 + p^{1/2} \operatorname{sn}^2(v, p)} \quad (51)$$

$$\operatorname{cn}(u, m) = \frac{\operatorname{cn}(v, p) \cdot \operatorname{dn}(v, p)}{1 + p^{1/2} \operatorname{sn}^2(v, p)} \quad (52)$$

Note that in both the descending and ascending Landen transformations, sn and dn are required in order to compute cn . In the computer program values of m greater than 0.6 are computed using the ascending transformation. Values of m less than or equal to

0.6 are computed using the descending transformation. The transformations are reapplied until higher powers of m or m_1 are deemed negligible. The currently used cutoff value is $m^2(m_1^2) = 10^{-20}$. Both of the Landen transformations converge quite rapidly. Thus the cutoff parameter value is attained in three or fewer applications of the pertinent transformations.

Some computational difficulty may be experienced in evaluating the hyperbolic functions used in the ascending Landen's transformation, for large values of the argument u . This problem can be alleviated somewhat by reducing the cn argument, u , to its principal value $-4K(k) \leq u \leq 4K(k)$. Further difficulty may be resolved by using the descending transformation throughout the modulus range where applicable.

When $k = u$, the cn^2 term in Eq. (40) reduces to $\cos^2(\psi_{ijk})/2$ and $H1_{ijk} = H2_{ijk} = (H_{ijk})/2 = B'$. Thus, for $k = 0$, Eq. (40) reduces to

$$\eta_{ijk} = B' \cos \psi_{ijk},$$

which is the usual wave elevation equation.

The matter of the frequency dependence of the trajectories of the wave orthogonals has been discussed briefly. In principle it would be possible to compute an initial angle θ_{ojk} for each frequency and at each station which give a path length and a path offset from the axis that would fall within established error limits. Such an iterative procedure would increase the computation time enormously and was rejected on this basis. Several schemes were tried in attempting to find a simple rule for the choice of θ_{ojk} which would give reasonable conformity in a given family of trajectories. The simplest rule turned out to be the best. A linear distribution of θ_{ojk} was chosen according to the following relation:

$$\theta_{ojk} = \theta_{ojk}^* [1 - 0.04(\omega - 0.2)] \quad (54)$$

where θ_{ojk}^* is a control angle for the family of trajectories. The choice of the above relation is quite an arbitrary one and a different and more complicated bottom topography could necessitate a different function or the iterative procedure discussed above.

The refraction angle at each station along a given path is computed from Snell's Law:

$$\theta_{ijk} = \arcsin \frac{\kappa_{oj} \sin \theta_{ojk}}{\kappa_{ij}} \quad (55)$$

The path length and offset from the axis are given by

$$s'_{ijk} = \sum_i \frac{\Delta s'}{\cos \theta_{i-1,j,k}} \quad (56)$$

$$y'_{ijk} = \sum_i \Delta s' \cdot \tan \theta_{i-1,j,k} \cdot \quad (57)$$

The system is tested for wave breaking by applying Eq. (19) to the envelope height, H_{ijk} , increased by a factor of 1.40 to account for non-linear peak up. If the test succeeds and breaking occurs then the increased value of envelope height is retained as H_b for use in computing decay after breaking, Eq. (20), and wave stability, Eq. (21). Indexing the breaking point as $i = b$ and any location in the surf zone beyond the breaking point as $i = a$, these equations become:

$$H_{ajk} = H_{bjk} \left(\frac{h_a}{h_b} \right)^{1.55-5S_a} \cdot \left(\frac{\alpha_{bjk}}{\alpha_{ajk}} \right) , \quad (58)$$

$$\left(\frac{H_a}{h_a} \right)_{\text{Stable}} = \frac{H_{bjk}}{h_{bjk}} \left(0.85 - 0.40 \frac{\omega_j^2 h_a}{g} \right) . \quad (59)$$

Once stability is found the envelope height, or rather the symmetrical envelope elevation $B = H/2$ is carried forward in the usual way.

Since the test for breaking is applied to the envelope, strictly, wave breaking can be considered to occur only if a phase wave crest occurs within the breaking band of frequencies. As a practical matter the prediction of the exact arrival of the phase wave is the most difficult and least reliable part of the whole procedure, so that the surf zone should be considered to extend over any region where breaking is predicted for any frequency within the envelope.

The boundary dissipation equation, Eq. (22), is applied to the envelope height between successive stations outside the breaking zone.

In the present computation the array consists of 100 stations, 120 frequencies, and 3 families of wave rays ($\theta_0^* = 0^\circ, 20^\circ, 40^\circ$). The computer program is listed in Van Mater [1970]. The program requires 23 minutes of running time on the IBM 7094 and provides about 14,000 lines of output.

HYDRODYNAMICS IN THE OCEAN ENVIRONMENT

Tuesday, August 25, 1970

Afternoon Session

Chairman: J. Hoyt
Naval Undersea Research and
Development Center, Pasadena

	Page
Three Dimensional Instabilities and Vortices Between Two Rotating Spheres J. Zierep, O. Sawatzki, Universität Karlsruhe	275
On the Transition to Turbulent Convection Ruby Krishnamurti, Florida State University	289
Turbulent Diffusion of Temperature and Salinity: -- An Experimental Study A. H. Schooley, U.S. Naval Research Laboratory	311
Self-Convecting Flows M. P. Tulin, Hydronautics, Inc. and J. Shwartz, Hydronautics-Israel, Ltd. and Israel Institute of Technology	321

THREE DIMENSIONAL INSTABILITIES AND VORTICES BETWEEN TWO ROTATING SPHERES

J. Zierep and O. Sawatzki
Universität Karlsruhe
Karlsruhe, West Germany

We study the motion of a viscous medium between two concentric rotating spheres. Investigating this type of flow is an extension of the well-known contribution of G. I. Taylor [1], who studied the motion between two rotating cylinders. Due to the action of the centrifugal force instabilities are possible. The main difference between the two flow fields is that for the spheres the centrifugal force is a function of the latitude. We have here an instability in a three-dimensional flow and it is possible that there exist different flow regimes -- stable and unstable ones -- side by side. This problem is closely related to the cellular convection flow, especially to those existing over nonuniformly heated surfaces [2, 3, 4]. The thermal buoyancy corresponds to the centrifugal force, the nonuniform heating corresponds to the latitudinal dependence of the centrifugal force.

Now some fundamental things about the used apparatus.* The experiments have been done primarily with the inner sphere (Aluminum) rotating and the outer one (Plexiglass) fixed. The gap was filled with silicon oil that contained aluminum powder as flow indicator. Measured has been mainly the frictional torque that keeps the angular velocity of the inner sphere constant. The temperature in the gap was controlled by thermocouples and photographs have been taken of the different flow configurations. The measurements have been done by Ritter and Wimmer [6] as part of their master thesis.

Figures 1 and 2 show the results for two different gap widths. Plotted is the friction torque coefficient ζ_M over a Reynolds number that ranges from 10^1 to 10^6 . Covering this wide range has been accomplished by 1) using silicon oils with viscosities between 3 and 1000 cSt and 2) by varying the angular velocity from 0 to 200 revolutions/sec.

In principle we have here independent of the width of the gap three different domains of fluid motion. For small Reynolds numbers

* For detailed information see [5].

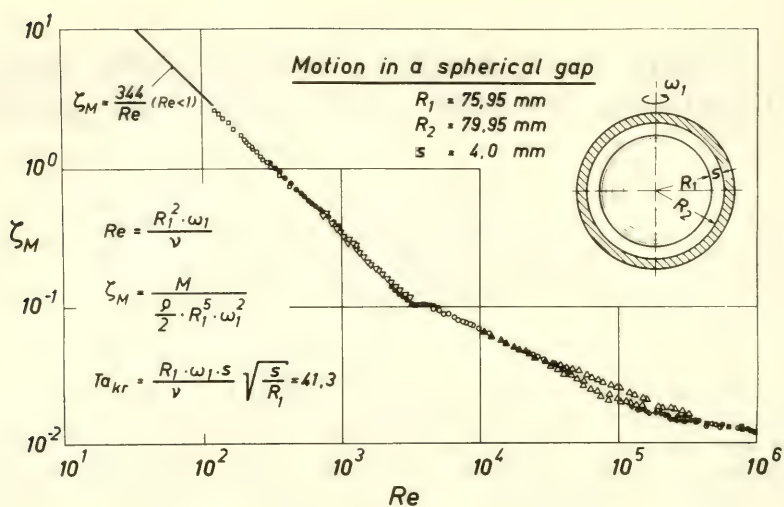


Fig. 1 $\zeta_M(Re)$ for the relative gap width $s/R_1 = 0.0527$

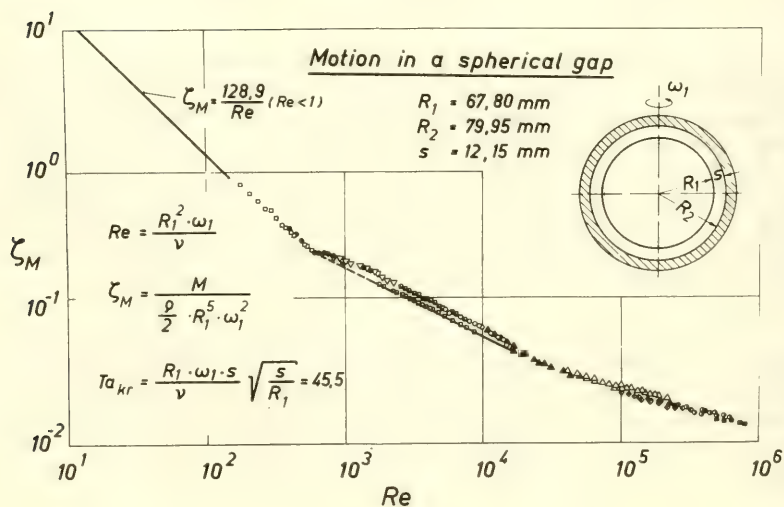


Fig. 2 $\zeta_M(Re)$ for the relative gap width $s/R_1 = 0.18$

the Navier Stokes equations give $\zeta_M \sim 1/\text{Re}$, the law for creeping flow. Surprisingly this holds up to $\text{Re} = 3.3 \cdot 10^3$ for the small gap and up to $\text{Re} = 600$ for the larger one. Next to this regime follows one of laminar boundary layer type with $\zeta_M \sim 1/\sqrt{\text{Re}}$. Finally the turbulent flow regime with $\zeta_M \sim 1/\sqrt[3]{\text{Re}}$ is reached after passing some possible instable flow configurations in the transition region. In general we have this behavior in all cases but quantitatively there are important differences depending on the relative width of the gap. The reason for this behavior is the multitude of the possible flow configurations.

First we study the case of the small relative width of the gap. For low Reynolds numbers (for instance $\text{Re} = 10$) the streamlines are concentric circles around the axis of rotation (Fig. 3). With

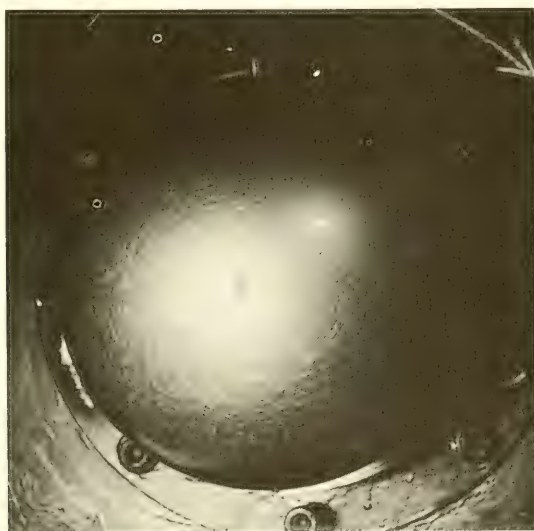


Fig. 3 For small Reynolds number the streamlines are concentric circles around the axis of rotation. $s = 5 \text{ mm}$, $\text{Re} = R_1^2 \omega_1 / \nu = 10$

increasing Reynolds number the streamlines change to spirals (Fig. 4). Close to the rotating sphere the spirals are moving from the poles to the equator but close to the fixed sphere the spirals are moving from the equator to the poles. The inner and the outer spirals join and form closed curves. With passing the critical Taylor number $\text{Ta} = 41.3$ Taylor vortices begin to develop close to the equator. It is remarkable that the critical Taylor number here has the same value as for the concentric cylinders. The axes of these vortices have spiral form and end free in the flow field. (Fig. 5). From

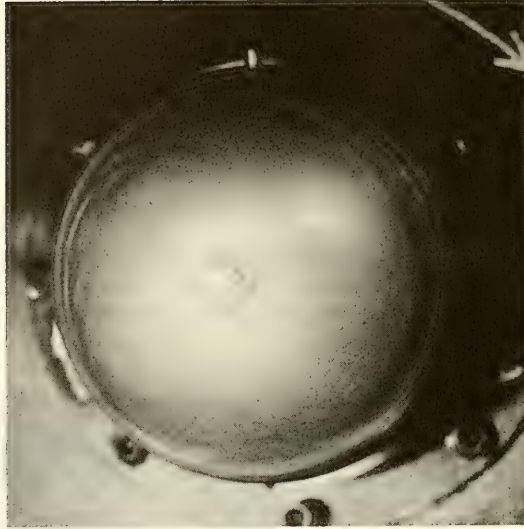


Fig 4 For larger Reynolds number the streamlines are spirals. $s = 5 \text{ mm}$, $Re = 2350$

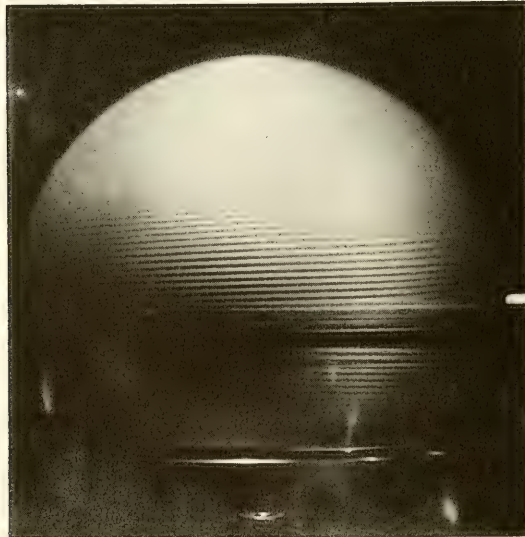


Fig 5 For large Reynolds number the vortex axes become spirals and end in the flow field. $s = 1.05 \text{ mm}$, $Re = 27,000$, $Ta = 41.6$

the end of the vortices up to the poles the laminar flow remains stable. With increasing Reynolds number, the axes of the vortices become wavy (Fig. 6) and the flow turns turbulent after passing some intermediate states (Figs. 7, 8). In this case photographs still show a remarkable distinct structure of the flow.

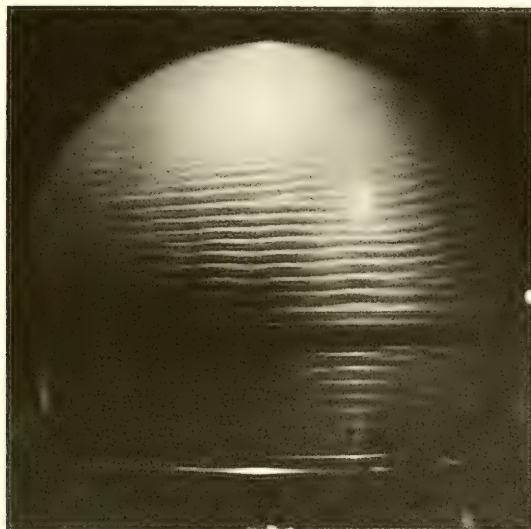


Fig. 6 The vortex axes become wavy for very large Reynolds number. $s = 2$ mm, $Re = 16,800$, $Ta = 68.8$

For the larger relative width of the gap this matter is much more complicated. In the transition from laminar to turbulent flow we found that altogether five basically different but reproducible main modes are possible. In the torque diagram all these modes are noticeable and they are remarkably stable as soon as they have become existent. For this reason we called them "stable instabilities." In the experiment these different modes can be established by applying a suitable acceleration of the angular velocity. In analogy to the rotating cylinders [7] we have here a case of nonuniqueness. The mode of instability that is finally realized depends on the initial condition given by the experimentator. Now the main modes I - V shall be discussed briefly.

I. In spite of having an overcritical state no vortices become visible. The transition to the turbulent flow occurs by passing through mode II, that is described below. Mode I is characterized by the fact

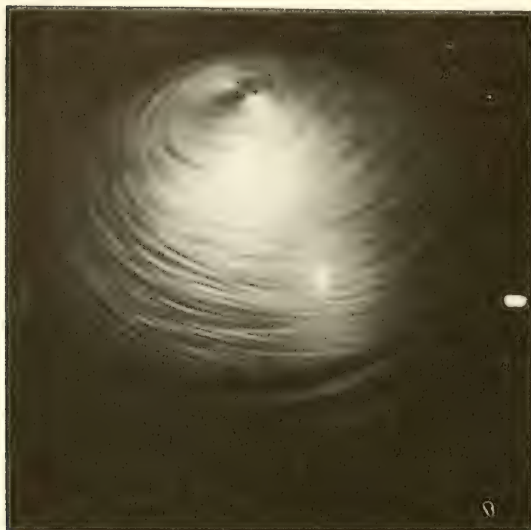


Fig 7 The turbulent motion. $s = 3.5$ mm, $Re = 53,500$,
 $Ta = 522$



Fig. 8 The turbulent motion. $s = 2$ mm, $Re = 158,000$,
 $Ta = 648$

that in the field between the two boundary layers of the rotating and the fixed sphere -- according to the large gap -- a flow is established that moves with a constant but smaller angular velocity than the inner rotating sphere. Obviously this type of motion prevents or at least delays the development of the Taylor vortices. A similar pattern is known to exist also in the gap between two discs [8] with one of them rotating.

II. This regime is characterized by a flow with vortices that begin at the poles (Fig. 9). The axes of these vortices are inclined

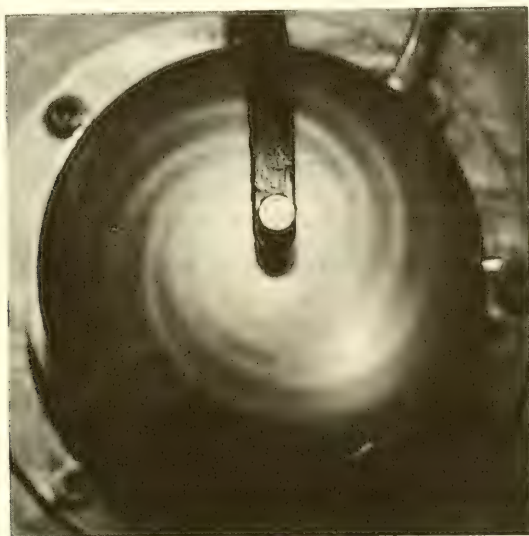


Fig. 9 Motion of Mode II. $s = 12.15$ mm, $Re = 8,300$,
 $Ta = 630$

slightly to the streamlines close to the fixed sphere. With increasing Reynolds number these vortices advance around the poles to the equator. The axes become more and more wavy and finally the flow turns turbulent. The physical explanation of these vortices is by no means evident. We have the conjecture that we have here a situation analogous to the occurrences close to a free rotating sphere [9] or disc [10]. Very often these vortices are called Stuart vortices. Contrarily to the familiar pattern of vortices, rotating with alternating direction the Stuart vortices rotate all in the same direction.

III. Two Taylor vortices develop symmetrical to the equator. Outside the vortex zone we have mode I flow. Surprisingly at the equator -- where the centrifugal force has its maximum -- the flow

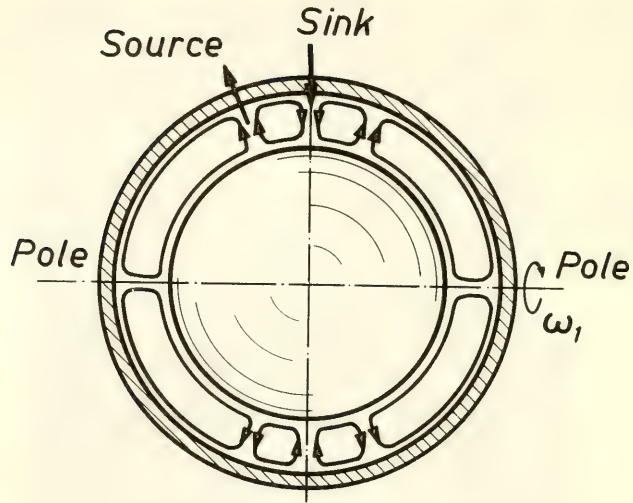


Fig 10 Sketch of Mode III

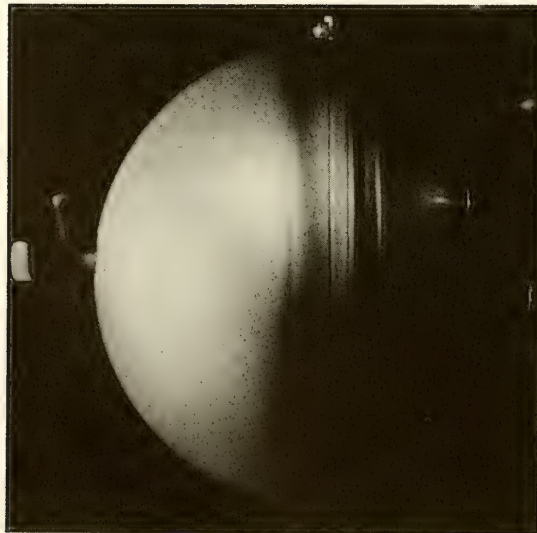


Fig 11 Motion of Mode III. $s = 8$ mm, $Re = 8,130$, $Ta = 318$

is directed inward (Figs. 10, 11). This can be explained by a cellular motion in the field between the pole and the vortex that forces the vortex to rotate in the mentioned direction. The result is the sink flow at the equator.

IV. Two pairs of Taylor vortices develop symmetrical to the equator but now with an outward motion at the equator (Figs. 12, 13). Mode III is a limit case of IV reached by increasing angular velocity. The cell close to the equator becomes smaller and smaller and in the limit the flow reverses at the equator.

V. This is an unsteady version of mode III. Vortices, generated at the equator, leave the equator under a small angle of about 10° (Fig. 14) and move on spiral trajectories to the pole.

It is interesting to see that the critical Taylor number increases with increasing gap width. Corresponding calculations for rotating cylinders with arbitrary gap width, done by Kirchgäßner [11], agree very well with our experimental results for spheres having the same direction (Fig. 15). The explanation for this is that in our case the instability first begins at the equator and we have there locally a similar situation as in the case of the two cylinders.

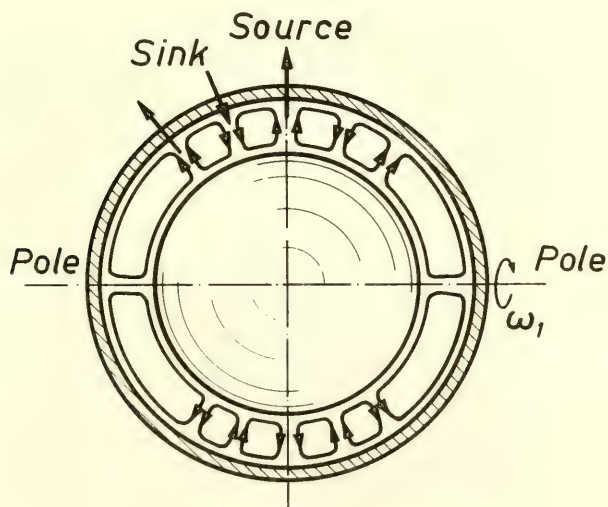


Fig. 12 Sketch of Mode IV

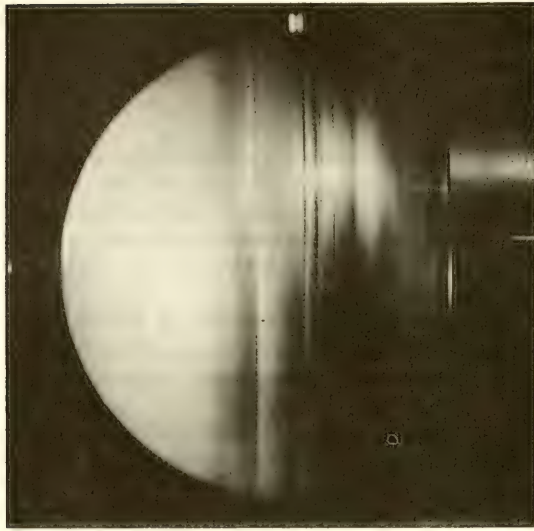


Fig. 13 Motion of Mode IV. $s = 12.15$ mm, $Re = 2,660$,
 $Ta = 201$



Fig. 14 Motion of Mode V. $s = 12.15$ mm, $Re = 1,210$,
 $Ta = 95.6$

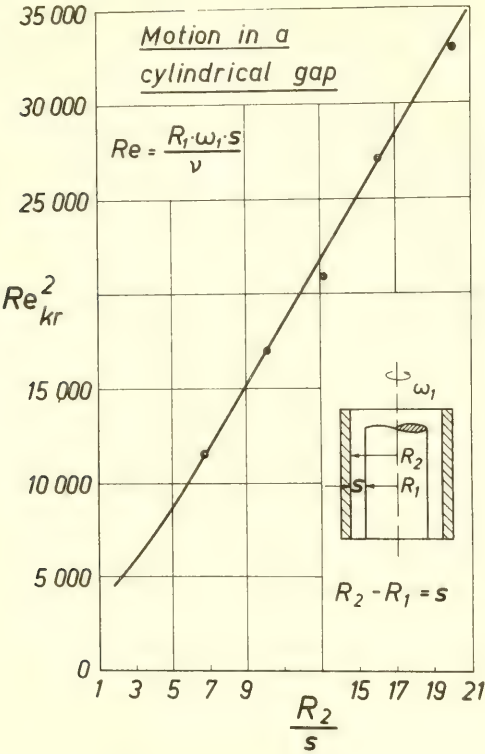


Fig.15 The critical Reynolds number for rotating cylinders [11] and the corresponding measurements for the spherical gap

As far as theory is concerned we have treated three problems. Without going into details we give a short summary.

a. In case of fully laminar flow and a small relative gap width the differential equations can be solved by using an approximation method like that of v. Karman - Polhausen. The results are simple expressions for the streamlines. Close to the walls these are logarithmic spirals that fit very well to the experimental results (Fig. 4).

b. Mode 1 -- with larger relative gap -- can also be treated easily. For the region close to the fixed and the moving sphere estimations can be used for the boundary layer thicknesses. For a first approximation results for the boundary layer of a rotating disc [12] can be used. Between these two boundary layers we have an already

mentioned full laminar flow. The Navier Stokes equations in spherical coordinates give a very simple solution here with the velocity linear in r . The analytical expressions for the three flow regions can be combined and a short and simple calculation gives a torque coefficient that fits surprisingly well to our experimental results.

c. The Stuart vortices -- already mentioned in connection with mode II -- all rotate in the same direction. Experiments done with a rotating free sphere [9] have confirmed this type of vortices. A simple cinematic consideration shows how one comes from the Taylor-Görtler vortices that have an alternating direction of rotation to the Stuart vortices. For this it is only necessary to superpose a suitable flow field to the Taylor-Görtler vortices with a flow direction cross to the vortex axes. With other words: to get Stuart vortices it is necessary that the Taylor vortices become embedded in a suitable flow field.

We are dealing here with a real three-dimensional effect that changes our vortex model. One realizes easily that for a rotating free sphere or in the gap between two spheres of which one is rotating the just mentioned situation exists.

REFERENCES

- [1] Taylor, G. J., "Stability of a Viscous Liquid Contained Between Two Rotating Cylinders," *Phil. Trans. A* 223, 289-293, 1923.
- [2] Zierep, J., "Thermokonvektiv Zellularströmungen bei inkonstanter Erwärmung der Grundfläche," *ZAMM* 41, 114-125, 1961.
- [3] Koschmieder, E. L., "On Convection of a Nonuniformly Heated Plane," *Beitr. z. Phys. d. Atmos.*, 39, 208-216, 1966.
- [4] Müller, U., "Über Zellularströmungen in Horizontalen Flüssigkeitsschichten Mit Ungleichmäßig Erwärmter Bodenfläche," *Beitr. z. Phys. d. Atmos.*, 39, 217-234, 1966.
- [5] Sawatzki, O., and Zierep, J., "Das Stromfeld Zwischen Zwei Konzentrischen Kugelflächen, von Denen die Innere Rotiert," *Acta Mechanica*, 9, 13-35, 1970.
- [6] Wimmer, M., and Ritter, C. F., "Die Strömung im Spalt Zweier Konzentrischer Kugeln," *Diplomarbeiten, Univ. Karlsruhe, Lehrstuhl für Strömungslehre* 1968, 1969.
- [7] Coles, D., "Transition in Circular Couette Flow," *J. Fluid Mech.* 21, 385-425, 1965.

- [8] Schultz-Grunow, F., "Der Reibungswidstand Rotierender Scheiben im Gehäuse," ZAMM 15, 191-204, 1935.
- [9] Sawatzki, O., "Das Strömungsfeld um eine Rotierende Kugel," Acta Mechanica, 9, 159-214, 1970.
- [10] Gregory, N., Stuart, J. T., and Walker, W. S., "On the Stability of Three-dimensional Boundary Layers with Application to the Flow Due to a Rotating Disc," Phil. Trans. Roy. Soc. A248, 155-199, 1955.
- [11] Kirchgaßner, K., "Die Instabilität der Strömung zwischen zwei rotierenden Zylindern gegenüber Taylor-Wirbeln für beliebige Spaltbreiten, ZAMP 12, 14-30, 1961.
- [12] Cochran, W. G., "The Flow Due to a Rotating Disc," Proc. Camb. Phil. Soc. A 140, 365-375, 1934.

* * * * *

DISCUSSION

L. van Wijngaarden
Twente Institute of Technology
Enschede, The Netherlands

The description of mode I reminds me of the result that Batchelor [1956] derived for laminar flow with closed streamlines of fluids with small viscosity: Thin boundary layers on solid boundaries separated by a region of constant vorticity. This result was derived for two-dimensional flow. In your case the flow is three-dimensional, but it might be that the same conditions which are necessary for Batchelor's result hold in this case of mode I.

REFERENCES

- Batchelor, G. K., "On steady laminar flow with closed streamlines at large Reynolds number," J. Fluid Mech., Vol. 1, p. 177, 1956.

* * * * *

REPLY TO DISCUSSION

J. Zierep
Universität Karlsruhe
Karlsruhe, West Germany

The general condition for the existence of closed streamlines, given by Batchelor in the cited reference, can be applied to the present case of a flow with rotational symmetry. We obtained information about the velocity distribution that has been confirmed by our analytical analysis, following a different path.

* * * * *

ON THE TRANSITION TO TURBULENT CONVECTION

Ruby Krishnamurti
Florida State University
Tallahassee, Florida

I. INTRODUCTION

The heat flow out of the sea floor has been observed in close to 2000 measurements; the mean value for all the oceans is found to be 1.4×10^{-6} cal/cm²sec. [Lee and Uyeda 1965] This is three orders of magnitude smaller than the solar heating at the sea surface and is surely negligible in any budget of the upper oceans. Yet, because this heat flux is imposed from below, it may be of some consequence in the dynamics of the abyssal circulation. If this heat were to be transferred purely by conduction through the sea water, a temperature gradient σ of 10^{-5} C°/cm would be required. The largest depth across which such a gradient can exist without convective overturning is determined by the critical value of the Rayleigh number R , which is defined as follows:

$$R = \frac{g\alpha}{K\nu} \sigma d^4$$

where g is the acceleration of gravity, α the thermal expansion coefficient, K the thermal diffusivity, ν the kinematic viscosity, and d is the depth of the layer in consideration. This largest depth that can transfer the imposed heat flux by conduction is only around 3 cm. If there are regions or time periods of the abyssal oceans in which horizontal advection of heat is not the dominant process, then this vertical convection, with its attendant vertical mixing of nutrients, can be an important process.

Some understanding of convective processes can be gained from laboratory studies of a horizontal layer of fluid which is heated from below and cooled from above. The following is a review of such laboratory studies and also a report of some recent experiments in rotating and non-rotating systems.

*This is contribution No. 33 of the Geophysical Fluid Dynamics Institute.

II. TRANSITION TO TURBULENT CONVECTION IN A NON-ROTATING LAYER OF FLUID

Unlike the fast transition to turbulence in plane parallel shear flows, the horizontal convecting layer undergoes a number of discrete transitions, remaining in each régime for a finite range of Rayleigh number. The transition to turbulent convection appears to result in the following manner: at sufficiently low values of the Rayleigh number the fluid system is stable to all small disturbances. As the value of R is increased the system becomes unstable to one kind of disturbance. As R is increased still further the fluid becomes unstable to more kinds of disturbances. At sufficiently large Rayleigh numbers the flow is unstable to so many kinds of disturbances, each occurring with uncontrolled phase, that the flow may be called turbulent. Before discussing the first three of these transitions, the experimental apparatus will be described.

Apparatus

One of the possible designs of experimental apparatus is shown in Fig. 1. The fluid layer occupies a region 51 by 49 cm, with a depth that can be chosen (usually between $1/2$ and 5 cm).

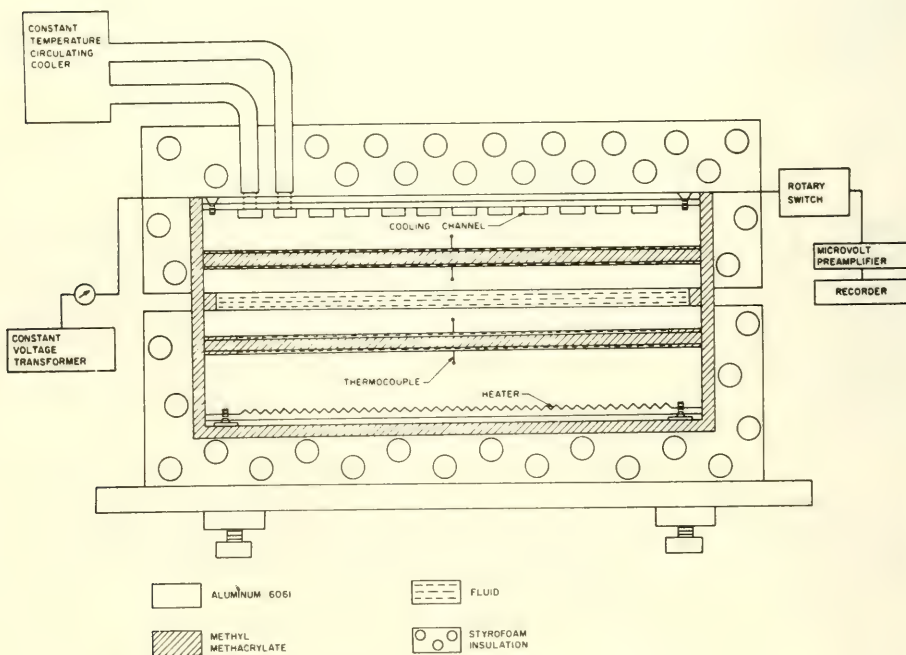


Fig. 1. Apparatus

The plexiglass tank containing the fluid also contains four blocks of aluminum 6061 T 651. Two of the blocks are 4 in. thick, two are 1 in. thick, each is 20 in. by 20 in. wide. The electrical heater, which is a fine mesh of resistance material embedded in silicon rubber, is attached to the bottom of the lowest block, which is 4 in. thick. The heat input is controlled by a variable transformer backed by a constant voltage transformer of the line voltage. Above this lowest aluminum block is a low-conductivity layer of methyl methacrylate. A layer of liquid sufficiently thin that it never convects for the temperature gradients occurring in these experiments effects constant thermal contact between the layers. Above this low conductivity layer is a block of aluminum 1 in. thick; above this is the convecting fluid, whose depth is defined by plexiglass spacers. The arrangement of blocks above the convecting layer is symmetric to that below except that the cooling is accomplished by cooling fluid from a constant-temperature circulator flowing in channels in the uppermost aluminum block. The channels for incoming and outgoing flows are side by side in order to minimize horizontal temperature gradients. The channels were cut in a complicated pattern and spaced so that the separation of channels was not close to an integral multiple of the expected convection cell size. The maximum flow rate of the cooling fluid is $2 \cdot 5$ gal/min. This apparatus was used in the studies which will be described with air, water, and silicone oils. For convection in mercury, the aluminum blocks were replaced by copper blocks of which two are 2 in. thick, two are 1 in. thick and each is 20 in. by 20 in. wide.

The thermal conductivity of the aluminum is about three orders of magnitude larger than that of the oils. The thermal conductivity of copper is 50 times as large as that of mercury. This is, of course, an attempt to approach the ideal condition of perfectly conducting boundaries. With poorly conducting boundaries a horizontal temperature ripple corresponding to the cellular structure in the convecting fluid penetrates into the boundaries and may control transitions to different cellular structures. Also the metal acts as a diffuser of any horizontal temperature variations arising from the discrete nature of the cooling channels. The large mass of metal (approximately 400 lb of aluminum or 700 lb of copper) acts as a large heat capacity so that temperatures in the blocks are very stable.

The heat transported by the convecting liquid is measured by concentrating the temperature gradient across the poor conductor in the manner devised by Malkus [1954]. In the steady state the heat H transported by the fluid is the average of the heat conducted across the two poor conductors:

$$H = k_p \frac{T_1 - T_2}{2d_p} + k_p' \frac{T_3 - T_4}{2d_p},$$

where k_p and k_p' are the molecular conductivities of the low conductivity layers, d_p is the depth of the layer, and T_1 , T_2 , T_3 and

T_4 are the temperatures of the four aluminum blocks. The subscripts are ordered from bottom to top. The conductivities k_p and k'_p are measured in terms of that of the liquid when it is known that the liquid layer is in a state of steady conduction. Then the following relations hold:

$$k_f \frac{T_2 - T_3}{d} = k_p \frac{T_1 - T_2}{d_p} = k'_p \frac{T_3 - T_4}{d_p},$$

where k_f is the molecular conductivity of the fluid. Thus, once the conductivity and depth of the poor conductors is determined, a measurement of the temperatures in the four metal blocks allows the determination of the Rayleigh number and the heat flux.

Fine aluminum flakes suspended in the liquid were used to visualize the flow. The aluminum flakes become aligned in a shear flow, and because they are flakes, reflect light more strongly in certain directions, depending upon the direction of the shear and of the illumination. In a uniform shear, the brightness is uniform; where there is a differential shear, there will be corresponding bright and dark regions. In the case of water, aluminum flakes would not stay in suspension sufficiently long, so another tracer called 'rheoscopic fluid AQW 010' was added to the water. This tracer displays differential shears, just as do the aluminum flakes, but remains in suspension about 10 times as long.

Since the fluid layer is bounded above and below by opaque boundaries, the plan form of convection is obtained by viewing the flow from the side as shown in Fig. 2. The tracers were illuminated at mid-depth by narrow overlapping beams of collimated light from two 2 W zirconium arc lamps. The two beams directed at each other allow visualization of shear regions at both positive and negative angles to the line of sight. This line of sight is perpendicular to the beam. As the light beam is moved horizontally, illuminating different regions of the fluid, a camera is moved horizontally on a threaded

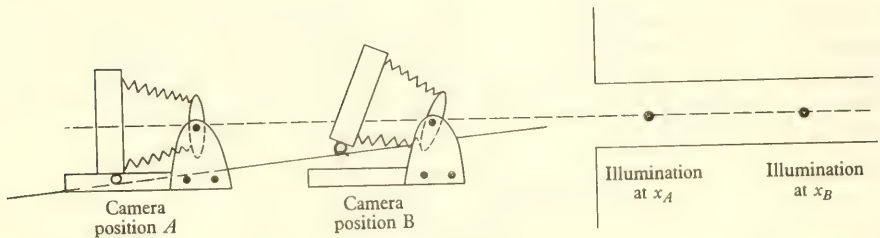


Fig. 2. Geometry for photographing plan form of convection

rod in order to keep the illuminated region in focus. Simultaneously, the back of the camera rolls on an inclined plane since the camera is free to rotate about an axis through its lens. Thus, different regions of the fluid produce images on different parts of the film. In this way, one obtains a picture of the flow pattern as if one were viewing from above.

For each steadily maintained external condition, the steadiness or non-steadiness of the resulting flow was to be determined. This was found to be too difficult by simply observing moving tracers through the fluid since there were gentle time dependencies with time scales of the order of several minutes to several hours. In order to have a record of the flow at an earlier time against which to compare the flow at a later time, the following photographic technique was devised. The apparatus used is shown schematically in Fig. 3. Two narrow overlapping beams of light illuminate aluminum flake tracers along a line in the x -direction, say, through the fluid. The beam remained fixed in space throughout the observation time. The camera was free to rotate about an axis through its lens. With the camera aperture open, a synchronous motor drew a wedge under the back of the camera at a rate determined by the time scale of the time dependence of the flow. Thus, the photograph displays an (x,t) representation of the flow, where t is the time coordinate. At $t = 0$, the camera recorded alternating bright and dark regions, corresponding to the cellular structure, as a narrow strip of image across the film. When the flow was steady, the cell boundaries remained fixed in time, thus producing straight lines parallel to the t -axis on the photograph. With the beam near the top (or bottom) of the convecting layer, the tracer particles have an x -component of velocity which is given by the slope of the trajectories in the (x,t) representation.

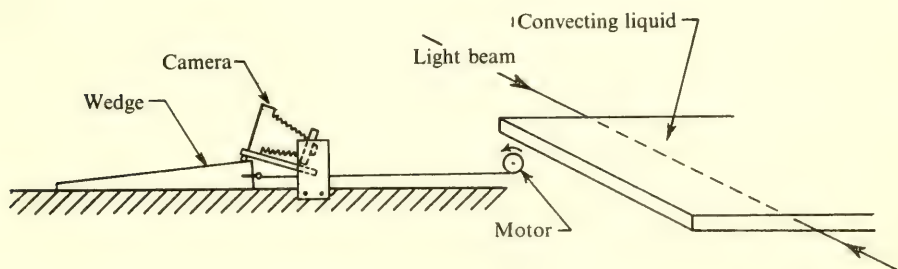


Fig. 3. The apparatus for photographing the time evolution of flow

The studies that will be described here were performed as externally steady, fixed heat flux experiments. Rayleigh number and heat flux were measured for fluids having Prandtl number from 10^{-2} to 10^4 . The Rayleigh number ranged from 10^3 to 10^6 . Except in the cases of air and mercury, the "plan form" of the convection was obtained by viewing from the side. The time dependence was determined by both the (x,t) photographs and thermocouples internal to the fluid. In the cases of air and mercury time dependence was determined only by the internal thermocouples.

The First Transition

In the order of increasing R , the first transition occurs at the well-known critical Rayleigh number R_c . This is a transition from the conduction state to one of steady cellular convection. It occurs independently of the Prandtl number Pr where $Pr = \nu/\kappa$. The nature of the flow and the change in slope of the heat flux curve have been predicted and experimentally verified. For the vertically symmetric problem the only stable finite amplitude solution of the infinite number of possible steady solutions is the two-dimensional roll [Schluter, Lortz and Busse 1965]. With a vertical asymmetry, such as that produced by changing mean temperature or by variation of material properties (ν, κ, α) with temperature, the conduction state is subcritically unstable to finite amplitude disturbance, and the flow near the critical point is hexagonal [Busse 1962; Segel and Stuart 1962; Krishnamurti 1968a,b]. In this discussion we restrict our attention to the case in which rolls are the realized flow just above R_c .

As the heat flux, and hence the Rayleigh number, are increased above R_c , steady two-dimensional rolls continue to be the observed flow up to approximately $12 R_c$, for $10 < Pr < 10^4$. The size of the rolls becomes larger in this range, as shown in Fig. 4, where the wave-number β is plotted against Rayleigh number. This increased size of the cell might be rationalized by an argument such as the following. By averaging over the entire fluid the non-dimensionalized temperature equation in the Boussinesq approximation one finds

$$H = R\sigma_m + \langle w\theta \rangle$$

where H is the dimensionless heat flux, σ_m is the vertical temperature gradient averaged over the entire fluid, w is the vertical velocity, θ is the departure of the temperature from a horizontal average, and brackets indicate averaging over the entire fluid. Thus $R\sigma_m$ is the heat flux due to conduction, $\langle w\theta \rangle$ is the convective heat flux. As the externally imposed heat flux is increased such that R exceeds R_c , the fluid transfers this larger flux through the correlation $\langle w\theta \rangle$. Consider a fluid parcel near the lower boundary. Its temperature θ is limited by the thermal diffusivity of the fluid material. As H is continually increased, the fluid is forced to

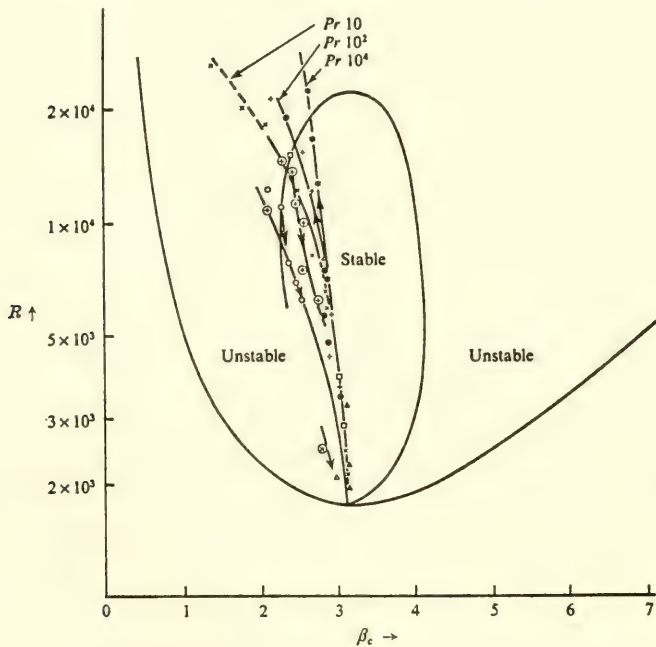
The Second Transition

The only theoretical study of stability of two-dimensional convection in the Rayleigh number range of the second transition is that of Busse [1968]. He shows that for infinite Prandtl number, two-dimensional rolls having wave-number β within a finite band (see Fig. 4) are stable to a restricted class of infinitesimal disturbances provided that $R < 22,600$. If $R > 22,600$ rolls are unstable for all β . Busse shows further that the roll plan form is then unstable to a disturbance of rectangular form with one side along the original roll axis. It is not known from this theory whether the resulting flow above 22,600 is steady. It is also not known how the selection of β from this band of possible wave-numbers occurs.

Laboratory studies [Krishnamurti 1970a] show that two-dimensional rolls do indeed become unstable near this Rayleigh number, which will be labelled R_{II} . The "plan forms" (obtained from the side) are shown in Fig. 5a where that on the left shows rolls below R_{II} , that on the right shows the flow pattern above R_{II} . The three-dimensional disturbance that forms on the rolls above R_{II} is consistent with Busse's instability to a rectangular disturbance. Since the method of photography displays regions of strong shear, the hypotenuse of the rectangle should appear bright. Thus, the nature of the growing mode (which is found experimentally to attain a steady state) is in agreement with Busse's result. It may be noted that the rectangular disturbance of his theory is one with symmetry in the vertical. The point of transition is also in good agreement with that computed by Busse, for that wave-number β which occurs in the experiment. Figure 5b shows the same transition when a circular boundary of plexiglass has been inserted into the rectangular region. Both Davis [1967] and Segel [1969] show that spatially modulated rolls will line up with their axes parallel to the short side of a rectangular container. In the almost square container, there appeared to be little preference of orientation of the rolls; rolls were seen along the line of sight as well as perpendicular to the line of sight in two different repetitions of the same experiment. The preference of rolls to line up with their axes parallel to the short side may be re-expressed as a preference of the rolls to meet the boundaries rather than lie along the boundaries. This effect is displayed in Fig. 5b. Presumably circular rolls did not develop because the plexiglass has thermal conductivity so close to that of the fluid that there was negligible distortion of the conduction temperature field and no fringing of the isotherms since there was fluid outside of the ring.

Associated with this change from steady two-dimensional to steady three-dimensional flow, there is observed a discrete change in slope of the heat flux curve (Fig. 5a). This corresponds to the second change of slope observed by Malkus [1954]. R_{II} showed no

move more rapidly to transport this increased heat flux. If the fluid must move faster, then the cells must be larger in order to allow the hot rising fluid to be in the vicinity of the cold upper boundary for a sufficiently long time to lose its heat before sinking and repeating the process. Although there are many ways in which the fluid could have transferred the increased heat flux, moving more rapidly with increased cell size is one of them. Of course, if the cells become very large, the viscous dissipation of energy near the horizontal boundaries would slow down the flow and defeat its own purpose. This will be discussed later. It is seen in Fig. 4 that, when the cell size is allowed to evolve freely (without being forced as in the experiments of Chen and Whitehead [1968]), approximately one-half of Busse's stability diagram is filled with observations, but the domain $\beta > \beta_c$ is conspicuously bare.



	d (cm)	R increasing	R decreasing
Pr 6.7	1.2	\times	\otimes
Pr 57	2	\square	
Pr 10^2	2	$+$	\oplus
Pr 0.86×10^3	3	\bullet	\circ
Pr 1.7×10^3	5	\blacktriangle	\triangle
Pr 0.85×10^4	2	\star	

Fig. 4. The observed cell size plotted on Busse's stability diagram for two-dimensional rolls

The Second Transition

The only theoretical study of stability of two-dimensional convection in this Rayleigh number range is that of Busse [1968]. He shows that for infinite Prandtl number, two-dimensional rolls having wave-number β within a finite band (see Fig. 4) are stable to a restricted class of infinitesimal disturbances provided that $R < 22,600$. If $R > 22,600$ rolls are unstable for all β . Busse shows further that the roll plan form is then unstable to a disturbance of rectangular form with one side along the original roll axis. It is not known from this theory whether the resulting flow above 22,600 is steady. It is also not known how the selection of β from this band of possible wave-numbers occurs.

Laboratory studies [Krishnamurti 1970a] show that two-dimensional rolls do indeed become unstable near this Rayleigh number, which will be labelled R_{II} . The "plan forms" (obtained from the side) are shown in Fig. 5a where that on the left shows rolls below R_{II} , that on the right shows the flow pattern above R_{II} . The three-dimensional disturbance that forms on the rolls above R_{II} is consistent with Busse's instability to a rectangular disturbance. Since the method of photography displays regions of strong shear, the hypotenuse of the rectangle should appear bright. Thus, the nature of the growing mode (which is found experimentally to attain a steady state) is in agreement with Busse's result. It may be noted that the rectangular disturbance of his theory is one with symmetry in the vertical. The point of transition is also in good agreement with that computed by Busse, for that wave-number β which occurs in the experiment, although the selection mechanism of that β is not understood. Figure 5b shows the same transition when a circular boundary of plexiglass has been inserted within the rectangular region. Both Davis [1967] and Segel [1969] show that spatially modulated rolls will line up with their axes parallel to the short side of a rectangular container. In the almost square container, there appeared to be little preference of orientation of the rolls; rolls were seen along the line of sight as well as perpendicular to the line of sight in two different repetitions of the same experiment. The preference of rolls to line up with their axes parallel to the short side may be re-expressed as a preference of the rolls to meet the boundaries rather than lie along the boundaries. This effect is displayed in Fig. 5b. Presumably circular rolls did not develop because the plexiglass has thermal conductivity so close to that of the fluid that there was negligible distortion of the conduction temperature field and no fringing of the isotherms since there was fluid outside of the ring.

Associated with this change from steady two-dimensional to steady three-dimensional flow, there is observed a discrete change in slope of the heat flux curve (Fig. 5). This corresponds to the second change of slope observed by Malkus [1954]. R_{II} showed no

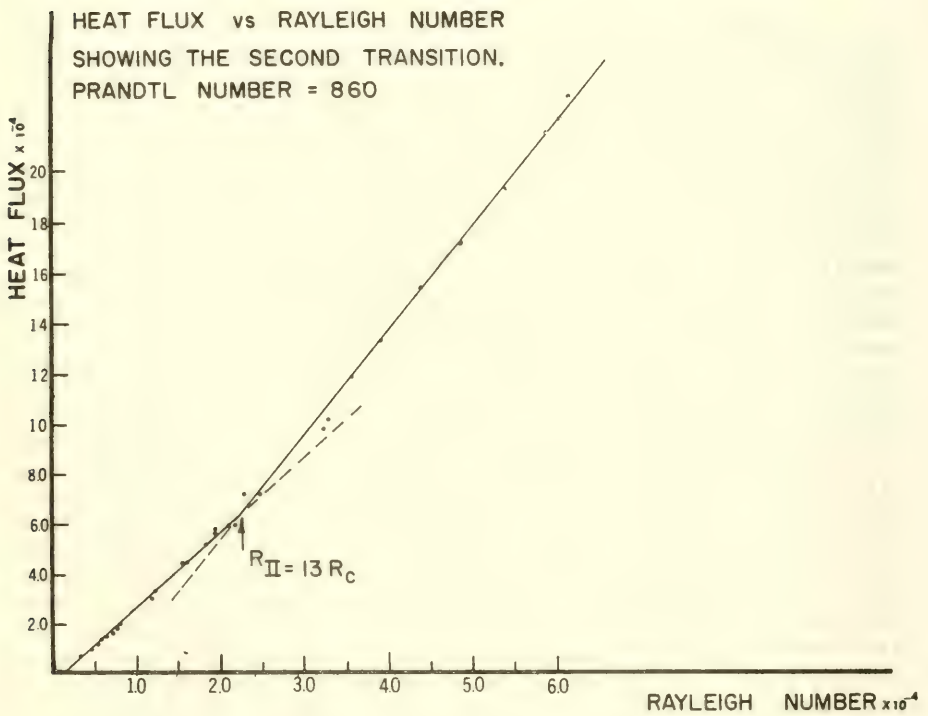
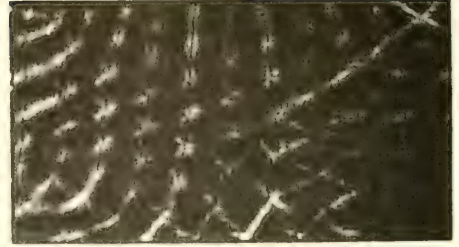
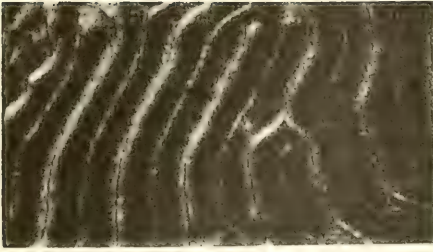


Fig. 5a. Heat flux plotted against Rayleigh number showing the second transition. Photographs show the corresponding change in plan form. The Prandtl number is 860.

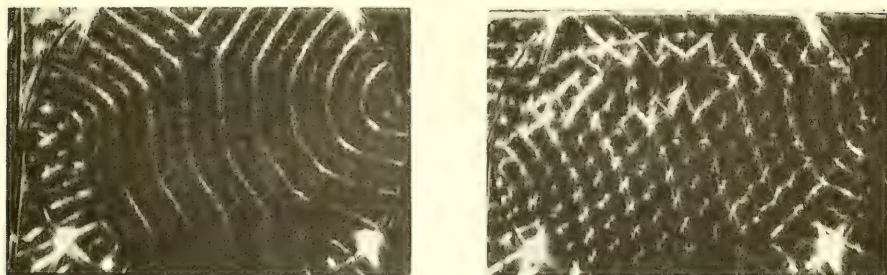


Fig. 5b. Photographs showing the plan form within circular side walls. The transition is the same as in Fig. 5a. The Prandtl number is 860.

definite Prandtl number dependence in the range $10 < \text{Pr} < 10^4$. There was a marked hysteresis both in the heat flux and plan form as the Rayleigh number was increased then decreased past R_{II} . This transition is shown by the curve labelled II in the régime diagram (Fig. 10).

The Third Transition

The third transition in order of increasing R occurs at a Rayleigh number which will be labelled R_{III} . It marks a change from steady three-dimensional to time-dependent flow, and has associated with it a discrete change in slope of the heat flux curve (Fig. 6) [Krishnamurti, 1970b]. The change in slope was measured for each of the fluids shown in Fig. 10, with $10^{-2} < \text{Pr} < 10^4$. The transition point is labelled as curve III. For Rayleigh numbers above this curve the flow showed two modes of time dependence. The one is a slow time dependence with time scale of the order of the thermal diffusion time d^2/κ . An (x,t) photograph showing this mode is seen in Fig. 8. The light beam was near the bottom of the fluid. It is a slow tilting of the cell with height. Below R_{III} there was never a noticeable tilt observed. Above R_{III} some cells would be tilted for times of the order of d^2/κ . Fig. 9 shows streak photographs of tracer particles in a vertical slice through the convecting fluid. Figure 9a shows steady flow in cells of rectangular cross section at Rayleigh number R_c and $\text{Pr} = 860$. Figures 9b and 9c show tilted cells at Rayleigh number $74 R_c$ and $89 R_c$, respectively, and $\text{Pr} = 860$. The tilted cells often occurred in pairs with the tilt always such that two rising particles were close together near the bottom boundary, flaring apart near the top. Two sinking particles were close together near the top, flaring apart near the bottom. Untilted cells, as in Fig. 9a are symmetrical about a horizontal line at mid-depth in the fluid. When integrated over the cell, the net vertical transport of the x -component of velocity, $\langle uw \rangle$ is zero.

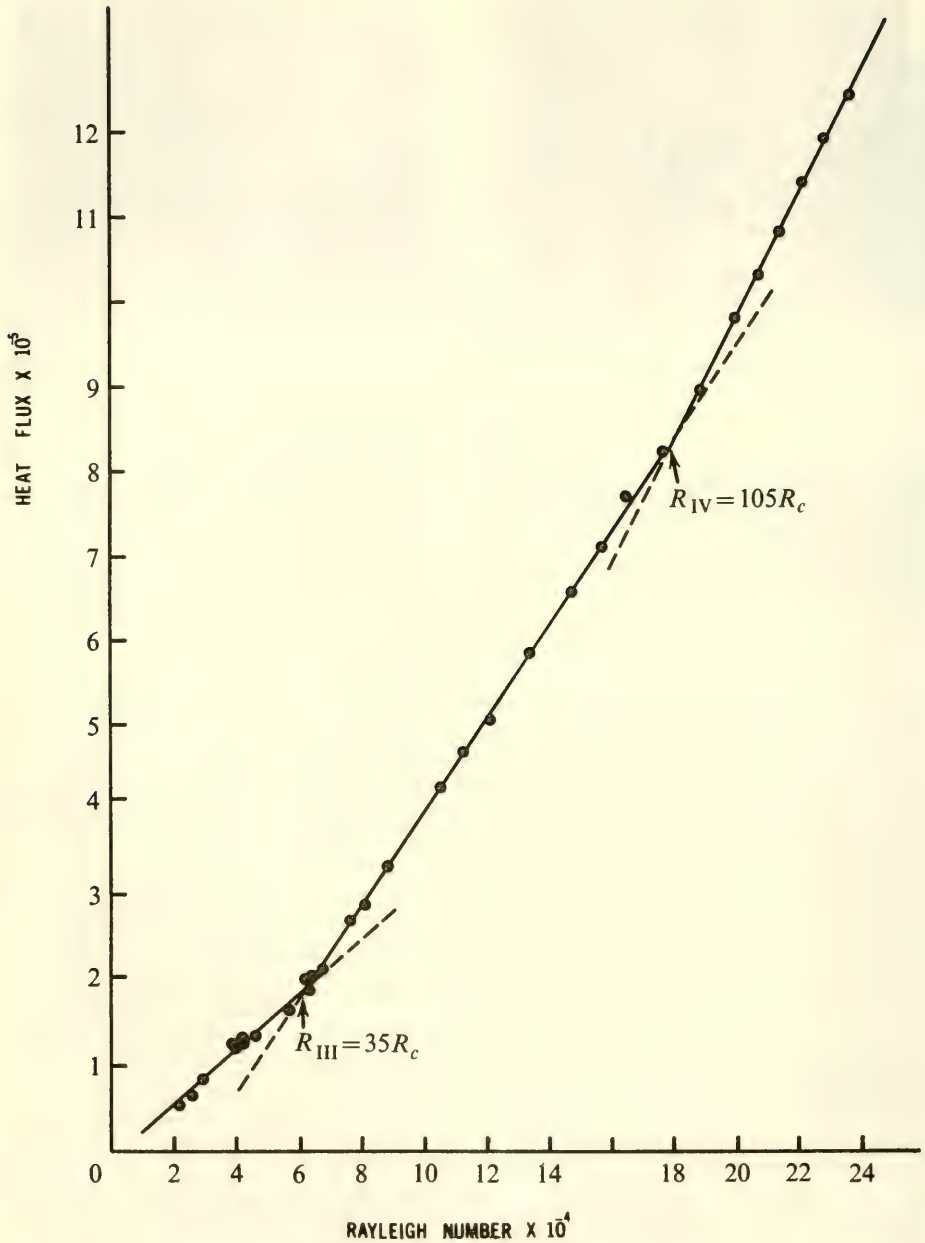
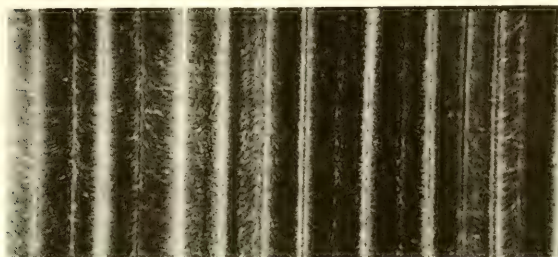
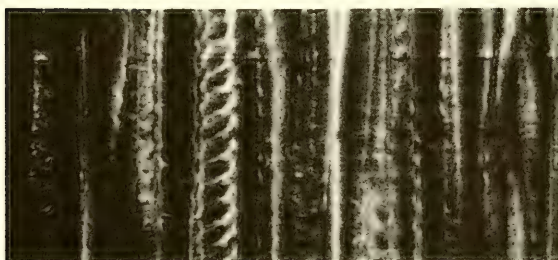


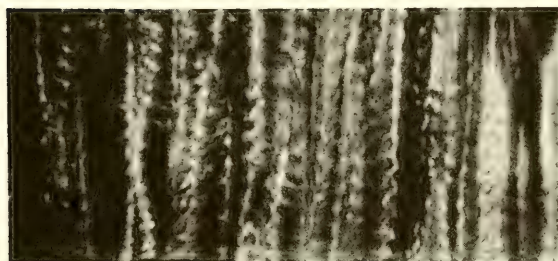
Fig. 6. Heat flux vs. Rayleigh number showing the third and fourth transitions. Prandtl number = 102.



a



b



c

Fig. 7. (x,t) photographs of convective flow. The position x through the tank is along the abscissa; the total width of the photograph represents 48 cm through the fluid. The time t is along the ordinate. The Prandtl number is 57.

- (a) $R = 28 R_c$; the total time is 17 minutes
- (b) $R = 200 R_c$; the total time is 17 minutes
- (c) $R = 335 R_c$; the total time is 15 minutes

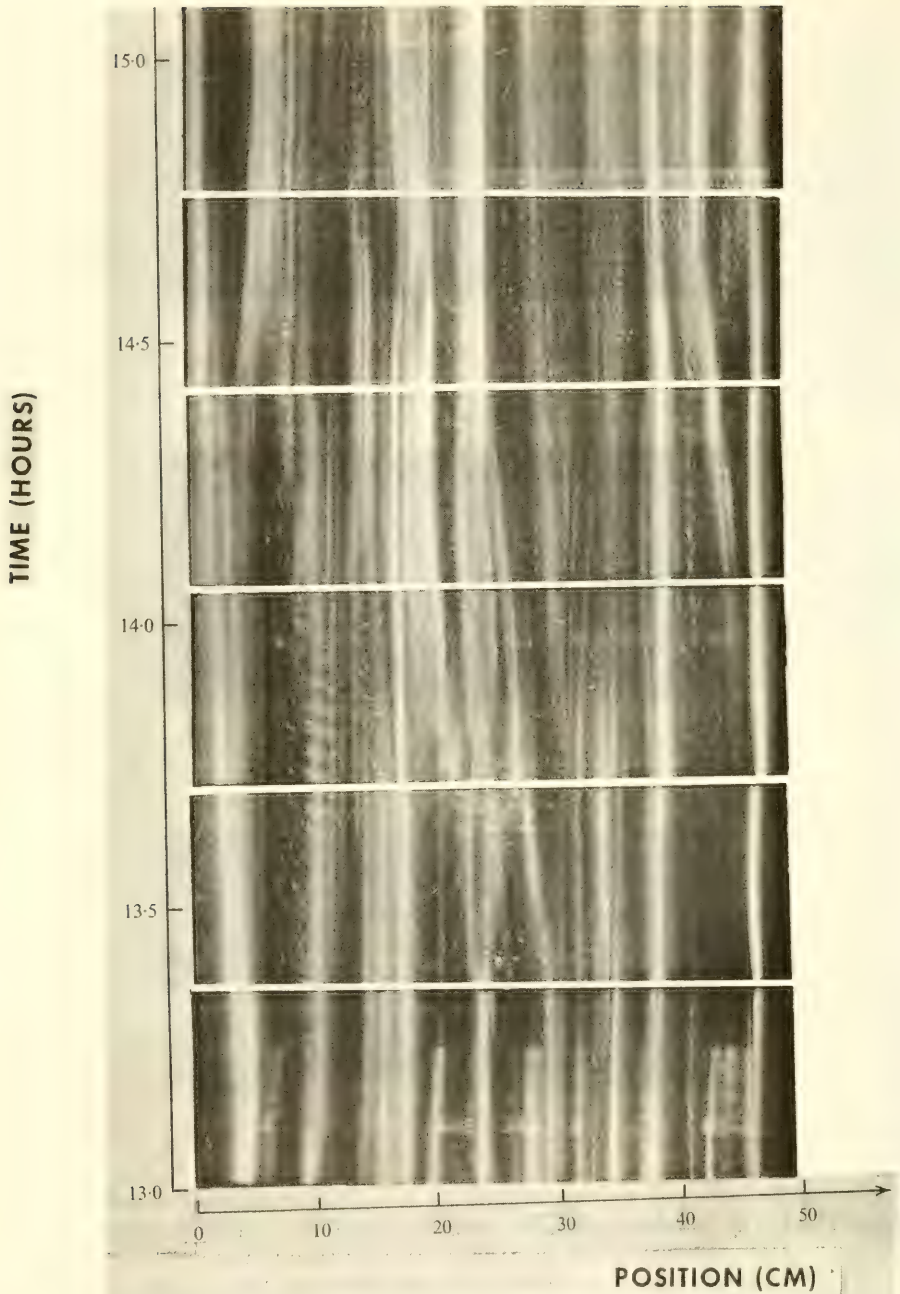


Fig. 8. (x, t) photograph at $45 R_c$, showing the slow time dependence corresponding to the tilting of the cells. The light beam is near the bottom of the fluid layer. The Prandtl number is 57.

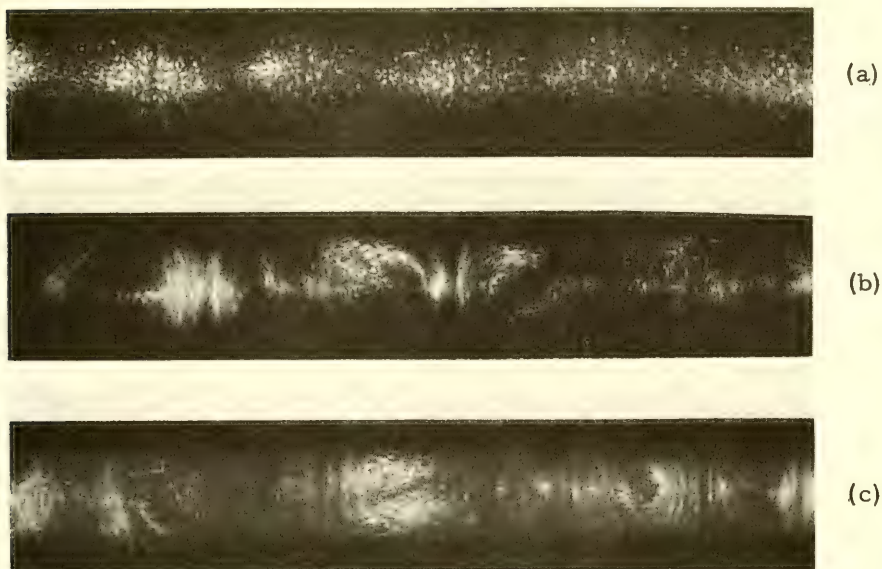


Fig. 9. Streak line photographs of tracers in a vertical slice through the convecting fluid. The Prandtl number is 860. (a) a vertical slice through steady two-dimensional rolls at $R = 6 R_c$. (b) Showing a pair of cells with a tilt relative to the vertical. $R = 74 R_c$. (c) Showing a tilted cell at $R = 89 R_c$.

In case of the tilted cells, however, $\langle uw \rangle$ over one cell is non-zero and is always in the sense of transporting positive x -component of momentum to regions where the flow is in the positive x -direction, transporting negative x -component to regions where the flow is in the negative x -direction. Again one might rationalize the increased slope of the heat flux curve by the following argument. As the externally imposed heat flux is increased more and more, the fluid must move faster and faster. Then, to accomplish the heat exchange at the boundaries, the cells must become wider and wider. The tilting of the cells can help to maintain this flow against the increased viscous dissipation along the boundaries. The tilting of cumulus convection cells in the earth's atmosphere has often been related with a vertical wind shear. The tilted cell is believed to be important in transporting momentum in the vertical direction, thus maintaining the wind aloft. It is interesting to note that in this laboratory situation convection cells tilt even in the absence of a mean wind shear.

The second mode of time dependence is an oscillatory mode with a much shorter time scale. Figure 7 shows (x, t) photographs taken with the light beam near the bottom of the layer of fluid. Figure 7b shows a bright region, which is a region of strong shear, move from one cell boundary to another. This process is repeated periodically in time. (x, t) photographs synchronized with a tem-

perature record at a point within the fluid showed a temperature anomaly each time a bright region moved pass the point. It is an oscillation in the sense that the temperature and flow show a time periodicity at a fixed point in the fluid. This oscillatory mode is illustrated in the following movie which shows convection in a Hele-Shaw cell having dimensions 24 in. wide, 2 in. tall, and 1/16 in. thick (that is 1/16 in. in the direction of the line of sight). It shows hot spots and cold spots (bright regions) forming and being advected by the mean circulation of the cell.

As the Rayleigh number is increased transition to turbulence appears to result from the increased number and frequency of these oscillations.

III. TRANSITION TO TURBULENT CONVECTION IN A ROTATING FLUID LAYER

This topic will be discussed very briefly. A horizontal layer of fluid heated below and cooled above is rotated about a direction parallel to the force of gravity. The linear stability theory has been treated by Chandrasekhar [1961]. The finite amplitude theory with very clear physical explanations is given by Veronis [1959]. Notable experiments have been performed by Fultz and Nakagawa [1955], by Rossby [1966], and others.

Recently, Küppers and Lortz [1969] have shown that for infinite Prandtl number there exists a critical Taylor number T_c beyond which there can be no stable steady convection in the vicinity of R_c . The Taylor number T is defined as

$$T = \frac{4\Omega^2 d^4}{\nu^2}$$

where Ω is the rotation rate, d the layer depth, and ν is the kinematic viscosity. For $T < T_c$ they show that the only stable finite amplitude solution is the two-dimensional roll solution. For $T > T_c$ there must be a transition from the conduction state to a time dependent flow as the Rayleigh number is increased beyond the critical.

The apparatus consisted of a fluid layer 1 or 2 cm in depth, 18 inches in diameter in the horizontal direction. The fluid was bounded below by a 2 in. thick aluminum block containing an electrical heater which is a fine mesh of resistance material. Above the fluid layer was bounded by a glass plate over which the cooling fluid circulated.

Photographs taken from above by a camera rotating with the fluid are shown in Fig. 11. Figure 11a shows rolls, Fig. 11b shows the cross instability forming on the rolls, of the same kind found in

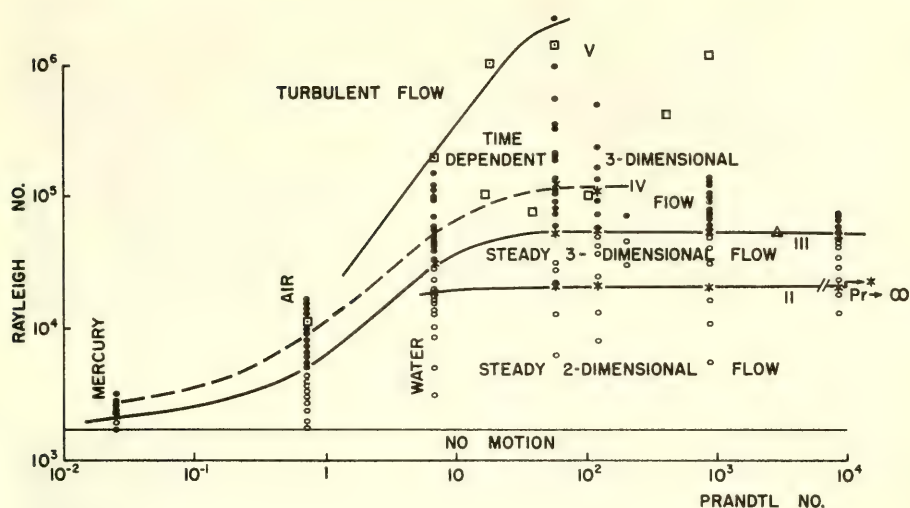


Fig. 10. The régime diagram. The circles represent steady flows, the circular dots represent time-dependent flows. The stars represent transition points. The open squares are Rossby's observations of time-dependent flow, the squares with a dot in the centre are Willis and Deardorff's observations [1967b] for turbulent flow. The triangle is Silveston's [1958] point of transition to time-dependent flow.

the non-rotating case. Figure 11c shows the break-down of rolls and waves forming on them. The disturbance forms an angle of $58^\circ \pm 2^\circ$ to the original roll axis, exactly as predicted by Kuppers and Lortz. Figure 11c is a transient state; 11d is the final steady state. In this state the over-all wavy pattern was not observed to change with time but the internal striations representing regions of strong shear were seen to change with a time scale of the order of one minute. (Here $d^2/\nu = 40$ sec, $d^2/\kappa \approx 1$ hr). Figure 12 shows the régime diagram for the rotating convection. The observed critical Taylor numbers compare only approximately with those computed by Kuppers [1970] for finite Prandtl number and rigid boundaries. The observed transitions occurred at $T_c = 1.5 \times 10^2$ for $Pr = 6.7$, $R \approx R_c$ and at $T_c = 7 \times 10^2$ for $Pr = 10^2$, $R \approx R_c$. The predicted values are $T_c = 7 \times 10^2$ for $Pr = 1$, $T_c = 1.7 \times 10^3$ for $Pr = 5$, and $T_c \approx 2 \times 10^3$ for $Pr \rightarrow \infty$.

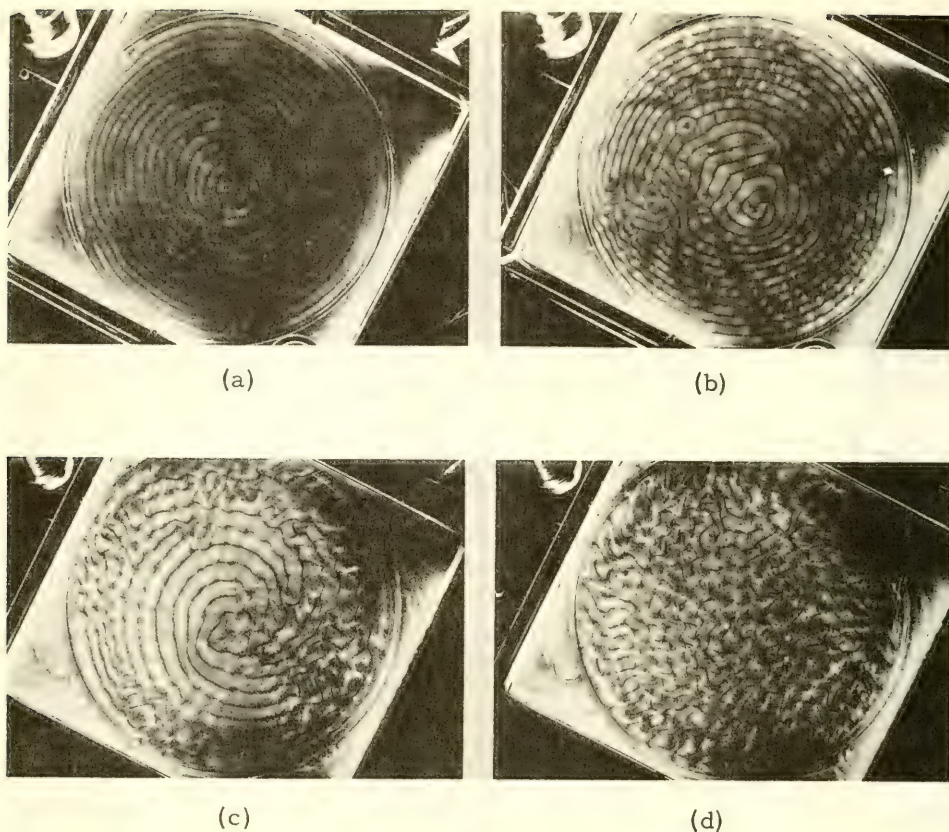


Fig. 11. Rotating Benard Convection, showing cross and wave instabilities on rolls

- (a) $R = 1.2 R_c$, $T = 1.1 \times 10^2$, $Pr = 6.7$ rolls
- (b) $R = 9.2 R_c$, $T = 1.1 \times 10^2$, $Pr = 6.7$; cross instability
- (c) $R = 2.1 R_c$, $T = 2.7 \times 10^3$, $Pr = 10^2$; showing the developing of waves
- (d) $R = 2.1 R_c$, $T = 2.7 \times 10^3$, $Pr = 10^2$, showing developed waves

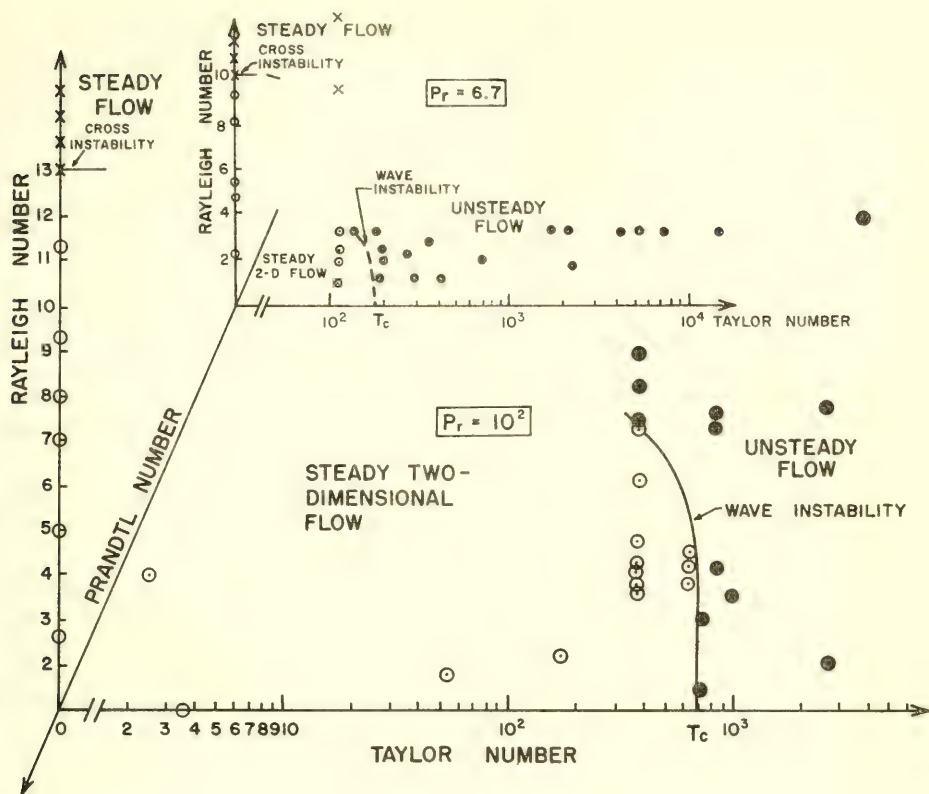


Fig. 12. The régime diagram for rotating Bénard convection

IV. SUMMARY AND CONCLUSIONS

Series of externally steady, fixed heat flux experiments were performed to measure Rayleigh number, heat flux and changes in flow of horizontal, non-rotating convection for $2.5 \times 10^{-2} \leq Pr \leq 0.85 \times 10^4$ and $10^3 < Ra < 10^6$. The régime diagram summarizing these experiments is shown in Fig. 10. Each of the curves I, II, III and IV marks a transition with a change of slope in the heat flux curve. The first is the transition from the conduction state to one of steady two-dimensional convection in the form of rolls.

There is a second transition characterized by the following properties:

- (i) There is a discrete change of slope of the heat flux curve at Rayleigh number R_{II} near $12 R_c$, showing no definite Prandtl number dependence in the range $10 < Pr < 10^4$.

- (ii) There is a change in the flow pattern from two-dimensional rolls to a three-dimensional flow which is periodic in space and steady in time. The change occurs at a Rayleigh number coinciding with R_{II} to within the error in determining R_{II} .
- (iii) There is hysteresis in the heat flux as well as in the flow pattern as R is increased from below or decreased from above, indicating that the transition is caused by a finite amplitude instability.

The third transition is indicated by curve III in Fig. 10. Above this curve, the flow is time dependent with a slow tilting of the cell in the vertical and a faster oscillation which has the nature of hot or cold spots advected with the mean flow. Transition to disorder is seen to result from an increased number and frequency of such oscillations.

Higher transitions observed by Malkus [1954] and confirmed by Willis and Deardorff [1967a] have not been discussed.

The small amplitude nonlinear theories have been quite successful in a small neighborhood of the critical point R_c . The observation that transition to turbulence occurs near R_c for small Prandtl number in non-rotating convection, and for $T > T_c$ for rotating convection, indicates the possibility of gaining further understanding of transition to turbulence through the nonlinear theories.

The research reported here was supported by the Office of Naval Research Contract N-00014-68-A-0159 and by grant number GK-18136 from the National Science Foundation.

REFERENCES

- Busse, F. H., Dissertation, University of Munich. (Translation from the German by S. H. Davis, the Rand Corporation, Santa Monica, California, 1966), 1962.
- Busse, F. H., "On Stability of Two-Dimensional Convection in Layer Heated from Below," *J. Math. and Physics*, 46, 140, 1968.
- Chandrasekhar, S., Hydrodynamic and Hydromagnetic Stability, Oxford, 1961.
- Chen, M. M. and Whitehead, J. A., "Evolution of Two-Dimensional Periodic Rayleigh Convection Cells of Arbitrary Wave-Numbers," *J. Fluid Mech.*, 31, 1, 1968.
- Davis, S. H., "Convection in a Box: Linear Theory," *J. Fluid Mech.*, 30, 465, 1967.

- Fultz, D. and Nakagawa, Y., "Experiments on Oven Stable Thermal Convection in Mercury," *Proc. Roy. Soc. A.* 231, 198, 1955.
- Krishnamurti, R., "Finite Amplitude Convection with Changing Mean Temperature, Part I, Theory," *J. Fluid Mech.*, 33, 445, 1968a.
- Krishnamurti, R., "Finite Amplitude Convection with Changing Mean Temperature, Part 2, An Experimental Test of the Theory," *J. Fluid Mech.*, 33, 457, 1968b.
- Krishnamurti, R., "On the Transition to Turbulent Convection, Part I, The Transition From Two- to Three-Dimensional Flow," *J. Fluid Mech.*, 42, 295, 1970a.
- Krishnamurti, R., "On the Transition to Turbulent Convection, Part 2, The Transition to Time Dependent Flow," *J. Fluid Mech.*, 42, 309, 1970b.
- Küppers, G. and Lortz, D., "Transition From Laminar Convection to Thermal Turbulence in a Rotating Fluid Layer," *J. Fluid Mech.*, 35, 609, 1969.
- Küppers, G., private communication, 1970.
- Lee, W. H. K. and Uyeda, S., *Terrestrial heat flow*, Washington, D.C., pp. 87-190. (American Geophysical Union, Geophysical Monograph series no. 8), 1965.
- Malkus, W. V. R., "Discrete Transitions in Turbulent Convection," *Proc. Roy. Soc. A* 225, 185, 1954.
- Rossby, H. T., Dissertation, M.I.T., 1966.
- Schluter, A., Lortz, A. and Busse, F., "On the Stability of Steady Finite Amplitude Convection," *J. Fluid Mech.*, 23, 129, 1965.
- Segel, L. A., "Distant Side-Walls Cause Slow Amplitude Modulation of Cellular Convection," *J. Fluid Mech.*, 38, 203, 1969.
- Segel, L. A. and Stuart, J. T., "On the Question of the Preferred Mode in Cellular Thermal Convection," *J. Fluid Mech.*, 13, 289, 1962.
- Silveston, P. L., *Forch. Ing. Wes.* 24, 29-32, 59-69, 1958.
- Veronis, G., "Cellular Convection with Finite Amplitude in a Rotating Fluid," *J. Fluid Mech.*, 5, 401, 1959.

- Willis, G. E. and Deardorff, J. W., "Development of Short-Period Temperature Fluctuations in Thermal Convection," *Phys. Fluids*, 10, 931-937, 1967a.
- Willis, G. E. and Deardorff, J. W., "Confirmation and Renumbering of the Discrete Heat Flux Transitions of Malkus," *Phys. Fluids*, 10, 1861, 1967b.

TURBULENT DIFFUSION OF TEMPERATURE AND SALINITY: — AN EXPERIMENTAL STUDY

Allen H. Schooley
*U.S. Naval Research Laboratory
Washington, D.C.*

ABSTRACT

Stratified temperature and salinity conditions in water have been established in a small laboratory tank. A method for making measurements and calculating the eddy diffusivities of temperature and salinity for different controlled levels of turbulence are described. The ratio of temperature and salinity molecular diffusivities is on the order of 100. The ratio of temperature and salinity eddy diffusivities, for the most turbulent conditions studied, is 14.

The dissipation of turbulent power density (P) due to viscous friction was found to be on the order of 10^7 larger than the power density (P') consumed in changing the thickness of the pycnocline. The experiments hint that P/P' may be relatively constant over a range of turbulence. If this is assumed to be true, there exists the possibility of estimating temperature (D) and salinity (D') eddy diffusivities by knowing the change of density, $(\Delta\rho)_T$ and $(\Delta\rho)_S$, with time (Δt) for a given depth difference (Δh) . Plots of D and D' in cm^2/sec vs. $(P'/\eta)^{1/2} = 110(\Delta\rho/\Delta t)^{1/2}(\Delta h)$ in sec^{-1} , are shown where (η) is the dynamic viscosity of water.

I. INTRODUCTION

The oceans are dominated by several turbulent processes. For each turbulent situation there are "eddy" diffusivities of temperature and salinity that are much larger than the molecular diffusivities. In spite of the difficulties in measuring eddy diffusivities at sea, there is considerable, though incomplete, literature on the subject [Neumann and Pierson, 1966]. Since turbulent ocean processes are inherently uncontrollable, several exploratory laboratory experiments were conducted in late 1964 and early 1965. This paper is the first publication of the results of these preliminary experiments.

II. APPARATUS.

Figure 1 shows the test cell where the experiments were conducted. It has transparent plastic walls and is 30 cm long, 9 cm high, and 2.5 cm thick. The bottom 4 cm was filled with either room temperature distilled water or a 0.25% solution of sodium chloride, depending whether thermal or salinity diffusion was to be studied. The molecular thermal diffusivity of pure water at atmospheric pressure and 20°C is $0.00143 \text{ cm}^2/\text{sec}$ (4% less than sea water). The molecular diffusivity of an aqueous NaCl solution is $0.0000141 \text{ cm}^2/\text{sec}$ (9% less than sea water) according to Hill [1962]. Convenient distilled water and NaCl solutions were used instead of sea water because of these relatively small differences.

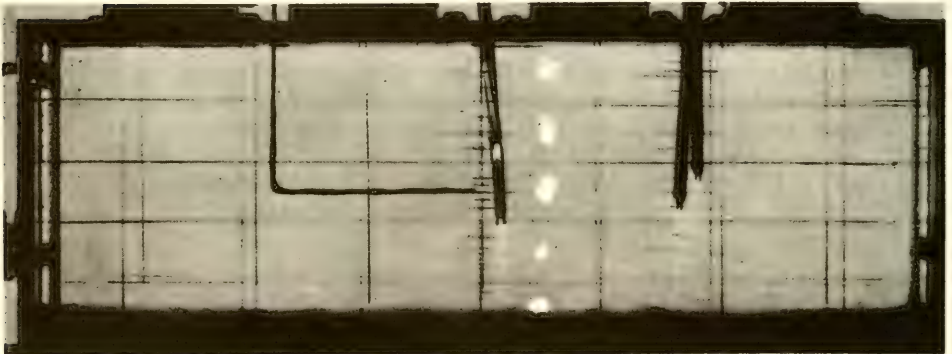


Fig. 1. Experimental cell. Temperature difference sensor near center. Salinity difference sensors at right. L shaped wire at left produces turbulence on demand.

When a thermal experiment was to be conducted, the top 4 cm of the cell was filled with water having a temperature several degrees above room temperature. A thin piece of balsa wood was floated on the top of the bottom layer and warm water introduced through a small nozzle directed perpendicularly to the top of the balsa wood. This procedure deflects the downward momentum of the warm water flow to the horizontal and filling was accomplished with a minimum of vertical mixing with the cooler more dense water below. When a salinity diffusion experiment was to be conducted, a top layer of pure water was introduced the same way. In this case the bottom water contained the salt solution.

A repeatable amount of turbulence was introduced by mechanically moving a stiff insulated wire back and forth at the interface between the two layers at a controlled rate and for a controlled length of time. The wire is shown in Fig. 1 at the 4 cm level where the interface was located when the cell was filled. (The cell is empty in Fig. 1.) The top of the "L" shaped wire is coupled to a mechanical system outside the picture. It is the bottom part of the "L" that was rotated back and forth laterally at the interface producing turbulence when desired. Table I gives the specifications for generating the amounts of turbulence that were used.

Table I. Specifications of the Turbulence Generator

Turbulence No.	Mixer Dimensions	Angle of Swing	Swings Per Sec
0	-	0	0
1	1.8 mm diam, 7 cm long	10.8°	2.5
2	"	"	5.4

When a thermal experiment was being conducted, the center sensor was used. It consists of a two element copper-constantan thermopile with junctions 2 cm apart. The upper junction was placed 1 cm above and the other 1 cm below the interface of the upper warm and the lower cooler water. The output of this sensor was 30 microvolts for each degree difference in temperature. It was connected to a small commercial micro-voltmeter and recorder which gave a time record of the temperature difference, 1 cm above and 1 cm below the interface. The record of vertical temperature difference decay, with time, gives data related to the effect of molecular diffusion when no turbulence is introduced. The vertical temperature difference decay, with controlled amounts of turbulence, was recorded by using a succession of carefully timed turbulent pulses interspaced with short intervals of quiescence.

When a salinity diffusion experiment was being conducted the two sensors on the right in Fig. 1 were used. They are identical

probes consisting of two closely spaced platinum wires set in epoxy. The conductivity of the solution at the points where each of the probes were located was read from a meter scale. The upper probe was placed one half cm above the interface and the other one half cm below. Standard salt solutions were used to calibrate the conductivity of the probes in order to measure salinity. This calibration was non-linear and temperature corrections were necessary.

Figure 2 illustrates the technique that was devised to facilitate measuring eddy diffusivity by the use of a series of turbulent pulses of the same amplitude and time. The ordinate of this chart is a record of the temperature difference (0 to 1.67°C/cm) measured by the thermopile shown in Fig. 1 vs. time, which progresses from left to right. The record starts at the upper left corner where the temperature difference starts to decrease due to molecular diffusion. At horizontal chart position #5 the mixer shown in Fig. 1 was activated for 15 seconds and then stopped for about 8 minutes. This 8 minute pause allows the pulse generated internal waves to damp out so that the temperature difference due to turbulent eddy diffusion can be measured and separated from the relatively slow molecular diffusion. Again at chart positions #6.4 and #7.8 similar 15 second pulsed of turbulence were introduced. The total time of turbulence was thus only 45 seconds, and three successive temperature differences due to eddy diffusion were recorded at three 15 second intervals of turbulence. The effect of eddy diffusion of NaCl was measured by the same technique using the conductivity sensors.

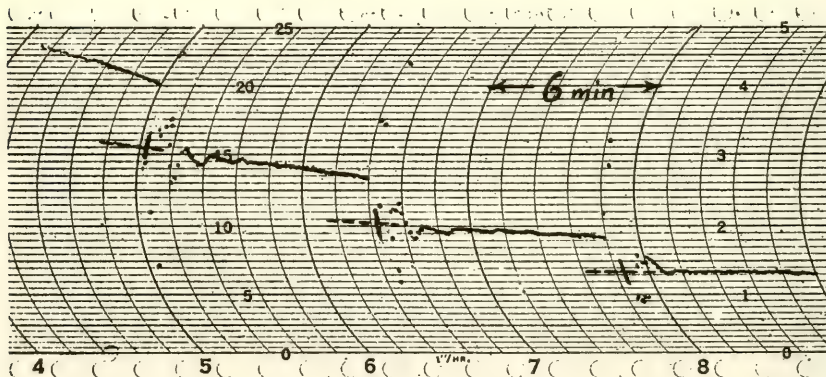


Fig. 2. Temperature difference ΔT vertically vs. time. The decay of ΔT by molecular diffusion is interrupted three times by turbulent pulses lasting 15 sec each.

III. THERMAL DIFFUSION

The model assumed is shown schematically in Fig. 3. At zero time t_0 and depth z_0 , a semi-infinite region of water at the temperature T_2 is assumed to be brought together with a semi-infinite region of water at temperature T_1 . Further, it is assumed that z_0 and T_0 are essentially constant for t_1, t_2, \dots . Eventually as t becomes large, the semi-infinite model breaks down in practice because the effective value of T_0 decreases.

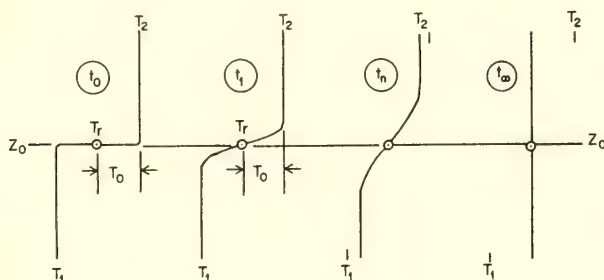


Fig. 3. Schematic presentation of temperature diffusion as a function of water depth z and time t . Semi-infinite depth is presented vertically with z_0 a reference. At time t_0 a sharp temperature discontinuity is assumed, and T_0 defined as $(T_2 - T_1)/2$. At t_1 diffusion has started and T_0 remains constant. For long times t_n, t_∞ the semi-infinite model breaks down because the effective value of T_0 does not remain constant in practice.

The heat flow for this model is governed by the one-dimensional diffusion equation

$$\frac{\partial T}{\partial t} = D \frac{\partial^2 T}{\partial z^2} \quad (1)$$

where D is the diffusivity, usually expressed in cm^2/sec .

Due to vertical symmetry the problem can be formulated using the T_0 part of Fig. 3, where $T_r = (T_1 + T_2)/2$ is the reference temperature. Taking $T_r = 0, z_0 = 0, t_0 = 0$ the initial and the boundary conditions for $z > 0$ and $t = 0$ is $T(z, 0) = T_0 = (T_2 - T_1)/2$. For $z = 0$ and $t > 0$; $T(0, t) = T_r$.

The analytical solution to this well-defined problem is

$$T(z, T) = T_0 [1 - \operatorname{erf}(x/2\sqrt{Dt})] + T_2 \quad (2)$$

where

$$\operatorname{erf}(x/2\sqrt{Dt}) \equiv 2/\sqrt{\pi} \int_0^{x/2\sqrt{Dt}} e^{-u^2} du.$$

From (1) the gradient of T at the boundary z_0 is

$$\left. \frac{\partial T}{\partial z} \right|_{z_0} = \frac{T_0}{\sqrt{\pi Dt}}$$

or

$$\left[\left. \frac{\partial T}{\partial z} \right|_{z_0} \right] = \frac{T_0^2}{\pi D} \left(\frac{1}{t} \right) \quad (3)$$

and

$$D = (T_0^2/\pi) \left[\frac{1}{t} \left/ \left(\left. \frac{\partial T}{\partial z} \right|_{z_0} \right)^2 \right] \quad (4)$$

Since T_0^2/π is constant for any one experiment, a plot of $1/t$ vs. $(\Delta T/\Delta z)^2$ for the data points should give a straight line through the origin with slope $D\pi/T_0^2$. Figure 4 is such a plot for the experiment of Fig. 2. A mean square fit gives a slope of 0.66 with a correlation coefficient of 0.99. Since $T_0 = 2.45^\circ\text{C}$, in this case the eddy diffusivity is $D = 2.45^2(0.66)/\pi = 1.26 \text{ cm}^2/\text{sec}$.

In practice all plots of the experimental data do not yield perfectly straight lines, particularly for larger values of t (smaller values of $1/t$) than are shown in Fig. 4. Calibration and experimental errors are always present. In addition, as is illustrated in Fig. 3, the effective value of T_0 is not constant for extended lengths of time ($t = t_n \rightarrow t_\infty$) because the experiments were necessarily conducted in a finite size container. However, Fig. 4 does represent consistency of the data with the simple analytical theory under the assumptions that have been made.

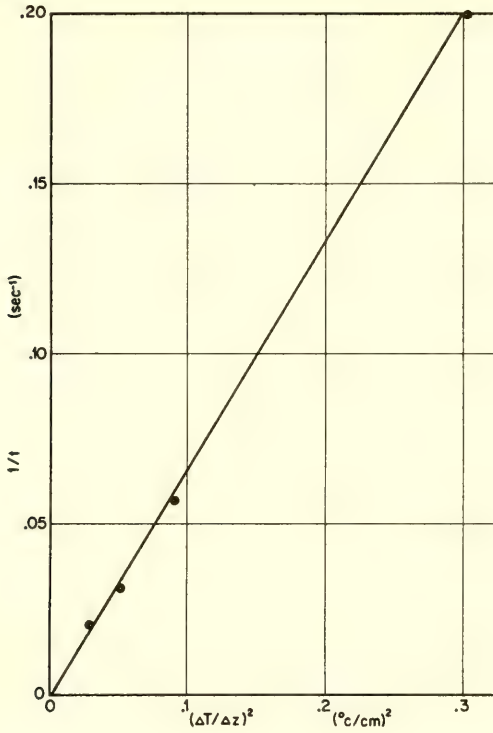


Fig. 4. Sample of experimental data showing $(\Delta T/\Delta z)^2$ is a linear function of $1/t$. This is in accord with theory that diffusivity $D = (T_0^2/\pi) [(1/t)/(\Delta T/\Delta z)^2]$.

IV. SALINITY DIFFUSION

The substitution of S for T in (4) is all that is necessary. Thus

$$D' = (S_0^2/\pi) \left[\frac{1}{t} / \frac{\Delta S}{\Delta z} \right]_{z_0}^2 \tag{5}$$

where D' is the diffusivity of NaCl dissolved in water in cm^2/sec , S , the mass concentration of salt in gm/cm^3 , t , the diffusion time in seconds, z , depth in cm, and S_0 , the initial salinity discontinuity in gm/cm^3 .

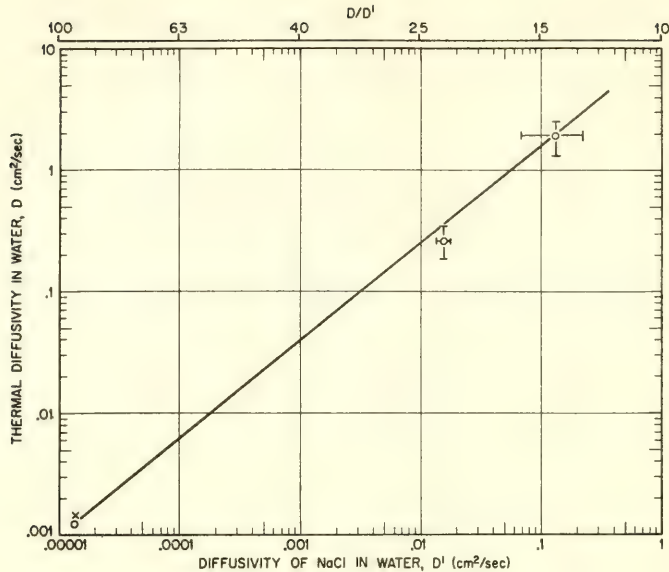


Fig. 5. Thermal diffusivity D vs. diffusivity of NaCl in water D' for zero turbulence at lower left, and increasing turbulence toward the upper right.

V. DISCUSSION OF RESULTS

Figure 5 shows thermal diffusivity D vertically, and salt diffusivity D' horizontally. The point marked (X) at the lower left represents the handbook values for the two molecular diffusivities. The nearby circular point was determined experimentally when the mixer of Fig. 1 was not used. The point nearest the center of Fig. 5 is an average of four experiments using turbulence #1 as listed in Table I. The maximum deviations from the mean are shown. The upper right point is for turbulent condition #2. The mean value was derived from seven experiments. Again maximum deviations from the mean are shown.

In Fig. 5 a straight line has been drawn connecting the molecular diffusivity point with the point of maximum eddy diffusivity. The intermediate point is somewhat below this line but there is clearly not enough experimental data to determine the shape of the curve. At the top of Fig. 5 a scale shows how the ratio of D/D' decrease with increasing turbulence.

Turbulence in a stratified fluid manifests itself in two ways.

There is heat energy liberated due to viscous friction. Also, a part of the turbulent energy is dissipated in changing the potential gravitational energy of the pycnocline by changing its thickness.

The power density associated with a change in potential energy can be shown for water to be approximately

$$P' = \frac{g(\Delta\rho)(\Delta h)^2}{8(\Delta t)} \quad \text{ergs/cm}^3 \text{ sec} \quad (6)$$

where g is acceleration of gravity in cm/sec^2 , $(\Delta\rho)$ is either $(\Delta\rho)_T$ or $(\Delta\rho)_S$ symbolizing the change in density due to temperature or salinity differences across the pycnocline in gm/cm^3 , (Δh) the change in thickness of the pycnocline in cm , and $(\Delta t) = (t_2 - t_1)$ in sec . For turbulence #1, $P'_1 = 0.0074 \text{ ergs/cm}^3 \text{ sec}$. For turbulence #2, $P'_2 = 0.055$.

The power density due to viscous friction P was estimated by measuring the temperature rise in the water due to turbulence #1 and #2 being maintained for measured lengths of time. For turbulence #1 this was about $P_1 = 0.014(10^7) \text{ ergs/cm}^3 \text{ sec}$. For turbulence #2, $P_2 = 0.082(10^7)$.

The ratio of $P_1/P'_1 = 1.9(10^7)$, and $P_2/P'_2 = 1.5(10^7)$. Thus, it appears that the power density due to viscous friction is on the order of 10^7 greater than the power density associated with a change in the pycnocline thickness.

However, the ratios for the two conditions of turbulence are different only by about 25%. This is interesting, for if it should turn out that P/P' is relatively constant over a practical range of turbulence, temperature and salinity diffusivities could be estimated directly from the time rate of change of pycnocline thickness (after internal waves are filtered out). Possible application to the ocean is intriguing.

For physical and dimensional reasons, let us divide P' by the dynamic viscosity of water $\eta = 0.01 \text{ gm/cm sec}$, and take the square root. Equation (6) then becomes

$$(P'/\eta)^{1/2} = 110(\Delta\rho/\Delta t)^{1/2}(\Delta h) \quad 1/\text{sec} \quad (7)$$

This equation contains variables that are relatively easy to measure and has the dimension of vorticity. It is plotted in Fig. 6 for the average values of the variables used in the small scale laboratory experiments.

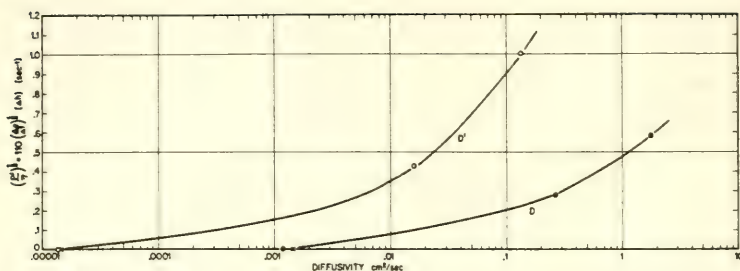


Fig. 6. Tentative extrapolation of experimentally determined diffusion coefficients D and D' vs. variables that are relatively easy to measure at sea.

VI. ACKNOWLEDGMENT

I am grateful to Prof. Håkon Mosby, Geofysisk Institutt, Bergen, Norway, for his interest and early participation in this exploratory project. I am indebted to Albert Brodzinsky, NRL, for applying his skill in mathematics and physics to the problems of data analysis.

REFERENCES

- Neumann, Gerhard, and W. J. Pierson, Jr., Principles of physical oceanography, Prentice-Hall, Englewood Cliffs, N.J., pp. 392-421, 1966.
- Hill, M. N. (Editor), The sea, Vol. 1, Wiley and Sons, N. Y., p. 27, 1962.

SELF-CONVECTING FLOWS

Marshall P. Tulin
Hydronautics, Incorporated
Laurel, Maryland
and
Josef Shwartz
Hydronautics-Israel, Ltd. and
Israel Institute of Technology

ABSTRACT

A theory for the motion of two-dimensional turbulent vortex pairs in homogeneous media has been developed based on separate velocity scaling of the internal and external flow fields involved in the motion and taking into account variations in volume, circulation, momentum, and energy. Based on the results obtained from this theory (I) a simplified theory (II) is derived to deal with the rising motion of turbulent vortex pairs in stratified media. The theoretical results are compared with systematic experimental observations.

In theory (I) the ratio of internal to external velocity scales, ψ , is introduced as an important variable and the theory is specifically derived for the two limiting cases of weak ($\psi \rightarrow 1$) and strong ($\psi \gg 1$) circulation. The weak circulation theory leads to results similar to those obtained in the past using theory based on complete similarity and momentum conservation; i.e., $z \sim t^{1/3}$. The strong circulation theory leads to results which depend very much on the way in which vorticity from the shear layer is ingested into the vortex pair. When ingested so as to cause annihilation (cancellation) of the ingested vorticity, the asymptotic trajectory is $z \sim t^{1/2}$. Under the same conditions the velocity ratio, ψ , increases toward an asymptotic value, and the virtual momentum coefficient for the motion tends to zero. As a result, the asymptotic motion (assuming vorticity annihilation) corresponds to a motion with complete similarity and with energy conservation.

A comparison of experimental observations of rise versus time and radius versus height with theory (I) lend strong support to the strong circulation theory and suggest that ingested vorticity may be largely annihilated.

Based on these finding for homogeneous flows, a simplified theory (II) for stratified media was developed upon the assumptions: (i) the motion is determined by conservation of volume, mass, and energy (neglecting vorticity and momentum); (ii) complete similarity ($dR/dz = \beta$, a constant). Good agreement was found between the predictions of this theory and the results of systematic experiments, and particularly for the maximum rise of height.

NOTATION

a	Density gradient in surrounding fluid, $a = (1/\rho_e)(d\rho_e/dz)$
A	Initial buoyancy parameter (theory), Eq. (44)
A_1	Vorticity mixing coefficient, Eq. (9)
b	Half distance between cores of vortex-pair
B	Stratification parameter (theory), Eq. (45)
c	Constant
C_D	Energy dissipation coefficient
D	Energy dissipation parameter, Eq. (46)
E	Total energy of convected mass
G	Experimental buoyancy parameter, Eq. (44)
j	Geometrical parameter, $j = 0$ for planar geometry, $j = 1$ for axial symmetry
k	Virtual potential energy coefficient, Eq. (38)
k_m	Virtual mass coefficient
K	Virtual kinetic energy coefficient, Eq. (37)
M_z	Vertical component of total momentum
n	Parameter defined by Eq. (47)
r	Radial distance from center of rising mass, $r^2 = \xi^2 + \eta^2 + \zeta^2$
R	Mean radius of rising mass
\bar{R}	Non-dimensional mean radius of rising mass, $\bar{R} = R/R_0$
S	Experimental density stratification parameter, Eq. (53)

t	Time
\bar{t}	Non-dimensional time, $\bar{t} = W_0 t / z_0$
t_{\max}	Time at which the maximum height of rise is reached
u, v, w	Velocity components, see Fig. 14
W	Vertical velocity of rising mass
\bar{W}	Non-dimensional vertical velocity of rising mass, $\bar{W} = W / W_0$
W^*	Vertical velocity of ideal vortex-pair
z	Height of rising mass center above its virtual origin
\bar{z}	Non-dimensional height of rising mass center, $\bar{z} = z / z_0$
z_{\max}	Maximum height reached by rising mass
β	Modified entrainment coefficient
γ	Local vorticity, Eq. (7)
Γ	Total circulation about a single vortex
ξ, η, ζ	Coordinate system, see Fig. 14
ρ	Local density inside convected mass
ρ_e	Density of surrounding fluid
ρ_i	Average density of convected mass, Eq. (43)
$\Delta\rho$	Density difference, $\Delta\rho = \rho_i - \rho_e$
ψ	Velocity ratio, W_i / W_e
μ	Non-dimensional vertical momentum, $(M_z / \rho) / W_{i0} R^2$

Subscripts

$()_0$	Initial conditions
$()_i$	Internal
$()_e$	External

I. INTRODUCTION

Ideal Vortex-Pairs. Flow visualization studies carried out by Scorer [1957], Woodward [1959] and Richards [1965], indicate that the shear layer which is formed between a moving isolated mass of fluid and the stationary surrounding medium tends to roll up and create a flow field which resembles (in two dimensions) the one associated with two line vortices of equal strength but opposite sign, separated by a distance $2b$, so-called "vortex-pairs." The possibility of vortex-pair motions in an inviscid fluid was considered and analyzed over 100 years ago by Sir W. Thomson [1867]. His analysis

applies only to an idealized vortex-pair in which each vortex has a highly concentrated core which is set into motion only by the influence of the other vortex. Such an ideal vortex-pair moves through the surrounding fluid in a direction perpendicular to the plane joining the vortex cores and with a velocity W^* determined only by the pair separation, $2b$, and the circulation about a single vortex, Γ , according to the relation

$$W^* = \frac{\Gamma}{4\pi b} \quad (1)$$

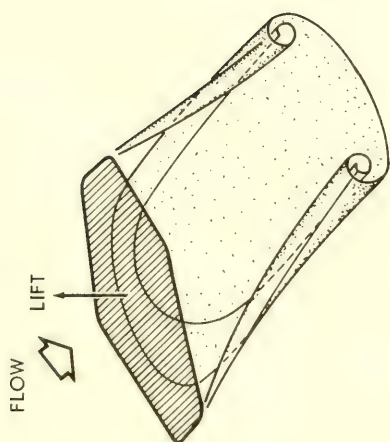
A unique feature of this idealized vortex-pair motion is the existence of a closed streamline and a finite captured mass, as indicated by the oval in Fig. 2a. Thomson [1867] calculated the semi-axes of the oval-shaped captured mass to be $2.09b$ and $1.73b$ so that the cross-sectional area is approximately $3.62\pi b^2$ and the ratio of width to thickness is 1.21.

Under certain circumstances it is entirely possible that carefully balanced vortex-pairs, approximating Thomson's idealization, can be formed. The motion around the vortex centers must be affected by viscosity in a real fluid, but as long as the viscous cores do not extend close to the bounding closed streamline, the flow within and without this streamline may be so closely matched that no large shearing motions or accompanying drag are associated with the motion of the captured mass. In fact, nearly ideal vortex-pairs are sometimes found in the wakes of lifting surfaces, Fig. 1a, and are known as "contrails," see Scorer [1958] and Spreiter and Sachs [1951]. Of course, the concentrated vorticity in the vortex cores tends to diffuse, and does so rapidly when the flow in the core is turbulent.

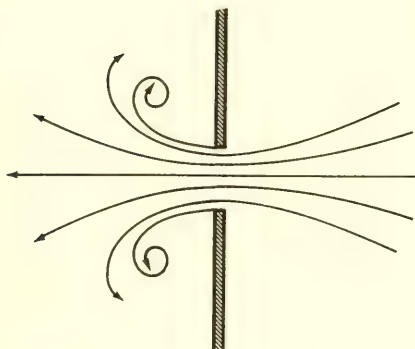
Turbulent Vortex-Pairs. The probable short lifetime of ideal vortex-pairs under turbulent conditions gives special importance to vortex-pairs whose behavior is governed by turbulent entrainment; indeed, it is these kinds of motions which are most commonly observed in nature, as in the case of a mass of fluid forced out rapidly through an aperture, Fig. 1b, or in the convection of isolated masses in nature, Fig. 1c, or in the bent-over and rising chimney plume.

Turbulent vortex-pairs are characterized by the fact that the interior motion does not match the outer flow at the boundary of the captured mass, so that a region of high shear exists there, accompanied by the production of vorticity and by turbulent entrainment. In other words, these vortex-pairs move with a velocity W not equal to the velocity W^* derived from Thomson's model, Eq. (1).

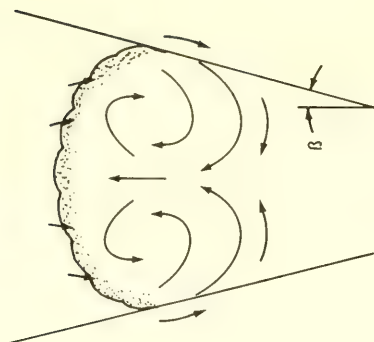
We may, in principle, generalize Thomson's model to consider those cases where the velocity of translation, W , has a more



(a) TRAILING VORTEX SHEET



(b) IMPULSIVE MOTION; FLUID FORCED THROUGH AN APERTURE



(c) FLOW IN AND AROUND NATURALLY OCCURRING THERMALS

Fig. 1. Examples of vortex-pairs

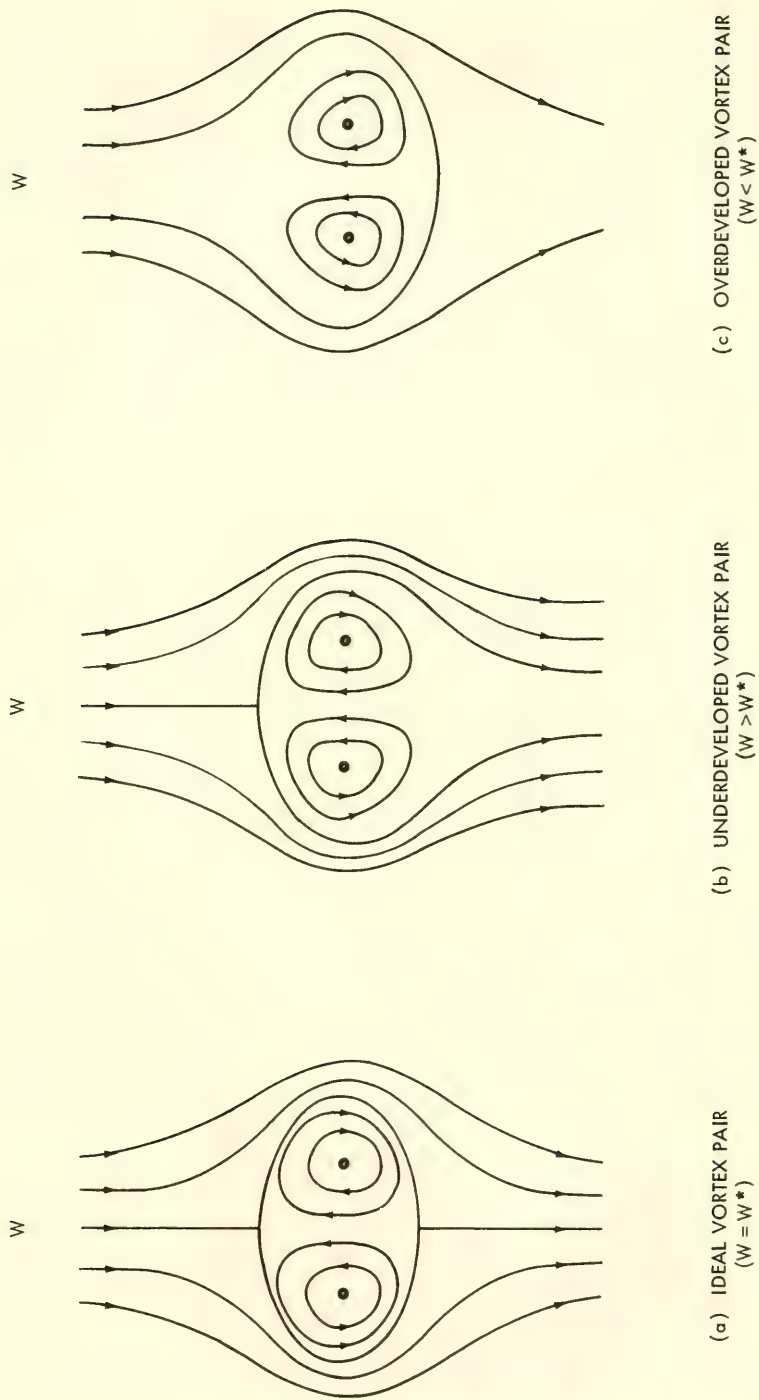


Fig. 2. Generalized vortex-pairs (observer moving with the cores)

general relation to the velocity W^* which characterizes the internal, rotational motions of the vortex-pair. Two distinct cases suggest themselves, in theory. In one case, $W > W^*$, and the convected mass loses volume to the surrounding fluid and continually shrinks in size; we denote this vortex-pair as "underdeveloped," see Fig. 2b. In the other case, $W < W^*$, and the "overdeveloped" vortex-pair gains mass through the entrainment of exterior fluid, Fig. 2c. Of these it is the latter motion which is most commonly observed in nature and forms the main subject of this work.

Within an overdeveloped motion, the velocity at the boundary inside the vortex-pair, as seen by an observer moving with it, will be larger than the velocity of the surrounding fluid just outside the boundary of the pair. Accompanying the velocity gradients thus created across this boundary, shear stresses are exerted by the vortex-pair on the surrounding fluid, resulting in the entrainment of outer fluid and a general increase in the volume of the convected mass, see Fig. 3. Within the high shear zones at the boundary on either side vorticity of sign opposite to that within the respective

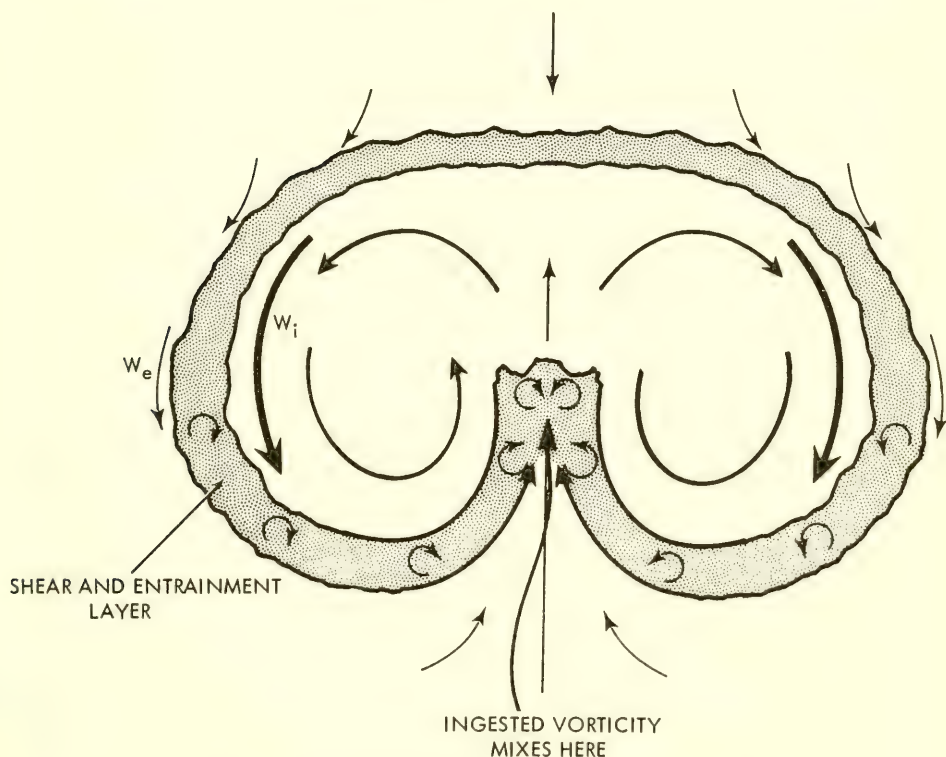


Fig. 3. Entraining vortex pair ($W_i > W_e$)

interior is created, and is pulled down around the bottom of the rising mass toward the plane of symmetry. To the extent that the ingested vorticity remains on its own side of this plane, the vorticity within the interior will be steadily reduced; of course, ingested vorticity of opposite sign does have a chance to mix and thus to annul itself, depending on the efficiency of mixing. Should effective annihilation of ingested vorticity occur, then the initial total vorticity within one side of the pair would be conserved in time.

As for the kinetic energy implicit in the motion of the vortex pair, it must be continuously reduced with time due to turbulent dissipation.

Self-Similarity in Vortex-Pair Motions. It is a striking characteristic of free turbulent flows in homogeneous media at sufficiently high Reynolds numbers that, under similar circumstances, the flows at different points in space or time can usually be reduced from one to another upon normalization by an appropriate length and velocity scale (self-similarity). This is true, for example, of the flow at different downstream sections of turbulent jets and wakes. It is therefore natural to expect that a turbulent vortex-pair exhibits complete self-similarity during its life time, and this assumption has been made in all theoretical treatments of the subject, starting with Morton, Taylor, and Turner [1956]. Two important consequences of this complete similarity are: (1) conservation of the ratio of internal and external velocity scales, W/W^* , during the motion; (2) linearity of the length scale of the convected mass with the distance traveled from a virtual origin.

This latter result, predicting that the traces of the side boundaries of the convected mass form a wedge, is independent of the dynamics of the motion and serves to provide a check on self-similarity. In fact, a number of previous experiments on self-convecting masses claim to confirm this behavior to a reasonable approximation, see, e.g., Scorer [1958], Woodward [1959] and Richards [1965].

It is obvious to ask whether a "natural" value of the velocity ratio W/W^* , or the same thing, of the constant $\beta = dR/dz$ is observed, independent of the original circumstances giving rise to the convected mass. The answer seems to be no. In the present experiments, two distinctly different ranges of value of dR/dz differing by a factor 2, have been repeatedly measured; these correspond to two different stroke lengths in the apparatus used to originate the vortex motions. Furthermore, although the present data may be claimed to correspond "in a reasonable approximation" to a constant value of dR/dz , yet quite consistent deviations from linearity exist between the traces of pair radius and distance traveled, see Fig. 4. These deviations are such that dR/dz seems actually to increase throughout the observed motions.

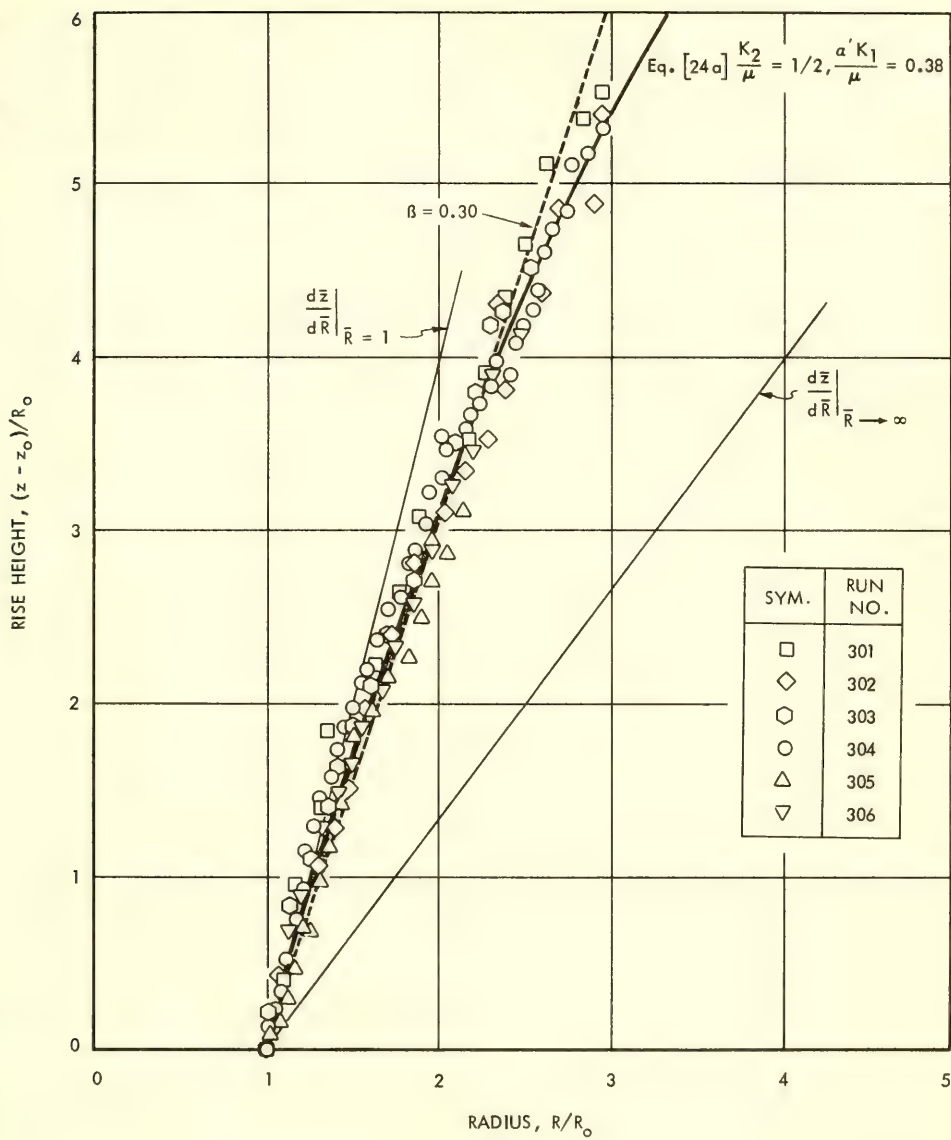


Fig. 4. The variation of vortex-pair radius with height in a homogeneous medium, experiment

In view of these facts, and for other reasons, it seems desirable to attempt a more general theory of the motion of turbulent vortex pairs, based on the assumption of separate velocity scaling of the internal and external motions; i.e. allowing W/W^* to vary continuously. Afterwards, a simplified theory pertaining to motions in stratified media will be developed and the results compared to experimental observations.

II. THEORY (HOMOGENEOUS FLOWS)

Separate Similarity of Internal and External Flows. We visualize the vortex-pair motion to be divided into internal and external flow fields, separated by a thin region of high shear, which also forms the boundary of the captured mass, see Fig. 3. We assume that each flow field is itself self-similar.

Internal.

$$w_i(x, y, t) = W_i(t) \cdot \overline{w}_i\left(\frac{x}{R}; \frac{y}{R}\right) \quad (2)$$

External.

$$w_e(x, y, t) = W_e(t) \cdot \overline{w}_e\left(\frac{x}{R}; \frac{y}{R}\right) \quad (3)$$

and similarly for the other velocity components.

We let $\psi = W_i/W_e$, where ψ is, in general, not constant in time as it is in the case of complete similarity.

We choose W_i as the circumferential velocity averaged over the inner boundary of one-half of the vortex pair and W_e the same except averaged over the outer boundary. (The inner and outer boundaries are separated by a thin shear layer.)

Volume Changes. The volume of fluid comprising the vortex pair increases continuously with time due to entrainment into it. Because of the similarity assumed, the rate of entrainment of volume must (in two dimensions) be proportional to a characteristic velocity and a characteristic length. We take for the former, the velocity difference $W_i - W_e$

$$\frac{d(\pi R^2)}{dt} = 2\pi R(W_i - W_e) \cdot \alpha(\psi) \quad (4)$$

or,

$$\frac{dR}{dz} = \frac{W_e}{W} (\psi - 1) \cdot \alpha(\psi) = (\psi - 1)\alpha'(\psi) \quad (5)$$

Note that the dependence of the proportionality constant α' on the velocity ratio ψ has been left unspecified.

Circulation Changes. The circulation Γ about one half of the vortex pair is, on account of the inner similarity, proportional to the length scale and inner velocity scale. On account of the way in which W_i was defined,

$$\Gamma \propto RW_i \quad (6)$$

The fluid entrained into the vortex pair from the surrounding high shear layer carries vorticity of opposite sign to that already within the interior, see Fig. 3 and thus reduces it to the extent it is not annihilated through mixing with vorticity being entrained in the opposite lobe. The strength of entrained vorticity must, on account of similarity, be proportional to the ratio of a pertinent velocity and length scale. In particular:

$$\gamma(\text{entrained}) \propto \frac{(W_e - W_i)}{R} \quad (7)$$

The flux of entrained vorticity takes the form:

$$\begin{aligned} \text{Vorticity Flux} &\propto \text{Volume Flux} \cdot \gamma(\text{entrained}) \\ &\propto [2\pi R(W_i - W_e) \cdot \alpha(\psi)] \left[\frac{W_e - W_i}{R} \right] \end{aligned} \quad (8)$$

Finally, the change in circulation may be related to the flux of vorticity:

$$\frac{d\Gamma}{dt} = -A_1 \cdot 2\pi\alpha(\psi) \cdot (W_i - W_e)^2 \quad (9)$$

or,

$$\frac{d(W_i R)}{dz} = -A_1 \alpha' \cdot (W_i - W_e) \cdot (\psi - 1) \quad (10)$$

The value of the parameter A_1 will depend in part upon the extent to which entrained vorticity from each side mixes together

causing annihilation. In the case of complete annihilation, $A_1 \equiv 0$.

Momentum Conservation. The momentum, M_z , of the vortex pair is conserved in motion through a homogeneous medium. It may on account of similarity be expressed in the form,

$$\frac{M_z}{\rho} = K_m(\psi) \cdot W_e R^2 = \text{const.} \quad (11)$$

where $K(\psi)$ is a momentum coefficient. Its form may be deduced through use of the identity, Lamb [1945], pg. 229,

$$\frac{M_z}{\rho} = \iint \gamma \zeta \, d\xi \, d\zeta \quad (12)$$

The latter integral can be taken separately over the interior and shear layer of the vortex pair, which yields terms upon making use of similarity,

$$\iint_{\text{int.}} \gamma \zeta \, d\xi \, d\zeta \propto W_i R^2 \quad (13)$$

$$\iint_{\text{shear layer}} \gamma \zeta \, d\xi \, d\zeta \propto (W_e - W_i) R^2 \quad (14)$$

As a result, the form of $K_m(\psi)$ consistent with our assumptions, is seen to be,

$$K_m(\psi) = K_1 - K_2 \psi \quad (15)$$

where K_1 and K_2 are undetermined constants.

Energy. The total kinetic energy in the vortex pair motion, taking account of similarity, may be expressed as the sum of two terms,

$$\frac{K.E.}{\rho} = K_i W_i^2 R^2 + K_e W_e^2 R^2 \quad (16)$$

while the dissipation takes the form,

$$\frac{d}{dt} \frac{KE}{\rho} = - W_i^3 R \cdot C_D(\psi) \quad (17)$$

where for large values of ψ , C_D must approach some limiting value C_D' , while for small values of ψ ($\psi \rightarrow 1$), $C_D \rightarrow C_D(1) \cdot (W_e/W_i)^3$.

Laws of Motion. Limiting Cases; Weak Circulation ($\psi \rightarrow 1$).
In this case the inner and outer flows are almost matched and the deviation from the ideal vortex motion is small. The laws of motion in their appropriate form become,

Volume.

$$\frac{dR}{dz} = (\psi - 1) \cdot \alpha'(1) \quad (5a)$$

Vorticity.

$$\frac{d(W_e R)}{dz} = - A_1 \alpha'(1) \cdot (\psi - 1)^2 \cdot W_e \quad (10a)$$

Momentum.

$$K_m(1) \cdot W_e R^2 = \text{const.} \quad (11a)$$

Energy.

$$K(1) \frac{d(W_e^2 R^2)}{dz} = - \left(\frac{W_e}{W} \right) W_e^2 R \cdot C_D(1) \quad (17a)$$

Combining (5a) and (10a) leads to the result,

$$W_e \propto \frac{1}{R^{1+A_1(\psi-1)}} \quad A_1 \neq 0 \quad (18)$$

Whereas, (11a) requires

$$W_e \propto \frac{1}{R^2} \quad \text{or} \quad z \propto t^{1/3} \quad (19)$$

so that the presumed motion can take place only if $A_1 = 0$ or $A_1 = (\psi - 1)^{-1}$. Combining (17a) and (10a) leads to the requirement that the velocity ratio be constant and have the value

$$\psi = 1 + \left[\frac{C_D(1)}{2K(1) \cdot \alpha(1)} \right] \quad (20)$$

At the same time, dR/dz is required to be constant and to have the value,

$$\psi \rightarrow 1 \quad \frac{dR}{dz} = \left(\frac{W_e}{W} \right) \cdot \frac{C_D(1)}{2K_e(1)} \quad (21)$$

We leave till later a discussion of comparison with experiment, but we may note now that the prediction (19) is similar to that of the previous theory based on complete similarity.

Strong Circulation ($\psi \gg 1$). In this case the interior circulation is very strong relative to the ideal value and the deviation from the ideal vortex motion is large. The appropriate laws of motion are,

Volume.

$$\frac{dR}{dz} = \psi \cdot \alpha'(\psi) \quad (5b)$$

Vorticity.

$$\frac{d(W_1 R)}{dz} = - A_1 \alpha'(\psi) \cdot W_1 \cdot \psi \quad (10b)$$

Momentum.

$$(K_1 - K_2 \psi) \cdot W_1 R^2 = \psi \cdot (M_z / \rho) \quad (11b)$$

Energy.

$$K_e W \frac{d}{dz} (W_1 R)^2 = - W_1^3 \cdot R \cdot C_D' \quad (17b)$$

Combining (10b) and (17b) leads to the requirement that $\alpha(\psi)$ be constant and equal to

$$\psi = \frac{C_D'}{2K_e \cdot A_1} \quad (21)$$

Since similarity requires that W_e/W be constant, we may hereafter take α' constant in (5b) and (10b). Combining (5b) and (10b) leads to the result

$$W_i \propto \frac{1}{R^{(1+A_1)}} \quad \text{or} \quad W_i/W_{i_0} \propto \left(\frac{R_0}{R}\right)^{1+A_1} \quad (22)$$

and, substituting (22) and (5b) into (11b) leads to the differential relation,

$$\left(K_1 - \frac{K_2}{\alpha'} \frac{d\bar{R}}{dz}\right) \bar{R}^{(1-A_1)} = \frac{\mu}{\alpha'} \cdot \frac{d\bar{R}}{dz} \quad (23)$$

which has the solution,

$$\frac{\alpha'}{\mu} K_1 \cdot \bar{z} = \frac{\bar{R}^{A_1}}{A_1} + \frac{K_2}{\mu} \bar{R} + \text{const.} \quad (A_1 \neq 0) \quad (24)$$

where

$$\mu = \frac{M_z/\rho}{W_{i_0} R_0^2}$$

and

$$\frac{\alpha'}{\mu} K_1 \bar{z} = \ln \bar{R} + \frac{K_2}{\mu} \bar{R} + \text{const.} \quad (A_1 = 0)$$

or

$$\frac{\alpha'}{\mu} K_1 \frac{(z - z_0)}{R_0} = \ln \bar{R} + \frac{K_2}{\mu} (\bar{R} - 1) \quad (24a)$$

Substituting dR/dz derived from (23) into (5b) yields a relation between ψ and R ,

$$\psi = \frac{K_1}{\mu \bar{R}^{(A_1-1)} + K_2} \quad (25)$$

and, finally, it may be shown that,

$$\frac{W_e}{W_{i_0}} = \frac{\mu}{K_1} \bar{R}^{-2} + \frac{K_2}{K_1} \bar{R}^{-(1+A_1)} \quad (26)$$

The type of motions which ensue from this theory in the case of strong circulation are seen to depend very much on the value of

A_1 , the constant appearing in the relation for circulation change, and which depends in part on the way in which vorticity is ingested into the vortex pair. In fact, the asymptotic behavior of the vortex pair changes radically as A_1 varies around the value unity. This is demonstrated in the table below.

Asymptotic Behavior ($\psi \gg 1$)				
	\bar{z}	ψ	W_e/W_{i0}	\bar{z}
$A_1 > 1$	$\frac{\mu \bar{R}^{A_1}}{A_1 \alpha' K_1}$	$K_1 \bar{R}^{-A_1+1}$	$K_1 \bar{R}^{-2}$	$\sim t^{1/(1+2/A_1)}$
$A_1 = 1$	$\bar{R} \left(\frac{\mu + A_1 K_2}{A_1 \alpha' K_1} \right)$	$K_1/\mu + K_2$	$K_1 \bar{R}^{-2}$	$\sim t^{1/3}$
$A_1 < 1$	$\bar{R}(K_2/\alpha' K_1)$	K_1/K_2	$K_1/K_2 \cdot \bar{R}^{-(1+A_1)}$	$\sim t^{1/(2+A_1)}$
$A_1 = 0$	$\bar{R}(K_2/\alpha' K_1)$	K_1/K_2	$K_1/K_2 \cdot \bar{R}^{-1}$	$\sim t^{1/2}$

For values of $A_1 > 1$, the velocity ratio is seen to decline, so that the strong circulation assumption must eventually become invalid. The case $A_1 = 1$ yields results qualitatively similar to the weak circulation case. In the case where $A_1 < 1$, however, the velocity ratio increases to the asymptotic value shown and, most interesting, the added momentum coefficient ($K_1 - K_2\psi$) vanishes asymptotically, so that the motion becomes determined by volume, vorticity, and energy balances alone. Finally, in the case where $A_1 \ll 1$ (effective annihilation of ingested vorticity), then asymptotically the motion becomes determined by volume and energy balances alone, yielding $\bar{z} \sim t^{1/2}$.

III. COMPARISON WITH EXPERIMENT (HOMOGENEOUS MEDIA)

In Figs. 5 and 6 are shown data from actual experiments on two-dimensional vortex pair motions in homogeneous fluids. Most of the data shown were obtained in experiments carried out in our own laboratory. Suffice it here to show a schematic of the facility which was used, Fig. 7, and to show Table 1, in which the properties and characteristics of the experimental vortex pairs are listed.

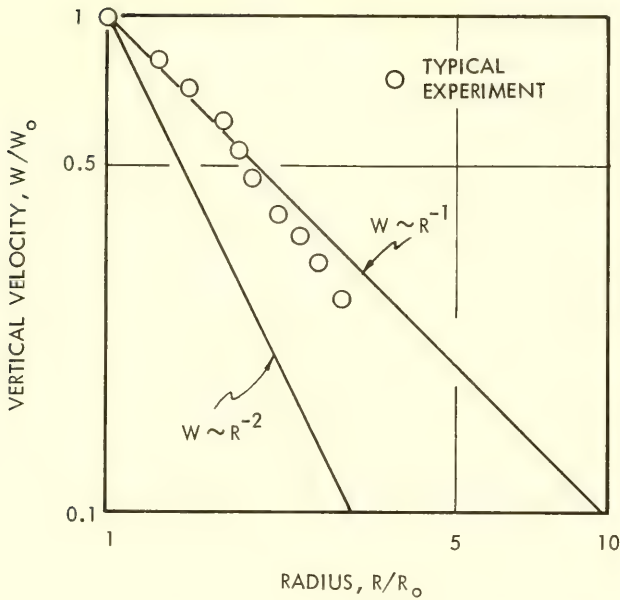


Fig. 5. The vertical velocity vs. radius of a vortex-pair moving in a homogeneous fluid

Most significant, we found in our experiments and from the data of Richards [1965] that the measured variation of vertical velocity and pair radius (two-dimensions) conformed more closely to the law $W \sim R^{-1}$ or $z \sim t^{1/2}$ than to the law derived in the past by others and which is based on complete similarity and momentum conservation; i.e., $W \sim R^{-2}$ or $z \sim t^{1/3}$. A test of the simple conservation of momentum, $W \sim R^{-2}$, using a typical trajectory is illustrated in Fig. 5 and, similarly, in Fig. 6 it is shown that the trajectories, so far as they have been observed experimentally, conform more closely to the asymptotic law derived earlier for the case of strong circulation, utilizing a small value of A_1 ($0 < A_1 < 0.2$).

In the case of strong circulation, the radius grows in a linear fashion asymptotically, but the theory predicts that during the initial phases of the motion the quantity dR/dz is less than its asymptotic value. A similar behavior was observed in our experiments, see Fig. 4. The matching up of these observed trajectories with the theory offers an opportunity to determine some of the constants of the theory. For this purpose we assume to begin with that $A_1 = 0$, since the comparison between observed and theoretical trajectories

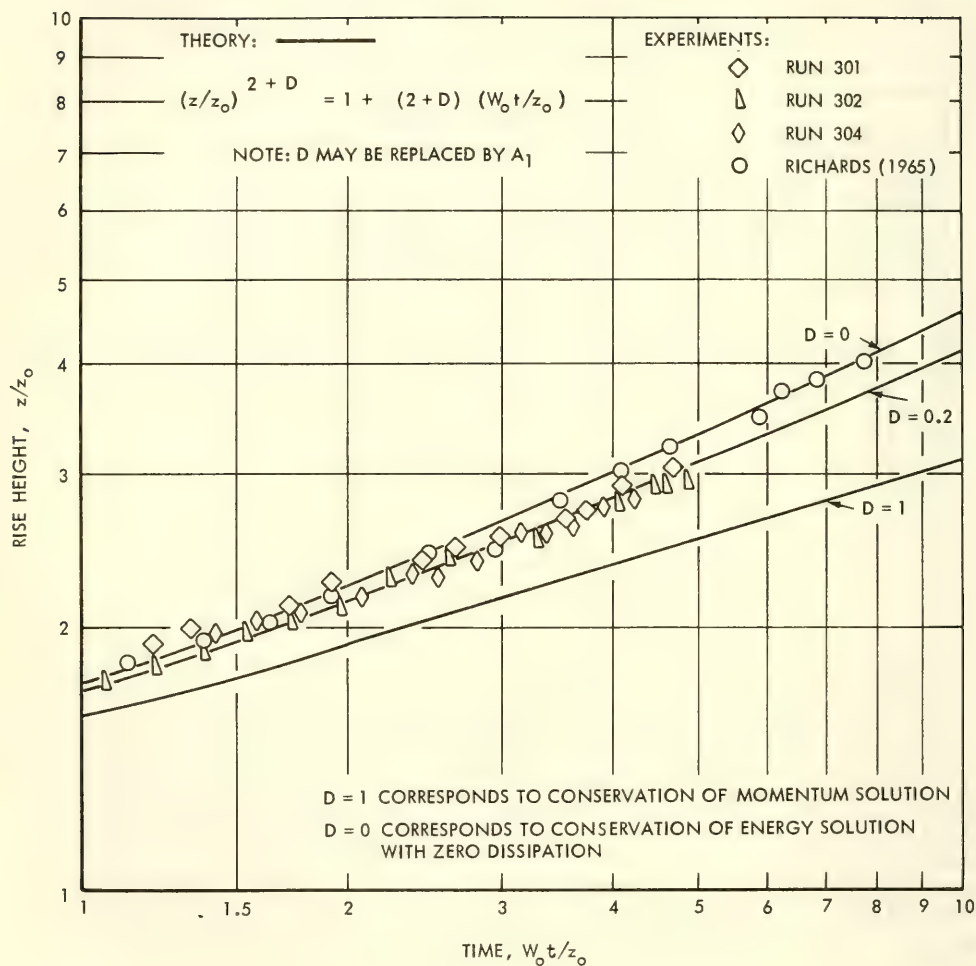


Fig. 6. The rise of vortex-pairs in a homogeneous medium; comparison of experiment and theory

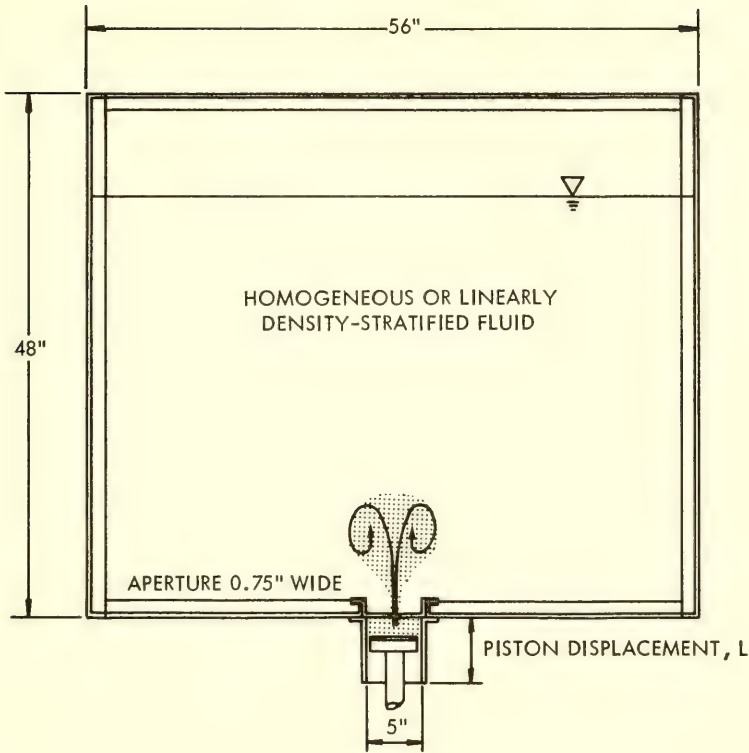


Fig. 7. Experimental facility for studying vortex-pair motion

suggests a small value. In this case,

$$\frac{(\alpha K_1)}{\mu} \left[\frac{z - z_0}{R_0} \right] = \ell n \bar{R} + \frac{K_2}{\mu} [\bar{R} - 1] \quad (24a)$$

The trajectory according to Eq. (24a) with $K_2/\mu = 1/2$ and $\alpha'K_1/\mu = 0.38$ is shown in Fig. 4. A fair fit with the experiments has been achieved, and noticeably better than is possible with any linear trajectory.

The strong circulation theory thus explains the two important features of vortex pair behavior which cannot be explained by the usual theory of complete similarity. These features are: (i) the tendency for forced vortex trajectories (homogeneous flow) to more nearly follow the law $z \sim t^{1/2}$ rather than $z \sim t^{1/3}$, and (ii) the tendency for the entrainment coefficient (dR/dz) to grow during the initial phase of the motion. These results suggest that in vortex

TABLE 1
Characteristic Properties and Parameters of Impulsively Generated Vortex-Pairs

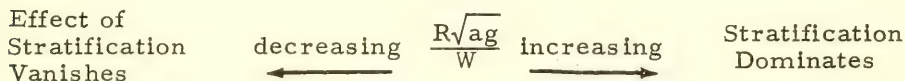
Series	Run	L (ft.)	a (ft. ⁻¹)	W _o (ft./sec)	R _o (ft.)	β	(Δρ/ρ _e) _o	z _o (ft.)	G	S	z _{max} - z _o (ft.)	t _{max} √ag	G/S
I	101	0.50	0.0177	0.295	0.160	0.310	0.00331	0.515	-1.200	1.735	0.283	1.66	-0.700
	201	0.50	0.0081	0.480	0.134	0.280	0.00269	0.478	-0.180	0.258	0.656	1.62	-0.700
	202	0.50	0.0081	0.532	0.133	0.320	0.00265	0.416	-0.125	0.160	0.621	1.48	-0.781
	203	0.50	0.0081	0.570	0.136	0.306	0.00275	0.495	-0.121	0.159	0.619	1.75	-0.758
	204	0.50	0.0081	0.270	0.146	0.320	0.00276	0.456	-0.555	0.743	0.416	1.51	-0.746
	205	0.50	0.0081	0.338	0.143	0.300	0.00283	0.476	-0.374	0.509	0.441	1.84	-0.735
	206	0.50	0.0081	0.296	0.148	0.286	0.00291	0.556	-0.595	0.920	0.386	1.75	-0.650
	208	0.50	0.0081	0.112	0.150	0.304	0.00265	0.493	-3.260	4.910	0.159	1.69	-0.657
	209	0.50	0.0081	0.122	0.150	0.321	0.00277	0.503	-2.780	3.790	0.139	1.75	-0.735
	401	0.50	0.0020	0.138	0.148	0.294	0.00067	0.503	-0.612	0.904	0.421	1.79	-0.676
	403	0.50	0.0020	0.296	0.143	0.274	0.00075	0.522	-0.143	0.199	0.686	1.56	-0.720
	404	0.50	0.0020	0.154	0.151	0.277	0.00072	0.546	-0.534	0.810	0.454	1.52	-0.658
	405	0.50	0.0020	0.318	0.143	0.300	0.00077	0.476	-0.117	0.145	0.661	1.73	-0.807
	406	0.50	0.0020	0.455	0.158	0.320	0.00079	0.494	-0.061	0.076	0.809	1.75	-0.800
	407	0.50	0.0020	0.110	0.162	0.244	0.00074	0.663	-1.300	2.330	0.364	1.80	-0.569
II	408	0.50	0.0020	0.098	0.160	0.256	0.00075	0.624	-1.568	2.600	0.316	1.70	-0.600
	410	0.50	0.0020	0.498	0.157	0.311	0.00077	0.505	-0.951	0.066	0.844	1.63	-0.770
	411	0.50	0.0020	0.336	0.155	0.320	0.00073	0.484	-0.101	0.133	0.659	1.60	-0.758
	501	0.50	0.0231	0.546	0.160	0.321	0.00846	0.498	-0.498	0.618	0.418	1.42	-0.735
	502	0.50	0.0231	0.645	0.156	0.332	0.00800	0.470	-0.408	0.554	0.434	1.52	-0.735
	503	0.50	0.0231	0.528	0.156	0.282	0.00827	0.553	-0.528	0.814	0.419	1.57	-0.650
	412	0.25	0.0020	0.266	0.127	0.560	-0.00041	0.227	-0.042	0.047	0.464	1.65	-0.885
III	413	0.25	0.0020	0.308	0.124	0.562	-0.00046	0.223	-0.035	0.034	0.523	1.68	-1.030
	414	0.25	0.0020	0.304	0.125	0.680	-0.00037	0.184	-0.024	0.024	0.459	1.75	-1.000
	301	0.50	0	0.550	0.147	0.300	0	0.490	0	0	-	-	-
	302	0.50	0	0.525	0.147	0.286	0	0.514	0	0	-	-	-
	303	0.50	0	0.336	0.155	0.302	0	0.514	0	0	-	-	-
	304	0.50	0	0.358	0.155	0.300	0	0.517	0	0	-	-	-
	305	0.50	0	0.109	0.150	0.280	0	0.536	0	0	-	-	-

motions in homogeneous flows the internal velocity scale grows steadily relative to the translational (external) velocity, the ratio approaching a value considerably larger than unity, while at the same time, the virtual momentum coefficient associated with the vortex motion approaches the value zero. The data also suggest that vorticity ingested from around one half of the vortex pair is almost annihilated through mixing with vorticity ingested from the opposite side.

IV. SIMPLIFIED THEORY (VORTEX PAIR MOTION IN STRATIFIED MEDIA)

Convected masses in nature are often rising or falling in a medium of varying density, as in the case of a chimney plume projected upwards into a stable atmosphere. The latter may be characterized by a characteristic time (the Vaissala period), $1/\sqrt{ag}$, where $a = - (1/\rho_e)(d\rho_e/dz)$ and ρ_e is the potential density of the atmosphere. The same definition can be used to characterize any density stratified media.

The motion of the convecting mass may also be characterized at any instant by the time, R/W . It is almost apparent that when the latter time is long in comparison to the Vaissala period that the effect of stratification will dominate, and conversely. That is,



Quite clearly, too, as the motion proceeds in time, the ratio R/W increases continuously, so that stratification must eventually dominate. When this happens, the vertical motion of vortex-pairs may become oscillatory, and is accompanied by the collapse and horizontal spreading of the convected mass, as illustrated in Fig. 8. This behavior is, of course, not consistent with similarity either complete or of the kind assumed in the preceding section.

It is sometimes desirable to be able to estimate the trajectory of a vortex pair while it is rising in a stratified media and particularly to predict the maximum height of rise and the time required to reach the maximum. For this purpose, we adopt here a simplified theory based essentially on the assumption of strong circulation and annihilation of ingested vorticity. In fact, the particular assumptions adopted would apply if the velocity ratio, ψ , had already closely approached its limiting value. These assumptions are: (i) the motion is determined by conservation of volume, mass, and energy (neglecting vorticity and momentum); (ii) complete similarity ($dR/dz = \beta$, a constant). For further justification of these

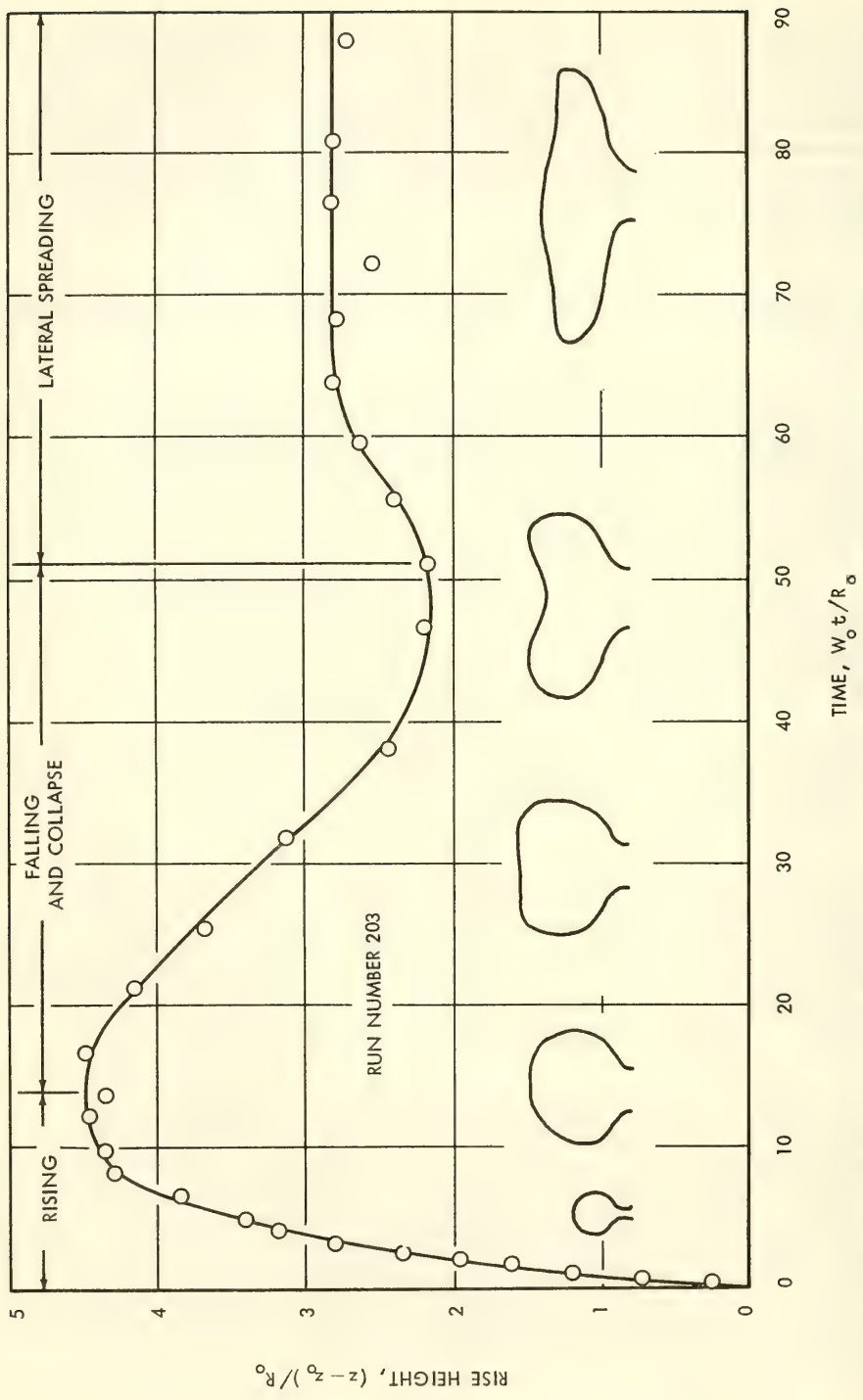


Fig. 8. Typical trajectory of a vortex-pair in a linearly density stratified medium

assumptions we shall depend finally upon a comparison between theoretical predictions and the results of systematic experiments.

The energy balance is expressed as follows,

$$\begin{aligned} \frac{\partial E}{\partial t} &= \frac{\partial}{\partial t} \int \left[\frac{\rho}{2} (u^2 + v^2 + w^2) + (\rho - \rho_e) g \zeta \right] d\xi \, d\eta \, d\zeta \\ &= - (\text{Rate of Dissipation of Energy}) \end{aligned} \quad (27)$$

See Fig. 14 for nomenclature.

For a self-similar, self-convecting flow, the dissipation of kinetic energy per unit volume which occurs due to the action of turbulent shear stresses must for dimensional reasons be of the form,

$$\frac{\text{Dissipation}}{\text{Unit Volume}} \propto \frac{\rho W^3}{R} \quad (28)$$

As a result, the energy balance, Eq. (27), for a self-convecting mass in a homogeneous medium of the same density takes the form,

$$\frac{K}{2} \frac{d(W^2 R^{2+j})}{dt} = - C_D \frac{W^3}{R} R^{2+j} \quad (29)$$

where

$$j = 0 \quad (\text{two-dimensional})$$

$$j = 1 \quad (\text{axisymmetrical})$$

and K is a constant of virtual energy, defined by the identity,

$$\int \frac{u^2 + v^2 + w^2}{2} d\xi \, d\eta \, d\zeta = \frac{K}{2} W^2 R^{2+j} \quad (30)$$

and where C_D is a dissipation coefficient.

Making use of (29), together with the relationship $R = \beta z$, it may be shown that the height of rise follows the law,

$$z^{(2+j)/2 + C_D/\beta K} \propto t \quad (31)$$

in a medium of uniform density with $\Delta\rho = 0$. The dissipation coefficient in nature, $D = C_D/\beta K$, may be determined by a comparison between theoretical trajectories such as given by (31) and observations of vortex pair rise in homogeneous media. As shown in Fig. 6, such a comparison leads to the conclusion that D is quite small ($D < 0.2$).

The trajectory given by (31) may be compared to the law which would apply if momentum were conserved,

$$z^{3+j} \propto t \quad (32)$$

which coincides with (31) only if $D = 1$. The variance of observed trajectories from the momentum law (32) is clearly seen in Figs. 5 and 6.

Volume conservation in a self-similar flow leads to a linear relation between the nominal radius of the mass and the height of rise from the virtual origin $z = 0$:

$$R = \beta z \quad (33)$$

Conservation of mass takes the form

$$\frac{d}{dt} \left[\left(\frac{4}{3} \right)^j \pi R^{2+j} \rho_i \right] = 2^j 2\pi R^{1+j} \rho_e W \beta \quad (34)$$

where ρ_e , is the density of the surrounding fluid at any given height z and ρ_i is the average density within the rising mass, defined by

$$\left(\frac{4}{3} \right)^j \pi R^{2+j} [\rho_i(z) - \rho_e(z)] = \int (\rho - \rho_e) d\xi (d\eta)^j d\zeta \quad (35)$$

where the integration is taken over the entire volume of the rising mass.

The formulation of conservation of energy is based upon (27) and (28)

$$\frac{d}{dt} \left[\frac{K}{2} \rho_i W^2 R^{2+j} + k(\rho_i - \rho_e) g z R^{2+j} \right] = - C_D \rho_i \frac{W^3}{R} R^{2+j} \quad (36)$$

where W and R are the observed and measured gross properties of the rising mass while K and k are the coefficients of the virtual kinetic and potential energies, respectively, defined in two dimensions, e.g., by

$$K\rho_i \frac{W^2 R^2}{2} = \int \frac{\rho}{2} (u^2 + w^2) d\xi d\zeta \quad (37)$$

and

$$k(\rho_i - \rho_e)zR^2 = \int (\rho - \rho_e)(z + \zeta) d\xi d\zeta \quad (38)$$

In most practical instances where one is dealing with a mass of fluid convected through a homogeneous or stratified medium such as the ocean or the atmosphere, the difference between the densities of the convected and surrounding masses is very small; that is $\Delta\rho/\rho_e \ll 1$, being usually of the order of 10^{-3} , and therefore ρ_i/ρ_e can be taken as 1. This assumption, frequently referred to as the Boussinesq approximation, see Phillips [1966], will be used throughout the analysis presented herein.

Using the Boussinesq approximation and the identity $dz = w dt$, the three conservation statements, Eqs. (33), (34) and (36), may be reduced to the following form in the case of a planar motion:

$$R = \beta z, \quad (39)$$

$$\frac{d\rho_i}{dz} + \frac{2\Delta\rho}{z} = 0,$$

or (40)

$$\frac{d}{dz} \left(\frac{\Delta\rho}{\rho_e} \right) + \frac{2}{z} \left(\frac{\Delta\rho}{\rho_e} \right) = a$$

$$z \frac{dW^2}{dz} + 2 \left(1 + \frac{C_D}{\beta K} \right) W^2 + \frac{2kg}{K} \left(\frac{\Delta\rho}{\rho_e} + az \right) z = 0 \quad (41)$$

where $a = -(1/\rho_e)(d\rho_e/dz)$ and $\Delta\rho = (\rho_i - \rho_e)$.

Finally, explicit general solutions of (40) and (41) may be found. They are:

$$\frac{\Delta\rho}{\rho_e} = \left[\left(\frac{\Delta\rho}{\rho_e} \right)_0 - \frac{az_0}{3} \right] \bar{z}^{-2} + \frac{az_0}{3} \bar{z} \quad (42)$$

$$\begin{aligned} \left(\frac{w}{w_0} \right)^2 = & \left[1 - \frac{A}{(1+2D)} + B \left(\frac{1}{1+D/2} - \frac{1}{1+2D} \right) \right] \bar{z}^{-n} \\ & + \left[\frac{(A+B)}{(1+2D)} \right] \bar{z}^{-1} - \left[\frac{B}{(1+D/2)} \right] \bar{z}^2 \end{aligned} \quad (43)$$

where

$$A \equiv \left(\frac{2k}{K} \right) G \quad \text{and} \quad G \equiv \frac{z_0 g}{W_0^2} \left(\frac{\Delta \rho}{\rho_0} \right)_0 \quad (44)$$

$$B \equiv \left(\frac{2k}{3K} \right) S \quad \text{and} \quad S \equiv \frac{z_0^2 a g}{W_0^2} \quad (45)$$

$$D \equiv \frac{C_D}{\beta K} \quad (46)$$

$$n \equiv 2(1 + D) \quad (47)$$

and

$$\bar{z} \equiv z/z_0 \quad (48)$$

The parameter G is a measure of the initial buoyancy of the convected mean relative to the initial momentum. G is taken as positive when a net buoyancy force is acting on the mass, i.e. $\Delta \rho < 0$. S is a measure of the added buoyancy which would result from moving the convected mass a vertical distance z_0 through a stratified medium. Since \sqrt{ag} is the frequency with which a finite volume of fluid of given density would oscillate in a stratified medium, often referred to as the Vaisala frequency, the parameter S can also be considered as the square of the ratio of the characteristic time of the convected motion, z_0/W_0 , and the reciprocal of the Vaisala frequency.

The maximum height of the rising mass, reached at the point where $W = 0$, is according to (43), given by the solution of the following:

$$\left[\frac{B}{(1 + D/2)} \right] \left(\frac{z_{\max}}{z_0} \right)^{2+n} - \left[\frac{A + B}{1 + 2D} \right] \cdot \left(\frac{z_{\max}}{z_0} \right)^{1+n} - \left[1 - \frac{A}{(1 + 2D)} \right] + B \left(\frac{1}{1 + D/2} - \frac{1}{1 + 2D} \right) = 0 \quad (49)$$

It is of interest to consider certain special cases:

1. A mass rising in a homogeneous medium with the same density as itself; i.e., $A = 0$ and $B = 0$. Then

$$\left(\frac{W}{W_0} \right) = \left(\frac{z}{z_0} \right)^{-n/2} \quad (50)$$

or,

$$\left(\frac{z}{z_0}\right)^{1+n/2} = 1 + \left(1 + \frac{n}{2}\right) \frac{W_0 t}{z_0} \quad (51)$$

This result suggests how to estimate the dimensionless quantity n (or D) through the analysis of the trajectories of rising masses in this special case.

2. A mass with initial density difference rising in a homogeneous medium; i.e., $B = 0$. Then

$$\left(\frac{W}{W_0}\right)^2 = \left[1 - \frac{A}{(1+2D)}\right] \bar{z}^{-n} + \left[\frac{A}{(1+2D)}\right] \bar{z}^{-1} \quad (52)$$

If $A > 0$, then no maximum height is reached, but if $A < 0$,

$$\frac{z_{\max}}{z_0} = \left[\frac{1 + 2D + |A|}{|A|} \right]^{1/(1+2D)} \quad (53)$$

The predicted rise of the mass as a function of time and the maximum rise of the mass for a range of values of A (< 0) and D , as obtained from Eqs. (52) and (53), are presented in Figs. 9 and 10. These figures demonstrate clearly the effect of the (negative) initial buoyancy and energy dissipation parameters on the time history of an impulsively started rising mass moving through a uniform surrounding fluid of smaller density.

2a. The same case as above but for $W_0 = 0$ and $A > 0$. First of all, (43) may be rewritten:

$$W^2 = W_0^2 \left(\frac{z_0}{z}\right)^n + \frac{2kgz_0}{(1+2D)K} \left(\frac{\Delta\rho}{\rho_e}\right)_0 \left(\frac{z_0}{z}\right)^n - \frac{2kgz_0}{(1+2D)K} \left(\frac{\Delta\rho}{\rho_e}\right)_0 \cdot \frac{z_0}{z}$$

or in this case

$$W^2 \cdot z = \left[\frac{-2kg}{\beta^2(1+2D)K} \right] \left(\frac{\Delta\rho}{\rho_e}\right) \cdot R_0^2 \left[1 - \left(\frac{R_0}{\beta z}\right)^{n-1} \right] \quad (54)$$

3. A mass with no initial buoyancy rising in a stratified medium, i.e., $A = 0$. Then,

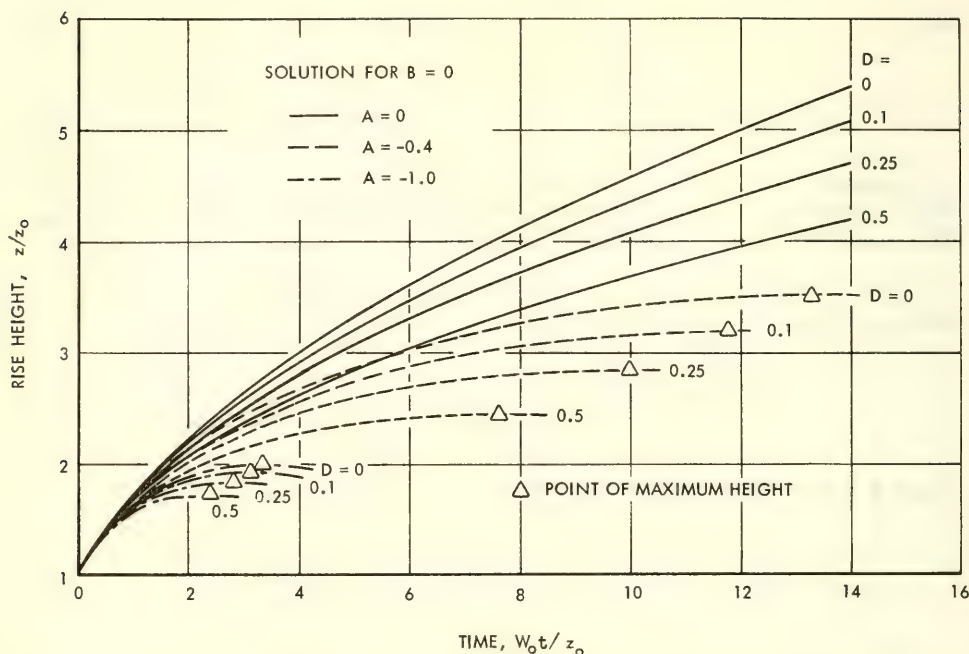


Fig. 9. The rise of an impulsively started heavy mass of fluid in uniform surroundings ($B = 0$), theory

$$\left(\frac{W}{W_0}\right)^2 = \left[1 + B\left(\frac{1}{1+D/2} - \frac{1}{1+2D}\right)\right] \bar{z}^{-n} + \frac{B}{(1+D/2)} \cdot \bar{z}^{-1} - \frac{B}{(1+D/2)} \cdot \bar{z}^{-2} \quad (55)$$

and the maximum rise of the mass, as a function of B , is obtained from Eq. (55) by setting $W = 0$.

Approximate integrated solution for the height of the convected mass, z , as a function of time can be readily obtained from Eq. (55) whenever $D \ll 1$ and $B \ll 1$. When these two requirements are satisfied, Eq. (55) can be rewritten as

$$\left(\frac{W}{W_0}\right)^2 = \bar{z}^{-2} - B\bar{z}^2 \quad (56)$$

and upon integration we obtain

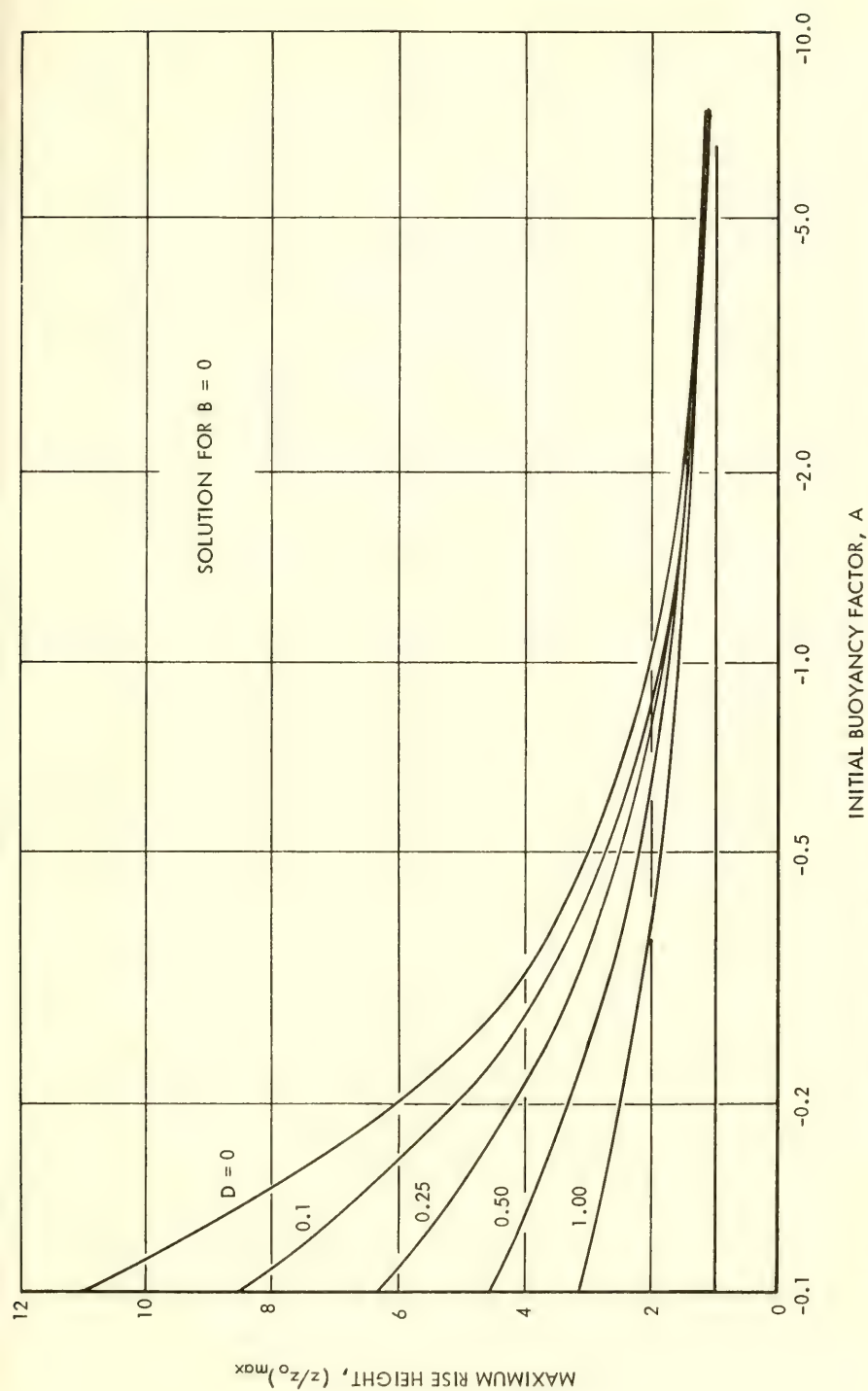


Fig. 10. The maximum rise of an impulsively started heavy mass of fluid in uniform surroundings ($B = 0$), theory

$$\sqrt{B} \bar{z}^2 = \sin \left[\sin^{-1} \sqrt{B} + 2\sqrt{Bt} \right] \quad (57)$$

where we have normalized the time t according to

$$t \equiv \frac{W_0 t}{z_0} \quad (58)$$

Equation (57) is particularly useful for the approximate determination of the maximum rise of a mass convected in a stratified medium and the time at which this maximum height is reached, \bar{t}_{\max} . For the maximum height we find

$$\bar{z}_{\max} = \left(\frac{1}{B} \right)^{1/4} \quad (59)$$

and the time required to reach this height is given by

$$\bar{t}_{\max} = \frac{\pi}{4\sqrt{B}} - \frac{1}{2} \quad (60)$$

This last result is especially interesting. In experiments on convected masses of fluid moving through a density stratified medium it was frequently observed that the time it takes the mass to reach its maximum height is inversely proportional to the Vaisala frequency of the stratified medium, i.e., $t_{\max} \sqrt{ag} = \text{const.}$ Equation (60) is just a statement of this same fact for small values of B (as usually exist in nature), since $\bar{t}_{\max} \sqrt{B} = \sqrt{2k/3K} (t_{\max} \sqrt{ag})$.

V. COMPARISON OF EXPERIMENTAL AND THEORETICAL RESULTS (STRATIFIED MEDIA)

In our experimental investigation we have studied the motion of impulsively started rising masses (or vortex-pairs) in both uniform and density-stratified surroundings. According to the theoretical considerations presented in the previous section, the time-histories of these motions, expressed in appropriate non-dimensional terms, are determined by three parameters, A , B and D , i.e., for given values of these parameters the rise and growth of the convected mass as a function of time can be predicted. A and B are determined by G and S and by a third parameter which is the ratio of the virtual kinetic and potential energy coefficients, K/k , according to Eqs. (44) and (45).

While the parameters G and S are determined in each case by the initial conditions of the rising vortex-pair, there is no

practical way for determining a priori the values of D and K/k . These latter parameters can be determined only by comparing certain sets of experimental results with corresponding theory.

A series of experiments on the motion of vortex-pairs in a homogeneous medium of the same density, Series III (see Table 1), where the parameters G and S (and therefore also A and B) are identically equal zero, may be used for determining the dissipation parameter D . The rise of the vortex-pairs in this case is predicted by Eq. (51) and is graphically depicted in Fig. 9 (with $A = 0$). The actual predicted rise of the convected mass depends on the numerical value of the parameter D (or n).

In Fig. 6 are shown a comparison between experimental and theoretical results on the rise of impulsively started masses in a uniform medium of the same density. In a log-log plot, the slope of the trajectory for large values of $(W_0 t/z_0)$ should be equal, according to our analysis, to $1/(2+D)$, and it can be used therefore for determining the value of the dissipation parameter D associated with the motion of the rising mass. Included in Fig. 6 are the experimental results of Richards [1965], on the rise of two-dimensional puffs in homogeneous surroundings. The best agreement with all experimental results is obtained when we choose $D = 0.2$.

The numerical value of K/k enters into the analysis only when there is an initial difference between the rising and surrounding fluid densities or when the surrounding fluid is stratified. This value will be also determined from a comparison of some experimental and theoretical results. For a vortex-pair convected in a density-stratified medium we found earlier that, for sufficiently small values of the parameters A , B and D , the time it takes the mass to reach its maximum height is inversely proportional to the Valsala frequency and is given by

$$(t_{\max} \sqrt{ag}) \approx \sqrt{\frac{3K}{2k}} \frac{\pi}{4} \quad (61)$$

This value decreases only very gradually as the value of B (or S) so that Eq. (61) is very useful for the experimental determination of K/k .

In Fig. 11 the value of the product $(t_{\max} \sqrt{ag})$, as measured in the experiments of Series I and II, is presented as a function of the stratification parameters S ; the initial conditions for each experiment presented in the Figure are included in Table 1. There are certain inherent inaccuracies in the experimental determination of t_{\max} which explain the scatter. Also shown in Fig. 11 are the asymptotic solution for the maximum rise time, Eq. (60), and the exact solution, according to Eq. (43), with $D = 0.2$ and $G/S = -0.715$.

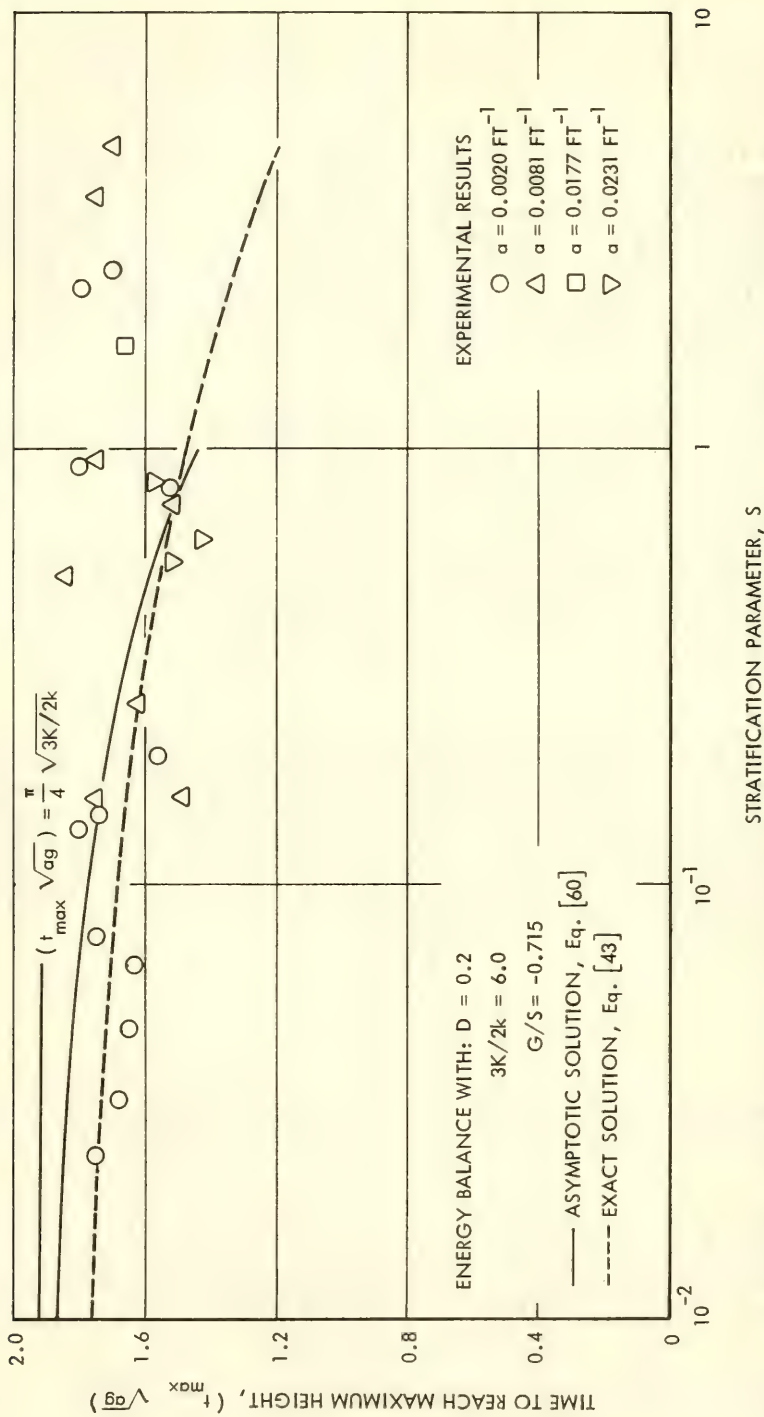


Fig. 11. Time of maximum rise for vortex-pairs convected in a density-stratified medium; comparison of experiment and theory

Close agreement between theoretical and experimental results was obtained when we used $3K/2k = 6$ or $K/k = 4$. We have included in the same figure the experimental results from Series III which had a markedly different value of β ; these too were found to agree very closely with the theoretical prediction based on $D = 0.2$ and $K/k = 4$, indicating that the dependence of these latter two parameters on β is probably very weak. We have used these values of D and K/k for all subsequent comparisons of experimental and theoretical results. The coefficient of virtual potential energy cannot be much different from unity, according to its definition in Eq. (38). The total kinetic energy of a rising vortex-pair was thus found to be about four times larger than the kinetic energy associated with its linear convection alone, an indication of the intensity of motion inside the vortex-pair, which contributes to its total kinetic energy. This finding lends important support to the strong circulation assumption.

A comparison between the predicted and actual maximum heights of rise of a vortex-pair convected in a linearly density-stratified medium is shown as Fig. 12. The figure includes a prediction based on the simplified asymptotic solution for small B (or S), Eq. (59), and a prediction obtained from the exact solution of Eq. (49) for \bar{z}_{\max} . Generally there is good agreement between the experimentally measured maximum height of vortex-pairs and the exact theoretical solution.

Finally, in Fig. 13, we compare the measured trajectories (height versus time) of vortex-pairs with their theoretically predicted trajectories. The vortex-pairs included in the Figure all had different starting conditions and they were moving through media with different density-stratifications. However, their trajectories, as depicted in the figure are shown to depend only on the values of the two lumped parameters G and S which combine their starting conditions with the properties of the surrounding medium.

The fact that trajectories of different vortex-pairs are grouped according to their G and S values confirms the validity of the scaling laws and scaling parameters used herein, while the agreement obtained between the experimental and theoretical trajectories lends further support to the validity of the simplified theory presented here for the motion of vortex-pairs in stratified media.

VI. SUMMARY AND CONCLUSIONS

A theory for the motion of two-dimensional turbulent vortex-pairs in homogeneous media has been developed based on separate velocity scaling of the internal and external flow fields involved in the motion. These two flow fields are depicted to be separated by a thin region of high shear, which also forms the boundary of the

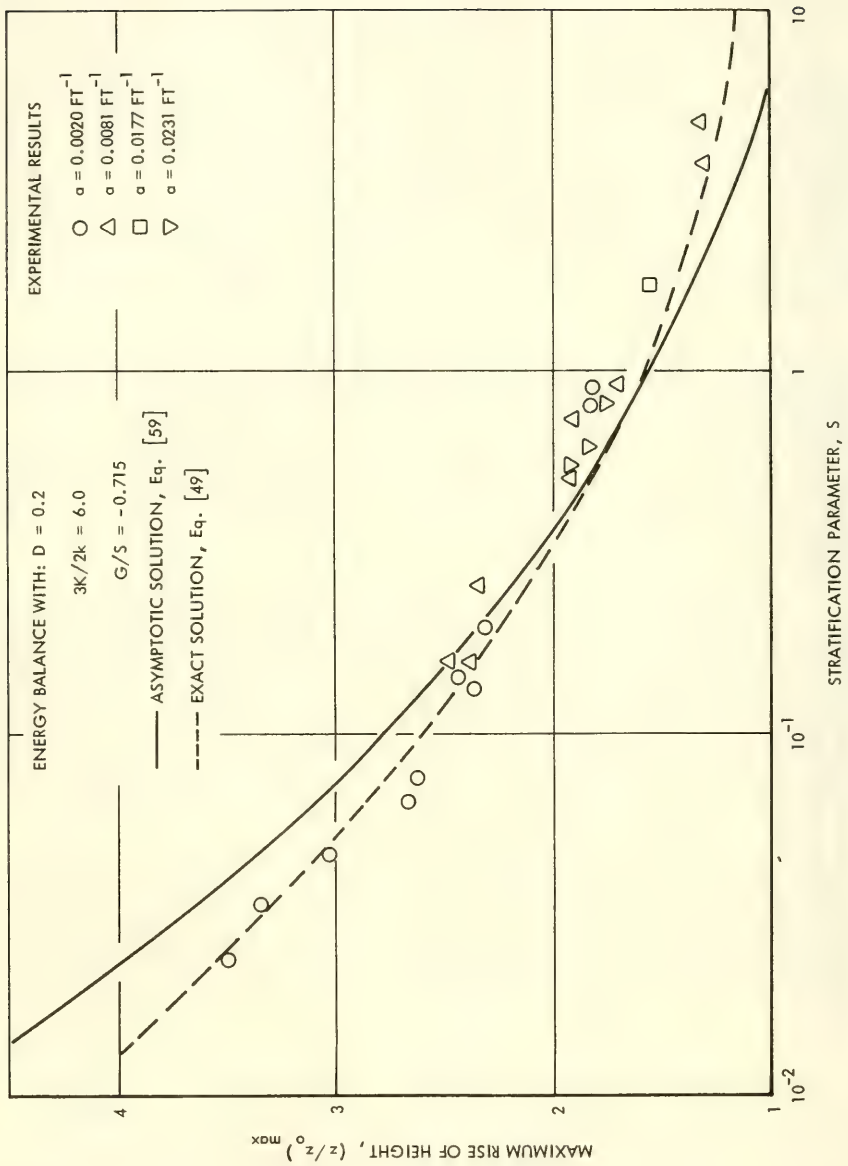


Fig. 12. The maximum rise of vortex-pairs convected in a density-stratified medium; comparison of experiment and theory

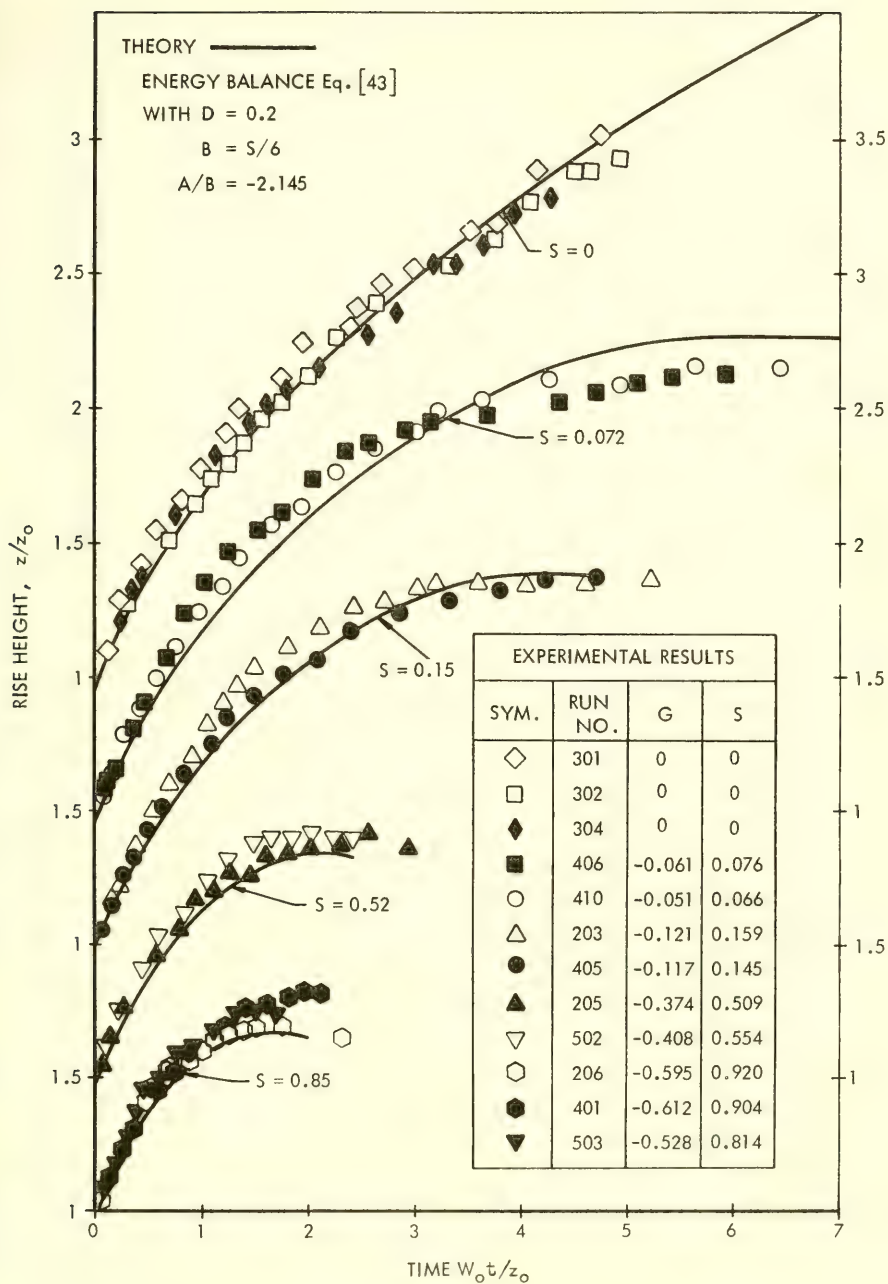


Fig. 13. The trajectory of vortex-pairs in stratified media; comparison of experiment and theory

captured mass. The theory takes into consideration variations in volume, circulation, momentum, and energy in the flow field. The ratio of internal to external velocity scales, ψ , is introduced as an important variable. The virtual momentum coefficient is shown to be linear in ψ , of the form $K_1 - K_2\psi$.

The theory is specifically derived for the two limiting cases of weak and strong circulation. In the former case, $\psi \rightarrow 1$ and the entrainment is weak; the asymptotic behavior of the trajectory is $z \sim t^{1/3}$ just as predicted by the usual theory based on complete similarity and momentum conservation.

In the case of strong circulation, $\psi \gg 1$, the asymptotic behavior of the trajectory depends very much on the way in which vorticity from the shear layer is ingested into the vortex pair. In the case where the shear layer from opposite sides is ingested in such a way as to cause annihilation of the ingested vorticity, then the asymptotic trajectory is $z \sim t^{1/2}$. Under the same conditions, the velocity ratio, ψ , increases toward the asymptotic value K_1/K_2 so that the virtual momentum coefficient tends to zero. As a result, the asymptotic motion assuming vorticity annihilation corresponds to a motion with complete similarity and with energy conservation. The ratio of growth of the pair radius with height is shown to increase, approaching a linear relation asymptotically.

Systematic experiments have been carried out, and the results for rise versus time and radius versus height are compared with the theory. They lend strong support to the strong circulation theory and further suggest that ingested vorticity is to a large degree annihilated.

Based on these findings for the case of homogeneous flows, a simplified theory is derived for the rising motion of vortex pairs in stratified media. The assumptions of the theory are: (i) the motion is determined by conservation of volume, mass, and energy (neglecting vorticity and momentum); (ii) complete similarity ($dR/dz = \beta$, a constant). General laws of motion in stratified media have been derived and solutions given; particularly interesting cases are discussed in detail.

Motions in stratified media were shown to depend on four non-dimensional parameters. Two of these depend upon the initial conditions of the motion and the stratification of the media. The other two are inherent in the details of the motion and had to be determined from experiments; one of these, the dissipation parameter $D = C_D/\beta K$ was found to be 0.2 while the other, the ratio of virtual kinetic and potential energy coefficients K/k was found to be 4. On the basis of these numbers it may be concluded that the dissipation rate is small and that the contribution of internal motions to the overall kinetic energy is large.

The experiments confirmed the environmental scaling param-

eters, which were used to collapse data taken under differing conditions. Good agreement was found between predicted and observed trajectories. Particularly good agreement was found for the maximum height of rise. The time required to reach maximum height was found to be inversely proportional to the Vaisala frequency, \sqrt{ag} , and was given approximately by $t_{\max}\sqrt{ag} = 1.8$, in good agreement with the theory. In general the experiments confirmed the utility of the simplified theory for predictions of the motion of vortex pairs in stratified media. This theory has been utilized elsewhere for the prediction of the behavior of chimney plumes rising into a stable atmosphere, with very good agreement between the theory and full scale observations, Tulin and Schwartz [1970], and also with excellent correlation with experiments to the penetration of a density discontinuity by a turbulent vortex-pair, Birkhead, Shwartz, and Tulin [1969].

ACKNOWLEDGMENT

This work was supported by the Naval Air Systems Command, the Air Programs Branch and the Fluid Dynamics Branch of the Office of Naval Research under Contract No. N00014-70-C-0345, which support is gratefully acknowledged.

REFERENCES

- Birkhead, J. L., Shwartz, J., and Tulin, M. P., "Penetration of a Density Discontinuity by a Turbulent Vortex-Pair," HYDRO-NAUTICS, Incorporated Technical Report 231-21, December 1969.
- Lamb, H., Hydrodynamics, Dover Publications, N.Y., 1945.
- Morton, B. R., Taylor, G. I., and Turner, J. S., "Turbulent Gravitational Convection from Maintained and Instantaneous Sources," Proc. of the Royal Society, A, Vol. 234, p. 1, 1956.
- Phillips, O. M., The Dynamics of the Upper Ocean, Cambridge University Press, Cambridge 1966.
- Richards, J. M., "Puff Motion in Unstratified Surroundings," J. of Fluid Mech., Vol. 21, No. 1, p. 97, 1965.
- Scorer, R. S., Natural Aerodynamics, Pergamon Press, 1958.
- Scorer, R. S., "Experiments on Convection of Isolated Masses of Buoyant Fluid," J. of Fluid Mech., Vol. 2, No. 6, p. 583, August 1957.
- Spreiter, J. R., and Sacks, A. H., "The Rolling Up of the Trailing Vortex Sheet and Its Effect on the Downwash Behind Wings," J. of Aero Sciences, Vol. 18, No. 1, p. 21, January 1951.

Thomson, Sir. W., "On Vortex Atoms," Philosophical Magazine, Series 4, Vol. 34, No. 227, p. 15, July 1867.

Tulin, M. P., and Schwartz, J., "Hydrodynamic Aspects of Waste Discharge," ALAA Paper No. 70-755, June 1970.

Woodward, B., "The Motion in and Around Isolated Thermals," Quart. J. of the Royal Meteorological Society, Vol. 85, p. 144, 1959.

ζ, η, ξ - CARTESIAN COORDINATES

u, v, w - CORRESPONDING VELOCITIES

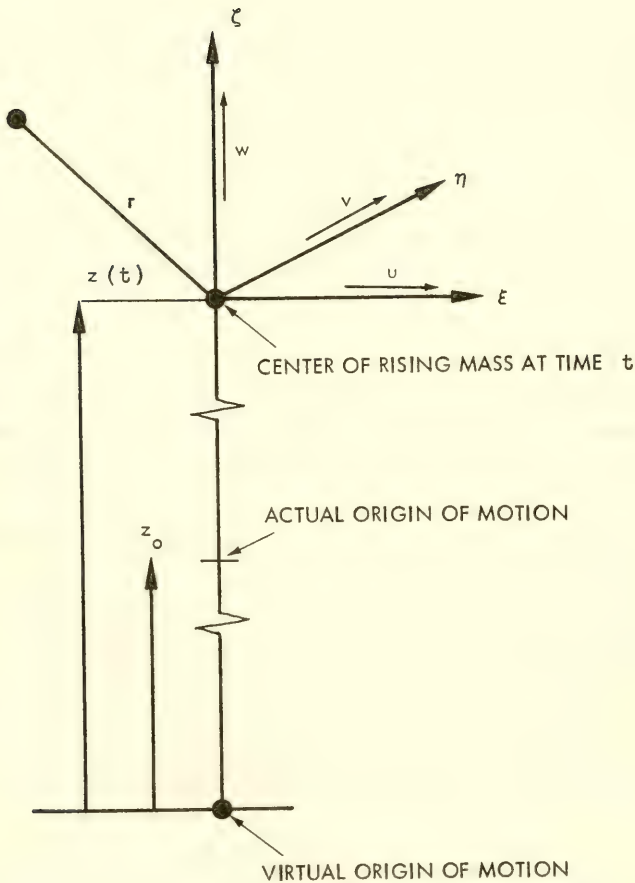


Fig. 14. Nomenclature

HYDRODYNAMICS IN THE OCEAN ENVIRONMENT

Thursday, August 27, 1970

Morning Session

Chairman: G. B. Whitham
California Institute of Technology

	Page
Radar Back-Scatter from the Sea Surface K. Hasselmann, M. Schieler, Universität Hamburg	361
Interaction Between Gravity Waves and Finite Turbulent Flow Fields D. Savitsky, Stevens Institute of Technology	389
Characteristics of Ship Boundary Layers L. Landweber, University of Iowa	449
Study of the Response of a Vibrating Plate Immersed in a Fluid L. Maestrello, T. L. J. Linden, The Boeing Company	477

RADAR BACK-SCATTER FROM THE SEA SURFACE

K. Hasselmann* and M. Schieler
*Institut fuer Geophysik
University of Hamburg*

ABSTRACT

Doppler spectra of electromagnetic backscatter from the sea surface are interpreted in terms of generalized Bragg models. The observed broadening of the spectra about the Bragg line is attributed to higher-order nonlinear processes. At conventional radar frequencies, good agreement with the measurements is achieved by an extension of the wave-facet interaction model considered by Wright, Bass et al. and other workers. The correlation of wave slopes and orbital velocities in the joint probability distribution of carrier-wave facets leads to significant differences between the Doppler spectra for vertical, horizontal and cross polarization. In the HF band, the Doppler broadening is interpreted in terms of quadratic wave-wave interactions. For the usual case that the electromagnetic wave lengths are small compared with the principal wavelengths of the sea, the theoretical Doppler spectrum consists of the lowest-order Bragg line and superimposed images of the complete ocean wave frequency spectrum folded on either side of the Bragg line. Both wave-facet and wave-wave interaction models give promise of extracting significant information on the "state of the sea" from electromagnetic Doppler return at wave lengths short compared with the dominant wave lengths of the sea.

*Presently at Woods Oceanographic Institution.

I. INTRODUCTION

The development of numerical wave prediction methods in the past years [1, 2, 17] has increased the need for wave data on a synoptic scale, both as a reference for testing and improving the models and as real-time input for the computations. Synoptic wave data would also be of value for numerical weather forecasting by providing indirect information on surface winds in otherwise poorly covered areas of the oceans. The growing interest in electromagnetic backscatter from the sea surface stems largely from the potentiality of the method for furnishing sea-state data of this kind. Radar scatterometers in satellites could scan most of the world oceans in a few hours. Alternatively, large areas of the ocean can be sampled using HF stations on land. Following the pioneering work of Crombie [6] and others, Ward [22] has recently detected the backscattered return of ionospheric HF modes from relatively small, 100 km square patches of the sea surface at distances up to 3000 km.

Unfortunately, both techniques suffer from wave length limitations. Cloud absorption and finite antenna size define an effective transmission window for satellite scatterometers in the conventional radar wave length range between a few fractions of a cm and about 50 cms. Backscatter measurements over long horizontal ranges are similarly restricted to ionospheric modes in the decameter band. In both cases, the electromagnetic wave lengths are considerably shorter than the principal components of the surface-wave spectrum, which normally lie in the range between 50 and 500 m. The bad wave length matching creates difficulties in relating the backscattered signals obtained by these methods to significant sea-state parameters.

Scattering experiments in both the centimeter-decimeter and decameter bands have now clearly established the basic validity of the first-order (Bragg) wave-wave interaction theory. According to this model, the backscattered radiation arises from interactions with two gravity-wave components whose wavenumbers \underline{k}^g are determined by the Bragg (resonance interaction) condition for constructive interference, $\underline{k}^g = \pm 2\underline{k}^i$, where \underline{k}^i represents the horizontal wavenumber component of the incident radiation. For non-normal incidence, the wave lengths of the scattering and incident components are then of the same order, which implies that the scattering surface waves normally lie in the high-wavenumber, equilibrium range of the surface-wave spectrum. It appears therefore from first-order theory that backscatter measurements may yield a useful independent determination of Phillips' constant [15, 22], but do not contain significant information on the more interesting low-wavenumber part of the wave spectrum which contains most of the wave energy.

Fortunately, the scattering measurements, while supporting the Bragg theory, also indicate that it should be regarded only as a first approximation. The Doppler spectra, in particular, exhibit

several features not predicted by the Bragg model. Generally, there is a marked dependence of the anomalies on sea state, suggesting that useful correlations between backscatter signatures and significant sea-state parameters may be discovered by extending the scattering theory to higher order.

Two generalisations have been proposed: the wave-facet interaction model [23, 4, cf. also 3, 9, 10, 20, 21], in which the Bragg-scattering waves are superposed on longer carrier waves, and the higher-order, wave-wave interaction model originally investigated by Rice [18]. The models have been applied hitherto mainly to the cross sections, which show only weak sea-state signatures. In the present paper, we consider their extension to the more strongly sea-state dependent Doppler spectra.

In the cm-dm bands, good agreement with the observed Doppler spectra is obtained with the wave-facet interaction model. The Doppler spectra are found to be quasi-Gaussian and can be characterized to good approximation by the mean frequency and the frequency bandwidth. Both parameters depend on moments of the wave spectrum which are governed by the high-energy, low-wave-number range of the spectrum. They can therefore be used to obtain independent estimates of, say, the mean waveheight and period.

The model allows only for electromagnetic interactions. Basically, the hydrodynamical modulation of short gravity waves by long carrier waves is of considerable interest, not only for the description of the surface wave field, but also for its energy balance. The interactions generally lead to an energy loss of the long waves at a rate which can be estimated from the observed upwind-downwind asymmetry of the cross sections [11][†]. However, because of the strong influence of white capping, the interactions cannot yet be described in sufficient detail to be included realistically in computations of the Doppler spectra. Their effect on the Doppler bandwidth is probably negligible, but the mean Doppler frequency may be more strongly modified.

The wave-facet interaction model is valid for electromagnetic wave lengths shorter than about 1 m. Thus it applies in the cm-dm radar band, but not in the dkm band. In the latter case, however, the Bragg theory can be generalised by straightforward extension of the wave-wave interaction analysis to higher order. The relevant

[†]Longuet-Higgins [13] has shown that the momentum loss of short waves breaking on the crests of longer waves results in an energy transfer to the long waves. However, the gain in long-wave kinetic energy due to this process can be shown to be slightly less than the loss of potential energy arising from the simultaneous mass transfer between short and long waves. The net result of both processes is a weak attenuation of the long waves [11].

perturbation parameter of the expansion is given by the ratio of the amplitude of the interacting surface wave to the wave length of the incident radiation. In the first order analysis, the perturbation parameter is proportional to the slope of the scattering Bragg wave, which is small for all electromagnetic wave lengths. At second and higher order, however, the electromagnetic waves interact with longer surface waves of higher amplitude. In this case, the perturbation parameter remains small only if the electromagnetic wave length is large compared with the amplitude of the entire wave field. This condition is satisfied by dkm waves, but not by cm-dm waves.

The requirements for the wave-facet and wave-wave interaction models are found to be mutually exclusive, so that the two expansions cannot be matched in a common region of validity. It is a fortunate coincidence that the theoretical wave length gap corresponds to the gap between the two presently available techniques for measuring electromagnetic backscatter on a synoptic scale.

The second order wave-wave interaction analysis yields a continuous Doppler spectrum superimposed on the first-order Bragg line. The continuum reduces to a particularly simple and useful form when the Bragg wave length is short compared with the wave lengths of the dominant surface waves -- the usual situation for ionospheric modes. In this case, the continuum is identical with the two-sided image of the surface-wave frequency spectrum, centered on the Bragg line as virtual frequency origin. The energy scale of the wave spectrum can be inferred from the observed energy of the Bragg line, independent of transmission or other calibration factors.

Doppler side-band structures observed by Ward [22] and others are not inconsistent with this interpretation. However, most Doppler spectra published hitherto have been analysed from rather short records, so that the continuum is generally not well defined statistically. Longer records are needed to decide whether the one-dimensional frequency spectrum of the surface-wave field can indeed be detected in the Doppler spectrum of backscattered ionospheric modes above the inherent ionospheric noise.

II. THE LOWEST-ORDER SCATTERING MODELS

For electromagnetic waves short compared with the dominant waves of the sea, one might attempt to describe the scattered field by a specular reflexion model, in which the sea surface is represented as an ensemble of locally plane, infinitesimal facets, each of which reflects the incident radiation according to the laws of geometric optics. The cross section σ for the backscattered radiation (the backscattered energy per unit solid angle per unit surface area of the ocean) is then proportional to the number density of facet normals

pointing towards the source. As the distribution of normals in a random surface-wave field is approximately Gaussian, the dependence of $\log \sigma$ on depression angle θ is given by a parabola, with maximum at normal incidence (90° depression angle) and half-width typically of the order 10° (Fig. 1).

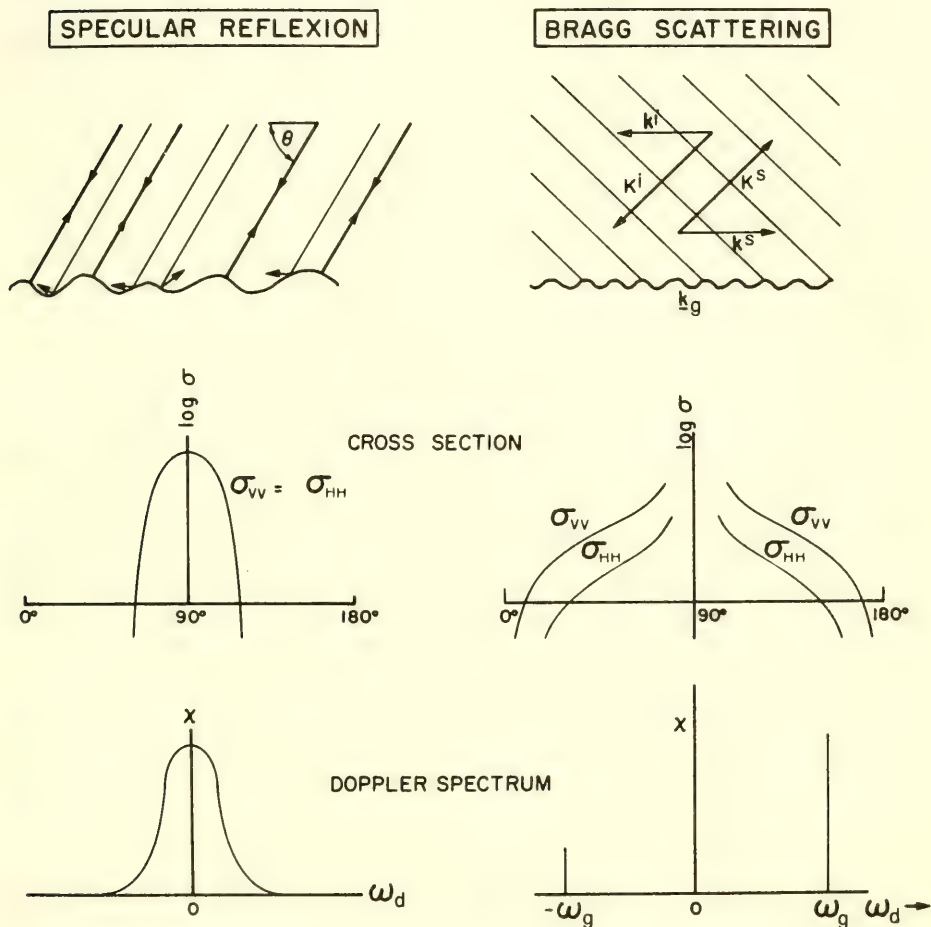


Fig. 1. Cross sections and Doppler spectra according to the specular reflection and first-order Bragg scattering models (qualitative)

The frequencies of the backscattered waves are shifted relative to the frequency of the incident radiation by the Doppler frequency $\omega_f = -2\mathbf{k}^i \cdot \mathbf{u}$ induced by the facet motion, where $\mathbf{K}^i = (\mathbf{k}^i, k_z^i)$ is the wavenumber of the incident radiation and \mathbf{u} the local orbital velocity of the waves. For an approximately linear wave field, \mathbf{u} is a Gaussian variable, and the Doppler spectrum also has a Gaussian shape.

As the backscattered waves are reflected at normal incidence, it follows by symmetry that the cross sections and Doppler spectra are independent of polarisation. Vertical and horizontal polarisation are denoted in Fig. 1 by V and H, respectively, the first index referring to the incident field, the second to the backscattered field. The cross-polarised return VH and HV vanishes.

Although applied successfully by Cox and Munk [5] to the analysis of sun glitter from the sea surface, the specular reflexion model fails to describe the observed electromagnetic backscatter at cm-dm and dkm wave lengths. It appears that for these wave lengths surface irregularities of length scale comparable with the radiation wave length cannot be neglected. Accordingly, recent models have been based on the Bragg scattering theory, in which these irregularities are regarded as the dominant scatterers.

It is assumed in the Bragg model that the slopes of the scattering surface waves are small and that their wave lengths are comparable with those of the radiation field. The backscattered field can then be expanded in powers of the surface displacement. The first-order field is linear in the surface displacement and can therefore be constructed by superposition from the field scattered by a single gravity-wave component $\zeta = Z \exp \{i\mathbf{k}^g \cdot \mathbf{x} - i\omega_g t\}$. This corresponds to the classical problem of refraction by a periodic lattice. The scattered field consists of two waves $s = \pm$ whose horizontal wavenumbers and frequencies are given by the Bragg (resonant interaction) conditions

$$\mathbf{k}^i + s\mathbf{k}^g = \mathbf{k}^s \quad (1)$$

$$\omega_i + s\omega_g = \omega_s$$

(The vertical wavenumber component k_z^i determining the scattering angle follows from the dispersion relation $|\omega_s| = c|\mathbf{k}^s|$, where c is the velocity of light).

Backscattering ($\mathbf{k}^s = -\mathbf{k}^i$) occurs for the gravity-wave components $\mathbf{k}^g = \pm 2\mathbf{k}^i$. The backscattering cross section is accordingly of the form

$$\sigma_{\alpha\beta} = \sigma_{\alpha\beta}^+ + \sigma_{\alpha\beta}^- \quad (2)$$

where

$$\sigma_{\alpha\beta}^s = T_{\alpha\beta} F_g(-2s\mathbf{k}^i) \quad (\alpha, \beta = V \text{ or } H, \quad s = \pm)$$

and $F_g(\mathbf{k})$ is the surface-wave spectrum, normalised such that the mean square surface displacement $\langle \zeta^2 \rangle = \int F_g(\mathbf{k}) d\mathbf{k}$. The cornered parentheses denote mean values. (The negative sign of the wave-number in the definition of $\sigma_{\alpha\beta}^s$ has been introduced so that $\sigma_{\alpha\beta}^+$ corresponds to a spectral line with positive Doppler shift, cf. Eq. (3).) $T_{\alpha\beta}$ is a scattering coefficient obtained by expanding the electromagnetic boundary conditions at the free surface [18]),

$$T_{VV} = \left| \frac{2\omega_i^2}{c^2} \sin^2 \theta \frac{(1-\epsilon)(\epsilon[1+\cos^2 \theta] - \cos^2 \theta)}{(\epsilon \sin \theta + \sqrt{\epsilon - \cos^2 \theta})^2} \right|^2$$

$$T_{HH} = \left| \frac{2\omega_i^2}{c^2} \sin^2 \theta \frac{1-\epsilon}{(\sin \theta + \sqrt{\epsilon - \cos^2 \theta})^2} \right|^2$$

$$T_{VH} = T_{HV} = 0$$

where ϵ is the dielectric constant of sea water.

The normalized Doppler spectrum $\chi_{\alpha\beta}(\omega_d)$, defined by $\int \chi_{\alpha\beta}(\omega_d) d\omega_d = \sigma_{\alpha\beta}$, where $\omega_d = \omega_s - \omega_i$, is given according to (1) by two lines at the gravity-wave frequencies $\pm \omega_g$,

$$\chi_{\alpha\beta}(\omega_d) = \chi_{\alpha\beta}^+(\omega_d) + \chi_{\alpha\beta}^-(\omega_d)$$

with

(3)

$$\chi_{\alpha\beta}^s(\omega_d) = \sigma_{\alpha\beta}^s \delta(\omega_d - s\omega_g)$$

Normally, one of the Bragg lines due to scattering from the surface wave component propagating in the downwind direction is very much stronger than the other line associated with the wave propagating in the opposite, upwind direction.

The general properties of the Bragg cross sections and Doppler spectra are indicated qualitatively in the right-hand panels of Fig. 1. In contrast to the specular reflexion model, there is a pronounced dependence on polarisation and appreciable backscatter at small and intermediate depression angles. The cross-polarised return again vanishes.

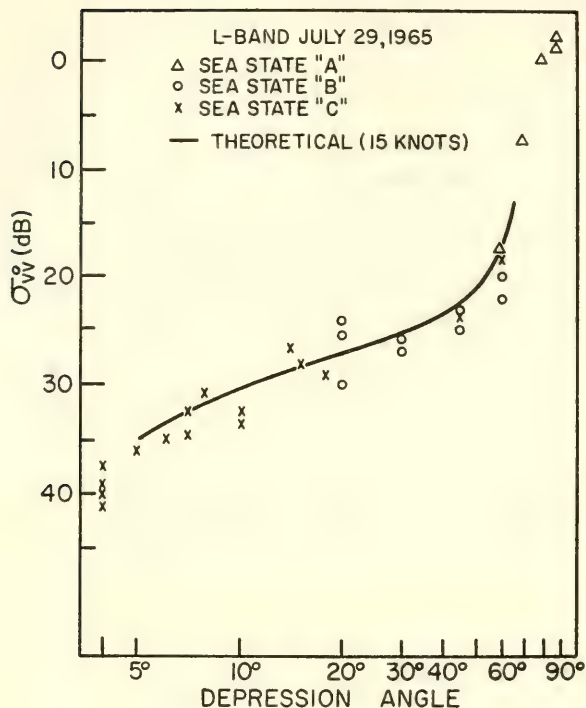


Fig. 2. Theoretical and observed Bragg backscatter cross sections for vertically polarised 24 cm (L band) waves (from Wright [23])

Figure 2 shows a comparison by Wright [23][†] of experimental and theoretical Bragg cross sections for vertically polarised cm-dm waves. The surface waves were represented by a Phillips' spectrum $F_g(k) = (\alpha/2)k^{-4}S(\psi)$, with a uniform half-plane angular spreading function, $S(\psi) = \pi^{-1}$ for $0 \leq |\psi| < \pi/2$, $S(\psi) = 0$ for $-\pi/2 < |\psi| \leq \pi$. The constant α was chosen to fit the observed cross sections, but is not inconsistent with other estimates from direct measurements of gravity-wave spectra (cf. also [15]). Shown in Fig. 3 are theoretical and experimental cross section ratios σ_{VV}/σ_{HH} . The agreement here is also very good, except for the shortest wave length (3.4 cm, 8910 MHz), where scattering by spray may be beginning to mask the

[†]The theoretical cross sections shown in Figs. 2 and 3 were, in fact, computed for the wave-facet interaction model considered in the next section. However, the deviations from the first-order Bragg model are negligible.

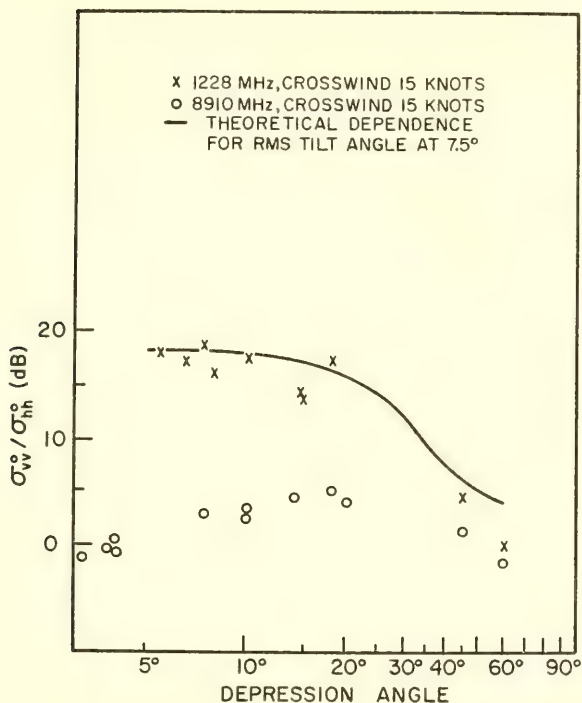


Fig. 3. Theoretical and observed ratios of Bragg backscatter cross sections for vertical and horizontal polarisation at wave lengths 24 cm (1228 MHz) and 3.4 cm (8910 MHz) (from Wright [24])

weak Bragg return for horizontal polarisation. Not predicted by first-order Bragg theory is the observed cross-polarised return, which is generally only slightly smaller than or comparable with the backscatter for horizontal polarisation; this can be explained by the wave-facet interaction model [23].

Although the observed cross sections σ_{vv} and σ_{hh} are in good agreement with theory, the Doppler spectra for these polarisations point to limitations of the first-order model. In the cm-dm bands, the Bragg lines are found to be broadened into Gaussian shaped distributions with bandwidths of the same order as the Bragg frequency (cf. Fig. 4., from Valenzuela and Laing [20]). Earlier measurements by Hicks *et al.* [13] indicate that the mean frequencies of the distributions -- which were not measured by Valenzuela and Laing -- may also be considerably higher, by factors of the order 2 to 4, than the theoretical Bragg frequency.

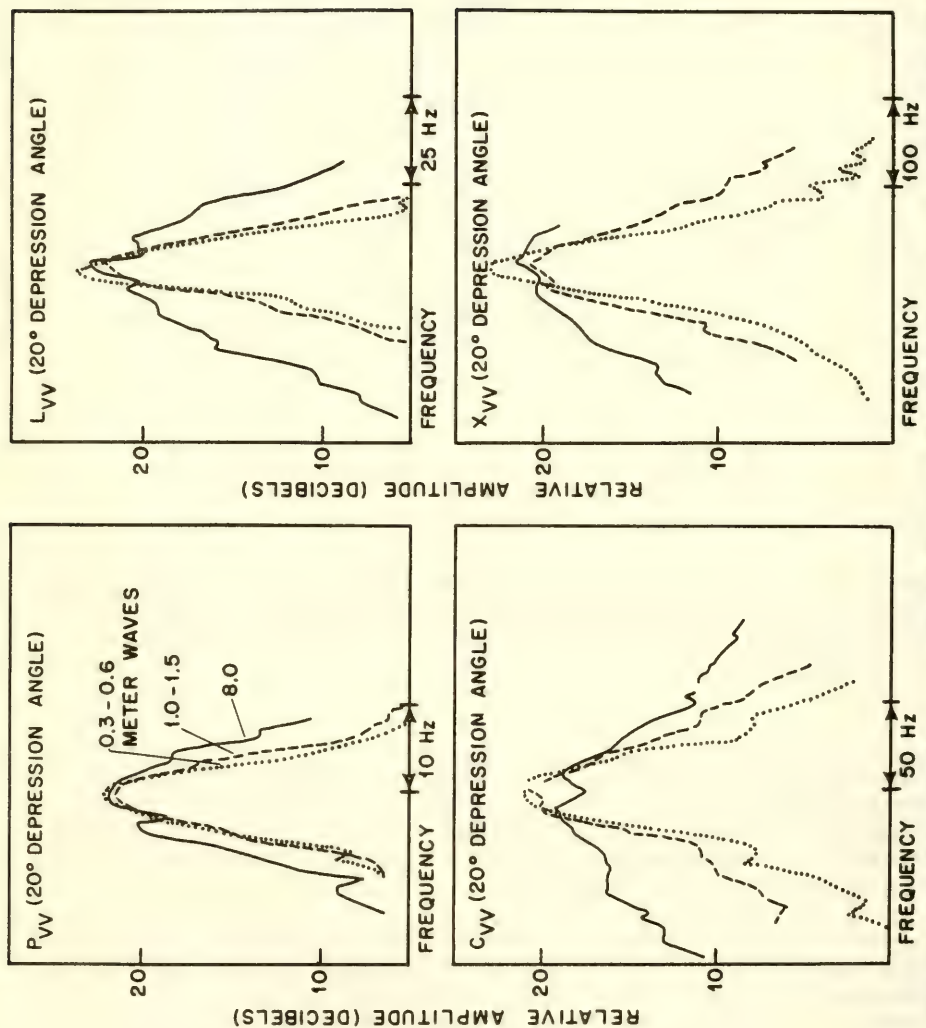


Fig. 4. Examples of vertically polarised Doppler backscatter spectra in bands P (70 cm), L (24 cm), C (6.7 cm) and X (3.4 cm). (From Valenzuela and Laing [20]).

In the decameter bands, the observed broadening and shift of the Bragg lines are much weaker. Instead, the Doppler spectra show pronounced side band structures (cf. Fig. 11, from Ward [22], and similar spectra in Crombie [6] and elsewhere). The basic difference in structure of the Doppler spectra observed in the cm-dm and dkm bands lends support to theoretical considerations calling for alternative expansion procedures in the two wave length ranges.

III. THE WAVE-FACET INTERACTION MODEL

In order to treat the scattering waves as small perturbations of a plane surface, it is assumed in the Bragg theory that the wave amplitudes are small compared with the wave length of the incident radiation. In a strict sense, the expansion is valid if this condition is satisfied not only for the Bragg waves, but for the entire surface displacement. Thus the theory is not rigorously applicable to short electromagnetic waves of a few cm wave length, although the long surface waves of high amplitude which violate the expansion condition do not enter in the final scattering expressions. Various workers [e.g. 3, 4, 10, 20, 21, 23] have suggested that this formal shortcoming may be remedied by dividing the surface-wave spectrum into two parts, a high-wavenumber scattering region, and the energy-containing region at low wavenumbers which defines the "sea." The "sea" is then treated as a random carrier wave which modulates the scattering by the superimposed Bragg waves. If the Bragg wave length π/k^i is short compared with a typical wave length $2\pi/k^c$ of the sea, the carrier wave may be represented locally as a plane facet, and the first-order scattering theory applied in the reference frame of the moving facet.

The model involves additional conditions besides the two-scale assumption that it is possible to define a facet diameter D intermediate between the carrier and scattering wave length scales,

$$(k^i)^{-1} \ll D \ll (k^c)^{-1} \quad (4)$$

The finite facet size implies an indeterminacy $\Delta k = O(1/D)$ of the scattering wavenumber, which corresponds to an angular spread $\Delta\theta = O\{(K^i D \sin \theta)^{-1}\}$ of the backscattered beam. The wave-facet interaction model is meaningful only if $\Delta\theta$ is small compared with the change in effective depression angle introduced by the facet slope $\partial\zeta/\partial x = O(k^c\zeta)$, where ζ is the carrier-wave amplitude. This requires $k^c\zeta DK^i \sin \theta \gg 1$, or, since $Dk^c \ll 1$, on account of [4],

$$K^i \zeta \sin \theta = k_3^i \zeta \gg 1 \quad (5)$$

Similarly, a wavenumber broadening Δk corresponds to a frequency broadening of the Bragg line of order $\Delta\omega = (d\omega_g/dk^g) \Delta k = (\omega_g/2k^g) \cdot \Delta k$ (ignoring capillary effects). The model assumes that this is small compared with the Doppler shift $\omega_f = -2K^i \cdot u$ induced by the facet velocity u . For $u = O(\omega_c \zeta)$, where ω_c is a typical carrier-wave frequency, this requires

$$DK^i \omega_c \zeta k^i / \omega_i = DK^i (k^i k^c)^{1/2} \zeta \gg 1$$

Substituting $Dk^c \ll 1$, this is equivalent to

$$K^i \zeta (k^i / k^c)^{1/2} \gg 1 \quad (6)$$

Since $k^i / k^c \gg 1$, the frequency condition (6) is less critical than the corresponding condition (5) for the angular resolution. The inequality (5) is normally fairly well satisfied at conventional radar wave lengths for surface-wave heights of order 1 m and higher (except for small depression angles, where the model breaks down, in any case because of shadowing effects). For electromagnetic wave lengths longer than about 1 m the inequality (5) is normally no longer valid, even though the two-scale inequality (4) may still apply.

The total backscattered energy is obtained in the wave-facet interaction model by summing over the contributions from all scattering facets. Introducing a facet probability distribution $p(\underline{\lambda})$ with respect to the five basic facet parameters $\underline{\lambda} = (\lambda_1, \lambda_2, \lambda_3, \lambda_4, \lambda_5)$, where

$$(\lambda_1, \lambda_2, \lambda_3) = (u_1, u_2, u_3) = \text{facet velocity (= local long-wave orbital velocity),}$$

and $(\lambda_4, \lambda_5) = (\partial \zeta / \partial x_1, \partial \zeta / \partial x_2) \equiv (n_1, n_2) = \text{facet slope, the Doppler spectrum is given by}$

$$\chi_{a\beta}^s = \int [\tilde{\sigma}_{a\beta}^s \delta(\omega_d - s\tilde{\omega}_g - \omega_f)] p(\underline{\lambda}) d\underline{\lambda} \quad (7)$$

where $\tilde{\sigma}_{a\beta}^s$, $\tilde{\omega}_g$ represent, respectively, the Bragg cross section and gravity-wave frequency in the facet reference frame.

To the modulated Doppler spectrum (7) of the first-order Bragg field should be added the modulated spectrum of the zero'th order field reflected from a plane facet, as described by the specular reflexion model. However, this is important only near vertical incidence and will be ignored in the following.

Experimentally, the probability distribution $p(\underline{\lambda})$ is found to be approximately Gaussian, in accordance with the theoretical distri-

bution for a random, linear gravity-wave field,

$$p(\underline{\lambda}) = (2\pi)^{-5/2} |C|^{-1/2} \exp \left\{ -\frac{1}{2} C_{ij}^{-1} \lambda_i \lambda_j \right\} \quad (8)$$

The covariance matrix C_{ij} can be evaluated from the surface-wave spectrum and the linear wave solutions,

$$C_{ij} = \begin{array}{cc|cc} \overline{g k_1^2/k} & \overline{g k_1 k_2/k} & & \\ \overline{g k_1 k_2/k} & \overline{g k_2^2/k} & & \\ \hline & & 0 & \\ & & g\overline{k} & -\overline{\omega k_1} & -\overline{\omega k_2} \\ & 0 & -\overline{\omega k_1} & \overline{k_1^2} & \overline{k_1 k_2} \\ & & -\overline{\omega k_2} & \overline{k_1 k_2} & \overline{k_2^2} \end{array} \quad (9)$$

where $\overline{k_a k_\beta/k} = \int F_g(k) (k_a k_\beta/k) dk$, etc.

We note that the facet Doppler shift ω_f is correlated not only with the facet velocity, but through the correlation $\langle u_3 n_i \rangle$ also with the facet slope,

$$\langle \omega_f n_i \rangle = -2k_3^i \langle u_3 n_i \rangle \quad (10)$$

For small wave slopes, the factor in square parentheses in Eq. (7) can be expanded in powers of n_i . The integration can then be carried out explicitly for each term of the expansion yielding a solution of the form

$$\chi_{\alpha\beta}(\omega_d) = \chi_{\alpha\beta}^+(\omega_d) + \chi_{\alpha\beta}^-(\omega_d)$$

with

$$\chi_{\alpha\beta}^s(\omega_d) = (\tilde{\sigma}_{\alpha\beta}^s)_0 \frac{\exp \left\{ -(\omega_d - s\omega_g)^2 / 2\langle \omega_f^2 \rangle \right\}}{(2\pi\langle \omega_f^2 \rangle)^{1/2}} [1 + q_1^s + q_2^s + \dots] \quad (11)$$

where q_1^s, q_2^s, \dots are polynomials in $(\omega_d - s\omega_g)$ of order 1, 2, ... in the facet slope,

$$q_1^s = \frac{\langle \omega_f n_i \rangle (\omega_d - s\omega_g)}{\langle \omega_f^2 \rangle} \left\{ \left(\frac{\partial}{\partial n_i} \tilde{\sigma}_{\alpha\beta}^s \right)_0 / (\tilde{\sigma}_{\alpha\beta}^s)_0 + \frac{s(\omega_d - s\omega_g)}{\langle \omega_f^2 \rangle} \left(\frac{\partial \tilde{\omega}_g}{\partial n_i} \right)_0 \right\} \quad (12)$$

$$\begin{aligned}
q_2^s = & \left\{ \langle n_i n_j \rangle + \frac{\langle \omega_f n_i \rangle \langle \omega_f n_j \rangle}{\langle \omega_f^2 \rangle} \left[(\omega_d - s \omega_g)^2 - \langle \omega_f^2 \rangle \right] \right\} \cdot \\
& \cdot \left\{ \frac{1}{2} \left(\frac{\partial^2 \tilde{\sigma}_{\alpha\beta}^s}{\partial n_i \partial n_j} \right)_0 / \tilde{\sigma}_{\alpha\beta}^s + s \frac{(\omega_d - s \omega_g)}{\langle \omega_f^2 \rangle} \left[\frac{1}{2} \left(\frac{\partial^2 \tilde{\omega}_g}{\partial n_i \partial n_j} \right)_0 + \left(\frac{\partial \tilde{\omega}_g}{\partial n_i} \frac{\partial \tilde{\sigma}_{\alpha\beta}^s}{\partial n_j} / \tilde{\sigma}_{\alpha\beta}^s \right)_0 \right] \right. \\
& \left. + \frac{(\omega_d - s \omega_g)^2 - \langle \omega_f^2 \rangle}{2 \langle \omega_f^2 \rangle} \left(\frac{\partial \tilde{\omega}_g}{\partial n_i} \frac{\partial \tilde{\omega}_g}{\partial n_j} \right)_0 \right\} \quad (13)
\end{aligned}$$

The subscript 0 refers to values at $\underline{n} = 0$.

To lowest order, the Doppler spectra for vertical and horizontal polarisation are identical Gaussian distributions with mean frequency $\langle \omega \rangle = s \omega_g$ and variance

$$\begin{aligned}
\langle (\omega - \langle \omega \rangle)^2 \rangle = \langle \omega_f^2 \rangle = & 2 \left\{ k_l^i k_m^j \langle u_l u_m \rangle + \langle k_3^i \rangle^2 \langle u_3^2 \rangle \right\} \quad (14) \\
& (l, m = 1, 2)
\end{aligned}$$

The distribution represents an ensemble of Bragg lines of equal energies displaced by their appropriate facet Doppler frequencies ω_f .

The higher-order corrections q_1^2, q_2^2, \dots represent distortions of the Gaussian distribution due to the variations in energy of the Bragg lines associated with variations in the carrier-wave slope. These affect the shape of the Doppler spectrum through the correlation between facet slopes and facet Doppler frequency, Eq. (10). The degree of distortion depends on the depression angle and polarisation. In the cross-polarised case, the zero'th and first-order terms disappear, since $(\tilde{T}_{VH})_0 = (\partial/\partial n_i \tilde{T}_{VH})_0 = 0$, so that the Doppler spectrum is non-Gaussian already to lowest order.

Computations of the Doppler spectrum were made for a Pierson-Moskowitz [16] spectrum using a half-plane cosine-to-the-fourth spreading factor,

$$F_g(k) = \begin{cases} \frac{4\alpha}{3\pi} k_l^{-4} \exp \{ -\beta(\omega_0/\omega)^4 \} & \text{for } k_l > 0 \\ 0 & \text{for } k_l < 0 \end{cases}$$

with $\alpha = 0.0081$, $\beta = 0.74$ and $\omega_0 = g/U$, where U is the wind velocity, assumed parallel to the x_l axis. The same spreading factor was taken for both scattering and carrier waves.

For a Pierson-Moskowitz spectrum, $\langle \omega_i^2 \rangle \sim U^2$ and $\langle \omega_i n_i \rangle \sim U$. The slope moments $\langle n_i n_j \rangle$ diverge logarithmically at high wavenumbers. To obtain finite $\langle n_i n_j \rangle$, the "carrier-wave" spectrum was cut off at an upper wavenumber $k_g/10$. The exact position of the cut-off is not critical for the evaluation of $\langle n_i n_j \rangle$, and the slope moments themselves enter only rather weakly in the second-order term q_2^s of the expansion (11). However, the existence of a divergence as such points to a conceptual difficulty of the wave-facet interaction model. It appears that for an asymptotic k^{-4} spectrum the carrier-wave region of the spectrum cannot be rigorously separated from the Bragg-scattering region.

Figure 5 shows the computed half-power bandwidths for the lowest-order Gaussian spectrum as a function of wave height. The values compare well with measurements by Valenzuela and Laing [20].

Deviations from the Gaussian form due to the higher-order corrections q_1^s and q_2^s are represented in Figs. 6 - 9 in terms of the mean frequency $\langle \omega \rangle / \omega_g$ and the frequency bandwidth $\langle (\omega - \langle \omega \rangle)^2 \rangle / \langle \omega^2 \rangle$, normalised by their appropriate values for the zero'th order Gaussian spectrum.

The strongest correction is found for the mean frequency, particularly for horizontal polarisation. The dependence on depression-angle and polarisation, shown in Fig. 6 for $U = 20$ m/s, is found to be very similar at all wind speeds. The absolute values of the frequency shifts increase approximately linearly with wind speed, Fig. 7. Qualitatively, the polarisation and wind-speed dependence of the mean Doppler frequency are in agreement with measurements made by Hicks *et al.* [13] at low depression angles of about 5° . However, the theory is not strictly applicable in this case on account of shadowing effects.

The bandwidth corrections (Figs. 8 and 9) remain rather small for depression angles less than 45° and limited azimuth angles ψ relative to the wind. Larger deviations in the cross-wind directions depend strongly on the spreading factors, which are rather uncertain for these angles. The experimental dependence of the Doppler bandwidth on radar frequency and polarisation [20] tends to be somewhat larger and have a different trend than the corrections shown in Figs. 8 and 9. Valenzuela and Laing [20] suggest that these effects may be due partly to spray. To a fair approximation, the observed bandwidths can be represented for small and intermediate angles ψ and θ by the zero'th order Gaussian bandwidth.

Both the bandwidth and mean frequency vary significantly with wave height and can therefore be used for estimates of sea state. For the one-parametrical family of spectra considered in the present example, the two estimates are not independent. However, in general the mean square bandwidth $\langle (\omega - \langle \omega \rangle)^2 \rangle \approx \langle \omega_i^2 \rangle$ (Eq. 14) and the mean

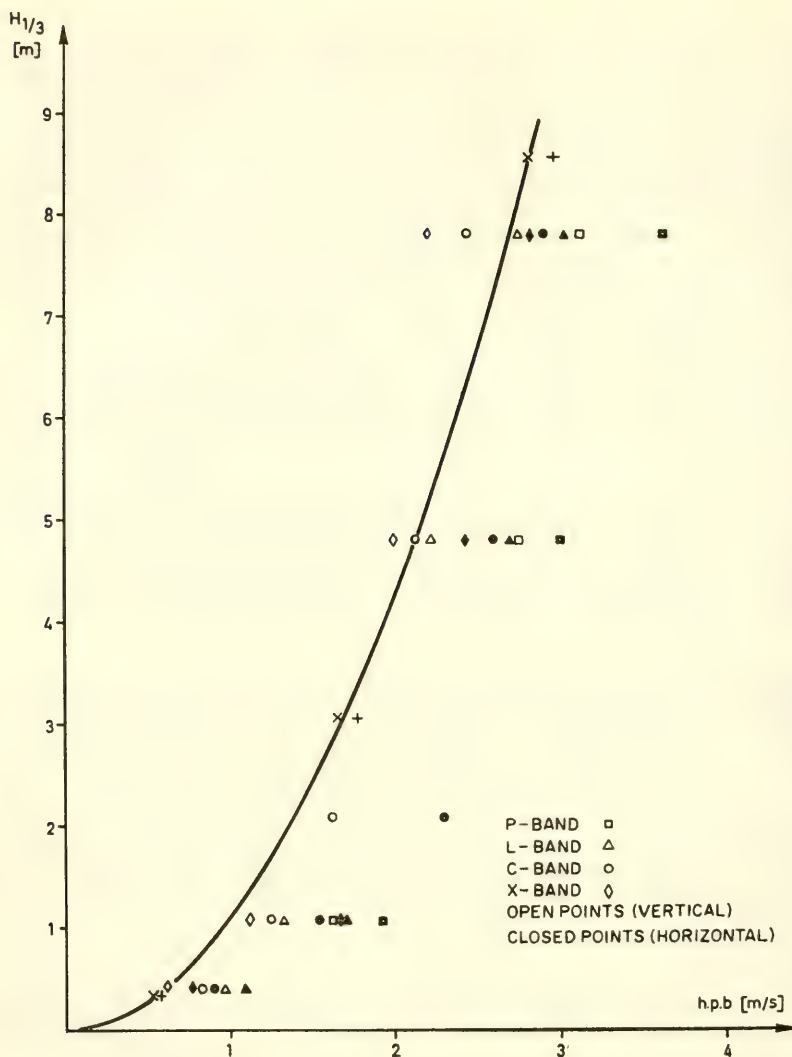


Fig. 5. Comparison of theoretical half-power bandwidths (h.p.b.) for zero'th order Gaussian spectrum with measurements by Valenzuela and Lang 20 . Doppler frequencies are in units of equivalent velocities $U_d = \omega_d / 2k^1$. Theoretically, a Pierson-Moskowitz spectrum with $\cos^4 \psi$ spreading function yields

$$\text{h.p.b. [m/s]} = 1.06 \left\{ \frac{\cos^2 \theta}{6} (4 \cos^2 \psi + 1) + \sin^2 \theta \right\}^{1/2} (H_{1/3} [\text{m}])^{1/2}$$

where the significant wave height $H_{1/3} \approx 4 \langle \zeta^2 \rangle^{1/2} = 0.209 U^2/g$. The computations were made for $\psi = 0^\circ$, $\theta = 20^\circ$.

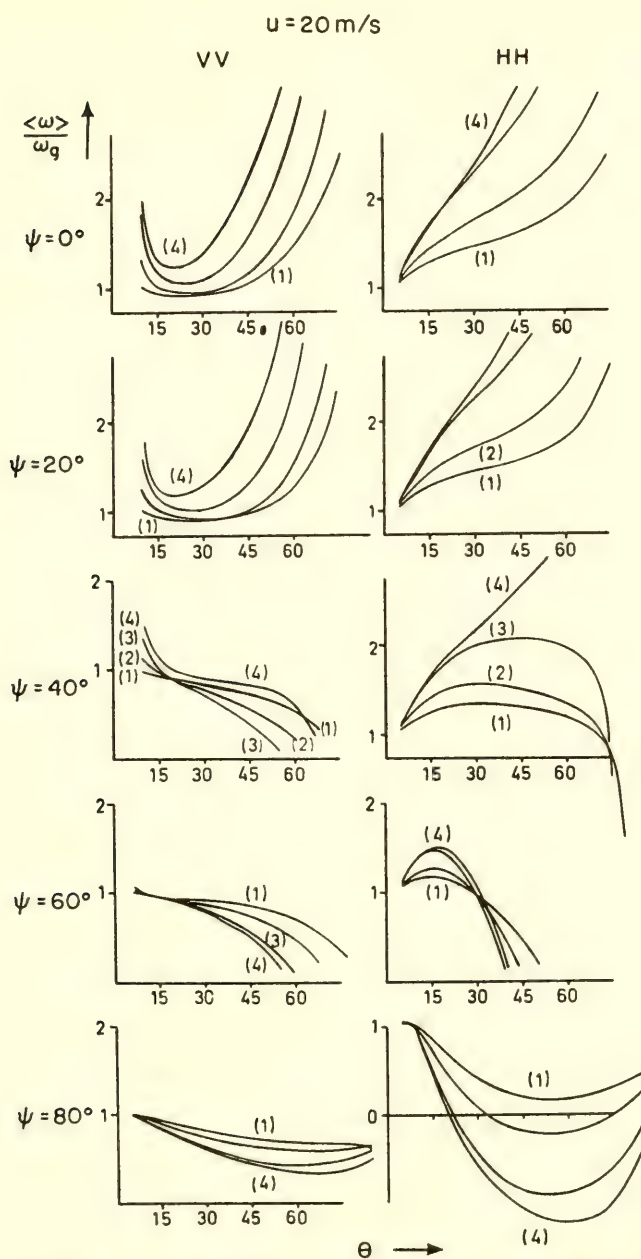


Fig. 6. Ratios of mean Doppler frequency $\langle \omega \rangle$ to Bragg frequency ω_g for the wave-facet interaction model at windspeed $U = 20 \text{ m/s}$. The indices 1, 2, 3, 4 refer to P, L, C and X bands, respectively. The computations include terms up to order q_2^2 in the expansion (11). To this approximation, the cross polarised case yields $\langle \omega \rangle = \omega_g$.

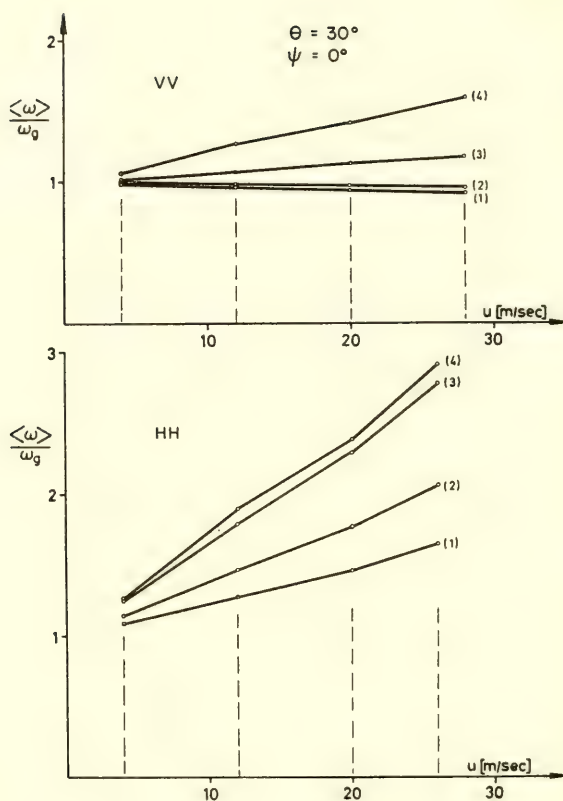


Fig. 7. Dependence of $\langle \omega \rangle / \omega_g$ on wind speed U for $\theta = 30^\circ$, $\psi = 0^\circ$. An approximately linear variation is found for all depression angles θ and azimuth angles ψ .

$u = 4 \text{ m/s}$

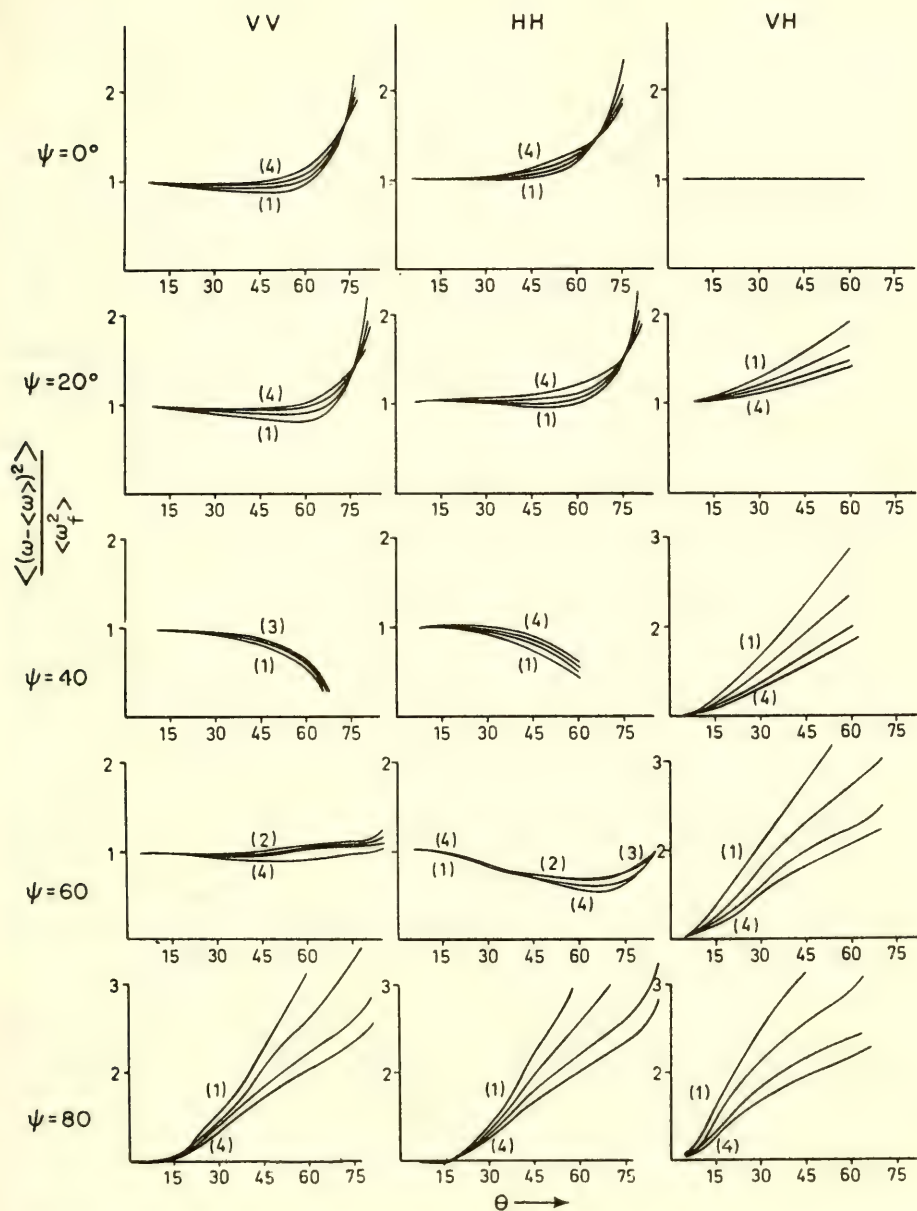


Fig. 8. Frequency variance of the Doppler spectrum computed to order q_2^s , normalised by the variance $\langle \omega_f^2 \rangle$ of the zero'th order Gaussian distribution ($U = 4 \text{ m/s}$).

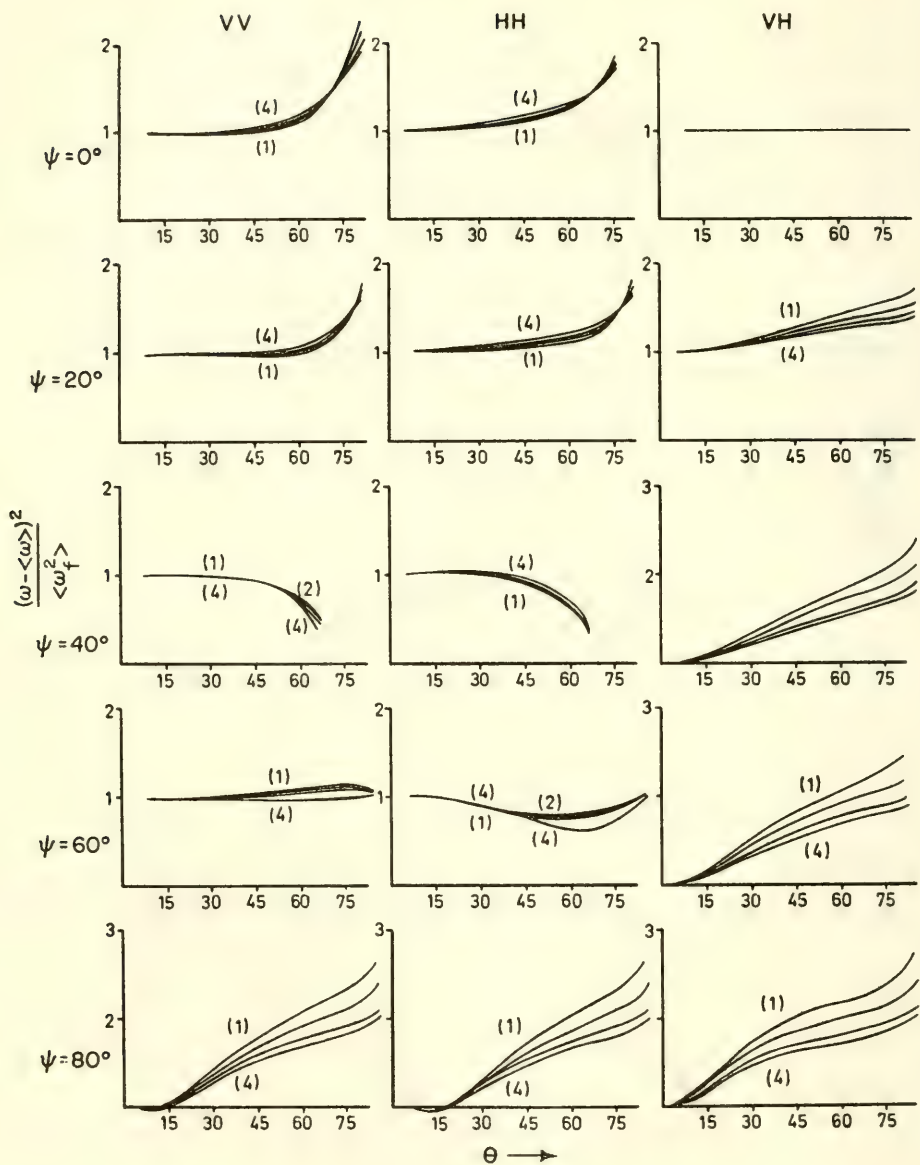
$u = 20 \text{ m/s}$


Fig. 9. Same as Fig. 8 with wind speed $U = 20 \text{ m/s}$

product $\langle \omega_i n_i \rangle$ (Eq. 10), which is responsible for most of the mean-frequency variation, depend on differently weighted moments of the gravity-wave spectrum. The two Doppler parameters can therefore be used to obtain independent estimates of two sea-state parameters --for example, the mean wave height and mean wave period.[†]

IV. HIGHER-ORDER WAVE-WAVE INTERACTIONS

For HF waves longer than about 10 m, the Bragg model can be generalised by straightforward extension of the wave-wave interaction expansion to higher order. In this case, the perturbation parameter $k_{3\zeta}^i$ is normally a small quantity even when ζ is defined as the surface displacement of the complete wave field, and there is no need to consider the long waves of high amplitude separately. In fact, the wave-facet interaction model is not applicable for HF waves on account of the angular resolution condition (5). The inequality $k_{3\zeta}^i \ll 1$ and condition (5) are mutually exclusive, representing a wave length gap between the wave-facet and higher-order wave-wave interaction models extending from a few fractions of a meter to about 10 meters.

At second order, the wave-wave interaction analysis yields scattered waves through interactions with pairs of gravity-wave components a, b satisfying the next-order Bragg conditions

$$\begin{aligned} \underline{k}^i + \sigma_a \underline{k}^a + \sigma_b \underline{k}^b &= \underline{k}^s \\ \omega_i + \sigma_a \omega_a + \sigma_b \omega_b &= \omega_s \quad (\sigma_a, \sigma_b = \pm) \end{aligned} \quad (15)$$

The second-order Doppler spectrum $\chi^{(2)}(\omega_d)$ is obtained by summing over all pairs of surface waves yielding a backscattered component with the appropriate horizontal wavenumber $\underline{k}^s = -\underline{k}^i$ and frequency $\omega_s = \omega_i + \omega_d$,

$$\chi^{(2)}(\omega_d) = \sum_{\sigma_a, \sigma_b} \int T^{(2)} F_g(\underline{k}^a) F_g(\underline{k}^b) \delta(\omega_d - \sigma_a \omega_a - \sigma_b \omega_b) d\underline{k}^a \quad (16)$$

where $\underline{k}^b = -\sigma_b(2\underline{k}^i + \sigma_a \underline{k}^a)$ (Eq. 15). $T^{(2)}$ is a scattering function determined by the second-order coupling coefficients occurring in the expansion of the boundary conditions about the undisturbed plane surface (cf. Ref. (18)). (The polarisation indices are irrelevant for the following discussion and are ignored.)

[†] Significant sea-state signatures are found only for the Doppler spectra and not the cross sections. On integrating Eq. (11) with respect to frequency the dependence on the moments $\langle \omega_f^2 \rangle$ and $\langle \omega_f n_i \rangle$ disappears, leaving only a weak sea-state dependence through the slope moments $\langle n_i n_j \rangle$.

The scattering function $T^{(2)}$ includes both electromagnetic and hydrodynamic interactions at the free surface. For wave lengths in the HF range and longer, the hydrodynamic interactions can probably be described to fair approximation by classical hydrodynamical theory, independent of the effects of wave breaking. Equation (16) represents the random-field expression of nonlinear effects such as nonsinusoidal wave forms[†], nonlinear phase velocities, etc., that have been variously suggested as explanation of the observed side bands of HF Doppler spectra.

In the limit of an incident wave short compared with the principal waves of the sea, the dominant interactions at finite depression angles are electromagnetic. The largest contributions to the integral in (16) arise in this case from interactions in which one of the gravity-wave components, say \underline{k}^a , lies near to the peak of the spectrum. Since $k^a \ll k^i$, the second component \underline{k}^b is then approximately equal to the Bragg component, $\sigma_b \underline{k}^b \approx -2\underline{k}^i$ (cf. Eq. (15) and Fig. 10). The side condition $\omega_d = \sigma_a \omega_a + \sigma_b \omega_b = \text{const}$ (expressed by the δ -function in the integral) defines an integration curve in the \underline{k}^a plane which is given approximately by the circle $k^a = \text{const}$. This follows by noting that, on account of Eq. (15), the variation δk^a corresponds to an equally large variation $\pm \delta k^b$. But for $k^a \ll k^b$, the associated frequency variation $\delta \omega_b$ is generally small compared with the variation $\delta \omega_a$, since $d\omega_b/dk^b \ll d\omega_a/dk^a$. Hence the side condition $\omega_d = \text{const}$ reduces to $\omega_a = \text{const}$. It is shown below that, at finite depression angles, $T^{(2)}$ is independent of \underline{k}^a for $k^a \ll k^b$, and the integration over the directions of \underline{k}^a for fixed k^a can then be readily carried out, yielding

$$\chi^{(2)}(\omega_d) = \chi^{(2)+}(\omega_d) + \chi^{(2)-}(\omega_d)$$

where

(17)

$$\chi^{(2)s}(\omega_d) = 2T^{(2)} F_g(-s2\underline{k}^i) [E_g(\omega_d - s\omega_g) + E_g(s\omega_g - \omega_d)]$$

and $E_g(\omega)$ is the one-dimensional frequency spectrum of the wave field, with $\langle \zeta^2 \rangle = \int_0^\infty E_g(\omega) d\omega$. (The factor 2 arises through interchange of the components a and b in Fig. 10.)

Thus each Bragg line appears as the carrier of a second-order, two-sided image of the surface-wave frequency spectrum. Physically, the Doppler continuum arises, as in the case of the wave-facet interaction model, through the modulation of the first-order

[†] These include the often invoked "higher interference orders" occurring in the Bragg scattering by a lattice. They are generated only if the periodic scattering field is not a purely sinusoidal disturbance but contains higher harmonics.

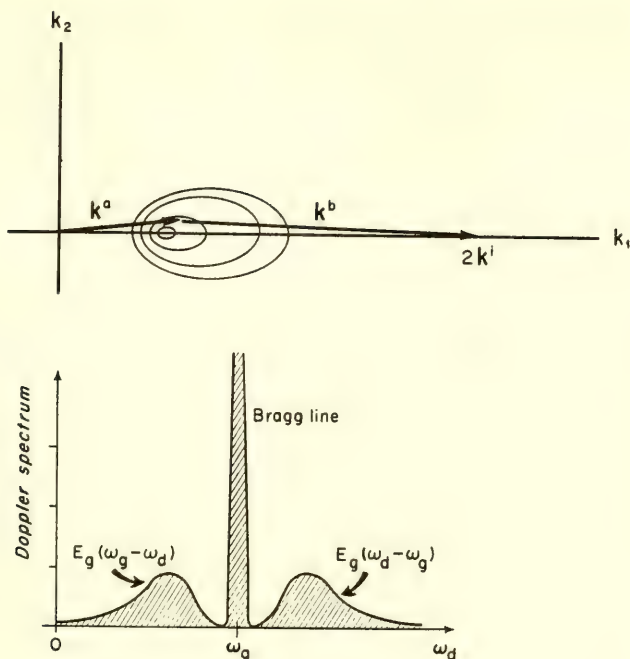


Fig. 10. Upper panel. Interacting gravity-wavenumbers $\underline{k}^a, \underline{k}^b$ for a spectral-peak wavenumber small compared with the Bragg wavenumber $2k^i$. Strong contributions to the second-order Doppler spectrum $\chi^{(2)}(\omega_d)$ arise when \underline{k}^a is close to the spectral peak. Contour lines indicate curves of constant spectral energy. Lower panel. The associated second-order Doppler spectrum $\chi^{(2)}$ consists of two images of the wave frequency spectrum E_g reflected on either side of the Bragg line.

Bragg field by long surface waves of high amplitude. However, in the present case the Doppler shift is not determined by the frequency shift $\omega_f = -2k^i u$ induced by the long-wave orbital velocities, but rather by the intrinsic long-wave frequencies ω_0 . Each low-frequency component splits the first-order Bragg line $\omega_s^{(1)} = \omega_i + \sigma_b \omega_0$ into two lines $\omega_s^{(2)} = \omega_s^{(1)} \pm \omega_0$. Since $u \approx \zeta \omega_0$, the regions of validity for the wave-facet and wave-wave interaction models may also be expressed, respectively, as $\omega_0 \ll \omega_f$ and $\omega_0 \gg \omega_f$.

A useful feature of the relation (17) is that it defines the surface-wave spectrum in absolute energy units independent of electromagnetic calibration factors, which are difficult to establish for long-range ionospheric mode propagation. Using Eqs. (3) and (2) to eliminate the surface-wave spectrum at the Bragg wavenumber, Eq. (17) becomes

$$E_g(\omega_d - s\omega_g) + E_g(s\omega_g - \omega_d) = \frac{T^{(1)}}{2T^{(2)}} \frac{\chi^{(2)s}(\omega_d)}{\epsilon^{(1)s}} \quad (s = \pm) \quad (18)$$

where $\epsilon^{(1)s} = \int \chi^{(1)s}(\omega_d) d\omega_d$ is the energy of the first-order Bragg line. The ratio $T^{(1)}/2T^{(2)}$ can be determined from theory, and $\chi^{(2)s}$ and $\epsilon^{(1)s}$ may be measured in arbitrary energy units.

In the relevant limit $k^a \ll k^b$, $T^{(1)}/2T^{(2)}$ may be deduced from the picture of a short scattering wave $\zeta_b = A_b \exp \{i(\underline{k}^b \underline{x} - \omega_b t)\}$ riding on a long carrier wave $\zeta_a = A_a \exp \{i(\underline{k}^a \underline{x} - \omega_a t)\}$ (which is now, however, assumed to satisfy the wave-wave interaction condition $A_a k_3^a \ll 1$, rather than the wave-facet interaction condition (5)). For small slopes $A_a k^a \ll 1$, the principal effect of the carrier wave is presumably to alter the phase of the scattered field by raising and lowering the local mean reference surface of the short scattering waves†. Thus if the first-order backscattered wave in the absence of the carrier wave is of the form

$$\varphi^{(1)} = C^{(1)} A_b A_i \exp \{i(\underline{k}^i + \sigma_b \underline{k}^b) \underline{x} - i(\omega_i + \sigma_b \omega_b) t + i k_3^s x_3\}$$

where A_i is the amplitude of the incident field, $C^{(1)}$ is a first-order coupling coefficient, and $\underline{k}^i + \sigma_b \underline{k}^b \approx -\underline{k}^i$, $k_3^s \approx -k_3^i$, the modulated scattered wave in the presence of the carrier wave will be given approximately by

$$\tilde{\varphi} = e^{2ik_3^i \zeta_b} \varphi^{(1)} \approx (1 + 2ik_3^i \zeta_b) \varphi^{(1)} \equiv \varphi^{(1)} + \varphi^{(2)} \quad (19)$$

Thus

$$\varphi^{(2)} = C^{(2)} A_a A_b A_i \exp \{-i \underline{k}^i \underline{x} - i(\omega_i + \omega_d) t - i k_3^i x_3\} \quad (20)$$

with $C^{(2)} = 2ik_3^i C^{(1)}$. Expressed in terms of a continuous energy spectrum, this is readily found to correspond to a scattering function ratio

† A more detailed investigation indicates that slope effects can be ignored if $k^a \ll k_3^i = k^i \sin \theta$.

$$\frac{T^{(2)}}{T^{(1)}} = \frac{1}{4} \left| \frac{C^{(2)}}{C^{(1)}} \right|^2 = (k_3^i)^2 \quad (21)$$

For small depression angles ($k_3^i \ll k^i$), the effect of the carrier-wave slope becomes comparable with the phase shift induced by the vertical displacement, and the relations (20), (21) should be modified to include additional terms dependent on k^0 . However, this requires a more detailed investigation of the electromagnetic and hydrodynamic interactions.[†]

Examples of Doppler spectra obtained by Ward [22] from the sea echo of 21.840 MHz (14 m) waves at ranges near 3000 km are shown in Fig. 11. The analysis was based on short records of one minute duration, so that the continuum is poorly resolved statistically and individual spectra vary strongly. However, there is some indication of two side-band structures appearing on either side of a central Bragg peak. Theoretically, the Bragg line should lie at 0.48 Hz, which agrees well with the central peak of the first spectrum shown, but is somewhat to the left of the main peaks in the other cases. The displacement of the side lobes relative to the Bragg peak is of the order 0.1 Hz expected for typical ocean-wave frequencies.

The ratio of the side-band energy $\epsilon^{(2)} = \int \chi^{(2)}(\omega_d) d\omega_d$ to the energy $\epsilon^{(1)}$ of the Bragg line is given according to Eqs. (18) and (21) by

$$\epsilon^{(2)} / \epsilon^{(1)} = 4(k_s^i)^2 \langle \zeta^2 \rangle$$

Ward estimates a depression angle of 12° , which yields

$$\epsilon^{(2)} / \epsilon^{(1)} = 0.036 \langle (\zeta [m])^2 \rangle$$

The observed ratios of order unity correspond to root mean square wave heights of about 5 m, which appear rather high, but not impossible.

More plausible estimates of the wave height may have resulted from a more accurate determination of the scattering function ratio $T^{(2)}/T^{(1)}$ at small depression angles. Contamination of the observed spectra by ionospheric Doppler shifts may be an alternative explanation of the high ratios $\epsilon^{(2)}/\epsilon^{(1)}$. A spurious interaction between the Bragg line and the low frequency ionospheric Doppler spectrum could also have been introduced in the present experiment by the data analysis, since the Doppler spectra appear to have been computed -- as is often done -- from the time series of

[†]Note added in proof: A detailed analysis has recently been carried out by D. E. Barrick "Dependence of Second-Order Doppler Side Bands in HF Sea Echo on Sea State," to appear in 1971 G-AP Internat. Symp. Digest.

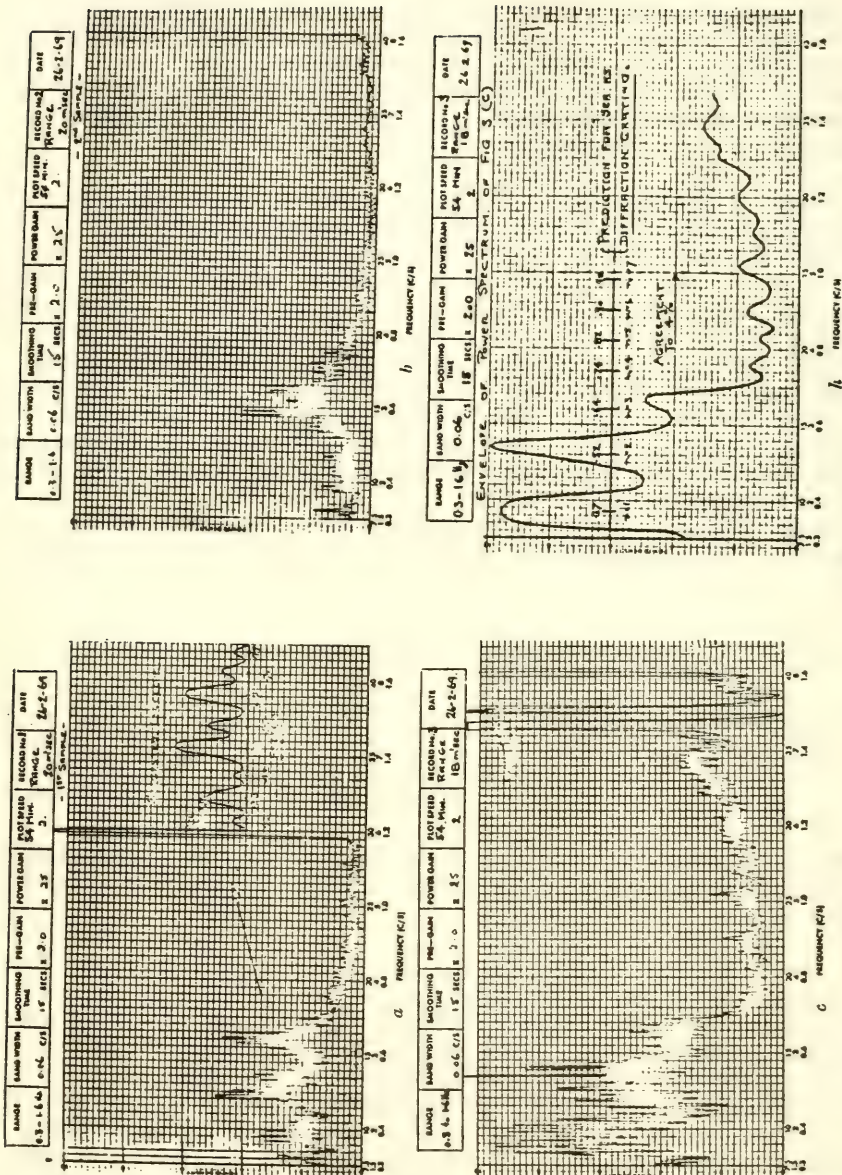


Fig. 11. Doppler spectra of 21.84 MHz (14 m) sea echo at ranges of 2700 km (18 ms) and 3000 km (20 ms), from Ward [22].

the signal phase (or phase cosine), which is nonlinearly related to the complex signal amplitude. More detailed investigations using longer time series are needed to decide whether the ocean wave spectrum can be extracted from the Doppler spectrum of long range HF sea echo in the presence of unavoidable ionospheric noise.

ACKNOWLEDGMENT

This work was supported in part by the Office of Naval Research under Contract No. ONR N00014-69-C-0057.

REFERENCES

1. Barnett, T. P., "Generation, dissipation and prediction of wind waves," *J. Geophys. Res.*, 73, 513-534, 1968.
2. Barnett, T. P., Holland, C. H. Jr. and Yager, P., "General technique for wind-wave prediction with application to the S. China Sea," *Westinghouse Res. Lab. Rep.*, June, 1969.
3. Barrick, D. E. and Peake, W. H., "A review of scattering from surfaces with different roughness scales," *Radio Sci.*, 3, 865-868, 1968.
4. Bass, F. G., Fuks, I. M., Kalmykov, A. I., Ostrovsky, I. E., and Rosenberg, A. D., "Very high frequency radiowave scattering by a disturbed sea surface," *IEEE Trans.*, AP-16, 554-568, 1968.
5. Cox, C. M. and Munk, W. H., "Measurement of the roughness of the sea surface from photographs of the sun's glitter," *J. Opt. Soc. Am.*, 44, 838-850, 1954.
6. Crombie, D. P., "Doppler spectrum of sea echo at 13.56 mc/s," *Nature*, 175, 681-682, 1955.
7. Daley, J. C., Ransone, J. T. Jr., Burkett, J. A. and Duncan, J. R., "Sea-clutter measurements on four frequencies," *Nav. Res. Lab. Rep.* 6806, 1968.
8. Daley, J. C., Ransone, J. T. Jr., Burkett, J. A. and Duncan, J. R., "Upwind-downwind-crosswind sea-clutter measurements," *Nav. Res. Lab. Rep.* 6881, 1969.
9. Ewing, G. C., ed., Oceanography from Space, Woods Hole Oceanogr. Inst., Ref. No. 65-10, 1965.
10. Guinard, N. W. and Daley, J. C., "An experimental study of a sea clutter model," *Proc. IEEE*, 58, 543-550, 1970.

11. Hasselmann, K., "On the mass and momentum transfer between short gravity waves and larger-scale motions," *J. Fluid Mech.*, 50, 189, 1971.
12. Hasselmann, K., "Determination of ocean wave spectra from Doppler radio return from the sea surface," *Nature*, 229, 16-17, 1971.
13. Hicks, B. L., Knable, N., Kavaly, J. J., Newell, G. S., Ruina, J. P. and Sherwin, C. W., "The spectrum of X-band radiation backscattered from the sea surface," *J. Geophys. Res.*, 65, 825-837, 1960.
14. Longuet-Higgins, M. S., "A nonlinear mechanism for the generation of sea waves," *Proc. Roy. Soc. A.* 311, 371-389, 1969.
15. Munk, W. H. and Nierenberg, W. A., "High frequency radar sea return and the Phillips saturation constant," *Nature*, 224, 1285, 1969.
16. Pierson, W. J. and Moskowitz, L., "A proposed spectral form for fully developed wind seas based on the similarity theory of S. A. Kitaigorodskii," *J. Geophys. Res.*, 69, 5181-5190, 1964.
17. Pierson, W. J., Tick, L. J. and Baer, L., "Computer based procedure for preparing global wave forecasts and wind field analysis capable of using wave data obtained by a space craft," 6th Naval Hydrodynamic Symposium, Washington, Office of Naval Res., Washington, D. C., 1966.
18. Rice, S. O., "Reflection of electromagnetic waves from slightly rough surfaces," *Comm. Pure Appl. Math.*, 4, 351-378, 1951.
19. Semenov, B., "An approximate calculation of scattering on the perturbed sea surface," *IVUZ Radiofizika (USSR)*, 9, 876-887, 1966.
20. Valenzuela, G. R. and Laing, M. B., "Study of Doppler spectra of radar sea echo," *J. Geophys. Res.*, 75, 551-563, 1970.
21. Valenzuela, G. R., Laing, M. B. and Daley, J. C., "Ocean spectra for the high frequency waves from airborne radar measurements," 1970 (subm. to *J. Mar. Res.*).
22. Ward, J. F., "Power spectra from ocean movements measured remotely by ionospheric radar backscatter," *Nature*, 223, 1325-1330, 1969.
23. Wright, J. W., "A new model for sea clutter," *IEEE Trans. AP*-16, 217-223, 1968.

INTERACTION BETWEEN GRAVITY WAVES AND FINITE TURBULENT FLOW FIELDS

Daniel Savitsky
Stevens Institute of Technology
Hoboken, New Jersey

ABSTRACT

A laboratory study of the interaction of deep water gravity waves progressing into a turbulent flow field produced by a finite width grid towed in a wide tank showed wave height attenuation of nearly 90% in the grid wake and wave height amplifications of nearly 75% in the still water outside the wake. The transverse gradient of longitudinal flow in the wake was predominantly responsible for the large wave deformations and precluded an evaluation of direct turbulence effects.

A simple, analytical solution using wave refraction, diffraction and superposition concepts is developed which qualitatively reproduces the measured results.

I. INTRODUCTION

As gravity waves progress from their source of origin, they encounter a variety of ocean environments which may interfere with their ordered motion and, consequently, alter the amplitude and direction of the wave system. Although an extensive literature exists on the mechanism of wave generation and their subsequent propagation through still water or a uniform flow, only recently has some attention been given to waves moving through a non-uniform flow -- and these have been restricted to relatively weak velocity gradients normal to the wave direction.

In a realistic ocean environment, gravity waves may encounter regions of turbulent flow, particularly in the upper layers. These oceanic turbulent flow fields can be developed by various geophysical mechanisms. For example, the action of unsteady wind shear stresses exerted against the surface of the sea; the breaking of wave crests

resulting in "splash turbulence" penetrating into the upper layers of the water; turbulent fields set up in intense currents; turbulence developed by high velocity, high Reynolds number flows in a tidal channel; ship wakes; etc. In each case, it is expected that wave attenuation will result from the interaction between the turbulent flow fields and wave motion. Such attenuation is of importance in developing relatively "quiet" local areas in the sea for launching or recovery of small craft or submarines, or in tracing the progress of, say, one storm passing through the intensive turbulence of another storm.

Phillips [1959] presents a theoretical study of the properties of waves on the free surface of a liquid in turbulent motion where the intensity of the turbulence is sufficiently small to preclude wave generation in itself and where the mean velocity of the flow is zero. There are two types of possible interaction, each of which results in the attenuation of the incident wave. One is an "eddy viscosity interaction" in which wave energy is transferred from the wave motion through a stretching of the vortex filaments in the turbulence which tends to increase ω^2 , the mean square vorticity associated with the turbulence itself. This straining process is of second order in wave height-length ratio and, hence, should be important for steep waves and when the turbulence scale is much less than that of the waves. The second type of interaction is a scattering phenomenon where random velocity fluctuations in the turbulence field will result in the convective distortion of the wave front, and produce a broad spectrum of scattered waves. This scattering effect is of first order in wave height-length ratio and, hence, predominates for waves of small slope. Phillips shows that, under typical conditions in the open sea, the attenuation from scattering will be greater than that from direct viscous dissipation for wave lengths greater than about 10 ft.

An experimental study was undertaken at the Davidson Laboratory, Stevens Institute of Technology, to investigate the interaction between mechanically generated progressive gravity waves and a controlled turbulence field developed by towing suitable grids in a towing tank. Since field measurements by Stewart and Grant [1962] supported the applicability of the Kolmogoroff hypothesis (that the statistical structure of turbulence has a universal form) to turbulence near the sea surface in the presence of waves, it was believed that grid-generated turbulence (known to satisfy the Kolmogoroff hypothesis) would indeed be representative of ocean turbulence on a model scale. Two experimental studies were undertaken. The first used a grid which spanned the width of a 12 ft wide towing tank and was towed in the direction of wave celerity at speeds less than the group velocity of the regular wave lengths generated by a plunger type wavemaker. In these studies, the test waves overtook and passed through the turbulence wake and grid. This so-called one-dimensional grid study was made in an attempt to develop a turbulent wake with uniform mean flow across any transverse section aft of the grid. Unfortunately, as will be subsequently discussed, a uniform flow field was not developed near the outer edges of the grid wake and this seriously

influenced the test results. The other series of experimental studies involved towing a 3-ft wide grid in a 75-ft wide towing tank. The intent of these tests was to allow any scattered wake system to be defracted outside the turbulence patch. However, the finite width grid also produced a pronounced longitudinal mean flow velocity gradient in transverse sections through the wake. Thus, in these latter tests, the generated waves were simultaneously subjected to three modification effects: (1) dissipation due to eddy viscosity; (2) scattering due to turbulent convective distortion of the wave front and (3) deformation of the wave due to mean flow velocity gradients.

Measurements were made of the wave deformation in the wakes of both the one- and two-dimensional grids. An analysis of these results indicated that the velocity gradients in the wakes had a dominating effect on the wave deformation and thus, unfortunately, precluded a reliable evaluation of the possible dissipative or scattering action of the turbulence field upon the incident wave. The studies are, nevertheless, of importance since they provide unique results, obtained under controlled laboratory conditions, describing the pronounced distortion of a deep water wave when encountering sharp current gradients, either naturally existing or artificially produced. It is shown that the wave distortion can be such as to provide locally areas of reduced wave motion which can be beneficial in launching or retrieving small craft or submersibles from a mother ship at sea.

The experimental results are described in some detail and an elementary analytical model is developed which, using the combined mechanics of wave refraction, defraction and superposition, at least qualitatively reproduces the features of the test results and, perhaps more important, describes a possible physical mechanism responsible for the observed large wave deformations.

These studies were supported by the Fluid Dynamics Branch of the Office of Naval Research, Department of the Navy, under Contract NR-062-254, Nonr263(36). They formed the basis for a dissertation submitted to the Graduate Division of the School of Engineering and Science in partial fulfillment of the requirements for the degree of Ph.D. at New York University.

II. EXPERIMENTAL PROCEDURES

Turbulence-generating grids have been used with great success in advancing the knowledge of turbulence in air flows, but have been used only occasionally in hydrodynamics -- particularly in towing tanks where a grid must be towed in quiet water to generate a turbulence field. Taylor [1935] has shown that disturbances generated in the wake of a grid transform rapidly into a quasi-isotropic turbulent field whether the grid is towed in quiet air or an airstream passes through the grid.

In the present task, vertical turbulence grids of finite draft and two mesh sizes were towed at various constant speeds in Tank No. 2 and 3 of the Davidson Laboratory in a direction normal to the plane of the grid. Regular waves, generated by a plunger type wavemaker in quiet water, traveled in the same direction as the grid tow (with initial crest lines parallel to the grid) progressed through the turbulent wake and grid into quiet water beyond the grid. Waves of various constant length and height were generated such that the group velocity of each regular wave was greater than the grid velocity. The wave lengths and water depth were such that deep water gravity waves were generated. Wave amplitudes were measured by resistance type wave wires which penetrated the fluid surface. Several of the wave wires were towed ahead and behind the grid (at the grid speed) while others were stationary and located both in and outside of the grid wake. The outputs of these wave probes were simultaneously recorded on a "Viscorder" oscillograph tape.

The details of test procedure, grid characteristics, and test conditions for the one-dimensional and two-dimensional turbulence grid studies are described separately below. Common to both studies was the observation that, for the grid sizes and grid velocities considered, the combination of physical grid and turbulent wake in smooth water did not produce a measurable wave system of its own. In fact, soon after passage of the grid and wake relative to a fixed point in the test tank, the water surface appeared unusually still. Further, the grid solidity was small enough that, when stationary, it did not noticeably affect the wave forms which passed through the stationary grid. Neither was there a measurable wave reflection from the grid.

One-Dimensional Grid Studies

The one-dimensional grid studies were conducted in Tank No. 3 of the Davidson Laboratory. This tank is 300 ft long, 12 ft wide and has a water depth of 6 ft. A plunger type wavemaker is located at one end of the tank and a slotted beach of 15° slope is located at the opposite end to absorb the wave energy with minimum reflection.

Grid Characteristics: A turbulence grid 11.5 ft wide spanned the tank width, penetrated the water surface to a depth of 1.6 ft, was attached to a standard carriage and towed in a direction away from the wavemaker. Figure 1 shows the test setup. Two mesh sizes were tested; one had a mesh $M = 0.36$ ft and was made of crossed square wooden slats 0.80 inches wide; the other had a mesh $M = 0.71$ ft and was made of crossed square wooden slats 1.60 inches wide. Thus, in both cases, the grid solidity was constant and equal to $S = 0.40$. The grid was towed at speeds of $V = 1.0$ and $V = 1.7$ ft/sec. The hydrodynamic drag and Reynolds No. of the grid ($Re_g = VM/\omega$) for these conditions are:

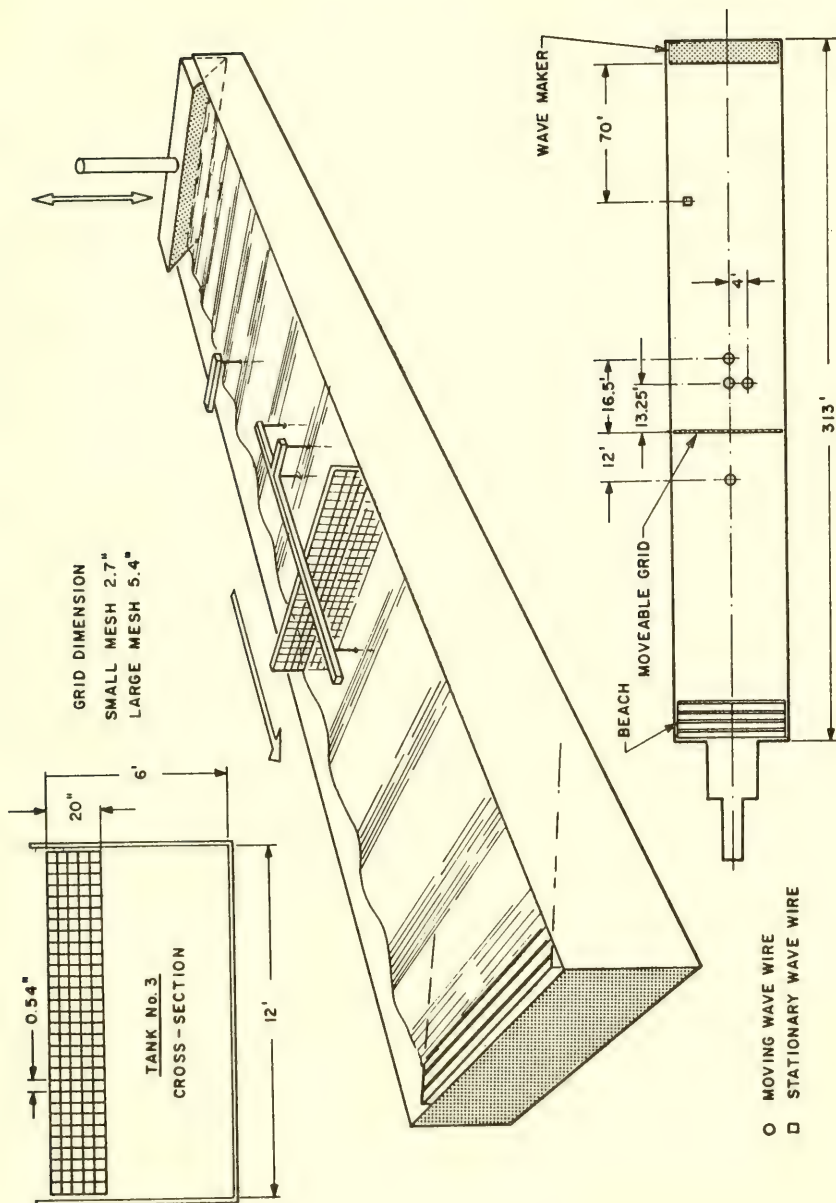


Fig. 1 Test Set-up One Dimensional Grid

<u>Mesh</u>	<u>Grid Velocity</u>	<u>Drag</u>	<u>Reynolds No.</u>
0.36 ft	1 ft/sec	13.2 lbs	28,000
0.26	1.7	37.9	49,000
0.71	1	13.2	56,800
0.71	1.7	37.9	96,500

Measurements were initially made of the mean value of the longitudinal velocity (in the grid direction) of the grid wake at the centerline of the grid and at a depth of 0.80 feet below the water surface. At a distance of 10.0 ft aft of the grid, the wake velocity was 0.40 V and decreased slowly with distance aft of the grid -- at a distance 20.0 ft aft of the grid, the mean velocity of the wake was 0.36 V . In these initial tests, a straight line of confetti was sprinkled across the 12 ft width of the tank parallel to the plane of the grid. Visual observations of this reference line after grid passage showed that the confetti moved essentially in one straight line parallel to the grid, thus indicating a lack of noticeable velocity gradients -- at least on the free surface. An analysis of the wave distortion data in this wake yielded anomalous results (these will be discussed in a subsequent section) that could not be explained by the assumption of a uniform longitudinal mean flow through transverse sections in the grid wake. Hence, a detailed survey was then made of the mean flow at distances of 10 ft and 20 ft aft of the grid. These results are shown in Fig. 2 which presents a plot of longitudinal mean flow (V_w) versus transverse distance from the grid centerline at a probe depth of 10 inches below the water surface. The wake velocities (V_w) are normalized on the basis of grid speed (V). It is clearly seen that the mean flow in the wake is essentially constant for a distance of approximately 5 ft from the grid centerline but then rapidly decreases between this point and the tank wall. The significance of this local velocity gradient will be subsequently discussed.

The wind tunnel results of Dryden [1937], who examined the turbulence aft of a rectangular grid having a mesh size $M = 0.41$ ft at a nearly similar Reynolds number, show that the turbulent velocity fluctuations u' as a function of distance, X , aft of the grid are:

$$\frac{V}{u'} = 10 + \frac{x}{M}.$$

Thus, for a distance 10 ft aft of the 0.36' mesh grid $x/M = 27.7$ and $u' = V/37.7$ or approximately 3% of the mean flow. At a distance of 20 mesh lengths aft of the grid, wind tunnel experiments have shown the establishment of quasi-isotropic turbulence.

GRID WIDTH = 11.50'; DRAFT = 20"; MESH SIZE = 5.4"

(GRID TOWED IN 12 FT WIDE TANK)

VELOCITY PROBE AT 10" DRAFT

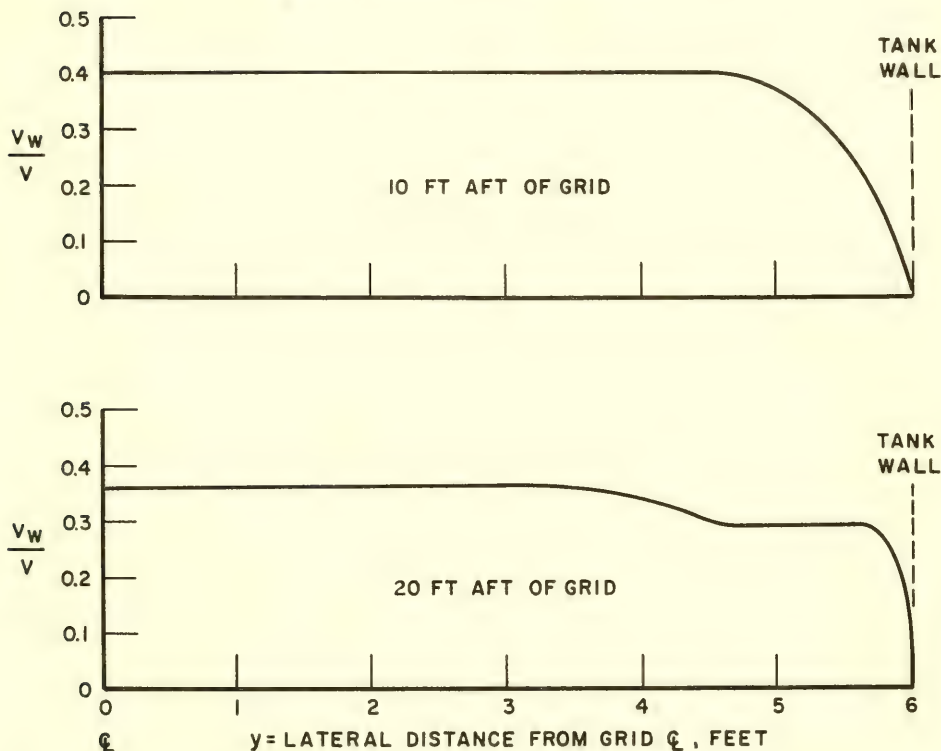
 V_W = WAKE VELOCITY ; V = GRID VELOCITY

Fig. 2 Longitudinal Velocity Distribution in Grid Wake

Wave Height Probes: Wave heights were measured by resistance type wave wires penetrating through the water surface. The position of the wave wires relative to the grid are shown in Fig. 1. It is seen that wave wires moving with the grid were located 12 ft ahead of and along the grid centerline; 13.25 ft and 16.50 ft aft of and along the grid centerline; and one located 13.25 ft aft and 4 ft transverse to the grid centerline. The wave wires 13.25 ft and 16.50 ft aft of the grid were used to obtain a measure of the apparent wave length in the turbulence field while the pair of wires 4 ft apart in the transverse plane 13.25 ft aft of the grid were used to measure any deformation of the wave crest line as it progressed through the turbulence. A stationary wave wire was located 60 ft forward of the wavemaker and was used to examine the regularity of the amplitude and period of the generated incident wave.

A range of wave heights and lengths used in these tests were as follows:

Wave Length λ , ft	Wave Period T, sec	Wave Celerity V_c , ft/sec	Group Velocity V_g , ft/sec	Wave Height H_w , ft
2.0	0.625	3.20	1.60	0.05
2.0	0.625	3.20	1.60	0.10
3.0	0.763	3.93	1.87	0.10
4.0	0.885	4.52	2.26	0.05
4.0	0.885	4.52	2.26	0.10
6.0	1.080	5.55	2.78	0.05
6.0	1.080	5.55	2.78	0.10
8.0	1.250	6.40	3.20	0.04
8.0	1.250	6.40	3.20	0.09

Test Procedure: Several experimental procedures were used in these studies. In one group of tests, the grid was held stationary 70 ft forward of the wavemaker until several waves had passed through the grid. The grid was then towed and wave measurements were made with the moving wave wires. For certain runs, after approximately 50 - 60 ft of grid tow, the aft moving wave wire (16.50 ft aft) was released from the tow and remained stationary in the tank. Thus, wave height measurements were taken both at a fixed position relative to the moving grid and at a fixed position in the tank (variable position relative to the grid). The other test procedure was to first tow the grid for a distance of approximately 50 ft which developed a turbulent wake and then start the waves which ran through the wake and overtook the moving grid. This technique avoided the possibility of a secondary wave formation as the incident wave ran through the moving grid. It was established that the results obtained with both test procedures were essentially similar.

Two-Dimensional Grid Studies

The two-dimensional grid studies were conducted in Tank No. 2 of the Davidson Laboratory. This tank is 75 ft square and has a water depth of 4.5 ft. A plunger mechanical type wavemaker spans one side of the tank and a sloping beach is installed on the opposite end to absorb the generated wave energy.

Grid Characteristics: Two turbulence grids, one 3 ft wide and another 5.5 ft wide, were separately towed in a direction away from the wavemaker. The grid centerline was 17 ft from one edge of the tank. Figure 3 shows the test setup. As in the one-dimensional tests, two mesh sizes -- $M = 0.36$ ft and $M = 0.71$ ft -- were

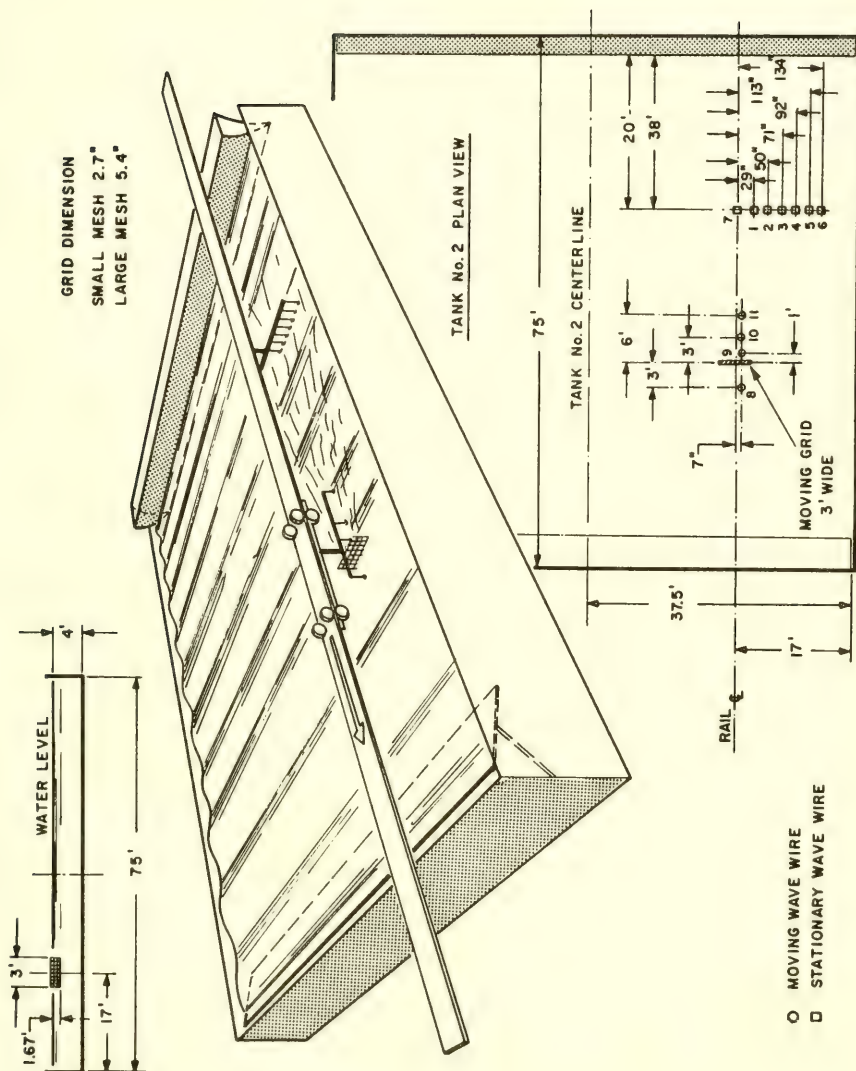


Fig. 3 Test set-up two-dimensional grid

tested. The grids were constructed of crossed square wooden slats 0.80 inches wide. The solidity, towing speeds and Reynolds number of the grids were the same as for the one-dimensional tests previously described. The hydrodynamic drag of the 0.36 ft mesh grid was 3.2 lbs and 9.25 lbs at tow speeds of 1.0 and 1.7 ft/sec respectively at a grid draft of 1.67 ft. At a grid draft of 0.84 ft, the hydrodynamic drags for this grid were 1.5 lbs and 4.33 lbs at 1.0 and 1.7 ft/sec. It is to be noticed that the grid drag increased as the square of the speed for all cases.

Measurements were made of the mean values of the longitudinal velocities at depths of 0.80 and 0.40 ft in the grid wake across several transverse sections aft of the 3 ft wide, 0.36 ft mesh grid with a 1.67 and 0.80 ft draft. A plot of the ratio of wake velocity to grid velocity is given in Fig. 4. These velocity ratios were the same for both grid drafts and towing speeds.

It is seen that there is a slow attenuation of velocity with distance aft of grid. Further, there is also a slow lateral spreading of the wake area. It is interesting to note that the wake velocities are all in the direction of grid tow. Surveys of the velocity field up to 5 ft from the grid centerline did not indicate a reverse flow. Visual observations did indicate a reverse flow along the bottom of the test tank.

An empirical formulation was established to represent the wake velocity V_w as a function of distance, x , aft of the grid and a distance, y , measured from the grid centerline normal to the x -direction. The wake equation is given by:

$$\frac{V_w}{V} = [0.45 - 0.00745x] \left[e^{-\left(\frac{y}{1.67+0.062x}\right)^8} \right]$$

where x and y are in units of feet.

The above formulation was developed for use in the analysis of wave deformation for regular waves running into a velocity gradient. This analysis is presented in a subsequent section of this report.

Wave Height Probes: The location of the wave amplitude measuring probes are shown in Fig. 3. It is seen that four probes were towed with the grid and 7 inches off its centerline; one 3 ft forward and three others 1 ft, 3 ft and 6 ft aft of the grid. In addition, seven stationary probes were located in a transverse line normal to the direction of grid tow and at distance 38 ft and then 20 ft ahead of the wavemaker. It will be noted that one of the stationary wave wires was directly on the grid centerline. This installation was accomplished by mounting the probe on the floor of the tank and providing a slot through the grid which passed over

GRID WIDTH = 36" ; DRAFT = 20" ; MESH SIZE = 2.7"
 (GRID TOWED IN 75 FT WIDE TANK)
 VELOCITY PROBE AT 10" DRAFT

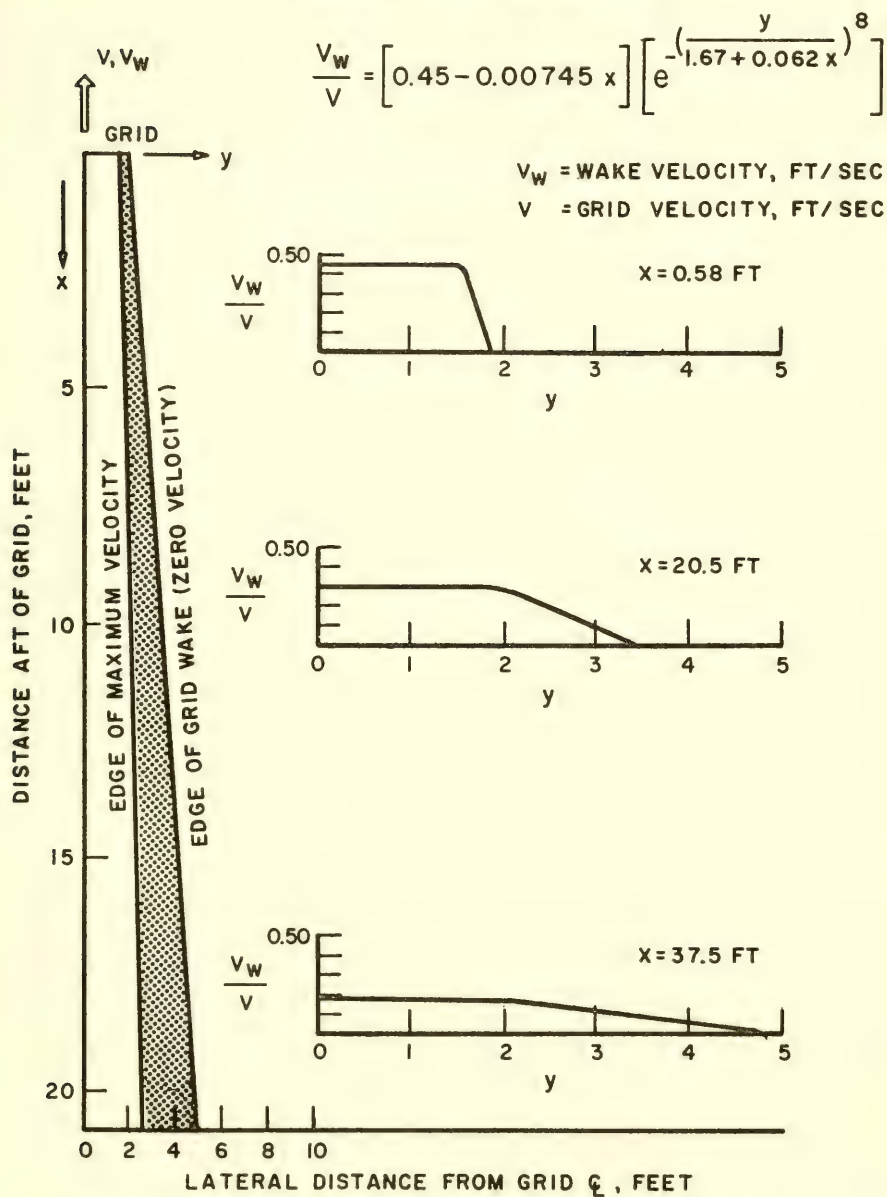


Fig. 4 Longitudinal velocity distribution in grid wake

the wave probe. Thus, the transverse probes covered an area from the grid centerline to a distance of nearly 9 ft outboard of the edge of the grid.

Test Procedure: The range of wave heights and lengths were essentially similar to those used in the one-dimensional tests. Also, the test procedures previously described were followed. The initial grid location was always 10 ft ahead of the wavemaker. After approximately 60 ft of tow, the grid was stopped and the wavemaker continued in operation until the wave amplitudes recorded in the line of transverse wave probes were again equal to the incident wave amplitude.

RESULTS OF EXPERIMENTAL INVESTIGATIONS

Selected test results are first described to illustrate the general behavior of waves in a turbulent flow field. An elementary analysis of the results is developed in the subsequent section.

One-Dimensional Grid Studies

As previously discussed, the original intention of the one-dimensional grid study was to provide a turbulent wake with constant longitudinal mean flow in any transverse section through the wake. Regular waves would be passed through the wake and measurements made of the dissipative effects of grid-controlled turbulence on wave amplitude attenuation. It was expected that the deep water gravity waves would pass through the turbulence field with the crest lines always remaining parallel to the grid and that the wave amplitude would be essentially constant along a given crest line and decrease as the wave progressed further into the turbulent area. Under these circumstances, the amplitude attenuation would be due both to viscous dissipation and to "wave stretching" as it moved into a longitudinal current from an originally quiet area.

This idealized situation did not develop but, rather, it was found that the wave crest lines were severely deformed; the wave amplitude was not constant across a given crest line; and, further, there were pronounced oscillations in the wave amplitude time history at each wave probe (whether moving or stationary) in the wake. In all cases, the control wave probe, which was fixed in quiet water aft of the turbulent wake, indicated a wave of constant amplitude and period continuously passing into the wake area.

General Behavior: An example of typical wave amplitude oscillations recorded by both the moving and stationary wave wires along the grid centerline is given in Fig. 5. The test conditions represented are for a wave length of 4.0 ft and a wave height of 1.2 inches. The grid velocity was 1.7 ft/sec. The phase speed of the wave is 5.4 ft/sec while the average wake velocity is approxi-

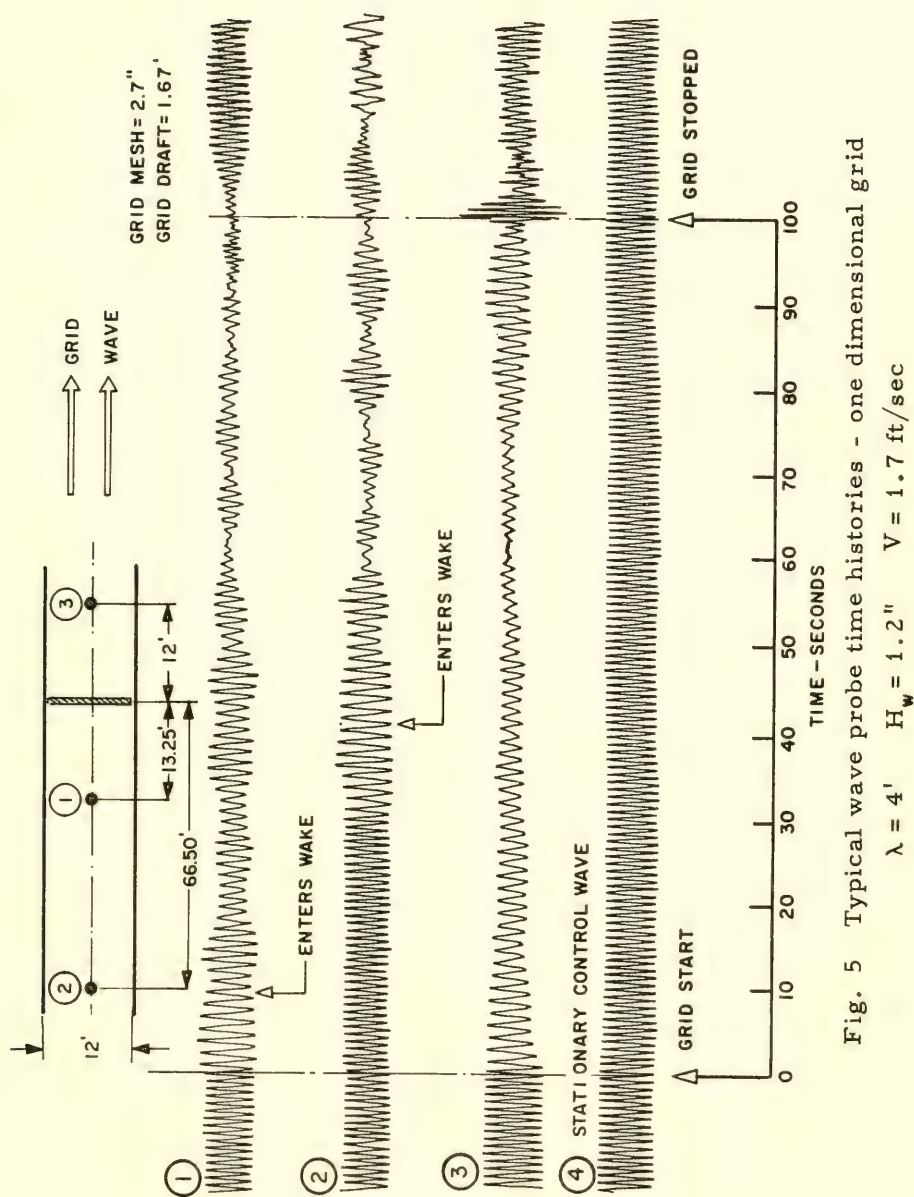
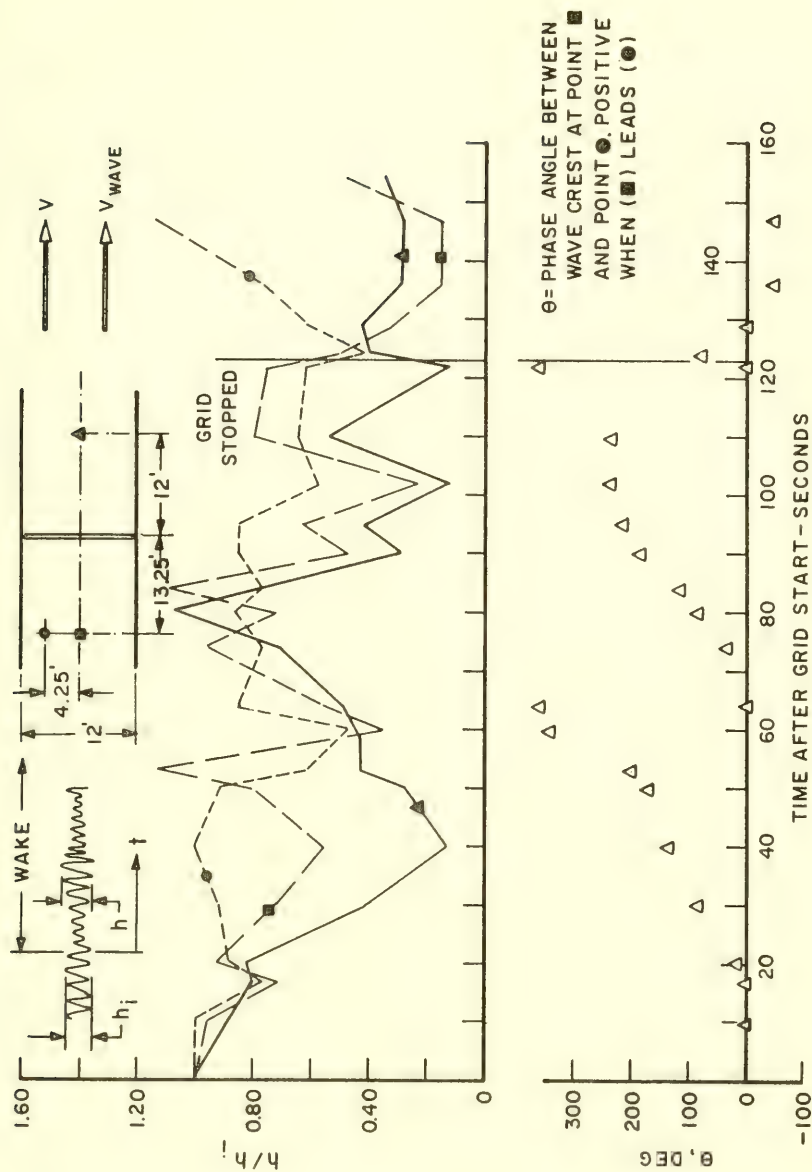


Fig. 5 Typical wave probe time histories - one dimensional grid

mately 0.60 ft/sec. Trace No. 1 is for the moving wave probe located 13.25 ft. aft of the grid; trace No. 2 is for a moving wave wire located 66.5 ft aft of the grid; trace No. 3 represents the moving wave wire 12 ft ahead of the grid, and trace No. 4 is for the stationary control wave wire located approximately 20 ft aft of the start of the turbulent wake. The times of start-up and stop of the grid motion and the time of entry of the moving wave wires into the wake are also indicated on this figure. Perhaps the most notable feature on this typical test record is the pronounced oscillation of the measured wave amplitude at all but the stationary wave wire. It is seen that, for the specified test conditions, the measured wave amplitudes varied from nearly zero to values somewhat larger than the incident wave. Further, the time between successive minimum values is approximately 9 - 10 seconds for the waves in the wake but considerably longer, although not as clearly defined, for the wave probe ahead of the grid. For longer wave lengths, the wave amplitude variations were reduced and the apparent period between minimum values increased. A reduction in grid speed reduced the wave amplitude variation and increased the apparent period between minimum values. There was no discernible effect of grid mesh size on these general observations.

It is to be noted from Fig. 5 that fluctuations in wave amplitude continued for a long time after the turbulence grid was stopped. This is, of course, due to the fact that the wake has a mean flow defined in Fig. 2 and, consequently, moves past the stationary grid. It is also interesting to note that wave deformation at wave wires 1 and 2 is first evident after approximately 3 seconds or, equivalently, after a wave crest has traveled nearly 5 ft into the wake.

Specific Behavior: The envelopes of wave height (h) variation with time, normalized on the basis of incident wave height (h_i), are plotted in Figs. 6 through 11 for a grid speed of approximately 1 ft/sec; a grid draft of 20 inches; and a mesh size of 2.7 inches. Data are presented for the 3, 4 and 8 ft wave lengths, each having a height of approximately 1 inch. The data for the 2 ft wave length are not presented since the wave heights were most irregular even in the non-turbulent flow area. The data for the 6 ft long wave were not unlike those for the 4 and 8 ft test waves and, hence, are not included in this paper. Two companion plots are presented for each wave length. For example, the data for the 3 ft long wave are given in Figs. 6 and 7. The envelopes of the ratio h/h_i for the three moving wave wires are plotted in Fig. 6 along with the phase angle between wave crests at the centerline and at a point 4 ft outboard of the centerline at a longitudinal distance of 13.25 ft aft of the grid. A zero phase angle represents a crest line parallel to the grid. The complementary data plot for the 3 ft wave is given in Fig. 7 where, in addition to the envelopes of h/h_i , the apparent wave length is plotted at a longitudinal centerline position approximately 15 ft aft of the grid. This wave length is computed from the data obtained at the two centerline wave wires located at a distance of 13.25 ft and 16.5 ft



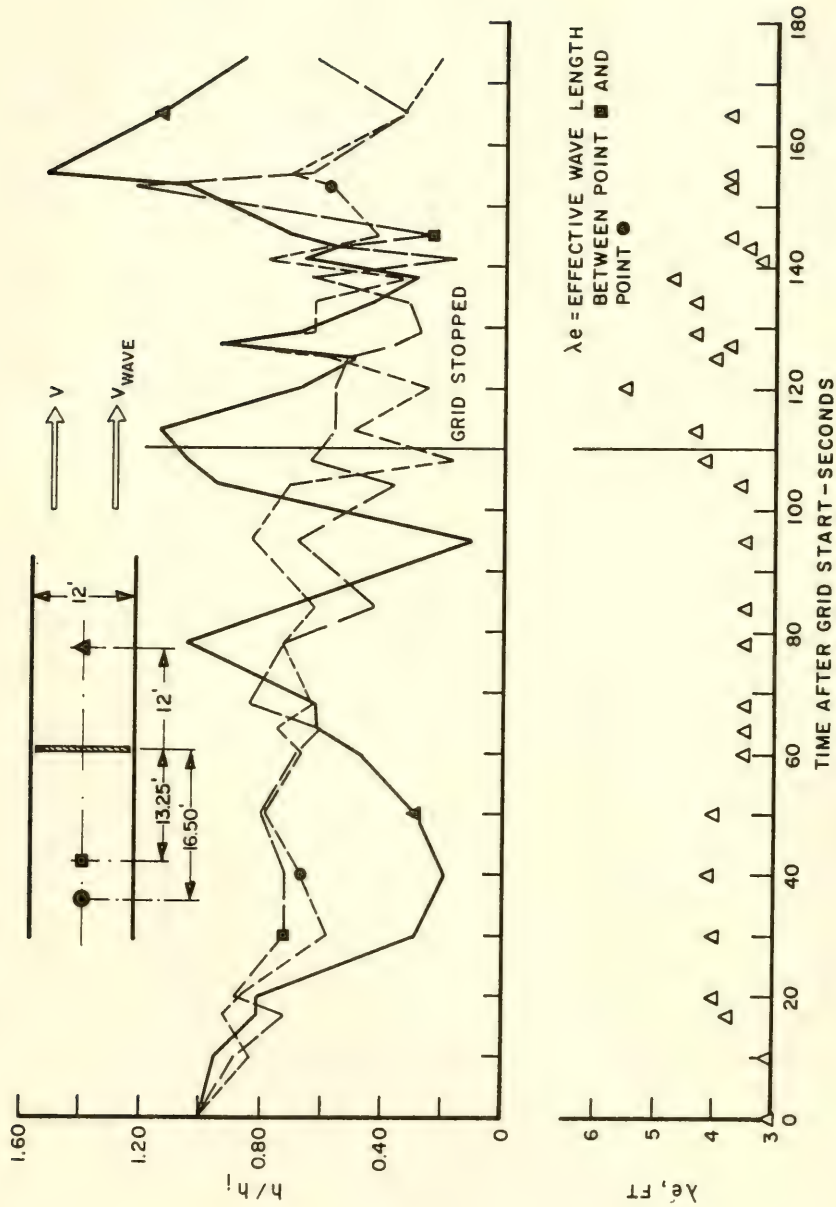


Fig. 7 Envelope of wave height at wave probes moving with one-dimensional grid
 $\lambda = 3'$ $H_w = 1.2''$ grid mesh = 2.7" draft = 1.67' $V = 1.1$ ft/sec

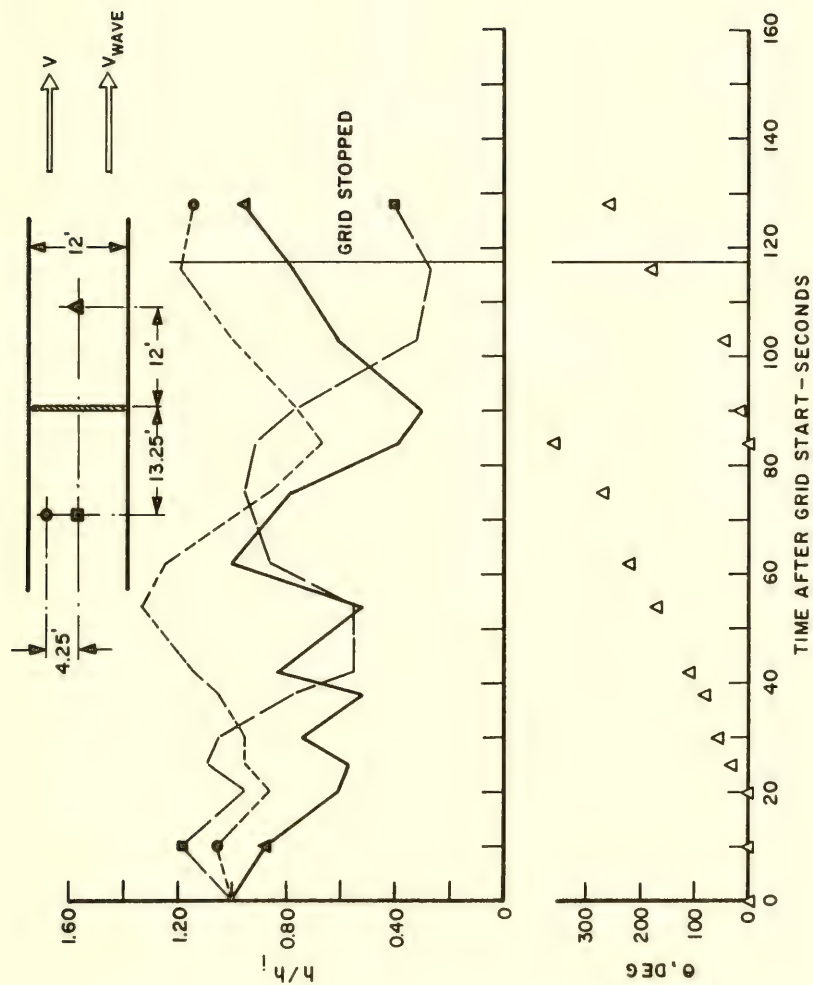


Fig. 8 Envelope of wave height at wave probes moving with one-dimensional grid
 $\lambda = 4'$ $H_w = 1.2''$ grid mesh = 2.7" draft = 1.67' $V = 1.0$ ft/sec

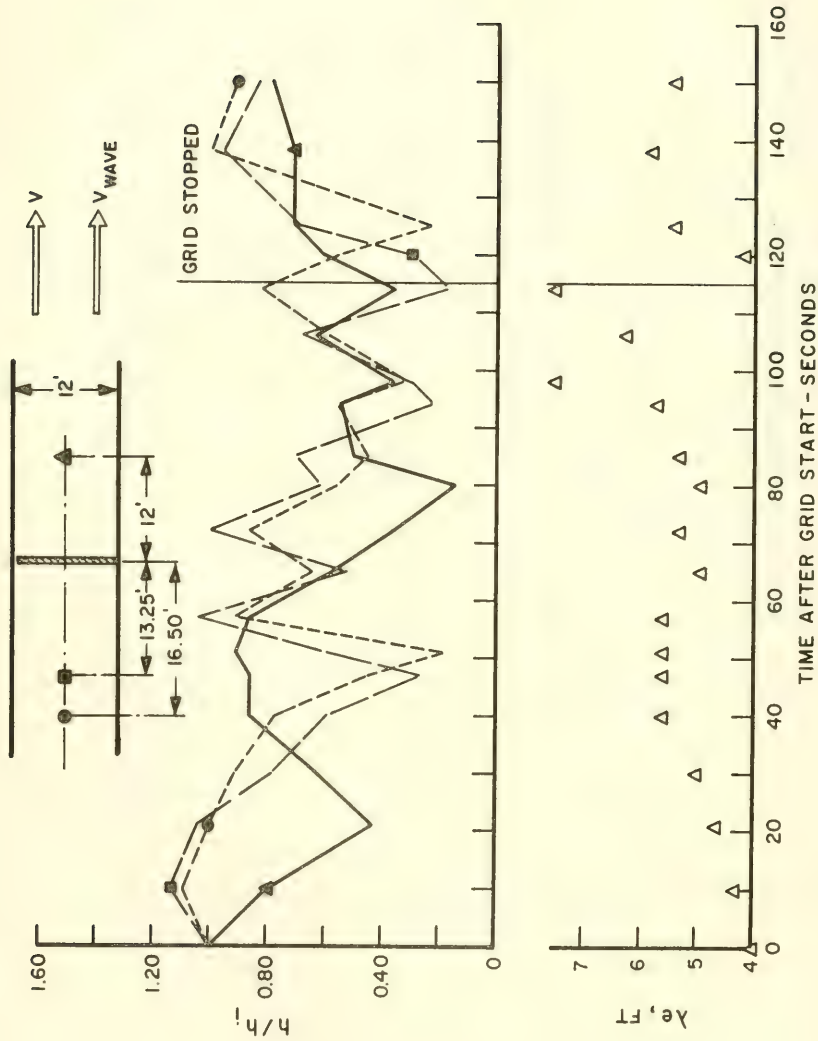


Fig. 9 Envelope of wave height at wave probes moving with one-dimensional grid
 $\lambda = 4'$ $H_w = 1.2''$ grid mesh = 2.7" draft = 1.27' $V = 1.1$ ft/sec

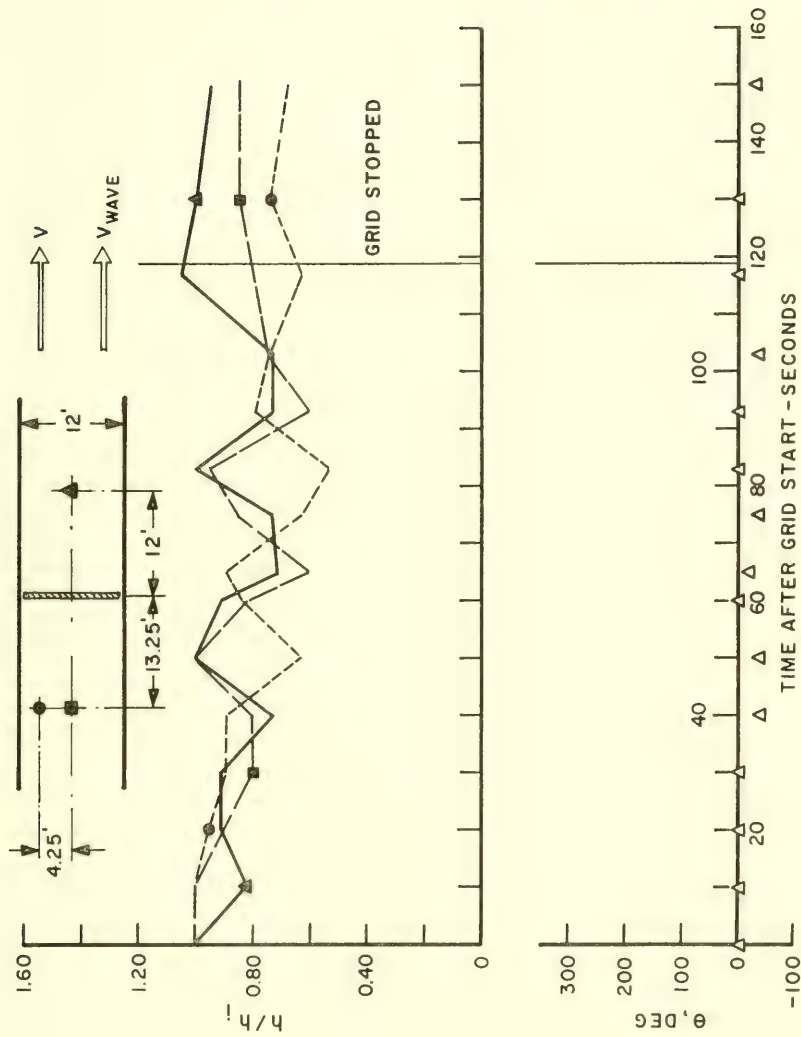


Fig. 10 Envelope of wave height at wave probes moving with one-dimensional grid
 $\lambda = 8'$ $H_w = 1.0''$ grid mesh = 2.7" draft = 1.27' $V = 1.1$ ft/sec

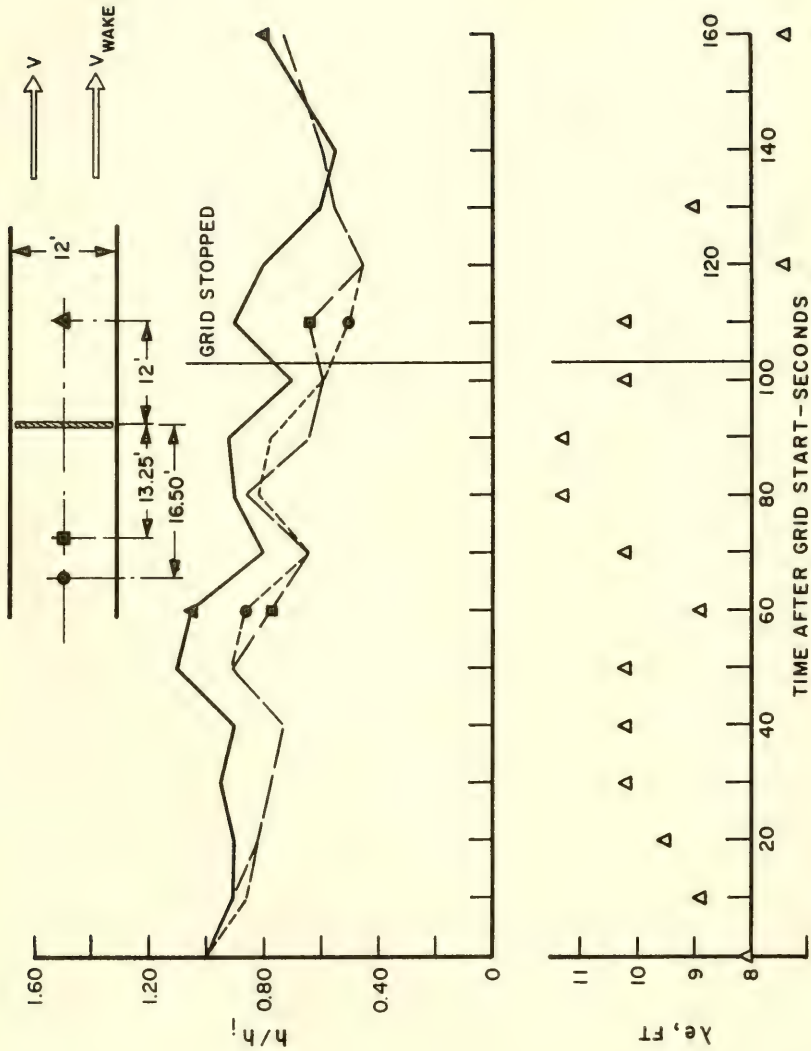


Fig. 11 Envelope of wave height at wave probes moving with one-dimensional grid
 $\lambda = 8'$ $H_w = 1.0''$ grid mesh = 2.7" draft = 1.27' $V = 1.1$ ft/sec

aft of the grid. Similar sets of plots are given in Figs. 8 and 9 for the 4 ft long wave and in Figs. 10 and 11 for the 8 ft long wave.

The irregular, oscillatory behavior of the wave height envelope is apparent in all plots and decreases as the wave length increases. Further, the average wave heights at 13.25 and 16.5 ft aft of the grid continuously decreases with increasing time of grid travel (which corresponds to an increasing length of turbulent wake through which the wave travels).

Repeat runs for otherwise identical test conditions did not produce identical time histories of wave height envelopes. This can be seen by comparing the time histories for a point 13.25 ft aft of the grid as shown in Figs. 6 and 7; 8 and 9; and 10 and 11. The time histories are much more nearly alike for the 8 ft long wave than for the 3 ft long wave.

Crest Line Deformation: An examination of the phase relation (θ) between the wave crest at a point 13.5 ft aft of and on the grid centerline and the wave crest at a point 4 ft transverse to this point indicates the first clear regularity to these one-dimensional test results. For the case of the 4 ft long wave (Fig. 6), it is seen that phase angle is zero, implying a crest line parallel to the grid for the first 20 seconds (20 ft of wake development) of grid travel. As time increases, the phase angle increases so that crest at the centerline precedes the wave crest 4 ft off the centerline. The phase angle increases nearly linearly with increasing time. For the 4 ft long wave (Fig. 8), a similar linear phase shift occurs except that the rate of phase shift is now somewhat slower. The phase shift for the 8 ft long test wave (Fig. 10) has a maximum value of only 45°. For this long wave, the centerline crest lags the outboard crest. A comparison of the wave amplitude shows nearly similar values at both wave probes when the phase is 0° or 360° and maximum differences when the phase angle is 180°.

Apparent Wave Length: The apparent wave length along the wake centerline was determined from an analysis of the time histories of the wave amplitudes at the two wave probes which were 3.25 ft apart (probes at distances of 13.25 ft and 16.50 ft aft of the grid). The apparent wave length generally increases with increasing time of grid travel. The 3 ft long wave (Fig. 7) attains a value of approximately 4 ft after 50 seconds of grid travel and then decreases to a value of 3.5 ft. The 4 ft test wave (Fig. 9) attains a value of nearly 6.5 ft after 100 seconds of grid travel while the 8 ft wave (Fig. 11) attains a value of approximately 11 ft after 90 seconds of travel. The wave lengthening is expected because of the longitudinal mean wake flow in the direction of wave celerity.

Effect of Grid Velocity: Figures 12 and 13 present the wave height envelopes for the 3 ft and 4 ft long waves when the grid speed

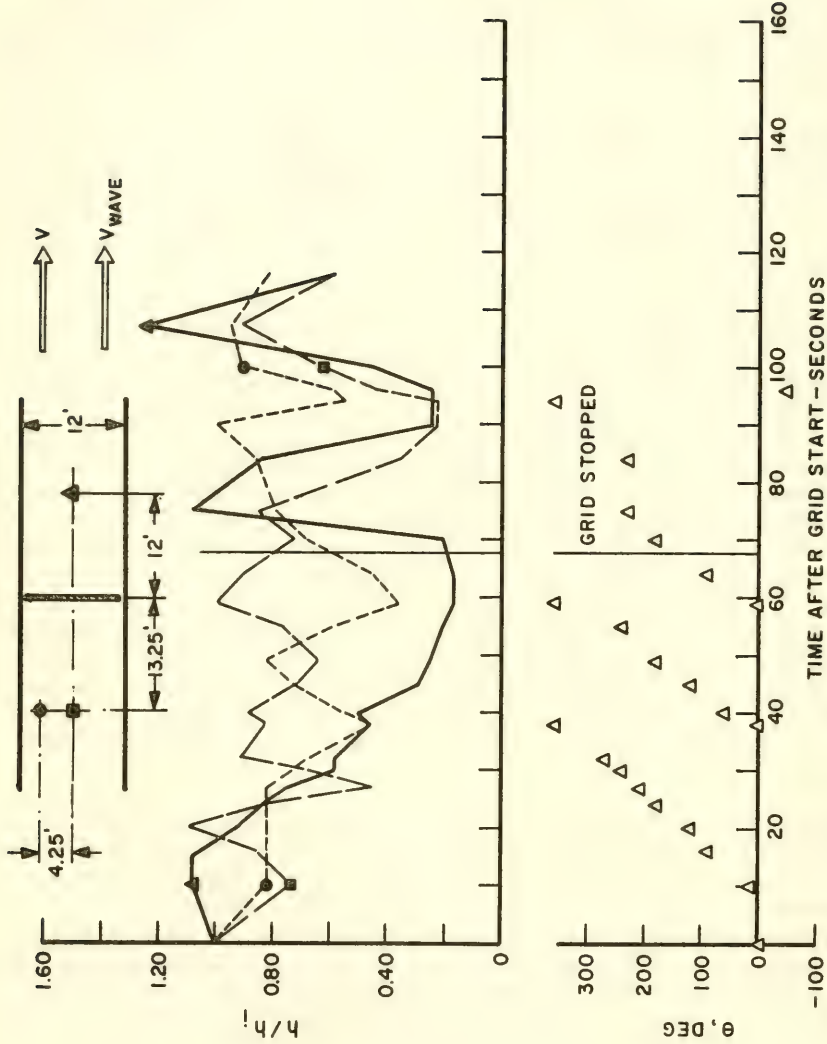


Fig. 12 Envelope of wave height at wave probes moving with one-dimensional grid
 $\lambda = 3'$ $H_w = 1.1''$ grid mesh = 2.7" draft = 1.27' $V = 1.7 \text{ ft/sec}$

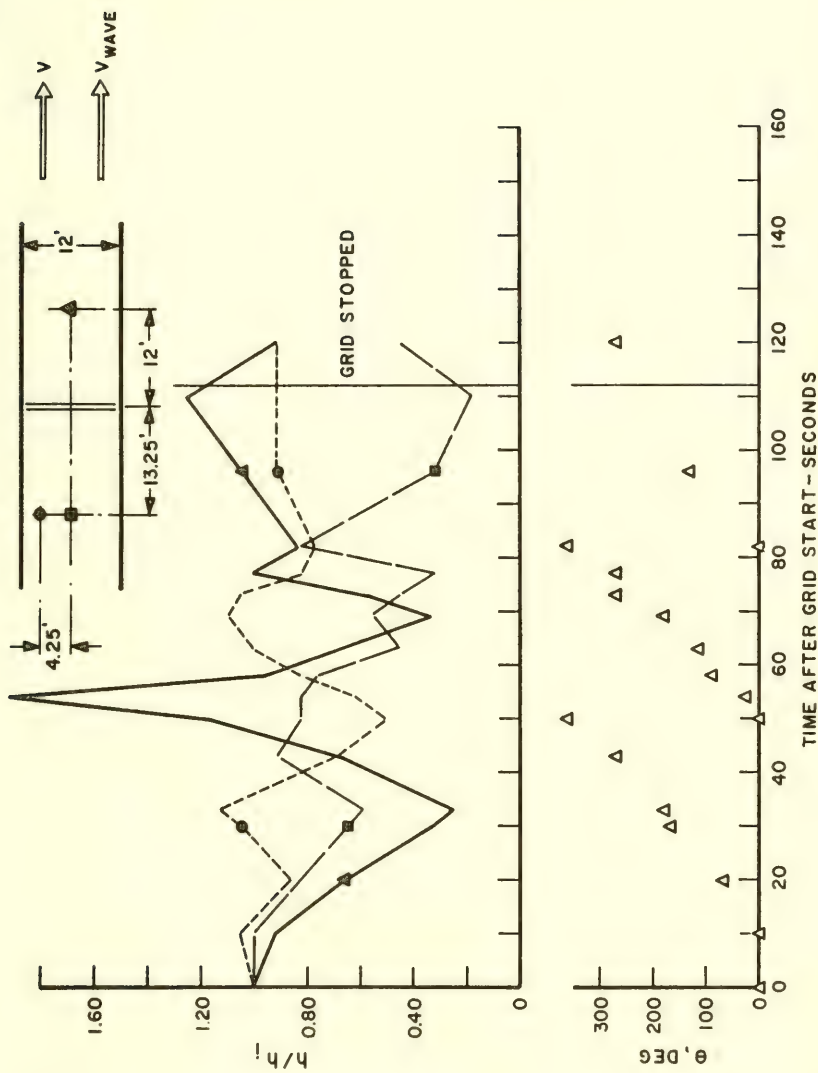


Fig. 13 Envelope of wave height at wave probes moving with one-dimensional grid
 $\lambda = 4'$ $H_w = 1.2''$ grid mesh = 2.7" draft = 1.27' $V = 1.7$ ft/sec

is increased to 1.7 ft/sec. These results are to be compared with those on Figs. 6 and 8 for a grid speed of 1.0 ft/sec. The major differences are that there are wider variations in wave amplitude at the higher grid speed and, further, the periodicity of the phase relation is reduced from 60 seconds to 40 seconds for the 3 ft wave and from 85 seconds to 50 seconds for the 4 ft wave. Unfortunately, sufficient data were not collected to determine the effect of grid velocity on apparent wave length. Similar data exist for the longer test wave lengths but, for the sake of brevity, these are not included in the present thesis.

Effect of Grid Mesh Size: Increasing the grid mesh size from 2.7" to 5.4" did not have a discernible effect upon the test results.

Two-Dimensional Grid Studies

The objective of these two-dimensional studies was to investigate the interaction between a turbulent flow field of finite dimensions and long-crested, deep water, gravity waves. As previously discussed, the grid wake characteristics were such that the waves were simultaneously subjected to dissipation effects due to eddy viscosity; scattering due to turbulent convective distortion of the wave front; and deformation of the wave due to mean flow velocity gradients. As in the one-dimensional investigations, it appears that the effect of the velocity gradients dominated in developing major wave distortions. Although the experimental program examined wide variations in wave length, wave height, grid mesh, grid width, grid draft, and grid speed, the presentation will be limited to a discussion of results for the following brief range of conditions:

$\lambda = 2.0; 6.0$ ft

$H_w = 1.0$ inches

Grid mesh = 2.7 inches

Grid draft = 0.83; 1.67 ft

Grid width = 3.0 ft

Grid velocity = 1.0, 1.6, 2.6 ft/sec

These limited combinations of parameters serve to illustrate the major effects of wake-wave interaction.

General Behavior: The behavior of the time history of the wave amplitudes at probe positions, either moving with the grid or stationary in the wake, were substantially different from the one-dimensional results previously discussed. The extensive irregularity in the wave amplitude were not observed -- particularly for those wave probes which traveled with the grid. There did appear to be some indication of an irregularity for those stationary wave probes located approximately two grid widths from centerline -- these were not, however, well defined. An examination of the crest line deformation as a given wave passed over the transverse line of stationary

probes indicated a slight concavity to the wave front with the crest along the grid centerline being in the lead by, at most, nearly 30 degrees for the 2 ft long wave at a grid speed of 1 ft/sec. It will be recalled that, in the one-dimensional tests, the phase between two transverse probes 4 ft apart continuously increased with time. In general, the wave height time histories were characterized by either a slow attenuation or amplification as the wave passed through the wake.

Figures 14 and 15 present the envelope of wave height time histories (normalized on the basis of incident wave height) along the transverse line of stationary wave probes fixed in the tank for 2 ft and 6 ft long waves respectively. The wave height was 1.0 inches and the grid dimensions were: width = 3.0 ft; draft = 1.7 ft; mesh = 2.7 in; speed = 1 ft/sec. For the probe on the centerline (No. 7), it is seen that there is a continuous decrease in amplitude starting from a time when the probe was 13 feet upstream of the grid. For the 2 ft wave (Fig. 14) the height is attenuated to approximately 10% of the incident wave height when the probe is 7 ft downstream of the grid and retains this reduced height for the entire time of data collection (80 seconds). It will be noted from Fig. 3 that, when the grid reaches the transverse wave probes, it has already developed a wake 28 ft long moving at a mean longitudinal velocity of approximately 35 per cent of the grid speed.

The probe 2.4 ft from the centerline (No. 1) also shows a continuous reduction in wave height with increasing time, finally attaining a value approximately 35% of the incident wave. Probe No. 2, located 4.2 ft from the centerline, indicates only small variation in wave height with time. The remaining outboard probes (No. 3, 4, 5) all show increases in wave height for the entire test run. These probes also indicate the existence of mild "beats" in the envelope of time histories although not as severe as for the one-dimensional case previously discussed. The maximum wave height occurs between probes 3 and 4 attaining a value approximately 75% larger than the incident wave. It is to be noted that, for all stationary wave probes, the height modifications are initially noted when the probes are still 13 ft upstream of the grid. In general, then, the characteristics of wave deformation in the wake show a significant reduction in wave height for approximately one grid width on either side of the centerline and an amplification beyond this region.

Figure 15 represents similar data for a 6 ft long wave -- all other conditions being equal. The general characteristics of wave deformation are identical to the 2 ft long wave except that the magnitudes of the changes are reduced. For example, the minimum wave height along the centerline is now 30 per cent of the incident wave while the maximum wave height is 35% larger than the incident wave.

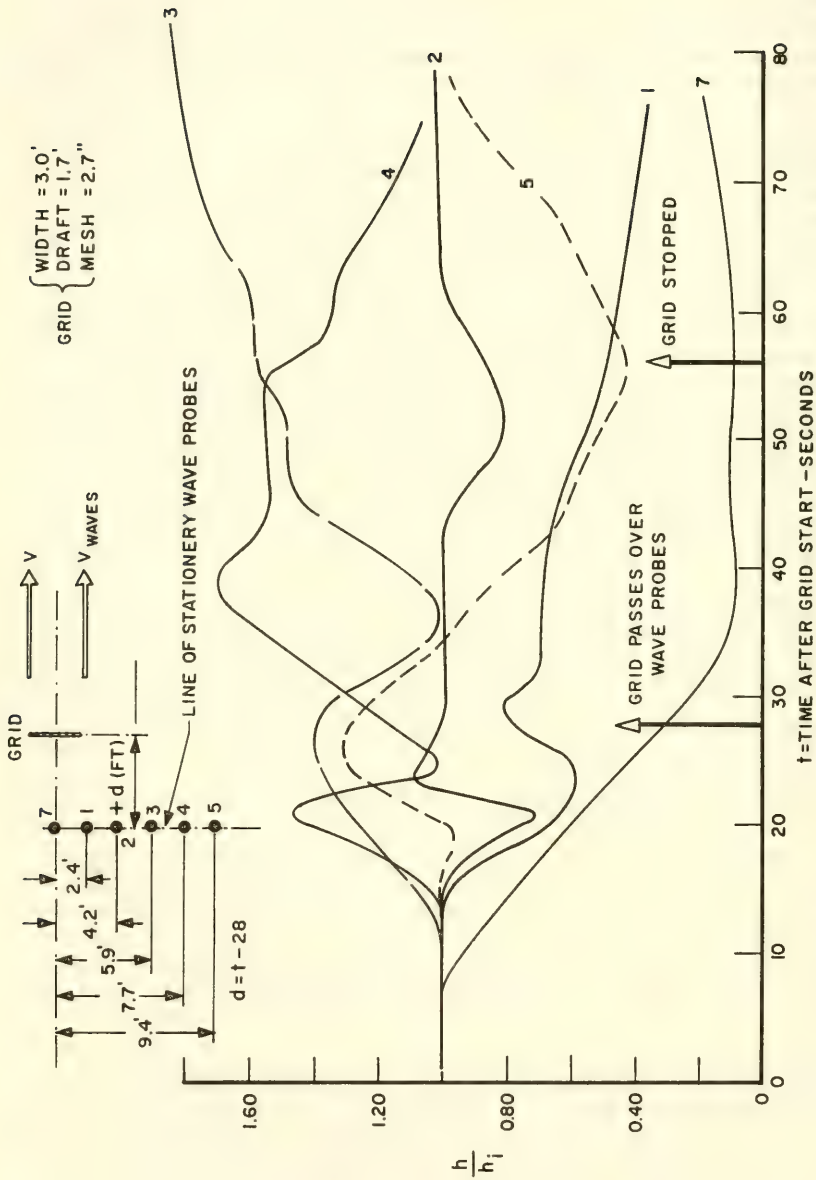


Fig. 14 Envelope of wave heights at stationary wave probes for 2-dimensional grid
 $\lambda = 2'$ $H_w = 1.0''$ $V = 1 \text{ ft/sec}$

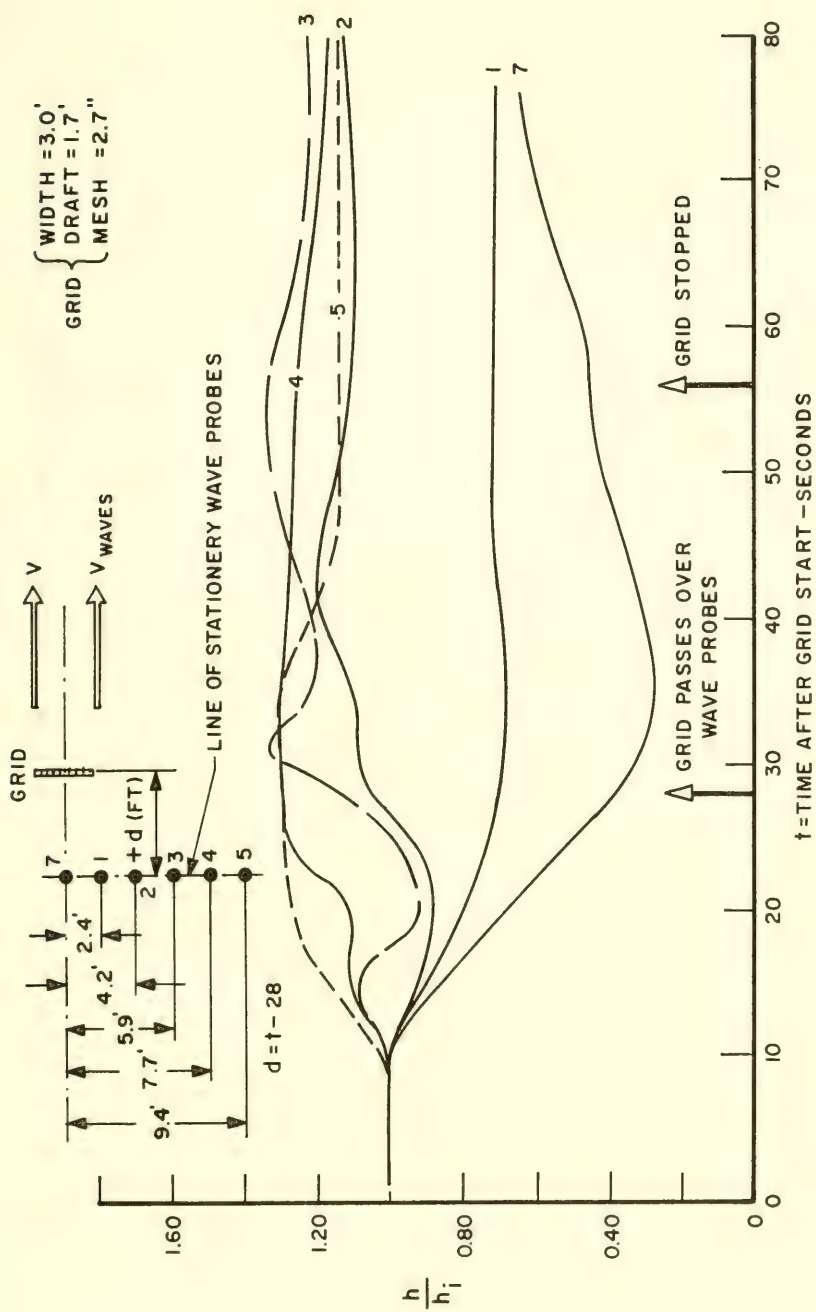


Fig. 15 Envelope of wave heights at stationary wave probes for 2-dimensional grid

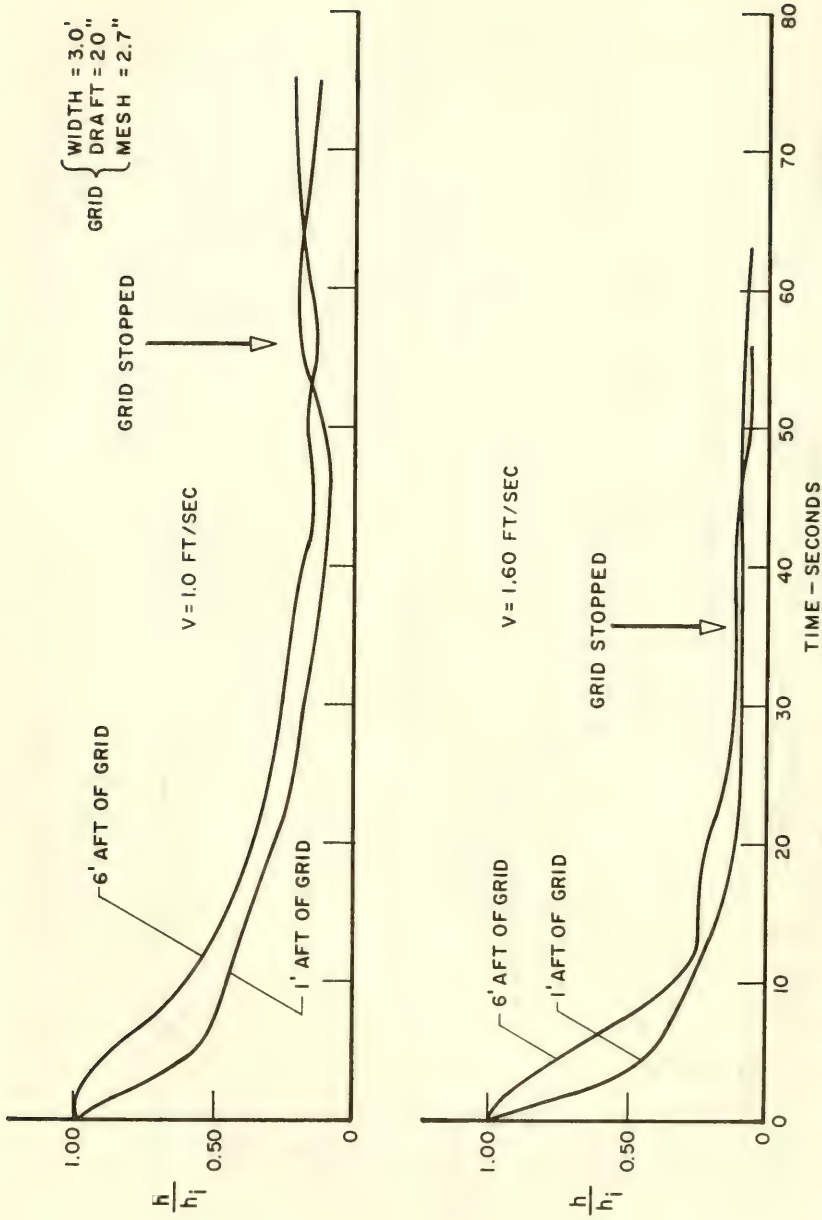


Fig. 16 Envelope of wave height at wave probes moving in wake of 2-dimensional grid
 $\lambda = 2'$ $H_w = 1.0''$

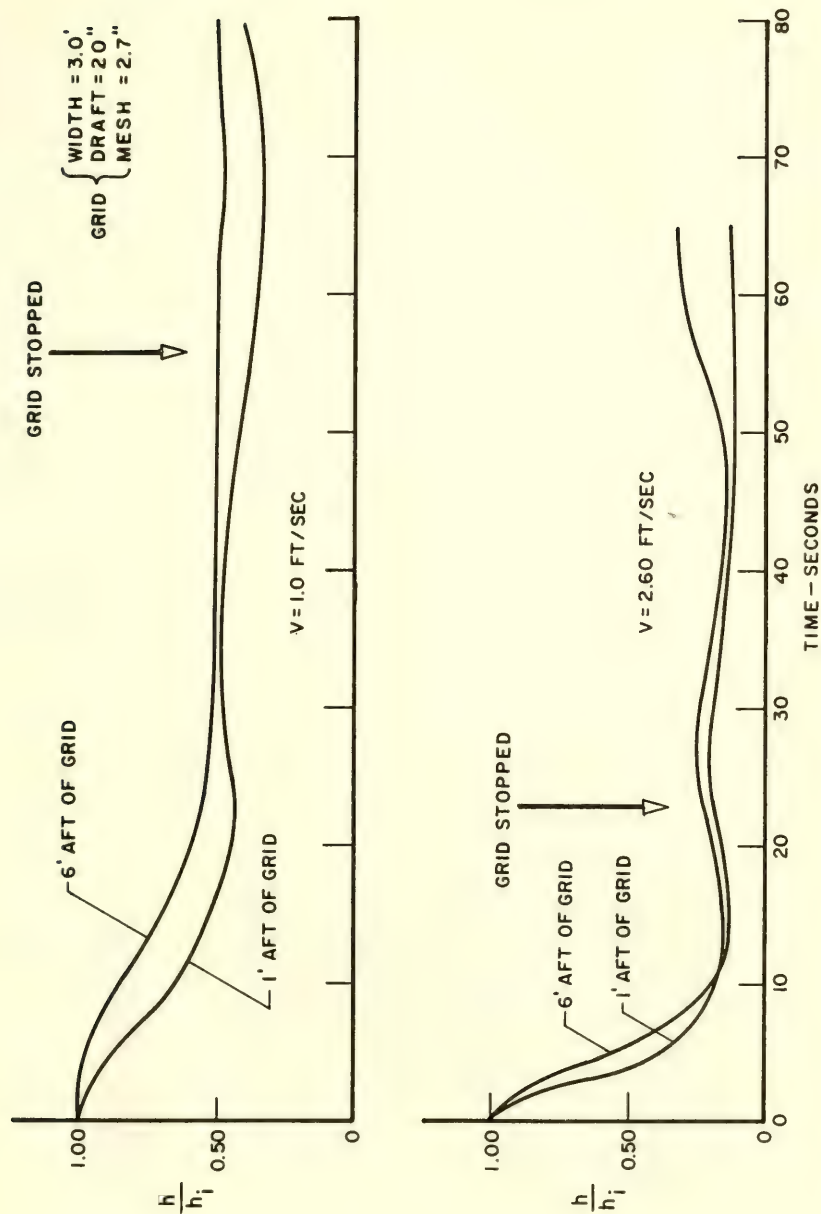


Fig. 17 Envelope of wave height at wave probes moving in wake of 2-dimensional grid

$$\lambda = 6' \quad H_w = 1.0''$$

The envelope of wave height at the moving probes is given in Figs. 16 and 17 for wave lengths of 2 ft and 6 ft respectively. The wave probe positions are at distances of 1 ft and 6 ft aft of the grid and just off its centerline. The grid was 3 ft wide, had a draft of 1.7 ft and a mesh size of 2.7 inches. Figure 16 presents results for grid speeds of 1.0 and 1.6 ft/sec, while Fig. 17 is for speeds of 1.0 and 2.6 ft/sec. It is seen that there is a continuous reduction in wave height with time. For the 2 ft long wave and a grid speed of 1.0 ft/sec, the amplitude is reduced to nearly 10 per cent of its initial value after approximately 20 ft of grid travel. It remains essentially at this value for the length of the test record which extended for 30 seconds after the grid was stopped. The effect of increasing the speed of the grid from 1.0 to 1.6 ft/sec reduced the wave height to nearly 8% of its initial value. It is to be noted that there is a distinct absence of oscillations in these time histories.

The results for the 6 ft long wave (Fig. 17) are essentially similar to those for the 2 ft long wave. At a grid speed of 1 ft/sec, the wave height is reduced to approximately 35 per cent of its initial value. When the grid speed was increased to 2.6 ft/sec, the wave height was reduced to 12 per cent of its initial value.

An overwater photograph of the wave deformation for a typical two-dimensional test is shown in Fig. 18. The reduction in wave height along the centerline wake area and the amplification outside this area are clearly visible in this photograph.

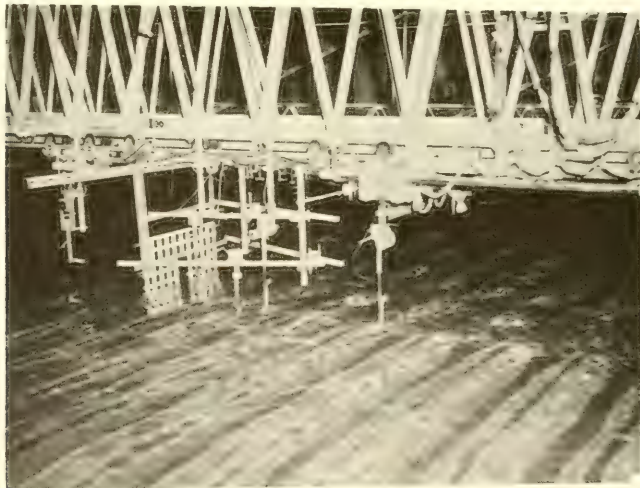


Fig. 18 Typical wave deformation for two-dimensional grid

Specific Results: To more clearly illustrate the modifications in wave height along a given crest line, transverse sections through the wake are plotted in Figs. 19 and 20 for a grid width of 3 ft, draft of 1.67 ft, mesh of 2.7" and speed of 1 ft/sec. The effect of a grid draft of 0.83 is given in Fig. 21. The results for the 2 ft wave are given in Fig. 19 while those for the 6 ft wave are given in Figs. 20 and 21. These data are obtained from simultaneous measurements of the recorded wave height at times corresponding to the indicated distances ahead of and behind the grid. A maximum phase shift of only 30° was discernible in the test records.

It is seen that a substantial reduction in wave amplitude exists for a distance of nearly one grid width on either side of the centerline. The maximum wave height amplification occurs at approximately two grid widths from the centerline and the wave amplitude appears to be unaffected at distances of approximately 4 grid widths from the centerline. This pattern exists for distances well aft of the grid. It is interesting to note that, as the wave passes through and ahead of the grid, where the wake does not exist, the deformed crest tends to return to its original uniform height. Again, it is seen that the 2 ft wave is much more attenuated and amplified compared to the 6 ft wave, all other conditions being equal. (Compare Figs. 19 and 20.) It is also interesting to note that reducing the grid draft from 1.67 ft to 0.83 ft has a negligible effect on wave deformation for the 6 ft wave. (Compare Figs. 20 and 21.)

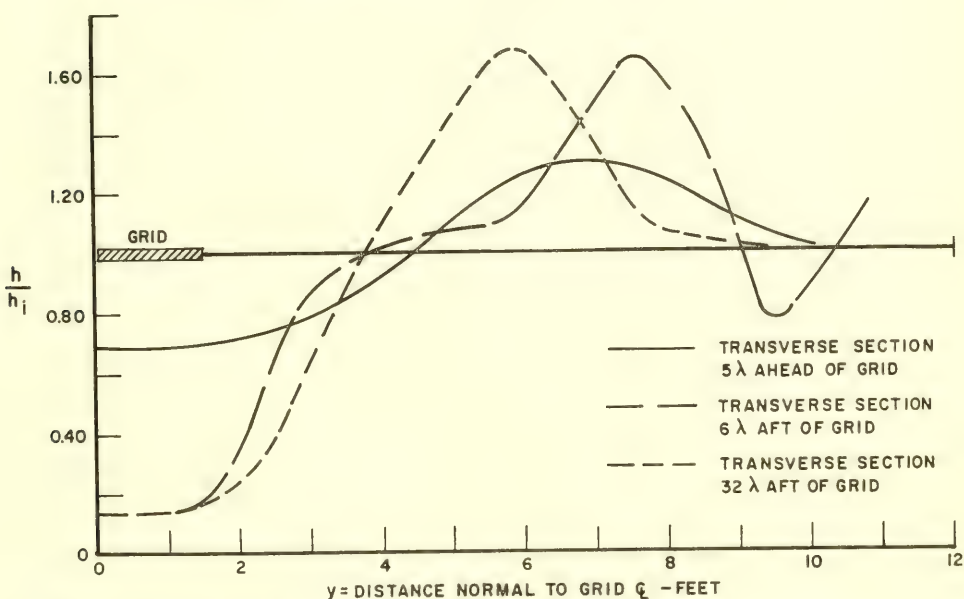


Fig. 19 Height of wave crest line in transverse sections normal to grid \mathcal{G} . $\lambda = 2'$, $H_w = 1''$, grid width = $3'$, mesh = $2.7''$, draft = $1.67'$, $V = 1$ ft/sec.

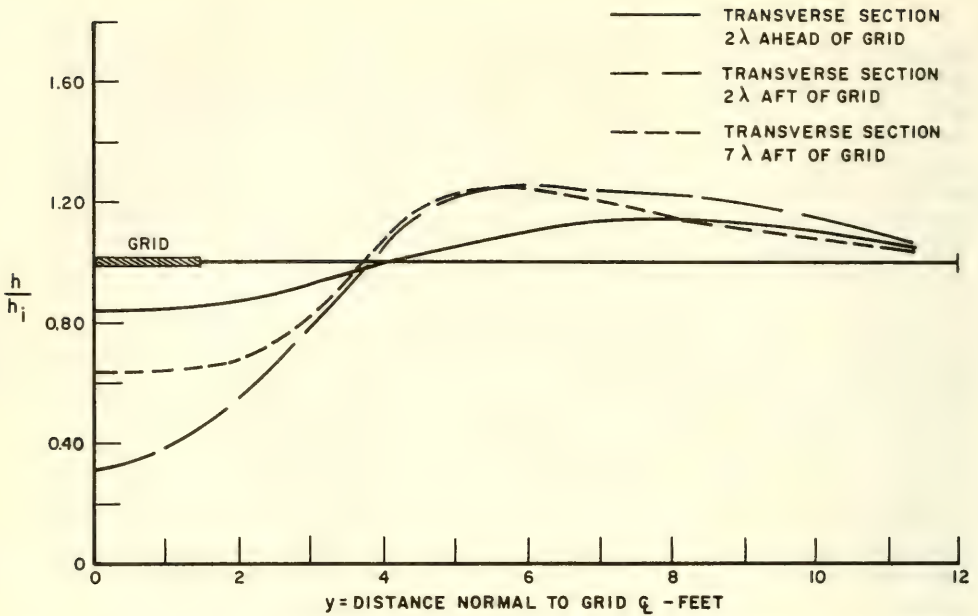


Fig. 20 Height of wave crest line in transverse sections normal to grid \mathcal{C} . $\lambda = 6'$, $H_w = 1''$, grid width = $3'$, mesh = $2.7''$, draft = $1.67'$, $V = 1$ ft/sec.

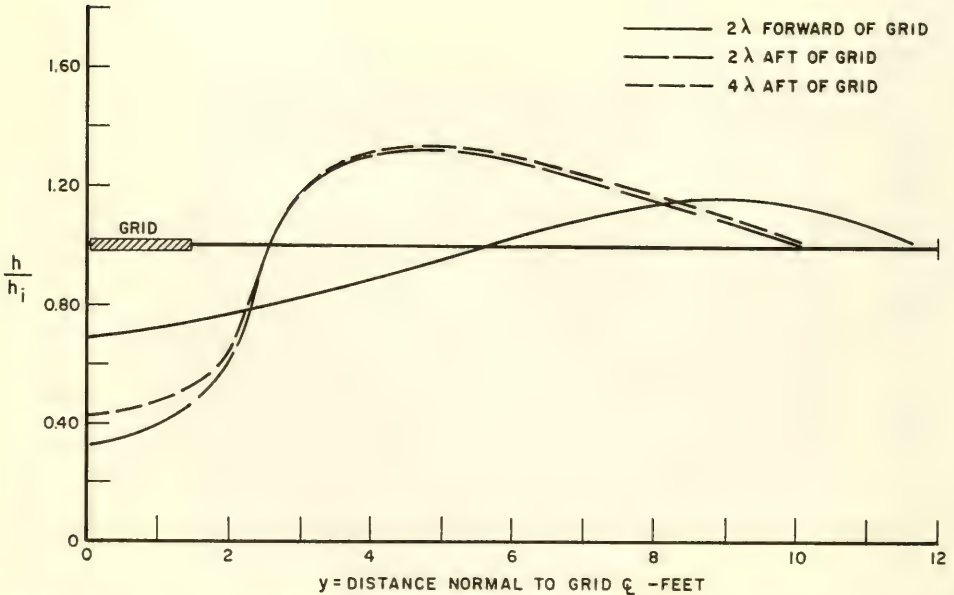


Fig. 21 Height of wave crest line in transverse sections normal to grid \mathcal{C} . $\lambda = 6'$, $H_w = 1''$, grid width = $3'$, mesh = $2.7''$, draft = $0.83'$, $V = 1$ ft/sec.

Increasing the mesh size from 2.7 to 5.4 inches has a negligible effect on the wave deformation. Increasing the width of the grid increased the area of wave attenuation and wave amplification.

III. ANALYSIS AND DISCUSSION

Viscous and Turbulent Effects

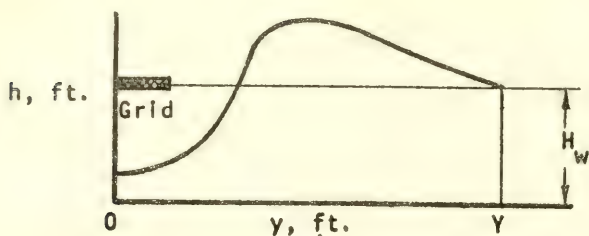
The initial analysis of the experimental results was directed to relating the observed wave deformations to possible physical mechanisms associated with the turbulent and viscous nature of the grid-generated wake. It was found that the large changes in wave height could not be accounted for by these considerations -- particularly in the two-dimensional grid studies. In this case, the square of the wave height was integrated along a crest line passing through the wake to obtain a measure of the energy in the deformed wave. This was compared with the energy in the incident wave for the same length of crest line. The results of this comparison are presented in Table 1 for wave and grid dimensions selected to be typically representative of the total test program. The length of integration, Y , along a given crest line was the distance between the grid centerline and the point where the wave height was again equal to the incident wave height. The crest length thus includes both the attenuated and amplified wave height regions. For a given test condition, the integrations were carried out for several transverse sections through the wake, both ahead of and aft of the grid. It is seen from Table 1 that the integrated expression representative of wave energy produces nearly similar results with and without the towed grid. In fact, for some test conditions, the integrated energy for waves in the presence of the grid results in values somewhat higher than for the case of no grid -- but this is attributed to experimental inaccuracies. It thus appears that viscous dissipative effects were quite small and, although they most certainly existed, their magnitude could not be accurately detected because the limited number of transverse wave probes were inadequate to trace the unexpected large wave height deformation which developed along a crest line.

A measure of the rms of the velocity fluctuations in the turbulent field yielded substantially the same values with or without waves passing through the wake. This was not surprising since the energy imparted by the grid to the fluid at a tow speed of 1 ft/sec was nearly an order of magnitude larger than the wave energy in a crestline length equal to the grid width.

For the one-dimensional tests, it will be recalled that the wave height at a given position in the wake exhibited large fluctuations and was characterized by irregularities in the recorded time histories. These results could certainly not be accounted for by dissipative mechanisms in the turbulent field. It appeared then that for both the one and two-dimensional studies the principal

TABLE I

Comparison of Wave Energy With and Without Towed Grid



$$E_g = \int_0^Y h^2 dy$$

(with towed grid)

$$E_{ng} = H_w^2 Y$$

(no grid)

Wave*

Grid*

Transverse Section

λ	H_w	L	D	M	V_G	Position**	E_{ng}	E_g
6.0	0.09	3.0	1.7	0.22	1.0 ft/sec	5 λ (F)	0.067 ft ³	0.069 ft ³
						6 λ (A)	0.063	0.060
						32 λ (A)	0.058	0.064
6.0	0.09	3.0	1.7	0.22	1.7	2 λ (F)	0.081	0.082
						2 λ (A)	0.081	0.083
						7 λ (A)	0.081	0.079
2.0	0.09	3.0	1.7	0.52	1.0	5 λ (A)	0.081	0.081
						6 λ (A)	0.087	0.092
						32 λ (A)	0.081	0.075
6.0	0.09	5.5	1.7	0.22	1.0	2 λ (F)	0.093	0.100
						2 λ (A)	0.087	0.099
						4 λ (A)	0.087	0.099
2.0	0.09	3.0	0.85	0.22	1.0	5 λ (F)	0.081	0.098
						6 λ (A)	0.072	0.078
						23 λ (A)	0.081	0.091
6.0	0.09	3.0	0.85	0.22	1.0	2 λ (F)	0.081	0.079
						2 λ (A)	0.070	0.076
						4 λ (A)	0.070	0.078

* Wave and grid dimension in feet; L = grid width; D = grid immersion; M = grid mesh

** (F) is transverse section forward of grid (ft)
(A) is transverse section aft of grid (ft)

mechanism of wave height deformation was due to a redistribution of energy along a crest line rather than to dissipative effects. In this regard, the results of Phillips [1959] were examined to determine possible convective distortions of the wave front resulting from scattering interference between wave and turbulence field. It was found that the observed results could not be accounted for by the turbulent scattering.

If, in the present studies then, turbulence is assumed to have had a minor effect on wave deformation, it remained to examine the possible interference between the mean flow gradient in the wake and the incident wave. The velocity profiles for the longitudinal mean flow aft of the grids are plotted in Figs. 2 and 4 for the one- and two-dimensional studies, respectively. In both cases there is a relatively sharp velocity gradient between a region of constant wake velocity to zero velocity at the tank wall for the one-dimensional case and to zero velocity in the still water adjacent to the finite grid wake in the two-dimensional case. By application and superposition of elemental theories of wave refraction, defraction and interference, it was found that the observed results could be, at least, qualitatively reproduced and physical mechanisms described to account for the large wave deformations observed.

A detailed analysis is first made of the two-dimensional tests since these results were free of possible wall reflection effects such as existed in the one-dimensional studies. Further, the 2-D analysis will provide the foundation for explaining the results of the 1-D studies which proved to be the more complex case.

Wave Interaction with Finite Velocity Field

Two-Dimensional Results. The longitudinal mean flow in the finite wake area aft of the grid is plotted in Fig. 4 and is quantified by an empirical formulation, Eq. (2).

$$\frac{V_w}{V} = [0.45 - 0.00745x] \left[e^{-\left(\frac{y}{1.67 + 0.062x}\right)^8} \right]$$

where

- V_w = mean value of longitudinal velocity in wake
- V = grid velocity
- x = distance aft of grid, ft
- y = distance normal to grid centerline, ft

In the present analysis, regular waves in still deep water encounter a variable current field $V_w(x,y)$ moving in the same direction as the waves. The waves are initially refracted by the current to an extent dependent upon the incident wave length, strength of current, and the velocity gradients in the wake. The orientation

of the wave-wake system is shown in Fig. 22.

For progressive deep water gravity waves in still water, the phase velocity of the wave, C_0 , is given by:

$$C_0^2 = g/k_0 \quad (3)$$

where g = acceleration of gravity, λ_0 = wave length in still water, k_0 = wave number = $2\pi/\lambda_0$, C_0 = wave velocity relative to still water. After the waves have run from still water into a current, the kinematical condition that must be satisfied is that the wave period, T , remains constant while the wave length, λ , velocity C , and height H_w change. Given a current velocity V_w , the constancy of wave period is expressed as:

$$\sigma = \frac{2\pi}{T} = k(C + V_w) = k_0(C_0 + V_{w_0}) \quad (4)$$

where the subscript, o , refers to the still water conditions.

Thus:

$$\frac{k_0}{k} = \frac{C + V_w}{C_0 + V_{w_0}} = \frac{C^2}{C_0^2}$$

For the present case $V_{w_0} = 0$ so that:

$$\frac{C^2}{C_0^2} - \frac{C}{C_0} - \frac{V_w}{C_0} = 0$$

and

$$C = \frac{1}{2}(C_0 + \sqrt{C_0^2 + 4V_w C_0}) \quad (5)$$

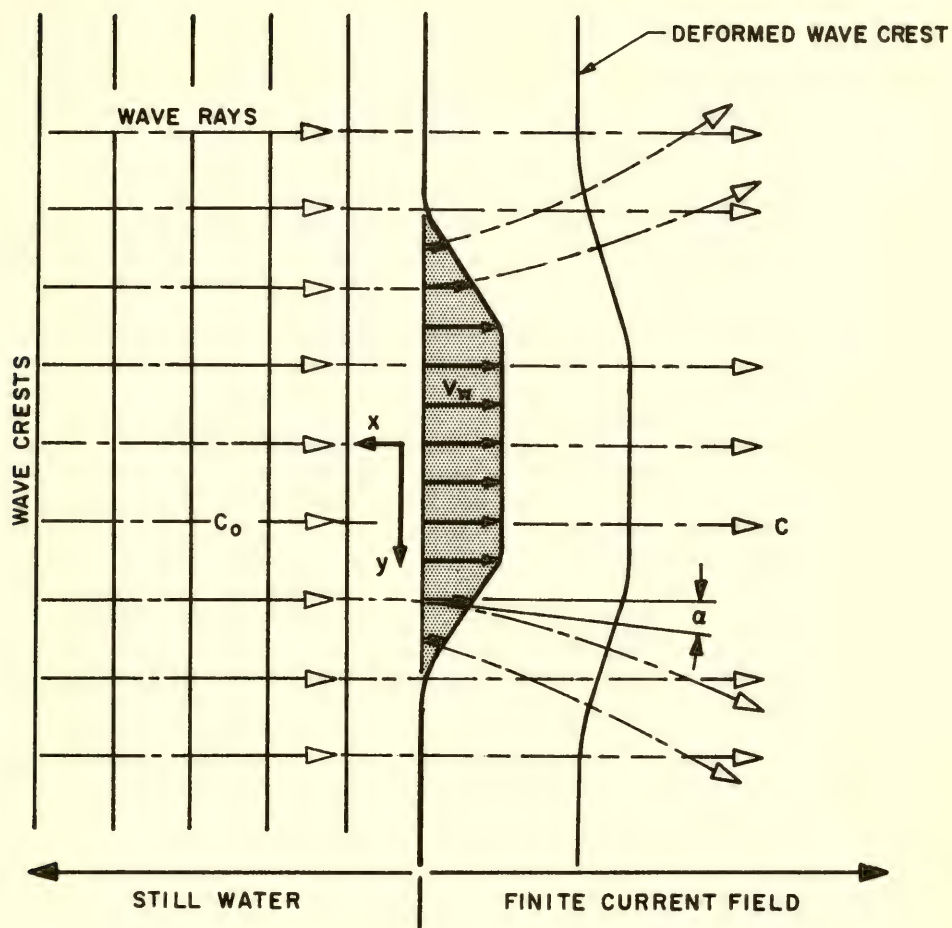
which is the wave speed relative to the water for waves progressing in the same direction as the current.

More generally, for waves whose crest line is at an angle relative to the x -axis:

$$C = \frac{1}{2}(C_0 + \sqrt{C_0^2 + 4V_w C_0 \cos \alpha}) \quad (6)$$

where α is the angle between a wave ray and the x -axis (Fig. 22).

The wave velocity relative to the bottom C' is the vector sum of the wave speed relative to the water and the local current.



v_w = LONGITUDINAL CURRENT FIELD IN WAKE

c_0 = WAVE VELOCITY, STILL WATER

c = WAVE VELOCITY, IN CURRENT

α = ANGLE BETWEEN WAVE RAY AND x AXIS

Fig. 22 Wave-wake system

$$\overline{C}' = \overline{V}_w + \overline{C} \quad (7)$$

The wave length for waves progressing in the same direction as the current is thus:

$$\frac{\lambda}{\lambda_0} = \left[\frac{1 + \sqrt{1 + 4(V_w/C_0)}}{2} \right]^2 \quad (8)$$

It can be seen that the effect of a following current is to increase the wave length relative to the water.

The analytical solution for the refraction of waves traveling through a finite current field is obtained by application of Fermat's principle that waves will travel in a path such that the travel time is a minimum. Applying the method of calculus of variations will lead to a time history of the path of individual wave rays passing through the current. For the purposes of this analysis, it will be assumed that the wake properties do not vary with time. This is a reasonable assumption since it has been demonstrated that, for a grid-speed of 1 ft/sec, the mean wake-velocity is an order of magnitude less than the wave speeds. Mathematically, the problem is to determine the minimum time path of a given wave ray through a current region defined by a position dependent velocity vector. The magnitude and direction of the current are known as functions of position (Eq. 2). The magnitude of the wave crest velocity relative to the water is C , given by Eq. (6). The problem is to determine the path of a wave ray such as to minimize the time necessary to travel from point A to a point B. Analogous optimization problems for dynamic systems are described by Bryson and Ho [1969].

The equations of motion are:

$$\begin{aligned} \dot{x}(t) &= -V_w(x, y) - C(x, y, \alpha) \cos \alpha \\ \dot{y}(t) &= -C(x, y, \alpha) \sin \alpha \end{aligned} \quad (9)$$

with initial conditions

$$\begin{aligned} x(0) &= x_0 \\ y(0) &= y_0 \end{aligned} \quad (10)$$

and at end of computation

$$x(t_f) = x_1$$

where t_f is an unspecified terminal time of integration between points A and B. It is required to find $\alpha(t)$ and t_f such that the above constraints are satisfied and that the performance index $J(\alpha)$ of elapsed time t_f is a minimum expressed mathematically,

$$J(\alpha) = \int_0^{t_f} dt \quad (11)$$

is a minimum.

From the methods of calculus of variations, the Hamiltonian of the system is:

$$H(x, y, \alpha, \lambda_x, \lambda_y) = 1 + \lambda_x(-V_w - C \cos \alpha) - \lambda_y C \sin \alpha \quad (12)$$

where λ_x and λ_y are Lagrange multipliers. The Euler-Lagrange equations are:

$$\dot{\lambda}_x = - \frac{\partial H}{\partial x}$$

$$\dot{\lambda}_y = - \frac{\partial H}{\partial y}$$

$$\dot{x} = \frac{\partial H}{\partial \lambda_x}$$

$$\dot{y} = \frac{\partial H}{\partial \lambda_y}$$

$$0 = \frac{\partial H}{\partial \alpha}$$

The terminal conditions are:

$$\begin{aligned} \lambda_y(t_f) &= 0 \\ H(t_f) &= 0 \end{aligned} \quad (14)$$

Since the Hamiltonian is not an explicit function of time, $\dot{H} = 0$ and H is a constant. Further, since $H = 0$ at the terminal condition, then it follows that $H = 0$ for all $0 \leq t \leq t_f$.

Evaluating $\partial H/\partial \alpha$ from (12) and using the condition $H = 0$ leads to a determination of the Lagrange multipliers.

$$\lambda_x = \frac{C \cos \alpha + \frac{\partial C}{\partial \alpha} \sin \alpha}{V_w(C \cos \alpha + \frac{\partial C}{\partial \alpha} \sin \alpha) + C^2}$$

$$\lambda_y = \frac{\frac{\partial C}{\partial \alpha} \cos \alpha - C \sin \alpha}{V_w(C \cos \alpha + \frac{\partial C}{\partial \alpha} \sin \alpha) + C^2}$$
(15)

The remaining differential equations are employed and, after extensive algebraic manipulations (which will not be reproduced herein), the following expression for $\dot{\alpha}(t)$, the angular trajectory for minimum travel time, is obtained.

$$\begin{aligned} \dot{\alpha}(t) = & \left[V_w C \frac{\partial^2 C}{\partial x \partial \alpha} - V_w \frac{\partial C}{\partial x} \frac{\partial C}{\partial \alpha} + C^2 \frac{\partial C}{\partial x} \sin \alpha + C \frac{\partial V_w}{\partial x} \frac{\partial C}{\partial \alpha} \sin^2 \alpha \right. \\ & + C^2 \frac{\partial V_w}{\partial x} \sin \alpha \cos \alpha + C^2 \frac{\partial^2 C}{\partial x \partial \alpha} \cos \alpha - 2C \frac{\partial C}{\partial x} \frac{\partial C}{\partial \alpha} \cos \alpha \\ & - C \frac{\partial V_w}{\partial x} \frac{\partial C}{\partial \alpha} \cos^2 \alpha - \frac{\partial V_w}{\partial x} \left(\frac{\partial C}{\partial x} \right)^2 \sin \alpha \cos \alpha + C^2 \frac{\partial C}{\partial y} \cos \alpha \\ & - C^2 \frac{\partial^2 C}{\partial y \partial \alpha} \sin \alpha + 2C \frac{\partial C}{\partial y} \frac{\partial C}{\partial \alpha} \sin \alpha + C^2 \frac{\partial V_w}{\partial y} \cos^2 \alpha \\ & \left. + 2C \frac{\partial V_w}{\partial y} \frac{\partial C}{\partial \alpha} \sin \alpha \cos \alpha + \frac{\partial V_w}{\partial y} \left(\frac{\partial C}{\partial \alpha} \right)^2 \sin^2 \alpha \right] / \\ & \left[-C^2 + C \frac{\partial^2 C}{\partial \alpha^2} - 2 \left(\frac{\partial C}{\partial \alpha} \right) \right] \end{aligned}$$
(16)

The partial derivatives of C and V_w contained in Eq. (16) are obtained from the definition of C and V_w as follows:

$$C = \frac{1}{2} \left[C_0 + \sqrt{C_0^2 + 4V_w C_0 \cos \alpha} \right]$$

$$V_w(x, y) = (0.45 - 0.0074x) \exp \left[- \left(\frac{y}{1.67 + 0.0062x} \right)^8 \right]$$

Thus:

$$\frac{\partial C}{\partial \alpha} = - V_w C_0 \sin \alpha (C_0^2 + 4V_w C_0 \cos \alpha)^{-1/2}$$

$$\frac{\partial C}{\partial x} = C_0 \cos \alpha (C_0^2 + 4V_w C_0 \cos \alpha)^{-1/2} \frac{\partial V_w}{\partial x}$$

$$\frac{\partial C}{\partial y} = C_0 \cos \alpha (C_0^2 + 4V_w C_0 \cos \alpha)^{-1/2} \frac{\partial V_w}{\partial y}$$

$$\begin{aligned} \frac{\partial^2 C}{\partial x \partial \alpha} &= C_0 \sin \alpha \frac{\partial V_w}{\partial x} \left[- (C_0^2 + 4V_w C_0 \cos \alpha)^{-1/2} \right. \\ &\quad \left. + 2C_0 \cos \alpha (C_0^2 + 4V_w C_0 \cos \alpha)^{-3/2} \right] \end{aligned}$$

$$\begin{aligned} \frac{\partial^2 C}{\partial y \partial \alpha} &= C_0 \sin \alpha \frac{\partial V_w}{\partial y} \left[- (C_0^2 + 4V_w C_0 \cos \alpha)^{-1/2} \right. \\ &\quad \left. + 2C_0 \cos \alpha (C_0^2 + 4V_w C_0 \cos \alpha)^{-3/2} \right] \end{aligned}$$

$$\begin{aligned} \frac{\partial^2 C}{\partial \alpha^2} &= - V_w C_0 \cos \alpha (C_0^2 + 4V_w C_0 \cos \alpha)^{-1/2} \\ &\quad - 2V_w^2 C_0^2 \sin^2 \alpha (C_0^2 + 4V_w C_0 \cos \alpha)^{-3/2} \end{aligned}$$

and

$$\begin{aligned} \frac{\partial V_w}{\partial x} &= -0.00745V \exp \left[- \left(\frac{y}{1.67 + 0.062x} \right)^8 \right] \\ &\quad + V(0.45 - 0.00745x) \exp \left[- \left(\frac{y}{1.67 + 0.062x} \right)^8 \right] \\ &\quad - 8 \left(\frac{y}{1.67 + 0.062x} \right)^7 \left[- \frac{0.062y}{1.67 + 0.062x} \right] \end{aligned}$$

$$\begin{aligned} \frac{\partial V_w}{\partial y} &= V(0.45 - 0.00745x) \exp - \left(\frac{y}{1.67 + 0.062x} \right)^8 \\ &\quad - 8 \left(\frac{y}{1.67 + 0.062x} \right)^7 \left(\frac{1}{1.67 + 0.062x} \right) \end{aligned}$$

These equations were programmed and evaluated on the PDP-10 computer. Refraction diagrams were obtained for several wave lengths, grid speeds, and initial wake lengths. The present report presents the results for

$$\lambda = 2, 6 \text{ ft}$$

$$\text{Grid width} = 3 \text{ ft}$$

$$\text{Grid submergence} = 1.67 \text{ ft}$$

$$\text{Grid mesh} = 2.7 \text{ in}$$

$$\text{Grid velocity} = 1 \text{ ft/sec}$$

$$\text{Wake length } (x_0) = 40 \text{ ft}$$

Actually, the empirical formulation for the wake velocity is associated with the above grid geometry. The results for the 2 and 6 ft waves are plotted in Figs. 23 and 24. These refraction diagrams are actually constructed by the so-called "orthogonal" method wherein a wave ray path is obtained from the computer solution. The crest lines shown on the diagrams are everywhere perpendicular to the orthogonals and represent the crest position at times corresponding to multiples of the wave period. This time interval, multiplied by the local wave speed at each point on the crest, determines the position of successive wave crests.

It is evident, for both wave lengths, that a large distortion of the wave front occurs for the length of wave crest initially located between a point 1 ft from the wake centerline and a point 3.5 ft from the centerline. In fact, this 2.5 ft length of crest is stretched to nearly eight times this length after the wave has traveled only 30 ft into the wake. The local crest line divergence for the 2 ft wave is larger than that for the 6 ft wave. A similar large stretching is evident for the length of wave crest between 3.5 and 5.0 ft from the centerline. Because of this extreme divergence of orthogonals for localized lengths of wave crest, it is not expected that refraction techniques alone are sufficient to represent the present wave-current interference effects. In fact, it is expected that diffraction along the wave crest must occur to provide for a flow of wave energy along the crest. This modification will be discussed subsequently.

The qualitative results obtained from the refraction analysis can be summarized by describing the behavior of adjacent finite crest lengths as the wave passes through the wake. The incident wave can be divided into four separate lengths as follows:

- 1) Crest length between $\frac{1}{2}$ and 1 ft.
- 2) Crest length between 1 ft and 3.5 ft.
- 3) Crest length between 3.5 ft and 5.0 ft.
- 4) Crest length beyond 5.0 ft.

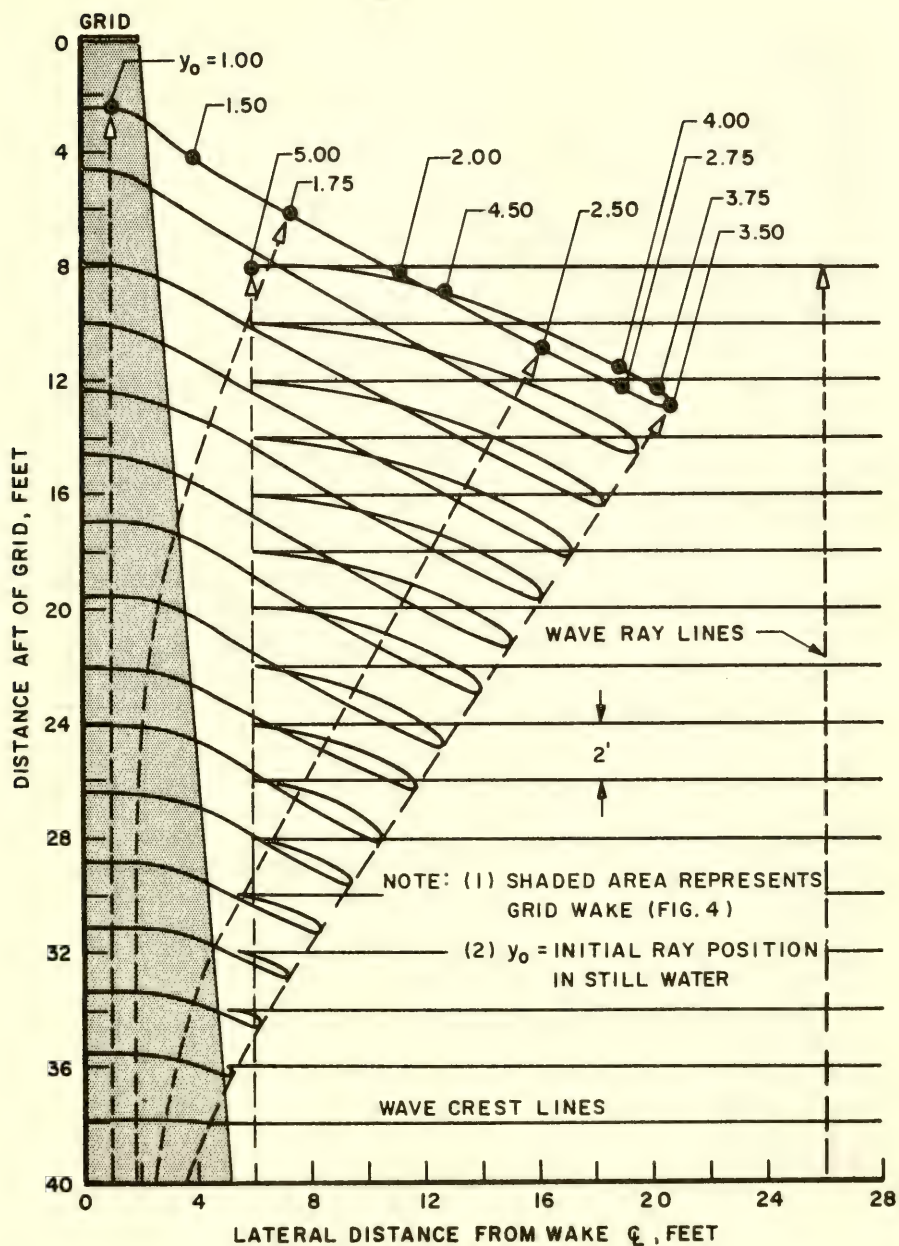


Fig. 23 Computed wave refraction diagram

$$\lambda = 2' \quad V = 1 \text{ ft/sec}$$

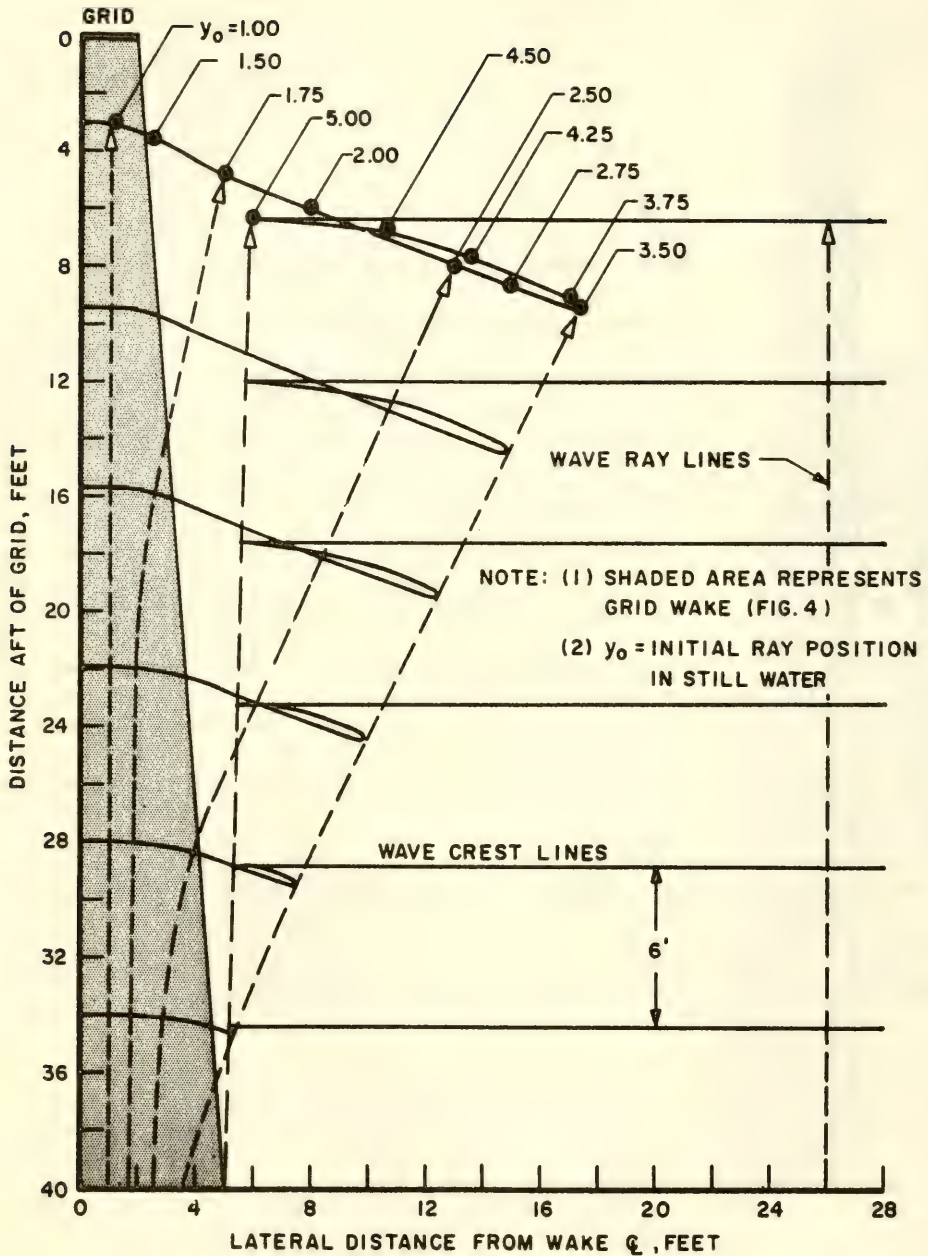


Fig. 24 Computed wave refraction diagram

$$\lambda = 6' \quad V = 1 \text{ ft/sec}$$

Crest Length Between $\frac{Q}{2}$ and 1 ft. In this region, the current field is essentially constant across any transverse section and increases slowly in the longitudinal direction. The effect on this finite wave is to increase the wave length in accordance with Eq. (8). For a mean flow of 0.30 ft/sec, the 2 ft wave length should increase by 20% while the 6 ft wave should increase by 10%. This is in reasonable agreement with the results in Figs. 23 and 24. Since the wave length increases, it is expected that the wave heights will decrease in order to maintain wave energy balance.

Phillips [1969] accounts for this wave energy balance in treating the case of long-crested waves running into a current in which the surface velocity varies only longitudinally. His results, plotted on Fig. 3.6 of his work, show that for the present conditions a wave height attenuation of approximately 15% is expected for the 2 ft wave and approximately 8% for the 6 ft wave. This is considerably less than the experimentally attained values of 80% to 90% attenuation previously discussed. Thus, the refraction procedure alone does not account for the results observed in the vicinity of the wake centerline. It will later be shown that diffraction effects applied to this length of wave crest can indeed result in large local attenuations of wave height.

Crest Length Between 1 ft and 3.5 ft. The orthogonals for this crest length diverge rapidly in a direction which causes the local wave crest to be redirected out of the wake area into the still water. This finite crest length advances in a constant direction relative to axis system at a speed and wave length equal to the incident wave. It then crosses the undeformed incident crest line at a distance 5 ft from the wake centerline. As a first order effect, it can be assumed that the wave heights decrease as the square root of the ratio of the initial wave ray separation to the separation at any subsequent position of the local crest. For the 2 ft long wave at a position 12 ft aft of the grid (28 ft into the wake), the wave height (Fig. 25) indicates that the average wave height for this local crest is approximately 30% of the incident wave height.

The deflection of this local wave crest length into the area of the incident wave could account for the irregularity observed in the wave height time histories at fixed points between 7 and 12 ft from the wake centerline.

Crest Length Between 3.5 and 5 ft. For this length of wave crest, it was seen that adjacent orthogonals converge and finally cross, resulting in a caustic curve [Pierson 1951]. On the basis of simple theory, the wave became infinitely high on the caustic which, of course, is not the case. At present, quantitative analysis of the wave height at and beyond caustics must still be developed for the case where variable currents produce wave distortions.

Crest Length Beyond 5 ft. This length of wave crest is always outside of the wake current and thus continuously progresses through still water with no alteration in wave length or speed. During its forward progress, it runs into the caustic area and deflected wave crest originating between 1 ft and 3.5 ft from the wake centerline.

Application of Analytical Results

Due to the omission of defraction effects for each wave crest segment, the refraction results discussed in this section are in themselves insufficient to represent the test results. They are nonetheless invaluable in forming the basis for providing qualitative information about the complex processes governing the interaction of a wave system with a finite current field.

Reflection Effects: The results of the refraction analysis are first used to compute wave heights along crest lines in transverse sections through the wake. The detailed results presented herein are for a transverse section 12 ft aft of the grid and for a current field extending 40 ft aft of the grid (as shown in Figs. 23 and 24). Thus, the wave has progressed 28 ft into the wake at the time of computation. The grid was 3 ft wide; had a mesh of 2.7 inches; a draft of 1.67 ft; and a tow speed of 1 ft sec. Computations were made for 6 ft and 2 ft long waves. The experimental results for these conditions have already been presented in Figs. 19 and 20.

Since the purpose of this computation is mainly to compare qualitatively the measured results with elemental analytical results, simplifying assumptions were introduced. First, it was assumed that the local wave height between adjacent orthogonals is inversely proportional to the square root of the distance between these adjacent rays. Thus,

$$\frac{H_w}{H_{w_0}} = \left(\frac{\ell_0}{\ell} \right)^{1/2} \quad (17)$$

where:

ℓ_0 = separation distance between adjacent rays in still water

ℓ = separation distance between adjacent rays on the deformed crest line

H_{w_0} = local wave height in still water

H_w = local wave height along deformed crest line

This enabled wave heights to be constructed along a wave crest from the centerline to a distance approximately 6 feet from the centerline. Beyond this point, there is a superposition of the deflected wave segment with the undisturbed length of the incident wave. In this area,

the two waves are combined in proper phase as indicated by the crest line plots in Figs. 23 and 24. The section of wave crest that develops into a caustic has not been included in this elemental construction. The results of this simple refraction analysis are plotted in Figs. 25 and 26 for the 6 ft and 2 ft wave lengths. It is seen that this procedure results in essentially unmodified crest heights just aft of the physical grid; then large reductions in wave height for areas transverse to the grid and, finally, increases in wave height in those areas where the deflected segment of the wave combines with the undeformed segment of the incident wave. The results of the refraction computations do not entirely agree with the experimental data -- particularly in the region of the grid wake where the test results show significant attenuations in wave height while the computed results show no wave height attenuation.

Considering the variation of computed wave height along the crest line (Figs. 25 and 26), it is seen that there is a large increase in wave height for positions less than and greater than approximately 6 ft from the grid centerline. At this 6 ft point, the computed wave height is a minimum. These transverse gradients cannot remain in equilibrium and thus represent a source of energy flow along the wave crest from the regions of large wave height to the point of low wave height. This is a diffraction phenomenon which exists simultaneously with refraction effects. A rigorous theoretical analysis of this problem appears to be extremely complex and is yet to be developed. For the purposes of the present study, a simplified analysis is developed which combines the results of elemental solutions of wave refraction, diffraction and superposition. Although not completely rigorous, this simplified approach is tenable and relatively easily applied.

Diffraction Effects: As normally considered, wave diffraction occurs when part of a wave is "cut off" as it moves past an obstruction such as a breakwater. The portion of the wave moving past the tip of the breakwater will be the source of a flow of energy in the direction essentially along the deformed wave crest and into the region in the lee of the structure. As explained by Wiegel, the "end" of the wave will act somewhat as a potential source and the wave in the lee of the breakwater will spread out with the amplitude decreasing exponentially along the deformed crest line. The mathematical solution of this phenomenon, which is taken from the theory of acoustic and light waves, is described by Penny and Price [1952], Johnson [1952] and Wiegel [1964]. The solutions for two basic diffraction phenomenon are presented by Wiegel: one is the case of a semi-infinite breakwater and the other is for the case of waves encountering a single gap in a very long breakwater. The solution for both cases are presented by Wiegel in the form of contour plots of equal diffraction coefficient, K , defined as the ratio of the wave height in the area affected by diffraction to the wave height in the area unaffected by diffraction. For the case of the wave passing through a single gap, the solutions are presented for various ratios of wave length to gap width.

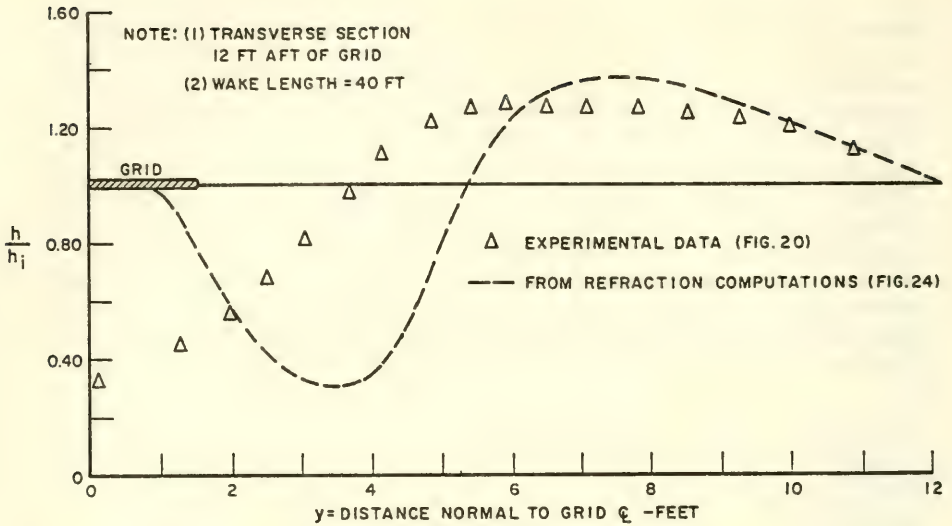


Fig. 25 Results of refraction computation versus measured crest height. $\lambda = 6'$; $H_w = 1''$; grid width = 3'; mesh = 2.7"; draft = 1.67"; $V = 1$ ft/sec.

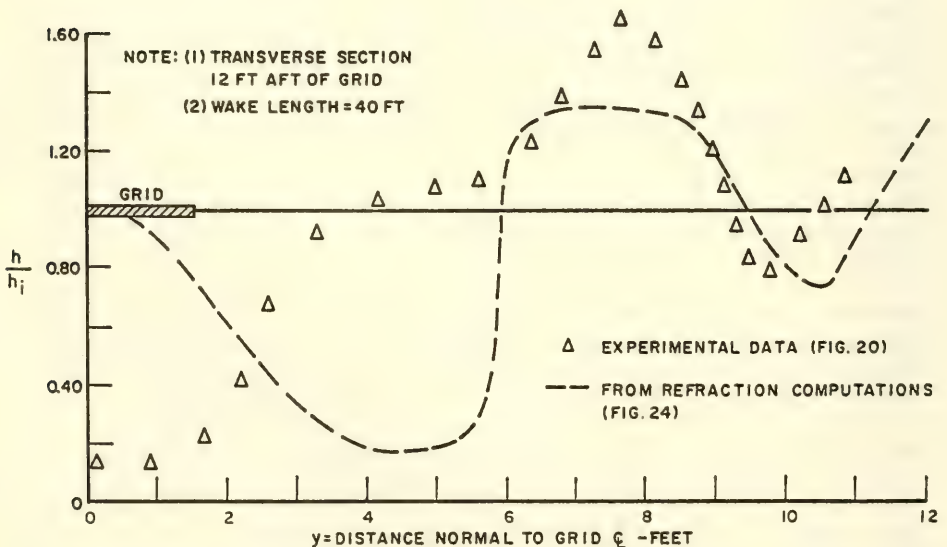


Fig. 26 Results of refraction computation versus measured crest height. $\lambda = 2'$; $H_w = 1''$; grid width = 3'; mesh = 2.7"; draft = 1.67"; $V = 1$ ft/sec.

In applying these diffraction results to the present study, it has been assumed that the refraction phenomenon previously discussed divides the wave crest into several segments which are separately diffracted as they pass through the grid wake. Specifically, the segment of the wave crest just aft of the grid is assumed to behave as though it was a section of the wave which passed through a breakwater gap equal to the grid width. The justification for this analogy follows from the refraction results given on Figs. 25 and 26 where it is shown that, for a distance of approximately one-half the grid width on either side of the grid centerline, the wave height in the wave cannot be maintained at a constant height since just outboard of this segment the refraction analysis yields a small wave height. Thus, it appears reasonable to assume that diffraction effects will be developed and that this centerline segment of the wave will reduce in amplitude and spread transversely along the crest as it proceeds into the grid wake. The diffraction coefficients will be taken to be those corresponding to a wave at a breakwater gap as given on pages 188-189 of Wiegel.

One other portion of the incident wave which appears to be modified by diffraction is that segment of the incident wave which is located 5 ft outboard of the grid centerline. From the wave refraction diagrams on Figs. 23 and 24, it is seen that wave rays and crest lines outboard of 5 ft are not influenced by the grid wake. Simple refraction considerations then result in a wave of constant amplitude along this length of the wave front. Again, this constant wave height cannot be maintained and a defraction process develops which causes a lateral spreading of the wave crest into the wake area with an attendant reduction in wave amplitude. This lateral flow of wave energy can be compared to the case of water passage past a semi-infinite breakwater, the solution for which is plotted on page 183 of Wiegel. Typical diffraction diagrams for the case of breakwater gap and semi-infinite barrier are given in Figs. 27 and 28 of this report.

The computed results for these two diffraction processes are plotted in Figs. 29 and 30 for the 6 ft and 2 ft wave lengths respectively. Again, the computations are made for transverse section approximately 28 ft into the grid wake. For the 6 ft wave, the ratio of effective "gap width" to wave length is $3/6 = 0.50$; for the 2 ft wave, the ratio is $3/2 = 1.50$. It is seen that the initial constant height wave segment between the grid centerline and 1.5 ft outboard is diffracted to approximately 0.30 of this height and is spread laterally to a distance nearly 12 ft from the grid centerline. Considering the diffraction of the entire wave segment initially 5 ft outboard of the grid centerline, it is seen that this section is spread inboard to the grid centerline with a corresponding reduction in wave height at approximately 0.30 of its initial height. It is seen that, for this wave segment, the attenuation of wave height as it spreads to the centerline is much more rapid for the 2 ft wave than for the 6 ft wave.

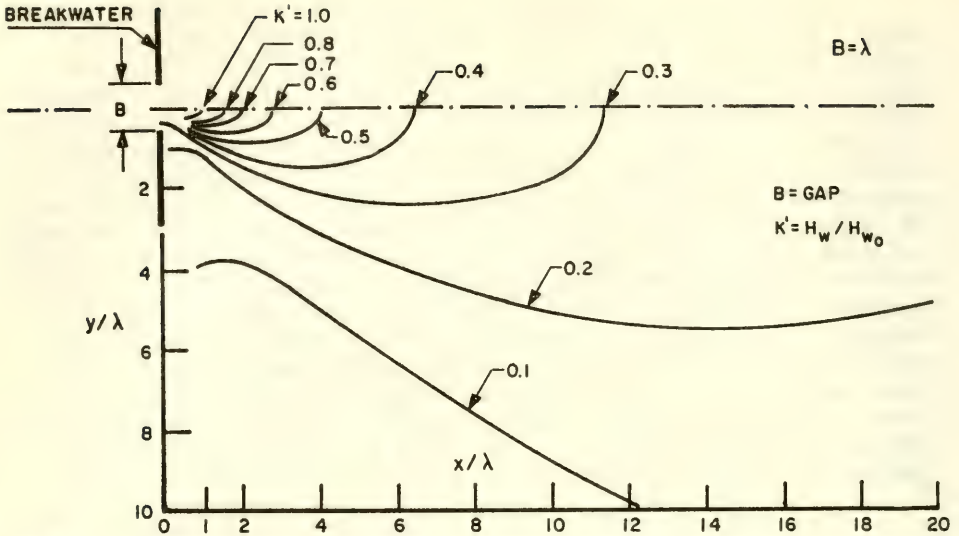


Fig. 27 Diffraction of waves at breakwater gap contours of equal defraction coefficient [Johnson 1952]

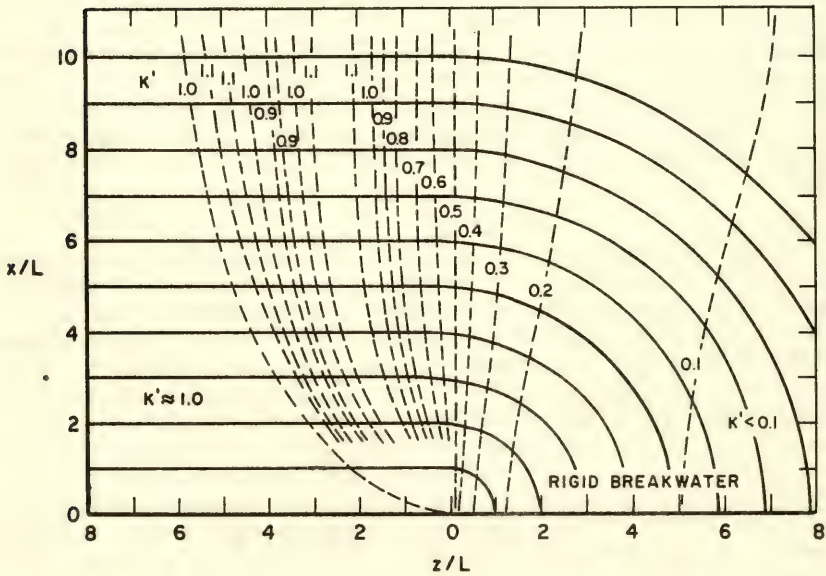


Fig. 28 Diffraction of waves passing semi-infinite breakwater [Penny and Price, 1952]

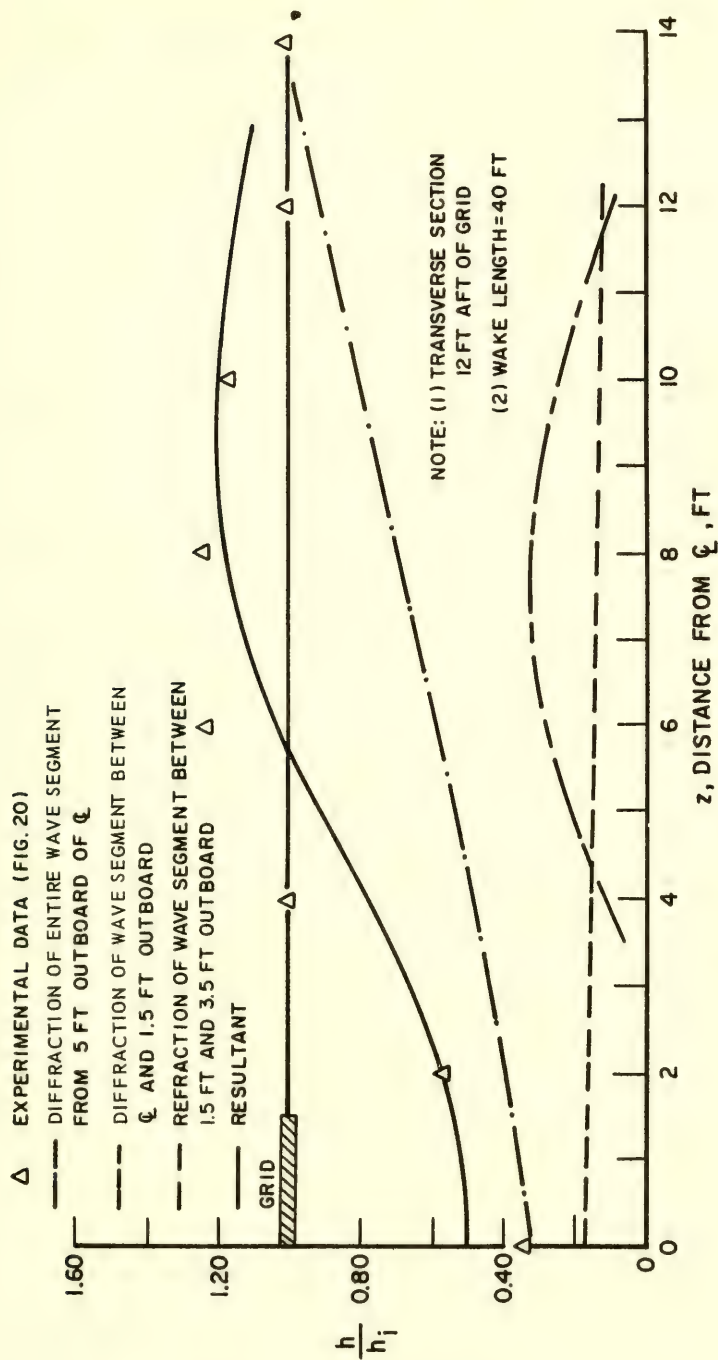


Fig. 29 Computed versus measured crest height

$\lambda = 6'$ $H_w = 1''$ grid width = 3' mesh = 2.7" draft = 1.67" $V = 1$ ft/sec

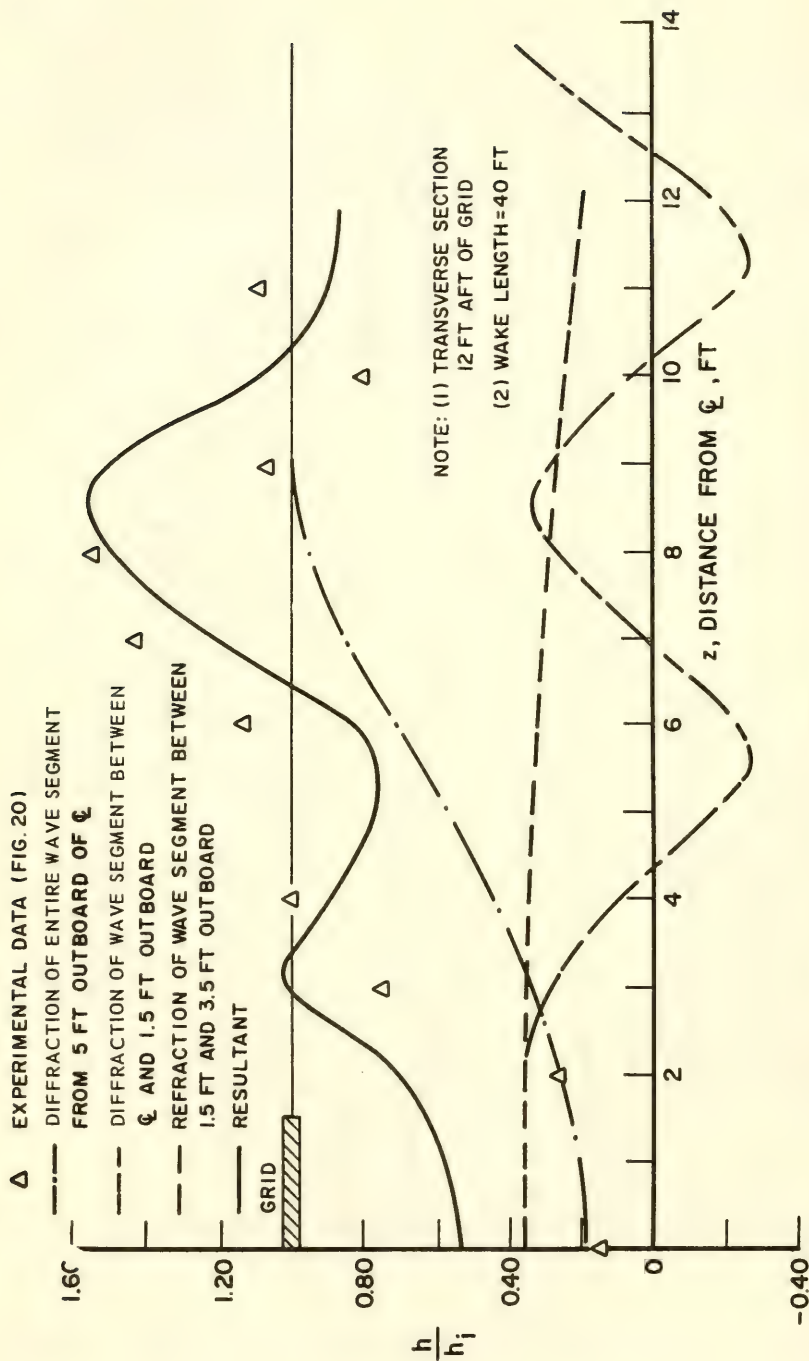


Fig. 30 Computed versus measured crest height

$\lambda = 2'$ $H_w = 1''$ grid width = 3' mesh = 2.7" draft = 1.67" $V = 1$ ft/sec

Superposition of Elemental Results

The results of the refraction and diffraction results have been superposed in order to provide an analytical estimate of the wave height distribution along a crest line as it progresses through the grid wake. The computations were carried out for a transverse section 12 ft aft of the grid for a grid wake 40 ft long. These are identical to the refraction calculations previously described. The following procedure is used in this superposition of elemental results:

a) The initial crest length between the grid centerline and 1.5 ft outboard is diffracted by the breakwater gap technique as plotted on Figs. 29 and 30.

b) The initial crest length 5 ft outboard of the grid centerline is diffracted by the technique of wave passage past a semi-infinite barrier as plotted on Figs. 29 and 30.

c) The segment of wave length initially between 1.5 ft and 3.5 ft is refracted by the orthogonal method and the wave heights are obtained by Eq. (17). The orientation (or phase) of this wave crest segment to the transverse section 12 ft aft of the grid is obtained from the computed refraction diagrams such as given in Figs. 23 and 24. The resultant wave heights for this segment are plotted on Figs. 29 and 30.

d) The segment of the wave crest between 3.5 ft and 5.0 ft outboard has been neglected in this simplified procedure since it develops into a caustic line.

e) The results of (a), (b), (c) and (d) are superposed to obtain the final wave height distribution.

The results of the above procedure are presented in Figs. 29 and 30 for the 6 ft and 2 ft wave respectively and compared with the experimental data. It is seen that agreement between computed and measured results is qualitatively acceptable for the 2 ft wave length and is good for the 6 ft wave length. It appears then that the physical processes responsible for the observed deformation of waves progressing into a finite current field have been established. It is strongly recommended that further studies of this problem be directed towards the development of a unified, rigorous theory which can be used to quantify this interesting wave-current interaction phenomenon.

One-Dimensional Results

No similar detailed analysis has been made of the one-dimensional results previously described. It does appear, however, that the transverse gradient in the longitudinal wake velocity existing at the outer edges produces a local wave refraction. This refracted wave segment must then be reflected from the tank walls and progress across the wake, running into similarly refracted wave segments from the opposite wall. These continuously crossing wave

segments passing over the incident wave may develop distortions in wave height time histories such as observed in the experiments. The wave height irregularity at any point in the wake thus precludes a reliable evaluation of the dissipative effects of the grid-produced turbulence since only two wave probes were used in this study.

IV. RECOMMENDATIONS FOR FURTHER STUDIES

The original objective of the present study was to investigate experimentally the interaction between gravity waves and turbulence fields generated in the wake of a towed grid. Unfortunately, the longitudinal mean flow velocity gradients in the wake had a dominating effect on wave deformation and thus precluded a direct evaluation of turbulence effects alone. Although, in a realistic ocean environment, turbulence fields can be generated by, and exist simultaneously with, velocity gradients in ocean currents, it is nevertheless of fundamental scientific interest to study separately the effects of turbulence fields with no mean flow interacting with gravity waves. The results of such an elemental turbulence study can then be combined with velocity gradients to represent wave passage through realistic ocean currents. Also, the results can be used alone to study the wave interaction with isolated turbulence fields such as exist, for example, in regions of "splash" turbulence developed by breaking waves.

It is thus recommended that the present study be continued but with an experimental apparatus designated to produce localized turbulence areas with no mean flow. The experimental procedure should be capable of generating turbulence fields of controlled eddy size, turbulence intensities, depth of penetration below the free surface, and length and width of turbulence patch. It is further recommended that the turbulence generator be capable of developing vortices with either a horizontal axis or a vertical axis or a combination of both.

The control of the vortex direction will be important in the study of the eddy viscosity interaction in which energy is transferred from the wave motion to the turbulence. As discussed by Phillips [1959], the passage of the wave results in straining the elements of the fluid near the surface in a manner periodic in time. The mean strain per cycle of the incident wave is of second order, namely $(\alpha/\lambda)^2$, where α is the amplitude and λ the wave length of the incident wave. The wave motion thus provides a mechanism for stretching the vortex lines that operates in addition to the stretching inherent in the turbulence itself, and so tends to increase $\overline{\omega}^2$, the mean square vorticity associated with the turbulence. It is expected that this possible mechanism for transfer of wave energy will be for waves interacting with vertical vortex fields. In this case, the vertical velocity gradient in the long-crested wave stretches the vertical vortices in the turbulence field, but should not effect the

horizontal vortices. An experimental setup designed to control the direction of the turbulent vortices can be most instructive in understanding this dissipative process.

The experimental procedure proposed to develop controlled turbulence fields with no mean flow is to sinusoidally oscillate a series of grids in a physically confined area in still water. The barrier confining the turbulent field can be constructed of four thin, vertical plates housing a rectangular box penetrating through the water surface to a depth below the lower ends of the oscillating grids. After oscillating the grids, the rectangular barrier can be lifted above the water surface just as the waves approach so that there is an interaction between waves and turbulence. The dimensions of this rectangular container can be varied to represent various sizes of turbulence areas. The use of an oscillating grid in a confined area has been investigated by Murray [1968] in his laboratory studies of horizontal turbulent diffusion. In his work, the grids which filled a 50 cm wide channel were composed of several rods 1 cm in diameter and 5 cm apart. The array consisted of 3 grids, each 30 cm apart, and had a stroke of 40 cm. The following conclusions concerning the generated turbulence are described by Murray.

1. There is no mean flow within the confined area of turbulence generation. This is precisely the objective of the proposed experimental procedure.
2. The oscillating array of grids produces turbulence fields which are essentially homogeneous and stationary.
3. The turbulent velocity distributions are Gaussian.
4. Taylor's statistical theory of turbulence effectively describes the variance, scale time, and scale length of the generated turbulence field.

In summary then, the proposed turbulence stimulation technique appears to be adequate for generating controlled and mathematically definable localized turbulence fields.

The experimental procedure will consist in mounting the turbulence generator over a section of the 75 ft square tank away from the side walls. The grid array would be oscillated to generate the turbulence field and mechanically generated gravity waves would approach this field. Just prior to the waves reaching the area of turbulence, the rectangular barrier surrounding the oscillating grids would be lifted clear of the water surface so that the waves would interact only with the turbulence. It is expected that the lateral diffusion of the turbulence area will be very slow compared to group velocity of the gravity waves so that, at least for the passage of several wave lengths, the turbulence properties may be assumed to be stationary.

Parametric variations in this study will include:

1. length and width dimensions of turbulence area;
2. depth of turbulence area below water surface;
3. spacing of vertical oscillating rods alone to investigate the interaction between vertically oriented vortices and gravity waves;
4. spacing of horizontal oscillating rods to investigate the interaction between horizontally oriented vortices and gravity waves;
5. combination of (3) and (4) to construct a grid having a rectangular mesh of varying dimensions to provide for various scales of two-dimensional turbulence;
6. vary speed of grid oscillation to obtain various levels of turbulence intensity;
7. vary length and height of gravity waves.

Measurements should be made of the wave-height time history at various locations both inside and outside of the turbulence patch. A spectral analysis of these wave height time histories should be carried out to determine the extent of wave scattering due to the presence of turbulence. Further, a hot film probe should be slowly towed through the turbulence area to characterize its statistical properties with and without the presence of passing waves.

It is believed that the suggested experimental procedure is practical and can provide data necessary for basic studies of gravity waves interacting with local turbulence areas.

V. CONCLUSIONS

An experimental study was undertaken to investigate the interaction between deep water gravity waves progressing into a turbulent flow field generated by a finite width grid moving in the wave direction in a large towing tank. It was found that the lateral gradient of the mean longitudinal flow in the wake had predominant influence on wave deformation and precluded an evaluation of the direct effect of turbulence.

The presence of the velocity gradients resulted in combined refraction, diffraction and interference between finite and adjacent segments of the incident crest line. Their combined effects were to reduce the wave heights in the wake area to approximately 10% of their original value. The wave heights outside of the wake were increased to values 75% larger than their original value.

An elementary analysis was performed of the refraction of waves entering a finite current field. A combination of these results with simple diffraction considerations qualitatively reproduced the measured crest line deformations. A unified theoretical study of this complex problem is required to provide quantitative results.

Recommendations for further investigation of wave interaction with turbulence field with no mean flow are made.

It appears that the present results may be useful in developing full-scale procedures for local "quieting" of the deep water waves behind support ship for retrieving or launching submersibles or landing craft in a following sea.

ACKNOWLEDGMENTS

The author wishes to express his appreciation to Dr. R. Hires of Stevens Institute of Technology for valuable discussions and technical advice rendered during the course of this study. He is also indebted to Professors W. J. Pierson, Jr. and G. Neumann of New York University for their continued encouragement and helpful suggestions throughout the study. Professor Eric S. Posmentier of New York University is thanked for his thorough review of the dissertation.

REFERENCES

- Bryson, A. E., Jr. and Ho, Hu-Chi, Applied Optimal Control Theory, Blaisdell Publishing Co., 1969.
- Johnson, J. W., "Generalized wave refraction diagrams," Proc. Second Conf. Coastal Eng., Berkeley, Calif., 1952.
- Johnson, J. W., "Generalized wave diffraction diagrams," Proc. Second Conf. Coastal Eng., Berkeley, Calif., the Engineering Foundation on Wave Research, pp. 6-23, 1952.
- Murray, S. P., "Simulation of horizontal turbulent diffusion of particles under waves," Coastal Engineering Proceedings of Eleventh Conference, London, England, Vol. 1, pp. 446-466, Sept. 1968.
- Penny, W. G. and Price, A. T., "The diffraction theory of sea waves by breakwaters and the shelter afforded by breakwaters," Phil. Trans. Roy. Soc. (London) Sec. A, 244, pp. 236-53, March 1952.

Phillips, O. M., "The scattering of gravity waves by turbulence,"
J. Fluid Mech., Vol. 5, part 2, pp. 177-192, 1959.

Phillips, O. M., The Dynamics of the Upper Ocean, Cambridge
University Press.

Pierson, W. J., Jr., "The interpretation of crossed orthogonals in
wave refraction problems," U. S. Army, Corps of Engineers,
Beach Erosion Board, Tech. Report No. 21, January 1951.

Stewart, R. W. and Grant, H. L., "Determination of the rate of
dissipation of turbulent energy near the sea surface in the
presence of waves," J. Geophysical Res., Vol. 67, No. 8,
pp. 3177-3180.

Taylor, G. I., Statistical Theory of Turbulence, Parts I-IV,
Proc. Royal Society A, 151, pp. 421-428.

Wiegel, R. L., Oceanographical Engineering, Prentice Hall, Inc.,
1964.

* * * * *

DISCUSSION

Dr. N. Hogben

*National Physical Laboratory, Ship Division
Feltham, Middlesex, England*

Dr. Savitsky has undertaken a very interesting investigation of the effect of turbulence on waves in an oceanographic context. His main finding is that waves can be dramatically attenuated by turbulence from travelling grids. He explains this in terms of refraction and diffraction and comments on the potential use for quieting sea waves.

Whilst listening to his presentation it occurred to me that his findings may also have an important bearing on the understanding of wavemaking by ships. It is a common experience that the wave system originating from the stern region of a ship tends to have much smaller amplitudes than would be predicted from the usual theories. I would be glad if Dr. Savitsky could comment on whether this suppression of wavemaking by ship sterns may be at least partly explained in terms of a refraction and diffraction analysis such as he has described in the paper, applied to the interaction between the vorticity and turbulence in the boundary layer and wake and the stern wave system.

* * * * *

REPLY TO DISCUSSION

Daniel Savitsky
Stevens Institute of Technology
Hoboken, New Jersey

It may be possible for ship wakes to locally attenuate the wave generated by the afterbody. If the mechanism described in the paper is applicable, it would necessarily require that wave amplitudes be larger at some distance transverse to the ship wake. This, of course, follows from considerations of preserving wave energy. Much further study of afterbody generated waves would be necessary to determine the association of ship-wave attenuation with the mechanism described in the present paper.

* * * * *

CHARACTERISTICS OF SHIP BOUNDARY LAYERS

L. Landweber
University of Iowa
Iowa City, Iowa

I. INTRODUCTION

When I accepted the invitation to lecture on ship boundary layers, my original plan was threefold: a) to review three-dimensional boundary-layer theory, b) to discuss the few available applications of the theory to ship forms, and c) to present certain unpublished results on ship boundary layers that have been reported in several theses at the University of Iowa. In the course of attempting to "catch-up" on the literature on three-dimensional boundary layers, so that I could pretend to be an authority on the subject, I encountered so many excellent review articles, that it became apparent that a review-of-reviews was hardly likely to match the immortality achieved in its category by the "song-of-songs." Rather it seemed to be more useful and interesting to examine the validity and applicability to ship forms of the assumptions of existing methods for computing three-dimensional boundary layers, and to suggest and partly to implement certain approaches which appear to be better suited to the ship problem.

Some of the common assumptions of three-dimensional boundary-layer theory are the following:

1. Assumption of small cross-flow -- that the direction of flow within the boundary layer deviates by only a small angle from the direction of the streamline at the outer edge of the boundary layer.
2. Assumption of methods of calculating two-dimensional boundary layers for determining the velocity component parallel to the outer streamline, even when the small cross-flow assumption is avoided.
3. The assumption of monotonic cross flow -- that as the wall is approached from the outer streamline, and angle of deviation of the boundary-layer streamlines increases monotonically up to a certain value at a small distance from the wall, beyond which it

remains nearly constant.

4. The assumption that three-dimensional boundary-layer problems are best treated with equations in streamline coordinates.

A stimulating article by Lighthill [1] on the fundamental significance of vorticity in a boundary layer initiated the development of a proposed method for treating ship boundary-layer problems. This will be presented in two sections; a first in which the vortex sheet on the ship hull, which generates the irrotational flow about it, is determined; a second in which the vorticity equations for a three-dimensional boundary layer, in terms of a triply orthogonal coordinate system, are derived. The significance of the first part is that it furnishes the initial values for the second.

So there will be no "review"; but it still seems desirable to touch upon the ship boundary-layer treatments of Lin and Hall [2], Webster and Huang [3], and Uberoi [4], and the contributions in the theses of Pavamani [5], Chow [6], and Tzou [7].

II. NATURE OF THE SHIP PROBLEM

In comparison with other three-dimensional boundary-layer problems, that for the ship is much more complex because of the presence of a free surface at which the body is moving partly immersed. Some ship boundary-layer problems will now be described.

1. The first step in a boundary-layer calculation, the determination of the irrotational flow outside the boundary layer (the outer flow) is a difficult problem. Solutions employing linearized free-surface boundary conditions and thin-ship theory furnish inadequate approximations. The development of more accurate methods of calculating the irrotational flow about ship forms is a current research problem [8].

2. At Froude numbers sufficiently low so that the free surface may be treated as a rigid plane, (zero-Froude-number case), the three-dimensional flow about the double model, obtained by reflecting the immersed portion in this plane, is of considerable interest. Methods of computing the irrotational flow for this case are available [8, 9]. Calculation of the viscous drag for this case, and its ratio to the frictional resistance of a flat plate of the same length, wetted area and Reynolds number, would yield the so-called form factor of the hull form which is required in one method of predicting ship resistance on the basis of model tests [4].

3. The three-dimensional boundary layer is very sensitive to the shape of the bow. The nature of the boundary layer near the forefoot, which determines whether or not bilge vortices will be generated, can also be studied at zero Froude number. Bows

frequently are designed with zones of reversing curvature, at which boundary-layer profiles with S-shaped cross-flows may occur.

4. At higher Froude numbers the boundary layer will lie over a hull surface area which depends upon the equilibrium trim and draft and the surface-wave profile along the hull at that Froude number. The curvature of the outer streamlines at the free surface strongly affects the cross-flow components of the boundary-layer velocity profiles [6,7], an effect which is completely ignored in boundary-layer studies at zero Froude number.

5. Near the stern the boundary layer thickness becomes of the same order of magnitude as the radii of curvature, and the methods of thin boundary-layer theory cannot be used without modification. A detailed study of boundary-layer characteristics in this region is desirable in connection with the development of improved rational methods of computing the viscous drag, and the design of stern appendages from the point of view of strength and cavitation. Of course, if such a calculation could be extended into the near wake, it would be a great boon to the propeller designer.

6. The draft and trim of a ship may vary greatly, depending upon its cargo. It operates at various speeds or Froude numbers, and if model tests are involved, the effect of the scale or Reynolds number would be of interest. Since the flow pattern would vary with each of these four parameters, one may wish to calculate the boundary layer for many combinations of parametric values.

III. SHIP BOUNDARY-LAYER CALCULATIONS

Ship boundary layers at zero Froude number have been calculated by Uberoi [4]. To determine the outer irrotational flow he introduced a distribution of n discrete sources lying within but close to the hull and determined their strengths by solving simultaneously n linear equations, obtained by satisfying the boundary condition on the hull at n points. This source distribution was then used to calculate the streamlines.

For calculating the boundary layer, the flow was treated as two-dimensional along each streamline, and the momentum thickness and shape parameter determined by an available two-dimensional semi-empirical procedure [10]. A better approximation could have been obtained with little additional effort had one of the available three-dimensional boundary-layer procedures assuming small cross-flow been used [11], since these would have taken into account the important three-dimensional property of the spreading of streamlines. Nevertheless, since the spreading of the streamlines is small except near the bow and stern, the results should furnish a useful approximation.

Finally, to determine the viscous drag, an empirical formula relating the shape parameter H_t with the outer velocity U_t at the tail (designated by the subscript t) and the velocity of the uniform stream at infinity, U_∞ ,

$$\frac{U_\infty}{U_t} = e^{H_t - 1}$$

is assumed, as well as that the equations of thin boundary-layer theory may be integrated to the very tail, a dubious assumption. Since this empirical relation is unlikely to be universally valid, the foregoing procedure, which is that usually employed to compute viscous drag, emphasizes the need for additional research on the characteristics of the thick boundary layer near the stern.

An approximate method for computing the boundary layer on a ship form at a nonzero Froude number has been developed and applied by Webster and Huang [3]. Guilloton's theory of ship wave resistance [12] as presented by Korvin-Kroukovsky [13] furnishes tables from which the outer flow can be determined along three streamlines on the hull. The boundary layer along these streamlines is then computed by a small cross-flow method employing streamline coordinates, due to Cooke [14]. This method has been applied to two Series-60 forms of 0.60 and 0.80 block coefficients, over a range of Froude and Reynolds numbers. Although the assumption of small cross-flow is basic to the method, it was nevertheless applied to estimate the locations of separation points on these streamlines on the basis of Cooke's criterion that separation occurs when the cross-flow is 90° .

Smith's comparative study of five different methods of computing a turbulent three-dimensional boundary [11] indicates that a method which does not assume small cross-flow, and which employs a three-dimensional extension of Head's entrainment hypothesis [15] for the variation of the streamwise shape parameter gives better predictions of the cross-flow than methods which assume small cross-flow, and a constant value of the shape parameter. All five methods, however, yielded values of the momentum thickness in poor agreement with experimental results. Smith conjectures that this failure is probably due to the adoption of empirical relations for the shear stress from two-dimensional theory.

These results of Smith indicate that the Webster-Huang procedure for calculating separation points could be improved considerably by the adoption of the best of the five methods. None of the methods, however, can be used reliably to calculate the viscous drag.

Lin and Hall [2] also employ streamline coordinates and the small cross-flow assumption in computing the boundary layer on a ship form. As in the method of Cooke [14], the momentum integral

equation in the streamwise direction becomes a differential equation for momentum thickness after assuming a power law of variation for the streamwise velocity profile and a semi-empirical relation from two-dimensional boundary-layer theory between the shear-stress coefficient and the momentum-thickness Reynolds number. An additional assumption, that the cross-flow angle varies as the square of the distance from the outer border of the boundary layer, is introduced to determine the cross-flow. Finally a new auxiliary relation between the shape parameter and the momentum thickness is derived by combining the streamwise momentum and energy integral equations and introducing one more assumption, another semi-empirical relation between the dissipation coefficient and the momentum thickness Reynolds number, also borrowed from two-dimensional theory.

Each of the five assumptions of the method used by Lin and Hall is of doubtful validity for a ship boundary layer. Boundary-layer data on ship forms, which are discussed in subsequent sections, indicate that the cross-flow is not everywhere small, that the two-dimensional relations are not generally valid in a three-dimensional boundary layer, that a power law is not a good approximation for the streamwise velocity profiles, and that the cross-flow angle cannot obey a quadratic relation.

Finally, a paper due to Gadd [16] , which the author has not yet seen, should be mentioned. He determines the outer potential flow, taking wavemaking into account, and applies this to calculate the boundary layer on an equivalent body of revolution, neglecting cross-flow. In referring to this paper, Shearer and Steel [17] remark that "Gadd has recently applied a three-dimensional boundary-layer theory to the pressure distributions obtained using the Hess and Smith method, taking account of the free surface, to give friction distributions which agree very well with measured values. Comparison of this theory with some of the experimental values detailed herein (in [17]) are given in ... " (in [16]).

IV. BOUNDARY-LAYER DATA FOR SHIP FORMS

It has been indicated that the relations for the shear stress used in calculating two-dimensional boundary layers may not be valid for a three-dimensional boundary layer. In order to investigate the applicability to ship forms of these and other empirical relations that have been proposed, it would be desirable to have a set of data, including pressure distributions, mean velocity profiles for both the streamwise and cross-flow directions, and shear stresses, for some shiplike forms.

Full scale boundary-layer measurements on a 210-foot ship, the USS Timmerman, have been reported by Sayre and Duerr [18]. Mean velocity profiles are given for four points along the hull, at speeds of 5, 10, 15 and 20 knots. The measured boundary-layer

thicknesses are in poor agreement with values computed from a formula for two-dimensional flow on a smooth flat plate. Although no other analysis was attempted, these data offer an opportunity to test procedures for computing a three-dimensional boundary layer, e.g., by the suggested modification of the method of Webster and Huang.

Some boundary-layer measurements on a 70-meter research vessel "Meteor" [19] and a 1:30-scale double model in a wind tunnel [20] have been reported by Wieghardt. The full-scale measurements, taken at a point 40 per cent of the draft from the free surface and 40 meters from the bow, yielded a value of the shear stress approximately equal to that for a flat plate, but a definitely lower value of the momentum thickness. The results for the boundary layer at the corresponding point on the model were consistent with the full scale measurements in spite of the neglect of free surface effects in the wind-tunnel tests. Several phenomena peculiar to ship boundary layers were displayed by the model study. One of these is the unusual shape of the boundary layer (vorticity-containing region) around the girth of a fore-ship section, showing bumps at the sides and a great increase in thickness at the keel, attributed by Wieghardt to secondary flow (i.e., large cross flow) initiated near the bow. The shear-stress coefficient at midship section was nearly constant at about $C_f = 0.0035$, but decreased to 0.0025 as the keel was approached, and then increased rapidly to 0.0039 at the keel. The momentum thickness θ varied even more, from a mean value of $\theta/x = 0.0013$ down the sides, increasing to a maximum of 0.0028 as the keel is approached, then falling to 0.0018 at the keel. These results indicate that, at least near the keel, the two-dimensional shear stress formulas frequently assumed in computing three-dimensional boundary layers, are very inaccurate. Wieghardt concludes that "much more experimental knowledge about the flow in ship boundary layers, including secondary flows and trailing vortices is needed for semi-empirical calculation methods for such three-dimensional boundary layers ..."

A project to obtain full-scale measurement of ship boundary layers is under way in Japan, and some results of this work were reported at the 12th International Towing Tank Conference in Rome [21]. The unusual shapes of certain velocity profiles astern of the parallel middle body were attributed to the presence of vortices separated from the hull. Clearly these profiles could not be represented by a power law. On one ship an array of five longitudinal vortices was observed in the wake, of which one pair originated at the bow, another pair was shed astern of amidships, and the fifth was due to the propeller.

A recent paper by Shearer and Steel [17] is noteworthy in that it presents the results of shear-stress and pressure surveys on two ship models at a particular Froude number. The effect of the Froude number on the shear-stress coefficient C_f was found to be small except at the uppermost measurement locations along a waterline at 25 per cent of the draft from the free surface, for which the

curve of C_f against longitudinal distance along the waterline undulated 180° out of phase with the wave profile. The most interesting feature of the C_f curves for various waterlines is their large variation along the waterline even at depths where the free-surface effect should be negligible, in agreement with Wieghardt's results. Furthermore, the variation was found to be sensitive to the shape of the bow. This again indicates that one is not free to assume a simple formula for the shear stress in calculating a three-dimensional boundary layer.

The boundary layer on an ellipsoid with axis ratios 20:4:1 and the incident flow in the direction of the longest axis was investigated in a wind tunnel by Pavamani [5]. He measured the distribution of both pressure and shear stress, the velocity profiles, as well as the flow directions in the boundary layer. With the equipment used it was not possible to probe the boundary layer in the regions of largest curvature. It was found however that the shear stress in a transverse section increased in the direction of increasing curvature.

Two shear-stress formulas that are used in computing three-dimensional turbulent boundary layers are one due to Young,

$$C_\tau = \frac{2\tau_0}{\rho U^2} = 0.0176 \left(\frac{U\theta}{\nu} \right)^{-0.2}$$

and another due to Ludwig-Tillmann,

$$C_\tau = 0.246 \times 10^{-0.678H} \left(\frac{U\theta}{\nu} \right)^{-0.268}.$$

Here τ_0 is the shear stress at the wall, ρ is the mass density of the fluid, U is the velocity at the outer edge of the boundary layer, θ is the boundary-layer momentum thickness computed for the streamwise component of the velocity, ν is the kinematic viscosity, and H is the shape parameter of the boundary-layer velocity profile. Although not done by Pavamani, his data can be used to compare the predictions by these formulas with his shear-stress measurements by Preston's method. Comparisons at two points in the midsection, one on the centerline and the other in the vicinity of the edge, and given in the following table.

COMPARISON OF MEASURED AND COMPUTED SHEAR STRESS
AT MIDSECTION OF 20:4:1 ELLIPSOID ($R_x = 10^6$)

	Measured	Young	Ludwig-Tillmann
at centerline	0.00330	0.00380	0.00283
near the edge	0.00466	0.00444	0.00318

These results for only two points already indicate that neither of the above formulas gives good agreement, although Young's seems to be preferable. It is planned to continue the analysis of Pavamani's data with the aims of representing his shear-stress data by an alternative formula, and to compare his measurements with computed values of the boundary-layer characteristics.

V. SHIP BOUNDARY-LAYER PHENOMENA

At a ship's bow certain streamlines of the outer flow pass downwards along a side, turn around the bilge, and continue along the underside of the hull. Because of the large curvature at the bilges, the cross-flow angle in the boundary layer may become large and the resulting secondary flow has been observed to roll-up into a pair of so-called bilge vortices [22]. Clearly the small cross-flow assumption is not suitable for treating this phenomenon.

It has been observed that these bilge vortices can be eliminated by attaching a large bulb to the bow [23]. A possible explanation of this effect is that the curvature reversals as an outer streamline passes from the bulb to the bow, and then around a bilge result in an S-shaped velocity profile, i.e., one in which the sign of the cross-flow angle changes in passing from the outer limit of the boundary layer to the wall. In any case, since bows are frequently designed so that streamlines would undergo changes in the sign of the curvature, S-shaped velocity profiles would occur, so that the assumption of monotonically varying cross-flow angle, and in particular its frequently assumed quadratic variation, would be improper.

The surface wave profile along the hull affects the boundary layer in two ways, as has been shown by Chow [6]. Climbing from a wave trough to a crest is equivalent to passing through a region of adverse pressure gradient. If the free-surface slope is large enough and continues long enough, separation will ensue near the free surface. Secondly, the curvature at a surface-wave crest along the hull tends to generate a secondary flow. Chow [6] has attributed a second zone of separation at some distance beneath the free surface to this phenomenon.

The conjectured mechanism of the effect of a surface wave on a boundary layer was confirmed by Tzou [7]. He simulated the free surface by a sinusoidal ceiling in a wind tunnel, and observed and photographed the flow directions in the boundary layer of a vertical ogival strut, as indicated by an array of fine threads supported at various distances from the wall. He also verified the effect by solving the Navier-Stokes equations and the equation of continuity numerically, by a combination of a finite-difference method together with the Blasius solution for a flat plate, for a simplified model of his experiment. These results indicate once again the unsuitability of the small cross-flow assumption for ship boundary layers.

VI. THE COORDINATE SYSTEM

A set of mutually orthogonal lines on a surface S can be selected in infinitely many ways. Such a net, together with the distance along the normal to S form a system of space coordinates which, in general, are triply orthogonal only on S . Although a non-orthogonal system of space coordinates is usually an awkward choice in formulating the Navier-Stokes equations, when these equations are simplified in accordance with the usual assumptions of thin boundary-layer theory, Squire [24] has shown that the boundary-layer equations are identical in form with that for a fully orthogonal system.

When the third coordinate is the distance ζ along the normal to S , the surfaces $\zeta = \text{const.}$ are, for obvious reasons, said to be parallel to S . It is shown in texts on differential geometry that the lines of principal curvature, and only these lines, have the property that the surface normals along them generate developable surfaces $\zeta = \text{const.}$ and $\eta = \text{const.}$, and that these, together with the parallel surfaces $\zeta = \text{const.}$, form a mutually orthogonal family. For this reason Howarth [25] and Landweber [26] employed the lines of principal curvature as surface coordinates in formulating the equations of motion. Nevertheless, according to Crabtree, *et al.*, [27], "this is an undesirable restriction," a feeling that seems to be shared by most of the contributors to the subject of three-dimensional boundary layers. Preferred is the streamline-coordinate system, although geodesics and rectangular coordinates have also been used. Only Howarth [28] has adopted the lines of principal curvature for the coordinate system in his treatment of the three-dimensional boundary layer near a stagnation point.

There are two good reasons for using streamline coordinates. One is that, in the cases to which they have been applied, the inviscid-flow streamlines could be readily obtained; the other is that practical, approximate methods of solving the boundary-layer equations, employing techniques developed for two-dimensional boundary layers, are available for the equations in streamline coordinates. The simplest of these methods are based on the assumption of small cross-flow in the boundary layer. According to Smith [11], however, who applied five of these methods to compute the boundary layer on a yawed wing, none of these was found to be completely satisfactory, as has already been indicated.

For the case of present interest, the boundary layer on a ship form, the first of the aforementioned reasons does not apply. Calculation of the velocity distribution and the streamlines on a ship form at the particular Froude number is a task of the same order of difficulty as that of solving the three-dimensional boundary-layer equations. For the zero-Froude-number case, methods are available for computing the potential flow [8,9]; at nonzero Froude numbers an approximate method due to Guilloton [12,13] furnishes tables for the calculation of three streamlines along a ship hull.

Another consideration is that the streamline pattern on a ship form is a function of four parameters, the Froude number, the Reynolds number, the trim angle and the draft-length ratio. Thus, if streamline coordinate were to be used, it would be necessary to calculate a great many coordinate systems. It appears to be more practical to select a unique coordinate system which depends only upon the geometry of hull and is independent of the above four parameters.

If it sufficed to study thin boundary layers, there would be a free choice of orthogonal surface coordinates on the hull surface. But the boundary layer near the stern cannot be considered thin, and a continuation of the boundary-layer calculations into this region could not be undertaken with the equations for an orthogonal coordinate system unless the surface coordinates had been selected to be lines of principal curvature.

VII. DETERMINATION OF LINES OF PRINCIPAL CURVATURE

First suppose that the equation of the surface S is given by

$$F(x, y, z) = 0 \quad (1)$$

where (x, y, z) are the rectangular Cartesian coordinates of a point P on S . Let $\overline{ds} = \overline{i} dx + \overline{j} dy + \overline{k} dz$ denote a vector element of arc along one of the lines of principal curvature, where $\overline{i}, \overline{j}, \overline{k}$ are unit vectors along the x, y, z axes. Then

$$\text{grad } F = \nabla F = \overline{i} F_x + \overline{j} F_y + \overline{k} F_z \quad (2)$$

is a vector along the normal at P and

$$d\nabla F = \overline{ds} \cdot \nabla \nabla F \quad (3)$$

is the change in this vector along the normal in moving an increment \overline{ds} from P to P' along a line of principal curvature. It can be shown [29] that the normals to S at P and P' intersect if and only if \overline{ds} is an element of arc of a line of principal curvature. This implies that the vectors

$$\overline{ds}, \quad \nabla F \quad \text{and} \quad \overline{ds} \cdot \nabla \nabla F$$

are coplanar, and hence that

$$\overline{ds} \cdot \nabla F \times (\overline{ds} \cdot \nabla \nabla F) = 0. \quad (4)$$

Also the condition that \overline{ds} be normal to ∇F is

$$\overline{ds} \cdot \nabla F = 0 \quad (5)$$

Equations (4) and (5) are the differential equations of the lines of principal curvature.

In terms of their components, (5) becomes

$$F_x dx + F_y dy + F_z dz = 0 \quad (6)$$

and from (4) we obtain

$$\begin{aligned} & (F_y F_{xz} - F_z F_{xy})(dx)^2 + (F_z F_{xy} - F_x F_{yz})(dy)^2 + (F_x F_{yz} - F_y F_{xz})(dz)^2 \\ & + (F_x F_{yy} - F_x F_{zz} + F_z F_{xz} - F_y F_{xy}) dy dz \\ & + (F_y F_{zz} - F_y F_{xx} + F_x F_{xy} - F_z F_{yz}) dz dx \\ & + (F_z F_{xx} - F_z F_{yy} + F_y F_{yz} - F_x F_{xz}) dx dy = 0. \end{aligned} \quad (7)$$

Because of the quadratic nature of (7), the simultaneous solution of (6) and (7) yields a pair of solutions for (dx, dy, dz) , which can be shown to be orthogonal. Thus, from an initial point P , one can calculate the lines of principal curvature in step-by-step fashion.

If the equation of the surface is given in the form

$$y = f(x, z) \quad (8)$$

where x is directed from bow to stern, z is positive upwards, and the plane $y = 0$ is the vertical plane of symmetry, then (6) and (7) can be combined into the differential equation of the projection of the lines of principal curvature on the plane of symmetry,

$$[pqt - s(1 + q^2)] \left(\frac{dz}{dx} \right)^2 + [(1 + p^2)t - (1 + q^2)r] \frac{dz}{dx} + [(1 + p^2)s - pqr] = 0 \quad (9)$$

where

$$p = f_x, \quad q = f_z, \quad r = f_{xx}, \quad s = f_{xz}, \quad t = f_{zz} \quad (10)$$

and the principal radii of curvature ρ are given by

$$(rt - s^2)\rho^2 + K[t(1+p^2) + r(1+q^2) - 2pqs]\rho + K^2 = 0 \quad (11)$$

where

$$K = [1 + p^2 + q^2]^{\frac{1}{2}}.$$

Other relations between the geometric parameters of the orthogonal coordinate system based on the lines of principal curvature are given in [26].

VIII. EQUATIONS OF VORTICITY IN A BOUNDARY LAYER

Lighthill [1] makes a convincing case for the primary importance of vorticity in a boundary layer. If the vorticity is known, the velocity field can be calculated by the Biot-Savart law. Secondly, vorticity is diffused and convected more gradually than other fluid properties and hence is more readily determinable numerically. From the mathematical point of view, Lighthill implies that it is easier to solve the diffusion equation for vorticity than the boundary-layer momentum equations governed by an outer irrotational flow.

Sherman [30] has also been impressed by Lighthill's views, and has contributed a more mathematical discussion of "sources of vorticity." Neither he nor Lighthill, however, have formulated the vorticity equations for a three-dimensional boundary layer. This will now be undertaken.

The Navier-Stokes equations for an incompressible fluid may be written in the vector form

$$\frac{\partial \bar{v}}{\partial t} - \bar{v} \times \bar{\omega} + \text{grad} \left(\frac{1}{2} \bar{v} \cdot \bar{v} + \frac{p}{\rho} + gz \right) = -\nu \text{curl } \bar{\omega} \quad (12)$$

where \bar{v} is the velocity at a point of the fluid, $\bar{\omega} = \text{curl } \bar{v}$ is the vorticity, t denotes time, p is the pressure, ρ the mass density, g the acceleration of gravity, z is a vertical coordinate, positive upwards, and ν is the kinematic viscosity. An immediate consequence of (12), obtained by applying the nonslip condition at the wall surface S , is

$$\text{grad} \left(\frac{p}{\rho} + gz \right) = -\nu \text{curl } \bar{\omega} \quad \text{on } S \quad (13)$$

which relates the vorticity at the wall to the pressure gradients of the flow outside the boundary layer. By taking the curl of the members of Eq. (12) we obtain the Helmholtz vorticity diffusion equation

$$\frac{\partial \bar{\omega}}{\partial t} = \text{curl} (\bar{v} \times \bar{\omega}) - \nu \text{curl curl } \bar{\omega} \quad (14)$$

a form from which the pressure gradient has been eliminated. The velocity, however, still appears.

In rectangular coordinates we would have

$$\text{curl curl } \bar{\omega} = \nabla \times (\nabla \times \bar{\omega}) = \nabla \nabla \cdot \bar{\omega} - \nabla^2 \bar{\omega} = - \nabla^2 \bar{\omega}$$

since $\nabla \cdot \bar{\omega} = 0$, and (14) could be written in the form

$$\begin{aligned} \frac{\partial \xi}{\partial t} &= \xi \frac{\partial u}{\partial x} + \eta \frac{\partial u}{\partial y} + \zeta \frac{\partial u}{\partial z} - u \frac{\partial \xi}{\partial x} - v \frac{\partial \xi}{\partial y} - w \frac{\partial \xi}{\partial z} + \nu \frac{\partial^2 \xi}{\partial x^2} \\ \frac{\partial \eta}{\partial t} &= \xi \frac{\partial v}{\partial x} + \eta \frac{\partial v}{\partial y} + \zeta \frac{\partial v}{\partial z} - u \frac{\partial \eta}{\partial x} - v \frac{\partial \eta}{\partial y} - w \frac{\partial \eta}{\partial z} + \nu \frac{\partial^2 \eta}{\partial y^2} \\ \frac{\partial \zeta}{\partial t} &= \xi \frac{\partial w}{\partial x} + \eta \frac{\partial w}{\partial y} + \zeta \frac{\partial w}{\partial z} - u \frac{\partial \zeta}{\partial x} - v \frac{\partial \zeta}{\partial y} - w \frac{\partial \zeta}{\partial z} + \nu \frac{\partial^2 \zeta}{\partial z^2} \end{aligned} \quad (15)$$

We wish to obtain the equivalent set of equations for a three-dimensional boundary layer, employing a triply orthogonal coordinate system (α, β, γ) , where $h_1 d\alpha$ and $h_2 d\beta$ are elements of arc along the lines of principal curvature on S , and γ is distance along the normal, with $\gamma = 0$ on S .

Let $\bar{e}_1, \bar{e}_2, \bar{e}_3$ denote unit vectors in the directions of increasing α, β, γ . Put

$$\bar{v} = \bar{e}_1 u + \bar{e}_2 v + \bar{e}_3 w, \quad \bar{\omega} = \bar{e}_1 \xi + \bar{e}_2 \eta + \bar{e}_3 \zeta.$$

From $\bar{\omega} = \text{curl } \bar{v}$ we have in this system of coordinates, with $h_3 = 1$,

$$\begin{aligned} \xi &= \frac{1}{h_2} \left[\frac{\partial w}{\partial \beta} - \frac{\partial (h_2 v)}{\partial \gamma} \right] = \frac{1}{h_2} \frac{\partial w}{\partial \beta} - \frac{\partial v}{\partial \gamma} - \frac{v}{h_2} \frac{\partial h_2}{\partial \gamma} \\ \eta &= \frac{1}{h_1} \left[\frac{\partial}{\partial \gamma} (h_1 u) - \frac{\partial w}{\partial \alpha} \right] = \frac{\partial u}{\partial \gamma} - \frac{1}{h_1} \frac{\partial w}{\partial \alpha} + \frac{u}{h_1} \frac{\partial h_1}{\partial \gamma} \\ \zeta &= \frac{1}{h_1 h_2} \left[\frac{\partial}{\partial \alpha} (h_2 v) - \frac{\partial}{\partial \beta} (h_1 u) \right] = \frac{1}{h_1} \frac{\partial v}{\partial \alpha} - \frac{1}{h_2} \frac{\partial u}{\partial \beta} \\ &\quad + \frac{1}{h_1 h_2} \left(v \frac{\partial h_2}{\partial \alpha} - u \frac{\partial h_1}{\partial \beta} \right) \end{aligned}$$

Put $h_1(\alpha, \beta, 0) = H_1$, $h_2(\alpha, \beta, 0) = H_2$; let K_1, K_2 be the curvatures in the plane tangent to S of the arcs $\alpha = \text{const.}$ and $\beta = \text{const.}$; let K_3, K_4 be the principal curvatures of the surface S corresponding to the directions of increasing α and β . Then we have [26]

$$h_1 = H_1(1 + K_3\gamma), \quad h_2 = H_2(1 + K_4\gamma) \quad (16)$$

whence

$$\frac{1}{h_1} \frac{\partial h_1}{\partial \gamma} = \frac{K_3}{1 + K_3\gamma}, \quad \frac{1}{h_2} \frac{\partial h_2}{\partial \gamma} = \frac{K_4}{1 + K_4\gamma} \quad (17)$$

and, also from [26]

$$\frac{1}{h_1 h_2} \frac{\partial h_2}{\partial \alpha} = \frac{K_1}{1 + K_4\gamma}, \quad \frac{1}{h_1 h_2} \frac{\partial h_1}{\partial \beta} = \frac{K_2}{1 + K_3\gamma} \quad (18)$$

Hence the expressions for ξ, η, ζ become

$$\xi = \frac{1}{h_2} \frac{\partial w}{\partial \beta} - \frac{\partial v}{\partial \gamma} - \frac{K_4 v}{1 + K_4\gamma} \quad (19)$$

$$\eta = \frac{\partial u}{\partial \gamma} - \frac{1}{h_1} \frac{\partial w}{\partial \alpha} + \frac{K_3 u}{1 + K_3\gamma} \quad (20)$$

$$\zeta = \frac{1}{h_1} \frac{\partial v}{\partial \alpha} - \frac{1}{h_2} \frac{\partial u}{\partial \beta} + \frac{K_1 v}{1 + K_4\gamma} - \frac{K_2 u}{1 + K_3\gamma}. \quad (21)$$

At the wall, the nonslip condition gives

$$\bar{\omega} = -\bar{e}_1 \frac{\partial v}{\partial \gamma} + \bar{e}_2 \frac{\partial u}{\partial \gamma}. \quad (22)$$

Since the shear-stress vector at the wall is

$$\bar{\tau} = \mu(\bar{e}_1 \frac{\partial u}{\partial \gamma} + \bar{e}_2 \frac{\partial v}{\partial \gamma}) \quad (23)$$

we see that

$$\bar{\tau} = \mu \bar{\omega} \times \bar{e}_3. \quad (24)$$

This indicates that the vorticity lines and the skin-friction lines on S form an orthogonal net, as is well known.

Since in a boundary layer w is small in comparison with u and v , and derivatives with respect to α and β are small in comparison with derivatives with respect to γ , we are justified in omitting the derivatives with respect to α and β in (19), (20) and (21). In a thick boundary layer it may be necessary to retain the terms $K_3\gamma$ and $K_4\gamma$ in the denominators of (19), (20), and (21), but we shall neglect these terms in the present treatment. Thus the expressions for the vorticity components in a boundary layer become

$$\xi = -\frac{\partial v}{\partial \gamma} - K_4 v \quad (25)$$

$$\eta = \frac{\partial u}{\partial \gamma} + K_3 u \quad (26)$$

$$\zeta = K_1 v - K_2 u. \quad (27)$$

Near the wall the γ derivatives are dominant so that the expression for the vorticity remains that given by (22). Farther into the boundary layer, however, the terms $K_1 v$, $K_2 u$, $K_3 u$, and $K_4 v$ may become appreciable when the curvatures are large, as at the bilges of a ship form.

When ξ and η are known, the corresponding values of u and v , obtained by integrating the differential equations (25) and (26), are given by

$$u = e^{-K_3 \gamma} \int_0^\gamma \eta e^{K_3 \gamma} d\gamma \quad (28)$$

$$v = -e^{-K_4 \gamma} \int_0^\gamma \xi e^{K_4 \gamma} d\gamma \quad (29)$$

somewhat more simply than by the Biot-Savart law.

We can now obtain the components of $\text{curl } \bar{\omega}$ in the boundary layer by replacing u , v , w by ξ , η , ζ in the right members of (25), (26), and (27). Thus we obtain

$$\text{curl } \bar{\omega} \cdot \bar{e}_1 = -\frac{\partial \eta}{\partial \gamma} - K_4 \eta \quad (30)$$

$$\text{curl } \bar{\omega} \cdot \bar{e}_2 = \frac{\partial \xi}{\partial \gamma} + K_3 \xi \quad (31)$$

$$\text{curl } \bar{\omega} \cdot \bar{e}_3 = K_1 \eta - K_2 \xi \quad (32)$$

and similarly, from (19), (20), and (21),

$$\begin{aligned} \text{curl } (\bar{v} \times \bar{\omega}) = & \bar{e}_1 \left[\frac{1}{h_2} \frac{\partial}{\partial \beta} (u\eta - v\xi) - \frac{\partial}{\partial \gamma} (w\xi - u\zeta) - K_4(w\xi - u\zeta) \right] \\ & + \bar{e}_2 \left[\frac{\partial}{\partial \gamma} (v\zeta - w\eta) - \frac{1}{h_1} \frac{\partial}{\partial \alpha} (u\eta - v\xi) + K_3(v\zeta - w\eta) \right] \\ & + \bar{e}_3 \left[\frac{1}{h_1} \frac{\partial}{\partial \alpha} (w\xi - u\zeta) - \frac{1}{h_2} \frac{\partial}{\partial \beta} (v\zeta - w\eta) \right. \\ & \left. + K_1(w\xi - u\zeta) - K_2(v\zeta - w\eta) \right] \end{aligned} \quad (33)$$

For the components of $\text{curl curl } \bar{\omega}$ in the boundary layer we obtain, neglecting small terms,

$$\text{curl curl } \bar{\omega} \cdot \bar{e}_1 = - \frac{\partial^2 \xi}{\partial \gamma^2} - (K_3 + K_4) \frac{\partial \xi}{\partial \gamma} \quad (34)$$

$$\text{curl curl } \bar{\omega} \cdot \bar{e}_2 = - \frac{\partial^2 \eta}{\partial \gamma^2} - (K_3 + K_4) \frac{\partial \eta}{\partial \gamma} \quad (35)$$

$$\text{curl curl } \bar{\omega} \cdot \bar{e}_3 = K_1 \frac{\partial \xi}{\partial \gamma} + K_2 \frac{\partial \eta}{\partial \gamma} + K_1 K_3 \xi + K_2 K_4 \eta. \quad (36)$$

Substituting these results into (14) yields the vorticity equations

$$\frac{\partial \xi}{\partial t} = \frac{1}{h_2} \frac{\partial}{\partial \beta} (u\eta - v\xi) - \frac{\partial}{\partial \gamma} (w\xi - u\zeta) - K_4(w\xi - u\zeta) + \nu \left[\frac{\partial^2 \xi}{\partial \gamma^2} + (K_3 + K_4) \frac{\partial \xi}{\partial \gamma} \right] \quad (37)$$

$$\frac{\partial \eta}{\partial t} = \frac{\partial}{\partial \gamma} (v\zeta - w\eta) - \frac{1}{h_1} \frac{\partial}{\partial \alpha} (u\eta - v\xi) + K_3(v\zeta - w\eta) + \nu \left[\frac{\partial^2 \eta}{\partial \gamma^2} + (K_3 + K_4) \frac{\partial \eta}{\partial \gamma} \right] \quad (38)$$

$$\frac{\partial \zeta}{\partial t} = \frac{1}{h_1} \frac{\partial}{\partial \alpha} (w\xi - u\zeta) - \frac{1}{h_2} \frac{\partial}{\partial \beta} (v\zeta - w\eta) + K_1(w\xi - u\zeta) - K_2(v\zeta - w\eta). \quad (39)$$

Here u and v are given in terms of the vorticity by (28) and (29); w can then be obtained from the continuity equation.

In order to start the calculation, conditions at time $t = 0$ are required. This may be taken to be the vortex sheet for irrotational flow about the hull in a uniform stream, since this gives the initial vorticity distribution when the body is impulsively accelerated from rest to its constant speed. A procedure for determining this vortex sheet is developed in the following section.

IX. INTEGRAL EQUATION FOR A VORTEX SHEET FOR IRROTATIONAL FLOW ABOUT A THREE-DIMENSIONAL FORM

A three-dimensional form bounded by a surface S is immersed in a uniform stream of velocity U in the positive x -direction, of unit vector \bar{i} . We shall suppose that the fluid is inviscid and incompressible. Let us assume that the disturbance of the flow due to the body may be represented by a vortex sheet of strength $\bar{\gamma} = \gamma \bar{\sigma}$ where $\bar{\sigma}$ is a unit vector tangent to the surface S such that the fluid within the body is at rest.

In crossing S in the direction of its outward normal, designated by the unit vector \bar{n} , there is a discontinuity in the tangential component of the velocity of the fluid, of magnitude γ , in the direction with unit vector

$$\bar{s} = \bar{\sigma} \times \bar{n}. \quad (40)$$

By continuity, since the fluid on the interior side of S is at rest, the velocity components in the $\bar{\sigma}$ and \bar{n} directions at the exterior side of S must also vanish, and hence the velocity at the exterior side of S is given by

$$\bar{u} = \gamma \bar{\sigma} \times \bar{n} = \bar{\gamma} \times \bar{n}. \quad (41)$$

Since, a priori, the mutually orthogonal directions of the streamlines, \bar{s} , and of the vortex lines, $\bar{\sigma}$, are unknown, it is necessary to introduce a set of orthogonal, curvilinear coordinate lines on S , $\xi = \text{const.}$ and $\eta = \text{const.}$ Denote unit vectors in the directions of increasing ξ and η by \bar{e}_1 and \bar{e}_2 , with sense such that $\bar{e}_1 \times \bar{e}_2 = \bar{n}$. Put

$$\bar{\gamma} = \bar{e}_1 \gamma_1 + \bar{e}_2 \gamma_2, \quad \bar{u} = \bar{e}_1 u + \bar{e}_2 v. \quad (42)$$

Then, by (41), we have

$$u = \gamma_2, \quad v = -\gamma_1. \quad (43)$$

An integral equation for the vorticity vector $\bar{\gamma}$ can be derived from the condition that the contributions to the velocity on the interior side of a point P of S must sum to zero. This gives

$$\frac{1}{4\pi} \int_S \bar{\gamma}_Q \times \nabla_P \left(\frac{1}{r_{PQ}} \right) dS_Q + \frac{1}{2} \bar{\gamma}_P \times \bar{n}_P = U \bar{i} \quad (44)$$

in which the integral, obtained from the Biot-Savart law, represents

the velocity at P induced by vortex elements at points Q of S , and, by (41), the negative of the second term is the contribution from the local vortex element $\bar{\gamma}_P$. Here r_{PQ} is the length of the chord joining the points P and Q of S and ∇_P denotes the gradient with respect to the coordinates of P .

The integral in (44) is not suitable for numerical evaluation in the given form because r_{PQ}^2 , which goes to zero as Q approaches P , occurs in the denominator of the integrand. This singularity can be eliminated, however, in the following manner.

First take the cross-product of (44) by \bar{n}_P to obtain

$$\frac{1}{4\pi} \int_S \left[\bar{\gamma}_Q \times \nabla_P \left(\frac{1}{r_{PQ}} \right) \right] \times \bar{n}_P dS_Q + \frac{1}{2} (\bar{\gamma}_P \times \bar{n}_P) \times \bar{n}_P = \bar{U} \times \bar{n}_P. \quad (45)$$

Since, in the neighborhood of P , both $\bar{\gamma}_Q$ and $\nabla_P(1/r_{PQ}) = \bar{r}_{PQ}/r_{PQ}^3$ lie very nearly in the tangent plane at Q , their cross-product is very nearly parallel to \bar{n}_Q , and hence the integrand of (45) is proportional to the angle between \bar{n}_P and \bar{n}_Q or r_{PQ}/R , where R is the radius of curvature of the arc of S subtended by the chord PQ . Thus the order of the singularity of the integrand of (45) has been reduced to that of $1/r_{PQ}$.

In order to eliminate this singularity, consider the relation

$$\begin{aligned} \left[\bar{\gamma}_P \times \nabla_Q \left(\frac{1}{r_{PQ}} \right) \right] \times \bar{n}_P &= \bar{\gamma}_P \cdot \bar{n}_P \nabla_Q \left(\frac{1}{r_{PQ}} \right) - \bar{\gamma}_P \bar{n}_P \cdot \nabla_Q \left(\frac{1}{r_{PQ}} \right) \\ &= - \bar{\gamma}_P \bar{n}_P \cdot \nabla_Q \left(\frac{1}{r_{PQ}} \right) \end{aligned} \quad (46)$$

since $\bar{\gamma}_P \cdot \bar{n}_P = 0$. Also we may write

$$\int_S \bar{n}_P \cdot \nabla_Q \left(\frac{1}{r_{PQ}} \right) dS_Q = \int_S \left[\bar{n}_P \cdot \nabla_Q \left(\frac{1}{r_{PQ}} \right) + \bar{n}_Q \cdot \nabla_Q \left(\frac{1}{r_{PQ}} \right) \right] dS_Q + 2\pi \quad (47)$$

since $\int_S \bar{n}_Q \cdot \nabla_Q (1/r_{PQ}) dS_Q$ is the flux through S due to a sink of unit strength at P . Applying (46) and (47), and noting that

$$\nabla_P \left(\frac{1}{r_{PQ}} \right) = - \nabla_Q \left(\frac{1}{r_{PQ}} \right)$$

we obtain from (45),

$$\int_S \left[(\bar{\gamma}_Q - \bar{\gamma}_P) \times \nabla_P \left(\frac{1}{r_{PQ}} \right) \right] \times \bar{n}_P dS_Q - \gamma_P \int_S (\bar{n}_P + \bar{n}_Q) \cdot \nabla_P \left(\frac{1}{r_{PQ}} \right) dS_Q = 4\pi U \bar{i} \times \bar{n}_P. \quad (48)$$

The singularity has been removed from the first integral in (48) because a factor proportional to r_{PQ} is contained in

$$\bar{\gamma}_Q - \bar{\gamma}_P \approx \bar{r}_{PQ} \cdot (\nabla \bar{\gamma})_P.$$

The second integrand is also singularity-free at P since

$$\bar{n}_P \cdot \nabla_P \left(\frac{1}{r_{PQ}} \right) \approx \frac{\bar{n}_P \cdot \bar{r}_{PQ}}{r_{PQ}^3} \approx \frac{-1}{2Rr_{PQ}}$$

and

$$\bar{n}_Q \cdot \nabla_P \left(\frac{1}{r_{PQ}} \right) \approx \frac{1}{2Rr_{PQ}}.$$

Thus we see that $(\bar{n}_P + \bar{n}_Q) \cdot \nabla_P (1/r_{PQ})$ is regular at P .

A procedure for obtaining a numerical solution of the integral equation (48) consists of replacing the integrals by quadrature formulas to obtain sets of linear equations. Expressing $\bar{\gamma}$ in terms of \bar{e}_1 and \bar{e}_2 as in (42), for each of n points P the quadrature formula yields a linear equation in the unknown values of u and v at n points Q . This gives n vector equations or, resolving in the directions \bar{e}_1 and \bar{e}_2 at P , $2n$ scalar equations in $2n$ unknowns. When Q coincides with P , the integrand is set equal to zero.

Taking the scalar products of the members of (48) by \bar{e}_{1P} and \bar{e}_{2P} , we obtain the pair of scalar equations

$$\int_S (\bar{\gamma}_Q - \bar{\gamma}_P) \times \nabla_P \left(\frac{1}{r_{PQ}} \right) \cdot \bar{e}_{1P} dS_Q + u_P \int_S (\bar{n}_P + \bar{n}_Q) \cdot \nabla_P \left(\frac{1}{r_{PQ}} \right) dS_Q = 4\pi U \bar{i} \cdot \bar{e}_{1P} \quad (49)$$

$$\int_S (\bar{\gamma}_Q - \bar{\gamma}_P) \times \nabla_P \left(\frac{1}{r_{PQ}} \right) \cdot \bar{e}_{2P} dS_Q + v_P \int_S (\bar{n}_P + \bar{n}_Q) \cdot \nabla_P \left(\frac{1}{r_{PQ}} \right) dS_Q = 4\pi U \bar{i} \cdot \bar{e}_{2P}. \quad (50)$$

In applying these equations, one needs to express $\bar{\gamma}_Q$ and \bar{n}_Q in

terms of the unit vectors \bar{e}_{1Q} , \bar{e}_{2P} and \bar{n}_P . This requires that the direction cosines of \bar{e}_{1Q} , \bar{e}_{2Q} , and \bar{n}_Q relative to \bar{e}_{1P} , \bar{e}_{2P} and \bar{n}_P be calculated for each combination of P and Q; i.e., $\frac{1}{2}n(n+1)$ tables of direction cosines. Furthermore, if (x_P, y_P, z_P) and (x_Q, y_Q, z_Q) are the coordinates of P and Q in a rectangular Cartesian coordinate system with unit vectors $\bar{i}, \bar{j}, \bar{k}$, then

$$\bar{r}_{PQ} = \bar{i}(x_Q - x_P) + \bar{j}(y_Q - y_P) + \bar{k}(z_Q - z_P)$$

and the expression of $\nabla_P(1/r_{PQ}) = \bar{r}_{PQ}/r_{PQ}^3$ in terms of \bar{e}_{1P} , \bar{e}_{2P} and \bar{n}_P requires that n tables of direction cosines of the latter set of vectors with respect to the $\bar{i}, \bar{j}, \bar{k}$ system also be obtained. These direction cosines and the components of \bar{r}_{PQ} can be readily determined if the equations of the surface are given in the form

$$x = F(\xi, \eta), \quad y = G(\xi, \eta), \quad z = H(\xi, \eta). \quad (51)$$

A procedure for solving (49) and (50) by iteration is suggested by the following modifications:

$$\begin{aligned} \int_S (\bar{Y}_Q - \bar{Y}_P)_n \times \nabla_P \left(\frac{1}{r_{PQ}} \right) \cdot \bar{e}_{1P} dS_Q + u_{P,n+1} \int_S (\bar{n}_P + \bar{n}_Q) \cdot \nabla_P \left(\frac{1}{r_{PQ}} \right) dS_Q \\ = 4\pi U \bar{i} \cdot \bar{e}_{1P} \end{aligned} \quad (52)$$

$$\begin{aligned} \int_S (\bar{Y}_Q - \bar{Y}_P)_n \times \nabla_P \left(\frac{1}{r_{PQ}} \right) \cdot \bar{e}_{2P} dS_Q + v_{P,n+1} \int_S (\bar{n}_P + \bar{n}_Q) \cdot \nabla_P \left(\frac{1}{r_{PQ}} \right) dS_Q \\ = 4\pi U \bar{i} \cdot \bar{e}_{2P} \end{aligned} \quad (53)$$

For ship forms the foregoing procedure can be used to determine the velocity and vorticity distributions and the streamlines and vortex lines on a double ship model at zero Froude number. At non-zero Froude numbers, a similar pair of integral equations can be derived, but these would be considerably more complicated because of the contributions of the wave potential to the velocity on the body surface S .

X. CONCLUSIONS

It has been indicated, on the basis of the limited available boundary-layer data on actual ships and ship models, that the various integral methods, with or without the small cross-flow assumption, and employing streamline coordinates, are of dubious applicability to ship forms because three additional assumptions concerning the

velocity profile, the cross-flow angle, and the shear-stress coefficient are not in accord with these data. If the energy integral equation is also used to obtain an auxiliary equation, then an additional assumption concerning the dissipation coefficient comes into question.

Two significant ship boundary-layer phenomena, the generation of secondary flows and possibly of vortices at the bilges near the bow and at a wave crest along the hull, indicate that cross-flow angles may become large, so that the small cross-flow assumption would be inappropriate. The possibility that the cross-flow may change in sense and that the velocity profiles may become S-shaped both at the bow and along the wave profile on the hull must also be taken into account.

Lines of principal curvature are recommended as the basis of the orthogonal coordinate system for treating ship boundary layers because, in contrast with alternative choices, this system remains orthogonal even in the thick boundary layer at the stern, and because, unlike the streamline coordinates, the former system does not change as the draft, trim, and the Froude and Reynolds numbers are varied. For this reason, equations for determining the lines of principal curvature have been included.

Since integral methods seem to be wedded to the use of streamline coordinates, the recommendation that these be replaced by the lines of principal curvature implies that a differential method must be adopted. One such method, based on the work of Bradshaw, Ferriss and Atwell [31] for a two-dimensional boundary layer, has been extended to the case of a three-dimensional surface by Nash [32]. An alternative approach based on determining the vorticity in the boundary layer, strongly promoted by Lighthill [1], motivated the derivations of the vorticity equations in principal-curvature coordinates and the integral equations of a vortex sheet for irrotational flow about a three-dimensional form. Considerable further development is required for application of these vorticity equations to a turbulent three-dimensional boundary layer.

Lastly it should be remarked that presently we cannot determine the outer flow about a ship form with sufficient accuracy for reliable boundary-layer calculations due to a combination of errors due to linearization of the free-surface boundary conditions, approximate satisfaction of the hull boundary condition, and the effects of viscosity on the wave making. In comparison with the outer-flow approximation for the flow about a body without a free surface, the effects of viscosity are experienced much farther upstream along the body because of the phenomenon of interference between waves generated near the bow and stern. Because of the strong interaction between the outer flow and that in the boundary layer and wake, it appears to be necessary to develop an iteration procedure, alternating between these regions, which hopefully would converge to a solution for the flow about a ship form.

ACKNOWLEDGMENT

This study was supported by the Office of Naval Research, under contract Nonr 1611-(07).

REFERENCES

- [1] Lighthill, M. J., Chapter II of Laminar Boundary Layers, editor L. Rosenhead, Oxford, Clarendon Press, 1963.
- [2] Lin, J. D. and Hall, R. S., "A Study of the Flow Past a Ship-Like Body," Univ. of Conn., Civil Engineering Department, Report No. CE 66-7, November 1966.
- [3] Webster, W. C. and Huang, T. T., "Study of the Boundary Layer on Ship Forms," Hydronautics, Inc., Tech. Report 608-1.
- [4] Uberoi, S. B. S., "Viscous Resistance of Ships and Ship Models," Hydro-Og Aerodynamisk Laboratorium Report No. Hy-13, September 1969.
- [5] Pavamani, F. S. A., "Three-Dimensional Turbulent Boundary Layer," M.S. Thesis, The Univ. of Iowa, August 1960.
- [6] Chow, S.-K., "Free-Surface Effects on Boundary-Layer Separation on Vertical Struts," Ph.D. Dissertation, The Univ. of Iowa, June 1967.
- [7] Tzou, T.-S., "Secondary Flow Near a Simulated Free Surface," M.S. Thesis, The Univ. of Iowa, June 1966.
- [8] Landweber, L. and Macagno, M., "Irrotational Flow About Ship Forms," The Univ. of Iowa, IIHR Report No. 123, December 1969.
- [9] Hess, J. L. and Smith, A. M. O., "Calculation of Potential Flow About Arbitrary Bodies," Progress in Aeronautical Sciences, Vol. 8, Pergamon Press, New York, 1966.
- [10] Thompson, B. G., "A Critical Review of Existing Methods of Calculating the Turbulent Boundary Layer," A.R.C. R. & M., August 1964.
- [11] Smith, P. D., "Calculation Methods for Three-Dimensional Turbulent Boundary Layers," A.R.C. R. & M. No. 3523, December 1966.

- [12] Guilloton, R., "Potential Theory of Wave Resistance of Ships with Tables for its Calculation," Trans. Soc. Naval Arch. & Marine Engrs., Vol. 59, 1951.
- [13] Korvin-Kroukovsky, B. V., and Jacobs, W. R., "Calculation of the Wave Profile and Wave Making Resistance of Ships of Normal Commercial Form by Guilloton's Method and Comparison with Experimental Data," Soc. of Naval Arch. & Marine Engrs., Tech. & Res. Bulletin No. 1-16, December 1954.
- [14] Cooke, J. C., "A Calculation Method for Three-Dimensional Turbulent Boundary Layers," A.R.C. R. & M. No. 3199, October 1958.
- [15] Head, M. R., "Entrainment in the Turbulent Boundary Layer," A.R.C. R. & M. No. 3152, September 1958.
- [16] Gadd, G. E., "The Approximate Calculation of Turbulent Boundary Layer Development on Ship Hulls," Paper W5 (1970) published by RINA for written discussion.
- [17] Shearer, J. R. and Steel, B. N., "Some Aspects of the Resistance of Full Ship Forms," Paper W4 (1970) published by RINA for written discussion.
- [18] Sayre, C. L. Jr., and Duerr, R. L., "Boundary-Layer Investigation of USS Timmerman," David Taylor Model Basin, Hydromechanics Laboratory R. & D. Report 1170, August 1960.
- [19] Wieghardt, K., "Boundary Layer Tests on the Meteor," Jahrbuch der Schiffbautechnischen Gesellschaft, 1968.
- [20] Wieghardt, K., "Boundary Layer Measurements on a Double Model," Proc. 12th International Towing Tank Conference, Rome 1969.
- [21] Executive Committee for the Project "Measurements of Boundary Layers of Ships," Proc. 12th International Towing Tank Conference, Rome 1969.
- [22] Tatinclaux, J. C., "Experimental Investigation of the Drag Induced by Bilge Vortices," Schiffstechnik, Bd. 17, May 1970.
- [23] Takahei, T., "Investigations on the Flow Around the Entrances of Full Hull Forms," Proc. 11th International Towing Tank Conference, Tokyo 1966.

- [24] Squire, L. C., "The Three-Dimensional Boundary-Layer Equations and Some Power Series Solutions," A.R.C. R. & M. 3006, 1957.
- [25] Howarth, L., "The Boundary Layer in Three Dimensional Flow -- Part I, Derivation of the Equations for Flow Along a General Curved Surface," Phil. Mag., Ser. 7, Vol. 42, 1951.
- [26] Landweber, L., "Appendix A. Equations in Curvilinear Orthogonal Coordinates," Advanced Mechanics of Fluids, Edited by H. Rouse, John Wiley & Sons, New York, 1959.
- [27] Crabtree, L. F., Küchemann, D., and Sowerby, L., "Three Dimensional Boundary Layers," Chapter VIII, p. 415 of Laminar Boundary Layers, Edited by L. Rosenhead, Oxford University Press, 1963.
- [28] Howarth, L., "The Boundary Layer in Three Dimensional Flow -- Part II, The Flow Near a Stagnation Point," Phil. Mag. Ser. 7, Vol. 42, 1951.
- [29] Smith, C., An Elementary Treatise on Solid Geometry, Macmillan & Company, London, 1891.
- [30] Sherman, F. S., "Introduction to Three-Dimensional Boundary Layers," Rand Corporation Memorandum RM-4843-PR, April 1968.
- [31] Bradshaw, P., Ferriss, D. H., and Atwell, N. P., "Calculation of Boundary Layer Development Using the Turbulent Energy Equation," J. Fluid Mech., Vol. 28, 1967.
- [32] Nash, J. F., "The Calculation of Three-Dimensional Turbulent Boundary Layers in Incompressible Flow," J. Fluid Mech., Vol. 37, Part 4, 1969.

DISCUSSION

Dr. N. Hogben

*National Physical Laboratory, Ship Division
Feltham, Middlesex, England*

This paper performs a valuable service in laying the foundations for a new method of calculating ship boundary layer properties in terms of the vorticity field. A verdict on the merit of this approach must await the results of actual computations and comparison with experiment. The purpose of this contribution is to supplement the review of experimental data given in the paper by drawing attention to work which I reported in 1964 (Ref. (*)). It comprised boundary layer explorations covering the surface of a model with mathematical form as defined by Wigley (Ref. (**)) having parabolic waterlines and section shapes. Measurements were made at 5 speeds in the range $0.16 < F_r < 0.32$ and it is of interest that features noted by Wieghardt as cited in the present paper were also observed. In particular considerable stretching of the boundary layer below the keel, likewise attributed to secondary flow effects, and bumps on the velocity profiles attributed to trailing vortices, were found.

REFERENCES

- (*) Hogben, N. , "Record of a boundary layer exploration on a mathematical ship model," Ship Division NPL Report No. 52, July 1964.
- (**) Wigley, W. C. S. , "Calculated and measured wave resistance of a series of forms defined algebraically," Trans. R.I.N.A. , 1942.

* * * * *

DISCUSSION

H. Lackenby
The British Ship Research Association
Northumberland, England

I certainly agree with Professor Landweber's plea for a more detailed study of the relatively thick boundary layers in way of ship sterns especially in very full tanker forms.

In Ref. 17 (Shearer and Steele) it is apparent that some of the models of the full tanker forms considered were suffering from gross separation at the stern. There is little doubt that this accounts for the viscous pressure resistance being as high as 30% of the total. Incidentally, in this reference the corresponding wave making resistance or gravitational component was stated to be only 3 to 5% of the total.

Reference is made in Professor Landweber's paper to conditions which bring about separation but not, as far as I can ascertain, to methods of calculating the shear stress after separation and the added pressure resistance which this brings about. I would be glad if the Author would care to comment on the development of calculation methods for these conditions. I would also mention that in some of the latest full tanker forms there is little doubt that separation is taking place on these ships at sea and the situation is having to be accepted.

The viscous component of ship resistance has always been an important one but owing to the developments in tanker forms it is becoming even more important than it was in this class of ship. Professor Landweber's paper is, therefore, of particular interest and importance at this time and I look forward to further developments in his approach to the problem.

* * * * *

REPLY TO DISCUSSION

L. Landweber
University of Iowa
Iowa City, Iowa

Mr. Lackenby emphasizes the importance of boundary-layer studies on tanker forms. Since the resistance of a tanker is mainly viscous, and the power-wasting phenomena of bilge-vortex formation and stern separation are viscous in origin, it is clear that such studies are needed, if only to develop designs which avoid their occurrence.

For the particular tanker form to which Mr. Lackenby refers, the wavemaking resistance was stated to be only 3 to 5 per cent of the total. Our experience has been that the wave resistance of a tanker model may be about 10 per cent of the total, and that if a proper bow bulb is fitted, it may be reduced to about 6 per cent. Since others have found that bulbs on tanker models reduce viscous, rather than wave resistance, this indicates that the problem remains to be resolved.

I would like to thank Dr. Hogben for reminding us of his important 1964 boundary-layer paper, one of the very few available studies of ship boundary layers. Explorations of this kind on other ship forms are urgently needed to guide the development of methods of computing ship boundary layers.

STUDY OF THE RESPONSE OF A VIBRATING PLATE IMMERSSED IN A FLUID

L. Maestrello

*NASA Langley Research Center
Hampton, Virginia*
and

T. L. J. Linden

*European Space Operations Center
Darmstadt, Germany*

I. INTRODUCTION

A large aircraft in supersonic flight undergoes large variations in flow field over its surface. This paper is concerned with studying the response of a structure excited by convected turbulence at nearly zero pressure gradient and by shock-boundary layer interaction, with the inclusion of the coupling due to the acoustic field on each side of a panel. Shock waves on thin-walled structures can impose severe loading problems, the most common of which is the self-induced oscillation which is generated by an oscillating shock. The shock wave can easily couple with the forcing frequency present in the environment, including panel resonances.

From interior noise point of view, the upper region of the airplane fuselage is considered the principal noise radiator. The aerodynamics in this region are known from the Prandtl-Mayer relation, and further downstream by shock-boundary interaction. In addition, the fuselage skin experiences traveling shock waves which run up and down the skin during the acceleration period, which might last twenty minutes for a Mach 3 airplane.

In supersonic flight, the vibration of the surface is influenced by the back pressure resulting from the radiation of sound on both sides of the surface, so that, the surface motion and radiation are coupled phenomena. The interior noise level is determined by skin panel vibrations. For radiation below the critical frequency, the major source of sound arises from the interaction of the bending wave with the discontinuity of the boundary. Above the critical frequency,

the action of discontinuities like tear stoppers, etc., have little effect on altering sound pressure level, since the sound radiation by the panel is in the form of Mach wave radiation.

The experiment described in this paper indicates that some simplifications in the model can be made, viz. (1) that there is no significant interaction between the plate and the aerodynamic forces on the plate; and (2) that the panel displacement is small in comparison to its thickness so that thin plate theory may be used. The plate is, however, acoustically coupled to the external flow field and the internal cavity.

Lyamshev [1968] has solved a similar problem for a complex structure. Dowell [1969] computed the transient, non-linear response of a simply supported plate coupled to an external flow field and a cavity. Dzygadło [1967] presented a linear analysis allowing mutual interaction between the plate and the external flow. Fahy and Pretlove [1967] have computed a first order approximation to the acoustic coupling of a flexible duct wall to the flow field through the duct. Maidanek [1966] considers an infinite, orthotropic plate coupled acoustically to an external flow field. Numerous other investigations have been reported on acoustically coupled structures with varying degrees of approximation, Irgens and Brand [1968], White and Cottis [1968], Strawderman [1967], Creighton [1970], Ffowcs-Williams [1966], Crighton and Ffowcs-Williams [1969], Dolgova [1969], Feit [1966], Lapin [1967], Pal'tov and Pupyrev [1967].

II. MEASUREMENTS

a) The Experimental Arrangement

The flow investigated was the sidewall boundary layer of the Jet Propulsion Laboratory 20-inch supersonic wind tunnel; the shock was induced by a 30° wedge mounted outside the boundary layer, off-center and on the same side that the measurements were made. This was done to offset the position of the reflected shock from the opposite wall. The position of the shock was determined by observing the displacement of a line of tufts, and by a static pressure survey. For zero pressure gradient, detail of flow field and panel response has been previously reported by Maestrello [1968].

The experiment was arranged to perform three basic measurements: mean velocity profile ahead of the shock with static pressure distribution across the shock, wall pressure fluctuations and measurement of displacement response of a simple panel structure. The titanium* test panel measure $12 \times 6 \times 0.062$ inches and was brazed on all four sides of a $3/4$ inch \times $3/4$ inch titanium frame. The brazing

*Ti-6AL-4V Titanium alloy containing 6% aluminum, 4% vanadium, 90% titanium.

was intended to simulate the clamped edge condition. The panel formed most of one wall of a rigid cavity measuring $14 \times 8 \times 6.6$ inches. The other surface of the panel was exposed to the flow field. The pressure differential across the panel was variable. The experiment was conducted at two pressure differentials, viz. 0.06 and 14 psi; the latter corresponds to the actual differential between wind tunnel pressure and local ambient.

The side wall of the tunnel was modified to accommodate two identical, rigid, steel plates, which supported the necessary instrumentation. One plate contained an array of holes in which pressure transducers were mounted. The pressure transducers were mounted on the center-line of the tunnel in the streamwise direction at the same locations where the mean static pressure measurements were made. Two types of pressure transducers were used; one, the conventional lead zirconate titanate type made by Atlantic Research, the other a capacitance type made by Photocon Corporation with sensitive diameters of 0.06 inch and 0.09 inch respectively. Correction due to finite size transducers was made adopting the Corcos [1963] approach. The panel displacement was measured with Photocon capacitance, displacement transducers mounted on brackets which could slide along a bar and could be set precisely by means of a screw mechanism.

The output of both pressure transducers and displacement transducer were recorded on Ampex FR-1800H 14-channel tape, recorded in the FM mode. Four channels were used for simultaneously recording data for correlation measurements. The maximum dynamic range was obtained by splitting each data channel into two tape tracks through phase matched filters to separate the lower and higher frequencies.

b) The Wall Pressure Field

Measurements indicated that the flow field in front of the shock closely approximated the properties of equilibrium of an adiabatic flat-plate boundary layer [Maestrello 1968]. The flow in front of the shock has the following characteristics: Mach number $M_e = 3.03$, free stream velocity $U_e = 2,100$ ft/sec, total temperature $T_t = 567^\circ$ R, boundary layer thickness $\delta = 1.37$ inch, boundary layer displacement thickness $\delta^* = 0.445$ inch, momentum thickness $\theta = 0.083$ inch, Reynolds number $R = U_e \delta / \nu = 4.87 \times 10^5$, skin friction coefficient $C_f = 1.27 \times 10^{-3}$, and $\overline{C}_f R \theta = 39.8$ Coles parameter [Coles 1964].

The pressure ratio across the shock is a well defined function of Mach number, for a 15° half-cone angle, the pressure ratio is approximately 8.5. Experimental results show, however, that this ratio is considerably smaller ($\Delta p = 2.3$). It is postulated that interaction with an expansion wave originating at the base of the wedge is responsible for lowering the pressure differential and producing an

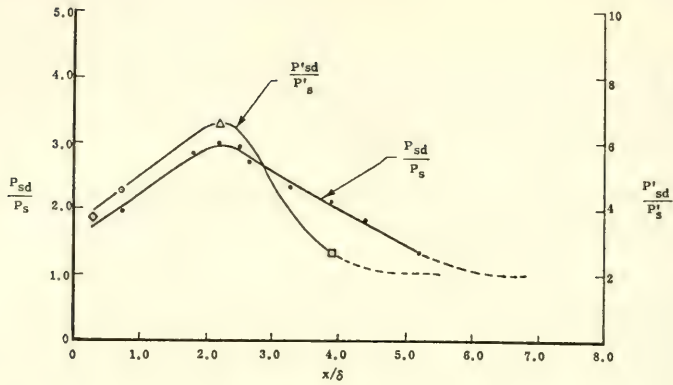


Fig. 1. Static Pressure Fluctuations and Mean Pressure Distribution Downstream of the Shock

effective decay downstream, Fig. 1. In the present case, the wedge angle induces a shock in the boundary layer large enough to cause a separation: farther downstream, the flow becomes reattached and goes back to the flat plate condition. This transition takes place within a few boundary layer thicknesses.

Downstream of the shock, the ratio of the mean pressure distribution p_{sd}/p_s and the ratio of the rms pressure fluctuation p'_{sd}/p'_s vary with a consistent relationship and both reach a maximum at $x/\delta \approx 2.3$, where subscripts s and sd , mean upstream and downstream of the shock, respectively, Fig. 1. Beyond $x/\delta \approx 6$ the effect of the shock on the static pressure vanishes. Kistler [1963] indicates a similar behavior between mean and fluctuating pressure in the separated region ahead of a forward-facing step at the same Mach number and upstream Reynolds number. The differences in the flow geometry only alter the magnitude of the pressure, in that the ratio of the mean pressure to the fluctuating pressure $p_{sd}/p'_{sd} \approx 14$ in the present experiment while Kistler found that $p_{sd}/p'_{sd} \approx 32$.

The normalized power spectral density measured upstream and downstream of the shock are shown in Fig. 2. The spectra are normalized by requiring $\int_0^\infty \pi(\omega) d\omega = 1$ in order to demonstrate the deviation from the zero pressure gradient case. For the spectra just downstream of the shock more energy is concentrated in a narrow low frequency band while further downstream at $x/\delta \approx 4$, the energy is distributed over a much broader bandwidth and approaches the shape and level of the spectrum taken upstream of

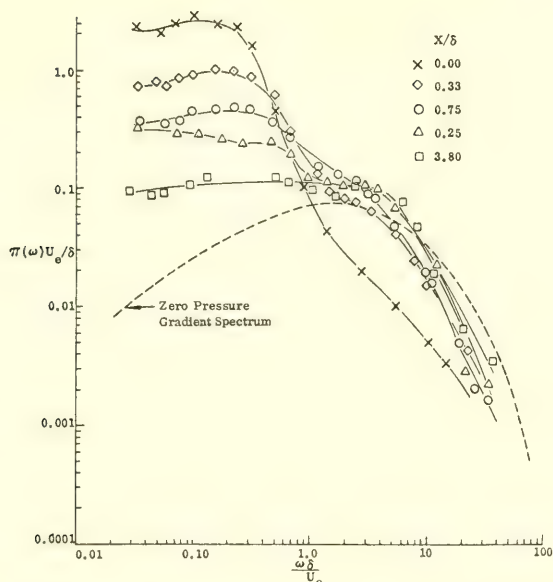


Fig. 2.. Power Spectral Density of the Wall Pressure Fluctuation

the shock. The normalized power spectral density found upstream of the shock corresponds to the zero pressure gradient, and peaks at $\omega\delta/U_e \approx 2$ while downstream the spectral density is modified in the region below the peak. It is significant that by altering the local flow conditions, only the low frequency ends of the spectra are appreciably affected. It is noticed that the pressure fluctuation measurements at $x/\delta \approx 0$ where the shock impinges show a noticeable deviation from the general pattern in the higher frequencies. This is attributed to an intermittent signal superimposed on the regular pressure signal as seen on the oscilloscope. It is possibly due to the characteristic fanning of the shock as it goes through the boundary layer.

Measurements of the cross-correlation are shown in Fig. 3. The cross-correlation characteristics are a function of position downstream of the shock. The cross-correlation between positions $x/\delta = 0.33$ and $x/\delta = 3.80$, the farthest apart, has characteristics similar to those found at zero pressure gradient boundary layer in that the ratio between the convection velocity and the freestream velocity $U_c/U_e = 0.72$ and that the correlation between those two points is still significant. The cross-correlation of the shortest distance between $x/\delta = 0.33$ and $x/\delta = 0.75$, shows that the con-

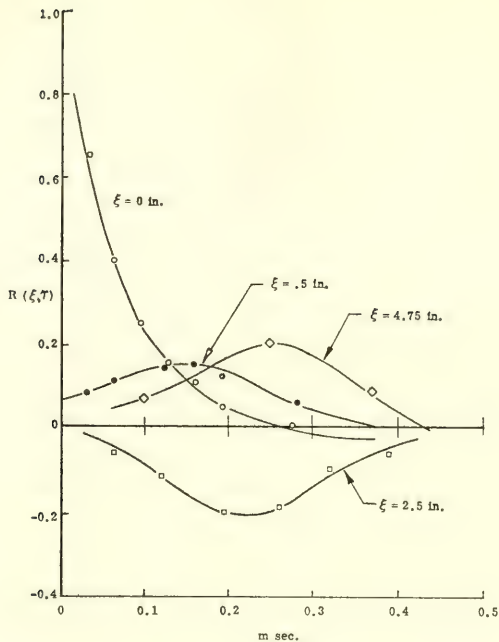


Fig. 3. Longitudinal Cross-Correlation of the Wall Pressure

vection velocity is very low $U_c/U_e = 0.13$ and the correlation is very weak. The correlation between $x/\delta = 0.33$ and $x/\delta = 0.25$, where $x/\delta = 2.25$ corresponds to the maximum static pressure ratio is negative. The shock induces the boundary layer to separate and the recirculation within the separation region permits the sign of the pressure to change. Kistler argued that the fluctuating pressure in the separated region arises from the combined action of the turbulent shear layer and the recirculating flow. The picture, however, is not yet clear enough to develop a model for time dependent loading, since the geometry of the separated region is the primary variable in estimating the pressure amplitude and resulting phase.

No measurement of the lateral cross-correlation was made during the test; however, for the purpose of computing the response of the panel, it is assumed that the pressure decays similarly to that in the case of zero pressure gradient $e^{-|\eta|/a_2}$ where $a_2 = 0.26$ and η is the spatial separation [Maestrello 1968]. This choice overestimates the lateral cross-correlation, since the flow field is far from being homogeneous. However, the overestimation may not be exceeded by a factor of 2.

c) The Panel Response Field

Measurements were made of the power spectral density and cross-correlation of the displacement. Typical results are shown in Figs. 4 and 5 for a pressure differential of 14 psi. The static deflection of the panel was 0.06 inches at the center, and the dynamic deflection was small in comparison with its thickness.

The displacement spectral density at the center of the panel show pronounced spikes, the lowest frequency of which corresponds to the lowest mode of the panel. The accuracy beyond a frequency of 3100 Hz was poor due to the spatial resolution of the capacitance transducer, and therefore the spectrum beyond 3100 Hz was ignored.

Space-time correlation measurements were made along the panel centerline from $x = x' = 3$ in. $y = y' = 3$ in. at one-inch intervals up to a maximum separation of 6 in. The correlogram indicates a convected feature with a phase velocity $\pm U_{cp} = 770$ ft/sec. This convection velocity corresponds to that found in the previous experiment using the same arrangements, except that no shock was present [Maestrello 1968].

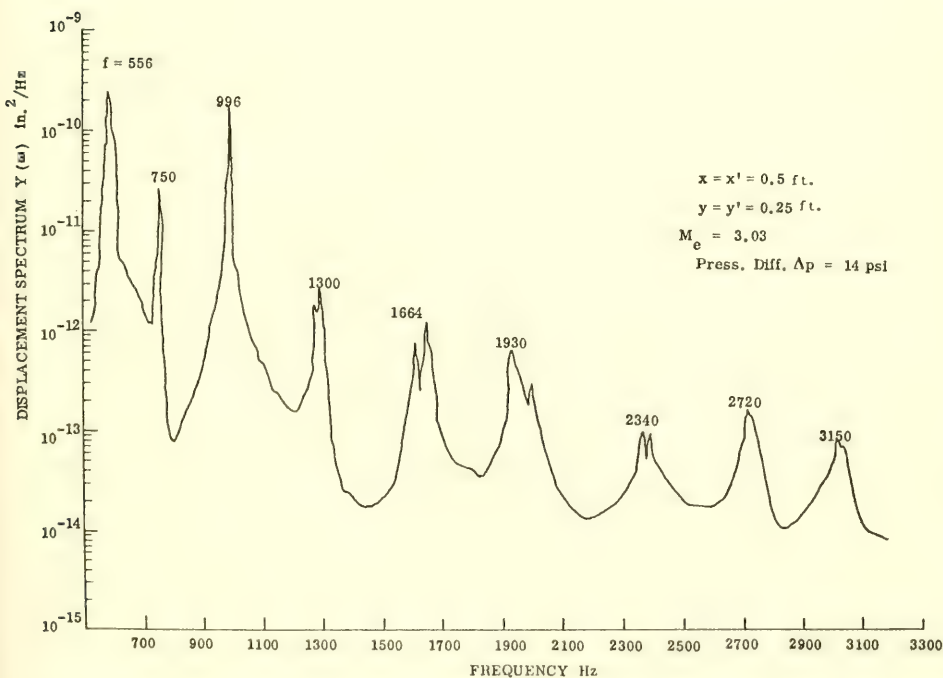


Fig. 4. Displacement Spectral Density

In comparing the results of the present and previous experiments, it is concluded that the sign change of the convection velocity is attributed to the presence of the shock. Furthermore, the cross-correlation of the wall pressure also reflects a phase change for a separation of 2.5 inches, which is in the same location as the phase change which occurs for the displacement correlation in Fig. 5.

III. ANALYSIS OF ACOUSTICALLY COUPLED PANELS

a) Two-dimensional Finite Panel

The vibration of the panel is induced by an arbitrary, external pressure field F . It is assumed that the panel motion does not interact with the turbulent boundary layer, i.e., the forcing field is not altered by the plate motion. However, the panel is acoustically coupled to the fluid on both sides of the panel.

The equation of motion for an harmonic component of the displacement, W , of a thin panel with a force, F , and a pressure differential, $p_2 - p_1 + \delta p$ acting upon it, obeys the equation

$$B\Delta^2 W - \rho_p \omega^2 W = F + p_2 - p_1 + \delta p \quad (1)$$

where the bending stiffness, B , may include hysteretic damping, and where ρ_p is the mass per unit area of the panel, ω is the angular frequency, p_2 is the acoustic pressure on the streamside of the panel, p_1 is the acoustic pressure below the panel and δp is the static pressure differential.

The perturbation pressures, p_1 and p_2 , are related to the velocity potentials, which satisfy time-independent wave equations in the appropriate regions. In solving these equations one uses a boundary condition which relates the potentials to the panel displacement. These relationships may be made more obvious through the use of Green's theorem. Thus, it is required to solve a system of three coupled partial differential equations, the first of which is not separable for the clamped edge boundary condition.

p_1 and p_2 may be found directly as function of W . Thus, consider first the cavity. The acoustic velocity potential, φ , satisfies the Helmholtz equation

$$\Delta \varphi + k^2 \varphi = 0 \quad (2)$$

with boundary condition $\partial \varphi / \partial n = 0$ on all walls except on the plate where $\partial \varphi / \partial n = -i\omega W$.

The Greens function, g , for a cavity with hard walls satisfies

$X = X' = 0.25 \text{ FT}$
 $Y = Y' = 0.25 \text{ FT}$
 PRESS. DIFF. $\Delta p = 14 \text{ psi}$
 400 Hz HI PASS FILTER
 $M_e = 3.03$

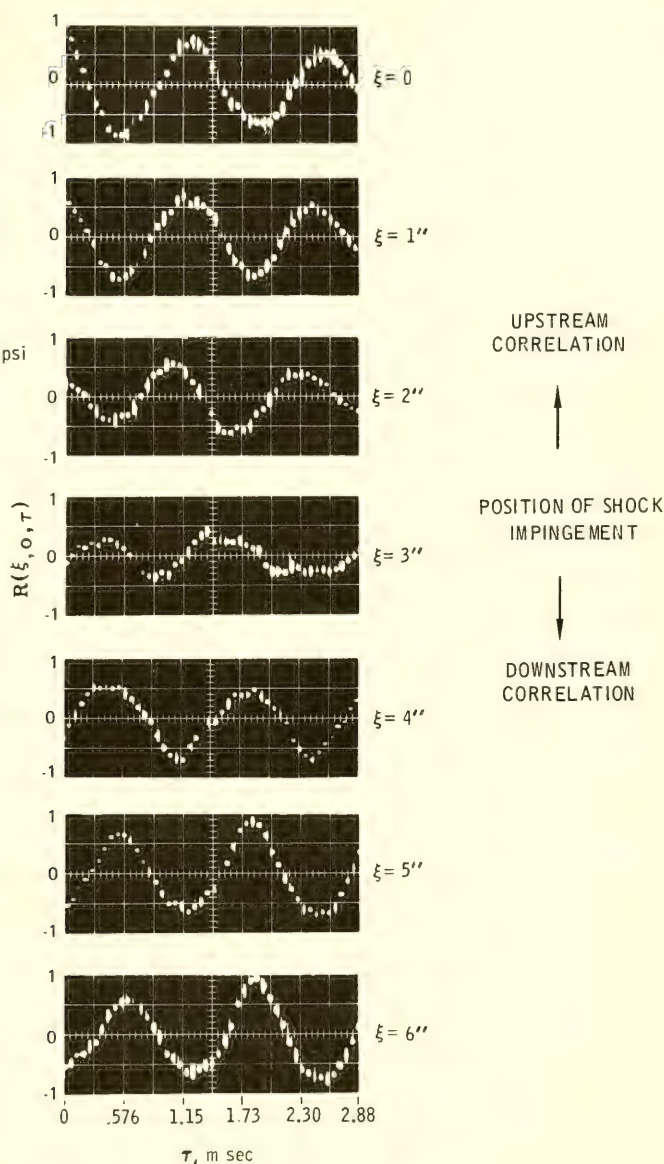


Fig. 5. Broad Band Space Time Correlation of the Panel Displacement Along the Center from $x = x' = 0.25 \text{ ft}$, $y = y' = 0.25 \text{ ft}$.

the equation

$$\Delta g(\vec{r} | \vec{r}) + k_c^2 g(\vec{r} | \vec{r}') = -4\pi\delta(\vec{r} - \vec{r}') \quad (3)$$

and is given by Morse and Feshbach, Vol. II [1953]

$$g(r/r') = -\frac{4\pi}{a_c b_c} \sum_{m=0} \sum_{n=0} \epsilon_m \epsilon_n \frac{\cos \frac{m\pi x}{a_c} \cos \frac{m\pi x'}{a_c} \cos \frac{n\pi y}{b_c} \cos \frac{n\pi y'}{b_c}}{k_{mn} \sin(k_{mn}d)} \\ \times \begin{cases} \cos k_{mn}z \cos k_{mn}(z'+d) & z > z' \\ \cos k_{mn}z' \cos k_{mn}(z+d) & z < z' \end{cases} \quad (4)$$

where

$$k_{mn}^2 = k_c^2 - \left(\frac{m\pi}{a_c}\right)^2 - \left(\frac{n\pi}{b_c}\right)^2$$

and $k_c = \omega/c_c$ where c_c is the speed of sound in the cavity of dimensions a_c, b_c, d .

By applying Green's theorem, the integral equation for φ is obtained,

$$\varphi(\vec{r}) = \frac{1}{4\pi} \int \int_{\text{plate}} g(\vec{r}/\vec{r}_s') \frac{\partial \varphi(\vec{r}_s')}{\partial n'} d\vec{r}_s' \quad (5a)$$

Now using the boundary conditions, this becomes

$$\varphi(\vec{r}) = -\frac{i\omega}{4\pi} \int \int_{\text{plate}} g(\vec{r}/\vec{r}_s') W(\vec{r}_s') d\vec{r}_s' \quad (5b)$$

The pressure p_1 is related to φ by

$$p_1 = -i\omega\rho_c\varphi$$

where ρ_c is the mass density of the fluid in the cavity.

To compute p_2 , it will be more convenient to operate with the differential equation. Let the acoustic velocity potential in the flow

field be denoted by ψ . By applying the Fourier transform on the (x, y) coordinates, one gets the ordinary differential equation

$$\frac{d^2 \hat{\psi}(\alpha, \beta, z)}{dz^2} + \zeta^2 \hat{\psi}(\alpha, \beta, z) = 0 \quad (6)$$

where

$$\zeta^2 = k^2 + (M^2 - 1)\alpha^2 - 2kM\alpha - \beta^2$$

$$\psi(x, y, z) = \int_{-\infty}^{\infty} \int_{-\infty}^{\infty} d\alpha d\beta e^{i(\alpha x + \beta y)} \hat{\psi}(\alpha, \beta, z)$$

$k = \omega/c$, M is the flow Mach number and c the speed of sound in the region above the plate. Only the positive exponential solution to Eq. (6) is chosen, since it is the solution representing outgoing waves. Thus,

$$\hat{\psi}(\alpha, \beta, z) = A(\alpha, \beta) e^{i\zeta z} \quad (7a)$$

The boundary condition, arising from the continuity of normal displacement is

$$\left. \frac{d\hat{\psi}(\alpha, \beta, z)}{dz} \right|_{z=0} = -ic \widehat{LW} \Big|_{z=0}$$

where the differential operator

$$L = k + iM \frac{\partial}{\partial x}$$

Thus,

$$\hat{\psi}(\alpha, \beta, z) = -c \frac{\widehat{LW}}{\zeta} e^{i\zeta z} \quad (7b)$$

Now, since

$$\widehat{LW} = \int_0^a \int_0^b dx' dy' e^{-i(\alpha x' + \beta y')} LW(x', y')$$

then

$$\psi(x, y, z) = - \frac{c}{4\pi^2} \int_0^a \int_0^b dx' dy' G(x, y, z | x', y', 0) L W(x', y') \quad (8)$$

where

$$G(\vec{r} | \vec{r}') = \int_{-\infty}^{\infty} \int_{-\infty}^{\infty} d\alpha d\beta \frac{e^{i[\alpha(x-x') + \beta(y-y') + \zeta(z-z')]}{\zeta} \quad (9)$$

which is found in Appendix A to be for supersonic flow,

$$G(\vec{r} | \vec{r}') = \begin{cases} \frac{2\pi i}{\sqrt{M^2 - 1}} \frac{e^{i\kappa(Mu + \sqrt{u^2 - R^2})}}{\sqrt{u^2 - R^2}} \\ 0 \quad \text{outside the Mach cone} \end{cases}$$

and for subsonic flow,

$$G(\vec{r} | \vec{r}') = \frac{2\pi i}{\sqrt{1 - M^2}} \frac{e^{i\kappa(Mu + \sqrt{u^2 + R^2})}}{\sqrt{u^2 + R^2}} \quad (10)$$

except in this case, $\kappa = k/\sqrt{1 - M^2}$ and $u = (x - x')/\sqrt{1 - M^2}$. If $\hat{L} \hat{W}$ had been evaluated as

$$(k - \alpha M) \hat{W}$$

then Eq. (8) would read

$$\psi(x, y, z) = - \frac{c}{4\pi^2} \int_0^a \int_0^b dx' dy' W(x', y') L^* G(x, y, z | x', y', 0) \quad (11)$$

This equation is formally correct if $L^* G$ is interpreted as a distribution, which is to say that one partially integrates to obtain Eq. (8).

Now using Eq. (8)

$$\begin{aligned} p_2(x, y, z) &= - i\rho_0 c L \psi(x, y, z) \\ &= \frac{i\rho_0 c^2}{4\pi^2} \int_0^a \int_0^b dx' dy' G(x, y, z | x', y', 0) |L|^2 W(x', y') \end{aligned} \quad (12)$$

where ρ_0 is the density of the fluid above the plate, and where partial integration has been utilized. Had Eq. (11) been used instead, Eq. (12) would read

$$p_2(x, y, z) = \frac{i\rho_0 c^2}{4\pi^2} \int_0^a \int_0^b dx' dy' W(x, y) |L|^2 G(x, y, z | x', y', 0) \quad (13)$$

which is reducible to Eq. (12) by partial integration. Thus, supersonic flow does not present any especial difficulty aside from the fact that G is singular all along the Mach cone, and this is an integrable singularity.

Inserting the expressions for p_2 and p_1 into Eq. (1) results in a single partial integro-differential equation to solve, viz.,

$$\begin{aligned} B\Delta^2 W - \rho_p \omega^2 W = F + \delta_p + \frac{i\rho_0 c^2}{4\pi^2} \int_0^a \int_0^b G(x, y, |x', y'|) |L|^2 W(x', y') dx' dy' \\ + \frac{\omega^2 \rho_c}{4\pi} \int \int_{\text{plate}} g(x_c, y_c | x'_c, y'_c) W(x, y) dx dy \quad (14) \end{aligned}$$

where the subscript c refers to the cavity, thus

$$x_c = x + \frac{a_c - a}{2}$$

$$y_c = y + \frac{b_c - b}{2}$$

Equation (14) presents a formidable computational problem. The Green's function g is known as an infinite series which is slow to converge ($1/n$) thus compounding the difficulty by an increasing number of necessary operations to maintain a given accuracy.

An alternative to solving Eq. (14) is to convert it to an integral equation for its Fourier amplitudes and to solve the resulting equation. The advantage is that this equation is simpler (though it is a singular integral equation). The following notation shall be employed:

$$\begin{aligned} \hat{f}(\vec{K}) &= \frac{1}{2\pi} \int_{\text{supp}\{f\}} d\vec{r} e^{-i\vec{K} \cdot \vec{r}} f(\vec{r}) \\ \hat{f}(\vec{r}) &= \frac{1}{2\pi} \int_{\vec{K}\text{-space}} d\vec{K} e^{i\vec{K} \cdot \vec{r}} \hat{f}(\vec{K}) \end{aligned}$$

The result of applying the Fourier transform to Eq. (1) is

$$B\Delta^2 \hat{W} - \rho_p \omega^2 \hat{W} = \hat{f} + \hat{p}_2 - \hat{p}_1 \quad (15)$$

where

$$f = F + \delta_p$$

The first term in (15) may be evaluated using Green's theorem; thus,

$$\Delta^2 \hat{W} = K^4 \hat{W} + \oint d\vec{r}_s \frac{\partial}{\partial n} \left[e^{-i\vec{K} \cdot \vec{r}} (\Delta W + K^2 W) \right] \quad (16a)$$

Now, for a plate clamped on its edge to a rigid, plane support, the following boundary conditions hold,

$$\left. \begin{aligned} W = \partial_n W &= 0 \\ \frac{\partial^2 W}{\partial s^2} = \frac{\partial^3 W}{\partial n \partial s^2} &= 0 \end{aligned} \right\} \quad \text{on edge}$$

where s is in the direction of the edge, i.e., the tangent. Thus,

$$\Delta^2 \hat{W} = K^4 \hat{W} + \Lambda[W] \quad (16b)$$

where

$$\Lambda[W] = \oint d\vec{r}_s \left(\frac{\partial^3 W}{\partial n^3} - i(\vec{K} \cdot \vec{n}) \frac{\partial^2 W}{\partial n^2} \right) e^{-i\vec{K} \cdot \vec{r}_s}$$

If more general boundary conditions are to be considered (e.g. elastic foundation) the above expression must be replaced by the right side of 16a. From the Eq. (7b) and the equation prior to Eq. (12) it is found that

$$\hat{p}_2 = \frac{i\rho_0 c^2 (k - \alpha M)^2}{\zeta} \hat{W}(\vec{K}) \quad (17)$$

From Eq. (5b) it is found that

$$\begin{aligned}\hat{p}_1 &= -\frac{\omega^2 \rho_0}{4\pi} \int_{\text{plate}} d\vec{r}_s g(\vec{K} | \vec{r}_s) W(\vec{r}_s) \\ &= -\Omega[W]\end{aligned}$$

where

$$g(\vec{k} | \vec{r}') = \frac{1}{2\pi} \int_{\text{plate}} d\vec{r} e^{-i\vec{k} \cdot \vec{r}} g(\vec{r} | \vec{r}') \quad (18)$$

Substituting these results into Eq. (15) gives

$$B\Gamma(\vec{K})\hat{W}(\vec{k}) + B\Lambda[W] - \Omega[W] = \hat{f}(\vec{K}) \quad (19)$$

where

$$\Gamma(\vec{K}) = K^4 - \frac{\rho_p \omega^2}{B} - \frac{i\rho_0 c^2 (k^2 - \alpha^2 M^2)}{B\zeta} \quad (19a)$$

Let ψ_n denote the finite Fourier transform of a beam eigenfunction, φ_n . It follows from the Fourier representation that the ψ_n form an orthogonal set on the infinite interval. Thus, expanding \hat{W} as

$$\hat{W}(\vec{K}) = \sum_{m,n} W_{mn} \psi_m(\alpha a) \psi_n(\beta b) \quad (20)$$

or alternatively, W as

$$W(\vec{r}) = \sum_{m,n} W_{mn} \varphi_m\left(\frac{x}{a}\right) \varphi_n\left(\frac{y}{b}\right) \quad (21)$$

and introducing these expressions into (19) and subsequently utilizing the orthogonality, gives

$$W_{mn} + \sum_{r,s} \Gamma_{mnrs} W_{rs} = \Phi_{mn} \quad (22)$$

where Φ_{mn} are the projections of

$$\Phi(\vec{k}) = \frac{\hat{f}(\vec{K})}{\Gamma(\vec{K})} = \sum_{m,n} \Phi_{mn} \psi_m(\alpha a) \psi_n(\beta b)$$

and

$$\Gamma_{mnrs} = \int_{-\infty}^{\infty} \int_{-\infty}^{\infty} d\vec{K} \frac{\psi_m^*(\alpha a) \psi_n^*(\beta b)}{\Upsilon(\vec{K})} \left(B\Lambda \left[\varphi_r \left(\frac{x}{a} \right) \varphi_s \left(\frac{y}{b} \right) \right] - \Omega \left[\varphi_r \left(\frac{x}{a} \right) \varphi_s \left(\frac{y}{b} \right) \right] \right)$$

The computation of the integral Γ_{mnrs} may be simplified by deforming the contour on the α -plane. Due to the manner in which the Fourier transform was chosen, the integrand, except the term $\Upsilon(\vec{k})$, is single-valued and analytic in the lower half-plane. The contour will, thus, be deformed in this half-plane. This deformation is determined by the analytic properties of the function $\Upsilon(\vec{k})$, Eq. (19a).

$$\Upsilon(\alpha, \beta) = (\alpha^2 + \beta^2)^2 - \frac{\rho_p \omega^2}{B} \frac{i \frac{\rho_0 \omega^2}{B} \left(1 - \frac{\alpha^2 M^2}{k^2} \right)}{\sqrt{k^2 + (M^2 - 1)\alpha^2 - 2kM\alpha - \beta^2}}$$

This function is two-sheeted with square-root type branch points at

$$\frac{kM \pm \sqrt{k^2 + (M^2 - 1)\beta^2}}{M^2 - 1}$$

The sheet associated with the positive value of the square root will be termed the physical sheet, since it corresponds to outgoing radiation.

The function has ten zeros on the two sheets, four zeros on each sheet with the same values, corresponding to resonances of the plate and the other two zeros are located near the branch points on one of the two sheets, independent of each other.

It is convenient to make the following substitutions

$$\mu = \frac{\rho_0}{\rho_p} \quad \text{and} \quad \gamma^4 = \frac{\rho_p \omega^2}{B}$$

The Eq. (19a) may be written

$$T(\alpha, \beta) = (\alpha^2 + \beta^2)^2 - \gamma^4 - \frac{i\mu\gamma^4\left(1 - \frac{\alpha^2 M^2}{k^2}\right)}{\sqrt{k^2 + (M^2 - 1)\alpha^2 - 2kM\alpha - \beta^2}}$$

In the present case, μ is a small number (≈ 0.0015) so that approximate values of the zeros may be found, expressed as a power series in μ . To the second order these zeros are

$$\alpha_s^\pm = A_s^\pm - \frac{\mu^2}{2} \frac{\left[1 - \left(\frac{A_s^{\pm 2} M^2}{k^2}\right)^2\right] \gamma^8}{\sqrt{[k^2 + (M^2 - 1)\beta^2](A_s^{\pm 4} + 2A_s^{\pm 2}\beta^2 + \beta^4 - \gamma^4)^2}}$$

where

$$A_s^\pm = \frac{kM \pm \sqrt{k^2 + (M^2 - 1)\beta^2}}{M^2 - 1}$$

$$\alpha_{(\pm)_1(\pm)_2} = A_{(\pm)_1(\pm)_2}$$

$$+ \mu \frac{i\gamma^4 \left[1 - \left(\frac{MA_{(\pm)_1(\pm)_2}}{k}\right)^2\right]}{4A_{(\pm)_1(\pm)_2}(\beta^2 + A_{(\pm)_1(\pm)_2}^2) \left[k^2 + (M^2 - 1)A_{(\pm)_1(\pm)_2}^2 - 2kMA_{(\pm)_1(\pm)_2} - \beta^2\right]^{1/2}}$$

where

$$A_{(\pm)_1(\pm)_2} = (\pm)_1 \sqrt{-\beta^2(\pm)_2} \gamma^2$$

The last four zeros exist on both sheets. The location of the first two zeros may be distinguished into three possibilities: when $\gamma < A_s^-$ then α_s^- and α_s^+ are respectively on the unphysical and physical sheets; as γ is increased such that $A_s^- < \gamma < A_s^+$, then α_s^- moves off the unphysical sheet and crosses over to the physical sheet and α_s^+ remains unchanged; as γ is further increased such that $A_s^+ < \gamma$ then α_s^+ crosses over to the unphysical sheet and α_s^- remains unchanged. A typical configuration for the poles and branch points is shown in Fig. 6.

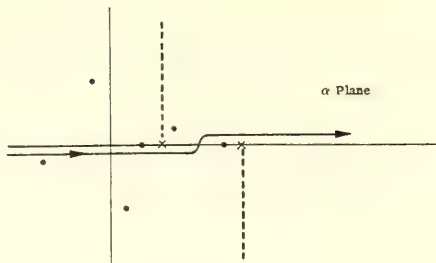


Fig. 6. Integration Contour for Γ_{mnr}

The above contour, Fig. 6, is deformed to circulations about poles and branch cut in the appropriate half-planes of analyticity as indicated below, Fig. 7, for the upper half-plane.

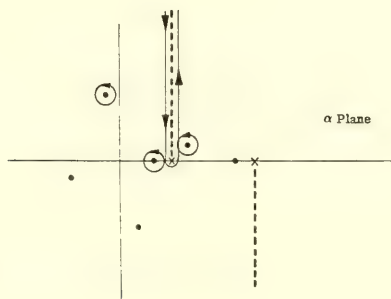


Fig. 7. Deformed Integration Contours for Γ_{mnr}

The function Υ has been analytically continued into the k -plane by giving k a small negative imaginary part; so that, the branch points and the poles are displaced off the real axis as indicated in the previous figures.

The branch-cut integral is given by

$$I(\beta) = \int_0^\infty dt \frac{\psi_m(a\alpha) [B\Lambda(\alpha, \beta) - \Omega(\alpha, \beta)] \left(-\frac{2i\rho_0 c^2 (k - \alpha M)^2}{\sqrt{k^2 + (M^2 - 1)\alpha^2 - 2kM\alpha - \beta^2}} \right)}{[B(\alpha^2 + \beta^2)^2 - \rho_p \omega^2]^2 + \left(\frac{\rho_0 c^2 (k - \alpha M)^2}{\sqrt{k^2 + (M^2 - 1)\alpha^2 - 2kM\alpha - \beta^2}} \right)}$$

where $\alpha = A_s^-$ - it. So that

$$\Gamma_{mns} = \int 2\pi i \sum \text{residues } d\beta + \int_{-\infty}^{\infty} \psi_n(\beta b) I(\beta) d\beta$$

The branch-cut integral is exponentially damped rather oscillatory, so it may be readily performed numerically using Laguerre-Gauss quadrature. The second integral is more difficult, it oscillates with a period $2\pi/b$.

In solving Eq. (22) maximum values of the indices are postulated. This is justified, since the index is inversely proportional to some length on the panel. Now there certainly exists, from the experimental point of view, a smallest length to which a disturbance may be localized. After having solved Eq. (22) the plate displacement is simply the Fourier transform of (21), thus,

$$W(\vec{r}) = \sum_{m,n} W_{mn} \varphi_m\left(\frac{x}{a}\right) \varphi_n\left(\frac{y}{b}\right) \quad (23)$$

where φ_m is a beam eigenfunction.

To find the sound pressure level in the cavity the expression for W from Eq. (23) is inserted into Eq. (5b) to give

$$p_l(\vec{r}) = \frac{\omega^2 \rho_c}{a_c b_c} \sum_{m,n} \sum_{r,s} W_{rs} I_{mr} J_{ns} \frac{\cos \frac{m\pi x_c}{a_c} \cos \frac{n\pi y_c}{b_c} \cos k_{mn}(z+d)}{k_{mn} \sin k_{mn} d}$$

where I_{mr} and J_{ns} are given in the appendix B.

Similarly, the radiation may be computed from Eq. (12).

The force is not a deterministic function as has been implicitly assumed from the outset, but a stochastic variable whose correlation properties are known, either via a model or directly from experimental data. Thus, it would only be meaningful to compute statistical averages of the response based on statistical averages of the force (i.e. cross-correlation). The procedure to be used is an amendment of a procedure due to Rosenblatt [1962], the notation is that of Rosenblatt.

Consider a homogeneous, stationary, random process $X_{\vec{r},t}$ (Rosenblatt writes this as $X_{\vec{r},t}(\omega)$ to explicitly indicate that it is a function defined on a sample space) with a cross-correlation defined as

$$R(\vec{r}, t; \vec{r}', t') = \langle X_{\vec{r},t} X_{\vec{r}',t'} \rangle \quad (24)$$

where $\langle \rangle$ is the expectation operator, i.e., R is defined through the ensemble average. Because the process is homogeneous and stationary,

$$R(\vec{r}, t; \vec{r}', t') = R(\vec{r} - \vec{r}', t - t')$$

or

$$R(\vec{r} - \vec{r}', t - t') d\vec{r} dt = \langle dM(x_{\vec{r},t}) dM(x_{\vec{r}',t'}) \rangle$$

where $dM(x_{\vec{r},t})$ is the Stieljes measure of the process. The procedure may be simply stated as the problem of finding a Fredholm expansion of R and subsequently representing $X_{\vec{r},t}$ by such an expansion. Such an expansion is provided by the eigenfunctions and eigenvalues of the integral equation

$$\psi(\vec{r}, t) = \lambda \int_{-\infty}^{\infty} R(\vec{r} - \vec{r}', t - t') \psi(\vec{r}', t') d\vec{r}' dt \quad (25)$$

The spectrum, is of course, continuous. The eigenfunctions are plane waves and the eigenvalues the inverse of the power spectral density as can be seen by applying the Fourier transform. Thus the desired expansion for R is

$$R(\vec{r} - \vec{r}', t - t') = \left(\frac{1}{2\pi}\right)^2 \int_{-\infty}^{\infty} e^{i[\vec{K} \cdot (\vec{r} - \vec{r}') - (\omega - \omega')] } \hat{R}(\vec{K}, \omega) d\vec{K} d\omega$$

Now let

$$Z_{\vec{K},\omega} = \frac{1}{(2\pi)^2 \sqrt{R(\vec{K}, \omega)}} \int_{-\infty}^{\infty} e^{i[\vec{K} \cdot \vec{r} - \omega t]} dM(x_{\vec{r},t}) \quad (26)$$

It follows from (24) and (26) that

$$\langle Z_{\vec{K},\omega} Z_{\vec{K}',\omega'} \rangle = \delta(\vec{K} - \vec{K}') \delta(\omega - \omega')$$

since $\langle dM(\vec{X}_{r,t}) dM(\vec{X}_{r',t'}) \rangle = R(\vec{r} - \vec{r}', t - t') d\vec{r} dt$.

Thus the $Z_{\vec{K},\omega}$ are independent random variables with unit variance and with zero mean if $EX_{r,t} = 0$. The transform of (26) is,

$$\vec{X}_{r,t} = \int_{-\infty}^{\infty} Z_{\vec{K},\omega} \sqrt{R(\vec{K},\omega)} e^{-i(\vec{K} \cdot \vec{r} - \omega t)} d\vec{K} d\omega \quad (27)$$

A simple calculation reveals that (27) satisfies (24).

These results will now be applied to the plate displacement. Thus, the cross-power spectral density (CPSD) of the plate response is given by (asterisk denotes complex conjugate)

$$\langle W(\vec{r}) W^*(\vec{r}') \rangle = \sum_{m,n,r,s} \varphi_m\left(\frac{x}{a}\right) \varphi_n\left(\frac{y}{b}\right) \varphi_r\left(\frac{x'}{a}\right) \varphi_s\left(\frac{y'}{b}\right) \langle W_{mn} W_{rs}^* \rangle \quad (28)$$

Now if the solution to Eq. (22) is represented as

$$W_{mn} = \sum_{i,j} \gamma_{mnij} \Phi_{ij}$$

then

$$\langle W_{mn} W_{rs}^* \rangle = \sum_{ijkl} \gamma_{mnij} \gamma_{rskl}^* \langle \Phi_{ij} \Phi_{kl}^* \rangle$$

Further,

$$\langle \Phi_{ij} \Phi_{kl}^* \rangle = \int_{-\infty}^{\infty} \int_{-\infty}^{\infty} d\vec{K} d\vec{K}' \frac{\psi_i(\alpha a) \psi_j(\beta b) \psi_k^*(\alpha' a) \psi_l^*(\beta' b)}{\Gamma(\vec{K}) \Gamma^*(\vec{K}')} \langle f(\vec{K}) f^*(\vec{K}') \rangle$$

The force F is now identified with $X_{\vec{r},t}$ so that

$$\begin{aligned} \langle \hat{f}(\vec{K}) \hat{f}^*(\vec{K}') \rangle &= [\hat{R}(\vec{K}, \omega) \hat{R}^*(\vec{K}', \omega)]^{1/2} \langle Z_{\vec{K},\omega} Z_{\vec{K}',\omega}^* \rangle \\ &= [\hat{R}(\vec{K}, \omega) \hat{R}^*(\vec{K}', \omega)]^{1/2} \delta(\vec{K} - \vec{K}') \end{aligned}$$

In summary then

$$\langle W_{mn} W_{rs}^* \rangle = \sum_{i,j,k,l} \gamma_{mnij} \gamma_{rskl}^* \int_{-\infty}^{\infty} d\vec{K} \frac{\psi_i(\alpha a) \psi_j(\beta b) |R(\vec{K}, \omega)| \psi_k^*(\alpha a) \psi_l^*(\beta b)}{|\Gamma(\vec{K})|^2} \quad (29)$$

Analogous to (28), the expression for the CPSD of P_1 can be written in terms of $EW_{mn}W_{rs}^*$ from (29). The same can also be done for the radiation.

b) One Dimensional Model

To simplify the computations we assume that the transverse plate dimension is very large and that no flexural waves propagate in the transverse direction. With these simplifications Eq. (22) may be written

$$W_n + \sum_m \Gamma_{nm} W_m = \Phi_n \quad (30)$$

where

$$\Gamma_{nm} = \int_{-\infty}^{\infty} dK \frac{\psi_n^*(Ka) \Lambda \left[\varphi_m \left(\frac{x}{a} \right) \right]}{\Upsilon(K)} \quad (31)$$

where

$$\Upsilon(K) = K^4 - \gamma^4 - \frac{i\mu\gamma^4 \left(1 - \frac{K^2 M^2}{k} \right)}{\sqrt{k^2 + (M^2 - 1)K^2 - 2kKM}}$$

and

$$\Phi_n = \int_{-\infty}^{\infty} dK \frac{\psi_n^*(aK) F(K)}{\Upsilon(K)} \quad (32)$$

The circumvention of the branch points in the above expressions will be described shortly.

If G_{mn} denotes the inverse matrix to $\delta_{mn} + \Gamma_{mn}$ then the solution to (30) is

$$W_n = \sum_m G_{nm} \phi_m$$

Now performing the ensemble averages as before gives

$$\langle W_m W_n^* \rangle = \sum_{r,s} G_{mr} \langle \phi_r \phi_s^* \rangle G_{ns}^* \quad (33)$$

but

$$\langle \phi_r \phi_s^* \rangle = \int_{-\infty}^{\infty} dK \frac{\psi_r^*(aK)}{\Upsilon(K)} \int_{-\infty}^{\infty} dK' \frac{\psi_s(aK')}{\Upsilon^*(K')} \langle F(K) F^*(K') \rangle$$

To make the discussion concrete let

$$\langle F(K) F^*(K') \rangle = P(\omega) \delta(K' - (K - \frac{\omega}{U_c}))$$

which corresponds to a spatially uncorrelated pressure field with convection velocity U_c and power spectrum $P(\omega)$.

Thus

$$\langle \phi_r \phi_s^* \rangle = P(\omega) \int_{-\infty}^{\infty} dK \frac{\psi_r^*(aK) \psi_s(aK - \frac{a\omega}{U_c})}{\Upsilon(K) \Upsilon^*(K - \frac{\omega}{U_c})} \quad (34)$$

The major contribution to the integral for Γ_{mn} , Eq. (31), comes about when the peak of ψ_n is close to the peaks of $1/\Upsilon(K)$; since ψ_n is a highly oscillatory function (period = $2\pi/a$) with a peak at χ_n/a and decaying with the distance from this point and $1/\Upsilon(K)$ is a non-oscillatory function with peaks whenever K equals the real part of the poles which are roughly located at γ times the four roots of unity and the trapped wave poles near the branch points $(k/(1+M))(k/(M-1))$. But for the frequencies we are considering (up to 3000 Hz) only the pole near $k/(1+M)$ lies on the physical sheet. For this frequency range the trapped wave pole is bounded by 0 and 0.15 and the pole near γ by 0 and 0.6. Now, the peak of ψ_n^* is given by χ_m/a which is numerically (see Appendix B) 0.155, 0.26, 0.36, 0.465, 0.57, 0.67, ... and the period is 0.206. The height of the peaks decays roughly as $(1/Ka)^3$ is 0.05 of the first. The function $1/\Upsilon(K)$ also has peaks that decay in the same manner. Thus, the infinite matrix Γ_{mn} has appreciably non-zero entries only in the upper left-hand corner. Consequently, we need only compute Γ_{mn} for the first 4 or 5 modes, say, and then invert this matrix + I to obtain the upper left square matrix of order 4 or 5 of G_{mn} and thus for higher modes

$$G_{mn} = \delta_{mn}$$

So that

$$\langle W_m W_n^* \rangle = \langle \phi_m \phi_n^* \rangle$$

for other than the first few modes.

The contour for the integral in (34), Fig. 8, is similar to one

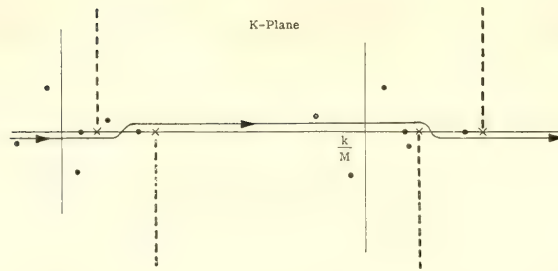


Fig. 8. Contour for $\langle \phi \phi^* \rangle$ in Eq. (34)

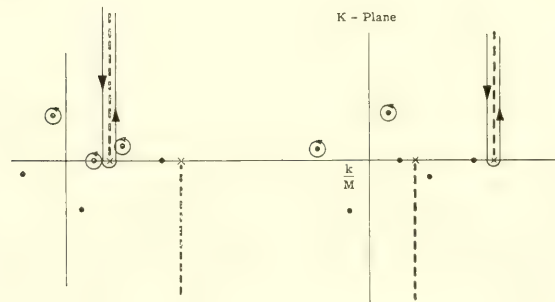


Fig. 9. Deformation of Contour in Fig. 8

described earlier but the term $\Upsilon^*(K - (k/m))$ introduces further poles and branch cuts. The contour and its deformation are shown in the Figs. 8 and 9. In Fig. 9 only the contours for that part of the integrand which is analytic in the upper half-plane are shown.

$\psi_m(K)$ may be written

$$\psi_m(K) = S_m(K) + T_m(K)e^{-iKa}$$

where

$$S_m(K) = -4N_m \frac{i\alpha_m(aK)^3 - \chi_m^3}{(aK)^4 - \chi_m^4}$$

and

$$\frac{1}{2} T_m(K) = N_m \left[(\chi_m + i\alpha_m aK) \left(\frac{\cos \chi_m}{(aK)^2 - \chi_m^2} - \frac{\operatorname{ch} \chi_m}{(aK)^2 + \chi_m^2} \right) \right. \\ \left. - (\alpha_m \chi_m - iaK) \left(\frac{\sin \chi_m}{(aK)^2 - \chi_m^2} + \frac{\operatorname{sh} \chi_m}{(aK)^2 + \chi_m^2} \right) \right]$$

with α_m and χ_m defined in Appendix B.

Now

$$\psi_m^*(K) \psi_n(K - \frac{\omega}{U_c}) = L(K) + U(K)$$

where

$$L(K) = S_m^*(K) \left(S_n(K - \frac{\omega}{U_c}) + T_n(K - \frac{\omega}{U_c}) e^{-i(K - \frac{\omega}{U_c})a} \right)$$

and

$$U(K) = e^{i(a\omega/U_c)} T_m^*(K) \left(S_n(K - \frac{\omega}{U_c}) + T_n(K - \frac{\omega}{U_c}) e^{i(K - \frac{\omega}{U_c})a} \right)$$

Thus, we have

$$\langle \phi_m \phi_n^* \rangle = P(\omega) \int_{-\infty}^{\infty} dK \frac{L(K) + U(K)}{T(K) T^*(K - \frac{\omega}{U_c})}$$

The above expression is evaluated as a sum of residue contributions plus branch-cut integrals.

$$\frac{1}{P(\omega)} \langle \phi_m \phi_n^* \rangle = 2\pi i \sum_{j=1}^5 \operatorname{Res} \left\{ \frac{L(z_j)}{T(z_j) T^*(z_j - \frac{\omega}{U_c})} \right\} + I_1 + I_2 \\ + 2\pi i \sum_{\substack{j=7 \\ j=9}}^{12} \operatorname{Res} \left\{ \frac{L(z)}{T(z) T^*(z - \frac{\omega}{U_c})} \right\} + I_3 + I_4$$

where the z_j are identified in the above figure.

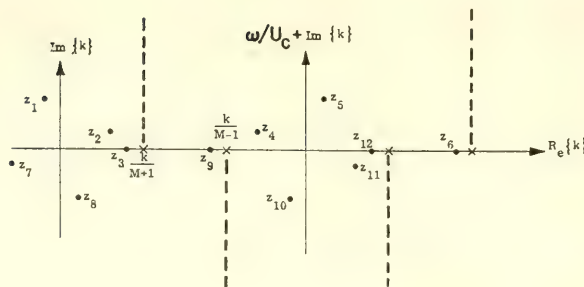


Fig. 10. Location of Poles and Branch Cuts

As indicated previously, z_6 and z_9 are not on the physical sheet for the range of frequencies considered (up to 14,000 Hz).

$$I_1 = \int_0^\infty dy \frac{U\left(\frac{k}{M+1} + iy\right)}{\Gamma^*\left(\frac{k}{M+1} - \frac{\omega}{U_c} + iy\right)} \left[\frac{1}{\Gamma^+\left(\frac{k}{M+1} + iy\right)} - \frac{1}{\Gamma^-\left(\frac{k}{M+1} - iy\right)} \right]$$

where $\Gamma^+\left(\frac{k}{M+1} + iy\right)$ is the expression following Eq. (31), the plus being included only to explicate that it is the positive side of the square root branch cut. $\Gamma^-\left(\frac{k}{M+1} + iy\right)$ is obtained from Γ^+ by replacing μ by $-\mu$.

$$I_2 = - \int_0^\infty dy \frac{U\left(\frac{k}{M-1} + \frac{\omega}{U_c} + iy\right)}{\Gamma\left(\frac{k}{M-1} + \frac{\omega}{U_c} + iy\right)} \left[\frac{1}{\Gamma^{+*}\left(\frac{k}{M-1} + iy\right)} - \frac{1}{\Gamma^{-*}\left(\frac{k}{M-1} + iy\right)} \right]$$

$$I_3 = - \int_0^\infty dy \frac{L\left(\frac{k}{M-1} - iy\right)}{\Gamma^*\left(\frac{k}{M-1} - \frac{\omega}{U_c} - iy\right)} \left[\frac{1}{\Gamma^{+*}\left(\frac{k}{M-1} - iy\right)} - \frac{1}{\Gamma^{-*}\left(\frac{k}{M-1} + iy\right)} \right]$$

$$I_4 = - \int_0^\infty dy \frac{L\left(\frac{k}{M+1} + \frac{\omega}{U} - iy\right)}{\Gamma\left(\frac{k}{M+1} + \frac{\omega}{U_c} - iy\right)} \left[\frac{1}{\Gamma^{+*}\left(\frac{k}{M+1} - iy\right)} - \frac{1}{\Gamma^{-*}\left(\frac{k}{M+1} - iy\right)} \right]$$

It is felt, that the effect of the pole at z_3 cancels the contribution of I_1 and similarly the residue at z_{12} cancels the contribution of I_3 .

Thus only I_2 and I_4 will contribute. Therefore

$$\frac{1}{P(\omega)} \langle \phi_m \phi_n^* \rangle = 2\pi i \sum_{\substack{j=1 \\ j \neq 3}}^5 \operatorname{Res}_{z=z_j} \left\{ \frac{U(z)}{\Gamma(z) \Gamma^*(z - \frac{\omega}{U_c})} \right\} + I_2 \\ + 2\pi i \sum_{\substack{j=7 \\ j \neq 9}}^{11} \operatorname{Res}_{z=z_j} \left\{ \frac{L(z)}{\Gamma(z) \Gamma^*(z - \frac{\omega}{U_c})} \right\} + I_4$$

By the same argument which eliminated I_1 and I_3 we may replace I_2 and I_4 by pretending that z_6 and z_9 are on the physical sheet and thus

$$I_2 = - 2\pi i \operatorname{Res}_{z=z_6} \left\{ \frac{U(z)}{\Gamma(z) \Gamma^*(z - \frac{\omega}{U_c})} \right\}$$

and

$$I_4 = - 2\pi i \operatorname{Res}_{z=z_9} \left\{ \frac{L(z)}{\Gamma(z) \Gamma^*(z - \frac{\omega}{U_4})} \right\}$$

To evaluate the residues it is necessary to determine

$$\Gamma'(z) = 4z^3 + \frac{i\mu\gamma^4(3zM^2k^2 + z^3M^4 - z^3M^2 - 3kM^3z^2 - k^2z - k^3M)}{\sqrt{k^2 + (M^2 - 1)z^2 - 2kMz}^3}$$

The following relationships among the poles are valid

$$z_4 = \frac{\omega}{U_c} + z_7^* \quad z_5 = \frac{\omega}{U_c} + z_8^* \quad z_6 = \frac{\omega}{U_c} + z_9$$

$$z_{10} = \frac{\omega}{U_c} + z_1^* \quad z_{11} = \frac{\omega}{U_c} + z_2^*$$

$$\lim_{z \rightarrow z_4} \left[\frac{z - z_4}{\Gamma^*(z - \frac{\omega}{U_c})} \right] = \lim_{z \rightarrow z_7^*} \left[\frac{z - z_7^*}{\Gamma^*(z)} \right] = \lim_{z \rightarrow z_7} \left[\frac{z - z_7}{\Gamma^*(z^*)} \right]$$

$$\Gamma^*(z) = z^{*4} - \gamma^4 + \frac{i\mu\gamma^4 \left(1 - \frac{z^{*2} M^2}{k^2} \right)}{\sqrt{k^2 + (M^2 - 1)z^{\frac{*2}{2}} - 2kMz^*}}$$

So

$$\Upsilon^*(z^*) = \Upsilon^-(z)$$

Thus

$$\lim_{z \rightarrow z_4} \left[\frac{z - z_9}{\Upsilon^*(z - \frac{\omega}{U_c})} \right] = \Upsilon^{-1}(z_7)$$

Similarly

$$\lim_{z \rightarrow z_5} \left[\frac{z - z_5}{\Upsilon^*(z - \frac{\omega}{U_c})} \right] = \Upsilon^{-1}(z_8)$$

$$\lim_{z \rightarrow z_6} \left[\frac{z - z_6}{\Upsilon^*(z - \frac{\omega}{U_c})} \right] = \Upsilon^{-1}(z_9)$$

$$\lim_{z \rightarrow z_{10}} \left[\frac{z - z_{10}}{\Upsilon^*(z - \frac{\omega}{U_c})} \right] = \Upsilon^{-1}(z_{11})$$

$$\lim_{z \rightarrow z_{11}} \left[\frac{z - z_4}{\Upsilon^*(z - \frac{\omega}{U_c})} \right] = \Upsilon^{-1}(z_2)$$

$$\begin{aligned} \frac{1}{2\pi i P(\omega)} \langle \phi_m \phi_n^* \rangle &= \frac{U(z_1)}{\Upsilon'(z_1) \Upsilon^*(z_1 - \frac{\omega}{U_c})} + \frac{U(z_2)}{\Upsilon'(z_2) \Upsilon^*(z_2 - \frac{\omega}{U_c})} \\ &+ \frac{U(\frac{\omega}{U_c} + z_7^*)}{\Upsilon(\frac{\omega}{U_c} + z_7^*) \Upsilon^{-1}(z_7)} + \frac{U(\frac{\omega}{U_c} + z_8^*)}{\Upsilon(\frac{\omega}{U_c} + z_8^*) \Upsilon^{-1}(z_8)} \\ &- \frac{U(\frac{\omega}{U_c} + z_9)}{\Upsilon(\frac{\omega}{U_c} + z_9) \Upsilon^{-1}(z_9)} \\ &+ \frac{L(z_7)}{\Upsilon'(z_7) \Upsilon^*(z_7 - \frac{\omega}{U_c})} + \frac{L(z_8)}{\Upsilon'(z_8) \Upsilon^*(z_8 - \frac{\omega}{U_c})} + \end{aligned}$$

$$+ \frac{L(\frac{\omega}{U_c} + z_1^*)}{\Upsilon(\frac{\omega}{U_c} + z_1^*)\Upsilon^{-1}(z_1)} + \frac{L(\frac{\omega}{U_c} + z_2^*)}{\Upsilon(\frac{\omega}{U_c} + z_2^*)\Upsilon^{-1}(z_2)} \\ - \frac{L(z_9)}{\Upsilon'(z_9)\Upsilon^*(z_9 - \frac{\omega}{U_c})}$$

In a similar, though simpler fashion, we may evaluate the integral in Eq. (32).

$$\Lambda \left[\phi_m \left(\frac{x}{a} \right) \right] = A_m(K) + B_m(K)e^{-iKa}$$

where

$$A_m(K) = -\frac{2N_m}{a} \left(\frac{\chi_m}{a} \right)^2 \left[\chi_m - \frac{\cos \chi_m - \operatorname{ch} \chi_m}{\sin \chi_m + \operatorname{sh} \chi_m} iKa \right]$$

and

$$B_m(K) = -\frac{2N_m}{a} \left(\frac{\chi_m}{a} \right)^2 \left[\frac{\chi_m (\cos \chi_m \operatorname{sh} \chi_m + \sin \chi_m \operatorname{ch} \chi_m) - iKa \sin \chi_m \operatorname{sh} \chi_m}{\sin \chi_m + \operatorname{sh} \chi_m} \right]$$

Thus $\psi_n^* \Lambda[\phi_m]$ may be decomposed into factors analytic in upper and lower half-planes, respectively. Denoting these terms by G^+ and G^- we have,

$$\Gamma_{mn} = \int_{-\infty}^{\infty} \frac{G^+(K) + G^-(K)}{\Upsilon(K)} dK$$

where

$$G^+(K) = A_m(K) (S_n^*(K) + T_n^*(K)e^{iKa})$$

and

$$G^-(K) = B_m(K) (T_n^*(K) + S_n^*(K)e)$$

The contour of integration is indicated below.



Fig. 11. Contour for Γ_{mn} Eq. (31)

The contour is deformed in the appropriate half-planes and branch cuts are replaced by poles as discussed previously. Thus,

$$\begin{aligned} \frac{1}{2\pi i} \Gamma_{mn} = & \text{Res}_{z=z_1} \left\{ \frac{G^+(z)}{T(z)} \right\} + \text{Res}_{z=z_1} \left\{ \frac{G^+(z)}{T(z)} \right\} \\ & - \text{Res}_{z=z_7} \left\{ \frac{G^-(z)}{T(z)} \right\} - \text{Res}_{z=z_8} \left\{ \frac{G^-(z)}{T(z)} \right\} \\ & + \text{Res}_{z=z_9} \left\{ \frac{G^-(z)}{T(z)} \right\} \end{aligned}$$

We now invert the matrix $\delta_{mn} + \Gamma_{mn}$. Let us denote this inverse by G_{ij} . Then

$$\langle W_m W_n^* \rangle = G_{mp} \langle \phi_p \phi_q^* \rangle \tilde{G}_{qn}$$

where the tilde denotes Hermitian conjugate and sum of p and q is implied. The final step, then, becomes the diagonalization of the CPSD matrix $\langle W_m W_u^* \rangle$ thus giving the PSD for the actual degrees of freedom of the system.

c) Acoustic Power, Power Radiated

In computing the power radiated, we make use of the unitary matrix U_{ij} which diagonalized the CPSD matrix. The average power radiated, to the far field, P , is given by

$$P \sim \langle \text{Im} \left\{ \psi^* \frac{\partial \psi}{\partial r} \right\} \rangle$$

With the use of the asymptotic form of the Hankel function, the asymptotic form of ψ may be computed. This form is

$$\psi(r, \theta) \xrightarrow{r \rightarrow \infty} \frac{A(\theta) e^{i \frac{kr(\sqrt{1-M^2 \sin^2 \theta} + M \cos \theta)}{M^2 - 1}}}{\sqrt{2\pi i k r} \sqrt{1 - M^2 \sin^2 \theta}}$$

where

$$A(\theta) = \int_0^a dx' e^{i \frac{kx'}{M^2 - 1} \left(\frac{\cos \theta}{\sqrt{1 - M^2 \sin^2 \theta}} - M \right)} W(x')$$

The acoustic velocity in the radial direction u_r is given by

$$\begin{aligned} u_r &= \frac{d\psi}{dr}(r, \theta) \\ &= \frac{ik(\sqrt{1 - M^2 \sin^2 \theta} + M \cos \theta)}{M^2 - 1} \psi(r, \theta) \end{aligned}$$

The pressure, p , a microphone in the far-field would measure is given by

$$\begin{aligned} \frac{1}{\rho c} P &= ik\psi - M \frac{\partial \psi}{\partial x} \\ &= ik\psi - \frac{ikM^2}{M^2 - 1} \psi \\ &= - \frac{ik\psi(r, \theta)}{M^2 - 1} \end{aligned}$$

The average radiated intensity is given by the expectation value

$$\begin{aligned} I &= \frac{1}{2} \text{Re} \langle p u^* \rangle \\ &= - \frac{ik\rho c}{M^2 - 1} \frac{ik(\sqrt{1 - M^2 \sin^2 \theta} + M \cos \theta)}{M^2 - 1} \frac{1}{2} \text{Re} \langle \psi \psi^* \rangle \\ &= \frac{\rho c k^2 (\sqrt{1 - M^2 \sin^2 \theta} + M \cos \theta)}{2(M^2 - 1)^2} \text{Re} \langle \psi \psi^* \rangle \end{aligned}$$

Now,

$$\langle \psi \psi^* \rangle = \frac{1}{(2\pi k r) \sqrt{1 - M^2 \sin^2 \theta}} \langle A(\theta) A^*(\theta) \rangle$$

where

$$\langle A(\theta) A^*(\theta) \rangle = \int_0^a dx \int_0^a dx' e^{i \frac{k(x' \cdot x)}{M^2 - 1} \left(\frac{\cos \theta}{\sqrt{1 - M^2 \sin^2 \theta}} - M \right)} \langle W(x') W^*(x) \rangle$$

and where

$$\langle W(x') W^*(x) \rangle = \sum_m \sum_n \langle W_m W_n^* \rangle \varphi_m(x') \varphi_n(x)$$

Let U_{ij} denote the unitary matrix which diagonalizes $\langle W_m W_n^* \rangle$, i.e., the transformation to the actual degrees of freedom. Further, let λ_m denote the power in the m^{th} degree of freedom, then we have

$$\langle W(x') W^*(x) \rangle = \sum_{i,j,m,n} \varphi_i(x') U_{mi} \lambda_i \delta_{ij} U_{nj}^* \varphi_n(x)$$

The integrals have already been encountered, they are simply the finite Fourier transform of the $\varphi_m(x)$ so that,

$$\langle A(\theta) A^*(\theta) \rangle = \sum_{i,j,m,n} \psi_i(z) U_{mi} \lambda_i \delta_{ij} U_{nj}^* \psi_j(-z)$$

where

$$z = \frac{ik \frac{\cos \theta}{\sqrt{1 - M^2 \sin^2 \theta}} - M}{M^2 - 1}$$

REFERENCES

- Corcos, G. M., "Resolution of Pressure in Turbulence," J. Acoust. Soc. Am., Vol. 35, N2, 1963.
- Crighton, D. G., "Radiation from Turbulence Near a Composite Flexible Boundary," PRDC. Rog. Soc. London A314, 153-173, 1970.
- Crighton, D. G. and Flowcs-Williams, J. E., "Real Space-Time Green's Functions Applied to Plate Vibration Induced by Turbulent Flow," J. Fluid Mech., Vol. 38, Part 2, pp. 305-313, 1969.
- Dolgoval, I. I., "Sound Radiation from a Boundary Layer," Soviet Physics Acoustics, Vol. 15, No. 1, July-Sept. 1969.
- Dowell, E. H., "Transmission of Noise from a Turbulent Boundary Layer Through a Flexible Plate Into a Closed Cavity," J. Acoust. Soc. Am., Vol. 46, 1969.
- Dzygadło, Z., "Forced Vibration of Plate of Finite Length in Plane Supersonic Flow," Proc. Vibration Problem, Warsaw, 1.8, 1967.
- Fahy, A. J. Petlove, "Acoustic Forces on a Flexible Panel Which is Part of Duct Carrying Airflow," J. Sound and Vibration, Vol. 5, 1967.
- Feit, D., "Pressure Radiated by a Point-Excited Elastic Plate," J. Acoust. Soc., Vol. 40, No. 6, pp. 1489-1494, 1966.
- Flowcs-Williams, J. E., "The Influence of Simple Supports on the Radiation From Turbulent Flow Near a Plane Compliant Surface," J. Fluid Mech., Vol. 26, Part 4, pp. 641-649, 1966.
- Lapin, A. D., "Radiation of Sound by a Vibrating Non-Uniform Wall," Soviet Physics - Acoustics, Vol. 13, No. 1, pp. 55-58, July-Sept. 1967.
- Lyamshev, L. M., "On the Sound Radiation Theory From Turbulent Flow Near an Elastic Inhomogeneous Plate," The 6th International Congress of Acoustics, Tokyo, 1968.
- Maestrello, L., "Radiation From and Panel Response to Supersonic Turbulent Boundary Layer," J. Sound Vibration, Vol. 10, 2, 1969.

- Magnus, W. and Oberhettinger, F., Formulas and Theorems for the Special Functions of Mathematical Physics, Chelsea, 1961.
- Morse, P. and Feshback, H., Methods of Theoretical Physics, Chap. 11, McGraw Hill, New York, 1953.
- Pol'tov, V. A. and Pupyzev, V. A., "Vibration and Sound Radiation of a Plate Under Random Loading, Soviet Physics - Acoustics, Vol. 13, No. 2, pp. 210-214, Oct.-Dec. 1967.
- Rosenblatt, M., Random Processes, Chapter VIII, Oxford University Press, New York, 1962.
- Strawderman, W. A., "The Acoustic Field in a Closed Space Behind a Rectangular Simply Supported Plate Excited by Boundary Layer Turbulence, USL Report No. 827, 1967.
- White, P. D. and Cottis, M. G., "Acoustic Radiation From a Plate -- Rib System Excited by Boundary Layer Turbulence, Measurement Analysis Corporation 702-06, 1968.

APPENDIX A

If we make the following changes in variables

$$\xi = \sqrt{(M^2 - 1)} \alpha - \kappa M$$

$$\kappa = \frac{k}{\sqrt{M^2 - 1}}$$

$$u = \frac{x - x'}{\sqrt{M^2 - 1}}$$

then expression for the Green's function in Eq. (9) becomes

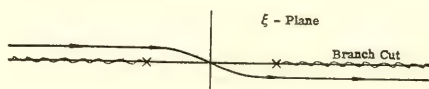
$$\begin{aligned} G(x, y, z | x', y', 0) &= \frac{e^{i\kappa Mu}}{\sqrt{M^2 - 1}} \int_{-\infty}^{\infty} \int_{-\infty}^{\infty} d\xi d\beta \frac{e^{i[\xi u + \beta(y-y') + z\sqrt{\xi^2 - (\kappa^2 + \beta^2)}]}}{\sqrt{\xi^2 - (\kappa^2 + \beta^2)}} \\ &= \frac{e^{i\kappa Mu}}{\sqrt{M^2 - 1}} \int_{-\infty}^{\infty} d\xi e^{i\xi u} \int_{-\infty}^{\infty} d\beta \frac{e^{i[\beta(y-y') + z\sqrt{(\xi^2 + \kappa^2) - \beta^2}]} }{\sqrt{\xi^2 - \kappa^2 - \beta^2}} \end{aligned}$$

(see M + F, Vol. 1, Page 823)

$$= \frac{\pi e^{i\kappa Mu}}{\sqrt{M^2 - 1}} \int_{-\infty}^{\infty} d\xi e^{i\xi u} H_0^{(1)}(R\sqrt{\xi^2 - \kappa^2})$$

$$R^2 = (y - y')^2 + z^2$$

The contour of integration for the above integral is shown below.



Define

$$I(u) = \int_{-\infty}^{\infty} d\xi e^{i\xi u} H_0^{(1)}(R\sqrt{\xi^2 - \kappa^2})$$

By considering the asymptotic form of the Hankel function, the above integral is seen to be convergent in the upper half-plane for values of u and R such that

$$u > R$$

that is, the region inside the Mach cone.

The contour may be deformed to be a contour along the branch cut as shown below.



Thus

$$\begin{aligned}
 I(u) &= \left[\int_{\kappa}^{\infty} \int_{\text{below cut}}^{\infty} - \int_{\infty}^{\kappa} \int_{\text{above cut}}^{\kappa} \right] e^{i\xi u} H_0^{(1)}(R\sqrt{\xi^2 - \kappa^2}) d\xi \\
 &= \int_{\kappa}^{\infty} e^{i\xi u} H_0^{(2)}(R\sqrt{\xi^2 - \kappa^2}) - \int_{\kappa}^{\infty} e^{i\xi u} H_0^{(1)}(R\sqrt{\xi^2 - \kappa^2}) d\xi \\
 &= -2 \int_{\kappa}^{\infty} e^{i\xi u} J_0(R\sqrt{\xi^2 - \kappa^2}) d\xi
 \end{aligned}$$

We thus get (see Magnus and Oberhettinger, p. 179)

$$I(u) = 2i \frac{e^{i\kappa\sqrt{u^2 - R^2}}}{\sqrt{u^2 - R^2}}$$

so that

$$\begin{aligned}
 G(\vec{r} | \vec{r}') &= \frac{2\pi i}{\sqrt{M^2 - 1}} \frac{e^{i\kappa(Mu + \sqrt{u^2 - R^2})}}{\sqrt{u^2 - R^2}} \\
 &= \frac{2\pi i}{\sqrt{M^2 - 1}} \frac{e^{i\kappa MR(\cos\theta + \sin\theta)}}{R \sin\theta}
 \end{aligned}$$

APPENDIX B

$$I_{mr} = \int_0^a \cos \frac{m\pi x_c}{a_c} \varphi_r\left(\frac{x}{a}\right) dx$$

$$x_c = x + \frac{a_c - a}{2}$$

$$\varphi_r\left(\frac{x}{a}\right) = \sin \frac{K_r x}{a} - \text{sh} \frac{K_r x}{a} + \alpha_r \left(\cos \frac{K_r x}{a} - \text{ch} \frac{K_r x}{a} \right)$$

$$\begin{aligned}
 \frac{1}{N_r} I_{mr} = & \frac{1}{\left(\frac{\alpha_r}{a} - \frac{m\pi}{a_c}\right)} \left\{ \alpha_r \left(\sin \left[\left(\frac{K_r}{a} - \frac{m\pi}{a_c} \right) a - \frac{m\pi}{a_c} \left(\frac{a_c - a}{2} \right) \right] + \sin \left[\frac{m\pi}{a_c} \left(\frac{a_c - a}{2} \right) \right] \right) \right. \\
 & \left. + \cos \left[\frac{m\pi}{a_c} \left(\frac{a_c - a}{2} \right) \right] - \cos \left[\left(\frac{K_r}{a} - \frac{m\pi}{a_c} \right) a - \frac{m\pi}{a_c} \left(\frac{a_c - a}{2} \right) \right] \right\} \\
 & + \frac{1}{2 \left(\frac{K_r}{a} + \frac{m\pi}{a_c} \right)} \left\{ \cos \left[\frac{m\pi}{a_c} \left(\frac{a_c - a}{2} \right) \right] - \cos \left[\left(\frac{K_r}{a} + \frac{m\pi}{a_c} \right) a + \frac{m\pi}{a_c} \left(\frac{a_c - a}{2} \right) \right] \right. \\
 & \left. + \alpha_r \left(\sin \left[\left(\frac{K_r}{a} + \frac{m\pi}{a_c} \right) a + \frac{m\pi}{a_c} \left(\frac{a_c - a}{2} \right) \right] - \sin \left[\frac{m\pi}{a_c} \left(\frac{a_c - a}{2} \right) \right] \right) \right\} \\
 & + \frac{\frac{\alpha_r}{a}}{\left(\frac{K_r}{a} \right)^2 + \left(\frac{m\pi}{a_c} \right)^2} \left\{ \cos \left[\frac{m\pi}{a_c} \left(\frac{a_c - a}{2} \right) \right] - \cos \left[\frac{m\pi}{a_c} \left(\frac{a + a_c}{2} \right) \right] (\operatorname{ch} K_r + \alpha_r \operatorname{sh} K_r) \right\} \\
 & + \frac{\frac{m\pi}{a_c}}{\left(\frac{K_r}{a} \right)^2 + \left(\frac{m\pi}{a_c} \right)^2} \left\{ \alpha_r \sin \left[\frac{m\pi}{a_c} \left(\frac{a_c - a}{2} \right) \right] - \sin \left[\frac{m\pi}{a_c} \left(\frac{a + a_c}{2} \right) \right] (\operatorname{sh} K_r + \alpha_r \operatorname{ch} K_r) \right\}
 \end{aligned}$$

where

$$\alpha_r = \frac{\cos K_r - \operatorname{ch} K_r}{\sin K_r + \operatorname{sh} K_r}$$

and the normalization N_r is given by [Dzygadło 1967]

$$\begin{aligned}
 N_r^{-2} = & \frac{1}{4K_r} (\operatorname{sh} 2K_r - \sin 2K_r) + \frac{1}{K_r} (\operatorname{sh} K_r \cos K_r - \sin K_r \operatorname{ch} K_r) \\
 & + \frac{\alpha_r}{2K_r} (\operatorname{ch} 2K_r - \cos 2K_r - 4 \sin K_r \operatorname{sh} K_r) \\
 & + \alpha_r^2 \left[1 + \frac{1}{4} (\sin 2K_r + \operatorname{sh} 2K_r) \right. \\
 & \left. - \frac{1}{K_r} (\sin K_r \operatorname{ch} K_r + \operatorname{sh} K_r \cos K_r) \right]
 \end{aligned}$$

and the eigenvalues K_r are the roots of the equation

$$\cos K_r \cosh K_r = 1$$

and are approximately given by

$$\kappa_1 = 4.730 \quad \kappa_2 = 7.853 \quad \kappa_r = \frac{\pi}{2} (2n + 1)$$

J_{ns} is the same as I_{ns} with a and a_c replaced by b and b_c , respectively.

APPENDIX C

$$\Lambda[w] = \oint d\mathbf{r}_s \left[\frac{\partial^3 w}{\partial n^3} - i(\vec{K} \cdot \vec{n}) \frac{\partial^2 w}{\partial n^2} e^{-i\vec{K} \cdot \vec{r}} \right]$$

Now

$$\begin{aligned} \Lambda \left[\varphi_m \left(\frac{x}{a} \right) \varphi_n \left(\frac{y}{b} \right) \right] &= Q(m, n, \alpha, \beta, a, b) \\ &- Q(n, m, \beta, \alpha, b, a) \end{aligned}$$

where φ is defined in Appendix A and

$$Q(m, n, \alpha, \beta, a, b)$$

$$= 2 \left(\frac{\kappa_n}{b} \right)^2 \left[\frac{\kappa_n}{b} - i\alpha_n \beta + e^{-i\beta b} \left(\frac{\kappa_n}{b} \operatorname{ch} \kappa_n + i\beta \frac{\operatorname{sh}^2 \kappa_n}{\sin \kappa_n - \operatorname{sh} \kappa_n} \right) \right] \int_0^a dx e^{-i\alpha x} \varphi_m \left(\frac{x}{a} \right)$$

The integral may be found by appropriately combining the following four integrals

$$\begin{aligned} \int_0^a \sin \kappa_n \frac{x}{a} e^{i\alpha x} dx &= \frac{1}{2i} \left[\frac{e^{i(\kappa_n + \alpha a)}}{i \left(\frac{\kappa_n}{a} + \alpha \right)} - \frac{e^{-i(\kappa_n - \alpha a)}}{i \left(\alpha - \frac{\kappa_n}{a} \right)} \right] \\ &= \frac{a}{2} \left[\frac{e^{i(\alpha a - \kappa_n)} - 1}{\alpha a - \kappa_n} - \frac{e^{i(\alpha a + \kappa_n)} - 1}{\alpha a + \kappa_n} \right] \end{aligned}$$

$$\int_0^a \cos \kappa_n \frac{x}{a} e^{i\alpha x} dx = \frac{a}{2i} \left[\frac{e^{i(\alpha a + \kappa_n)} - 1}{\alpha a + \kappa_n} + \frac{e^{i(\alpha a - \kappa_n)} - 1}{\alpha a - \kappa_n} \right]$$

$$\int \operatorname{sh} \kappa_n \frac{x}{a} e^{i\alpha x} = \frac{ai}{2} \left[\frac{e^{\frac{i(\alpha a + i\kappa_n)}{\alpha a + i\kappa_n} - 1}}{\alpha a + i\kappa_n} - \frac{e^{\frac{i(\alpha a - i\kappa_n)}{\alpha a - i\kappa_n} - 1}}{\alpha a - i\kappa_n} \right]$$

$$\int \operatorname{ch} \kappa_n \frac{x}{a} e^{i\alpha x} = \frac{a}{2i} \left[\frac{e^{\frac{i(\alpha a + i\kappa_n)}{\alpha a + i\kappa_n} - 1}}{\alpha a + i\kappa_n} + \frac{e^{\frac{i(\alpha a - i\kappa_n)}{\alpha a - i\kappa_n} - 1}}{\alpha a - i\kappa_n} \right]$$

and where α_n is given in Appendix B.

APPENDIX D

$$\Omega[w] = \frac{\omega^2 \rho_c}{4\pi} \int_{\text{Plate}} d\vec{r}_s / \hat{g}(\vec{k}/\vec{r}_s) \vec{W}(\vec{r}_s)$$

$$\Omega[\varphi_r(x/a)\varphi_s(y/b)] = \omega^2 \rho_c \sum_{\substack{m=0 \\ n=0}}^{\infty} \epsilon_m \epsilon_n \frac{f_m(\alpha a_c) f_n(\beta b_n) I_{mr} I_{ns}}{\kappa_{mn} \sin \kappa_{mn} d}$$

where

$$f_m(x) = x e^{i(m\pi - x)} / [x^2 - (m\pi)^2]$$

and I_{mr} is given in Appendix B.

HYDRODYNAMICS IN THE OCEAN ENVIRONMENT

Thursday, August 27, 1970

Afternoon Session

Chairman: T. Inui
University of Tokyo, Tokyo, Japan

	Page
Recent Research on Ship Waves J. N. Newman, Massachusetts Institute of Technology	519
Variational Approaches to Steady Ship Wave Problems M. Bessho, The Defense Academy, Yokosuka, Japan	547
Wavemaking Resistance of Ships with Transom Stern B. Yim, Naval Ship Research and Development Center	573
Bow Waves Before Blunt Ships and Other Non-Linear Ship Wave Problems G. Dagan, Technion-Israel Institute of Technology, Haifa, Israel, and M. P. Tulin, Hydronautics, Inc.	607
Shallow Water Problems in Ship Hydrodynamics E. O. Tuck and P. J. Taylor, University of Adelaide, Adelaide, South Australia	627

RECENT RESEARCH ON SHIP WAVES

J. N. Newman
Massachusetts Institute of Technology
Cambridge, Massachusetts

50-6700
253-1000

253-6807

ABSTRACT

This paper is concerned with various aspects of the far-field wave pattern generated by a ship or other moving body in steady translation. Section II contains a brief derivation of the classical Kelvin wave pattern, based upon linear inviscid wave theory. In Section III full-scale aerial photographs are presented for the waves generated by the Ferry Boat UNCATENA, and compared both with the theory and with photographic observations of a small scale model of the same vessel. In Section IV we discuss a towing tank experiment, designed to compare the waves generated by a "wavy wall" with the nonlinear theory for this hull form. Finally, in Section V, a third-order solution is outlined for the Kelvin wave system, which indicates the occurrence of a nonlinear instability on the cusp line.

I. INTRODUCTION

Ship waves are intriguing from several viewpoints. To the observer of a moving vessel, either layman or professional, they are a fascinating pattern on the free surface -- in otherwise calm water one might, in fact, regard them as a thing of beauty. To the naval architect they are of primary interest as a source of energy radiation, and hence of wave drag on the vessel. More generally, to ship hydrodynamicists of all disciplines, they are a source of complication, interacting with, and affecting the boundary conditions of, such fields as viscous drag, propeller-hull interactions, sea-keeping, and maneuverability. To a naval vessel ship waves are a possible source of detection, visible for hundreds of wavelengths or ship lengths downstream and to each side of the vessel's track. Similarly, to the operators of all types of vessels, they are a source of damage to property and of personal injury to persons, in or beneath the water surface, or on the shoreline. And, to the theoretical hydrodynamicist, they are the source of seemingly endless challenges, both analytical and computational.

The classical analysis of ship waves using linearized inviscid wave theory, originated in the nineteenth century by Kelvin and Mitchell, has enabled us to understand and predict the qualitative features of ship waves. The period since 1900 has seen a wide variety of refinements and applications of this basic model, and the present unsatisfactory state-of-the-art in no way detracts from the dedicated contributions of Havelock and others, some of whom are in this audience, who labored with ship-wave theory before it was facilitated by digital computers and a more widespread understanding of the methods of mathematical physics.

As in most other branches of ship hydrodynamics, our present knowledge of ship waves is sufficient only for a qualitative understanding of the phenomena, and does not permit quantitative predictions with the accuracy required by most engineering situations. In the past decade many ambitious scientists and engineers have, therefore, abandoned the assumptions of linearization, or of an inviscid fluid. Some of these attempts at fundamental improvements of the Kelvin-Michell approach were summarized by the author in a Panel Report (Newman [1968]) to the Seventh Symposium on Naval Hydrodynamics. The present paper is not intended to cover such a broad range of contributions, but only to report on my own recent and very limited activities in this area, both experimental and theoretical. In the experimental domain, photographic observations have been made of the Ferry Boat UNCATENA and of a small scale model of the same vessel, in order to verify the Kelvin wave pattern prediction and to search for variations in the wave system resulting from scale effects. In addition, a series of experiments have been made in a towing tank with the objective of confirming the striking nonlinear phase-jumps predicted by Howe [1967, 1968]. Finally, in an extensive theoretical investigation, which is reported upon in more detail elsewhere (Newman [1971]), we consider the possibility of third-order nonlinear resonant interactions in ship waves, motivated by the importance of these interactions in the field of ocean waves (Phillips [1966]). For the sake of completeness, we shall first give a brief outline of the classical Kelvin ship-wave system.

II. THE KELVIN SHIP-WAVE PATTERN

Disregarding the local effects close to a ship hull, we can assume that ship waves are a distribution, in wavenumber space, of individual plane water waves. Generally speaking, these are observed to be of small amplitude relative to their wavelength, and the relevant Reynolds numbers are of order 10^6 to 10^9 , so that we are led to a linear potential-flow model. The individual plane wave system can then be described by the free-surface elevation

$$\zeta(x_0, y_0) = A e^{ik(x_0 \cos \theta + y_0 \sin \theta) - i\omega t} \quad (1)$$

where A is the wave amplitude, k is the wavenumber ($2\pi/\lambda$, if λ is the wavelength), θ the direction of propagation of the wave with respect to variations of time t . The kinematic and dynamic properties of the wave motion can be readily determined from the velocity potential, which differs from the above only by a factor

$$(-ig/\omega)e^{kz_0}$$

if the fluid depth is large, the vertical z_0 -axis is positive upwards with $z_0 = 0$ the plane of the undisturbed free surface, and the (x_0, y_0, z_0) coordinates are fixed with respect to the bulk of the fluid volume. Finally, with the above restrictions, the frequency ω and wavenumber k obey the dispersion relation

$$k = \omega^2/g.$$

The most general distribution of these elementary plane waves is obtained by integrating over all scalar wavenumbers k (or frequencies ω) and wave directions θ , so that

$$\zeta(x_0, y_0) = \int_0^\infty dk \int_0^{2\pi} d\theta A(k, \theta) e^{ik(x_0 \cos \theta + y_0 \sin \theta) - i\omega t}. \quad (2)$$

However, steady-state ship waves are independent of time, when viewed from a moving coordinate system which translates with the ship, say with velocity V in the $+x$ direction, and this condition restricts the frequency, or wavenumber, of the contributions to the integrand in (2). If (x, y) denote moving coordinates with

$$x_0 = x + Vt$$

$$y_0 = y,$$

then by direct substitution

$$\zeta(x, y) = \int_0^\infty dk \int_0^{2\pi} d\theta A(k, \theta) e^{ik(x \cos \theta + y \sin \theta) + it(kV \cos \theta - \omega)}. \quad (3)$$

This integral will depend on time, for arbitrary amplitude functions $A(k, \theta)$, unless

$$\omega = kV \cos \theta \quad (4)$$

or from the dispersion relation,

$$k = (g/V^2) \sec^2 \theta. \quad (5)$$

Finally, if the ship's velocity V is positive, it follows from (4) (or from an obvious physical argument) that the wave direction θ must lie in the interval $-\pi/2 \leq \theta \leq \pi/2$. Thus we arrive at the "free-wave" description of the ship-wave system

$$\zeta(x, y) = \int_{-\pi/2}^{\pi/2} d\theta A(\theta) e^{i(g/V^2) \sec^2 \theta (x \cos \theta + y \sin \theta)} \quad (6)$$

which is the starting point for many analyses of wave resistance.

Kelvin's ship-wave pattern may be obtained from (6) by noting that if the polar radius $R = (x^2 + y^2)^{1/2}$ is large compared to the typical wavelength $2\pi V^2/g$, then from the method of stationary phase the dominant contributions to (6) will arise from those angles θ where the phase function

$$(g/V^2) \sec^2 \theta (x \cos \theta + y \sin \theta) \quad (7)$$

is stationary, or

$$\frac{\partial}{\partial \theta} \sec^2 \theta (x \cos \theta + y \sin \theta) = 0. \quad (8)$$

Carrying out the indicated differentiation, it follows that

$$x \tan \theta + y(2 \sec^2 \theta - 1) = 0,$$

or that the significant ship waves will be situated at points such that

$$-|y/x| = \frac{\sin \theta \cos \theta}{2 - \cos^2 \theta}. \quad (9)$$

The behavior of this function is indicated in Fig. 1, and the essential features of a Kelvin system are immediately clear:

1. The waves are confined to a sector $|y/x| < 8^{-1/2} \approx \tan 19^\circ 28'$.
2. On the boundaries of this sector, or cusp line, the waves are oriented at an angle $|\theta| = \cot^{-1} 2^{1/2} \approx 35^\circ 16'$.

3. In the interior of the sector, two distinct wave systems will occur, the diverging ($|\theta| > 35^\circ$) and transverse ($|\theta| < 35^\circ$) systems.

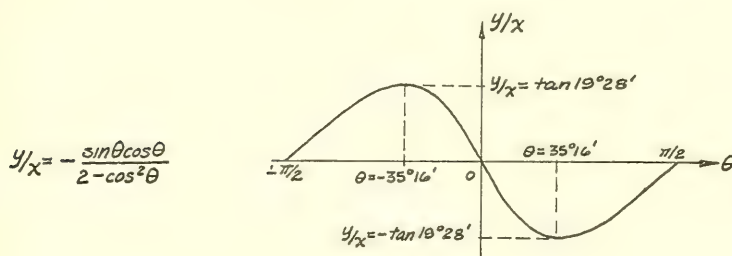


Fig. 1 Plot of y/x , from Eq. (9), as a function of the wave direction θ .

Finally, if the loci of a given wave crest are plotted, by requiring that the wave phase (7) be constant, while (9) is satisfied, the familiar Kelvin wave pattern shown in Fig. 2 is obtained. (The phase difference of $\pi/2$ between the two wave systems along the cusp line is not explainable from the above simplified argument, but is a natural consequence of the method of stationary phase. Fig. 2 is reproduced from Lunde [1951].)

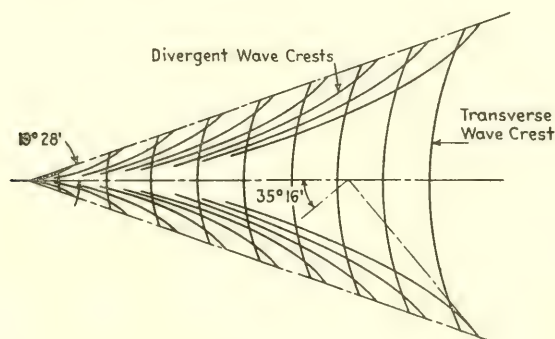


Fig. 2 Wave crests of the Kelvin wave system (from Lunde [1951])

The amplitude of the individual elements in the Kelvin wave system will vary, in accordance with the function $A(\theta)$ or the "free-wave spectrum" of the vessel. Moreover, the wave amplitude will vary as $R^{-1/2}$ for large R , in consequence of the radial spreading

of wave energy. This result follows, too, from the stationary phase approximation, which, in addition, tells us that the attenuation rate is changed to $R^{-1/3}$ on the cusp line. A uniformly valid expansion near the cusp line has been obtained by Peters [1949] and by Ursell [1960]. The latter work includes numerical computations.

III. PHOTOGRAPHIC OBSERVATIONS OF SHIP WAVES

Kelvin's ship-wave pattern, as developed in the preceding section or as originally developed by Lord Kelvin using an initial-value approach, is well known and widely accepted, since the final results are consistent with our observations of ship waves. Nevertheless, and perhaps to the surprise of many, the author knows of no definitive experimental confirmation of the Kelvin pattern. Aerial photographs are generally of the near-field (e.g., Guilloton [1960]; Inui [1962]) or from oblique angles (Wehausen and Laitone [1960], Fig. 23). Stoker's "Water Waves" contains striking high-altitude photographs which are from directly above the vessels, but during turning maneuvers or while in convoys. One exception to the above may be a special volume* on aerial reconnaissance prepared during World War II, but this is not generally available, nor has it been used at all for a comparison with theory.

Two years ago I had the opportunity to obtain aerial photographs of the Ferry Boat M. V. UNCATENA. This vessel is 147 feet long by 28 feet waterline beam and 9 feet draft, displaces 400 tons, and operates at a speed of $15\frac{1}{2}$ knots between Woods Hole and Martha's Vineyard, Massachusetts. Propulsion is from three propellers, turning at 1,200, 1,000, and 1,200 rpm. The water depth in the area where photographs were made ranges from 50 feet to 80 feet, with depths of 70 feet predominant. Originally, this vessel was chosen for observation because of the severe wave systems which it generated, in consequence of its high (0.38) Froude number. Preliminary observations from a surface vessel indicated the most severe waves to be substantially shorter than those which are predicted on the cusp line of the Kelvin wave system, but it is apparent from the subsequent photographic observations that these waves, in fact, are located inside the $19^{\circ}28'$ boundary of the cusp line.

Three of the photographs obtained are shown here as Figs. 3 - 5. These were made with a Hasselblad 2-1/4 X 2-1/4 inch camera and a wide-angle lens of 38 mm focal length. Figures 3 and 4 were taken consecutively, looking directly downward from an altitude of 1,000 feet. Figure 5 is an oblique shot from 1,600 feet. As is clear from these photographs, the predominant waves generated are a portion of the diverging wave system, lying inside of the $19\frac{1}{2}^{\circ}$ cusp line. In Figs. 3 and 4 we have drawn in boundary lines $\pm 19^{\circ}28'$

*"Speed of Shipping," revised edition, Central Interpretation Unit, revised November 1943.

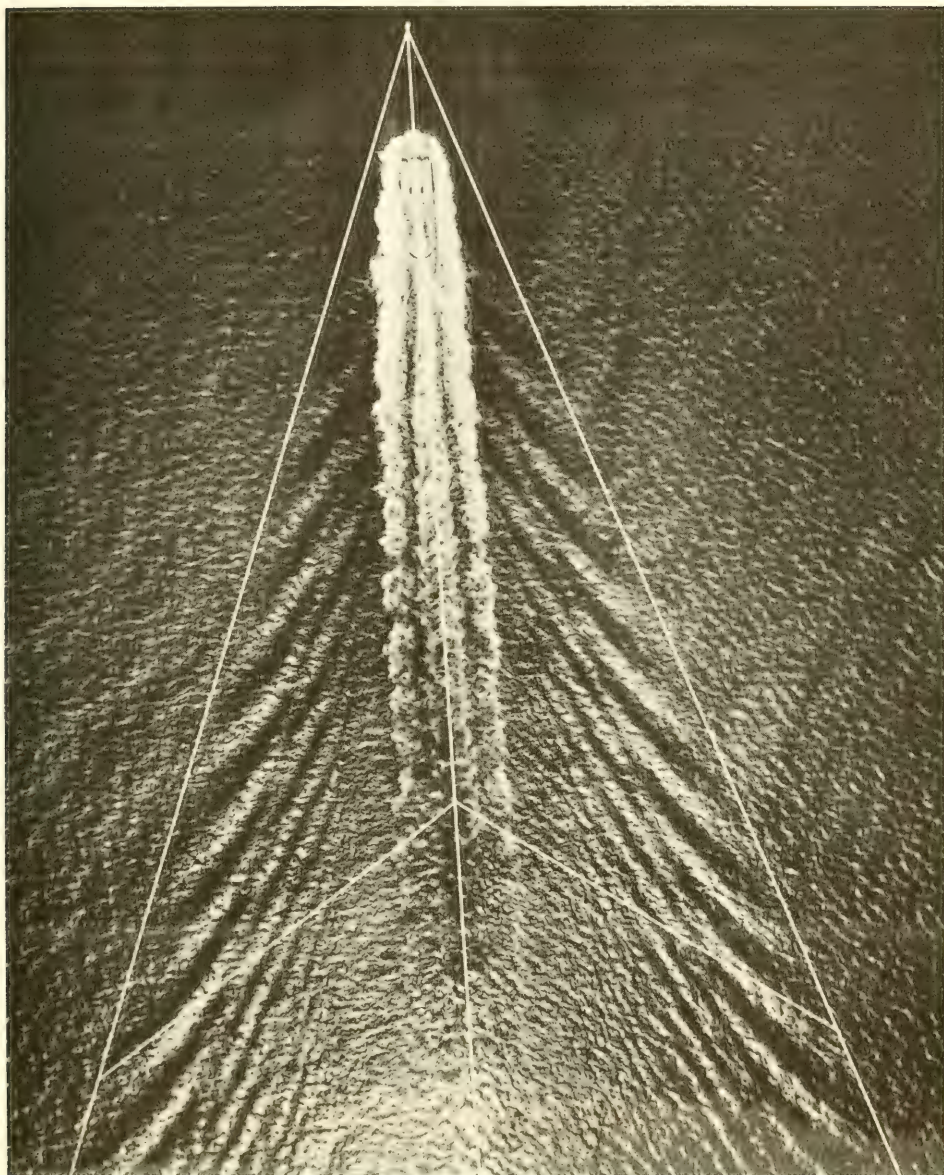


Fig. 3 Aerial view of the UNCATENA wave system with $19^{\circ}28'$ boundary lines and typical $35^{\circ}16'$ cusp-crest tangent lines superimposed

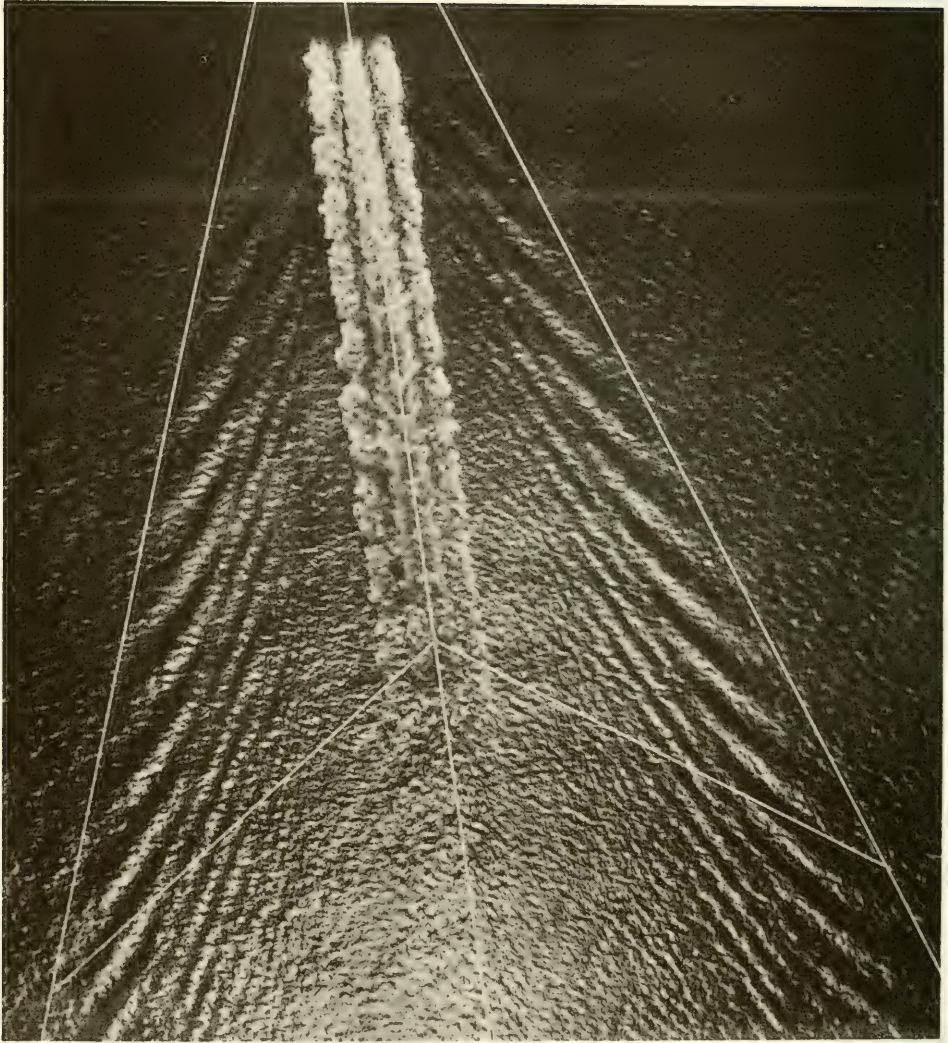


Fig. 4 Aerial view of the UNCATENA, further downstream, with the $19^{\circ}28'$ boundary lines and typical $35^{\circ}16'$ tangent lines superimposed



Fig. 5 Aerial oblique view of the UNCATENA from ahead of the bow

from the center of the wake, which, in principle, should lie on the cusp line or boundary of the wave system. The apex of this center is to some extent arbitrary, since, without further knowledge of the amplitude function $A(\theta)$, as it appears in Eq. (6), for this particular vessel, the location of the ship's bow relative to the origin of the (x,y) coordinates is arbitrary. It is clear, in fact, from Fig. 3 that the apex of the UNCATENA cusp lines is somewhat ahead of its bow, by a distance of about one ship length. This conclusion is consistent with other observations of ship waves (e.g., Gadd [1969]), and we emphasize here that, in principle, there is no contradiction between this observation and the linear Kelvin prediction.

Also shown in Figs. 3 and 4 is a typical pair of $35^{\circ}16'$ angles, which should be tangent to the wave crests on the cusp lines. Both the $19^{\circ}28'$ boundary angle and the $35^{\circ}16'$ wave crest angle are substantially confirmed by these observations, within the accuracy obtainable from these photographs. In fact, we have not observed any phenomena in these tests which are inconsistent with the linear Kelvin description of the far-field waves, in spite of the obviously nonlinear near-field disturbance associated with this vessel, especially at its bow. There is also no noticeable effect on the waves from the ship's viscous wake and propeller wake region, in spite of the persistence of this wake far-downstream. (However, the latter wake effects may be expected to affect the transverse waves near the centerline; this effect could not be detected here because of

the relatively weak transverse wave system of this vessel, and the fact that aerial photographs from directly above tend to emphasize the shorter, and hence steeper, diverging waves.)

As can be seen in all three photographs, but most noticeably in the downstream portion of Fig. 5, the diverging wave system includes three discrete groups of waves, separated by relatively calm regions or "nodes." The observation of three wave groups is also noted by Wehausen in the text adjoining Fig. 23 of Wehausen and Laitone [1960]. The explanation of this phenomenon is somewhat controversial. One possibility is in terms of the conventional "bow" and "stern" waves, and possibly others associated with the shoulder or knuckle of the vessel. My own view is that, while this synthesis is applicable near the ship, it is inappropriate in the far-field where the stationary phase approximation developed in the previous section is valid. Indeed, if two discrete "bow" and "stern" wave systems are superposed, in the Kelvin stationary phase approximation, the result is only one wave system, provided that the observation distance downstream is large compared to the separation distance between the two disturbances. There will, of course, be interference effects, with regions of reinforcement and other regions of cancellation, just as in the simpler radiation and diffraction patterns which we associate with nondispersive wave problems. In the present context these will be introduced via the amplitude function $A(\theta)$, and my own view is that the nodal regions between the three observed wave systems correspond to zeros of the function $A(\theta)$ for this particular vessel. Indeed, it is not difficult to perceive, in some parts of these photographs, a phase difference of 180° across the nodal regions. In principle, there should be additional nodal lines and discrete diverging waves in the interior portion of the wave system, but these will correspond to relatively short waves which are not so strongly generated by this vessel, and more quickly attenuated by viscous and other effects.

As one possible measure of the validity of Froude's hypothesis, that ship-wave effects are dependent only on the Froude number and the hull form, a series of photographs have also been made with a scale model of the UNCATENA. For this purpose a six-foot (scale ratio of 24) fiberglass model was constructed, and equipped with a single battery-powered electric motor and screw propeller, and a radio-controlled rudder system. Figures 6 and 7 show the model, as fitted with its single propeller and rudder, with an antenna mast for the radio control receiver. Test runs were made with this model on the Charles River, with photographic observations from the Boston University Bridge at a height of approximately 50 feet. These photographs were made with a Minolta 35 mm camera and 28 mm focal-length lens. Figures 8 - 10 show the model wave system from various oblique angles. Unfortunately, no observations could be made from directly above, so that measurements of the wave angles are not obtainable for the model scale. Figures 8 - 11 show indeed that close to the model discrete bow and stern wave systems are

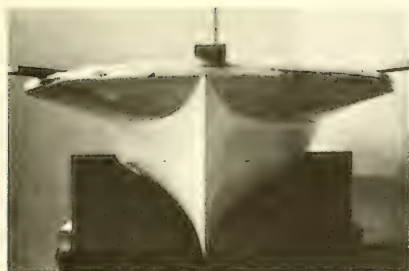


Fig. 6 UNCATENA model
bow view

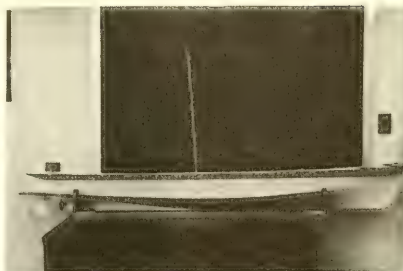


Fig. 7 UNCATENA model
side view

distinguishable, whereas further downstream these blend into a single diverging wave pattern with several nodal regions. It is apparent that, on the model scale, more than three wave groups can be distinguished far downstream; in Fig. 10 four or possibly five discrete groups can be noted. Since viscous attenuation is stronger at the smaller Reynolds numbers corresponding to the model scale, it must be presumed that the attenuation of the short diverging waves in the full-scale tests is due to other effects, such as the higher level of ambient waves and turbulence in the full-scale flow. Another noticeable difference is the obvious presence of transverse waves in the model tests, especially in Fig. 9 which is from approximately the same viewing angle as the full-scale photograph shown in Fig. 5.



Fig. 8 UNCATENA model and wave system
(compare with Fig. 5)



Fig. 9 UNCATENA model and wave system
aerial view



Fig. 10 UNCATENA model and wave system

This infers a significant difference between the transverse wave amplitudes for the model and full-scale, which could have important ramifications on the predictions of wave resistance from conventional model testing, but this tentative conclusion may be biased by minor differences in camera angles or lighting*, and it is felt that a quantitative measurement of the transverse wave amplitudes for the model and full-scale vessel should be made, with wave buoys or stereo photographs.

IV. TANK TESTS OF A WAVY WALL

In perhaps the only truly nonlinear analysis of ship waves carried out to date, Howe [1967, 1968] has considered the waves generated by a "wavy wall" or ship hull form consisting of a slowly damped sine wave. This geometrical form generates preferentially only one wave system. By suitable choice of the hull wavelength and velocity, a diverging wave system can be generated which, according to Howe's theory and based on the analysis of slowly varying finite amplitude waves as originally developed by Whitham [1965], will become unstable. The most striking feature of Howe's computations, resulting from this instability, is the occurrence of a shock or "phase-jump" across which there is an abrupt change in phase and wavenumber. Figure 11 is reproduced from Howe [1968], and shows the calculated wave system and the region where a phase-jump is predicted. Also shown, on the abscissa and with an exaggerated scale, are the waterlines of the hull form.

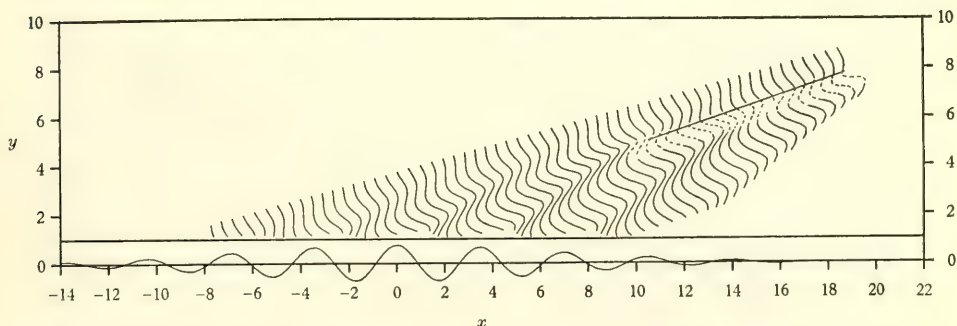


Fig. 11 Cross sections of the free surface perpendicular to the phase-jump. The broken line segments indicate a possible form for the free surface in the neighborhood of the phase-jump (from Howe [1968]).

*In color slides shown during the oral presentation of this paper, some weak transverse waves can be noted in the full-scale tests.

It should be noted that Howe's choice of a specific problem to which to apply the Whitham technique was based largely on the relative ease of verifying the results with a suitable experiment. We therefore set out to conduct such an experiment in the MIT Ship Model Towing Tank. For this purpose a model was constructed of Formica plastic laminate, bent to conform to Howe's damped sine wave, with fiberglass and polyester resin reinforcement and fairing of the back side of the Formica. The model was 10.4 feet long, by 1.5 feet vertical depth, and was immersed to a wetted draft of 1.0 feet. This "model" was fitted to the towing carriage in an off-center position to maximize the effective width of the tank and minimize reflections from the tank walls. The tank width is 8.4 feet, and the model was set up to give a separation of 5.5 feet between the wavy side and the facing tank wall. Tests were carried out at a speed of 4 feet per second, and the wave system was observed visually, photographically, and with a pair of wave probes which were placed at varying distances from the model to obtain a total of sixteen longitudinal wave records.

Figures 12 and 13 show the model in operation, and the resulting wave system. In no case was a phase-jump observed, in the region where it was anticipated. One can discern a somewhat irregular local effect along a longitudinal line about one foot from the tank wall, but this phenomena extends to the front of the wave group, is parallel to the longitudinal axis, and, moreover, originates further away from the model than the predicted phase-jumps. This discrepancy is unexplained, although D. J. Benney (private communication) has pointed out that the existence of phase-jumps can be questioned,



Fig. 12 Photograph of the wavy wall and wave pattern looking downstream



Fig. 13 Photograph of the wavy wall and wave pattern looking upstream

in principle, on the grounds that its existence violates the preassumed condition of a slowly varying wave system which is the basis for Howe's work.

V. THIRD-ORDER INTERACTIONS IN KELVIN WAVE SYSTEMS

One of the fundamental properties of a linear boundary-value problem is the principle of superposition; thus, for example, Kelvin's ship-wave pattern, although originally derived for a single "pressure point," is valid for any distribution of singularities and hence for arbitrary ship hulls. But as soon as the assumption of linearity is discarded, the possibilities for nonlinear interactions, among the previously independent components of the solution, must all be examined. In water-wave theory it was shown ten years ago by Phillips (cf. Phillips [1966]) that for deep water gravity waves the second-order interactions are relatively uninteresting, but when third-order effects are included it is possible for "resonant" interactions to occur. Thus two or three primary waves can interact, over large scales of time and distance, so as to transfer a substantial portion of their energy into a completely new wave system of a different wavenumber. This striking result has been confirmed by others, both theoretically and experimentally, and can be regarded as well established.

Motivated by the occurrence of third-order interactions in ocean wave systems, and by the striking nonlinear effects obtained for a special case of the ship-wave problem by Howe [1967, 1968] as noted in the previous section, I have studied the third-order perturbation solution of the Kelvin wave problem. The details of this investigation are "messy," to say the least, and will be presented in a separate paper (Newman [1971]), but I shall briefly describe the technique employed and the form of the results. First, as a preliminary approach to this problem, we may examine the possibility that, at any point in the Kelvin wave field, the transverse and diverging waves are such as to satisfy the criteria developed by Phillips for resonance between two primary waves. It is not difficult to show, in fact, that the wavenumbers of the diverging and transverse waves are not resonant, except possibly on or near the cusp line, where the simple stationary phase results are invalid.

To develop a complete solution of the ship-wave problem valid to third-order would be a formidable task; local effects near the hull, and nonlinearities associated with the boundary condition on the hull would have to be included, and the possibility of a breaking wave near the bow would raise fundamental questions of validity of the solution. Instead, we focus on nonlinearities associated only with wave propagation on the free surface, and taking place slowly over scales of many wavelengths, so that local effects and hull nonlinearities can both be neglected. The first-order linearized velocity potential must satisfy the familiar free-surface condition

$$g\phi_{|z} + V^2\phi_{|xx} = 0 \quad \text{on} \quad z = 0 \quad (10)$$

where subscripts denote partial derivatives. The notation and coordinate system are as defined in Section II. By suitably non-dimensionalizing the coordinates, we may replace (10) by the condition

$$\phi_{|z} + \phi_{|xx} = 0 \quad \text{on} \quad z = 0. \quad (11)$$

The general solution of this free-surface condition and of Laplace's equation, not including local effects near the disturbance, is (cf. Eq. (6))

$$\phi = \int_0^{2\pi} d\theta f(\theta) e^{kz + i\mathbf{k} \cdot \mathbf{x}} \quad (12)$$

where $k = (g/V^2) \sec^2 \theta$, $\mathbf{k} = (k \cos \theta, k \sin \theta)$, and $\mathbf{x} = (x, y)$. (In Section II the wave angles were restricted to the sector $-\pi/2 < \theta < \pi/2$. Here we allow all values of θ in the integrand of (12), in order to avoid taking the real part of the complex exponential; Eq. (12) will be real if $f(\theta) = f^*(\pi - \theta)$, and to avoid difficulties with the radiation condition we shall assume that (12) holds only if x is large and negative.)

The second-order free-surface condition, analogous to (11), is

$$\phi_{2z} + \phi_{2xx} = 2\nabla\phi_1 \cdot \nabla\phi_{1x} - \phi_{1x}(\phi_{1zz} + \phi_{1xxz}). \quad (13)$$

By inserting the first-order solution (12) for ϕ_1 in (13), and replacing products by repeated integrals, it follows that a particular solution of (13) will be

$$\phi_2 = \int_0^{2\pi} d\theta \int_0^{2\pi} d\theta_2 f(\theta) f(\theta_2) W(\theta_1, \theta_2) e^{k_{12}z + i\mathbf{k}_{12} \cdot \mathbf{x}} \quad (14)$$

where

$$\mathbf{k}_{12} = \mathbf{k}(\theta_1) + \mathbf{k}(\theta_2).$$

The weight function W is an algebraic function, determined by the various derivatives in (13), and it can be shown that this function contains only removable singularities. Thus by repeated application of the method of stationary phase, $\phi_2 = O(R^{-1})$ for large distances R from the disturbance, and this second-order potential will be

masked by the first-order potential $\phi_1 = O(R^{-1/2})$.

Extending these results to third-order involves straightforward but tedious analysis. The third-order free-surface condition is analogous to (13), but involves more terms on the right-hand side:

$$\begin{aligned}\phi_{3z} + \phi_{3xx} = & -\frac{1}{2}\nabla\phi_1 \cdot \nabla(\nabla\phi_1)^2 + 2\phi_{1x}(\nabla\phi_1 \cdot \nabla\phi_{1xz} \\ & + \nabla\phi_{1z} \cdot \nabla\phi_{1x}) + 2(\nabla\phi_1 \cdot \nabla\phi_{2x} + \nabla\phi_2 \cdot \nabla\phi_{1x}) \\ & - \phi_{1x}(\phi_{2zz} + \phi_{2xxz})\end{aligned}\quad (15)$$

A particular solution, analogous to (14), is given by the triple integral

$$\phi_3 = \int_0^{2\pi} d\theta_1 \int_0^{2\pi} d\theta_2 \int_0^{2\pi} d\theta_3 f(\theta_1) f(\theta_2) f(\theta_3) W(\theta_1, \theta_2, \theta_3) e^{k_{123} + i k_{123}' x} \quad (16)$$

where

$$\underline{k}_{123} = \underline{k}(\theta_1) + \underline{k}(\theta_2) + \underline{k}(\theta_3).$$

The weight function $W(\theta_1, \theta_2, \theta_3)$ is singular at points where its denominator vanishes or where

$$k_{123} - (\sec \theta_1 + \sec \theta_2 + \sec \theta_3)^2 = 0 \quad (17)$$

and it is necessary, therefore, to study the roots of this equation. It can be shown that the strongest singularities occur along the cusp line; for example, at the point

$$\theta_1 = \theta_2 = \theta_3 - \pi = 35^\circ 16'.$$

The integral (16) is improper at these points and we, therefore, conclude, as in many linear wave problems, that a steady-state solution cannot be assumed a priori, but must be derived as the appropriate limit of an initial value problem.

An expedient initial value problem is obtained by regarding the right-hand side of (15) as a pseudo-pressure distribution, imposed on the free surface from an initial state of rest, and then looking for the steady-state limit which results. To avoid unnecessary algebra we rewrite (15) in the unsteady form

$$\phi_{3z} + \phi_{3xx} - 2\phi_{3xt} + \phi_{3tt} = e^{\epsilon t} P(x, y) \quad (18)$$

where P denotes the right-hand side of (15). A solution corresponding to (16) is readily obtained, and in the limit $\epsilon \rightarrow 0$ we find that the only modification is to replace Eq. (17) for the roots of the denominator of W by the new equation

$$k_{123} + (\epsilon + i \sum_{j=1}^3 \sec \theta_j)^2 = 0. \quad (19)$$

Thus the singularities in (16) become slightly complex, and for $\epsilon > 0$ the integrals in (16) are proper.

Finally, the behavior of (16) as $\epsilon \rightarrow 0$ must be examined. Here the algebraic details are critical, since cancellation occurs between many of the leading-order terms. In view of the numerous possibilities for error, the following surprising result must be regarded as tentative, and I would hope that it will be verified independently by others who are willing to tackle the algebra involved.

As $\epsilon \rightarrow 0$, Eq. (16) predicts waves on the cusp line of the same form ($\theta = 35^\circ$) as the first-order solution, but with an amplitude which tends to infinity logarithmically in ϵ . Thus there can be no steady-state solution of the third-order initial value problem, as posed in Eq. (18) and, presumably, in the more general case of a "steady" moving disturbance initiated from a state of rest. Ultimately, as in the analogous case for ocean waves, the logarithmic growth rate will be modified by further nonlinearities, but, nevertheless, we must conclude that significant amounts of energy can be exchanged, through nonlinear processes, in the region of the cusp line, among adjacent wavenumbers.

VI. CONCLUSIONS AND RECOMMENDATIONS

The caption above is the standard one for theses and reports. In this paper we have obviously raised more questions than we have answered. The observations of the UNCATENA show that Kelvin's wave patterns are confirmed, even for a highly nonlinear near-field, provided the observation point is sufficiently far downstream (much further than is possible in a conventional towing tank). But are the differences noted in the photographs of the full-scale vessel and the 1/24th-scale model due to differences in photographic conditions and experimental errors, or are the transverse waves (and very short diverging waves) of substantially larger amplitude on the model scale? Here we would emphatically recommend further experiments in which the wave heights can be measured quantitatively, both for the full-scale vessel and for its model. This task can be simplified if only

the transverse waves are examined, but the difficulties of carrying out full-scale measurements in an ambient wave system are well known. (In spite of their appearance to the contrary, Figs. 3 - 5 were made early in the morning of a relatively calm day to ensure little ambient wave motion. The low rising sun in the model photographs is explained similarly!)

Turning to the wavy wall tests described in Section IV, we have attempted, without success, to verify a theoretical anomaly -- Howe's phase-jumps. It is an open question whether this failure is due to experimental error (an obvious possibility is the effective modification of the wavy wall shape due to viscous effects), or if, in fact, the phase discontinuity obtained by Howe is a consequence of pushing Whitham's slowly varying finite amplitude technique too far, with a solution which is not always slowly varying but contains local "singularities" or "shocks." It is not likely that this question can be answered by further experimental work, unless possibly a viscous correction can be incorporated in the model's shape (to allow for a turbulent boundary layer in the presence of a slowly varying sinusoidal pressure gradient!).

Finally, in Section V, we have outlined a nonlinear analysis of the Kelvin wave system which predicts an instability along the cusp line, but for which (unlike Howe's instability) the conclusion depends critically on a delicate avoidance of algebraic errors. Having thus gone out on a limb, I can only express the hope that independent verification is soon forthcoming.

VII. ACKNOWLEDGMENTS

The three experiments described here were carried out with the generous assistance of many persons. The full-scale photographs of the UNCATENA were made by Mr. F. Claude Ronnie of the Woods Hole Oceanographic Institution; the Woods Hole Oceanographic Institution also furnished the aircraft for these tests and the services of Mr. Robert Weeks as pilot. The subsequent experiments were performed by several MIT graduate students: David MacPherson and William McCreight built the fiberglass mold and model of the UNCATENA; Albert Bradley kindly loaned his radio control system; and the model completion and testing was carried out by Charles Flagg and Nan King, with photographs made by Ronald Walrod. Messrs. Flagg and King also built and tested the wavy wall model, and photographs of this test were again provided by Mr. Walrod. The propeller for the UNCATENA model was kindly loaned by Professor Daniel Savitsky of the Davidson Laboratory, Stevens Institute of Technology, and the wave probes used for the wavy wall test by Professor Jerome Milgram of MIT.

REFERENCES

- Gadd, G., "Ship Wavemaking in Theory and Practice," *Trans. Royal Inst. Nav. Archs.*, Vol. 111, 4, pp. 487-506, 1969.
- Guilloton, R. S., "The Waves Generated by a Moving Body," *Trans. Inst. Nav. Archs.*, Vol. 102, 2, pp. 157-174, 1960.
- Howe, M. S., "Non-Linear Theory of Open-Channel Steady Flow past a Solid Surface of Finite-Wave-Group Shape," *J. Fluid Mech.*, Vol. 30, 3, pp. 497-512, 1967.
- Howe, M. S., "Phase Jumps," *J. Fluid Mech.*, Vol. 32, 4, pp. 779-790, 1968.
- Inui, T., "Wave-Making Resistance of Ships," *Trans. Soc. Nav. Archs. and Mar. Engs.*, Vol. 70, pp. 283-353, 1962.
- Lunde, J. K., "On the Linearized Theory of Wave Resistance for Displacement Ships in Steady and Accelerated Motion," *Trans. Soc. Nav. Archs. and Mar. Engs.*, Vol. 59, pp. 25-85, 1951.
- Newman, J. N., "Panel Report -- Nonlinear and Viscous Effects in Wave Resistance," *Seventh Symposium on Naval Hydrodynamics*, Rome, 1968.
- Newman, J. N., "Third-Order Interactions in Kelvin Ship-Wave Systems," *J. of Ship Research*, Vol. 15, 1, pp. 1-10, 1971.
- Peters, A. S., "A New Treatment of the Ship Wave Problem," *Communs. Pure and Appl. Math.*, Vol. 2, pp. 123-148, 1949.
- Phillips, O. M., "The Dynamics of the Upper Ocean," *Cambridge University Press*, 1966.
- Ursell, F., "On Kelvin's Ship-Wave Pattern," *J. Fluid Mech.*, Vol. 8, 3, pp. 418-431, 1960.
- Wehausen, J. V., and Laitone, E. V., "Surface Waves," *Handbuch der Physik*, Vol. IX, Springer-Verlag, 1960.
- Whitham, G. B., "A General Approach to Linear and Non-Linear Dispersive Waves Using a Lagrangian," *J. Fluid Mech.*, Vol. 22, pp. 273-284, 1965.

DISCUSSION

SOME DEVELOPMENTS IN SHIP WAVE PATTERN RESEARCH

N. Hogben

*National Physical Laboratory, Ship Division
Feltham, Middlesex, England*

I. INTRODUCTION

This note briefly reports two developments in ship wave pattern research. The first concerns progress in application of the 'Equivalent Source Array' concept described in Ref. 1; the second is the development of a fully automated system of recording and analyzing the waves, a more detailed account of which is being prepared as Ref. 2.

II. EQUIVALENT SOURCE ARRAYS

An 'Equivalent Source Array' means for the present purpose, a source distribution which according to linear theory would generate a given wave pattern. It can be used for evaluating and interpreting the correlation between wave theory and experiment and also for predicting the effects of wavemaking on changing tank width and depth.

In Ref. 1, this concept was invoked to interpret wave pattern measurements behind a series of 3 models with parabolic hull forms and systematically varied beam. More recently, a similar investigation has been made of the wave patterns behind 3 trawler type hull forms (a parent and 2 derivatives) tested by Everest (Ref. 3). In the case of these more realistic models, the 'equivalent source arrays' were found to vary significantly with speed as indicated by the sample results for one of the models shown in Fig. 1. It may be seen that sources and sinks appear at a distance ahead of the bow which increased with increasing Froude number. This effective lengthening of the array may be explained in terms of 2nd order increases of wave phase velocity due to nonlinearity of the waves generated in the bow regions.

III. AUTOMATED RECORDING AND ANALYSIS

A prototype for a fully automated recording and analysis system has now been developed and operated. It comprises a stationary array of 4 capacitance probes with paper tape output and a com-

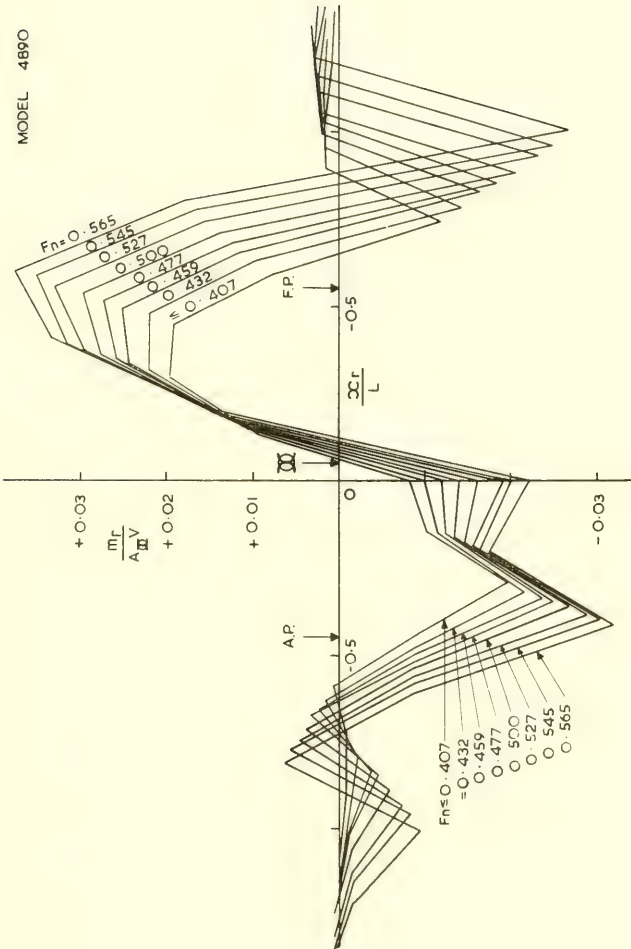


Fig. 1a Equivalent source arrays

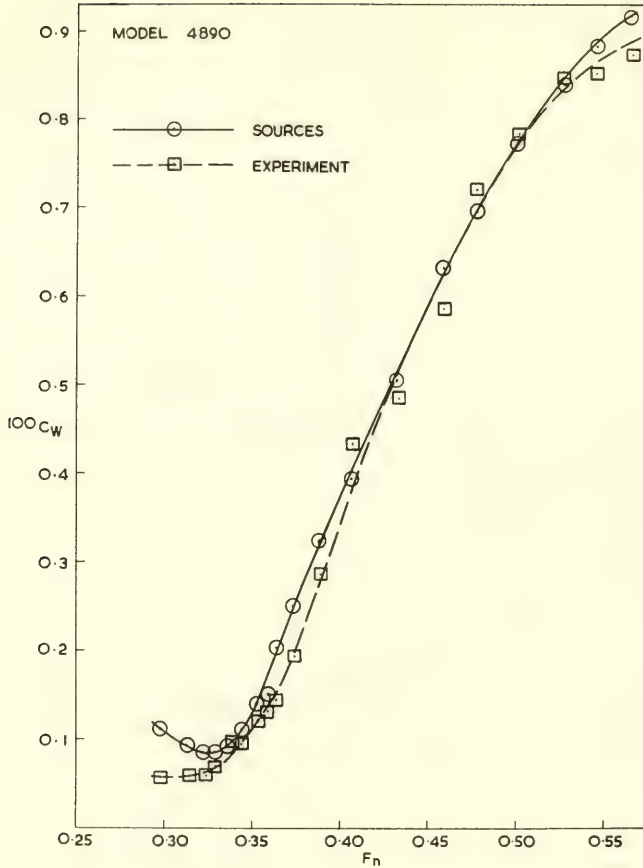


Fig. 1b Wave pattern resistance

puter program which analyses the tapes as punched by the recording digitizer. The probes themselves are as described in Ref. 4. The computer program uses the Matrix method of analysis developed with this application in view and described in Refs. 4 and 5. It works by a least square fitting of an appropriate function to the wave surface defined over a suitable grid of positions.

Some sample results for a 20 foot model of one of the trawler type models tested by Everest (Ref. 3), are shown in Figs. 2 and 3. Fig. 2 is a copy of part of a computer output. At the top a tabulation defining the wave ordinates $Z(X_R, Y_R)$ 'as measured' by listing R , X_R , Y_R and Z (R is a serial number, X_R , Y_R are longitudinal and transverse coordinates respectively in feet, and Z is the wave

R	X	Y	Z
1	+ 25.218	+ 8.000	+ 1.643
2	+ 25.436	+ 6.000	+ 0.244
3	+ 25.653	+ 4.000	+ 0.722
4	+ 25.871	+ 1.333	+ 0.893
5	+ 26.307	+ 6.000	+ 0.7
6	+ 26.524	+ 4.000	
7	+ 26.742	+ 1.?	
	27.177		
	.395		0.739
146	+ 59.	+ 1.333	- 0.623
147	+ 60.058	+ 8.000	- 0.538
148	+ 60.275	+ 6.000	- 0.804
149	+ 60.493	+ 4.000	+ 0.353
150	+ 60.711	+ 1.333	- 1.111

CASE 535.100 SPEED 8.710

N	THETA	A _N	B _N	100DC _W	AL	F _S	F _C
0	00.00	0.695	-1.112	0.0608	08.481	-0.0371	0.0232
1	32.09	-0.460	-0.111	0.0051	10.019	-0.0030	-0.0124
2	45.87	-0.636	0.683	0.0235	12.191	0.0319	-0.0298
3	53.12	-0.127	0.218	0.0019	14.144	0.0166	-0.0097
4	57.70	0.005	-0.277	0.0024	15.887	-0.0334	0.0006
5	60.92	-0.028	-0.397	0.0050	17.468	-0.0748	-0.0052
6	63.35	-0.048	-0.217	0.0016	18.923	-0.0635	-0.0139
7	65.25	-0.137	-0.021	0.0006	20.276	-0.0093	-0.0620
8	66.80	0.056	0.145	0.0008	21.546	0.1011	0.0387
9	68.09	0.076	0.068	0.0003	22.747	0.0728	0.0812
10	69.18	0.185	0.038	0.0012	23.888	0.0621	0.3033
11	70.13	-0.068	0.047	0.0002	24.977	0.1174	-0.1708
12	70.96	0.003	-0.082	0.0002	26.021	-0.3172	0.0100
13	71.68	-0.074	0.063	0.0003	27.025	0.3709	-0.4387
14	72.35	-0.021	0.062	0.0001	27.993	0.5631	-0.1856

100CW= 0.1041

[This is to be compared with 100CW=0.09375 obtained by Everest with 15 foot model of the same form (Ref. 4).]

R	X	Y	CZ	DZ
1	+ 25.218	+ 8.000	+ 1.661	+ 0.018
2	+ 25.436	+ 6.000	+ 0.194	- 0.051
3	+ 25.453	+ 4.000	+ 0.764	+ 0.042
		+ 1.333	+ 0.852	- 0.041
			+	
	59.840	+ 1.553	0.14	478
147	+ 60.058	+ 8.000	- 0.502	+ 0.036
148	+ 50.275	+ 6.000	+ 0.766	- 0.038
149	+ 60.493	+ 4.000	+ 0.607	+ 0.254
150	+ 60.711	+ 1.333	- 0.693	+ 0.418

RMS RESID 00.163 RMS Z 01.080

Fig. 2 Sample computer output

elevation in inches). In the middle is a tabulation of wave spectrum parameters accompanied by the resulting wave resistance coefficient $100 C_w$. The first 4 columns define the amplitudes and resistance contributions of the various wave modes in notation which corresponds to that used for example in Ref. 4. The last 3 columns define functions used for computing 'equivalent source arrays' in notation explained in Ref. 1. It may be seen that the resistance coefficient $100 C_w$ checks reasonably well with a result obtained by Everest for a smaller model of the same form, using manual pointers on transverse cuts analyzed by the method of Eggers (Ref. 6).

At the bottom is a tabulation defining the wave ordinates $CZ (X_R, Y_R)$ 'as fitted' in the same format as the 'as measured' results but with an extra column listing the difference between measurement and fit. Fig. 3 shows a sample profile plotted from the computer output.

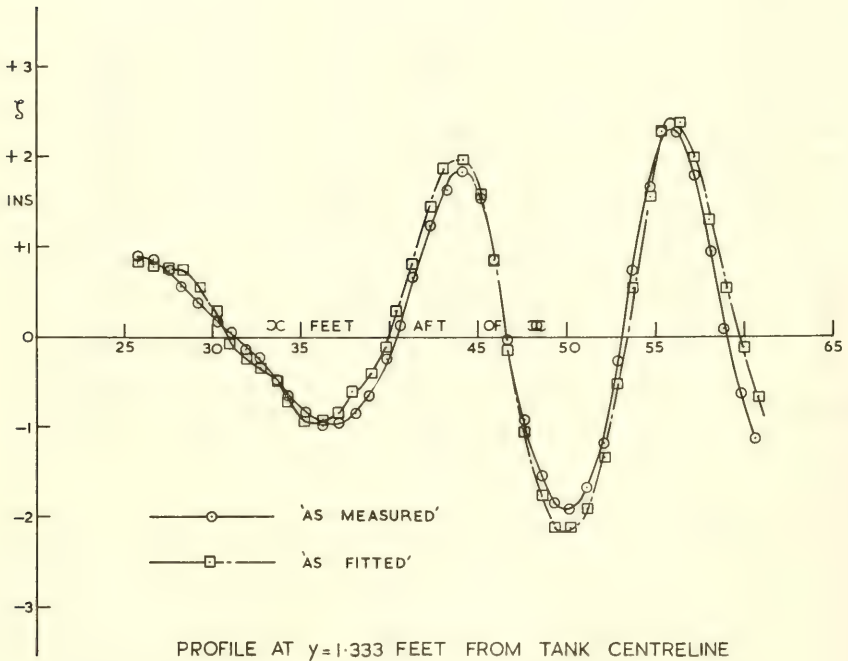


Fig. 3 Profile at $y = 1.333$ feet from tank centerline

ACKNOWLEDGMENTS

Appreciation is expressed for the contributions of Mr. B. Garner and Mr. H. G. Loe in developing the automated wave recording system and of Mr. E. J. Neville and Mr. M. Wilsdon in conducting the experiments.

REFERENCES

1. Everest, J. T. and Hogben, N., "An experimental study of the effect of beam variation and shallow water on 'thin ship' wave predictions," Trans. RINA paper W11 (1969) issued for written discussion.
2. Hogben, N., "Automated analysis of wave patterns behind towed models," in preparation as Ship Division Report No. 143.
3. Everest, J. T., "Some comments on the performance in calm water of a single hull trawler form and corresponding catamaran ships made up from symmetrical and asymmetrical hulls," NPL Ship Division Report No. 129, February 1969.
4. Gadd, G. E. and Hogben, N., "The determination of wave resistance from measurements of the wave pattern," NPL Ship Division Report No. 70, November 1965.
5. Hogben, N., "The computing of wave resistance from a wave pattern by a matrix method," NPL Ship Division Report No. 56, October 1964.
6. Eggers, K. W. H., "Über die ermittlung des wellenwiderstandes eines schiffsmodells durch analyse seines wellensystems," Schiffstechnik Vol. 9, part 46, p. 79, 1962.

VARIATIONAL APPROACHES TO STEADY SHIP WAVE PROBLEMS

Masatoshi Bessho
The Defense Academy
Yokosuka, Japan

INTRODUCTION

Although there have been many fruitful engineering applications of the theory of the wave-making resistance of ships, it is still not possible to completely explain the wave resistance of the usual surface-piercing ships. The so-called order theory gives us insight into the structure and composition of our approximate theory; however, we do not yet have a consistent and practical theory which is universally acceptable.

The author has speculated on what would be the best approximation to our boundary value problem. In this connection, is there a useful principle which corresponds to the Rayleigh-Ritz principle in the theory of elasticity? The present paper will provide a partial answer.

Our first aim is to introduce a variational principle which corresponds to the linearized boundary value problem. This is accomplished by introducing Flax's expression from wing theory. [6]

Our second aim is to find an alternate expression which will enable us to treat blunt bodies, since Flax's method is useful only for thin wings. Gauss' variational expression [24,25] for the boundary problem of a harmonic function is introduced for this purpose. This is shown to be equivalent to extremizing the Lagrangian or kinetic potential. The resulting dynamical interpretation of the boundary value problem is similar to the approaches of many other authors who have studied free surface problems by using the Lagrangian [3,12,13,14].

I. FLAX'S VARIATIONAL PRINCIPLE

The variational principle introduced by A. H. Flax in wing theory [6] may be directly applied to our problem. Those unfamiliar with this principle are directed to Appendix A.

If the Kutta-Joukowski condition [6,7,8] is satisfied at the trailing edge, we have the reciprocity relation

$$\iint_S p\tilde{w} \, dx \, dy = \iint_S \tilde{p}w \, dx \, dy \quad (1.1)$$

by (A.8) and (A.24), where p is the pressure, w is the vertical velocity component, and tildas denote reverse flow quantities. The integration is over the wetted portion of the ship hull S .

Let $\zeta(x,y)$ be the free surface elevation. The variation of the integral

$$I = \iint_S [(p - \tilde{p})\zeta_x - \tilde{p}w] \, dx \, dy \quad (1.2)$$

due to variations of p and \tilde{p} takes the form

$$\delta I = \iint_S [\delta p(\zeta_x - \tilde{w}) - \delta \tilde{p}(\zeta_x + w)] \, dx \, dy. \quad (1.3)$$

Since the variations δp and $\delta \tilde{p}$ are arbitrary, the pressure which extremizes the integral I is equivalent to the solution of the boundary value problem (A.25) and (A.26); that is, the problem for the perturbation potential ϕ with the conditions

$$\begin{aligned} \zeta_x &= -w = \phi_z \\ \zeta_x &= \tilde{w} = -\tilde{\phi}_z \end{aligned} \quad (1.4)$$

on the free surface. The stationary value of I is the drag; namely,

$$[I] = \iint_S p_0 \zeta_x \, dx \, dy, \quad (1.5)$$

where p_0 denotes the correct solution. [6,24,26] Thus, the boundary value problem is converted to a variational problem, the solution of which is suggested by various methods of approximation. [6]

If we introduce the error integral,

$$E^* = \iint_S (p - p_0)(\tilde{w} - \zeta_x) \, dx \, dy, \quad (1.6)$$

we see from (1.1), (1.4), and (1.5) that

$$E^* = D - I. \quad (1.7)$$

Therefore, Flax's principle produces an approximate solution which makes the error integral (1.6) stationary. [23]

This method suggests powerful means for obtaining approximate solutions, but unfortunately it has been applied only to thin hydroplanes and wings. [7]

II. GAUSS' VARIATIONAL PRINCIPLE

In this section, we assume there is no free surface. Then the velocity potential has the following representations for the source-sink and doublet distributions:

$$\phi_i(P) = \frac{1}{4\pi} \int_S \frac{\sigma_i(Q)}{r(P, Q)} dS(Q), \quad i = 0, 1, 2, \dots \quad (2.1)$$

and

$$\phi_i(P) = \frac{1}{4\pi} \iint_S \mu_i(Q) \frac{\partial}{\partial \nu} \frac{1}{r(P, Q)} dS(Q), \quad i = 0, 1, 2, \dots \quad (2.2)$$

Here, quantities with the suffix zero stand for the correct solutions while those with other suffices are not necessarily correct. For these potentials we have the following reciprocity relations:

$$\iint_S \phi_1 \sigma_2 dS = \iint_S \sigma_1 \phi_2 dS, \quad (2.3)$$

$$\iint_S \mu_2 \phi_{1\nu} dS = \iint_S \mu_1 \phi_{2\nu} dS, \quad (2.4)$$

and

$$\iint_S \phi_1 \phi_{2\nu} dS = \iint_S \phi_2 \phi_{1\nu} dS. \quad (2.5)$$

Gauss's variational principle for the Dirichlet problem states that if we consider the functional

$$G = \frac{1}{2} \iint_S (\phi - 2f)\sigma dS, \quad (2.6)$$

where

$$f = \phi_0 \text{ is given on } S, \quad (2.7)$$

then the function ϕ which gives the maximum value to G is the solution of the Dirichlet problem. [9,10] This is easily verified by making use of the reciprocity (2.3).

In the same way, we may construct a variational principle for the Neumann problem as follows: Let us consider the extremum problem for the functional

$$H = \frac{1}{2} \iint_S (\phi_\nu - 2f_\nu) \mu \, dS, \quad (2.8)$$

where

$$f_\nu = \phi_{0\nu} \text{ is given on } S. \quad (2.9)$$

This problem is seen to be equivalent to the present boundary value problem by making use of (2.4).

Alternately, we may construct a variational problem by making use of (2.5); namely, by introducing the functional

$$J = \frac{1}{2} \iint_S \phi (2f_\nu - \phi_\nu) \, dS, \quad (2.10)$$

and taking the variation, we have

$$\delta J = \iint_S \delta \phi (f_\nu - \phi_\nu) \, dS. \quad (2.11)$$

From this we see the equivalence to the boundary value problem. [24,25]

Now, since

$$\iint_S \phi_1 \phi_{2\nu} \, dS = \iiint_D \nabla \phi_1 \nabla \phi_2 \, d\tau, \quad (2.12)$$

where D is the entire water domain and $d\tau$ is a volume element, a natural measure of the error of an approximate solution ϕ is

$$E = \frac{1}{2} \iiint_D [\nabla(\phi - \phi_0)]^2 \, d\tau, \quad (2.13)$$

which becomes

$$E = \frac{1}{2} \iint_S (\phi - \phi_0)(\phi_\nu - \phi_{0\nu}) \, dS = J_0 - J, \quad (2.14)$$

by Green's theorem. Here,

$$J_0 = \frac{1}{2} \iint_S \phi_0 \phi_{0\nu} \, dS \quad (2.15)$$

is the correct value. We see clearly that

$$\delta E = - \delta J. \quad (2.16)$$

Since E is non-negative, we have the inequality [10]

$$J_0 \geq J. \quad (2.17)$$

It is well-known that among all functions ϕ having a finite energy integral,

$$T = \frac{1}{2} \iiint_D [\nabla \phi]^2 \, d\tau, \quad (2.18)$$

and a given normal derivative on S , the one which minimizes T is a harmonic function [1,4]. Accordingly, if we solve this minimization problem, say by the relaxation method, we have the inequality

$$T \geq J_0. \quad [1,4] \quad (2.19)$$

This is the dual of (2.17) and we now have the variational problem (2.7) as an involutory transformation of the latter minimization problem. (See, for example, the textbook on variational calculus [11].)

III. A VARIATIONAL PROBLEM FOR THE LAGRANGIAN

The preceding principle can be easily extended to flow in a gravitational field. Let us consider the functional

$$L = T - V, \quad (3.1)$$

where

$$T = \frac{1}{2} \iiint_D [\nabla \phi]^2 d\tau \quad (3.2)$$

and

$$V = \frac{g}{2} \iint_F \zeta^2 dx dy \quad (3.3)$$

are the total kinetic and potential energies, respectively. L is just the kinetic potential or Lagrangian. [5] Assume that the function ϕ has a given normal derivative

$$\phi_\nu = -x_\nu \text{ on } S \text{ and } F. \quad (3.4)$$

Taking the variation of L , we have

$$\begin{aligned} \delta L = & - \iiint_D \phi \nabla^2 \delta \phi d\tau + \iint_S \phi \delta \phi_\nu dS + \\ & \iint_F [\phi \delta \phi_\nu + \{(\frac{1}{2} \nabla \phi)^2 - g\zeta\} \delta \nu] dS. \end{aligned}$$

Making use of (3.4), which is also true for the new deflected free surface, we have

$$\delta L = - \iiint_D \phi \nabla^2 \delta \phi d\tau + \frac{1}{\rho} \iint_F p \delta \nu dS, \quad [3, 14] \quad (3.5)$$

where

$$p/\rho = -\phi_x - \frac{1}{2}(\nabla \phi)^2 - g\zeta. \quad (3.6)$$

Hence, if the pressure at the free surface vanishes, the stationary value of L will be attained when $\delta \phi$ is harmonic. This is just an extension of Kelvin's minimum energy principle. [1, 4]

On the other hand, if $\delta \phi$ is harmonic, then the stationary value of L is attained when the free surface pressure is constant and zero. The latter is an extension of Riabouchinsky's principle of minimum added mass. [3, 14]

The variational problem can be transformed so that the constraint condition is converted to a natural condition. Let us add a term which is zero at the stationary point. Consider the functional

$$P = T - V - \int \int_{S+F} \phi(x_\nu + \phi_\nu) dS. \quad (3.7)$$

Assume that ϕ is harmonic and, for simplicity, assume that the integral over an inspection surface at infinity vanishes. Making use of Green's theorem we have

$$\begin{aligned} P &= - \int \int \int_D [\phi_x + \frac{1}{2}(\nabla\phi)^2] d\tau - \frac{g}{2} \int \int_F \zeta^2 dx dy \\ &= \frac{1}{\rho} \int \int \int_D p d\tau + \text{Const}, \end{aligned} \quad (3.8)$$

where

$$\text{Const} = \frac{g}{2} \int \int H^2 dx dy - \frac{g}{2} \int \int_S z^2 dx dy, \quad (3.9)$$

and H is the depth to the bottom.

Taking the variation, we have

$$\delta P = \frac{1}{\rho} \int \int_F p \delta \nu dS - \int \int_{F+S} \delta \phi (\phi_\nu + x_\nu) dS. \quad (3.10)$$

Therefore, when

$$p = 0 \text{ on } F \text{ and } \phi_\nu + x_\nu = 0 \text{ on } S \text{ and } F, \quad (3.11)$$

P is stationary. This result was first given by J. C. Luke [12,13], who pointed out that the volume integral of the pressure is equivalent to the Lagrangian.

Furthermore, we may write (3.8) as

$$P = M - H, \quad (3.12)$$

where

$$H = T + V \quad (3.13)$$

and

$$M = - \iiint_D \phi_x d\tau. \quad (3.14)$$

M is the total momentum of the system in the x-direction and becomes equal to twice T,

$$M = 2T = - \iint_{S+F} \phi x_\nu dS = \iint_{S+F} \phi \phi_\nu dS, \quad (3.15)$$

when ϕ satisfies the boundary condition.

Hence, $\delta P = 0$ means that

$$\delta H = \delta M. \quad (3.16)$$

That is, when the variation of the total energy equals that of the total momentum in the x-direction, the potential satisfies the boundary conditions (3.11).

For purposes of application, it may be convenient to write P as

$$P = - \iint_{S+F} \phi(x_\nu + \frac{1}{2}\phi_\nu) dS - \frac{g}{2} \iint_F \zeta^2 dx dy. \quad (3.17)$$

This principle is applied to a regular, two-dimensional wave-train in Appendix B. In general, there is some difficulty in the application of this theory since the integrals P and L may not be finite. This is because the kinetic energy exceeds the potential energy for a finite amplitude wave. [1,2,4]

One way to bypass this difficulty may be to assume a flow model like the Riabouchinsky model [3] in cavitation theory (see Fig. 2); however, this may be impossible in the three-dimensional case. Another way may be to introduce Rayleigh's friction coefficient so that the waves far downstream will die out. In any case, there are still some problems which make us hesitant to begin the actual numerical computations.

Finally, let us consider the linearization of the free surface condition. Neglecting higher order terms in the integral over the water's surface and assuming that

$$g\zeta(x,y) = -\phi_x(x,y,0), \quad (3.18)$$

we have

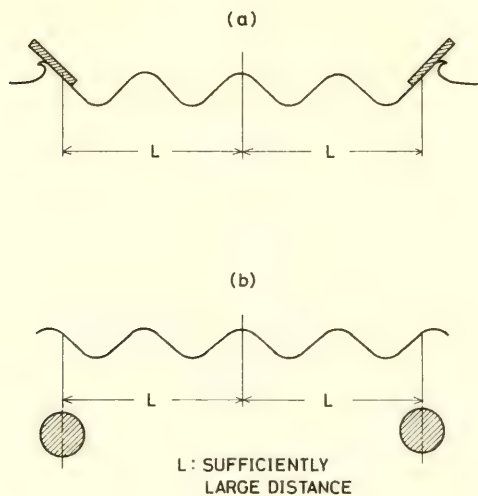


Fig. 2. Riabouchinsky Models

$$P = P_F + P_S, \quad (3.19)$$

where

$$P_S = - \iint_S \phi(x_\nu + \frac{1}{2} \phi_\nu) dS, \quad (3.20)$$

and

$$P_F = - \frac{1}{2g} \iint_F \phi(\phi_{xx} + g\phi_z) dS. \quad (3.21)$$

Accordingly, if we set

$$\phi_{xx} + g\phi_z = 0 \quad \text{on} \quad F, \quad (3.22)$$

which is just the dynamic boundary condition, then

$$P_F = 0, \quad (3.23)$$

and we are left with a variational calculus problem for P_S .

IV. THE LINEARIZED PROBLEM

The variational problem for P_S (3.20) is not satisfactory since there is no reciprocity relation for this form. We must introduce the reversed flow potential as was done for Flax's principle.

Let us consider the integral

$$L^*(\phi_1, \tilde{\phi}_2) = L^*(\tilde{\phi}_2, \phi_1) = -\frac{1}{2} \iint_D \nabla \phi_1 \nabla \tilde{\phi}_2 d\tau - \frac{g}{2} \iint_F \xi_1 \xi_2 dx dy. \quad (4.1)$$

Assuming that ϕ_1 and $\tilde{\phi}_2$ are harmonic and satisfy the free surface condition, we have, by Green's theorem,

$$L^*(\phi_1, \tilde{\phi}_2) = -\frac{1}{2} \iint_S \phi_1 \tilde{\phi}_{2\nu} dS = -\frac{1}{2} \iint_S \tilde{\phi}_2 \phi_{1\nu} dS, \quad (4.2)$$

where S is the surface of a submerged body. This is the reciprocity theorem for a submerged body. [8]

If $\tilde{\phi}_\nu = -\phi_\nu$, then

$$L^*(\phi, \tilde{\phi}) = \frac{1}{2} \iint_S \phi \phi_\nu dS = L(\phi, \phi), \quad (4.3)$$

where

$$L(\phi, \phi) = \frac{1}{2} \iint_D (\nabla \phi)^2 d\tau - \frac{g}{2} \iint_F \zeta^2 dx dy. \quad (4.4)$$

L^* is called the modified Lagrangian integral [5]. Note that $L(\phi, \phi)$ has a finite value in the linearized case but not in the finite amplitude case.

If S is the wetted part of a surface-piercing body which is under the waterline before the free surface is disturbed, there is an additional term from the surface integral. [15, 16, 19, 20, 21] The reciprocity theorem, in this case, is

$$\begin{aligned} L^*(\phi_1, \tilde{\phi}_2) &= -\frac{1}{2} \int_L \phi_1 \tilde{\zeta}_2 dy - \frac{1}{2} \iint_S \phi_1 \tilde{\phi}_{2\nu} dS \\ &= \frac{1}{2} \int_L \tilde{\phi}_2 \zeta_1 dy - \frac{1}{2} \iint_S \tilde{\phi}_2 \phi_{1\nu} dS. \end{aligned} \quad (4.5)$$

When $\phi_1 = \phi$, $\tilde{\phi}_2 = \tilde{\phi}$ and $\phi_\nu = -x_\nu$, L^* becomes

$$L^*(\phi, \tilde{\phi}) = \frac{1}{2} \int_L \tilde{\phi} \zeta x_n dS + \frac{1}{2} \iint_S \tilde{\phi} x_\nu dS, \quad (4.6)$$

where n is the inner normal to the waterline curve L in the horizontal plane. Thus, the first term in the right-hand side of (4.6) is the correction for the change of the wetted surface S . [16] This is justified, on the one hand, by the dynamical meaning of the Lagrangian and, on the other hand, by the linearization procedure of the preceding section.

For the case of a pressure distribution over the water surface, we may integrate (4.5) by parts and make use of the formulas in Appendix A. This results in the expression

$$\begin{aligned} L^*(\phi_1, \tilde{\phi}_2) &= -\frac{1}{2} \iint_S \phi_{1x} \tilde{\zeta}_2 dx dy = \frac{1}{2} \iint_S \tilde{\phi}_2 x \zeta_1 dx dy \\ &= \frac{1}{2\rho} \iint_S [p_1 + \rho g \zeta_1] \tilde{\zeta}_2 dx dy = \frac{1}{2\rho} \iint_S [\tilde{p}_2 + \rho g \tilde{\zeta}_2] \zeta_1 dx dy. \end{aligned} \quad (4.7)$$

Thus, the reciprocity becomes [8]

$$\mathfrak{L}^*(p_1, \tilde{p}_2) = \frac{1}{2\rho} \iint_S p_1 \tilde{\zeta}_2 dx dy = \frac{1}{2\rho} \iint_S \tilde{p}_2 \zeta_1 dx dy \quad (4.8)$$

where

$$\mathfrak{L}^*(p_1, \tilde{p}_2) = L^*(\phi_1, \tilde{\phi}_2) - \frac{g}{2} \iint_S \zeta_1 \tilde{\zeta}_2 dx dy. \quad (4.9)$$

Making use of these reciprocities, we may easily show the equivalence of the boundary value problem to the variational problem for the functional I^* , where

$$I^* = \frac{1}{2} \iint_S [\phi \tilde{\phi}_\nu - (\phi - \tilde{\phi}) x_\nu] dS, \quad (4.10)$$

for a submerged body, and

$$I^* = -\frac{1}{2\rho} \iint_S [p \tilde{\zeta} - (p - \tilde{p}) \zeta_0] dx dy, \quad (4.11)$$

for a pressure distribution. [24, 26]

Alternate representations for these integrals are

$$I^* = L^*(\phi_0, \tilde{\phi}_0) - L^*(\phi - \phi_0, \tilde{\phi} - \tilde{\phi}_0), \quad (4.12)$$

and

$$I^* = \mathfrak{L}^*(p_0, \tilde{p}_0) - \mathfrak{L}^*(p - p_0, \tilde{p} - \tilde{p}_0), \quad (4.13)$$

where the suffix zero stands for the correct solution. These formulas show that the variational principle extremizes the Lagrangian of the error and that the stationary values are just given by the Lagrangian.

The difficulty arises in the case of a surface-piercing body. From (4.12), the functional to be extremized is

$$I^* = -L^*(\phi, \tilde{\phi}) + \frac{1}{2} \int_L (\tilde{\phi} \zeta_0 - \phi \tilde{\zeta}_0) dy + \frac{1}{2} \iint_S (\tilde{\phi} - \phi) x_\nu dS. \quad (4.14)$$

Taking the variation, we have the boundary conditions equivalent to this variational problem,

$$\phi_x = -g \zeta_0, \quad \tilde{\phi}_x = g \tilde{\zeta}_0 \quad \text{on } L, \quad (4.15)$$

$$\phi_\nu = -\tilde{\phi}_\nu = -x_\nu \quad \text{on } S. \quad (4.16)$$

But we have no knowledge of the surface elevation on L , a priori, as this problem may be indeterminant. [17, 23] We must remember here that the solution is unique only when the detachment points are fixed by the theory of cavitation. [3, 14]

This difficulty may be avoided by introducing a homogeneous solution for the two-dimensional, linearized case (see Appendix C).

For the present case, we might proceed as follows: Let us consider the difference between a surface piercing body and the limiting case of a submerged body moving very close to the free surface as in Fig. 3. [23] The boundary condition on the water surface above the submerged body must be $\phi_z = 0$, but since the top is also the free surface, this is equivalent to

$$\phi_z = \zeta_x(x, y) = 0 \quad \text{on } \overline{F}, \quad (4.17)$$

or integrating, we have

$$\phi_x(x, y, 0) = -g\zeta(x, y) = \text{Const} = \text{func}(y) \quad \text{on } \overline{F}. \quad (4.18)$$

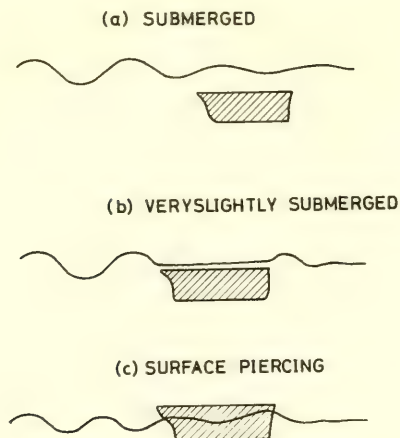


Fig. 3. Slightly Submerged Ship

This formula shows that there may be a thin layer of uniform flow over the top of the submerged body.

When this layer moves with the body,

$$\phi_x(x, y, 0) = -g\zeta(x, y) = -1 \quad \text{on} \quad \overline{F}, \quad (4.19)$$

and we clearly have the case of a surface-piercing body.

On the other hand, the boundary value problem of a submerged body is equivalent to the variational problem (4.10). After solving this problem, we may calculate the surface elevation over the top water plane by (4.18), but it will differ from (4.19), in general. In this case, it might be necessary to introduce another potential which satisfies condition (4.19), in addition to the above potential. This procedure may not be practical because the treatment of the top water plane is difficult.

In this case, it would be more convenient to consider the following two boundary value problems: Let us split the velocity potential into two parts,

$$\phi = \phi_1 + \phi_2, \quad (4.20)$$

with boundary conditions

$$\phi_{1x} = 0 \quad \text{on } L \quad (4.21)$$

$$\phi_{1\nu} = -x_\nu \quad \text{on } S$$

$$\zeta_2 = \tilde{\zeta}_2 = \zeta_{20}, \text{ given on } L \quad (4.22)$$

$$\phi_{2\nu} = 0 \quad \text{on } S$$

The corresponding functionals are of the form (4.10) for ϕ_1 , and of the form (4.14), without the third term on the right-hand side, for ϕ_2 .

For the present case, ζ_{20} must be equal to $1/g$ by (4.19); however, in general, it will be arbitrary and, perhaps, a constant of the form (4.18). ϕ_2 is called the homogeneous solution. [18, 22, 26]

Finally, it should be noticed that the Lagrangian is closely related to the far-field potential. For a submerged body, we have, from the boundary conditions, (A.9), (A.11), and (4.3),

$$\begin{aligned} B &= - \int_S x x_\nu dS + 2L(\phi, \phi) \\ &= 2L(\phi, \phi) + \nabla, \end{aligned} \quad (4.23)$$

where ∇ is the displaced volume. For a surface-piercing body, interpreting condition (A.10) as a correction for the real wetted surface, we have

$$\iint_S x \phi_\nu dS + \frac{1}{g} \int_L x \phi_x dy = \nabla, \quad (4.24)$$

where ∇ is the displacement volume under the still waterline. Therefore, we can write (A.11) as

$$B = \nabla + 2L^*(\phi, \tilde{\phi}_1 + \tilde{\phi}_2), \quad (4.25)$$

where ϕ_1 and ϕ_2 are defined by (4.21) and (4.22), with $\zeta_{20} = 1/g$.

For a pressure distribution, we have, from (A.18) and (4.8),

$$B = 2\rho \mathcal{L}^*(p, \tilde{p}_2), \quad (4.26)$$

where p_2 is a homogeneous solution, as is ϕ_2 , and $\tilde{\zeta}_2 = 1/g$. Since B is also a measure of the total lift, this formula shows that the homogeneous solution for the constant surface elevation influences the lift, as we have easily verified by the reciprocity (4.8). [26] It should be noticed that, in this case, the condition $A = 0$ in (A.18) insures the continuity of the planing hull.

Kotchin's function (A.17) is also given in the form

$$H(\theta) = - \iint_S \phi_e x_\nu dS - \int_L \phi_e \zeta dy + 2L^*(\phi, \tilde{\phi}_d), \quad (4.27)$$

where $\tilde{\phi}_d$ has the boundary values

$$\tilde{\phi}_{d\nu} = -\phi_{e\nu} \quad \text{on} \quad S$$

and (4.28)

$$g\tilde{\zeta}_d = \tilde{\phi}_{dx} = -\phi_{ex} \quad \text{on} \quad L$$

$\tilde{\phi}_d$ is called the diffraction potential. [23, 26] Here, the second term of (4.27) may be omitted as in (4.25).

For a submerged body, there is no integration along L and H may be written as

$$H(\theta) = - \iint_S (\phi_e + \tilde{\phi}_d) x_\nu dS. \quad (4.29)$$

Finally, for a pressure distribution,

$$H(\theta) = 2\rho\mathfrak{L}^*(p, \tilde{p}_d), \quad (4.30)$$

where

$$\tilde{\zeta}_d = -\frac{1}{g} \phi_{ex}. \quad (4.31)$$

V. CONCLUSION

We have presented two variational principles for the boundary value problem associated with the waves of a ship advancing at a constant speed: The first is Flax's principle, which makes use of the stationary character of the drag. This principle is useful only for

planing boats or for submerged thin wings. [6,24] The second is based on Gausz's principle, which converts the boundary value problem to a variational problem. This method is shown to be an extension of Riabouchinsky's principle of minimum virtual mass. [3,24]

The latter principle is based on the stationary character of the Lagrangian and has recently been used by Luke, in a more general form, to study water wave dispersion problems. [3,12,13] We also have analogous principles for light and sound wave diffraction and for the radiation of energy due to the heaving, swaying, and rolling oscillations of ships. [25,27,28,29,30]

The variational principles emphasize the dynamical meaning of the boundary value problems and permit us to solve them approximately by the Rayleigh-Ritz-Galerkin procedure. [6,28,29] However, when we try to apply these principles to our problem, there are two difficulties:

The first is that our system is not conservative because of the trailing wave. This may be bypassed by introducing an artificial model, as in Fig. 2, or by introducing a reversed flow for the linearized case.

The second difficulty is for the surface-piercing body, in which case the wave profile is not known, a priori, even in the linearized case. This difficulty may be avoided by introducing homogeneous solutions [27] which appear in the case of a surface pressure distribution. [26]

Finally, although a variational method does not necessarily represent a new method of analysis, it does suggest new methods of approximation. For this reason, it may be useful, especially for engineering purposes.

REFERENCES

1. Lamb, H., Hydrodynamics, 6th Ed., Cambridge University Press, 1932.
2. Wehausen, J. V. and Laitone, E. V., "Surface Waves," Handbuch der Physik Bd. 9, Springer and Co., 1960.
3. Gilbarg, D., "Jets and Cavities," Handbuch der Physik Bd. 9, Springer and Co., 1960.
4. Milne-Thomson, L. M., Theoretical Hydrodynamics, 4th ed., Macmillan and Co., 1962.

5. Morse, P. M., and Feshbach, H., Methods of Theoretical Physics, in 2 volumes, student ed., McGraw Hill and Co., 1953.
6. Flax, A. H., "General Reverse Flow and Variational Theorems in Lifting-Surface Theory," *J. Aeronaut. Sci.*, vol. 19, 1952.
7. Ursell, F., and Ward, G. N., "On Some General Theorems in the Linearized Theory of Compressible Flow," *Q. J. Math. and Mech.*, vol. 3, 1950.
8. Hanaoka, T., "On the Reverse Flow Theorem Concerning Wave-Making Theory," *Proc. 9th Japan Nat. Congress for Appl. Mech.*, 1959.
9. Frostman, O., Potential d'Equilibre et Capacité des Ensembles, Lund Univ., 1935.
10. Inoue, M., Theory of Potential, Kyoritsu, Tokyo, 1952 (Japanese).
11. Hayashi, T., and Mura, T., Variational Calculus, Corona, Tokyo, 1958 (Japanese).
12. Luke, J. C., "A Variational Principle for a Fluid with a Free Surface," *J. Fluid Mech.*, vol. 27, 1967.
13. Lighthill, M. J., "Application of Variational Methods in the Non-Linear Theory of Dispersive Wave Propagation," *Proc. IUTAMSymposia*, Vienna, 1966.
14. Garabedian, P. R. and Spencer, D. C., "Extremal Methods in Cavitational Flow," *J. Ratl. Mech. Anal.*, vol. 1, 1952.
15. Wehausen, J. V., "An Approach to Thin Ship Theory," *Proc. Int. Semi. on Theor. Wave-Resistance*, Michigan, 1963.
16. Ylm, B., "Higher Order Wave Theory of Ships," *J. Ship Res.*, September, 1968.
17. Kotik, J., and Morgan, R., "The Uniqueness Problem for Wave Resistance Calculated from Singularity Distributions Which are Exact at Zero Froude Number," *J.S.R.*, March 1969.
18. Van Dyke, M., Perturbation Methods in Fluid Mechanics, Academic Press, 1964.
19. Bessho, M., "On the Theory of the Wave-Resistance," *J. Zosen Kyokai*, vol. 105, 1959.

20. Bessho, M., "On the Theory of the Wave-Resistance," (2nd Rep.), J.Z.K., vol. 106, 1960.
21. Bessho, M., "On the Formula of Wave-Making Force Acting on a Ship," J.Z.K. vol. 110, 1961.
22. Bessho, M. and Mizuno, T., "On Wave-Making Resistance of Half Immersed Circular Cylinder and Vertical Plate," Rept. of Defense Academy (Japanese), vol. 1, 1963.
23. Bessho, M., "On the Boundary Value Problem in the Theory of Wave-Making Resistance," Memo. Defense Academy, vol. 6, 1967.
24. Bessho, M., "Gauss' Variational Principle in Boundary Value Problems," Read at Sea-Keeping Sub Com. of Japan Tow. Tank Comm., October 1967.
25. Bessho, M., "On Boundary Value Problems of an Oscillating Body Floating on Water," M.D.A., vol. 8, 1968.
26. Bessho, M. and Nomura, K., "A Contribution to the Theory of Two-Dimensional Hydroplaning," M.D.A., vol. 10 (in print).
27. Miles, J. and Gilbert, F., "Scattering of Gravity Waves by a Circular Dock," J.F.M., vol. 34, 1968.
28. Mizuno, T., "On Swaying Motion of Some Surface-Piercing Bodies," M.D.A., vol. 9, 1969.
29. Mizuno, T., "On Sway and Roll Motion of Some Surface-Piercing Bodies," read at Spring Meeting of Jap. Soc. Nav. Arch., 1970.
30. Isshiki, H., "Variational Principles Associated with Surface Ship Motions," read at Korea-Japan Seminar on Ship Hydrodynamics, Seoul, 1970.

APPENDIX A

The Linearized Velocity Potential [2,23]

Let us consider the flow of water around a ship S , taking the coordinate system as in Fig. 1 and the velocity of the stream at upstream infinity to be unity.

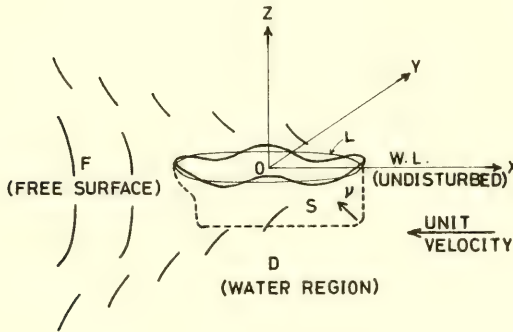


Fig. 1. Coordinate System

The pressure $p(x, y)$ on the water surface is given by

$$\frac{1}{\rho} p(x, y) = - \phi_x(x, y, 0) - g\zeta(x, y), \quad (\text{A.1})$$

in the linearized theory, where ρ is the water density; g , the gravity constant; ζ , the surface elevation, and ϕ , the perturbation potential ($d\phi = -u dx - v dy - w dz$). The suffix stands for differentiation.

The kinematic condition on the water surface is

$$\phi_z(x, y, 0) = \zeta_x(x, y). \quad (\text{A.2})$$

Since the pressure on the free surface is constant, the potential must satisfy the condition

$$\phi_{xx}(x, y, 0) + g\phi_z(x, y, 0) = 0. \quad (\text{A.3})$$

A solution which has a source singularity at a point Q and

satisfies the above water surface condition can be expressed as

$$4\pi S(P, Q) = \frac{1}{r(P, Q)} - \frac{1}{r(P, \bar{Q})} - \frac{g}{\pi} \lim_{\mu \rightarrow +0} \int_{-\pi}^{\pi} \int_0^{\infty} \frac{e^{k(z+z') + ik(\tilde{\omega} + \tilde{\omega}')} dk d\theta}{k \cos^2 \theta - g + \mu l \cos \theta}, \quad (A.4)$$

where $P \equiv (x, y, z)$, $Q \equiv (x', y', z')$, $\bar{Q} \equiv (x', y', -z')$, $r(P, Q) = \overline{PQ}$ and $\tilde{\omega} = x \cos \theta + y \sin \theta$, $\tilde{\omega}' = x' \cos \theta + y' \sin \theta$. Hereafter, we will call this the fundamental singularity. This solution approaches the following values asymptotically:

$$S(P, Q) \xrightarrow{x \gg x'} \frac{1}{4\pi} \left\{ \frac{1}{r(P, Q)} + \frac{1}{r(P, \bar{Q})} \right\}, \quad (A.5)$$

$$S(P, Q) \xrightarrow{x \ll x'} \frac{g}{\pi} \operatorname{Im} \int_{-\pi/2}^{\pi/2} e^{g \sec^2 \theta \{ (z+z') + i(\tilde{\omega} + \tilde{\omega}') \}} \sec^2 \theta d\theta. \quad (A.6)$$

By considering the integral

$$\iint [\phi_\nu(Q) S(P, Q) - \phi(Q) S_\nu(P, Q)] dS(Q)$$

about a point P in the interior of the fluid, we have the expression

$$\phi(P) = \iint_{S+F} [\phi_\nu S - \phi S_\nu] dS.$$

Since ϕ and S satisfy condition (A.3) on F , we have, finally,

$$\begin{aligned} \phi(P) = & \iint_S [\phi_\nu(Q) S(P, Q) - \phi(Q) S_\nu(P, Q)] dS(Q) \\ & - \frac{1}{g} \int_L [\phi(Q) S_{x'}(P, Q) - \phi_{x'}(Q) S(P, Q)] dy', \end{aligned} \quad (A.7)$$

where L is the curve on which F cuts S .

When the water motion is due to a pressure distribution over the water surface, we have

$$\phi(P) = \frac{1}{\rho g} \iint_S p(Q) S_{x'}(P, Q) dx' dy', \quad (A.8)$$

where we have used (A.1) and integrated (A.7) by parts. We have also assumed that the potential and surface elevation are continuous over S and F , including L .

Making use of asymptotic characters (A.5) and (A.6) of S , we obtain the asymptotic expansions of ϕ as follows:

$$\phi(p) \xrightarrow{x \gg 1} \frac{1}{2\pi r} A + \frac{x}{2\pi r^3} B, \quad (\text{A.9})$$

where $r = \overline{PO}$ and

$$A = \iint_S \phi_\nu dS + \frac{1}{g} \int_L \phi_x dy, \quad (\text{A.10})$$

$$B = \iint_S [\phi_\nu x - \phi x_\nu] dS - \frac{1}{g} \int_L [\phi - x\phi_x] dy. \quad (\text{A.11})$$

The expression for A may also be written as

$$A = \iint_S \phi_\nu dS - \frac{1}{g} \iint_F \phi_{xx} dx dy = \iint_S \phi_\nu dS + \iint_F \phi_z dx dy, \quad (\text{A.10}')$$

by using (A.3). Thus A is the total outward flux from the water domain. This must be zero; otherwise, we would have a large source of the resistance other than from the wave and splash.

We also have the kinematic condition on the surface of the ship,

$$\phi_\nu = -x_\nu \quad \text{on} \quad S. \quad (\text{A.12})$$

Therefore,

$$\iint_S \phi_\nu dS = - \iint_S x_\nu dS = 0, \quad (\text{A.13})$$

where S is the wetted surface of the ship below the undisturbed water surface. From (A.10) and (A.13), we have

$$\frac{1}{g} \int_L \phi_x dy = - \int_L \xi dy = 0. \quad (\text{A.14})$$

But this condition is not adequate in practical cases. One way to avoid this difficulty may be to take the real wetted surface as S . On the other hand, for the consistency of the theory, it may be

preferable to take

$$\phi(p) \xrightarrow{x \gg 1} \frac{x}{2\pi r^3} B, \quad (\text{A.9}')$$

instead of (A.9).

Far downstream, we have

$$\phi(p) \xrightarrow{x \ll -1} \frac{g}{\pi} \text{Im} \int_{-\pi/2}^{\pi/2} \phi_e(P, \theta) H(\theta) \sec^2 \theta \, d\theta, \quad (\text{A.15})$$

where

$$\phi_e(P, \theta) = \exp [g \sec^2 \theta (z + i\tilde{\omega})] \quad (\text{A.16})$$

and

$$H(\theta) = \iint_S [\phi_y \phi_e - \phi \phi_{ey}] \, dS - \frac{1}{g} \int_L (\phi \phi_{ex} - \phi_x \phi_e) \, dy. \quad (\text{A.17})$$

For a pressure distribution, we have simply

$$A = 0$$

and

$$B = \frac{1}{\rho g} \iint_S p(x, y) \, dx \, dy, \quad (\text{A.18})$$

where

$$H(\theta) = \frac{1}{\rho g} \iint_S p(x, y) \phi_{ex} \, dx \, dy. \quad (\text{A.19})$$

If the flow direction is reversed, the conditions corresponding to (A.1), (A.2), and (A.3) are as follows:

$$\frac{1}{\rho} \tilde{p}(x, y) = \tilde{\phi}_x(x, y, 0) - g \tilde{\zeta}(x, y), \quad (\text{A.20})$$

$$\tilde{\phi}_z(x, y, 0) = -\tilde{\zeta}_x(x, y), \quad (\text{A.21})$$

and

$$\tilde{\phi}_{xx}(x, y, 0) + g\tilde{\phi}_z(x, y, 0) = 0, \quad (\text{A. 22})$$

so that the fundamental singularity is the same as that for the direct flow, except that the wave follows on the downstream side. This may be expressed as

$$\tilde{S}(P, Q) = S(Q, P), \quad (\text{A. 23})$$

we also have

$$S_{x^*}(P, Q) = \tilde{S}_x(Q, P). \quad (\text{A. 24})$$

The boundary conditions for this case are

$$\tilde{\phi}_\nu = -\phi_\nu = x_\nu \quad \text{on} \quad S, \quad (\text{A. 25})$$

and

$$\tilde{\phi}_z = -\tilde{w} = -\phi_z = w = -\zeta_x \quad \text{on} \quad S. \quad (\text{A. 26})$$

APPENDIX B

The Progressing Wave

Let us obtain the solution for a periodic progressing wave, moving at constant unit speed, by the variational method of §3.

We take the form of the complex potential to be

$$\phi + i\psi = -ia \exp(kz - ikx), \quad (\text{B. 1})$$

where the origin is on the undisturbed water level.

The integrals to be evaluated are

$$P = M - T - V, \quad \frac{1}{\rho} M = - \int_{-\pi/k}^{\pi/k} dx \int_{-\infty}^0 \phi_x dz, \quad (\text{B. 2})$$

$$\frac{1}{\rho} T = \frac{1}{2} \iint (\nabla \phi)^2 dx dz, \quad \frac{1}{\rho} V = \frac{g}{2} \int \zeta^2 dx,$$

where $2\pi/k$ is the wavelength.

Assuming a surface disturbance of the form,

$$\zeta = b + c \cos kx + d \cos 2kx, \quad (\text{B.3})$$

and integrating the expressions for M , T , and V , we have

$$\frac{1}{\rho} M = \pi c a \left[1 + k(b + \frac{d}{2}) + \frac{k^2}{8} (c^2 + 4b^2 + 2d^2 + 4bd) \right],$$

$$\frac{1}{\rho} T = \frac{\pi a^2}{2} \left[1 + 2kb + k^2 (c^2 + 2b^2 + d^2) + k^3 c^2 (2b + d) \right], \quad (\text{B.4})$$

$$\frac{1}{\rho} V = \frac{\pi g}{2k} (c^2 + d^2 + 2b^2).$$

Differentiating P with respect to a , b , c and d , and equating the derivatives to zero (by the principle (3.16)), we obtain the following stationary values, neglecting higher order terms:

$$c \doteq a(1 + \frac{5}{8} k^2 a^2),$$

$$b \doteq O(k^3),$$

$$d \doteq \frac{1}{2} k a^2,$$

$$g/k \doteq 1 - k^2 a^2,$$

(B.5)

$$\frac{k}{2\pi} T \doteq \frac{\rho g}{4} c^2 (1 + \frac{3}{4} k^2 c^2),$$

$$\frac{k}{2\pi} V \doteq \frac{\rho g}{4} c^2 (1 + \frac{1}{4} k^2 c^2),$$

(B.6)

$$\frac{k}{2\pi} P \doteq \frac{k}{2\pi} (T - V) \doteq \frac{\rho g}{8} k^2 c^4.$$

These expressions agree with other well-known results. [1, 2]

APPENDIX C

A Variational Principle for the Stream Function

In the two-dimensional case, we may use a stream function instead of the velocity potential. Let us introduce the stream function as follows:

$$\phi_x(x, z) = \psi_z(x, z), \quad \phi_z(x, z) = -\psi_x(x, z). \quad (C.1)$$

Then, the boundary conditions for ψ become

$$\psi_z(x, 0) - g\psi(x, 0) = 0 \quad \text{and} \quad \tilde{\psi}_z(x, 0) - g\tilde{\psi}(x, 0) = 0, \quad (C.2)$$

$$\psi_0(x, z) = -\tilde{\psi}_0(x, z) = -z \quad \text{on} \quad S, \quad (C.3)$$

$$\zeta(x) = -\psi(x, 0) \quad \text{and} \quad \tilde{\zeta}(x) = \tilde{\psi}(x, 0). \quad (C.4)$$

Introducing a modified Lagrangian integral,

$$L^*(\psi_1, \tilde{\psi}_2) = -\frac{1}{2} \iint_D \nabla \psi_1 \nabla \tilde{\psi}_2 \, dx \, dy - \frac{g}{2} \int_F \zeta_1 \tilde{\zeta}_2 \, dx, \quad (C.5)$$

we have, directly, the reciprocity

$$L^*(\psi_1, \tilde{\psi}_2) = L^*(\tilde{\psi}_2, \psi_1) \quad (C.6)$$

$$\int_S \psi_1 \tilde{\psi}_{2\nu} \, dS = \int_S \tilde{\psi}_2 \psi_{1\nu} \, dS$$

In particular, from (C.3),

$$L^*(\psi_0, \tilde{\psi}_0) = -\frac{1}{2} \int_S \tilde{\psi}_0 \psi_{0\nu} \, dS = -\frac{1}{2} \int_S z \psi_{0\nu} \, dS = \frac{1}{2} \int_S \psi_0 \psi_{0\nu} \, dS$$

$$= \frac{1}{2} \iint_D (\nabla \psi_0)^2 \, dx \, dy - \frac{g}{2} \int_F \zeta_0^2 \, dx = L(\psi_0, \psi_0). \quad (C.7)$$

The variational problem with the function

$$\begin{aligned}
 I^* &= L^*(\psi_0, \tilde{\psi}_0) - L^*(\psi - \psi_0, \tilde{\psi} - \tilde{\psi}_0) \\
 &= \frac{1}{2} \int_S (\psi \tilde{\psi}_n - \psi_0 \tilde{\psi}_n - \tilde{\psi}_0 \psi_n) dS.
 \end{aligned} \tag{C.8}$$

is equivalent to the boundary value problem for ψ . Here, the boundary values, ψ_0 and $\tilde{\psi}_0$, are given by (C.3). Since a stream function has an arbitrary constant, we should also consider the modified problem with boundary conditions

$$\psi_0 = -\tilde{\psi}_0 = C: \text{ constant on } S, \tag{C.9}$$

which is the homogeneous problem. [22]

If condition (C.9) holds, the surface elevation at the fore and aft ends is C (instead of zero for the condition (C.3)), but the x -component of the velocity at the same points is $-(1+gc)$, by (C.2). Hence, the water flows in and out the body unless $C = -1/g$. Thus an adequate condition for a surface piercing body is

$$\psi = -z - \frac{1}{g} \quad \text{on } S. \tag{C.10}$$

Throughout this section, we have treated a class of functions ψ and ξ which are finite and continuous everywhere. As long as the integrals considered exist, the method may be applied with some minor changes to other classes of functions.

The question of the uniqueness of solutions will be left to the future.

WAVEMAKING RESISTANCE OF SHIPS WITH TRANSOM STERN

B. Yim

*Naval Ship Research and Development Center
Washington, D.C.*

ABSTRACT

The wave resistance of ships, having transom sterns and bow bulbs, is analyzed by an indirect method. The total wave resistance of a combination of singularity distributions for such ships is minimized with various parameters of the bulb and the transom stern at each Froude number. The effect of free surface on the body streamlines near the stern is also analyzed.

INTRODUCTION

There has been an increasing interest in ships having transom sterns, not only for high-speed ships like destroyers but also for cargo vessels, because of the advantages of more cargo room as well as modern improvements in techniques of loading and unloading cargoes over the stern. Recently a theoretical study was made by this author [1], and a mathematical model was suggested in view of applying a higher-order ship-wave theory [2]. In this paper, we shall look at the problem again from a different angle, i. e., approaching the problem in a more practical manner.

There are usually two approaches to the ship hydrodynamics problems, direct and indirect. In the direct approach one starts with a given ship and finds a corresponding mathematical representation for it, then, calculates physical quantities, and verifies the results by experiments. On the other hand, one could start with a mathematical model such as a singularity distribution, and calculate the physical quantities of the model, find the corresponding ship form, check the behavior with the experimental results, and utilize the knowledge in designing practical ships. This is an indirect approach. Both approaches are useful in the development of ship science. In Reference 1 by a direct approach, it was found that the transom stern might be represented by a sink line along the stern, having a strength

proportional to the stern draft. Now, we would like to use the indirect approach to the transom stern theory. Noting that a sink line on the free surface is tantamount to the constant pressure distribution ahead of the line and that it produces a negative cosine regular wave and a depression in the free surface immediately behind the sink line, we expect to get streamlines similar to the transom-stern ship from a combination of a normal ship-singularity distribution and the transom sink.

First the free-surface streamline due to a two-dimensional sink line is plotted to establish the validity of this model, which will be used later for plotting the streamline near the transom. Then, several simple original ship singularities are considered so that basic ship models can be modified to those having transom sterns. Since the transom sink is supposed to behave like a stern bulb [1] to cancel stern waves, a bow bulb [3,4] made of a source is also considered together with the stern sink to cancel bow waves as well as to supply source strength which helps form a closed body. Thus, optimum strengths for the bow bulb source together with the transom stern sink are calculated to minimize the total wave resistance.

The wave resistances with and without the bow bulb and the transom stern are calculated. The Sretensky formula for wave resistance is used since it is much simpler to program in the high-speed computing machine than the Havelock formula. Finally, approximate waveforms near the stern are investigated, which will help in designing a good afterbody near the transom stern.

This is part of a project in which the ultimate goal is to understand more the physical meaning of a transom stern in the wavemaking resistance of a ship; to obtain better design criteria for ships with transom sterns; to find out the possibility of an improved ship design with the gained knowledge, and, hopefully, to design a good ship with a transom stern, making full use of high-speed computers as well as testing the model in a towing tank.

Although this is a small part of ship-designing problems, it is not easy to complete in a short time. At this stage, it is merely hoped that this paper will achieve several objectives: (1) to validate the mathematical model of a ship having a transom stern as a stepping stone to analytical investigation of transom sterns, (2) to determine the practical ranges of parameters within which the application of bulbous bows and transom sterns would be beneficial, and (3) to initiate a computational procedure which would be used for an overall design program using a high-speed digital computer.

II. A SINK ON THE TWO-DIMENSIONAL FREE SURFACE

Lamb [5] showed a formula for the free-surface shape due to a point sink with the strength M located at $x = 0$, $y = 0$, moving with constant speed U to $-x$ direction on the free surface, where $+x$ is on the mean free surface pointing right, and $+y$ points vertically upward. The wave height is

$$\eta = \frac{2\pi M}{U} \left\{ -2 \cos k_0 x + \frac{k_0}{\pi} \int_0^\infty \frac{e^{-mx}}{m^2 + k_0^2} dm \right\}, \text{ in } x > 0 \quad (1)$$

where

$$k_0 = \frac{g}{U^2}$$

$$k_0 \int_0^\infty \frac{e^{-mx}}{m^2 + k^2} dm = \left\{ \left(\frac{\pi}{2} - \text{Si } k_0 x \right) \cos k_0 x + \text{Ci } k_0 x \sin k_0 x \right\} \quad (2)$$

in $x > 0$

$$\text{Si } u = u - \frac{u^3}{3 \cdot 3!} + \frac{u^5}{5 \cdot 5!} - \dots \quad (3)$$

$$\text{Ci } u = \gamma + \log u - \frac{u^2}{2 \cdot 2!} + \frac{u^4}{4 \cdot 4!} - \dots \quad (4)$$

$$\gamma = 0.577215665 \quad (5)$$

and g is the acceleration of gravity. If this is compared with the wave height due to the distribution of constant pressure p_0 on $x < 0$, it can be easily seen that

$$\frac{p_0}{\rho g} = \frac{2\pi |M|}{U} \quad (6)$$

holds. Thus, from the Bernoulli equation the form of the free surface in $x < 0$ can be given by

$$\eta = -\frac{p_0}{\rho g} \left(1 + \frac{k_0}{\pi} \int_0^\infty \frac{e^{-mx}}{m^2 + k_0^2} dm \right), \text{ in } x < 0 \quad (7)$$

The wave height for $x \leq 0$ is plotted in Fig. 1 and it clearly shows

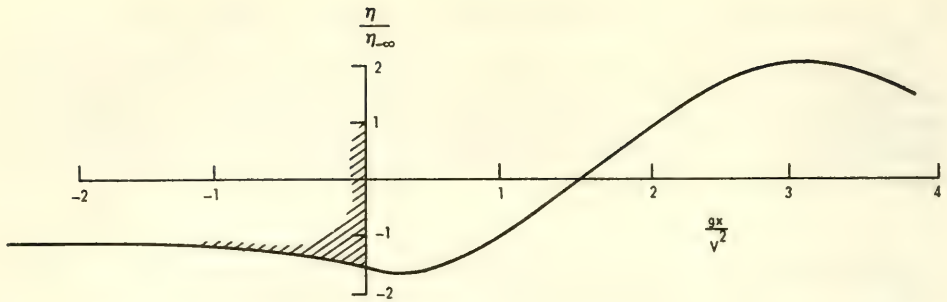


Fig. 1. Stem Waveform by a Sink Line Transform Stem

the appropriateness of this flow model in the vicinity of the transom stern. The integral term is the local disturbance which dies down rapidly with $|x|$, and the expression of η in $x < 0$ can be interpreted as the body streamline of the half body which is formed by a sink on the free surface with a total flux equal to $u\eta_{-\infty} = up_0/(\rho g) = 2\pi M$. This kind of two-dimensional half body was treated by Afremov [6] in investigating the flow near a transom stern, thus obtaining pressure distribution of the two-dimensional half body,

$$y = -\eta_0 e^{ax}, \quad \text{in } x \leq 0 \quad (8)$$

with the parameter $a \geq 0$. He obtained a sharp rise of pressure near the edge of the transom stern where the pressure is zero, the value of atmospheric pressure. This sudden rise of pressure at the stern can also be observed from experiments of planning ships [7].

However, the application of the two-dimensional analyses is generally valid only near the transom stern. In addition, in designing the afterbody near the transom stern, the investigation of hydrodynamic interactions between other parts of ship hull and transom stern is important, especially the superposition of ship wave systems from bow, stern, and any discontinuities of the hull; this will be discussed later.

III. SHIPS WITH TRANSOM STERNS AND BOW BULBS

It seems reasonable to say that the general representation of a ship with a transom stern and a bow bulb may be achieved by combining singularity distributions: a source distribution along a given base surface with either point or line doublets or sources for the bow bulb, and a line sink distribution for the transom stern along a line

that is on the free surface, at the stern, and perpendicular to the ship centerplane. In the previous section it is known that the transom stern can be represented by a sink line at the stern, it is therefore natural to deduce that the sink could contribute in cancelling stern waves [1]. Since a moving point sink produces negative cosine regular waves behind, the proper main hull should have a hull shape that produces positive cosine stern waves. To investigate the best shape of transom sterns, in a simple way, we have chosen two simple bare-hull forms, represented in the Michell sense by the following equations:

$$y_1 = \frac{B_1}{4L} \{1 - \cos(2\pi x)\}, \quad \text{in} \quad \begin{matrix} -1 < x < 0 \\ -\frac{H}{L} < z < 0 \end{matrix} \quad (9)$$

and

$$y_2 = -\frac{2B_2}{L}(x + x^2), \quad \text{in} \quad \begin{matrix} -1 < x < 0 \\ -\frac{H}{L} < z < 0 \end{matrix} \quad (10)$$

where L , B_1 , and H are the ship length, the beam, and the draft, respectively; (x, y, z) is the right-hand rectangular cartesian coordinate system with the origin O on the free surface; the x axis is in the direction of the uniform flow velocity at infinity; and the z axis is vertically upward. The hull in Eq. (9) produces the favorable stern waves for the transom stern but has cusps in both ends and is called a cusped cosine ship here. The hull in Eq. (10) is rather a common parabolic hull form, not particularly favorable for the transom stern. The corresponding source distributions by the Michell approximation are

$$\sigma_1 = \frac{UB_1}{4L} \sin(2\pi x) \quad (11)$$

in

$$D(y = 0, -1 < x < 0, -H/L < z < 0) \quad (12)$$

and

$$\sigma_2 = -\frac{UB_2}{\pi L}(1 + 2x), \quad \text{in} \quad D \quad (13)$$

The theory of superposition can be allowed in the sense of the Michell ships. For convenience, we set

$$\sigma = \sigma_1 + \sigma_2 \quad (14)$$

with

$$B = B_1 + B_2 \quad (15)$$

where B is the beam of a superposed ship.

For the transom stern, a triangular shape of stern draft is considered as

$$z = \pm \alpha y - H_s/L, \quad \text{in} \quad -\frac{B}{2L} < y < \frac{B}{2L} \quad (16)$$

where α denotes the deadrise which takes on a negative value for $y < 0$, and a positive value for $y > 0$,

$$\frac{H_s}{L} = - \left| \alpha \frac{B}{2L} \right| \quad (17)$$

is the maximum stern draft; and α is a parameter to be determined for the total optimum wave resistance. Following Ref. 1, the source distribution for the transom stern is taken as

$$\sigma_s = - \frac{U}{4\pi} \left(\frac{H_s}{L} \mp \alpha y \right) \quad (18)$$

although actual shape of the transom stern corresponding to this source distribution will be found later by streamline plotting. In addition, a point source located at bow stern, $x = -1$, $y = 0$, $z = z_b$ with the strength σ_b is considered as a source type of bulb that contributes to form a closed body with the sink distribution at the stern as well as to reduce bow waves.

IV. WAVE RESISTANCE

The wave resistance due to the source distributions mentioned previously can be written according to Sretensky [8]

$$\frac{R}{\frac{1}{2}\rho U^2 L^2} = \frac{16\pi^2 k}{w} \sum_{m=0}^{\infty} \epsilon_m \frac{2b^2}{2b^2 - 1} (P^2 + Q^2) \quad (19)$$

where

$$k = \frac{gL}{U^2} = \frac{1}{F_n^2}$$

$$\epsilon_m = \begin{cases} 1 & \text{when } m = 0 \\ 2 & \text{when } m \geq 1 \end{cases} \quad (20)$$

$$b = \sqrt{\frac{1}{2} + \frac{1}{2} \sqrt{1 + \left(\frac{4\pi m}{kw}\right)^2}} \quad (21)$$

Lw = tank width where the ship is tested,

$$P + iQ = \int_s \sigma(x, y, z) \exp \left\{ kb(zb + ix) + i2\pi y \frac{m}{w} \right\} dS(x, y, z) \quad (22)$$

Substituting in Eq. (22) all the source distributions for the bare hulls, the transom stern, and the bow bulb, and performing the integration, we obtain

$$P_1 = \left[\left\{ 1 - \cos(kb) \right\} \left\{ \frac{\pi}{k^2 b^2 - 4\pi^2} \frac{B_1}{L} - \frac{2B_2}{\pi k^2 b^2 L} \right\} + \frac{\sin(kb)B_2}{\pi kbL} \right] \cdot E \quad (23)$$

$$P_2 = \frac{-1}{8\pi^3 \left(\frac{m}{w}\right)^2} \left\{ 1 - \cos \left(B_2 \pi \frac{m}{w} \right) \right\} \quad (24)$$

$$P_3 = \cos(kb) \exp(kz_1 b^2) \quad (25)$$

$$Q_1 = \left[\sin(kb) \left\{ \frac{\pi B_1 / (2L)}{k^2 b^2 - 4\pi^2} - \frac{2B_2}{\pi k^2 b^2 L} \right\} + \frac{B_2}{\pi kbL} + \cos(kb) \frac{B_2}{\pi kbL} \right] \cdot E \quad (26)$$

$$Q_2 = 0 \quad (27)$$

$$Q_3 = -\sin(kb) \exp(kz_1 b^2) \quad (28)$$

where subscripts 1, 2, and 3 correspond to the bare hull, transom sink, and bow bulb, respectively,

$$E = \left\{ 1 - \exp \left(-kb \frac{2H}{L} \right) \right\} \frac{1}{kb} \quad (29)$$

$$P = P_1 + \alpha P_2 + \frac{\sigma_b}{U} P_3 \quad (30)$$

and

$$Q = Q_1 + \alpha Q_2 + \frac{\sigma_b}{U} Q_3 \quad (31)$$

with the functions P and Q evaluated and substituted into Eq. (19), the wave resistance may be minimized with respect to such parameters as α and σ_b .

V. OPTIMUM TRANSOM STERN AND BOW BULB

A usual technique is employed to obtain the optimum values of α and σ_b for given k , B_1/L , B_2/L , z_1 , and H/L . Namely, we solve two linear simultaneous equations in α and σ_b

$$\begin{aligned} \frac{\partial R}{\partial \alpha} &= 2\alpha(\overline{P_2^2} + \overline{Q_2^2}) + 2\sigma_b(\overline{P_2 P_3} + \overline{Q_2 Q_3}) + 2(\overline{P_1 P_2} + \overline{Q_1 Q_2}) = 0 \\ \frac{\partial R}{\partial \sigma_b} &= 2\alpha(\overline{P_2 P_3} + \overline{Q_2 Q_3}) + 2\sigma_b(\overline{P_3^2} + \overline{Q_3^2}) + 2(\overline{P_1 P_3} + \overline{Q_1 Q_3}) = 0 \end{aligned} \quad (32)$$

for α and σ_b , where

$$P_i P_j \equiv \frac{16\pi^2 k}{w} \sum_{m=0}^{\infty} \epsilon_m \frac{2b^2}{2b^2 - 1} P_i P_j \quad (33)$$

etc.

from the formula of wave resistance. Cases of $B_2 = 0$, $B_1 \neq 0$; $B_2 \neq 0$, $B_1 = 0$ and $B_1 \neq 0$, $B_2 \neq 0$ were calculated for each Froude number F_n , which will be shown later.

VI. SLENDER BODY THEORY

For the case of $B_2 = 0$, the cross sectional area curve is a cusp at both ends. Thus a slender body theory can easily be applied here. The result will be only the change of

$$E \rightarrow 1 \quad (34)$$

and

$$\frac{B_1}{L} \rightarrow \frac{A}{L^2} \quad (35)$$

in P_1 and Q_1 in Eqs. (23) and (26) of the wave resistance of the previously described Michell ship, where A is the area of the mid-

ship section.

The slender ship approximation is useful for the ship with a transom stern because this may give better chances to represent the ship shape near the transom than Michell approximation. Yet for the case of low Froude numbers it is well known that the usual slender ship theory is also very poor. To improve this situation, the slender ship theory can be modified further from that developed by Maruo [11].

In the equations of wave resistance Eqs. (19) through (22), by consecutive applications of integration by part to Eq. (22)

$$\begin{aligned}
 P + iQ &= \int_S \sigma \exp \left\{ kb(zb + ix) + i2\pi y \frac{m}{w} \right\} dS \\
 &= \frac{1}{ikb} \left\{ \int_{c(0)} \sigma(0, y, z) \exp \left(kzb^2 + i2\pi y \frac{m}{w} \right) dc \right. \\
 &\quad - \int_{c(-l)} \sigma(-1, y, z) \exp \left\{ kb(zb - i) + i2\pi y \frac{m}{w} \right\} dc \\
 &\quad \left. - \int_{-l}^0 dx e^{ikxb} \frac{d}{dx} \int_{c(x)} \sigma \exp \left(kzb^2 + i2\pi y \frac{m}{w} \right) dc \right\} \\
 &= \frac{1}{ikb} \left\{ \int_{c(0)} \sigma(0, y, z) \exp \left(kzb^2 + i2\pi y \frac{m}{w} \right) dc \right. \\
 &\quad \left. - \int_{c(-l)} \sigma(-1, y, z) \exp \left\{ kb(zb - i) + i2\pi y \frac{m}{w} \right\} dc \right\} \\
 &\quad + \frac{1}{k^2 b^2} \left[\left\{ \frac{d}{dx} \int_{c(x)} \sigma \exp \left(kzb^2 + i2\pi y \frac{m}{w} \right) dc \right\} e^{ikxb} \right]_{x=-1}^{x=0} \\
 &\quad - \int_{-l}^0 dx e^{ikxb} \frac{d^2}{dx^2} \int_{c(x)} \sigma \exp \left(kzb^2 + i2\pi y \frac{m}{w} \right) dc \quad (36)
 \end{aligned}$$

where

$$dS = dx \, dc \quad (37)$$

The last integral can be approximated by

$$\frac{1}{k^2 b^2} \int_{-1}^0 dx e^{ikxb} M''(x)$$

where

$$M(x) \equiv \int_{c(x)} \sigma(x, y, z) dc \quad (38)$$

This reduces the influences of the line singularity approximation of ship hull singularities in two ways, (1) by the factor $1/b^2$, which corresponds to $\cos^2 \theta$ in the Havelock wave resistance formula, (2) by the factor $1/k^2$ which is the smaller if the Froude number is the smaller. Of course, the number of terms have been increased in the singularities along $c(0)$, which is the intersection of the free surface and the transom stern, and $c(-1)$, which is the straight bow stem line.

VII. STREAMLINES

To establish the validity of the mathematical model of the ship with the transom stern, the double model [9,10] scheme is inadequate because free-surface waves play a vital role in the flow field of a transom stern.

Fortunately a slender ship model [11,12] gives an easy representation of the wave height along the train of ship. The wave height is

$$\zeta(x_1, y_1) = \frac{\varphi_{x_1}}{k}(x_1, y_1, 0) \quad (39)$$

and

$$\begin{aligned} \varphi(x_1, y_1, 0) = & -\frac{k}{\pi U} \iint_S \sigma(x, y, z) dS \\ & \times \operatorname{Re} \int_{-\pi}^{\pi} \sec^2 \theta \int_0^{\infty} \frac{e^{it\omega}}{t - k \sec^2 \theta - i\mu \sec \theta} dt d\theta \quad (40) \end{aligned}$$

where

$$\omega = (x_1 - x) \cos \theta + (y_1 - y) \sin \theta \quad (41)$$

and S is the ship surface.

The inner double integral was treated by Havelock and was represented by both a Bessel and a Struve functions. [13,14] We will consider, for simplicity, a source distribution which becomes

zero at both ends of a ship such as we considered in Eq. (11), although this is not a basic necessity for evaluating physical quantities, namely,

$$\sigma(0, y, z) = \sigma(-1, y, z) = 0$$

By making use of this assumption we integrate the wave-height Eq. (39) by parts

$$\begin{aligned} \zeta(x_1, y_1) &= \frac{\varphi_{x_1}}{k} (x_1, y_1, 0) \\ &= -\frac{1}{\pi U} \int_{-1}^0 e^{-i\pi x \cos \theta} dx \frac{d}{dx} \int_{c(x)} \sigma dc \operatorname{Re} \int_{-\pi}^{\pi} \int_0^{\infty} \frac{\sec^2 \theta e^{t(i\omega_1 + z)}}{t - k \sec^2 \theta - i\mu \sec \theta} dt d\theta \\ &= \frac{\operatorname{Re}}{\pi U} \int_{-\pi}^{\pi} \int_0^{\infty} \frac{I(x_1, y_1; t, \theta)}{t - k \sec^2 \theta - i\mu \sec \theta} dt d\theta \end{aligned} \quad (42)$$

where

$$\omega_1 = x_1 \cos \theta + (y_1 - y) \sin \theta \quad (43)$$

$$I(x_1, y_1; t, \theta) = - \int_{-1}^0 e^{-itx \cos \theta} dx \frac{d}{dx} \int_{c(x)} \sigma \sec^2 \theta e^{t(i\omega_1 + z)} dc \quad (44)$$

Integrating I by parts with respect to x , we obtain

$$\begin{aligned} I(x_1, y_1; t, \theta) &= \frac{1}{it} \left[\frac{d}{dx} \int_{c(0)} \sigma(0, y, z) \sec^3 \theta e^{t(i\omega_1 + z)} dc \right. \\ &\quad - \frac{d}{dx} \int_{c(-1)} \sigma(-1, y, z) \sec^3 \theta \exp \left\{ ti(\overline{x_1 + 1} \cos \theta + \overline{y_1 - y} \sin \theta) + tz \right\} dc \\ &\quad \left. - \int_{-1}^0 dx e^{-itx \cos \theta} \frac{d^2}{dx^2} \int_{c(x)} \sigma(x, y, z) \sec^3 \theta e^{t(i\omega_1 + z)} \right] dc \end{aligned} \quad (45)$$

For simplicity $\sigma_x(0, y, z)$ and $\sigma_x(-1, y, z)$ are assumed to be uniformly distributed, respectively, along the stern on the free surface and along the bow stern vertically. For investigation of the flow field near the transom stern, the contribution of $\sigma_x(0, y, z)$ to the wave height may be approximated by two-dimensional values; the contribution of $\sigma_x(-1, y, z)$ may be approximated by the stationary phase; and the contribution from the last integral of $I(x, y; t, \theta)$ may be approximated by a slender body theory, and will be investigated first, here.

Now let us investigate the last (third) term of the above integral I. From the slender body theory

$$\begin{aligned} \frac{d^2}{dx^2} \int_{c(x)} \sigma(x, y, z) \exp \{ti(x_1 \cos \theta + \overline{y_1 - y} \sin \theta) + tz\} dc \\ = \frac{d^2 M(x)}{dx^2} \exp \{ti(x_1 \cos \theta + y_1 \sin \theta)\} \end{aligned} \quad (46)$$

With this approximation, we go back to the wave-height Eq. (42) and consider the values only on $y_1 = 0$

$$\zeta_3(x_1, 0) = - \frac{Re}{\pi U} \int_{-1}^0 dx M''(x) \int_{-\pi}^{\pi} \int_0^{\infty} \frac{\sec^3 \theta e^{ti(x_1 - x) \cos \theta}}{it(t - k \sec^2 \theta - i\mu \sec \theta)} dt d\theta \quad (47)$$

Changing the contour of integration with respect to t in a complex plane such as Havelock [13] used, we have

$$\begin{aligned} \zeta_3(x_1, 0) &= - \frac{1}{k\pi U} \int_{-1}^0 dx M''(x) \int_{-\pi}^{\pi} \sec \theta d\theta \int_0^{\infty} \frac{\sin(km\overline{x_1 - x} \sec \theta)}{m(1+m)} dm d\theta \\ &\quad + \int_{-1}^{x_1} dx M''(x) \int_{-\pi}^{\pi} 2\pi \sec \theta \cos(k\overline{x_1 - x} \sec \theta) d\theta \\ &= \frac{\pi}{Uk} \int_{-1}^0 dx M''(x) \left[\left\{ \frac{2}{\pi} \log |x_1 - x| - Y_0(k|x_1 - x|) \right\} \right. \\ &\quad \times \left. \text{sign}(x_1 - x) + H_0(k\overline{x_1 - x}) \right] \\ &\quad + \frac{4\pi}{Uk} \int_{-1}^{x_1} dx M''(x) Y_0(k|x_1 - x|) \end{aligned} \quad (48)$$

where Y is the Neumann function, H is the Struve function, and $\text{sign}(x_1 - x)$ is $+1$ for $x_1 - x > 0$ and -1 for $x_1 - x < 0$.

When only the integral of the first term of I in Eq. (45) is taken, we may approximate the wave height as follows, for $x_1 < 0$:

$$\begin{aligned}
 \zeta_1 &= \frac{\text{Re } \sigma_x}{\pi U} \int_{-B/2}^{B/2} dy \int_{-\pi}^{\pi} d\theta \int_0^{\infty} dt \frac{\sec^3 \theta e^{it(x_1 \cos \theta - y \sin \theta)}}{it(t - k \sec^2 \theta - i\mu \sec \theta)} \\
 &= \int_0^{x_1} dx \text{Re } \frac{\sigma_x}{\pi U} \int_{-B/2}^{B/2} dy \int_{-\pi}^{\pi} d\theta \int_0^{\infty} dt \frac{\sec^2 \theta e^{it(x \cos \theta - y \sin \theta)}}{t - k \sec^2 \theta - i\mu \sec \theta} + J \\
 &= \int_0^{x_1} dx \text{Re } \frac{\sigma_x}{k\pi U} \int_{-B/2}^{B/2} dy \int_{-\pi}^{\pi} d\theta \int_0^{\infty} dt \left[-1 + \frac{t - i\mu \sec \theta}{t - k \sec^2 \theta - i\mu \sec \theta} \right] \\
 &\quad \times e^{it(x \cos \theta - y \sin \theta)} + J \\
 &= - \int_0^{x_1} dx \frac{\sigma_x}{kU} \int_{-B/2}^{B/2} dy \frac{2}{\sqrt{x^2 + y^2}} + \int_0^{x_1} \frac{\sigma_x}{k\pi U} dx \lim_{y_1 \rightarrow \infty} \int_{-\pi/2}^{\pi/2} d\theta \int_0^{\infty} dt \\
 &\quad \times \frac{4e^{i\pi x \cos \theta} \sin(ty_1 \sin \theta)}{\sin \theta (t - k \sec^2 \theta - i\mu \sec \theta)} + J \\
 &= -4 \int_0^{x_1} dx \frac{\sigma_x}{kU} \log \frac{\sqrt{x^2 + B^2/4} + B/2}{|x|} + 4 \frac{\sigma_x}{kU} \int_0^{x_1} dx \int_0^{\infty} \frac{e^{itx} dt}{t - k - i\mu} + J
 \end{aligned}
 \tag{49}$$

Note that $t = 0$ is not a singularity because of the zero of $\sin \{t(x_1 \cos \theta - y \sin \theta)\}$ in the numerator of the real integrand. The integrand J is defined as follows:

$$\begin{aligned}
 J &= \text{Re } \frac{\sigma_x}{\pi U} \int_{-B/2}^{B/2} dy \int_{-\pi}^{\pi} d\theta \int_0^{\infty} \frac{\sec^3 \theta e^{-i\pi y \sin \theta} dt}{it(t - k \sec^2 \theta - i\mu \sec \theta)} \\
 &= \text{Re } \frac{2\sigma_x}{\pi U} \int_0^{B/2} dy \int_0^{\pi} d\theta \int_0^{\infty} \frac{dt}{k i} \sec \theta \left\{ \frac{-1}{t} \right. \\
 &\quad \left. + \frac{1}{t - k \sec^2 \theta - i\mu \sec \theta} \right\} (e^{-ity \sin \theta} + e^{ity \sin \theta}) \\
 &= \text{Re } \frac{\sigma_x}{\pi U} \lim_{B \rightarrow \infty} 4\pi \int_0^{\pi} \frac{d\theta \cos \theta}{ik \sin \theta} e^{ik \frac{B}{2} \sec^2 \theta \sin \theta} \\
 &= 2\sigma_x \pi / (k^2 U)
 \end{aligned}
 \tag{50}$$

Letting

$$I_1 \equiv \int_0^{x_1} dx \int_0^\infty \frac{e^{itx} dt}{t - k - i\mu}$$

we have

$$I_1 = \int_0^\infty \frac{e^{mx_1} - 1}{m^2 + k^2} dm \quad \text{in } x_1 < 0$$

$$= -\frac{\pi}{2k} + \frac{1}{k} \left\{ \left(\frac{\pi}{2} - \text{Si} kx_1 \right) \cos kx_1 + \text{Ci} kx_1 \sin kx_1 \right\},$$

and

$$I_1 = \frac{2\pi}{k} \cos kx_1 - \frac{3\pi}{2k} - \frac{1}{k} \left\{ \left(\frac{\pi}{2} - \text{Si} kx_1 \right) \cos kx_1 \right. \\ \left. + \text{Ci} kx_1 \sin kx_1 \right\}, \quad \text{in } x_1 > 0$$

Therefore, for $x_1 < 0$

$$\zeta_1 \doteq \frac{\sigma_x}{kU} \left[4x_1 (\log |x_1| - 1) - 4 \int_0^{x_1} dx \log (\sqrt{x^2 + B^2/4} + B/2) \right. \\ \left. + \frac{4}{k} \left\{ \left(\frac{\pi}{2} - \text{Si} kx_1 \right) \cos kx_1 + \text{Ci} kx_1 \sin kx_1 \right\} \right] \quad (52a)$$

and for $x_1 > 0$

$$\zeta_1 \doteq \frac{\sigma_x}{kU} \left[4x_1 (\log x_1 - 1) - 4 \int_0^{x_1} dx \log (\sqrt{x^2 + B^2/4} + B/2) \right. \\ \left. + \frac{8\pi}{k} \cos kx_1 - \frac{4\pi}{k} - \frac{4}{k} \left\{ \left(\frac{\pi}{2} - \text{Si} kx_1 \right) \cos kx_1 \right. \right. \\ \left. \left. + \text{Ci} kx_1 \sin kx_1 \right\} \right] \quad (52b)$$

The wave height related to the second term of I can be approximated by the method of stationary phase, [5] neglecting the local disturbance:

$$\zeta_2 = -4 \sqrt{\frac{2\pi}{kx}} \frac{\sigma_x(-1, 0, 0)}{U} (1 - e^{-kH}) \cos \left(kx + \frac{\pi}{4} \right) \quad (53)$$

The wave height near the stern due to a point source at the bow can be approximated also by the method of stationary phase:

$$\zeta_b = 4k \frac{\sigma_b}{U} \exp(kz_1) \sqrt{\frac{2\pi}{kx_1}} \cos(kx_1 + \frac{\pi}{4}) \quad (54)$$

The wave height near the stern due to the transom stern sink, approximated by the two-dimensional one, was given earlier, say ζ_s .

As a result, the total sum of ζ_3 , ζ_2 , ζ_b , and ζ_s would represent an approximate wave height in the wake of the ship near the transom stern. The streamlines on the body near the stern can be obtained by considering the pressure which is given by the singularity representation as was done in Eqs. (6) and (7). The streamlines near the bow may be obtained by a double model approximation. The integrated scheme to produce approximate body streamlines will be programmed for a high-speed computer in the near future.

VIII. NUMERICAL RESULTS AND DISCUSSIONS

The optimal strength of singularities for the transom stern and for the bow bulb are shown in Figs. 2, 4, and 6. The former is shown in terms of the deadrise angle α of the afterbody near the stern. The latter is shown in terms of the radius of the corresponding half body produced by the point source located in the infinite medium. These are all functions of Froude numbers for the given hull shapes. The wave resistance at each Froude number is computed for the given hull with the transom stern and the bow bulb optimal at a given Froude number; see Figs. 3, 5, 7, and 8.

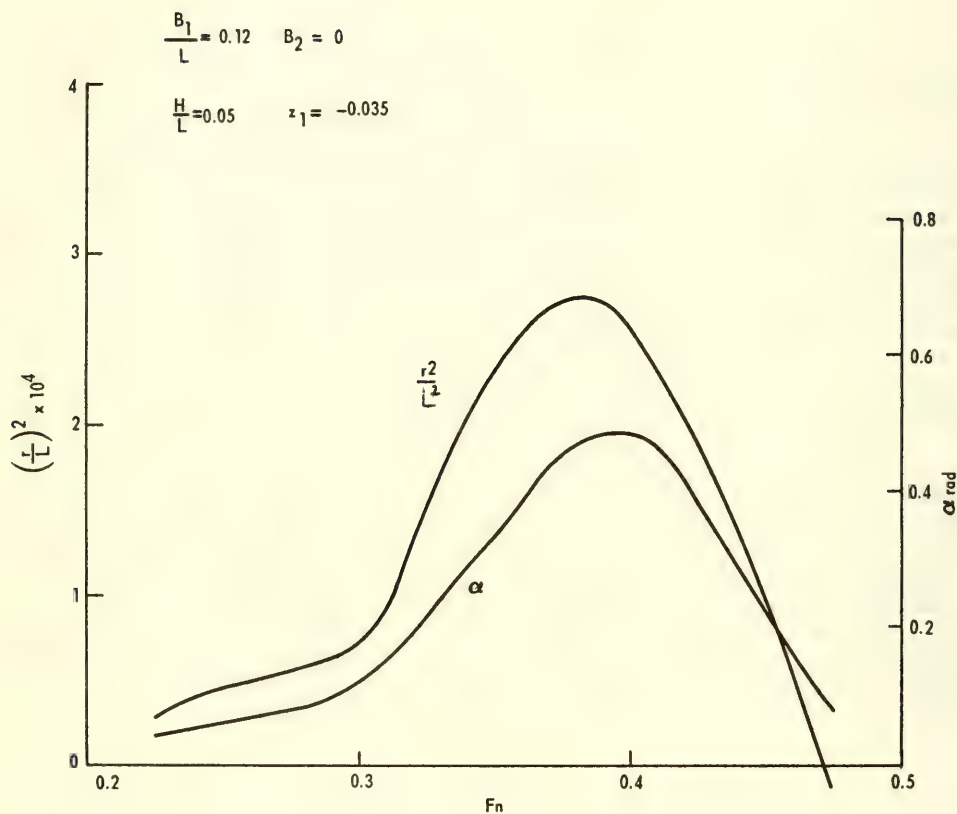


Fig. 2. Optimal Values of Bulb Size and Transom Dead Rise Angle for a Cusped Cosine Ship Using the Michell Ship Theory

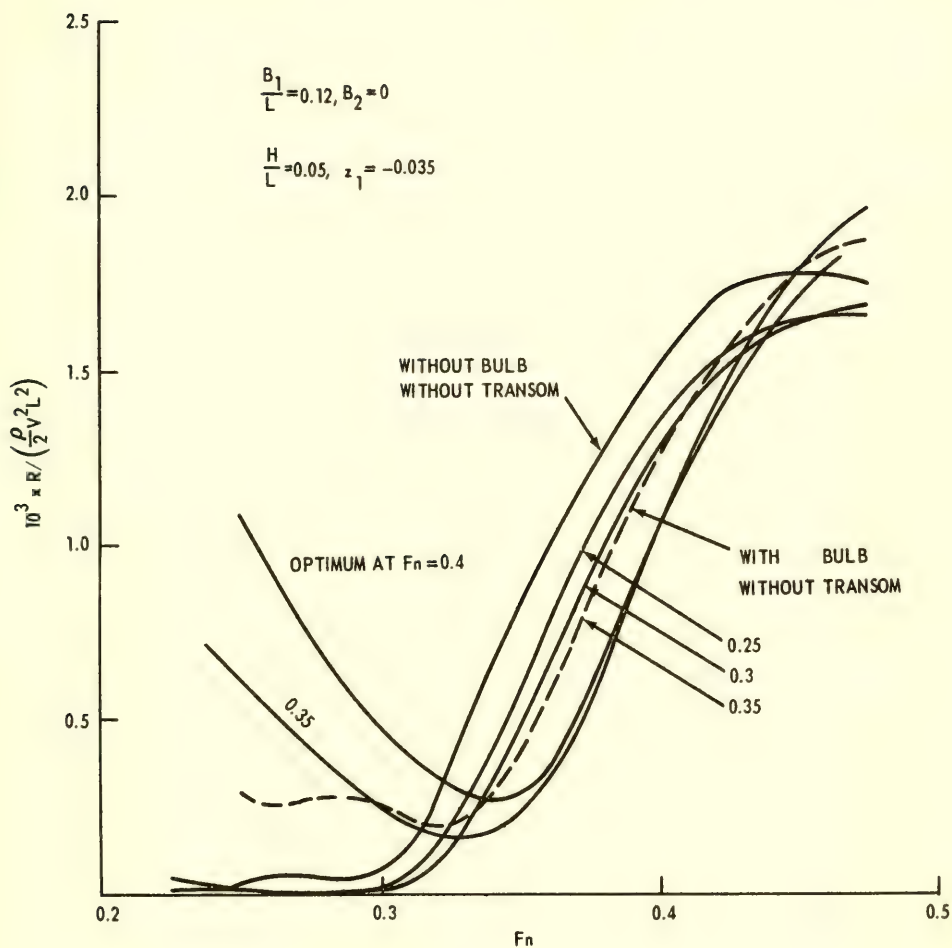


Fig. 3. Wave Resistance of Cusped Cosine Ships with Optimum Bows and Transom Sterns, using the Michell Ship Theory

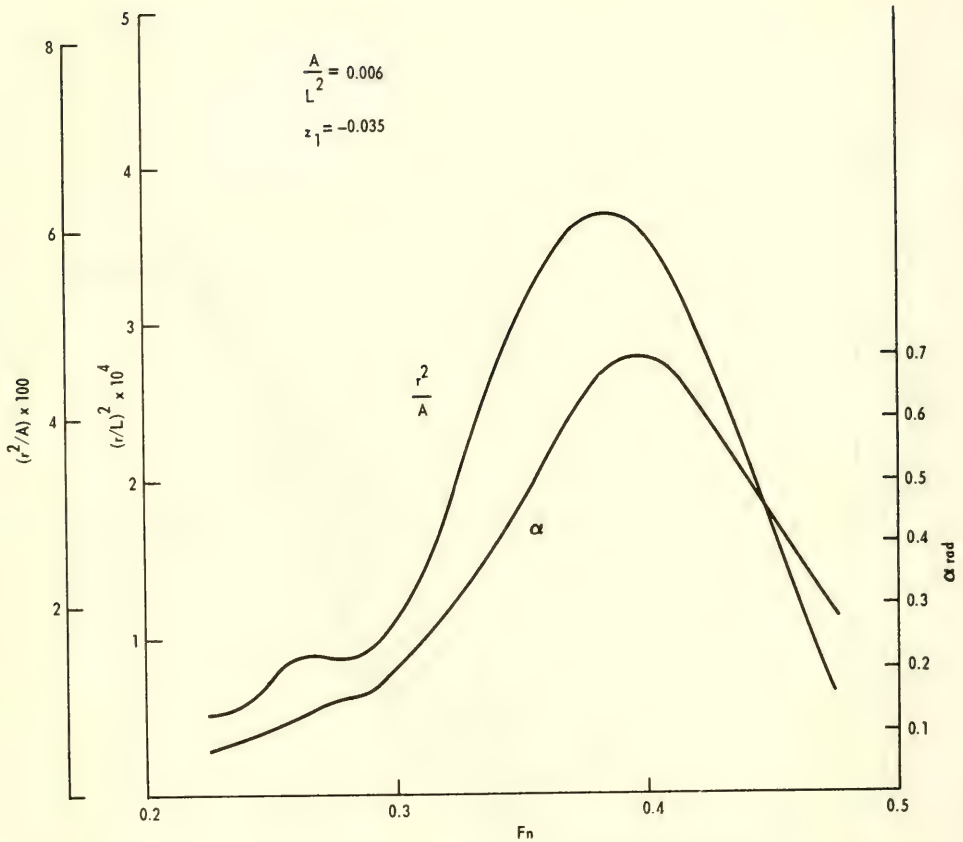


Fig. 4. Optimal Values of Bulb Size and Transom Deadrise Angle for a Cusped Cosine Ship, using the Slender Body Theory

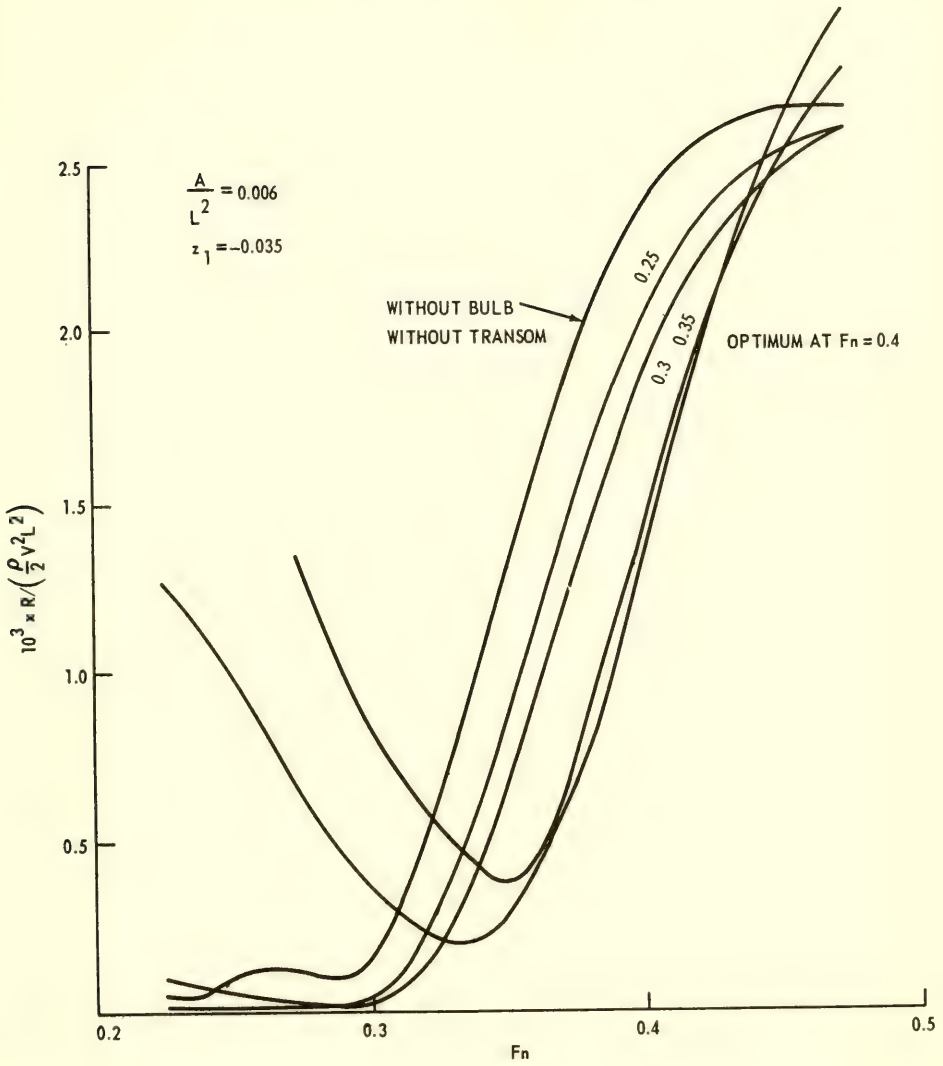


Fig. 5. Wave Resistance of Cusped Cosine Ships with Optimum Bulbous Bows and Transom Sterns, using the Slender Ship Theory

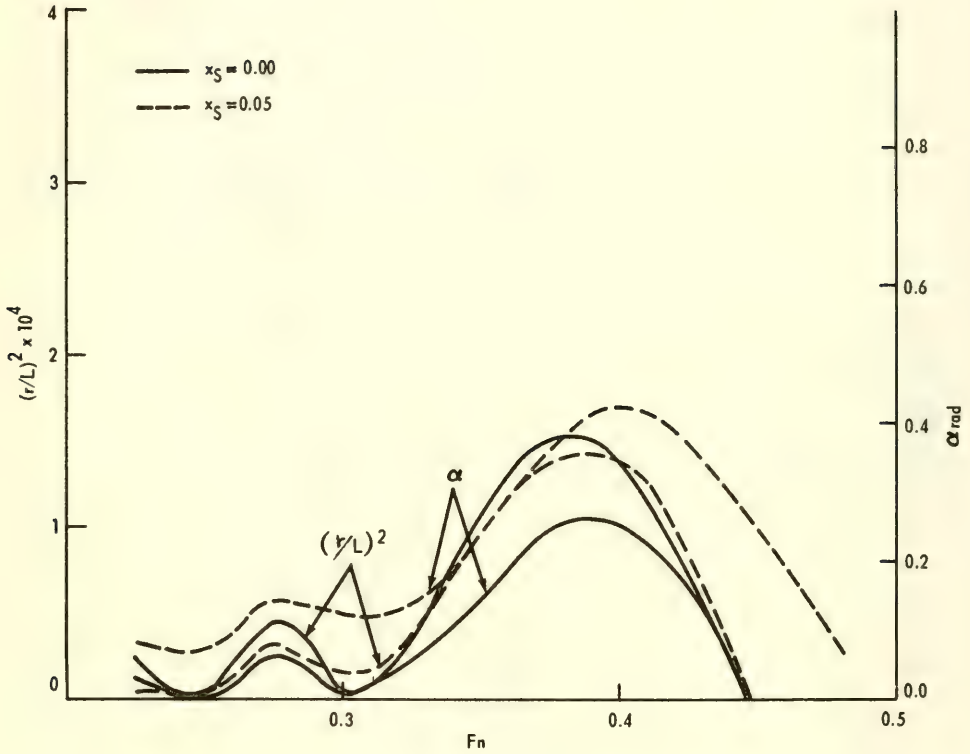


Fig. 6. Optimal Values of Bulb Size and Transom Deadrise Angle for Cusped Cosine-Parabolic Ships $B_1 = B_2$, $B_1/L = 0.06$, $H/L = 0.05$, $z_1 = -0.035$

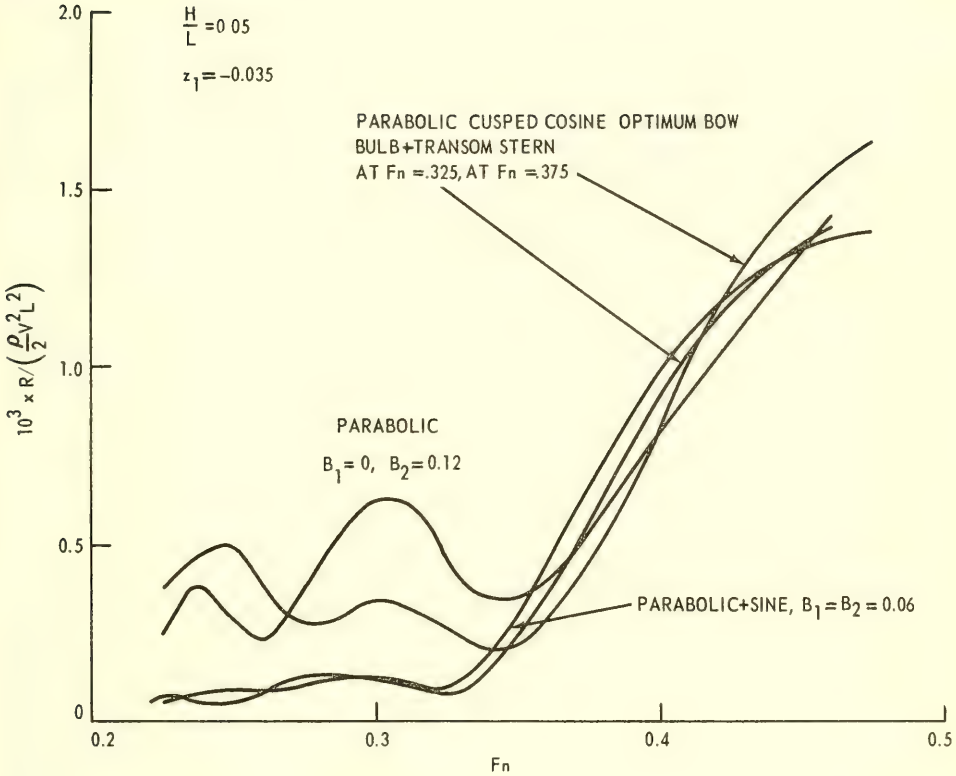


Fig. 7. Wave Resistance of Ships of Cusped Cosine and Parabolic Waterlines with and without Bulb and Transom Sterns ($x_s = 0$)

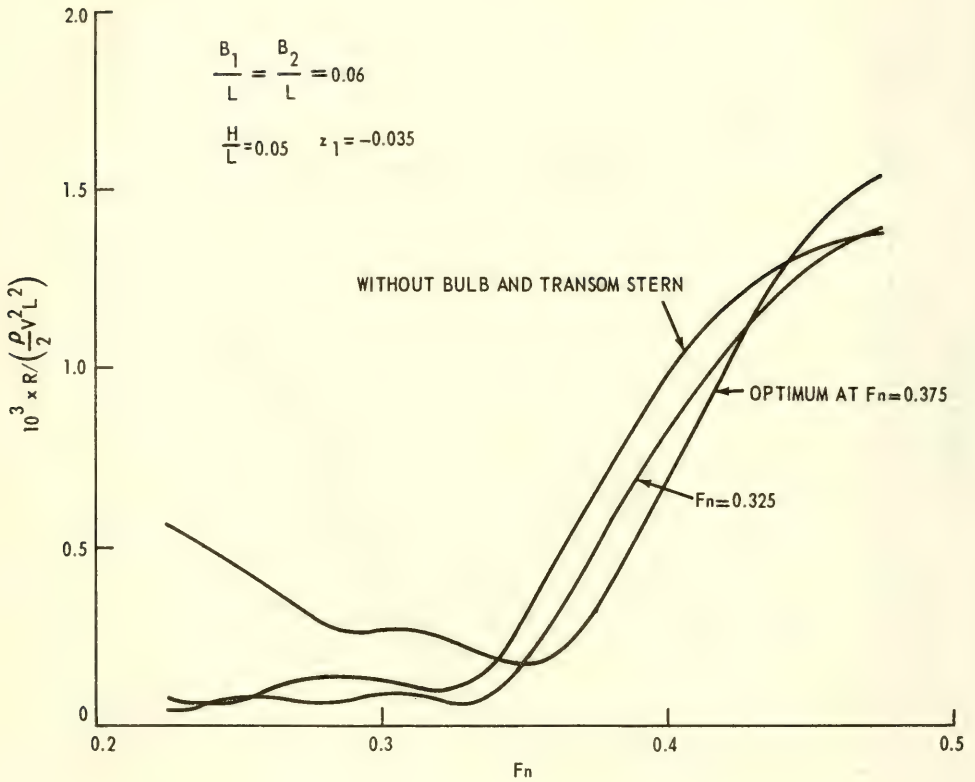


Fig. 8. Wave Resistance of Ships of Cusped Cosine and Parabolic Waterlines with and without Bulbous Transom Stern ($x_s = 0.05$)

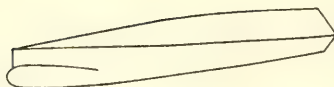
For a slender body model, Eqs. (11) and (35) are used for the bare-hull source distribution, which is called a cusped cosine ship here. For a Michell thin ship model, computations are performed for Eq. (11) for cusped cosine and parabolic ships. For the combined bare-hull source distribution, the influence of the location of transom stern x_s is shown in Figs. 6 through 8. It can be understood that there is an optimal location for the minimum wave resistance as in the case of a bulbous bow; however, it is not computed here.

It is interesting and reasonable to see that the optimum size of the bulb becomes the smaller for the large Froude numbers over 0.4, and eventually the strength becomes negative at $F_n > 0.5$. In other words, for a large Froude number, a ship behaves like a single point doublet far behind the ship so that the only way to reduce the wave height is to reduce the ship volume.

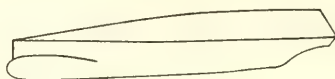
Indeed it is possible to take advantage of the transom stern as well as the bulbous bow to reduce wave resistance in the Froude number range $F_n < 0.5$ by a proper combination of the ship hull shape and the transom stern and the bow bulb. For the case of a high-speed ship such as a planing boat, there is no alternative to evade the detrimental cavitation without having the full separation occur at the transom stern, whether it is beneficial to the wave resistance or not.

The numerical results of streamlines are not given in the present paper because of their complexity. The approximate method of computation of the streamlines near the stern is shown in the previous section. When the ship draft is fairly large, compared with the wavelength, the ship shape from the singularities can be approximately computed from the double model. However, for a transom stern, the free surface follows immediately behind the usually shallow drafted afterbody. Thus, the modified slender body theory used in the previous sections, combined with a double model approach to the forward part of ship hull seems to be promising. Some imaginative approximate configurations from the concerned source distributions are shown in Fig. 9.

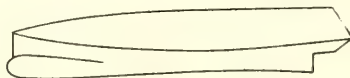
Last, but not least, the importance of experiments on the design of ships with transom sterns should be emphasized. There are very few experimental results available [15]. However, this has to be done in close coordination with the theory so as not to grope in the dark. The theory is now on a solid foundation. More time and effort are needed to achieve experimentally usable and complete results on ships with transom stern. In the future, the author hopes to finish a systematic computer program for designing ships with bulbous bow and transom stern that includes information about the wave resistance, the bulb size, the transom-stern draft, and the main hull shape.



A Cusped Cosine Ship with Bulb and Transom Stern 1



A Cusped Cosine Ship with Bulb and Transom Stern 2



A Cusped Cosine - Parabolic with Bow Bulb and
Transom Stern ($x \neq 0$)

Fig. 9. Imaginative Diagram for Ships with Bulb and Transom Stern

ACKNOWLEDGMENT

This work was carried out under the General Hydrodynamic Research Program of the Naval Ship Research and Development Center. The author expresses his thanks to Mr. J. B. Hadler, Head, Ship Powering Division, NSRDC, for his encouragement in numerous discussions. Thanks are also due to Dr. P. C. Pien for his valuable advice, Mr. H. M. Cheng for reviewing the manuscript and his help in editing, and Mrs. L. Greenbaum for her patient effort in the preparation of the manuscript.

REFERENCES

1. Yim, B., "Analyses of Waves and the Wave Resistance due to Transom-Stern Ships," Journal of Ship Research, Vol. 13, No. 2, June 1969.
2. Yim, B., "Higher Order Wave Theory of Ships," Journal of Ship Research, Vol. 12, No. 3, Sept. 1968.
3. Maruo, H., "Problems Relating to the Ship Form of Minimum Wave Resistance," Proceedings of Fifth Symposium on Naval Hydrodynamics, ONR, Department of the Navy, 1964.

4. Yim, B., "Some Recent Developments in Theory of Bulbous Ships," Proceedings of Fifth Symposium on Naval Hydrodynamics, ONR, Department of the Navy, 1964.
5. Lamb, H., "Hydrodynamics," Cambridge University Press, Cambridge, England, 1932, Sixth Edition.
6. Afremov, A. Sh., "Sbornik Statey po Gidromekhanika i Dinamike Sudna," USSR, 1967, pp. 130-146.
7. Sottorf, W., "Experiments with Planing Surfaces," Tech. Memo. No. 739, NACA, 1934.
8. Sretensky, L. N., "On the Wave-Making Resistance of a Ship Moving Along in a Canal," Philosophical Magazine, Vol. 22, Seventh Series, 1936.
9. Inui, T., "60th Anniversary Series, Vol. 2," The Society of Naval Architecture of Japan, 1957.
10. Pien, P. C., and Strom-Tejsen, J., "A Hull Form Design Procedure for High Speed Displacement Ships," Transaction of The Society of Naval Architects and Marine Engineers, 1968.
11. Maruo, H., "Calculation of the Wave Resistance of Ships, the Draught of Which is as Small as the Beam," Journal of the Society of Naval Architects of Japan, 1962.
12. Tuck, E. O., "The Steady Motion of a Slender Ship," Ph.D. Thesis, Cambridge, 1963.
13. Havelock, T. H., "Ship Waves: the Calculation of Wave Profiles," Proc. of the Royal Society, A, Vol. 135.
14. Wigley, W. C. S., "Ship Wave Resistance," Trans. N.E. Coast Inst. Engineers and Shipbuilders, Vol. 47, pp. 153-196, 1931.
15. Michelsen, F. C., Moss, J. L., Young, B. J., "Some Aspects of Hydrodynamic Design of High Speed Merchant Ships," Trans. of SNAME, Vol. 76, 1968.

LIST OF SYMBOLS

A	Midship section area
b	Defined by Eq. (21)
B	Ship beam
B_1, B_2	Ship beams associated with two hull forms given by Eqs. (9) and (10), respectively

Ciu	Cosine function defined by Eq. (4)
D	Domain defined by Eq. (12)
E	Defined by Eq. (29)
F_n	Froude number, $U/(gL)^{1/2}$
g	Acceleration of gravity
H	Draft of ship
H_s	Stern draft
I	Expression defined by Eq. (44)
I_1	Expression given by Eq. (51)
J	Expression defined by Eq. (50)
k	Lg/U^2
L	Ship length
M	Source strength
p_0	Pressure
P	Expression defined by Eq. (22)
P_1, P_2, P_3	Expressions defined by Eqs. (23), (24) and (25), respectively
Q	Expression defined by Eq. (22)
Q_1, Q_2, Q_3	Expressions defined by Eqs. (26), (27) and (28), respectively
r	Bulb radius
R	Wave resistance
S	Ship surface
Siu	Sine function defined by Eq. (3)
U	Velocity at $x \rightarrow -\infty$
V	Ship speed
Lw	Tank width
x, y, z	Rectangular coordinates
x_s	The x coordinate of the location of transom stern sink
y_1, y_2	Ship hull forms given by Eqs. (9) and (10), respectively
z_1	The z coordinate of the location of the point source for bulb
α	Dead rise angle of transom stern defined by Eq. (16)
ζ	Wave height
η	Two-dimensional wave height
$\zeta_1, \zeta_2, \zeta_3$	Wave heights due to the first, second and third term of I in Eq. (45)
ζ_b	Wave height due to bulb source

ζ_s	Wave height due to transom stern sink
σ	Source strength for ship hull
σ_1, σ_2	Source strength given by Eqs. (11) and (12), respectively
σ_b	Source strength for bow bulb
σ_s	Source strength for transom stern
ρ	Density of water
γ	Quantity given by Eq. (5)

* * * * *

DISCUSSION

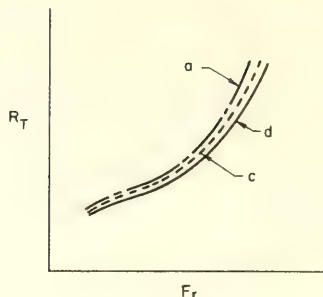
Georg P. Weinblum
Institut für Schiffbau
Hamburg, Germany

Some general remarks may be permitted, especially from the point of view of application.

So far investigations of more practical character deal preferably with the bow wave formations, while linearized wave resistance theory treats with equal love the forebody and the afterbody of displacement ships. Few experiments only have been conducted to check, *ceteris paribus*, the advantage of form symmetry with respect to the midship section in real fluid. Such tests have been performed by the present writer with bulbous forms by comparing simplified ship hulls:

- a) without a bulb (naked hull),
- b) a bulbous bow only,
- c) a stern bow only,
- d) bulbs symmetrically arranged at bow and stern.

These experiments are useful in the present context, starting from the author's and my personal viewpoint, that in ideal fluid a similarity can be reached in wave effects due to a transom stern and a bulbous bow (because of a similarity in form representation by dipole arrangements). The sketch annexed shows an impressive improvement by the symmetrical bulbous ship design (d), and this indicates, that the combination bulbous bow + transom stern should be useful as shown theoretically by the author.



The application of linearized wave resistance theory to slow full ships following our present state of knowledge overstrains this theory heavily. This theory should not be discarded, however, completely as long as it is used as a heuristic principle only, i.e. as means to look for solutions which must be checked experimentally.

It is recommended to use in this sense several earlier interesting papers published by the author. Considering the present critical attitude towards linearized wave resistance theory in general, I wish to state that its use (including perhaps some correcting "improvements" for practical purpose still can be highly recommended in case of medium or especially high Froude numbers. It should be remembered that in the range of the large wave resistance hump values computed by Michell's theory may differ by an amount only from experimental results which corresponds to the scatter of the latter derived from models in different scale. Therefore I welcome the author's present second approach on the subject of transom sterns although the correlation between form and generating singularities (so far rather indicated than carried out) may still require further studies.

With regard to the author's statement about lack of systematic experimental evidence it is suggested to look into report No. 167 Institut fuer Schiffbau Hamburg and to check if something useful can be found there.

* * * * *

DISCUSSION

S. D. Sharma and L. J. Doctors
University of Michigan
Ann Arbor, Michigan

In an oral discussion at the Symposium Professor Maruo and the first-named discussor challenged the validity of the author's Fig. 1 because they felt that the wave profile should have been discontinuous at the location of the line sink or the pressure step, $x = 0$. Dr. Yim insisted that his figure was correct, arguing that a similar curve is shown in Lamb's "Hydrodynamics," p. 405. In the meantime, we have examined the problem more closely and arrived at the following conclusions.

Let us examine the case of the pressure step first. Consider a two-dimensional pressure distribution,

$$p(x) = p_0 \{1 + \text{sgn}(x)\} / 2, \quad (\text{D1})$$

on the mean free surface, $z = 0$, moving steadily with speed U along the direction of Ox . The resulting motion can be described by a velocity potential $\phi(x, z)$ subject to the conditions

$$\phi_{xx}(x, z) + \phi_{zz}(x, z) = 0, \quad (\text{D2})$$

$$p(x) - \rho U \phi_x(x, 0) + \rho g \zeta(x) + \rho \mu U \phi(x, 0) = 0, \quad (\text{D3})$$

$$U \zeta_x(x) + \phi_z(x, 0) = 0, \quad (\text{D4})$$

$$\phi_{x,z}(x, -\infty) = 0, \quad (\text{D5})$$

where $z = \zeta(x)$ describes the free surface elevation and the limit $\mu \rightarrow +0$ is understood as usual. It is easy to verify that the solution is

$$\phi(x, y) = - (p_0 / \pi \rho U) \int_0^\infty \frac{\exp(ikx + kz)}{k(k - k_0 + i\mu)} dk, \quad k_0 = g/U^2, \quad (\text{D6})$$

$$\zeta(x) = - (p_0 / \rho g) \{1 + \text{sgn}(x)\} / 2 - i(p_0 / \pi \rho g) \int_0^\infty \frac{\exp(ikx)}{k - k_0 + i\mu} dk. \quad (\text{D7})$$

The limit $\mu \rightarrow +0$ then leads to the following real expression

$$\begin{aligned} \rho g \zeta(x)/P_0 = & -\{1 + \operatorname{sgn}(x)\}/2 - \frac{\operatorname{sgn}(x)}{\pi} \int_0^{\infty} \frac{\exp(-w|k_0 x|)}{1+w^2} dw \\ & - \{1 - \operatorname{sgn}(x)\} \cos(k_0 x), \end{aligned} \quad (D8)$$

which is indeed continuous at $x = 0$ although the wave slope ζ_x becomes infinite at that point. This is evident in the accompanying Figure (see Curve 1), but does not show up on the scale used by the author in his Fig. 1.

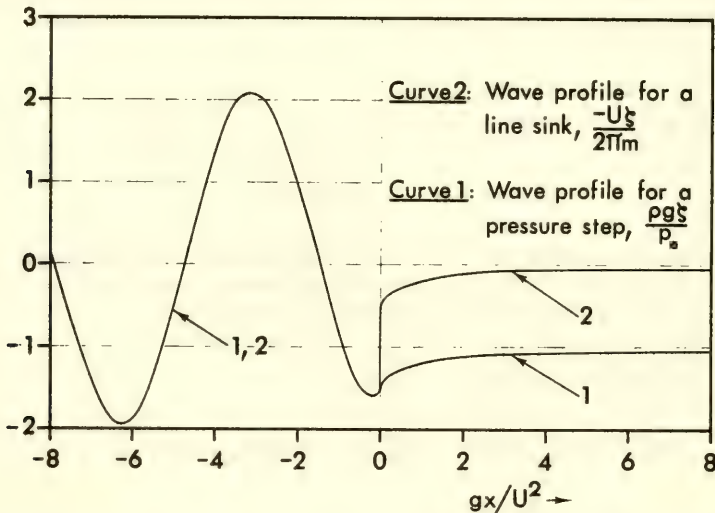


Fig. D1. Comparison of Wave Profiles for a Line Sink and a Pressure Step

On the other hand, one can also approach the problem as the limiting case of a submerged line source as the submergence tends to zero. The velocity potential for a line source of strength m (that is, output $2\pi m$ per unit length of line) on the line $x = 0$, $z = -f$ is found to be

$$\phi(x, z) = m \ln \sqrt{\frac{x^2 + (z+f)^2}{x^2 + (z-f)^2}} + 2mk_0 \int_0^{\infty} \frac{\exp\{k(z-f+ix)\}}{k(k-k_0+i\mu)} dk, \quad (D9)$$

and the wave profile

$$\zeta(x) = U\phi_x(x, 0)/g, \quad (D10)$$

now becomes

$$-U\zeta(x)/2\pi m = -\frac{\operatorname{sgn}(x)}{\pi} \int_0^\infty \frac{e^{-wk_0|x|} \{\cos(wk_0f) + w \sin(wk_0f)\}}{1+w^2} dw - \{1 - \operatorname{sgn}(x)\} e^{-k_0f} \cos(k_0f). \quad (D11)$$

It is obvious that for $f = 0$ the wave profile of the line source becomes discontinuous at $x = 0$. For any nonzero value of f the profile remains theoretically continuous at $x = 0$. However, for all practical purposes it is discontinuous in the limit $f \rightarrow 0$ as shown in the accompanying figure (see Curve 2) for $k_0f = 0.00001$.

If we assume $p_0/\rho g = -2\pi m/U$, then the potentials of the pressure step (D6) and the line source (D9) become identical in the limit $f \rightarrow 0$. But the wave profiles differ by the first term of (D8). Incidentally, the author's Eq. (1) differs from our (D11) by a factor of 2. But his relation (6) seems to have a compensating error of factor 1/2 so that his wave profile (7) does agree with our (D8). We have not investigated what effect this discrepancy has on the author's further calculations of wave resistance. But we did notice an obvious slip in Eq. (18) for the strength of the line sink representing the transom stern. If σ_s is regarded as a line density, apparently a factor L is missing on the R.H.S. On the other hand, if σ_s is interpreted as a surface density, then the R.H.S. should contain the Delta function $\delta(0)$ as a factor.

We also find the idea of using a line sink to represent the transom stern rather unconvincing. The line sink would tend to force the flow around the corner of the transom, which in practice occurs only at low speeds, but in a highly viscous manner not tractable by ideal fluid theory. The case of real interest is the one at high speeds where the flow separates smoothly from the transom. In this regime, we feel that the line sink should not be used so that the excess sources in the hull can produce a semi-infinite half-body. We would appreciate the author's comments on this point.

Notwithstanding minor differences of opinion, we wish to congratulate the author on his imaginative approach to a very interesting problem.

* * * * *

REPLY TO DISCUSSION

B. Yim

*Naval Ship Research and Development Center
Washington, D.C.*

The author would like to acknowledge Prof. Weinblum's encouragement. The author fully agrees with him on everything he mentioned. As is indicated in the text, the model of the transom stern assumes the linear free-surface condition although, in practice, very often nonlinear phenomena, e.g., a rooster-tail or cavity collapse, do occur. Therefore, this point also needs care, in addition to the error in Michell's thin ship theory or the slender ship theory.

* * * * *

REPLY TO DISCUSSION

B. Yim

*Naval Ship Research and Development Center
Washington, D.C.*

The author sincerely appreciates the deep interest shown by Drs. Sharma and Doctors regarding his paper.

About the validity of Fig. 1, the author will attempt to make a detailed explanation. First, the author would like to point out that the discussers agree by their Eqs. (D6) and (D9) that, with $p_0/\rho g = -2\pi m/U$, the potential due to a point sink located on the free surface at $x = 0$ and the potential due to the corresponding uniform pressure distribution along the free surface from $x = -\infty$ to $x = 0$ are identical everywhere in the flow field and on the boundary. This fact has long been known. Thus, velocities of the two cases are identical everywhere, and the wave heights of the two cases are identical from the relation (D10). Namely, one problem with the given pressure distribution is in fact the same problem with the properly given source distribution as in many fluid mechanics problems. Admitting this fact, it is impossible to claim that the representation by pressure gives

the smooth boundary and that the representation by source gives the discontinuous boundary. To elaborate a little more, the discussers did not notice that the boundary ahead of the location of sink or at $x < 0$, $z = 0$ is no longer a free surface but has become a part of body boundary formed by the sink flow field, where the pressure is a constant different from zero. This may be understood better if we consider another identity of potentials due to a point sink on $x = 0$, $z = 0$ and a uniform distribution of doublet in $-x$ direction on $-\infty < x < 0$, $z = 0$. The body boundary created by the two-dimensional sink is considered to form a part of a transom stern heuristically in the second section to justify the three-dimensional mathematical model in the following sections. It will be easily noticed with a real scale how readily acceptable the boundary would be and how proper and simple this model is.

Here the author also appreciates being advised that the factor of 2 is missing on M in his equations in the second section of the author's paper. This factor has nothing to do with any of the numerical results. In fact, the second section has no numerical relation with the results derived in other sections.

* * * * *

BOW WAVES BEFORE BLUNT SHIPS AND OTHER NON-LINEAR SHIP WAVE PROBLEMS

Gedeon Dagan

Technion-Israel Institute of Technology

Haifa, Israel

and

Marshall P. Tulin

Hydronautics, Incorporated

Laurel, Maryland

NOTATION

a	Draft at bow of a completely blunt shape (dimensionless)
b, \tilde{b}	Outer and inner coordinates of point B in the ξ and $\tilde{\xi}$ planes
$c_{1i}, c_{2i}, d_{1i}, d_{2i}, e_{1i}, e_{2i}, \tilde{d}_{1i}, \tilde{d}_{2i}$	Arbitrary constants
C_D	Drag coefficient
D'	Drag force; $\tilde{D} = D' / \rho U'^2 T'$
$f' = \phi' + i\psi'$	Complex potential; $F = f' / g^{1/2} T'^{3/2}$; $f = f' g / U'^3$; $\tilde{f} = f' / U' T'$
$Fr_L = U' / (gL')^{1/2}$	Length Froude number
$Fr_T = U' / (gT')^{1/2}$	Draft Froude number
$h'(x')$	Function describing the body shape; $H = h' / T'$; $h = h' g / U'^2$
l_f'	Forebody length; $l_f = l_f' g / U'^2$
l'	Characteristic length; $l = l' g / U'^2$
$N = \eta' / T'$	Dimensionless free-surface elevation
$\tilde{p} = p' / \rho U'^2$	Dimensionless pressure
t'	Jet thickness; $t = t' g / U'^2$; $\tilde{t} = t' / T'$
T'	Draft
$w' = u' + iv'$	Complex velocity; $w = \tilde{w} = w' / U'$; $W = w' / (gT')^{1/2}$

U'	Velocity at infinity
$z' = x' + iy'$	Complex variable; $z = z'g/U'^2$; $\tilde{z} = z'/T'$; $Z = z'/T'$
β	Angle at bow
$\delta_1, \delta_2, \Delta_1$	Gauge functions
$\epsilon = T'g/U'^2$	Small parameter
$\zeta = \xi + i\mu$	Auxiliary variable; $\tilde{\zeta} = \zeta/\epsilon$
η'	Free-surface elevation; $\eta = \eta'g/U'^2$; $\tilde{\eta} = \eta'/T'$; $N = \eta'/T'$
$\tilde{\Omega} = \ln(1/\tilde{w})$	Logarithm of complex velocity = $\tau + i\theta$

I. INTRODUCTION

The conventional linearized theory of ship waves is based on a first-order perturbation expansion in which the length Froude number is of order one, while the beam Froude number (thin ships) and/or the draft Froude number (slender of flat ships) tend to infinity. While the theory is in fair agreement with laboratory results in the case of schematical fine shapes (e.g. Weinblum et al. [1952]), it is of a qualitative value at best in the case of actual hulls. To improve the accuracy of the linearized solutions, second order nonlinear effects have been considered, either in the free-surface condition or in the body condition (e.g. Tuck [1965], Eggers [1966]).

A different nonlinear effect, overlooked until recently for the case of displacement ships, is that associated with the bow bluntness. It is well known from the theory of inviscid flow past airfoils or slender bodies (Van Dyke [1957]) that the linearized solution is singular near a blunt nose in the stagnation region. The singularity may be removed by an inner expansion in which the length scale is a local one associated with the nose bluntness.

In the case of a free-surface flow with gravity the phenomenon is more complex. The pressure rise in the stagnation region is associated with the free-surface rise and the formation of a breaking wave or spray and the existence of a genuine bow drag. The inner expansion of the Bernoulli equation shows that the inertial nonlinear terms become more important than the free gravity term, for sufficiently high local Froude numbers.

The bow nonlinear effects have been recognized a long time ago in the case of planing plates (Wagner [1932]), but they have been always associated with a relatively high Fr_L , such that the lift/buoyancy ratio is of order one. Here we are primarily interested in the case of displacement ships which move at a small Fr_L and the hull

position beneath the unperturbed level is practically independent of Fr_L . Nonlinear inertial effects may be important nevertheless near a blunt bow.

A systematical experimental confirmation of the role played by the bow bluntness has been provided recently by Baba [1969]. From towing-tank tests with three geosims of a tanker ($C_b = 0.77$) it was found that in ballast conditions at a $Fr_T \approx 1.2$ a breaking wave appears before the bow. At the maximum Fr_L tested ($Fr_L = 0.24$, $Fr_T = 1.7$, Fig. 1a) the energy dissipated in the breaking wave contributed 18 per cent of the total resistance, while the energy radiated by waves gave only 6 per cent. Baba has suggested a two-dimensional representation of the breaking wave of this experiment, as if it were uniform and normal to the bow (Fig. 1b), and has estimated equivalent length as half the beam. The drag coefficient per unit length, corresponding to a two-dimensional flow across the breaking wave is $C_D = D'/0.5 \rho U'^2 T' = 0.08$ for $Fr_T = 1.7$. Sharma [1969] has indicated a larger breaking wave resistance for a higher block coefficient tanker and has suggested that the bow bulbs main effect is to reduce the breaking wave resistance. With the development of large tankers, as well as large and rapid cargo ships, the study of the bow free-surface nonlinear effect becomes particularly important.

We present here some of the results of our last year's studies, which are reported in detail in two reports (Dagan and Tulin [1969, 1970]).

In this first stage we have attacked the two-dimensional problem of free-surface flow past a blunt body of semi-infinite length. The two-dimensional study is a necessary step in the development of a theory for three-dimensional bows since it provides a valuable gain in insight at the expense of relatively simple computations. Moreover, it gives an estimate of the bow drag of flat ships and opens the way to more realistic computations by further approximations.

Taking the length as semi-infinite is very useful from a mathematical point of view and it is equivalent to the limit $Fr_L \rightarrow 0$. This assumption is entirely justified for the small Fr_L considered here and for determining the bow flow, which is not sensibly influenced by the trailing edge condition.

II. THE FREE SURFACE STABILITY (SMALL Fr_T EXPANSION)

We consider the two-dimensional gravity flow past the body of Fig. 2. The box-like shape has been adopted for the sake of computational simplicity, but the method can be easily extended to any other shape.

When Fr_T is small the free-surface is smooth. We assume that breaking wave inception is related to the instability of the free-surface. According to Taylor's criterion (Taylor [1950]), the

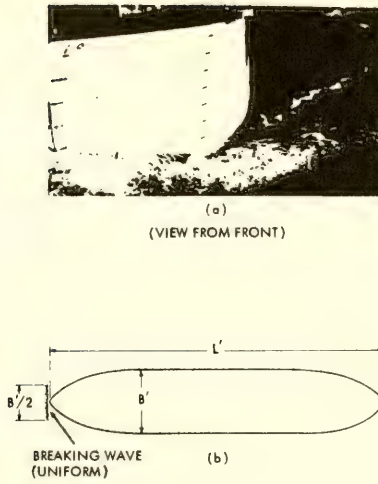


Fig. 1. Baba's [1969] experimental results. (a) Breaking wave before a tanker; (b) Baba's two-dimensional representation of the breaking wave.

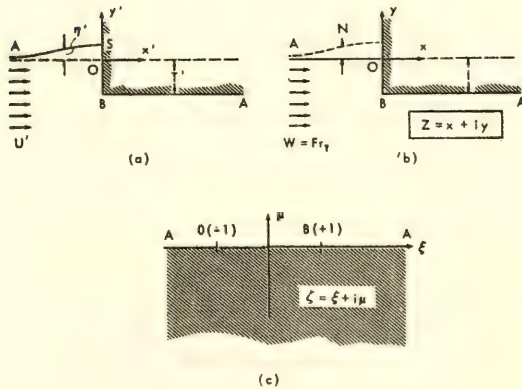


Fig. 2. Small Fr_T flow past a box-like shape body. (a) The physical plane; (b) the linearized dimensionless physical variables; (c) the auxiliary ζ plane.

free-surface becomes unstable when the normal acceleration vanishes. In our case this occurs when the centrifugal effect related to the free-surface curvature offsets the gravity acceleration. Since we expect the free-surface to become steep as Fr_T increases, there must be a critical Fr_T characterizing instability.

The gravity free-surface problem is, however, nonlinear. To linearize it we consider a small Fr_T perturbation expansion, i.e. and expansion for a state near rest. Referring the variables to T' (Fig. 2) and $(gT')^{1/2}$ and expanding as follows:

$$F(Z) = \Phi + i\Psi = Fr_T F_1(Z) + Fr_T^3 F_2(Z) + \dots \quad (1)$$

$$W(Z) = U - iV = Fr_T W_1(Z) + Fr_T^3 W_2(Z) + \dots \quad (2)$$

$$N(X) = Fr_T^2 N_1(X) + Fr_T^4 N_2(X) + \dots \quad (3)$$

we obtain from the exact free surface and body boundary conditions the following equations:

at first order (Fig. 2b)

$$\Psi_1 = 0 \quad (\text{ASBA}) \quad (4)$$

$$W_1 = 1 \quad (X \rightarrow -\infty) \quad (5)$$

i.e. a flow beneath a rigid wall replacing the free-surface at its unperturbed elevation. In addition

$$N = \frac{1}{2} (1 - U_1^2) \quad (X < 0, Y = 0)$$

second order

$$\Psi_2 = -U_1 N_1 \quad (\text{AS}, X < 0, Y = 0) \quad (7)$$

$$\Psi_2 = 0 \quad (\text{SBA}, X > 0, Y = H(x)) \quad (8)$$

i.e. a flow generated by a source distribution along the degenerated free-surface, and

$$N_2 = -U_1 U_2 \quad (X < 0, Y = 0) \quad (9)$$

It is easy to ascertain that Ψ_2 is zero at infinity such that

the total source flux is zero. Similarly N_2 is zero at both the origin and infinity. In fact the first order solution gives the exact values of N at infinity and at the stagnation point, the higher order approximations correcting only the free-surface shape between these two anchor points. The above expansion is consistent and hopefully uniformly convergent. It differs from that suggested by Ogilvie [1968] who has kept terms of different order in the same equation in order to obtain waves far behind a submerged body.

The solution of the first order approximation for the box-like shape body (Fig. 2a) is obtained in terms of the auxiliary variable ζ as

$$W_1 = \left(\frac{\zeta + 1}{\zeta - 1} \right)^{1/2} \quad F_1 = \zeta / \pi \quad (10)$$

where the mapping of the linearized Z plane (Fig. 2b) onto ζ (Fig. 2c) is given by

$$Z = \frac{1}{\pi} (\zeta^2 - 1)^{1/2} + \frac{1}{\pi} \ln [(\zeta^2 - 1)^{1/2} - \zeta] \quad (11)$$

Hence, by Eq. (6) we have

$$N_1 = \frac{1}{1 - \xi}$$

For the second order approximation (Eq. (7)) we get

$$\Psi_2 = \frac{(\xi + 1)^{1/2}}{(\xi - 1)^{3/2}} \quad (\xi < -1, \mu = 0) \quad (12)$$

Ψ_2 given along the ζ real axis (Eqs. (8) and (12)), leads by a Cauchy integral to

$$\begin{aligned} \Phi_2(\xi) &= -\frac{1}{\pi} \operatorname{Re} \int_{-1}^{-\infty} \Psi_2(\lambda) \frac{d\lambda}{\xi - \lambda} \\ &= -\frac{1}{\pi} \left\{ \frac{2}{1 - \xi} + \left(\frac{\xi + 1}{\xi - 1} \right)^{1/2} \frac{\ln [-\xi - (\xi^2 - 1)^{1/2}]}{1 - \xi} \right\} \end{aligned} \quad (13)$$

U_2 and N_2 as functions of ξ , are easily found from Eqs. (13) and (9) (for details see Dagan and Tulin [1969]). The shape of the free-surface at second order is given in Fig. 3. As expected, the profile becomes steep as Fr_τ increases.

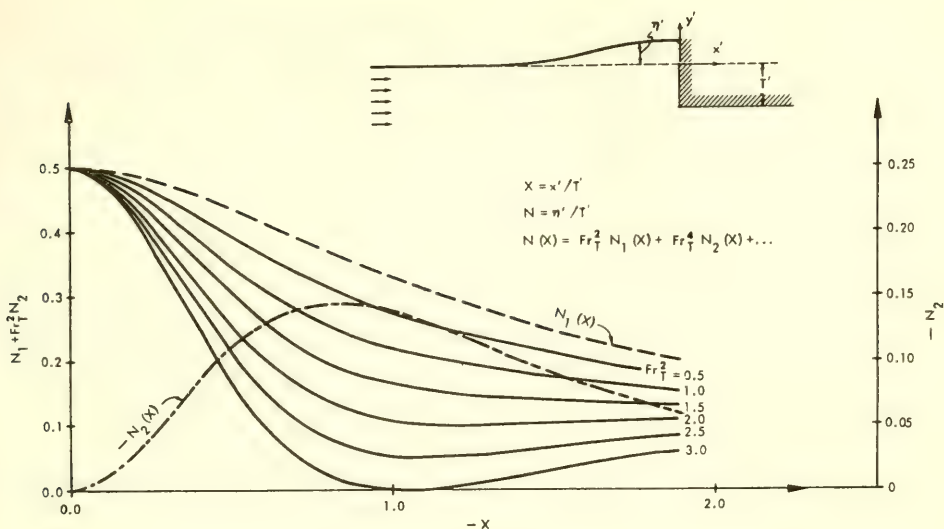


Fig. 3. The free-surface shape in front of a rectangular body

The dimensionless pressure gradient component normal to the free-surface is proportional to

$$\begin{aligned}
 & -1 + Fr_T^4 \left[\frac{1}{2} \left(\frac{dN_1}{dX} \right)^2 - U_1^2 \frac{d^2 N_1}{dX^2} \right] \\
 & + Fr_T^6 \left(\frac{dN_1}{dX} \frac{dN_2}{dX} - U_1^2 \frac{d^2 N_2}{dX^2} - 2 U_1 U_2 \frac{d^2 N_1}{dX^2} \right)
 \end{aligned} \quad (14)$$

where the first two terms of the expansion contribute to order Fr_T^6 in the pressure gradient. Taylor's marginal stability is reached for the value of Fr_T which renders Eq. (14) equal to zero. This value has been found to be $Fr_T \approx 1.5$ and the point of instability at $X = 0.3$.

Although the expression for the pressure gradient can hardly be expected to converge rapidly at such a high Fr_T , the result is of the order of magnitude of that found by Baba and would seem to confirm the mechanism of free-surface disruption assumed by us.

The effect is nonlinear since only when taking into account the second order term does the steepening of the free-surface depend strongly on Fr_T . There is no bow drag in the small Fr_T limit.

The present method suggests a possible way for determining

the influence of the bow shape on the breaking wave inception, and therefore serves in selecting shapes which retard the phenomenon. Its application to three-dimensional bows is left for future studies.

III. THE HIGH FROUDE NUMBER APPROXIMATION (THE JET MODEL)

(a) The Outer Expansion

As Fr_T increases the breaking wave develops. Energy is dissipated there and the momentum loss is associated with an induced bow drag. To treat analytically this free-surface nonlinear problem we have to adopt a flow model which: (i) permits an ideal fluid representation of the phenomenon and (ii) lends itself to the linearization of the free-surface condition.

We adopt here the jet model, well known from planing theories, and neglect the returning jet flow, such that the jet momentum loss is equivalent to that of the breaking wave (Fig. 4a). Moreover we expand the exact equations of flow in an $\epsilon = 1/Fr_T^2$ small parameter expansion, consistent with the usual linearized ship wave theory.

The expansion, and the associated model, are probably valid for sufficiently high Fr_T , and we only may hope, like in other asymptotic solutions, that the results are sufficiently accurate even for moderate Fr_T .

We consider now an outer expansion with the outer variables made dimensionless by referring them to U' and U'^2/g (see Notation). Using a procedure followed in similar problems in the past (Tulin [1965], Wu [1967]) we carry out the expansion in an auxiliary ζ plane (Fig. 4c) related to the complex potential plane (Fig. 4b) through the transformation

$$\frac{df}{d\zeta} = 1 - \frac{t}{\pi\zeta} \quad (15)$$

We assume now that the jet thickness t and the distance to the stagnation point b are both $o(1)$, such that under the outer process $\epsilon \rightarrow 0$, $\zeta = O(1)$ they coalesce with the origin of the ζ plane (Fig. 4e).

Under these conditions we obtain by a systematical expansion of the complex velocity

$$w(\zeta) = 1 + \delta_1(\epsilon)w_1(\zeta) + \delta_2(\epsilon)w_2(\zeta) + \dots \quad (16)$$

after taking into account that by definition the body profile has the

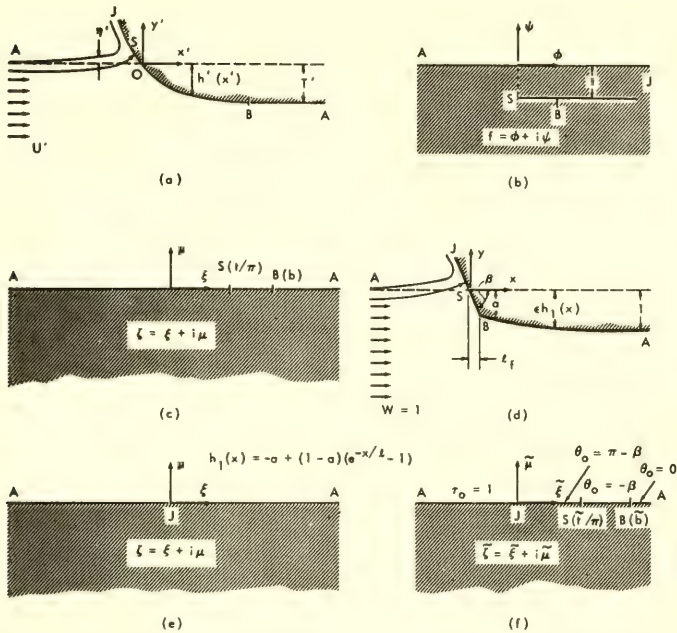


Fig. 4. High Fr_T flow past a blunt body. (a) The physical plane; (b) the complex potential plane; (c) the auxiliary ξ plane; (d) flow past a completely blunt shape (physical plane, outer variables); (e) the body first-order boundary condition in the outer expansion; (f) the zero order boundary conditions in the inner expansion.

equation

$$h(x) = \epsilon h_1(x) \tag{17}$$

at first order

$$\delta_1 = \epsilon \tag{18}$$

$$\text{Re}(w_1 + ik_1) = 0 \qquad (\xi < 0, \quad \mu = 0) \tag{19}$$

$$\text{Im} k_1(\xi) = -h_1(\xi) \qquad (\xi > 0, \quad \mu = 0) \tag{20}$$

where

$$k_1(\zeta) = \int_{-\infty}^{\zeta} w_1 d\zeta$$

and

$$z = \zeta - \epsilon \int_{-\infty}^{\zeta} w_1 d\zeta \quad (21)$$

at second order

$$\delta_2 = \epsilon^2$$

$$\operatorname{Re} \left(\frac{dw_2}{d\zeta} + iw_2 \right) = - \operatorname{Re} \left[(w_1 + 2\bar{w}_1) \frac{dw_1}{d\zeta} \right] \quad (\xi < 0, \mu = 0) \quad (22)$$

$$\operatorname{Im} w_2 = - \frac{1}{2} \operatorname{Im} w_1^2 \quad (\xi > 0, \mu = 0) \quad (23)$$

$$w_2 \rightarrow 0 \quad (\xi \rightarrow -\infty) \quad (24)$$

We determine now the first order solution by replacing the body along $\xi > 0$ by an unknown pressure distribution (equivalent to a vortex distribution, see Stoker [1957]) of strength $g_1(\xi)$. The function $k_1(\zeta)$ satisfying Eq. (19) and the radiation condition becomes

$$k_1(\zeta) = \frac{1}{\pi} \int_0^{\infty} e^{-i(\zeta-\nu)} \operatorname{Ei} [i(\zeta-\nu)] g_1(\nu) d\nu \quad (25)$$

Eq. (20) becomes now

$$\frac{1}{\pi} \int_0^{\infty} \operatorname{Re} e^{-i(\xi-\nu)} \operatorname{Ei} [i(\xi-\nu)] g_1(\nu) d\nu = -h_1(\xi) \quad (26)$$

The integral Eq. (26), with a displacement kernel, may be solved by the Wiener-Hopf technique.

The Fourier transform of Eq. (27) reads

$$M(\lambda)G_1^+(\lambda) = \frac{1}{\sqrt{2\pi}} [N_1^-(\lambda) + H_1^+(\lambda)] \quad (27)$$

where M , G_1 , H_1 , and N_1 are the transforms of the kernel, g_1 , h_1 and the free-surface profile, respectively.

The kernel's transform has been factorized by Carrier et al.

[1967]

$$M(\lambda) = \frac{1}{(2\pi)^{1/2}} \frac{1}{1+|\lambda|} = [M^+(\lambda)][M^-(\lambda)]$$

$$= \left\{ \frac{1}{\sqrt{1+\lambda}} \exp \left[\frac{1}{\pi i} \int_0^\lambda \frac{\ell_n u}{1-u^2} du \right] \right\} \left\{ \frac{1}{\sqrt{2\pi}} \frac{1}{\sqrt{1+\lambda}} \exp \left[-\frac{1}{\pi i} \int_0^\lambda \frac{\ell_n u}{1-u^2} du \right] \right\} \quad (28)$$

The separation of Eq. (27) can now be accomplished, provided that we select a given body shape $h_1(x)$.

We limit ourselves here to the case of the completely blunt shape of Fig. 4d. The forebody length ℓ_f is of order ϵ , such that at the limit $\epsilon \rightarrow 0$ the bow degenerates at first order into a point singularity at the origin. Any shape with the same length scale of the forebody will yield the same first order body condition.

With (Fig. 4e)

$$\begin{aligned} H_1^+(\lambda) &= \frac{1}{(2\pi)^{1/2}} \int_0^\infty e^{i\lambda\xi} h_1(\xi) d\xi \\ &= -\frac{1}{(2\pi)^{1/2}} \frac{1}{i\lambda} + \frac{1-a}{(2\pi)^{1/2}} \frac{1}{i\lambda-1/\ell} \end{aligned} \quad (29)$$

we obtain from the separation of Eq. (27)

$$G_1^+(\lambda) = \frac{i}{2\pi} \left[\frac{1}{\lambda} - (1-a) \frac{1}{\lambda+i/\ell} \right] \frac{1}{M^+(\lambda)} \frac{1}{M^-(0)} + \frac{\sum_{i=0}^n c_{1i} \lambda^i}{M^+(\lambda)} \quad (30)$$

where the last term, representing eigensolutions, results from the application of Liouville's theorem, c_{1i} being arbitrary.

Equation (30) cannot be inverted exactly, because of the integral appearing in $M^+(\lambda)$, but the inversion can be carried out for large λ by expanding $M^+(\lambda)$. After carrying out this process (see Dagan and Tulin [1970]) we arrive at the following expression for $g_1(\xi)$ in the vicinity of the origin

$$g_1(\xi) = \frac{a}{(\pi\xi)^{1/2}} + O(\xi^{1/2} \ln \xi) + \sum_{i=0}^n \frac{d_{1i}}{\xi^{i+3/2}} \quad (\xi \rightarrow 0) \quad (31)$$

where d_{1i} are related in a unique manner to c_{1i} .

From Eq. (31) we obtain

$$w_1(\zeta) = -\frac{a}{(\pi\zeta)^{1/2}} + O(\zeta^{1/2} \ln \zeta) + \sum_{i=0}^n \frac{d_{1i}}{\zeta^{i+3/2}} \quad (\zeta \rightarrow 0) \quad (32)$$

which is the central part of our analysis.

The expression of the second order solution, satisfying Eqs. (22), (23), and (32), was found to be

$$w_2(\zeta) = \frac{a^2}{2\pi\zeta} + O(\ln \zeta) + \sum_i \frac{d_{2i}}{\zeta^{i+3/2}} \quad (33)$$

Summarizing the results for the outer expansion, we have, with the estimate $t = O(\epsilon^2)$

$$w = 1 - \frac{\epsilon a}{(\pi\epsilon)^{1/2}} + \epsilon \sum_i \frac{d_{1i}}{\zeta^{i+3/2}} + \frac{\epsilon^2 a^2}{2\pi\zeta} + \epsilon^2 \times \sum_i \frac{d_{2i}}{\zeta^{i+3/2}} + \epsilon O(\zeta^{1/2} \ln \zeta) \quad (34)$$

$$z \sim \zeta - \epsilon \left[a i + 2a \left(\frac{\zeta}{\pi} \right)^{1/2} \right] + \epsilon \sum_i \frac{e_{1i}}{\zeta^{i+1/2}} + \frac{\epsilon^2}{2\pi} \ln \zeta - \frac{t}{\pi} \ln \zeta + \epsilon^2 \sum_i \frac{e_{2i}}{\zeta^{i+1/2}} \quad (35)$$

e_{1i} and e_{2i} being again constants related to c_{1i} , c_{2i} .

The velocity has the familiar square root singularity at first order and a source singularity at second order. The free-surface is continuous and attached to the bottom at first order, while at second order it rises at infinity. The eigensolutions of the problem, which represent in fact the linearized solutions of a free-surface flow past a flat horizontal plate, as well as the flow details near the bow will be subsequently determined with the aid of an inner solution. It is worthwhile to mention here that only at second order are the details of the adopted model (i.e. the jet) manifested in the solution. Any other model attached to the bow will produce an identical first order solution.

(b). The Inner Expansion and Its Matching with the Outer Solution

We stretch now the coordinates and adopt the following inner variables,

$$\tilde{\zeta} = \zeta/\epsilon; \quad \tilde{w} = w; \quad \tilde{z} = z/\epsilon; \quad \tilde{t} = t/\epsilon; \quad \tilde{b} = b/\epsilon \quad (36)$$

and expand the function $\tilde{\Omega} = \ell n(1/\tilde{w}) = \tau + i\theta$ in a perturbation series

$$\tilde{\Omega} = \tilde{\Omega}_0 + \Delta_1(\epsilon)\tilde{\Omega}_1 + \dots \quad (37)$$

For the body of Fig. 4d we obtain from the inner expansion of the exact equations the boundary conditions for $\tilde{\Omega}_0$ specified in Fig. 4f, which represent a nonlinear free-surface flow without gravity. The conditions at infinity are provided by the matching with the outer expansion. Only in the case of the straight bow of Fig. 4e are the inner conditions so simple. In a general case we have to solve an integral equation for θ [Wu, 1967] or to start with a given $\theta(\tilde{\zeta})$.

The solution of \tilde{w}_0 is readily found in the form

$$\tilde{w}_0 = \frac{(\tilde{\zeta})^{1/2} - (\tilde{t}/\pi)^{1/2}}{(\tilde{\zeta})^{1/2} + (\tilde{t}/\pi)^{1/2}} \left[\frac{(\tilde{\zeta})^{1/2} + \tilde{b}}{(\tilde{\zeta})^{1/2} - \tilde{b}} \right]^{\beta/\pi} \exp \left(\sum_i \frac{\tilde{d}_{oi}}{\tilde{\zeta}^{1+1/2}} \right) \quad (38)$$

where the exponential represents the eigensolutions of the problem, \tilde{d}_{oi} being arbitrary constants.

Expanding \tilde{w}_0 for large $\tilde{\zeta}$ we obtain

$$\tilde{w}_0 = 1 - 2[(\tilde{t}/\pi)^{1/2} - \beta\tilde{b}/\pi] \frac{1}{\tilde{\zeta}^{1/2}} + 2[(\tilde{t}/\pi)^{1/2} - \beta\tilde{b}/\pi]^2 \frac{1}{\tilde{\zeta}} + \frac{\tilde{d}_{o1}}{\tilde{\zeta}^{1/2}} + \dots \quad (39)$$

$$\begin{aligned} \tilde{z} = \int \frac{1 - \tilde{t}/\pi\tilde{\zeta}}{\tilde{w}_0} d\tilde{\zeta} = \tilde{\zeta} - 4[(\tilde{t}/\pi)^{1/2} - \beta\tilde{b}/\pi] + 2[(\tilde{t}/\pi)^{1/2} - \beta\tilde{b}/\pi]^2 \ell n \tilde{\zeta} \\ - \frac{\tilde{t}}{\pi} \ell n \tilde{\zeta} - a i + 2\tilde{d}_{o1}\tilde{\zeta}^{1/2} + \dots \end{aligned} \quad (40)$$

Before proceeding to the matching we rule out the eigensolutions appearing in Eqs. (38), (39) and (40) because they lead either to an infinite velocity in the jet or to an infinite jet thickness, depending on whether \tilde{d}_{oi} are positive or negative. The matching of \tilde{w}_0 and \tilde{z} (Eqs. (39) and (40)) with w and z (Eqs. (34) and (35)) now gives

$$\tilde{t} = \epsilon a^2, \quad \tilde{b} = \frac{a\pi^{1/2}\epsilon^{1/2}}{2\beta}, \quad d_{1i} = 0, \quad d_{2i} = 0 \quad (41)$$

and both inner and outer solutions are uniquely determined.

Our estimates of t and b are confirmed, Eq. (41) showing that $t = O(\epsilon^2)$ and $b = O(\epsilon^{3/2})$. The nonlinear character of the problem is manifest in the inner expansion.

We have now a uniform solution which can be written by adding the inner and outer solutions and subtracting their common part.

(c) The Bow Drag

The horizontal force acting on the bow is found by the pressure integration in the inner zone (Fig. 4f)

$$\tilde{D} = \int_B^J \tilde{p} \, d\tilde{y} = \frac{1}{2} \operatorname{Im} \int_B^J (1 + \tilde{w}^2) \, d\tilde{z} = \frac{1}{2} \operatorname{Im} \int_{\tilde{b}}^0 \left(\frac{1}{\tilde{w}} + \tilde{w} \right) \left(1 - \frac{\tilde{t}}{\pi \tilde{\zeta}} \right) d\tilde{\zeta} \quad (42)$$

Since \tilde{w} is analytical in the lower $\tilde{\zeta}$ half plane the integration along BJ may be replaced by integration at infinity (at H) and around the origin J. After expanding $1/\tilde{w}_0 + \tilde{w}_0$ at infinity and near the origin, we get for \tilde{D}

$$\tilde{D} = \frac{\epsilon a^2}{2} (1 + \cos \beta/\pi) \quad (43)$$

The same result, excepting the $\cos \beta/\pi$ term, may be obtained directly from the first order outer expansion.

To roughly compare the result of Eq. (43), with Baba's findings, let's assume that the bow is completely blunt with $\beta = \pi/2$ and $a = 1$. For $\epsilon = 1/\operatorname{Fr}_\tau^2 \approx 0.34$ we have

$$C_D = 2\tilde{D} = 0.34 \quad (44)$$

which is roughly four times larger than the value estimated by Baba.

At this stage it is difficult to find which of the following factors explain this discrepancy: The asymptotic character of the solution, the lack of details on the bow shape or, may be the most important, the crude representation by Baba of a three-dimensional flow by a two-dimensional equivalent (Fig. 1a). Future experiments

and theoretical developments will give the answer to this question.

The method presented here is applicable to other bow shapes, like blunt round bows. In this latter case the bow drag appears at higher order than in the completely blunt case. The extension to other shapes, as well as to three-dimensional bodies is left for future studies.

IV. CONCLUSIONS

Theoretical models of breaking wave inception and of a free-surface bow drag have been derived for the case of a two-dimensional gravity free-surface flow past a blunt body. In both cases the effects are nonlinear and are related to the important role played by the inertial term of the Bernoulli equation in the vicinity of the bow.

The results are of the order of magnitude of those found by Baba [1969], but an improved verification has to be done by carrying out two-dimensional experiments. The theory presented here may be extended, with additional approximations, to three-dimensional flows.

ACKNOWLEDGMENT

The present work has been supported by the Office of Naval Research under Contract No. Nonr-3349(00), NR 062-266 with HYDRONAUTICS, Incorporated.

REFERENCES

- Baba, E., "Study on Separation of Ship Resistance Components," Mitsubishi Tech. Bul. No. 59, pp. 16, 1969.
- Carrier, F. G., Krook, M., and Pearson, C. E., Functions of a Complex Variable, McGraw-Hill, pp. 438, 1966.
- Dagan, G., and Tulin, M. P., "Bow Waves Before Blunt Ships," HYDRONAUTICS, Incorporated Technical Report 117-14, 1969.
- Dagan, G., and Tulin, M. P., "The Free Surface Bow Drag of a Two-Dimensional Blunt Body," HYDRONAUTICS, Incorporated Technical Report 117-17, 1970.
- Eggers, K. W. H., "On Second Order Contributions to Ship Waves and Wave Resistance," Proc. 6th Symp. of Naval Hydrodynamics, 1966.

- Ogilvie, T. F., "Wave Resistances: The Low Speed Limit,"
The Univ. of Michigan, Dept. of Naval Arch., Rep. No. 002,
pp. 29, 1968.
- Stoker, J. J., Water Waves, Wiley, New York, 1957.
- Taylor, G. I., "The Instability of Liquid Surfaces' When Accelerated
in a Direction Perpendicular to Their Plane, I," Proc. Roy.
Soc., London, A, 201, pp. 192, 1950.
- Tuck, E. O., "A Systematic Asymptotic Procedure for Slender
Ships," J. Ship Res., Vol. 8, No. 1, pp. 15-23, 1965.
- Tulin, M. P., "Supercavitating Flows -- Small Perturbation Theory,"
Proc. of the Internat. Symp. on the Application of the Theory
of Functions in Continuous Mechanics, 2nd Vol., pp. 403-
439, 1965.
- Wagner, H., "Über Gleitvorgänge an der Oberfläche von Flüssig-
keiten," Zamm, Vol. 12, No. 4, pp. 193-216, 1932.
- Weinblum, G. P., Kendrik, J. J. and Todd, M. A., "Investigation
of Wave Effects Produced by a Thin Body," David Taylor
Model Basin Report No. 840, pp. 19, 1952.
- Wu, T. Y., "A Singular Perturbation Theory for Nonlinear Free-
Surface Flow Problems," Int. Shipbldg. Prog. Vol. 14,
No. 151, pp. 88-97, 1967.

* * * * *

DISCUSSION

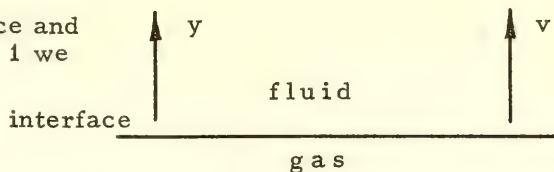
L. van Wijngaarden

*Twente Institute of Technology
Enschede, The Netherlands*

I would like to ask a question about the authors' interpretation of Taylor's instability. They use as a criterion for marginal stability that the normal component of the pressure gradient at the interface between gas and fluid vanishes. This is indeed the case for a plane interface.

For a plane interface and variables indicated in Fig. 1 we have

$$\rho \frac{\partial v}{\partial t} = - \frac{\partial p}{\partial y}.$$



For negligible gas density Taylor's result is:

Fig. 1

$$\text{stable:} \quad \frac{\partial v}{\partial t} < 0; \quad \frac{\partial p}{\partial y} > 0.$$

$$\text{instable:} \quad \frac{\partial v}{\partial t} > 0; \quad \frac{\partial p}{\partial y} < 0.$$

$$\text{marginal stability:} \quad \frac{\partial p}{\partial y} = 0.$$

The question is whether this criterion ($\partial p / \partial y = 0$) holds also for more general interfaces. As an example consider the spherically symmetric implosion of an empty gas bubble (Fig. 2). The equation for the radius R is

$$R \ddot{R} + \frac{3}{2} \dot{R}^2 = - \frac{p_\infty}{\rho}$$

where p_∞ is the pressure far away in the fluid, $p_\infty > 0$. From this relation

$$R \ddot{R} = - \frac{p_\infty}{\rho} - \frac{3}{2} \dot{R}^2 < 0.$$

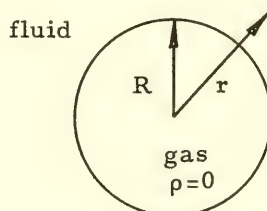


Fig. 2

The inviscid equation for the only velocity component v is

$$\frac{\partial v}{\partial t} + v \frac{\partial v}{\partial r} = - \frac{1}{\rho} \frac{\partial p}{\partial r}.$$

Since $v(r) = R^2 \dot{R} / r^2$, it follows that at $r = R$

$$\frac{1}{\rho} \frac{\partial p}{\partial r} = - \ddot{R} + \frac{2 \dot{R}^2}{R}.$$

This vanishes never and according to the foregoing criteria the motion is stable.

However Plesset and Mitchell [1956] proved that in fact this spherically symmetric implosion is unstable. This demonstrates that for interfaces which are appreciably curved like in the author's case, the criterion for marginal stability is not always that the normal pressure gradient vanishes.

REFERENCES

Plesset, M. S. and Mitchell, T. P., "On the Stability of the Spherical Shape of a Vapor Cavity in a Liquid," *Quart. of App. Math.*, 13, 4, 1956.

* * * * *

DISCUSSION

Prof. Hajime Maruo
Yokohama National University
Yokohama, Japan

I congratulate the success of Dr. Dagan's beautiful analysis of the wave-breaking resistance discovered by Baba. As in the discussion at the 12th ITTC, this resistance component has been regarded so far, as a portion of the wave resistance. However the present analysis indicates that it is not the case. The wave-breaking resistance seems to have a nature akin to that of the spray resistance. Which is the better classification, the author considers, whether it belongs to the wave resistance or to the spray resistance?

* * * * *

REPLY TO DISCUSSION

Gedeon Dagan

*Technion-Israel Institute of Technology
Haifa, Israel*

The authors have indeed applied Taylor's instability criterion to a flow field which is different from that considered originally by Taylor: The free-surface is curved, the basic flow is not uniform and the instability is local.

For a plane free-surface Taylor [1950] has shown that any disturbance, of arbitrary wave length, is unstable for $\partial p / \partial y < 0$; moreover, the rate of growth of the disturbance amplitude becomes large for small wave lengths. It is reasonable, therefore, to assume that for wave lengths which are much smaller than the radius of the curvature of the free-surface, Taylor's criterion is locally valid.

The radius of curvature of the free-surface (r') may be quite large. At instability $V'^2 / gr' \cong 1$, i.e. $r' / T' \cong V'^2 / gT'$. For the marginal Froude number characterizing instability, $Fr_T \cong 1.5$, it was found that $V' / V'_\infty \cong 0.7$. Hence, in this case, $r' / T' = (V'^2 / V_\infty'^2) Fr_T^2 \cong 1$. For a draft T' of order of a few meters, disturbances of wave lengths much smaller than r' are physically conceivable.

Although the example suggested by Prof. van Wijngaarden, of a collapsing spherical bubble, shows undoubtedly that Taylor's criterion cannot be applied indiscriminately, its resemblance with the case of a steady free-surface is questionable. The inspection of Plesset and Mitchell [1956] article reveals that only for $R/R_0 \rightarrow 0$ (R being the actual radius of the bubble and R_0 its initial radius) the disturbances are unstable, although the pressure gradient is positive. The two cases are quite different.

We agree in principle with Prof. van Wijngaarden's criticism concerning the need for a more rigorous treatment of the local stability of a steady curved free-surface. Unfortunately, the basic flow itself has been determined only approximately and further refinements of the stability criterion do not seem justified at this stage. The aim of the computations presented in the paper was limited to offering a model of the free-surface breaking and the order of magnitude of the marginal Froude number.

* * * * *

REPLY TO DISCUSSION

M. P. Tulin

Hydronautics, Incorporated
Laurel, Maryland

The wave-breaking resistance is undoubtedly similar to the spray resistance rather than to the wave drag. It is a local phenomenon related to the shape of the body. The energy is not radiated, but dissipated locally. On this ground, the theoretical analysis presented in the paper is based on a model of a semi-infinite body, with neglect of the downstream conditions.

* * * * *

SHALLOW WAVE PROBLEMS IN SHIP HYDRODYNAMICS

E. O. Tuck and P. J. Taylor
University of Adelaide
Adelaide, South Australia

ABSTRACT

In this paper we discuss two basic problems in shallow water ship hydrodynamics, namely the squat problem and the problem of wave force due to beam seas. Squat is an important phenomenon in very shallow water because of the danger of scraping bottom. Apart from reviewing and extending existing work on sinkage and trim in canals and in a wide expanse of shallow water, we indicate here how the shallow water results can be obtained from a finite depth theory as the depth becomes small. Unsteady problems associated with motions or of forces on a ship in beam seas are also of practical importance, as for a ship standing at an exposed mooring facility. We provide here sample computations of the side force on a tanker hull in regular beam seas.

I. INTRODUCTION

It must be stated at the outset that this paper is concerned principally with shallow water, and not with finite depth of water, except in Section 4. The distinction between these two cases is important from the theoretical point of view and needs to be emphasized here since those more accustomed to dealing with water of effectively infinite depth tend to refer to "shallow water" whenever the effect of the bottom is considered.

We take the expression "finite depth" to classify a range of water depths in which there are significant changes to the flow problems as compared with infinite depth, and significant but not necessarily dominant effects of the water bottom on the behavior of the ship. On the other hand, the "shallow water" regime is one in which the depth is so small that the narrowing of the field of flow has a

dominant effect on the ship hydrodynamics.

A degree of quantitateness may be attached to this concept of shallowness in a number of ways. Physically and most significantly we require the depth to be so small that the hydrodynamic part of the pressure distribution in the field of flow not too close to a disturbing influence such as a ship is to a good first approximation independent of the vertical coordinate z . Thus the only pressure variation with z is hydrostatic.

If there are waves present, ambient or made by the ship, it is consistent with the above that their wavelength be much greater than (say 5 - 10 times) the water depth, and hence the resulting shallow-water theory is sometimes called a "long wave theory." However, this terminology can be misleading, since most of the results obtained also apply when free surface effects are negligible, as for a ship moving at very low Froude number, when the wavelength is vanishingly small. An additional requirement for significant effects of shallowness in the ship hydrodynamics context is that the draft of the ship be comparable with the water depth, so that the water bottom does have a profound effect on the ship.

In this paper we are concerned principally with two major problems, which are apparently quite distinct from each other, but in which similar phenomena appear. The first problem is the classical squat problem, associated with steady forward movement of the ship in calm water, while the second is an unsteady problem associated with the response of, or forces on, a ship without forward motion in beam seas.

Squat is the change in draft and trim of the ship as a result of hydrodynamic pressure variations over its hull. Acceleration of fluid particles as they pass the middle sections of the ship tends to produce a diminution of pressure there, and hence a downward force. There is also an upward force near the bow and stern stagnation points, but the effect of these forces is small since there is a much smaller area over which the positive hydrodynamic pressure can act. In any case, the developing boundary layer and ultimate flow separation tends to eliminate the upward force at the stern.

Thus we expect a net downward force, which leads to a downward displacement, an increase in draft, or sinkage. At the same time we might expect a much less significant angular trim effect, in which the presence of the small upward force at the bow and the lack of such a force at the stern may give a bow-up trim. These conclusions are confirmed qualitatively at reasonably low speeds.

In fact, of course, being a simple Bernoulli effect, squat is present in any depth of water. An interesting and immediate conclusion we may draw is that, like all Bernoulli effects, squat depends predominantly on the square of the ship's speed. This seems not to

have been noticed by pilots and ship's captains, who are generally aware of the problem of squat as a danger to the vessels under their control, but are prepared to adopt a linear rule-of-thumb such as "a foot for every 5 knots"!

In shallow water, squat is obviously a most important problem, if only because it may cause a ship to actually scrape the bottom. But not only is this danger present, but the magnitude of the sinkage is actually increased by the proximity of the water bottom. This is clear physically, since the effective channel of flow is constricted by the additional boundary, leading to even greater acceleration of fluid particles across the middle sections of the ship.

Another interesting additional phenomenon in shallow water is a result of a close analogy between long-wave theory and linear aerodynamics, in which the Froude number $F = U/\sqrt{gh}$ based on water depth h plays the role of the Mach number. Thus we expect extraordinary effects in the neighborhood of $F = 1$, c.f. the "sound barrier," and indeed both theory and experiment confirm that this critical speed is of crucial importance. Theory, at least in its linearized form, predicts infinite sinkage at $F = 1$, while in both experiments and in observations at sea we obtain a dramatic increase in draft associated with the generation of a type of permanent wave or bore accompanying the ship near $F = 1$.

The squat problem is discussed in Sections 2 - 4, each section presenting a different aspect of the problem. In Section 2 there is a lateral as well as horizontal constriction to the field of flow, and a hydraulic-type theory applies, while with the removal of the lateral boundaries in Section 3 the true shallow-water theory can be used. In Section 4, for the only time in this paper we use a finite-depth approach and present calculations of sinkage and trim which are close to the shallow-water results when the water depth/ship length ratio is reasonably small.

Problems of ship motions in shallow water, i.e. of flows of an unsteady nature, are of special interest again because of the dangers inherent in large motions when there is very little water beneath the keel. However, even if this danger of grounding were not present, one might be wary of using present theories of ship motions for cases when the water depth is known to be significant, since theories such as strip theory deal (successfully) with infinite water depth only.

For definiteness we concentrate here on a particular mode of fluid flow, that involved in pure sideways (sway) motion of the ship or of force on it. This mode is of interest for a number of reasons, some practical, some theoretical. From the practical point of view we expect this mode of motion or force to be of great significance when a ship is berthed or positioned in such a way that the dominant seas are from abeam, or when it is being manoeuvred sideways by

tugs or bow thrusters.

From the theoretical point of view, this mode is interesting in that it provides a transition between the case of a fully-grounded ship where the clearance is zero and the whole flow must pass around the ends of the ship, and the case when the depth is sufficiently large compared with the draft of the ship to allow nearly all the flow to pass beneath the keel. At draft/depth ratios intermediate between zero and unity (but close to unity) the ship acts like a porous wall, some fluid particles passing "through" (i.e. under) it, while others are diverted toward the bow or the stern.

Just as the steady problem has an aerodynamic analogy, so the unsteady problem is shown in Section 5 to be analogous to an acoustic scattering problem, with the ship playing the role of a partly permeable acoustic barrier of negligible thickness (assuming the ship is thin). Some results may be obtained directly from the acoustic literature for such ribbon-like barriers, but new computations are needed for the general porous case.

In Section 6 we describe techniques for obtaining the effective acoustic porosity of the ship, i.e. the extent to which each section of the ship blocks (or rather, fails to block) the flow of fluid particles beneath it. This porosity is then used in Section 7 to obtain sway exciting forces on a Series 60 ship at zero speed.

II. ONE DIMENSIONAL THEORIES OF SQUAT IN SHALLOW, NARROW CANALS

Perhaps the most easily treated shallow-water problem involving ships is that for ships moving in a waterway so restricted in both width and depth that the problem may be treated as if one-dimensional. The effect of the ship is then little more than that of an obstruction in an (open) pipe.

This approach clearly has very important applications to canals and river traffic, and it is not surprising that a number of similar analyses have been made in response to actual squat problems arising in the use of such restricted waterways. For instance Garthune et al. [1948] and Moody [1964], following the method of Lemmerman [1942], derive a squat formula for use in the Panama canal, Constantine [1961], following Kreitner [1934], was concerned with the Manchester ship canal, Sjostrom [1965] with the Suez canal, Tothill [1967] with the St. Lawrence seaway and Sharpe and Fenton [1968] with the Yarra river, Australia. No doubt every important shallow and narrow waterway has had its independent squat investigation.

The theoretical development is in the main quite elementary, once we accept the one-dimensional hypothesis, which can itself be

justified either by careful asymptotic analysis or by physical reasoning. Suppose the canal has cross-section area $A(x, Z(x))$, when the water surface at station x is defined by $z = Z(x)$, z being a co-ordinate measured vertically upward from the equilibrium water surface. If, similarly, the ship has section area $S(x, Z(x))$ at station x , and the water has only an x -component of velocity $u(x)$, then continuity requires $u(A - S) = \text{constant}$, while Bernoulli's equation applied at the free surface gives $\frac{1}{2}u^2 + gZ = \text{constant}$.

If we take $Z = 0$ far upstream, where $u = U$, $S = 0$ and $A = A_0$, we have

$$u(A - S) = UA_0 \quad (2.1)$$

and

$$\frac{1}{2}u^2 + gZ = \frac{1}{2}U^2. \quad (2.2)$$

In this formulation the ship is fixed in position and the fluid streams past it in the x -direction. Elimination of u gives

$$\sqrt{U^2 - 2gZ} (A(x, Z) - S(x, Z)) = UA_0, \quad (2.3)$$

a transcendental equation from which the water surface elevation $Z(x)$ at station x may be determined in principle, for a canal of arbitrary section (not necessarily uniform or vertical sided), and a ship which occupies any proportion of the available canal area at any station.

In this most general case we should then return to the Bernoulli equation to obtain the pressure on the hull (which turns out to be hydrostatic) and integrate to obtain the force and moment on the ship. In principle the net vertical force would exactly balance the ship's weight and the trim moment would be zero, if we had started with the ship in its correct squatting position. In practice we should have to devise some kind of iteration procedure to move from an initial guess to the correct position. Such a general and exact study seems not to have been carried out, although it would be of some considerable interest.

Most investigators avoid this problem by treating an idealized ship which is a straight-sided cylinder, and ignoring end effects. In that case Z is constant over the length of the ship, and it follows that the ship simply rides up ($Z > 0$) with the water, maintaining constant displacement. If at the same time we restrict attention to the case when the canal is constant in section area, and in the region of interest at the free surface has a width W independent of Z (locally vertical sides), then we have from (2.3) that

$$\sqrt{U^2 - 2gZ} (A_0 + WZ - S) = UA_0 \quad (2.4)$$

where S is now constant. On squaring, (2.4) gives a cubic equation which may be solved directly for Z . Alternatively, following Constantine [1961], we may treat the problem in an inverse manner, solving for the speed as a function of Z and obtaining in non-dimensional form

$$F = \left[\frac{2d(1-d-s)^2}{1-(1-d-s)^2} \right]^{\frac{1}{2}} \quad (2.5)$$

where

$$F = U/\sqrt{gh} \quad (2.6)$$

$$d = -Z/h \quad (2.7)$$

and

$$s = S/A_0, \quad (2.8)$$

with

$$h = A_0/W \quad (2.9)$$

as the mean depth.

Constantine [1961] discusses the nature of the flow predicted by (2.5) and presents curves of F against d . Equation (2.5) permits only a restricted range of Froude numbers F for any given blockage coefficient s , namely

$$0 < F < F_1(s) \quad \text{and} \quad F_2(s) < F < \infty, \quad (2.10)$$

where $F_1(s)$, $F_2(s)$ are critical Froude numbers* shown in Fig. 1. No steady flow is possible in the "trans-critical" region $F_1 < F < F_2$, and Constantine [1961] discusses how an unsteady bore forms ahead of the ship if it attempts to exceed F_1 . Notice from Fig. 1 that the trans-critical regime becomes narrow if s is small, and as the blockage tends to zero there remains a single critical Froude number $F_1 = F_2 = 1$.

The last result is relevant to an alternative linearized approach to solution of (2.3) not utilized by the previously referenced investigators, but described in a somewhat different context by Tuck [1967]. Instead of specializing the shape of the ship, one now makes the approximation that its section area S is everywhere small compared with the canal section area A . If we again take for definiteness the case of a canal whose undisturbed section area A is independent of x and equal to A_0 , the water elevation Z will likewise

* Roots of the equation $s = 1 - \frac{3}{2} F^{2/3} + \frac{1}{2} F^2$.

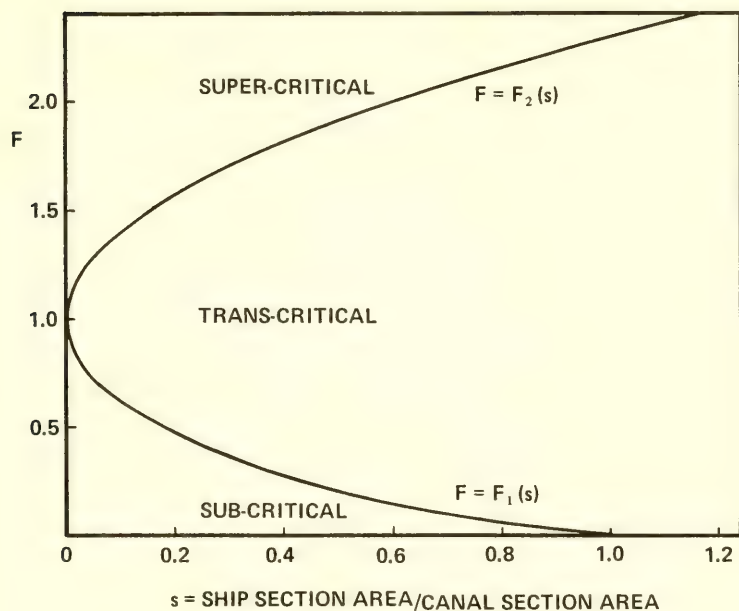


Fig. 1 Critical zones for squat in a canal

be small relative to the mean depth of water, and we can replace (2.3) by its Taylor series expansion with respect to Z , writing

$$\left(U - \frac{gZ}{U} + \dots\right)(A(x,0) + A_z(x,0)Z + \dots - S(x,0) - \dots) = UA_0. \quad (2.11)$$

On collecting terms of leading order in (2.11) and setting

$$A_0 = A(x,0) \quad (2.12)$$

$$S(x) = S(x,0) \quad (2.13)$$

$$W(x) = A_z(x,0), \quad (2.14)$$

we have

$$-\frac{gZ}{U} A + UWZ - US = 0,$$

i.e.

$$d = s \frac{F^2}{1 - F^2} \quad (2.15)$$

where F , d , s , h are again defined by (2.6) - (2.9) respectively, although all these quantities may now in principle vary with station coordinate x . However, if they do not, (2.15) can easily be shown to be the result of direct approximation of (2.5) for small s .

The most interesting feature of (2.15) is of course the singularity at the critical Froude number $F = 1$, which is to be expected from the fact that the former transcritical region $F_1 < F < F_2$ has shrunk down to an isolated "forbidden" Froude number at $F = 1$. We shall make use of linearized results like (2.15) throughout the remainder of this paper; however, it is well to bear in mind in each case that we may expect singularities at the critical Froude number and that, should these be of concern, they may be explained, studied or removed by non-linear considerations similar to those of the present section.

III. TWO-DIMENSIONAL THEORY OF SQUAT IN WIDE, SHALLOW WATER

The theories of the previous section are useful only in widths of water comparable with the beam of the ship. Since the important blockage parameter is the ratio of the maximum ship cross-section area to the cross-section area of the channel, naive use of these theories for very wide channels leads to the conclusion that the squat effect tends to zero for a given ship as the channel width tends to infinity. But of course the basic Bernoulli effect must still be present, even in an infinite expanse of water, so that there will still be squat, and indeed substantial squat in this case.

Analysis of shallow-water flow past ship-like bodies in infinitely-wide water was first attempted by Michell [1898] in his famous wave-resistance paper. The relatively greater importance of Michell's infinite depth formula, the derivation of which constitutes the first part of his paper, has perhaps led to little interest being taken in the second part of the paper, where he treats a shallow water problem. This is unfortunate, since Michell's approach is what we might now call an aerodynamic analogy, even though his paper ante-dates aerodynamics!

The problem treated by Michell concerns steady flow at speed U in the x -direction past an obstacle of thin cylindrical form, with equation

$$y = \pm \frac{1}{2}b(x), \quad |x| < \ell, \quad (3.1)$$

extending from the bottom $z = -h$ to the top $z = 0$ of the water. It is apparent right from the outset that with this model of a ship we can expect no prediction of squat, for the "ship" has vertical sides everywhere, and no fluid passes under it. Michell's only concern was with wave resistance.

The mathematical problem is specified by a disturbance velocity potential ϕ such that the fluid velocity is $\nabla(Ux + \phi)$, satisfying Laplace's equation

$$\frac{\partial^2 \phi}{\partial x^2} + \frac{\partial^2 \phi}{\partial y^2} + \frac{\partial^2 \phi}{\partial z^2} = 0, \quad -h < z < 0, \quad (3.2)$$

the bottom condition

$$\frac{\partial \phi}{\partial z} = 0 \quad \text{on} \quad z = -h, \quad (3.3)$$

the linearized free surface condition

$$g \frac{\partial \phi}{\partial z} + U^2 \frac{\partial^2 \phi}{\partial x^2} = 0 \quad \text{on} \quad z = 0, \quad (3.4)$$

and the linearized hull boundary condition

$$\frac{\partial \phi}{\partial y} = \pm \frac{1}{2} U b'(x) \quad \text{on} \quad y = 0_{\pm}. \quad (3.5)$$

Both equations (3.4), (3.5) are linearized on the basis that the ship is thin, i.e. that its slope $b'(x)$ is everywhere small, so that ϕ and its derivatives are small, as is the free surface elevation.

We now apply the assumption that the depth h is small. The corresponding approximate equations may be obtained formally by stretching the z -coordinate with respect to h , then carrying out an asymptotic expansion in terms of the small parameter h/l , see Wehausen and Laitone [1960]. However, the leading terms are easily obtained by simply expanding ϕ in a Taylor series with respect to z , about the bottom value $z = -h$, i.e.

$$\begin{aligned} \phi(x, y, z) &= \phi(x, y, -h) + (z+h) \phi_z(x, y, -h) \\ &+ \frac{1}{2} (z+h)^2 \phi_{zz}(x, y, -h) + \dots \end{aligned} \quad (3.6)$$

The second term in the expansion (3.6) vanishes by (3.3), and we use (3.1) to express ϕ_{zz} in terms of ϕ_{xx} and ϕ_{yy} , writing

$$\phi(x, y, z) = \phi(x, y, -h) - \frac{1}{2}(z+h)^2 \nabla^2 \phi(x, y, -h) + \dots \quad (3.7)$$

where $\nabla^2 = (\partial^2/\partial x^2) + (\partial^2/\partial y^2)$. On substitution in (3.4) we obtain immediately to leading order in h the equation

$$-gh\nabla^2 \phi(x, y, -h) + U^2 \phi_{xx}(x, y, -h) = 0,$$

or

$$\left[(1 - F^2) \frac{\partial^2}{\partial x^2} + \frac{\partial^2}{\partial y^2} \right] \phi(x, y, -h) = 0, \quad (3.8)$$

where $F = U/\sqrt{gh}$.

Equation (3.8) is formally identical to the equation describing linearized aerodynamics in a two-dimensional flow of a compressible fluid, with the Froude number F playing the role of the Mach number (see e.g. Sedov [1965]). Indeed, the problem of solving (3.8) subject to (3.5) is identical to that for subsonic ($F < 1$) or supersonic ($F > 1$) flow over a non-lifting wing of thickness $b(x)$, and we may use directly the results obtained in aerodynamics. Of course Michell was not so fortunate, and we should say that aerodynamicists could have used Michell's results, the first solution of any boundary-value problem for a non-trivial general boundary.

The character of Eq. (3.8) is different according as $F < 1$ when it is elliptic and $F > 1$ when it is hyperbolic, and different mathematical properties and solution techniques apply in these two cases. Here we quote only the final result for the hydrodynamic part of the pressure distribution over the body surface, namely

$$p = \begin{cases} \frac{-\rho U^2}{2\pi\sqrt{1-F^2}} \int_{-\infty}^{\infty} \frac{b'(\xi) d\xi}{x-\xi}, & F < 1 \\ \frac{\rho U^2}{2\pi\sqrt{F^2-1}} b'(x), & F > 1, \end{cases} \quad (3.9)$$

the bar denoting a Cauchy principal value. Note that the pressure given by (3.9) is a function of x only. The z -dependence has been neglected as part of the shallow-water approximation and there is no y -dependence because of the thin-ship approximation. The complete pressure distribution is obtained by adding to (3.9) the hydrostatic pressure.

The only possible force on this cylindrical body is in the x -direction, and there is no net moment. Michell found by integration

of p times the slope $b'(x)$ that the net force (wave resistance) is

$$F_1 = \begin{cases} 0, & F < 1, \\ \frac{\rho U^2 b}{2\sqrt{F^2 - 1}} \int_{-\ell}^{\ell} [b'(x)]^2 dx, & F > 1. \end{cases} \quad (3.10)$$

No doubt Michell was disappointed in his conclusion of zero wave resistance in the more important sub-critical regime, and indeed this conclusion may have contributed to the neglect of his shallow-water results. However, we can expect no other result from the present theory, which lacks a dissipation mechanism in the sub-critical regime to leading order. This feature it has in common with linearized aerodynamics. However, in aerodynamics the drag vanishes even according to nonlinear theory for Mach numbers everywhere less than unity, whereas in the present water-wave problem it is only to leading order that the wave-making dissipation mechanism disappears. No second-order calculations seem to have been carried out to find the non-zero subcritical wave-resistance, and this is a problem which merits attention.

Michell's analysis for a wall-sided "ship" was extended to ships of arbitrary cross-section by Tuck [1966]. In this case we can expect to predict a squat effect, and, although the analysis in the 1966 paper is rather complicated, the main conclusion is quite simple. By the method of matched asymptotic expansions (Van Dyke, [1964]), Tuck showed essentially that Michell's result (3.9) for the pressure still holds, providing we interpret the function $b(x)$ as the mean thickness of the ship at station x , averaged over the full depth of the water, i.e. set

$$b(x) = \frac{1}{h} S(x) \quad (3.11)$$

where $S(x)$ is, as in Section 2, the cross-sectional area of the ship at station x . Thus, for example, we obtain again Michell's wave resistance formula (3.10) but with (3.11) used to rewrite it in terms of $S(x)$.

On the other hand, the modified geometry of the ship does now allow non-zero vertical-plane forces and moments, and we find an upward heaving force

$$F_3 = \begin{cases} \frac{\rho U^2}{2\pi h\sqrt{1-F^2}} \int_{-\ell}^{\ell} dx \int_{-\ell}^{\ell} d\xi B'(x) S'(\xi) \log |x-\xi|, & F < 1 \\ -\frac{\rho U^2}{2h\sqrt{F^2-1}} \int_{-\ell}^{\ell} S'(x) B(x) dx, & F > 1 \end{cases} \quad (3.12)$$

and a bow-up pitching moment

$$F_5 = \begin{cases} -\frac{\rho U^2}{2\pi h\sqrt{1-F^2}} \int_{-\ell}^{\ell} dx \int_{-\ell}^{\ell} d\xi (xB(x))' S'(\xi) \log |x-\xi|, & F < 1, \\ -\frac{\rho U^2}{2h\sqrt{F^2-1}} \int_{-\ell}^{\ell} S'(x) xB(x) dx, & F > 1, \end{cases} \quad (3.14)$$

where $B(x)$ is the width of the ship at the waterline at station x . In fact the force written down in (3.12) is invariably negative at subcritical speeds so that a sinkage is to be expected rather than a lift.

Tuck [1966] also gives formulae for the actual sinkage and trim displacements of the ship in response to these forces, assuming equilibrium with hydrostatic restoring forces, and provides some computed results which are in reasonable quantitative and excellent qualitative agreement with experiments of Graff *et al.* [1964]. There is a need for more experiments, especially in the very low water depth range, but it would appear from the comparisons so far made that the theory is quantitatively accurate so long as the depth is less than about one eighth of a ship length, and the Froude number based on depth is less than about 0.7.

It may be worth observing here that the integrals in (3.12) - (3.15) are fairly insensitive to the shape of the section curves $B(x)$, $S(x)$. For instance, the ratio

$$\lambda = - \frac{\ell^2 \int_{-\ell}^{\ell} dx \int_{-\ell}^{\ell} d\xi B'(x) S'(\xi) \log |x-\xi|}{\int_{-\ell}^{\ell} B(x) dx \cdot \int_{-\ell}^{\ell} S(x) dx} \quad (3.16)$$

is nearly an absolute dimensionless constant, taking values between 2.0 and 2.4 over a very wide range of $B(x)$, $S(x)$ curve shapes, including actual ships and mathematically defined curves. Thus a nearly universal approximation to the subcritical vertical force is

$$F_3 = -\lambda \frac{\rho U^2}{2\pi h \sqrt{1-F^2} \ell^2} \int_{-\ell}^{\ell} B(x) dx \int_{-\ell}^{\ell} S(x) dx \quad (3.17)$$

with a fixed value of λ . From this follows a similar approximation to the actual sinkage, say a displacement of δ downwards, where

$$\delta = \frac{\lambda}{2\pi} \frac{F^2}{\sqrt{1-F^2}} \frac{\int_{-\ell}^{\ell} S(x) dx}{\ell^2}. \quad (3.18)$$

Finally, introducing the displaced volume

$$V = \int_{-\ell}^{\ell} S(x) dx \quad (3.19)$$

and making a further assumption (justified in most practical situations) that $F \ll 1$, we have

$$\delta = \frac{2\lambda}{\pi} \frac{U^2}{gh} \frac{V}{L^2} \quad (3.20)$$

where $L = 2\ell$ is the ship length.

In practical terms, if δ , L and h are in feet, V in cubic feet and U in knots, and if we insert reasonable (conservative) values for λ and g , (3.20) implies

$$\delta = 0.13 \frac{U^2 V}{h L^2}. \quad (3.21)$$

We put forward this formula (3.21) quite seriously for practical use by anyone interested in a quick estimate of squat in a wide expanse of shallow water. One should note the quadratic dependence on forward speed, the inverse dependence on water depth, the proportionality to displacement (at fixed length) and inverse square dependence on length (at fixed displacement).

In a subsequent paper, Tuck [1967] extended the 1966 work to the case where the ship is moving along the center of a rectangular channel of width w , considering only the sub-critical case. The assumption made was that w is comparable with the ship length L ; however the results obtained were uniformly valid, in the sense that the infinite-width results were reproduced as $w/L \rightarrow \infty$, while as $w/L \rightarrow 0$ we obtain predictions which may also be obtained by elementary (linear) one-dimensional theory as in Section 2. An inter-

esting mathematical feature of this small width limit is that the singularity at $F = 1$ becomes stronger as $w/L \rightarrow 0$, changing from inverse square root (e.g. (3.12)) to inverse first power (e.g. (2.15)).

Another conclusion in the 1967 paper was that the ratio between the sinkage at width w and that at infinite width was almost independent of the shape, size or speed of the ship, depending only on the parameter $(w/L)\sqrt{1-F^2}$. Thus, starting with any estimate (even (3.21)!) of the infinite width sinkage, we may further estimate the effect of finite width by use of the universal curve given in the 1967 paper. For example, at low values of F , a channel width of two ship lengths increases the sinkage by 10%, one ship length by 33%, over the infinite width values. For channel widths less than one ship length a one-dimensional theory as in Section 1 is sufficiently accurate and probably to be preferred.

IV. THREE-DIMENSIONAL THEORY OF SQUAT IN INFINITE WIDTH, FINITE DEPTH

We begin the present section by presenting the solution! Suppose $S(x)$ is the cross-section area curve of a slender ship moving at velocity U in water of finite constant depth h , and let

$$S^*(k) = \int_{-\ell}^{\ell} S(x) e^{ikx} dx. \quad (4.1)$$

Then consider

$$\begin{aligned} \phi = & \frac{iU}{4\pi^2} \int_{-\infty}^{\infty} dk k S^*(k) e^{-ikx} \int_{-\infty}^{\infty} d\lambda \frac{e^{-i\lambda y}}{q} \\ & \cdot \left[e^{qz} + \frac{e^{-qh} \cosh qz}{\sinh qh} - \frac{k^2 \cosh q(z+h)}{\sinh qh(k^2 - \kappa q \tanh qh)} \right] \end{aligned} \quad (4.2)$$

where $\kappa = g/U^2$ and $q = (k^2 + \lambda^2)^{\frac{1}{2}}$.

Although the expression (4.2) is extremely complicated, it has the following properties, easily checked:

$$(i) \quad \nabla^2 \phi = 0, \quad -h < z < 0, \quad r = (y^2 + z^2)^{\frac{1}{2}} \neq 0, \quad (4.3)$$

$$(ii) \quad \partial \phi / \partial z = 0 \quad \text{on } z = -h, \quad (4.4)$$

$$(iii) \quad \kappa (\partial \phi / \partial z) + (\partial^2 \phi / \partial x^2) = 0 \quad \text{on } z = 0, y \neq 0, \quad (4.5)$$

$$(iv) \quad \phi \rightarrow \frac{U}{\pi} S'(x) \log r + f(x) + O(r \log r) \quad \text{as } r \rightarrow 0. \quad (4.6)$$

The physical interpretation of ϕ is as follows. The contribution from the first term "e^{qz}" inside the square brackets is just the potential of a line distribution of sources, of strength proportional to $S'(x)$, in a fluid which extends to infinity in all directions. The contribution from the second term inside the square brackets corrects for the presence of a bottom wall at $z = -h$, while the last term in the square brackets corrects for the presence of a free surface at $z = 0$.

The last property (4.6) indicates that the given solution (4.2) can serve as an outer approximation (see Tuck [1964]) and will match an inner approximation which satisfies the correct boundary condition on a slender hull surface. Thus (4.2) gives the disturbance potential for flow around a slender ship in finite depth of water, no shallowness assumptions having been made.

The function $f(x)$ in (4.6) is of crucial importance, and may clearly be considered in three parts, arising from the three terms in the square brackets in (4.2). Let us write

$$f(x) = f_{\infty}(x) + g(x) \quad (4.7)$$

where

$$f_{\infty}(x) = -\frac{US'(x)}{2\pi} \log 4(\ell^2 - x^2) + \frac{U}{2\pi} \int_{-\ell}^{\ell} d\xi \frac{S'(x) - S'(\xi)}{|x - \xi|} \quad (4.8)$$

(Tuck and von Kerczek [1968]) is the corresponding function for the double-body flow in an infinite fluid (no bottom or free surface), while $g(x)$ is the contribution from the second two terms in the square bracket of (4.2), and takes the value

$$g(x) = \frac{iU}{4\pi^2} \int_{-\infty}^{\infty} dk \, k S^*(k) e^{-ikx} A^*(k) \quad (4.9)$$

where

$$A^*(k) = -2 \int_k^{\infty} \frac{dq}{\sqrt{q^2 - k^2}} \left[1 + \frac{kq}{k^2 - kq \tanh qh} \right]. \quad (4.10)$$

In the integral (4.10), if $kh < 1$ there is a pole on the real q -axis at $q = q_0(k)$, where

$$k^2 = \kappa q_0 \tanh q_0 h \quad (4.11)$$

and this pole must be avoided by passing beneath it in order that the waves are behind the ship.

Thus the real part of $A^*(k)$ may be written as a Cauchy principal value integral, which can be evaluated by standard numerical quadratures, whereas the imaginary part of $A^*(k)$ can be obtained from the residue at the pole, and we have

$$\Im A^*(k) = \begin{cases} \frac{\pi \kappa}{\sqrt{q_0^2 - k^2}} \frac{q_0}{k} \frac{dq_0}{dk}, & \kappa h < 1 \\ 0, & \kappa h > 1. \end{cases} \quad (4.12)$$

Once A^* is determined, $g(x)$ follows by further numerical quadratures from (4.9), if actual numerical values of $g(x)$ are required.

However, our main aim is to find the forces on the ship, which follow from $g(x)$ via the pressure distribution, given by

$$p(x, y, z) = p_{\infty}(x, y, z) - \rho U g'(x) \quad (4.13)$$

where $p_{\infty}(x, y, z)$ is the pressure on a double body in an infinite fluid. Hence the vertical force is

$$\begin{aligned} F_3 &= F_3^{\infty} - \rho U \int_{-\ell}^{\ell} dx B(x) g'(x) \\ &= F_3^{\infty} - \frac{\rho U^2}{4\pi^2} \int_{-\infty}^{\infty} dk k^2 S^*(k) \overline{B^*(k)} A^*(k), \end{aligned} \quad (4.14)$$

and the trim moment is

$$\begin{aligned} F_5 &= F_5^{\infty} + \rho U \int_{-\ell}^{\ell} dx x B(x) g'(x) \\ &= F_5^{\infty} + \frac{\rho U^2}{4\pi^2} \int_{-\infty}^{\infty} dk k^2 S^*(k) \overline{x B^*(k)} A^*(k), \end{aligned} \quad (4.15)$$

where $F_3^{\infty}, F_5^{\infty}$ are the corresponding quantities for the "submerged" half of the infinite fluid double body, $B(x)$ is again the waterplane

width curve, $B^*(k)$, $xB^*(k)$ are Fourier transforms (cf. (4.1)) of $B(x)$, $xB(x)$ respectively, and a bar denotes a complex conjugate.

The quantities F_3^∞ , F_5^∞ must be computed separately, e.g. by computer programs such as those of Hess and Smith [1964] or Tuck and von Kerczek [1968]. Alternatively, one may estimate them experimentally. It is important to note that F_3^∞ , F_5^∞ are independent of water depth and of Froude number; indeed, when divided by ρU^2 these are constants which are a property of the hull geometry alone.

An interesting special case is a ship with fore-and-aft symmetry, where (neglecting viscosity) $F_5^\infty = 0$. In addition, since $S(-x) = S(x)$ and $-xB(-x) = -xB(x)$, S^* is real and even with respect to k whereas xB^* is imaginary and odd. As a result, only the imaginary part (4.12) of $A^*(k)$ contributes to the integral in (4.15), and we have

$$F_5 = \frac{\rho U^2}{2\pi^2} \int_0^\infty dk k^2 S^* \Im(xB^*) \Im A^* \quad (4.16)$$

$$= \begin{cases} 0, & F = (kh)^{-\frac{1}{2}} < 1 \\ \frac{\rho g}{2\pi} \int_0^\infty \frac{dq_0 q_0 k}{\sqrt{q_0^2 - k^2}} S^*(k) \Im xB^*(k), & F > 1. \end{cases} \quad (4.17)$$

Similar, but more complicated, results are obtained for $F_3 - F_3^\infty$ and $F_5 - F_5^\infty$ when the ship does not possess fore-and-aft symmetry. Evaluation of the supercritical trim moment F_5 from (4.17) requires only a single numerical quadrature (apart from the prior estimation of the Fourier transforms S^* , xB^*). However, in the general case an additional numerical quadrature is needed to determine the real part of $A^*(k)$ from (4.10).

The shallow-water limit of the above finite-depth results corresponds to letting $kh \rightarrow 0$, i.e. we let the depth tend to zero relative to a typical effective wavelength $2\pi/k$. In particular, from (4.11) we have $q_0 h \rightarrow 0$ as $kh \rightarrow 0$ and hence $k \rightarrow \sqrt{kh} q_0$, or $q_0 \rightarrow Fk$. Thus for $F > 1$, (4.17) gives for ships with fore-and-aft symmetry that

$$F_5 \rightarrow \frac{\rho g}{2\pi} \frac{F^2}{\sqrt{F^2 - 1}} \int_0^\infty dk k S^* \Im xB^* \quad (4.18)$$

$$= - \frac{\rho U^2}{2\pi \sqrt{F^2 - 1}} \int_{-\ell}^\ell S'(x) xB(x) dx, \quad (4.19)$$

in agreement with (3.15). It is quite straightforward to show in a similar manner that all of the shallow-water results of Section 3 are reproduced in the corresponding limit, even when fore-and-aft symmetry is not assumed.

In carrying out this shallow-water limit, one may wonder what happens to the "double-body" terms F_3^∞ and F_5^∞ . The answer is that they are of course quite independent of water depth and hence nothing happens to them, and in principle they remain in the formulae. However, when the depth is small the shallow-water terms formally dominate the total expression for F_3 or F_5 , so that F_3^∞ and F_5^∞ may be neglected.

In Fig. 2 we present computed finite-depth sub-critical sinkage and super-critical trim for a ship with parabolic waterline and section-area curves, a length of 600 ft, beam of 60 ft, draft of 20 ft, and block coefficient 0.533. This geometry and size was chosen for analytical convenience, but is not unlike a destroyer hull. The super-critical trim was calculated directly from (4.17) by a single numerical quadrature (since this hull has fore-and-aft symmetry), whereas the sub-critical sinkage required an extra numerical integration of (4.10), and, furthermore, required separate estimation of the infinite-fluid contribution F_3^∞ in (4.14).

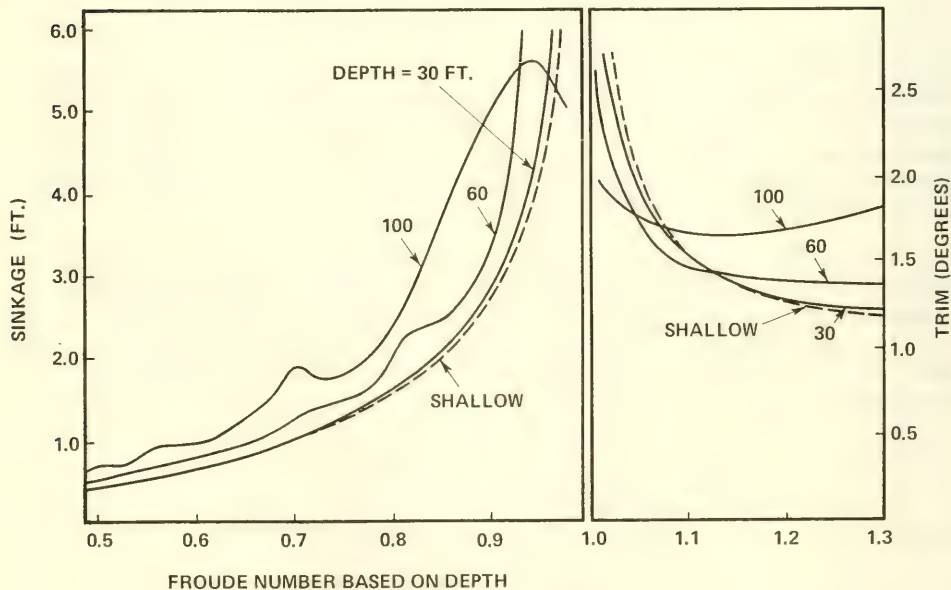


Fig. 2 Finite depth squat for a ship 600 ft long and 20 ft draft

Instead of using sophisticated numerical techniques for F_3^∞ , in the present case we estimated F_3^∞ by assuming that the under-water hull could be approximated by an equivalent spheroid, with the same length and displacement. If we define the slenderness ϵ by

$$\epsilon = \sqrt{\frac{12}{\pi} \frac{V}{L^3}}, \quad (4.20)$$

which is equal to the beam/length ratio of the equivalent spheroid, the exact infinite fluid force on the submerged half of the spheroid can be obtained from the formula given by Havelock [1939] in the form

$$F_3^\infty = -\rho U^2 \cdot \int_{-l}^l B(x) dx \cdot C_S(\epsilon) \quad (4.21)$$

where

$$C_S(\epsilon) = \frac{1}{2} + \frac{1}{2}(1 - 3\epsilon^2 + 2\epsilon^3) \left(1 - \frac{\epsilon^2}{2\sqrt{1-\epsilon^2}} \log \frac{1+\sqrt{1-\epsilon^2}}{1-\sqrt{1-\epsilon^2}}\right)^{-2}. \quad (4.22)$$

In fact, since ϵ is generally small, an adequate slender-body approximation to (4.22) is

$$C_S(\epsilon) = -\epsilon^2 \left(\log \frac{1}{2}\epsilon + \frac{3}{2}\right) + \epsilon^3 + O(\epsilon^4 \log \epsilon). \quad (4.23)$$

The result (4.22) is of course in exact agreement with Havelock's [1939] more general formula for ellipsoids whose sections are not circular. On the other hand (4.23) is within 10% of computations based on Havelock's formula for general ellipsoids, providing $\epsilon < 0.2$ and the half-beam/draft ratio of the general ellipsoid lies between 0.65 and 7.0, a range of parameters which includes the usual ship dimensions. Some preliminary numerical computations using the theory of Tuck and Von Kerczek [1968] have shown that (4.23) is a good estimate for non-ellipsoidal geometries, while Havelock [1939] himself made satisfactory comparisons between his ellipsoid estimates and experiments of Horn [1937] on actual ship models, so that there are grounds for believing that (4.21) subject to (4.23) gives a useful prediction of the infinite fluid zero Froude number sinkage force.

The finite depth computations were carried out for water depths of 100, 60 and 30 feet. The results for the smallest of these depths are in very close agreement with the shallow-water theory of Section 3, shown dashed on Fig. 2, over the complete range of Froude numbers shown. This indicates that a water depth/ship length

ratio of 1 in 20 is quite adequately shallow for the use of shallow-water theory. But the results at twice this depth are also in reasonably good agreement with shallow-water theory, the latter theory underestimating sinkage by about 20%. The corresponding underestimate at 100 ft depth is about 40%, so that one should consider a water-depth/ship length ratio of 1 in 6 as too great to use shallow-water theory for sinkage.

However, it must be pointed out that the difference between the finite depth and shallow water predictions of sinkage is predominantly due to the influence of the term F_3^∞ in (4.14). If this (positive) term is left out of (4.14) the finite depth computations at all depths merely oscillate about a mean which is quite close to the shallow-water curve. These oscillations are clearly visible in Fig. 2; they are quite similar to the humps and hollows in theoretical wave resistance curves, and have the same explanation, as an interference effect. One may thus speculate that, by ignoring these oscillations, we may obtain a useful empirical scheme for computing finite depth sinkage by adding the shallow water estimate (e.g. (3.21)) to the infinite fluid zero Froude number estimate computed by (4.23). Further work needs to be done to test this suggestion, which is of some significance since computations based on the theory of the present section are too complicated and expensive of computer time for general use.

No direct comparisons of the finite depth computations with experiment have yet been made, but the differences between the finite-depth and shallow-water results appear to be in the right direction to explain most of the discrepancies already noted by Tuck [1966] between shallow-water theory and the experiments of Graff *et al.* [1964]. In particular, more detailed computations for a depth of 100 ft, ($h/L = 0.167$) show that the peaks in the sinkage and trim curves occur at about the right Froude numbers, 0.94 and 0.98 respectively, and that the trim starts to become significant at a Froude number as low as 0.8.

V. THE ACOUSTIC ANALOGY FOR UNSTEADY LATERAL FLOW

In the remainder of this paper we shall be concerned with a very special aspect of the problem of ship motions in shallow water, namely computation of the exciting force on a stationary ship under the influence of regular beam seas. A more general formulation and partial solution of the problem of ship motions in shallow water is given by Tuck [1970]. Most other work on ship motions in shallow water, e.g. Freakes and Keay [1966], Kim [1968], concerns finite depth rather than shallow water. An exception is a number of papers by Wilson (e.g. [1959]) on responses of moored ships in harbors, but no account is taken there of ship geometry. Mention must also be made of the thesis by Ogilvie [1960], in which the shallow-water asymptotic expansion was developed rigorously for a class of two-

dimensional diffraction problems.

We now suppose that, except for the scattering effect of the ship, the flow field is described by an incident plane wave moving in the y -direction, with wavelength $2\pi/k$, frequency σ , and amplitude A , where k and σ are related by the shallow-water dispersion relation

$$\sigma = \sqrt{gh} k. \quad (5.1)$$

The potential of this wave will be taken to be the real part of $\phi_0 e^{-i\sigma t}$, where

$$\phi_0 = A \sqrt{\frac{g}{h}} \frac{e^{iky}}{ik}. \quad (5.2)$$

In fact, (5.1) and (5.2) are of course already approximations to the exact formula (e.g. Wehausen and Laitone [1960]) for small-amplitude waves in finite depth h ; for instance the exact expression for ϕ_0 is that given by (5.2) multiplied by $\cosh k(z+h)/\cosh kh$, which tends to unity as $kz \rightarrow 0$.

This incident wave is modified by the presence of the ship. We suppose that the total field is then the real part of $(\phi_0 + \phi)e^{-i\sigma t}$, where $\phi = \phi(x, y, z)$ is the disturbance potential, which is to be found. The exact equations satisfied by ϕ are (3.2), (3.3), an unsteady free surface condition analogous to (3.4), namely

$$g \frac{\partial \phi}{\partial z} - \sigma^2 \phi = 0 \quad \text{on} \quad z = 0 \quad (5.3)$$

and a boundary condition on the ship's hull of the form

$$\frac{\partial}{\partial n} (\phi_0 + \phi) = 0 \quad (5.4)$$

where $\partial/\partial n$ denotes differentiation normal to the hull.

We construct first an outer shallow-water approximation to ϕ in the same way as in Section 3, i.e. by expanding in a Taylor series with respect to $(z+h)$. Equation (3.7) still applies, but on substitution of (3.7) in (5.3) we now find

$$-gh \left(\frac{\partial^2}{\partial x^2} + \frac{\partial^2}{\partial y^2} \right) \phi(x, y, -h) - \sigma^2 \phi(x, y, -h) = 0,$$

i.e. $\phi(x, y, -h)$ satisfies the Helmholtz equation

$$\nabla^2 \phi + k^2 \phi = 0 \quad (5.5)$$

in the (x, y) plane.

The Helmholtz equation is of course simply the "reduced" wave equation, and so applies to any scalar wave problem in two dimensions, for sinusoidal time dependence. In particular, it describes linear acoustics in two dimensions (e.g. Morse [1948]), and many results obtained in solving acoustic problems may be utilized.

For example, we may treat immediately the scattering of a thin cylindrical ship, as in Michell's model of Section 3, which extends from top to bottom of the water. An important difference from the theory of Section 3 is that, even in the limit as the thickness tends to zero, the thin "ship" is capable of scattering beam waves. Thus, to leading order, the problem is independent of thickness, and reduces to acoustic scattering by a ribbon or strip of zero thickness placed broadside on to the waves, with a "hard" boundary condition

$$\frac{\partial \phi}{\partial y} = -A \sqrt{\frac{g}{h}} = \text{constant on } y = 0_{\pm}, \quad |x| < \ell. \quad (5.6)$$

The exact solution can be written down as a series of Mathieu functions (Morse and Rubenstein [1938]). Results for the scattering cross section, the far-field polar diagram and the force on the strip can be computed from this series, but only with some difficulty, especially for high frequency. Alternatively, integral equation formulations of the problem can lead to useful high and low frequency asymptotic solutions (Hönl, Maue and Westphal [1961]) or even to efficient numerical solutions (Taylor [1971]). Such numerical results are included with the discussion of the general case in Section 7.

Once again this idealized ship is deficient from the practical point of view. In particular, it allows no account to be taken of flow beneath the keel of the ship. In any situation of real interest, wave energy is not only scattered, diffracting around the ends of the ship, but also transmitted underneath the ship if there is any reasonable amount of clearance. The most interesting situation is that which applies when the amounts of disturbance scattered and transmitted are of the same order of magnitude; we shall see later that this is true for draft/water depth ratios in the range 0.5 to 0.95.

We shall retain the approximation that the ship is thin, and hence slender, since it must have small draft. However, the

possibility of fluid passing underneath the ship means that we must replace the "hard" boundary condition (5.6) by a more general condition, expressing in effect a relationship between the velocity $(\partial\phi/\partial y) + A\sqrt{g/h}$ of fluid passing "through" (i.e. under) the strip $y = 0_+$, $|x| < \ell$ and the pressure difference (proportional to potential difference) across the strip, which causes this underflow. Thus we write

$$\frac{\partial\phi}{\partial y} + A\sqrt{\frac{g}{h}} = \mp P\phi \quad \text{on } y = 0_+, |x| < \ell, \quad (5.7)$$

where $P = P(x)$ is the "porosity" of the ship section at station x . If the ship is actually touching the bottom, then $P = 0$ and (5.7) reduces to (5.6); at the other extreme, if there is substantial clearance, $P \rightarrow \infty$ and the jump in potential ϕ across the strip tends to zero, leading as expected to zero force on the ship.

In the following section we indicate how to obtain the porosity $P(x)$ for any given ship and sea bottom geometrical configuration. The problem of solving (5.5) subject to (5.7) is then identical to that for acoustic scattering by a "semi-soft" or porous ribbon with finite acoustic impedance, see e.g. Morse [1948]. However, no general procedure seems to be available in the acoustic literature for solving this type of problem, and we present in Section 7 a numerical approach based on an integral equation formulation.

It should be remarked that as $k \rightarrow 0$ the present problem reduces to uniform steady streaming flow across the ship, the free surface being replaced by a rigid wall. This problem was discussed by Newman [1969], who presented solutions for the added mass of the ship in such a flow. The present theory can be considered a generalization of Newman's theory to allow for waves, and gives results which agree with Newman's in the limit as $k\ell \rightarrow 0$, i.e. as the waves become long compared with the length of the ship.

VI. THE DETERMINATION OF THE EFFECTIVE POROSITY

The problem formulated in the previous section is to be interpreted as an outer problem, which provides a solution for the scattered field ϕ everywhere except within a beam or two of the center plane $y = 0$ of the ship. In this latter region, the outer solution must match an inner approximation which describes the detailed flow field beneath the hull. This flow can easily be shown (Tuck [1970], Newman [1969]) to be locally two-dimensional in the (x, z) plane, and to satisfy the two-dimensional Laplace equation

$$\frac{\partial^2 \phi}{\partial y^2} + \frac{\partial^2 \phi}{\partial z^2} = 0 \quad (6.1)$$

in that plane. Furthermore, the free surface condition reduces to a rigid-wall boundary condition

$$\frac{\partial \phi}{\partial z} = 0 \quad \text{or} \quad z = 0. \quad (6.2)$$

Thus the inner problem is identical to that treated by Newman [1969], who assumed that (6.2) was valid everywhere.

The boundary condition at "infinity" for this inner solution is that the inner solution should match the behavior of the outer solution in a common domain of validity, say many beams away from $y = 0$, but not so far away that y is as large as l or $2\pi/k$. In effect, this simply means that the inner boundary condition (5.7) for the outer solution becomes the outer boundary condition for the inner solution. Thus the inner approximation to the disturbance potential ϕ must satisfy

$$\frac{\partial \phi}{\partial y} + A \sqrt{\frac{g}{h}} \rightarrow \mp P\phi \quad \text{as} \quad y \rightarrow \pm \infty \quad (6.3)$$

which is satisfied if ϕ is asymptotically independent of y , i.e.

$$\phi \rightarrow \mp \frac{A\sqrt{g/h}}{P} \quad \text{as} \quad y \rightarrow \pm \infty \quad (6.4)$$

implying

$$\frac{\partial \phi}{\partial y} \rightarrow 0 \quad \text{as} \quad y \rightarrow \pm \infty. \quad (6.5)$$

The boundary condition on the hull is (5.4) but where now $\partial/\partial n$ denotes differentiation normal to the hull cross section Γ at station x , and where, since ky is small in the inner region, we may replace the incident wave ϕ_0 by

$$\phi_0 \rightarrow A \sqrt{\frac{g}{h}} \left(\frac{1}{ik} + y \right), \quad (6.6)$$

i.e. by an incident stream of speed $A\sqrt{g/h}$. Then (5.4) becomes

$$\frac{\partial \phi}{\partial n} = -A \sqrt{\frac{g}{h}} \frac{\partial y}{\partial n} \quad \text{on} \quad \Gamma. \quad (6.7)$$

Thus the inner approximation to ϕ is the potential for flow due to

motion of the section Γ as if it were an infinitely long rigid cylinder moving in the y -direction with velocity $A\sqrt{g/h}$, the fluid at $y = \pm \infty$ being at rest.

The problem specified by (6.1) subject to (6.2), the bottom condition (3.3), the hull condition (6.7) and the rest condition (6.5) is a classical Neumann boundary value problem, and ϕ is determined by these conditions apart from an additive constant. If in addition we prescribe the natural symmetry condition that ϕ is an odd function of y , in conformity with (6.4), then ϕ is uniquely determined, and the actual limit of ϕ as $y \rightarrow \pm \infty$ must, via (6.4), provide a determination of P .

A number of techniques are available for solving this two-dimensional boundary-value problem. If the section is sufficiently simple (e.g. rectangular) a solution may be found by conformal mapping methods (Flagg and Newman [1971]). For actual and quite general ship sections we have (Taylor [1971]) developed a computer program based on the methods used by Frank [1967] for a similar problem.

In this method one represents the flow by a distribution of sources around the section Γ , with variable but unknown density. These sources individually satisfy the "free" surface and bottom conditions (6.2) (3.3), but not, of course the hull boundary condition (6.7) on Γ . We now attempt to choose the source density function in order to satisfy (6.7), thereby obtaining an integral equation from which the source density is in principle obtainable.

Since analytic solutions for general Γ are out of the question, we adopt a numerical approach in which Γ is first approximated by a set of straight line segments, on each of which we assume the source density to be constant. The integral equation then reduces to a set of linear algebraic equations for these unknown constant source strengths, and this set of equations is solved by direct matrix inversion.

It is convenient to define a blockage coefficient

$$C(x) = \frac{1}{P(x)}, \quad (6.8)$$

as the inverse of the porosity. With this definition, we see from (6.4) that to obtain $C(x)$ we merely divide the potential ϕ by minus the speed $A\sqrt{g/h}$ of the motion of the section Γ and take the limit as $y \rightarrow +\infty$. Thus, if our aim is solely to determine $C(x)$ or $P(x)$, we may, without loss of generality, take $A = -\sqrt{h/g}$ for the purpose of the present section only, and identify C as the limit of ϕ as $y \rightarrow +\infty$, a quantity which is readily evaluated from the numerical solution for the generating source strengths.

The program has been tested by comparison with Flagg and Newman's [1971] computations for a rectangular section, and gives good agreement over the range of dimension of interest. For instance, with a rectangle of total width 0.25 and a (submerged) draft 0.1 in water of depth 0.125, Flagg and Newman's [1971] computations give $C = 0.598$, while our program with 24 segments on the bottom of the rectangle and 12 segments on each side gives $C = 0.603$. Although this accuracy (1%) is already very good in the present application, it can easily be and has been improved by use of a larger number of segments, especially in the neighborhood of the corners.

Another check is by means of asymptotic estimates for small clearances (Taylor [1971]). A formula which is valid for arbitrary sections, providing they have substantially vertical sides $2b$ units apart and a substantially flat bottom c ($\ll h, b$) units from the water bottom, is

$$C = \frac{bh}{c}. \quad (6.9)$$

For strictly rectangular sections, this formula may be improved by estimation of the next term in an asymptotic expansion for small c/h , giving

$$C = \frac{bh}{c} + \frac{2h}{\pi} \log \frac{h}{4c} + \frac{2h}{\pi} - b + O(c). \quad (6.10)$$

For the rectangular section used as an example above, (6.9) gives $C = 0.625$ while (6.10) gives $C = 0.597$.

Indeed, it must be noted that rectangles are not a fair test for the computer program, since the generating source strength becomes infinite at the sharp corner. We should therefore expect far better accuracy for smooth ship-like sections. For instance, the program gives results with accuracies of better than 1% when applied to the oval-shaped sections generated by a single isolated dipole in a channel (Lamb [1932]).

Figure 3 shows computations of $C(x)/\ell$ for a Series 60, block 0.80, tanker hull (Todd [1963]), with beam/draft ratio of 2.5 and length/beam ratio of 8.0, the ship length being 2ℓ . The results are for two depths of water only, with draft/depth ratios of 0.8 and 0.9. In neither of these cases is there a great deal of water beneath the keel, but this is the interesting range, since it is necessary that the clearance be relatively small to achieve significant flow blockage. Thus at a draft/depth ratio of 0.4, the typical values of C/ℓ are already below 0.125 over the whole length of the ship, which leads to a maximum force (see the following section) less than a quarter of that for the full-blocked situation.

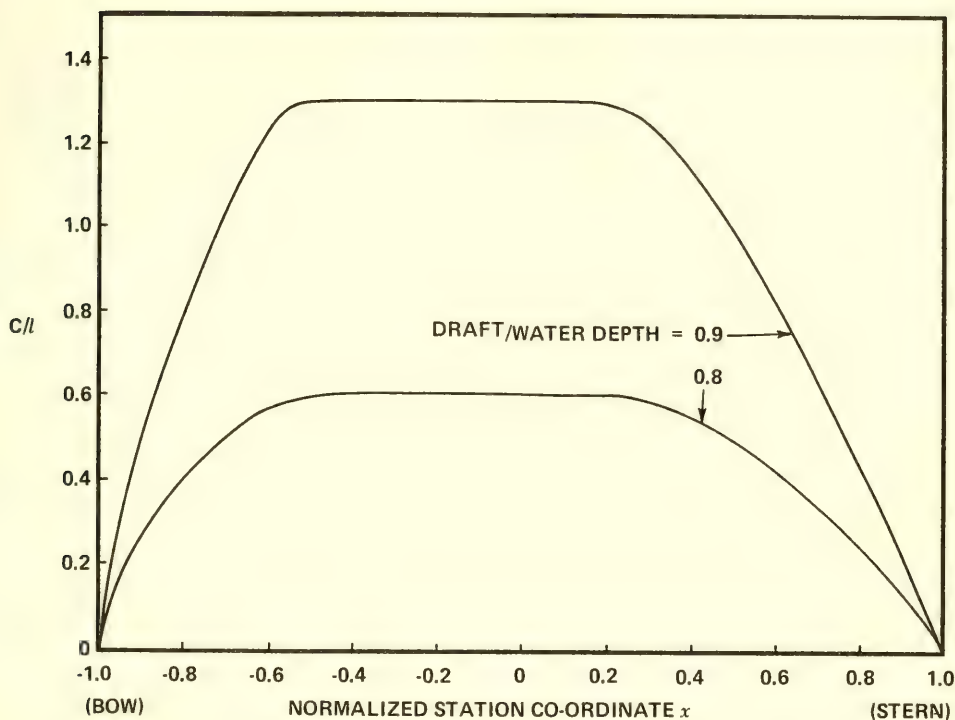


Fig. 3 Blockage coefficient $C(x)$ for Series 60, block 0.80 ship

VII. THE SIDE FORCE DUE TO BEAM SEAS

Once we have obtained the blockage coefficient $C(x)$ or its inverse the porosity $P(x)$ for any given ship-water bottom geometry, we have all the information about the ship that is necessary to solve the outer acoustic-like problem to determine the wave force on the ship. Numerical techniques for solving the problem formulated in Section 5 are described by Tuck [1970] and by Taylor [1971] and will not be discussed in detail here.

It is sufficient to observe that the outer problem can be reduced to solution of an integral equation, using methods analogous to those described by Hönl, Maue and Westphal [1961], in which $P(x)$ appears as an input quantity. This integral equation can be solved by direct numerical quadrature, followed by matrix inversion, leading to numerical values for the basic unknown potential $\phi(x, 0_+, -h)$.

This potential is proportional to the pressure difference across the ship, and hence we may obtain the net force F_2 on the

ship in beam seas in the form

$$F_2 = -2i\sigma\rho h \int_{-l}^l \phi(x, 0_+, -h) dx. \quad (7.1)$$

Figure 4 shows computations of $|F_2|/2\rho g h l A$ for the Series 60, block 0.80 ship whose blockage coefficient $C(x)$ was given in Fig. 3. This particular scaling of the force was chosen so that the high frequency or short wave limit $kl \rightarrow \infty$ is 2.0. This limit corresponds physically to the case when the ship acts as a perfect reflector many wavelengths long, so that a pure standing wave exists in its neighborhood. This is true for all values of $P(x)$, i.e. for all draft/water depth ratios, because as the waves get shorter and shorter they are less able to penetrate beneath the hull.

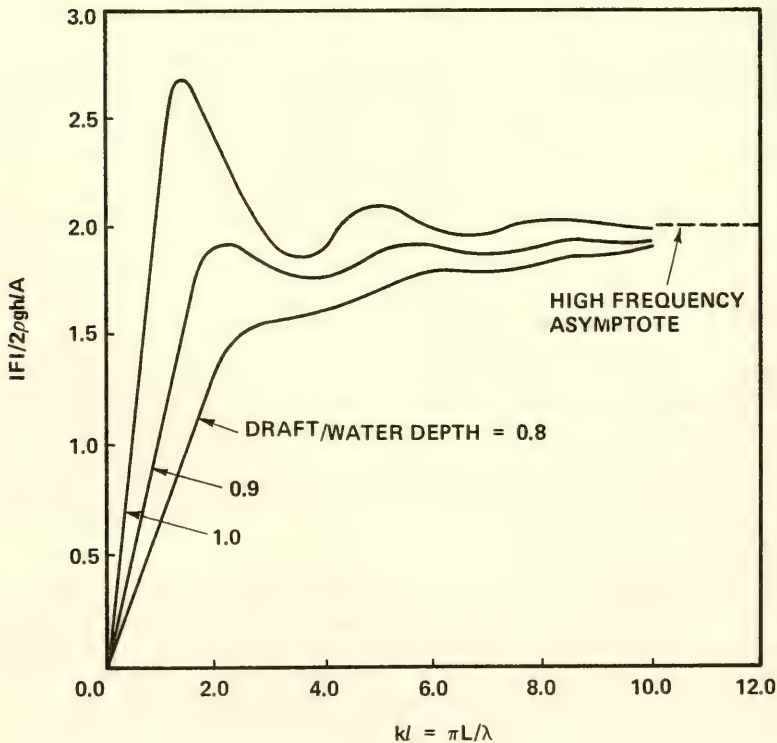


Fig. 4 Side force on Series 60, block 0.80 ship, due to beam seas

The results for zero clearance show pronounced wobbles as a function of frequency. This is to be expected, and is due to interference between the waves diffracted around the two ends of the ship. For non-zero $P(x)$ there is a similar but much reduced effect, since part of the wave energy is transmitted directly beneath the ship, and a less strong diffraction pattern produced.

The force decreases markedly as the clearance is increased and the ship presents less of a barrier to passage of wave energy. If in fact the clearance is large, $P \rightarrow \infty$ or $C \rightarrow 0$, it follows from (5.7) that $\phi(x, 0_+, -h) \rightarrow -A\sqrt{g/h} C(x)$ and hence that

$$F_2 \rightarrow 2ipghkA \int_{-l}^l C(x) dx. \quad (7.2)$$

The physical interpretation of this limit is that the effect of the free surface on the disturbance flow field about the ship diminishes as the clearance increases, until the flow is effectively the same as the low frequency limit in which the force is in phase with the fluid particle accelerations. This is in line with an interpretation (Newman [1969]) of $C(x)$ as related to the added mass of the section at x , with the free surface replaced by a rigid wall. The resulting force F_2 is of course numerically small, if $C(x)$ is itself small.

On the other hand, the only cases shown in Fig. 4 correspond to clearances small enough to give significant blockage $C(x)$, and hence a net force comparable with the standing-wave value $4pghlA$. It would appear that this limiting value is a useful, usually conservative, estimate for clearances of this order, but that it should be used with caution for low frequencies (very long swell) or for non-small clearances. In the latter case, e.g. with draft/water depth < 0.5 , the standing wave limit may be a substantial over-estimate of the total force.

The computations presented here are samples only. They may be considered extensions of similar computations given by Tuck [1970] for a mathematically idealized ship with a blockage coefficient

$$C(x) = c_0 \sqrt{l^2 - x^2}. \quad (7.3)$$

In fact the results for the Series 60 ship are not greatly different from those given by Tuck [1970], a reflection of the fact that (7.3) is not an unreasonable approximation to the shape of the curves in Fig. 3. Further computations, including other ship geometries and clearances, and treating the case of incident seas from directions other than abeam, are given by Taylor [1971].

REFERENCES

- Constantine, T., "On the movement of ships in restricted waterways," *J. Fluid Mech.*, vol. 9, pp. 247-256, 1961.
- Flagg, C. and Newman, J. N., Unpublished manuscript, 1971.
- Frank, W., "Oscillation of cylinders in or below the free surface of deep fluids," N.S.R.D.C. Report No. 2375, Washington, D.C., 1967.
- Freakes, W. and Keay, K. L., "Effects of shallow water on ship motion parameters in pitch and heave," MIT, Dept. of Nav. Arch. and Mar. Eng., Report No. 66-7, Cambridge, Mass., 1966.
- Garthune, Rosenberg, B., Cafiero, D. and Olson, C. R., "The performance of model ships in restricted channels in relation to the design of a ship canal," N.S.R.D.C. Report No. 601, Washington, D. C., 1948.
- Graff, W., Kracht, A., and Weinblum, G., "Some extensions of D. W. Taylor's standard series," *Trans. S.N.A.M.E.*, vol. 72, p. 374, 1964.
- Havelock, T. H., "Note on the sinkage of a ship at low speeds," *Z. angew. Math. Mech.*, vol. 19, pp. 202-205, 1939.
- Hess, J. L. and Smith, A. M.O., "Calculation of non-lifting potential flow about arbitrary three-dimensional bodies," *J. Ship. Res.*, vol. 8, pp. 22-44, 1964.
- Hönl, H., Maue, A. W. and Westphal, K., "Theorie der Beugung," *Handbuch der Physik*, vol. 25, pp. 218-573, S. Flugge (ed.), Springer, Berlin, 1961.
- Horn, F., *Jahrbuch der Schiffsbau techn. Gesellsch.*, vol. 38, p. 177, 1937.
- Kim, C. H., "The influence of water depth on the heaving and pitching motions of a ship moving in longitudinal regular head waves," *Schiffstechnik*, vol. 15, pp. 127-132, 1968.
- Kreitner, J., "Über den Schiffswiderstand auf beschränktem Wasser," *Werft Reederei Hafen*, vol. 15, 1934.
- Lamb, H., "Hydrodynamics," (6th ed.) C.U.P. and Dover, 1932.
- Lemmerman, In "Resistance and propulsion of ships," Van Lammeren, W. (ed.), H. Stam, Holland, 1942.

- Michell, J. H., "The wave resistance of a ship," *Phil. Mag.* (5), vol. 36, pp. 430-437, 1898.
- Moody, C. G., "The handling of ships through a widened and asymmetrically deepened section of Gaillard cut in the Panama canal," N.S.R.D.C. Report 1705, Washington, D. C., 1964.
- Morse, P. M., "Vibration and sound," (2nd ed.) McGraw-Hill, New York, 1948.
- Morse, P. M. and Rubenstein, P. J., "The diffraction of waves by ribbons and slits," *Phys. Rev.*, vol. 54, pp. 895-898, 1938.
- Newman, J. N., "Lateral motion of a slender body between two parallel walls," *J. Fluid Mech.*, vol. 39, pp. 97-115, 1969.
- Ogilvie, T. F., "Propagation of waves over an obstacle in water of finite depth," Ph.D. thesis, University of California, Berkeley, 1960.
- Sedov, L. I., "Two-dimensional problems in hydrodynamics and aerodynamics," (translation), Interscience, New York, 1965.
- Sharpe, B. B. and Fenton, J. D., "Report of investigation of a proposed dock at Yarraville," University of Melbourne, Dept. of Civil Eng., 1968.
- Sjostrom, C. H., "Effect of shallow water on speed and trim," Paper read to N.Y. section, S.N.A.M.E., 1965.
- Taylor, P. J., Unpublished thesis, University of Adelaide, 1971.
- Todd, F. H., "Series 60, methodical experiments with models of single-screw merchant ships," N.S.R.D.C. Report No. 1712, Washington, D. C., 1963.
- Tothill, J. T., "Ships in restricted channels," *Marine Technology*, vol. 4, pp. 111-128, 1967.
- Tuck, E. O., "A systematic asymptotic expansion procedure for slender ships," *J. Ship. Res.*, vol. 8, pp. 15-23, 1964.
- Tuck, E. O., "Shallow-water flows past slender bodies," *J. Fluid Mech.*, vol. 26, pp. 81-95, 1966.
- Tuck, E. O., "Sinkage and trim in shallow water of finite width," *Schiffstechnik*, vol. 14, pp. 92-94, 1967.

- Tuck, E. O., "Ship motions in shallow water," *J. Ship. Res.*, vol. 14, no. 4, 1970.
- Tuck, E. O. and von Kerczek, C., "Streamlines and pressure distribution on arbitrary ship hulls at zero Froude number," *J. Ship Res.*, vol. 12, pp. 231-236, 1968.
- Van Dyke, M., "Perturbation methods in fluid mechanics," Academic Press, New York, 1964.
- Wehausen, J. V. and Laitone, E. V., "Surface waves," *Handbuch der Physik*, vol. 9, S. Flugge (ed.), Springer, Berlin, 1960.
- Wilson, B. W., "The energy problem in the mooring of ships exposed to waves," *Bull. No. 50, Perm. Int. Assoc. of Nav. Cong.*, Brussels, 1959.

* * * * *

DISCUSSION

Prof. Hajime Maruo
Yokohama National University
Yokohama, Japan

In the present analysis, the problem of the shallow water effect is discussed on the basis of a self-consistent linearized theory. According to the investigations into the same problem both theoretical and experimental, which were carried out at the University of Tokyo several years ago, nonlinear phenomena appeared remarkably in the trans-critical speed range. This problem can be analyzed by a similar way to the nonlinear theory of the transonic flow of a compressible fluid. At that time, however, the theory of the transonic gas flow had not been well developed, and the former investigations were obliged to confine themselves in the analysis by the analogy with the simple one-dimensional duct flow. Nowadays the theory of the transonic flow around a body has been developed to a great extent. The mathematical technique used in it may be available to the problem of the nonlinear shallow water effect.

* * * * *

REPLY TO DISCUSSION

E. O. Tuck and P. J. Taylor
University of Adelaide
Adelaide, South Australia

We certainly agree with the comments of Professor Maruo regarding the importance of nonlinear phenomena in the trans-critical speed range. Indeed, the transonic analogy was discussed in the paper by Tuck [1966] and further work on this aspect of the problem was suggested.

* * * * *

HYDRODYNAMICS IN THE OCEAN ENVIRONMENT

Friday, August 28, 1970

Morning Session

Chairman: Adm. R. Brard
Marine National Bassin D'Essais
Des Carenes, Paris, France

	Page
Singular Perturbation Problems in Ship Hydrodynamics T. F. Ogilvie, University of Michigan	663
Theory and Observations on the Use of a Mathematical Model for Ship Maneuvering in Deep and Confined Waters N. H. Norrbin, Statens Skeppsprovsningsanstalt, Sweden	807
The Second-Order Theory for Nonsinusoidal Oscillations of a Cylinder in a Free Surface C. M. Lee, Naval Ship Research and Development Center	905

SINGULAR PERTURBATION PROBLEMS IN SHIP HYDRODYNAMICS

T. Francis Ogilvie
University of Michigan
Ann Arbor, Michigan

NOTATION

a_{ij}	added-mass coefficient
b_{ij}	damping coefficient
$b(x, z)$	hull offset
c_{ij}	restoring-force coefficient
$C(x)$	contour of body in the cross section at x
$F_j^m(t)$	force in j -th mode due to body motion
$F_j^w(t)$	force in j -th mode due to incident waves
g	gravity constant
$g(x, z; \epsilon)$	Y offset of camber surface
$G(x, z)$	$g(x, z; \epsilon)/\epsilon$
$h(x, z; \epsilon)$	half-thickness of body (equal to $b(x, z)$ for a symmetrical body)
$H(x, z)$	$h(x, z; \epsilon)/\epsilon$
$H(x)$	part of free-surface deflection in problems in two dimensions (see Eq. (5-15))
H	projection of a body onto the $y = 0$ plane (the center-plane of a ship)
i	$\sqrt{-1}$
i, j, k	unit vectors parallel to three Cartesian axes
k, ℓ, m	Fourier-transform variables corresponding to x, y, z respectively
$K_n(z)$	modified Bessel function of second kind
L	length of a ship, or the segment of the x axis between bow and stern cross sections

m_j	($j = 1, \dots, 6$) a set of functions defined over the surface of a slender body (see (2-75))
$m(x)$	added mass per unit length of a slender body
n_j	($j = 1, \dots, 6$) a set of functions defined over the surface of a slender body, equal to the components of the unit normal vector for $j = 1, 2, 3$ (see (2-72))
$n(x)$	damping coefficient per unit length of a slender ship
\mathbf{n}	unit vector normal to body surface (usually taken positive into the body)
\mathbf{N}	unit vector in a plane $x = \text{constant}$, normal to body contour in that cross section
p	pressure
r	radius coordinate in cylindrical coordinate system
$r_0(x, \theta)$	radius coordinate of a slender body
\mathbf{r}	$x\mathbf{i} + y\mathbf{j} + z\mathbf{k}$
s	half-span of a horseshoe vortex or a lifting line
$s(x)$	local half-span in wing cross section at x , or cross section area of a slender body (taken as the cross section area of the <u>submerged</u> part, for a ship)
S	half-span of a wing of large aspect ratio
$T(x)$	keel depth of a ship at cross section at x
T_{ij}	transfer functions between motion variables and forces on body
U	speed of a body, or speed of an incident stream (the latter invariably being taken in the positive x direction)
$\mathbf{v}(x, y, z)$	fluid velocity at (x, y, z) with uniform stream at infinity, $U = 1$, flowing around a body
$x \ y \ z$	Cartesian coordinates
$X \ Y \ Z$	stretched Cartesian coordinates, e.g., $x = X, y = \epsilon Y, z = \epsilon Z$ for a slender-body problem, xyz being far-field coordinates, XYZ near-field
$Z_n(x, y; \epsilon)$	terms in a near-field expansion of $\zeta(x, y; \epsilon)$ (cf. $\zeta_n(x, y; \epsilon)$)
$\alpha_n(x, z; \epsilon)$	$\phi_n(x, 0, z; \epsilon)$ in thin-body problem
$\gamma_n(x, z; \epsilon)$	normal velocity component in the plane of a sheet of dipoles
δ	motion-amplitude parameter in ship-motion problems
ϵ	small parameter in most problems considered
$\zeta(x, y, t)$	displacement of the free surface

$\zeta_n(x,y;\epsilon)$	terms in a far-field expansion of $\zeta(x,y;\epsilon)$ (cf. $Z_n(x,y;\epsilon)$)
$\zeta(z)$	function mapping the complex variable z onto an auxilliary (ζ) plane (in Section 5)
$\eta(x,y)$	steady part of free-surface deflection in ship-motion problem
$\eta(x)$	free-surface deflection in problems in two dimensions
$\eta_0(x)$	part of free-surface deflection in low-speed problem in two dimensions (see (5-7))
θ	angle variable in cylindrical coordinate system
$\theta(x,y,t)$	time-dependent part of free-surface deflection in ship-motion problem
κ	g/U^2 , a wave number in steady-motion problems
$\lambda_n(z)$	density of dipoles on a line (see (2-40))
$\mu_n(z)$	density of dipoles on a line (see (2-40))
$\mu_n(x,z;\epsilon)$	density of dipoles on a surface
ν	ω^2/g , a wave number in oscillation problems
$\xi_j(t)$	displacement in the j -th mode of motion (see Section 2.32)
ρ	water density
$\sigma_n(x;\epsilon)$	density of sources on a line
$\sigma_n(x,z;\epsilon)$	density of sources on a surface
$\phi(x,y,z,t)$	velocity potential (the arguments may vary, but ϕ generally denotes the complete potential function in a problem)
$\phi_0(x,y)$	in Section 5.4, potential for the problem in which the free surface is replaced by a rigid wall
$\phi_n(x,y,z;\epsilon)$	terms in a far-field expansion of $\phi(x,y,z;\epsilon)$
$\phi_j(x,y,z)$	normalized potential functions (see (2-73), (3-28))
$\Phi_n(x,y,z;\epsilon)$	terms in a near-field expansion of $\phi(x,y,z;\epsilon)$
$\Phi_j(x,y,z)$	normalized potential functions (see (3-44))
$\chi(x,y,z)$	velocity potential for the perturbation of a unit-strength incident stream by a slender ship
$\psi_j(x,y,z)$	normalized potential functions (see (2-76))
$\psi(x,y,z,t)$	time-dependent part of velocity potential in ship-motion problem (with forward speed)
$\Psi_j(x,y,z)$	normalized potential functions (see (3-45))
ω	radian frequency of sinusoidal oscillations
$\Omega_j(x,y,z)$	normalized potential functions (see (3-46))

MISCELLANEOUS CONVENTIONS

- 1) Velocity Potential: The velocity is always the positive gradient of the potential function.
- 2) Coordinates and Orientation: In problems involving a steady incident flow, that flow is always in the positive x direction. The vertical axis is the y axis in 2-D problems, the z axis in 3-D problems.
- 3) Time Dependence: In problems of sinusoidal oscillation, the time dependence is always in the form of the exponential function, $e^{i\omega t}$. In such problems, the real part only is intended to be used, but we do not indicate this explicitly in general.
- 4) Fourier Transforms: These are denoted by an asterisk. For example,

$$\sigma^*(k) = \int_{-\infty}^{\infty} dx e^{-ikx} \sigma(x); \quad \sigma(x) = \frac{1}{2\pi} \int_{-\infty}^{\infty} dk e^{ikx} \sigma^*(k);$$

$$\phi^{**}(k, l; z) = \int_{-\infty}^{\infty} \int_{-\infty}^{\infty} dx dy e^{-i(kx + ly)} \phi(x, y, z).$$

- 5) Principal-Value Integrals: These are denoted by a bar through the integral sign:

$$\bar{\int}_{-\infty}^{\infty} \frac{d\xi f(\xi)}{\xi - x}.$$

- 6) Order Notation: There are three symbols used: O , o , \sim .

- a) " $y = O(x)$ " means: $|y/x| < M$ as $x \rightarrow 0$, where M is a constant not depending on x .
- b) " $y = o(x)$ " means: $|y/x| \rightarrow 0$ as $x \rightarrow 0$.
- c) " $y \sim f(x)$ " means $|y - f(x)| = o(f(x))$ as $x \rightarrow 0$.

I. INTRODUCTION

This paper is a survey of a group of ship hydrodynamics problems that have certain solution methods in common.

The problems are all formulated as perturbation problems, that is, the phenomena under study involve small disturbances from a basic state that can be described adequately without any special difficulties. The methods of solution make explicit use of the fact that the disturbances of the basic state are small. Mathematically, this is formalized by the introduction of one or more small parameters which serve as measures of the smallness of various quantities. The solutions obtained will generally be more nearly valid for small values of the parameter(s).

However, the problems will also be characterized by the fact that they are ill-posed in the limit as the small parameter(s) approaches zero. Thus, we call them singular perturbation problems. Special techniques are needed for treating such problems, and we have two which are especially valuable:

- 1) The Method of Matched Asymptotic Expansions, and
- 2) The Method of Multiple-Scale Expansions.

The first has a well-developed literature, and it has been made particularly accessible to engineers by Van Dyke [1964]. The second, which has a longer history, is perhaps less well-known, but we now have a textbook treatment of it too, thanks to Cole [1968]. Because of the availability of such books, my treatment of the methods in general will be extremely terse.

The necessity for treating ship hydrodynamics problems as perturbation problems arises most often in the incredible difficulty of handling the boundary condition which must be satisfied at the free surface. Even after neglecting viscosity, surface tension, compressibility, the motion of the air above, and a host of lesser matters, one can still make little progress toward solving free-surface problems unless one assumes that disturbances are small -- in some sense. Historically, it has commonly been assumed that the boundary conditions may be linearized; in fact, this has so commonly been assumed that many writers hardly mention the fact, let alone try to justify it.

The two methods emphasized in this paper can also be applied to problems involving an infinite fluid. In fact, neither method was applied specifically to free-surface problems until quite recent times. Section 2 of this paper is devoted to several infinite-fluid problems. My justification, quite frankly, is almost entirely on didactic grounds. The methods can be made much clearer in these simpler problems, and so I include them here, although in some

cases the infinite-fluid problems can be treated adequately by more elementary methods.

Most of the material in this paper has appeared in print elsewhere. My intention has been to present a coherent account of the treatment of singular perturbation problems in ship hydrodynamics, and so I have reworked solutions by other people and put them into a common notation and a common format. In some cases, I have made conscious decisions to follow certain routes and to ignore others. I am sure that I have made many such decisions unconsciously too. I have tried to give credit where it is due, but I am also sure that I have committed some sins of omission in the references. I apologize to those whom I may have slighted in this way.

1.1. Nature of the Problems and Their Solutions

We never really derive the perturbation solution of the exact* problem; we derive, at best, an exact solution of a perturbation problem. That is, we formulate an exact boundary-value problem, simplify the problem, solve the simplified version, and then hope that that solution is an approximation to the solution of the exact problem.

Thus, there will almost always be open questions about the validity of our solutions, and these questions can only be resolved through comparisons with exact solutions and experiments. We can have little hope of being rigorous. In fact, it is difficult to provide completely convincing arguments for doing some of the things that we do; in many cases, our approach is justified by the fact that it works! Much progress has been made in this field by people who try approaches "to see what will happen."

This does not imply that we shoot in the dark. It does suggest that we often depend more on intuition (or experience, which is the same thing) than on mathematical logic in deciding how to solve problems. The small disturbance assumptions by which free-surface problems have traditionally been linearized must have been tried first on this basis. The predictions which result from making such assumptions agree fairly well with observations of nature, and so we are encouraged to go on making the same assumptions in new problems. We may expect to be successful sometimes.

There are also open questions about the uniqueness of solutions. Engineers do not often worry about such matters, but they should certainly be aware of certain situations in which the dangers of

*"Exact" means only that nonlinear boundary conditions are treated exactly. I neglect viscosity, surface tension, compressibility, etc., and still call the problem "exact."

non-uniqueness are especially great. The history of the study of free-surface problems provides numerous examples of invalid solutions being published by authors who were not sufficiently careful on this score. We have learned to be careful about imposing a radiation condition when necessary, although newcomers to the field are still occasionally trapped.* Questions about stability of our solutions are not so well appreciated, but of course solution stability is just one aspect of solution uniqueness. A particularly startling example has been pointed out in recent years by Benjamin and Feir [1967]: Ordinary sinusoidal waves in deep water are unstable. This has now been demonstrated both theoretically and experimentally. It comes as no great surprise to those experimenters who had tried to generate high-purity sinusoidal waves for ship-motions experiments, but it was certainly quite a surprise to the theorists, who apparently did not suspect any such phenomenon before its discovery by Benjamin and Feir.

Since we shall be considering small-perturbation problems, we may expect the solutions to appear in the form of series expressions (not necessarily power series!). Often, we are content to obtain one term in such a series. Practically never do we face the question of whether the series converges. In fact, we usually just hope that the series has some validity, at least in an asymptotic sense.

The question will arise from time to time, "How small must the small parameter be in order that a one- (or two- or three- or n-) term expansion give valid predictions?" In ship-hydrodynamics problems, it is quite safe to assert that the only answer to such a question must be based on experimental evidence. In fact, even in simple problems, the knowledge of a few terms is not likely to help much with this question. For example, suppose that one tries to solve the simple differential equation: $y''(x) + y(x) = 0$, by means of a series of odd powers of x . How does one know that a two-term approximation is accurate to within one per cent even if x is as large as unity? One might compute the third term, of course, and compare it with the second term, hoping to guess what the effect of further terms would be. If it were too difficult to compute that third term, one could only hope that the solution had some validity, and perhaps one would try to find some experimental evidence on which to hazard a guess about validity. So it is in our ship-hydro-

* Within the last few years, a leading German journal published an article on wave resistance in water of finite depth, in which it was concluded that a body had identically zero resistance if it were symmetrical fore and aft. The author was, I believe, primarily a numerical analyst, not familiar with the pitfalls of free-surface problems. He did not impose a numerical condition equivalent to a radiation condition. (This is one reference that I intentionally omit.)

dynamics problems. It will be necessary to discuss this point further at an appropriate place.

A related question concerns the precise definition of the small parameters that we use to formulate the approximate problems. In this paper I avoid defining the small parameter quantitatively. It is usually unnecessary and it is dangerous. I shall return to this point also.

1.2. Matched Asymptotic Expansions

For most of our problems, the approach advocated by Van Dyke [1964] is entirely adequate. I shall assume that the reader is familiar with (or has access to) Van Dyke's book. Only a few definitions and concepts will be mentioned here.

Perhaps the simplest problem that demonstrates the applicability of the method of matched asymptotic expansions is the following: Find the solution of the differential equation,

$$\epsilon \ddot{y} + 2\dot{y} + y = 0,$$

subject to the initial conditions:

$$y(0) = 1; \quad \dot{y}(0) = 0.$$

The parameter ϵ is to be considered small, and, in fact, we want to know how the solution of this problem behaves as $\epsilon \rightarrow 0$. Now, if we set $\epsilon = 0$, the order of the differential equation is reduced, and two initial conditions cannot be satisfied. Therefore, one cannot obtain a series expansion for the solution by a simple iteration scheme which starts with the solution for the limit case, $\epsilon = 0$.

The exact solution for this problem is:

$$y(t) = \frac{-p_2 e^{p_1 t} + p_1 e^{p_2 t}}{p_1 - p_2},$$

where

$$p_1 = \frac{-1 - \sqrt{1 - \epsilon}}{\epsilon} \approx -2/\epsilon;$$

$$p_2 = \frac{-1 + \sqrt{1 - \epsilon}}{\epsilon} \approx -1/2.$$

If we consider that $t = O(1)$ as $\epsilon \rightarrow 0$, then the following approximation is valid for $y(t)$:

$$y(t) \sim e^{-t/2} \left\{ 1 + \frac{\epsilon}{8} (2 - t) + \frac{\epsilon^2}{32} (6 - 3t + 2t^2) + \dots \right\}.$$

This approximation could be obtained step-by-step, iteratively:

$$2\dot{y}_n + y_n = -\epsilon \ddot{y}_{n-1},$$

where $y(t) \sim \sum y_n(t)$. However, it is not uniformly valid at $t = 0$, and the constants cannot be determined. On the other hand, we could consider that $t = O(\epsilon)$ as $\epsilon \rightarrow 0$ and rearrange the exact solution accordingly. This is most easily done if we set $t = \epsilon\tau$ and rewrite everything in terms of τ . The approximation for $y(t)$ is then:

$$y(t) \sim 1 + \epsilon \left(\frac{1}{4} - \frac{\tau}{2} \right) + \epsilon^2 \left(\frac{3}{16} - \frac{\tau}{4} + \frac{\tau^2}{8} \right) + \dots$$

$$- e^{-2\tau} \left\{ \frac{\epsilon}{4} + \epsilon^2 \left(\frac{3}{16} + \frac{\tau}{8} \right) + \dots \right\}.$$

This approximation could be obtained completely from the differential equation by an iteration scheme in which we let $y(t) \sim \sum Y_n(\tau; \epsilon)$, the individual terms satisfying the equation:

$$Y_n''(\tau) + 2Y_n'(\tau) = -\epsilon Y_{n-1}(\tau) \quad [Y_n' \equiv dY/d\tau]$$

and the conditions:

$$Y_1(0) = 1; \quad Y_n(0) = 0, \quad n > 1; \quad Y_n'(0) = 0, \quad n \geq 1$$

However, this solution is not uniformly valid for $\tau \rightarrow \infty$; in fact, one would hardly suspect that it represents a solution decaying exponentially with time.

The difficulty arises because the problem is characterized by two time scales, $1/p_1$ and $1/p_2$, and the two are grossly different. One of the two exponentials in the exact solution decays very rapidly and the other decays at a moderate rate. The contrast in these two time scales, along with the fact that each has its dominant effect in a distinct range of time, allows us to apply the method of matched asymptotic expansions to this problem. The Van Dyke prescription for doing this is as follows:

Define the n term outer expansion of $y(t)$ as $[y_1(t) + \dots + y_n(t)]$; define the m term inner expansion of $y(t)$ as $[Y_1(\tau) + \dots + Y_m(\tau)]$. In the n term outer expansion, substitute $t = \epsilon\tau$ and rearrange the result into a series ordered according to ϵ ; truncate this expression after m terms, which gives the m term inner expansion of the n term outer expansion. Similarly, in the m term inner expansion, substitute $\tau = t/\epsilon$ and rearrange the result into a series ordered according to ϵ ; truncate this expression after n terms, which gives the n term outer expansion of the m term inner expansion. The matching rule states that:

The m term inner expansion of the n term outer expansion = the n term outer expansion of the m term inner expansion.

In the example discussed in the previous paragraphs, the outer solution could not be obtained by a simple iteration scheme. The matching principle can now be used to determine the constants in the outer solution, and so an iteration scheme is now available, requiring, however, that inner and outer expansions be obtained simultaneously. In the example, the inner solution could be obtained completely and independently of the outer, but this is an accident which occurred because of the simple nature of the problem above. Ordinarily, in cases in which one might consider using the method of matched asymptotic expansions, one must proceed step-by-step to find first a term in one expansion, then a term in the other expansion, and so on.

It is worthwhile to be fairly precise about certain definitions. We use the equivalence sign, " \sim ", frequently. For example, we write:

$$\phi(x, y, z; \epsilon) \sim \sum_{n=0}^N \phi_n(x, y, z; \epsilon)$$

This means that:

$$\left| \phi - \sum_{n=0}^N \phi_n \right| = o(\phi_N) \quad \text{as} \quad \epsilon \rightarrow 0 \quad \text{for fixed values of } (x, y, z).$$

Also, it implies that $\phi_{n+1} = o(\phi_n)$ as $\epsilon \rightarrow 0$. The qualification that (x, y, z) should be fixed is very important. In the example above, we would have the equivalent statement for the outer expansion:

$$\left| y(t; \epsilon) - \sum_{n=1}^N y_n(t; \epsilon) \right| = o(y_N) \quad \text{as} \quad \epsilon \rightarrow 0 \quad \text{for fixed } t,$$

and, for the inner expansion:

$$|y(t;\epsilon) - \sum_{n=1}^N Y_n(\tau;\epsilon)| = o(Y_N) \quad \text{as} \quad \epsilon \rightarrow 0 \quad \text{for fixed } \tau.$$

In the latter, we evaluate the difference on the left-hand side for smaller and smaller values of t ($= \epsilon\tau$) as $\epsilon \rightarrow 0$; in other words we restrict the range of t more and more as $\epsilon \rightarrow 0$. This is in contrast to the interpretation of the outer expansion, in which we simply fix t at any value while we let $\epsilon \rightarrow 0$. In even more physical terms, we may say that the inner expansion describes the solution during the time when the $e^{p_1 t}$ term is varying rapidly, and the outer expansion describes the solution when the $e^{p_1 t}$ term has effectively reached zero and the $e^{p_2 t}$ term is varying significantly. This separation into two distinct regimes is characteristic of problems in which we apply the method of matched asymptotic expansions. Of course, the real key to the success of the method is in the procedure by which the two aspects of the solution are matched to each other. After all, they do represent just two aspects of the same solution.

Usually, we insist that our asymptotic expansions be consistent. A precise definition of this term is awkward, but perhaps it is clear if we state that each term in such a series depends on ϵ in a simple way that cannot be broken down into simpler terms of different orders of magnitude. For example, the following two series are equal:

$$\begin{aligned} [1 + \epsilon + \epsilon^2 + \epsilon^3 + \dots] &= [1 + \frac{1}{2}\epsilon + \frac{1}{4}\epsilon^2 + \frac{1}{8}\epsilon^3 + \dots] \\ &+ [\frac{1}{2}\epsilon + \frac{1}{4}\epsilon^2 + \frac{1}{8}\epsilon^3 + \dots] \\ &+ [\frac{1}{2}\epsilon^2 + \frac{1}{4}\epsilon^3 + \dots] \\ &+ [\frac{1}{2}\epsilon^3 + \dots] + \dots \end{aligned}$$

On the right-hand side, let:

$$f_0(\epsilon) = 1 + \frac{1}{2}\epsilon + \frac{1}{4}\epsilon^2 + \frac{1}{8}\epsilon^3 + \dots;$$

$$f_n(\epsilon) = \frac{\epsilon^n}{2} f_0(\epsilon), \quad \text{for } n > 0.$$

Then we can write:

$$\sum_{n=0}^N \epsilon^n \sim \sum_{n=0}^N f_n(\epsilon) \quad \text{as} \quad \epsilon \rightarrow 0.$$

These happen to be convergent series (if $\epsilon < 1$), but we can interpret them as asymptotic series just as well. The series on the left is "consistent"; the one on the right is not, because individual terms have their own ϵ substructure.

The striving for consistency can become a religion, but it is not a reliable faith. Consistency (or the lack of it) tells us nothing about the relative accuracy of otherwise equivalent asymptotic expansions. In fact, we could define a third asymptotic series with terms given by:

$$g_0(\epsilon) = 1/(1-\epsilon); \quad g_n(\epsilon) = 0 \quad \text{for} \quad n > 0.$$

This series is grossly inconsistent, but one term gives the exact answer for the sum of the previous series! Occasionally one can make educated guesses about such things, replacing a few consistently arranged terms by a simple, inconsistent expression having much greater accuracy in practical computations. Mathematically, these different asymptotic series are equivalent, and, if ϵ is small enough, they will all give the same numerical results. But we want in practice to be able to use values of ϵ that are sometimes not "small enough."

We shall work with consistent series, for the most part, in spite of such possibilities of improvement through the use of inconsistent series. Most newcomers to this field of analysis find that there is a considerable element of art in the application of the method of matched asymptotic expansions, and I personally consider that the improvement of the expansions through the development of inconsistent expansions is the highest form of this art. Except in one respect, I do not intend to pursue the possibilities of inconsistent expansions in this paper.

The exception that I make is the following: Many singular perturbation problems lead to asymptotic-expansion solutions of the form:

$$\sum_{n=0}^N \sum_{m=0}^n a_{nm} \epsilon^n (\log \epsilon)^m,$$

where a_{nm} does not depend on ϵ . We can, of course, write this out in a long string of terms quite consistently arranged. However, my practice will be to treat the sum:

$$h_n(\epsilon) \equiv \epsilon^n \sum_{m=0}^n a_{nm} (\log \epsilon)^m$$

as a single term (albeit inconsistent) in the series $\sum h_n(\epsilon)$. An alternative way of describing this practice is to say that I consider $\log \epsilon = O(1)$ as $\epsilon \rightarrow 0$! I have encountered some practical problems which could apparently not be solved by the Van Dyke matching principle unless treated in this way, and I have never seen or heard of a problem in which this practice led to difficulties. There are some good arguments for proceeding in this way, but I know of no proof that either way is the correct way. (Some of my colleagues will call this a cheap trick, rather than a higher expression of an art form.)

The classical example in physics of this kind of mathematical problem is the boundary layer first described by Prandtl in 1904. The thickness of the boundary layer becomes smaller and smaller as the small parameter, $1/\sqrt{R}$ approaches zero (R is the Reynolds number), but the presence of the boundary layer cannot be neglected, because then the governing differential equation becomes lower order, and the body boundary conditions cannot all be satisfied. Unfortunately, Prandtl did not realize the generality of the analysis which he introduced into the viscous-fluid problem, and, lacking the modern formalism for treating such problems, he could not obtain higher-order approximations.

Perhaps I should include a discussion of Prandtl's problem in this paper, since it might be considered as a "singular perturbation problem in ship hydrodynamics." However, I shall not do this, for several reasons. Van Dyke's coverage of the problem is excellent, I think. Also, the analysis concerns only laminar boundary layers, and they are really of quite limited interest in ship hydrodynamics. Finally, the formal procedure breaks down completely at the leading edge of a body, and the singularities that occur there cause major difficulties in all attempts to use the formalism to obtain higher-order approximations.

One final point should be emphasized, even at the risk of insulting the intelligence of readers who have read this far. Whenever we write, " $\epsilon \rightarrow 0$," we are implying the existence of a sequence of physical problems in which the geometry of some fundamental parameter varies. For example, in Prandtl's boundary-layer problem, we may consider that viscosity changes as $\epsilon = 1/\sqrt{R} \rightarrow 0$. In the simple ordinary-differential-equation example presented above, we may think of a spring-mass system in which the mass is changed systematically from one experiment to the next. Later, when we treat slender-body theory, we consider a sequence of problems in which the body changes each time. The theory always implies the possible existence of such a series of problems, and the quality of the predictions improves as the problem more nearly fits

the limit case. Thus, we shall be able to apply the results of slender-body theory to bodies which are not especially slender. In such cases, we may expect that the predictions will be less accurate than the predictions that we would make for a much more slender body. But we never know a priori how slender the body must be for a certain accuracy to be realized, and it would be wrong to assert that the theory applies only to needle-like bodies. All that we can say is that it would be more accurate for such bodies than for not-so-slender bodies.

1.3. Multiple-Scale Expansions

In the problems of the previous section, we had two greatly contrasting scales for the independent variable. The fact that enabled us to obtain two separate expansions was that each of the scales dominated the behavior of the solution in a particular region of space or a particular period of time. The major practical concern was to ensure that the separate expansions matched, because they really represented just different aspects of the same solution.

The present section is devoted to problems in which there are again two greatly contrasting scales. However, in these problems, it will not be possible to isolate the effects of each scale into a more or less distinct region of space or time. The effects of the two scales mingle together completely. However, we may still expect to be able to identify these effects somehow, just because the two scales are so different.

There are classical problems of this kind, the most famous being related to nonlinear effects on certain periodic phenomena. Cole [1968] discusses a number of these problems. Perhaps the simplest example of all is a linear one: Find approximate solutions for small ϵ in the problem of a linear oscillator with very small damping, where the differential equation might be written:

$$\ddot{y} + 2\epsilon\dot{y} + y = 0.$$

To be specific, let the solution satisfy the initial conditions: $y(0) = 1$ and $\dot{y}(0) = 0$. Physically, we expect that the system will oscillate with gradually decreasing amplitude. It would be desirable if the approximate solution at least did not contradict this expectation.

We might try representing $y(t;\epsilon)$ by an asymptotic expansion with respect to ϵ : $y(t;\epsilon) \sim \sum y_n(t;\epsilon)$. We would find immediately that the first term in this expansion is just: $y_0(t;\epsilon) = \cos t$. This seems quite reasonable, since it represents a steady oscillation at the frequency approximate to the undamped oscillator. The second term in the expansions would be obtained from:

$$\ddot{y}_1 + y_1 = -2\epsilon \dot{y}_0 = 2\epsilon \sin t, \quad \text{with} \quad y_1(0) = \dot{y}_1(0) = 0.$$

It is impossible to obtain a steady-state particular solution of this problem. In fact, the solution is:

$$y_1(t; \epsilon) = \epsilon [\sin t - t \cos t].$$

Thus, we obtain an expansion in which the second term grows linearly with time. One might expect that succeeding terms will grow even faster. This expansion is correct, and, for small values t , it could be used for numerical predictions. But we would certainly prefer to obtain an expansion which is uniformly* valid, even for very large t .

The exact solution is easily found, of course. It is:

$$y(t; \epsilon) = e^{-\epsilon t} \left[\cos \sqrt{1-\epsilon^2} t + \frac{\epsilon}{\sqrt{1-\epsilon^2}} \sin \sqrt{1-\epsilon^2} t \right].$$

The approximate solution becomes worse and worse with increasing t because the frequency is wrong and because the exponential factor is expanded in a power series in t . If we watch the oscillating mass on a time scale appropriate to the period of the oscillation, we do not see the exponential decay and the slight shift of frequency caused by the damping. On the other hand, if we watch for a very long time, the effects of damping accumulate gradually. Thus, the effects of the "slow-time" scale, $1/\epsilon$, persist throughout the history of the motion as observed on a real-time scale, but these effects never occur suddenly. It is this fact which enables us to separate them out of the real-time problem.

There seems to be less reliable formalism available for handling such problems than in the case of the method of matched asymptotic expansions. More is left to the insight and ingenuity of the individual problem solver. In the example discussed above, the procedure is fairly clear: Expand $y(t; \epsilon)$ in a series such as this:

$$y(t; \epsilon) \sim y_0(\hat{t}, \tau; \epsilon) + y_1(\hat{t}, \tau; \epsilon) + \dots,$$

where we define:

$$\hat{t} = \epsilon t; \quad t = \tau + f_1(\tau; \epsilon) + f_2(\tau; \epsilon) + \dots,$$

*Strictly speaking, the series really is uniformly valid except at $t = \infty$.

and the functions f_n are to be determined in such a way that the approximation is uniformly valid for all t . In treating this particular problem, Cole immediately assumes that $t \propto \tau$ and further that $t/\tau = 1 + O(\epsilon^2)$. These extra assumptions speed the solution considerably, but it is not clear how one would know to make them if the exact solution were not available. The exact solution takes the form:

$$y(t; \epsilon) = e^{-\hat{t}} [\cos \tau + (\hat{t}/\tau) \sin \tau],$$

in terms of the new variables. (The factor (\hat{t}/τ) does not depend on t .) Here it is clear how the two time scales enter into the solution as well as the problem. One may expect the relationship between t and τ to be equivalent to the expansion of the quantity $\sqrt{(1-\epsilon^2)}$. The reader is referred to Cole's book for further discussion of the solution of such problems.

One problem that will be discussed later is a close relative of the classical problems mentioned above. The solution by Salvesen [1969] of the higher-order problem of the wave resistance of a submerged body leads to a situation in which the first approximation is periodic downstream and that period is modified in the third-order approximation. (Otherwise the waves downstream in the higher approximation would grow larger and larger, without limit.) A similar problem involves the oscillation of a body on the free surface, in which the wave length of the radiated waves must be modified in the third approximation. For example, see Lee [1968].

A quite different application of this method is the problem of very low speed motion of a body under or on a free surface. The simplest such case has been discussed by Ogilvie [1968]. For a translating submerged body, there are two kinds of length scales: length scales associated with body dimensions and submergence, and the length scale U^2/g , which is associated with the presence of the free surface. Presumably, the latter has effects primarily near the free surface, in a "boundary layer" with thickness which varies with U^2/g as that variable approaches zero. But the effects of the body dimensions are also important near the free surface (or at least near a part of it). Thus the effects of the two length scales cannot be separated into distinct regions. A brief discussion of this problem appears in Section 5.42 of the present paper.

There may be many other problems of ship hydrodynamics in which this approach would be valuable. For example, many authors have obtained approximate solutions of problems involving submerged bodies by alternately satisfying a body boundary condition, then the free-surface condition, then again the body condition, etc. At each stage, when one condition is being satisfied, the other is being violated, but it is assumed that the errors become smaller and

smaller with each iteration. Such a procedure is discussed, for example, by Wehausen and Laitone [1960], who point out the usefulness of Kochin functions in such procedures. However, there is often a question about the precise nature of such expansions. In the first approximation, for example, the effects of the free-surface are likely to drop off exponentially with distance from the surface. This makes it inappropriate to treat depth of submergence as a large parameter in the usual manner, because exponentially small orders of magnitude are either trivial or exceedingly difficult to handle. I do not believe that anyone has yet shown how to treat this problem systematically.

II. INFINITE-FLUID PROBLEMS

It is mainly the presence of the free surface in our problems that forces us to seek ever more sophisticated methods of approximation. However, the nature of the approximations can often be appreciated more easily by applying those methods to infinite-fluid problems. In this section, I discuss a number of problems that are geometrically similar to the ship problems that are my real concern. In some cases, it must be realized that the methods used here are not necessarily the best methods for the infinite-fluid problems. However, without the complications which accompany the presence of the free surface, one can better understand the significance of the coordinate distortions, the repeated re-ordering of series, and the matching of expansions.

The reader who feels comfortable with matched asymptotic expansions is invited to skip this chapter.

2.1. Thin Body

A "thin body" has one dimension which is characteristically much smaller than the other dimensions. In aerodynamics, the common example is the "thin wing," and, in ship hydrodynamics, one frequently treats a ship as if it were thin. In such problems, the incident flow is usually assumed to approach the body approximately edge-on, and so the thinness assumption allows one to linearize the flow problem.

In this section, thin-body problems are treated by the method of matched asymptotic expansions. This is not the way thin-body problems are normally attacked, and, in fact, I do not recall ever having heard of such a treatment. At the outset, I must point out that there are good reasons why this has been the case. If the body is symmetrical about a plane parallel to the direction of the incident flow, one does not need inner and outer expansions for solving the problem. And if the body lacks such symmetry, the lowest-order problem cannot be solved analytically, and so the method of matched

asymptotic expansions does not offer the possibility that one may be able to obtain higher-order approximations.

In fact, the problem of a thin body in an infinite fluid is not a genuine singular perturbation problem (although it may contain some sub-problems that are singular, such as the flow around the leading edge of an airfoil). However, I believe that the problem of a thin ship is singular; I shall discuss this in Section 4. There has been a considerable amount of misunderstanding as to what constitutes the near field and what constitutes the far field in the thin-ship wave-resistance problem, and the rectification of such misunderstanding requires a careful statement of the problem.

It is conceivable that this interpretation of the thin-ship problem may be useful in formulating a rational mathematical idealization of the maneuvering-ship problem.

For convenience, I separate the thin-body problem into two parts: a) the symmetrical-body problem, and b) the problem of a body of zero thickness. To treat an arbitrary thin body, with both thickness and camber, one should certainly consider both aspects at once. It is not really difficult to do this, and indeed the problem of an unsymmetrical body of zero thickness actually involves thickness effects (at higher orders of magnitude than in the symmetrical-body problem)⁴. I have kept the problems separate here only for clarity in discussing certain phenomena that occur.

2.11. Symmetrical Body (Thickness Effects). Let the body be defined by the equation:

$$y = \begin{cases} \pm h(x, z; \epsilon) & \text{for } (x, 0, z) \text{ in } \mathbf{H}, \\ 0 & \text{for } (x, 0, z) \text{ not in } \mathbf{H}, \end{cases} \quad (2-1)$$

where \mathbf{H} is the part of the $y = 0$ plane which is inside the body. (It is the centerplane if the body is a ship.) The "thinness" of the body is expressed by writing:

$$h(x, z; \epsilon) = \epsilon H(x, z), \quad (2-2)$$

where ϵ is a small parameter and $H(x, z)$ is independent of ϵ . The body is immersed in an infinite fluid which is streaming past it with a speed U in the positive x direction. The flow, in the absence of the body, can be described by the velocity potential: Ux .

It will sometimes be convenient to say that the body is defined by the equation: $y = \pm h(x, z; \epsilon)$, implying that the function $h(x, z; \epsilon)$ is identically zero if $(x, 0, z)$ is not in \mathbf{H} . Also, note that we shall

frequently drop the explicit mention of the ϵ dependence.

As $\epsilon \rightarrow 0$, the body shrinks down to a sheet of zero thickness aligned with the incident flow. Thus, the first term in an asymptotic expansion of the velocity potential in the far field is just the incident-stream potential. In general, let the far-field expansion be expressed as follows:

$$\phi(x, y, z; \epsilon) \sim \sum_{n=0}^N \phi_n(x, y, z; \epsilon), \text{ where } \phi_{n+1} = o(\phi) \text{ as } \epsilon \rightarrow 0 \text{ for fixed } (x, y, z). \quad (2-3)$$

Then we have:

$$\phi_0(x, y, z; \epsilon) = Ux. \quad (2-4)$$

The far field is the entire space except the $y = 0$ plane. Since the potential $\phi(x, y, z; \epsilon)$ satisfies the Laplace equation throughout the fluid domain, the individual terms in the above expansion satisfy the Laplace equation in the far field:

$$\phi_{n_{xx}} + \phi_{n_{yy}} + \phi_{n_{zz}} = 0 \quad \text{for } |y| > 0. \quad (2-5)$$

At infinity, we expect (on physical grounds) that:

$$\nabla(\phi - Ux) \rightarrow 0. \quad (2-6)$$

Therefore, for $n > 0$, every ϕ_n must be singular on the $y = 0$ plane or be a constant throughout space. The latter would be too trivial a result to consider, and so we assume that ϕ_n is indeed singular on the $y = 0$ plane.

But what kind of singularities will be needed? Because of the symmetry of the problem, it is not difficult to show that a sheet of sources will suffice. One can use Green's theorem to show this. Alternatively, one can use transform methods for solving the Laplace equation, which is practically equivalent to solving by separation of variables. Whatever method is used, the result is the same; $\phi_n(x, y, z; \epsilon)$ has a representation:

$$\phi_n(x, y, z; \epsilon) = - \frac{1}{4\pi} \int_{-\infty}^{\infty} \int_{-\infty}^{\infty} \frac{\sigma_n(\xi, \zeta; \epsilon) d\xi d\zeta}{[(x-\xi)^2 + y^2 + (z-\zeta)^2]^{1/2}}, \quad (2-7)$$

where $\sigma_n(x, z; \epsilon)$ is an unknown source-density function. The outer

expansion is just the sum of these:

$$\phi(x, y, z; \epsilon) \sim Ux - \frac{1}{4\pi} \sum_{n=1}^N \int_{-\infty}^{\infty} \int_{-\infty}^{\infty} \frac{\sigma_n(\xi, \zeta; \epsilon) d\xi d\zeta}{[(x-\xi)^2 + y^2 + (z-\zeta)^2]^{1/2}}. \quad (2-8)$$

This is the most general possible outer expansion for this problem.

It will be necessary presently to know the inner expansion of the above outer expansion. To find it, define an inner variable:

$$Y = y/\epsilon, \quad (2-9)$$

substitute for y in the outer expansion, and re-order the resulting expression with respect to ϵ . A direct approach to this process is difficult, but the following method, in four steps, allows us to obtain the desired results to any number of terms in a fairly simple way:

1) Take the Fourier transform of ϕ_n with respect to x :

$$\begin{aligned} \phi_n^*(k; y, z; \epsilon) &= -\frac{1}{4\pi} \int_{-\infty}^{\infty} d\zeta \sigma_n^*(k; \zeta; \epsilon) \int_{-\infty}^{\infty} \frac{dx e^{-ikx}}{[x^2 + y^2 + (z-\zeta)^2]^{1/2}} \\ &= -\frac{1}{2\pi} \int_{-\infty}^{\infty} d\zeta \sigma_n^*(k; \zeta; \epsilon) K_0(|k| \sqrt{y^2 + (z-\zeta)^2}) \end{aligned}$$

where K_0 is the modified Bessel function usually denoted this way, and $\sigma_n^*(k; z; \epsilon)$ is the Fourier transform of the function $\sigma_n(x, z; \epsilon)$. The convolution theorem was used in the first step above.

2) Take the Fourier Transform next with respect to z :

$$\begin{aligned} \phi_n^{**}(k; y; m; \epsilon) &= -\frac{1}{2\pi} \sigma_n^{**}(k, m; \epsilon) \int_{-\infty}^{\infty} dz e^{-imz} K_0(|k| \sqrt{y^2 + z^2}) \\ &= -\frac{\sigma_n^{**}(k, m; \epsilon)}{2(k^2 + m^2)^{1/2}} e^{-(k^2 + m^2)^{1/2} |y|}, \end{aligned}$$

where $\sigma_n^{**}(k, m; \epsilon)$ is the double transform of $\sigma_n(x, z; \epsilon)$.

3) Substitute: $y = \epsilon Y$ and expand the exponential function into a power series:

$$\begin{aligned}\phi_n^{**}(k; y; m; \epsilon) = & -\frac{\sigma_n^{**}(k, m; \epsilon)}{2(k^2 + m^2)^{1/2}} \left[1 + \frac{1}{2!} \epsilon^2 Y^2 (k^2 + m^2) \right. \\ & \left. + \frac{1}{4!} \epsilon^4 Y^4 (k^2 + m^2)^2 + \dots \right] \\ & + \frac{1}{2} \sigma_n^{**}(k, m; \epsilon) \left[\epsilon |Y| + \frac{1}{3!} \epsilon^3 |Y|^3 (k^2 + m^2) \right. \\ & \left. + \frac{1}{5!} \epsilon^5 |Y|^5 (k^2 + m^2)^2 + \dots \right].\end{aligned}$$

4) Note that:

$$-\frac{\sigma_n^{**}(k, m; \epsilon)}{2(k^2 + m^2)^{1/2}} = \phi_n^{**}(k; 0; m; \epsilon) \equiv \alpha_n^{**}(k, m; \epsilon). \quad (2-10)$$

Also, we observe that, if $f^{**}(k, m)$ is the Fourier transform of $f(x, z)$, then $(k^2 + m^2)f^{**}(k, m)$ is the Fourier transform of $-(f_{xx} + f_{zz})$. Defining the inverse transform of $\alpha_n^{**}(k, m; \epsilon)$:

$$\alpha_n(x, z; \epsilon) = \phi_n(x, 0, z; \epsilon), \quad (2-11)$$

and inverting the above series term-by-term, we obtain:

$$\begin{aligned}\phi_n(x, y, z; \epsilon) \sim & \alpha_n(x, z; \epsilon) + \frac{1}{2} \epsilon |Y| \sigma_n(x, z; \epsilon) - \frac{1}{2!} \epsilon^2 |Y|^2 (\alpha_{n_{xx}} + \alpha_{n_{zz}}) \\ & - \frac{1}{2 \cdot 3!} \epsilon^3 |Y|^3 (\sigma_{n_{xx}} + \sigma_{n_{zz}}) \\ & + \frac{1}{4!} \epsilon^4 |Y|^4 [\alpha_{n_{xxx}} + 2\alpha_{n_{xxz}} + \alpha_{n_{zzz}}] + \dots.\end{aligned} \quad (2-12)$$

This is the inner expansion of a typical term in the outer expansion.

In order to combine the expansions of the separate terms into a single inner expansion of the outer expansion, let us assume that σ_n and α_n are both $O(\epsilon^n)$. (It is not necessary to assume this, it is merely convenient.) Then we have for the desired expansion:

$$\phi(x, y, z; \epsilon) \sim Ux \quad O(1)$$

$$+ \alpha_1(x, z; \epsilon) \quad O(\epsilon)$$

$$+ \alpha_2(x, z; \epsilon) + \frac{1}{2} |y| \sigma_1(x, z; \epsilon) \quad O(\epsilon^2)$$

$$+ \alpha_3(x, z; \epsilon) + \frac{1}{2} |y| \sigma_2(x, z; \epsilon) - \frac{1}{2} |y|^2 (\alpha_{1xx} + \alpha_{1zz}) \quad O(\epsilon^3)$$

$$+ O(\epsilon^4). \quad (2-13)$$

Note that we have reverted to far-field variables. We must here consider that $y = O(\epsilon)$ in order to recognize the orders of magnitude as indicated above.

Next we must find the inner expansion of the exact solution. Substitute $y = \epsilon Y$ in the formulation of the problem. The Laplace equation transforms as follows:

$$\phi_{YY} = -\epsilon^2(\phi_{xx} + \phi_{zz}). \quad (2-14)$$

The kinematic condition on the body is:

$$\pm \phi_x h_x - \phi_y \pm \phi_z h_z = 0 \quad \text{on} \quad y = \pm h(x, z),$$

which transforms into:

$$\phi_Y = \pm \epsilon^2(\phi_x H_x + \phi_z H_z) \quad \text{on} \quad Y = \pm H(x, z). \quad (2-15)$$

We assume that there exists a near-field asymptotic expansion of the solution:

$$\phi(x, y, z; \epsilon) \sim \sum_{n=0}^N \Phi_n(x, Y, z; \epsilon), \quad \text{where} \quad \Phi_{n+1} = o(\Phi_n) \quad \text{as} \quad \epsilon \rightarrow 0, \\ \text{for fixed } (x, Y, z). \quad (2-16)$$

We could show carefully that:

$$\Phi_0(x, Y, z; \epsilon) = Ux.$$

(Perhaps it is obvious to most readers.) We then express the con-

ditions on the near-field expansion as follows:

$$[L] \quad \Phi_{1YY} + \Phi_{2YY} + \Phi_{3YY} + \dots \\ \sim -\epsilon^2 [\Phi_{1xx} + \Phi_{1zz} + \Phi_{2xx} + \Phi_{2zz} + \dots]; \quad (2-17)$$

$$[H] \quad \Phi_{1Y} + \Phi_{2Y} + \Phi_{3Y} + \dots \sim \pm \epsilon^2 [UH_x + \Phi_{1x} H_x + \Phi_{1z} H_z + \dots] \\ \text{on } Y = \pm H(x, z). \quad (2-18)$$

Solution of the Φ_1 problem. From the [L] condition above, it is clear that:

$$\Phi_{1YY} = 0 \quad (2-19)$$

in the fluid domain. Therefore Φ_1 must be a linear function of Y . In view of the symmetry of the problem, we can set:

$$\Phi_1(x, Y, z; \epsilon) = A_1(x, z; \epsilon) + B_1(x, z; \epsilon) |Y|, \quad \text{for } |Y| > H(x, z). \quad (2-20)$$

The body condition reduces to:

$$\Phi_{1Y}(x, \pm H(x, z), z; \epsilon) = \pm \epsilon^2 UH_x(x, z) = \pm B_1(x, z; \epsilon) = O(\epsilon^2). \quad (2-21)$$

It appears that we have determined the value of $B_1(x, z; \epsilon)$ -- but this is wrong, as we shall see in a moment. The two-term inner expansion appears to be:

$$\phi(x, y, z; \epsilon) \sim Ux + A_1(x, z; \epsilon) + B_1(x, z; \epsilon) |Y|.$$

Its outer expansion is obtained by setting $Y = y/\epsilon$:

$$\phi(x, y, z; \epsilon) \sim Ux + \frac{1}{\epsilon} B_1(x, z; \epsilon) |y| + A_1(x, z; \epsilon). \\ O(1) \quad O(\epsilon) \quad O(\epsilon^2)$$

The order-of-magnitude estimates were obtained as follows: B_1 is $O(\epsilon^2)$, from (2-21). If our expansion is consistent (as we insist), then A_1 is also $O(\epsilon^2)$, by (2-20). Now, in the outer expansion of the inner expansion, the B_1 term is lower order than the A_1 term.

The two-term outer expansion of the two-term inner expansion is:

$$\phi(x, y, z; \epsilon) \sim Ux + \frac{1}{\epsilon} B_1(x, z; \epsilon) |y| .$$

$$O(1) \quad O(\epsilon)$$

On the other hand, the two-term inner expansion of the two-term outer expansion is, from (2-13),

$$\phi(x, y, z; \epsilon) \sim Ux + \alpha_1(x, z; \epsilon).$$

There is no linear term here at all, and it seems that we cannot match the two expansions.

It is a very comforting feature of the method of matched asymptotic expansions that things go wrong this way when we have made unjustified assumptions. Our mistake was this: When we found that apparently $B_1 = \epsilon^2 UH_x = O(\epsilon^2)$, we eliminated the possibility that there might be a term which is $O(\epsilon)$ in the inner expansion*. Now we rectify this error. Once again, let Φ_1 be given by (2-20), but suppose that both "constants" are, in fact, $O(\epsilon)$. The body boundary condition immediately yields the condition that:

$$B_1(x, z; \epsilon) = 0 ,$$

and so we have:

$$\Phi_1(x, Y, z; \epsilon) = A_1(x, z; \epsilon) .$$

The inner expansion, to two terms, is now given by:

$$\phi(x, y, z; \epsilon) \sim Ux + A_1(x, z; \epsilon).$$

When we match this to the inner expansion of the outer expansion, we find that:

$$A_1(x, z; \epsilon) = \alpha_1(x, z; \epsilon) = \phi_1(x, 0, z; \epsilon).$$

(See 2-11.) Now we have matched the expansions satisfactorily, but

*This trouble would have been avoided if I had started by assuming that the expansion is a power series in ϵ , as many people do in such problems. However, that procedure can lead to even greater difficulties sometimes.

the result is not yet of much use, since we do not know either function, A_1 or α_1 . It is worth noting, however, that the inner expansion can be rewritten:

$$\phi(x, y, z; \epsilon) \sim Ux + \phi_1(x, 0, z; \epsilon).$$

Thus, to two terms the inner expansion is determined entirely by the far-field solution, the latter being evaluated on the centerplane. In other words, in the near-field view, the fluid velocity (to this degree of approximation) is caused entirely by remote effects.

Solution of the Φ_2 problem: This is much more straightforward, and the results are more interesting. We may expect that $\Phi_2 = O(\epsilon^2)$, since we still have the nonhomogeneous body condition to satisfy. In this case, then,

$$\Phi_2(x, Y, z; \epsilon) = A_2(x, z; \epsilon) + B_2(x, z; \epsilon) |Y|,$$

and the body condition requires that $B_2(x, z; \epsilon) = \epsilon^2 UH_x(x, z)$. The three-term inner expansion is:

$$\begin{array}{ccccccc} \phi(x, y, z; \epsilon) \sim & Ux & + & \alpha_1(x, z; \epsilon) & + & A_2(x, z; \epsilon) & + & \epsilon^2 UH_x(x, z) |Y| \\ & O(1) & & O(\epsilon) & & O(\epsilon^2) & & O(\epsilon^2) \end{array}$$

The two-term outer expansion of this three-term inner expansion is:

$$\begin{array}{ccccccc} \phi(x, y, z; \epsilon) \sim & Ux & + & \alpha_1(x, z; \epsilon) & + & U h_x(x, z; \epsilon) |y| \\ & O(1) & & O(\epsilon) & & O(\epsilon) \end{array}$$

The three-term inner expansion of the two-term outer expansion is, from (2-13):

$$\phi(x, y, z; \epsilon) \sim Ux + \alpha_1(x, z; \epsilon) + \frac{1}{2} |y| \sigma_1(x, z; \epsilon).$$

(The α_2 in (2-13) is not carried over to the above expansion, since it originates in the third term of the outer expansion.) These two match if:

$$\sigma_1(x, z; \epsilon) = 2UH_x(x, z; \epsilon) = O(\epsilon). \quad (2-22)$$

Thus, finally, we have found $\sigma_1(x, z; \epsilon)$, the source density in the first far-field approximation, as a function of the body geometry. It is the familiar result from thin-ship theory. In addition, we can

now also write down $\alpha_1(x, z; \epsilon)$ by combining (2-7) and (2-11):

$$\alpha_1(x, z; \epsilon) = -\frac{1}{2\pi} \int \int_{\mathbf{H}} \frac{U h_x(\xi, \zeta; \epsilon) d\xi d\zeta}{[(x-\xi)^2 + (z-\zeta)^2]^{1/2}} = O(\epsilon).$$

We have the two-term outer expansion -- with everything in it known -- and the three-term inner expansion -- with the "constant" $A_2(x, z; \epsilon)$ not yet determined.

Solution of the higher-order problems: From the [L] condition, (2-17), it can be seen that $\Phi_2(x, Y, z; \epsilon)$ is not linear in Y . However, the differential equation for Φ_2 is easily solved, the body boundary condition can be satisfied, and matching can be carried out with the outer expansion. The result is:

$$\Phi_3(x, Y, z; \epsilon) = A_3(x, z; \epsilon) + B_3(x, z; \epsilon) |Y| - \frac{1}{2} \epsilon^2 Y^2 (\alpha_{1_{xx}} + \alpha_{1_{zz}}),$$

where

$$B_3(x, z; \epsilon) = \epsilon^2 [(\alpha_{1_x} H)_x + (\alpha_{1_z} H)_z],$$

$$A_3(x, z; \epsilon) = \alpha_3(x, z; \epsilon).$$

We also obtain σ_2 , through the matching,

$$\sigma_2(x, z; \epsilon) = 2[(\alpha_{1_x} h)_x + (\alpha_{1_z} h)_z],$$

and this information also gives us α_2 and A_2 .

Summary: Symmetrical Body. The results for both near- and far-field expansion are stated in terms of the far-field coordinates (the natural coordinates of the problem) in Table 2-1. In a sense, the results are rather trivial. There could be difficulties near the edges of \mathbf{H} , but, barring such possibilities, the inner expansion could be obtained from the outer expansion and then matched to the body boundary condition. This is actually the classical thin-ship approach. The outer expansion is uniformly valid near the thin body, except possibly near the edges.

In the classical approach to the thin-body problem, there is usually a legitimate question concerning the analytic continuation of the potential function into the region of space occupied by the body. Sometimes one avoids the problem by restricting attention to bodies which can legitimately be generated by a sheet of sources, but this is not very satisfying. The method of matched asymptotic expansions avoids the question altogether by eliminating the need to ask it. What

TABLE 2-1
SYMMETRICAL THIN BODY

Near-Field (Inner) Expansion

$$y = O(\epsilon)$$

$$\begin{aligned} \phi(x, y, z; \epsilon) \sim & Ux + \alpha_1(x, z; \epsilon) + \underbrace{\alpha_2(x, z; \epsilon) + \frac{1}{2} \sigma_1(x, z; \epsilon) |y|}_{O(\epsilon^2)} \\ & O(1) \quad O(\epsilon) \quad O(\epsilon^2) \\ & \underbrace{+ \alpha_3(x, z; \epsilon) + \frac{1}{2} \sigma_2(x, z; \epsilon) |y| - \frac{1}{2} |y|^2 (\alpha_{1xx} + \alpha_{1zz})}_{O(\epsilon^3)} \\ & + O(\epsilon^4) \end{aligned}$$

Far-Field (Outer) Expansion

$$y = O(1)$$

$$\begin{aligned} \phi(x, y, z; \epsilon) \sim & Ux - \frac{1}{4\pi} \sum_{n=1}^N \iint_{\mathbf{H}} \frac{\sigma_n(\xi, \zeta; \epsilon) d\xi d\zeta}{[(x-\xi)^2 + y^2 + (z-\zeta)^2]^{1/2}} \\ & O(1) \quad O(\epsilon^n) \end{aligned}$$

From Matching

$$\sigma_1(x, z; \epsilon) = 2Uh_x(x, z; \epsilon) ;$$

$$\sigma_2(x, z; \epsilon) = 2[(\alpha_{1x} h)_x + (\alpha_{1z} h)_z] ;$$

etc.;

$$\alpha_n(x, z; \epsilon) = -\frac{1}{4\pi} \iint_{\mathbf{H}} \frac{\sigma_n(\xi, \zeta; \epsilon) d\xi d\zeta}{[(x-\xi)^2 + (z-\zeta)^2]^{1/2}} .$$

we are really saying is this: From very far away, the disturbance appears as if it could have been generated by a sheet of sources, but close-up we allow for the possibility that this observation from afar may be somewhat inaccurate. In fact, there is no analytic continuation presumed in the present method.

One can show by the use of Green's theorem that the far-field picture is valid even if the analytic continuation is not possible. A particularly appealing (to me) version of such a proof has been provided by Maruo [1967] for the much more complicated problem of a heaving, pitching slender ship moving with finite forward speed on the surface of the ocean.

I suppose that the uniformity of the thin-body solution is the result of the fact that a well-posed potential problem can be stated by giving a Neumann boundary condition over a surface. The situation will be quite different when we consider slender-body theory: in the far field, it would be necessary to give boundary conditions on a line, and that does not lead to a well-posed potential problem in three dimensions. Similarly, we may expect trouble at the confluence of two boundary conditions, and this indeed occurs when we try to treat a ship problem by the method discussed above. The free-surface conditions cannot be satisfied, and the difficulty can be traced back to the behavior of the far-field potential near the intersection of the centerplane and the undisturbed free surface.

2.12. Unsymmetrical Body (Lifting Surface). For the sake of simplicity, let the body have zero thickness. Then it can be represented as follows:

$$y = g(x, z; \epsilon) = \epsilon G(x, z) \quad \text{for} \quad (x, 0, z) \quad \text{in} \quad \mathbf{H}, \quad (2-23)$$

where \mathbf{H} is now the projection of the body onto the $y = 0$ plane. Again, there is a uniform incident flow in the positive x direction.

The analysis is quite similar to the symmetrical-body case, at least in the near field, and so most of the details will be omitted here. In the near field, let there be an expansion:

$$\phi(x, y, z; \epsilon) \sim \sum_{n=0}^N \Phi_n(x, Y, z; \epsilon),$$

just as in (2-16). The first term is, again, $\Phi_0(x, Y, z; \epsilon) = Ux$. The terms again satisfy the transformed Laplace equation, (2-17):

$$[L] \quad \Phi_{1_{YY}} + \Phi_{2_{YY}} + \Phi_{3_{YY}} + \Phi_{4_{YY}} + \dots \\ \sim -\epsilon^2 [\Phi_{1_{xx}} + \Phi_{1_{zz}} + \Phi_{2_{xx}} + \Phi_{2_{zz}} + \dots];$$

the body boundary condition is now:

$$\begin{aligned}
 [H] \quad & \Phi_{1Y} + \Phi_{2Y} + \Phi_{3Y} + \Phi_{4Y} + \dots \\
 & \sim \epsilon^2 [UG_x + (\Phi_{1x} G_x + \Phi_{1z} G_z) + (\Phi_{2x} G_x + \Phi_{2z} G_z) + \dots] \\
 & \text{on} \quad Y = G(x, z). \quad (2-24)
 \end{aligned}$$

The solution for Φ_1 is generally an expression linear in Y , but, for the same reasons as in the symmetrical-body problem, only the "constant" term can ultimately be matched to the far-field solution, and so we take for Φ_1 :

$$\Phi_1(x, Y, z; \epsilon) = A_1^\pm(x, z; \epsilon) \mp O(\epsilon).$$

The superscript \pm has been attached to the solution to indicate that this quantity may be different on the two sides of the body. This was not necessary in the previous problem, because of the symmetry, but in the present near-field problem the body completely isolates the fluid on its two sides and there is no reason to assume that A_1 is the same on both sides of the body. (It turns out, in fact, that $A_1^- = -A_1^+$.)

One next obtains:

$$\Phi_2(x, Y, z; \epsilon) = A_2^\pm(x, z; \epsilon) + B_2^\pm(x, z; \epsilon) Y.$$

From the body boundary condition, the following is true:

$$\Phi_{2Y}(x, G, z; \epsilon) = B_2^\pm(x, z; \epsilon) = \epsilon^2 UG_x(x, z). \quad (2-25)$$

Thus, we find that

$$B_2^+(x, z; \epsilon) = B_2^-(x, z; \epsilon) \equiv B_2(x, z; \epsilon).$$

Similarly, one can proceed:

$$\Phi_3(x, Y, z; \epsilon) = A_3^\pm(x, z; \epsilon) + B_3^\pm(x, z; \epsilon) Y - \frac{1}{2} \epsilon^2 Y^2 (A_{1xx}^\pm + A_{1zz}^\pm),$$

where

$$B_3^\pm(x, z; \epsilon) = \epsilon^2 [(GA_{1x}^\pm)_x + (GA_{1z}^\pm)_z].$$

It is interesting to note the following about the symmetry: It turns out that Φ_1 and Φ_2 are odd with respect to Y , but Φ_3 is neither even nor odd. The linear term in Φ_3 , namely, $B_3^\pm(x, z; \epsilon)Y$, is even, since it turns out that $B_3^+ = -B_3^-$. Careful study of the Φ_2 problem shows that it actually implies that there is a generation of fluid in the body, but the rate of generation is higher order than the Φ_2 term. Physically, of course, there can be no fluid generated, and so a compensating source-like term appears in Φ_3 .

The far field is again the entire space except for the plane $y = 0$. The relations (2-3) to (2-6) are again valid, as well as the discussion of them. But now it will not suffice to provide only source singularities on the centerplane; clearly we must also provide singularities which lead to antisymmetric potential functions. In fact, since the body has zero thickness, we shall expect the leading-order approximation to be strictly antisymmetric. These requirements are all met by a distribution of dipoles which are oriented with the y axis. The potential of such a sheet of dipoles can be expressed:

$$f(x, y, z) = \frac{y}{4\pi} \int_{-\infty}^{\infty} \int_{-\infty}^{\infty} \frac{\mu(\xi, \zeta) d\xi d\zeta}{[(x-\xi)^2 + y^2 + (z-\zeta)^2]^{3/2}}. \quad (2-26)$$

The inner expansion of such an integral can be obtained by the same Fourier-transform technique that was used before. One finds that:

$$f^{**}(k; y; m) = \frac{1}{2} (\text{sgn } y) \mu^{**}(k, m) e^{i|y|(k^2 + m^2)^{1/2}}.$$

The exponential function can be expanded into a series, which is then inverted term-by-term. Define a new function (cf. (2-10)):

$$\gamma^{**}(k, m) = (k^2 + m^2)^{1/2} \mu^{**}(k, m) = - \frac{(\mu_{xx} + \mu_{zz})^{**}}{(k^2 + m^2)^{1/2}}. \quad (2-27)$$

The following relationships exist between the two functions $\mu(x, z)$ and $\gamma(x, z)$:

$$\mu(x, z) = \frac{1}{2\pi} \int_{-\infty}^{\infty} \int_{-\infty}^{\infty} \frac{\gamma(\xi, \zeta) d\xi d\zeta}{[(x-\xi)^2 + (z-\zeta)^2]^{1/2}}; \quad (2-28)$$

$$\gamma(x, z) = - \frac{1}{2\pi} \int_{-\infty}^{\infty} \int_{-\infty}^{\infty} \frac{[\mu_{xx} + \mu_{zz}] d\xi d\zeta}{[(x-\xi)^2 + (z-\zeta)^2]^{1/2}}. \quad (2-29)$$

(Note the comparison between (2-28) and the relation between α_n and σ_n in Table 2-1. In fact, (2-29) gives the inversion of the formula in Table 2-1.) The inner expansion of $f(x, y, z)$ can now be written in terms of these two functions:

$$f(x, y, z) = \frac{1}{2} \{ \mu(x, z)(\operatorname{sgn} y) - \gamma(x, z)y - \frac{1}{2!} y^2 (\operatorname{sgn} y)(\mu_{xx} + \mu_{zz}) \\ + \frac{1}{3!} y^3 (\gamma_{xx} + \gamma_{zz}) + \frac{1}{4!} y^4 (\operatorname{sgn} y)(\mu_{xxxx} + 2\mu_{xxzz} + \mu_{zzzz}) + \dots \} . \quad (2-30)$$

This may be compared with (2-12).

Now let us assume that the two-term outer expansion is:

$$\phi(x, y, z; \epsilon) \sim Ux + \frac{y}{4\pi} \int_{-\infty}^{\infty} \int_{-\infty}^{\infty} \frac{\mu(\xi, \zeta; \epsilon) d\xi d\zeta}{[(x-\xi)^2 + y^2 + (x-\zeta)^2]^{3/2}}$$

Furthermore, assume that μ_1 and γ_1 are both $O(\epsilon)$. (If these assumptions are too restrictive, that fact will become clear in the subsequent steps of the method of matched asymptotic expansions.) Then the inner expansion of the two-term outer expansion is:

$$\phi(x, y, z; \epsilon) \sim Ux \pm \underbrace{\mu_1(x, z; \epsilon)}_{O(1)} - y \underbrace{\gamma_1(x, z; \epsilon)}_{O(\epsilon^2)} \mp \frac{1}{2} \underbrace{y^2 (\mu_{1xx} + \mu_{1zz})}_{O(\epsilon^3)} .$$

I have kept four terms, as indicated by the order-of-magnitude notes under the terms. (Recall that $y = O(\epsilon)$ in the inner expansion.)

Matching with the appropriate forms of the outer expansion of the inner expansion, we find that:

$$A_1^{\pm}(x, z; \epsilon) = \pm \mu_1(x, z; \epsilon); \quad (2-31)$$

$$B_2^{\pm}(x, z; \epsilon) = -\epsilon \gamma_1(x, z; \epsilon). \quad (2-32)$$

From (2-25), we find that:

$$\gamma_1(x, z; \epsilon) = -\epsilon U G_x(x, z) = -U g_x(x, z; \epsilon). \quad (2-33)$$

It appears now that we could use this knowledge of γ_1 in (2-28) for determining μ_1 . But this is wrong. Note from (2-30) that $\gamma_1(x, z)$

is the normal velocity component on the $y = 0$ plane caused by the distribution of dipoles, $\mu_1(x, z)$, over the same plane. Now we would presumably restrict the dipole distribution to the region \mathbf{H} , and so (2-29) is valid if the range of integration is reduced to just \mathbf{H} , since the integrand is identically zero outside \mathbf{H} . But the same is not true in (2-28). There is a generally non-zero normal component of velocity, $\gamma_1(x, z)$, over the entire plane, and the range of integration in (2-28) cannot be reduced to just \mathbf{H} . Unfortunately, we know $\gamma_1(x, z)$ only on \mathbf{H} , from (2-33), and so we have solved nothing.

This difficulty is hardly surprising, since we are really formulating here the classical lifting-surface problem, and its solution requires either the solution of a two-dimensional singular integral equation or the introduction of further simplifications -- which will be discussed presently.

In the lifting-surface problem, we really should distribute dipoles over two regions, the centerplane \mathbf{H} and the part of the plane $y = 0$ which is directly downstream of \mathbf{H} . Let the latter be called \mathbf{W} . Pressure must be continuous across \mathbf{W} , since there is no body there to support a pressure jump. In the usual aerodynamics manner, one can then show that $\partial\mu_1/\partial x$ must be zero on \mathbf{W} . In this way, the integration range in (2-29) can be reduced to an integral over just \mathbf{H} .

Of course, lifting surface theory is usually worked out in terms of vorticity distributions. I happen to prefer using dipole distributions, mainly because then I do not have to worry about whether a vortex line might be ending in the fluid region. The connection is fairly simple between the two versions, of course. A single discrete horseshoe vortex extending spanwise between $z = s$ and $z = -s$ and downstream to $x = \infty$ corresponds to a sheet of dipoles of uniform density, spread over the plane region bounded by the vortex line. The potential function can be written, for unit vortex strength,

$$\begin{aligned}\phi(x, y, z) &= \frac{y}{4\pi} \int_{-s}^s d\zeta \int_0^\infty \frac{d\xi}{[(x-\xi)^2 + y^2 + (z-\zeta)^2]^{3/2}} \\ &= \frac{y}{4\pi} \int_{-s}^s \frac{d\zeta}{y^2 + (z-\zeta)^2} \left[1 + \frac{x}{[x^2 + y^2 + (z-\zeta)^2]^{1/2}} \right] \\ &= \frac{1}{4\pi} \left[\tan^{-1} \frac{y}{z-s} - \tan^{-1} \frac{y}{z+s} + \tan^{-1} \frac{y\sqrt{[x^2 + y^2 + (z-s)^2]}}{x(z-s)} \right. \\ &\quad \left. - \tan^{-1} \frac{y\sqrt{[x^2 + y^2 + (z+s)^2]}}{x(z+s)} \right].\end{aligned}$$

The normal velocity component in the plane of the vortex is:

$$\phi_y(x, 0, z) = \frac{1}{4\pi} \left(\frac{1}{z-s} \left[1 + \frac{[x^2 + (z-s)^2]^{1/2}}{x} \right] - \frac{1}{z+s} \left[1 + \frac{[x^2 + (z+s)^2]^{1/2}}{x} \right] \right).$$

A lifting line can be described in a similar way if we allow the dipole density to vary with the spanwise coordinate, z . For simplicity, let us assume that $\mu(z) = \mu(-z)$, and that $\mu(s) = 0$. The potential for a lifting line is:

$$\phi(x, y, z) = \frac{y}{4\pi} \int_{-s}^s d\zeta \mu(\zeta) \int_0^\infty \frac{d\xi}{[(x-\xi)^2 + y^2 + (z-\zeta)^2]^{3/2}} \quad (2-34)$$

$$= - \frac{y}{4\pi} \int_0^s ds' \mu'(s') \int_{-s'}^{s'} d\zeta \int_0^\infty \frac{d\xi}{[(x-\xi)^2 + y^2 + (z-\zeta)^2]^{3/2}}, \quad (2-35)$$

and the normal velocity component is:

$$\phi_y(x, 0, z) = - \frac{1}{4\pi} \int_{-s}^s \frac{ds' \mu'(s')}{z-s'} \left[1 + \frac{[x^2 + (z-s')^2]^{1/2}}{x} \right]. \quad (2-36)$$

Note that this reduces to the result for the single horseshoe vortex if a) we set $\mu'(z) = \delta(z+s) - \delta(z-s)^*$, and b) we integrate over a span from $-s-\beta$ to $s+\beta$, where β is a very small positive number. This may lend some credibility to the procedure frequently advocated by aerodynamicists in wing problems, viz., when integrating by parts in the spanwise direction, extend the range of integration slightly beyond the wing tips so that quantities which become infinite at the tips do not yield infinite contributions that cannot be integrated. (This is terrible mathematics, but apparently the physics is sound, since the results seem to be correct.)

Finally, we can use the above procedures to derive the corresponding expressions for a lifting surface. The important quantity is the normal velocity component, given by:

$$\phi_y(x, 0, z) = - \frac{1}{4\pi} \int_L d\xi \int_{-s(\xi)}^{s(\xi)} d\zeta \frac{\mu_{xz}(\xi, \zeta)}{z-\zeta} \left[1 + \frac{[(x-\xi)^2 + (z-\zeta)^2]^{1/2}}{x-\xi} \right], \quad (2-37)$$

* $\delta(z)$ is the usual Dirac delta function.

where L is the range of x covered by the lifting surface (the length of L being generally the chord length), and $s(x)$ is the half-span at cross section x . On H (the projection of the wing on the plane $y = 0$), the normal velocity component, ϕ_y , is known, either by direct application of the body boundary condition or by matching to a near-field solution, and we obtain the usual integral equation for a lifting surface.

We shall not be concerned here with the various methods of attempting directly to solve this integral equation, either by analytical or numerical methods. In fact, analytical methods do not exist, so far as I know, except for a few special geometries, such as elliptical planforms. The pair of equations (2-28) and (2-29) forms a remarkable analogy to a standard boundary-value problem in two dimensions which is analyzed thoroughly by Muskhelishvili [1953]. One three-dimensional case has been solved analytically by a method that has some similarity to the standard methods for the 2-D problem; this was done by Kochin [1940]. Even his circular-planform wing led to so much difficulty, it seems unlikely that it will be generalized to other planforms.

Analytical solutions have also been obtained for circular and then elliptic planforms by formulating the problem in terms of an acceleration potential in coordinate systems appropriate to such shapes of figures. This was all done long ago. See Kinner [1937] and Krienes [1940].

There are many numerical techniques for obtaining approximate solutions of this problem. However, I ignore these and proceed to analyze a special configuration which can be treated approximately as a limiting case of the general lifting-surface problem.

2.2. High-Aspect-Ratio Wing

It is an interesting historical fact that Prandtl's boundary-layer solution really contains the essence of the method of matched asymptotic expansions, but Prandtl failed to observe that the same technique would work in his lifting-line problem. In the boundary-layer problem, he really required the matching of two complementary, asymptotically valid, partial solutions. It was probably Friedrichs [1955] who first recognized that the high-aspect-ratio lifting-surface problem could be treated the same way. Van Dyke [1964] discusses the derivation of lifting-line theory in some detail from the point of view of matched asymptotic expansions. My presentation is not different from Van Dyke's in any startling ways. There are some differences, partly because I have in mind applications to planing problems eventually, partly because I am not an aeronautical (or aerospace) engineer at heart.

The conventional approach to solving the problem of a wing of

high aspect ratio is to simplify (2-37) by arguments that relate the sizes of the terms involving $(x-\xi)^2$ and $(z-\zeta)^2$. (Quite comparable arguments are used in the conventional approach to the theory of slender wings.) If the radical in (2-37) can be simplified, then the ξ integration can be performed, and one is left with just the integral over ζ . In this way, the 2-D integral equation is reduced to a one-dimensional integral equation, which is of a standard form.

Using the method of matched asymptotic expansions, we return to the original formulation of the problem and derive a sequence of simpler problems, rather than try to work out approximate solutions of the integral equation. The large-aspect-ratio wing is "slender" in the spanwise direction. This means that cross sections parallel to the $z = 0$ plane vary gradually in size and shape as z varies; in particular, the maximum dimension in the z direction, say $2S$ (the span), is much greater than the maximum dimension in the cross sections. We shall make whatever further assumptions of this kind that we need in order to keep the solution well-behaved. The small parameter can be defined as the inverse of the aspect ratio, that is,

$$\epsilon = 1/(\text{AR}) = (\text{area of } \mathbf{H})/4S^2,$$

where \mathbf{H} is the projection of the wing onto the $y = 0$ plane. As before, it is not necessary to be so specific about the definition of ϵ , and in fact it may be misleading. A wing with aspect ratio equal to 100 might be slender in the required sense if, for example, there were discontinuities in chord length in the spanwise direction. In any case, the wing shrinks down to a line, part of the z axis, as $\epsilon \rightarrow 0$.

Let the body be defined by the following relation:

$$y = g(x, z) \pm h(x, z), \quad (2-38)$$

for $(x, 0, z)$ in \mathbf{H} . See Figure (2-1). It is not necessary that the body be a thin one, in the sense of the previous section. I do, however, specify that it should be symmetric with respect to z , for the sake of simplicity in what follows. Both of the functions $g(x, z)$ and $h(x, z)$ really depend on ϵ , of course*, but we shall generally omit explicit mention of the fact.

There is an incident flow which, at infinity, is uniform in the x direction. Let the far-field solution be represented by the asymptotic expansion:

*In fact, g and h are both $O(\epsilon)$.

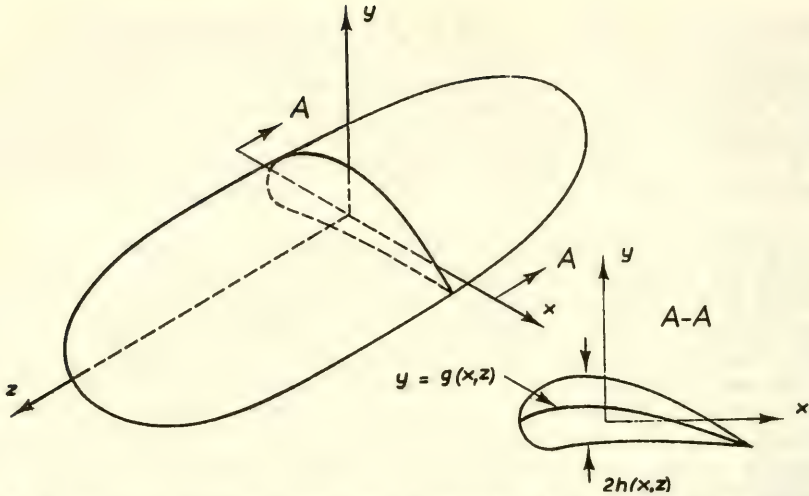


Fig. (2-1). Coordinates for the High-Aspect-Ratio Wing

$$\phi(x, y, z) \sim Ux + \sum_{n=1}^N \phi_n(x, y, z), \text{ where } \phi_{n+1} = o(\phi_n) \text{ as } \epsilon \rightarrow 0, \\ \text{for fixed } (x, y, z). \quad (2-39)$$

(Again, the dependence on ϵ is suppressed in the notation.) Since the body shrinks to a line ($x = 0, y = 0, |z| < S$) in the limit as $\epsilon \rightarrow 0$, the terms denoted by ϕ_n all represent flow perturbations which arise in the neighborhood of this singular line. They can be expressed in terms of singularities on that line, and the strengths of such singularities should be $o(1)$ as $\epsilon \rightarrow 0$. In an ideal fluid, we could expect the occurrence of dipoles, quadripoles, etc., on the singular line. We also take the realistic point of view that viscosity cannot be completely neglected and that there may be some circulation as a result. In the usual aeronautical point of view, this implies that there may be a vortex line present, complete with a set of trailing vortices. In the point of view adopted in the previous section, I assume that there may be a sheet of dipoles behind the singular line. I also make the usual assumption that these wake dipoles (or vortices) lie in the plane $y = 0$. This part of the $y = 0$ plane ($0 < x < \infty, |z| < S$) will be denoted by \mathbf{W} . (Note that \mathbf{H} has all but disappeared in the far field view. It is only a line.)

We can now write the outer expansion in the following form:

$$\begin{aligned}
\phi(x, y, z) \sim Ux + \frac{y}{4\pi} \sum_{n=1}^N \int_{-S}^S \int_0^\infty \frac{\gamma_n(\zeta) d\zeta}{[(x-\xi)^2 + y^2 + (x-\zeta)^2]^{3/2}} \\
+ \frac{y}{4\pi} \sum_{n=1}^N \int_{-S}^S \frac{\mu_n(\zeta) d\zeta}{[x^2 + y^2 + (z-\zeta)^2]^{3/2}} \\
+ \frac{x}{4\pi} \sum_{n=1}^N \int_{-S}^S \frac{\lambda_n(\zeta) d\zeta}{[x^2 + y^2 + (z-\zeta)^2]^{3/2}} + \dots \quad (2-40)
\end{aligned}$$

The first sum contains terms which are exactly of the form given in (2-34), that is, they represent a lifting line with a strength $\sum \gamma_n(z)$. The second and third sums represent lines of dipoles oriented vertically and longitudinally, respectively. It is implied above that the sums are asymptotic expansions, in our usual far-field sense.

We shall presently require the inner expansions of these terms. We obtain the inner expansions by assuming that $r = (x^2 + y^2)^{1/2} = O(\epsilon)$, which implies that both x and y are small.

Inner expansion of the lifting-line potential: Each of the double integrals containing a γ can be rewritten as a single integral:

$$\begin{aligned}
& \frac{y}{4\pi} \int_{-S}^S \int_0^\infty \frac{\gamma(\zeta) d\zeta}{[(x-\xi)^2 + y^2 + (z-\zeta)^2]^{3/2}} \\
&= - \frac{1}{4\pi} \int_{-S}^S d\zeta \gamma'(\zeta) \left(\tan^{-1} \frac{y}{z-\zeta} + \tan^{-1} \frac{y\sqrt{x^2 + y^2 + (z-\zeta)^2}}{x(z-\zeta)} \right). \quad (2-41)
\end{aligned}$$

Now break this into two parts:

1) The first term in brackets on the right-hand side does not depend on x . As $y \rightarrow 0$ (i.e., for $y = O(\epsilon)$), its contribution can be represented:

$$\pm \frac{1}{4} \gamma(z) - \frac{y}{4\pi} \int_{-S}^S \frac{d\zeta \gamma'(\zeta)}{z-\zeta} [1 + O(\epsilon^2)],$$

where the double sign is chosen according to whether $y > 0$ or $y < 0$, respectively, and the special integral sign indicates that the Cauchy principal value is intended. This representation is valid only for $|z| < S$, but that is no restriction here. It may be noted that

Every term in (2-51) must be of the same order of magnitude at a point in the near field, that is for $r = O(\epsilon)$. If a term were of some other order of magnitude with respect to ϵ , the definition of "consistency" would eliminate it from this series. The orders of magnitude of most of the unknown constants can then be written down. Since the first term, Ux , is $O(\epsilon)$, we can make the following statements:

$$\eta_0, A_{00} = O(\epsilon); \quad A_{01}, B_{01} = O(\epsilon^2); \quad A_{0n}, B_{0n} = O(\epsilon^{n+1}).$$

The term containing the logarithm does not fit the pattern quite so well -- unless we follow my arbitrary practice of saying that $\log \epsilon = O(1)$. (See the discussion of "consistency" in Section 1.2.) Then we can say that:

$$\delta_0 = O(\epsilon).$$

The Laurent series expression for the near-field expansion is very convenient when it comes to finding the outer expansion of the inner expansion. All we need to do is to interpret r differently and rearrange the terms according to their dependence on ϵ . Thus, if we consider that $r = O(1)$, the outer expansion of the one-term inner expansion is:

$$\begin{aligned} \phi(x, y, z) \sim \Phi_0(x, y, z) \sim & \underset{O(1)}{Ux} + \underset{O(\epsilon)}{\delta_0 \log r} + \underset{O(\epsilon)}{\eta_0 \tan^{-1} \frac{y}{x}} + \underset{O(\epsilon)}{A_{00}} \\ & + \underset{O(\epsilon^2)}{\frac{A_{01} \cos \theta}{r}} + \underset{O(\epsilon^2)}{\frac{B_{01} \sin \theta}{r}} + O(\epsilon^3). \quad (2-51') \end{aligned}$$

This obviously matches the one-term outer expansion, with an asymptotically small error which is $O(\epsilon)$.

We could keep two terms in (2-51'); that would be the two-term outer expansion of the one-term inner expansion, which would have to match the one-term inner expansion of the two-term outer expansion. From (2-51') and (2-45b), we thus construct the equality:

$$Ux + \delta_0 \log r + \eta_0 \tan^{-1} \frac{y}{x} + A_{00} = Ux + \frac{1}{2} \gamma_1(z) \left[1 - \frac{1}{\pi} \tan^{-1} \frac{y}{x} \right].$$

This can be true only if the following are separately true:

$$\delta_0 = 0; \quad \eta_0 = -\frac{1}{2\pi} \gamma_1(z); \quad A_{00} = \frac{1}{2} \gamma_1(z). \quad (2-52)$$

$$\phi(x, y, z) \sim \sum_{n=0}^N \Phi_n(x, y, z), \quad \Phi_{n+1} = o(\Phi_n) \quad \text{as } \epsilon \rightarrow 0, \\ \text{with } (x/\epsilon, y/\epsilon, z) \text{ fixed.} \quad (2-48)$$

The first term in this expansion satisfies the conditions:

$$\Phi_{0_{xx}} + \Phi_{0_{yy}} = 0 \quad \text{in the fluid region,} \quad (2-49)$$

$$\frac{\partial \Phi_0}{\partial N} = 0 \quad \text{on the body.} \quad (2-50)$$

From (2-45a), it is clear that the one-term inner expansion, $\phi(x, y, z) \sim \Phi_0(x, y, z)$, must match the one-term outer expansion, $\phi(x, y, z) \sim Ux$. Thus $\Phi_0(x, y, z)$ is the solution of a two-dimensional potential problem, and a rather conventional problem at that: In a section through the body drawn perpendicular to the spanwise axis, the potential satisfies the Laplace equation in two-dimensions, a homogeneous Neumann condition on the body, and a uniform-flow condition at infinity. The direction of the uniform flow is the same as the direction of the actual incident stream as viewed in the far field.

Since Φ_0 does satisfy the Laplace equation in two dimensions, the methods of complex-variable functions are available for determining its properties. In particular, if we assume that $\nabla \Phi_0$ is bounded everywhere in the fluid region and single-valued too, then Φ_0 can be expressed as the real part of an analytic function of a complex variable, the analytic function being such that its derivative can be expressed by a Laurent series. Thus, we can write for $\Phi_0(x, y; z)$:

$$\Phi_0(x, y; z) = Ux + \delta_0 \log r + \eta_0 \tan^{-1} \frac{y}{x} + A_{00} + \frac{A_{01} \cos \theta}{r} \\ + \frac{B_{01} \sin \theta}{r} + \frac{A_{02} \cos 2\theta}{r^2} + \frac{B_{02} \sin 2\theta}{r^2} + \dots, \quad (2-51)$$

where $r = (x^2 + y^2)^{1/2}$. The "constants" are all unknown functions of z , the spanwise coordinate. The first term represents a uniform stream at infinity, and I have already performed one matching to determine this term. The second and third terms represent a source and a vortex, respectively; the fourth term, a constant, is included for generality; the fifth and sixth terms represent a dipole; etc. Such an expansion as (2-51) is valid outside any circle about the origin which encompasses the body cross section.

I have taken the trouble of writing out the inner expansion of the outer expansion in three ways just to point out how, in this problem, there is an additional term in the lowest-order expression each time we add another term of higher order in the outer expansion. Each of the three terms included in (2-44) contributes to the ϵ term in (2-45c). This phenomenon occurs frequently, and its occurrence is the reason that one must proceed step-by-step in the matching. In the present problem, one would be in some difficulty if he tried to write down an arbitrary number of terms in each expansion and immediately start matching.

Next we formulate the near-field problem. Instead of making the formal changes of variable, $x = \epsilon X$ and $y = \epsilon Y$, we shall simply understand now that, in the near field,

$$x = O(\epsilon) \quad \text{and} \quad y = O(\epsilon); \quad \text{also} \quad \partial/\partial x = O(\epsilon^{-1}) \quad \text{and} \quad \partial/\partial y = O(\epsilon^{-1}).$$

Of course, differentiation with respect to z does not affect orders of magnitude.

The Laplace equation can be written in the form:

$$\phi_{xx} + \phi_{yy} = -\phi_{zz}, \quad (2-46)$$

where the right-hand side is ϵ^2 higher order than the left-hand side. The boundary condition on the body is:

$$0 = \phi_x(g_x \pm h_x) - \phi_y + \phi_z(g_z \pm h_z) \quad \text{on} \quad y = g \pm h. \quad (2-47)$$

The last condition is equivalent to requiring that $\partial\phi/\partial n = 0$ on the body, where $\partial/\partial n$ denotes differentiation in the direction normal to the body surface. An alternative statement is the following:

$$\frac{\partial\phi}{\partial N} = \frac{(\pm g_x + h_x)\phi_x \mp \phi_y}{\sqrt{1 + (g_x \pm h_x)^2}} = -\frac{(h_z \pm g_z)\phi_z}{\sqrt{1 + (g_x \pm h_x)^2}} \quad \text{on} \quad y = g \pm h, \quad (2-47')$$

where $\partial\phi/\partial N$ is the rate of change in a plane perpendicular to the z axis, measured in the direction normal to the body contour in that cross section plane. Note that the left-hand side is $O(\phi/\epsilon)$, since differentiation in the N direction has the same order-of-magnitude effect as differentiation with respect to x or y . The right-hand side, on the other hand, is $O(\phi\epsilon)$, since g and h are both $O(\epsilon)$.

Now let there be an inner expansion:

$$\gamma_1(z) = O(\epsilon); \quad \mu_1(z), \quad \lambda_1(z), \quad \gamma_2(z) = O(\epsilon^2);$$

also, all other terms in (2-40) are $o(\epsilon^2)$. These statements can all be proven. The description of the problem is greatly simplified, however, by their being assumed now.

We can write the three-term outer expansion now:

$$\phi(x, y, z) \sim Ux + \phi_1(x, y, z) + \phi_2(x, y, z), \quad (2-44)$$

where

$$\phi_1(x, y, z) = \frac{y}{4\pi} \int_{-S}^S \int_0^\infty \frac{\gamma_1(\xi) d\xi d\zeta}{[(x-\xi)^2 + y^2 + (z-\zeta)^2]^{3/2}}; \quad (2-44a)$$

$$\begin{aligned} \phi_2(x, y, z) = & \frac{y}{4\pi} \int_{-S}^S \int_0^\infty \frac{\gamma_2(\xi) d\xi d\zeta}{[(x-\xi)^2 + y^2 + (z-\zeta)^2]^{3/2}} \\ & + \frac{1}{4\pi} \int_{-S}^S \frac{[y\mu_1(\xi) + x\lambda_1(\xi)] d\xi}{[x^2 + y^2 + (z-\xi)^2]^{3/2}}. \end{aligned} \quad (2-44b)$$

The inner expansion of the one-term outer expansion is, of course:

$$\phi(x, y, z) \sim Ux, \quad [O(\epsilon)] \quad (2-45a)$$

to any number of terms. (Recall that $x = O(\epsilon)$ in the near field.) The inner expansion of the two-term outer expansion is:

$$\begin{aligned} \phi(x, y, z) \sim & Ux + \frac{1}{2} \gamma_1(z) \left[1 - \frac{1}{\pi} \tan^{-1} \frac{y}{x} \right] \quad [O(\epsilon)] \\ & - \frac{y}{4\pi} \int_{-S}^S \frac{d\zeta}{z-\zeta} \frac{\gamma_1'(\zeta)}{z-\zeta}. \quad [O(\epsilon^2)] \end{aligned} \quad (2-45b)$$

Finally, the inner expansion of the three-term outer expansion is:

$$\begin{aligned} \phi(x, y, z) \sim & Ux + \frac{1}{2} \gamma_1(z) \left[1 - \frac{1}{\pi} \tan^{-1} \frac{y}{x} \right] + \frac{y\mu_1(z) + x\lambda_1(z)}{2\pi(x^2 + y^2)} \quad [O(\epsilon)] \\ & - \frac{y}{4\pi} \int_{-S}^S \frac{d\zeta}{z-\zeta} \frac{\gamma_1'(\zeta)}{z-\zeta} + \frac{1}{2} \gamma_2(z) \left[1 - \frac{1}{\pi} \tan^{-1} \frac{y}{x} \right]. \quad [O(\epsilon^2)] \end{aligned} \quad (2-45c)$$

this term represents a distribution of vorticity extending to infinity both upstream and downstream. Thus, it leads to a discontinuity across the $y = 0$ plane, even upstream. The second term must compensate for this behavior, since there can be no discontinuities in the region $x < 0$.

2) The second term in brackets on the right-hand side of (2-41) must be considered carefully with respect to the branches of the square-root function. With a bit of effort, one can show that, as $r \rightarrow 0$, its contribution is:

$$\frac{\gamma(z)}{4} \left(1 - \frac{2}{\pi} \tan^{-1} \frac{y}{x} \right) (1 + O(\epsilon^2)), \quad 0 < \tan^{-1} \frac{y}{x} < \pi;$$

$$\frac{\gamma(z)}{4} \left(3 - \frac{2}{\pi} \tan^{-1} \frac{y}{x} \right) (1 + O(\epsilon^2)), \quad \pi < \tan^{-1} \frac{y}{x} < 2\pi.$$

Combining this result with the previous one, we find that the inner expansion of a lifting-line potential function can be written as follows:

$$\begin{aligned} & \frac{\gamma}{4\pi} \int_{-s}^s \int_0^\infty \frac{\gamma(\xi) d\xi d\zeta}{[(x-\xi)^2 + y^2 + (z-\zeta)^2]^{3/2}} \\ & \sim \left[\frac{1}{2} \gamma(z) \left[1 - \frac{1}{\pi} \tan^{-1} \frac{y}{x} \right] - \frac{\gamma}{4\pi} \int_{-s}^s \frac{d\zeta}{z-\zeta} \frac{\gamma'(\zeta)}{\zeta} \right] [1 + O(\epsilon^2)], \\ & \text{for } 0 < \tan^{-1} \frac{y}{x} < 2\pi. \quad (2-42) \end{aligned}$$

Inner expansion of the dipole-line potential: An integration by parts with respect to ζ transforms these integrals into an appropriate form so that one can let $r \rightarrow 0$ and thereby obtain the first terms in the desired expansions. Typical terms in the second and third sums of (2-40) have the following inner expansions:

$$\frac{1}{4\pi} \int_{-s}^s \frac{[y\mu(\xi) + x\lambda(\xi)] d\xi}{[x^2 + y^2 + (z-\xi)^2]^{3/2}} \sim \left[\frac{y\mu(z) + x\lambda(z)}{2\pi(x^2 + y^2)} \right] [1 + O(\epsilon^2 \log \epsilon)]. \quad (2-43)$$

Note the occurrence of the logarithm of ϵ !

Inner expansion of the outer expansion: In order not to confuse the picture, I shall make more assumptions now, namely:

The first of these three equations means only that there is no net source strength in the 2-D problem. The second relates the 2-D vortex strength, η_0 , to the dipole density, γ_1 , in the far field. The latter can obviously be interpreted also as a vortex strength. The third quality relates the "constant" term, A_{00} , in the near-field solution to the far-field solution's dependence on z , the spanwise coordinate. It is important to include such a term as this in the near-field solution, because it provides a three-dimensional effect in the otherwise two-dimensional problems.

Presumably, the near-field problem can be solved somehow. If the body is simple enough, an analytic solution may be obtainable; with the available powerful methods of the theory of functions of a complex variable, it is even reasonable to hope to find such solutions. However, even if numerical methods must be used, the solution can be found. Then all of the constants in (2-51) except A_{00} are known. The constant of most interest at this moment is η_0 ; it will be non-zero only if some mechanism has been included that can generate and determine a circulation around the body. I shall assume that a Kutta condition is available for this purpose, since the present section is concerned with wings. Then, with η_0 known, we can find the first approximation to the vorticity (and dipole density) in the far field, by means of (2-52). At the same time, A_{00} is determined.

Nothing more can be done now unless we find a higher-order term in either the near- or far-field expansion. It is interesting to pursue the near-field solution further first.

When we substitute the expansion, (2-48), into the Laplace equation, (2-46), and keep only leading-order terms, we obtain the partial differential equation for Φ_1 :

$$\Phi_{1xx} + \Phi_{1yy} = -\Phi_{0zz}, \quad \text{in the fluid domain.}$$

Now Φ_0 was found to be $O(\epsilon)$, and we might reasonably expect that Φ_1 would be $O(\epsilon^2)$. In fact, this turns out to be quite correct. In the equation just above, this means that the left-hand side is $O(1)$ and the right-hand side is $O(\epsilon)$. Asymptotically, then, we have that:

$$\Phi_{1xx} + \Phi_{1yy} = 0 \quad \text{in the fluid domain.}$$

We again have a purely two-dimensional boundary-value problem to solve, if we can state the boundary conditions appropriately. From (2-47'), we find by the same arguments that:

$$\frac{\partial \Phi_1}{\partial N} = 0 \quad \text{on the body.}$$

We do not know the conditions at infinity yet, but let us assume that the condition on Φ_1 is similar to that on Φ_0 , i.e., the gradient of Φ_1 should be bounded.

This problem is identical to the Φ_0 problem, and so we can represent its solution outside of some circle by another series like the one in (2-51). We have not determined yet what the coefficients of the increasing terms are like, and so we allow two more arbitrary terms (the first two terms in the following):

$$\begin{aligned} \Phi_1(x, y; z) = & \alpha_1 x + \beta_1 y + \delta_1 \log r + \eta_1 \tan^{-1} \frac{y}{x} + A_{10} + \frac{A_{11} \cos \theta}{r} \\ & + \frac{B_{11} \sin \theta}{r} + \frac{A_{12} \cos 2\theta}{r^2} + \frac{B_{12} \sin 2\theta}{r^2} + \dots \quad (2-53) \end{aligned}$$

All terms must be the same order of magnitude if $r = O(\epsilon)$. Assuming that order to be ϵ^2 , we have:

$$\alpha_1, \beta_1 = O(\epsilon); \quad \delta_1, \eta_1, A_{10} = O(\epsilon^2); \quad A_{11}, B_{11} = O(\epsilon^3); \text{ etc.}$$

With this information in hand, we combine the first two terms in the inner expansion and then we obtain the outer expansion of the two-term inner expansion:

$$\begin{aligned} \phi(x, y, z) \sim & Ux \quad O(1) \\ & + \eta_0 \tan^{-1} \frac{y}{x} + A_{00} + \alpha_1 x + \beta_1 y \quad O(\epsilon) \\ & + \frac{A_{01} \cos \theta}{r} + \frac{B_{01} \sin \theta}{r} + \delta_1 \log r + \eta_1 \tan^{-1} \frac{y}{x} + A_{10} \quad O(\epsilon^2) \end{aligned} \quad (2-54)$$

First we can keep just the first two orders of magnitude and match them with the two-term inner expansion of the two-term outer expansion, given in (2-45b). Using (2-52), we see that everything already matches except for the terms $\alpha_1 x + \beta_1 y$ and the integral in (2-45b). For these to match, we require that:

$$\alpha_1 = 0; \quad \beta_1 = -\frac{1}{4\pi} \int_S^S \frac{d\zeta}{z - \zeta} \gamma_1'(\zeta). \quad (2-55)$$

Physically, this means that the Φ_1 problem should have had as the condition at infinity:

$$|\Phi_1 - \beta_1 y| \rightarrow 0 \quad \text{as} \quad r \rightarrow \infty,$$

that is, there is a uniform stream at infinity, moving at a right angle to the actual incident uniform stream. This is the downwash velocity. With this condition at infinity known, the Φ_1 problem can be solved by the same method used for the Φ_0 problem, and all of the terms in (2-53) are then known, except A_{10} .

We have all of the information available to match the three-term outer expansion of the two-term inner expansion with the two-term inner expansion of the three-term outer expansion. Using (2-45c) and all of the terms in (2-54), we obtain the equation:

$$\begin{aligned} Ux + \eta_0 \tan^{-1} \frac{y}{x} + A_{00} + \beta_1 y + \frac{A_{01} \cos \theta}{r} + \frac{B_{01} \sin \theta}{r} + \delta_1 \log r + \eta_1 \tan^{-1} \frac{y}{x} \\ + A_{10} = Ux + \frac{1}{2} \gamma_1(z) \left[1 - \frac{1}{\pi} \tan^{-1} \frac{y}{x} \right] + \frac{y\mu_1(z) + x\lambda_1(z)}{2\pi(x^2 + y^2)} \\ - \frac{y}{4\pi} \int_{-s}^s \frac{d\zeta}{z - \zeta} \frac{\gamma_1'(\zeta)}{\zeta} + \frac{1}{2} \gamma_2(z) \left[1 - \frac{1}{\pi} \tan^{-1} \frac{y}{x} \right]. \end{aligned}$$

The unknown quantities are: A_{10} , μ_1 , λ_1 , γ_2 . This equation is satisfied only if:

$$\delta_1 = 0; \quad \eta_1 = -\frac{1}{2\pi} \gamma_2(z); \quad A_{10} = \frac{1}{2} \gamma_2(z);$$

$$\mu_1(z) = 2\pi B_{01}; \quad \lambda_1(z) = 2\pi A_{01}.$$

From this matching step, we see that all quantities introduced so far are now completely known. There is no source strength in the second approximation*; there is a correction to the vorticity in the far-field description; there is a correction to the "constant" in the near-field problem; and the density of both vertical and longitudinal dipoles in the far field is known. It is interesting to note that the last were determined entirely from the lowest-order near-field solution, that is, from Φ_0 . When quadripoles first enter, it will be found that they too are determined in strength from Φ_0 solely.

The next term would be much more difficult to obtain, since, in the near field, it entails solving a Poisson equation in which the

*It would have been possible to eliminate the $\delta \log r$ terms in both problems above by noting that the body boundary conditions allow for no net source strength.

nonhomogeneous part depends on Φ_0 , which we have not obtained explicitly. (The right-hand side of (2-46) finally has an effect.) Also, spanwise effects occur in the body boundary condition, (2-47), for the first time. Therefore I shall put this problem to rest at this point. Table 2-2 shows the sequence of steps that we have followed in this problem.

TABLE 2-2
HIGH-ASPECT-RATIO WING -- SUMMARY

Terms	Far-Field Expansion	Near-Field Expansion	Quantity Determined by Matching
1	$\phi_0 = Ux$	Φ_0	1 Condition at infinity for Φ_0 problem 2 Vorticity, $\gamma_1(z)$, in far field
2	$\phi_0 + \phi_1$	$\Phi_0 + \Phi_1$	3 Downwash velocity (condition at infinity for Φ_1 problem) 4 Correction to vorticity in far field; densities of vertical, horizontal dipoles in far field
3	$\phi_0 + \phi_1 + \phi_2$		

One point in particular should be noted: The near-field problem was not linearized. If one can predict the flow around the two-dimensional forms which appear in the near-field problem, one is not limited to consideration of, say, thin wings. All that is necessary is that the spanwise length be much greater than the dimensions in the two-dimensional problems and that there be gradual change in the body and flow geometry in the spanwise direction. Needless to say, the latter condition is usually violated at the wing tips, and so the analysis breaks down there. It may be hoped that the prediction of important physical quantities is not affected too seriously thereby, but higher and higher approximations certainly cannot be found until the extra singularities at the tips are removed somehow.

2.3. Slender Body

In the previous section, we considered the flow around a slender body which was oriented with its long dimension perpendicular to the incident flow. Now we consider the flow around a slender body which is oriented with its long dimension approximately parallel to the incident flow. The same geometrical restrictions will be applied to the body in this problem, namely, that its transverse dimensions should be small compared with its long dimension and that cross-section shape, size, and orientation should vary gradually along the length.

Although both this section and the previous section concern slender bodies in an incident flow, convention says that only this section really presents "slender-body theory."

In ship hydrodynamics problems, slender-body theory has been applied mostly to nonlifting bodies, i. e., bodies not generating trailing vortex systems.* I shall limit myself here to such problems too. Specifically, I assume that there is no separation of the flow from the body; furthermore, there are no sharp edges at which a Kutta condition might be applied. The potential function should be continuous and single-valued throughout the fluid domain.

This restriction is not generally desirable. Certainly an important aspect of aerodynamics is the calculation of lift on a slender body which does generate a vortex wake; modern high-speed delta-wing aircraft and many slender missiles are genuine slender lifting bodies. There are several important ship-hydrodynamics problems which may ultimately be best analyzed by a slender-wing[†] approach. Most important, perhaps, is the problem of a maneuvering ship. An attempt is made in this direction by Fedyayevskiy and Sobolev [1963], but it is not very successful because they use the conventional methods of slender-wing theory, and these break down in application to wings which are not more-or-less delta shaped.[‡] A modern approach to slender-wing theory is given by Wang [1968].

* Obviously, a ship is a "lifting body," but I think it is commonly understood that the term implies a dynamic lift process, and that is the way I use it.

[†] "Slender wing," "wing of very low aspect ratio," and "slender lifting surface" are all equivalent terms in my usage.

[‡] Conventional slender-wing theory can be used for wings in which the span increases monotonically downstream, ending in a squared-off trailing edge. If the incident stream is uniform and steady, the wing does not have to end at the location of the maximum span, but the part of the wing aft of this location must be uncambered. Not all of these conditions are satisfied in the interesting ship maneuvering problems.

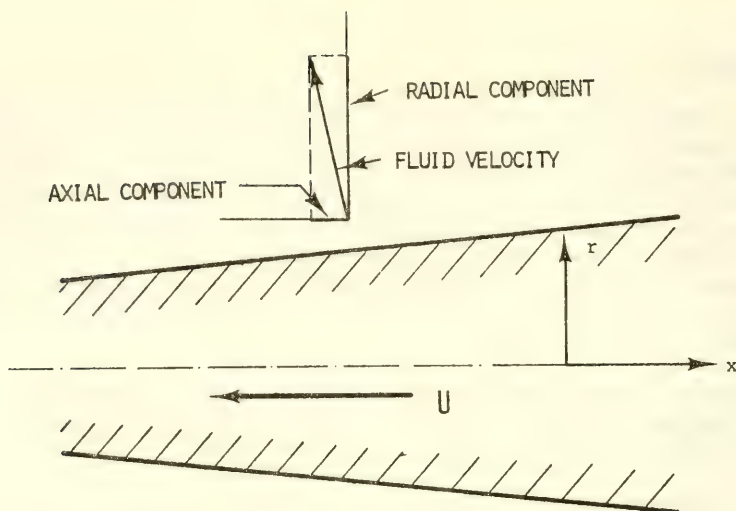


Fig. (2-2). Fluid Velocity Near a Slender Body in Steady Motion

The physical ideas behind slender-body theory were developed fifty years ago, and the original way of looking at this problem is perhaps still the best way. Take a reference frame which is fixed with respect to the fluid at infinity. As a slender body moves past, one may imagine that its greatest effect on the fluid is to push it aside; the body also imparts to the fluid a velocity component in the axial direction, but this component should be quite small compared with the transverse component. Both components should be small compared with the forward speed of the body.

In modern slender-body theory, we attempt to formalize this estimate of the relative velocity-component magnitudes. We devise a procedure that automatically arranges velocities in the anticipated order:

- 1) Forward speed
- 2) Transverse perturbation
- 3) Longitudinal perturbation

When this pattern comes out of the boundary-value problem, we then investigate further to see what other patterns follow from the same assumptions. The whole body of assumptions, results, and intermediate mathematics constitute what we call "slender-body theory."

In aerodynamics, the original intuitive approach of Munk was not completely displaced until the late 1940's. The newer, more systematic approach which developed then is described well by Ward

[1955]. For the first time, it was possible to predict with some confidence how the flow around the various cross sections interacted. There were some difficulties in principle, even with the new approach; what we now call the "outer expansion" of the problem was in effect forced to satisfy body boundary conditions. The difficulty is somewhat comparable to trying to force a Laurent-series solution to satisfy prescribed conditions which are stated on a contour inside the minimum circle of convergence. A readable, refreshing account of slender-body theory in the 1950's has been provided by Lighthill [1960].

During the early 1960's, slender-body theory was applied to ship hydrodynamics problems by several investigators. Probably the earliest to try this on a major scale was Vossers [1962]; he attacked a variety of steady- and unsteady-motion problems by slender-body theory. He used a Green's function approach, which apparently avoids the fundamental difficulty in principle of the previous method. However, it is really too much to hope to obtain asymptotic estimates of five-fold integrals -- without making mistakes. Apparently Vossers did hope for too much, but Joosen [1963] and [1964] corrected many of his mistakes. Newman [1964] also advocated the Green's-function approach and produced some interesting results.

The modern (i.e., fashionable) alternative is to use the method of matched asymptotic expansions. In ship hydrodynamics, Tuck [1963a] first used this method in his doctoral thesis at Cambridge University. It avoids the difficulties in principle of Ward's approach, and it is easier to work with than the Green's-function method. Of course, the method of matched asymptotic expansions has its own set of difficulties of principle. However, it is the method that I shall pursue here.*

In any case, the analysis can be no better than the assumptions which are made at the beginning. Therefore I shall be (perhaps painfully) explicit about the assumptions.

2.31. Steady Forward Motion. Let the body surface be specified by the equation:

* A very recent account of slender-body theory, particularly with respect to its applications in ship hydrodynamics, has been published by Newman [1970]. I think that his presentation and mine generally complement each other (and perhaps occasionally contradict too). Newman has provided a survey that seems comparable in intent to the one by Lighthill [1960], mentioned above, whereas I am trying to place slender-body theory into a hierarchy of singular perturbation problems. My emphasis is on the development and application of the method of solution.

$$r = r_0(x, \theta) \quad x \quad \text{in} \quad \Lambda,$$

where $r = (y^2 + z^2)^{1/2}$, and θ is an angle variable measured about the x axis. It will be assumed that $r = O(\epsilon)$. In this section, I take the most conventional definition of θ , namely, that it be measured in a right-handed sense from the y axis. (In ship problems, it is more convenient to measure the angle from the negative vertical axis.) Λ is the part of the x axis which coincides with the longitudinal extent of the body; typically, one might take it to be the interval, $-L/2 < x < L/2$, but I shall not insist that the origin be located at the mid-length section. Figure 2-3 shows a typical cross section.

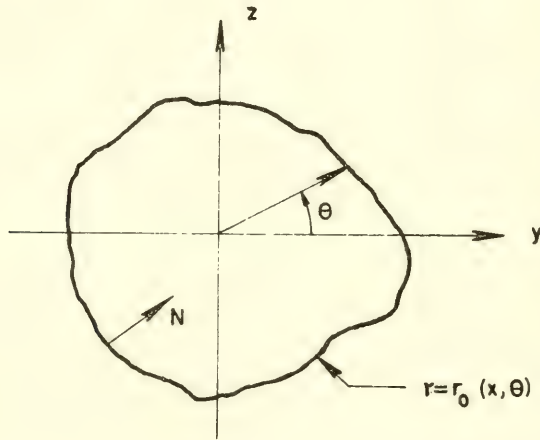


Fig. (2-3). Cross Section of the Slender Body

As usual, assume that there exists a velocity potential, $\phi(x, y, z)$, which satisfies the Laplace equation. There is an incident stream which, in the absence of the body, is a uniform flow in the positive x direction, with the velocity potential Ux . It will be convenient to use cylindrical coordinates, (x, r, θ) , in which case the Laplace equation takes the form:

$$\phi_{rr} + \frac{1}{r} \phi_r + \frac{1}{r^2} \phi_{\theta\theta} + \phi_{xx} = 0, \quad \text{for} \quad r > r_0(x, \theta). \quad (2-57)$$

The kinematic boundary condition on the body can be written:

$$\phi_x r_{0x} - \phi_r + \frac{1}{r_0} \phi_\theta r_{0\theta} = 0 \quad \text{on} \quad r = r_0(x, \theta). \quad (2-58)$$

With respect to the physical arguments presented at the

beginning of the section, note that our frame of reference is now moving with the body. Therefore, the velocity components should be ordered:

$$\partial\phi/\partial x \sim U = O(1); \quad \partial\phi/\partial y, \partial\phi/\partial z, \partial\phi/\partial r = o(1);$$

$$\partial(\phi - Ux)/\partial x = o(\partial\phi/\partial r).$$

In each case, of course, the appropriate limit operation is that $\epsilon \rightarrow 0$, where ϵ is the slenderness of the parameter. These order relations should be valid near the body.

Far away, there will be the uniform stream, which is $O(1)$, but there is no reason to assume that the perturbation velocity will have components with differing orders of magnitude.

These order-of-magnitude relations all come about automatically if, in the near field, we define new variables:

$$r = \epsilon R, \quad y = \epsilon Y, \quad z = \epsilon Z,$$

and assume that differentiation with respect to x, Y, Z, R , and θ all have no effect on the order of magnitude of a quantity. Thus, suppose that the potential in the near field can be written: $\phi(x, y, z) = Ux + \Phi(x, Y, Z)$. Then the derivatives have the following orders of magnitude:

$$\frac{\partial\phi}{\partial x} = U + \frac{\partial\Phi}{\partial x} = O(1) + O(\Phi); \quad \frac{\partial\phi}{\partial y} = \frac{\partial\Phi}{\partial y} = \frac{1}{\epsilon} \frac{\partial\Phi}{\partial Y} = O(\Phi/\epsilon);$$

$$\frac{\partial\phi}{\partial z} = O(\Phi/\epsilon); \quad \frac{\partial\phi}{\partial r} = O(\Phi/\epsilon).$$

It will turn out that $\Phi = O(\epsilon^2)$. This means that the transverse velocity components, ϕ_y, ϕ_z , and ϕ_r are all $O(\epsilon)$, that is, they are proportional to the slenderness parameter. Note also that a circumferential velocity component would be given by $(1/r)\partial\phi/\partial\theta = (1/\epsilon R)\partial\Phi/\partial\theta = O(\Phi/\epsilon)$, when we interpret $R = O(1)$ (that is, in the near field), and so circumferential and radial velocity components have the same order of magnitude. The perturbation of the longitudinal velocity component is $O(\Phi) = O(\epsilon^2)$, which is, appropriately, a higher order of magnitude than that of the transverse velocity components.

In the far field, we assume that differentiation with respect to any of the natural space variables has no order-of-magnitude effect. Thus, we use the Cartesian coordinates (x, y, z) and the

cylindrical coordinates (x, r, θ) in a very conventional manner. As $\epsilon \rightarrow 0$, the slender body becomes more and more slender, shrinking down to a line which coincides with part of the x axis. (This is the line segment that I defined as Λ previously.) In the limit, there is no body at all and thus no disturbance of the incident uniform flow. In the far field, the disturbance is always $o(1)$. Therefore the far field consists of the entire space except the x axis, and the potential function must satisfy the Laplace equation everywhere except possibly on the x axis.

At infinity, it is reasonable to require that the perturbation of the incident flow should vanish, which implies that the perturbation potential must be regular even at infinity. A velocity potential cannot be regular throughout space, including infinity, unless it is trivial. Therefore the velocity potential must be singular somewhere, and the only place in the far field where such behavior is permitted is on the x axis. Our far-field slender-body problems all reduce to finding appropriate singularity distributions on the x axis.

The Far-Field Singularity Distributions. In the far field, the first term in the asymptotic expansion for the potential function will be Ux . All of the following terms must represent flow fields for which the velocity approaches zero at infinity; they represent distributions of singularities on the x axis. The nature of the singularities can only be determined in the matching process, and so we must generally be prepared to handle all kinds of singularities.

One of the easier ways of doing this is to apply a Fourier transform to the Laplace equation, replacing the x dependence by a wave-number dependence. The resulting partial differential equation in two dimensions can be solved by separation of variables in cylindrical coordinates. When we require that the potential functions be single valued, we find that the solutions must all be products of:

$$K_n(|k|r) \quad \text{or} \quad I_n(|k|r) \quad \text{and} \quad \sin n\theta \quad \text{or} \quad \cos n\theta,$$

where K_n and I_n denote modified Bessel functions. Since I_n is poorly behaved when its argument is large, we reject it, so that the solution consists of terms:

$$K_n(|k|r)[\alpha \cos n\theta + \beta \sin n\theta].$$

The quantities α and β are constants with respect to r and θ , but they are both functions of k . They also depend on the index n , of course. The general solution is obtained by combining all such possible solutions. Any term in the far-field expansion of the potential function might be of the form:

$$\phi_m(x, y, z) = \frac{1}{2\pi} \sum_{n=0}^{\infty} \int_{-\infty}^{\infty} dk e^{ikx} K_n(|k|r) [a_{mn}^*(k) \cos n\theta + b_{mn}^*(k) \sin n\theta], \quad (2-59)$$

where $a_{mn}^*(k)$ and $b_{mn}^*(k)$ are unknown functions. The most general far-field expansion comprises the incident-flow potential, Ux , and a sum of terms like the above, that is,

$$\phi(x, y, z) \sim Ux + \sum_{m=1}^M \phi_m(x, y, z) \quad \text{for fixed } (x, y, z) \quad \text{as } \epsilon \rightarrow 0. \quad (2-60)$$

It will be necessary to have the inner expansion of the outer expansion. This means that we must interpret r to be $O(\epsilon)$ in the above expressions, instead of $O(1)$ as heretofore, and rearrange terms according to their dependence on ϵ . The easiest procedure is to replace any of the K_n functions in (2-59) by its series expansion for small argument. We obtain formulas such as the following:

$n = 0$:

$$\begin{aligned} & \frac{1}{2\pi} \int_{-\infty}^{\infty} dk e^{ikx} K_0(|k|r) a_{m0}^*(k) \\ & \sim -\frac{\log r}{2\pi} \int_{-\infty}^{\infty} dk e^{ikx} a_{m0}^*(k) - \frac{1}{2\pi} \int_{-\infty}^{\infty} dk e^{ikx} a_{m0}^*(k) \log \frac{C|k|}{2}; \end{aligned} \quad (2-61a)$$

$n > 0$:

$$\begin{aligned} & \frac{1}{2\pi} \int_{-\infty}^{\infty} dk e^{ikx} K_n(|k|r) a_{mn}^*(k) \begin{pmatrix} \cos \\ \sin \end{pmatrix} n\theta \\ & \sim \frac{2^{n-1} (n-1)!}{2\pi r^n} \begin{pmatrix} \cos \\ \sin \end{pmatrix} n\theta \int_{-\infty}^{\infty} \frac{dk}{|k|^n} e^{ikx} a_{mn}^*(k). \end{aligned} \quad (2-61b)$$

Physically, the $n = 0$ integral represents the potential for a line of sources. This can be seen directly from (2-61a): As $r \rightarrow 0$, the function is proportional to $\log r$, which is the potential function for a source in two dimensions. However, the strength of the apparent 2-D source is a function of x . In fact, the integral defining that strength is identical to the integral which gives the inverse of a Fourier transform. Let $a_{m0}(x)$ be the function having $a_{m0}^*(k)$

as its Fourier transform, and further define:

$$\sigma_m(x) \equiv -2\pi a_{m0}(x).$$

Then the result in (2-61a) can be rewritten:

$$\frac{1}{2\pi} \int_{-\infty}^{\infty} dk e^{ikx} K_0(|k|r) a_{m0}^*(k) \sim \frac{1}{2\pi} \sigma_m(x) \log r - \frac{1}{4\pi} f_m(x), \quad (2-61a')$$

where

$$f_m(x) = \int_{-\infty}^{\infty} d\xi \sigma_m'(\xi) \log 2|x-\xi| \operatorname{sgn}(x-\xi). \quad (2-61a'')$$

By manipulating the full integral containing K_0 , one can also show that:

$$\frac{1}{2\pi} \int_{-\infty}^{\infty} dk e^{ikx} K_0(|k|r) a_{m0}^*(k) = -\frac{1}{4\pi} \int_{-\infty}^{\infty} \frac{\sigma_m(\xi) d\xi}{[(x-\xi)^2 + r^2]^{1/2}}, \quad (2-62)$$

which is easily recognized as the potential function for a line distribution of sources.

Similarly, the other integrals can be interpreted in terms of dipoles, quadripoles, etc. In particular, we see that for $n=1$ the inner expansion of the integral reduces to the potential in two dimensions for a dipole. We may consider the variable x as a parameter, and then we have a different 2-D dipole strength at each x .

The Sequence of Near-Field Problems. In the near field, we can formalize our procedure by making the changes of variables already mentioned, $r = \epsilon R$, $y = \epsilon Y$, $z = \epsilon Z$, then assuming that differentiation with respect to R , Y , or Z does not affect orders of magnitude. Instead of doing this, I shall simply retain the ordinary variables, r , y , and z , and I ask the reader to recall that differentiation with respect to any of these three variables causes a change in order of magnitude. Thus, for example, $\partial \phi / \partial r = O(\phi/\epsilon)$ in the near field.

In cylindrical coordinates, the Laplace equations and the body boundary condition can be written as follows:

$$[L] \quad \phi_{rr} + \frac{1}{r} \phi_r + \frac{1}{r^2} \phi_{\theta\theta} = -\phi_{xx}; \quad (2-57')$$

$$[H] \quad \frac{\partial \phi}{\partial N} = \mathbf{N} \cdot \nabla \phi = \frac{-\phi_r + (1/r_0^2) r_{0\theta} \phi_\theta}{\sqrt{[1 + (r_{0\theta}/r_0)^2]}} = \frac{\phi_x r_{0x}}{\sqrt{[1 + (r_{0\theta}/r_0)^2]}}$$

on $r = r_0(x, \theta)$. (2-58')

The definition of \mathbf{N} is analogous to that in (2-47'). It is a unit vector lying in the cross section plane at some x , perpendicular to the contour of the body in that cross section. It has the three components:

$$\mathbf{N} = \frac{(0, -1, r_{0\theta}/r_0)}{\sqrt{[1 + (r_{0\theta}/r_0)^2]}},$$

measured in the x , r , and θ directions, respectively. Equation (2-58'), like (2-58), expresses the fact that $\partial \phi / \partial n = 0$, where \mathbf{n} is the unit vector normal to the body surface.

Let the inner expansion be expressed as follows:

$$\phi(x, y, z) \sim \sum_{n=0}^N \Phi_n(x, y, z) \quad \text{as } \epsilon \rightarrow 0 \quad \text{for fixed } (x, y/\epsilon, z/\epsilon).$$

Substitute this expansion into the [L] and [H] conditions above:

$$[L] \quad \nabla_{y,z}^2 (\Phi_0 + \Phi_1 + \Phi_2 + \Phi_3 + \dots) = -(\Phi_{0xx} + \Phi_{1xx} + \dots);$$

$$[H] \quad \frac{\partial \Phi_0}{\partial N} + \frac{\partial \Phi_1}{\partial N} + \frac{\partial \Phi_2}{\partial N} + \dots = -\frac{r_{0x}(\Phi_{0x} + \Phi_{1x} + \dots)}{\sqrt{[1 + (r_{0\theta}/r_0)^2]}};$$

The operator $\nabla_{y,z}^2$ is the 2-D Laplacian in the y - z plane, that is,

$$\nabla_{y,z}^2 \equiv \frac{\partial^2}{\partial y^2} + \frac{\partial^2}{\partial z^2} = \frac{\partial^2}{\partial r^2} + \frac{1}{r} \frac{\partial}{\partial r} + \frac{1}{r^2} \frac{\partial^2}{\partial \theta^2}.$$

It can be proven that the first term in the expansion, Φ_0 , represents just the uniform stream:

$$\Phi_0(x, y, z) = Ux.$$

This appears so obvious that I pass on immediately to the Φ_1 problem. From the [L] and [H] conditions, we find:

$$[L_1] \quad \nabla_{y,z}^2 \Phi_1 = 0 \quad \text{in the fluid domain;}$$

$$[H_1] \quad \frac{\partial \Phi_1}{\partial N} = - \frac{U r_{0x}}{\sqrt{[1 + (r_{0\theta}/r_0)^2]}} \quad \text{on} \quad r = r_0. \quad (2-63)$$

Finding Φ_1 is strictly a problem in two dimensions. In fact, it is just the problem that the early aerodynamicists put forth intuitively at the beginning of their slender-body analysis. (It was also the end of their analysis!) For an arbitrary body shape, we might have to solve this boundary-value problem numerically; that is not much of a problem today. However, we are not yet ready to work with numbers, because the formulation of the problem is not quite complete: we have not specified the behavior of Φ_1 at infinity. To do so requires that we match the unknown solution of this problem to the far-field expansion.

First, note what (2-63) tells us about the order of magnitude of Φ_1 . The right-hand member is $O(\epsilon)$ and the left-hand member is $O(\Phi_1/\epsilon)$ (because of the differentiation in the transverse direction), which together imply:

$$\Phi_1 = O(\epsilon^2).$$

Actually, (2-63) says only that Φ_1 cannot be higher order than ϵ^2 ; it could be lower order if the matching introduced some effect that required ϵ^2 to be $o(\Phi_1)$, but this does not happen.

This Φ_1 problem is remarkably similar to the Φ_0 problem in Section 2.2. If we can assume that $\nabla \Phi_1$ is bounded at infinity, then we can express Φ_1 in a series just like the one in (2-51). Whether $\nabla \Phi_1$ really is bounded at infinity can only be determined from the matching, of course, but we go ahead with the assumption, trusting that our method will show us if we have made unwarranted assumptions.

It should be noted too that there are important differences between this problem and the problem of Section 2.2. The Neumann-type of condition on the body was homogeneous there, but it is not homogeneous here. Thus, one may expect that there may be a non-zero net source strength inside the body in the present problem. What happens at infinity is also different. In the earlier problem, the potential had to represent a uniform flow at infinity, and we supposed that there might be the proper circumstances that a circulation flow could occur. In the present problem, the uniform flow

at infinity has been included in Φ_0 , and so we might expect that Φ_1 will represent a flow with velocity vanishing at infinity, and there appears to be no reason to expect a circulation in the 2-D problem.

It would be tedious to go through the same arguments that were used previously, and so I shall only summarize the results that would be obtained after a careful matching process. In the near field, Φ_1 does indeed yield a velocity field which is bounded in magnitude at infinity, and there is no circulation. Thus, it can be represented by the series:

$$\Phi_1(x, y, z) = C_1 + \frac{A_{10}}{2\pi} \log r + \frac{A_{11} \cos \theta + B_{11} \sin \theta}{2\pi r} + \dots \quad (2-64)$$

The "constants" are all functions of x . In the near field, all terms must be the same order of magnitude, by definition, and so A_{11} and B_{11} are $O(\epsilon A_{10})$. (I am, as usual, ignoring quantities which are $O(\log \epsilon)$.) In the matching, the $1/r$ terms are lost in the first round, and the $\log r$ and constant terms are forced to match the inner expansion of the outer expansion.

In the outer expansion, (2-60), only a line of sources in the ϕ_1 term of (2-60) can match the near-field expansion properly. That is, in (2-59) and (2-60), we have the following:

$$a_{1n}^*(k) = b_{1n}^*(k) = 0 \quad \text{except for } n = 0.$$

The two-term outer expansion and its two-term inner expansion are:

$$\phi(x, y, z) \sim Ux + \frac{1}{2\pi} \int_{-\infty}^{\infty} dk e^{ikx} K_0(|k|r) a_{10}^*(k) \quad (2-65a)$$

$$\sim Ux + \frac{1}{2\pi} \sigma_1(x) \log r - \frac{1}{4\pi} f_1(x), \quad (2-65b)$$

where (2-61a') has been used to express the latter.

Matching between the near-field and far-field then shows that:

$$A_{10} = \sigma_1(x) \quad (2-66a)$$

$$C_1 = -\frac{1}{4\pi} f_1(x). \quad (2-66b)$$

In obtaining an actual solution, one proceeds through the following steps: 1) Matching shows that Φ_1 represents a flow with bounded velocity at infinity. 2) Then the Φ_1 problem is completely

formulated and can be solved. 3) From the solution of the Φ_1 problem, the function $A_{10}(x)$ can be determined, which, through the matching, gives $\sigma_1(x)$, and the far-field two-term expansion is known. 4) From the matching relation for $C_1(x)$, along with formula (2-61a"), the near-field potential is known completely to two terms, and the $C_1(x)$ term includes the most important effects of interaction among sections. This sequence of steps shows what an intimate relationship exists between near- and far-field expansions.

The source strength, $\sigma_1(x) = A_{10}(x)$, can be computed without the necessity of solving the flow problem. In the near-field picture, draw a circle which encloses the body section. The net flux rate across this circle is just A_{10} . From the body boundary condition, (2-63), one can show that there is a net flux rate across the body surface, and it is given by $Us'(x)$, where:

$$s(x) = \frac{1}{2} \int_0^{2\pi} d\theta \, r_0^2(x, \theta) = \text{cross section area at } x. \quad (2-67a)$$

The two fluxes must be equal, and so we find that:

$$\sigma_1(x) = A_{10}(x) = Us'(x). \quad (2-67b)$$

Thus, the source strength is proportional to the rate of change with x of the body cross sectional area.

I shall not pursue the solution to higher order of magnitude, although there is no insuperable difficulty in doing so. Rather, I prefer to point out several interesting facts about the solution and then close this section.

In the far field, the solution to two terms is axially symmetric, although the body is not a body of revolution. The near-field two-term expansion is not symmetric in this way unless the body is circular and is aligned with the incident flow. However, the near-field solution can be represented by the series,

$$\phi(x, y, z) \sim Ux + \frac{\sigma_1(x)}{2\pi} \log r - \frac{1}{4\pi} f_1(x) + \frac{A_{11} \cos \theta + B_{11} \sin \theta}{2\pi r} + \dots,$$

and, at large r , the axially symmetric terms dominate this series.

If the far-field expansion is carried to three terms, it will be found that the third term can be interpreted in terms of a line of dipoles, both vertically and horizontally oriented. Such terms will be of the form given in (2-61b), with $n = 1$; they contain unknown functions $a_{21}^*(k)$ and $b_{21}^*(k)$, which must be determined through matching. These unknown functions will depend entirely on the

solution of the Φ_1 problem discussed above. In fact, one finds explicitly that:

$$A_{11}(x) = \int_{-\infty}^{\infty} \frac{dk}{|k|} e^{ikx} a_{21}^*(k); \quad B_{11}(x) = \int_{-\infty}^{\infty} \frac{dk}{|k|} e^{ikx} b_{21}^*(k).$$

Thus, the two-term inner expansion contains enough information to determine the strength of the dipoles which appear in the third term of the far-field expansion. The same inner expansion would determine the strengths of quadripoles in the fourth term of the far-field expansion, etc., etc.

On the other hand, the far-field expansion (even at the second term) contains much information about three-dimensional effects, information which is largely lacking in the near-field expansion. I have already pointed out that only the "constant" term contains important information about 3-D effects in the two-term near-field expansion. The rest of the Φ_1 solution depends on just the shape of the local section and the local rate of change of section shape and size. If higher-order near-field terms are found, it will be seen that they are influenced even by the two-term outer expansion. In fact, the "constant" term in Φ_1 can be interpreted as a modification to the incident stream, caused by the presence of all the other cross sections of the body. The effects of this extra incident flow on the transverse velocity field are not perceived until one finds a higher order expansion of the solution in the near field.

The briefest account of slender-body theory would be seriously lacking without mention of the possibly catastrophic effects of body ends. If a body has a blunt end, then $s(x)$ increases linearly in some neighborhood of the end. Accordingly, $s'(x)$ is discontinuous, jumping from a value of zero just beyond the end to a finite value at the end. This is an obvious violation of our assumptions about "slenderness." But trouble develops even without a blunt-ended body. For example, if the tip is pointed (but not cusped), there will still be a stagnation point right at the point. Thus this case violates the assumption that longitudinal perturbation of the incident flow velocity is a second-order quantity.

Sometimes these end effects can be overlooked with impunity. There are major examples later in this paper. However, even when we have such luck, we must be prepared to have higher-order expansions go awry.

2.32. Small-Amplitude Oscillations at Forward Speed. In this section, we consider the same kind of body as in Section 2.31, namely, a slender body which is aligned approximately with an incident stream. However, now we formulate a time-dependent problem in which the body performs small-amplitude oscillations while it moves through the fluid.

It would be entirely feasible to consider the general problem in which the body oscillates with the six degrees of freedom of a rigid body. (We could even include more degrees of freedom by allowing deformations of the body.) However, the major concepts should be clear if we allow only two degrees of freedom, a) a lateral translation, comparable to the heave or sway of a ship, and b) a rotation, like the pitch or yaw of a ship.

In this section, I shall depart from my usual approach and first treat the problem for a perfectly general body, then introduce the slenderness property at the very end. This introduces a bit of variety, but more important is the fact that some general properties of the physical system can be pointed out, without any confusion over the effects of assuming slenderness of the body.

We use two coordinate systems: $Oxyz$ is fixed in the body with its origin at the center of gravity, and $O'x'y'z'$ is an inertial system which moves with the mean motion of the body center of gravity. With respect to the stationary fluid at infinity, the mean motion is a translation at speed U in the negative x' direction; thus, in the $O'x'y'z'$ system, there appears to be a flow past the body in the positive x' direction.

The two reference systems differ because the body oscillates in the z direction, the instantaneous displacement being denoted by $\xi_3(t)$, and rotates about the y axis, the angular displacement being denoted by $\xi_5(t)$. In a more general problem, we could let $\xi_1(t)$, $\xi_2(t)$, and $\xi_3(t)$ denote surge, sway, and heave (displacements along the x , y , and z axes, respectively) and $\xi_4(t)$, $\xi_5(t)$, and $\xi_6(t)$ denote roll, pitch, and yaw (rotations about the x , y , and z axes, respectively). It will be assumed explicitly that $\xi_j(t)$ is a small quantity, so that squares and products can be neglected in comparison with the quantity itself. Furthermore, it will be assumed that $\xi_j(t)$ varies sinusoidally in time and it will be represented by the real part of a complex function varying as $e^{i\omega t}$. We shall not usually bother to indicate that only the real part of a complex quantity is to be implied. Thus we can write:

$$\dot{\xi}_j(t) = i\omega\xi_j(t). \quad (2-68)$$

The relationship between the two coordinate systems is as follows (see Figure (2-4)):

$$\begin{aligned} x &= x' \cos \xi_5 - (z' - \xi_3) \sin \xi_5 \approx x' - z' \xi_5; \\ y &= y'; \\ z &= x' \sin \xi_5 + (z' - \xi_3) \cos \xi_5 \approx x' \xi_5 + z' - \xi_3. \end{aligned} \quad (2-69)$$

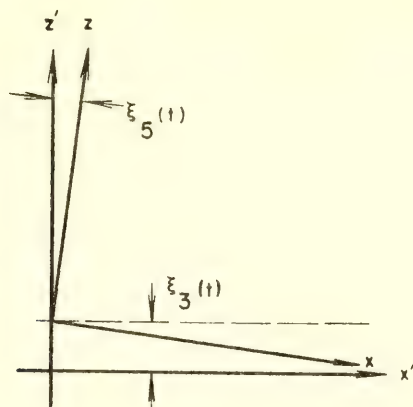


Fig. (2-4). Two Coordinate Systems for Oscillation Problem

The absolute velocity of the center of gravity is:

$$\begin{aligned}
 -U\mathbf{i}' + i\omega\xi_3\mathbf{k}' &= (-U\cos\xi_5 - i\omega\xi_3\sin\xi_5)\mathbf{i} \\
 &\quad + (-U\sin\xi_5 + i\omega\xi_3\cos\xi_5)\mathbf{k} \quad (2-70) \\
 &= -U\mathbf{i} + (i\omega\xi_3 - U\xi_5)\mathbf{k} \quad (2-70')
 \end{aligned}$$

where $(\mathbf{i}, \mathbf{j}, \mathbf{k})$ are unit vectors in the $Oxyz$ system, and $(\mathbf{i}', \mathbf{j}', \mathbf{k}')$ are unit vectors in the $O'x'y'z'$ system.

Let the body surface be defined by the equation:

$$S(x, y, z) = 0. \quad (2-71)$$

Denote the unit vector normal to the surface, inwardly directed, by \mathbf{n} :

$$\mathbf{n} = n_1\mathbf{i} + n_2\mathbf{j} + n_3\mathbf{k}. \quad (2-72a)$$

It is convenient to make a number of other definitions, as follows:

- 1) n_j : Extend the above definition of n_j to $j = 4, 5, 6$ as follows:

$$\mathbf{r} \times \mathbf{n} = n_4 \mathbf{i} + n_5 \mathbf{j} + n_6 \mathbf{k} \quad (2-72b)$$

where

$$\mathbf{r} = x\mathbf{i} + y\mathbf{j} + z\mathbf{k}.$$

In particular, note that:

$$n_3 = \mathbf{n} \cdot \mathbf{k} \quad \text{and} \quad n_5 = zn_1 - xn_3. \quad (2-72')$$

2) ϕ_i : This is a normalized velocity potential. It satisfies:

$$\left. \begin{aligned} \phi_{i_{xx}} + \phi_{i_{yy}} + \phi_{i_{zz}} &= 0 && \text{in fluid region;} \\ \frac{\partial \phi_i}{\partial n} &= n_i && \text{on } S(x, y, z) = 0; \\ |\nabla \phi_i| &\rightarrow 0 && \text{at infinity.} \end{aligned} \right\} \quad (2-73)$$

3) $\mathbf{v}(x, y, z)$: This is a normalized fluid velocity, equal to the fluid velocity at (x, y, z) when an incident stream flows past the body, the stream having unit velocity, \mathbf{i} , at infinity. It can be represented as follows:

$$\mathbf{v}(x, y, z) = \nabla [x - \phi_i(x, y, z)]. \quad (2-74)$$

4) m_i : This quantity is related to the rate of change of $\mathbf{v}(x, y, z)$ in the neighborhood of the body, as follows:

$$m_1 \mathbf{i} + m_2 \mathbf{j} + m_3 \mathbf{k} \equiv \mathbf{m} \equiv -(\mathbf{n} \cdot \nabla) \mathbf{v}; \quad (2-75a)$$

$$m_4 \mathbf{i} + m_5 \mathbf{j} + m_6 \mathbf{k} \equiv -(\mathbf{n} \cdot \nabla)(\mathbf{r} \times \mathbf{v}). \quad (2-75b)$$

In particular, note that:

$$m_3 = \frac{\partial \phi_{iz}}{\partial n} \equiv \phi_{i_{zn}}; \quad (2-75a')$$

$$m_5 = -\frac{\partial}{\partial n} (\mathbf{j} \cdot \mathbf{r} \times \mathbf{v}) = -\frac{\partial}{\partial n} (zv_1 - xv_3)$$

$$= -\frac{\partial}{\partial n} [z(1 - \phi_{ix}) + x\phi_{iz}] = -n_3 + \frac{\partial}{\partial n} (z\phi_{ix} - x\phi_{iz}). \quad (2-75b')$$

- 5) ψ_i : This is another useful normalized velocity potential. It is related to m_i the way ϕ_i is related to n_i . It satisfies:

$$\left. \begin{aligned} \psi_{i,xx} + \psi_{i,yy} + \psi_{i,zz} &= 0 && \text{in fluid region;} \\ \frac{\partial \psi_i}{\partial n} &= m_i && \text{on } S(x, y, z) = 0; \\ |\nabla \psi_i| &\rightarrow 0 && \text{at infinity.} \end{aligned} \right\} \quad (2-76)$$

In particular, it can be seen that these conditions are satisfied for $i = 3, 5$ if:

$$\psi_3(x, y, z) = \phi_{1_z}(x, y, z); \quad (2-76')$$

$$\psi_5(x, y, z) = -\phi_3(x, y, z) - (z\phi_{1_x} - x\phi_{1_z}). \quad (2-76'')$$

(The last term does satisfy the Laplace equation.)

Now we can write down the velocity potential for the combined translation and oscillation in terms of the above-defined quantities. It is a well-known fact of classical hydrodynamics that the fluid motion can be expressed as a superposition of six separate motions, each of which would be caused by the motion of the body in one of the rigid-body degrees of freedom. However, it is essential for the use of this fact that the description be made in terms of a coordinate system fixed with respect to the body. Note that there is no linearization implicit in this superposition, in the sense that there is no requirement that motions be small in any way. In the body-fixed reference frame, the velocity potential is:

$$\begin{aligned} &[-U \cos \xi_5 - i\omega \xi_3 \sin \xi_5] \phi_1(x, y, z) \\ &+ [-U \sin \xi_5 + i\omega \xi_3 \cos \xi_5] \phi_3(x, y, z) + i\omega \xi_5 \phi_5(x, y, z). \end{aligned}$$

The nature of the superposition is obvious when we compare the first two coefficients here with (2-70). However, it must also be recalled that the velocity potential obtained in this way gives the absolute velocity of the fluid, that is, the gradient of this potential is the velocity in a reference frame fixed to the fluid at infinity.* Thus, we must add to this potential an extra term to provide for the

* This can be concluded also by recalling the definition of ϕ_i : its gradient vanishes at infinity.

apparent incident stream in the observation reference frame. The latter has the velocity potential Ux' , and so the complete potential is:

$$\begin{aligned}\phi(x', y', z', t) = & Ux' - (U \cos \xi_5 + i\omega \xi_3 \sin \xi_5) \phi_1(x, y, z) \\ & + (-U \sin \xi_5 + i\omega \xi_3 \cos \xi_5) \phi_3(x, y, z) + i\omega \xi_5 \phi_5(x, y, z)\end{aligned}\quad (2-77)$$

$$\begin{aligned}\simeq & Ux' - U\phi_1(x, y, z) + [i\omega \phi_3(x, y, z)] \xi_3(t) \\ & + [i\omega \phi_5(x, y, z) - U\phi_3(x, y, z)] \xi_5(t).\end{aligned}\quad (2-77')$$

The potential ϕ has been defined basically in terms of the inertial reference frame, although most of the right-hand side here is expressed in terms of the body-fixed system. Note that not only the incident stream is defined in terms of primed coordinates, but also the body motion is really defined in those coordinates as well; in particular, heave motion is a translation of the body along an axis fixed with respect to the fluid at infinity.

The Bernoulli equation must be used for computing the pressure:

$$-\frac{p}{\rho} = \phi_t + \frac{1}{2} (\phi_x'^2 + \phi_y'^2 + \phi_z'^2).$$

The linear approximations of the derivatives here are as follows:

$$\begin{aligned}\phi_t = & [(i\omega)^2 \phi_3 + (i\omega U) \phi_{1z}] \xi_3(t) \\ & + [(i\omega)^2 \phi_5 - (i\omega U) \phi_3 + (i\omega U)(z \phi_{1x} - x \phi_{1z})] \xi_5(t); \\ \phi_{x'} = & U[1 - \phi_{1x}] + [i\omega \phi_{3x}] \xi_3(t) + [i\omega \phi_{5x} - U \phi_{3x} - U \phi_{1z}] \xi_5(t); \\ \phi_{y'} = & -U[\phi_{1y}] + [i\omega \phi_{3y}] \xi_3(t) + [i\omega \phi_{5y} - U \phi_{3y}] \xi_5(t); \\ \phi_{z'} = & -U[\phi_{1z}] + [i\omega \phi_{3z}] \xi_3(t) + [i\omega \phi_{5z} - U \phi_{3z} + U \phi_{1x}] \xi_5(t).\end{aligned}$$

Some simplification has been done through the dropping of quadratic terms in ξ_j . Substituting these expressions into the Bernoulli equation and simplifying somewhat, one finds that:

$$-\frac{p}{\rho} = \frac{U^2}{2} \mathbf{v}^2 + [(i\omega)^2 \phi_3 + (i\omega U)(\psi_3 + \mathbf{v} \cdot \nabla \phi_3)] \xi_3(t) \\ + [(i\omega)^2 \phi_5 + (i\omega U)(\psi_5 + \mathbf{v} \cdot \nabla \phi_5) - U^2(\psi_3 + \mathbf{v} \cdot \nabla \phi_3)] \xi_5(t).$$

In the terms containing ξ_j , one can use primed and unprimed coordinates interchangeably, since the difference leads to terms of higher order.

The force (moment) corresponding to the j -th mode of oscillation is given by:

$$F_j(t) = \int_S dS n_j p(x, y, z, t) \equiv \sum_i T_{ji} \xi_i(t) + F_{j0},$$

where S is the surface of the body at any instant and F_{j0} is the steady force component. (For $j = 1, 2, 3$, the latter is zero.) The "transfer functions" T_{ji} are:

$$T_{33} = -\rho \int_S dS n_3 [(i\omega)^2 \phi_3 + (i\omega U)(\psi_3 + \mathbf{v} \cdot \nabla \phi_3)];$$

$$T_{35} = -\rho \int_S dS n_3 [(i\omega)^2 \phi_5 + (i\omega U)(\psi_5 + \mathbf{v} \cdot \nabla \phi_5) - U^2(\psi_3 + \mathbf{v} \cdot \nabla \phi_3)];$$

$$T_{53} = -\rho \int_S dS n_5 [(i\omega)^2 \phi_3 + (i\omega U)(\psi_3 + \mathbf{v} \cdot \nabla \phi_3)];$$

$$T_{55} = -\rho \int_S dS n_5 [(i\omega)^2 \phi_5 + (i\omega U)(\psi_5 + \mathbf{v} \cdot \nabla \phi_5) - U^2(\psi_3 + \mathbf{v} \cdot \nabla \phi_3)].$$

These formulas can be simplified considerably, even before we introduce the slenderness approximation. We use two theorems: One is an extension of Stokes' theorem, proven by Tuck (see Ogilvie and Tuck [1969]):

$$\int_S dS n_j (\mathbf{v} \cdot \nabla \phi_i) = - \int_S dS m_j \phi_i.$$

The other theorem is Green's theorem; in applying it, we note that all of the functions decrease sufficiently rapidly far away that there is no need to account for effects at infinity.* Thus, in T_{33} and T_{35} we have:

* ϕ_1 and ϕ_3 appear to represent dipoles at infinity; thus, both are proportional to $1/r^2$ as $r \rightarrow \infty$. ϕ_5 appears to represent a quadrupole, thus is proportional to $1/r^3$ at infinity.

$$\int_S dS n_3 (\psi_3 + \mathbf{v} \cdot \nabla \phi_3) = \int_S dS (\phi_{3n} \psi_3 - \psi_{3n} \phi_3) = 0.$$

Similarly, in T_{55} ,

$$\int_S dS n_5 (\psi_5 + \mathbf{v} \cdot \nabla \phi_5) = 0.$$

In T_{35} , we manipulate one integral as follows:

$$\begin{aligned} \int_S dS n_3 (\psi_5 + \mathbf{v} \cdot \nabla \phi_5) &= \int_S dS (n_3 \psi_5 - m_3 \phi_5) \\ &= \int_S dS (n_3 \psi_5 - \psi_{3n} \phi_5 + \psi_3 \phi_{5n} - \psi_3 n_5) \\ &= - \int_S dS n_3 \phi_3 + \int_S dS z (n_3 \phi_{1x} - n_1 \phi_{1z}). \end{aligned}$$

Similarly, in T_{53} and T_{55} , we find:

$$\int_S dS n_5 (\psi_3 + \mathbf{v} \cdot \nabla \phi_3) = \int_S dS n_3 \phi_3 - \int_S dS z (n_3 \phi_{1x} - n_1 \phi_{1z}).$$

The last integral in the last two expressions can be rewritten:

$$\begin{aligned} \int_S dS z (n_3 \phi_{1x} - n_1 \phi_{1z}) &= \mathbf{j} \cdot \int_S dS z \mathbf{n} \times \nabla \phi_1 \\ &= \mathbf{j} \cdot \int_S dS [\mathbf{n} \times \nabla (z \phi_1) - \mathbf{n} \times (\phi_1 \mathbf{k})] \\ &= \int_S dS n_1 \phi_1, \end{aligned}$$

the last equality following from application of Stokes' theorem to the first term. Combining all of these results, we find for the T_{ji} :

$$\begin{aligned} T_{33} &= -\rho(i\omega)^2 \int_S dS n_3 \phi_3; \\ T_{35} &= -\rho(i\omega)^2 \int_S dS n_3 \phi_5 + \rho(i\omega U) \int_S dS (n_3 \phi_3 - n_1 \phi_1); \end{aligned}$$

$$T_{33} = -\rho(i\omega)^2 \int_S dS n_3 \phi_3 - \rho(i\omega U) \int_S dS (n_3 \phi_3 - n_1 \phi_1);$$

$$T_{55} = -\rho(i\omega)^2 \int_S dS n_5 \phi_5 + U^2 \int_S dS (n_3 \phi_3 - n_1 \phi_1).$$

These results have been obtained with no assumptions made about the shape of the body. The only assumption was that the sinusoidal oscillations had very small amplitude.

Now, finally, let us assume that the body is slender. The only effect is that we lose the terms containing $n_1 \phi_1$. For a slender body, n_3 and n_5 are $O(1)$ as the slenderness parameter, ϵ , approaches zero, whereas n_1 is $O(\epsilon)$. From (2-73), we see that ϕ_1 is therefore higher order than ϕ_3 and ϕ_5 by a factor of ϵ . Thus:

$$\left[\int_S dS n_1 \phi_1 / \int_S dS n_3 \phi_3 \right] = O(\epsilon^2).$$

Seldom in practical problems do we ever retain terms with such a great difference in orders of magnitude, and so we neglect the terms containing $n_1 \phi_1$ if the body is slender.

In the ship-motion problem, the quantity corresponding to T_{33} will be

$$(i\omega)^2 \left[a_{33} + \frac{1}{i\omega} b_{33} \right],$$

where a_{33} and b_{33} are the heave added-mass and damping coefficients, respectively.* The other T_{ij} 's have a similar interpretation in terms of pitch added-moment-of-inertia and damping coefficients, cross-coupling coefficients, etc. We note that there are three kinds of terms here:

a) Terms independent of U . These are all of the same form:

$$T_{ij}^{(0)} = - (i\omega)^2 \int_S dS n_i \phi_j. \quad (2-78)$$

b) Terms proportional to U . These occur only in the cross terms, T_{ij} , with $i \neq j$. For a slender body, we have:

*In the ship-motion problem, ϕ_j is complex. Here, of course, ϕ_j is purely real, and so there is no analog to b_{ij} .

$$T_{35} = T_{35}^{(0)} - (U/i\omega) T_{33}^{(0)}; \quad (2-79)$$

$$T_{53} = T_{53}^{(0)} + (U/i\omega) T_{33}^{(0)}. \quad (2-80)$$

c) A term proportional to U^2 . This occurs only in T_{55} :

$$T_{55} = T_{55}^{(0)} + (U/i\omega)^2 T_{33}^{(0)}. \quad (2-81)$$

Even at zero forward speed, there is coupling between the heave and pitch modes, unless the body is symmetrical fore-and-aft. If the body is symmetrical, one can show that $T_{35}^{(0)}$ and $T_{53}^{(0)}$ are zero. But even in this case, the existence of forward speed causes a loss of symmetry, and so a pure-heave motion causes a pitch moment, and a pure-pitch motion causes a heave force. The symmetry between T_{35} and T_{53} should be noted: The speed-independent parts are equal, whereas the speed-dependent parts are exactly opposite.

One remarkable fact is that there is no interaction between the oscillatory motion and the perturbation of the uniform stream by the steady forward motion. If the above formulas are derived from the kinetic-energy formula by use of the Lagrange equations, this fact is perhaps obvious. When we derive expressions for force and moment on an oscillating ship, it is anything but obvious.

For the sake of completeness, I write out here the final formulas for the T_{ij} 's for a slender body in an infinite fluid. We note first that, by the same procedures used in the steady-forward-motion problem, the following is true to a first approximation:

$$\phi_{jyy} + \phi_{jzz} = 0, \quad \text{in the near field.}$$

From (2-72'), it is rather obvious that, for a slender body,

$$n_5 = -x n_3 [1 + O(\epsilon^2)],$$

and thus, from (2-73):

$$\phi_5 = -x \phi_3 [1 + O(\epsilon^2)].$$

Now let:

$$m(x) \equiv \rho \int_{C(x)} d\ell n_3 \phi_3 \equiv \text{added mass per unit length}, \quad (2-82)$$

where $C(x)$ is the contour around the body in the cross section at x . Then clearly,

$$T_{33}^{(0)} = T_{33} = -\rho(i\omega)^2 \int_L dx \int_{C(x)} d\ell n_3 \phi_3 = - (i\omega)^2 \int_L dx m(x),$$

where L is the domain of the length of the body. Similarly, we obtain:

$$T_{35}^{(0)} = T_{53}^{(0)} = \rho(i\omega)^2 \int_L dx x \int_{C(x)} d\ell n_3 \phi_3 = (i\omega)^2 \int_L dx x m(x);$$

$$T_{55}^{(0)} = - (i\omega)^2 \int_L dx x^2 m(x).$$

Collecting these results, we have:

$$\begin{aligned} T_{33} &= - (i\omega)^2 \int_L dx m(x); \\ T_{35} &= (i\omega)^2 \int_L dx xm(x) - \frac{U}{i\omega} T_{33}; \\ T_{53} &= (i\omega)^2 \int_L dx xm(x) + \frac{U}{i\omega} T_{33}; \\ T_{55} &= - (i\omega)^2 \int_L dx x^2 m(x) + \left(\frac{U}{i\omega}\right)^2 T_{33}. \end{aligned} \tag{2-83}$$

III. SLENDER SHIP

Of all the problems discussed in this paper, the slender-ship problem has led to the most important practical consequences. Therefore it is not unreasonable to devote the longest chapter to the problem. Even so, some aspects will not be covered; perhaps the most important missing example is the case of sinkage and trim of a ship.

In the four sections, two steady-motion and two unsteady-motion problems are discussed. The first steady-motion problem is the wave-resistance problem, that is, the problem of a ship in steady forward motion on the surface of an infinite ocean. In the second section, the problem treated is essentially the same, but the Froude number is assumed to be related to the slenderness parameter in such a way that Froude number approaches infinity as slenderness approaches zero; this rather unnatural relationship is discussed at some length. In the third section, I discuss in some detail the problem of heave and pitch motions of a ship at zero forward speed; the results are not at all surprising, but the method is quite clear in this case, which helps one in approaching the final section. It is concerned with the problem which is the combination of the first and third problems: heave and pitch motions of a ship with forward speed.

3.1. The Moderate-Speed, Steady-Motion Problem

The theory presented here is due to Tuck [1963a]*. The analysis -- as far as I carry it here -- is not very much more difficult than the analysis of the infinite-fluid problem, and so it will only be sketched here.

The theory is attractive for its simplicity and its elegance, but unfortunately it has not been successful in predicting wave resistance. The reasons are not entirely clear, although they have been discussed for many years. See, for example, Kotik and Thomsen [1963]. The difficulty could very well be that real ships are just not slender enough for a one-term expansion (or perhaps any number of terms) to give an accurate prediction of wave resistance. This is the old question, "How small must the 'small' parameter be?" Another possibility is that the error arises because the lowest-order slender-body theory places the source of the disturbance precisely on the level of the undisturbed free surface, and so there are no attenuation effects due to finite submergence of parts of the hull. (These two possible causes of error are not entirely separate.) Still another possible cause is considered in Section 3.2.

The hull surface will be specified by the equation:

$$r = r_0(x, \theta). \quad (3-1)$$

Now it will be convenient to measure θ from the negative z axis, since most ships are symmetrical about the midplane. We assume that $r_0 = O(\epsilon)$ and that $\partial^n r_0 / \partial x^n = O(\epsilon)$, as needed.

There is a velocity potential satisfying the Laplace equation and the same kinematic body boundary condition, (2-58), as in the infinite-fluid problem. The incident stream is again taken in the positive x direction, that is, with velocity potential Ux . The two free-surface conditions are:

$$g\zeta + \frac{1}{2} [\phi_x^2 + \phi_y^2 + \phi_z^2] = \frac{1}{2} U^2, \quad \text{on} \quad z = \zeta(x, y); \quad (3-2)$$

$$\zeta_x \phi_x + \zeta_y \phi_y - \phi_z = 0, \quad \text{on} \quad z = \zeta(x, y). \quad (3-3)$$

Finally, there is a radiation condition to be satisfied.

* This reference is not readily available, but the material which is of interest here can also be found in Tuck [1963b], Tuck [1964a], and Tuck [1964b], all of which are gathered into Tuck [1965a].

As usual, we assume that there is a far-field expansion:

$$\phi(x, y, z) \sim \sum_{n=0}^N \phi_n(x, y, z), \quad \text{where} \quad \phi_{n+1} = o(\phi_n) \quad \text{as} \quad \epsilon \rightarrow 0, \\ \text{for fixed } (x, y, z). \quad (3-4)$$

and a near-field expansion:

$$\phi(x, y, z) \sim \sum_{n=0}^N \Phi_n(x, y, z), \quad \text{where} \quad \Phi_{n+1} = o(\Phi_n) \quad \text{as} \quad \epsilon \rightarrow 0, \\ \text{for fixed } (x, y/\epsilon, z/\epsilon). \quad (3-5)$$

These expansions are substituted into all of the exact conditions, from which we obtain two sequences of problems which must be solved simultaneously.

In the far field, the first term in the expansion for ϕ must be just the incident uniform-stream potential, Ux , since the body vanishes as $\epsilon \rightarrow 0$ and the asymptotic representation $\phi \sim \phi_0 = Ux$ satisfies the free-surface conditions (trivially). The second term represents a line of singularities on the x axis. One really ought to allow the most general possible kind of singularities on this line, but it is no surprise to find that just sources are sufficient at first, and so we consider the special case of a line of sources on the free surface. One can show that higher-order singularities could not be matched to the near-field solution. Alternatively, one can construct a far-field solution using Green's theorem and show that it really represents just a line distribution of sources. See, for example, Maruo [1967].

One can use the classical Havelock source potential to express the desired potential for a line of sources, but Tuck's procedure is more convenient in the slender-body problem: Apply a double-Fourier transform operation to the Laplace equation, reducing it to an ordinary differential equation with z as independent variable:

$$-(k^2 + l^2)\phi^{**}(k, l; z) + \phi_{zz}^{**}(k, l; z) = 0,$$

where k and l are the transform variables, and the asterisks denote the transforms. Assume for the moment that the line of sources is located at $z = z_0 < 0$. The above differential equation can be solved generally, with a different solution above and below $z = z_0$. The solution in the upper region is forced to satisfy the linearized free-surface condition, the solution in the lower region must vanish at great depths, and the two must have the discontinuity at $z = z_0$ appropriate to the source singularities. Finally, one may

allow $z_0 \rightarrow 0$. In physical variables, the result is:

$$\begin{aligned} \phi_1(x, y, z) = & -\frac{1}{2\pi^2} \int_{-\infty}^{\infty} dk e^{ikx} \sigma^*(k) K_0(|k|r) \\ & - \lim_{\mu \rightarrow 0} \frac{U^2}{4\pi^2} \int_{-\infty}^{\infty} dk e^{ikx} k^2 \sigma^*(k) \int_{-\infty}^{\infty} \frac{d\ell e^{i\ell y + z\sqrt{(k^2 + \ell^2)}}}{\sqrt{(k^2 + \ell^2)} [g\sqrt{(k^2 + \ell^2)} - (Uk - i\mu/2)^2]}, \end{aligned} \quad (3-6)$$

where μ denotes a fictitious Rayleigh viscosity, guaranteeing that the proper radiation condition is satisfied, and $\sigma^*(k)$ is the Fourier transform of $\sigma(x)$, the source density.*

The two-term outer expansion is:

$$\phi(x, y, z) \sim Ux + \phi_1(x, y, z),$$

which has the two-term inner expansion:

$$\phi(x, y, z) \sim Ux + \frac{1}{\pi} \sigma(x) \log r - \frac{1}{2\pi} f(x) - g(x), \quad (3-7)$$

where

$$f(x) = \int_{-\infty}^{\infty} d\xi \sigma'(\xi) \log 2|x - \xi| \operatorname{sgn}(x - \xi) \quad (3-8a)$$

$$= -\frac{1}{\pi} \int_{-\infty}^{\infty} dk e^{ikx} \sigma^*(k) \log \frac{C|k|}{2}; \quad (3-8b)$$

$$g(x) = \lim_{\mu \rightarrow 0} \frac{U^2}{4\pi^2} \int_{-\infty}^{\infty} dk e^{ikx} k^2 \sigma^*(k) \int_{-\infty}^{\infty} \frac{d\ell}{\sqrt{(k^2 + \ell^2)} [g\sqrt{(k^2 + \ell^2)} - (Uk - i\mu/2)^2]}. \quad (3-9)$$

The expansion should be compared with the corresponding expansion for a line of sources in an infinite fluid, as given in (2-65). We now have an extra term, $g(x)$, and the terms containing $\sigma(x)$ and $f(x)$ differ by a factor of two from the earlier result. The latter variation is not important; it results from the fact that the line of sources was taken at $z = z_0 < 0$, and those sources merged with their images when we let $z_0 \rightarrow 0$.

* Define $\sigma(x) \equiv 0$ for values of x ahead of and behind the ship.

The most interesting feature of this inner expansion of the two-term outer expansion is that the wave effects are all contained in $g(x)$ -- a function of just x . In the infinite-fluid problem, all 3-D effects in the near field were included (in the first approximation) in the single function of x , $f_1(x)$. We now have a generalization of this for the free-surface problem.

In the near field, it is easy to show that the first term in the asymptotic expansion of the potential is again just the uniform-stream potential, Ux . The next term, Φ_1 , must satisfy the Laplace equation in two dimensions (in the cross-plane) and the same body boundary condition as before, (2-63):

$$\frac{\partial \Phi_1}{\partial N} = - \frac{U r_{0x}(x, \theta)}{[1 + (r_{0\theta}/r_0)^2]^{1/2}} \quad \text{on} \quad r = r_0(x, \theta). \quad (3-10)$$

As in the infinite-fluid problem, this conditions suggests that

$$\Phi_1 = O(\epsilon^2),$$

since $r_0 = O(\epsilon)$ and $\partial/\partial N = O(\epsilon^{-1})$.

Now consider the free-surface conditions. In the Bernoulli equation, note the orders of magnitude:

$$g\zeta + U\Phi_{1x} + \frac{1}{2}(\Phi_{1x}^2 + \Phi_{1y}^2 + \Phi_{1z}^2) + \dots = 0 \quad \text{on} \quad z = \zeta(x, y).$$

$O(\zeta) \quad O(\epsilon^2) \quad O(\epsilon^4) \quad O(\epsilon^2) \quad O(\epsilon^2)$

The term containing Φ_{1x}^2 can be dropped, but the others containing Φ_1 are all the same order of magnitude, and we have no reason to suppose that the ζ term is higher order. In the kinematic condition, note the orders of magnitude:

$$U\zeta_x + \Phi_{1x}\zeta_x + \Phi_{1y}\zeta_y - \Phi_{1z} + \dots = 0 \quad \text{on} \quad z = \zeta(x, y).$$

$O(\zeta) \quad O(\zeta\epsilon^2) \quad O(\zeta) \quad O(\epsilon)$

Clearly, we can drop the term containing Φ_{1x} , but no others.

Now we must relate the order of magnitude of ζ with the order of magnitude of Φ_1 . From the kinematic condition, one might suppose that $\zeta = O(\epsilon)$. However, the dynamic condition then implies that $\zeta \sim 0$, which means only that ζ is higher order than we assumed. In fact, the only assumption which is consistent with both conditions is that:

$$\zeta = O(\epsilon^2).$$

The kinematic condition then reduces to:

$$\Phi_{1z} = 0 \quad \text{on} \quad z = 0; \quad (3-11)$$

thus, Φ_1 represents the flow which would occur in the presence of a rigid wall at $z = 0$. From the dynamic free-surface condition, we can compute the first approximation to the wave shape:

$$g\zeta(x, y) \sim - (U\Phi_{1x} + \frac{1}{2} \Phi_{1y}^2) \Big|_{z=0}. \quad (3-12)$$

It may appear to be a paradox that we have a flow without waves, from which we compute a wave shape! But, like all paradoxes, it is a matter of interpretation and understanding. We shall return to this point presently.

Since Φ_1 satisfies the Laplace equation in two dimensions and a rigid-wall condition on $z = 0$, it can be continued analytically into the upper half space as an even function of z . All of the arguments used in the infinite-fluid problem can then be carried over directly. In particular, at large distance from the origin, we can write, as in (2-64),

$$\Phi_1 \sim C_1 + \frac{A_{10}}{2\pi} \log r + O(1/r), \quad \text{as} \quad r \rightarrow \infty.$$

The two-term inner expansion can be matched to the two-term outer expansion. We obtain

$$A_{10} = 2\sigma(x);$$

$$C_1 = -\frac{1}{2\pi} f(x) - g(x).$$

Note that there is again a factor of 2 difference from the infinite-fluid results, (2-66). Of course, the term $g(x)$ is new here.

We can again determine A_{10} and thus σ in terms of body shape, without the necessity of solving the near-field hydrodynamic problem. By the simple flux argument, we find that:

$$A_{10} = 2Us'(x), \quad (3-13a)$$

where $s(x)$ is the cross-sectional area of the submerged part of the hull. With this convention, we find that

$$\sigma(x) = U s'(x), \quad (3-13b)$$

just as in the infinite-fluid problem. Again, we have been able to determine the complete two-term outer expansion without explicitly solving the near-field problem. This occurs because the source-like behavior which dominates far away from the body (still in the near-field sense) can be found simply in terms of the rate of change of cross section, and it provides all the information needed for determining the two-term far-field expansion.

Enough information is now available to determine a first approximation of the wave resistance. It can be computed in either of two ways: 1) integrate the near-field pressure over the hull surface, or 2) use the far-field expansion and the momentum theorem. In either case, one obtains:

$D_W \equiv$ wave resistance

$$\sim -\frac{1}{2} \rho \int_{-\infty}^{\infty} \int_{-\infty}^{\infty} d\sigma(x) d\sigma(\xi) Y_0(\kappa |x-\xi|),$$

where

$\sigma(x)$ = source density, given in (3-13b),

$$\kappa = g/U^2,$$

$$d\sigma(x) = \frac{d\sigma(x)}{dx} dx,$$

$Y_0(z)$ = Bessel function of the second kind, of order zero, argument z .

This is the slender-body wave-resistance formula which is so notoriously inaccurate. At speeds for which one would hope to use it, it gives values that are too high by a factor of 3 or more. Generally, one could not (and should not) expect to correct such errors by including higher-order terms, and so it is rather futile to pursue this analysis further.

Streamlines, Waves, Pressure Distributions. I mentioned previously the apparent paradox of prescribing a rigid-wall free-surface condition, then using the solution of that problem to compute wave shapes, as in formula (3-12). Such a procedure really can be quite rational.

Once a velocity potential is known everywhere, it is a fairly

simple task for a computer to figure out the velocity field and to produce streamlines. Figure (3-1) shows the streamlines around a Series 60 hull, calculated from the near-field slender-body solution by Tuck and Von Kerczek [1968]. The upper boundary of the figure is the rigid-wall streamline. Figure (3-2) shows the same streamlines in two other views. These drawings are accurate (in principle) to order ϵ . This means, loosely speaking, that they show the streamlines on a scale which is appropriate for measuring beam and draft of the ship. Thus, we see that some of the streamlines start near mid-draft, pass under the bottom, then return to approximately their original depth. These are variations which show on a scale intended for measuring quantities which are $O(\epsilon)$.

The wave height, on the contrary, is $O(\epsilon^2)$, as we found earlier. Therefore it should not show in these figures. Our assumptions have led to the conclusion that wave height is small compared with beam and draft. Thin-ship theory, on the other hand, predicts that wave height and beam are comparable -- without being very explicit about the ratio of wave height to draft.

In the section of Fig. (3-2) showing hydrodynamic pressure along streamlines, only the waterplane curve (denoted by **W**) is really consistent. On any streamline, the pressure will vary mostly because of the changing hydrostatic head along the streamline. Such pressure variations are $O(\epsilon)$. If we were to work out a second-order theory and plot the streamlines, the shift in streamline position from first-order theory to second-order theory would lead to a hydrostatic pressure change which is $O(\epsilon^2)$. This is the same as the order of magnitude of the hydrodynamic pressure, but it is ignored in the figure.

On the other hand, if we were inside the ship measuring pressure at a point on the hull, we would not care which streamline went past that point. We could use the Bernoulli equation to estimate the pressure at any point, and the estimate consistent to order ϵ^2 would be found from the equation:

$$0 = \frac{p}{\rho} + gz + U\Phi_{1x} + \frac{1}{2} (\Phi_{1y}^2 + \Phi_{1z}^2).$$

3.2. The High-Speed, Steady-Motion Problem

In the preceding analysis, we have said nothing explicit about the speed other than assuming that it was finite. The first term in the velocity-potential expansions was Ux , and all other terms were assumed to be small in comparison.

In principle, there is no reason to provide or allow a connection between Froude number and our slenderness expansion parameter. However, the practical manner in which a perturbation analysis is used may justify our making such an unnatural assumption. In practice, we work out an asymptotic expansion, which provides

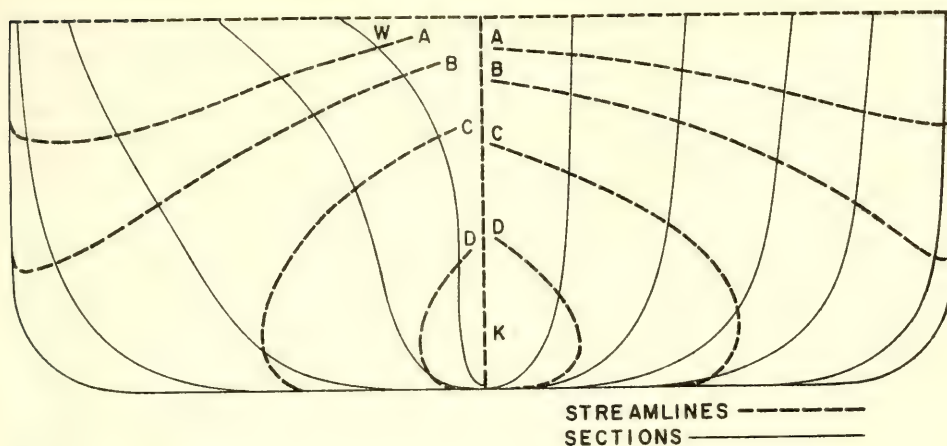


Fig. (3-1). Steady-Motion Streamlines on Ship Hull According to First-Order Slender-Body Theory (Body-Plan View). From Tuck and Von Kerczek [1968].

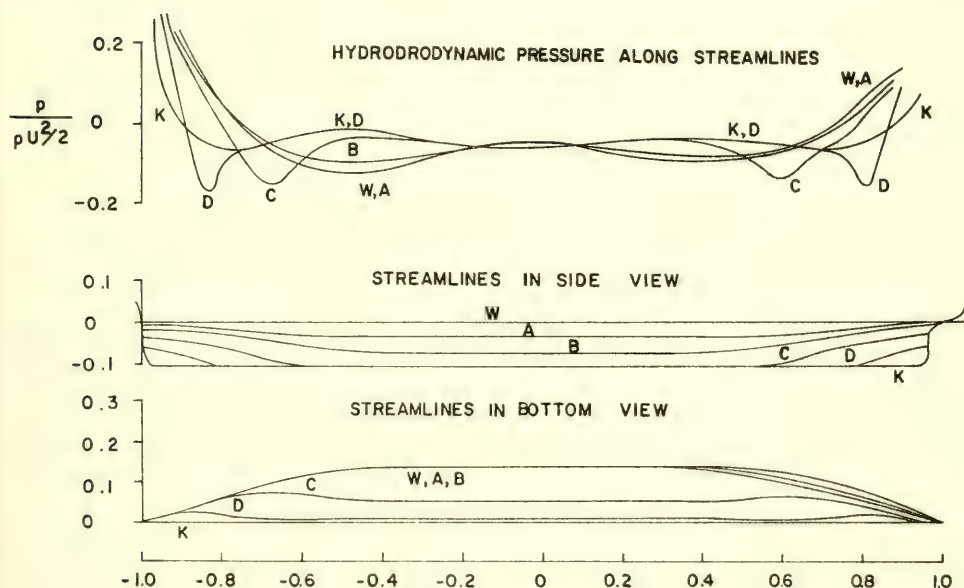


Fig. (3-2). Steady-Motion Streamlines and Hydrodynamic Pressure on Ship Hull According to First-Order Slender-Body Theory (Side and Plan Views). From Tuck and Von Kerczek [1968].

a description that becomes approximately valid (in a certain sense) as the small parameter approaches zero. But we use the expansion under conditions in which the small parameter is quite finite, and we just hope that the resulting error is not too big. The size of that error may depend on other parameters of the problem, and we may possibly reduce the error by allowing such other parameters to vary simultaneously with the basic slenderness parameter.

In the steady-motion problem that we have been considering, the small parameter ϵ could be thought of as the beam/length ratio. There is a completely different length scale in the problem, namely, $U^2/g = F^2 L$, where F is the Froude number and L is ship length. This length is proportional to the wavelength of a wave with propagation speed equal to ship speed. When we assume that $F = O(1)$ as $\epsilon \rightarrow 0$, we imply that the speed is such as to produce waves which can be measured on a scale appropriate for measuring ship length, and we imply that this speed is unrelated to slenderness.

If we are interested in problems of very-low-speed ships or very-high-speed ships, in which the generated waves are, respectively, much shorter or much longer than ship length, it is entirely conceivable that our severely truncated asymptotic expansions may be made even more inaccurate by the extreme values of Froude number. We may increase the practical accuracy by assuming, say, that wavelength approaches zero or infinity, respectively as $\epsilon \rightarrow 0$. This is not to imply that there really is a connection between speed and slenderness. It is done only in the hope that wavelength and ship length may be more accurately represented when we use the theory with a finite value of ϵ .

Formally, the low-speed problem may be treated simply as a special case of Tuck's analysis, as described in Section 3.1. One finds that the appropriate far-field problem contains a rigid-wall free-surface boundary condition (in the first approximation). Thus, both near- and far-field approximations are without real gravity-wave effects. However, this formal approach is quite improper. The difficulty is so serious that we devote a special section later to the low-speed problem. It is perhaps the most singular of all of our singular perturbation problems. The difficulty, in essence, is that we have treated all perturbation velocity components as being small compared with U , and this leads to nonsense if we allow U to approach zero.

At high speed, a slender-body theory can be developed along lines paralleling Tuck's analysis. This has been done by Ogilvie [1967]. The resulting near-field and far-field boundary-value problems are quite different from Tuck's however. No numerical results have been obtained yet from this analysis.

Near-field and far-field regions are defined just as in the previous slender-body problem. In the far-field, the velocity-potential expansion starts with the uniform-stream term, Ux ,

followed by a term representing a line of singularities. The near-field expansion also starts with the uniform-stream term, followed by a term which satisfies the Laplace equation in two dimensions.

The differences appear first in the boundary conditions satisfied by these expansions. The proper way of setting up these conditions is to nondimensionalize everything and then assume that Froude number, F , is related to the slenderness parameter, ϵ , in such a way that $F \rightarrow \infty$ as $\epsilon \rightarrow 0$. It is easier just to let the gravity constant, g , approach zero in this limit. The only interesting new case, it turns out, is: $g = O(\epsilon)$. We now assume this to be the case.

Since g appears only in the dynamic free-surface boundary condition, the body boundary condition will be the same as in the moderate-speed problem, Eq. (3-10), and in the infinite fluid problem, Eq. (2-63).

In the far field, the disturbance vanishes as $\epsilon \rightarrow 0$. Therefore the free-surface disturbance is $o(1)$. If we let the expansion of the velocity potential, $\phi(x, y, z)$, be expressed:

$$\phi(x, y, z) \sim Ux + \sum_{n=1}^N \phi_n(x, y, z), \quad \text{for fixed } (x, y, z),$$

the dynamic and kinematic free-surface conditions are, approximately:

$$\begin{aligned} 0 &\simeq U\zeta_x - \phi_{1z}, & \text{on } z = 0. \\ 0 &\simeq g\zeta + U\phi_{1x}, \end{aligned} \tag{3-14}$$

We do not know the relative orders of magnitude of ζ and ϕ , a priori, but a study of the possibilities shows that only one combination is possible, namely, that ζ and ϕ_1 are the same order of magnitude. Then, in the dynamic condition, the term containing g is higher order than the other term, and it can be neglected in the first approximation, that is,

$$\phi_{1x} = 0, \quad \text{on } z = 0, \tag{3-14}$$

which implies also that

$$\phi_1 = 0 \quad \text{on } z = 0. \tag{3-15}$$

Thus, the free surface acts like a pressure-relief surface, with no

restraining effect of gravity (to this order of magnitude).

This condition points to a fundamentally different kind of solution from that of the previous problems. If we continue the function ϕ_1 analytically into the upper half-space, it must be odd with respect to the surface $z = 0$. Thus ϕ_1 cannot represent a line of sources. The least singular solution represents a line of dipoles, oriented vertically. Assuming that ϕ_1 will consist only of such dipoles, we can write it:

$$\phi_1(x, y, z) = \frac{\sin \theta}{r} \int_0^\infty d\xi \mu(\xi) \left[1 + \frac{x - \xi}{[(x - \xi)^2 + r^2]^{1/2}} \right], \quad (3-16)$$

where $y = r \cos \theta$ and $z = r \sin \theta$. The two-term outer expansion and the two-term inner expansion of the two-term outer expansion are, respectively:

$$\begin{aligned} \phi(x, y, z) &\sim Ux + \phi_1(x, y, z) \\ &\sim Ux + \frac{2 \sin \theta}{r} \int_0^x d\xi \mu(\xi). \end{aligned} \quad (3-17)$$

I am now assuming that the bow of the ship is located at $x = 0$; then, in matching to the near-field solution, we can show that the dipole density must be zero upstream of the ship bow. This expansion is unaffected by the downstream dipoles.

In the near field, we assume the usual expansion:

$$\phi(x, y, z) \sim Ux + \sum_{n=1}^N \Phi_n(x, y, z) \quad \text{for fixed } (x, y/\epsilon, z/\epsilon).$$

The term Φ_1 satisfies the 2-D Laplace equation:

$$\Phi_{1yy} + \Phi_{1zz} = 0.$$

The body boundary condition suggests that $\Phi_1 = O(\epsilon^2)$, just as it did before in Eq. (3-10).

From the dynamic free-surface condition,

$$0 = g\zeta + U\Phi_{1x} + \frac{1}{2} (\Phi_{1y}^2 + \Phi_{1z}^2) \quad \text{on } z = \zeta(x, y),$$

we see that $\zeta = O(\epsilon)$ (since $g = O(\epsilon)$). This causes a new problem. We would like, as usual, to change this condition at $z = \zeta(x, y)$ to a

modified condition at $z = 0$. But this is not possible. For example, the term Φ_{1x} would be transformed:

$$\begin{array}{ccccccc} \Phi_{1x}(x,y,\zeta(x,y)) & = & \Phi_{1x}(x,y,0) & + & \zeta(x,y)\Phi_{1xz}(x,y,0) & + & \dots \\ O(\epsilon^2) & & O(\epsilon^2) & & O(\epsilon) & & O(\epsilon) \end{array}$$

Every term, in fact, will be the same order of magnitude, and so this ordinary kind of expansion fails. We must continue to apply the condition on the actual (unknown) location of the free surface.*

The kinematic free-surface condition is also nonlinear and must be satisfied on the unknown location of the free surface:

$$0 \simeq U\zeta_x + \Phi_{1y}\zeta_y - \Phi_{1z} \quad \text{on} \quad z = \zeta(x,y).$$

Each term here is $O(\epsilon)$, and so none can be ignored.

We are left in the rather uncomfortable position of having to solve a nonlinear problem just to obtain a first approximation to the near-field potential function. However, that nonlinear problem is a two-dimensional problem, which is not an insignificant advantage, and, as we shall see, it is possible in principle to predict the location of the free surface, thus avoiding the necessity of searching for it.

We do not have a condition to apply at infinity in the Φ_1 (near-field) problem. It is not so straightforward in this case to predict the form of the solution as $r \rightarrow \infty$, but Ogilvie [1967] showed that:

$$\Phi_1(x,y,z) = \frac{A_{11} \sin \theta}{r} [1 + O(1/r)] \quad \text{as} \quad r \rightarrow \infty,$$

where A_{11} is a constant to be determined. There is no source-like behavior. This might have been expected, of course, since the inner expansion of the outer expansion, (3-17), showed the characteristics of a two-dimensional dipole. An intermediate expansion can be used to show that these statements are correct.

A numerical procedure for solving this problem may be the following: Suppose that at some x we know the value of Φ_1 on the free surface, $z = \zeta(x,y)$, and that we also know $\zeta(x,y)$ at that x .

*If we expand: $\zeta \sim \sum \zeta_n$, we could apply the condition on $z = \zeta_1$, then apply the usual kind of transformation, as above, so that conditions on higher-order terms would be applied on a priori known surfaces.

Using Green's theorem, we can write:

$$\Phi_1(x; y, z) = \frac{1}{2\pi} \int \left[\frac{\partial \Phi_1}{\partial N} \log r' - \Phi_1 \frac{\partial}{\partial n} (\log r') \right] dl',$$

where $r'^2 = [(y-y')^2 + (z-z')^2]$, and the integration is carried out in the cross section, with (y', z') ranging over the body contour, the free-surface contour, and a closing contour at infinity. The last of these contours contributes nothing and can be ignored. We assumed that Φ_1 is known on the free surface, and, from the body boundary condition, we know $\partial \Phi_1 / \partial N$ on the hull. If we let the field point, $(x; y, z)$, approach the hull surface, we obtain an integral equation, with Φ_1 unknown on the hull and $\partial \Phi_1 / \partial N$ unknown on the free surface. This is not quite the usual form for an integral equation, but it should be possible to solve it approximately by essentially standard numerical methods. Then the Green's-theorem integral can be used to express Φ_1 at all points in that cross section. Thus, the solution of an integral equation in one dimension allows the potential to be found.

This procedure has not used the information contained in the free-surface conditions. Usually, we look on the free surface conditions as complications that cause tremendous difficulty in the finding of solutions. Now we take an opposite point of view: Supposing that we have solved the above problem at some x , we use the kinematic conditions to predict the value of ζ just downstream:

$$\begin{aligned} \zeta(x + \Delta x, y) &= \zeta(x, y) + \Delta x \zeta_x(x, y) + \dots \\ &= \zeta(x, y) + \frac{\Delta x}{U} [\Phi_{1z}(x, y, \zeta(x, y)) - \Phi_{1y} \zeta_y] + \dots \end{aligned}$$

Similarly, we predict the value of Φ_1 on the free surface just downstream:

$$\Phi_1 \Big|_{\zeta(x+\Delta x, y)} = \Phi_1 + (\Delta x) [\Phi_{1x} + \zeta_x \Phi_{1z}] + \dots,$$

where the right-hand side is evaluated at $(x, y, \zeta(x, y))$, and the dynamic boundary condition is used to evaluate Φ_{1x} .

Now we are ready to start over. Presumably having solved the problem at some x , we have used the free-surface conditions to formulate the equivalent problem at $x + \Delta x$. The most serious difficulty may very well be in starting the whole process, and there seems to be no elegant prescription for carrying out that essential first step; in some problems, it is possible that a linearized solution may suffice for a start, but this is not certain. Another serious difficulty may be the stability of the method.

This analysis has led to the possibility of predicting waves with amplitude which is $O(\epsilon)$, that is, waves comparable in amplitude to ship beam and draft. Such a possibility makes the analysis worth further investigation, but it is also the cause of the major difficulty, viz., the necessity of solving a nonlinear problem in the near field.

When the above analysis was offered for publication in 1967, one of the referees called attention to the fact that the conclusions seemed to be quite at variance with those of Rispin [1966] and Wu [1967]. Simple observation shows that, at very great distance, the dominant fluid motion should be gravity-related free-surface waves, whereas my high-Froude-number analysis predicts no true wave motion in the far field. Actually, all aspects of the problem are in complete harmony if we consider a "far-far field" in which distance from the ship is $O(\epsilon^{-1})$, that is, much greater than ship length. The two free-surface conditions then fall into the usual linearized format, and we would expect to find progressive waves in such a region.

This is quite reasonable. At very high Froude number, one expects typical waves to be very long -- in this case, considerably longer than the ship. The appropriate distortion of coordinates is an isotropic compression in scale far, far away, in contrast to our usual anisotropic stretching of coordinates in the cross-plane near the body. In their two-dimensional planing problems, Rispin [1966] and Wu [1967] performed just such a distortion. Their problem is discussed at some length later, when we come to two-dimensional problems.

The present problem is an interesting case in which an inconsistent expansion might be useful in the far field. Suppose that we arbitrarily replace the free-surface condition, (3-15), by the usual moderate-speed condition,

$$U^2 \phi_{xx} + g \phi_y = 0, \quad \text{on} \quad z = 0.$$

If Froude number is indeed very high, then this condition is quite equivalent to (3-15). But the potential function which satisfies this condition does not represent just the simple line of dipoles implied by (3-16). There will be all of the well-known extra terms involving the free surface. If such an inconsistent far-field solution can be matched to the near-field solution, then the waveless far-field solution obtained previously can be avoided. Perhaps this is worth further study.

3.3. Oscillatory Motion at Zero Speed

A systematic study of the zero-speed ship-motions problem by means of the method of matched asymptotic expansions does not

yield any results that were not obtained previously by simpler means. However, it is instructive to consider this problem by this method because the results are rather obvious and it is then clear how the formalism is used in place of some common physical arguments. Then, in the more complicated forward-speed problem, in which physical insight is less reliable, the same formalism can be applied with reasonable faith in its predictions.

Only the slender-body idealization of a ship has led to useful prediction methods in the ship-motion problem.* The thin-ship model, which was intensively studied from the late 1940's until the early 1960's, was useful for certain restricted aspects of the problem. For example, the damping of heave and pitch motions, as predicted by thin-ship theory, is fairly accurate. But the complete theory is deficient. A straightforward one-parameter analysis leads to the prediction of resonances in heave and pitch with no added-mass or damping effects, as shown by Peters and Stoker [1954]. (See also Peters and Stoker [1957] and Stoker [1957].) A multi-parameter thin-ship analysis is apparently satisfactory in principle, as demonstrated by Newman [1961], but no one has used it for prediction purposes. It is too complicated.

Slender-body theory at one time appeared to have comparable difficulties, but these have been largely removed in recent years, and a theory which is essentially rational now exists and is fairly successful in predicting ship motions.

In early versions of the slender-body theory of ship motions, all inertial effects (both ship and fluid) were lost in the lowest-order approximation, along with hydrodynamic damping effects. The theory was even more primitive than the classical Froude-Krylov approach. Excitation was computed from the pressure field of the waves, undisturbed by the presence or motions of the ship, and the restoring forces were simply the quasi-static changes in buoyancy and moment of buoyancy. Even the mass of the ship was supposed to be negligible in the lowest-order theory.

These deficiencies are removed by assuming that the frequency of motion is high, in an asymptotic sense. That is, if one assumes that the frequency of sinusoidal oscillation is $O(\epsilon^{-1/2})^{**}$, then the ship inertia force is the same order of magnitude as the excitation and the buoyancy restoring forces. The hydrodynamic force and moment also enter into the calculation of ship motions at the lowest order of magnitude. This was all recognized, for example, by Newman and Tuck [1964]. However, correcting the slender-body

*Note that "strip theory" is a special case of "slender-body theory."

** ϵ is the usual slenderness parameter.

theory in this way was rejected by many workers on the ground that the resulting theory would be valid only for very short incident waves, whereas the most important ship motions are known to occur when the waves have wave lengths comparable to ship length.

The choice was this: 1) Follow the reasonable usual assumptions of slender-body theory and obtain a rather useless theory*. 2) Accept the formal assumption that frequency is high and obtain a much more interesting theory -- which turns out to be very similar to the intuitive but quite successful "strip theory" of ship motions. In what follows, I make the second choice.

The reasons for the success of this choice have become clear in the last few years. In one of the most important practical problems, namely, the prediction of heave and pitch motions in head seas, we can truly say that we are dealing with a high-frequency phenomenon. Because of the Doppler shift in apparent wave frequency, fairly long waves are encountered at rather high frequencies; the waves are long enough to cause large excitation forces, and the frequencies are high enough to cause resonance effects. At zero speed, on the other hand, incident waves with frequency near the resonance frequencies of a ship are likely to be much shorter in length than the ship, and so their net excitation effect is much reduced through interference. For typical ships on the ocean, most of the heave and pitch motion at zero speed is caused by waves with length comparable to ship length, and so the frequencies of such motion are well below the resonance frequencies. Thus, at zero speed, prediction of ship motions can be treated largely on a quasi-static basis; the system response is "spring-controlled" rather than "mass controlled."

The problem is very much like the simple spring-mass problem discussed in Section 1.2. If the mass of a spring-mass system is very small, we can ignore inertia effects at low frequency. Thus, if the system is described by the differential equation:

$$m\ddot{y} + ky = Fe^{i\omega t},$$

the exact and approximate solutions, given by:

*Newman and Tuck showed, for example, that the lowest-order perturbation potential resulting from ship oscillations satisfies a rigid-wall free-surface condition, even with forward speed included. Maruo [1967] has the same result for the forced-oscillation problem. Newman and Tuck performed calculations with a second-order theory for the zero-speed case and found practically no change in their predictions due to second-order effects. They did not make such calculations in the forward-speed problem.

$$y_{ex} = Fe^{i\omega t} / (k - m\omega^2), \quad y_{ap} = Fe^{i\omega t} / k,$$

respectively, are approximately equal if ω is small enough. If we solve this equation on the understanding that ω is very large, we must keep all quantities in the exact solution. But that solution will reduce numerically to the approximate solution if we evaluate it with a small value of ω .

We could say that the solution obtained on the assumption of high frequency becomes inconsistent if we apply it to problems at low frequency, but, if the appropriate small parameter is small enough, an inconsistent approximation is no worse numerically than a consistent approximation.

Once more I would warn against trying to make absolute judgments of what is "small" and what is "not small." I avoid careful definitions of my small parameters largely for this reason; if the definition is not precise, one can never be tempted to put numbers into the definition! In the problem ahead, we cannot possibly judge analytically how "slender" the ship must be or how "high" the frequency must be for the results to have some validity.

In all of the discussions of ship motions, I use the same notation as in the study of oscillatory motion in an infinite fluid. See Section 2.32.

The ship in its mean position will be defined by the equation:

$$S_0(x, y, z) = -z + d(x, y) = 0, \quad (3-18)$$

where $d(x, y) = O(\epsilon)$; the instantaneous hull position is defined by the following equation:

$$S(x, y, z, t) = -z + d(x, y) + \xi_3(t) - x\xi_5(t) = 0. \quad (3-19)$$

The ship is heading toward negative x (although it does not matter in the zero-speed case). Upward heave and bow-up pitch are considered positive.

We assume that all motions have very small amplitude. Symbolically, we write that:

$$\xi_i(t) = O(\epsilon\delta) \quad \text{as either } \epsilon \text{ or } \delta \text{ approaches zero.}$$

where ϵ is the usual slenderness parameter, and δ is a "motion-amplitude" parameter. This convenient assumption allows us to

vary the motion amplitude for a given ship (i.e., for fixed ϵ), and it also guarantees that the motions are small compared with the ship beam and draft, even as the latter approach zero as $\epsilon \rightarrow 0$. Velocity potential, wave height, motion variables, and all other dependent variables may be expected to have double asymptotic expansions, valid as $\epsilon \rightarrow 0$ and $\delta \rightarrow 0$. We shall consistently carry terms which are linear in δ . The steady-motion problems already treated correspond to the $\delta = 0$ case; at zero speed, the $\delta = 0$ case is trivial. The problem ahead is to solve the linear motions problem -- "linear" in terms of motion amplitude. With respect to the slenderness parameter, we shall consistently carry up to ϵ terms.

It should be noted that the slenderness assumption is not needed in formulating a linear motions problem at zero forward speed; it is convenient, however, in practical application of the theory.

All motions are assumed to be sinusoidal at radian frequency ω . I use a complex exponential notation, so that: $\xi_i(t) = i\omega\xi_i(t)$. Also, it is assumed that $\omega = O(\epsilon^{-1/2})$, and so symbolically we can write: $\partial/\partial t = O(\epsilon^{-1/2})$.

The potential function, $\phi(x, y, z, t)$, satisfies the Laplace equation and the following boundary conditions:

$$[A] \quad 0 = g\zeta + \phi_t + \frac{1}{2}[\phi_x^2 + \phi_y^2 + \phi_z^2], \quad \text{on} \quad z = \zeta(x, y, t); \quad (3-20a)$$

$$[B] \quad 0 = \phi_x \zeta_x + \phi_y \zeta_y - \phi_z + \zeta_t, \quad \text{on} \quad z = \zeta(x, y, t); \quad (3-20b)$$

$$[C] \quad 0 = \phi_x S_x + \phi_y S_y - \phi_z + S_t, \quad \text{on} \quad S(x, y, z, t) = 0. \quad (3-21)$$

We consider first the problem of a ship which is forced by some external means to heave and pitch in calm water. In the far field, the slenderness assumption leads us to expect that the potential function can be represented by a line of singularities on the x axis. From previous experience, we might hope that a line of sources would suffice in the first approximation; this turns out to be correct. Since these sources represent an oscillating ship, the strengths of the sources will also vary sinusoidally. Suppose that there is a source distribution on the x axis:

$$\text{Re} \{ \sigma(x) e^{i\omega t} \}, \quad -\infty < x < \infty.$$

Define $\sigma(x)$ to be identically zero beyond the ends of the ship. Obviously, $\sigma(x) = o(1)$ as $\delta \rightarrow 0$, since there is no fluid motion at all for $\delta = 0$. Therefore, in the first approximation, we may

linearize the free-surface conditions. More precisely, we could assume the existence of asymptotic expansions, $\phi \sim \sum \phi_n$ and $\zeta \sim \sum \zeta_n$, and let the first term in each be $o(1)$ as $\delta \rightarrow 0$. The linearized free-surface conditions take their usual form:

$$[A] \quad 0 = g\zeta + \phi_t, \quad \text{on} \quad z = 0;$$

$$[B] \quad 0 = -\phi_z + \zeta_t, \quad \text{on} \quad z = 0.$$

These can be combined into the following:

$$\phi_z - \nu\phi = 0, \quad \text{on} \quad z = 0, \quad (3-22)$$

where $\nu = \omega^2/g = O(\epsilon^{-1})$. In the far field, it is very difficult to guess how differentiation alters orders of magnitude. If the oscillation frequency is very high, then the resulting waves are very short; it would be reasonable, perhaps, to try stretching the coordinates, and there would be no obvious basis for doing this anisotropically. The approach which I take here is somewhat different: Solve the above-stated linear problem exactly, then observe the behavior of the solution for high frequency of oscillation. In other words, the problem is not stated in a consistent manner, but when we have the solution we rearrange it and make it consistent.

The desired potential function can be written in the following form:

$$\phi(x, y, z, t) = \text{Re} \{ \phi(x, y, z) e^{i\omega t} \}, \quad (3-23)$$

where:

$$\phi(x, y, z) = -\frac{1}{2\pi} \int_{-\infty}^{\infty} d\xi \, \sigma(\xi) \underbrace{\int_0^{\infty} \frac{k \, dk}{k - \nu} e^{kz} J_0(k \sqrt{[(x-\xi)^2 + y^2]})}_{\text{wiggly arrow}} \quad (3-23a)$$

$$= -\frac{1}{4\pi} \int_{-\infty}^{\infty} dk \, e^{ikx} \sigma^*(k) \underbrace{\int_{-\infty}^{\infty} \frac{d\ell \, e^{i\ell y + z\sqrt{(k^2 + \ell^2)}}}{\sqrt{(k^2 + \ell^2)} - \nu}}_{\text{wiggly arrow}}. \quad (3-23b)$$

The form in (3-23a) can be obtained readily by superposing a distribution of free-surface sources: J_0 is the ordinary Bessel function of order zero, and the wiggly arrow shows that the integral is to be interpreted as a contour integral, indented at the pole in the obvious sense indicated. Form (3-23b) is obtained by a transform method; $\sigma^*(k)$ is the Fourier transform of $\sigma(x)$; details may be found in Ogilvie and Tuck [1969]. Again, the inner integral is to be interpreted as a contour integral; there are two poles in this case. In both formulas, the path of the contour has been chosen so that the

solution has a satisfactory behavior at infinity, viz., it represents outgoing waves.

We need the inner expansion of this potential function, that is, we must find its behavior as $r = (y^2 + z^2)^{1/2} \rightarrow 0$. The basic idea here in finding the inner expansion is to use the second form of solution, convert the contour integral into an integral along a closed contour, and use the calculus of residues. The integrand of the inner integral has four singularities, located at $\ell = \pm \ell_0$ and at $\ell = \pm i|k|$, where $\ell_0 = (\nu^2 - k^2)^{1/2}$. The first two are simple poles, but the second two are branch points. We "connect" the latter via the point at infinity; see Fig. (3-3). It is drawn for the case that $|k| < \nu$; if $|k| > \nu$, all four singularities are purely imaginary. The contour is closed as shown if $y > 0$. (Otherwise, the contour is closed below.) The integrals along the large circular arcs approach zero as the radius of the arcs approaches infinity. Then the inner integral in $\phi(x, y, z)$ is equal to $2\pi i$ times the residue at $\ell = -\ell_0$, less the value of the contour integral down and back up the imaginary axis. The latter can be shown to be $O(\epsilon)$, and so the inner integral in $\phi(x, y, z)$ is:

$$\underbrace{\int_{-\infty}^{\infty} \frac{d\ell}{(k^2 + \ell^2)^{1/2} - \nu} e^{i\ell y + z\sqrt{k^2 + \ell^2}}}_{\text{contour integral}} = - \frac{2\pi i \nu}{(\nu^2 - k^2)^{1/2}} e^{\nu z - iy\sqrt{\nu^2 - k^2}} + O(\epsilon)$$

Next, we assume that the source distribution is smooth enough that $\sigma(x)$ does not vary rapidly on a length scale comparable with ship beam. This assumption implies that $\sigma^*(k)$ decreases rapidly with increasing values of k , and so the value of the above inner integral -- a function of k -- does not really matter except when k is small in magnitude. Accordingly, we expand the above expression in a manner appropriate for small $|k|$. We obtain

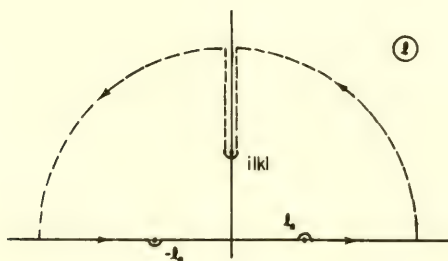


Fig. (3-3). Contour of Integration Defining the Velocity Potential of a Line of Pulsating Sources: Zero-Speed Case

$$\begin{aligned}
\phi(x, y, z) &\simeq \frac{1}{4\pi^2} \int_{-\infty}^{\infty} dk e^{ikx} \sigma^*(k) \frac{2\pi i \nu}{(\nu^2 - k^2)^{1/2}} e^{\nu z - i y \sqrt{\nu^2 - k^2}} \\
&\simeq \frac{i}{2\pi} e^{\nu z - i \nu y} \int_{-\infty}^{\infty} dk e^{ikx} \sigma^*(k) \{1 + \dots\} \\
&= i e^{\nu z - i \nu y} \sigma(x) + \dots \quad (3-24)
\end{aligned}$$

With the time dependence reintroduced, we have:

$$\phi(x, y, z, t) \simeq \text{Re} \{ i \sigma(x) e^{\nu z} e^{i(\omega t - \nu y)} \} + \dots \quad (3-25)$$

This approximation represents a travelling wave; for $y > 0$, in particular, the wave is moving away from the line of sources. For $y < 0$, we must start over, closing the contour for the k integration on the lower side of the k plane. It turns out that the result is the same if only we replace y by $|y|$. Thus, we have an outgoing wave for $y < 0$ also. In both cases, the outgoing wave has the form appropriate for a gravity wave in two dimensions.

In the approximations above, it is necessary to require that r be not extraordinarily large; if one assumes that $r = O(1)$ and $\omega = O(\epsilon^{-1/2})$, then the above results follow logically. Thus the very simple approximation above is valid even in part of the far field. It is an example of the well-known physical principle that nearly unidirectional waves can be generated if the wave generator is much larger than a wave length.

If we let $r = O(\epsilon)$, no change occurs in this approximation. Since $\nu = O(\epsilon^{-1})$, it is not permissible to expand the exponential functions even when y and z are $O(\epsilon)$. The only effect of passing from far field to near field now is to change the scale of the observed wave motion.

This far-field analysis has provided information that was probably quite obvious intuitively: In the near-field, the condition at infinity is that there should be outgoing, two-dimensional, gravity waves*. With this information in hand, we can move on to the formulation and solution of the near-field problem.

In the near-field, we make the usual slender-body assumptions:

* I cannot imagine that anyone would ever have doubted this fact, even without the above analysis to show it. But in the forward-speed problem, the condition at infinity in the near field is not at all obvious, and such an analysis seems necessary.

$$\frac{\partial}{\partial y}, \frac{\partial}{\partial z}, \frac{\partial}{\partial r} = O(\epsilon^{-1}).$$

To a first approximation, the potential function satisfies the Laplace equation in two dimensions:

$$\phi_{yy} + \phi_{zz} \sim 0,$$

and the linear free-surface condition

$$\phi_z - \nu \phi \sim 0 \quad \text{on} \quad z = 0. \quad (3-22)$$

With the assumptions made above, the two terms here are of the same order of magnitude. (If we did not assume high frequency, we would obtain just the rigid-wall boundary condition, $\phi_z = 0$.) This condition implies that we shall be solving a gravity-wave problem in two dimensions. At infinity, we know from the far-field solution that the appropriate condition is an outgoing-wave requirement. All that remains is to put the body boundary condition, (3-21), into the appropriate form.

Let $\partial/\partial N$ denote differentiation in the direction normal to the body contour in a cross section. Then, from (3-19) and (3-21),

$$\begin{aligned} \frac{\partial \phi}{\partial N} &= \frac{\phi_z - \phi_y S_y}{(1+d_y^2)^{1/2}} = \frac{\phi_x S_x + S_1}{(1+d_y^2)^{1/2}} \\ &= \frac{\dot{\xi}_3 - x\dot{\xi}_5 - \xi_5 \phi_x + d_x \phi_x}{(1+d_y^2)^{1/2}} \sim \frac{\dot{\xi}_3 - x\dot{\xi}_5}{(1+d_y^2)^{1/2}}. \end{aligned} \quad (3-26)$$

The last simplification involves an error which is $O(\epsilon^2)$ higher order than the retained terms. To the same approximation, we can write (see (2-72')):

$$n_3 = \mathbf{n} \cdot \mathbf{k} \sim \frac{1}{(1+d_y^2)^{1/2}}; \quad n_5 \sim -x n_3.$$

Thus, the boundary condition is:

$$\frac{\partial \phi}{\partial N} \sim n_3 \dot{\xi}_3 + n_5 \dot{\xi}_5; \quad \text{on} \quad z = d(x, y). \quad (3-27)$$

As in the infinite-fluid problem (cf. (2-73)), we can define normalized potential functions, $\phi_i(x, y, z)$:

$$\phi_{iyy} + \phi_{izz} = 0, \quad \text{in the fluid region;} \quad (3-28a)$$

$$\frac{\partial \phi_i}{\partial N} = n_i, \quad \text{on } z = d(x, y); \quad (3-28b)$$

$$\phi_{iz} - \nu \phi_i = 0, \quad \text{on } z = 0, \quad (3-28c)$$

where $\nu = \omega^2/g$. In the present case, the functions satisfy the 2-D Laplace equation and a 2-D body boundary condition, and they must satisfy the linearized free-surface condition. Instead of the previous simple condition at infinity, we must impose the 2-D outgoing-wave radiation condition and a condition of vanishing disturbance at great depths. Thus, the boundary-value problem is much more complicated than in the infinite-fluid case, but, thanks to the slenderness assumption, we have only 2-D problems to solve, and, thanks to the small-amplitude assumption, the problems are linear.

The actual velocity potential function can now be expressed:

$$\phi(x, y, z, t) \sim \text{Re} \left[\sum_{j=3,5} i\omega \xi_j(t) \phi_j(x, y, z) \right]. \quad (3-29)$$

It must be observed that each ϕ_j is complex, because of the radiation condition. It is necessary to devise an appropriate numerical scheme for solving these problems. Both mapping techniques and integral-equation methods have been successfully applied. Note, incidentally, that the heave/pitch problem requires solution of just the ϕ_3 problem, since the slenderness assumption allows the approximation to be made that $\phi_5 \simeq -x\phi_3$.

The result of this analysis is a pure strip theory, that is, the flow appears to take place in cross sections as if each cross section were independent of the others. It is consistent to follow the solution of this problem with a computation of the pressure field at each cross section, from which force-per-unit-length, then force and moment on the ship can be found after appropriate integrations. We obtain the following formulas for the force and moment on the ship resulting from the motion of the ship:

$$F_j^m(t) = -\rho \int_{S_0} ds \, n_j [g(\xi_3 - x\xi_5) + (i\omega)^2 (\xi_3 \phi_3 + \xi_5 \phi_5)], \quad (3-30)$$

where $j = 3$ for heave force and $j = 5$ for pitch moment, and the symbol S_0 denotes that the integration is to be taken over the hull surface in its mean or undisturbed position, which is specified by Eq. (3-18). The first term, involving g , is just a buoyancy effect.

The following terms are purely hydrodynamic; they will be expressed in terms of added-mass and damping coefficients, as follows: Let:

$$m(x) + \frac{1}{i\omega} n(x) \equiv \rho \int_{C(x)} d\ell \, n_3 \phi_3, \quad (3-31)$$

where $C(x)$ is the contour of the immersed part of the cross section of x . Cf. (2-82). We call $m(x)$ the "added mass per unit length" and $n(x)$ the "damping coefficient per unit length." Using the slender-body approximations that $\phi_5 \approx -x\phi_3$ and $n_5 \approx -xn_3$, we find for $F_j^m(t)$:

$$F_3^m(t) = -\rho g \int_{S_0} dS \, n_3 (\xi_3 - x\xi_5) - (i\omega)^2 \int_L dx \, (\xi_3 - x\xi_5) [m(x) + n(x)/i\omega]; \quad (3-32)$$

$$F_5^m(t) = \rho g \int_{S_0} dS \, xn_3 (\xi_3 - x\xi_5) + (i\omega)^2 \int_L dx \, x(\xi_3 - x\xi_5) [m(x) + n(x)/i\omega].$$

Finally, we abbreviate these formulas:

$$F_j^m(t) = - \sum_{i=3,5} [(i\omega)^2 a_{ji} + (i\omega) b_{ji} + c_{ji}] \xi_i(t), \quad (3-33)$$

where

$$\begin{aligned} a_{33} &= \int_L dx \, m(x); & b_{33} &= \int_L dx \, n(x); \\ a_{35} &= a_{53} = - \int_L dx \, xm(x); & b_{35} &= b_{53} = - \int_L dx \, xn(x); \\ a_{55} &= \int_L dx \, x^2 m(x); & b_{55} &= \int_L dx \, x^2 n(x); \\ c_{33} &= \rho g \int_{S_0} dS \, n_3 = 2\rho g \int_L dx \, b(x, 0); \\ c_{35} &= c_{53} = - \rho g \int_{S_0} dS \, xn_3 = - 2\rho g \int_L dx \, xb(x, 0); \\ c_{55} &= \rho g \int_{S_0} dS \, x^2 n_3 = 2\rho g \int_L dx \, x^2 b(x, 0); \end{aligned}$$

$b(x, z)$ is the hull offset at a point (x, z) on the centerplane.

The wave-excitation problem can be formulated as a singular perturbation problem, but such a problem has never been satisfactorily solved, even for the zero-speed case. Fortunately, another approach is available for obtaining the wave excitation; this is the very elegant theorem proven by Khaskind [1957]. It allows one to compute the wave excitation force, including the effects of the diffraction wave, without solving the diffraction problem. Since we thus avoid the singular perturbation problem altogether, only the final results are presented here. (Reference may be made to Newman [1963] for details of the zero-speed case.) Let the incident wave have the velocity potential:

$$\phi_0(x, z, t) = \frac{igh}{\omega} e^{\nu z + i(\omega t - \nu x)};$$

the corresponding wave shape is given by:

$$\zeta_0(x, t) = h e^{i(\omega t - \nu x)}.$$

This is the head-seas case. For an arbitrary body, the heave force due to the incident waves is:

$$F_3^W(t) = \rho g h e^{i\omega t} \int_{S_0} dS e^{\nu z - i\nu x} \{ (1 - \nu \phi_3) n_3 + i\nu \phi_3 n_1 \}.$$

If the body is a slender ship, with axis parallel to the wave-propagation direction, this formula simplifies to the following:

$$F_3^W(t) \simeq \rho g h e^{i\omega t} \int_L dx e^{-i\nu x} \int_{C(x)} d\ell n_3 e^{\nu z} (1 - \nu \phi_3). \quad (3-34a)$$

The corresponding expression for pitch moment on a slender body is:

$$F_5^W(t) \simeq \rho g h e^{i\omega t} \int_L dx e^{-i\nu x} (-x) \int_{C(x)} d\ell n_3 e^{\nu z} (1 - \nu \phi_3). \quad (3-34b)$$

In the expression $(1 - \nu \phi_3)$ in the integrand, the first term leads to the force (moment) which would exist if the presence of the ship did not alter the pressure distribution in the wave; in other words, it gives the so-called "Froude-Krylov" excitation. This fact can be proven by applying Gauss' theorem to the integral. Dynamic effects in the wave ("Smith effect") are properly accounted for. The second term gives all effects of the diffraction wave.

A final rewriting of the wave-force formula is worthwhile. The above approximate expression for $F_3^W(t)$ can be manipulated into the following:

$$F_3^w(t) \approx 2\rho g \int_L dx \, b(x,0) \zeta_0(x,t) \left[1 - \frac{\nu}{b(x,0)} \int_{-\tau(x)}^0 dz \, e^{\nu z} b(x,z) \right] \\ + i\rho\omega \int_L dx \, \zeta_{01}(x,t) \int_{C(x)} dl \, n_3 \phi_3 e^{\nu z}.$$

The first term shows the Froude-Krylov force quite explicitly; the product of $\zeta_0(x,t)$ and the quantity in brackets is often called an "effective waveheight," the second factor being a quantitative representation of the Smith effect. The second integral term has been expressed in terms of the vertical speed of the wave surface, $\zeta_{01}(x,t)$. This term should be compared with the force expression for the calm-water problem, (3-30). For a slender body, the hydrodynamic part of the latter can be written, for $j = 3$,

$$-i\rho\omega \int_{S_0} dS \, n_3 [\dot{\xi}_3(t) \phi_3 + \dot{\xi}_5(t) \phi_5] \approx -i\rho\omega \int_L dx \, [\dot{\xi}_3(t) - x \dot{\xi}_5(t)] \int_{C(x)} dl \, n_3 \phi_3.$$

The last quantity in brackets is the vertical speed of the cross section at any particular x . Comparison with the second term of $F_3^w(t)$ shows that the latter is almost exactly the same as the hydrodynamic force that we would predict if each section of the ship had a vertical speed $-\dot{\zeta}_{01}(x,t)$. This analogy would be exact, in fact, if the exponential factor, $e^{\nu z}$, were not present in the $F_3^w(t)$ formula.

Except for that factor, what we have found is that Korvin-Kroukovsky's well-known "relative-velocity hypothesis" is approximately correct according to the analysis above. The hypothesis is particularly accurate for very long waves, in which case $e^{\nu z} \approx 1$ over the depth of the ship, but it is less accurate for short waves. Again, it should be noted that we have no absolute basis for saying whether a particular wave is short or long in this respect. In computing the Froude-Krylov part of the force, it is well-known that the exponential-decay factor must be included in practically all cases of practical interest; this has been amply demonstrated experimentally. It suggests that one should be wary of dropping the exponential factor in the diffraction-wave force expression.

Summary. In the far field, we assumed that the effects of the heaving/pitching ship could be represented by a line of pulsating singularities located at the intersection of the ship centerplane and the undisturbed free surface. For a first approximation, we tried using just sources, and these were sufficient to allow matching with the near-field solution. In particular, the inner expansion of the outer expansion showed that the near-field expansion would satisfy a two-dimensional outgoing-wave radiation condition, at least in the first approximation. With this fact established, we formulated the near-field problem; it reduced ultimately to the determination of a velocity potential in two dimensions, the potential satisfying a linear

free-surface condition and an ordinary kinematic body boundary condition, as well as the outgoing-wave condition. This is a standard problem which must generally be solved numerically with the aid of a large computer; such programs exist. The force and moment were expressed as integrals of added-mass-per-unit-length and damping-per-unit-length, both of which could be found from the velocity potential for the 2-D problem. Finally, the determination of the wave excitation force and moment was carried out by application of the Khaskind formula, which permits us to avoid the singular perturbation problem involved in solving for the diffraction wave.

3.4. Oscillatory Motion with Forward Speed

The problem of predicting the hydrodynamic force on an oscillating ship with forward speed is not fundamentally much different from the same problem in the zero-speed case. It is considerably more complex, to be sure, but no new assumptions are needed.

The approach here is that of Ogilvie and Tuck [1969]. Alternative approaches have been devised by numerous other authors; some of these were mentioned in the last section. The distinguishing characteristics of the Ogilvie-Tuck approach are: 1) application of the method of matched asymptotic expansions, and 2) assumption that frequency is high in the asymptotic sense that $\omega = O(\epsilon^{-1/2})$, while Froude number is $O(1)$. Also, the problem is broken down into a series of linear problems by the use of a "motion-amplitude" parameter, δ , which is a measure of the amplitude of motion relative to the size of ship beam and draft.

The reference frame is assumed to move with the mean motion of the center of gravity of the ship. Thus it appears that there is a uniform stream at infinity, and we take this stream in the positive x direction. The z axis points upward from an origin located in the plane of the undisturbed free surface, and the y axis completes the right-handed system. (Positive y is measured to starboard.)

Let the velocity potential be written:

$$\phi(x, y, z, t) = Ux + U\chi(x, y, z) + \psi(x, y, z, t), \quad (3-35a)$$

where $U[x + \chi(x, y, z)]$ is the solution of the steady-motion problem discussed in Section 3.1. For the moment, we simply assume that $\psi(x, y, z, t)$ includes everything that must be added to the steady-motion potential so that $\phi(x, y, z, t)$ is the solution of the complete problem. We shall also divide the free-surface deformation function into two parts:

$$\zeta(x, y, t) = \eta(x, y) + \theta(x, y, t), \quad (3-35b)$$

where $\eta(x,y)$ is the free-surface shape in the steady-motion problem (the $\zeta(x,y)$ of Section 3.1), and $\theta(x,y,t)$ is whatever must be added so that $\zeta(x,y,t)$ is the complete free-surface deformation.

The body surface is defined mathematically just as in Section 3.3 for the zero-speed problem; see (3-18) and (3-19). The same assumptions are made about orders of magnitude:

$$\xi_i(t) = O(\epsilon \delta) ; \quad \omega = O(\epsilon^{-1/2}) .$$

From these assumptions and the subsequent analysis, it turns out that

$$\psi(x,y,t) = O(\epsilon^{3/2} \delta), \quad \theta(x,y,t) = O(\epsilon \delta),$$

as either ϵ or $\delta \rightarrow 0$. We can look on the complete solution as a double expansion in ϵ and δ . From this point of view, the expansion for the potential can be written:

$$\begin{aligned} \phi(x,y,z,t) = & \{ Ux + U\chi_1(x,y,z) + \dots \} \\ & O(\delta^0 \epsilon^0) \quad O(\delta^0 \epsilon^2) \\ & + \{ \psi_1(x,y,z,t) + \psi_2(x,y,z,t) + \dots \} + o(\delta). \quad (3.36) \\ & O(\delta^1 \epsilon^{3/2}) \quad O(\delta^1 \epsilon^2) \end{aligned}$$

The order of magnitude of the term $U\chi_1(x,y,z)$ was found in Section 3.1. The order of magnitude of ψ_1 may be somewhat surprising. Physically, it implies that the effects of ship oscillations dominate the effects of steady forward motion -- in the first approximation. These orders of magnitude were derived by Ogilvie and Tuck. Here, I shall not prove them, but I hope to make them appear plausible. It should be noted that the high frequency assumption was made just so that the orders of magnitude would come out this way. (Cf. the discussion in Section 2.3, in which it was pointed out that the formalism for the steady-motion slender-body problem is established to force certain expected results to come out of the analysis. We are doing the same here, forcing strip theory to come out as the first approximation.)

The linearity of the ψ_1 problem permits us to assume that the time dependence of ψ_1 and of the corresponding first term in a θ expansion can be represented by a factor $e^{i\omega t}$.

In order to find any effects of interaction between steady motion and oscillatory motion, it is necessary to solve for the term

$\psi_2(x, y, z, t)$. Thus, we must retain two terms in the time-dependent part of the potential function. (The problem is still linear, however, in terms of δ .) It is not convenient to be repeatedly attaching subscripts to the symbols, and so I shall simply write out equations and conditions which are asymptotically valid to the order of magnitude appropriate to keeping ϵ^2 terms in the expansion of $\psi(x, y, z, t)$.

In the far field, the effect of the oscillating ship can be represented in terms of line distributions of singularities. Again, we try to get along with just a distribution of sources, and we are successful if we allow for the existence of both steady and pulsating sources. The steady-source distribution is exactly the same as in the steady-motion problem. Let the density of the unsteady sources be given by $\sigma(x)e^{i\omega t}$; define $\sigma(x) \equiv 0$ for the values of x beyond the bow or stern. The corresponding potential function must satisfy the Laplace equation in three dimensions, a radiation condition, and the usual linearized free-surface condition:

$$(i\omega)^2\psi + 2i\omega U\psi_x + U^2\psi_{xx} + g\psi_z = 0 \quad \text{on} \quad z = 0. \quad (3-37)$$

Then it can be shown that:

$$\psi(x, y, z, t) \sim -\frac{e^{i\omega t}}{4\pi^2} \int_{-\infty}^{\infty} dk e^{ikx} \sigma^*(k) \int_C \frac{dl \exp[i l |y| + z\sqrt{k^2 + l^2}]}{\sqrt{k^2 + l^2} - \nu(1 + Uk/\omega)^2}, \quad (3-38)$$

where $\sigma^*(k)$ is the Fourier transform of $\sigma(x)$, and the contour C is taken as in Fig. (3-4), where k_1 and k_2 are the real roots* ($k_1 < k_2$) of the equation:

*There are two real roots if $\tau \equiv \omega U/g > 1/4$; the other two roots are a complex pair. Since we assume that $\omega = O(1/\sqrt{\epsilon})$, then also $\tau = O(1/\sqrt{\epsilon})$, and we are assured that $\tau \gg 1/4$. However, if $\tau \downarrow 1/4$, the complex pair come together, and our estimates are all very bad. Of course, it is well known that the ship-motion problem is singular at $\tau = 1/4$. For still smaller values of τ , there are four real roots of the above equation, and the solution can again be interpreted physically and mathematically. From experimental evidence, it appears that our final formulas can be applied for any forward speed, at least in head seas, but the presence of a singularity at $\tau = 1/4$ shows that this is accidental. Our theory is a high-frequency, finite-speed theory, and it really should not be possible to let U vary continuously down to zero.

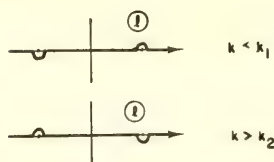


Fig. (3-4). Contour of Integration Defining the Velocity Potential of a Line of Pulsating Sources: Forward-Speed Case

$$\left[1 + \frac{Uk}{\omega}\right]^4 - \left[\frac{k}{v}\right]^2 = 0,$$

and the contour is indented as shown at the poles on the real axis in the k plane. The contour C extends from $-\infty$ to $+\infty$. The poles in the k plane all fall on the imaginary axis if $k_1 < k < k_2$, and then C is the entire real axis, with no special interpretations being necessary.

The above expression for $\psi(x, y, z, t)$ is a one-term outer expansion, but it is not a consistent one-term expansion. It is shown by Ogilvie and Tuck that a much simpler expression is possible if $r = (y^2 + z^2)^{1/2}$ is $O(1)$ as $\epsilon \rightarrow 0$; emphasis should be placed here on the restriction that r is not extraordinarily large. If $\sigma^*(k)$ is restricted in a rather reasonable way, it follows that:

$$\psi(x, y, z, t) \sim \frac{i}{2\pi} e^{i\omega t} \int_{-\infty}^{\infty} dk e^{ikx} \sigma^*(k) e^{v(z-iy|y|)(1+Uk/\omega)^2}. \quad (3-39)$$

We can take this as our one-term outer expansion of $\psi(x, y, z, t)$.

The inner expansion of this expression is obtained by letting $r = O(\epsilon)$. Then we find that:

$$\psi(x, y, z, t) \sim i e^{i\omega t} e^{v(z-iy|y|)} [\sigma(x) - 2i(\omega U/g)(z - i|y|)\sigma'(x)]. \quad (3-40)$$

Since $vr = O(1)$, it is not appropriate to expand the exponential function further. This is a two-term inner expansion of the outer expansion of ψ ; the first term represents an outgoing, two-dimensional, gravity wave, just as in the zero-speed problem (see (3-25)), but the second term represents a wave motion in which the amplitude

increases linearly with distance from the x axis. The latter is a rather strange kind of potential function; it represents a wave which becomes larger and larger, without limit, at large distance. However, one must remember that this is the inner expansion of the outer expansion of $\psi(x,y,z,t)$; it means that there are waves near the x axis which seem to increase in size when viewed in the near field. At very great distances, one must revert to the previous integral expressions for $\psi(x,y,z,t)$.

We must next find an inner expansion which satisfies conditions appropriate to the near field and which matches the above far-field expansion. One finds readily that:

$$\psi_{yy} + \psi_{zz} = 0 \quad \text{in the fluid region,}$$

to the order of magnitude that we consistently retain. Thus, the partial differential equation is again reduced to one in two dimensions, and so we seek to restate all boundary conditions in a form appropriate to a 2-D problem.

The body boundary condition must be carefully expressed in terms of a relationship to be satisfied on the instantaneous position of the body. This condition can then be restated as a different condition to be applied on the mean position of the hull. It can be shown that:

$$\frac{\partial \psi}{\partial N} \sim \frac{\xi_3 - x\xi_5}{(1+d_y^2)^{1/2}} + \frac{-U\xi_5 + U(\xi_3 - x\xi_5)(h_0\chi_{yz} - \chi_{zz})}{(1+d_y^2)^{1/2}} \quad \text{on } z = d(x,y). \quad (3-41)$$

[$\epsilon^{1/2}\delta$] [$\epsilon\delta$]

The derivative on the left has the same meaning as in the previous slender-body analyses: It is the rate of change in a cross section plane, in the direction normal to the hull contour in that plane. The first term on the right-hand side is the same as in the zero-speed problem; see (3-26). The quantity $-U\xi_5$ has a simple physical interpretation: it is a cross-flow velocity caused by the instantaneous angle of attack. The remaining terms all arise as a correction on the steady-motion potential function, $U\chi$; the latter satisfies a boundary condition on the mean position of the ship, which is not generally the actual position of the ship, and so it must be modified.

Intuitive derivations of strip theory usually omit the terms involving χ . However, in a consistent slender-body derivation, they are the same order of magnitude as the angle-of-attack term. (This says nothing about which is the more nearly valid approach!)

The free-surface condition reduces ultimately to:

$$\psi_{tt} + g\psi_z \sim -2U\psi_{tx} - 2U\chi_y\psi_{ty} - U\chi_{yy}\psi_t \quad \text{on } z = 0. \quad (3-42)$$

$$[\epsilon^{1/2}\delta] \quad [\epsilon\delta]$$

The orders of magnitude are noted, again on the basis of information not derived here. This condition can be compared with the linear condition used in the far field, (3-37). The two terms on the left here are obviously the same as the terms $(i\omega)^2\psi + g\psi_z$ in (3-37), and the first term on the right here, $-2U\psi_{tx}$, is the same as the term $2i\omega U\psi_x$ in (3-37). The other two terms on the right-hand side here are basically nonlinear in origin; they involve interactions between the oscillation and the steady perturbation of the incident stream. The term $U^2\psi_{xx}$ which appears in (3-37) is missing here because it is $O(\epsilon^{3/2}\delta)$ in the near field by our reckoning.

Again it is worthwhile to compare this boundary condition with its nearest equivalent in other versions of slender-body theory or strip theory of ship motions. If we did not assume that frequency is very large, slender-body theory would require in the first approximation that $\psi_z = 0$, since the other terms are all higher order. This is just the free-surface boundary condition obtained in this problem by Newman and Tuck [1964] and by Maruo [1967]. Higher order approximations would involve nonhomogeneous Neumann conditions on $z = 0$. On the other hand, in most derivations of strip theory, it is assumed that the free-surface condition is: $\psi_{tt} + g\psi_z = 0$ on $z = 0$. This agrees with the lowest-order condition obtained by Ogilvie and Tuck, as given above. However, the assumption of this boundary condition in the usual strip-theory derivation is quite arbitrary, and no means is available to extend it to higher-order approximations. The assumptions made by Ogilvie and Tuck were chosen explicitly so that the simplest approximation would be just strip theory, and we see here that that goal was achieved. This basis for choosing assumptions was selected only because strip theory had proven to be the most accurate procedure available for predicting ship motions.*

The method of solution used by Ogilvie and Tuck is to find several functions each of which satisfies some part of the nonhomogeneous conditions. In particular, let the solution be expressed in the following form:

$$\psi(x, y, z, t) = \sum_j [i\omega\Phi_j + U\Psi_j + (i\omega)^2 U\Omega_j] \xi_j(t), \quad (3-43)$$

*In other words, we stopped fretting about how irrational strip theory was and set out to derive it formally!

where $j = 3$ and 5 , and Φ_j , Ψ_j , and Ω_j satisfy the following conditions, respectively:

$$\Phi_{jyy} + \Phi_{jzz} = 0; \quad \Phi_{jn} = n_j \quad \text{on} \quad z = d(x, y); \quad \Phi_{jz} - \nu \Phi_j = 0 \quad \text{on} \quad z = 0; \quad (3-44)$$

$$\Psi_{jyy} + \Psi_{jzz} = 0; \quad \Phi_{jn} = m_j \quad \text{on} \quad z = d(x, y); \quad \Psi_{jz} - \nu \Phi_j = 0 \quad \text{on} \quad z = 0; \quad (3-45)$$

$$\Omega_{jyy} + \Omega_{jzz} = 0; \quad \Omega_{jn} = 0 \quad \text{on} \quad z = d(x, y);$$

$$\Omega_{jz} - \nu \Omega_j = - (1/g)[2\Phi_{jx} + 2\chi_y \Phi_{jy} + \chi_{yy} \Phi_j] \quad \text{on} \quad z = 0. \quad (3-46)$$

The quantities n_j were defined previously, in (2-72), as the six components of a generalized normal vector. Also, the quantities m_j were defined earlier, by (2-75). In the present notation, let $\mathbf{v}(x, y, z)$ (see (2-74)) be defined by

$$\mathbf{v}(x, y, z) = \nabla[x + \chi(x, y, z)].$$

Then m_j is again given by the previous formulas. Now it requires just a bit of manipulating to show that the assumed solution above indeed satisfies the body and free-surface boundary conditions; I omit the proof.

The above near-field solution must match the far-field solution, which has an inner expansion given in (3-40). In connection with the latter, a comment was made earlier that the near-field solution would have to represent a wave motion in which one component grows linearly in amplitude as $|y| \rightarrow \infty$. Now we can see that just such an interpretation must be given to the Ω_j functions, for otherwise we cannot possibly find solutions to the problems set above for Ω_j . The nonhomogeneous free-surface condition on Ω_j can be compared to the free-surface condition that would result if a pressure distribution were applied to the free surface. In fact, if a pressure field were applied externally on $z = 0$, the pressure being given by

$$p(x, y, t) = i\rho\omega U \xi_j(t)[2\Phi_{jx} + 2\chi_y \Phi_{jy} + \chi_{yy} \Phi_j],$$

then the potential function would have to be $(i\omega)^2 U \Omega_j \xi_j(t)$, with $\Omega_j(x, y, z)$ satisfying the conditions stated previously. This

"pressure distribution" is periodic in time, and it is also periodic in y as $|y| \rightarrow \infty$; the latter comes from the term containing $\Phi_{j\infty}$. Furthermore, the time and space periodicities are related to each other in just the way that one would expect for a plane gravity wave. This can be proven by studying the boundary-value problem for Φ_j . Thus, there is an effective pressure distribution over an infinite area, and it excites waves at just the right combination of frequency and wave length so that we have a resonance response. In an ordinary two-dimensional problem, there would be no solution satisfying all of these conditions. However, our solution need not be regular at infinity; it must only match the far-field expansion. And the far-field expansion predicts an appropriate singular behavior at infinity. It is shown by Ogilvie and Tuck that the solution of this inner problem does exactly match the above far-field solution. The way the pieces of the puzzle all fit together is rather typical of the method of matched asymptotic expansions, and it indicates at least that the manipulations of asymptotic relations were probably done correctly! (It still says nothing about the correctness of the assumptions.)

There is no benefit to be derived by repeating here the solution of the above detailed problems. Rather, we jump to the results for the heave force and the pitch moment, and we do little more than compare these results with the comparable formulas in two previous problems:

CASE 1: The oscillating slender body, with forward speed, in an infinite fluid (Section 2.32)

CASE 2: The oscillating slender body (ship), at zero forward speed, on a free surface (Section 3.3)

In all cases, let the force (moment) be expressed in the form:

$$F_j^m(t) = - \sum_{i=3,5} [(i\omega)^2 a_{ji} + (i\omega) b_{ji} + c_{ji}] \xi_i(t).$$

We define c_{ji} to be independent of frequency and of forward speed. (We must make some such arbitrary convention, or the separation into a_{ji} and c_{ji} components is not unique.) With this convention, c_{ji} represents just the buoyancy restoring force (moment). Thus, $c_{ji} = 0$ for all j, i in case 1; in cases 2 and 3, c_{ji} is given by:

$$[c_{ji}] = 2\rho g \int_L dx \{1, -x\} \begin{pmatrix} 1 \\ -x \end{pmatrix} b(x, 0).$$

Table 3-1 shows a_{ji} and b_{ji} for the three problems. In Cases 1 and 2, the results have been obtained from Sections 2.32 and 3.3, respectively. For Case 3, the present problem, the lengthy derivation will be found in Ogilvie and Tuck [1969]. Some points should be noted:

1. All of the terms in Case 3 include the corresponding Case 2 terms, i.e., the added mass and damping at forward speed can be computed in terms of the added mass and damping at zero speed, plus a speed-dependent component. Formally, we could also say that Case 1 includes all of the Case 2 terms, with $n(x)$ set equal to zero. From this point of view, the only differences among the three cases are the forward-speed effects.

2. The coupling coefficients b_{35} and b_{53} include a forward-speed term $\mp Ua_{33}$ in both Case 1 and Case 3. This means, first of all, that there can be some damping even in the infinite-fluid problem. Secondly, it means that this contribution to the damping coefficients is not altered by the presence of the free surface. Note that in neither case is it necessary to ignore the steady perturbation of the incident stream (the χ terms in (3-41), for example) in order to obtain this result.

3. The other coupling coefficients, a_{35} and a_{53} , contain similar speed-dependent terms in Case 3; they arise at the same point in the analysis as the terms discussed in 2 above. We could arbitrarily include such terms, $\pm(U/\omega)b_{33}$, in Case 1 too, without causing any errors since b_{33} is zero anyway in Case 1.

4. In Case 1, there is a speed-dependent term in a_{55} which is lacking in Case 3. The reason for the lack is that such a term is higher order in terms of ϵ in the ship problem, because of the assumption that $\omega = O(\epsilon^{-1/2})$. There was no need for a high-frequency assumption in Case 1, and so the extra term could legitimately be retained.

5. If, in Case 3, one arbitrarily includes the forward-speed term, $-(U/\omega)^2 a_{33}$, in the a_{55} coefficient, making it identical to the Case 1 coefficient, then it is consistent to modify b_{55} in a similar way, namely by changing it to:

$$b_{55} = \int_L dx x^2 n(x) - (U/\omega)^2 b_{33}.$$

The relationship between these forward-speed effects is quite the same as that discussed above in paragraphs 2 and 3. In the b_{55} coefficient of Case 1, we could also introduce an extra term, $-(U/\omega)^2 b_{33}$, without causing any error, since b_{33} is zero anyway in this case. Thus we can maintain the symmetry between Case 1 and Case 3.

TABLE 3-1

ADDED-MASS AND DAMPING COEFFICIENTS IN THREE PROBLEMS

	CASE 1 - Body with Forward Speed in Infinite Fluid	CASE 2 - Ship with Zero Forward Speed on Free Surface	CASE 3 - Body with Forward Speed on Free Surface
a_{33}	$\int_L dx m(x)$	$\int_L dx m(x)$	$\int_L dx m(x)$
b_{33}	0	$\int_L dx n(x)$	$\int_L dx n(x)$
a_{35}	$-\int_L dx xm(x)$	$-\int_L dx xm(x)$	$-\int_L dx xm(x) + (U/\omega^2)b_{33} - (2\rho\nu U/\omega) \operatorname{Im} \{I\}$
b_{35}	$-Ua_{33}$	$-\int_L dx xn(x)$	$-\int_L dx xn(x) - Ua_{33} - (2\rho\nu U) \operatorname{Re} \{I\}$
a_{53}	$-\int_L dx xm(x)$	$-\int_L dx xm(x)$	$-\int_L dx xm(x) - (U/\omega^2)b_{33} + (2\rho\nu U/\omega) \operatorname{Im} \{I\}$
b_{53}	$+Ua_{33}$	$-\int_L dx xn(x)$	$-\int_L dx xn(x) + Ua_{33} + (2\rho\nu U) \operatorname{Re} \{I\}$
a_{55}	$\int_L dx x^2 m(x) - (U/\omega^2)a_{33}$	$\int_L dx x^2 m(x)$	$\int_L dx x^2 m(x)$
b_{55}	0	$\int_L dx x^2 n(x)$	$\int_L dx x^2 n(x)$

NOTE 1) In all cases, $m(x)$ and $n(x)$ are defined:

$$m(x) + \frac{1}{i\omega} n(x) \equiv \rho \int_{C(x)} dl n_3 \phi_3,$$

where $C(x)$ is the wetted part of the cross section contour at x , and n_3 and ϕ_3 have the same meaning as in Section 2.32 and 3.3. In CASE 1, ϕ_3 is a real quantity, and so $n(x) = 0$.

NOTE 2) The quantity I in Case 3 is defined as follows: Let $\phi = \phi_3$ and let ϕ_∞ be a 2-D potential function which is sinusoidal in y , such that $|\phi - \phi_\infty| \rightarrow 0$ as $y \rightarrow \infty$. Then:

$$I \equiv \int_L dx \left[\int_{b(x,0)}^{\infty} dy [\phi^2(x,y,0) - \phi_\infty^2(x,y,0)] - \frac{1}{2\nu} \phi_\infty^2(x,b(x,0),0) \right],$$

where $b(x,z)$ gives the hull offset corresponding to the point $(x,0,z)$ on the centerplane.

6. The only forward-speed terms not yet discussed are those in Case 3 which involve the integral I. They arise from the inclusion of the functions Ω_j in the potential function, as in (3-43), and the necessity for including those functions is a consequence of the fact that the right-hand side of (3-42), the free-surface condition, is not zero. Now, the right-hand side of (3-42) represents an interaction between the forward motion and the oscillation. One might try to simplify matters by assuming that one can neglect the effects of χ , the perturbation of the incident stream by the body. But this reduces (3-42) to the following:

$$\psi_{tt} + g\psi_z \simeq -2U\psi_{tx}, \quad \text{on } z = 0. \quad (3-47)$$

$$O(\epsilon^{1/2}\delta) \quad O(\epsilon\delta)$$

The right-hand side is still not zero, and we would still have the Ω_j functions to contend with. In fact, it may be recalled that this remaining term on the right-hand side was the one that caused the major trouble in interpreting the Ω_j problems. Neglect of the χ terms leads to the condition on Ω_j (cf. (3-46)):

$$\Omega_{jz} - v\Omega_j = -(2/g)\Phi_{jz}, \quad \text{on } z = 0, \quad (3-48)$$

and it is the one remaining right-hand term which causes the solution for Ω_j to diverge at infinity. The usual procedure at this point is to set $\Omega_j = 0$, turn the other way, and just ignore these problems. The results are in remarkably good agreement with experimental observations, and one still wonders how this can be rationalized mathematically.

Finally, we should at least mention the problem of predicting wave excitations in the forward-speed problem. The singular perturbation problem involved in solving for the diffraction waves has not been satisfactorily worked out yet, at least, not in a manner compatible with the approach presented above.

One might hope to avoid the diffraction problem by using the Khaskind relations, as in the zero-speed problem. (See Section 3.3.) In fact, Newman [1965] has derived what I call the Khaskind-Newman relations. These provide a generalization of Khaskind's formula, relating the wave excitation on a moving ship to the problem of forced oscillations of the ship when the ship is moving in the reverse direction. Unfortunately for our purposes, Newman's derivation is based on an a priori linearization of the free-surface, in the sense that our terms involving χ can be neglected. Therefore, the appropriate diffraction problem cannot really be avoided in this way. Also, it is necessary to have available the potential function for the forced-motion problem, and this includes at least a part of the Ω_j functions even if the χ dependence is ignored.

In a not-yet published paper, Newman has applied the Khaskind-Newman relations in the forward-speed problem by arbitrarily ignoring the Ω_j functions in the forced-motion potential function. He finds for the heave excitation force:

$$F_3^w(t) \approx \rho g h (1 + U \omega_0 / g) e^{i \omega t} \int_L dx e^{-i \nu_0 x} \int_{C(x)} dl n e^{\nu_0 z} \cdot \left[1 - \nu_0 \Phi_3 + \frac{U \nu_0}{i \omega} (\chi_z + \Psi_3) - \frac{U \nu_0}{\omega} \right],$$

where, as before, ω is the frequency of oscillation (that is, the frequency of encounter) and $\nu = \omega^2/g$; the frequency measured in an earth-fixed reference frame is denoted by ω_0 , and we define $\nu_0 = \omega_0^2/g$. The actual wave length of the incident waves is $\lambda = 2\pi/\nu_0$. The two frequencies are related as follows: $\omega = \omega_0 + U \omega_0/g$. These formulas are all valid for the head-seas case only.

This formula should be compared with (3-34a), which was the corresponding result in the zero-speed problem. The first term in brackets yields the Froude-Krylov force, and the second term yields a pure-strip-theory prediction of the diffraction wave force, which can be interpreted approximately in terms of the relative-motion hypothesis. The remaining terms represent an interaction between forward speed and the incident waves.

Again, it should be pointed out that more than just nonlinear effects have been neglected in setting Ω_j equal to zero. In fact, the usual linear free-surface condition for ship-motions problems can be written:

$$\psi_{tt} + g\psi_z = -2U\psi_{tx} - U^2\psi_{xx}, \quad \text{on } z = 0.$$

(Cf. (3-37) and (3-47).) Even the inclusion of the Ω_j terms still omits some effects usually considered as linear, namely, the effects of the term $-U^2\psi_{xx}$ in this boundary condition. These effects are higher order in the theory presented here solely because of the high-frequency assumption.

IV. THIN-SHIP THEORY AS AN OUTER EXPANSION

It has already been shown how one can view a symmetrical thin-body problem in terms of inner and outer expansions; the usual description of the flow around such a body is really just the first term of an outer or far-field expansion. It was not at all obvious that one had to use such a powerful method on such a problem, but it was clear that one could do this. Probably the only advantage of doing

so in the infinite-fluid case was that one could avoid possible questions about the validity of analytically continuing the potential function inside the body surface. On the other hand, one had then to face all kinds of difficulties in principle in justifying use of matched asymptotic expansions. It was a rather academic exercise.

The situation may be quite different in the thin-ship problem. The purpose of this chapter is to show one can obtain the first results of thin-ship theory in the same way as for the infinite-fluid problem but that a second-order solution leads to fundamental difficulty. The latter appears to suggest that a combination thin-body/slender-body approach may be appropriate. A limited amount of other evidence may be cited to support this idea.

I wish to emphasize that there are no new results in this chapter. It is all a matter of interpretation. Perhaps someone will be able to show that the problem discussed here has a trivial explanation. On the other hand, perhaps someone will be stimulated to do further research on the subject. In either case, I shall be happy with the outcome.

The problem may be partially stated just as the infinite-fluid, thin-body problem was stated. Let there be a velocity potential, $\phi(x, y, z)$, which satisfies the Laplace equation,

$$[L] \quad \phi_{xx} + \phi_{yy} + \phi_{zz} = 0,$$

everywhere in the fluid domain and the body boundary condition,

$$[H] \quad 0 = \phi_x h_x + \phi_y + \phi_z h_z, \quad \text{on} \quad y = \pm h(x, z) = \pm \epsilon H(x, z).$$

Now we add on the two free-surface conditions:

$$[A] \quad \frac{1}{2} U^2 = g\zeta + \frac{1}{2} [\phi_x^2 + \phi_y^2 + \phi_z^2], \quad \text{on} \quad z = \zeta(x, y);$$

$$[B] \quad 0 = \phi_x \zeta_x + \phi_y \zeta_y - \phi_z, \quad \text{on} \quad z = \zeta(x, y).$$

Also, we must specify a radiation condition.

In the far field, where $y = O(1)$, we assume the existence of the expansions:

$$\left. \begin{aligned} \phi(x, y, z) &\sim \sum_{n=0}^N \phi_n(x, y, z), \\ \zeta(x, y) &\sim \sum_{n=1}^N \zeta_n(x, y), \end{aligned} \right\} \quad \text{for fixed } (x, y, z);$$

$$\left. \begin{aligned} \phi(x, y, z) &\sim \sum_{n=0}^N \Phi_n(x, y, z), \\ \zeta(x, y) &\sim \sum_{n=1}^N Z_n(x, y), \end{aligned} \right\} \text{ for fixed } (x, y/\epsilon, z).$$

We assume right away that:

$$\phi_0(x, y, z) = \Phi_0(x, y, z) = Ux.$$

In the far field, the ship vanishes as $\epsilon \rightarrow 0$, and so we take the entire outside of the plane $y = 0$ (below the free surface) as the far field. It is easily seen that the second term in the outer expansion must be of the form:

$$\phi_1(x, y, z) = -\frac{1}{4\pi} \iint_{\mathbf{H}} \sigma_1(\xi, \zeta) G(x, y, z; \xi, 0, \zeta) d\xi d\zeta, \quad (4-1)$$

where \mathbf{H} is the portion of the centerplane of the ship below $z = 0$, $\sigma_1(x, z)$ is an unknown source density, and $G(x, y, z; \xi, \eta, \zeta)$ is the usual Green's function for a linearized problem of steady motion with a free surface. It has the important property:

$$G_{xx} + \kappa G_z = 0, \quad \text{on} \quad z = 0, \quad (4-2)$$

where $\kappa = g/U^2$. Of course, the potential ϕ_1 , also has this property:

$$\phi_{1xx} + \kappa \phi_{1z} = 0, \quad \text{on} \quad z = 0.$$

For later convenience, we define

$$\alpha_1(x, z) \equiv \phi_1(x, 0, z), \quad (4-3)$$

and so $\alpha_1(x, z)$ has the property too:

$$\alpha_{1xx} + \kappa \alpha_{1z} = 0, \quad \text{on} \quad z = 0. \quad (4-4)$$

With $\phi_1(x, y, z)$ given by (4-1), the two-term outer expansion is:

$$\phi(x, y, z) \sim Ux + \phi_1(x, y, z),$$

and the inner expansion of the two-term outer expansion is:

$$\phi(x, y, z) \sim Ux + \alpha_1(x, z) + \frac{1}{2} |y| \sigma_1(x, z) + \dots$$

$$O(1) \quad O(\epsilon) \quad O(\epsilon^2)$$

I have taken my usual liberty of indicating unproven orders of magnitude. I am not really assuming these orders of magnitude; I am saying that one can prove that these are correct, and I display them here now simply as an aid to the reader.

Now consider the near field. Just as in the infinite-fluid problem, one may stretch coordinates, $y = \epsilon Y$, and follow through the consequences. This is effectively what I do, without writing the change of variable explicitly. Thus, the Laplace equation yields the condition:

$$\phi_{1yy} = 0,$$

and so ϕ_1 must be a linear function of y . The same analysis as used in the infinite-fluid problem, Section 2.11, leads to the conclusion that Φ_1 is even more restricted than this. It must be a constant with respect to y . Thus, let:

$$\Phi_1(x, y, z) \equiv A_1(x, z).$$

The two-term inner expansion is then:

$$\phi(x, y, z) \sim Ux + A_1(x, z).$$

Matching gives the unsurprising result that:

$$A_1(x, z) = \alpha_1(x, z). \quad (4-5)$$

In other words, once again the inner expansion starts out simply as the inner expansion of the outer expansion; it is not necessary to formulate a near-field problem to obtain this result.

The same arguments lead to the prediction that:

$$\Phi_2(x, y, z) = A_2(x, z) + U h_x(x, z) |y|. \quad (4-6)$$

Thus the three-term inner expansion is formed, and it can be matched with the three-term inner expansion of the two-term outer-expansion, yielding the familiar result once again that:

$$\sigma_1(x, z) = 2U\eta_x(x, z).$$

(See (2-22).) This obviously had to come out this way, since we have not yet introduced any effects of the presence of the free surface. It should be noted that only the function $A_2(x, z)$ is not already determined. (Knowledge of $\sigma_1(x, z)$ allows us to express $\alpha_1(x, z)$ explicitly, from (4-1) and (4-3).)

A systematic treatment of the free surface-conditions leads to the following:

$$[A] \quad 0 = gZ_1 + U\Phi_{1x} \quad O(\epsilon)$$

$$+ gZ_2 + U\Phi_{2x} + UZ_1\Phi_{1xz} + \frac{1}{2}(\Phi_{1x}^2 + \Phi_{1z}^2) + \frac{1}{2}(\Phi_{2y}^2) \quad O(\epsilon^2)$$

$$+ \dots, \quad \text{on } z = 0;$$

$$[B] \quad 0 = UZ_{1x} - \Phi_{1z} \quad O(\epsilon)$$

$$+ UZ_{2x} - \Phi_{2z} - Z_1\Phi_{1zz} + \Phi_{1x}Z_{1x} + \Phi_{2y}Z_{2y} \quad O(\epsilon^2)$$

$$+ \dots, \quad \text{on } z = 0.$$

The lowest-order conditions in [A] and [B] together require that:

$$\Phi_{1xx} + K\Phi_{1z} = 0, \quad \text{on } z = 0.$$

We see that this is automatically satisfied by our $\Phi_1(x, y, z) = A_1(x, z) = \alpha_1(x, z)$. (See (4-4).) The first term in the expansion for wave shape in the near field is also determined:

$$Z_1(x, y) \doteq -\frac{U}{g}\bar{\Phi}_{1x}(x, 0).$$

This really says only that the free surface appears in the near field to be raised (or lowered) by just the limiting value (as $y \rightarrow 0$) of $\zeta(x, y)$ in the far field. Again, a rather trivial result.

When we consider the ϵ^2 terms in the free-surface conditions, it is a different matter. The two conditions can be combined into the following:

$$\begin{aligned}
 0 = \Phi_{2xx} + \kappa \Phi_{2z} - \frac{U}{g} (\alpha_{1x} \alpha_{1xz})_x + \frac{1}{2U} (\alpha_{1x}^2 + \alpha_{1z}^2)_x \\
 + \frac{U}{2} (h_x^2)_x - \frac{1}{U} \alpha_{1x} \alpha_{1zz} + \frac{1}{U} \alpha_{1xx} \alpha_{1x} \mp \frac{g}{U} h_x Z_{2y}.
 \end{aligned}
 \tag{4-7}$$

In condition [A], we note that differentiation of the ϵ^2 terms with respect to y yields:

$$0 = gZ_{2y} \pm U^2 h_{xx}.$$

Therefore, in the complicated free-surface condition above, (4-7), only the first two terms involve y ; all of the other terms are functions of just x . From (4-7) and (4-6), we can thus write the following:

$$0 = [h_{xxx}(x, 0) + \kappa h_{xz}(x, 0)] U|y| + (\text{a function of } x).$$

This must be true for any y , and so we obtain the condition:

$$0 = h_{xxx} + \kappa h_{xz}, \quad \text{on} \quad z = 0.$$

If the ship is wall-sided at $z = 0$, the second term is separately zero, and so we would have to require that $h_{xxx} = 0$ at $z = 0$.

Now this is clearly unacceptable. Why should our theory work only for such a special case? (The waterline is made of circular arcs in this case.)

As a result of our having stretched the coordinates, we came to the prediction that the fluid velocity near the thin body consists of a tangential component which is essentially independent of the local conditions plus a normal component which depends only on local conditions. Near the free surface, such results are simply untenable.

I present here a formalism which apparently avoids this difficulty. Again, I point out that no new results are obtained. However, it does seem possible that the procedure might be fruitful if studied further.

The idea is to define a third region, complete with its own asymptotic expansions of ϕ and ζ . This region will be essentially the same as the near field in a slender-body analysis, that is, it is a region in which $y = O(\epsilon)$ and $z = O(\epsilon)$ as $\epsilon \rightarrow 0$. It follows from this assumption that $\partial/\partial y$ and $\partial/\partial z$ both have the effect of changing orders of magnitude by a factor $1/\epsilon$. What is most important is that this region is interposed between the thin-body near field and

the free surface. Thus, it is no longer necessary or even proper to try to make the previous inner expansion satisfy the free-surface conditions.

We expect, as usual, that the first term in the expansion of ϕ in this new near field will be just Ux . Furthermore, we can expect the next term to be rather trivial, since the second term in the previous near-field expansion did actually satisfy the free-surface condition. Using the usual arguments of slender-body theory, we find in fact that the three-term expansion of ϕ in this new field is:

$$\phi(x, y, z) \sim Ux + a_1(x, 0) + Uh_x(x, 0)|y| - \frac{1}{\kappa} z a_{1xx}(x, 0).$$

$$O(1) \quad O(\epsilon) \quad O(\epsilon^2) \quad O(\epsilon^2)$$

The corresponding wave shape is found to be:

$$\begin{aligned} \zeta(x, y) \sim & -\frac{U}{g} a_{1x}(x, 0) & O(\epsilon) \\ & -\frac{U}{g} \left[Uh_{xx}(x, 0)|y| + \frac{U^3}{g^2} a_{1x}(x, 0) a_{1xxx}(x, 0) \right] & \\ & -\frac{1}{2g} \left[a_{1x}^2(x, 0) + U^2 h_x^2(x, 0) + \left(\frac{U^2}{g} \right) a_{1xx}^2(x, 0) \right] & \left. \vphantom{\begin{aligned} \zeta(x, y) \sim \end{aligned}} \right\} O(\epsilon^2) \\ & + \dots \end{aligned}$$

It can be shown in straightforward fashion that these results match the far-field expansion as $\sqrt{(y^2 + z^2)} \rightarrow \infty$ and they match the previous (thin-body) near-field expansion as $z \rightarrow -\infty$. Furthermore, they satisfy the free-surface conditions without the necessity for imposing unacceptable restrictions on the body shape. There is just one aspect that requires special care: The free-surface conditions cannot be satisfied on the surface $z = 0$ in this near field. The reason is that the first term of the ζ expansion is $O(\epsilon)$, and differentiation with respect to z is assumed to change orders of magnitude by $1/\epsilon$. Thus, suppose that we want to evaluate some function $f(z)$ on $z = \zeta$ in terms of its value (and values of its derivatives) on $z = 0$. The usual procedure is to write:

$$f(\zeta) = f(0) + \zeta f'(0) + \frac{1}{2} \zeta^2 f''(0) + \dots$$

$$O(f) \quad O(\epsilon) \cdot O(f/\epsilon) \quad O(\epsilon^2) \cdot O(f/\epsilon^2)$$

With our set of assumptions, this expansion is useless; we cannot

terminate it. The one simplification which is admissible here is to evaluate $f(z)$ and its derivatives on $z = Z_1$, where $\zeta = Z_1 + o(\epsilon)$.*

I have not worked out any more terms in any of these expansions, but I suppose that the next term in this near-field expansion will be much more interesting. In the far field, it is well-known that the third term in the expansion of the potential function will include the effects of what appears to be a pressure distribution over the free surface. It was shown by Wehausen [1963] that at the intersection of the undisturbed free surface and the hull surface the solution is singular, and he represented the singular part by a line integral taken along this line of intersection. From the point of view of the method of matched asymptotic expansions, it should be possible to represent the far-field effects of that line integral in terms of an equivalent line of singularities on the x axis. The strength of the singularities would be determined, as usual, by matching the solution to the near-field expansion. At this stage, thin-ship theory will have become a singular perturbation problem.

V. STEADY MOTION IN TWO DIMENSIONS (2-D)

Sometimes we study two-dimensional problems with the intent of incorporating the solutions into approximate three-dimensional solutions, as in the treatment of high-aspect-ratio wings and in slender-body theory. And sometimes we investigate two-dimensional problems simply because the corresponding three-dimensional problems are too difficult.

The problems discussed in this section are in the second group. It is not likely that any of these problems and their solutions will have practical application before several more years have passed, even in the context of strip theories. Here are some of the most fundamental difficulties related to the presence of the free surface.

The first two subsections concern a 2-D body which pierces the free surface. Such a problem is intrinsically nonlinear. We might try to formulate the problem as a perturbation problem, in this case involving a perturbation of a uniform stream. However, there must be a stagnation point somewhere on the body, and at that point the perturbation velocity is equal in magnitude to the incident stream velocity. It is not small! If the stagnation point is near the free surface, the free-surface conditions cannot be linearized. We must find methods which are adaptable to highly nonlinear problems.

Such a method is the classical hodograph method, used since

*The same difficulty arises also in Sections 3.2 and 5.42.

the nineteenth century for solving free-streamline problems. But it introduces a new difficulty: It cannot be used to treat free streamlines which are affected by gravity, which means that only infinite-Froude-number problems can be treated directly. This leads to a further great difficulty, which is discussed in some detail in Section 5.1.

In Section 5.3, a brief discussion is presented of the problem studied by Salvesen [1969]. It contains two aspects of interest: It is a case in which the free-surface conditions can be linearized because of the depth of the moving body, and I have already commented in the Introduction that there are very interesting fundamental questions involved in such procedures. Also, it presents a clear example of the classical phenomenon discussed in the section on multiple scale expansions: The wave length obtained in the first approximation must be modified in subsequent approximations, or the solution becomes unbounded at infinity -- where we know perfectly well that the waves are bounded in amplitude.

Finally, Section 5.4 describes two recent attempts to approach the problem of extremely low-speed motion. The difficulty is basically this: In the usual linearization, we assume that all velocity components (at least in the vicinity of the free surface) are much smaller than the forward speed -- which becomes nonsense if we subsequently decide to let U , the forward speed, approach zero. What is needed is a perturbation scheme in which somehow the small parameter is proportional to U . Then it is certainly permissible to allow U to approach zero. Section 5.41 shows a very straightforward procedure for doing this; however, it leads to a sequence of Neumann problems, and so the wave nature of the fluid motion is lost. In Section 5.42, an alternative method is discussed. It is an application of the multiple scale expansion procedure to which Section 1.3 was devoted.

5.1. Gravity Effects in Planing

Before we try to treat this problem properly, let us consider briefly a well-known approach to the 2-D planing problem and determine why it is not completely satisfactory. In the middle 1930's, A. E. Green wrote several papers on the subject, and the essence of his approach is well-presented by Milne-Thomson [1968]. A flat plate is located with its trailing edge at the origin of coordinates, as shown in Fig. (5-1). There is an incident stream with speed U coming from the left, and, at infinity upstream, there is a free surface at $y = h$. The effects of gravity are neglected. The fluid is assumed to leave the trailing edge smoothly (a Kutta condition), and a jet of fluid is deflected forward and upward by the plate. In the absence of gravity, the jet never comes down to trouble us again. In the figure, A marks the leading edge of the plate and C marks the stagnation point.

The physical plane shown in Fig. (5-1) is also the complex

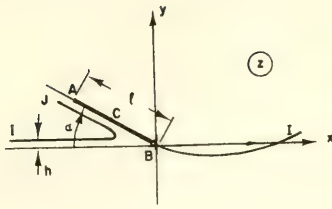


Fig. (5-1). Planing Problem in the Physical Plane

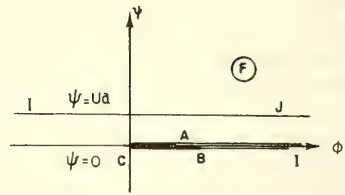


Fig. (5-2). Planing Problem in the Plane of the Complex Potential.

$z = x + iy$ plane. Let $F(z) = \phi(x,y) + i\psi(x,y)$ be the complex velocity potential for this problem. Then $F(z)$ effects a mapping of the z plane onto an F plane, as shown in Fig. (5-2), in which points are marked to correspond to Fig. (5-1). It is assumed that $\phi = 0$ and $\psi = 0$ at the stagnation point. Furthermore, we have set $\psi = Ua$ on the upstream free-surface streamline, IJ, which implies that a is the thickness of the jet and that Ua is the rate at which fluid leaves in the jet. Of course, $F(z)$ is not known yet.

We can also consider that the z plane is mapped by the function $w(z) = dF/dz$. $w(z)$ is the "complex velocity," that is, $w = u - iv$, where u and v are the velocity components in the x and y directions, respectively. The entire fluid region is mapped by $w(z)$ into the region bounded by a half-circle and its diameter, as shown in Fig. (5-3). Again, points are marked to correspond to Fig. (5-1). The diameter is the image of the planing surface, on which the direction of the velocity vector is known, and the circle is the image of the entire free surface, on which the magnitude of the velocity vector is known (from the Bernoulli equation). Again, we note that the mapping function itself is not yet known.

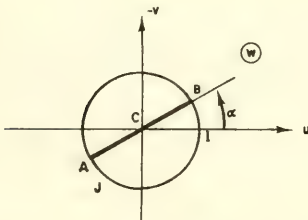


Fig. (5-3). Planing Problem in the Plane of the Complex Velocity.

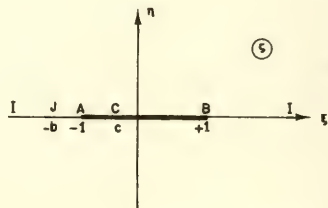


Fig. (5-4). Planing Problem in the Auxiliary (ζ) Plane.

The functions $w(z)$ and $F(z)$ are, of course, very simply related, although neither is known explicitly yet. In order to obtain another relationship, one introduces the $\zeta = \xi + i\eta$ plane, in which the fluid domain is mapped into the lower half-space, as shown in Fig. (5-4). We can write out the explicit expressions for mapping the F and w planes into the ζ plane. The first is accomplished by means of the Schwarz-Christoffel transformation:

$$\frac{dF}{d\zeta} = \frac{Ua}{\pi(b+c)} \frac{\zeta - c}{\zeta + b} \equiv H(\zeta),$$

which can actually be integrated, yielding:

$$F(z(\zeta)) = \frac{Ua}{\pi} \left(\frac{\zeta - c}{b+c} - \log \frac{\zeta + b}{b+c} \right).$$

The second mapping can be shown to take either of the equivalent forms:

$$\begin{aligned} w(z(\zeta)) &= Ue^{i\alpha} \frac{\zeta - c}{(1 - \zeta c) + i\sqrt{(1 - c^2)}\sqrt{(\zeta^2 - 1)}} \\ &= Ue^{i\alpha} \frac{(1 - \zeta c) - i\sqrt{(1 - c^2)}\sqrt{(\zeta^2 - 1)}}{\zeta - c}. \end{aligned} \quad (5-1)$$

The solution is then completed by using the relationship between F and w , along with these expressions, to obtain the relationship between z and ζ . Since:

$$\frac{dz}{d\zeta} = \frac{dz}{dF} \frac{dF}{d\zeta} = \frac{H(\zeta)}{w(z(\zeta))},$$

of which the right-hand side is known, we can integrate to obtain:

$$\begin{aligned} z(\zeta) &= \int_1^\zeta \frac{H(\zeta')}{w(z(\zeta'))} d\zeta' \\ &= \frac{ae^{-i\alpha}}{\pi(b+c)} \left(-c(\zeta-1) + (1+bc) \log \frac{\zeta+b}{b+1} + i\sqrt{(1-c^2)}\sqrt{(\zeta^2-1)} \right. \\ &\quad \left. - ib\sqrt{(1-c^2)} \log [\zeta + \sqrt{(\zeta^2-1)}] \right. \\ &\quad \left. - i\sqrt{(1-c^2)}\sqrt{(b^2-1)} \log \frac{1+b\zeta - \sqrt{(b^2-1)}\sqrt{(\zeta^2-1)}}{\zeta+b} \right) \end{aligned}$$

So now we have z as a function of ζ , as well as F and w as functions of ζ .

There are three parameters in this solution, a , b , and c , none of which has been determined yet. By letting $|\zeta| \rightarrow \infty$, Green came to the conclusion that the flow far away is a uniform stream as required only if:

$$c = -\cos \alpha \quad \text{and} \quad \sqrt{(1 - c^2)} = \sin \alpha. \quad (5-2)$$

(Both statements are necessary to avoid an ambiguity in sign.) Also, one can use the $z(\zeta)$ formula to evaluate z at the leading edge of the plate:

$$z(-1) = -le^{-i\alpha}.$$

(Compare Figs. (5-1) and (5-4).) This provides a relationship among a , b , and c . But there are no more conditions to be found unless we introduce more information about the physical problem. For example, we could use the solution with unspecified values of a and b , and work out the formula for lift on the plate. (Milne-Thomson gives the formula.) If then we fix the value of lift, we have another condition on a and b . However, this is rather a backwards way of going at the problem. We are most likely to want to solve the entire problem just to find the lift and other interesting physical quantities, and so we have not gained much if we must assume the value of the lift as a given datum.

There is another anomaly in this result: The value of h (See Fig. (5-1)) has not been used in any way. In the formula for $z(\zeta)$, let $\zeta = \xi$, with $|\xi|$ very large. Then every value of z computed in this way gives a point on the free surface far away from the planing surface. With a considerable amount of tedious algebra, one can eliminate ξ and express y as a function of x (at least asymptotically, as $|x| \rightarrow \infty$). The first term is the most interesting:

$$y \sim -\frac{a\sqrt{(1 - c^2)}}{\pi(b + c)} [\log |x| + \text{constant}].$$

Thus, far away from the planing surface, the free surface apparently drops off logarithmically to $-\infty$. The slope of the free surface approaches zero ($\propto 1/|x|$) and so there is no violation of our assumption that the flow at infinity is simply a streaming motion parallel to the x axis. But obviously the assumption that the trailing edge was located at a height h below the free-surface level at infinity was quite meaningless, and it cannot be enforced in the solution.

There are thus two difficulties: 1) The above solution is not unique (a common difficulty in free-streamline problems); 2) It has unacceptable behavior at infinity.

These difficulties were resolved by Rispin [1966] and Wu [1967], who recognized that the solution of Green's problem is part of a near-field (inner) expansion of the complete solution. An inner expansion does not necessarily satisfy the obvious conditions at infinity; it must only match some outer expansion in a proper way. Rispin and Wu produced the appropriate outer expansions and showed that matching does occur. The effects of gravity appear first in the far field, which is hardly surprising, for two reasons: 1) Far away, one expects to find gravity waves as the only disturbance. 2) The divergence of the free-surface shape in Green's solution is so weak that one might expect the smallest amount of gravity effect to bring the free surface into the region where we expect to find it: thus, the small effect of gravity eventually would have a large consequence, but only far away from the planing surface.

Rispin defines the small parameter:

$$\beta \equiv g\ell/U^2 = 1/F^2,$$

where F is the usual Froude number. In the near field, the natural coordinates are used, which means effectively that ℓ is considered to be $O(1)$. Smallness of β is achieved by allowing $g \rightarrow 0$ or $U \rightarrow \infty$. Rispin treats his small parameter properly by nondimensionalizing everything, so that he then does not have to specify whether $U \rightarrow \infty$ or $g \rightarrow 0$. Rather than change all variables now, I shall treat g as a small parameter, as in Section 3.2; the results are the same as Rispin's, of course.

In the far field, typical lengths are assumed to be $O(1/\beta)$ in magnitude, or $O(1/g)$, in my loose notation. We could define new coordinates, say,

$$\hat{z} = \beta z; \quad \hat{x} = \beta x; \quad \hat{y} = \beta y,$$

and consider that $\hat{z} = O(1)$ as $g \rightarrow 0$ in the far field, while $z = O(1)$ as $g \rightarrow 0$ in the near field. Rather than do this, we shall just keep in mind that such orders of magnitude are to be assumed. Also, we note that $d/dz = O(1)$ in the near field and $d/dz = O(\beta)$ in the far field.

This problem is reversed from the most common kind of stretched-coordinate problem: The inner problem is solved by natural coordinates, and the outer coordinates are compressed. Note, however, that there is no distortion of coordinates between near- and far-fields. There is just a change of scale.

In the far field, the planing surface appears to vanish in the limit, and so the first term in a far-field expansion must represent just the incident uniform stream. That is, if the outer expansion is represented:

$$F(z;\beta) \sim \sum_{n=0}^N F_n(z;\beta), \quad w(z;\beta) \sim \sum_{n=0}^N W_n(z;\beta), \quad \text{for fixed } \beta z \\ \text{as } \beta \rightarrow 0,$$

then clearly we have:

$$F_0(z;\beta) = Uz, \quad \text{and} \quad W_0(z;\beta) = U.$$

This one-term outer expansion must match the one-term inner expansion, the latter being just Green's solution. This much of the matching procedure is rather obvious, and Green already used this fact to determine the value of c , as given in (5-2).

The next term in the outer expansion is not quite so obvious. In order to facilitate the matching process, Rispin solved the problem in the ξ plane, just as we did above for Green's problem. The free-surface boundary condition on W_1 is not much different from the familiar linearized condition. One can show fairly simply that:

$$\operatorname{Re} \left[\frac{dW_1}{d\xi} + \frac{igA}{U^2} W_1 \right] = 0 \quad \text{on} \quad \eta = 0,$$

where $A = a/\pi(b+c)$. (The factor A is just the value of $dz/d\xi$ far away from the planing surface.) Note that the first term is $O(\beta W_1)$ because of the differentiation, and the second term is the same order because of the g factor. The solution for W_1 must be analytic in the lower half-space and satisfy this condition on $\eta = 0$, $|\xi| > 0$; note the exclusion of the origin, where singularities may occur.

As usual, we try to restrict the singularities to the simplest kind possible. In this case, we would find nothing in the near field to match with if we allowed all kinds of singularities in W_1 . A sufficiently general solution* is the following:

$$W_1(\xi;\beta) = ie^{-igA\xi/U^2} \int_{\infty}^{\xi} dt e^{igAt/U^2} \left[\frac{C_1}{t} + \frac{C_2}{t^2} \right],$$

where C_1 and C_2 are real constants yet to be determined (in the matching).

* Rispin discusses more general solutions, which are needed in constructing higher-order solutions.

The two-term outer expansion is now:

$$w(z;\beta) \sim U + W_1(\zeta;\beta),$$

with W_1 given as above. Its inner expansion to one term is easily found:

$$w(z;\beta) \sim U - \frac{iC_2}{\zeta}.$$

We cannot really say positively that these two terms are the same order of magnitude, but it turns out that they must be if this expression is to match the two-term outer expansion of the one-term inner expansion. The latter is obtained readily from Green's solution for $w(z(\zeta))$ which was given in (5-1). It is:

$$w(z;\beta) \sim U + \frac{iU \sin \alpha}{\zeta}.$$

Then, obviously, we find that:

$$C_2 = -U \sin \alpha.$$

We cannot determine the other constants, C_1 , from the solutions so far obtained. It is necessary to solve for the second term in the inner expansion, and Rispin carries this through. Then, he matches the two-term outer expansion of the two-term inner expansion with the two-term inner expansion of the two-term outer expansion, finding that $C_1 = -aU/\pi$. Thus, C_1 is proportional to the rate at which fluid leaves in the jet; the C_1 term represents a sink, in fact. (The C_2 term represents a vortex.)

Rispin obtains estimates for h as well, but the results are rather complicated, and it would add no perspicuity to the present section to repeat them. The important point in principle is that it is possible now to specify the value of h and not come to a contradiction as a result. The far-field description has effectively provided a height reference, because of the effect of gravity. This effect does not change the first-order inner solution, but it does modify the second-order term. (The velocity magnitude is not constant on the free surface in the second approximation.)

In the second-order term of the inner expansion, there is another interesting phenomenon, namely, the apparent angle of attack changes. This means, physically, that the occurrence of gravity waves modifies the inflow to the planing surface. In the

near field, it is still not possible to see the waves that exist far away, but the latter have the effect of making the incident stream appear to be rotated somewhat. It is like a downwash effect (although the physical origin is quite different).

If one were given a planing problem such as we formulated early in this section, with the incident stream and all geometric parameters prescribed, it would be necessary to solve for the parameters a and b . One equation relating these parameters has already been mentioned, namely, the equation relating the length of the plate to these parameters. The other equation comes from the expression (which was not written out here) for h as a function of a and b .

Rispin avoided much tedious algebra by solving the inverse problem. He assumed that a , b , and c were given, then solved to find h . He also had to treat the angle of attack as an unknown quantity, and he found an asymptotic expansion for it. (Note that only two of the basic parameters can be prescribed arbitrarily, unless we are prepared also to let ℓ be an unknown quantity.)

One final comment on Rispin's work must be made. He finds terms of six orders of magnitude: $O(1)$, $O(\beta \log \beta)$, $O(\beta)$, $O(\beta^2 \log^2 \beta)$, $O(\beta^2 \log \beta)$, and $O(\beta^2)$. But he finds also that they cannot be determined one at a time. Rather, they must be taken in groups: a) the $O(1)$ terms, b) the terms linear in β (the logarithm being ignored), and c) the terms involving β^2 . This is the same kind of matching procedure that would have been used if he had adopted the working rule that logarithms should be treated as if they were $O(1)$. (See Section 1.2.)

5.2. Flow Around Bluff Body in Free Surface

A problem related to that of Rispin [1966] and Wu [1967] has been studied by Dagan and Tulin [1969]. They have concerned themselves with the flow at the bow of a blunt ship, where any kind of linearization procedure must be completely wrong. In order to handle such a situation, they have adopted essentially the same procedure that the previous authors used, namely, they set up inner- and outer-expansion problems in which the nonlinearity is confined initially to the near field and the effects of gravity are confined initially to the far field. Then, by limiting their study to a two dimensional problem, the nonlinear near-field problem can be solved by the hodograph method, and the far-field problem is a simple variation of a well-studied problem in water-wave theory. The geometry of their problem is shown in Fig.(5-5), which is reproduced from their paper. They argue that at very low speed there will be a smooth flow up to and then down under the bow, with a stagnation point at the location of highest free-surface rise, but that that flow becomes unstable as speed increases, until finally a jet forms, as

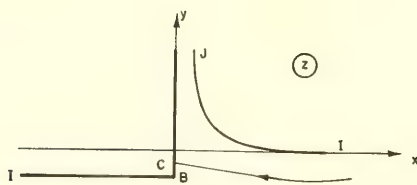


Fig. (5-5). Bluff Body in the Free Surface

sketched in Fig. (5-5). Regardless of whether their description of the flow at very low speed is correct*, this jet model appears to be entirely reasonable physically; a barge-like body usually causes a region of froth just ahead of the bow, and this froth is probably caused by such a jet being thrown upward and forward, then dropping downward (which the theory overlooks). Thus it seems appropriate to study the formation of such a free-surface jet by the use of free-streamline theory, and one may expect that the details of the formation of the jet are not terribly sensitive to the effect of gravity.

The body, as shown in Fig. (5-5), extends downstream to infinity. (In a sense, the whole problem is part of the inner expansion of a much larger problem, in which the stern of the body would be visible and in which waves would follow the body.) Thus, there is no Kutta condition or equivalent which can effectively cause a circulation type of flow in the fluid region. In Green's problem, for example, the flow at great distances appears to have been caused by a vortex. It is this property that causes the apparent logarithmic deflection of the free surface far away from the body, and it is this property that requires the far-field description (as in Rispin's problem) to contain a logarithmic singularity at the origin. Dagan and Tulin have no such logarithmic solutions.

They find that the jet appears, from far away, to be caused by a singularity of algebraic type. Specifically, the outer expansion of their inner expansion shows the complex velocity behaving like $Z^{-3/2}$, where Z is the complex variable defined in the physical plane, shown in Fig. (5-5). Thus, their far-field expansion must exhibit a singularity at the origin of this same type.

This result, if correct, is most interesting, for, as Dagan and Tulin point out, it means that the far-field expression for

* Their Section III. 2 has some questionable aspects.

pressure is not integrable, and so one must use the near-field expansion for any force calculation. Furthermore, it is a disturbing result, because it suggests that many previous attempts to incorporate bow-wave nonlinearities into linear-theory singularities have been futile exercises.

Personally, I am not yet willing to admit that the possibility of having the complex velocity behave like $Z^{-1/2}$ is really to be rejected, as Dagan and Tulin claim. Wagner [1932] analyzed the region of the jet and the stagnation point for the flow against a flat plate of infinite extent downstream, and he showed that this flow, from far away, has the behavior of a flow around the leading edge of an airfoil, that is, the velocity varied with $Z^{-1/2}$. Physically it seems rather difficult to imagine that, by curving the body around just behind the stagnation point, one causes such a drastic change in the apparent singularity.

Dagan and Tulin present a figure (their Fig. 2) in which they have placed many symbols showing beam/draft ratios of more than a hundred ships, and it is quite evident that most ships have values of this ratio considerably greater than unity. They then use this fact as an alleged justification for claiming that their 2-D model of the bow flow (as in Fig. (5-5)) will have some validity in describing the flow around the bow of an actual ship -- since most ships are presumably of the "flat" variety. However, this claim is completely misleading. The theory might apply to a scow, but not to a ship. After all, beam/draft ratio is measured amidships, and even ships with the largest block coefficients have entrance angles less than 180° .

Also, it is appropriate to mention again the warning against defining a small parameter precisely and then trying to interpret on some absolute basis whether a particular value of the parameter is "small enough." For example, it is conceivable that a thin-ship analysis would be valid for a ship with beam/draft ratio of 10, whereas a flat-ship analysis might fail for the same ship. I am not saying that this is likely, but it is possible. In one problem, a value of 10 might be "small," whereas in another problem a value of 1/10 might be "not small."

Notwithstanding these objections, the paper by Dagan and Tulin has provided a refreshing change in outlook on the bow-flow problem, and perhaps it will be more fruitful eventually than the usual attempts to place complicated singularities at the bow in the frame-work of linearized theory.

5.3. Submerged Body at Finite Speed

Since the principal difficulty in solving free-surface problems follows from the nonlinear conditions at the free surface, we are always seeking new arguments to justify linearizing the conditions. One possible basis for linearizing is that a body is deeply submerged. Then its effect on the free surface will presumably be small, even if it is not appropriate to linearize the problem in the immediate neighborhood of the body itself.

Such problems were discussed by Wehausen and Laitone [1960], where the previous history may also be found. Tuck [1965b] introduced a more systematic treatment for the case of a circular cylinder. Salvesen [1969] solved the problem for a hydrofoil (with Kutta condition and thus with circulation), and he compared his results with the data from experiments which he conducted. In the earlier studies of such problems, the approach was usually an iterative one in which the body boundary condition was first satisfied, then an additional term was added to the solution so that the free-surface condition would be satisfied; the latter would cause the body boundary condition to be violated, and so another term would have to be added to correct that error, but then there would again be an error in the free-surface condition. And so on. The free-surface condition that was satisfied once during each cycle was generally the conventional linearized condition. Thus, if the procedure converged, one obtained a solution which exactly satisfied the body boundary condition and the linearized free-surface condition. The contribution of Tuck seems to have been in systematizing the procedure in terms of a small parameter varying inversely with depth of the body and in pointing out that a consistent iteration scheme involves using the exact free-surface conditions as a starting point. Then, as the boundary condition on the body is corrected at each stage, so also is the free-surface condition made more and more nearly exact.

Tuck concluded, in fact, that it was more important to include nonlinear, free-surface effects than to improve the satisfaction of the body boundary condition if one were most interested in certain free-surface phenomena, e.g., predicting wave resistance and near-surface lift. Salvesen agreed with this conclusion only on the condition that the body speed be not too large. At fairly high speed, his results indicated that precision in satisfying the body boundary condition was just as important as precision in satisfying the free-surface condition. Figure (5-6) is taken from Salvesen's paper; it shows the theoretical wave resistance of a particular body as a function of (depth) Froude number, the resistance being calculated by three different approximations: 1) linearized free-surface theory, 2) theory in which the free-surface condition is satisfied to second order, and 3) theory in which both the free-surface condition and the body boundary condition are satisfied to second order. The differences are quite apparent.

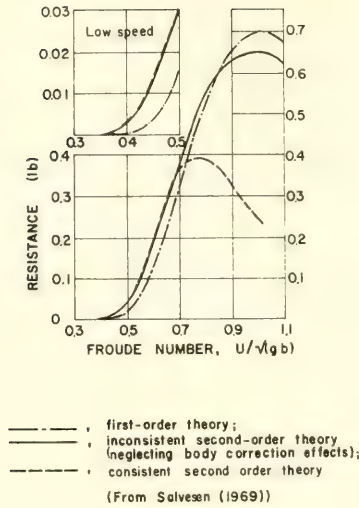


Fig. (5-6). Theoretical Wave-Resistance Curves for $\epsilon = t/b = 0.30$.

The figure is a very interesting one. The difference between the linear-theory curve and either of the other two curves is presumably a second-order quantity, and yet that difference is -- in one case -- of the same order of magnitude numerically as the linear-theory curve itself. The problem is worth further discussion.

Salvesen defines his small parameter as follows:

$$\epsilon \equiv t/b,$$

where t is the thickness (or some other characteristic dimension) of the body, and b is the submergence of the body below the undisturbed free-surface level. It is not assumed that the body is "thin" in any sense; it could be a circular cylinder (Tuck's problem), for example. Salvesen's calculations and experiments were carried out for a rather fat, wing-shaped body with a sharp trailing edge. The body was symmetrical about the horizontal plane at depth b . If the free surface had not been present, there would have been no lift on the body.

A complex velocity potential, $F(z) = \phi(x,y) + i\psi(x,y)$, can be defined for the problem, with $z = x + iy$ measured from an origin located in the body at a depth b below the undisturbed free surface.

Salvesen expands the complex potential in a series which he groups in two alternate ways:

$$F(z) = [Uz + F_{b0}] + [F_{f1} + F_{b1}] + \dots \quad (5-3)$$

$$= Uz + [F_{b0} + F_{f1}] + [F_{b1} + F_{f2}] + \dots \quad (5-4)$$

These terms are defined in terms of the iteration scheme already mentioned. The grouping in (5-3) is to be used near the body, and the grouping in (5-4) applies far away from the body; in particular, the latter applies on and near the free surface. Salvesen points out that this distinction means that: a) near the body, we are considering the zero-order flow to be that flow which would occur in the presence of the body and the absence of the free surface, and b) near the free-surface, the basic flow is just the uniform incident stream. Thus, in (5-3), we must determine F_{b0} so that $[Uz + F_{b0}]$ satisfies the kinematic boundary condition on the body and so that $|\nabla F_{b0}| \rightarrow 0$ as $|z| \rightarrow \infty$ (in any direction).

Next, Salvesen assumes that F_{b0} is $O(\epsilon)$ far away from the body. The two terms so far obtained do not satisfy a free-surface condition, and so F_{f1} must be determined so that, when it is added to the first two terms, the sum satisfies the appropriate free-surface condition, which is:

$$\text{Re} \{F'_{b0} + F'_{f1} + i\kappa F_{b0} + i\kappa F_{f1}\} = 0 \quad \text{on} \quad y = b \quad (5-5)$$

where $\kappa = g/U^2$. Since F_{b0} is assumed to be $O(\epsilon)$ near the surface, then the same should be true for F_{f1} .

Now the three terms in the series do not satisfy the body condition, and so F_{b1} is determined so that, when it is added to the first three terms, the sum satisfies the condition properly. Then F_{b1} is assumed to be $O(\epsilon^2)$ near the free surface, and a new function F_{f2} is found to provide a further correction needed near the free surface.

It is in this last step that the Tuck-Salvesen approach differs from the previous treatments of such problems. If F_{b1} is really $O(\epsilon^2)$, then the free-surface condition ought to be satisfied to that order of magnitude. It can be shown that this implies the following condition on F_{f2} :

$$\begin{aligned} &\text{Re} \{F'_{b1} + F'_{f2} + i\kappa F_{b1} + i\kappa F_{f2}\} \\ &= \eta_1 \text{Im} \{F''_{b0} + F''_{f1} + i\kappa F'_{b0} + i\kappa F'_{f1}\} - (1/2U) |F'_{b0} + F'_{f1}|^2. \end{aligned} \quad (5-6)$$

The right-hand side of this equation takes account of the nonlinearity of the free-surface conditions, since obviously it involves just the potential function from the previous cycle of the iteration. η_1 is the free-surface elevation from the previous approximation; it is given by:

$$\eta_1(x) = - (U/g) \operatorname{Re} \{ F'_{b0} + F'_{f1} \},$$

with the right-hand side evaluated on $y = b$. One might try to cut corners in (5-6) in either of two ways, namely, 1) ignore the right-hand side by setting it equal to zero, 2) Drop the terms involving F_{b1} on the left-hand side. The first is equivalent to retaining just a linear free-surface condition. The second is equivalent to neglecting the effect of the second-order body correction at the free surface; this is the "inconsistent" second-order theory to which Fig. (5-6) refers.

Apparently, Salvesen did not prove one important step in his development, namely, his claim that F_{b0} is $O(1)$ near the body and $O(\epsilon)$ far away from the body. In fact, with his definition of $\epsilon = t/b$, it appears that the statement is wrong. The potential F_{b0} represents just a thickness effect, since it is the solution of the problem of a symmetrical body in a uniform stream. Although the body can be replaced by a distribution of sources, the disturbance will appear from far away to have been caused by a dipole, and so it must have the form: $F_{b0} \sim C/z$. If the body were a circular cylinder, we could evaluate C : $C = Ut^2$, where t is the radius of the cylinder. The complex fluid velocity on the free surface caused by the body is, in the first approximation, $-C/z^2 = O(\epsilon^2)$, since $z = x + ib$ on the level of the undisturbed free surface. This conclusion contradicts Salvesen's assumption that the free-surface disturbance is $O(\epsilon)$, but perhaps it does not matter. At this point, the results would presumably be just the same if he had defined: $\epsilon \equiv (t/b)^{1/2}$. (The argument above for a circular cylinder agrees with Tuck's conclusions.)

When the first free-surface correction is found, namely, F_{f1} , its effect in the neighborhood of the body is not diminished by an order of magnitude, since at least one part of F_{f1} involves an exponential decay with depth, the exponent being $\kappa(y - b)$. Near the body, $y \approx 0$, and so the exponential-decay factor is $e^{-\kappa b}$, and it has been assumed that κb is $O(1)$. (See Salvesen's paper.)

Since F_{f1} is $O(\epsilon^2)$ near the body, the order of magnitude of the next correction term, F_{b1} , must be the same. This time, however, the nature of the body disturbance is quite different from a dipole disturbance. The effective incident flow corresponding to F_{f1} is not a uniform stream, and so the presence of a sharp trailing edge on the body requires that a Kutta condition be imposed, and then a circulation flow occurs. From far away, it appears that F_{b1}

is caused by a combination of a vortex and a dipole. If the strengths of the two apparent singularities were comparable, the vortex behavior would dominate the dipole behavior far away, and the induced velocity would diminish in proportion to $1/z$, rather than $1/z^2$, which was the case for the dipole. Thus, F_{b1} would be $O(\epsilon^3)$ near the free surface. In the absence of a sharp trailing edge which can cause the formation of a vortex flow, the corresponding F_{b1} would be $O(\epsilon^4)$. This matter remains to be resolved.

There are other interesting aspects to this problem. One relates to the interpretation of the small parameter, $\epsilon = t/b$. In defining such a dimensionless perturbation parameter, one normally assumes that the smallness of ϵ can be realized physically either by letting t be extremely small or by letting b be very large. In the present problem, this choice is not really available to us. The reason is that there is another length scale in the problem, namely, $1/\kappa = U^2/g$, and this length scale appears generally in combination with the dimension b . It has been assumed that $\kappa b = O(1)$ as $\epsilon \rightarrow 0$. Therefore, if we want to consider the problem of a body which is more and more deeply submerged, ($b \rightarrow \infty$), then we must also restrict our attention to higher and higher speeds. This is awkward.

Finally, one more important aspect must be mentioned. The relation between wave number, κ , and forward speed, U , namely, $\kappa = g/U^2$, is based on linearized free-surface theory. In general, if one seeks to find the nature of nonlinear waves which can propagate without change of form, the wave length of those waves is not related to their speed in this simple fashion. To be sure, the relationship is approximately correct if the waves are not terribly big in amplitude, and so one might expect that the wave length or the wavenumber can be expressed as an asymptotic series in ϵ

$$\kappa \sim \kappa_0 + \kappa_1 + \kappa_2 + \dots,$$

with $\kappa_0 = g/U^2$. This can indeed be done, but it turns out to be much more convenient to assume that κ is precisely given and then to find the value of forward speed that corresponds to that wave number. Thus, one expands the forward speed, U , into an asymptotic expansion:

$$U \sim u_0 + u_1 + u_2 + \dots$$

This procedure is discussed by Wehausen and Laitone [1960], and Salvesen uses it in his hydrofoil problem. I was able to omit mention of it in writing Eqs. (5-5) and (5-6) because it turns out that $u_1 = 0$, and so the effect of this speed shift (or period shift) does not enter the problem until the third approximation is being sought. However, this is a classic example of the kind of expansion described in

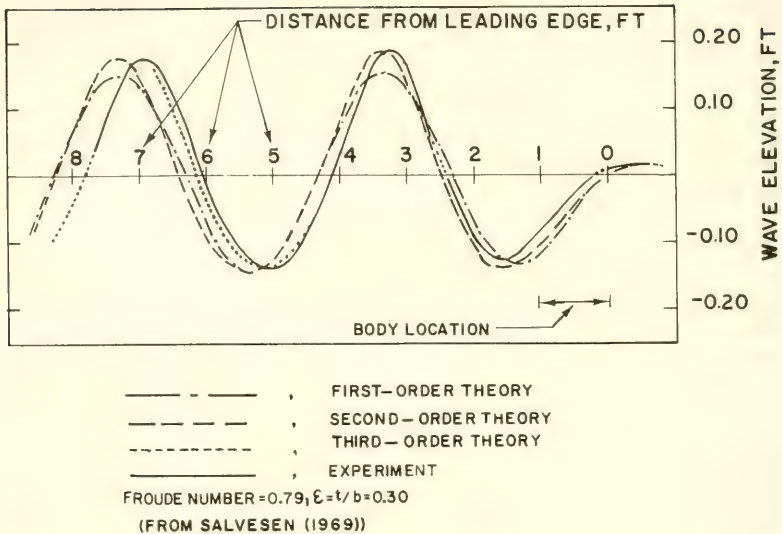


Fig. (5-7). Third-Order Effect on Wave Length

Section 1.3. If one did not allow for a variation in either κ or U , the third approximation would not be valid at infinity, and so one would have great difficulty in predicting wave resistance, since that quantity depends explicitly on the wave height at infinity.

Figure (5-7) is taken from Salvesen [1969]. It shows very clearly the change in wave length that arises in the third-order solution. In fact, it appears in this case that the change of wave length is practically the only third-order effect. This figure also speaks well for Salvesen's experimental technique!

5.4. Submerged Body at Low Speed

Salvesen [1969] computed the wave height behind a hydrofoil up to the third approximation, as already mentioned in Section 5.3. Although his third approximation is not really consistent, he gives what appear to be sufficient arguments to demonstrate that the consistent result would not be much different from the results presented in his paper. Figure (5-8), from Salvesen [1969], presents the wave-height computations in a way that shows the relative importance of the first-, second-, and third-order term. Let the wave amplitude be expressed by the series:

$$H \sim H_1 + H_2 + H_3, \quad \text{where} \quad H_{n+1} = o(H_n) \quad \text{as} \quad t \rightarrow 0.$$

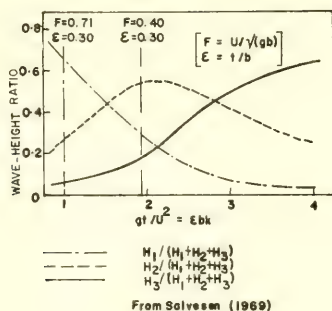


Fig. (5-8). First-, Second-, and Third-Order Wave Heights at Low Speeds.

(t is the thickness of the foil, as in the last section.) Then the figure shows the three ratios, $H_n/(H_1 + H_2 + H_3)$, for $n = 1, 2, 3$; that is, each curve shows the relative contribution to the wave height of one of the first three terms in the wave-height expansion. As speed decreases (toward the right-hand side of the figure), the second-order part comes to dominate the linear-theory part, and then the third-order part dominates the first two. It seems quite likely that the fourth-order term would take over if the graph were extended, then the fifth-, sixth-, ... order terms.

Salvesen's analysis is based on the condition that t (or, more properly, t/b , where b is the body depth) is very small; the Froude number is simply a parameter unrelated to t , which is equivalent to saying that Froude number $\equiv U/\sqrt{gb}$ is $O(1)$ as $t/b \rightarrow 0$. Perhaps it is not surprising if Salvesen's expansion is not uniformly valid with respect to Froude number. That is all that Fig. (5-8) really says.

The reason for its nonuniformity has already been mentioned: In the expansion of the solution near the free surface, it has been assumed that the lowest-order approximation is just the uniform-stream term, Ux ; all other terms in the expansion of the potential must be very small compared to this term. And this is nonsense if we consider the limit process $U \rightarrow 0$. Of course, we might have been lucky: It could have turned out that the velocity perturbation approached zero more rapidly than U . But it does not. And so we have here a genuine singular perturbation problem.

Let us consider a sequence of steady-motion experiments, each lasting for an infinite length of time. We arrange the sequence of experiments according to decreasing values of body speed, U ,

and we suppose that all conditions except forward speed are identical in all experiments. We shall discuss what happens when " $U \rightarrow 0$," and we shall understand by the limit operation that we are passing through the sequence of experiments toward the limit case in which there is no forward speed at all. In each experiment, U is a constant.*

As $U \rightarrow 0$, we certainly expect all fluid motion to vanish. But we would like to know to what extent the velocity field vanishes in proportion to U (that is, what part is $O(U)$), what part vanishes more rapidly than U (that is, what part is $o(U)$), and what part, if any, vanishes less rapidly than U .

In an infinite fluid, the velocity everywhere is exactly proportional to U . Far away, the velocity approaches zero; it drops off like $1/r$ if there is a circulation around the body, and it drops off like $1/r^2$ if there is no circulation. But in both cases the constant of proportionality is $O(U)$. No matter how distant our point of observation is from the body, the velocity is $O(U)$ as $U \rightarrow 0$.

At very low speed, one expects that gravity will force the free surface to remain plane. The constant-pressure condition will be violated to the extent that the magnitude of the fluid velocity on that plane is not quite constant, but the error in satisfying the dynamic condition will be proportional to the square of the fluid velocity magnitude. The kinematic condition will be satisfied in a trivial manner. Accordingly, it seems quite reasonable to assume that the free-surface disturbance is $O(U^2)$ as $U \rightarrow 0$, and so the velocity potential in the first approximation is the same as if the free surface were replaced by a rigid wall. Let the rigid-wall velocity potential be denoted by $\phi_0(x, y)$. Clearly, it is true that:

$$\phi_0(x, y) = O(U).$$

This follows by the same arguments as those used in the preceding paragraph. The more important problem is to determine the order of magnitude of $[\phi(x, y) - \phi_0(x, y)]$, where $\phi(x, y)$ is the exact velocity potential for the case of the body moving at speed U under the free surface.

In order to be specific now, let $\phi_0(x, y)$ be the velocity potential in two dimensions which satisfies the conditions:

$$\frac{\partial \phi_0}{\partial n} = 0, \text{ on body; } |\phi_0 - Ux| \rightarrow 0, \text{ as } x \rightarrow -\infty; \frac{\partial \phi_0}{\partial y} = 0 \text{ on } y = 0.$$

*This is the same point that I belabored in the last paragraph of Section 1.2. Again, I apologize to those to whom it is obvious.

The body is at rest in our reference frame.

The rigid-wall solution satisfies all conditions of the free-surface problem except the dynamic condition on the free surface. The latter could be used to define the free-surface shape. Thus, if the free-surface disturbance is expressed by

$$\eta(x) \sim \eta_0(x) + \eta_1(x) + \dots,$$

the dynamic free-surface boundary condition says that:

$$\eta(x) \sim \eta_0(x) \equiv \frac{1}{2g} [U^2 - \phi_{0,x}^2(x, 0)]. \quad (5-7)$$

Of course, the kinematic condition is now violated, but an additional velocity field which is $O(U^2)$ can correct that. And so it appears plausible that:

$$\phi(x, y) - \phi_0(x, y) = o(U). \quad (5-8)$$

One point should be noticed from this conclusion. The limit process " $U \rightarrow 0$ " implies that Froude number goes to zero. Nothing has been said about the length scale used in defining Froude number, but it does not matter so long as all dimensions are fixed. The submergence and the body dimensions may be quite comparable, for example. Thus, we are not considering t/b as small, in the sense that Salvesen did. However, both t and b are supposed to be large compared with the length U^2/g ; we imply this if we state that all dimensions must be fixed as $U \rightarrow 0$.

It would be wrong to take $\phi_0(x, y)$ as the potential for the flow around the body in an infinite fluid (without either free surface or a rigid-wall substitute). The body can be quite near to the free surface in Salvesen's sense, and so the effect of its image cannot be neglected. Furthermore, at least part of the effect of the image is $O(U)$, even if the body is very far away from the free surface, and such an effect must be included in the first term of the approximation which is supposed to be valid as $U \rightarrow 0$.

The next problem is to find $[\phi(x, y) - \phi_0(x, y)]$. We consider two possible approaches in the following subsections.

5.41. A Sequence of Neumann Problems. As above, let there be a velocity potential, $\phi(x, y)$, which provides the solution of the exact problem:

$$g\eta(x) + \frac{1}{2} [\phi_x^2 + \phi_y^2] - \frac{1}{2} U^2 = 0, \quad \text{on } y = \eta(x); \quad (5-9)$$

$$\phi_x \eta_x - \phi_y = 0, \quad \text{on } y = \eta(x); \quad (5-10)$$

$$\frac{\partial \phi}{\partial n} = 0, \quad \text{on the body}; \quad (5-11)$$

$$\phi(x, y) - Ux \rightarrow 0, \quad \text{as } x \rightarrow -\infty; \quad (5-12)$$

The rigid-wall potential, $\phi_0(x, y)$, satisfies (5-11) and (5-12) too, but it does not satisfy the free-surface conditions, of course; instead, we have

$$\frac{\partial \phi_0}{\partial y} = 0, \quad \text{on } y = 0. \quad (5-13)$$

Now we introduce one more potential function, the difference between the above two potentials:

$$\Phi(x, y) \equiv \phi(x, y) - \phi_0(x, y). \quad (5-14)$$

It must satisfy the body boundary condition, of course, and it vanishes far upstream. On the free surface, which we now define as:

$$y = \eta(x) = \eta_0(x) + H(x), \quad (5-15)$$

where $\eta'_0(x)$ is defined as in (5-7), the new potential satisfies the two conditions:

$$0 = gH(x) - \frac{1}{2} \phi_{0x}^2(x, 0) + \frac{1}{2} [\phi_{0x}^2 + \phi_{0y}^2 + 2\phi_{0x}\Phi_x + 2\phi_{0y}\Phi_y + \Phi_x^2 + \Phi_y^2]_{y=\eta(x)}; \quad (5-16)$$

$$0 = [\eta_0(x) + H'(x)][\phi_{0x} + \Phi_x]_{y=\eta(x)} - [\phi_{0y} + \Phi_y]_{y=\eta(x)}. \quad (5-17)$$

These conditions are still exact. An obvious approach to solving for $\Phi(x, y)$ and $H(x)$ is to re-express these conditions on $y = \eta(x)$ as conditions on $y = 0$. Here I shall assume that this can be done in the usual way.* Then it follows from the exact conditions

* This is the crucial point which distinguishes this section from the next section.

that the following are appropriate simplifications:

$$0 \simeq gH(x) + \phi_{0x}\Phi_x, \quad \text{on} \quad y = 0; \quad (5-18)$$

$$\Phi_y \simeq \eta'_0(x)\phi_{0x} - \eta_0(x)\phi_{0yy} \quad \text{on} \quad y = 0. \quad (5-19)$$

The second condition is a Neumann condition; the right-hand side is known, and the condition is prescribed on a known, fixed surface. In fact, (5-19) is satisfied by the real part of:

$$\frac{1}{\pi} \int_{-\infty}^{\infty} \frac{ds \, p(s)}{s - z},$$

where

$$z = x + iy,$$

$$p(x) = \eta_0(x)\phi_{0x}(x, 0). \quad (5-20)$$

This follows from the Plemelj formula. (See, e.g., Muskhelishvili [1953].) The function $p(x)$ can be interpreted in terms of the fluid velocity which is needed to correct the flow field because of the error incurred by taking the free surface at $y = \eta_0(x)$ while using the potential function $\phi_0(x, y)$ to prescribe the velocity field. This is the same correction which was discussed above in connection with (5-8). Now we may observe that, since $\eta_0 = O(U^2)$ and $\phi_0(x, y) = O(U)$, it follows that $p(x) = O(U^3)$. Thus also:

$$|\nabla\Phi| = O(U^3) \quad \text{as} \quad U \rightarrow 0. \quad (5-21)$$

This is certainly a much stronger conclusion than (5-8)!

The integral expression given above is not the solution of the Φ problem, even in the first approximation, since it does not satisfy the body boundary condition. However, since the existence of Φ arises from a defect of ϕ_0 in meeting the free-surface conditions, it is difficult to imagine that the above estimate of the order of magnitude of Φ is not correct.

Numerical procedures could readily be worked out for solving problems of the above type. In fact, all that is needed is one algorithm which handles the problem of a given distribution of the normal velocity component on a surface in the presence of a plane rigid wall. The integral part of the solution given above would

lead to a non-zero normal velocity component on the body, and this would have to be offset by a flow which does not change the condition at the plane $y = 0$. Presumably, all higher-order approximations would be solutions of problems which are identical in form to this one.

A variation on this approach has been discussed several times by Professor L. Landweber, although he has not published the work. He points out that the usual linearized free-surface condition,

$$\frac{\partial^2 \phi}{\partial x^2} + \kappa \frac{\partial \phi}{\partial z} = 0, \quad \text{on} \quad z = 0, \quad \text{where} \quad \kappa = g/U^2,$$

becomes the rigid-wall condition when $U \rightarrow 0$, and so one might try an iteration scheme in which ϕ is expanded in a series, $\phi \sim \sum \phi_n$, and the terms are obtained as the solutions in an iteration scheme:

$$\frac{\partial \phi_1}{\partial y} = 0, \quad \frac{\partial \phi_n}{\partial y} = -\frac{1}{\kappa} \frac{\partial^2 \phi_{n-1}}{\partial x^2} \quad (\text{for } n > 1) \quad \text{on} \quad y = 0.$$

In order to test the scheme, Professor Landweber proposed trying to obtain the potential function for a Havelock source in this way; this obviates the need to satisfy a body boundary condition, and the known potential for the source can be expanded in a series in terms of $1/\kappa$.

Neither of the above schemes appears very promising to me. Salvesen's findings about the singular low-speed behavior seem to condemn any approach which overlooks the peculiar nature of the free-surface problem at low speeds. The next section should make clear why I am pessimistic about these approaches. It should be obvious even now that the wave-like nature of the problems has been lost, but the difficulty is more serious than that.

5.42. A Dual-Scale Expansion. According to linearized wave theory, the wave-like nature of a free surface disturbance loses its identity exponentially with depth. A disturbance created at the free surface is attenuated rapidly with depth, and a disturbance created at some depth causes a free-surface disturbance which decreases with the depth of the cause. The depth effect is essentially proportional to $e^{\kappa y}$, where, as above, $\kappa = g/U^2$ and y is measured as positive in the upward direction.

As U approaches zero, this depth-attenuation factor approaches zero for any fixed y . In other words, the free-surface effects are restricted to a thin layer which approaches zero thickness as $U \rightarrow 0$. We might say that the free-surface is separated from the main body of the fluid by this "boundary layer" in which there is

a rapid transition from conditions at the surface to conditions inside the bulk of the fluid. From our experience with viscous boundary layers, we should expect the occurrence of large derivatives in this region and also some difficulty in satisfying boundary conditions on a face of the boundary layer.

In a viscous boundary layer, of course, the derivatives are much greater in one direction than in another, and this fact allows us to stretch coordinates anisotropically and apply the limit processes of the method of matched asymptotic expansions. In the free-surface boundary layer, however, this does not appear to be a possible approach. From the linear theory, we expect that there will be a wave motion with wave lengths which are $O(U^2/g)$. Thus, derivatives will be large in at least two directions inside the boundary layer -- in the direction normal to the layer and in one direction parallel to the layer.

When I tried to solve this problem two years ago (see Ogilvie [1968]), I did not apply very systematic procedures. Rather, I simply assumed that the first approximation to Φ , as defined in (5-14), would have certain properties, namely,

$$\bar{\Phi}(x,y) = O(U^5); \quad \Phi_x(x,y), \quad \Phi_y(x,y) = O(U^3);$$

also, the surface deflection function would be given by (5-15), with:

$$H(x) = O(U^4); \quad H'(x) = O(U^2).$$

The order of magnitude of Φ was chosen just so that the velocity components would be $O(U^3)$, and I assumed that differentiation changes a quantity by $1/U^2$ in order of magnitude. The arguments leading up to (5-21) contributed heavily to the conjecture about velocity components, and the $1/U^2$ effect of differentiation was chosen just because the free-surface characteristic length is U^2/g . It is important to note that the rigid-wall potential, ϕ_0 , is still part of the solution, and these statements about orders of magnitude and differentiation do not apply to it. In fact, I assume that ϕ_0 is completely known, and so it is not necessary to conjecture about the effects of differentiation.

In terms of the general approach of the multiple-scale expansion method, I have assumed that an approximation to the solution can be represented as the sum of two functions. The first depends only on the length scale appropriate to the body geometry. The second function depends primarily on lengths measured on a scale appropriate to U^2/g , but it also depends on the first function and thus on lengths typical of the body. However, it seems to be possible to keep clear when differentiations are being carried out with respect to each of the length scales.

Physically, the situation may be described in the following way: If U is small enough, the body extends over a distance of many wave lengths of the surface disturbance. The initial disturbance is caused by the body, of course; this is the "rigid-wall" motion, and its dimensions are characteristic of the body. It causes a free-surface disturbance, with the result that waves are created. But these waves are very, very short, whereas the initial disturbance from the body appears to be just a slight nonuniformity in flow conditions when viewed on the scale comparable to the wave length. The method is, in fact, quite similar to classical methods such as the W-K-B method.

When the assumptions listed above are actually applied, we find that the approximate free-surface conditions given in (5-18) and (5-19) must be replaced by the following:

$$gH(x) + \phi_{0x}(x, 0)\Phi_x(x, \eta_0(x)) \simeq 0; \quad (5-22)$$

$$\tilde{\Phi}_y(x, \eta_0(x)) - \phi_{0x}(x, 0)H'(x) \simeq p'(x);$$

the function $p(x)$ is the same that was given in (5-20). Note that Φ in both conditions here is to be evaluated on $y = \eta_0(x)$, rather than on $y = 0$. The reason is the same that was given in Section 3.2 in the near-field problem: If we tried in the usual way to expand $\Phi(x, \eta_0)$, say as follows:

$$\Phi(x, \eta_0) = \Phi(x, 0) + \eta_0\Phi_y(x, 0) + \frac{1}{2}\eta_0^2\Phi_{yy}(x, 0) + \dots,$$

we would find that every term on the right-hand side is the same order of magnitude according to my assumptions. In particular, $\eta_0 = O(U^2)$, and, symbolically, we have: $\partial/\partial y = O(1/U^2)$. So this expansion procedure is not useful.

The two conditions above can be combined consistently into the following:

$$\Phi_y(x, \eta_0(x)) + \frac{1}{g}\phi_{0x}^2(x, 0)\Phi_{xx}(x, \eta_0(x)) \simeq p'(x). \quad (5-23)$$

This is remarkably similar to the free-surface condition for another problem. In the ordinary linearized theory of gravity waves, suppose that a pressure distribution, $p(x)$, is travelling at a speed U . The free-surface condition would be:

$$\Phi_y(x, 0) + \frac{U^2}{g}\Phi_{xx}(x, 0) = p'(x),$$

if $\Phi(x, y)$ were the potential function for the problem. Replace U by $\phi_{0x}(x, 0)$, the "local stream speed," and evaluate the condition on $y = \eta_0(x)$; then this condition transforms into the condition found for $\Phi(x, y)$ in the low-speed problem. Thus, on a "local" scale (in which a typical length is U^2/g), the free-surface condition is just a very ordinary condition; one cannot see that the stream velocity changes slightly along the free surface, because the change occurs on a scale in which a typical measurement would be a body dimension; the change is very gradual. Also, the level of the undisturbed free surface appears to change gradually, as given by (5-7); this change also cannot be detected on the "local" scale.

It is now clear that the two length scales are quite distinct. We cannot separate the fluid-filled region into distinct parts in each of which only one length scale needs to be considered. Rather, the gradual changes which appear on the body-size scale appear to modify the short-length wave motion in the manner of a modulation.

In trying to find a potential function which satisfies (5-23), I made a nonconformal mapping: $x' = x$, $y' = y - \eta_0(x)$. Then Φ satisfies a complicated partial differential equation in terms of x' and y' , but the terms in the equation can be arranged according to their dependence on U , and it is found that the leading-order terms are simply the terms in the Laplacian, that is,

$$\Phi_{x'x'} + \Phi_{y'y'} \sim 0;$$

all other terms are higher order. In this new coordinate system, the free-surface condition, (5-23), is transformed too, but again the leading-order terms are just the same after the transformation (but expressed as functions of x' and y'). Furthermore, the boundary condition is then to be applied on $y' = 0$. Let us now drop the primes on the new variables, for convenience. Then the problem is as follows: Find a velocity potential, $\Phi(x, y)$, which satisfies the Laplace equation in two dimensions and the free-surface condition:

$$\Phi_y(x, y) + \frac{1}{g} \phi_{0x}^2(x, 0) \Phi_{xx}(x, 0) = p'(x),$$

where

$$p(x) = \eta_0(x) \phi_{0x}(x, 0).$$

In addition, the potential must satisfy a body boundary condition; this has not been carefully formulated yet, and, in any case, the only solution that has been produced so far is one that satisfies the free-surface condition but not a body condition. There may be

some good justification (or rationalization) for proceeding this way, but it is really an open question.

With such restrictions and reservations expressed, we can write down a "solution" of the above problem. Define:

$$\phi \equiv \operatorname{Re} \{f_0(z)\}; \quad \Phi(x, y) \equiv \operatorname{Re} \{F(z)\};$$

$$k(z) \equiv g \left[\frac{df_0}{dz} \right]^{-2}.$$

Note that:

$$f'_0(x) = \phi_{0x}(x, 0); \quad k(x) = g[\phi_{0x}(x, 0)]^{-2}$$

Then the solution is given by:

$$F'(z) = -\frac{1}{\pi i} \int_{-\infty}^{\infty} ds p'(s) \int_{-\infty}^z \frac{d\zeta}{s - \zeta} k(\zeta) \exp \left[-i \int_{\zeta}^z du k(u) \right].$$

The ζ integral is a contour integral starting at $x = -\infty$, located entirely in the lower half-space. It should pass above the location of the singularity in $k(z)$. This solution represents no disturbance at the upstream infinity, as one would expect.

Far downstream, this solution can be approximated:

$$F'(z) \approx 2le^{-i\kappa z} \int_{-\infty}^{\infty} ds p''(s) \exp \left[i\kappa s - i \int_s^z du [k(u) - \kappa] \right],$$

where $\kappa = g/U^2$. Then, from (5-22), we obtain the wave shape far aft of the body:

$$H(x) \approx -\frac{2U}{g} \int_{-\infty}^{\infty} ds p''(s) \sin [\kappa(x - s) + K(s)],$$

where

$$K(s) = \int_s^{\infty} du [k(u) - \kappa].$$

Calculation of the wave resistance is then very simple in principle. (In practice, it is a very tedious calculation.) Note that the expression for the wave shape downstream does not require knowledge of

$F'(z)$ (or $\Phi(x,y)$), that is, the surface disturbance far away is a real wave, but its shape and size depend only on the solution of the rigid-wall problem. This is not true of the wave disturbance in the vicinity of the body.

It would be very useful, I am sure, to formulate this problem carefully by the method of multi-scale expansions. The approach described by Ogilvie [1968] is very heuristic and leaves much to be desired.

ACKNOWLEDGMENT

The preparation of this paper was supported by a grant of the National Science Foundation (Grant GK 14375).

REFERENCES

- Benjamin, T. P., and Feir, J. E., "The disintegration of wave trains on deep water. Part 1. Theory," *Journal of Fluid Mechanics*, 27, 417-430, 1967.
- Cole, Julian D., Perturbation Methods in Applied Mathematics, Blaisdell Pub. Co., Waltham, Mass., 1968.
- Dagan, G., and Tulin, M. P., Bow Waves Before Blunt Ships, Technical Report 117-14, Hydronautics, Inc., 1969.
- Fedyayevskiy, K. K., and Sobolev, G. V., Control and Stability in Ship Design. English translation: JPRS: 24,547; OTS: 64-31239; Joint Publications Research Service, Clearinghouse for Federal Scientific and Technical Information, U.S. Dept. of Commerce, 1963.
- Friedrichs, K. O., "Asymptotic Phenomena in Mathematical Physics," *Bull. American Mathematical Society*, 61, 485-504, 1955.
- Joosen, W. P. A., "The Velocity Potential and Wave Resistance Arising from the Motion of a Slender Ship," *Proc. International Seminar on Theoretical Wave Resistance*, pp. 713-742, Ann Arbor, Michigan, 1963.
- Joosen, W. P. A., "Slender Body Theory for an Oscillating Ship at Forward Speed," *Fifth Symposium on Naval Hydrodynamics*, ACR-112, pp. 167-183, Office of Naval Research, Washington, 1964.

- Khaskind, M. D., "The Exciting Forces and Wetting of Ships," (in Russian), *Izvestia Akademii Nauk S.S.S.R., Otdelenie Tekhnicheskikh Nauk*, 7, 65-79, 1957. (English translation: David Taylor Model Basin Translation No. 307 (1962)).
- Kinner, W., "Die kreisförmige Tragfläche auf potentialtheoretischer Grundlage," *Ing.-Arch.*, 8, 47-80, 1937.
- Kochin, M. E., *Theory of Wing of Circular Planform*, NACA Tech. Memo 1324, (An English translation of the Russian paper), 1940.
- Kotik, J. and Thomsen, P., "Various Wave Resistance Theories for Slender Ships," *Schiffstechnik*, 10, 178-186, 1963.
- Krienes, K., "Die elliptische Tragfläche auf potentialtheoretischer Grundlage," *Zeit. angewandte Mathematik und Mechanik*, 20, 65-88, 1940.
- Lee, C. M., "The Second-Order Theory of Heaving Cylinders in a Free Surface," *Jour. Ship Research*, 12, 313-327, 1968.
- Lighthill, M. J., "Mathematics and Aeronautics," *Jour. Royal Aeronautical Society*, 64, 375-394, 1960.
- Maruo, H., "Application of the Slender Body Theory to the Longitudinal Motion of Ships among Waves," *Bulletin of the Faculty of Engineering, Yokohama National University*, 16, 29-61, 1967.
- Milne Thomson, L. M., *Theoretical Hydrodynamics*, 5th Ed., Macmillan Co., New York, 1968.
- Muskhelishvili, N. I., *Singular Integral Equations*, English translation by J. R. M. Radok, P. Noordhoff N. V., 1953.
- Newman, J. N., "A Linearized Theory for the Motion of a Thin Ship in Regular Waves," *Jour. Ship Research*, 5:1, 34-55, 1961.
- Newman, J. N., "The Exciting Forces on Fixed Bodies in Waves," *Jour. Ship Research*, 6:3, 10-17, 1962 (reprinted as David Taylor Model Basin Report 1717).
- Newman, J. N., "A Slender Body Theory for Ship Oscillations in Waves," *Jour. Fluid Mechanics*, 18, 602-618, 1964.
- Newman, J. N., "The Exciting Forces on a Moving Body in Waves," *Jour. Ship Research*, 9, 190-199, 1965 (reprinted as David Taylor Model Basin Report 2159).

- Newman, J. N., "Applications of Slender-Body Theory in Ship Hydrodynamics," Annual Review of Fluid Mechanics, Ed. by M. Van Dyke and W. G. Vincenti, Annual Reviews, Inc., 1970.
- Newman, J. N. and Tuck, E. O., "Current Progress in the Slender Body Theory for Ship Motions," Fifth Symposium on Naval Hydrodynamics, ACR-112, pp. 129-162, Office of Naval Research, Washington, 1964.
- Ogilvie, T. F., "Nonlinear High-Froude-Number Free-Surface Problems," Jour. Engineering Mechanics, 1, 215-235, 1967.
- Ogilvie, T. F., Wave Resistance: The Low-Speed Limit, Report No. 002, Dept. of Naval Arch. and Mar. Eng., University of Michigan, Ann Arbor, Michigan, 1968.
- Ogilvie, T. F. and Tuck, E. O., A Rational Strip Theory of Ship Motions: Part 1, Report No. 013, Dept. of Naval Arch. and Mar. Eng., University of Michigan, Ann Arbor, Michigan, 1969.
- Peters, A. S. and Stoker, J. J., The Motion of a Ship, as a Floating Rigid Body, in a Seaway, Report No. IMM-203, Institute of Mathematical Sciences, New York University, 1954.
- Peters, A. S. and Stoker, J. J., "The Motion of a Ship, as a Floating Rigid Body, in a Seaway," Comm. Pure and Applied Mathematics, 10, 399-490, 1957.
- Rispin, P. P., A Singular Perturbation Method for Nonlinear Water Waves Past an Obstacle, Ph.D. thesis, Calif. Inst. of Tech., 1966.
- Salvesen, N., "On higher-order wave theory for submerged two-dimensional bodies," Jour. Fluid Mechanics, 38, 415-432, 1969.
- Stoker, J. J., Water Waves, Interscience Publishers, 1957.
- Tuck, E. O., The Steady Motion of Slender Ships, Ph.D. thesis, Cambridge University, 1963a.
- Tuck, E. O., "On Vossers' Integral," Proc. International Seminar on Theoretical Wave Resistance, pp. 699-710, Ann Arbor, Michigan, 1963b.
- Tuck, E. O., "A Systematic Asymptotic Expansion Procedure for Slender Ships," 8:1, 15-23, 1964a.
- Tuck, E. O., "On Line Distributions of Kelvin Sources," Jour. Ship Research, 8:2, 45-52, 1964b.

- Tuck, E. O., The Application of Slender Body Theory to Steady Ship Motion, Report 2008, David Taylor Model Basin, Washington, 1965a.
- Tuck, E. O., "The effect of non-linearity at the free surface on flow past a submerged cylinder," Jour. Fluid Mechanics, 22, 401-414, 1965b.
- Tuck, E. O. and Von Kerczek, C., "Streamlines and Pressure Distribution on Arbitrary Ship Hulls at Zero Froude Number," Jour. Ship Research, 12, 231-236, 1968.
- Van Dyke, M., Perturbation Methods in Fluid Mechanics, Academic Press, New York, 1964.
- Vossers, G., Some Applications of the Slender Body Theory in Ship Hydrodynamics, Ph.D. thesis, Technical University of Delft, 1962.
- Wagner, H., "Über Stoss- und Gleitvorgänge an der Oberfläche von Flüssigkeiten," Zeit. f. Ang. Math. u. Mech., 12, 193-215, 1932.
- Wang, K. C., "A New Approach to 'Not-so-Slender' Wing Theory," Jour. Mathematics and Physics, 47, 391-406, 1968.
- Ward, G. N., Linearized Theory of Steady High-Speed Flow, Cambridge University Press, 1955.
- Wehausen, J. V., "An Approach to Thin-Ship Theory," Proc. International Seminar on Theoretical Wave Resistance, pp. 821-852, Ann Arbor, Michigan, 1963.
- Wehausen, J. V. and Laitone, E. V., "Surface Waves," Encyclopedia of Physics, IX, pp. 446-778, Springer-Verlag, Berlin, 1960.
- Wu, T. Y., "A Singular Perturbation Theory for Nonlinear Free Surface Flow Problems," International Shipbuilding Progress, 14, 88-97, 1967.

THEORY AND OBSERVATIONS ON THE USE OF A MATHEMATICAL MODEL FOR SHIP MANEUVERING IN DEEP AND CONFINED WATERS

Nils H. Norrbin
Statens Skeppsprövningsanstalt
Sweden

ABSTRACT

This paper summarizes an experimental and analytical study of ship maneuvering, with special emphasis on the use of a research-purpose simulator for evaluating the behaviour of large tankers in deep water as well as in harbour entrances and canals. In an introductory Section some new results from full-scale measurements and simulator studies are given to illustrate the demands put on a mathematical model in the two extreme applications: course-keeping in deep water and manoeuvring in a canal bend.

Well-known derivations of rigid body dynamics and homogeneous flow solutions for forces in the ideal case are included to form skeleton of the mathematical model. Separate equations handle helm and engine controls. Coefficients and parameters are made non-dimensional in a new system — here designated the "bis" system as different from the SNAME "prime" system generally used — in which the units for mass, length and time, respectively, are given by the mass of the ship, m , the length, L , and the time required for travelling one ship length at a speed corresponding to $V = F_{nL} = 1, \sqrt{L/g}$.

Semi-empirical methods are suggested for estimates of the force and moment derivatives. Special consideration is given to added mass and rudder forces in view of their predominant importance to course-keeping behaviour; the rudder forces measured on a scale model are corrected for differences in wake and screw

loading before application to full-scale predictions. Non-linear contributions to hull forces are included in second order derivatives, relevant to the cross-flow concept.

The extension of the mathematical model to the confined-water case is based upon the theoretical results by Newman and others, and upon relations found from special experiments. In the model the hydrodynamic interferences appearing in forces and moments due to the presence of port and starboard side wall restrictions and bottom depth limitations are represented by additional terms containing higher order derivatives with respect to three suitable confinement parameters, $\eta = \eta_s + \eta_p$, $\bar{\eta} = \eta_s - \eta_p$, and ζ . In a canal the asymmetrical forces are considered as due to the added effects from port (p) and starboard (s) walls rather than as the effect of an off-centreline position; primarily η is a measure of this position, $\bar{\eta}$ a measure of the bank spacing.

The mathematical model is here applied for evaluation of model test data obtained for a Swedish 98 000 tdw tanker in the VBD laboratories. Oblique towing and rotating arm tests were performed in "deep" and shallow water. Oblique towing tests were also run at various distances from a vertical wall in the deep tank, and in two Suez-type canal sections. The effect of shallow water was especially large in force nonlinearities. Missing data for bottom and wall effects on added mass and inertia are taken from theory and from test results due to Fujino, respectively.

The deep-water predictions for zig zag test and spiral loop prove to be in good agreement with full-scale trial results. Analogue computer diagrams are given to show the effects of shallow water upon definite manoeuvres and upon course-change transients following auto-pilot trim knob settings. Finally a few results are included to illustrate auto-pilot position control of the tanker in free water, in shallow water, between parallel walls and in a canal.

I. INTRODUCTION

On Course-Keeping in Deep Water

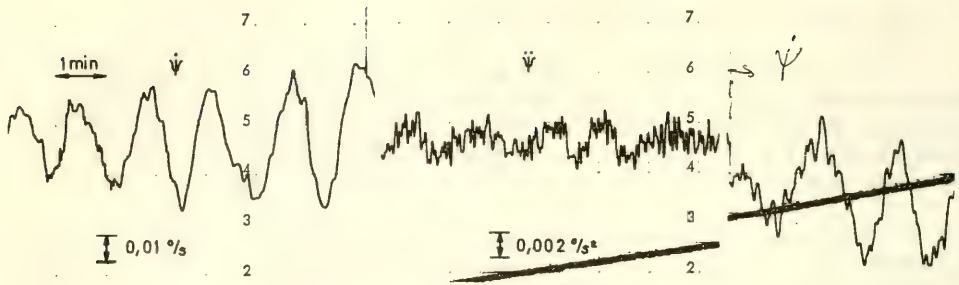
The average depth of the oceans is some 3800 m. Small native crafts still steer their ways between nearby islands in these oceans. New ships are built to transport ever larger quantities of containers or bulk cargoes at a minimum of financial expense between the continents.

It is not necessarily obvious that the helmsman shall be able to control a mammoth tanker on a straight course. A few years ago ship operators were stirred by the published results of an analytical study, interesting in itself, which in fact did indicate, that manual control of ships would be impossible beyond a certain size. Upon request by the shipbuilders a series of real-time simulator studies were initiated at SSPA in autumn 1967 to investigate manual as well as automatic control of large tankers then building, [1].

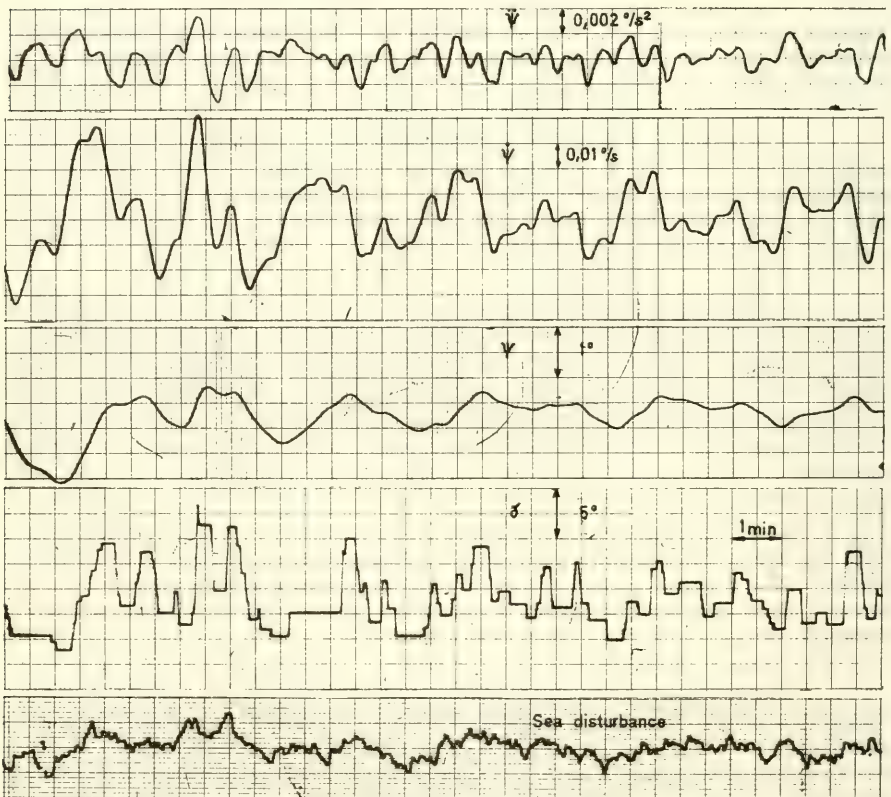
At an early stage of these tests the helmsman was found to constitute a remarkably adaptive control, which could not be simulated by a simple transfer function. As could be expected a rate display proved to make course keeping more easy; the rate signal was even more essential to the auto pilot.

The simulator findings were confirmed in subsequent prototype trials. The diagrams of Fig. 1 compare simulator and prototype rates of change of heading and yaw accelerations for a large tanker as steered by the author in a Force 6 following sea. (In the simulator case the sea disturbance was represented by a cut-off pseudo-random white noise of predetermined root mean square strength, that was fed into the yaw loop.) This particular tanker is dynamically unstable on a straight course, and the steady-state $\psi(\delta)$ -diagram from a deep-water spiral test exhibits a hysteresis loop with a total height of 0.5 °/s and a total width of a little more than 3° of helm. If yaw rate is maintained within some 40 per cent of the loop height value it has been found possible to control the straight heading by use of small helm only.

The use of the computer-type simulator for the prediction of ship behaviour implies the adoption of a suitable mathematical model and the knowledge of a number of coefficients in this model. An alternative technique that simulates full-scale steering by controlled free-sailing ship models is still in use. Mostly the steering has been exercised by manual operation of the controls, and it has been claimed that at least comparative results should then be valid. It is likely that the truth of this statement depends on the actual speed and size (and time constants) of the prototype ship as well as of the model scale ratio used.



Full scale single-channel record (Helmsman: Author)



Simulator records (Helmsman: Author)

Fig. 1. Manual steering of an unstable 230 000 tdw tanker in quatering sea. Prototype and simulator records.

Time is scaled as square root of length. Human response time may be "scaled" within certain limits only. The $\dot{\psi}(\delta)$ -diagrams of Fig. 2 demonstrate results of simulated steering of the tanker prototype already referred to, as well as of her fictive models of four different sizes. (Note that curves run anti-clockwise with time.) The smallest "model" is in scale 1:100, i.e. it has a length of 3.1 m, which should permit free-sailing tests in several in-door facilities. The two helmsmen, which each one seem to represent one kind of steering philosophy and who were allowed a short training period in each case, both failed to maintain the proper control of the two smaller "models."

The control of a ship on a straight course is governed mainly by the effective inertia, by the yaw damping moment, by the rudder force available, and by the time this force is applied. A mathematical model intended for studies of manual or automatic steering may therefore be quite simple; in contrast to the test basin model it may include proper corrections for the large scale effects often present in rudder force data. (Cf. Section VII.)

Figure 3 repeats the original simulator $\dot{\psi}(\delta)$ -curves from real-time straight running, recorded by use of the "complete" mathematical model, but it also presents results from tests with a linear model as well as with a model, which contains no other hydrodynamic contributions than those in lateral added inertias and rudder forces. No major differences were experienced in using these three models of increasing simplicity.

On Manoeuvring in Confined Waters

Manoeuvring, involving yaw rates and drift velocities, which are not small compared to the forward speed, demands a mathematical model of considerable complexity. A useful presentation of non-linear characteristics has been given by Mandel, [2]. One particular non-linear model designed to include manoeuvres in confined waters will be more fully discussed in subsequent Sections of this paper.

The average depth of the oceans is some 3800 m. But ocean voyages start and terminate at ports behind the shallow waters of the inner continental shelves. Additional confinements are presented by many of the important gateways of world trading, such as the Straits of Dover and Malacca, the Panama Canal, and the Suez Canal now closed.

The maximum draughts of "large" ships have always been limited by bottom depths of docks and harbours, and of canals and canal locks. With few exceptions the requirements placed on under-keel clearances — by ship owners or by authorities — have been chosen solely with a view to prevent actual ship grounding or excessive canal bed erosions. Thus the Suez Canal Authorities accepted

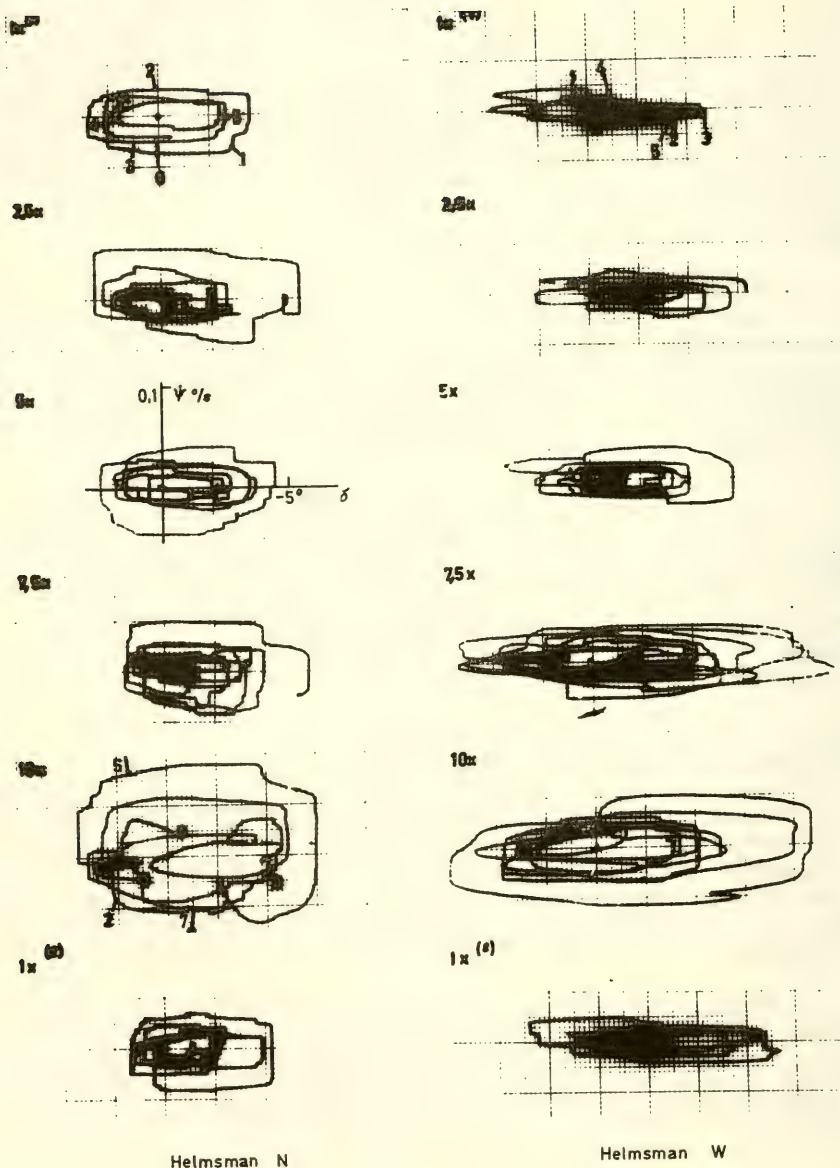
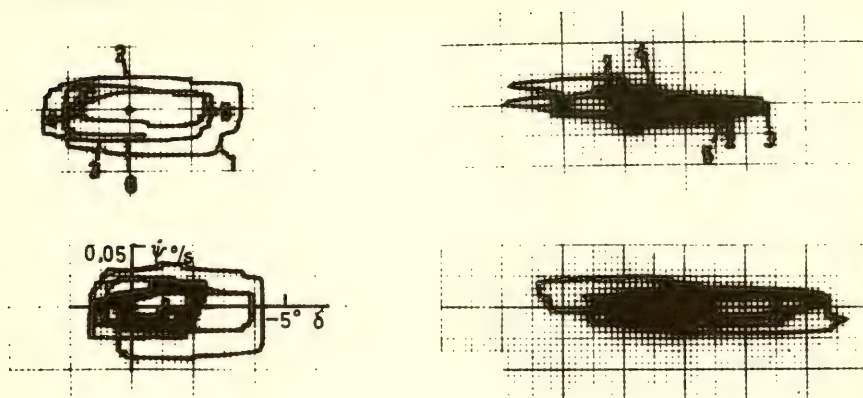
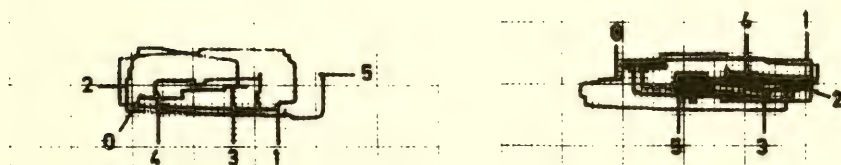


Fig. 2. Simulator tests of manual steering of an unstable 230 000 tdw tanker in real and speeded up time. Yaw rate versus helm angle. (Numbers along curves indicate minutes in real time.)

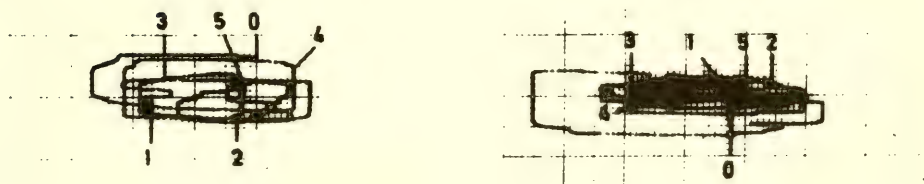
"Complete" model:



Linear model:



Model using inertia and rudder forces only:



Helmsman N

Helmsman W

Fig. 3. Simulator tests of manual steering of an unstable 230 000 tdw tanker using alternative mathematical models. Yaw rate versus helm angle.

a nominal blockage ratio of 1:4 for ships in northbound transit at a maximum speed of 13 kilometres per hour, corresponding to a mean back-flow velocity of some 1.5 m/s.

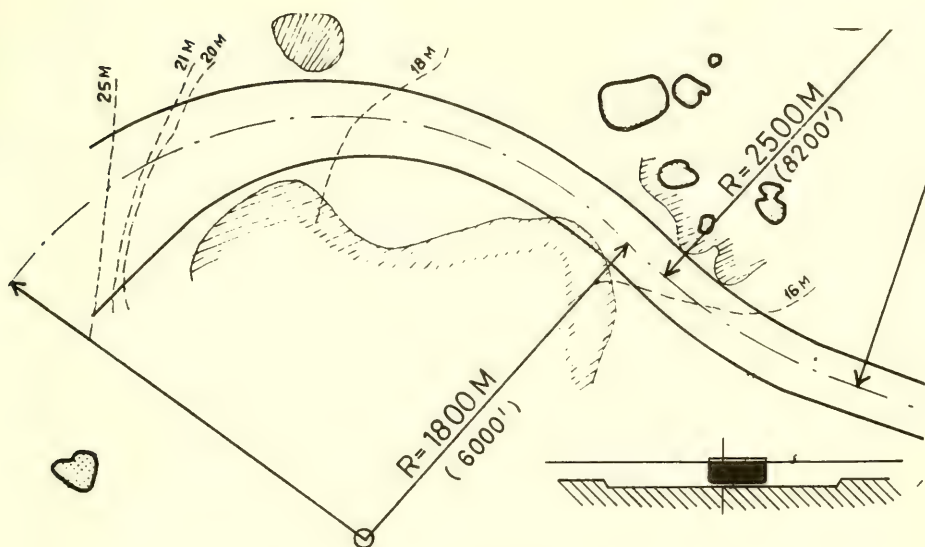
Today new limits are imposed by the depths of ocean sills as well as by the depths and widths of open sea port approaches. The potential dangers of a large oil tanker navigating in such waters under, say, the influence of an unexpected change of cross current must not be denied. Whatever nautical experience the master or pilot may possess, he is still in need of actual data and of means to convert this information to helm and engine orders. Automatic systems on a predictor basis are likely to appear in a near future, [3].

In the planning for dredged entrance channels and harbour turning basins the maneuvering properties of the ships must no longer be overlooked. The upper drawing of Fig. 4, reproduced from Ref. [4], shows part of the plan view and a typical section of the buoyed channel for 200 000 tdw tankers unloading at a new oil terminal. Before entering the 90° starboard turn the speed is brought down to less than 2 knots, and the tanker then proceeds under slow acceleration by own power. Braking tugs are used on quarters, and forward tugs assist in the S-bend. The lower diagram of Fig. 4 is taken from SSPA records of yaw rates in the passage; the initial curvature corresponds to $r' = 0.175$, and the maximum rate of change of angular velocity is of the order of $0.0005 \text{ }^\circ/\text{s}^2$ at a forward speed of 2.3 knots.

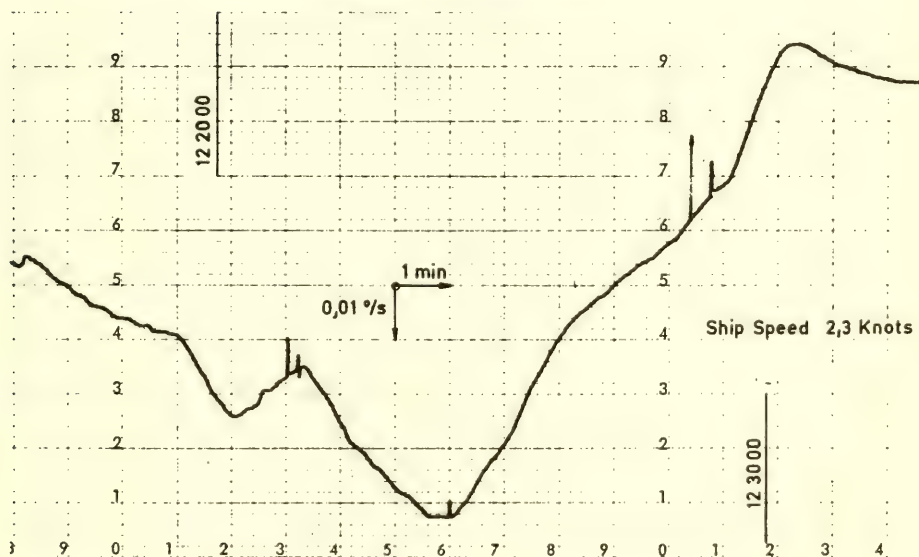
In general the lateral forces on the ship will all increase as water depth turns smaller, and the dynamical stability is also likely to increase. From extensive measurements by Fujino it appears, however, that the picture is not so simple, and that for some ships there may be a "dangerous" range of depth-to-draught ratios, in which the dynamic stability gets lost, [5].

Recent model tests indicate that the large-value non-linearities, such as the lateral cross-flow drag at high values of drift, do increase even more than the linear contributions governing the inherent stability conditions. Whereas these non-linearities may be omitted in the mathematical model of the ship in a canal the bank effects here introduce destabilizing forces, that are again highly non-linear.

The effects of well-known forces experienced by a ship sailing parallel to the bank of a canal are clearly apparent in the record from a Suez Canal transit here reproduced in Fig. 5, [6]. (The positions in the canal as well as the width between beach lines were derived from triangulation by use of two simple sighting instruments designed for the purpose.) Upon approach to the Km 57 bend the ship is slightly to port of the canal centre line. The pilot orders port helm for two minutes, by which the ship is pushed away from the near bank and the desired port turn is also initiated. Back on centre line the ship mainly turns with the canal. In spite of a starboard checking rudder



Plan and typical section of dredged channel



Part of yaw rate record in transit

Fig. 4. Example of yaw rates recorded on 210 000 tdw tanker in harbour approach.

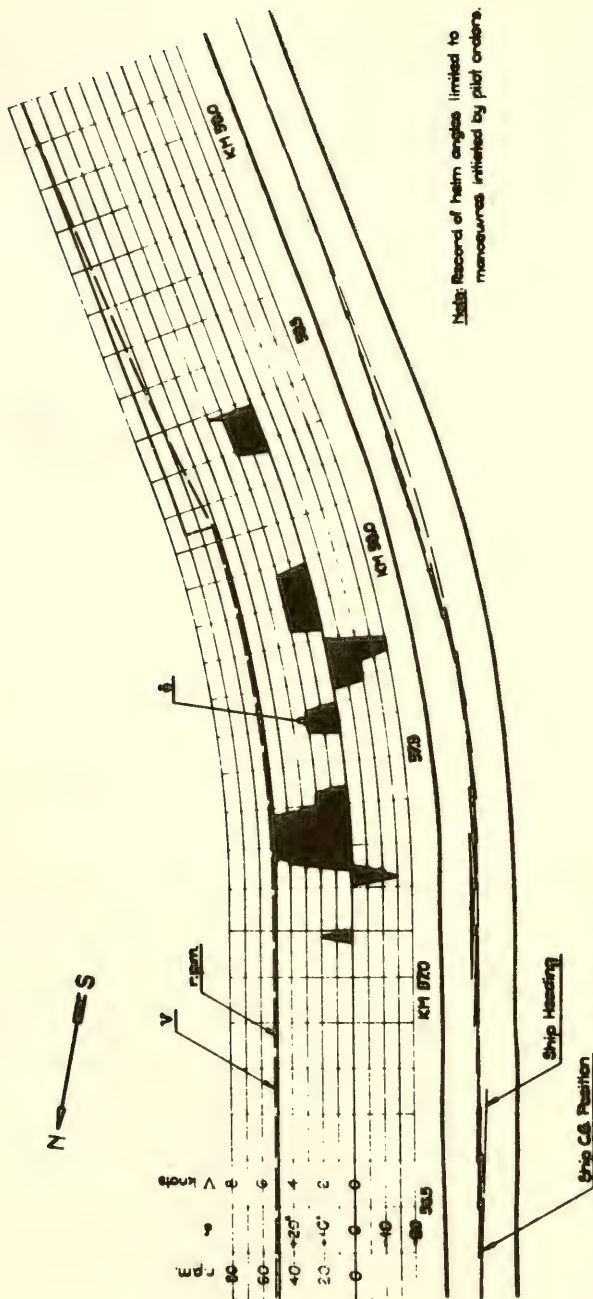


Fig. 5. 60 000 tdw tanker southbound through Suez Canal on 36' draught.
Abstract of Records in KM 57 Bend.

she again moves closer to the port bank, and again port rudder has to be applied, etc.

So far analytical studies of ships moving in canals have been dealing with straight running. It is believed that the mathematical model which is presented here may also be extended to the case of slowly widening and bending canals.

II. SYMBOLS AND UNITS, ETC.

When applicable the symbols and abbreviations here used have been chosen in accordance with the ITTC recommendations, [7]. Some new symbols are introduced to define the position and orientation of a ship in confined waters. (See also Section X.)

The system of axes fixed in space is $O_0x_0y_0z_0$, that fixed in the body or ship is $Oxyz$. The point of reference O lies at distance $L_{pp}/2$ forward of A.P. of the ship. (Cf. Fig. 6 and Section IV.)

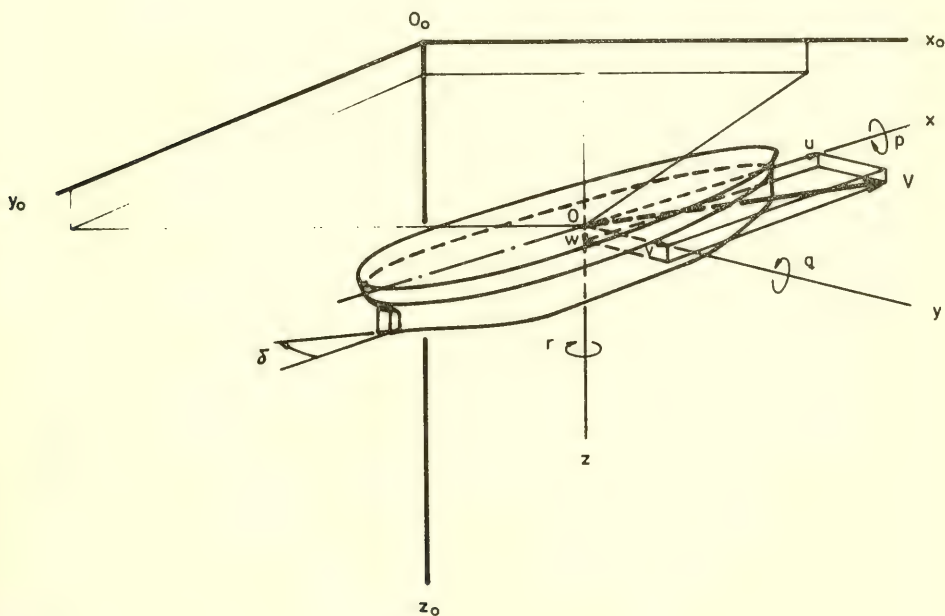


Fig. 6. Inertia frame and body axes, etc.

Dimensional numbers are given in metric units unless otherwise stated. Generally coefficients and relations are expressed in non-dimensional forms. In addition to the non-dimensionalizing "prime" system usually adopted use is here made of a new "bis" system, further presented in Section III.

A dot above a variable stands for a derivation with respect to time. Partial derivatives of forces and moments are designated by the proper subscript attached to the force or moment symbol.

TABLE I

Symbol	Definition	Physical Dimension	Remarks
A_c	Channel section area	L^2	
A	Section area of hull	L^2	
A_{ij}	Added mass. $i = 1, 2, 3; j = 1, 2, 3$	M	
	" " $i = 4, 5, 6; j = 4, 5, 6$	ML^2	
	" " $i = 1, 2, 3; j = 4, 5, 6$	ML	
A_H	Added mass in horizontal oscill. in a free surface, neglecting gravity	M	
A'_H	Added mass in horizontal oscill., unbounded fluid	M	
A_r	Total proj. area of rudder	L^2	
A_{rm}	Moveable proj. area of rudder	L^2	
B	Beam of hull	L	
C_D	Cross-flow drag coeff., 3-dim.	-	
D	Diameter of propeller	L	
\vec{F}	Force vector	MLT^{-2}	
F_{nh}	Froude number on depth	-	$F_{nh} = V/\sqrt{gh}$
F_{nL}	Froude number on length	-	$F_{nL} = V/\sqrt{gL} = V''$
I	Moment of inertia	ML^2	
I_{ij}	Mass product of inertia	ML^2	$I''_{zz} = k_{zz}^2$
J	Propeller advance coefficient	-	$J = u(1 - w)/nD$
K	Rolling moment about x axis	ML^2T^{-2}	
K_Q	Propeller torque coeff.	-	$K_Q = -Q^P/\rho n^2 D^5$
K_T	Propeller thrust coeff.	-	$K_T = T^P/\rho n^2 D^4$

Symbol	Definition	Physical Dimension	Remarks
L	Length of hull	L	$L = L_{pp}$
M	Pitching moment about y axis	ML^2T^{-2}	
\vec{M}	Moment vector	ML^2T^{-2}	
N	Yawing moment about z axis	ML^2T^{-2}	$N'' = N/mgL$
Q	Torque about propeller shaft	ML^2T^{-2}	Q^T = turbine torque
R	Turning radius	L	$r' = L/R$
R	Resistance	MLT^{-2}	$X(R) = -R$
T	Hull draught	L	
T^P	Propeller thrust	MLT^{-2}	
T_L	Kinetic energy of liquid	ML^2T^{-2}	
\vec{U}	Total flow velocity	LT^{-1}	
\vec{V}	Velocity of origin of body axes	LT^{-1}	$V'' = V/\sqrt{gL}$
\vec{V}^c	Speed of water current	LT^{-1}	
\vec{V}_l	Ship speed over ground	LT^{-1}	
W	Channel width in general	L	
\overline{W}	Bank spacing, half of	L	$2\overline{W} = W_b - W_p$
X, Y, Z	Hydrodynamic forces along body axes	MLT^{-2}	
Y^R	Y-force due to rudder	MLT^{-2}	
Y^{RR}	Y-force on rudder proper	MLT^{-2}	
a	Depth to top of rudder	L	
a	Water surface elevation	L	
a_Λ	Slope of lift coefficient curve	-	
b	Height of rudder	L	
c	Flow velocity past rudder	LT^{-1}	
c_D	Cross-flow drag coeff., 2-dim.	-	
g	Gap between rudder and hull	L	
\vec{g}	Gravity vector	LT^{-2}	
h	Depth of water	L	
\vec{h}	Vector in general	Undef.	
k_{ii}	Coefficients of accession to inertia	-	$i = 1, 2, 3$

Symbol	Definition	Physical Dimension	Remarks
k'_{ii}	Coefficients of accession to inertia	-	$i = 4, 5, 6$
k_r	Corr. factor for rudder inflow	-	Cf. eq. (7.4)
k_v	Corr. factor for rudder inflow	-	
k_{zz}	Non-dim. radius of gyration	-	
m	Mass of body	M	$m'' = 1$
n	Number of revs. of prop. in unit time	T^{-1}	
p	Pressure in general	$ML^{-1}T^{-2}$	
q	Stagnation pressure	$ML^{-1}T^{-2}$	
p, q, r	Angular velocity components	T^{-1}	
r_{ome}	Max. radius of equivalent body of revolution	L	
s	Lateral thrust factor	-	Cf. Section VII
s	Sinkage	L	
t	Time	T	$t'' = t/\sqrt{L/g}$
t	Thrust deduction factor	-	
u, v, w	Components of \vec{V} along body axes	LT^{-1}	
w	Wake fraction	-	
x, y, z	Orthogonal coordinates of a right-handed system of body axes	L	
x_0, y_0, z_0	Orthogonal coordinates of a right-handed system of space axes (inertia frame)	L	
Δ	Weight displacement	MLT^{-2}	$\Delta = \mu\rho g\nabla_0 = mg$
∇	Volume displacement	L^3	Normal approx.: $\nabla = \nabla_0$
∇_0	Volume displacement at rest	L^3	
Λ	Aspect ratio	-	
Λ_r	Aspect ratio of rudder	-	$\Lambda_r = b^2/A_r$
$\bar{\Lambda}_r$	Do for rudder + plane wall image	-	$\bar{\Lambda}_r = 2\Lambda_r$
Φ	Velocity potential	L^2T^{-1}	$\Phi'' = \Phi/L\sqrt{gL}$

Symbol	Definition	Physical Dimension	Remarks
$\bar{\Omega}$	Angular velocity of ship	T^{-1}	
α	Angle of attack	-	
β	Angle of drift	-	$\tan \beta = -v/u$
γ	Frequency parameter	-	$\gamma = V\omega/g = u''\omega''$
γ	Coeff. of heading error term in proportional rudder control	-	"Rudder ratio"
δ	Rudder angle (deflection)	-	
δ^*	Rudder angle ordered by auto pilot	-	
δ_e	"Effective" rudder angle	-	$\delta_e = \delta$ for $v=r=0$
ϵ	Phase lead angle	-	
ζ	Restricted water depth parameter	-	$\zeta = T/(h - T)$
η	Ship-to-bank distance parameter	-	$\eta = \eta_s + \eta_p$
$\bar{\eta}$	Bank spacing parameter	-	$\bar{\eta} = \eta_s - \eta_p$
η_p	Port bank distance parameter	-	$\eta_p = L/(W_p - y_0)$
η_s	Starboard bank distance parameter	-	$\eta_s = L/(W_s - y_0)$
θ	Angle of pitch	-	
μ	Body mass density ratio	-	$\mu = m/\rho\nabla_0$. For norm. surface ships $\mu = 1$
ρ	Mass density of water	ML^{-3}	
σ	Coeff. of rate of change of heading term in proportional rudder control	T	"Rate (time) constant"
φ	Prismatic coefficient	-	
ϕ	Angle of roll or heel	-	
ψ	Angle of yaw, or heading error	-	
ω	Circular frequency	T^{-1}	$\omega'' = \omega\sqrt{L/g}$
ω'	Reduced frequency	-	$\omega' = \omega L/V \approx \omega''/u''$

III. NON-DIMENSIONALIZING BY USE OF THE "BIS" SYSTEM

The use of non-dimensional coefficients is accepted in all branches of ship theory, and when motion studies are considered even the variables of the equations are often normalized.

Within the field of maneuvering a unit for time is usually the time taken by a body to cover the distance of its own length, and the unit for velocity then is most naturally given by the momentary speed $V = (u^2 + v^2)^{1/2}$. If the body does not move forward this definition is less attractive. In the system just mentioned — which is recommended by ITTC and which in most cases is fully adequate — symbols for non-dimensional quantities usually are indicated by a prime.

The unit for length almost always is chosen equal to the length L of the body, and for the common surface ship more specified $L = L_{pp}$.

The unit for mass is mostly taken as the mass of a certain volume of the liquid, defined in terms of the body or ship geometry. In the "prime" system already referred to reference volumes are, say, $\frac{1}{2}L^3$ [8] or $\frac{1}{2}L^2T$ [9], the latter one used with the reference area LT suggested by the wing analogy.

In case of bodies, which are supported mainly by buoyancy lift, the main hull contour displacement ∇_0 is perhaps the most natural reference volume: if body mass then is $m = \mu \cdot \rho \cdot \nabla_0$ the non-dimensional mass is equal to μ . (When treating heavy aircraft dynamics Glauert chose $\mu\rho\nabla$ in place of $\rho\nabla$ for the mass unit, [10].) In normal ship dynamics $\mu = 1$, whereas for heavy torpedoes $\mu = 1.3 - 1.5$, say; the symbol μ will be rejected in certain applications.

Here a consistent normalization of motion modes and forces will be made in a new system, the "bis" system, where the unit for mass is $m = \mu\rho\nabla_0$, the unit for length is L and the unit for linear acceleration is equal to g , the acceleration of gravity. From this the unit for time is $\sqrt{L/g}$, and it also follows the Table below:

TABLE II

Unit for	"bis" system	"prime" system	
mass (M)	$\mu\rho\nabla_0$	$\frac{\rho}{2} L^3$	$\frac{\rho}{2} L^2 T$
length (L)	L	L	L
time (T)	$\sqrt{L/g}$	L/V	L/V
linear velocity	\sqrt{gL}	V	V
linear acceleration	g	V^2/L	V^2/L
angular velocity	$\sqrt{g/L}$	V/L	V/L
angular acceleration	g/L	V^2/L^2	V^2/L^2
force	$\mu\rho g\nabla_0$	$\frac{\rho}{2} V^2 L^2$	$\frac{\rho}{2} V^2 L T$
moment	$\mu\rho g\nabla_0 L$	$\frac{\rho}{2} V^2 L^3$	$\frac{\rho}{2} V^2 L^2 T$
Reference area	$\mu \frac{2\nabla_0}{L}$	L^2	LT

It will be noted that, in the system suggested, a non-dimensional velocity is given by the corresponding Froude number, and that all forces are related to the displacement gravity load $\Delta = \mu\rho g\nabla_0$ of the body. (Cf. quotients such as R/Δ , "resistance per tons of displacement," used in other fields of applied naval architecture.)

It is customary to form a non-dimensional force coefficient by dividing by the product of a stagnation pressure ($q = (\rho/2)V^2$) and a reference area, and of course the new system will not demand any different rules. In place of the velocity V, however, here is chosen that particular velocity which corresponds to $F_{nL} = 1$, i.e. the normalized stagnation pressure is $q = (\rho/2)gL$. The reference area then is seen to equal $\mu(2\nabla_0/L)$.

IV. KINEMATICS IN FIXED AND MOVING SYSTEMS

The two orthogonal systems of axes here used, $0_0x_0y_0z_0$ fixed in space — the inertia frame — and $0xyz$ fixed in the body, are shown in Figs. 6 and 7. The orientation of the body axes may be derived, from an original identification with the inertia frame, by

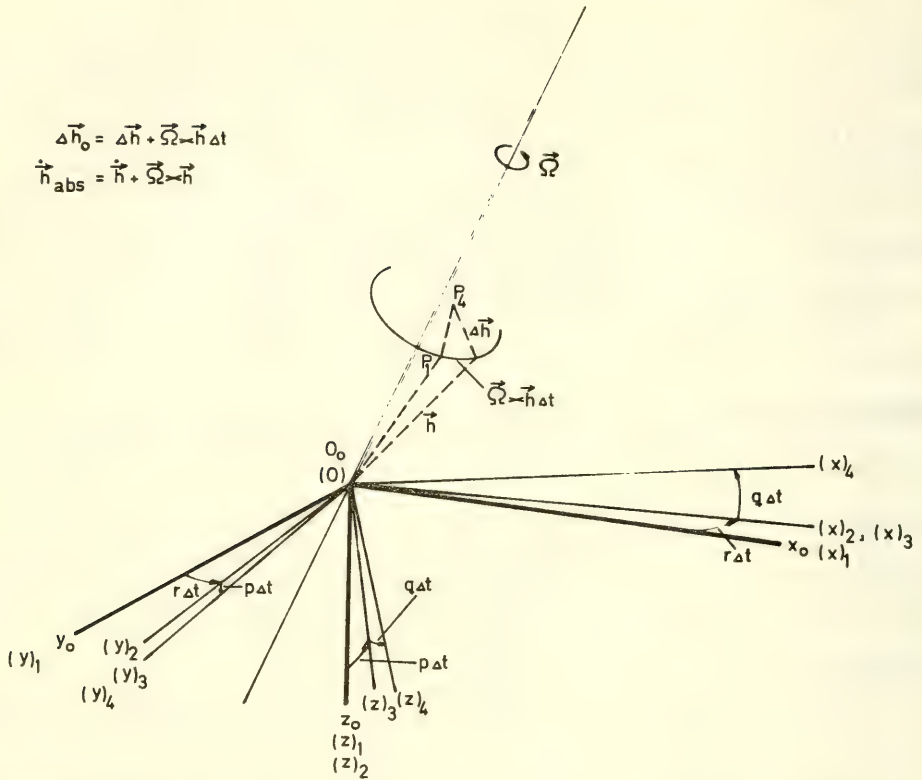


Fig. 7. Graphical deduction of the absolute time derivative of a vector $OP_1 = h$ defined in the moving body system

the successive rotations through the angle of yaw, ψ , the angle of pitch, θ , and the angle of roll, ϕ , respectively, defined around the body axes z , y , and x in their progressively changed positions.

In a certain moment of time the relation between the space vector $0_0 \vec{P} = \vec{x}_{0P}$ and radius vector $0P = \vec{x}_P$, invariant in the body system, is given by

$$\vec{x}_{0P} - \vec{x}_{00} = \Lambda \vec{x}_P \quad (4.1)$$

where the orthogonal transformation matrix reads

$$\Lambda = \begin{bmatrix} \cos \psi \cos \theta & -\sin \psi \cos \phi + \cos \psi \sin \theta \sin \phi & \sin \psi \sin \phi + \cos \psi \sin \theta \cos \phi \\ \sin \psi \cos \theta & \cos \psi \cos \phi + \sin \psi \sin \theta \sin \phi & -\cos \psi \sin \phi + \sin \psi \sin \theta \cos \phi \\ -\sin \theta & \cos \theta \sin \phi & \cos \theta \cos \phi \end{bmatrix} \quad (4.2)$$

When applied in opposite direction the transformation is

$$\vec{x}_p = \Lambda^{-1} (\vec{x}_{op} - \vec{x}_{o0}) = \tilde{\Lambda} (\vec{x}_{op} - \vec{x}_{o0}) \quad (4.3)$$

where $\tilde{\Lambda}$ is the transposed matrix, in which rows and columns appear in interchanged positions.

In particular, note that the gravity vector $\vec{g}_0 = g\hat{z}_0$ will be given by the column vector

$$\vec{g} = \tilde{\Lambda} \begin{vmatrix} 0 \\ 0 \\ g \end{vmatrix} = \begin{vmatrix} -g \sin \theta \\ g \cos \theta \sin \phi \\ g \cos \theta \cos \phi \end{vmatrix} \quad (4.4)$$

in the moving system.

From Fig. 7 will be seen how the absolute (total) value of the time derivative of any vector \vec{h} in the body system may be calculated from the relation

$$\dot{\vec{h}}_{abs} = \dot{\vec{h}} + \vec{\Omega} \times \vec{h} \quad (4.5)$$

The angular velocity vector $\vec{\Omega}$ may now be expressed in terms of the Eulerian angles and their time derivatives: For the vector \vec{h} there is $\dot{\vec{h}}_0 = \dot{\Lambda} \vec{h}$ and

$$\dot{\vec{h}}_{abs} = \tilde{\Lambda} (\dot{\Lambda} \vec{h} + \dot{\vec{h}}) = \dot{\vec{h}} + \tilde{\Lambda} \dot{\Lambda} \vec{h} \quad (4.6)$$

and so the column vector $\vec{\Omega}$ is obtained from the corresponding anti-symmetric angular velocity matrix for the product $\tilde{\Lambda} \dot{\Lambda}$,

$$\vec{\Omega} = \begin{vmatrix} p \\ q \\ r \end{vmatrix} = \begin{vmatrix} \dot{\phi} - \dot{\psi} \sin \theta \\ \dot{\psi} \cos \theta \sin \phi + \dot{\theta} \cos \phi \\ \dot{\psi} \cos \theta \cos \phi - \dot{\theta} \sin \phi \end{vmatrix} \quad (4.7)$$

The angular velocity components resolved in the inertia frame are

$$\begin{aligned} \dot{\phi} &= p + q \sin \phi \tan \theta + r \cos \phi \tan \theta \\ \dot{\theta} &= q \cos \phi - r \sin \phi \\ \dot{\psi} &= r \cos \phi \sec \theta + q \sin \phi \sec \theta \end{aligned} \quad (4.8)$$

In the special case of motion in a horizontal plane in absence of rolling and pitching it is $\dot{\psi} = r$.

In Section VIII an expression will be required for the absolute acceleration of a mass element dm at station $P(x, y, z)$ in a body moving through the water with velocity \vec{V} . From (4.5) then

$$\vec{V}_P = \begin{vmatrix} u \\ v \\ w \end{vmatrix} + \begin{vmatrix} 0 & -r & q \\ r & 0 & -p \\ -q & p & 0 \end{vmatrix} \begin{vmatrix} x \\ y \\ z \end{vmatrix} = \begin{vmatrix} u & -ry & +qz \\ v & +rx & -pz \\ w & -qx & +py \end{vmatrix} \quad (4.9)$$

and by a repeated application of the transformation formula

$$(\vec{a}_P)_{\text{obs}} = \begin{vmatrix} \dot{u} - rv + qw - (q^2 + r^2)x + (pq - \dot{r})y + (rp + \dot{q})z \\ \dot{v} - pw + ru - (r^2 + p^2)y + (qr - \dot{p})z + (pq + \dot{r})x \\ \dot{w} - qu + pv - (p^2 + q^2)z + (rp - \dot{q})x + (qr + \dot{p})y \end{vmatrix} \quad (4.10)$$

In the presence of a homogeneous steady current \vec{V}_0^c a term $\vec{\Lambda} \vec{V}_0^c$ is to be added to the right-hand member of Eq. (4.9). In practical applications this current may be assumed to take place in planes parallel to the horizontal, so that \vec{V} is fully identified by u_0^c and v_0^c . It is easy to show that the column matrix for the acceleration in (4.10) will remain unchanged. To the surface ship

in horizontal maneuvers, this homogeneous current will only mean a steady shift of the path; alternatively, if a certain straight course is required heading shall compensate for the steady drift. The local finite current, on the other hand, generates varying outer disturbances and shall be handled by other means.

V. FLOW PHENOMENA AND FORCES ON A SHIP IN FREE WATER

Ideal-fluid Concepts

As a source of reference for further discussions this Section recapitulates some of the characteristics of the flow past a ship in free or open water.

When a double-body ship form — i.e., a body which is symmetrical about the xy-plane — moves forward in a large volume of ideal-fluid water the streamlines adjust themselves according to the laws of continuity. The shape of those streamlines remain the same at all speeds. The increase of relative velocity past the wider part of the body corresponds to a back-flow or return flow of the water previously in rest. This disturbance in the potential flow pattern extends far into the fluid volume — a beam-width out from the side of the body the super-velocity still has a value, which is some 80 per cent of that just outside the body.

From a resistance point of view the steady forward motion within this ideal homogeneous fluid may lack some realism. According to the d'Alembert's Paradox the body will experience no resultant force. However, if the body is to be accelerated the kinetic energy of the fluid must be increased. This energy increase is manifested by a resistance, which for a given geometrical form is proportional to the mass of displaced fluid and the amount of acceleration, i.e. to the product of an "added mass" and the acceleration component in the direction considered. The resultant force is not necessarily orientated in the same direction.

In the simple steady motion the total energy certainly will remain constant, but as the body moves forward through virgin fluid there takes place in each transverse section a repeated particle acceleration and transformation of energy. The impuls pressure distribution thus generated will normally be unsymmetric, and so a free moment results on the body. This moment may be expressed by a combination of total-body added mass coefficients.

In the general case of a complex motion in the ideal homogeneous fluid all the forces and moments will then be available in terms of added masses and inertias, according to the theories

originated by Kirchhoff [11] and Lamb [12]. In spite of the fact that these forces will be modified by the presence of viscosity in the real fluid, and that new forces will also be generated by the viscous effects, these ideal results should be considered when formulating the mathematical model.

If \vec{U} is the velocity vector of the local fluid element the total kinetic energy is given by $T_L = (\rho/2) \int U^2 d\tau$, or in a potential flow generated by the impuls pressure $\rho\Phi$

$$T_L = - \frac{\rho}{2} \int \Phi \frac{\partial \Phi}{\partial n} dS \quad (5.1)$$

The integration is to be extended over the total boundary, i.e. over the wetted surface of the body. Let the potential be written in linearized form as

$$\Phi = \Phi_1 u + \Phi_2 v + \Phi_3 w + \Phi_4 p + \Phi_5 q + \Phi_6 r \quad (5.2)$$

with respect to the six component body velocities u_i . The six coefficients Φ_i then are functions of the body geometry and of the position in relation to the body.

The condition for fluid velocity $-\partial\Phi/\partial n$ at the body boundary to equal the body normal velocity may be formulated by use of the directional cosines for the normal in the $Oxyz$ -system, whereby

$$2T_L = \sum_{i=1}^6 \sum_{j=1}^6 A_{ij} u_i u_j$$

or

$$\begin{aligned} 2T_L = & -X_{\dot{u}} u^2 - Y_{\dot{v}} v^2 - Z_{\dot{w}} w^2 - 2Y_{\dot{w}} vw - 2X_{\dot{w}} wu - 2X_{\dot{v}} uv \\ & - K_{\dot{p}} p^2 + M_{\dot{q}} q^2 - N_{\dot{r}} r^2 - 2M_{\dot{r}} qr - 2K_{\dot{r}} rp - 2K_{\dot{q}} pq \\ & - 2(X_{\dot{p}} u + Y_{\dot{p}} v + Z_{\dot{p}} w)p - 2(X_{\dot{q}} u + Y_{\dot{q}} v + Z_{\dot{q}} w)q \\ & - 2(X_{\dot{r}} u + Y_{\dot{r}} v + Z_{\dot{r}} w)r \end{aligned} \quad (5.3)$$

Here there are 21 different added masses (A_{ij}) or "acceleration derivatives." Force derivatives with respect to a linear acceleration are of dimension M , and moment derivatives with respect to an angular acceleration are of dimension ML^2 , as are the mass moments of inertia. Cross coupling derivatives such as $X_{\dot{p}} = -A_{14}$ are of dimension ML .

If the body has a plane of symmetry there remain 12 different acceleration derivatives, and for a body of revolution generated around the x axis there are only the three derivatives A_{11} , A_{22} and A_{66}

The motion of the ideal liquid takes place in response to the force and moment expended by the moving solid. At any time this motion may be considered to have been generated instantaneously from rest by the application of a certain impulse wrench. The rate of change — cf. Eq. (4.5) — of the impulse wrench is equal to the force wrench searched for. Again, the work done by the impulse is equal to the increase of kinetic energy, and as shown by Milne-Thomson [13] the force and moment on the body may therefore be expressed in terms of the kinetic energy of the liquid,

$$\vec{F} = - \frac{d}{dt} \left(\frac{\partial T_L}{\partial \vec{V}} \right) - \vec{\Omega} \times \frac{\partial T_L}{\partial \vec{V}} \quad (5.4)$$

$$\vec{M} = - \frac{d}{dt} \left(\frac{\partial T_L}{\partial \vec{\Omega}} \right) - \vec{\Omega} \times \frac{\partial T_L}{\partial \vec{\Omega}} - \vec{V} \times \frac{\partial T_L}{\partial \vec{V}}$$

(The partial derivations shall be considered as gradient operators.) The complete formal expressions for the inertia forces in the ideal fluid have been derived from Eqs. (5.3) and (5.4) by Imlay [14], and they are here given in Eq. (5.5).

$$\begin{aligned} \overline{X}_{id} = & X_{\dot{u}} \dot{u} + X_{\dot{w}} (\dot{w} + uq) + X_{\dot{q}} \dot{q} + Z_{\dot{w}} wq + Z_{\dot{q}} q^2 + X_{\dot{v}} \dot{v} + X_{\dot{p}} \dot{p} + X_{\dot{r}} \dot{r} \\ & - Y_{\dot{v}} vr - Y_{\dot{p}} rp - Y_{\dot{r}} r^2 - X_{\dot{u}} ur - Y_{\dot{w}} wr + Y_{\dot{v}} vq + Z_{\dot{p}} pq - (Y_{\dot{q}} - Z_{\dot{r}}) qr \end{aligned}$$

$$\begin{aligned} \overline{Y}_{id} = & X_{\dot{v}} \dot{u} + Y_{\dot{w}} \dot{w} + Y_{\dot{q}} \dot{q} + Y_{\dot{v}} \dot{v} + Y_{\dot{p}} \dot{p} + Y_{\dot{r}} \dot{r} + X_{\dot{v}} vr - Y_{\dot{w}} vp + X_{\dot{r}} r^2 \\ & + (X_{\dot{p}} - Z_{\dot{r}}) rp - Z_{\dot{p}} p^2 - X_{\dot{w}} (up - wr) + X_{\dot{u}} ur - Z_{\dot{w}} wp - Z_{\dot{q}} pq + X_{\dot{q}} qr \end{aligned}$$

$$\begin{aligned} \overline{Z}_{id} = & X_{\dot{w}} (\dot{u} - wq) + Z_{\dot{w}} \dot{w} + Z_{\dot{q}} \dot{q} - X_{\dot{u}} uq - X_{\dot{q}} q^2 + Y_{\dot{w}} \dot{v} + Z_{\dot{p}} \dot{p} + Z_{\dot{r}} \dot{r} + Y_{\dot{v}} vp \\ & + Y_{\dot{r}} rp + Y_{\dot{p}} p^2 + X_{\dot{v}} up + Y_{\dot{w}} wp - X_{\dot{v}} vq - (X_{\dot{p}} - Y_{\dot{q}}) pq - X_{\dot{r}} qr \end{aligned}$$

$$\begin{aligned}\overline{K}_{id} = & X_{\dot{p}}\dot{u} + Z_{\dot{p}}\dot{w} + K_{\dot{q}}\dot{q} - X_{\dot{v}}wu + X_{\dot{r}}uq - Y_{\dot{w}}w^2 - (Y_{\dot{q}} - Z_{\dot{r}})wq + M_{\dot{r}}q^2 \\ & + Y_{\dot{p}}\dot{v} + K_{\dot{p}}\dot{p} + K_{\dot{r}}\dot{r} - (Y_{\dot{q}} - Z_{\dot{r}})vr + Z_{\dot{p}}vp - M_{\dot{r}}r^2 - K_{\dot{q}}rp + X_{\dot{w}}uv \\ & - (Y_{\dot{v}} - Z_{\dot{w}})vw - (Y_{\dot{r}} + Z_{\dot{q}})wr - Y_{\dot{p}}wp - X_{\dot{q}}ur + (Y_{\dot{r}} + Z_{\dot{q}})vq \\ & + K_{\dot{r}}pq - (M_{\dot{q}} - N_{\dot{r}})qr + Y_{\dot{w}}v^2\end{aligned}$$

$$\begin{aligned}\overline{M}_{id} = & X_{\dot{q}}(\dot{u} + wq) + Z_{\dot{q}}(\dot{w} - uq) + M_{\dot{q}}\dot{q} - X_{\dot{w}}(u^2 - w^2) - (Z_{\dot{w}} - X_{\dot{u}})wu \\ & + Y_{\dot{q}}\dot{v} + K_{\dot{q}}\dot{p} + M_{\dot{r}}\dot{r} + Y_{\dot{p}}vr - Y_{\dot{r}}vp - K_{\dot{r}}(p^2 - r^2) + (K_{\dot{p}} - N_{\dot{r}})rp \\ & - Y_{\dot{w}}uv + X_{\dot{v}}vw - (X_{\dot{r}} + Z_{\dot{p}})(up - wr) + (X_{\dot{p}} - Z_{\dot{r}})(wp + ur) \\ & - M_{\dot{r}}pq + K_{\dot{q}}qr\end{aligned}$$

$$\begin{aligned}\overline{N}_{id} = & X_{\dot{r}}\dot{u} + Z_{\dot{r}}\dot{w} + M_{\dot{r}}\dot{q} + X_{\dot{v}}u^2 + Y_{\dot{w}}wu - (X_{\dot{p}} - Y_{\dot{q}})uq - Z_{\dot{p}}wq - K_{\dot{q}}q^2 \\ & + Y_{\dot{r}}\dot{v} + K_{\dot{r}}\dot{p} + N_{\dot{r}}\dot{r} - X_{\dot{v}}v^2 - X_{\dot{r}}vr - (X_{\dot{p}} - Y_{\dot{q}})vp + M_{\dot{r}}rp + K_{\dot{q}}p^2 \\ & - (X_{\dot{u}} - Y_{\dot{v}})uv - X_{\dot{w}}vw + (X_{\dot{q}} + Y_{\dot{p}})up + Y_{\dot{r}}ur + Z_{\dot{q}}wp \\ & - (X_{\dot{q}} + Y_{\dot{p}})vq - (K_{\dot{p}} - M_{\dot{q}})pq - K_{\dot{r}}qr\end{aligned}$$

(5.5)

Forces in Horizontal Motions - General

Especially, for a body which is symmetrical with respect to its xz-plane and which is moving in the extension of its xy-plane, there are

$$\begin{array}{l|l}\overline{X}_{id} = X_{\dot{u}}\dot{u} - Y_{\dot{v}}vr - Y_{\dot{r}}r^2 & + X_{\dot{v}}(\dot{v} - ur) + X_{\dot{r}}\dot{r} \\ \overline{Y}_{id} = Y_{\dot{v}}\dot{v} + X_{\dot{u}}ur + Y_{\dot{r}}\dot{r} & + X_{\dot{v}}(\dot{u} + vr) + X_{\dot{r}}r^2 \\ \overline{N}_{id} = N_{\dot{r}}\dot{r} + (Y_{\dot{v}} - X_{\dot{u}})uv + Y_{\dot{r}}(\dot{v} + ur) & + X_{\dot{v}}(u^2 - v^2) + X_{\dot{r}}(\dot{u} - vr)\end{array}\quad (5.6)$$

By careful application of sound reasoning it is suggested that terms

to the right of the bar may be dropped. Terms containing the coefficient $Y_{\dot{r}}$ have been retained in view of the fore-and-aft unsymmetry present particularly in propelled bodies.

The coefficients for \dot{u} in X , for \dot{v} in Y , and for r in N — with signs reversed — are the most commonly well-known added masses and added moment of inertia respectively. These inertia coefficients also appear in some of the cross-coupling terms.

Lamb's "coefficients of accession to inertia" relate added masses to the mass of the displaced volume ∇ (k_{ij} , $i = 1, 2, 3$) and added moments of inertia to the proper moments of inertia of the same displaced volume (k'_{ij} , $i = 4, 5, 6$). Lamb calculated k_{11} , $k_{22} = k_{33}$ and $k'_{55} = k'_{66}$ for the spheroid of any length-to-diameter ratio, [15]. For ellipsoids with three unequal axes the six different coefficients were derived by Gurewitsch and Riemann; convenient graphs are included in Ref. [16]. For elongated bodies in general the total added inertias may be calculated from knowledge of two-dimensional section values by strip methods, applying the concept of an equivalent ellipsoid in correcting for three-dimensional end effects. (See further below.)

Of special interest in Eq. (5.6) is the coefficient $Y_{\dot{v}} - X_{\dot{u}}$ in the "Munk moment," [17]. (See also discussion in [18].) This free broaching moment in the stationary oblique translation within an ideal fluid defines the derivatives

$$N''_{uv} = - \frac{k_{22} - k_{11}}{\mu}, \quad N^i_{\beta} = \frac{2\nabla}{L^3} (k_{22} - k_{11}) \quad (5.7)$$

(Cf. Table II.) The factor $k_{22} - k_{11}$ may be looked upon as a three-dimensional correction factor.

Due to energy losses in the viscous flow of a real fluid past a submerged body the potential flow picture breaks down in the afterbody. In oblique motion there appears a stabilizing viscous side force. So far no theory is available for the calculation of this force, but semi-empirical formulas give reasonable results for conventional bodies of revolution. Force measurements on a divided double-body model of a cargo ship form have demonstrated that some de-stabilizing force is still carried on the afterbody but that most of the moment is due to the side force on the forebody, predictable from low-aspect-ratio wing or slender body theories, [18].

Similar measurements on a divided body in a rotating arm shall be encouraged. Contrary to the case of stationary pure translation the pure rotation in an ideal fluid involves non-zero axial and lateral forces. From Eq. (5.6) the side force is given by $X_{\dot{u}}ur$, whereas the moment here is $Y_{\dot{r}}ur$. For bodies of revolution the distribution of the lateral force may be calculated as shown by Munk

[17] whereas strip theory and two-dimensional added mass values may be used for other forms. The magnitude of ideal side force as well as moment are small, however, and in a real fluid the viscous effects are dominating.

There are reasons to believe that the main results of the theories for the deeply submerged body will also apply to the case of a surface ship moving in response to control actions at low or moderate forward speeds. Potential flow contribution to damping as well as inertia forces depend on the added mass characteristics of the transverse sections of the hull, and as long as these characteristics are not seriously affected by the presence of the free surface the previous statement comes true. However, an elongated body performing lateral oscillations of finite frequencies will generate a standing wave system close to the body as well as progressive waves, by which energy is dissipated. The hydrodynamic characteristics then are no longer functions of the geometry only. At a higher speed or in a seaway displacement and wave interference effects will further violate the simple image conditions.

VI. CALCULATIONS AND ESTIMATES OF HULL FORCES

On Added Mass in Sway and Added Inertia in Yaw

A brief review will here be given of the efforts made to calculate the added mass and inertia of surface ships in lateral motions. Four facts will be in support of this approach: The added masses are mainly free from viscous effects; the added masses appear together with rigid body masses in the equations of motions, and relative errors are reduced — this is especially true in the analytical expression for the dynamic stability lever, which involves only the small $X_{\dot{\psi}}$; the added masses are experimentally available only by use of non-stationary testing techniques, and in many places experimental data must therefore be supplemented with calculated values; the added masses are no unique functions of geometry only, and experiments must be designed to supply the values pertinent to the problems faced.

The velocity potential for the two-dimensional flow past a section of a slender body must satisfy the normal velocity condition at the contour boundary as well as the kinematical condition for the relative depression velocity at the free constant-pressure surface. In case of horizontal as well as vertical oscillations this latter linearized conditions is $\omega^2 + g(\partial\Phi/\partial z) = 0$ — cf. Lamb [12] — or, introducing the non-dimensional potential $\Phi'' = \Phi/L\sqrt{gL}$ and $\omega'' = \omega\sqrt{L/g}$,

$$\frac{\partial\Phi''}{\partial z''} = -\omega''^2 \cdot \Phi'' \quad (6.1)$$

For steady horizontal drift at moderate forward speeds one finds a similar condition

$$\frac{\partial \Phi''}{\partial z''} = \beta^2 \cdot F_{nL}^2 \cdot \frac{\partial^2 \Phi''}{\partial y''^2} \quad (6.2)$$

which shall govern the local accelerations of the flow in the transverse plane penetrated by the moving body, [18].

As is seen from the two equations above the vertical velocities at the water surface are zero in the limit of zero frequency or zero drift, and negligible for $\omega \ll \sqrt{g/L}$ or $\beta^2 F_{nL}^2 \ll 1$. The water surface may therefore be treated as a rigid wall, in which the underwater hull and streamlines are mirrored, i.e. the image moves in phase with the hull.

For high frequencies, where $\omega \gg \sqrt{g/L}$, the condition at the free surface is $\Phi = 0$. The water particles move up and down normal to the surface, but no progressive waves are radiated. At the juncture of the horizontally oscillating submerged section contour and the free surface this condition may be realized by the added effect of an image contour, which moves in opposite phase. (Cf. Weinblum [19].) The value of added mass in this case, "neglecting gravity," is smaller than the deeply submerged value by an amount equal to twice the image effect.

Added masses A_H' for two-dimensional forms oscillating laterally with very low frequencies in a free surface have been calculated by Grim [20] and by Landweber and Macagno [21], using a LAURENT series with odd terms to transform the exterior of a symmetric contour into the exterior of a circle (TEODORSEN mapping). By retaining the first three terms this transformation yields the well-known two-parameter LEWIS forms [22]; other combinations of three terms have been studied by Prohaska in connection with the vertical vibrations of ships [23]. Two terms (and one single selectable parameter for the excentricity) define the semi-elliptic contour as that special case with given draught, for which the added mass is a minimum. Landweber and Macagno also made calculations of the added masses A_H in the high-frequency case. For the semi-elliptic contour $A_H/A_H' = 4/\pi^2$, which result was first found by Lockwood-Taylor, [24].

A basic theory for the dependence of the hydrodynamic forces on finite frequencies was developed for the semi-submerged circular cylinder by Ursell, [25]. By use of a special set of non-orthogonal harmonic polynomials he found the velocity potential and stream function that satisfied the boundary conditions and represented a diverging wave train at infinity. Based upon similar principles Tasai extended the calculations of added masses (and damping forces) for two-dimensional LEWIS forms to include the total

practical range of swaying frequencies, [26] . His results are condensed in a number of convenient tables and diagrams; the added mass values are seen to vary even outside the limit values corresponding to zero and infinite frequencies.

An application of a generalized mapping function technique to ship section forms of arbitrary shape was performed by Porter, who studied the pressure distribution and forces on heaving cylinders, [27] . A way of solving the two-dimensional problem without resort to conformal mapping was developed by Frank, who represented the velocity potential by a distribution of wave sources over the submerged part of the contour, now defined by a finite number of off-sets. The varying source strength was determined from an integral equation based on the kinematical boundary condition

Vufts [29] contributed an extensive experimental and theoretical study of the hydrodynamic coefficients for pure and coupled swaying, heaving and rolling cylinders, based on the previous works by Ursell, Porter and de Jong, [30] . The coefficients of the THEODORSEN mapping function were defined by a least square fit of the geometry of the cylinder contours to off-sets in 31 points. Of special interest is the good agreement obtained between experiments and the theoretical predictions for the added mass of a typical midship section; the oscillation experiments do not cover the very low frequencies, however. Although small the difference in the calculations for the actual section fit and for an approximate LEWIS form was mainly confirmed by the experiments.

When used with the strip method the integrated section contributions to total added mass and inertia shall be reduced by the appropriate "longitudinal inertia factors" for three-dimensional effects. Following Lewis these factors are usually taken equal to those derived for the prolate spheroid in a similar mode of motion. This is only an engineering artifice, and it is certainly not correct, say, in case of accelerations in yaw for normal hull forms; thus these correction factors are mostly omitted in hydrodynamic studies of sufficiently slender bodies.

In a discussion of the strip theory Tuck [31] included the results of all the added mass and damping coefficients of a surface ship at zero forward speed, calculated by use of Frank's close-fit method with 15 off-sets for each of 23 stations. The total added mass (A_{22}^0) and moment of inertia (A_{66}^0) of a Series 60 Block .70 form are here represented by full lines in Fig. 8. Tuck also examined the forward speed corrections to be applied to the integrated values; thus, especially, he put $A_{66} = A_{66}^0 + (U^2/\omega^2) \cdot A_{22}^0$, or in present notation

$$N_f''(u'', \omega'') = N_f''(\omega'')_{u''=0} + \frac{u''^2}{\omega''^2} \cdot Y_v''(\omega'')_{u''=0} \quad (6.3)$$

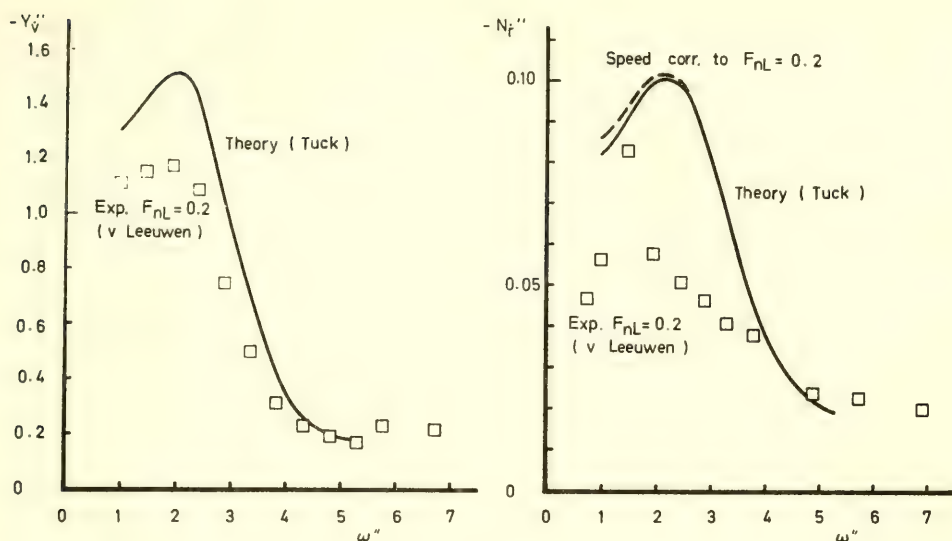


Fig. 8. Total added mass and added moment of inertia for a Series 60 Block .70 form according to theory and experiments.

(Note that the strip theory is not valid for small "reduced frequencies" $\omega' = \omega''/u''$, where it shall be replaced by a slender body theory, [31].) The dotted curves in the diagrams indicate predictions for $F_{nL} = u'' = 0.20$.

The Series 60 Block .70 form was subjected to oscillator experiments in lateral modes at several frequencies and forward speeds by van Leeuwen, [32]. The results for the naked hull with rudder at $F_{nL} = 0.20$ are compared with the predictions from strip theory in Fig. 8. The experimental values fall well below these predictions in the entire range of frequencies, especially in case of the moments in yaw. Although it is inherent in the testing technique that very low frequencies could not be included van Leeuwens results do cover the critical range around $\omega'' \cdot u'' = 1/4$.

Consider a surface body in steady motion along the centreline between two parallel walls width W apart; the diverging bow wave displays an angle to the centreline. If the motion is steady the reflected wave will pass aft of the body only if $W/L > \tan \beta$, regardless of the speed. For the simple travelling pressure point the cusp line angle is equal to $19^\circ 47'$ according to the Kelvin theory, whereas slightly different values may be observed for real ship forms. In case the body is oscillating (as in the simple example may

be illustrated by a pulsating source) additional waves will form, which move with speed g/ω . At low frequencies these waves move faster than the body, so that the diverging wave front folds forward, and at a certain forward speed there is now a new requirement on basin width to avoid wall interference. For combinations of ω and V (or u), in which $\gamma = \omega"u" = 0.272$, the opening angle equals $\beta = 90^\circ$, and with a further reduction in speed it rapidly reduces again to 55° as γ approaches $1/4$. This latter condition is associated with a special phenomenon of critical wave damping, as has been shown from theory as well as experiments by Brard, [33].

In model tests with a ship form in lateral oscillations a narrow range of critical frequencies may be identified by a change of the distribution of the hydrodynamic forces, which was clearly demonstrated by van Leeuwen's analysis.

Whereas there is a discrepancy in the absolute values of added masses compared in Fig. 8 this discrepancy could be reduced by the application of a three-dimensional corrector; more elaborate theories of forward speed effects for slender bodies at low frequencies may further improve the comparison. In the main, therefore, it may be stated that the variation of added mass with frequency is well documented.

Added Masses in Maneuvering Applications

The performance problems set up in maneuvering studies usually involve a short-time prediction of a transient response to a control action, and it is therefore convenient to be in the position to use ordinary non-linear differential equations with constant coefficients. This, of course, is in contrast to the linearized spectrum approach to the statistical seakeeping problem, which will more readily accept frequency-dependent coefficients. (Frequency- or time-dependence as a result of viscous phenomena will be touched upon below.) Which values of added mass are now to be used in the equations for the manoeuvring ship? It shall be noted that it is hard to judge from the behaviour of a free-sailing ship or ship model which is the correct answer unless special motions are carefully examined.

It was early suggested by Weinblum that the low added mass values of the high-frequency approximation should be adequate for use in dealing with problems of directional stability, where starting conditions should simulate impulsive motion, [19]. Weinblum also drew attention to Ref. [34], in which Havelock proved that the high-frequency values appeared in horizontal translations with uniform acceleration, regardless of the initial velocity.

The impulsive pressures experienced on the tapered bow and stern portions of a slender body in oblique translation may be calcu-

lated from the sectional area curve slope and the added mass characteristics of the transverse sections, as shown by Munk [17] and experimentally verified for the submerged doublebody ship form in Ref. [18]. The good agreement obtained between total yawing moments measured on this form and its surface ship geosim suggests that the deeply submerged added mass values should apply in this case. It is observed, however, that the water particles in way of a certain section station here are not repeatedly accelerated from rest as is the case when considering the cylindrical part of the hull. Again, if the principle of superposition of damping and inertia components to the total hydrodynamic force shall be retained for general motions it shall be necessary to adopt the zero-frequency added mass values.

An illustrative discussion of added masses with special application to the design and analysis of experiments is due to Motora in Ref. [35]. For the determination of the added mass in sway to be used in the aperiodic equations of a maneuvering ship he recorded the direction of the acceleration imparted to a model by a force suddenly applied in a certain direction. The added mass then could be found from a reasonable estimate of virtual mass in surge. To obtain the added moment of inertia in yaw he recorded the angular acceleration following the impact by a pendulum, the momentum loss of which was also known. He suggested that the inertia values so derived should correspond to the impact or high-frequency type, but the results included from tests with a series of ship models indicate sway mass values of the same order as those valid for the deeply submerged case, and moments of inertia in yaw of magnitudes corresponding to finite frequency surface values.

In a recent paper Motora and co-authors [36] compare the results of new experiments and calculations of an "equivalent" added mass for a ship model in a sway motion, which is initiated by a ramp- or step-form impact input of finite duration. The calculations are based on Tasai's section values in the frequency domain [26], and in agreement with the experiments they confirm that the value of the equivalent added mass defined is a function of impact duration. (Cf. Fig. 9.) If the duration is infinitely small only the equivalent added mass is equal to its high-frequency value, and it becomes larger the longer the duration. Thus these results help to explain the earlier findings for added masses as well as for added moments of inertia, for which latter the impact technique then used did generate rather short input impulses.

For application to normal ship maneuvers it may now seem justified to use the low-frequency or deeply submerged values.

In recent years it has been widely accepted that the acceleration derivatives for a surface ship model may be evaluated from a set of "planar-motion-mechanism" tests in pure sway or yaw. The acceleration amplitudes are varied by an adjustment of oscillator

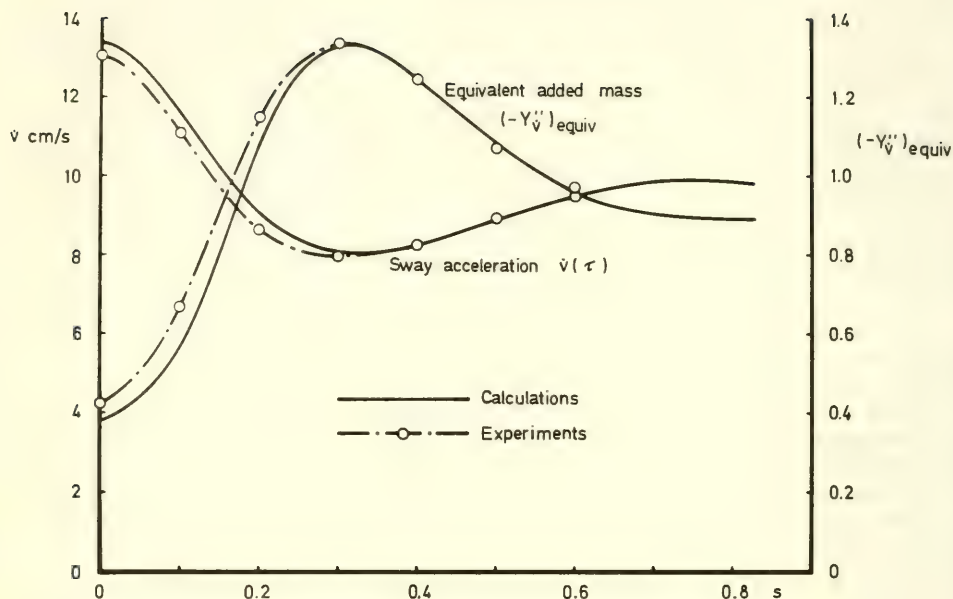


Fig. 9. Motora's equivalent added mass coefficient as defined by acceleration due to step input impact of duration τ

amplitudes, whereas the frequency is kept as low as running length permits, [32]. A typical reduced frequency $\omega' = \omega \cdot L/V$ will be of order 0.5, corresponding to $\omega'' = \gamma/u''$, $\omega'' = \omega' \cdot u'' = 0.1$ in Fig. 8. The derivatives so obtained may be expected to be somewhat higher than the zero-frequency values.

The theoretical zero-frequency added mass values for two-dimensional LEWIS forms as well as for semi-submerged ellipsoids of finite lengths indicate the main dependence on principal geometrical characteristics. Especially, for very large length-to-draught ratios the ellipsoid values tend to those of a semi-elliptic cylinder, $(\pi/2)\rho T^2$, so that $-Y_v'' = T/B$. Moreover, it will be seen from [21] that for LEWIS forms in general $-Y_v''$ likewise is rather close to T/B for fullness coefficients corresponding to midship sections.

The ellipsoid family has a constant prismatic coefficient $\varphi = 2/3$. The correction for finite length involves a slight dependence on B/T , as may be seen from Fig. 10. In a more general case

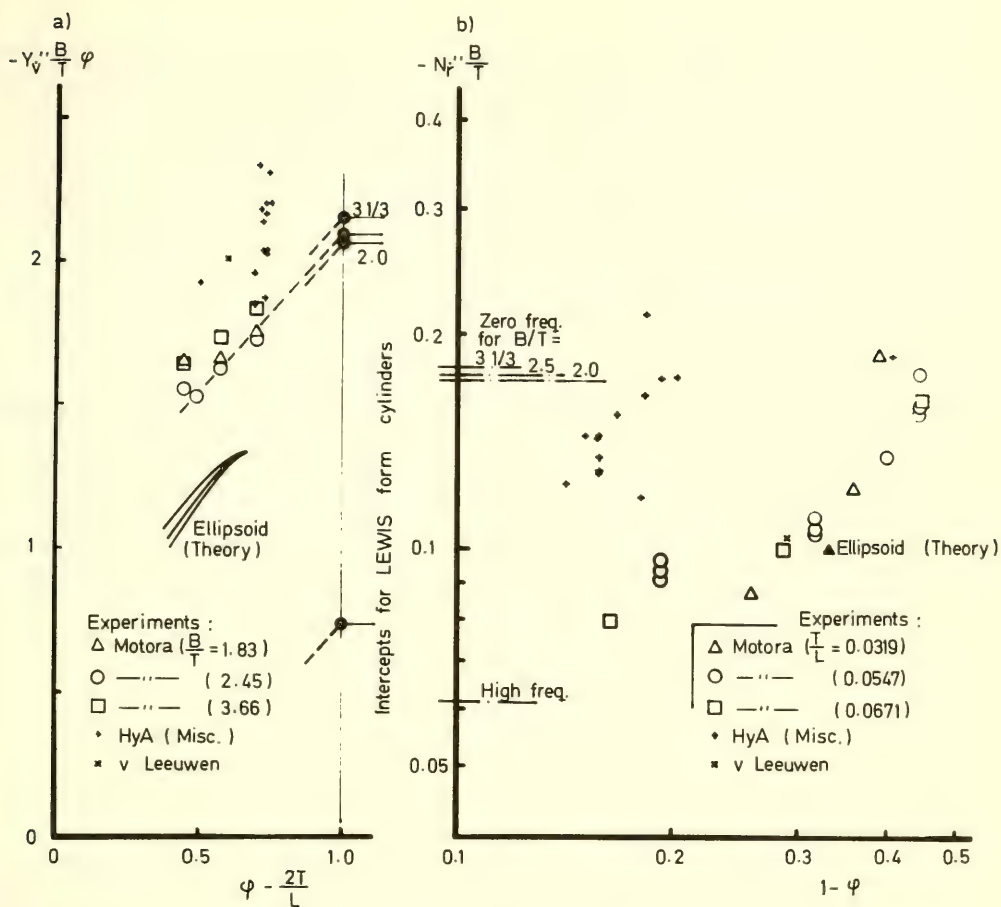


Fig. 10. Non-dimensional added mass (a) and added moment of inertia (b) from theory and experiments τ

this correction will also depend on ϕ and on lateral profile, etc. For the inclusion of ship form values in Fig. 10a the diagram is drawn to a base of $\phi - (2T/L)$. The ordinates are given by the product $-Y_v'' (B/T)\phi$, by which the intercepts on the vertical $\phi - (2T/L) = 1$ then corresponds to the infinitely long cylinders.

In addition to the ellipsoid and LEWIS cylinder values the diagram include the experimental results by Motora just referred to as well as a number of oscillator results, chiefly from tests run for SSPA in the HyA PMM. The general character of the three-dimensional corrector is clearly seen, and it is suggested that the diagram may be used for approximate estimates.

Non-dimensional added moments of inertia, in terms of

product $-N_f'' \cdot B/T$, are displayed in Fig. 10b, compiling experiment data from different sources. Here the two-dimensional LEWIS-form values for high as well as low frequencies are indicated by off-sets to the left in the diagram. Motora's 1960 impact test data, which appear on a level close to the high-frequency prediction, do not indicate any definite dependence on draught-to-length ratio. These data as well as low-frequency PMM data clearly indicate an increase of moment of inertia with reduced fullness. This trend may be expected in view of the deep and narrow bow and stern sections in fine forms — certainly the deeply-submerged ellipsoid is not representative for a ship form in yaw acceleration.

Semi-Empirical Relations for the Four Basic Stability Derivatives

Among the large number of first-order force and moment derivatives, that are used to describe the linearized hydrodynamics of the moving hull, only four appear in the analytical criterion for inherent dynamic stability with fixed controls. These are the stability derivatives proper, Y_{uv} , N_{uv} , Y_{ur} and N_{ur} . From simple analogy with the zero-aspect-ratio wing theory of Jones [37] they turn out as in Table III.

TABLE III

Non-dim. system:	"Prime"			"Bis"
Ref. area:		LT	L^2	$2\nabla/L$
Symbol and analogy value:	$Y_v' = -Y_\beta'$	$-\frac{\pi}{2} \cdot \frac{2T}{L}$	$-\pi \cdot \left(\frac{T}{L}\right)^2$	$Y_{uv}'' = -\frac{\pi}{2} \cdot \frac{LT^2}{\nabla}$
	$N_v' = -N_\beta'$	$-\frac{\pi}{4} \cdot \frac{2T}{L}$	$-\frac{\pi}{2} \cdot \left(\frac{T}{L}\right)^2$	$N_{uv}'' = -\frac{\pi}{4} \cdot \frac{LT^2}{\nabla}$
	Y_r'	$\frac{\pi}{4} \cdot \frac{2T}{L}$	$\frac{\pi}{2} \cdot \left(\frac{T}{L}\right)^2$	$Y_{ur}'' = \frac{\pi}{4} \cdot \frac{LT^2}{\nabla}$
	N_r'	$-\frac{\pi}{8} \cdot \frac{2T}{L}$	$-\frac{\pi}{4} \cdot \left(\frac{T}{L}\right)^2$	$N_{ur}'' = -\frac{\pi}{8} \cdot \frac{LT^2}{\nabla}$

Although this analogy has been verified in principle for a submerged double-body model as well as for the surface model at small Froude numbers [18], it shall not be expected to furnish an adequate numerical prediction. It suffices to point on the alternative relation for a closed body in a perfect fluid, given by Eq. (5.7), and to the fact that at least some negative lift is still carried on the run of normal ship-form hull. The bow lift or transverse force is not

concentrated to the leading edge as in case of a rectangular wing but distributed over the forebody as an effect of fullness and section shape. Certain modifications to the hull form are known to affect the force derivatives, but do not appear in the simple form parameters of Table III. The fin effect of screw and rudder contributes to the derivatives even in the case of vanishing aspect ratio of the hull.

From the analysis of a large number of derivatives it has been found that the scatter of data in a plot of, say, Y''_{uv} versus the parameter LT^2/∇ is somewhat smaller than the scatter of Y'_v on base of aspect ratio $2T/L$.

The diagrams Fig. 11-12 include stability derivative data for normal ship form models with normal-sized rudders propelled at medium Froude numbers on even keels. The dotted lines shown correspond to the simple wing analogy. The full lines are derived by linear regression and upon the tentative assumption of a - 1:2 relation of moment and force intercepts at zero aspect ratio. Their equations are given as

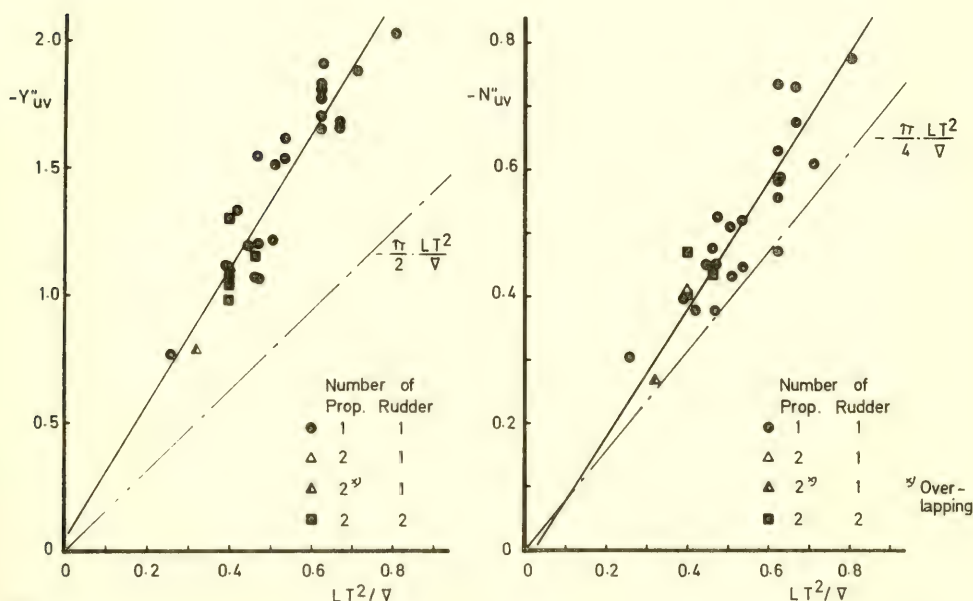


Fig. 11. Stiffness force and moment derivative data with mean regression line. (Cubic fit to experimental results.)

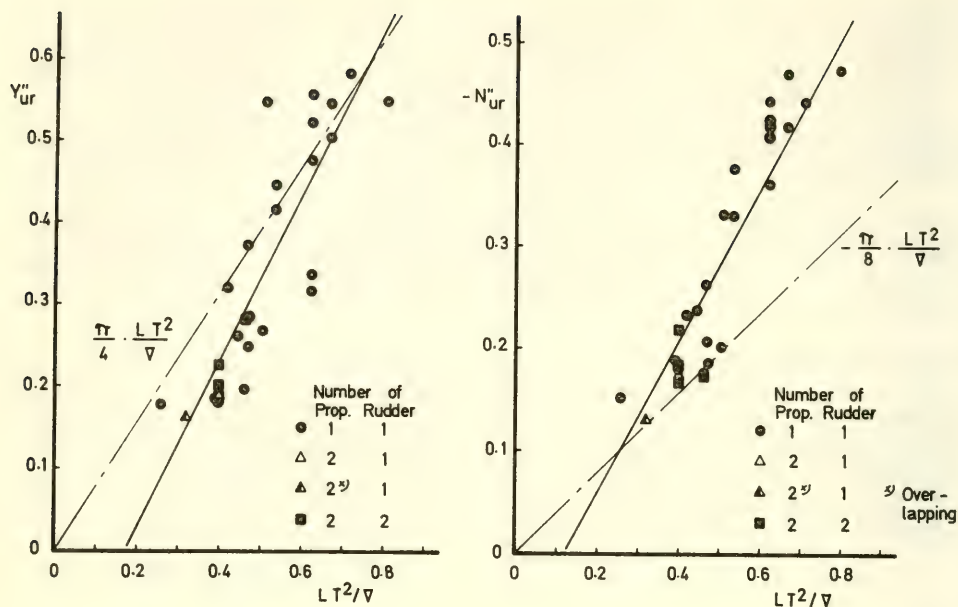


Fig. 12. Rotary force and moment derivative data with mean regression line. (Cubic fit to experimental results.)

$$Y''_{uv} = -2.66 \frac{L T^2}{V} - 0.04 = -1.69 \cdot \frac{\pi}{2} \cdot \frac{L T^2}{V} - 0.04$$

$$N''_{uv} = -1.01 \frac{L T^2}{V} + 0.02 = -1.28 \cdot \frac{\pi}{4} \cdot \frac{L T^2}{V} + 0.02$$

(6.4)

$$Y''_{ur} = 1.02 \frac{L T^2}{V} - 0.18 = 1.29 \cdot \frac{\pi}{4} \cdot \frac{L T^2}{V} - 0.18$$

$$N''_{ur} = -0.74 \frac{L T^2}{V} + 0.09 = -1.88 \cdot \frac{\pi}{8} \cdot \frac{L T^2}{V} + 0.09$$

and of the data 100, 86, 67 and 79 per cent respectively, appear within ± 20 per cent of these mean values.

It is obvious that these expressions should be regarded as guide values only, but they may also be used for comparative studies, especially when steering on a straight course is of main concern. In this latter case it is more important to have a proper knowledge of the control derivatives, whereas Eq. (6.4) may furnish adequate estimates for the hull forces; they again shall be corrected for alternative control arrangement alternatives, however.

In the next Section an approximate method will be given for finding the control derivatives of a rudder of conventional design. In the hypothetical case of an isolated rudder experiencing the nominal inflow at the stern of the ship it would be easy to calculate its contribution to the total "hull + rudder amidship" derivatives from a knowledge of its control effectiveness. In general the interference effects in behind condition are much more complicated, and in fact the contribution searched for mostly is quite small. Even more, then, the effect of a modification to rudder and control derivatives comes out as a very small change in the stability derivatives. The diagram in Fig. 13 is compiled to correlate the effects of such modifications as reported by Eda and Crane [38] and documented in test results available at SSPA. Obviously new experiments are required.

Reference shall here also be given to the methods of estimating stability derivatives for surface ships as suggested and successfully tested by Jacobs, [39].

The aerodynamic wing analogy should only be valid for small Froude numbers as the limit solution of a general lifting surface integral equation. The effects of finite Froude numbers on the lateral stability derivatives of a thin ship of small draught-to-length ratio was studied by Hu, [40]. According to Hu the force and

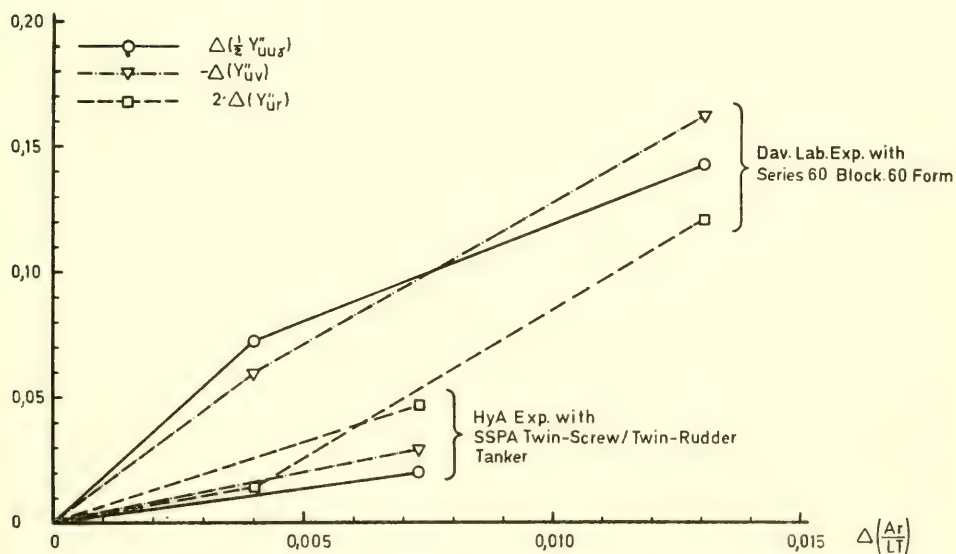


Fig. 13. Change of control force derivatives and total force derivatives in sway and yaw with change of relative size of rudder.

moment derivatives at $F_{nL} = 0.1$ are increased by some 20 per cent above their zero-speed values, an increase which is not fully realized in model tests. A comparison of the results of this theory with various experiments is presented by Newman, [41]. Newman also points out that the free surface may give rise to a steady side force as a thickness effect, and indicates a solution to that problem.

From an inspection of the experimental results for the drift moment, which are the more consistent, a first approximation to the speed dependence is given by

$$(N''_{uv})_u = (N''_{uv})_0 + \frac{1}{2} N''_{uvu} u \quad (6.5)$$

where $\frac{1}{2} N''_{uvu} \approx 1.3 (N''_{uv})_0$. This suggests that the zero-speed values will be some 20 per cent lower than those indicated by the mean line of Fig. 11.

Viscous Frequency Effects and Small-Value Non-Linearities in Lateral Forces

In dealing with the free-surface effects on added masses it was concluded that so far the frequencies involved in manoeuvring motions were to be regarded as low, but that frequency (or memory) effects should be expected to appear in time histories were viscous phenomena were of more concern.

The extreme exemplification is furnished by the pitching submarine, the stern planes of which are operating in the downwash behind the bow planes, but in case of submarines as well as normal surface ships also the very stern portion of the hull is exposed to velocities induced by vortices trailing from upstream hull and appendages. Moreover, local separation within the three-dimensional boundary layer flow over the stern directly affects the cross-flow momentum and the impulsive pressures. The forces and moments experienced by the hull in transient motions can then only be calculated by use of convolution integrals over the entire time history, such as derived by Brard in case of a special descriptive model, [42].

For application to the mathematical model defined by ordinary differential equations it is again still possible to use frequency dependent coefficients, but unfortunately this frequency dependence is likely to be subjected to scale effects. It is therefore advisable to design experiments for Strouhal numbers or reduced frequencies, which are low enough to produce steady-state values. From a summary of published data in Ref. [41] the limiting frequency will be expected to be somewhere in the region $1 < \omega' < 4$. From a more recent analysis of sinusoidal free-sailing tanker model data Nomoto suggests that this limiting frequency is approached already at $\omega' \approx 0.5$, [43]. This indicates that the high-frequency part of a normal

ship steering transfer function is obscured by the viscous frequency dependence. (Cf. Section IX.)

The steady motion of a full form may also be accompanied by a non-steady separation and shedding of vortices, which will violate captive measurements, or it will modify the force field and be a cause of unpredictable scale effects. In Ref. [44] Nomoto drew the attention to an "unusual" kind of separation, which had been observed not on the leeward but on the outer side of the after-body of turning models. (Later on he reported the same phenomenon taking place on full scale ships combining high block coefficients and low length-to-beam ratios.) This separation may be responsible for an almost constant increase in yaw damping moment — see diagram in Fig. 14a — and so indirectly for the small-rate non-linearity displayed in the yaw-rate-versus-helm diagram from spiral tests with these hulls.

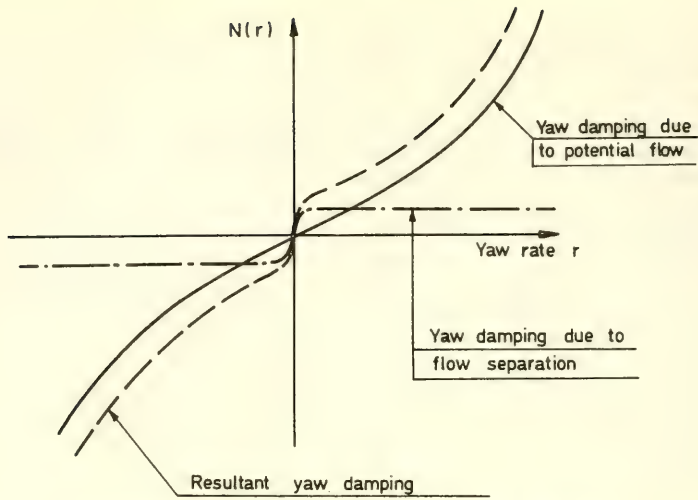
Unsymmetrical separation may also take place on a hull moving along a straight line with a small angle of drift. If transverse force and moment both are mainly linear functions of angle of drift the centre of pressure will remain in a forward position, only gradually moving aft with onset of viscous crossflow. A three-dimensional separation, which suddenly develops on one side of the hull, may explain the strange behaviour of the centre-of-pressure curve of a tanker model tested by Bottomley [45], here reproduced in Fig. 14b. New tests with modern hulls sometimes indicate similar trends.

It is fully possible to approximate these effects by a small-value non-linearity term in the mathematical model, which may then be used, say, for the prediction of a ship behaviour which is extremely sensitive to winds of varying directions [46]; if the separation is peculiar to the model only this prediction is meaningless, however.

Large-Value Non-Linearities in Lateral Forces

The predominant non-linearities present in the lateral forces are due to viscous cross-flow resistances, and they can only be established by experimental procedures. It will be assumed that the empirical relationships may be expressed by finite polynomials, derived by curve-fitting, and that these same relationships therefore also may be fully defined by a finite number of terms in the Taylor expansions. This convention motivates the use of appropriate numerical factors in front of the derivatives within the hydrodynamic coefficients.

From pure athwartship towing it is possible to define a Y-force $-C_0 \cdot L T \cdot v^2$, the sign of which is governed by $|v|/v$. Thus $Y(v^2, |v|/v) = \frac{1}{2} Y_{vv(|v|/v)} \cdot v^2 |v|/v$, or, for convenience, $\frac{1}{2} Y_{|v|v} |v| v$.



- a) Nomoto's explanation of effect of 3-dim. stern flow separation (Above)
- b) Lateral force centre of pressure acc. to measurements by Baker and Bottomley (Below)

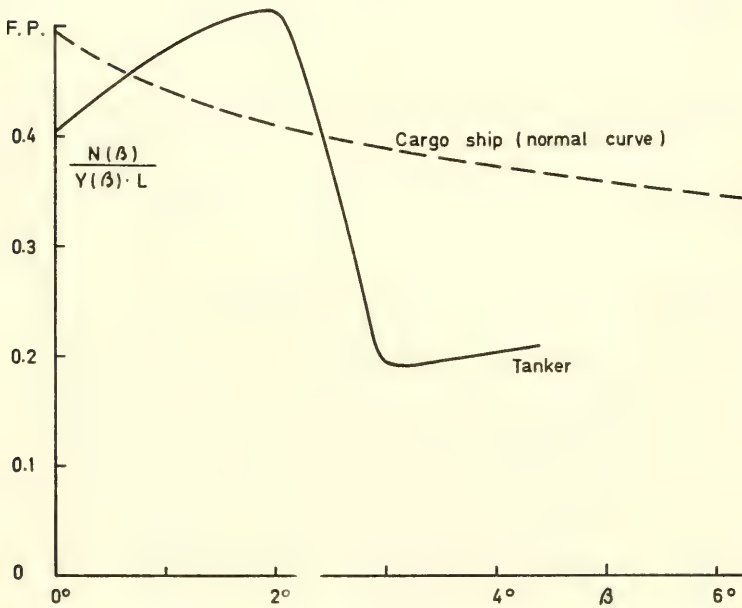


Fig. 14. Small-value non-linearities in full form model testing.

Note that the factor $\frac{1}{2}$ has been retained, which should not have been the case if v and $|v|$ had been treated as independent variables; this, however, would only have been a formal artifice with no physical significance.

In straight-line oblique motion the non-dimensional lateral force is $Y''(u'', v'', v''^2, |v''|/v'')$, or, in accepted writing

$$Y''(u'', v'') = Y''_{uv} u'' v'' + \frac{1}{2} Y''_{|v|v} |v''| v'' \quad (6.6)$$

where $\frac{1}{2} Y''_{|v|v} = -C_D \cdot L^2 T / 2 \nabla$. It is obvious that here two terms are added, which each one corresponds to a certain flow field. In the discussion of the "linear" term it was pointed out that the ideal flow picture would remain valid over the bow portion of the hull, and in view of the finite time required for the development of the viscous cross-flow these conditions may still be true at larger angles of drift. (Cf. non-linear theories for the lift of zero-aspect-ratio wings.)

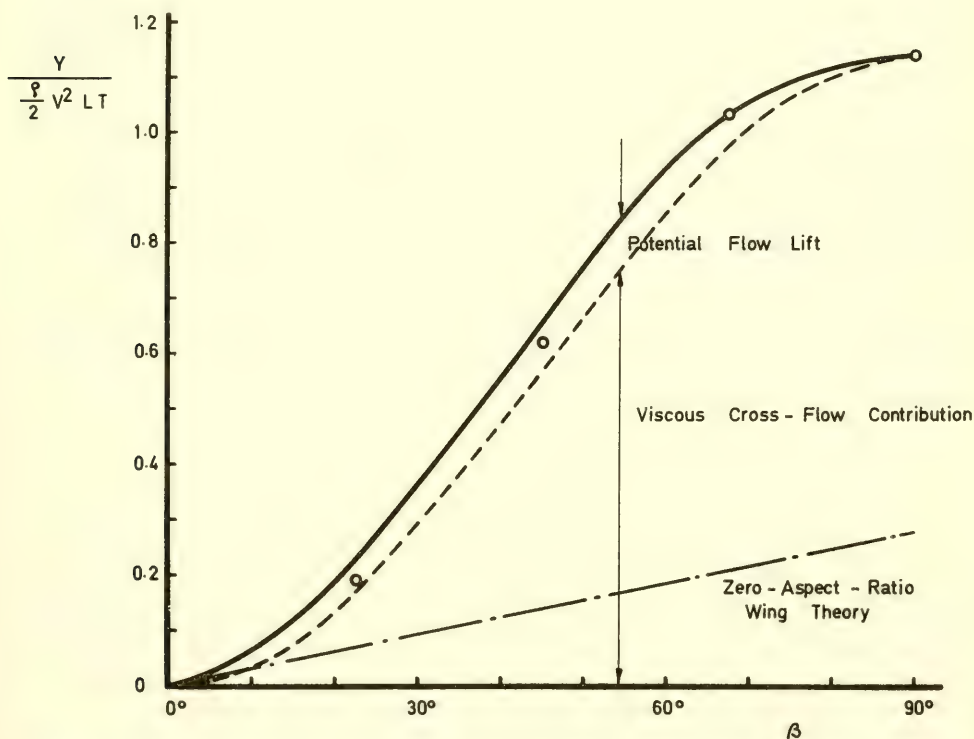


Fig. 15. Calculated and measured lateral forces on a cargo liner model in oblique towing.

An experimental evidence of the practical validity of the superposition in Eq. (6.6) is illustrated in Fig. 15, based on force measurements at SSPA on a 3.55 m model of a cargo liner with rudder and bilge keels, [47]. In this diagram the quotient $Y/(\rho/2)V^2LT = (2\nabla/L^2T)Y''/(u''^2 + v''^2)$ is plotted versus $\beta = -\arctg v/u$, and the viscous cross-flow component is seen to dominate the entire range of $10^\circ < \beta < 90^\circ$.

The variation of cross-flow drag coefficients with drifting speed and hull geometry has also been discussed in several papers by Thieme and by other authors, [48, 49, 50]. In lack of experimental results for a special case in the non-linear range it shall be possible to use these results; a typical value of cross-flow drag of a tanker form is $C_D = 0.7$. The contribution of cross-flow drag to moment-due-to-sway may then be ignored.

In a similar way it is possible to approximate the non-linear rotary derivatives. If $c_D (> C_D)$ is the mean section drag coefficient the moment-due-to-yaw derivative is $\frac{1}{2}N''_{rlr} = - (c_D/32) \cdot (L^2T/2\nabla)$, except for a three-dimensional correction factor. (For rough estimates $\frac{1}{2}N''_{rlr} = 0.03 \cdot \frac{1}{2}Y''_{vlv}$, which is verified from experiments.) The force-yaw velocity derivative now is zero to this approximation. Additional effects of skegs and screws contribute to non-zero values of $\frac{1}{2}N''_{vlv}$ as well as $\frac{1}{2}Y''_{rlr}$.

In the general case the local cross-flow resistance is proportional to $|v + xr|(v + xr)$, and from symmetry relations the coupling terms are seen to include the derivatives Y_{vlr} and Y_{vrl} , etc. (In the cubic fits more often used these couplings are represented by terms in Y_{vvr} and Y_{vrr} , etc. — cf. Abkowitz, [51].)

The contribution to Y due to the combined sway and yaw may be written $Y_{vlv}|v|v(r/v) + Y_{vlr}|r|r(v/r)$, i.e., Y_{vlr} may be looked upon as the derivative of Y_{vlv} with respect to yaw velocity r per unit v , etc.

Forward Speed and Resistance

The principal effects of viscous and free-surface phenomena on the resistance to steady forward motion are well-known to naval architects. The correlations of wavemaking and separation with ship geometry are still less satisfactory. However, alternative methods are available for full scale powering predictions from standard series or project model data. As will be further discussed in next Section the adequate synthesis should supply information not only on shaft horse power and r.p.m. but also on hull resistance and wake fraction. Speed trial data therefore require an analysis such as proposed and used by Lindgren; in case of very large and slow-running ships it may be necessary to include scale effects also in the open-water characteristics of the screw propeller, [52].

A simple guide to ship resistance values may be obtained from the mean line of Fig. 16, which summarizes the results of a limited number of SSPA trial trip data in terms of the total specific resistance $R/\Delta = -[X'']_{v=r=0}$ on basis of Froude number F_{nL} or u . (A similar plot of "total resistance in lbs to displacement in long tons" versus Taylor speed-length quotient, based on model data, was published by Saunders, [53].) The mean line also reflects the general trend of the resistance-speed-dependence for the individual ships in the proximities of their design speeds.

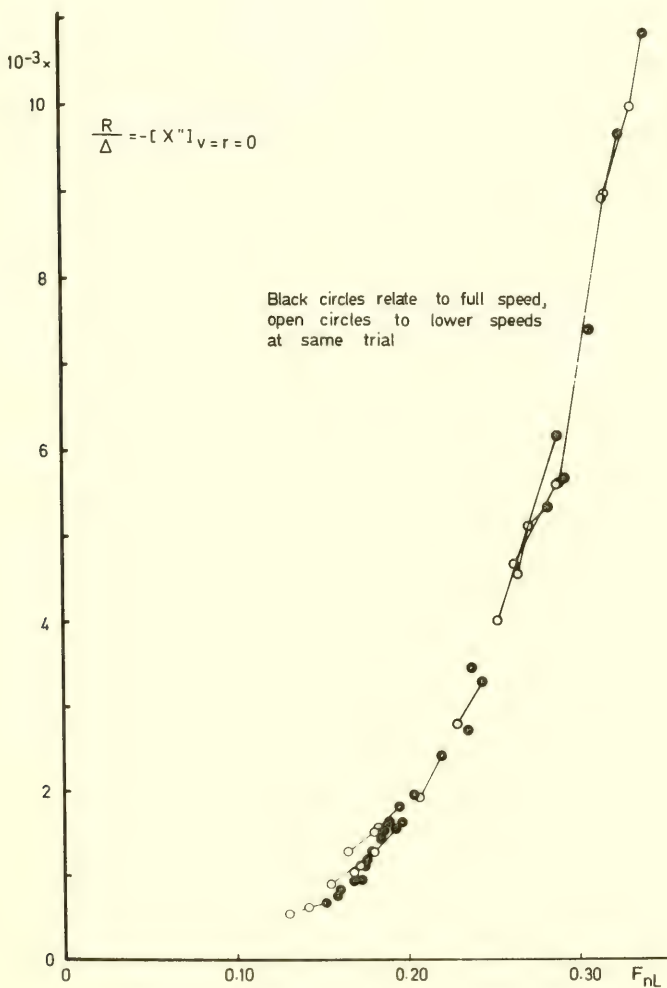


Fig. 16. Specific resistance figures as evaluated from ship trial data at SSPA.

A close approximation to a resistance curve with typical humps and hollows requires a multi-term polynomial in u . Established practice in naval architecture makes use of a single exponential term $R_1(u/u_1)^p$ to characterize the curve in the vicinity of u_1 . For large slow-running tankers $p \approx 2$ over the entire speed range of interest, which is associated with an almost constant advance ratio for the screw. In confined waters it may be necessary to include a higher-order term; see Section IX.

Forward Resistance Due to Lateral Motions

When the ship deviates from the true forward motion additional forces appear in axial direction. The main cause of speed loss in a turning motion is due to the axial component of the centripetal mass force and the hydrodynamic contribution $X_{rv} \cdot rv$, of second importance is rudder drag and finally the axial force due to oblique-hull lift and wave-making shall be considered.

Ideal-flow hydrodynamics identifies X_{rv} with $-Y_{\dot{\psi}}$, i.e. the mass effect is virtually almost doubled. (Cf. (5.6).) A recent analysis of turning trial data indicates much lower values of X_{rv} .

In a steady turn the ship proceeds with her bow pointing inwards, so that $(m + X_{rv})rv = -(m + X_{rv})V^2/R \cdot \beta$ indicates a force opposed to forward thrust. In running on a straight course the frequency of the yawing motion normally is so low that yaw rate and drift angle are in phase during most (but not all) of the time, and so an average parasite resistance results.

Let the response to a sinusoidal motion of the rudder be $\dot{\psi} = \dot{\psi}_a \cdot \sin(\omega t + \epsilon_r)$ and $\beta = \beta_a \cdot \sin(\omega t + \epsilon_\beta)$. Averaging over a number of complete periods gives

$$\overline{rv} = \frac{r_a \beta_a}{2} \cos(\epsilon_r - \epsilon_\beta) \quad (6.7)$$

As the normal merchant ship will pivot round a point closely aft of the bow at low frequencies a rough estimate of the average product is given by $(\overline{rv})_{\omega \rightarrow 0} \approx -(\overline{OP}/2)\dot{\psi}_a$.

A plane wing in a uniform flow will experience an induced drag as given by $C_{Di} = (1/\pi\Lambda)C_L^2$. According to certain experiments this simple relation may still be used with a correction factor for the twisted flow over a rudder behind a screw. The calculation of rudder lift will be shortly discussed in the next Section; using a nominal aspect ratio equal to twice the geometrical one the correction factor just mentioned will be of the order of 1.2 - 1.4.

Typical estimates for tankers give as a guide value a relative increase in forward resistance due to a rudder deflection of δ radians $\Delta X(\delta)/X(u) \approx 3.5$ or $5 \cdot \delta^2$. For small sinusoidal helm angles on a straight course the quasi-stationary application gives $\Delta X(\delta)/X(u) \approx 1.75$ or $2\delta_a^2$, which may be compared with the relation given from propulsion tests with a Mariner ship model in Japan, $\Delta T(\delta)/T = 2 \cdot \delta_a^2$, [54].

At propeller advance conditions removed from the steady forward motion state the induced rudder drag will be given by $\frac{1}{4} X_{cc\delta\delta} \cdot |c| c \delta^2$, where $c = c(u, n)$ is the effective flow velocity past the rudder and where the coefficient $\frac{1}{4} X_{cc\delta\delta}$ is proportional to the control derivative $\frac{1}{2} Y_{cc\delta}$ and to the ratio $\frac{a_\Lambda}{\Lambda}$. In computer applications a soft-type limiter will be used to simulate the conditions for a stalled flow.

The viscous lift experienced by a slender ship hull in oblique translation is also accompanied by an induced drag, but the axial component of the resultant force still is expected to be positive. (According to the zero-aspect-ratio wing analogy the resultant force will bisect the angle between the normal to the hull and the normal to the flow. With increasing aspect ratios the resultants move towards the normal to the flow.) The break-down of the ideal flow over the stern causes a change of viscous pressure resistance, however, and wave-making effects will cause a further increase of forward resistance.

These effects are here illustrated in Fig. 17 by results of axial force measurements on the surface ship model and the submerged double-body form otherwise described in Ref. [18]. From an inspection of these and other surface ship model experiments it is suggested to use a term

$$X(u, v) = \frac{1}{6} X_{uvvv} u |v| v^2 \quad (6.8)$$

to represent the axial force due to lateral drift. An approximate value of the derivative is given by $\frac{1}{6} X_{uvvv}'' = -200$.

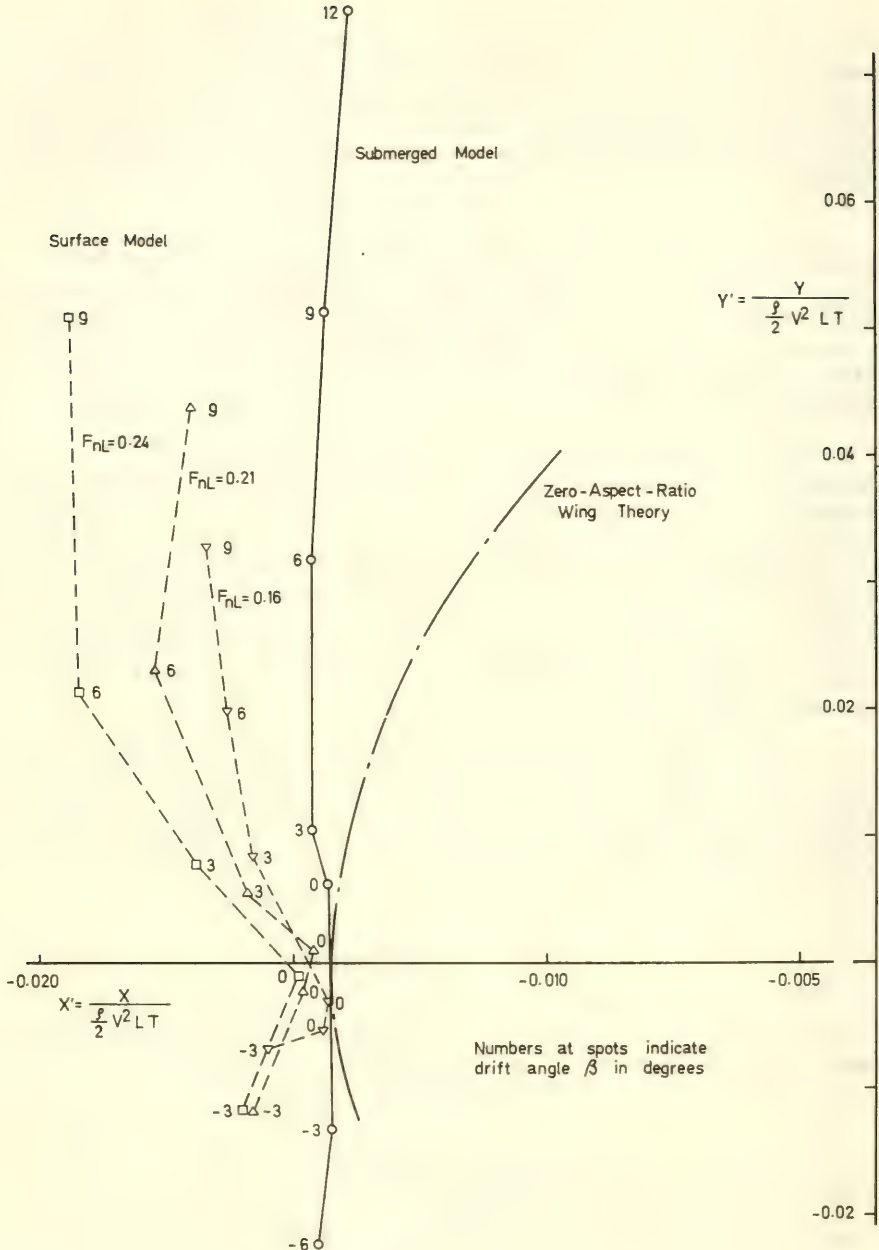


Fig. 17. Change of longitudinal force with hull lift in oblique towing of ship model and submerged double-body geosim

VII. SPEED AND STEERING CONTROL

In general the subject of steering and maneuvering may not be separated from that of propulsive control, and this is specially true in case of ship behaviour at slow speeds. Moreover, in model testing the interactions between hull, propeller, and rudder are likely to cause the main problems of model-to-ship-conversion, including scale effects of a hydrodynamic nature as well as other model effects due to the dynamics of the testing equipment.

Large seagoing ships are usually propelled by a single centre line screw, or by wingward twin screws. In case of a tandem contra-rotating propeller arrangement most of the characteristics discussed below may be calculated for an equivalent single propeller. In case of close-shafted twin screws of overlapping or interlocking types the interaction with the rudder should be specially considered.

It has been repeatedly proven by handling experience that twin screw ships should be fitted with twin rudders. Recent model tests indicate that with a suitable design of the rudders, including a certain neutral position toe-out, this arrangement may favourably compete with the centre line rudder alternative also from a propulsive performance point of view.

In the application of the first-order steering theory, first introduced by Nomoto in 1956 and strictly valid only for inherently stable ships, there appear only two constants: a (desired high) "gain" K , which represents the ratio of rudder turning moment to yaw damping, and a (desired low) "time constant" T , which measures the sluggishness of the ship response, and which represents the ratio of ship inertia to yaw damping. As was subsequently also shown by Nomoto [55] the non-dimensional quotient K'/T' turns out to be proportional to the parameter LA_r/∇ for ships with similar stern arrangements. This quotient may therefore be looked upon as a rudder-on-ship effectiveness factor, proportional to the initial yaw acceleration imparted to the ship by a given helm.

Some ten years ago maneuvering trials were run with three tankers of the Götaverken 40 000 tdw series, all similar except for the stern arrangements, [56]. The SSPA analysis of zig-zag tests with respect to the rudder-on-ship effectiveness factor just mentioned offers a unique illustration of the merits of these arrangements, Fig. 18. In particular, note that the two alternatives with rudder behind screw (screws) prove to be equivalent in case of same total area of rudder, and that the use of the larger area of a twin alternative therefore is especially favourable.

A propeller or a rudder, or the combination of a propeller and a rudder, acts as a stabilizing fin as well as a manoeuvring device; the contributions to the fin effect from the propeller and from the rudder-behind-propeller are of equal order. It should be

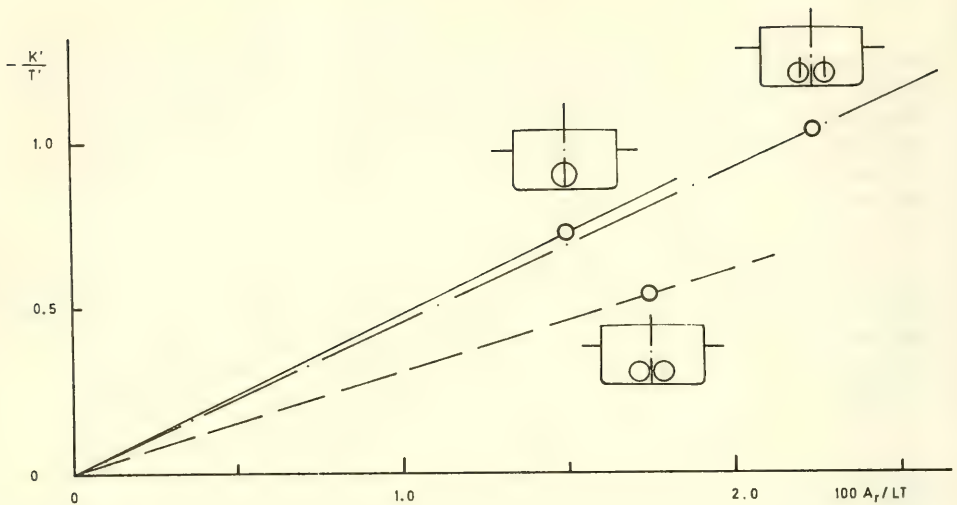


Fig. 18. Results from first-order analysis of full-scale zig zag tests with three 40 000 tdw tankers, similar except for stern arrangements.

realized that a minor modification to a rudder does not appreciably affect this fin effect or the size of a hysteresis loop in the yaw-velocity-versus-steady-helm diagram of an unstable ship. However, the higher control force per degree of helm then possibly achieved will help in actual directional control, where the history of yaw velocities and helm angles takes place well within the height of the steady-state loop. (See also Section I.)

The general propulsion case will be represented by an arrangement including one centre line screw and two wing screws, developing thrusts T_C , T_S and T_P , respectively. Hull interference generates axial forces $t_C T_C$, $t_S T_S$ and $t_P T_P$, in the opposite directions, as well as lateral or sideward forces $s_S \cdot T_S$ and $s_P \cdot T_P$. In order to adhere to the thrust deduction concept the factors t — which are not necessarily constants — will be taken as positive, so that the force in positive x direction is $-t \cdot T$. The factor s_S will be positive, and $s_P = -s_S$. Roughly $s_S = t_S \cdot \cot \alpha$, where α is the effective waterline angle in front of the propeller.

Normally the lateral forces due to T_S and T_P are in balance, but if $T_P \neq T_S$ there is a resultant force applied some $0.4 L$ behind the C.G. of the ship. The turning moment thus obtained is much larger than that produced by the axial forces along the shaft lines, [57].

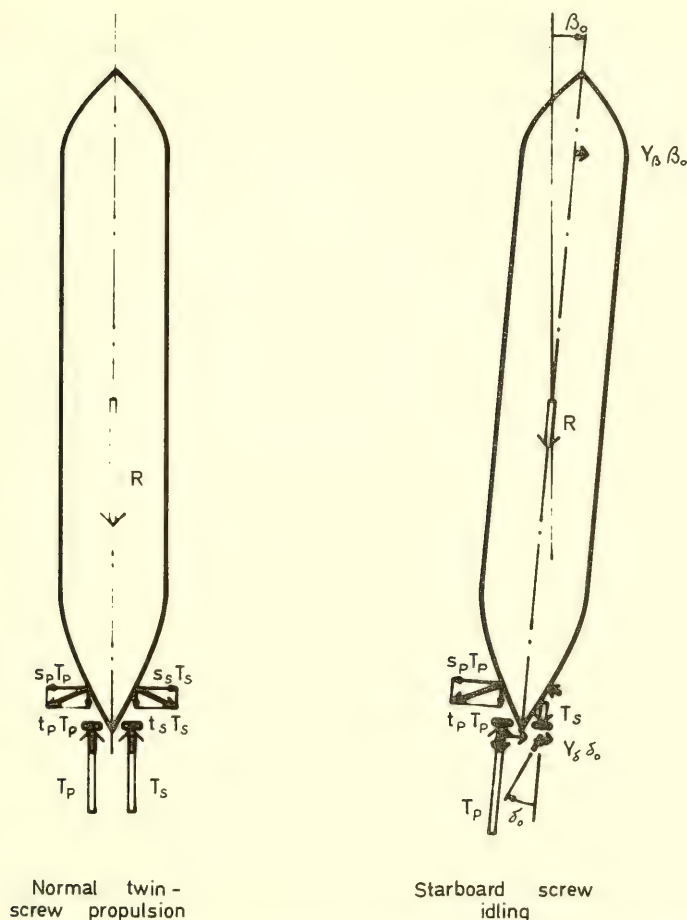


Fig. 19. Force fields on twin-screw tanker on straight steady course.

The diagrams in Fig. 19 illustrate the symmetric force field around a twin-screw tanker in normal straight course conditions, and the steady state situation when running with starboard propeller idling. The non-symmetric suction force on the port quarter is balanced by the forces due to drift and checking rudders. The drift angle is a fraction of a degree only, and some 90 per cent of the compensation force is due to the rudders, set at some 5 to 7 degrees. With the twin rudder arrangement it should be possible to maintain 75 per cent of the speed in this condition. The induced resistance due to rudder lift would be larger in case of a single rudder between the propellers, but the main cause of speed loss of a ship propelled by one of its screws only is the additional drag from the idling

propeller; again, that drag may well be increased by a factor of 3 if the propeller is locked.

The characteristics of a propeller in axial open-water flow are usually given by tables or curves of well-known K_T and K_Q coefficients versus advance ratio J . In yawed flow the propeller also experiences a lateral force and a (small) pitching moment, [58].

In behind conditions the effective angle of drift at the propeller still is roughly $2/3$ of the nominal local angle, high enough to let the propeller contribute the fin effect already mentioned. (The sidewash behind the propeller then has a further straightening effect on the flow to the rudder.) The effective advance ratio is modified by the effective wake in the factor $1 - w$; here w will be chosen as for thrust identity. The effective wake, again, is modified by the drift of the ship, being higher for a starboard drift angle than for a port one and a right-handed propeller [59]; here that effect will be taken as of second order.

Finally, the vertical asymmetry of the flow field is responsible for the appearance of a lateral force on the propeller of a ship even if drift or yaw are zero. In case of a single screw ship this latter force may be put equal to 3 to 5 per cent of the thrust, [60]. A right-handed screw tends to throw the stern of a loaded ship towards starboard, thus requiring a small starboard helm to be carried on straight course. Other free-running model tests prove that draught conditions may change this picture, and that the ship on light draught may have a tendency to turn to starboard, [61].

The hydrodynamic thrust T (T_c , T_s , T_p) and torque Q (Q_c , Q_s , Q_p) — which is negative in case of a right-handed screw on a driving shaft — will be given as quasi-stationary functions of instantaneous values of forward ship speed, u , and screw r.p.s., n (n_c , n_s , n_p). The thrust is a major factor governing the flow velocity past the rudder, and this velocity likewise will be given in terms of u and n . Rudder control derivatives usually are determined from model tests in one or two conditions of screw loading only. In order to find an adequate prediction of full scale control derivatives for the more general propulsion case it is necessary to combine model results with a simple procedure for calculating the total control force due to rudder deflection.

From the hydrodynamical point of view the typical all-movable rudder in behind condition is equivalent to a twisted wing on a pointed afterbody. There are a number of additional complications, however: The spanwise velocity distribution is highly non-uniform, the flow along the chord is accelerating or decelerating, the gap between wing and body is within a retarded boundary layer flow and it also varies with the angle of deflection, the boundary conditions at the free surface violate the vertical symmetry aspect even if there is no suction-down of air, the shape of the body stern

is far from say a simple axisymmetric cone. The modern half-spade rudder on a fixed horn (the Mariner-type) is a hybrid of the all-movable and the flapped types, and other common forms all have their special characteristics. The procedure here adopted is not a substitute for the detailed calculations necessary for a certain project design, but it will furnish a good estimate of control forces and make possible the extended use of model results referred to above.

The Rudder or "Control" Derivatives

It will be assumed that for each rudder configuration may be defined "equivalent" values of rudder area, rudder aspect ratio, rudder angle and rudder advance velocity.

A detailed study of the velocity field in the slipstream of a propelled tanker model and of the pressure distribution over the rectangular rudder fitted to this model was reported by Lötveit, [62]. The distortion of the spanwise loading due to slip-stream rotation was clearly demonstrated, but the diagrams did not indicate any definite influence of the rudder image in the hull and free surface; the gap distance from top of rudder to stern profile was some 12 per cent of rudder height. Straightforward calculations of rudder lift from known relations of lift curve slope versus geometric aspect ratio and an average advance velocity based on the simple momentum theory proved to give good agreement with the rudder forces measured by a force balance or integrated from the pressure field.

Unfortunately in this case no simultaneous measurements were made of the total hull-and-rudder forces, and there is still a lack of such data for normal surface ship forms. However, already from the old experiments by Baker and Bottomley [63] it was seen that the total force due to rudder deflection was increased by some 40 per cent in presence of a deep cruiser stern close above the rudder, and that a third of the total force then was carried by the hull.

Let b be the height of the rudder at the stock, or the higher value forward of it, and let a be the depth to top of rudder at the same station. With a projected area A_r of the rudder the aspect ratio of rudder + plane image is equal to $\bar{\Lambda} = 2b^2/A_r$. The lift curve slope $a_{\bar{\Lambda}}$ is taken from the theoretical curve derived from the Weissinger theory [64], or from empirical curves available.

The geometrical aspect ratio usually is of the order of 1.5, i.e. the rudder is not a low-aspect-ratio fin, but it seems still to be possible to make use of the results for wing-body interferences applicable to such fins. In particular, the ratio of the lift on a rigid combination of a wing and a cylindrical central body, L_{aa}^{WB} , to the lift of the abridged wing alone, L_a^W , is simply given by

$(1 + a/a+b)^2$, [65]. Next, for the calculation of the lift carried on the axially oriented body and on the wing deflected to the flow, it is observed that the exact theory by Mirels [66] may be approximated by $L_{\alpha 0}^{WB} \approx \sqrt{L_{\alpha}^{WB} \cdot L_{\alpha\alpha}^{WB}} = L_{\alpha}^{WB} (1 + a/a+b)$. Except for a correction factor the control derivative for the ship will be calculated as

$$\frac{1}{2} Y''_{c|c|\delta} = \frac{L^3}{2\nabla} \cdot \frac{u^2}{c^2} \cdot Y'_{\delta} = a_{\Lambda} \left(1 + \frac{a}{a+b}\right) \frac{A_r}{L T} \frac{L^2 T}{2\nabla} \quad (7.1)$$

where $Y''_{c|c|\delta}$ unlike Y'_{δ} is defined also for zero forward speed. The modern half spade or Mariner type rudder has a fixed horn, which divides the upper part of the rudder in ratio $A_h/(A_u - A_h)$. The right-hand member of (7.1) may then be multiplied by a factor $1 - (1/4) \cdot (A_h/A_r)$.

The effective rudder advance velocity c (squared) is calculated from the mean square velocity of the screw race and an estimated mean square velocity past the rudder outside the race. If w is the wake factor as integrated by the propeller (thrust identity) the effective square velocity above the race in a normal single screw arrangement may be taken as $u^2(1 - \frac{4}{3}w)^2$. Inside the race, which in average conditions has a diameter some 10 per cent smaller than the propeller, the ultimate mean square velocity is given by $u^2(1 - w)^2(1 + (8/\pi) \cdot (K_T/J^2))$, where, for $u > 0$,

$$K_T = K_{T00} + \frac{J}{|J|} \cdot K_{T0} + K_{TJ}J + \frac{1}{2} K_{TJJ}J \quad (7.2)$$

is to be approximated from the open water propeller diagram. Whereas the thrust may be analytically defined for all combinations of u and n — see below — the working conditions of the rudder are known only for a positive thrust, in which case

$$c^2 = \frac{1}{2} c_{uu}^2 u^2 + c_{un}^2 un + \frac{1}{2} c_{nn}^2 |n|n + \frac{1}{2} c_{nn}^2 n^2 \quad (7.3)$$

From an analysis of a large number of control derivative measurements on models it appears that a correction factor of 0.7 - 0.8 shall be applied to (7.1) when combined with (7.3) to give the force $Y(u, n, \delta) = \rho \nabla / L \cdot \frac{1}{2} Y''_{cc\delta} \cdot c^2 \delta$. This correction factor is understood to take care of gap effects and non-ideal geometry of the hull + rudder arrangement, etc.

The four constants in Eq. (7.3) depend on screw characteristics and wake factors, and they are therefore unique for the model scale. To facilitate a correction for this scale effect in the control derivatives the diagram in Fig. 20 has been compiled, chiefly from Ref. [67] and data available at SSPA. The slope of curves of wake factors against ship or model lengths increases with hull fullness; especially SSPA experience of full scale tanker trials rarely include

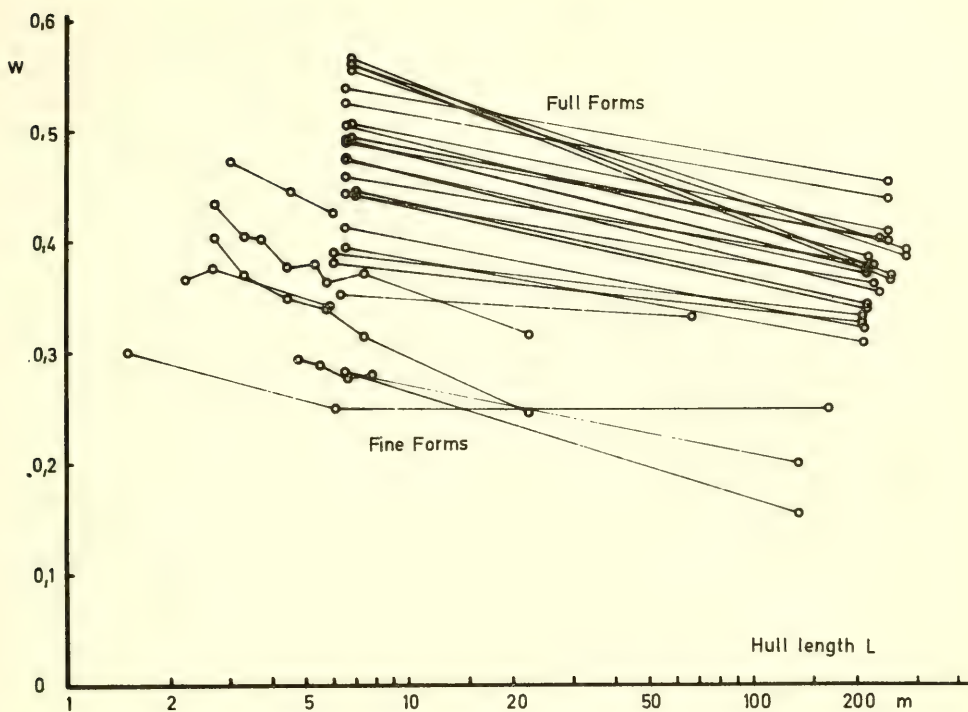


Fig. 20. Scale effects on wake factor w as integrated by propeller in model and full scale.

effective wake factors above 0.38.

In Fig. 21 the control moment derivative N_{δ}'' for a 98 000 tdwtanker is presented as a function of forward speed u and shaft speed n , for a 1:70 scale model as well as for the prototype. (Extrapolation to slowly reversed propeller is shown dotted.) In particular it is seen from the diagram that the turning moment from the rudder at self propulsion point of ship is only some 60 per cent of the model test value.

During a maneuver the effective change of angle of attack of the rudder is a function of nominal helm deflection δ , drift v , and yaw rate r , and change of screw loading. Again accepting this quasi-stationary model it is

$$\delta_e = \delta + \left(k_v \cdot \frac{v}{c} + k_r \frac{L \dot{\psi}}{2c} \right) |\delta| \quad (7.4)$$

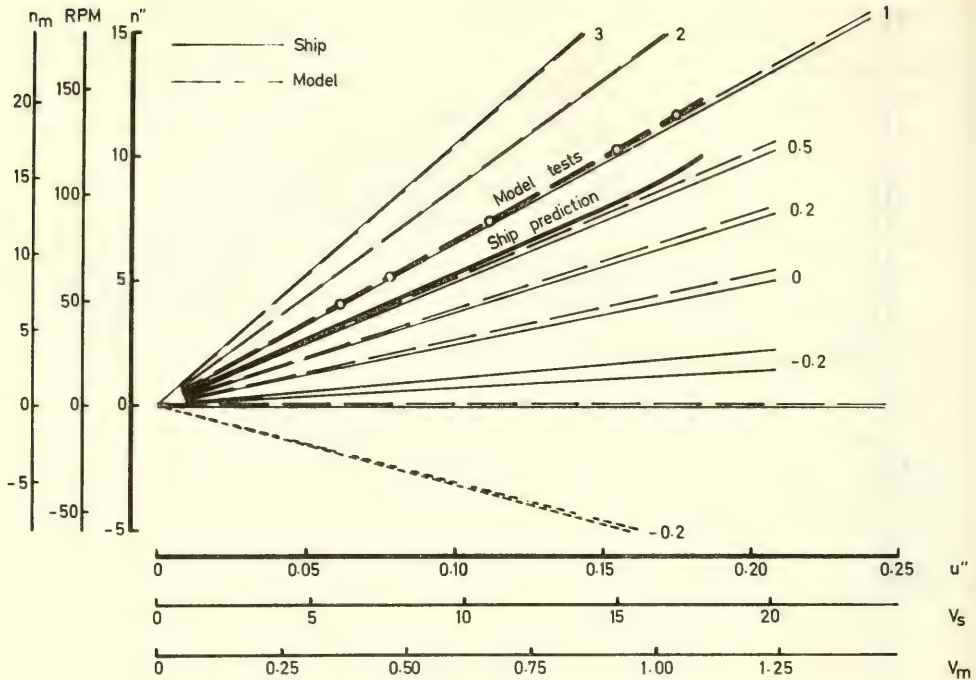


Fig. 21. Relative change of rudder control force with change of propeller advance conditions for 3.6 m model and 98 000 tdw tanker prototype. Diagram based on model tests at VBD and SSPA, and on speed trials.

where typical values are $k_v = -0.5$ and $k_r = 0.5$. (An alternative but less explicit method to include the same phenomena is given by Strom-Tejsen and Chislett [68], who make use of a number of coupling derivatives such as $Y_{\delta rr}^1$, etc.)

Helm Control

The manual or automatic pilot exerts the control through the steering gear, which is supposed to have a time constant T_E , causing a small delay in the rudder angle δ obtained. The value of T_E may vary say between 0.4 and 4 s, the first figure being a good catalogue value and the second one not seldom realized in shipboard testing. The steering gear or telemotor system often has a backlash of about half a degree.

The function of an auto-pilot may be said to be essentially

of the "proportional + rate control" type, although an integrator control shall be added to take care of stationary deviations. Commercial type auto-pilots include special features, which shall be included in simulator applications.

With the simple ideal auto-pilot "calling for" the rudder angle $\delta^* = \gamma\psi + \sigma\dot{\psi}$ the transfer function of the feed-back loop is

$$Y_2 = Y_{\delta\delta^*} \cdot Y_{\delta^*\psi} = \frac{\gamma(1 + \frac{\sigma}{Y}s)}{1 + T_E s} \quad (7.5)$$

Typical values for the gain or "rudder ratio" γ and rate constant σ of a tanker auto pilot in deep water setting are $\gamma = 3$ (degrees helm per degree heading error) and $\sigma = 135$ seconds (or 135 degrees helm per degree per second of change of heading). (See Section XIII.)

Although the course keeping characteristics of say an inherently unstable tanker may be studied in a Bode diagram by use of a total system open loop transfer function $Y_1 Y_2$, where the ship dynamics open loop Y_1 is defined from the linearized equations, this method is mostly avoided if an analogue computer is available. In case of small value non-linearities — such as dead zones or lags — in gyro compass and telemotors the equations-of-motion technique is unavoidable.

Much effort has been devoted to present the function of a manual helmsman in terms of a transfer function. The helmsman is a highly adaptive control system, which makes the task more difficult, but which also makes it more important. In many cases it is impossible to run real-time simulations because of lack of time, in other cases it is impossible to run comparative simulations just because of the learning ability of the operator.

Hooft tried to evaluate criteria for manual steering of large tankers by use of a transfer function, in which the gain and time constants were derived by extrapolation from high frequency pilot dynamics, [69]. Undoubtedly new basic information is required.

Propeller Thrust and Shaft Torque

A majority of ocean-going ships are propelled by fixed-blade screws driven by diesel engines or steam turbines, the normal steady state outputs of which in principle are characterized by constant torque Q^E — proportional to fuel pump stroke — and constant power — proportional to steam inlet pressure — respectively. In running conditions the mechanical torque losses Q^F depend on sign of r.p.m. but are more or less independent of its magnitude. Shaft r.p.m. is governed by the simultaneous equations for longitudinal resistance and for thrust and torque, for $u > 0$ here given as

$$gT'' = L^{-1} \cdot \frac{1}{2} T''_{uu} u^2 + T''_{un} u n + L \cdot \frac{1}{2} T''_{lnln} |n|n + L \cdot \frac{1}{2} T''_{nn} n^2$$

$$(Q_n^{E''} - Q_n'')_n = L^{-1} g \cdot Q_k^{E''} K + L^{-1/2} g^{+1/2} \cdot Q_n^{E''} \cdot n + L^{-1} g \cdot Q_n^{F''} \frac{n}{|n|} \quad (7.6)$$

$$+ L^{-2} \cdot \frac{1}{2} Q''_{uu} u^2 + L^{-1} Q''_{un} u n + \frac{1}{2} Q''_{lnln} |n|n + \frac{1}{2} Q''_{nn} n^2$$

with

$$\frac{1}{2} T''_{uu} = \frac{L^3 \nabla}{(L/D)^2} \cdot (1 - w)^2 \cdot \frac{1}{2} K_{TJJ}, \text{ etc.}$$

The steady-state hydrodynamic thrust and torque are given as functions of forward speed, u , and rate of revolutions, n , based on open water K_T and K_Q characteristics; K_T and K_Q are first approximated by square functions of $J = (u/nD)(1 - w)$ or $1/J$. (Note that a linearization of these characteristics does not result in a linearization of the (u, n) -dependence.) The Nordström data [70] may be used when reversing or transient maneuvers are considered. In general it is then necessary to confine the analytical functions to limited ranges of propeller advance coefficients, i.e. to use alternative coefficients as in Eq. (7.2). Harvald has presented useful information on the propulsive factors at arbitrary steady-state advance conditions, [71]. The effects of separating boundary layer flow along the stern of a retarding ship are still less predictable.

The added mass and moment of inertia involved in unsteady maneuvering of the propeller are functions of the momentaneous advance coefficients as well as of the rate of change of r.p.m. In small changes from normal propulsive conditions the added inertia is small as blade angles of attack are small. Naval architects often use a value of 30 per cent of rigid screw inertia for the added inertia; although this figure originates from model tests with screws oscillating at zero advance coefficient it may still be used as an effective average value during the short reversing stage of an engine maneuver. In fact this stage is dominated by the large control torques and by the way they are used.

When simulating maneuvers with diesel-powered ships it shall be observed that normal r.p.m. control is not possible for n less than some 35 - 40 per cent of design shaft speed n_0 . The torque delivered is here rapidly reduced, mainly due to loss of charge air pressure. (For high r.p.m. Q_n^E is almost zero.) Slow speed maneuvering must be performed by intermittent use of the propeller, which requires repeated starting of the engine. Reversing maneuvers must await drop of speed to some 60 per cent of the full speed value, at which lower speed braking air may be applied. There is also a

certain astern r.p.m. which must be attained before fuel may be injected to start engine back. For a discussion of detailed features of diesel maneuvering the reader is referred to a paper by Ritterhoff, [72].

The energy-converting efficiency of a turbine wheel has a maximum of some 80 per cent at a certain ratio of blade velocity to nozzle steam velocity, attainable at the design point. Assuming this ratio equal to 0.5, and a parabolic curve of efficiency symmetric to the design point, the following simple formula is obtained for the torque output:

$$Q^E = 2\kappa Q_0^E \left(1 - \frac{1}{2} \cdot \frac{n/n_0}{\kappa}\right) \quad (7.7)$$

Here Q_0^E and n_0 refer to torque and shaft speed at design conditions for full steam inlet $\kappa = 1$. The formula furnishes a good approximation also for present multi-staged ship turbines. In practical applications to studies of slow-speed port approach maneuvering it must be realized that steam production may then be limited to say $\kappa = 0.7$.

VIII. MODELLING THE DEEP-WATER HORIZONTAL MANEUVER

The General Case

The ship will be regarded as a rigid body moving under the influence of the gravity force mg and the buoyancy force $-\rho \cdot \nabla_0 \cdot \vec{g}$ — where ∇_0 is the volume displacement at rest — as well as under that of the external forces, including the control forces applied by use of rudders and thrusters. Before reducing the problem to the normal merchant ship case the more general form of the rigid body dynamics will be included.

The centres of mass (G) and buoyancy (B) may be off-set from the origin of the moving system (0), and it is then practical to apply Newton's laws in a summation of the acceleration forces on the mass elements (cf. (4.10) and (4.4)):

$$\sum \begin{bmatrix} dm & 0 & 0 \\ 0 & dm & 0 \\ 0 & 0 & dm \end{bmatrix} \begin{bmatrix} a_x \\ a_y \\ a_z \end{bmatrix}_{\text{abs}} = \begin{bmatrix} X \\ Y \\ Z \end{bmatrix} + \begin{bmatrix} m-\rho\nabla_0 & 0 & 0 \\ 0 & m-\rho\nabla_0 & 0 \\ 0 & 0 & m-\rho\nabla_0 \end{bmatrix} \tilde{\Lambda} \begin{bmatrix} 0 \\ 0 \\ g \end{bmatrix}$$

$$\sum \begin{bmatrix} dm & 0 & 0 \\ 0 & dm & 0 \\ 0 & 0 & dm \end{bmatrix} \begin{bmatrix} 0 & -z & y \\ z & 0 & -x \\ -y & x & 0 \end{bmatrix} \begin{bmatrix} a_x \\ a_y \\ a_z \end{bmatrix}_{\text{abs}} =$$

$$\begin{bmatrix} K \\ M \\ N \end{bmatrix} + \begin{bmatrix} 0 & -(mz_G - \rho \nabla_0 z_B) & my_G - \rho \nabla_0 y_B \\ mz_G - \rho \nabla_0 z_B & 0 & -(mx_G - \rho \nabla_0 x_B) \\ -(my_G - \rho \nabla_0 y_B) & mx_G - \rho \nabla_0 x_B & 0 \end{bmatrix} \tilde{\Lambda} \begin{bmatrix} 0 \\ 0 \\ g \end{bmatrix} \quad (8.1)$$

Upon summation the coefficient matrices of the acceleration terms, the mass and inertia tensors, expose as

$$m = \begin{bmatrix} m_{xx} & 0 & 0 \\ 0 & m_{yy} & 0 \\ 0 & 0 & m_{zz} \end{bmatrix} = \sum dm \quad (8.2)$$

$$I = \begin{bmatrix} I_{xx} & -I_{xy} & -I_{zx} \\ -I_{xy} & I_{yy} & -I_{yz} \\ -I_{zx} & -I_{yz} & I_{zz} \end{bmatrix} = - \sum \vec{x} \vec{x} dm$$

where the elements are defined by

$$\begin{aligned} \sum x dm &= m \cdot x_G & \sum (y^2 + z^2) dm &= I_{xx} & \sum xy dm &= I_{xy} \\ \sum y dm &= m \cdot y_G & \sum (z^2 + x^2) dm &= I_{yy} & \sum yz dm &= I_{yz} \\ \sum z dm &= m \cdot z_G & \sum (x^2 + y^2) dm &= I_{zz} & \sum zx dm &= I_{zx} \end{aligned} \quad (8.3)$$

Many authors prefer to introduce the virtual masses and moments of inertia into the equations given above. Here the "added" masses will consistently be assigned to the hydrodynamic reaction forces in the right-hand members; in Section V it was seen that these forces may include other inertia terms otherwise easily overlooked.

In most practical applications the xz -plane is a plane of symmetry, so that $y_G = y_B = 0$ and $I_{xy} = 0$. Except in a few special cases, such as when dealing with hydrofoil crafts, etc. — the discussion of which is outside the scope of this paper — other terms may be safely ignored in view of the smallness of the products of inertia and the perturbation velocities involved.

The Merchant Type Displacement Ship

In what follows the discussion is restricted to displacement ships, for which $m = \rho \nabla_0$ and $\nabla \approx \nabla_0$. Forward speed is always associated with a sinkage and change of trim, most obvious as "squatting" in waters of finite depth, but the manoeuvring dynamics will be sufficiently well described by the equations in four degrees of freedom, i.e. the surge, sway, roll and yaw. Then

$$\begin{aligned} m\{\dot{u} - rv - x_G \dot{r}^2 + z_G r \dot{p}\} &= X \\ m\{\dot{v} + ru + x_G \dot{r} - z_G \dot{p}\} &= Y \\ I_{xx} \dot{p} - I_{zx} \dot{r} - mz_G(\dot{v} + ru) &= K - mg(z_G - z_B) \sin \phi \\ I_{zz} \dot{r} - I_{zx} \dot{p} + mx_G(\dot{v} + ru) &= N \end{aligned} \quad (8.4)$$

Whereas the initial roll as well as the steady outward heel may be appreciable in case of say a highspeed destroyer these angles are also known to be quite insignificant in the tanker case. In steady turning a heel, proportional to $-(L/R_c) \cdot F_{nL}^2$, may produce an effective camber of the waterline flow around a fine hull, but this hardly applies to merchant ship forms.

Leaving the roll equation the present deep-water model is given as in Eq. (8.5). It shall be pointed out that the derivative Y_{ur}'' includes the potential-flow contribution X_u'' and the derivative N_{ur}'' the potential-flow contribution Y_r'' . In the forward speed equation X_{vr}'' is given a value that is smaller than its ideal value equal to $-Y_v''$.

$$\begin{aligned} (1 - X_u'')\dot{u} &= L^{-1} \cdot \frac{1}{2} X_{uu}'' u^2 + L^{-2} g^{-1} \cdot \frac{1}{24} X_{uuuu}'' u^4 + g \cdot T''(1 - t) \\ &+ (1 + X_{vr}'')v\dot{\psi} + L(x_G'' + \frac{1}{2} X_{rr}'')\dot{\psi}^2 + L^{-2} g^{-1} \cdot \frac{1}{6} X_{uvvv}' u |v| v^2 \\ &+ L^{-1} \frac{1}{4} X_{c|c|d\delta\delta}'' |c| c \delta_e^2 \end{aligned}$$

$$\begin{aligned}
(1 - Y_v'') \dot{v} &= L(Y_f'' - x_G'') \dot{\psi} + (Y_{ur}'' - 1) u \dot{\psi} + L^{-1/2} g^{-1/2} \cdot \frac{1}{2} Y_{uur}'' u^2 \dot{\psi} \\
&+ L^{-1} Y_{uv}'' uv + L^{-3/2} g^{-1/2} \cdot \frac{1}{2} Y_{uuv}'' u^2 v + L^{-1} \cdot \frac{1}{2} Y_{lvlv}'' |v|v \\
&+ L \cdot \frac{1}{2} Y_{rlrl}'' |\dot{\psi}| \dot{\psi} + Y_{lvrl}'' |v| \dot{\psi} + Y_{vrl}'' v |\dot{\psi}| \\
&+ L^{-1} \cdot \frac{1}{2} Y_{lclcd}'' |c|c \delta_e + k_{\psi} g T'' \\
(k_{zz}^2 + N_f'') \ddot{\psi} &= L^{-1} (N_v'' - x_G'') \dot{v} + L^{-1} (N_{ur}'' - x_G'') u \dot{\psi} + L^{-3/2} g^{-1/2} \cdot \frac{1}{2} N_{uur}'' u^2 \dot{\psi} \\
&+ L^{-2} N_{uv}'' uv + L^{-5/2} g^{-1/2} \cdot \frac{1}{2} N_{uuv}'' u^2 v + L^{-2} \cdot \frac{1}{2} N_{lvlv}'' |v|v \\
&+ \frac{1}{2} N_{rlrl}'' |\dot{\psi}| \dot{\psi} + L^{-1} \cdot N_{lvrl}'' |v| \dot{\psi} + L^{-1} \cdot N_{vrl}'' v |\dot{\psi}| \\
&+ L^{-2} \cdot \frac{1}{2} N_{lclcd}'' |c|c \delta_e + L^{-1} k_N g T''
\end{aligned} \tag{8.5}$$

Eq. (8.5) is to be combined with Eqs. (7.3), (7.4) and (7.6). In case of twin-screw ships (7.6) is to be properly modified and terms corresponding to $s_p \cdot T_p$ and $s_s \cdot T_s$ are to be introduced in (8.5).

Some Elementary Concepts

So far as small motions are considered forward speed and r.p.m. remain almost constant and the rudder force and moment may be regarded as functions of nominal helm δ . The yaw-rate/helm relation is given by the transfer function

$$Y_{\dot{\psi}\delta} = K \cdot \frac{1 + T_3 s}{1 + (T_1 + T_2)s + T_1 T_2 s^2} \tag{8.6}$$

and the open loop heading response by $Y_1 = (1/s) \cdot Y_{\dot{\psi}\delta}$, which may be used with Y_2 from Eq. (7.5) to study the closed-loop system with transfer function $F = Y_1 / (1 + Y_1 Y_2)$.

The static gain and the three time constants in (8.6) are built up from the coefficient of Eq. (8.5). T_3 is always positive. The two constants T_1 and T_2 are given by the roots of the characteristic equation. If $s_1 = -(1/T_1)$, the root to the right on the real axis, turns positive the ship is inherently unstable. The analytical criterion for dynamic stability suggests the dynamic stability lever

$$1_r'' - 1_v'' = \frac{x_G'' - N_{ur}''}{1 - Y_{ur}''} - \frac{N_{uv}''}{Y_{uv}''} \quad (8.7)$$

to be a suitable measure for the degree of stability. In particular it provides a good illustration when studying the effects onto the stability characteristics of changes in the stability derivatives.

Most modern large tankers are slightly unstable, or marginal stable, i.e. $1_r = 1_v$. For such ships the pivoting point position is given by the simple relation

$$\frac{\overline{OP}}{L} = - \frac{1 - Y_{ur}''}{Y_{uv}''} \quad (8.8)$$

which may be approximated by $\overline{OP}/L = 0.45 + (1/3)(\delta_{pp}(B/T) - 2)$. For a typical tanker this corresponds to $\overline{OP}/L = 0.5$. (The formula in fact indicates an acceptable value also for the destroyer, about 0.3.) Again, the pivoting point position — or the drift angle β — is a critical parameter to study when entering shallow waters.

IX. CONFINED WATER FLOW PHENOMENA AND SOME RESULTS FROM THEORY

Mostly on Resistance

In his notes for a third volume of "Hydrodynamics in Ship Design" Saunders collected a number of citations, ranging from Scott-Russel to Moody, which all illustrate the classical picture of ship behaviour in confined waters as it has been derived from observations in full scale and in model tests, [73]. He also concluded that, by 1960, the ventures and progresses made in analytical studies of ship manoeuvring in shallow waters remained scarce. One exception was offered by the papers by Brard, [74]. The problems of interaction between meeting or passing ships, or between ships travelling abreast — closely related to the bank effect problem of the single ship — had been dealt with by Weinblum [75], Havelock [76], and Silverstein [77].

Undoubtedly much more effort had by then been devoted to the changes of frictional and wave resistance of ships in axial motion in confined waters, and an important survey and contribution had been given by Schuster [78].

Ocean-going ships generally move at low speeds in shallow or narrow waterways, and hence the deformation of the wave system is small. According to Schuster the wave resistance is not notably affected by a limited depth for speeds below $F_{nh} = 0.7$, at which speed the excentricity of the orbital ellipse corresponds to a diameter

difference of about 5 per cent. In case of a bottom depth of 15 m this again corresponds to a ship speed of 16 knots.

In Ref. [79] Weinblum demonstrated that the wavemaking in a canal is a complicated function of speed, depth and width. In general it is therefore not possible to define a single effective length to characterize the canal dimensions in a speed number. However, effective canal speed includes the back-flow, and just as a critical speed in shallow water is defined by the speed of the solitary wave, \sqrt{gh} , experimental evidence advocates a critical speed in a certain canal corresponding to a certain Boussinesque number $B = F_{nh}\sqrt{(h/\bar{W}) + 1}$. (Here \bar{W} is equal to half the mean width of the section.) For a rectangular section Muller proved that the maximum wave resistance occurred at $F_{nh} = (2(h/\bar{W}) + 1)^{-1/2}$, [80]. In a canal 15 m deep and 120 m wide this corresponds to $F_{nh} = 0.81$. Again, let it be assumed that a significant change of the wave resistance due to the confinements will be found only at a speed equal to or higher than 70 per cent of this critical speed: this now gives a speed of about 13 knots, much too high to be experienced in canal transits involving normal blockage ratios. It may be concluded that the additional resistance terms to appear in the speed equation normally need not to account for the oscillatory wave-making components.

Reference shall here be given to recent studies of the unsteady flow conditions existing within a critical speed range for a ship in a canal; this range tends to zero when the width of the canal tends to infinity, [81, 82].

At sub-critical speeds the wave-making itself may influence the lateral force and moment on a ship moving along a bank, as shown by Silverstein, [77]. In case of the low Froude numbers met with in practice also these effects may probably be ignored, and the water surface may thus be treated as a solid wall. At $F_{nL} = 0.078$ or $F_{nh} = 0.32$, realized for a 98 000 tdw tanker proceeding at a speed of 14 km/h through the Suez canal, the longitudinal waves will have a length of some 10 m, i.e. only 4 per cent of the length of the ship.

The back-flow producing an increase of frictional resistance will also produce an increase of sinkage, and in case of small bed clearances this will of course indirectly affect the lateral forces sensitive to the clearance. These secondary effects must be born in mind when comparing predictions from theory with results from force measurements on models, which are free to heave and trim. In the normal evaluation and presentation of such measurements, however, it will be considered more practical always to use the nominal under-keel clearance.

The viscous resistance, including frictional as well as viscous pressure resistance, may be calculated accepting a plate

friction line and a form factor, characteristic for the super-velocities along the hull. This resistance now may be written $[X^V]_{\bar{W}=h=\infty} = \frac{1}{2} X_{uu}^V u^2$, where u is the forward speed of the ship. In confined waters there are additional supervelocities, the effect of which is equivalent to a back-flow along the hull and waterway bottom, where another boundary layer is generated. The two boundary layers will reduce the effective under-keel clearance, which tend to increase the trim by stern. Separation and unsymmetrical eddy-making within the boundary layers may initiate yawing tendencies in straight running, or change the behaviour of the ship in manoeuvres.

Graff has suggested to consider part of the mean back flow, ΔU_b , to be due to the lateral restriction, and the other part, ΔU_h , to be due to the finite depth, [83]. In normal applications ΔU is small compared to u , so that

$$X^V = \frac{1}{2} X_{uu}^V u^2 \left(1 + \frac{2\Delta U_b}{u}\right) \left(1 + \frac{2\Delta U_h}{u}\right) = \frac{1}{2} X_{uu}^V u^2 (1 + K_b)(1 + K_h) \quad (9.1)$$

The effects of a plane bottom at distance h below the ship waterline and a pair of parallel vertical walls, each one at distance \bar{W} from the ship centreline, are those produced by an infinite array of image bodies with spacings equal to $2h$ and $2\bar{W}$ respectively. At the double-body ship centreline the lateral perturbation velocities cancel whereas the axial components add together. (This simple concept is not valid for \bar{W} or h small compared to B or T , in which case additional doublet distributions are required to prevent a deformation of the body contour.) Graff choose to calculate an approximate value of K_b for an elliptic cylinder, extending from the surface down to the bottom and having a beam given by the three-dimensional form displacement. (Thus K_b is dependent on canal depth, although the final calculation is purely two-dimensional.) For the calculation of K_h he used an equivalent spheroid and results for supervelocities earlier published by Kirch, [84]. His final results are given in graphs and compared with model measurements, which confirm that this method offers acceptable values of resistance allowances for moderate confinements. It is thereby also possible to define a suitable form of resistance derivatives to be evaluated from model experiments from case to case.

In particular, a limited re-analysis of some of the data given by Graff indicates that the resistance increase in shallow water will be proportional to the increase of an under-keel clearance parameter $\zeta = T/(h-T)$. Further analysis of the results for sinkage in shallow water according to Tuck's theory are likewise in favour of the use of this parameter. (See below.)

In waterways severely restricted in width as well as in depth the increase of resistance is a complex function of blockage conditions.

From model tests with a Rhine vessel [85] it appears that the added resistance at a given forward speed may be approximated by an expression of the form $\Delta R = a \cdot (BT/\bar{W}h) + b \cdot (BT/\bar{W}h) \cdot \zeta$, or, roughly,

$$\Delta X(u, \zeta, \bar{\eta}) = \frac{1}{2} X_{uu\zeta\bar{\eta}} u^2 \zeta \bar{\eta} + \frac{1}{4} X_{uu\zeta\bar{\eta}}^2 \zeta^2 \bar{\eta}^2 \quad (9.2)$$

where $\bar{\eta}/2 = L/\sqrt{W}$ is a bank spacing parameter defined from the mean width $2\bar{W}$ of the canal cross section. (See Section X.)

The higher resistance in confined waterways is associated with a lower propeller efficiency, and the total propulsive efficiency is further reduced by an increase of the thrust deduction. The influence of flow restrictions on thrust deduction and wake factors has also been considered in a paper by Graff, [86]. In most simulator applications this latter influence may be ignored. However, the computed values of r.p.m. and speed attained at a given engine setting should be compared with, say, diagrams compiled by Sjöstrom, [87].

Sinkage and Lateral Forces

Within the last decade the application of slender-body theory has furnished new understanding and quantitative estimates to the old experience on sinkage and lateral motions in confined waters. Further developments of the theories and more accurate measurements are required to bridge a gap still remaining in force predictions.

In an essentially forward motion of the ship in shallow water the back-flow is increased all round the frame sections, and according to the first-order theory of Tuck the dynamic pressure is largely constant in the water around a cross section of the hull and over the bottom bed close below it, [88]. Upon assumption of a water depth of same order as the draught, the draught and beam being small compared to the length of ship and waves, and by use of the new technique of "matched asymptotic expansions" Tuck derived formulae for the vertical forces and so also for the sinkage and trim at sub- and super-critical speeds.

In case of ships with fore-and-aft symmetry the theory predicts zero trim for subcritical speeds, and zero sinkage for supercritical speeds. For small to moderate Froude numbers based on depth the sinkage varies as speed squared, and, using the under-keel clearance parameter defined here, according to the upper curve of Fig. 22.

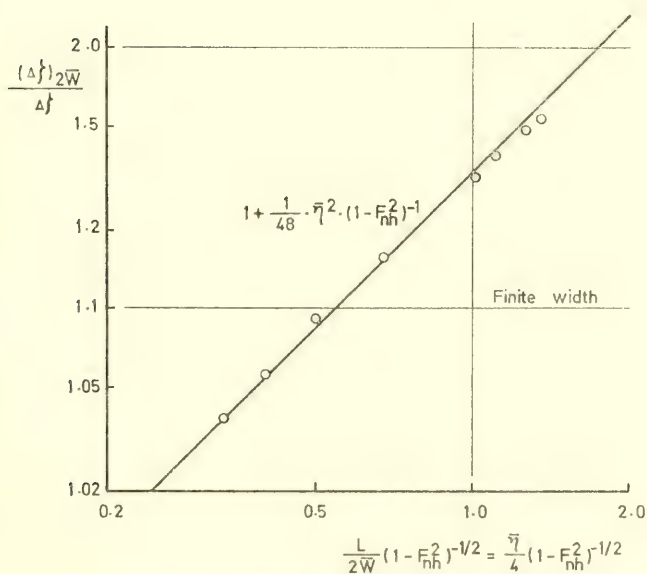
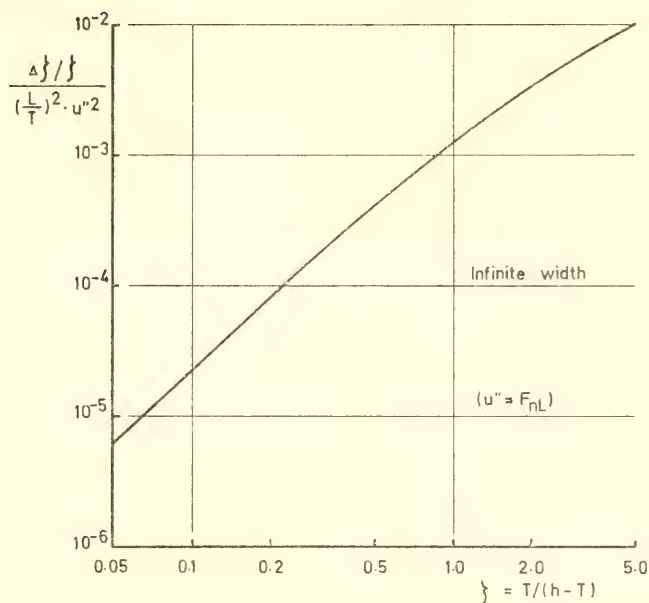


Fig. 22. Sinkage in shallow water of infinite and finite width, recalculated from Tuck's results.

In Ref. [89] Tuck has extended the theory to canals of finite width, in which the ratio of sinkage into the water (or trim) in the canal to the sinkage (or trim) in shallow water is given by a unique curve on basis of a simple width-and-speed parameter. Replotting this curve as in the lower diagram of Fig. 22 Tuck's results are shown to yield a square dependence on the bank-spacing parameter $\bar{\eta}$ when $F_{nh}^2 \ll 1$.

In canals presenting higher blockage the total sinkage or "squat" is dominated by the contribution from water level lowering as a consequence of flow continuity. From the Bernoullie and continuity equations an approximate relation for the hydrostatic ship sinkage in terms of ship lengths is given by

$$\sqrt{\frac{\phi_L}{\alpha_{WL}}} \cdot \frac{\frac{A}{A_c} \cdot F_{nL}^2}{1 - \frac{A}{A_c} - \frac{L W_{beach}}{A_c} \cdot F_{nL}^2}$$

Here ϕ_L and α_{WL} are the prismatic and waterline-area coefficients of the ship. Other methods of the practical calculation of squat are discussed in Ref. [90].

At low speeds wave making is concentrated to bow and stern of the ship, where changes of the local velocities do not influence the blockage conditions, and it shall be possible to calculate the forces on the ship without regard to wave making. The absolute speed still is a parameter, as it is seen to affect the hydraulic as well as the dynamic squat in a canal.

Kan and Hanaoka first presented low-aspect-ratio wing results for the calculation of transverse forces and moments on a ship in oblique or turning motions in shallow water, [91]. As the theory predicts the same correction factor to be applied to all deep-water values it seems to be essentially a two-dimensional theory as it is in deep water. Newman studied the same problem by use of the method of matched asymptotic expansions and by the assumption of a three-dimensional flow, differently orientated close to the body and close to the bottom (and upper image wall), [92]. His results bear out the effects of finite length, most obvious in case of moments due to yaw acceleration.

Newman considers the inner flow to be a two-dimensional cross-flow of reduced velocity, at each section depending on a blockage parameter in the velocity potential. The outer solution assumes flow to take place in planes parallel to the bottom wall at nominal transverse velocity as the body is reduced to a cut normal to the flow, this being physically similar to the flow past a porous plate. The results as applied to forces on a wing of low aspect ratio (or to a ship) are given in a simple diagram in [92], and here

they are used for comparisons with ship model values in Figs. 33 and 34. (A limited comparison of sway force and moment derivatives derived for the SSPA tanker model was included in [92]. A small adjustment of model force derivative appears in the present comparison, due to modified assumptions for non-linear viscous cross-flow contribution; cf. Section X.)

The lateral forces acting on a body of revolution in axial motion in close presence of a vertical wall have also been studied by Newman, [93]. The source distribution inside the body is mirrored in the wall, and in addition the calculations require the original distribution to be off-set towards the wall. This three-dimensional source distribution defines the velocity potential and so the forces may be found by use of the Lagally theorem. As expected from experience and approximate image theories for bodies not close to the wall there is an attraction towards the wall, increasing monotonically up to a finite value of body-and-wall contact. It is concluded that for geometrically related bodies with same sectional-area distribution the suction force will be inversely proportional to the length, whereas the yawing moment will be independent of length variation. The results also indicate that there will be a bow-away-from-wall moment for bodies with a stern, which is blunt compared to the bow, and vice versa.

In Fig. 23 calculations by Newman's method are compared with the results of force measurements on a tanker model towed along the vertical wall of a ship model basin. (Cf. Section X.) Basin depth was equal to $0.29 L_{pp}$, total basin width equal to $2.7 \cdot L_{pp}$. The diagram is plotted on ratio of wall distance to maximum radius of equivalent body of revolution, defined by length and displacement of model hull + image. The better agreement is obtained for that equivalent body, which also has the same sectional area curve, but even then the experimental results are some 25 per cent in excess of the prediction. At larger separations the difference is still larger. Comparative calculations using Silversteins "not-too-near-wall" results for an equivalent ovoid [77], are included in the diagram; in this case the prediction is better for larger separations, but in all much too high.

As long as the body is not too close to wall contact the Newman theory gives a linear dependence for the lateral force on ratio of body radius to centre-line wall distance, i.e. it is proportional to η_s or η_p defined for starboard or port wall distances in next Section. This linear dependence suggests that the lateral force on the ship between two parallel vertical walls may be obtained by adding the effects from each one, which idea may also be supported by the new presentation of old DTMB data [94, 95] given in Fig. 24. The diagram includes force and moment measurements on a twin-screw tanker model in several canal sections of simple rectangular form.

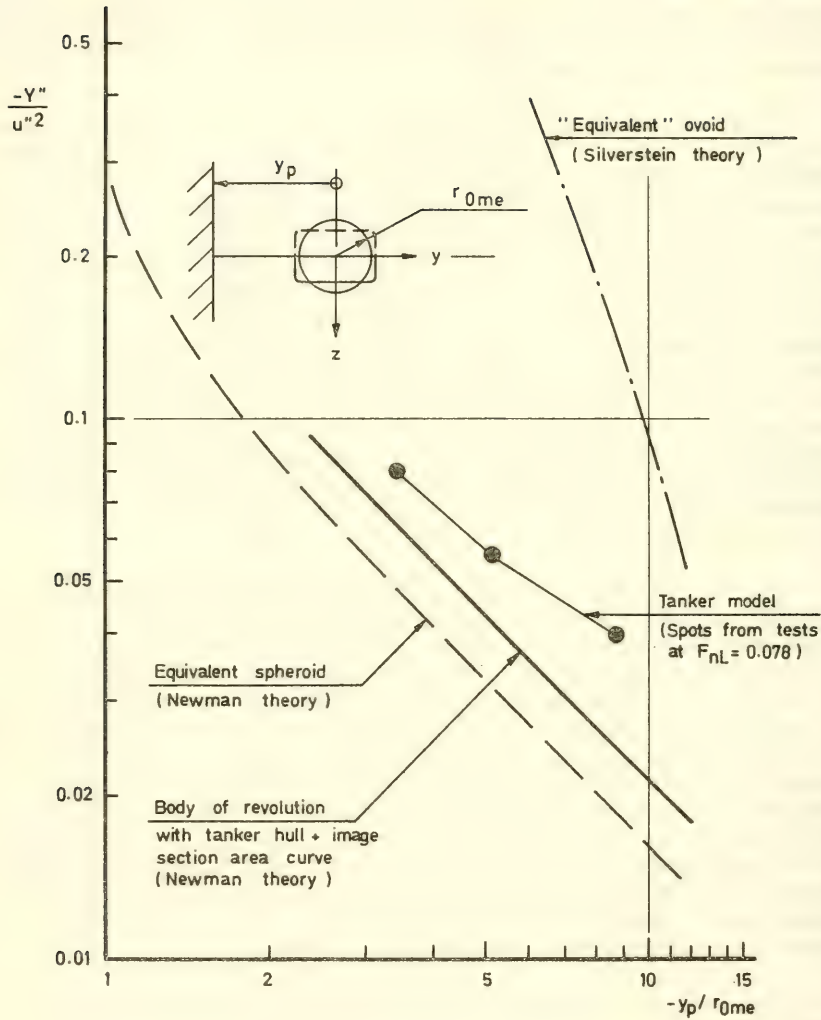


Fig. 23. Lateral force on a body moving parallel to a vertical wall. Measurements on propelled tanker model and theoretical results for bodies of revolution.

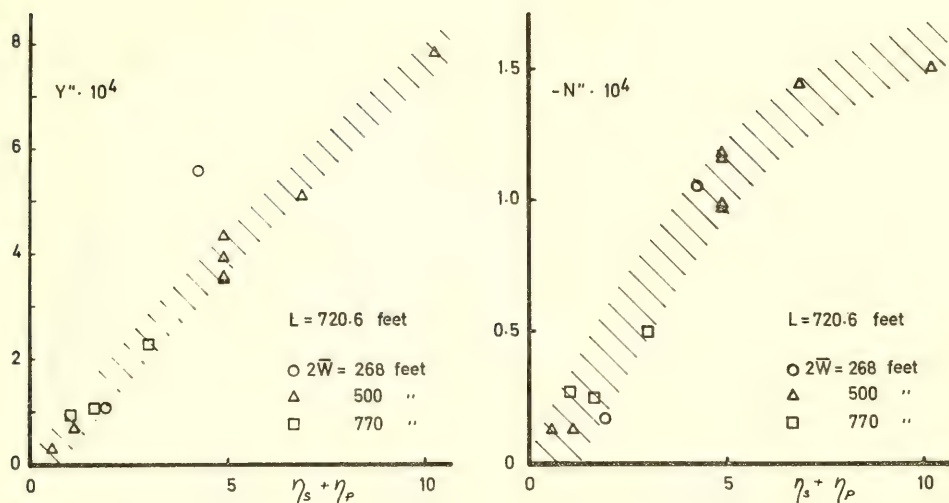


Fig. 24. Asymmetric forces and-moments on a twin-screw tanker model moving parallel to the vertical walls of canals of differing widths and depths (From DTMB test data)

The theoretical results for bow-away-from-wall moments are somewhat modified in practice, where bow wave and screw action contribute to make the tendency felt in ships of all types. Thus, in general a ship that moves off the centre-line of a canal must use helm towards the near wall and it takes up a small bow-from-wall equilibrium angle. Typical values derived from [94] for the 721' tanker off-set 50' from centre-line of the 500' \times 45' section are 15° helm and 1° drift.

The motion in shallow port approaches may involve much larger drift angles, and the behaviour of the ship is markedly affected by the increase of lateral cross flow resistance due to under-keel blockage. The diagram in Fig. 25 is compiled from shallow water test data in Ref. [49], and from Japanese data in Ref. [96], which also include measurements in presence of a wall. Again the parameters ζ and η are used for the presentation. For moderate ζ cross-flow drag increases in proportion to ζ , just as the linear force derivatives, but the dependence on η is of higher order. The cross-coupling between ζ and η may probably be ignored in practical applications.

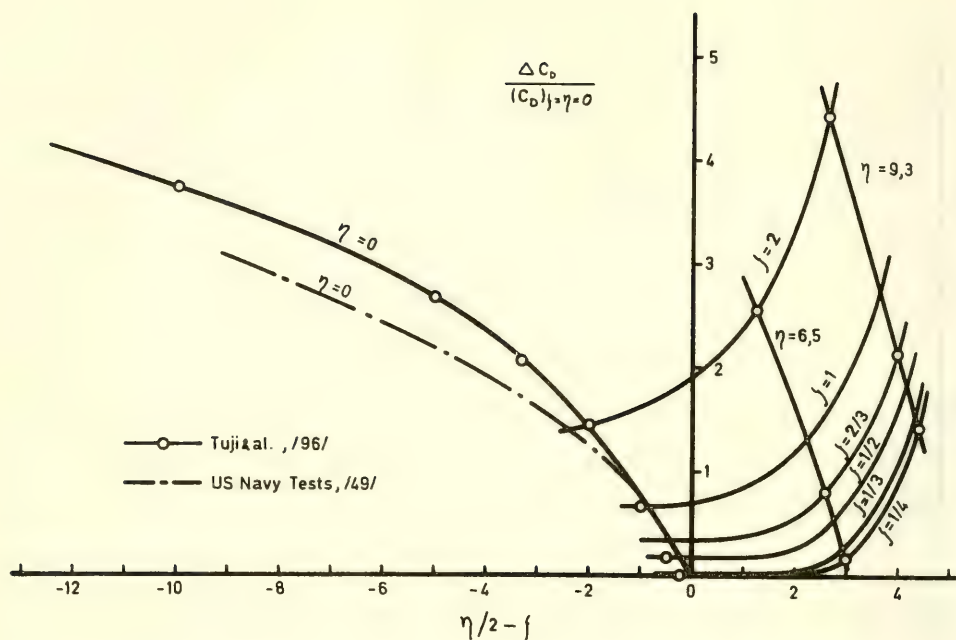


Fig. 25. Ship model cross flow drag coefficients as influenced by change of depth and presence of vertical wall

X. FORMAL REPRESENTATION OF CONFINEMENT EFFECTS

Waterway Description

The uniform straight canal with a rectangular section is the most simple case of a waterway confined in depth and width, but even there several parameters are required to characterize the flow phenomena taking place. It was seen in the last Section that the wall distance parameter η and the under-keel clearance parameter ζ both were useful tools for the description of certain effects. Their first merit, of course, is due to the zero values defined in unrestricted deep water.

Figs. 26 and 27 show a more general section of a canal. Such a canal is usually described by its mean depth between the bed lines, its widths at bed and beach lines, and its cross section area, related to the midship section of a transiting ship by the blockage ratio. The position of the ship in the canal is mostly given by the off-centre distance, and by the angle to the canal centre-line. Here approximate expressions involving the new parameters only will be given for the main geometric characteristics.

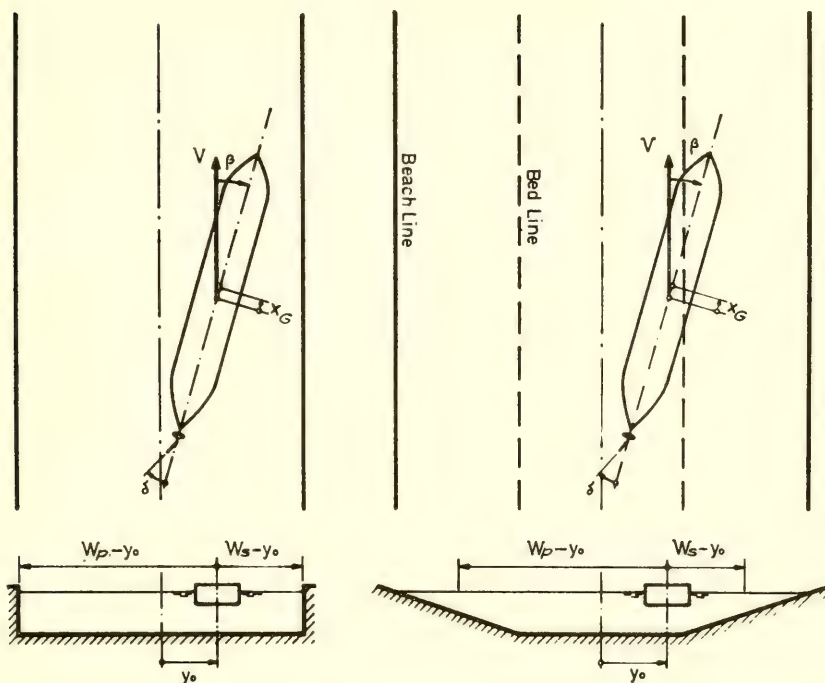


Fig. 26. Ship moving parallel to walls in a straight canal

The depth h is considered constant between the bed lines. The mean width $2\bar{W}$ is defined as the quotient between cross section area A_c and depth h . The ratio $2\bar{W}/B$ is a better parameter for width-to-beam relations the more shallow is the canal. For use with theoretical results for thin ships the width parameter will here not be related to beam but to ship length L .

As seen from Fig. 27 the bank and ship positions may be given by coordinates normal to a datum line essentially parallel to the main direction of the canal. The orientation of the ship is given by the heading angle ψ , measured from the same datum line. The basic geometric parameters are defined as

Under-keel clearance parameter	$\zeta = T/(h - T)$	
Port bank distance parameter	$\eta_p = L/(W_p - y_0)$	(10.1)
St'bd bank distance parameter	$\eta_s = L/(W_s - y_0)$	

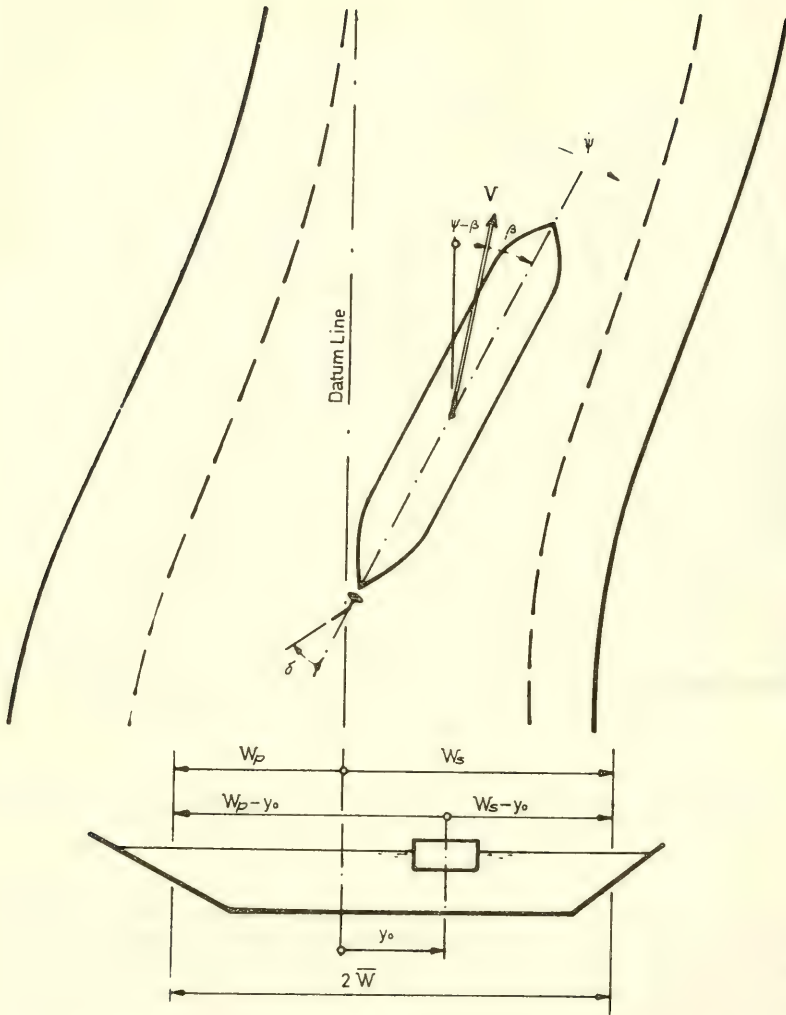


Fig. 27. Ship moving in a canal of slowly changing form

Note that $W_s > y_0 > W_p$, so that $\eta_s > 0$ and $\eta_p < 0$. It is also convenient to introduce

$$\eta = \eta_s + \eta_p \quad (10.2)$$

$$\bar{\eta} = \eta_s - \eta_p$$

The mean width of the canal at the station considered is

$$2\overline{W} = W_s - W_p = -\frac{\overline{\eta}}{\eta_s \eta_p} \cdot L \quad (10.3)$$

where the parameter ratio in the right member is constant for all lateral positions of the ship in the cross section. Especially, when ship on centre-line so that $\eta_s = -\eta_p = \overline{\eta}_0/2$, there is $L/2\overline{W} = \overline{\eta}_0/4$. In fact $\overline{\eta}/4$ alone is an acceptable approximation to the "ship length-to-canal width" parameter ratio also at ship positions slightly off-set from the centre-line: with $y_0 = \overline{W}/4$ $\overline{\eta}/4$ over-estimates the ratio $L/2\overline{W} = \overline{\eta}_0/4$ with less than 7 per cent. As a consequence $\overline{\eta}$ and ζ may be used to define an approximate blockage ratio

$$\frac{BT}{2\overline{W}h} = \frac{1}{4} \cdot \frac{B}{L} \cdot \frac{\overline{\eta}\zeta}{1+\zeta} \quad (10.4)$$

For small ζ the blockage ratio is proportional to $\overline{\eta}\zeta$, for large ζ to $\overline{\eta}$ alone.

Force Representation

The asymmetric forces appearing in presence of a single wall or in a canal are highly increased by an increase of the under-keel clearance parameter, and the general model will include complex couplings. If a single canal depth is studied on basis of special model tests it is of course possible to express the wall effect forces in terms of η_p and η_s only. Although the geometry of the inflow to the propeller may be modified in confined water it is assumed that the control derivatives remain unchanged and that changes of rudder forces are due to changes of screw loading only.

When suitable theoretical and experimental information becomes available it shall be possible to include the effects of ship motions towards the wall and of the angular orientation along it. At present solutions to the problem of motions oblique to a wall seem to be known only for elementary singularities such as circular cylinders and spheres, [97]. In particular, these results give a repulsion by the wall on the body moving toward or away from it, but, again of course, an attraction on the body moving parallel to it.

For the present investigation it shall be assumed that the effects of the walls on a ship moving not too close to them will be approximated by the quasi-steady asymmetry, and that the added masses may be taken as those derived for low-frequency oscillations in the centre of the confinement.

In the previous Section was shown that the attraction force

on the ship in motion parallel to a wall is essentially inversely proportional to the separating distance, i.e. $Y(u, \eta_s) = \frac{1}{2} Y_{uu\eta_s} \cdot u^2 \eta_s$, and that the effects of two walls may be approximated by superposition. Thus for $Y(u, \eta_s, \eta_p)$

$$\frac{1}{2} Y_{uu\eta_s} u^2 \eta_s + \frac{1}{2} Y_{uu\eta_p} u^2 \eta_p = \frac{1}{2} Y_{uu\eta} u^2 \eta \quad (10.5)$$

where $Y_{uu\eta} = Y_{uu\eta_s} = Y_{uu\eta_p}$.

As the ship moves closer to one of the walls, or as the walls are closer, this expression shall be completed by terms in η_s^2 and $|\eta_p| \eta_p$, or alternatively, in $\eta \bar{\eta}$.

The effect of a limited bottom depth is included by additional terms in $\eta \zeta$ and $\eta \bar{\eta} \zeta$. The forces due to steady sway and yaw are assumed to be increased in proportion to $uv \bar{\eta}$ and $ur \bar{\eta}$, and to $uv \bar{\eta} \zeta$ and $ur \bar{\eta} \zeta$ respectively. The dependence of added inertias on the confinements are represented by terms in $v \zeta$ and $v \bar{\eta}^2 \zeta, r \zeta$ and $r \bar{\eta}^2 \zeta$, all so far evaluated from the results published by Fujino, [5].

XI. MODEL TESTS

Test Program and Model

Five years ago an experiment program was designed for a tanker model with a view to put to test the analytical model set up as well as to obtain basic simulator data for a first canal transit study. Full scale measurements should subsequently be made with the 98 000 tdw prototype in the Suez Canal, but these plans could not be fulfilled, of course.

In November 1965 a first series of three component force measurements were ordered to be run with a 1:70 scale model at the VBD Laboratories in Duisburg. The test program included straight-line oblique towing of the propelled model in "deep" and shallow water in the large Shallow Water Tank and rotating arm tests at same depths in the Manoeuvring Tank. It also included straight-line oblique towing of the same propelled model in two Suez-Canal-type sections with a water depth equal to that of the shallow water tests. Most of these tests were run at self-propulsion point of model, determined from straight course speed runs in the waterways studied. All tests were performed at maximum "Suez draught." Resistance and propulsion tests had earlier been completed at SSPA with a 1:35 scale model on several draughts, and ship speed trials were analyzed to support the prediction of full scale screw loadings and control derivatives on model test draught. (Cf. Section VII.)

Additional tests in the VBD Shallow Water Tank were ordered in April 1966 to establish near-to-wall stiffness derivatives from straight-line motion close to one of the vertical basin walls in "deep" water. After a series of repeated tests with a modified recording system the full captive model test program was completed in April 1967. The test data are included in reports [98] and tables from VBD.

The test program is condensed in Table IV. It shall be observed that no acceleration derivatives could be obtained from these tests. Most of the force measurements were made at a model speed of 0.465 m/s corresponding to a ship speed of 7.6 knots or 14 km/h.

The ship prototype was a single-screw/single-rudder turbine tanker of the Kockums 90 000 - 100 000 tdw series, delivered to the owners in October 1965 for use in the crude oil trade through the Suez Canal on a reduced draught. The main dimensions of ship and 1:70 scale model are given in Table V, and the body plan is shown in Fig. 28. The prototype has a Mariner-type rudder, normal bow and no bilge keels; a few tests were run to investigate the effects of a bulbous bow and of bilge keels of common design.

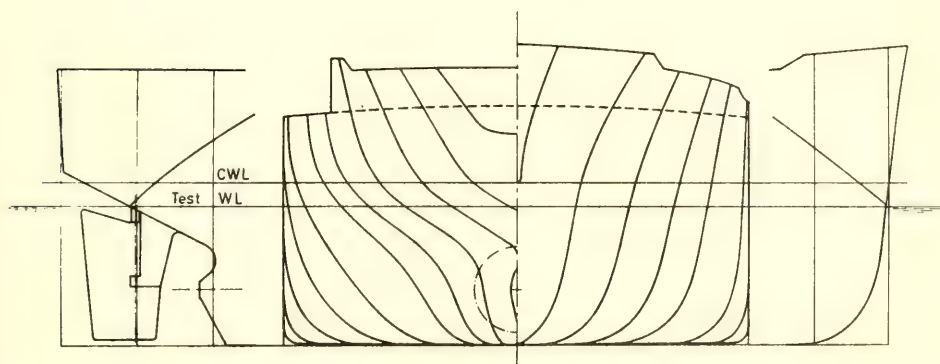


Fig. 28. Model of 98 000 tdw tanker -- body plan and profiles.
Model tested on "Suez draught"

TABLE IV. Test Program for Tanker Model ($L_{pp} = 3.614$ m, $T = 0.165$ m)

Series	FW	RAF	NW	SW	RAS	CS I	CS II
Waterway designation	Free Water	Free Water	Near to wall	Shallow Water	Shallow Water	Canal I	Canal II
Model dimensions:							
Water depth, h	mm	1050	1050	214	214	214	214
Basin diameter, $2R_b$	mm	-	-	-	24500	-	-
Tank width, W_{bed}	mm	9800	-	9800	-	1020	1200
Tank width, W_{beach}	mm	9800	-	9800	-	2300	2484
Tank width, $2\bar{W}$	mm	9800	-	9800	-	1660	1842
$\xi = T/(h - T)$		0.19	0.19	3.37	3.37	3.37	3.37
L/R_b	-	-	-	-	0.29	-	-
$\bar{\eta}_0/4 = L/2\bar{W}$	0.37	-	0.37	0.37	-	2.18	1.96
Parameter variation:							
Range of $r' = L/R$	-	-0.36-+0.54	-	-	-0.36-+0.54	-	-
Max η_s or $ \eta_p $	0	-	4.33	0	-	7.95	6.63
Range of β or ψ	$\pm 6^\circ$	0°	$\pm 6^\circ$	$\pm 6^\circ$	0°	$\pm 6^\circ$	$\pm 6^\circ$
Range of δ	$\pm 25^\circ$	0°	0°	$\pm 25^\circ$	0°	$\pm 25^\circ$	0°

TABLE V

		Ship	1:70 Model
Length, $L_{pp} = L$	m	253.00	3.614
Beam, B	m	38.94	0.556
Design draught, T_{CWL}	m	13.45	0.192
Suez draught (38'), T	m	11.58	0.165
Displacement, Suez draught, ∇	m ³	91 933	0.2680
Slenderness ratio, Suez draught, $- \frac{L_{pp}}{\nabla^{1/3}}$	-	5.606	
Midship coefficient, Suez draught, $-\beta$	-	0.991	
CB forward of $L_{pp}/2$, x_G/L_{pp}	-	+0.0185	
Long. radius of gyration/ L_{pp}	-	0.23	
Propeller diameter, D	m	7.15	0.1021
Pitch ratio, P/D	-	0.74	
Area ratio, A_d/A_o	-	0.65	
Number of blades, z	-	5	
Rudder area, total, A_r	m ²	64.8	0.0132
Horn area/ A_r	-	0.182	
Relative rudder area, $A_r/L_{pp}T$	-	0.0221	
Height at stock, b	m	9.80	0.140

Results for Force and Moment Coefficients

Figs. 29 - 32 show plot of force and moment coefficients from tests in deep (free) and shallow water, and the analytical approximation obtained by stepwise regression analysis. Results from the near-to-wall experiments have been given in Fig. 23.

In the evaluation it was consistently assumed that the changes of first and second order derivatives due to finite depth could be approximated by terms proportional to ζ . As the tests did include two values of ζ only, one of which very small, this does not effect the derivatives derived for these two depth conditions, nor the "true-deep-water" values.

Further, because of the scatter of experimental data it proved suitable to perform the analysis with an assumed value for the deep-water cross-flow resistance corresponding to $C_D = 0.7$; cf. Section VI.

In agreement with earlier findings the test results indicate a very marked influence of shallow water on the non-linear force contributions, and on the lateral force due to yaw in particular. It shall be observed that the analysis involves a change of sign in the first-order rotary force derivative as water depth is reduced.

The force and moment derivatives derived from shallow water and canal tests will be presented in next Section.

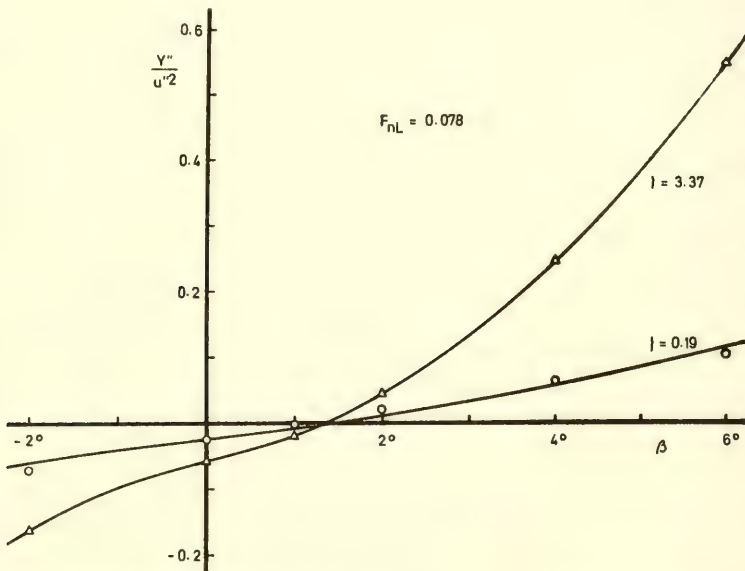


Fig. 29. 98 000 tdw tanker — Force coefficient $Y''(\beta)/u''^2$ in deep and shallow water.

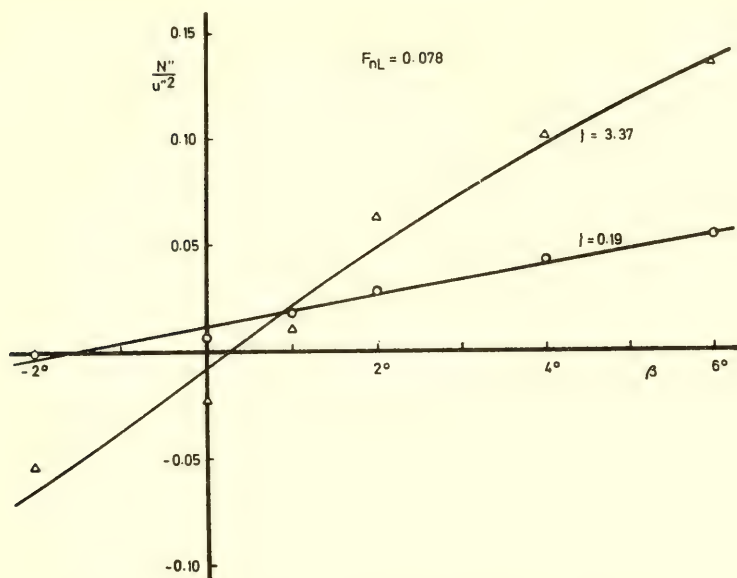


Fig. 30. 98 000 tdw tanker — Moment coefficient $N''(\beta)/u''^2$ in deep and shallow water.

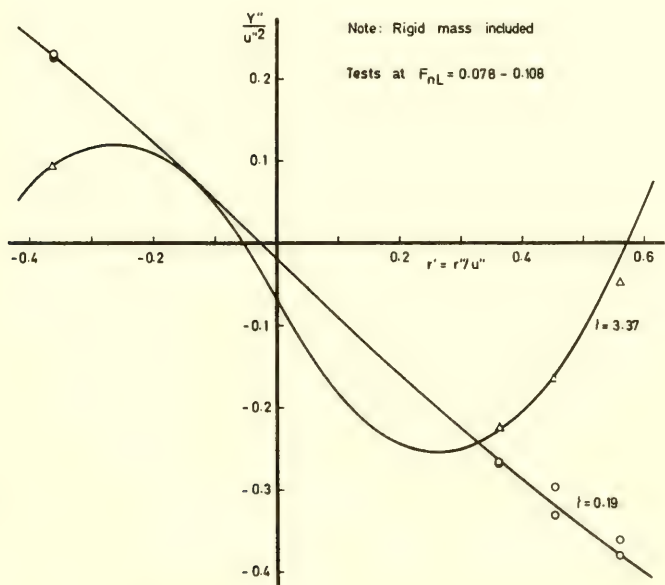


Fig. 31. 98 000 tdw tanker — Total force coefficient $Y''(r')/u''^2$ in deep and shallow water.

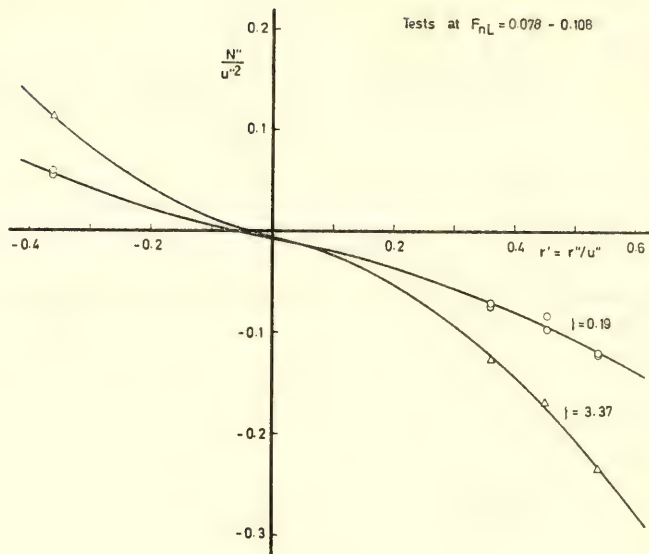


Fig. 32. 98 000 tdw tanker — Moment coefficient $N''(r')/u''^2$ in deep and shallow water.

XII. RESULTS FOR CONFINEMENT DERIVATIVES

Figs. 33 - 38 present available empirical or semi-empirical results for the main lateral hydrodynamic derivatives appearing in the confinement terms of the completed mathematical model. The derivatives $Y_{uv\eta}$ and $N_{uv\eta}$ for the 98 000 tdw tanker have been derived from the near-to-wall tests in deep water, and are not shown here. (Cf. Fig. 23.)

In Fig. 33 the shallow water results obtained for the SSPA tanker are compared with the experimental results published by Fujino [5], and with calculations from Newman's theory, [93]. The SSPA analysis is based on a linear dependence of the derivatives on ζ and the results are given by plots on straight lines, also suggested by the theory. Fujino's derivatives are evaluated separately for each depth. In general the theory seems to underestimate the influence of finite depth, especially for the stiffness moment.

Increase of added mass and added moment of inertia as obtained from Fujino's experiments and Newman's theory is shown in Fig. 34, again in poor agreement.

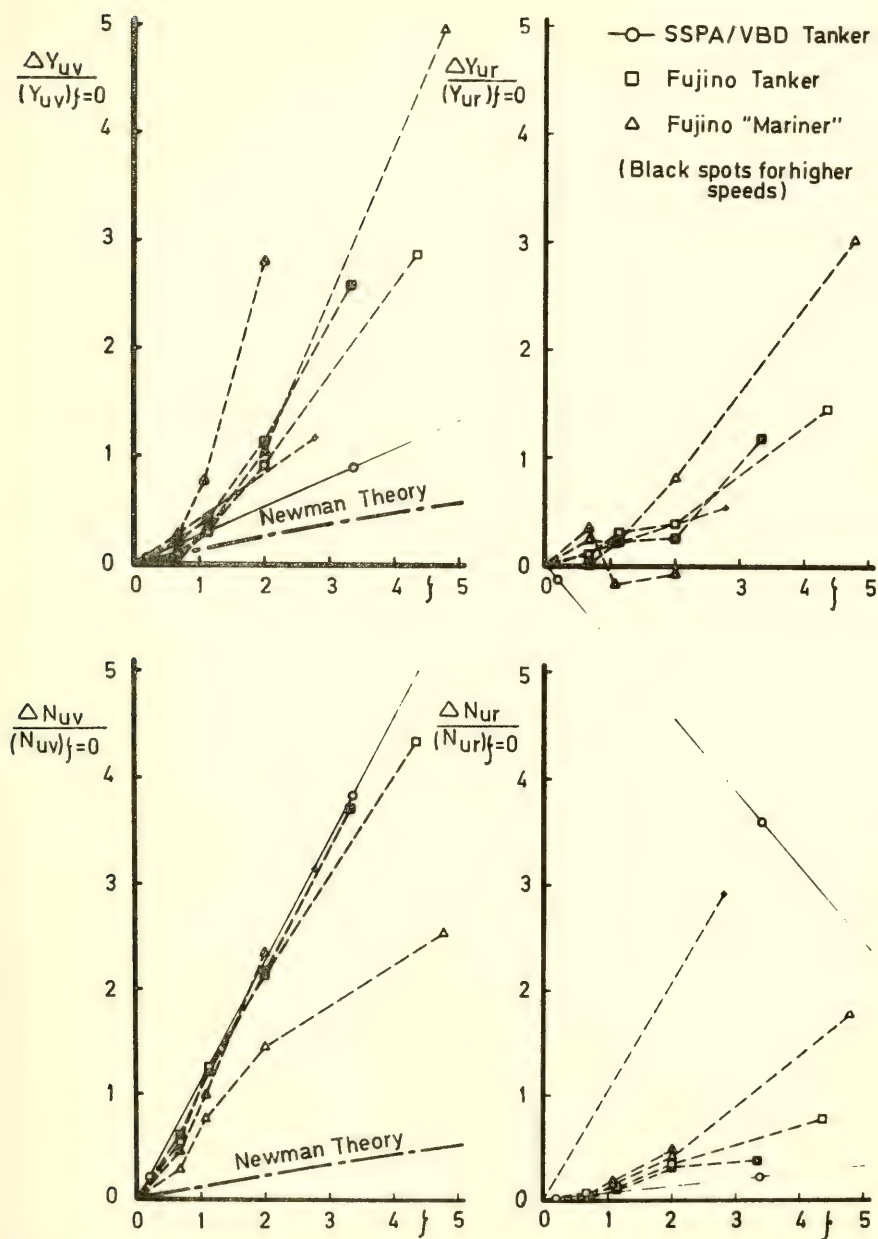


Fig. 33. Stability derivatives as influenced by finite depth -- results for SSPA tanker compared with Fujino tests and Newman theory.

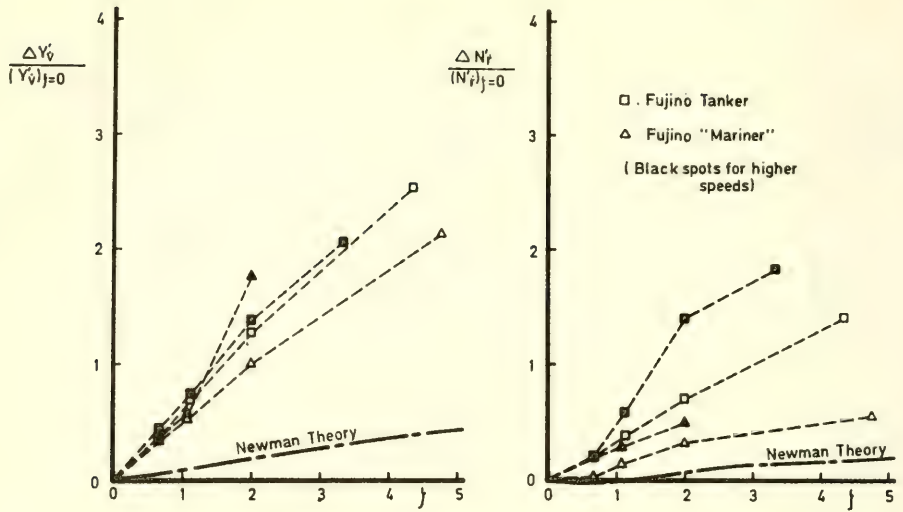


Fig. 34. Increase of linear and rotary acceleration derivatives with increase of parameter ζ according to Fujino tests and Newman theory.

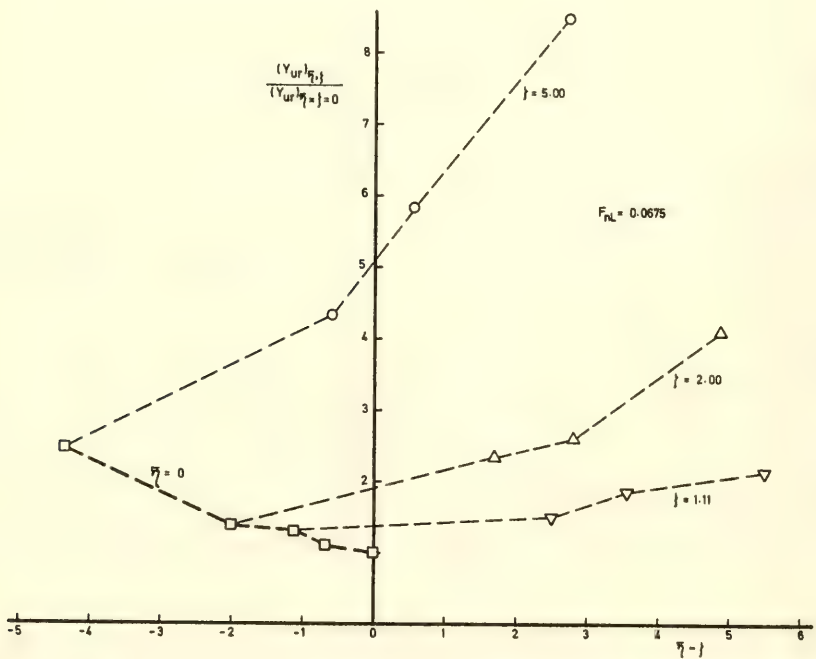


Fig. 35. Rotary force derivative for tanker as a function of waterway depth and width, replotted from Fujino PMM data

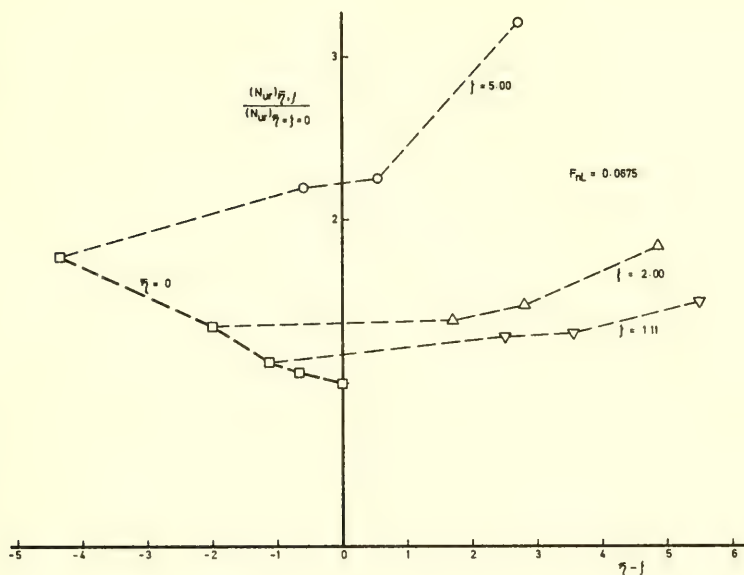


Fig. 36. Rotary moment derivative for tanker as a function of waterway depth and width, replotted from Fujino PMM data.

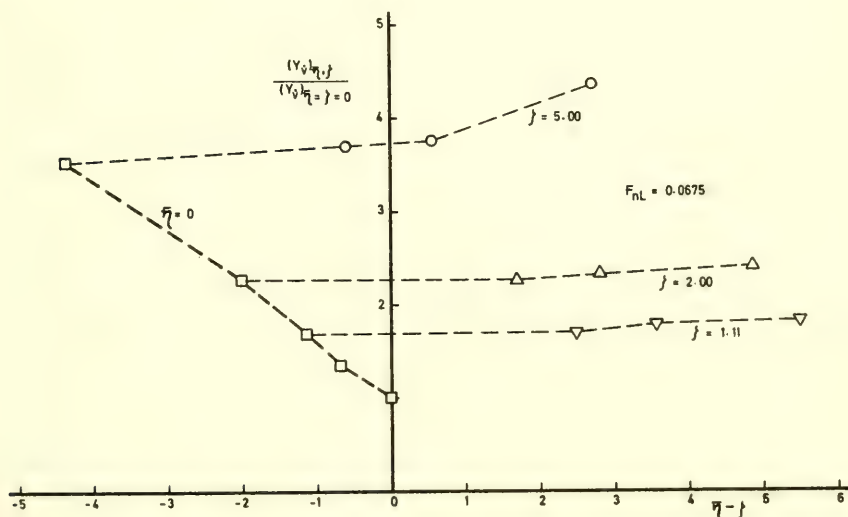


Fig. 37. Rel. change of lateral acceleration force derivative for a tanker as a function of waterway depth and width, replotted from Fujino PMM data.

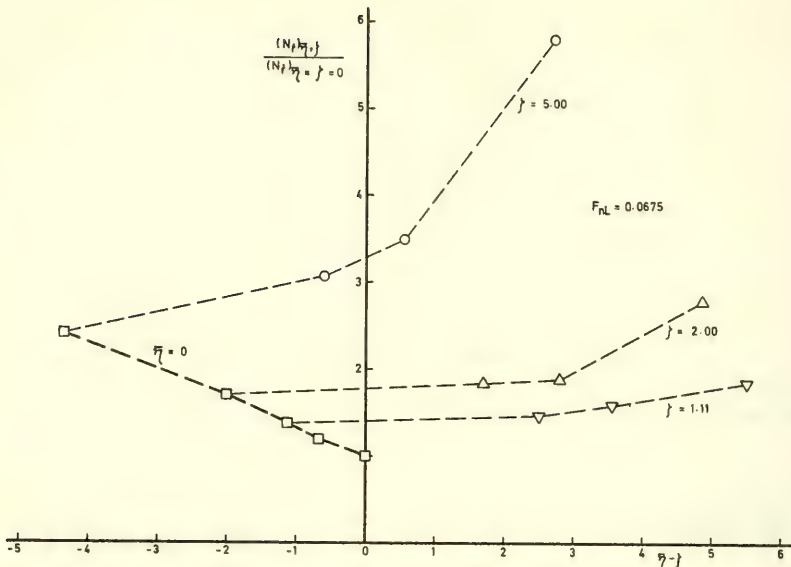


Fig. 38. Rel. change of rotary acceleration moment derivative for a tanker as a function of waterway depth and width, replotted from Fujino PMM data.

The diagrams in Fig. 35 - 38 are compiled from Fujino's measurements of rotary and acceleration derivatives in shallow waters and in canals. The dotted curves suggest a linear increase of all these derivatives with ζ in unrestricted water, and a more complex dependence of ζ and η in a canal. (Cf. end of Section X.)

XIII. SOME ASPECTS OF SHIP BEHAVIOUR IN CONFINED WATERS

Here a few comments will be given on some of the results obtained in a computer and simulator study performed for the 98 000 tdw tanker. The diagrams in Figs. 39 - 45 all include results directly drawn on the analogue computer recorder.

The only full scale maneuvering trials with the prototype ship so far available are a $20^\circ/20^\circ$ zig-zag test and a Dieudonné spiral, both run at full speed on full draught. These results are compared with the computer predictions — or hindcasts — for the ship on Suez draught in Figs. 39 and 40. As the difference in draught is not likely to have a significant influence the agreement is quite good. It shall be observed that the derivatives with respect to

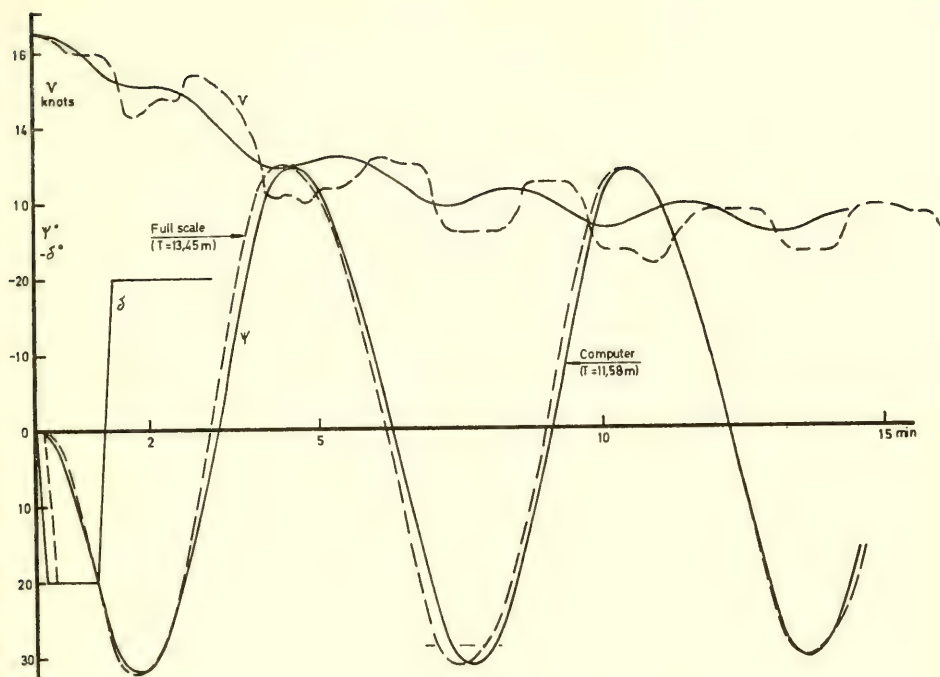


Fig. 39. 98 000 tdw tanker zig-zag test in deep water. Comparison of full scale trials and computer prediction.

$v|r|$ and $|v|r$ are not derived from measurements with this model but taken from an analysis of rotating arm tests with another tanker form, and the almost exact prediction of overswing angles might be somewhat accidental.

The good correlation of speed loss in the zig-zag maneuver is satisfying. The phase difference is likely to be due to the stern position of the ship's pressure-type speed log.

The ship (and simulator model) is slightly unstable on straight course in deep water; the total loop width is about 3.5° at slow speed as well as at high. In Fig. 41 is also shown the spiral prediction for shallow water ($\zeta = 3.37$ or $h/T = 1.3$). Here the initial stability is further impaired, whereas the stability in a turn is increased. A major factor governing the dependence of initial stability on water depth is the change of Y_{ur} . From Fig. 33 was seen that $Y_{ur}\zeta$ is negative for this model, so that the value of $1_r'' = (x_G'' - N_{ur}'' - N_{ur}\zeta'')/(1 - Y_{ur}'' - Y_{ur}\zeta'')$ may diminish much faster with increasing ζ than does $1_v'' = (N_{uv}'' + N_{uv}\zeta'')/(Y_{uv}'' + Y_{uv}\zeta'')$.

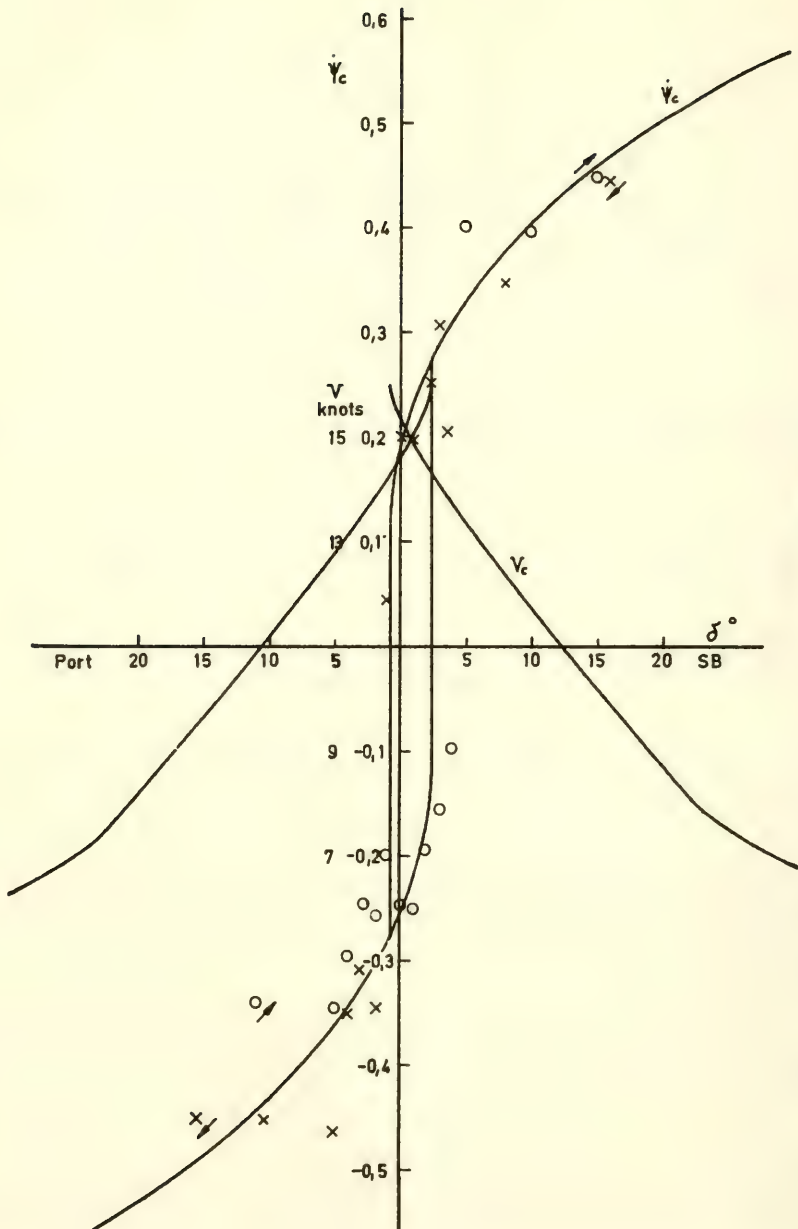


Fig. 40. 98 000 tdw tanker — $\dot{\psi}_c(\delta_c)$ -diagram from spiral tests in deep water. Comparison of full scale trials (x,o) and computer prediction (—).

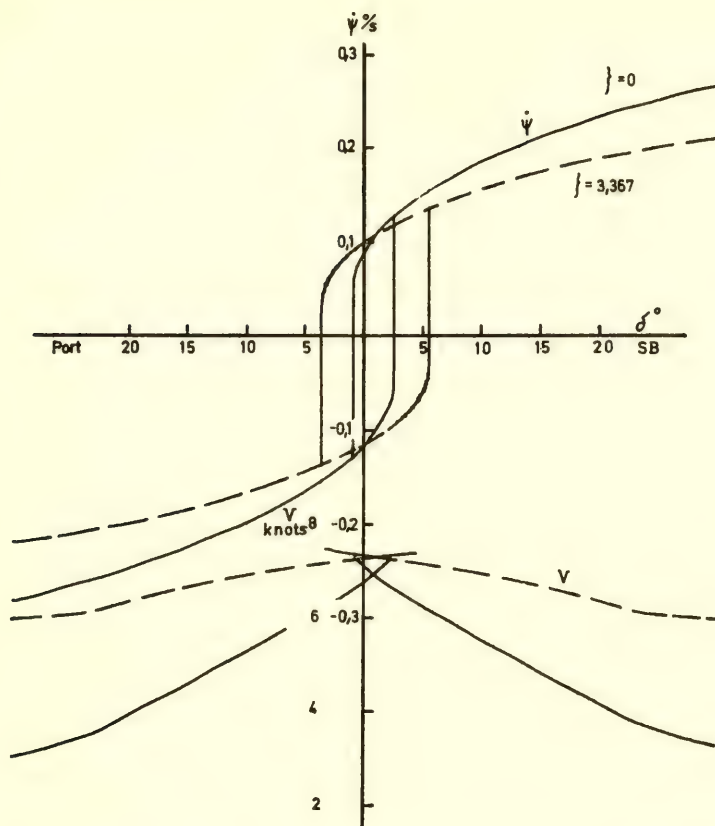


Fig. 41. 98 000 tdw tanker — Low speed spiral diagram from computer predictions for deep and shallow water

A similar trend is not unique, but it shall be observed that it may be necessary to include higher order derivatives in ζ to account for a finite range of "dangerous depth" as defined by Fujino, [5].

Figure 42 shows predictions for 20° rudder step responses in change of heading, yaw rate, and drift angle. The small drift angle obtained in the shallow water case is associated with the large increase of cross-flow drag. Similar results have earlier been reported by Schmidt-Stiebitz, [99].

From simulator and full scale experience is known that the helmsman may have some difficulties of controlling the ship in maneuvers that involve a change of course in shallow waters. Maneuvers by use of auto pilots are repeatable and well suited for

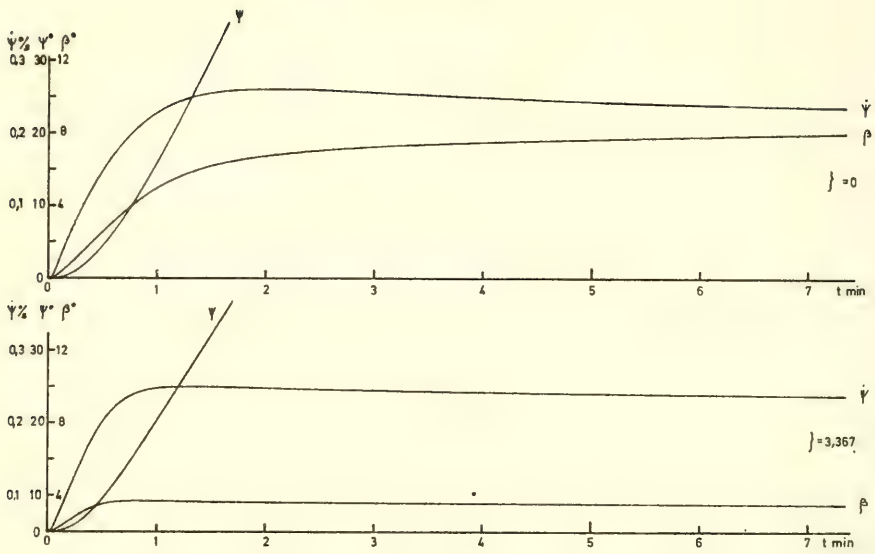


Fig. 42. 98 000 tdw tanker — Computer predictions of 20" rudder step response in deep and shallow water. Approach speed 7.6 knots.

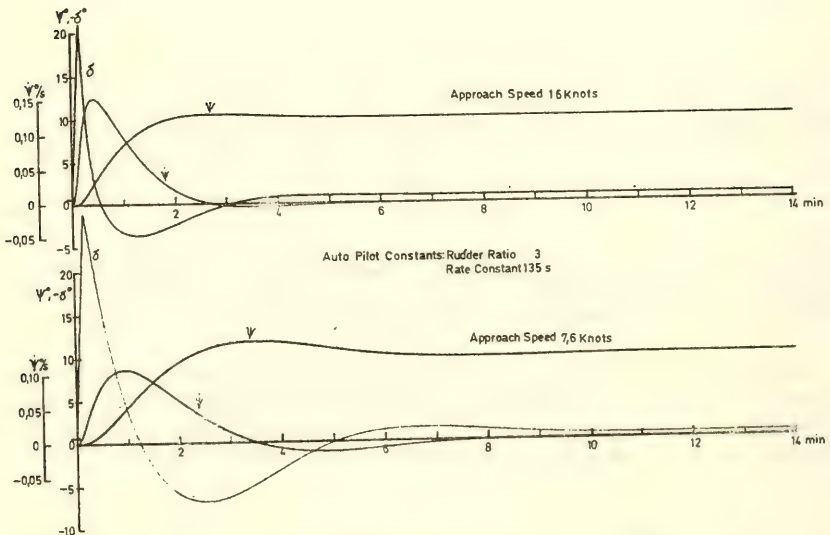


Fig. 43. 98 000 tdw tanker — Computer predictions of 10° course change manoeuvres by use of auto pilot knob setting. Two speeds in deep water.

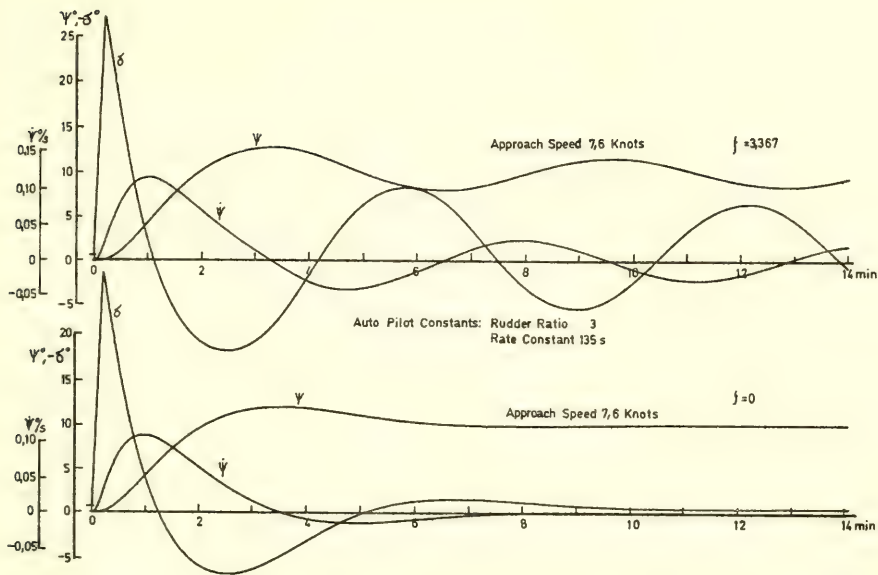


Fig. 44. 98 000 tdw tanker — Computer predictions of 10° course change maneuvers by use of auto pilot knob setting. Shallow and deep water.

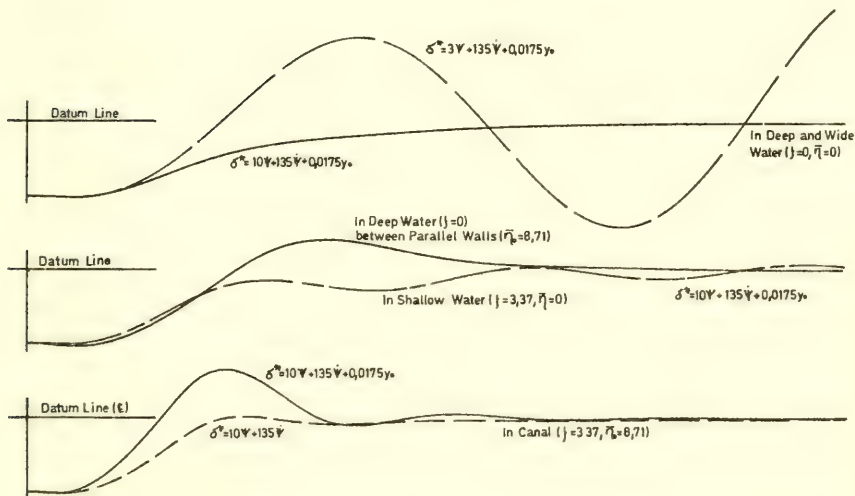


Fig. 45. 98 000 tdw tanker — Computer predictions of on-track control by auto pilots in deep and confined waters. Approach speed 7.6 knots. Initial off-set 20 m to starboard.

comparative studies. The diagrams in Figs. 43 and 44 refer to 10^0 course change maneuvers predicted for the tanker at two speeds in deep water and at the lower speed in shallow water, all executed using the same normal setting of auto pilot controls. There are several overswings in shallow water, and checking helm is large.

The final diagrams in Fig. 45 furnish a condensed illustration to the changing problems of course control in shallow waters and in canals. These problems are also dealt with by Eda and Savitsky [100], and in considerable detail by Fujino, [101].

It is assumed that the ship is moving at low speed on a straight course parallel to the required track (in a buoyed channel, say) but off-set 20 m to the starboard side. A signal proportional to this lateral error, calling for 1 degree rudder per m off track, is fed into the auto pilot. The upper curves for the free water conditions demonstrate that the rudder ratio setting must be increased (from normal 3 to say 10) in order to stabilize the ship on the required track. This control works reasonably satisfactory also in shallow water, but it tends to make the ship over-shoot the centre-line in the alternative case between parallel walls in deep water. Obviously the presence of the near wall accelerates the first swing towards and beyond the centre-line.

The two lower curves of Fig. 45 relate to the ship in a typical part of the Suez canal. In the shallow water the effect of the near wall is even more pronounced, and the stern of the ship is in danger of hitting the bank. However, by turning down the lateral error knob to zero the auto pilot is made to behave like the experienced helmsman, already referred to in the introduction. Thus, the ship first sheers bow-off the wall before the auto pilot applies a counter-rudder in order to slowly press the ship laterally away from the wall. The ship is seen to be almost steady on to the centre-line within two ship lengths.

REFERENCES

1. Norrbin, N. H., and Göransson, S., "The SSPA Steering and Maneuvering Simulator," (in Swedish), SSPA Allm. Rapport No. 28, April 1969.
2. Mandel, Ph., "Ship Maneuvering and Control," in "Principles of Naval Architecture" (revised), New York 1967.
3. van Berlekom, W., "Summary of a Simulator Study of Maneuvering Large Tankers in the Approach to a Port at Brofjorden," SSPA PM No. 1643-10, Sept. 1969. (Contract Report)

4. Bohlin, A., "Problems Arising from the Use of Very Large Ships in Connection with the Alignment and Depth of Approach Channels and of Maneuvering Areas," Paper S. II-3, Proc. XXII^e Congr s International de Navigation, Paris 1969.
5. Fujino, M., "Experimental Studies on Ship Maneuverability in Restricted Waters," Part I, Intern. Shipb. Progr., Vol. 15, No. 168, Aug. 1968.
6. Norrbin, N. H., and Simonsson, E. Y., "Observations onboard a 60 000 t.dw. Tanker Maneuvering through the Suez Canal," unpublished papers, SSPA and Uddevalla Shipyard, Nov. 1964.
7. ITTC, "Recommended Symbols Classified by Subject," Appendix II of Presentation Committee Report to the 10th ITTC, London 1963.
8. SNAME, "Nomenclature for Treating the Motion of a Submerged Body Through a Fluid," SNAME Technical and Research Bulletin No. 1 - 5, New York 1950.
9. Norrbin, N. H., "A Study of Course Keeping and Maneuvering Performance," SSPA Publ. No. 45, G teborg 1960. (Also Publ. in DTMB Report 1461, Washington D. C. 1960.)
10. Glauert, H., "A Non-Dimensional Form of the Stability Equations of an Aeroplane," ARC R & M No. 1093, London 1927.
11. Kirchhoff, G., "Ueber die Bewegung eines Rotationsk rpers in einer Fl ssigkeit," Crelle, Vol. LXXI, Heft 237, 1869.
12. Lamb, H., "Hydrodynamics," Cambridge University Press, Cambridge 1932 (6th ed.).
13. Milne-Thomson, L. M., "Theoretical Hydrodynamics," Mac Millan, London 1955 (3rd ed.).
14. Imlay, F. H., "The Complete Expressions for Added Mass of a Rigid Body Moving in an Ideal Fluid," DTMB Report 1528, July 1961.
15. Lamb, H., "The Inertia Coefficients of an Ellipsoid Moving in Fluid," ARC R & M No. 623, 1918.
16. Kotschin, N. J., Kibel, I. A., and Rose, N. W., "Theoretische Hydromechanik," Bd. I (from Russian), Akademie-Verlag, Berlin 1954.
17. Munk, M., "The Aerodynamic Forces on Airship Hulls," NACA Report No. 184, 1923.

18. Norrbin, N. H., "Forces in Oblique Towing of a Model of a Cargo Liner and a Divided Double-Body Geosim," SSPA Publ. No. 57, 1965.
19. Weinblum, G., "On Hydrodynamic Masses," DTMB Report 809, April 1952.
20. Grim, O., "Die Hydrodynamischen Kräfte beim Rollversuch," Schiffstechnik, 3. Bd., 14/15 Heft, Febr. 1956.
21. Landweber, L., and de Macagno, M. C., "Added Mass of Two-Dimensional Forms Oscillating in a Free Surface," J. Ship Research, Vol. 1, No. 3, Nov. 1957.
22. Lewis, F. M., "The Inertia of the Water Surrounding a Vibrating Ship," Trans. SNAME, Vol. 37, 1929.
23. Prohaska, C. W., "The Vertical Vibration of Ships," Shipb. and Mar. Eng. Builder, Oct-Nov 1947.
24. Lockwood-Taylor, J., "Some Hydrodynamical Inertia Coefficients," Phil. Mag. (Series 7) Vol. 9, No. 55, 1930.
25. Ursell, F., "On the Heaving Motion of a Circular Cylinder on the Surface of a Fluid," Quart. J. Mech. and Applied Math., Vol. II, Pt. 2, 1949.
26. Tasai, F., "Hydrodynamic Force and Moment Produced by Swaying Oscillation of Cylinders on the Surface of a Fluid," JSNA, Vol. 110, 1961.
27. Porter, W. R., "Pressure Distribution, Added Mass, and Damping Coefficients for Cylinders Oscillating in a Free Surface," University of California, Inst. of Engng Res., Series 82, Issue No. 16, July 1960.
28. Frank, W., "Oscillation of Cylinders in or below the Free Surface of Deep Fluids," NSRDC Report 2357, 1967.
29. Vugts, J. H., "The Hydrodynamic Coefficients for Swaying, Heaving and Rolling Cylinders in a Free Surface," Laboratorium voor Scheepsbouwkunde, Delft, Report No. 194, Jan. 1968.
30. de Jong, B., "Berekening van de hydrodynamische coëfficiënten van oscillerende cylinders," Laboratorium voor Scheepsbouwkunde, Delft, Report No. 174, March 1967.
31. Tuck, E. O., "A New Approach to the Strip Theory of Forced Ship Motion," NSRDC Tech. Note, Sept. 1966.

32. van Leeuwen, G., "The Lateral Damping and Added Mass of an Oscillating Shipmodel," Shipbuilding Laboratory, Delft, Publ. No. 23, July 1964.
33. Brard, R., "Introduction à l'étude théorique du tangage en marche," Bull. ATMA, No. 47, 1948.
34. Havelock, T., "The Resistance of a Submerged Cylinder in Accelerated Motion," Quart. Journ. Mech. Appl. Math., Vol. 2, Part 4, Dec. 1949.
35. Motora, S., "On the Measurement of Added Mass and Added Moment of Inertia of Ships in Steering Motion," Proc. First Symposium on Ship Maneuverability, Washington 1960, DTMB Report 1461, 1960.
36. Motora, S., Fujino, M., Sugiura, M., and Sugita, M., "Equivalent Added Mass of Ships in the Collision," Journ. Soc. Nav. Arch. Japan, Vol. 126, Dec. 1969.
37. Jones, R. T., "Properties of Low-Aspect-Ratio Pointed Wings at Speeds Below and Above the Speed of Sound," NACA Report No. 835, 1946.
38. Eda, H., and Crane, C. L. Jr., "Steering Characteristics of Ships in Calm Water and Waves," Trans. SNAME, Vol. 73, 1965.
39. Jacobs, W. R., "Estimation of Stability Derivatives and Indices of Various Ship Forms, and Comparison with Experimental Results," Dav. Lab. Report 1035, Sept. 1964.
40. Hu, P. N., "Forward Speed Effect on Lateral Stability Derivatives of a Ship," Dav. Lab. Report R-829, Aug. 1961.
41. Newman, J. N., "Some Hydrodynamic Aspects of Ship Maneuverability," Proc. Sixth Symposium on Naval Hydrodynamics, Washington, D. C. 1966.
42. Brard, R., "A Vortex Theory for the Maneuvering Ship with Respect to the History of Her Motion," Proc. Fifth Symposium on Naval Hydrodynamics, Bergen 1964.
43. Nomoto, K., and Karaano, K., "A New Procedure of Maneuvering Model Experiment," JSNA, Vol. 126, Dec. 1969.
44. Nomoto, K., "Unusual Scale Effect on Maneuverabilities of Ships with Blunt Bodies," Proc. 11th ITTC, Tokyo 1966.
45. Bottomley, G. H., "Maneuvering of Ships, Parts II-IV," Trans. IESS, Vols. 67, 70, and 74, 1923-1931.

46. Kent, J. L., "Ships in Rough Water," Thomas Nelson and Sons Ltd., London 1958.
47. Ambjörn, G., "Släpförsök med fartygsmodeller i sned och tvär ställning mot körriktningen..." (with English summary), Trans. Chalmers Univ. of Technology, No. 123, Göteborg 1952.
48. Thieme, H., "Schleppversuche bei Queranströmung," Schiff und Hafen, 6. Jahrg., Heft 6, 1954.
49. SNAME, "Notes on Ship Controllability," SNAME Technical and Research Bulletin No. 1-27, New York 1966.
50. Crane, C. L., Jr., "Studies of Ship Maneuvering — Response to Propeller and Rudder Actions," Proc. Ship Control Systems Symposium, Encl. to Vol. 1, US Marine Engng. Lab., Annapolis 1966.
51. Abkowitz, M. A., "Lectures on Ship Hydrodynamics — Steering and Maneuverability," HyA Report No. Hy-5, May 1964.
52. Lindgren, H., "Ship Trial Analysis and Model Correlation Factors," SSPA Publ. No. 54, 1963.
53. Saunders, H., "Hydrodynamics in Ship Design," Vol. II, Chapter 56, publ. by SNAME, New York 1957.
54. Matora, S., and Koyama, T., "Some Aspects of Automatic Steering of Ships," Japan Shipb. & Marine Engng., July 1968.
55. Nomoto, K., "Analysis of Kempf's Standard Manoeuvre Test and Proposed Steering Quality Indices," First Symposium on Ship Maneuverability, Washington D.C., DTMB Report 1461, Oct. 1960.
56. Nordén, I., "Fartyg med två roder," Götaverken Journal Skeppsbyggaren, No. 4, 1960.
57. Norrbin, N. H., "Steuern bei geringer Fahrt," Hansa, 101. Jahrg., Heft 10, May 1964.
58. Ribner, H. S., "Propellers in Yaw," NACA Report No. 820, 1945.
59. Ditlev Jorgensen, H., and Prohaska, C. W., "Wind Resistance," Appendix IV of Performance Comm. Report to the 11th ITTC, Tokyo 1966.

60. Wereldsma, R., "Experimental Determination of Thrust Excentricity and Transverse Forces Generated by a Screw Propeller," Intern. Shipb. Progr., Vol. 9, No. 95, July 1962.
61. Norrbin, N. H., "Circle Tests with a Radio-Controlled Model of a Cargo Liner," SSPA Publ. No. 53, Goteborg 1963.
62. Lötveit, M., "A Study of Rudder Action with Special Reference to Single-Screw Ships," Trans. NECI, Vol. 75, 1959/60.
63. Baker, G. S., and Bottomley, G. H., "Maneuvering of Ships, Part I -- Unbalanced Rudders of Single-Screw Ships," Trans. IEES, Vol. 65, 1921/22.
64. Weissinger, J., "Über die Auftriebsverteilung von Pfeilflügeln," Forschungsbericht deutscher Luftfahrtforschung Nr 1553, 1942. (Transl. NACA TM 1120.)
65. Spreiter, J. R., "The Aerodynamic Forces on Slender Plane- and Cruciform-Wing and Body Combinations," NACA Report No. 962, 1950.
66. Mirels, H., "Lift Effectiveness of Slender Wings on Cylindrical Bodies," J. Aero. Sci., Vol. 20, No. 7, July 1953. (Readers Forum.)
67. Yazaki, A., and Yokoo, K., "On the Roughness Allowance and the Scale Effect on the Wake Fraction of Super-Tankers," Proc. 11th ITTC, Tokyo 1966.
68. Strøm-Tejsen, J., and Chislett, M. S., "A Model Testing Technique and Method of Analysis for the Prediction of Steering and Maneuvering Qualities of Surface Ships," 6th Symposium on Naval Hydrodynamics, Washington D.C., 1966. (Also HyA Report Hy-7, Copenhagen 1966.)
69. Hooft, J. P., "The Maneuverability of Ships on a Straight Course," Intern. Shipb. Progress, Vol. 15, No. 162, Feb. 1968.
70. Nordström, H. F., "Screw Propeller Characteristics," SSPA Publ. No. 9, Goteborg 1948.
71. Harvald, S. A., "Wake and Thrust Deduction at Extreme Propeller Loadings," SSPA Publ. No. 61, Goteborg 1967.
72. Ritterhoff, J., "Beitrag zur Erhöhung der Sicherheit von Schiffsantriebsanlagen durch Untersuchung ihres Manöververhaltens," Schiff und Hafen, 22. Jahrg., Heft 3, March 1970.

73. Saunders, H., "Hydrodynamics in Ship Design," Vol. III, Chapter 6, publ. by SNAME, New York 1965.
74. Brard, R., "Maneuvering of Ships in Deep Water, in Shallow Water, and in Canals," Trans. SNAME Vol. 59, 1951.
75. Weinblum, G., "Theoretische Untersuchungen der Strömungsbeeinflussung zweier Schiffe aufeinander beim Begegnen und Ueberholen auf tiefem und beschränktem Wasser," Schiffbau 34. Jahrg., 1933.
76. Havelock, T. H., "Wave Resistance — The Mutual Action of Two Bodies," Proc. Roy. Soc., Series A, Vol. 155, London 1936.
77. Silverstein, B. L., "Linearized Theory of the Interaction of Ships," Inst. Engng. Research, Report Series 82, Issue 3, Univ. of California, Berkeley 1957.
78. Schuster, S., "Untersuchungen über Strömungs- und Widerstandsverhältnisse bei der Fahrt von Schiffen in beschränktem Wasser," Jahrb. STG, Bd. 46, 1952.
79. Weinblum, G., "Wellenwiderstand auf beschränktem Wasser," Jahrb. STG, Bd. 39, 1938.
80. Müller, O., "Aus dem Grenzgebiet des Wasser- und schiffbaulichen Modellversuchswesens," Schiffbau, 36. Jahrg., 1935.
81. Constantine, T., "On the Movement of Ships in Restricted Waterways," J. Fluid Mechanics, Vol. 9, Part 2, Oct. 1960.
82. Hooft, J. P., "On the Critical Speed Range of Ships in Restricted Waterways," Intern. Shipb. Progress, Vol. 16, No. 177, May 1969.
83. Sturtzel, W., and Graff, W., "Untersuchungen über die Zunahme des Zähigkeitswiderstandes auf flachem Wasser," 85. Mitteilung der VBD, Forschungsberichte des Landes Nordrhein-Westfalen Nr. 1777, 1967.
84. Kirsch, M., "Die Erzeugung von Rotationskörpern aus gegebenen Singularitäten-Verteilungen," Schiff und Hafen, Heft 11, 1959.
85. Sturtzel, W., and Heuser, H. H., "Widerstands- und Propulsionsmessungen für den Normalselbstfahrer Typ Gustav Koenigs," Forschungsberichte des Landes Nordrhein-Westfalen, Heft 868, 1960.

86. Graff, W., "Untersuchungen über Änderungen von Sog und Nachstrom auf beschränkter Wassertiefe in stehendem und strömenden Wasser," *Schiffstechnik*, 8. Bd, Heft 44, Nov. 1961.
87. Sjoström, C. H., "Effect of Shallow Water on Speed and Trim," *Naval Engineers Journal*, April 1967.
88. Tuck, E. O., "Shallow Water Flows Past Slender Bodies," *Journ. Fluid Mechanics*, Vol. 26, Part 1, Sept. 1967.
89. Tuck, E. O., "Sinkage and Trim in Shallow Water of Finite Width," *Schiffstechnik*, 14. Bd, Heft 73, Sept. 1967.
90. Hay, D., "Harbour Entrances, Channels and Turning Basins," *The Dock and Harbour Authority*, Jan. 1968.
91. Kan, M., and Hanaoka, T., "Analysis for the Effect of Shallow Water upon Turning," (in Japanese), *Journ. SNAJ*, Vol. 115, 1964.
92. Newman, N. J., "Lateral Motion of a Slender Body Between Two Parallel Walls," *Journ. Fluid Mechanics*, Vol. 39, Part 1, Oct. 1969.
93. Newman, N. J., "The Force and Moment on a Slender Body of Revolution Moving Near a Wall," *DTMB Report 2127*, Dec. 1965.
94. Garthune, R. S., Rosenberg, B., Cafiero, D., and Olson, C.R., "The Performance of Model Ships in Restricted Channels in Relation to the Design of a Ship Canal," *DTMB Report 601*, Aug. 1948.
95. Schoenherr, K. E., "Data for Estimating Bank Suction Effects in Restricted Water and on Merchant Ship Hulls," *Proc. First Symposium on Ship Maneuverability*, Washington D. C., *DTMB Report 1461*, Oct. 1960.
96. Tuji, T., Mori, N., and Yamanouchi, Y., "On the Water Force Acting on a Ship in Oblique Flow (Restricted Water Effect)," *Contr. to the 12th ITTC*, Rome 1969.
97. Kennard, E. H., "Irrotational Flow of Frictionless Fluids, Mostly of Invariable Density," *DTMB Report 2299*, Feb. 1967.
98. Nussbaum, W., "Messung von Quer- und Längskräften am Modell eines Grosstankers," *VBD Berichten Nr. 396 I-II and 406*, June-Sept. 1966. (Contract Reports.)

99. Schmidt-Stiebitz, H. , "Die Manövriereigenschaften der Schiffe in Abhängigkeit von Schiffsform und Fahrwasser," Schiff und Hafen, 16. Jahrg., Heft 2, Feb. 1964.
100. Eda, H., and Savitsky, D. , "Experimental and Analytical Studies of Ship Controllability in Canals," Dav. Lab. Techn. Note 809, Sept. 1969.
101. Fujino, M. , "Experimental Studies on Ship Maneuverability in Restricted Waters -- Part II," Intern. Shipb. Progr., Vol. 17, No. 186, Feb. 1970.

THE SECOND-ORDER THEORY FOR NONSINUSOIDAL OSCILLATIONS OF A CYLINDER IN A FREE SURFACE

Choung Mook Lee

*Naval Ship Research and Development Center
Washington, D.C.*

ABSTRACT

A nonlinear hydrodynamic response resulting from vertical oscillation of a horizontal cylinder in a free surface at the sum of two monochromatic frequencies is investigated. The fluid surrounding the cylinder is assumed incompressible, its motion irrotational and its depth infinite.

It is shown for the case of a semi-submerged circular cylinder that when the two frequencies are close to each other the hydrodynamic force associated with the difference of the two frequencies is greater than the steady force. In the limit as the two frequencies become equal the above two forces also become equal. It therefore appears reasonable to include the difference-frequency force in the calculation of the maximum steady force when the excitation of a body consists of narrow-band frequencies.

I. INTRODUCTION

The hydrodynamic problem dealing with a horizontal cylinder undergoing a vertical simple harmonic motion in a free surface has been investigated by many authors. Ursell [1949] treated a semi-circular cylinder using the method of multipole expansion and obtained the pressure distribution, added mass, and damping of the cylinder. Later Tasai [1959] and Porter [1960] extended Ursell's work to cylinders of ship-like sections using conformal mapping. Frank [1967] dealt with the foregoing problem by the Green's function which resulted in a distribution of singularities. Lee [1968], following Porter's work, extended the potential solution to second-

order in a perturbation series in the ratio of motion amplitude to half-beam. In the present work this cylinder-oscillation problem is extended to the case where the cylinder is oscillated at the sum of two monochromatic frequencies. In this case the second-order forces acting upon the cylinder include the effects of interactions between two frequencies, in particular, the sum and difference frequencies of the basic spectrum. The magnitudes of these second-order hydrodynamic quantities provide a measure of the non-linearity of the frequency response of an inviscid incompressible fluid to a periodic disturbance generated by an oscillating body in a free surface.

Hydrodynamic quantities such as added mass and damping obtained from the theory of oscillating cylinders in a free surface with a monochromatic frequency are extensively used in the studies of ship motions. Most of these studies are based on the assumption of linear frequency response of ships to waves. Recently Tasai [1969] and Grim [1969] emphasized the necessity of further investigation on nonlinear ship responses to waves. The present investigation is an attempt to provide information on the nonlinear relation between the motions of a body and surrounding fluid. This information might lead to the study of nonlinear ship motions in waves, perhaps by using the scheme suggested by Hasselmann [1966].

The problem to be investigated in this work is the following. An infinitely long horizontal cylinder which is symmetric about its vertical axis is semi-submerged and forced to oscillate vertically at the sum of two monochromatic frequencies. The maximum displacement of the cylinder from its mean position is assumed to be small compared to the half-beam of the cylinder. The fluid in which the cylinder oscillates is assumed inviscid, incompressible, and infinitely deep. The motion is assumed to have existed for a period significantly long that the initial transient phenomenon of the response of the fluid has completely decayed. This problem can be formulated as a boundary-value problem for a velocity potential. The kinematic and dynamic conditions to be satisfied on the free surface are nonlinear and the position of the free surface is a priori unknown. An exact solution of this problem in a closed form cannot be attained, so an approximate solution based on a linearization of the problem is pursued in this work. The linearization of the problem is carried out by a perturbation expansion of the velocity potential in terms of a small parameter formed by the ratio of the half-beam to a typical displacement amplitude of the cylinder motion. The first-order perturbation potential consists of two potentials, $\phi_1(x, y, t)$ and ϕ_2 , each of which involves only one of the two fundamental frequencies. The second-order perturbation potential consists of five potentials. Two of them are ϕ_3 and ϕ_4 which are associated respectively with frequencies of twice the fundamental frequencies. Two more are ϕ_5 and ϕ_6 which are associated respectively with the sum and the difference of the fundamental frequencies, and the last one, $\phi_7(x, y)$, is independent of the frequencies and is a steady potential. The

solutions for the first-order potentials were given by Ursell [1949], Tassai [1959], Porter [1960], and Frank [1967] among others. The solutions for three of the second-order potentials, ϕ_3 , ϕ_4 , and ϕ_7 , were given by Parassis [1966] and Lee [1966]. In the present investigation, the solutions for the remaining second-order potentials, ϕ_5 and ϕ_6 , will be given.

These solutions are based on the method of multipole expansions similar to that employed by Lee [1966]. An interesting problem arising from the present work is a surface-wave problem concerning a non-decaying pressure distribution on the free surface. The solution of this pressure-distribution problem is shown in detail in Appendix C. The potential ϕ_6 , associated with the difference frequency, is of particular significance in practical problems. ϕ_6 is a potential which is slowly-varying in time if two fundamental frequencies are close. In the case of bodies with insignificant restoring forces, such as submersibles and floating platforms, any hydrodynamic force, which is constant in time or varies slowly with time, could cause large excursions from the mean positions of such bodies if it acts for a long time. ϕ_6 must be calculated in order to determine this slowly-varying hydrodynamic force.

In the present work numerical results obtained from the solution of ϕ_6 are shown. These include the pressure-distribution about a semi-submerged circular cylinder, the hydrodynamic force acting on it, and the outgoing waves. These results are shown with other first- and second-order quantities for comparison purposes.

II. FORMULATION OF THE PROBLEM

A Cartesian coordinate system is used with origin at the interaction of the undisturbed free surface and the vertical line of symmetry of the cylinder. The x -axis is in the undisturbed free surface and the y -axis is directed upward.

Any point in the space is described in complex notation by

$$z = x + iy = re^{i\theta}. \quad (1)$$

The region outside the cylinder and the cylinder boundary is mapped from the region outside a circle in the ζ -plane and its circumference by the conformal transformation

$$\frac{z}{a} = \zeta + \sum_{n=0}^{\infty} a_{2n+1} \zeta^{-(2n+1)}, \quad (2)$$

$$\zeta = \xi + i\eta = \lambda e^{i\alpha}, \quad \lambda \geq 1, \quad (3)$$

where a and a_{2n+1} are real constants.

Points on the surface of the cylinder at its mean position are given by

$$\begin{aligned} x_0 &= a \left\{ \lambda_0 \cos \alpha + \sum_{n=0}^{\infty} \frac{a_{2n+1} \cos (2n+1)\alpha}{\lambda_0^{2n+1}} \right\}, \\ y_0 &= a \left\{ \lambda_0 \sin \alpha - \sum_{n=0}^{\infty} \frac{a_{2n+1} \sin (2n+1)\alpha}{\lambda_0^{2n+1}} \right\}, \end{aligned} \quad (4)$$

where λ_0 is the radius of the reference circle. When the cylinder is at the rest position its half breadth and draft are given respectively by

$$b = x_0(\lambda_0, 0), \quad (5)$$

$$d = |y_0(\lambda_0, -\pi/2)|. \quad (6)$$

The forced motion of the body is assumed to be the sum of two vertical simple harmonic motions with different frequencies. The motion of a point fixed in the body is expressed by

$$y(t) = h_0(\sin \sigma_1 t + \sin \sigma_2 t) \quad (7)$$

where σ_1 is greater than σ_2 and h_0 represents the amplitude of the individual simple harmonic motions.

The fluid is assumed to be incompressible and its motion to be irrotational so the continuity of mass in terms of velocity potential, $\Phi(x, y, t)$ is expressed by

$$\left(\frac{\partial^2}{\partial x^2} + \frac{\partial^2}{\partial y^2} \right) \Phi = \nabla^2 \Phi = 0. \quad (8)$$

The boundaries of the fluid are the free surface which extends to infinity along both the positive and negative x -axes, the fluid bottom which is at infinity, and the immersed surface of the cylinder.

If we let the equation of the free surface be expressed by

$$y = Y(x, t), \quad |x| > b, \quad (9)$$

the kinematic and dynamic boundary conditions on the free surface can be given respectively by

$$\Phi_x(x, Y(x, t), t) Y_x(x, t) - \Phi_y + Y_t = 0, \quad (10)$$

and

$$\Phi_t(x, Y(x, t), t) + gY + \frac{1}{2}(\Phi_x^2 + \Phi_y^2) = 0, \quad (11)$$

where a constant atmospheric pressure and an absence of surface tension on the free surface have been assumed. Taking the substantial derivative of Eq. (11) and eliminating $Y(x, t)$ by using Eq. (10), we obtain

$$\begin{aligned} \Phi_{tt}(x, Y(x, t), t) + g\Phi_y + 2\Phi_x\Phi_{tx} + 2\Phi_y\Phi_{ty} \\ + \Phi_x^2\Phi_{xx} + 2\Phi_x\Phi_y\Phi_{xy} + \Phi_y^2\Phi_{yy} = 0. \end{aligned} \quad (12)$$

Let the equation of the cylinder surface at its rest position be given by

$$S(x_0, y_0) = f(x_0) - y_0 = 0 \quad (13)$$

where $f(x_0)$ represents an implicit functional relation between x_0 and y_0 through the parameters λ_0 and α . Then the equation of the oscillating surface can be written as

$$S(x_0, y_0 + y(t)) = f(x_0) + h_0(\sin \sigma_1 t + \sin \sigma_2 t) - y = 0. \quad (14)$$

The kinematic condition to be satisfied on the cylinder surface is

$$\nabla\Phi(x_0, y_0 + y(t), t) \cdot \underline{n} = V_n = -\frac{S_t}{|\nabla S|} \quad (15)$$

where \underline{n} is the unit normal vector on the cylinder surface and points into the fluid and V_n is the normal component of the cylinder-surface velocity. Since

$$\underline{n} = \frac{\nabla S}{|\nabla S|} = \frac{(f'(x_0), -1)}{|\nabla S|},$$

Eq. (15) becomes

$$\Phi_x(x_0, y_0 + y(t), t) f'(x_0) - \Phi_y = -h_0(\sigma_1 \cos \sigma_1 t + \sigma_2 \cos \sigma_2 t). \quad (16)$$

In terms of the stream function which is the harmonic conjugate of Φ the boundary condition on the body is

$$\frac{\partial \psi}{\partial s} = \frac{\partial \Phi}{\partial n} = -\frac{dy(t)}{dt} \frac{\partial x}{\partial s}$$

where s is the arc length of the cylinder contour in the counter-clockwise direction. Thus we have

$$\psi(x_0, y_0 + y(t), t) = -x_0 \frac{dy(t)}{dt}.$$

To complete the specification of the boundary-value problem, following conditions should be also given; the symmetry of the flow about the y -axis implies that

$$\Phi(x, y, t) = \Phi(-x, y, t),$$

the zero normal component of the fluid velocity on a rigid surface at the infinitely deep horizontal bottom is described by

$$\Phi_y(x, -\infty, t) = 0,$$

and the solution should represent outgoing plane waves as $|x| \rightarrow \infty$.

III. PERTURBATION EXPANSION

Assume a frequency-response system in which the relation between the input X and the output Y is given by

$$Y = AX + BX^2$$

where the input X is given by

$$X = e^{-j\sigma_1 t} + e^{-j\sigma_2 t}$$

and A and B are constants; it can then be shown that the frequency components involved in the output Y are σ_1 , σ_2 , $2\sigma_1$, $2\sigma_2$, $\sigma_1 + \sigma_2$, $\sigma_1 - \sigma_2$, and a "d.c." shift. Therefore, we make a perturbation expansion of the complex velocity potential

$$H(z, t) = \Phi(x, y, t) + i\psi(x, y, t)$$

in terms of a perturbation parameter $\epsilon = h_0/b$ in the following fashion:

$$\begin{aligned} H &= \epsilon H^{(1)} + \epsilon^2 H^{(2)} + \epsilon^3 H^{(3)} + \dots \\ &= \epsilon(\Phi^{(1)} + i\psi^{(1)}) + \epsilon^2(\Phi^{(2)} + i\psi^{(2)}) + \epsilon^3(\Phi^{(3)} + i\psi^{(3)}) + \dots \end{aligned} \quad (17)$$

Each velocity potential and stream function given above is further expanded as

$$\begin{aligned} \Phi^{(1)} &= \phi_1(x, y, t) + \phi_2(x, y, t) \\ &= \varphi_1(x, y)e^{-j\sigma_1 t} + \varphi_2(x, y)e^{-j\sigma_2 t}, \end{aligned} \quad (17a)$$

$$\begin{aligned} \Phi^{(2)} &= \phi_3(x, y, t) + \phi_4(x, y, t) + \phi_5(x, y, t) + \phi_6(x, y, t) + \phi_7(x, y, t) \\ &= \varphi_3(x, y)e^{-j2\sigma_1 t} + \varphi_4e^{-j2\sigma_2 t} + \varphi_5e^{-j(\sigma_1 + \sigma_2)t} \\ &\quad + \varphi_6e^{-j(\sigma_1 - \sigma_2)t} + \varphi_7(x, y) \end{aligned} \quad (17b)$$

$$\begin{aligned} \psi^{(1)} &= \psi_1(x, y, t) + \psi_2(x, y, t) \\ &= \Psi_1(x, y)e^{-j\sigma_1 t} + \Psi_2(x, y)e^{-j\sigma_2 t}, \end{aligned} \quad (17c)$$

$$\begin{aligned} \psi^{(2)} &= \psi_3(x, y, t) + \psi_4(x, y, t) + \psi_5(x, y, t) + \psi_6(x, y, t) + \psi_7(x, y) \\ &= \Psi_3(x, y)e^{-j2\sigma_1 t} + \Psi_4e^{-j2\sigma_2 t} + \Psi_5e^{-j(\sigma_1 + \sigma_2)t} \\ &\quad + \Psi_6e^{-j(\sigma_1 - \sigma_2)t} + \Psi_7(x, y) \end{aligned} \quad (17d)$$

etc., where

$$\varphi_k = \varphi_{kc} + j\varphi_{ks}, \quad \Psi_k = \Psi_{kc} + j\Psi_{ks},$$

for $k = 1, 2, \dots, 6$, and $j = \sqrt{-1}$. In these expressions, only the real

parts are needed, so whenever there appears an expression of the product of two complex functions one of which is a time harmonic involving with $j = \sqrt{-1}$, it should be understood that the real part of the expression is to be taken.

The convergence of these perturbation expansions will not be discussed. As usual it is hoped that the first few terms of the expression would yield an adequate approximation to the exact solution of the complex potential $H(x, y, t)$.

The expansion given in Eqs.(17) and the Bernoulli equation (11) suggest that we also assume the expansion

$$\begin{aligned} Y(x, t) = \epsilon [& Y_1(x) e^{-j\sigma_1 t} + Y_2 e^{-j\sigma_2 t}] \\ & + \epsilon^2 [Y_3(x) e^{-j2\sigma_1 t} + Y_4 e^{-j2\sigma_2 t} \\ & + Y_5 e^{-j(\sigma_1 + \sigma_2)t} + Y_6 e^{-j(\sigma_1 - \sigma_2)t} + Y_7(x)] + O(\epsilon^3) \end{aligned} \quad (18)$$

where

$$Y_k = Y_{kc} + jY_{ks} \quad \text{for} \quad k = 1, 2, \dots, 6.$$

Substituting these expansions into the Laplace equation and the boundary conditions and equating the terms of the same order in ϵ as well as of the same harmonic time dependence, we obtain a set of linear boundary-value problems. In this linearization process the instantaneous boundary of the fluid is expanded in Taylor's series about the undisturbed position of the fluid boundary.

The linearized boundary conditions for the functions φ_j ($j = 1, 2, 3, 4, 7$) are shown in Appendix A where it is shown that in the limiting case of $\sigma_1 = \sigma_2$ the relations $\varphi_1 = \varphi_2$, $\varphi_3 = \varphi_4 = \varphi_5/2$ and $\varphi_6 = \varphi_7$ can be established. These identities mean that when $\sigma_1 = \sigma_2$ the perturbation expansion given in Eqs.(17) reduces to that for the case of a simple harmonic oscillation which was investigated by Lee [1968].

The linearized boundary conditions for the functions φ_5 and φ_6 are given next.

3.1 The Boundary-Value Problem for $\varphi_5(x, y)$

φ_5 is harmonic in $y < 0$ except in the portion occupied by the cylinder at its mean position. On the free surface

$$\varphi_{5y}(x, 0) - K_5 \varphi_5 = h_5(x) \quad (19)$$

where

$$K_5 = (\sigma_1 + \sigma_2)^2 / g,$$

$$\begin{aligned} h_5(x) = & -j\sigma_1 / (2g) \{ \varphi_1(x, 0)(\varphi_{2yy} - K_2\varphi_{2y}) - 2(\varphi_{1x}\varphi_{2x} + \varphi_{1y}\varphi_{2y}) \} \\ & - j\sigma_2 / (2g) \{ \varphi_2(x, 0)(\varphi_{1yy} - K_1\varphi_{1y}) - 2(\varphi_{1x}\varphi_{2x} + \varphi_{1y}\varphi_{2y}) \} \end{aligned} \quad (20)$$

in which

$$K_i = \frac{\sigma_i^2}{g}, \quad i = 1, 2.$$

On the cylinder surface,

$$\varphi_{5x}(x_0, y_0)f'(x_0) - \varphi_{5y} = m_5(x_0, y_0) \quad (21)$$

where

$$m_5(x_0, y_0) = -j \frac{b}{2} \{ (\varphi_{1xy}(x_0, y_0) + \varphi_{2xy})f'(x_0) - \varphi_{1yy} - \varphi_{2yy} \}, \quad (22)$$

or, in terms of stream functions,

$$\Psi_5(x_0, y_0) = -j \frac{b}{2} (\Psi_{1y}(x_0, y_0) + \Psi_{2y}). \quad (23)$$

In the far field $\varphi_{5y} \rightarrow 0$ as $y \rightarrow -\infty$ and φ_5 should represent outgoing plane waves as $|x| \rightarrow \infty$. Furthermore there is a symmetric-flow condition which is expressed by $\varphi_5(x, y) = \varphi_5(-x, y)$.

3.2 The Boundary-Value Problem for $\varphi_6(x, y)$

φ_6 is harmonic in $y < 0$ except in the portion occupied by the cylinder at its mean position. On the free surface

$$\varphi_{6y}(x, 0) - K_6\varphi_6 = h_6(x) \quad (24)$$

where

$$K_6 = (\sigma_1 - \sigma_2)^2 / g,$$

$$h_6(x) = -j\sigma_1/(2g)\{\varphi_1(x,0)(\bar{\varphi}_{2yy} - K_2\bar{\varphi}_{2y}) - 2(\varphi_{1x}\bar{\varphi}_{2x} + \varphi_{1y}\bar{\varphi}_{2y})\} \\ + j\sigma_2/(2g)\{\bar{\varphi}_2(\varphi_{1yy} - K_1\varphi_{1y}) - 2(\varphi_{1x}\bar{\varphi}_{2x} + \varphi_{1y}\bar{\varphi}_{2y})\} \quad (25)$$

and the bar signs mean the complex conjugates, i.e.

$$\bar{\varphi}_i = \varphi_{ic} - j\varphi_{is} \quad \text{for} \quad i = 1, 2.$$

On the cylinder surface

$$\varphi_{6x}(x_0, y_0)f'(x_0) - \varphi_{6y} = m_6(x_0, y_0) \quad (26)$$

where

$$m_6 = j \frac{b}{2} \{\bar{\varphi}_{2yy}(x_0, y_0) - \varphi_{1yy} - (\bar{\varphi}_{2xy} - \varphi_{1xy})f'(x_0)\} \quad (27)$$

or, in terms of the stream functions,

$$\Psi_6(x_0, y_0) = j \frac{b}{2} (\Psi_{1y} - \Psi_{2y}). \quad (28)$$

In the far field $\varphi_{6y} \rightarrow 0$ as $y \rightarrow -\infty$ and φ_6 should represent outgoing waves as $|x| \rightarrow \infty$. The symmetric-flow condition implies that

$$\varphi_6(x, y) = \varphi_6(-x, y).$$

IV. SOLUTIONS FOR φ_5 AND φ_6

It will be assumed that solutions for the first-order potentials φ_1 and φ_2 are known. The method of multipole expansions for finding φ_1 and φ_2 is described in Appendix B.

The main difference between the first- and second-order problems is in the free-surface conditions. A first-order problem has a homogeneous differential equation for the free-surface condition (see e.g. (A-1) of Appendix A) whereas a second-order problem has an inhomogeneous one (see e.g. (19)). When there exists a non-constant pressure distribution on a free surface of negligible surface tension the first-order free-surface condition for an incompressible irrotational flow is represented by an inhomogeneous differential

equation such as Eq. (19) or (24). The term on the right-hand side of the equation of the first-order free-surface condition represents the pressure distribution on the free surface. Thus the problems for the second-order potentials φ_5 and φ_6 presented in Sections 3.1 and 3.2 are the same type of boundary-value problems as those for the first-order potentials except for the "non-constant pressure" on the free surface. If we assume there is no body in the fluid, then these problems can be treated as problems for surface waves arising from variable free-surface pressure distributions. Solutions for these problems are given in Wehausen and Laitone [1960]. If we denote the velocity potential associated with the problem of variable pressure distribution on the free surface by W and if we assume that it is known, we can use it to find the potentials φ_5 and φ_6 . This is done by introducing a new function $G \equiv \varphi - W$, where φ could be either φ_5 or φ_6 , so that the free-surface condition for G is given by a homogeneous equation such as $G_y(x,0) - KG = 0$ where K is either K_5 or K_6 . The boundary-value problem for G is then identical to those for the first-order potentials and the solutions to these are well known. Once G is known the solution for φ is readily obtained from $\varphi = G + W$. This scheme was used by Lee [1968] to find the second-order potentials φ_3 and φ_4 . However there are certain requirements on the "free-surface pressure functions," h_5 and h_6 given by Eqs. (20) and (25) respectively, to be satisfied before the known methods can be used to find the potential W . These requirements are that the functions $h_5(x)$ and $h_6(x)$ should be absolutely integrable in $(-\infty, \infty)$ and should satisfy the Hölder condition. Although the proof of these statements may not seem obvious from Eqs. (20) and (25), it can be shown that both h_5 and h_6 satisfy the Hölder condition and as $|x| \rightarrow \infty$

$$h_5 = O(1/x^2) \tag{29}$$

and

$$h_6 = a_0 e^{j\{(K_1-K_2)|x|-\beta\}} + O(1/x^2) \tag{30}$$

where a_0 and β are given by

$$a_0 = \frac{2\pi^2}{g} Q_1 Q_2 K_1 K_2 (\sigma_1 - \sigma_2) \tag{30a}$$

and

$$\beta = q_1 - q_2 - \pi/2. \tag{30b}$$

Here the quantities Q_k and q_k for $k = 1, 2$ are associated with the

first-order potentials and can be best described by the expressions of asymptotic behavior of the first-order potentials such as

$$\varphi_k \sim -j\pi Q_k e^{K_k y} e^{j(K_k |x| - q_k)} \quad \text{for } k = 1, 2 \quad \text{as } |x| \rightarrow \infty.$$

It is apparent from Eq. (30) that h_6 is not absolutely integrable. This implies the necessity of further consideration in deriving the solution of W which is associated with h_6 .

4.1 Solution for a Case Where Free-Surface Pressure Distribution is Specified

In this section we consider a potential-flow problem with a given pressure distribution on the free surface. We restrict our attention to the pressure distributions which have harmonic time dependence and are even in x . Furthermore we consider the two special cases: the one where the pressure distribution decays in the manner of $1/x^2$ as $|x| \rightarrow \infty$ and the one where the pressure distribution behaves like that for outgoing plane waves as $|x| \rightarrow \infty$. Let $w(x, y, t)$ be a harmonic function defined in $y < 0$ and with its time dependence of the form

$$w(x, y, t) = W(x, y) e^{-i\omega t}$$

where $W = W_c + jW_s$ and ω is an angular frequency. The free-surface boundary condition is

$$W_y(x, 0) - KW = h(x) \quad (31)$$

where $K = \omega^2/g$ and h is a known pressure distribution and is even in x . We expect that the solution of W should represent outgoing plane waves as $|x| \rightarrow \infty$ and furthermore that $W_y(x, -\infty) = 0$. We seek solutions to this problem in two cases.

$$\text{Case 1:} \quad h(x) = O(1/x^2) \quad \text{as } |x| \rightarrow \infty. \quad (32)$$

The solution for this case is given in Wehausen and Laitone [1960] in the form of a complex potential

$$\begin{aligned} F(z) &= W(x, y) + iW^*(x, y) \\ &= 1/\pi \int_{-\infty}^{\infty} h(\xi) e^{-iK(z-\xi)} E_1(-iK(z-\xi)) d\xi + 2i \int_x^{\infty} h(\xi) e^{-iK(z-\xi)} d\xi \\ &\quad + (j-i) \int_{-\infty}^{\infty} h(\xi) e^{-iK(z-\xi)} d\xi. \end{aligned} \quad (33)$$

Here E_1 is the exponential integral defined by

$$E_1(z) = \int_0^\infty \frac{e^{-t}}{t} dt \quad \text{for} \quad |\arg(z)| < \pi.$$

$$\text{Case 2:} \quad h(x) = Ae^{jK'|x|} + O(1/x^2) \quad \text{as} \quad |x| \rightarrow \infty \quad (34)$$

where $K' (\neq K)$ is a wave number and A is a complex constant with $A = A_c + jA_s$.

Before trying to solve for W , we introduce a harmonic function $W_1(x, y)$ which is even in x and satisfies

$$W_{1y}(x, 0) - KW_1 = Ae^{jK'|x|}$$

$$W_{1y}(x, -\infty) = 0$$

and

$$W_1 \sim Be^{jK'|x|} \quad \text{as} \quad |x| \rightarrow \infty$$

where B is a complex constant with $B = B_c + jB_s$. The solution for W_1 is found in Appendix C as

$$W_1(x, y) = \frac{Ae^{K'y}}{K' - K} e^{jK'|x|} - j \frac{A}{\pi} \operatorname{Rei} \left[\frac{e^{iK'z} E_1(iK'z)}{K + K'} + \frac{e^{-iK'z} E_1(-iK'z)}{K' - K} \right]. \quad (35)$$

Now we let

$$W_2 \equiv W - W_1 \quad \text{in} \quad y < 0.$$

It can then be shown that

$$W_{2y}(x, 0) - KW_2 = h(x) - Ae^{jK'|x|} \equiv h_2(x)$$

where

$$h_2(x) = O(1/x^2) \quad \text{as} \quad |x| \rightarrow \infty$$

and that

$$W_{2y}(x, -\infty) = 0 \quad \text{and} \quad W_2(x, y) = W_2(-x, y).$$

The solution to this problem is given by Eq. (33) as

$$\begin{aligned}
 F_2(z) &= W_2(x, y) + iW_2^*(x, y) \\
 &= \frac{1}{\pi} \int_{-\infty}^{\infty} h_2(\xi) e^{-iK(z-\xi)} E_1(-iK(z-\xi)) d\xi + 2i \int_x^{\infty} h_2(\xi) e^{-iK(z-\xi)} d\xi \\
 &\quad + (j-i) \int_{-\infty}^{\infty} h_2(\xi) e^{-iK(z-\xi)} d\xi.
 \end{aligned} \tag{36}$$

Thus Eqs. (35) and (36) finally give

$$\begin{aligned}
 W &= W_1 + W_2 \\
 &= \frac{Ae^{K'y}}{K' - K} e^{jK'|x|} - j \frac{A}{\pi} \operatorname{Re}_i \left[\frac{e^{iK'z} E_1(iK'z)}{K' + K} + \frac{e^{-iK'z} E_1(-iK'z)}{K' - K} \right] \\
 &\quad + \operatorname{Re}_i \left[\frac{1}{\pi} \int_{-\infty}^{\infty} h_2(\xi) e^{-iK(z-\xi)} E_1(-iK(z-\xi)) d\xi + 2i \int_x^{\infty} h_2(\xi) e^{-iK(z-\xi)} d\xi \right. \\
 &\quad \left. + (j-i) \int_{-\infty}^{\infty} h_2(\xi) e^{-iK(z-\xi)} d\xi \right].
 \end{aligned} \tag{37}$$

If we seek a solution to the problem described in Section 3.1 except the body-boundary condition, given by Eq. (21), we can obtain it from Eq. (33) of Case 1 of this section as

$$\begin{aligned}
 F_5(z) &= W_5(x, y) + iW_5^*(x, y) \\
 &= \frac{1}{\pi} \int_{-\infty}^{\infty} h_5(\xi) e^{-iK_5(z-\xi)} E_1(-iK_5(z-\xi)) d\xi + 2i \int_x^{\infty} h_5(\xi) e^{-iK_5(z-\xi)} d\xi \\
 &\quad + (j-i) \int_{-\infty}^{\infty} h_5(\xi) e^{-iK_5(z-\xi)} d\xi,
 \end{aligned} \tag{38}$$

in which we let $h_5(x) = 0$ in $-b < x < b$ since the velocity potentials are undefined in this line interval. In the same way, if we seek a solution which satisfies all the conditions except the body-boundary condition given by Eq. (26) in Section 3.2, we can obtain it from Eq. (37) of Case 2 with the constant A replaced by $a_0 e^{-j\beta}$ (compare Eq. (30) with (34)). If we express the solution in the form of a complex potential and let $K' = K_1 - K_2$, we find that

$$\begin{aligned}
 F_6(z) &= W_6(x, y) + iW_6^*(x, y) \\
 &= \frac{a_0 e^{K'y}}{K' - K_6} e^{j(K'|x| - \beta)} \pm i j e^{j(K'|x| - \beta)} \\
 &\quad - j \frac{a_0 e^{-j\beta}}{\pi} \left[\frac{e^{iK'z} E_1(iK'z)}{K' + K_6} + \frac{e^{-iK'z} E_1(-iK'z)}{K' - K_6} \right] \\
 &\quad + \frac{1}{\pi} \int_{-\infty}^{\infty} h_6(\xi) e^{-iK_6(z-\xi)} E_1(-iK_6(z-\xi)) d\xi + 2i \int_x^{\infty} h_6(\xi) e^{-iK_6(z-\xi)} d\xi \\
 &\quad + (j - i) \int_{-\infty}^{\infty} h_6(\xi) e^{-iK_6(z-\xi)} d\xi, \tag{39}
 \end{aligned}$$

where \pm signs correspond to $x \leq 0$ and $h_6(x) = 0$ in $-b < x < b$.

4.2 Solutions for φ_5 and φ_6

We will now show how to use the solutions obtained in the preceding section to find φ_5 and φ_6 . We introduce a new harmonic function G_k defined by

$$G_k(x, y) = \varphi_k - W_k \tag{40}$$

in the domain of $y < 0$ except for the portion occupied by the cylinder. Here the subscript k can be either 5 or 6 unless specified as one or the other. The boundary-value problems posed in Sections 3.1 and 3.2 can be written in terms of G_k as

$$G_{ky}(x, 0) - K_k G_k = 0, \tag{41}$$

$$G_{kx}(x_0, y_0) f'(x_0) - G_{ky} = m_k(x_0, y_0) - (W_{kx}(x_0, y_0) f'(x_0) - W_{ky}), \tag{42}$$

or in terms of the harmonic conjugates of G_k , denote by G_k^* , the above boundary condition can be written as

$$G_5^*(x_0, y_0) = -j \frac{b}{2} (\Psi_{1y}(x_0, y_0) + \Psi_{2y}) - W_5^* \equiv B_5(x_0, y_0) \tag{42a}$$

and

$$G_6^*(x_0, y_0) = j \frac{b}{2} (\Psi_{1y}(x_0, y_0) - \Psi_{2y}) - W_6^* \equiv B_6(x_0, y_0). \tag{42b}$$

Furthermore G_k is even in x , $G_{ky} \rightarrow 0$ as $y \rightarrow -\infty$, and G_k

should represent outgoing waves as $|x| \rightarrow \infty$.

These boundary-value problems are almost identical to those for the first-order velocity potentials. Thus we find them by the same method used to find the first-order potentials which is described in Appendix B. It is often called the "multipole-expansion method" since the potential is expanded in an infinite series of poles, located at the origin, of increasing order with unknown strengths. Each pole satisfies Laplacian equation everywhere except at the origin, the linear free-surface condition of the type $\Phi_y(x, 0) - K\Phi = 0$ and the infinite-depth condition, and is even in x . However, since each pole vanishes as $|x| \rightarrow \infty$ the radiation condition of outgoing plane waves is not satisfied. To circumvent this a source singularity which has all these properties plus the property of outgoing waves at $|x| = \infty$ is added to the multipole-expansion series. The unknown source and multipole strengths are found by satisfying the remaining condition which is the boundary condition on the body. Specifically we assume the solution for G_k to be

$$G_k(x, y) = \sum_{m=0}^{\infty} (b_{km} + jc_{km}) M_{km}(x(\lambda, \alpha), y(\lambda, \alpha)) e^{-iq_k y}. \quad (43)$$

Here $b_{k0} = Q_k$ = unknown strength of a source at the origin, $c_{k0} = 0$,

$$M_{k0} = - \int_0^{\infty} \frac{e^{py} \cos px}{p - K_k} dp - j\pi e^{K_k y} \cos K_k x \quad (44)$$

= a source of unit strength at the origin,

where \int_0^{∞} indicates that a Cauchy principal value is to be used,

$$M_{km} = \frac{\cos 2m\alpha}{\lambda^{2m}} + K_k a \frac{\sin (2m-1)\alpha}{(2m-1)\lambda^{2m}} - \sum \frac{(2n+1)a_{2n+1}}{2m+2n+1} \frac{\sin (2m+2n+1)\alpha}{\lambda^{2m+2n+1}} \quad \text{for } m \geq 1 \quad (45)$$

= multipoles of unit strength at the origin,

b_{km} and c_{km} for $m \geq 1$ are unknown multipole strengths, and q_k represents unknown phase relations between the forced motion of the body and the pulsating singularities at the origin. The expression for the harmonic conjugate of G_k is

$$G_k^*(x, y) = \sum_{m=0}^{\infty} (b_{km} + jc_{km}) M_{km}^*(x(\lambda, \alpha), y(\lambda, \alpha)) \quad (46)$$

where

$$M_{k0}^* = \int_0^\infty \frac{e^{py} \sin px}{p - K_k} dp + j\pi e^{K_k y} \sin K_k x, \quad (47)$$

$$M_{km}^* = - \frac{\sin 2m\alpha}{\lambda^{2m}} + K_k a \left\{ \frac{\cos (2m-1)\alpha}{(2m-1)^{2m-1}} - \sum_{n=0}^{\infty} \frac{(2n+1)a_{2n+1}}{2m+2n+1} \frac{\cos (2m+2n+1)\alpha}{\lambda^{2m+2n+1}} \right\} \quad \text{for } m \geq 1. \quad (48)$$

Our task is now to find the unknown coefficients b_{km} and c_{km} and the phase relationship q_k from the boundary conditions on the body surface given in Eq. (42). Since the boundary conditions on the body are simpler when written in terms of the stream functions G_k^* than in terms of the potential functions G_k , we use the Eqs. (42a) and (42b) to obtain these unknown quantities. Thus we find that

$$\sum_{m=0}^{\infty} (b_{km} + jc_{km}) M_{km}^*(x_0, y_0) e^{-jq_k} = B_k(x_0, y_0). \quad (49)$$

Since the q_k 's are independent of the points (x_0, y_0) on the body, we see by choosing an arbitrary point on the body, say $(x'_0(\lambda_0, \alpha'), y'(\lambda_0, \alpha'))$, that

$$e^{-jq_k} = \frac{B_k(x'_0, y'_0)}{\sum_{m=0}^{\infty} (b_{km} + jc_{km}) M_{km}^*(\lambda_0, \alpha')}. \quad (50)$$

Substitution of Eqs. (50) into (49) yields

$$\sum_{m=0}^{\infty} (b_{km} + jc_{km}) \left(M_{km}^*(\lambda_0, \alpha) - \frac{B_k(x_0, y_0)}{B_k(x'_0, y'_0)} M_{km}^*(\lambda_0, \alpha') \right) = 0,$$

and use of the earlier definition of $b_{k0} = Q_k$ and $c_{k0} = 0$ in this equation yields

$$\begin{aligned} \sum_{m=1}^{\infty} \left(\frac{b_{km}}{Q_k} + \frac{jc_{km}}{Q_k} \right) \left\{ M_{km}^*(\lambda_0, \alpha) - \frac{B_k(x_0, y_0)}{B_k(x'_0, y'_0)} M_{km}^*(\lambda_0, \alpha') \right\} \\ = \frac{B_k(x_0, y_0)}{B_k(x'_0, y'_0)} \left(\int_0^\infty \frac{e^{py'_0} \sin px'_0}{p - K_k} dp + j\pi e^{K_k y'_0} \sin K_k x'_0 - \right. \end{aligned}$$

$$- \int_0^\infty \frac{e^{py_0} \sin px_0}{p - K_k} dp - j\pi e^{K_k y_0} \sin K_k x_0. \quad (51)$$

Since this equation is valid for all values of α in the interval $(-\pi/2, 0)$ on the circle of radius λ_0 , in principle we can take an infinite number of α 's to set up an infinite system of a linear algebraic equation which can then be solved for b_{km}/Q_k and c_{km}/Q_k . In practice, the infinite series is truncated, so only a finite number of these unknowns is sought; this finite number is equal to the number of chosen α 's. The proof for the convergence of such a truncation scheme was given by Ursell [1949]. Once the values of a number N of b_{km}/Q_k and c_{km}/Q_k (i.e. $m = 1, 2, \dots, N$) is known the values of q_k and Q_k are readily obtained from Eq. (50) by

$$q_k = \tan^{-1} \left\{ \frac{-\operatorname{Im}_j A}{\operatorname{Re}_j A} \right\}, \quad (52a)$$

$$Q_k = |A|, \quad (52b)$$

where

$$A = \frac{B_k(x'_0, y'_0)}{\sum_{m=0}^N \left(\frac{b_{km}}{Q_k} + \frac{j c_{km}}{Q_k} \right) M_{km}^* (\lambda_0, \alpha')}. \quad .$$

Thus we finally can express the solutions of the velocity potentials Q_k by

$$\varphi_k(x, y) = G_k(x, y) + W_k(x, y) \quad \text{for} \quad k = 5, 6. \quad (53)$$

V. PRESSURE, FORCE, AND WAVE

5.1 Pressure on the Cylinder Surface

If we expand P which denotes the pressures on the cylinder in the same way as Φ was expanded in Eq. (17), we find that

$$\begin{aligned} P(x_0, y_0 + y(t), t) = & \epsilon \left\{ P_I(x_0, y_0 + y(t)) e^{-j\sigma_1 t} + P_{II} e^{-j\sigma_2 t} \right\} \\ & + \epsilon^2 \left\{ P_{III} e^{-j2\sigma_1 t} + P_{IV} e^{-j2\sigma_2 t} + P_V e^{-j(\sigma_1 + \sigma_2) t} \right. \\ & \left. + P_{VI} e^{-j(\sigma_1 - \sigma_2) t} + P_{VII}(x_0, y_0 + y(t)) \right\} + O(\epsilon^3). \end{aligned}$$

We expand P_i ($i = I, II, \dots, VII$) in Taylor series about the mean position of the cylinder (x_0, y_0) and substitute

$$\begin{aligned} y(t) &= h_0(\sin \sigma_1 t + \sin \sigma_2 t) \\ &= \epsilon b(\sin \sigma_1 t + \sin \sigma_2 t) \end{aligned}$$

in this expansion. We rearrange the terms in powers of ϵ and in time harmonics to obtain

$$\begin{aligned} P &= \epsilon \left\{ p_1(x_0, y_0) e^{-j\sigma_1 t} + p_2 e^{-j\sigma_2 t} \right\} \\ &+ \epsilon^2 \left\{ p_3 e^{-j2\sigma_1 t} + p_4 e^{-j2\sigma_2 t} + p_5 e^{-j(\sigma_1 + \sigma_2)t} \right. \\ &\left. + p_6 e^{-j(\sigma_1 - \sigma_2)t} + p_7(x_0, y_0) \right\} + O(\epsilon^3). \end{aligned} \quad (54)$$

From the Bernoulli equation,

$$P = -\rho \Phi_t(x_0, y_0 + y(t), t) - \rho g(y_0 + y(t)) - \frac{\rho}{2} (\Phi_x^2 + \Phi_y^2),$$

we eliminate the static pressure $\rho g y_0$, expand the right-hand side in accordance with Eq. (17) and equate terms which are of the same power of ϵ and of the same time harmonics. We then find the expressions for p_i ($i = 1, 2, \dots, 7$) in terms of velocity potentials φ_i and their derivatives. The expressions for these p_i 's are

$$p_i = j\rho(\sigma_i \varphi_i(x_0, y_0) - gb) \quad \text{for } i = 1, 2 \quad (55)$$

$$p_{i+2} = -\rho \left\{ -j2\sigma_i \varphi_{i+2} + \frac{b\sigma_i}{2} \varphi_{iy} + \frac{1}{4}(\varphi_{ix}^2 + \varphi_{iy}^2) \right\} \quad \text{for } i = 1, 2 \quad (56)$$

$$\begin{aligned} p_5 &= -\rho \left\{ -j(\sigma_1 + \sigma_2) \varphi_5(x_0, y_0) + \frac{1}{2}(\varphi_{1x} \varphi_{2x} + \varphi_{1y} \varphi_{2y}) \right. \\ &\quad \left. + \frac{b}{2}(\sigma_1 \varphi_{1x} + \sigma_2 \varphi_{2y}) \right\}, \end{aligned} \quad (57)$$

$$\begin{aligned} p_6 &= -\rho \left\{ -j(\sigma_1 - \sigma_2) \varphi_6(x_0, y_0) + \frac{1}{2}(\varphi_{1x} \bar{\varphi}_{2x} + \varphi_{1y} \bar{\varphi}_{2y}) \right. \\ &\quad \left. - \frac{b}{2}(\sigma_1 \varphi_{1y} + \sigma_2 \varphi_{2y}) \right\}, \end{aligned} \quad (58)$$

$$p_7 = \frac{b}{2} \sum_{i=1}^2 \left\{ b\sigma_i \varphi_{i2y}(x_0, y_0) - \frac{1}{2}(\varphi_{ix} \bar{\varphi}_{ix} + \varphi_{iy} \bar{\varphi}_{iy}) \right\}, \quad (59)$$

where the bar sign means the complex conjugate e.g.

$$\overline{\varphi}_{2x} = \varphi_{2cx} - j\varphi_{2sx}.$$

If we let

$$\delta_i = \tan^{-1} (\operatorname{Re}_j p_i / \operatorname{Im}_j p_i) \quad \text{for} \quad i = 1, 2, \dots, 6,$$

we can express these pressures in the form

$$p_i = j |p_i| e^{-j\delta_i} \quad \text{for} \quad i = 1, 2, \dots, 6$$

or, in association with the time harmonics,

$$p_i e^{-j\omega_i t} = |p_i| \sin(\omega_i t + \delta_i) \quad \text{for} \quad i = 1, 2, \dots, 6$$

where

$$\omega_i = \begin{cases} \sigma_i & \text{for } i = 1, 2 \\ 2\sigma_{i-2} & \text{for } i = 3, 4 \\ \sigma_1 + \sigma_2 & \text{for } i = 5 \\ \sigma_1 - \sigma_2 & \text{for } i = 6. \end{cases} \quad (61)$$

5.2 Vertical Hydrodynamic Force on the Body

The vertical hydrodynamic force acting upon the body is given by

$$F = -2 \int_{\ell_0(t)}^{\ell(t)} P \cos(n, y) d\ell.$$

Here $\ell_0(t)$ is the instantaneous position of the point of intersection between the bottom of the body and the y -axis, $\ell(t)$ the instantaneous position of the point of contact of the body with the free surface, and $\cos(n, y)$ the direction cosine of the unit normal vector on the body surface in the y -direction. The positive direction of the unit normal vector is into the fluid, and the integral is taken along the cylinder contour. Eq. (54) enables us to show that for the family of cylinders

mapped according to Eq. (2)

$$\begin{aligned} F = 2 \int_0^b dx_0 & \left[\epsilon \left\{ p_1(x_0, y_0) e^{-j\sigma_1 t} + p_2 e^{-j\sigma_2 t} \right\} \right. \\ & + \epsilon^2 \left\{ p_3 e^{-j2\sigma_1 t} + p_4 e^{-j2\sigma_2 t} + p_5 e^{-j(\sigma_1 + \sigma_2) t} \right. \\ & \left. \left. + p_6 e^{-j(\sigma_1 - \sigma_2) t} + p_7 \right\} \right] + O(\epsilon^3). \end{aligned} \tag{62}$$

If we let

$$\begin{aligned} F = \epsilon & (f_1 e^{-j\sigma_1 t} + f_2 e^{-j\sigma_2 t}) \\ & + \epsilon^2 (f_3 e^{-j2\sigma_1 t} + f_4 e^{-j2\sigma_2 t} + f_5 e^{-j(\sigma_1 + \sigma_2) t} \\ & + f_6 e^{-j(\sigma_1 - \sigma_2) t} + f_7) + O(\epsilon^3), \end{aligned} \tag{63}$$

then we find that

$$\begin{aligned} f_i &= 2 \int_0^b p_i(x_0(\lambda_0, \alpha), y_0(\lambda_0, \alpha)) dx \\ &= 2 \int_{-\pi/2}^0 p_i(x_0(\lambda_0, \alpha), y_0(\lambda_0, \alpha)) T(\alpha) d\alpha \quad \text{for } i = 1, 2, \dots, 7 \end{aligned} \tag{64}$$

where the expressions for p_i are given in Eqs. (55) through (58) and

$$T(\alpha) = -a \left\{ \lambda_0 \sin \alpha + \sum_{n=0}^{\infty} \frac{(2n+1)a_{2n+1}}{\lambda_0^{2n+1}} \sin (2n+1) \alpha \right\}.$$

If we let

$$\gamma_i = \tan^{-1} (\operatorname{Re}_j f_i / \operatorname{Im}_j f_i) \quad \text{for } i = 1, 2, \dots, 6,$$

we can show that

$$\begin{aligned} f_i e^{-j\omega_i t} &= j |f_i| e^{-j\gamma_i} e^{-j\omega_i t} \\ &= |f_i| \sin (\omega_i t + \gamma_i) \quad \text{for } i = 1, 2, \dots, 6 \end{aligned} \tag{66}$$

where the ω_i 's are defined in Eq. (61).

5.3 Outgoing Waves at $|x| = \infty$

Equation (11) shows that

$$Y(x, t) = -\frac{1}{g} \left\{ \Phi_x(x, Y(x, t), t) + \frac{1}{2} (\Phi_x^2 + \Phi_y^2) \right\}.$$

If we substitute the expansions given in Eqs. (17) and (18) into this equation and equate the terms of the same order and time harmonic, we find that

$$Y_i(x) = j \frac{\sigma_i}{g} \varphi_i(x, 0) \quad \text{for } i = 1, 2, \quad (67)$$

$$Y_{i+2}(x) = \frac{1}{g} \left\{ j 2 \sigma_i \varphi_{i+2}(x, 0) - \frac{K_i}{2} \varphi_i \varphi_{iy} - \frac{1}{4} (\varphi_{ix}^2 + \varphi_{iy}^2) \right\} \quad \text{for } i = 1, 2, \quad (68)$$

$$Y_5(x) = j \frac{\sigma_1 + \sigma_2}{g} \varphi_5(x, 0) - \frac{\sigma_1 \sigma_2}{2g} (\varphi_1 \varphi_{2y} + \varphi_2 \varphi_{1y}) \\ - \frac{1}{2g} (\varphi_{1x} \varphi_{2x} + \varphi_{1y} \varphi_{2y}), \quad (69)$$

$$Y_6(x) = j \frac{\sigma_1 - \sigma_2}{g} \varphi_6(x, 0) + \frac{\sigma_1 \sigma_2}{2g} (\varphi_1 \bar{\varphi}_{2y} + \varphi_2 \bar{\varphi}_{1y}) \\ - \frac{1}{2g} (\varphi_{1x} \bar{\varphi}_{2x} + \varphi_{1y} \bar{\varphi}_{2y}), \quad (70)$$

$$Y_7(x) = -\frac{1}{4g} \sum_{i=1}^2 (\varphi_{ix}(x, 0) \bar{\varphi}_{ix} + \varphi_{iy} \bar{\varphi}_{iy} - 2K_i \varphi_i \bar{\varphi}_{iy}). \quad (71)$$

If we let $|x| \rightarrow \infty$ (or $\lambda \rightarrow \infty$ for $\alpha = 0$ or $-\pi$) only the pulsating sources contribute non-vanishing values (see the expression for the first-order potentials in Appendix B, and for φ_3 and φ_4 in Lee [1968]). Thus we find that

$$\varphi_i(x, 0) \sim -Q_i e^{-jq_i} \lim_{|x| \rightarrow \infty} \left(\int_0^\infty \frac{e^{py} \cos px}{p - K_i} dp + j\pi e^{K_i y} \cos K_i x \right) \Big|_{y=0} \\ = -j\pi Q_i e^{j(K_i |x| - q_i)} \quad \text{for } i = 1, 2, 3, 4, \quad (72)$$

where the Q_i 's are the source strengths, the q_i 's the phase re-

relationship between the forced motion and the pulsating singularities at the origin, and

$$K_i = \frac{\sigma_i^2}{g},$$

$$K_{i+2} = \frac{4\sigma_i^2}{g}, \quad \text{for } i = 1, 2.$$

We can also show from Eqs. (43) through (45) by letting $|x| \rightarrow \infty$ (or $\lambda \rightarrow \infty$ for $\alpha = 0$ or $-\pi$) that

$$\begin{aligned} G_i(x, 0) &\sim -Q_i e^{-jq_i} \lim_{|x| \rightarrow \infty} \left(\int_0^\infty \frac{e^{py} \cos px}{p - K_i} dp + j\pi e^{K_i y} \cos K_i x \right) \Big|_{y=0} \\ &= -j\pi Q_i e^{j(K_i |x| - q_i)} \quad \text{for } i = 5, 6 \end{aligned} \quad (73)$$

where

$$K_5 = \frac{(\sigma_1 + \sigma_2)^2}{g},$$

$$K_6 = \frac{(\sigma_1 - \sigma_2)^2}{g},$$

and then Eqs. (38) and (39) can be used to show that

$$W_5(x, 0) \sim j \int_{-\infty}^\infty h_5(\xi) e^{jK_5(|x| - \xi)} d\xi, \quad (74)$$

$$W_6(x, 0) \sim \frac{a_0 e^{j\{(K_1 - K_2)|x| - \beta\}}}{K_1 - K_2 - K_6} + j \int_{-\infty}^\infty h_6(\xi) e^{jK_6(|x| - \xi)} d\xi, \quad (75)$$

where a_0 and β are defined in Eqs. (30). The far-field behavior of the derivatives of the functions φ_i ($i = 1, 2, 3, 4$), G_i ($i = 5, 6$), W_5 , and W_6 can be shown to differ from those exhibited in Eqs. (72) through (75) by factors of the appropriate wave numbers K_i . If these results are applied to Eqs. (67) through (71) and some manipulations are carried out, we can show that as $|x| \rightarrow \infty$

$$Y_i(x) \sim \frac{\pi}{g} Q_i \sigma_i e^{j(K_i |x| - q_i)} \quad \text{for } i = 1, 2, \quad (76)$$

$$Y_{i+2}(x) \sim \frac{2\pi}{g} Q_{i+2} \sigma_i e^{j(4K_i|x| - q_{i+2})} + \frac{(\pi Q_i K_i)^2}{2g} e^{j(2K_i|x| - 2q_i)} \\ + \frac{4\sigma_i}{g} \left| \int_b^\infty h_{i+2}(\xi) \cos 4K_i \xi \, d\xi \right|^2 e^{j(4K_i|x| - \theta_{i+2})} \quad \text{for } i = 1, 2 \quad (77)$$

where $h_3(x)$ and $h_4(x)$ are defined in Eq. (A-2) of Appendix A and

$$\theta_{i+2} = \tan^{-1} \left\{ \frac{-\operatorname{Im}_j \left(\int_b^\infty h_{i+2}(\xi) \cos 4K_i \xi \, d\xi \right)}{-\operatorname{Re}_j \left(\int_b^\infty h_{i+2}(\xi) \cos 4K_i \xi \, d\xi \right)} \right\}, \\ Y_5(x) \sim \frac{\pi}{g} Q_5 (\sigma_1 + \sigma_2) e^{j(K_5|x| - q_5)} \\ + \frac{\pi^2}{2g^2} Q_1 Q_2 \sigma_1 \sigma_2 (K_1 + K_2) e^{j\{(K_1 + K_2)|x| - q_1 - q_2\}} \\ + \frac{2(\sigma_1 + \sigma_2)}{g} \left| \int_b^\infty h_5(\xi) \cos K_5 \xi \, d\xi \right|^2 e^{j(K_5|x| + \theta_5)} \quad (78)$$

where

$$\theta_5 = \tan^{-1} \left\{ \frac{-\operatorname{Im}_j \left(\int_b^\infty h_5(\xi) \cos K_5 \xi \, d\xi \right)}{-\operatorname{Re}_j \left(\int_b^\infty h_5(\xi) \cos K_5 \xi \, d\xi \right)} \right\}, \\ Y_6(x) \sim \frac{\pi}{g} Q_6 (\sigma_1 - \sigma_2) e^{j(K_6|x| - q_6)} \\ + \frac{\pi^2}{2g^2} Q_1 Q_2 \sigma_1 \sigma_2 (K_1 - K_2) e^{j\{(K_1 - K_2)|x| - (q_1 - q_2)\}} \\ + \frac{2(\sigma_1 - \sigma_2)}{g} \left| \int_b^\infty h_6(\xi) \cos K_6 \xi \, d\xi \right|^2 e^{j(K_6|x| + \theta_6)} \quad (79)$$

where

$$\theta_6 = \tan^{-1} \left\{ \frac{-\operatorname{Im}_j \left(\int_b^\infty h_6(\xi) \cos K_6 \xi \, d\xi \right)}{-\operatorname{Re}_j \left(\int_b^\infty h_6(\xi) \cos K_6 \xi \, d\xi \right)} \right\},$$

$$Y_7(x) \sim 0.$$

VII. NUMERICAL RESULTS

A semi-circular cylinder of unit radius ($b = 1$) is chosen for sample calculations of the pressure distributions, hydrodynamic forces, and out-going waves. The inputs for the calculations are the values of the fundamental frequencies σ_1 and σ_2 . Three values of σ_1 are chosen such that the corresponding length of gravity waves in deep water, $\lambda_1 = 2\pi g/\sigma_1^2$, are equal to $2b$, $10b$, and $20b$. For each value of σ_1 the values of the second frequency σ_2 are chosen so that the wave lengths obtained by $\lambda_2 = 2\pi g/\sigma_2^2$ lie in the interval of $\lambda_1 < \lambda_2 < 2\lambda_1$ which is equivalent to $\frac{1}{2}(b\sigma_1^2/g) < b\sigma_2^2/g < b\sigma_1^2/g$. The reason such a narrow range of σ_2 is chosen stems from our practical interests. When the forcing frequencies are close the difference between any two frequencies is very small. Thus any hydrodynamic force response associated with the difference-frequency within this band can often be treated as a d.c. force in practical situations. It is of interest to examine how significant the magnitude of the hydrodynamic force of difference-frequency is compared with the pure d.c. force.

Numerical results are obtained here for the d.c. component of hydrodynamic pressure, p_7 , hydrodynamic force, f_7 , and for those quantities which are associated with the difference frequency, p_6 , f_6 , and Y_6 which represent outgoing waves at $|x| = \infty$. The quantities associated with the sum-frequency, p_5 , f_5 , and y_5 , are not computed because these quantities can often be approximated from the known values associated with the frequencies $2\sigma_1$ or $2\sigma_2$ when $\sigma_1 \approx \sigma_2$. For comparison purposes the quantities p_i , f_i , and y_i for $i = 2$ and 4 which are borrowed from Lee [1968] are also shown with the quantities presently calculated.

The deep-water gravity wave length based on the difference frequency is given by

$$\lambda_6 = \frac{2\pi g}{(\sigma_1 - \sigma_2)^2} = \lambda_1 \frac{\lambda_2/\lambda_1}{1 + (\lambda_2/\lambda_1) - 2\sqrt{\lambda_2/\lambda_1}}$$

where

$$\lambda_1 = \frac{2\pi g}{\sigma_1^2} \quad \text{and} \quad \lambda_2 = \frac{2\pi g}{\sigma_2^2}.$$

λ_6/λ_1 as a function of λ_2/λ_1 is shown in Fig. 1. This figure shows the wave length corresponding to the difference-frequency $\sigma_1 - \sigma_2$ compared to the fundamental wave lengths λ_1 and λ_2 .

In the rest of the figures the abscissas are $\bar{\lambda}$ which is defined as $\bar{\lambda} = \lambda_2/\lambda_1$. For the values of $\lambda_1 = 2b$, $10b$, and $20b$, the corre-

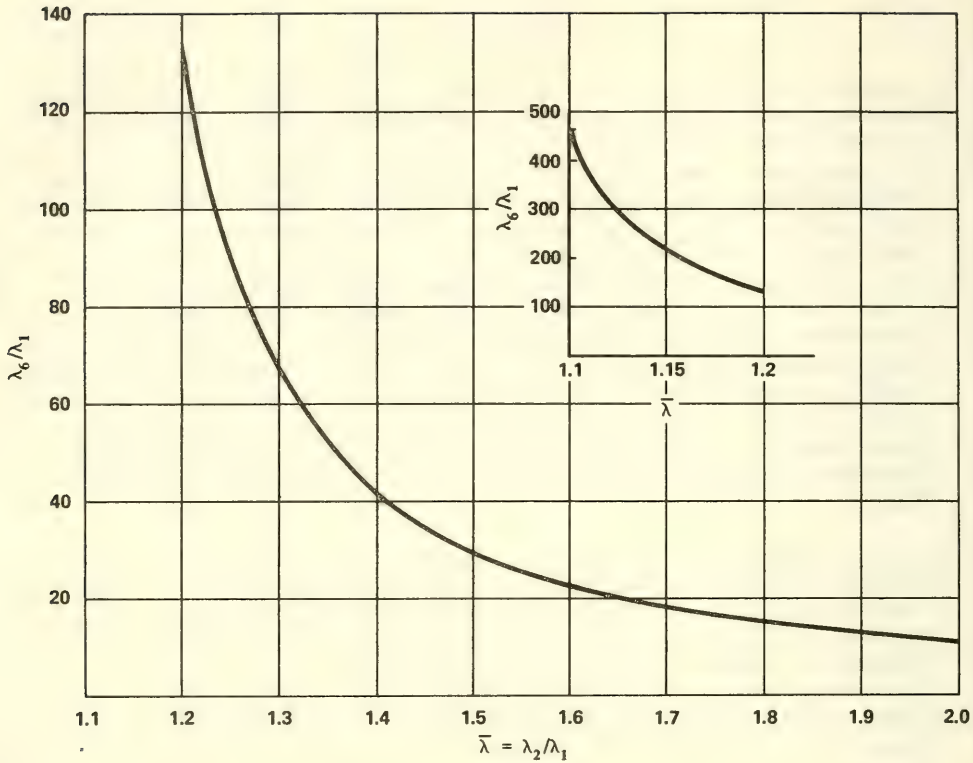


Fig. 1 Difference-frequency wave length
vs. fundamental-frequency wave length

sponding frequencies are respectively

$$\sigma_1 (= \sqrt{2\pi g/\lambda_1}) = \sqrt{\pi g/b}, \quad \sqrt{\pi g/5b}, \quad \text{and} \quad \sqrt{\pi g/10b}.$$

σ_2 is obtained from $\bar{\lambda} = \lambda_2/\lambda_1 = \sigma_1^2/\sigma_2^2$ as

$$\sigma_2 = \sqrt{2\pi g/(\lambda_1 \bar{\lambda})}.$$

Thus we have

$$\text{for } \lambda_1 = 2b, \quad \sigma_2 = \sqrt{\pi g/(b\bar{\lambda})}$$

$$\text{for } \lambda_1 = 10b, \quad \sigma_2 = \sqrt{\pi g/(5b\bar{\lambda})}$$

for $\lambda_1 = 20b, \quad \sigma_2 = \sqrt{\pi g/(10b\bar{\lambda})}.$

In Table 1, the values of $\delta_2 = \sigma_2^2 b/g$ and $\delta_6 = (\sigma_1 - \sigma_2)^2 b/g$ are given for $\bar{\lambda} = 1.0$ (0.1) 2.0 at each given $\lambda_1 = 2b, 10b,$ and $20b$. Thus the results in the subsequent figures can be referred to appropriate individual dimensionless frequencies such as $\delta_2, \delta_4 = 4\sigma_2^2 b/g = 4\delta_2,$ and $\delta_6 = 2\pi g/\lambda_1(1 + 1/\bar{\lambda} - 2\sqrt{1/\bar{\lambda}})$ once λ_1 and $\bar{\lambda}$ are given.

TABLE 1

δ_2 and δ_6 versus λ_1 at three different values at λ_1 and δ_1

	$\lambda_1 = 2b$ and $\delta_1 = \pi$		$\lambda_1 = 10b$ and $\delta_1 = \pi/5$		$\lambda_1 = 20b$ and $\delta_1 = \pi/10$	
$\bar{\lambda}$	δ_2	δ_6	δ_2	δ_6	δ_2	δ_6
1.05	2.992	0.182×10^{-2}	0.598	0.365×10^{-3}	0.299	0.182×10^{-3}
1.1	2.856	0.680×10^{-2}	0.571	0.136×10^{-2}	0.286	0.680×10^{-3}
1.2	2.618	0.238×10^{-1}	0.524	0.477×10^{-2}	0.262	0.238×10^{-2}
1.3	2.417	0.475×10^{-1}	0.483	0.950×10^{-2}	0.242	0.475×10^{-2}
1.4	2.244	0.753×10^{-1}	0.449	0.151×10^{-1}	0.224	0.753×10^{-2}
1.5	2.094	0.106	0.419	0.212×10^{-1}	0.209	0.106×10^{-1}
1.6	1.963	0.138	0.393	0.276×10^{-1}	0.196	0.138×10^{-1}
1.7	1.848	0.170	0.370	0.341×10^{-1}	0.185	0.170×10^{-1}
1.8	1.745	0.203	0.349	0.406×10^{-1}	0.175	0.203×10^{-1}
1.9	1.653	0.237	0.331	0.474×10^{-1}	0.165	0.237×10^{-1}
2.0	1.570	0.270	0.315	0.540×10^{-1}	0.157	0.270×10^{-1}

In Figs. 2, 3, and 4 the maximum hydrodynamic pressures at three points on the cylinder, $\theta = -90^\circ, -45^\circ,$ and $-5^\circ,$ are shown as functions of $\bar{\lambda}$ for $\lambda_1 = 10b$. The maximum pressures $|p_6|$ and $|p_7|$ are obtained from Eqs. (58) and (59). The pressures are non-dimensionalized by ρgb and are denoted with bar signs e.g. $\bar{p}_6 = |p_6|/\rho gb$. The values of \bar{p}_1 and \bar{p}_3 which are not shown in these figures are respectively equal to \bar{p}_2 and \bar{p}_4 at $\bar{\lambda} = 1.0$. The maximum hydrodynamic forces $\bar{f}_2 (= |f_2|/2\rho gb^2), \bar{f}_4, \bar{f}_6,$ and \bar{f}_7 which are obtained from Eq. (64) are shown as functions of $\bar{\lambda}$ in Figs. 5, 6, and 7 for $\lambda_1 = 2b, 10b,$ and $20b,$ respectively. Figure 8 shows the phase angles $\gamma_2, \gamma_4,$ and γ_6 which are defined by Eq. (65)

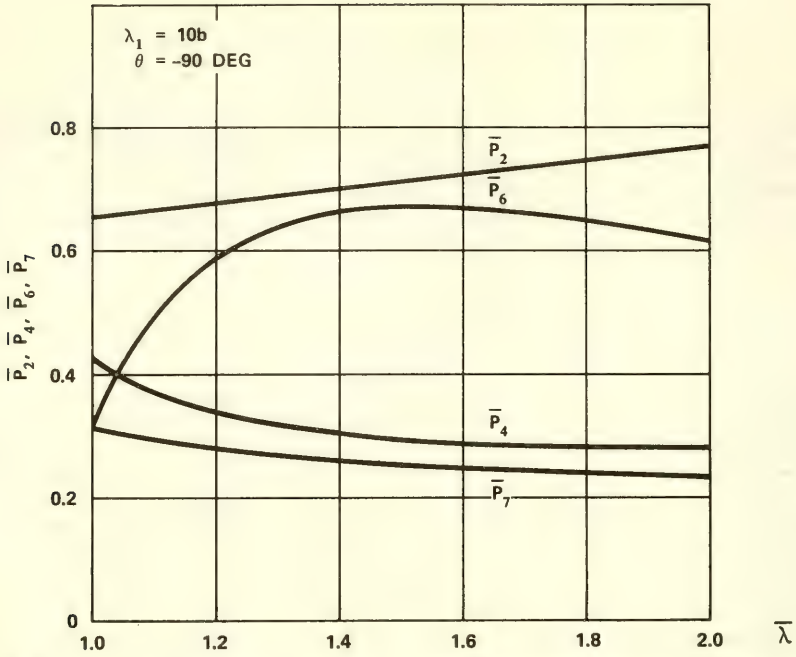


Fig. 2 First- and second-order pressures vs. $\bar{\lambda} = \lambda_2/\lambda_1$ at $\theta = -90^\circ$ for $\lambda_1 = 10b$

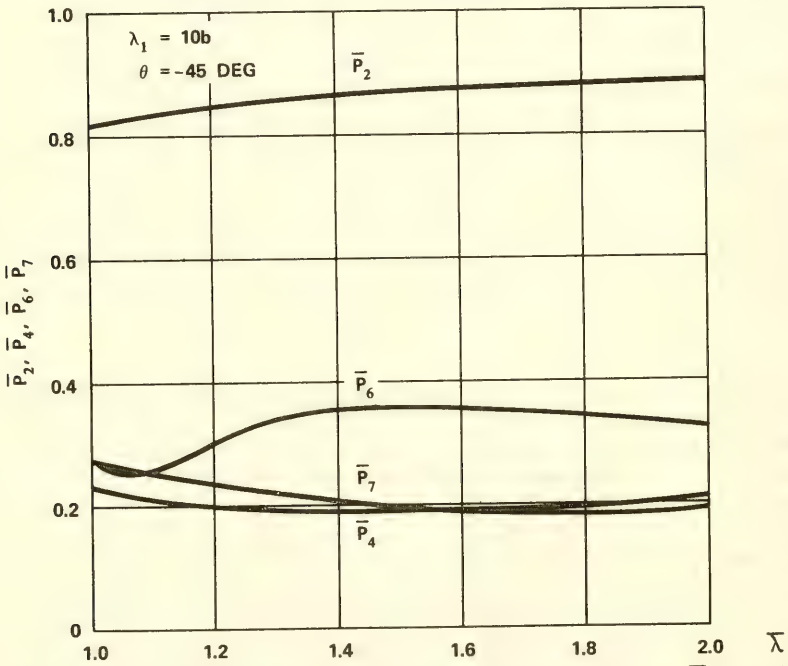


Fig. 3 First- and second-order pressures vs. $\bar{\lambda} = \lambda_2/\lambda_1$ at $\theta = -45^\circ$ for $\lambda_1 = 10b$

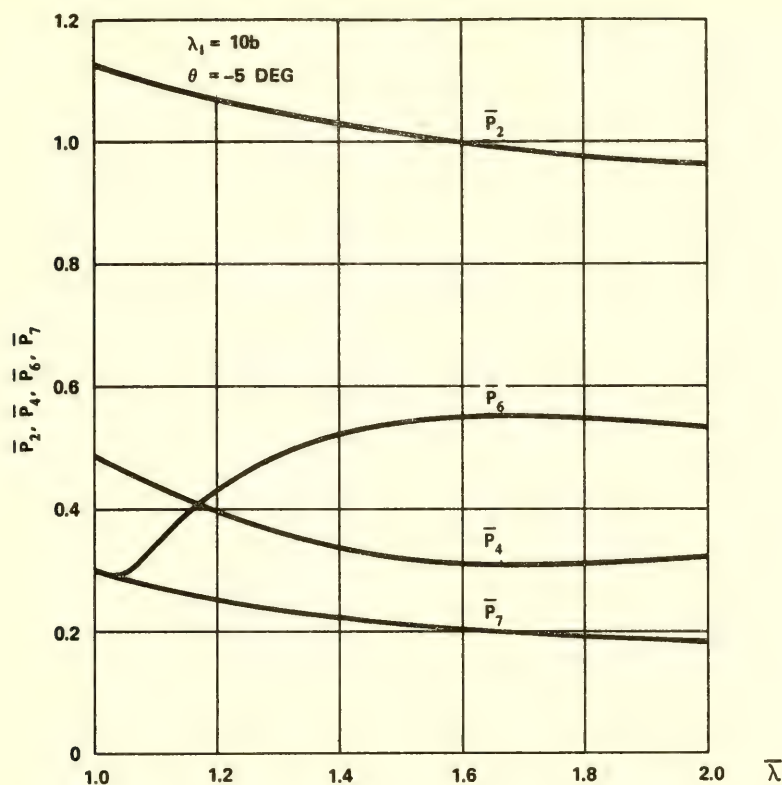


Fig. 4 First- and second-order pressures vs. $\bar{\lambda} = \lambda_2/\lambda_1$ at $\theta = -5^\circ$ for $\lambda_1 = 10b$

for $\lambda_1 = 10b$. The radiating-wave amplitudes at $|x| = \infty$ are shown in Fig. 9 for $\lambda_1 = 10b$. In this figure \bar{Y}_2 is defined by $\bar{Y}_2 = |Y_2|/b = \pi Q_2 \sigma_2 / (bg)$ and \bar{Y}_{6a} and \bar{Y}_{6b} are obtained in the following way. We can show from Eq. (79) that

$$Y_6(x) e^{-j(\sigma_1 - \sigma_2)t} \sim A_1 \cos \left\{ K_6 |x| - (\sigma_1 - \sigma_2)t - q_6 \right\} \\ + A_2 \cos \left\{ K_6 |x| - (\sigma_1 - \sigma_2)t + \theta_6 \right\} \\ - Y_{6b} \cos \left\{ (K_1 - K_2) |x| - (\sigma_1 - \sigma_2)t - (q_1 - q_2) \right\}$$

where

$$A_1 = \frac{\pi}{g} (\sigma_1 - \sigma_2) Q_6,$$

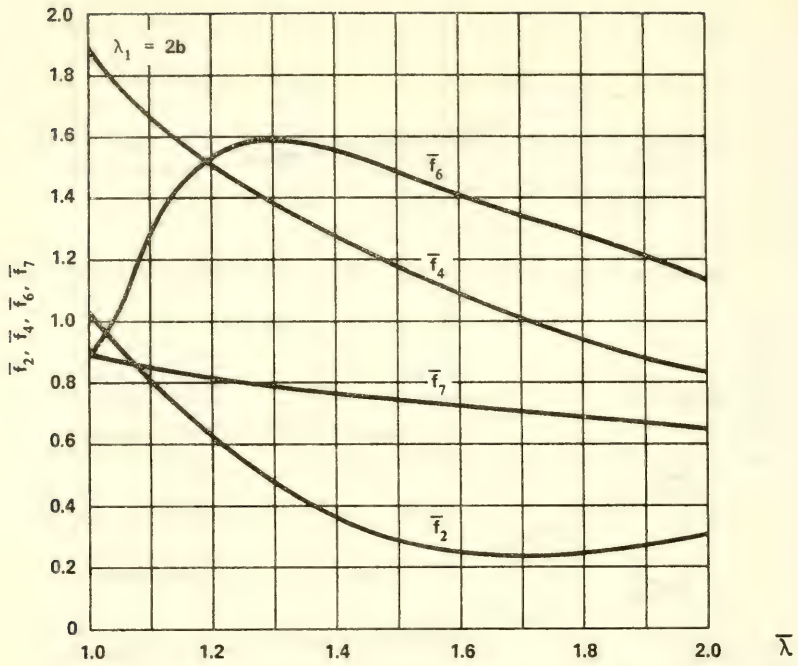


Fig. 5 First- and second-order forces vs. $\bar{\lambda}$ for $\lambda_1 = 2b$

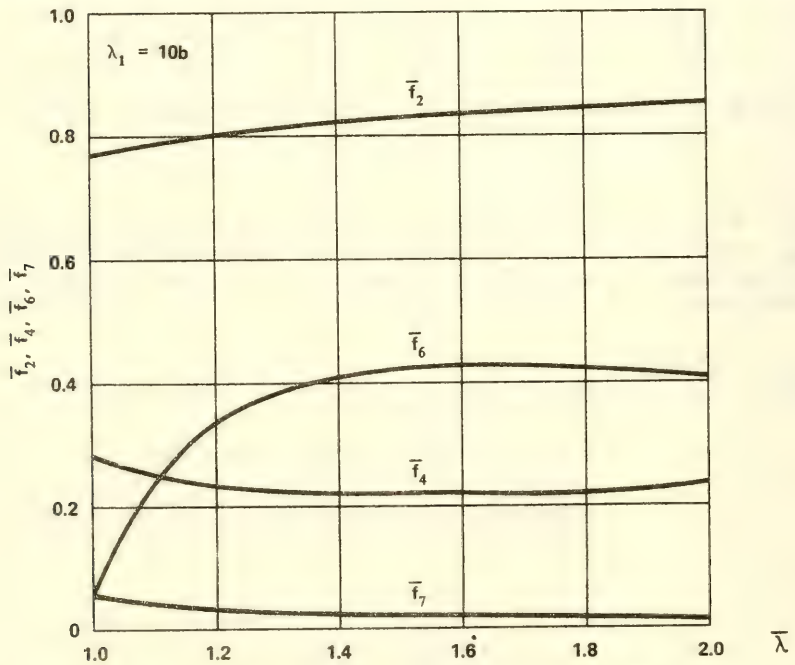


Fig. 6 First- and second-order forces vs. $\bar{\lambda}$ for $\lambda_1 = 10b$

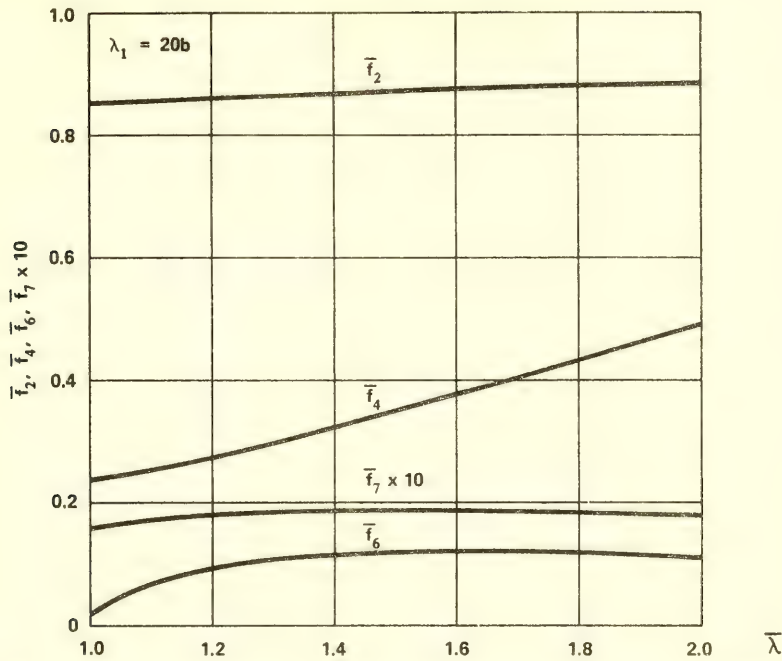


Fig. 7 First- and second-order forces vs. $\bar{\lambda}$ for $\lambda_1 = 20b$

$$A_2 = \frac{2}{g} (\sigma_1 - \sigma_2) \left| \int_b^\infty h_6(\xi) \cos K_6 \xi \, d\xi \right|^2,$$

$$Y_{6b} = \frac{\pi^2}{2g^2} Q_1 Q_2 \sigma_1 \sigma_2 (K_1 - K_2).$$

Furthermore we can reduce the above expression to

$$\begin{aligned} Y_6(x) e^{-j(\sigma_1 - \sigma_2)t} &\sim Y_{6a} \cos \{ K_6 |x| - (\sigma_1 - \sigma_2)t + \theta_6' \} \\ &\quad - Y_{6b} \cos \{ (K_1 - K_2) |x| - (\sigma_1 - \sigma_2)t - (q_1 - q_2) \} \end{aligned}$$

where

$$Y_{6a} = [A_1^2 + A_2^2 + 2A_1 A_2 \cos (q_6 + \theta_6)]^{1/2},$$

$$\theta_6' = \tan^{-1} \left\{ \frac{A_2 \sin \theta_6 - A_1 \sin q_6}{A_2 \cos \theta_6 + A_1 \cos q_6} \right\}.$$

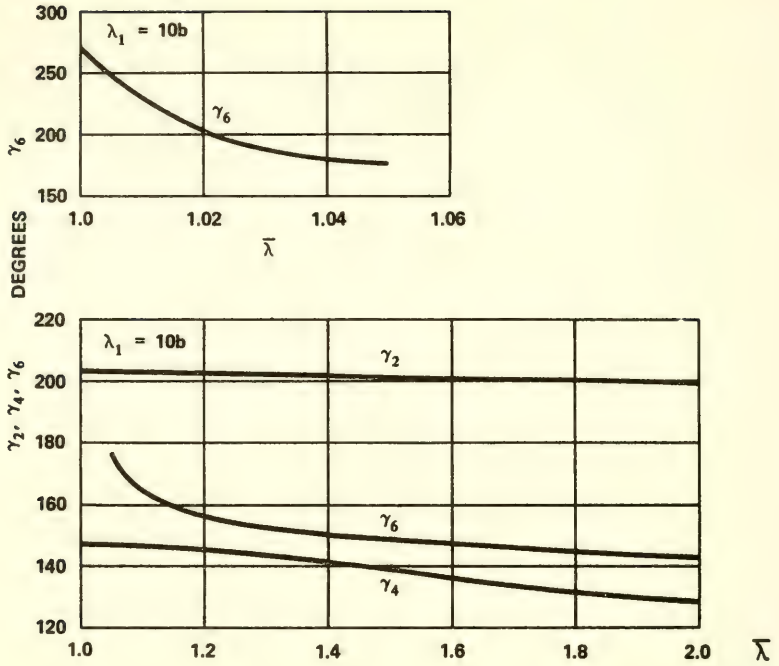


Fig. 8 Phase angles of first- and second-order forces vs. $\bar{\lambda}$ for $\lambda_1 = 10b$

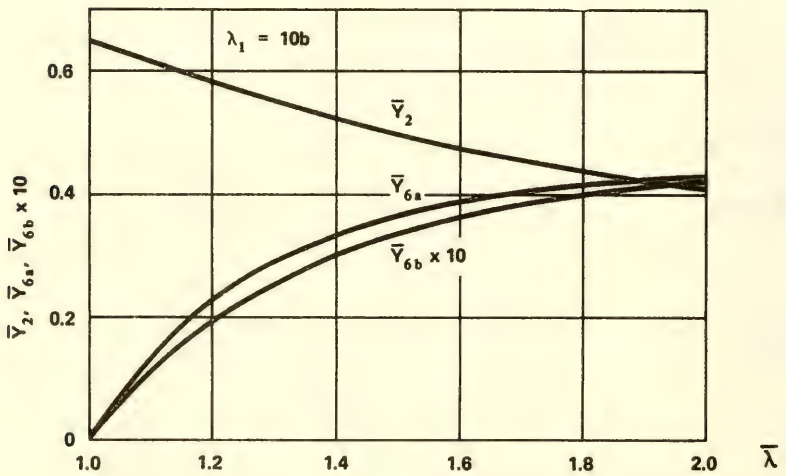


Fig. 9 First- and second-order wave amplitudes at $|x| = \infty$ vs. $\bar{\lambda}$ for $\lambda_1 = 10b$

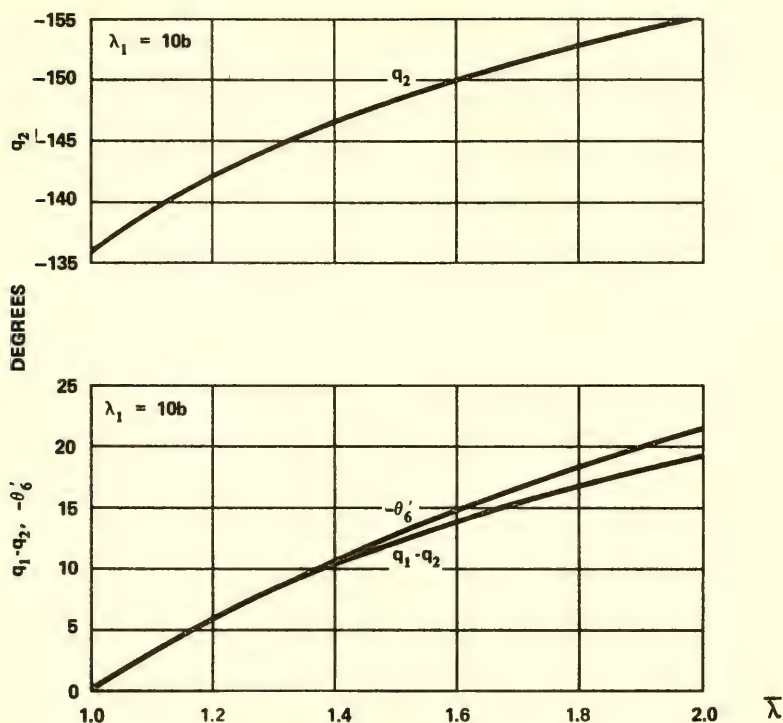


Fig. 10 Phase angles of first- and second-order waves at $|x| = \infty$ vs. $\bar{\lambda}$ for $\lambda_1 = 10b$

We then define

$$\bar{Y}_{6a} = \frac{Y_{6a}}{b} \quad \text{and} \quad \bar{Y}_{6b} = \frac{Y_{6b}}{b}.$$

In Fig. 10 the phase angles q_2 (see Eq. (76)), θ'_6 , and $q_1 - q_2$ are shown as functions of $\bar{\lambda}$ for $\lambda_1 = 10b$.

VII. DISCUSSION

If the forcing motion on a floating body has a very narrow frequency band, most of the second-order hydrodynamic responses occur in a frequency range of about twice the forcing frequencies. However, two components of the second-order force are exceptions to this case. One is the steady-state force and the other is the force with frequency equal to the difference-frequency between a pair of the frequencies in the narrow-band spectrum. If the value of the difference-frequency, $\sigma_1 - \sigma_2$, is very small, the force which

is associated with the difference-frequency changes very slowly in time and often may be treated as a pseudo-steady force. In fact we can show that in the limiting case of $\sigma_1 = \sigma_2$ that the difference-frequency force reduces to the steady-state force or in our notation, $f_6 = f_7$ when $\sigma_1 = \sigma_2$. It is shown in Appendix A that for $\sigma_1 = \sigma_2$

$$\varphi_1 = \varphi_2, \quad \varphi_3 = \varphi_4 = \varphi_5/2, \quad \text{and} \quad \varphi_6 = \varphi_7.$$

Equations (55) through (57) show immediately that $p_1 = p_2$, $p_3 = p_4 = p_5/2$, and $p_6 = p_7$. Substitution of these relations into Eq. (64) leads to $f_6 = f_7$ for $\sigma_1 = \sigma_2$. We observe in Figs. 5, 6, and 7 that as $\bar{\lambda} \rightarrow 1.0$, i.e. $\sigma_2 \rightarrow \sigma_1$, $|f_6| \rightarrow |f_7|$ and in Fig. 8 that $\gamma_6 \rightarrow -\pi/2$ as $\bar{\lambda} \rightarrow 1.0$. Since $f_6|_{\sigma_1=\sigma_2} = |f_6| \sin \gamma_6$ from Eq. (66) and f_7 is negative in this case, we see that $\gamma_6|_{\sigma_1=\sigma_2} = -\pi/2$ in order to maintain the relation $f_6 = f_7$ for $\sigma_1 = \sigma_2$.

For sufficiently small values of $\sigma_1 - \sigma_2$, we can show that the expression of the forcing motion becomes

$$\begin{aligned} \frac{y(t)}{h_0} &= \sin \sigma_1 t + \sin \sigma_2 t \\ &\approx 2 \sin \sigma_2 t \cos \frac{(\sigma_1 - \sigma_2)}{2} t \end{aligned} \quad (80)$$

and the corresponding expression for the hydrodynamic force can be derived from Eqs. (63) and (66) as

$$\begin{aligned} F &\approx \epsilon 2 |f_2| \cos \frac{\sigma_1 - \sigma_2}{2} t \sin (\sigma_2 t + \gamma_2) \\ &+ \epsilon^2 \left\{ 4 |f_4| \cos (\sigma_1 - \sigma_2) t \sin (2\sigma_2 t + \gamma_4) \right. \\ &\left. + |f_6| \sin \gamma_6 \cos (\sigma_1 - \sigma_2) t + f_7 \right\} + O(\epsilon^3). \end{aligned} \quad (81)$$

This is a beat oscillation for small values of $\sigma_1 - \sigma_2$. The response of hydrodynamic forces to this beating motion is made of two kinds of beat oscillations: a slowly-varying sinusoidal oscillation, and a steady component. For comparison purposes the relative magnitudes of the different components of the hydrodynamic force given in Eq. (81) are shown in Table 2 for $\lambda_1 = 10b$ and $\lambda_2 = 11b$ i.e. $\bar{\lambda} = 1.1$. The values in Table 2 are obtained from Fig. 6.

TABLE 2

The magnitudes of hydrodynamic forces for $\lambda_1 = 10b$ and $\overline{\lambda} = 1.1$

$2\overline{f}_2$	1.58
$4\overline{f}_4$	1.00
$\overline{f}_6 \sin \gamma_6 $	0.01
\overline{f}_7	0.04
$(\overline{f}_i = \frac{ f_i }{2\rho gb^2} \quad \text{for} \quad i = 2, 4, 6, 7)$	

It is clear from Table 2 that the first-order force dominates the second-order forces. For instance, if we assume $\epsilon = 0.1$ the ratio of the first-order force to the largest second-order force is $2\epsilon|f_2|/4\epsilon^2|f_4| \approx 16$. It is also clear that the magnitudes of the difference-frequency force and the steady force are much smaller than the first-order force, so they appear unimportant. However, when such forces act upon a body which has very small restoring force for a sufficiently long period of time a considerable excursion from its mean position can occur. One can see from Figs. 5 through 7 that the $|f_6|$ is larger than the $|f_7|$ in $1.0 < \overline{\lambda} < 2.0$. This means that for a sufficiently small value of the difference-frequency an estimate of the maximum "steady" force acting on an oscillating body should include the difference-frequency force.

If we assume that the motion of a wave maker is described by Eq. (80), the expression for the free-surface elevation, $Y(x)$, for large x can be given in the form

$$\begin{aligned} Y(x) \sim & \epsilon 2C_1 \cos \frac{\sigma_1 - \sigma_2}{2} t \cos (K_2|x| - \beta_1 - \sigma_2 t) \\ & + \epsilon^2 \{ 4C_2 \cos (\sigma_1 - \sigma_2) t \cos (4K_2|x| - \beta_2 - 2\sigma_2 t) \\ & + 4C_3 \cos (\sigma_1 - \sigma_2) t \cos (2K_2|x| - \beta_3 - 2\sigma_2 t) \\ & + Y_6(x) \cos (\sigma_1 - \sigma_2) t \} + O(\epsilon^3) \end{aligned} \tag{82}$$

where $C_1, C_2, C_3, \beta_1, \beta_2$, and β_3 are quantities which can be obtained from Eqs. (76) through (78) and $Y_6(x)$ is given by Eq. (79). We can see from the above equation that the far-field outgoing waves are made of four independent wave components. The terms other than the one associated with Y_6 represent beating phenomena with

the beating frequencies of $(\sigma_1 - \sigma_2)/2$ and $\sigma_1 - \sigma_2$. Although the values of C_2 and C_3 are not shown in Fig. 10, they are found from Lee [1968] to be about the same order of magnitude as \bar{Y}_{60} and \bar{Y}_{6b} . This means that the dominant contribution to the free-surface wave elevation comes from the first-order term whose beating frequency is $(\sigma_1 - \sigma_2)/2$.

We can conclude that the hydrodynamic force and the outgoing waves associated with the difference-frequency of two nearly equal frequencies are much smaller than the corresponding first-order quantities and are of the same order of magnitude as the other second-order quantities. An examination of the figures suggest that if the difference-frequency is sufficiently small an estimate of the effective "steady" force can be obtained by doubling the pure steady force. However, since the magnitude of the difference-frequency force is always larger than the steady component this estimate may be a low one.

ACKNOWLEDGMENT

The author would like to express his gratitude to Professors T. F. Ogilvie and J. N. Newman for their encouragement and valuable discussions during the course of this work.

REFERENCES

- Frank, W., "Oscillation of cylinders in or below the free surface of deep fluids," Report 2375, Naval Ship Research and Development Center, 1967, 46 pp.
- Grim, O., "Non-linear phenomena in the behavior of a ship in a seaway," presented at the 12th International Towing Tank Conference, Rome, Italy, 1969.
- Hasselmann, K., "On nonlinear ship motions in irregular waves," J. Ship Res., Vol. 10, No. 1, pp. 64-68, 1966.
- Lee, C. M., "The second-order theory of heaving cylinders in a free surface," J. Ship Res., Vol. 12, No. 4, pp. 313-327, 1968. Also published as Report No. NA-66-7, College of Engineering, University of California, Berkeley, 1966, 151 pp.
- Lighthill, M. J., "On waves generated in dispersive systems by travelling forcing effects, with applications to the dynamics of rotating fluids," J. Fluid Mech., Vol. 27, Part 4, pp. 725-752, 1967.

- Parissis, G. G., "Second order potentials and forces for oscillating cylinders on a free surface," Report No. 66-10, Dept. of Naval Arch. and Marine Engr., MIT, 1966, 141 pp.
- Porter, W. R., "Pressure distributions, added mass, and damping coefficients for cylinders oscillating in a free surface," Inst. Eng. Res., University of California, Berkeley, Series 82, Issue No. 16, 1960, 181 pp.
- Tasai, F., "On the damping force and added mass of ships heaving and pitching," (in Japanese) J. Zosen Kiokai, Vol. 105, pp. 47-56, 1959. Translated in English in Series 82, Issue 15, Inst. of Engr. Res., University of California, Berkeley, 1960, 24 pp.
- Tasai, F. and Takagi, M., "Theory and calculation of ship responses in regular waves," (in Japanese) Symposium on Seaworthiness, Society of Naval Architects of Japan, pp. 1-52, 1969.
- Ursell, F., "On the heaving motion of a circular cylinder," Quart. J. Mech. Appl. Math., Vol. 2, pp. 218-231, 1949.
- Wehausen, J. V. and Laitone, E. V., "Surface waves," Encyclopedia of Physics, Vol. IX, pp. 446-778, Springer-Verlag, Berlin, 1960.

APPENDIX A

Description of the Boundary-Value Problems for the Potentials φ_i for $i = 1, 2, 3, 4$, and 7

The application of the perturbation expansions given by Eqs. (17) and (18) to the exact boundary conditions given by Eqs. (12) and (16) yields the following:

On the free surface:

$$\varphi_{iy}(x, 0) - K_i \varphi_i = 0 \quad \text{for} \quad i = 1 \text{ and } 2, \quad (\text{A-1})$$

where $K_i = \sigma_i^2/g$,

$$\begin{aligned} \varphi_{iy}(x, 0) - 4K_{i-2}\varphi_i = & -j \frac{\sigma_{i-2}}{2g} \left\{ \varphi_{i-2}(x, 0)(\varphi_{(i-2)yy} - K_{i-2}\varphi_{(i-2)y}) \right. \\ & \left. - 2(\varphi_{(i-2)x}^2 + \varphi_{(i-2)y}^2) \right\} \equiv h_i(x) \end{aligned} \quad (\text{A-2})$$

for $i = 3$ and 4 , and

$$\varphi_{7y}(x, 0) = \sum_{k=1}^2 -\frac{\sigma_k}{2g} \operatorname{Re} j \left[j\varphi_k(x, 0)(\bar{\varphi}_{kyy} - K_k \bar{\varphi}_{ky}) \right] \equiv h_7(x) \quad (\text{A-3})$$

where $\bar{\varphi}_k = \varphi_{kc} - j\varphi_{ks}$.

On the body:

$$\varphi_{ix}(x_0, y_0)f'(x_0) - \varphi_{iy} = -b\sigma_i \quad \text{for } i = 1 \text{ and } 2, \quad (\text{A-4})$$

$$\begin{aligned} \varphi_{ix}(x_0, y_0)f'(x_0) - \varphi_{iy} &= -\frac{jb}{2} (\varphi_{(i-2)xy}(x_0, y_0)f'(x_0) - \varphi_{(i-2)yy}) \\ &\equiv m_i(x_0, y_0) \quad \text{for } i = 3 \text{ and } 4, \end{aligned} \quad (\text{A-5})$$

and

$$\begin{aligned} \varphi_{7x}(x_0, y_0)f'(x_0) - \varphi_{7y} &= -\frac{b}{2} \operatorname{Im} j \left[(\varphi_{1xy}(x_0, y_0) + \varphi_{2xy})f'(x_0) - \varphi_{1yy} - \varphi_{2yy} \right] \\ &\equiv m_7(x_0, y_0). \end{aligned} \quad (\text{A-6})$$

In the far field

$$\varphi_{iy}(x, -\infty) = 0 \quad \text{for } i = 1, 2, 3, 4, \text{ and } 7$$

and at $|x| = \infty$ the potentials φ_i for $i = 1, 2, 3$, and 4 should represent outgoing plane waves. For the steady potential φ_7 the condition at $|x| = \infty$ should be determined by the law of mass conservation (see Lee [1968]).

Symmetric flow condition:

$$\varphi_i(x, y) = \varphi_i(-x, y) \quad \text{for } i = 1, 2, 3, 4, \text{ and } 7.$$

In the limiting case of $\sigma_1 = \sigma_2$ the forcing motion given by Eq. (7) reduced to

$$y(t) = 2h_0 \sin \sigma_1 t$$

and if we let $\epsilon = 2h_0/b$, the perturbation expansion given by Eq. (17) reduces to

$$\Phi(x, y, t) = \epsilon \varphi_1(x, y)e^{-j\sigma_1 t} + \epsilon \varphi_3(x, y)e^{-j2\sigma_1 t} + \epsilon^2 \varphi_7(x, y)$$

which is the same expansion as that assumed by Lee [1966]. We can easily establish the identities $\varphi_1 = \varphi_2$ and $\varphi_3 = \varphi_4$. It will now be shown that for $\sigma_1 = \sigma_2$ we also have $\varphi_5 \equiv 2\varphi_3$ and $\varphi_6 \equiv \varphi_7$. Equation (20) gives

$$\begin{aligned} h_5(x) = & -j \frac{\sigma_1}{2g} \left\{ \varphi_1(x, 0)(\varphi_{2yy} - K_2 \varphi_{2y}) \right. \\ & - 2(\varphi_{1x} \varphi_{2x} + \varphi_{1y} \varphi_{2y}) \left. \right\} - j \frac{\sigma_2}{2g} \left\{ \varphi_2(\varphi_{1yy} - K_1 \varphi_{1y}) \right. \\ & - 2(\varphi_{1x} \varphi_{2x} + \varphi_{1y} \varphi_{2y}) \left. \right\}, \end{aligned}$$

so for $\sigma_1 = \sigma_2$

$$h_5(x) = -j \frac{\sigma_1}{g} \left\{ \varphi_1(x, 0)(\varphi_{1yy} - K_1 \varphi_{1y}) - 2(\varphi_{1x}^2 + \varphi_{1y}^2) \right\}.$$

Comparison of this with Eq. (A-2) shows that

$$h_5(x) = 2h_3(x).$$

Equation (22) gives

$$m_5(x_0, y_0) = -j \frac{b}{2} \left\{ (\varphi_{1xy}(x_0, y_0) + \varphi_{2xy})f'(x_0) - \varphi_{1yy} - \varphi_{2yy} \right\},$$

so for $\sigma_1 = \sigma_2$

$$m_5 = -jb \left\{ \varphi_{1xy}(x_0, y_0)f'(x_0) - \varphi_{1yy} \right\}.$$

Comparison of this with Eq. (A-5) shows that $m_5 = 2m_3$. The far field conditions and the symmetric-flow condition for both φ_5 and φ_3 are essentially identical. The above results lead to the conclusion that $\varphi_5 = 2\varphi_3$. φ_6 can be shown to be equal to φ_7 by a similar proof if $h_6(x)$ (Eq. (25) for $\sigma_1 = \sigma_2$) is compared with $h_7(x)$ (Eq. (A-3)) and $m_6(x)$ (Eq. (27) for $\sigma_1 = \sigma_2$) is compared with $m_7(x)$ (Eq. (A-6)).

APPENDIX B

Evaluation of the First-Order Velocity Potential

There are two first-order potentials, φ_1 and φ_2 , involved in this work. Since their solutions are essentially identical (they differ only in the frequencies), φ_1 will be chosen as the representative first-order potential. As shown in Appendix A, the boundary-value problem for φ_1 is

$$\nabla^2 \varphi_1 = 0, \quad (\text{B-1})$$

$$\varphi_{1y}(x, 0) - K_1 \varphi_1 = 0, \quad (\text{B-2})$$

$$\varphi_{1x}(x_0, y_0) f'(x_0) - \varphi_{1y} = -b\sigma_1, \quad (\text{B-3})$$

$$\varphi_{1y}(x, -\infty) = 0, \quad (\text{B-4})$$

$$\varphi_1(x, y) = \varphi_1(-x, y), \quad (\text{B-5})$$

and the radiation condition can be explicitly written as

$$\lim_{x \rightarrow \pm\infty} \text{Re} j(\varphi_{1x} \mp jK_1 \varphi_1) = 0. \quad (\text{B-6})$$

There are two methods for the solution of the above problem. One of them is the method of multipole expansions (see Ursell [1949]) which is essentially an eigenfunction expansion of the unknown function. The other is the method of source distribution (see Frank [1967]) i.e. the method of Green's function. A brief description of the method of multipole expansions will be given. First we consider the problem without the boundary condition on the body given in Eq. (B-3). If we transform the problem into the ζ -plane¹ we find that

$$\nabla^2 M(\lambda, \alpha) = 0, \quad (\text{B-7})$$

$$K_1 a \left\{ \lambda - \sum_{n=1}^{\infty} \frac{(2n+1)a_{2n+1}}{\lambda^{2n+1}} \right\} M(\lambda, 0) - \frac{\partial M}{\partial \alpha} = 0, \quad (\text{B-8})$$

¹Here, it should be recalled that the transformation given by Eq. (2) maps the ξ - and η -axes into the x - and y -axes and maps the contour of the semi-circle in the ζ -plane onto the contour of the cylinder in the z -plane.

$$M(\lambda, \alpha) = M(\lambda, \pi - \alpha), \quad (\text{B-9})$$

and in place of Eq. (B-4) and (B-6) we require

$$M \rightarrow 0 \quad \text{as} \quad \lambda \rightarrow \infty \quad \text{in} \quad -\pi \leq \alpha \leq 0. \quad (\text{B-10})$$

The solution of this problem is

$$M_m(\lambda, \alpha) = \frac{\cos 2m\alpha}{\lambda^{2m}} + K_1 a \left\{ \frac{\sin (2m-1)\alpha}{(2m-1)\lambda^{2m-1}} - \sum_{n=0}^{\infty} \frac{(2n+1)a_{2n+1}}{2m+2n+1} \frac{\sin (2m+2n+1)\alpha}{\lambda^{2m+2n+1}} \right\} \quad (\text{B-11})$$

where m is a positive integer. M_m is often called the multipole of order m . Although this expression for M_m trivially satisfies Eq. (B-6) in the ζ -plane, the expression above still does not represent the outgoing plane waves. To satisfy this radiation condition we introduce a source function $M_0(x, y)$ which satisfies all the required conditions except the boundary condition on the body. The expression for the function M_0 is

$$M_0(x, y) = \int_0^{\infty} \frac{e^{ky} \cos kx}{K_1 - k} dk - j\pi e^{K_1 y} \cos K_1 x \quad (\text{B-12})$$

where \int_0^{∞} means that a Cauchy principal value is to be used. Therefore we represent our solution as

$$\varphi_1 = \sum_{m=0}^{\infty} (b_m + jc_m) M_m(x(\lambda, \alpha), y(\lambda, \alpha)) e^{-jq} \quad (\text{B-13})$$

where b_m and c_m are the unknown strengths of the singularities, q is the phase difference between the motions of the body and the fluid, $b_0 = Q$ = source strength, and $c_0 = 0$. The unknown constants b_m , c_m , and q are to be determined from the boundary condition on the body given by Eq. (B-3).

We introduce the stream function Ψ_1 which is the harmonic conjugate of the velocity potential φ_1 . The Cauchy-Riemann relation gives $\partial\varphi_1/\partial n = \partial\Psi_1/\partial s$ along the contour of the cylinder where s is the arc length of the contour in the counter-clockwise direction. The boundary condition for Ψ_1 on the cylinder can be shown to be

$$\Psi_1(x_0, y_0) = -b\sigma_1 x_0. \quad (\text{B-14})$$

The expression for Ψ_1 in terms of the harmonic conjugates of M_m

denoted by N_m is easily found to be

$$\Psi_1 = \sum_{m=0}^{\infty} (b_m + jc_m) N_m(x(\lambda, \alpha), y(\lambda, \alpha)) e^{-jq}. \quad (B-15)$$

where

$$N_m = -\frac{\sin 2m\alpha}{\lambda^{2m}} + K_1 a \left\{ \frac{\cos (2m-1)\alpha}{(2m-1)\lambda^{2m-1}} - \sum_{n=0}^{\infty} \frac{(2n+1)a_{2n+1}}{2m+2n+1} \frac{\cos (2m+2n+1)\alpha}{\lambda^{2m+2n+1}} \right\} \quad \text{for } m \geq 1, \quad (B-16)$$

and

$$N_0 = - \int_0^{\infty} \frac{e^{ky} \sin kx}{K_1 - k} dk + j\pi e^{K_1 y} \sin K_1 x. \quad (B-17)$$

Substituting Eq. (B-15) into (B-14), we get

$$\sum_{m=0}^{\infty} (b_m + jc_m) N_m(x(\lambda, \alpha), y(\lambda, \alpha)) e^{-jq} = -b\sigma_1 x_0. \quad (B-18)$$

We choose any point on the contour of the cylinder between $\theta = 0$ and $\theta = -\pi/2$, say (x'_0, y'_0) in z -plane and (λ_0, α') in the ζ -plane, to show that

$$e^{-jq} = -b\sigma_1 x'_0 / \left\{ \sum_{m=1}^{\infty} (b_m + jc_m) N_m(\lambda_0, \alpha') + Q N_0(x'_0, y'_0) \right\}. \quad (B-19)$$

Equation (B-19) can be substituted into (B-18) to give

$$\sum_{m=1}^{\infty} A_m N_m(\lambda_0, \alpha) - N_m(\lambda_0, \alpha') \frac{x_0}{x'_0} = N_0(x'_0, y'_0) - N_0(x_0, y_0) \quad (B-20)$$

where

$$A_m = \frac{b_m + jc_m}{Q}.$$

In principle we can choose an infinite number of points on the cylinder $(-\pi/2 < \theta < 0)$ to set up an infinite number of simultaneous equations from Eq. (B-20) for the unknown coefficients A_m . However the

infinite series in Eq. (B-20) is truncated to a finite series to obtain an approximate solution by a matrix inversion. After finding some finite number² of b_m and c_m and using these coefficients in Eq. (B-19) we find the values of Q and q .

APPENDIX C

Solution for the Problem of Sinusoidal Pressure Distribution on a Free Surface

We seek a solution for the following boundary-value problem:

$$\begin{aligned}\nabla^2 W_I(x, y) &= 0 \quad \text{in} \quad y < 0, \\ W_{Iy}(x, 0) - KW_I &= Ae^{jK'|x|}\end{aligned}\tag{C-1}$$

where $K = \omega^2/g$, A is a real constant, and $K' = \omega'^2/g \neq K$. Furthermore we require that

$$W_{Iy}(x, -\infty) = 0,$$

$$W_I \sim Be^{K'y}e^{jK'|x|} \quad \text{as} \quad |x| \rightarrow \infty$$

where B is a complex constant, and

$$W_I(x, y) = W_I(-x, y).$$

If we let

$$W_I = W_{Ic} + jW_{Is},$$

we can easily show that

$$W_{Icy}(x, 0) - KW_{Ic} = A \cos K'x, \tag{C-2}$$

$$W_{Isy}(x, 0) - KW_{Is} = A \sin K'|x|. \tag{C-3}$$

²The exact number is determined in the sense of "an approximate in the mean" for the function on the right-hand side of Eq. (B-20) by the series on the left-hand side.

The value for the function W_{lc} which has all the required properties can be shown to be

$$W_{lc} = \frac{Ae^{K'y}}{K' - K} \cos K'x. \quad (C-4)$$

It takes little more effort to solve for W_{ls} . We find it by using a transform. Let

$$W_{ls}^* = \int_{-\infty}^{\infty} e^{-ipx} W_{ls}(x, y) dx.$$

The Laplace equation requires that

$$-p^2 W_{ls}^* + W_{lsyy}^* = 0$$

or

$$W_{ls}^*(p; y) = c(p) e^{lpy}. \quad (C-5)$$

If this is substituted into the Fourier transform of Eq. (C-3), the left-hand side yields

$$W_{lsy}^* - KW_{ls}^* = (|p| - K)c(p)$$

and the right-hand side yields

$$\begin{aligned} A \int_{-\infty}^{\infty} e^{-ipx} \sin K'|x| dx &= 2A \int_0^{\infty} e^{-ipx} \sin K'x dx \\ &= \frac{A}{i} \int_0^{\infty} (e^{i(K'-p)x} - e^{i(K'+p)x}) dx = \frac{-2AK'}{p^2 - K'^2}, \end{aligned} \quad (C-6)$$

where the apparent improper integral above is interpreted as a generalized function.³ Thus we find that

$$(|p| - K)c(p) = \frac{-2AK'}{p^2 - K'^2} \quad \text{or} \quad c(p) = \frac{-2AK'}{(p^2 - K'^2)(|p| - K)}$$

³Another way of interpreting this is that of Lighthill [1967] who let $\omega' = \omega_0 + j\epsilon$, $\epsilon \geq 0$ so that $e^{jK'|x|} = e^{jK'_0|x|} e^{-\mu x}$ where $K'_0 = (\omega_0^2 - \epsilon^2)/g$ approaches K' when $\mu (= \epsilon 2\omega_0/g) \rightarrow 0$.

If this expression is substituted into (C-5) and the transform is converted we find that

$$\begin{aligned}
 W_{1s}(x, y) &= -\frac{AK'}{\pi} \int_{-\infty}^{\infty} \frac{e^{|p|y}}{(p^2 - K'^2)(|p| - K)} e^{ipx} dp \\
 &= -\frac{2AK'}{\pi} \int_0^{\infty} \frac{e^{py} \cos px}{(p^2 - K'^2)(p - K)} dp \\
 &= -\frac{A}{\pi} \int_0^{\infty} e^{py} \cos px \left\{ \frac{1}{(K + K')(p + K')} \right. \\
 &\quad \left. + \frac{1}{(K' - K)(p - K')} - \frac{2K'}{(K'^2 - K^2)(p - K)} \right\} dp. \quad (C-7)
 \end{aligned}$$

Apparently there are poles at $p = K'$ and $p = K$. However if the inverse transform of the right-hand side of Eq. (C-6) is taken, it is readily seen that the integral must be integrated as a principal-value integral in order to recover the original function $A \sin K'|x|$. This means that the integral in Eq. (C-7) associated with the second and third terms in the square bracket should be taken as P. V. integrals.

If we let

$$I_1 \equiv \int_0^{\infty} \frac{e^{py} \cos px}{p + K'} dp = \text{Re}_i \int_0^{\infty} \frac{e^{-ipz}}{p + K'} dp,$$

and make the change of variable $t = i(p + K')x$, we can show that

$$I_1 = \text{Re}_i e^{iK'z} \int_{iKz}^{\infty} \frac{e^{-t}}{t} dt = \text{Re}_i [e^{iK'z} E_1(iK'z)].$$

Again the change of variable $t = i(p - K')z$ enables us to show that

$$\begin{aligned}
 I_2 &= \int_0^{\infty} \frac{e^{py} \cos px}{p - K'} dp = \text{Re}_i \int_0^{\infty} \frac{e^{-ipz}}{p - K'} dp \\
 &= \text{Re}_i [e^{-iK'z} E_1(-iK'z) \mp i\pi e^{-iK'z}]
 \end{aligned}$$

where \pm signs correspond to the case of $x \geq 0$. Similarly the change of variable $t = i(p - K)z$ in $I_3 \equiv \int_0^{\infty} (e^{py} \cos px)/(p - K) dp$ leads to

$$I_3 = \text{Re}_i [e^{-iKz} E_1(-iKz) \mp i\pi e^{-iKz}]$$

for $x \geq 0$. This integral is the last term in Eq. (C-7), and we observe that $\lim_{|x| \rightarrow \infty} I_3 = -\pi e^{Ky} \sin K|x|$. This implies the existence of a sinusoidal wave with wave number K in the far field. It obviously violates the radiation condition that the outgoing waves have wave number K' . However a careful examination of the integral I_3 shows that it is just one of the homogeneous solutions of the problem which can be discarded, if desired, because of the radiation condition. Thus substituting the expressions obtained above for I_1 and I_2 into Eq. (C-7) and discarding the last integral in that equation, we find that

$$\begin{aligned} W_{Is}(x, y) &= -\frac{A}{\pi} \left[\frac{I_1}{K+K'} + \frac{I_2}{K'-K} \right] \\ &= -\frac{A}{\pi} \operatorname{Re}_i \left[\frac{e^{iK'z} E_1(iK'z)}{K+K'} + \frac{e^{-iK'z} E_1(-iK'z)}{K'-K} \right] + \frac{Ae^{K'y}}{K'-K} \sin K'|x|. \end{aligned} \quad (C-9)$$

We combine Eqs. (C-4) and (C-9) to finally obtain

$$\begin{aligned} W_I(x, y) &= \frac{Ae^{K'y} e^{jK'|x|}}{K'-K} \\ &\quad - j \frac{A}{\pi} \operatorname{Re}_i \left[\frac{e^{iK'z} E_1(iK'z)}{K+K'} + \frac{e^{-iK'z} E_1(-iK'z)}{K-K'} \right]. \end{aligned} \quad (C-10)$$

Since $\lim_{|x| \rightarrow \infty} e^{\pm iz} E_1(\pm iz) = 0$, we see that

$$\lim_{|x| \rightarrow \infty} W_I = \frac{A}{\pi} \frac{e^{K'y}}{K'-K} e^{jK'|x|}$$

as is required.

* * * * *

DISCUSSION

Edwin C. James
California Institute of Technology
Pasadena, California

I would like to direct a question to Dr. Lee concerning the pure steady force. Apparently this type of force can arise in free surface problems and is attributed to a mean drift of mass in the direction of wave propagation. The action of such a force applied to an unrestrained body results in a sinkage or a lift. The question is then, how does one physically explain the steady force when the symmetry of the problem dictates that the mass transport at the station $x = 0$ should be zero?

* * * * *

REPLY TO DISCUSSION

Choung Mook Lee
Naval Ship Research and Development Center
Washington, D.C.

A mass transport phenomenon arises in the higher-order theory of surface waves (see, e.g. Wehausen and Laitone [1960, pp. 660-661]). Since the present work deals with a second-order problem of free-surface waves, it may be expected that mass-transport will occur in the present problem also. Although I have not touched upon this subject in the text, I discussed it in some detail in my previous work (Lee [1968, pp. 317-318]).

As the discussor pointed out, there is no mass flux across the y -axis. Then, the question arises as to the origin of the mass to supply mass transport. I answered this question in this previous work by showing that the role of the steady potential $\varphi_7(x,y)$ is to counteract the mass transport phenomenon. This means that φ_7 should behave like a steady sink whose strength is equal to the total mass drift through two vertical control planes encompassing the cylinder, divided by 2π . The lowest-order contribution from φ_7 to the steady force is fourth order, as is proved by Bernoulli's equation. Thus, the second-order steady force still exists while the mass transport phenomenon is nullified by the pure steady potential φ_7 .

HYDRODYNAMICS IN THE OCEAN ENVIRONMENT

Friday, August 28, 1970

Afternoon Session

Chairman: T. Y. Wu
California Institute of Technology

	Page
The Drifting Force on a Floating Body in Irregular Waves J. H. G. Verhagen, Netherlands Ship Model Basin, The Netherlands	955
Dynamics of Submerged Towed Cylinders M. P. Païdoussis, McGill University	981
Hydrodynamic Analyses Applied to a Mooring and Positioning of Vehicles and Systems in a Seaway P. Kaplan, Oceanics	1017
Wave Induced Forces and Motions of Tubular Structures J. R. Paulling, University of California, Berkeley	1083
Simulation of the Environment and of the Vehicle Dynamics Associated with Submarine Rescue H. G. Schreiber, Jr., J. Bentkowsky, and K. P. Kerr, Lockheed Missiles and Space Company, Sunnyvale	1111

THE DRIFTING FORCE ON A FLOATING BODY IN IRREGULAR WAVES

J. H. G. Verhagen
Netherlands Ship Model Basin
The Netherlands

I. INTRODUCTION

A floating body in waves experiences a hydrodynamic pressure force which is exerted by the surrounding fluid. Several factors contribute to this wave pressure. One of them is undoubtedly the conventional unsteady exciting force, which makes the body oscillate at frequencies in the region comprising the bulk of the energy containing waves.

Another factor originates from higher order forces due to various non-linear effects. In general these non-linear effects are too small to influence the high-frequency motions of the body. They can, however, be of importance in that part of the frequency domain in which the wave energy is very small, i.e. in the low-frequency range, in particular if one of the natural frequencies of oscillation of the body lies in that range.

In the limiting case -- zero frequency -- one arrives at the well-known drifting force.

It will be obvious, to assume that the force on a floating body in irregular waves comprises not only a steady part but also a slowly varying part, slow in comparison with the mean period of the wave spectrum. The steady as well as the slowly varying part of the wave force, both of which are proportional to the square of the wave height, are denoted by "drifting force." The present paper is concerned with the slow drift oscillation of a moored vessel in irregular waves. It is based on general observations revealed by an extensive test program on the behavior of moored bodies in a seaway.

II. GENERAL OBSERVATIONS OF TEST RESULTS

A study of the test results on the behavior of moored floating bodies in irregular seas revealed the following general observations:

1. The horizontal modes of motion -- surge, sway and yaw -- show two separate frequency regions. A low frequency region corresponding to the low natural frequencies of the moored system, and a frequency region corresponding to those of the energy containing waves.
2. The long periodic motion is excited by waves or by a wave group with amplitudes high compared to the mean wave height. In the considered cases, where a linear stiffness of the mooring system is employed, it appeared that the amplitude of the long periodic motion for a given vessel and mooring system is proportional to the square of the significant wave height divided by the mean wave period $\frac{H_s^2}{T_w}$ for various long crested seaways coming from a given direction.
3. For a given body and mooring system tested in various seaways no clear relation could be discovered between the time averaged excursion from the equilibrium position in still water and the amplitude of the long periodic motion.

These observations are obtained from extensive model tests conducted in the Seakeeping Laboratory of the N.S.M.B. at Wageningen.

The behavior is not unique to moored vessels. Also the towing force of a vessel towed in irregular seas show the same tendency as well as for instance, the slow oscillations in torque and thrust of the propeller of a self-propelled model as observed in the seakeeping model tests.

III. DISCUSSION OF THE RESULTS

The third point of the above mentioned observations deserves particular attention. The drifting force on a floating body in regular waves -- the time averaged position of the body is fixed in space -- is dependent on the joint action of waves and body motions. The force is proportional to the square of the wave height and dependent on the phase between wave and vessel motion.

If we consider an irregular wave as build up of a regular wave whose amplitude is a slowly varying function of time (slow as compared to the wave period) and a stochastic variable phase, the corresponding energy spectrum will be narrow. The drifting force on the floating body in that case will show the same dependency of the time as the square of the wave amplitude. The amplitude of modulation will be the same order of magnitude as the time averaged drift force.

For a given moored system with approximately linear spring stiffness and damping coefficient the same linear relationship must be found between mean excursion and low frequency amplitude of motion for various seaways. This appears not true. Especially in heading waves large discrepancies can occur. From this observation I am led to suppose that it will be not allowed to describe a practical wave spectrum by a slowly modulated regular wave in order to explain the obtained test results.

Based on the mentioned observations I am led to suggest the following hypothesis.

Hypothesis: The wave forces on a moored body in irregular waves which are responsible for the excitation of the mass-spring system in its resonance frequency are the second order low-frequency wave forces on the body in fixed condition, i.e. the drift force due to the reflection of waves.

The influence of the ship motions can be neglected.

One of the conclusions of this hypothesis is that the exciting force for the long-periodic motion is a function of wave characteristics and shape of the body alone, and not dependent on the mooring system or on the weight distribution of the moored body.

The hypothesis is supported by numerical motion calculation for comparison with experiments, which will be shown later on. It is needed however to extend the number of comparisons in order to obtain the restrictions of the proposition.

The proposition can be made acceptable in the following way: Suppose the irregularity of the wave could be described by a more or less regular wave pattern in which a few discrete steep waves are present. Intuitively it can be stated that the occurrence of a few high waves in an otherwise nearly regular wave pattern gives rise to some violent ship motions. Through inertia effects these motions occur mostly after the corresponding high waves have passed the vessel.

Hence, interaction between the high waves and the resulting motion on the pressure distribution around the ship's hull is drastically reduced, by the mentioned retardation between exciting force and resulting motion. Hence, the effect of such a single high wave on the floating body is consequently restricted to the instantaneous effect, i.e. the effect of the wave reflection, on a fixed body. The corresponding exciting force due to reflection is only dependent on body form and wave characteristics.

Conclusion: The mean drifting force on a floating body in irregular waves is dependent on the joint action between waves and body motion.

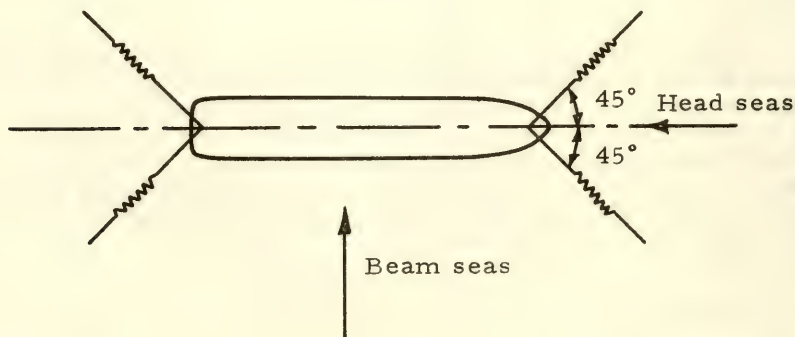
The slow drifting oscillations of a moored vessel are caused by forces due to the reflection of the waves against the fixed obstacle.

The remarkable observation that the amplitude of the long-periodic motion for a given body and mooring system in various seaways of given direction is proportional to $\zeta_{w1/3}^2 / \bar{T}$ can now be explained as follows: The force due to reflection of irregular waves against a fixed obstacle is proportional to $\zeta_{w1/3}^2$ if the body dimensions (L) in the wave direction is not too small compared to the mean wave length λ ($L/\lambda > \frac{1}{2} \pi$). A "high" wave can be defined more formally as a wave with amplitude a fixed number times the significant wave height. The change of occurrence per unit time of our so-called "high" wave is then proportional to $1/\bar{T}$ provided all of the considered random waves are Gaussian distributed, are at least distributed in the same way. If the combination of floating body and mooring system is considered as a mass-spring system with linear stiffness and damping coefficients the resulting long-periodic motions will be proportional to $\zeta_{w1/3} / \bar{T}$. In consequence of the many assumptions made in the above reasoning, one should be careful to adapt the explanation without reservation. A firm foundation is needed.

IV. MODEL TEST RESULTS

An extensive test program has been carried out in the Sea-keeping Laboratory of the N.S.M.B. on a number of models in order to obtain systematic information on the station-keeping abilities of moored vessels in a seaway. Some results of motion tests on one of the vessels will be given in this paper.

The vessel is moored between four horizontal linear springs and tested in various seaways approaching from ahead and from abeam. A sketch of the mooring system is given below.



The stiffness of each spring amounted to 5 tons/m. and is independent of the elongation. The main particulars of the vessel are:

Length - beam ratio	= 5.3
Beam - draft ratio	= 3.65
Block coefficient	= 0.750
Midship section coefficient	= 0.997
Waterplane coefficient	= 0.896

Wave spectra were produced similar in shape to those analysed by Pierson and Moskowitz for fully developed seas. These spectra can be described by:

$$S_{\zeta}(\omega) = \frac{A}{\omega^5} e^{-B/\omega^4}$$

Both the produced and the hypothetical spectra are given in the Figs. 1 through 5.

The significant wave height is defined as:

$$\zeta_{w 1/3} = 4\sqrt{m_0}$$

The average wave period is

$$\bar{T} = 2\pi \frac{m_0}{m_1}$$

where

$$m_k = \int_0^{\infty} \omega^k S_{\zeta}(\omega) d\omega$$

The distribution of the wave elevations confirm well to the normal probability distribution.

The motions of the vessel and the forces in the horizontal springs were measured in three irregular head seas and three irregular beam seas each with different characteristics. The duration of each test run corresponded to approximately half an hour for the full scale vessel. This time period is considered to be sufficiently long for a reliable statistical treatment of the recorded quantities. A typical recording of a horizontal motion of the moored vessel is given in Fig. 6. A low-frequency motion in the natural period of the ship-spring system is present upon which high-frequency motions are superimposed. The spectral density of the surge and sway motions are given in Figs. 7 through 12. The distribution of the forces and of the motions deviates from the normal distribution though in many cases the deviation is not large.

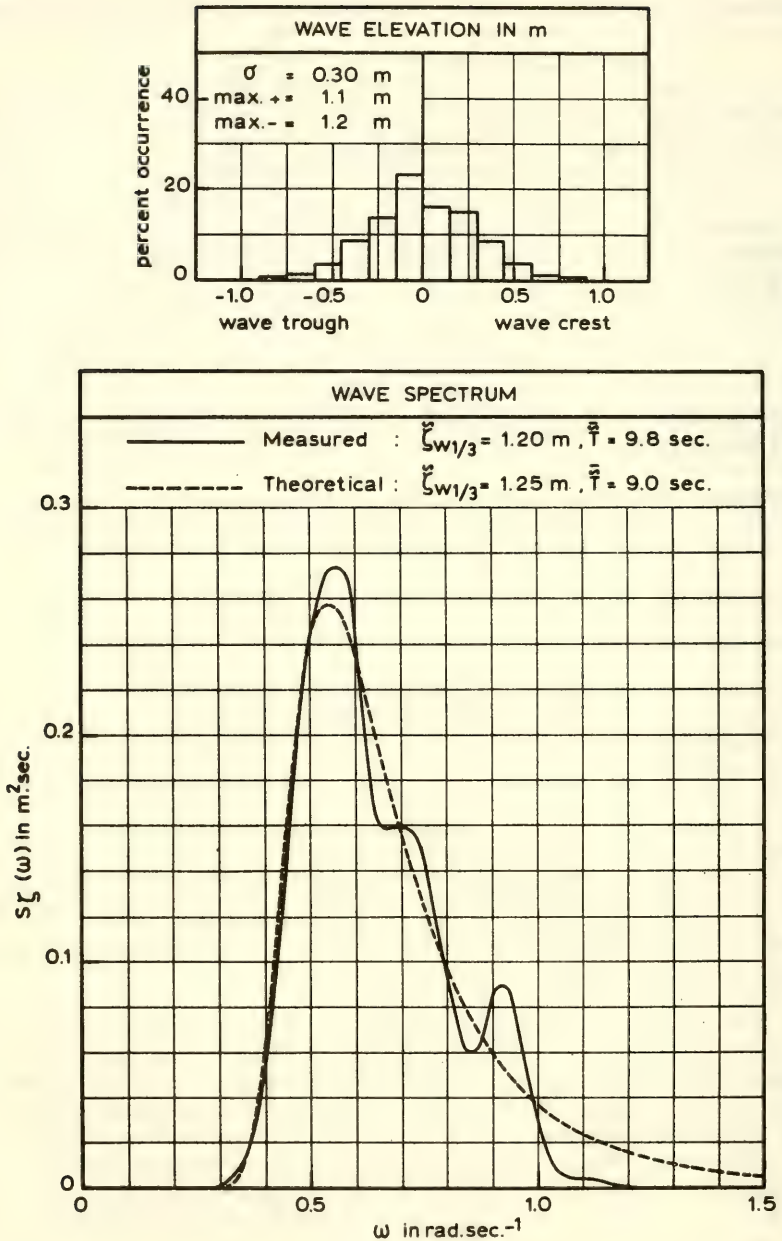


Fig. 1. Wave distribution and spectrum

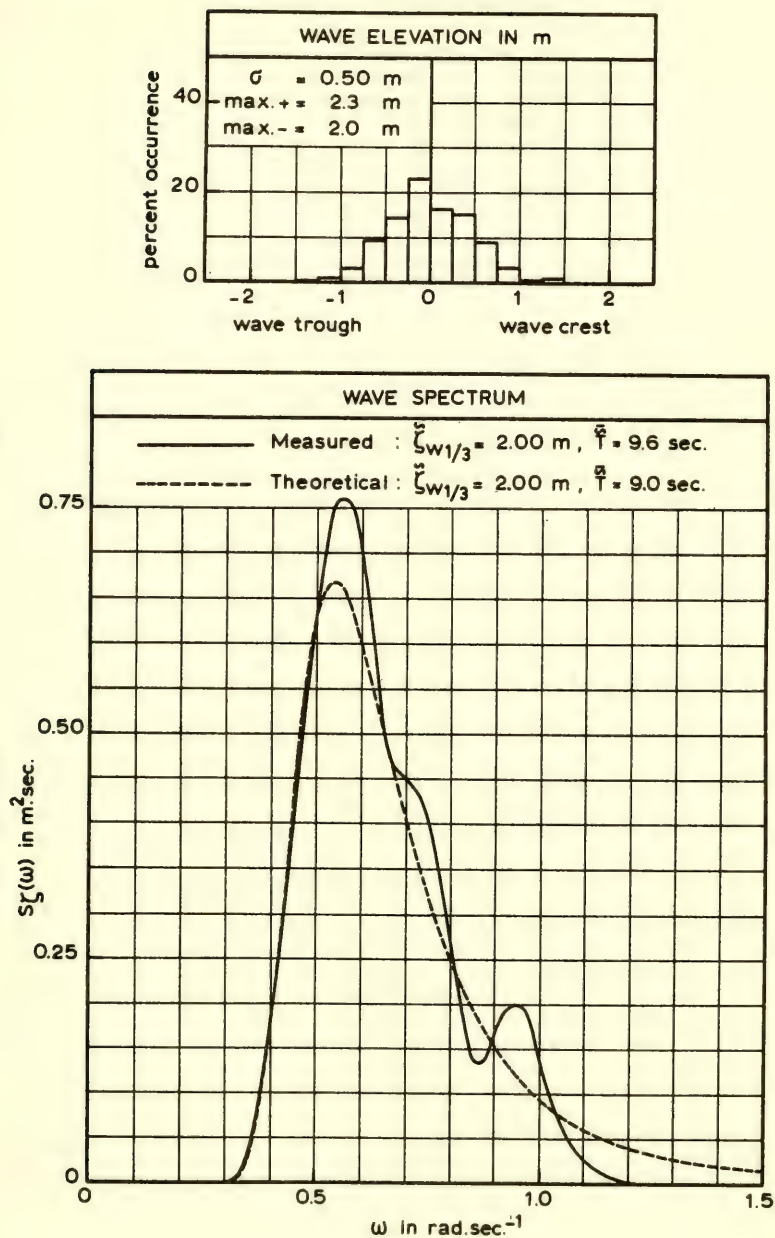


Fig. 2. Wave distribution and spectrum

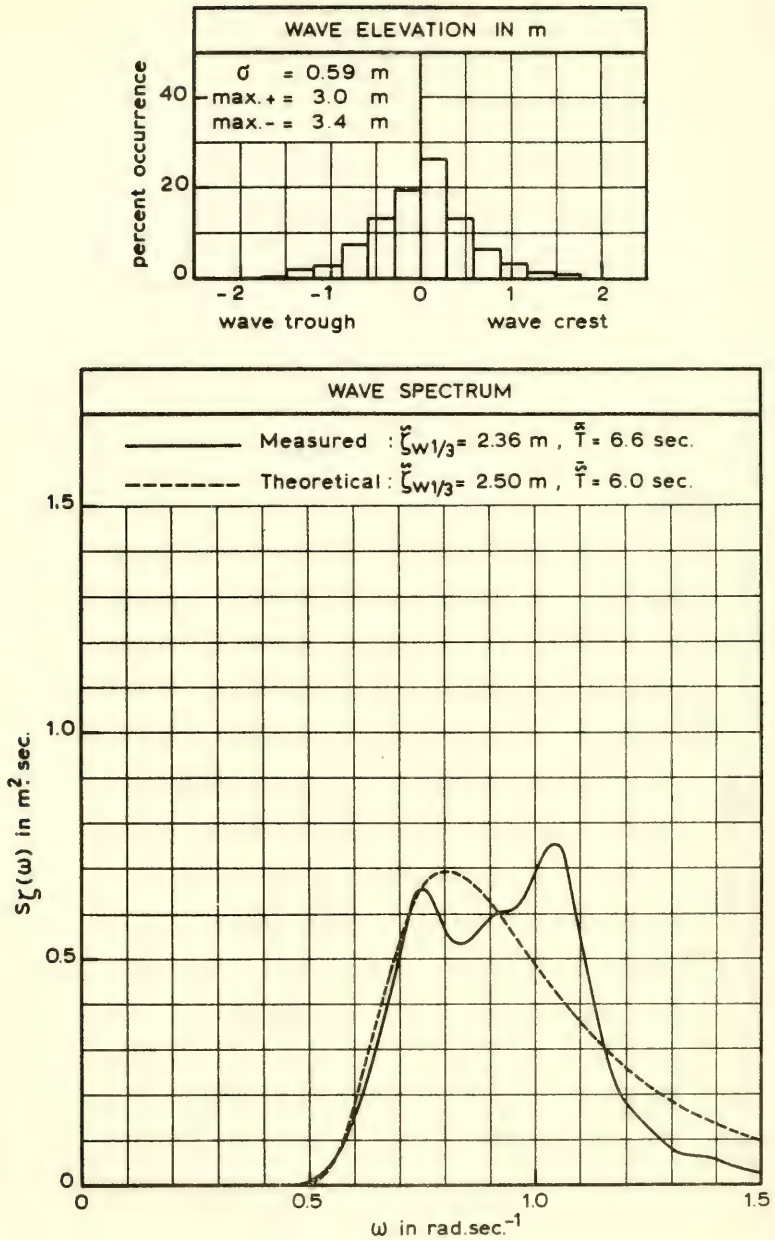


Fig. 3. Wave distribution and spectrum

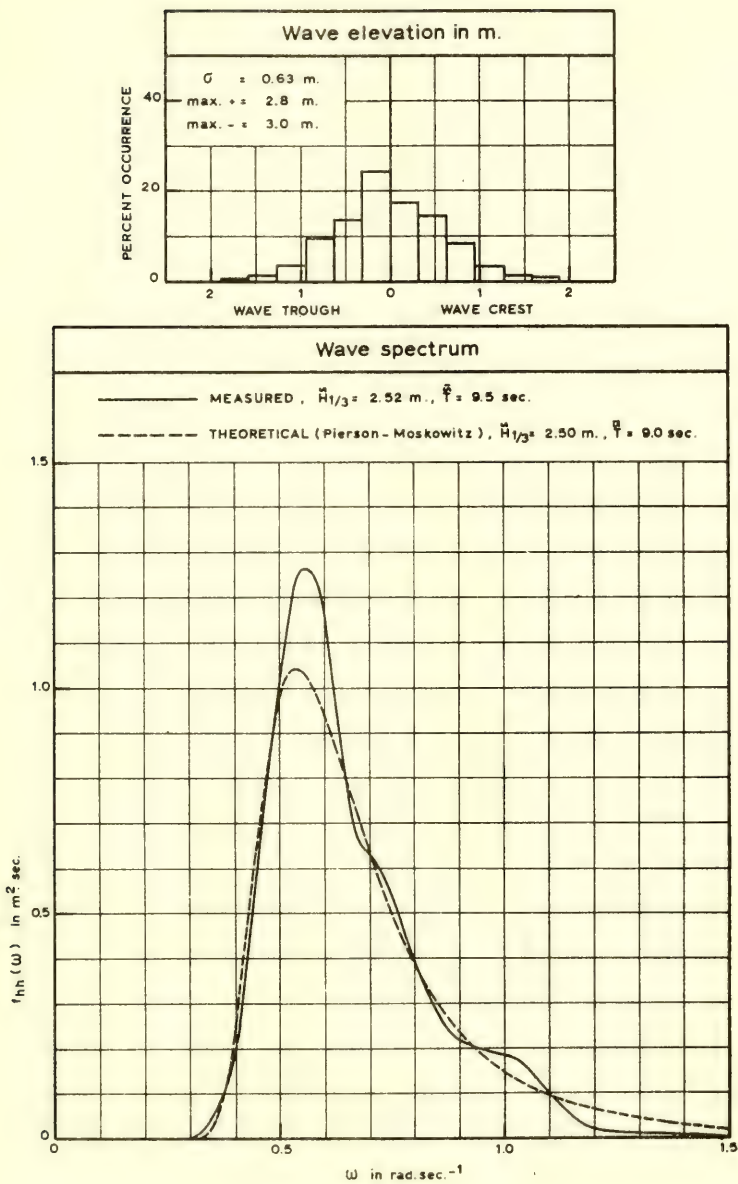


Fig. 4. Wave distribution and spectrum

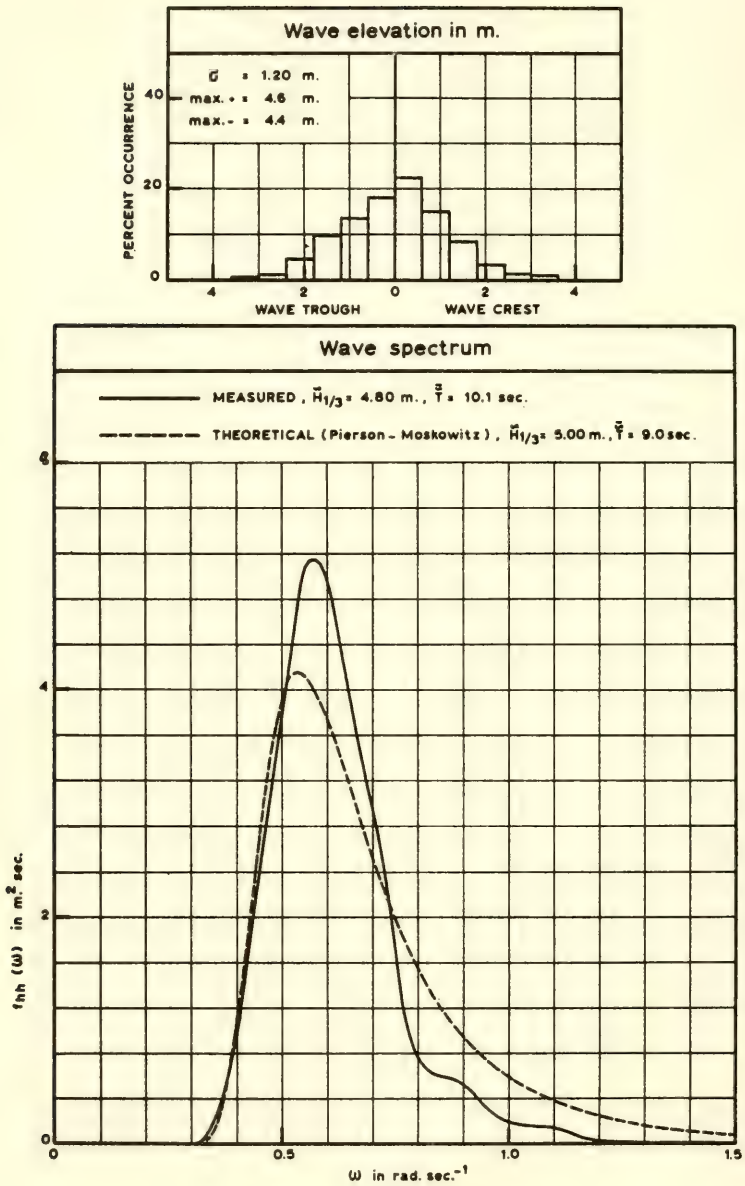


Fig. 5. Wave distribution and spectrum

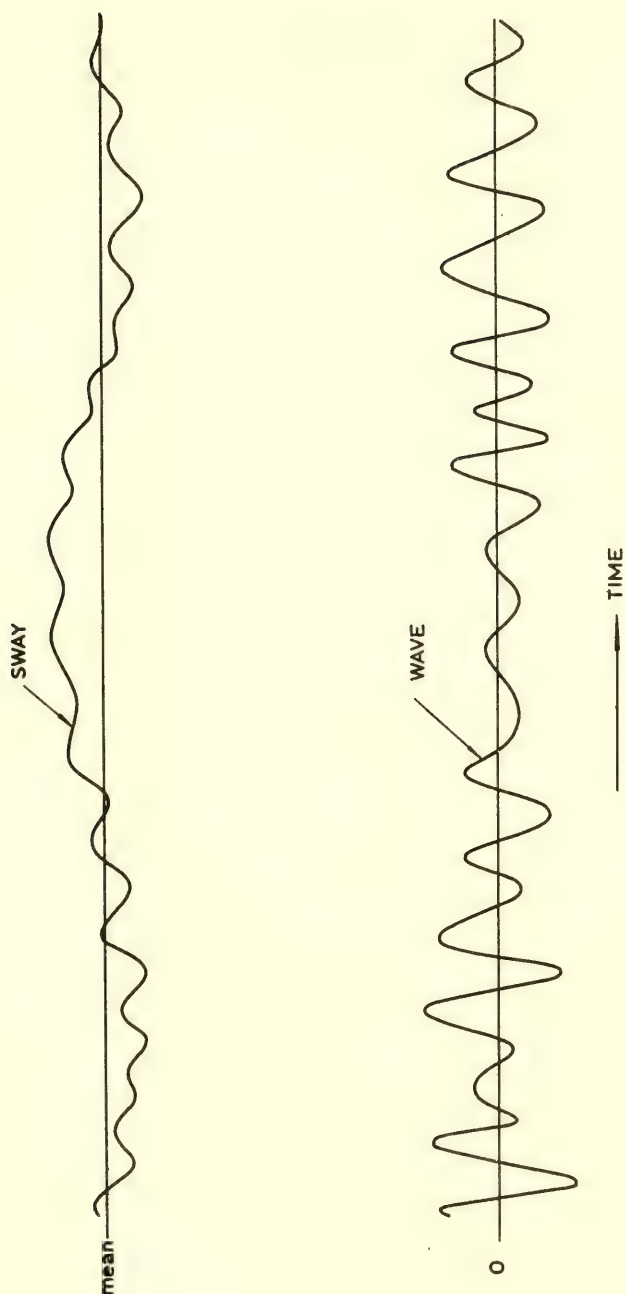


Fig. 6. Irregular wave and sway motion

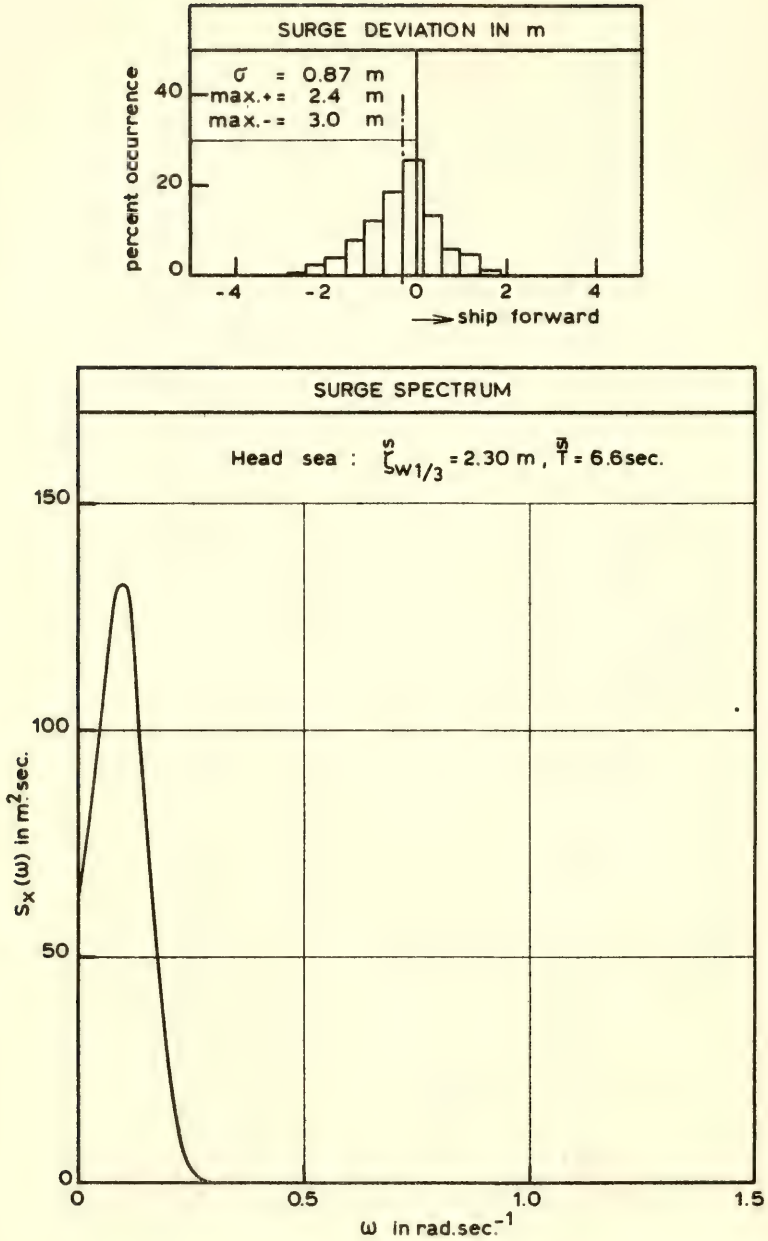


Fig. 7. Distribution and spectrum of surge

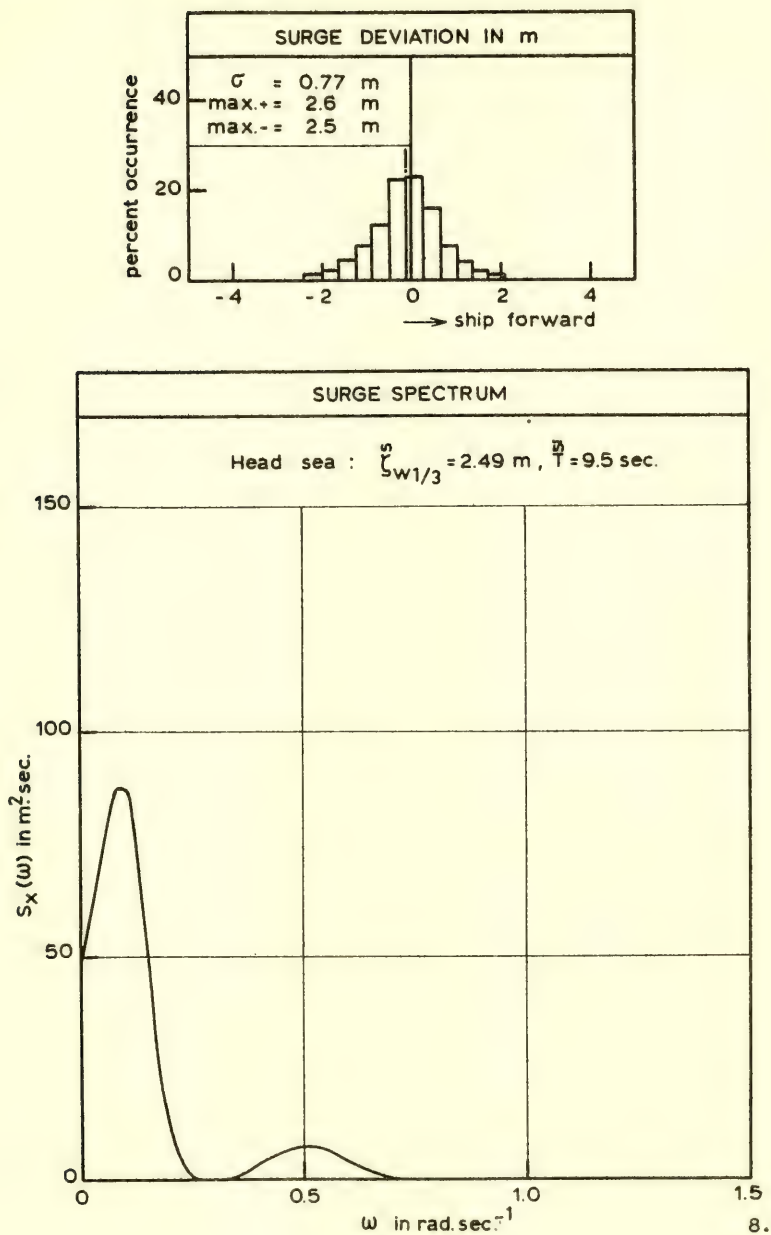


Fig. 8. Distribution and spectrum of surge

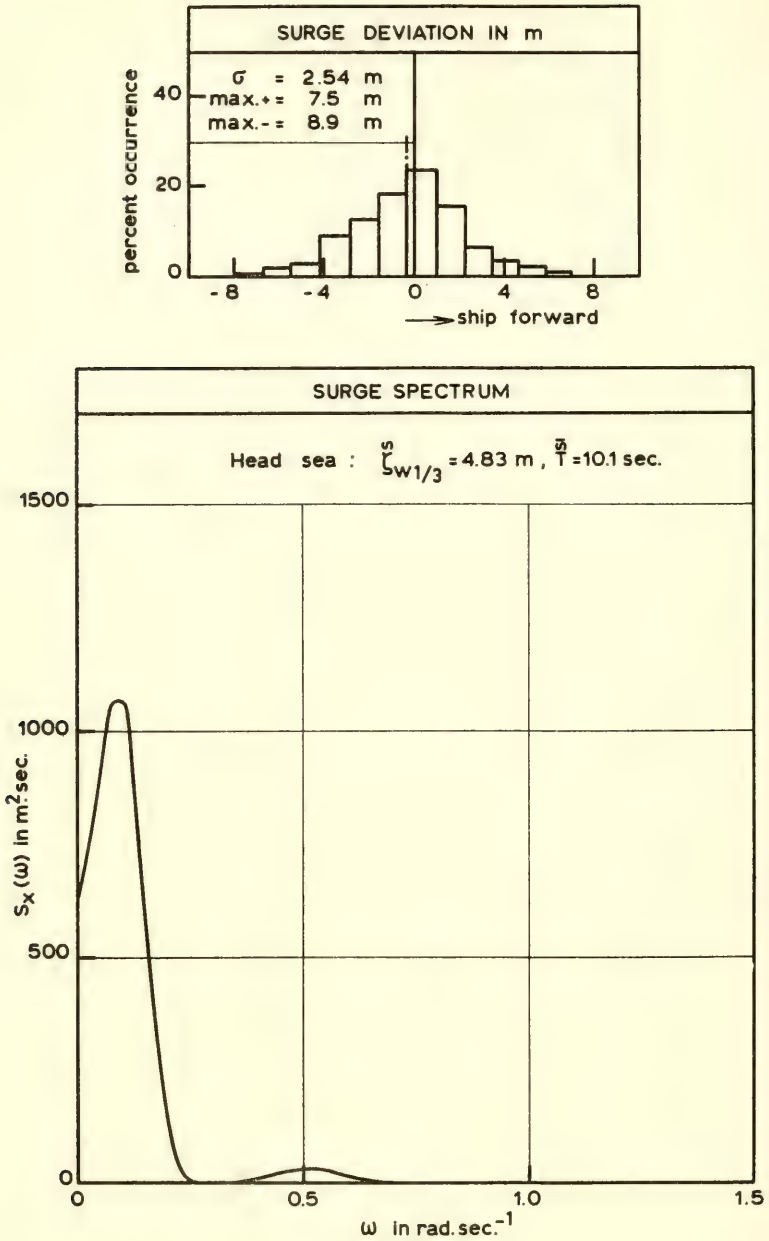


Fig. 9. Distribution and spectrum of surge

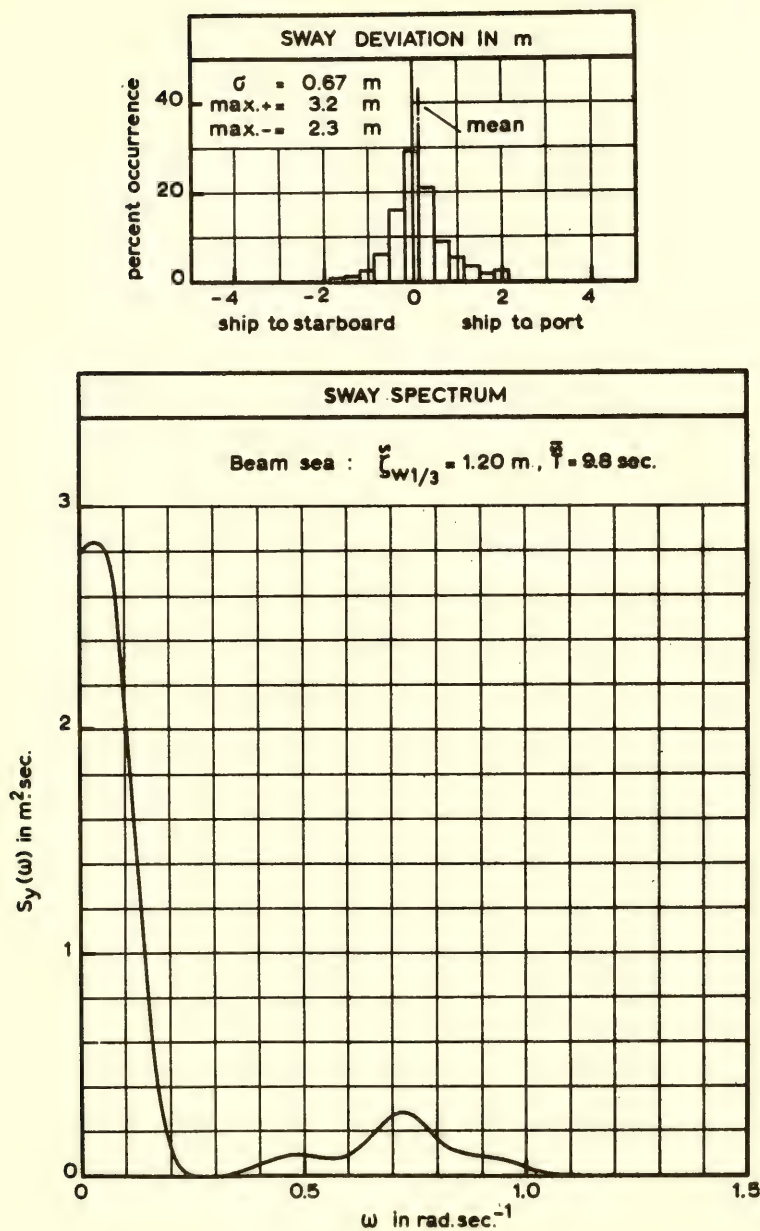


Fig. 10. Distribution and spectrum of sway

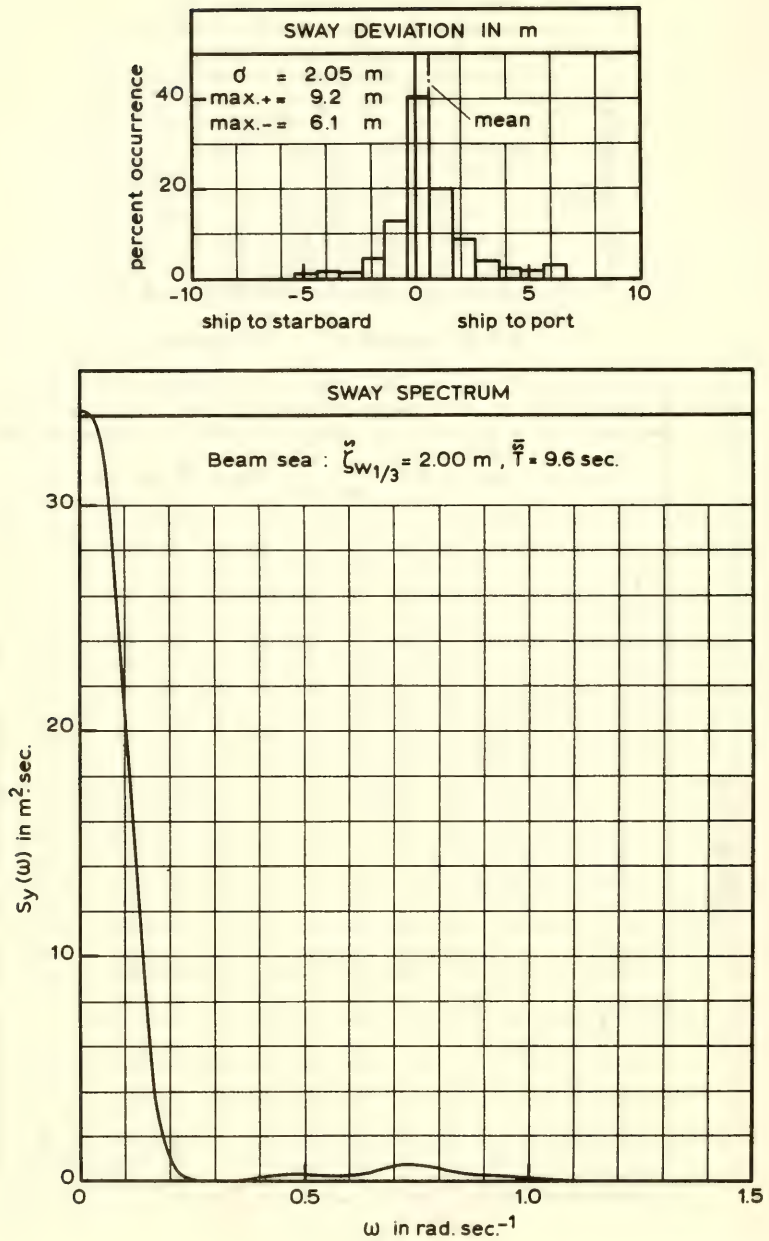


Fig. 11. Distribution and spectrum of sway

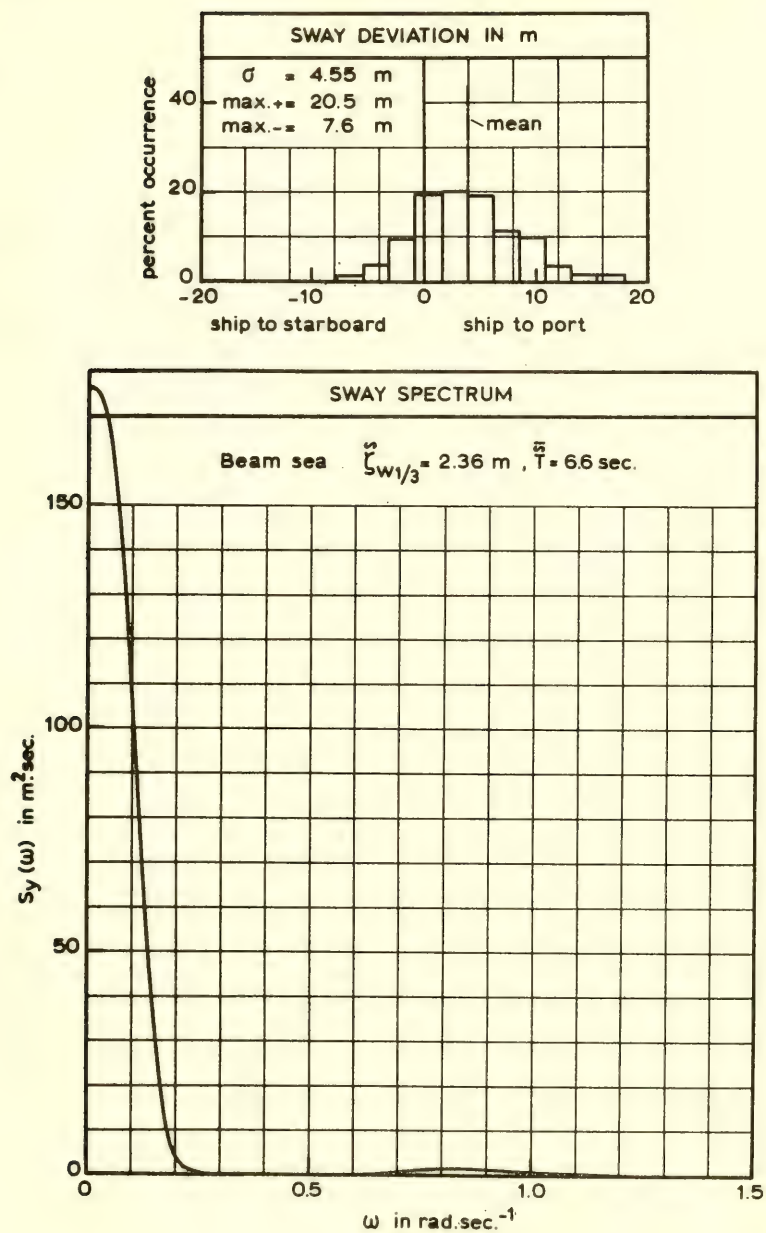


Fig. 12. Distribution and spectrum of sway

V. COMPARISON BETWEEN EXPERIMENTAL RESULTS AND CALCULATIONS

Some tentative calculations have been carried out amplifying and illustrating the aforementioned suppositions.

Mean Drifting Force

The mean drifting force on the moored vessel in the long-created irregular waves has been determined by a linear superposition of mean drifting forces in the regular wave components of the known wave spectrum. As has been shown by Maruo [1] a.o. the principle of superposition can also be applied to determine the non-linear mean drifting force. For head seas the mean longitudinal drifting force is

$$\overline{F}_x = \frac{4\rho g B^2}{L} \int_0^\infty \frac{F_x(\omega)}{\rho g \zeta_0^2 B^2 / L} S_\zeta(\omega) d\omega \quad (1)$$

In beam seas the mean lateral drifting force is

$$\overline{F}_y = 2\rho g L \int_0^\infty \frac{F_y(\omega)}{\frac{1}{2}\rho g \zeta_0^2 L} S_\zeta(\omega) d\omega \quad (2)$$

Formulas for the mean drifting force in regular waves on freely floating, completely restrained or elastic moored bodies are obtained by Maruo [2] and Newman [3]. Numerical calculations are usually carried out on specific formulas for the drifting force on a slender body. [3] As is well known, the agreement of these calculations with experiment is on the whole not very satisfactory. The slender body approximation results f.i. in a vanishing mean lateral drifting force. Therefore an engineering approach is preferred using available experimental data on a similar ship form. The estimated curves of the longitudinal drifting force in regular head waves at zero forward speed and the transverse force in beam waves are given in Figs. 13 and 14. Using these data the expressions (1) and (2) for the mean drifting force in irregular waves can be solved. The results compared with the experimental results are shown in Table I. The agreement is reasonable.

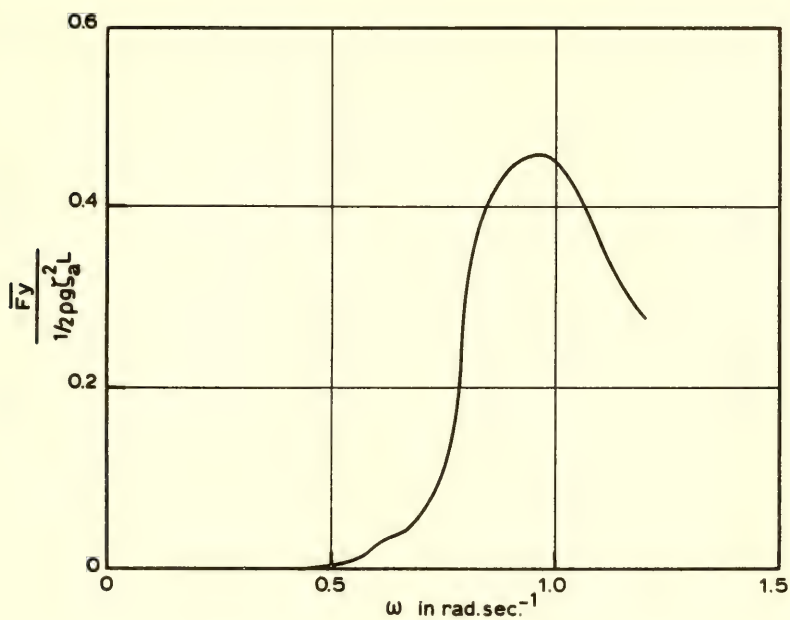


Fig. 13. Longitudinal drift force for head seas

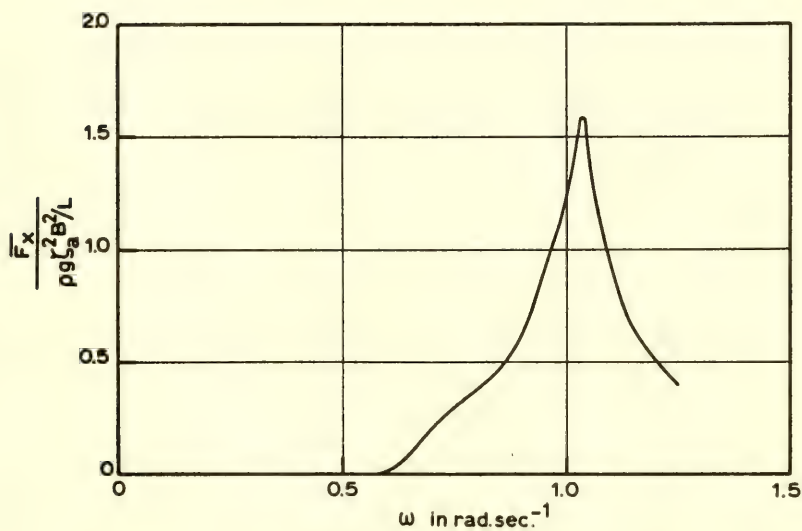


Fig. 14. Lateral drift force for beam seas

TABLE I

Wave characteristics			Mean drifting forces in tons			
Significant height $\zeta_{w/3}$ in m	Average period \bar{T} in sec	Wave direction	Longitudinal force measured	Longitudinal force calculated	Transverse force measured	Transverse force calculated
2.30	6.6	head	2.9	3.4		
2.49	9.5	head	1.2	1.1		
4.83	10.1	head	3.3	2.7		
1.19	9.8	beam			1.4	1.7
1.96	9.6	beam			4.9	5.6
2.30	6.6	beam			29.6	23.4

The low frequency drifting force

This part of the drifting force has been estimated as follows: The measured wave height record $\zeta_0(t)$ is squared $\zeta^2(t)$. This squared wave height function can again be analysed by a spectral analysis. The spectral density function of $\frac{1}{2}\zeta^2(t)$ is determined. For an example see Fig. 15. As can be seen from this figure it contains the sum and difference frequencies of the original wave height spectrum. The difference frequencies are now of special interest. They are related to the envelope of the original wave height record.

The r.m.s. value of the low-frequency energy variation is:

$$\sigma_{E \text{ diff}} = \left[\int_{\text{diff. freq.}} S_{\frac{1}{2}\zeta^2}(\omega) d\omega \right]^{1/2}$$

$\sigma_{E \text{ diff}}$ is proportional to the mean square value of the fluctuating part of the wave height envelope. The energy in the fluctuating part of the envelope curve depends largely on the occurrence of "high" waves. As discussed earlier the occurrence of "high" waves is proportional to $1/\bar{T}$ per unit time. So the relation between the r.m.s.

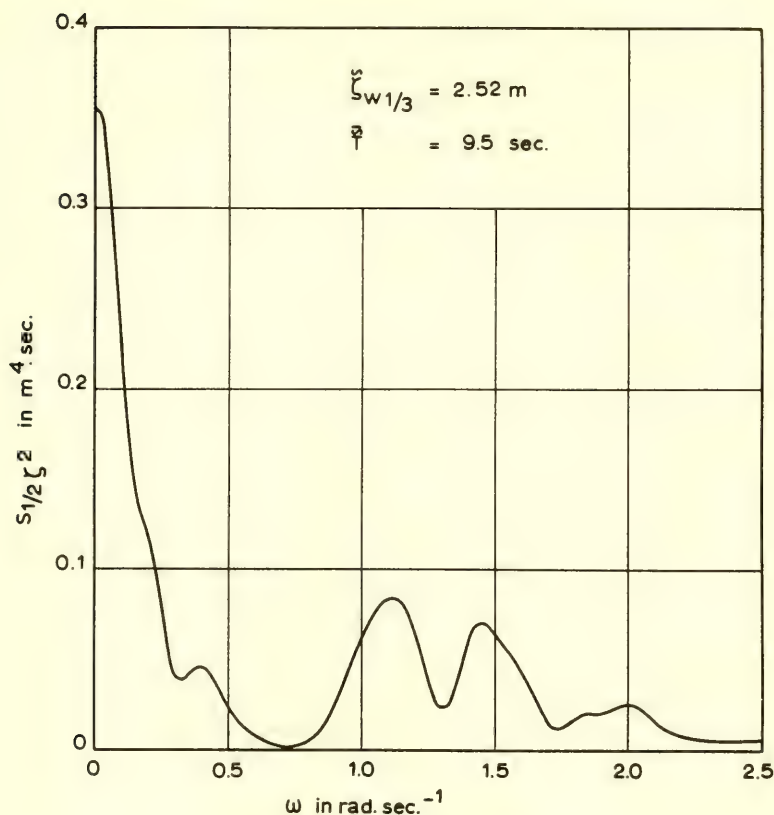


Fig. 15. Spectral density function of a half times the square of the wave height

value of the low-frequency energy variation and the characteristics of the waves becomes

$$\sigma_{E \text{ diff}} = \text{constant} \cdot \frac{\zeta_{w1/3}^2}{T}$$

Figure 17 shows that the produced wave spectra fit this relation quite well.

Now the exciting force must be determined keeping the vessel in a fixed position. In that case the exciting force is due to wave reflection alone. In regular head waves this force is

$$F_x = \frac{1}{2} \rho g a^2 B \overline{\sin^2 \alpha}$$

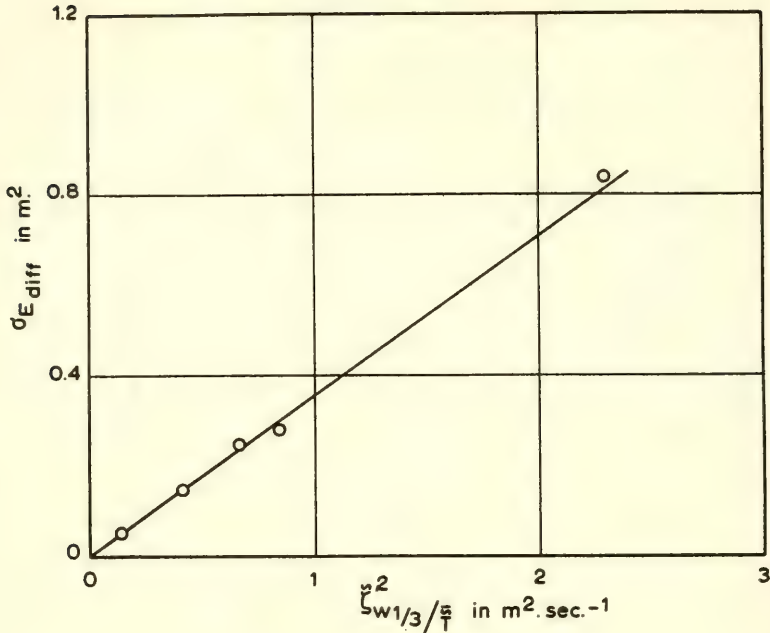


Fig. 16. Relation between the low-frequency energy variation and wave characteristics

when a is the wave amplitude and $\overline{\sin^2 \alpha}$ is the mean square of the angle between the tangent at the ship's waterline and the longitudinal axis.

Now the r.m.s. value of the low-frequency exciting force becomes

$$\sigma_{Fx} = \rho g \sigma_{E \text{ diff}} \overline{B \sin^2 \alpha}$$

and the r.m.s. value of the low-frequency motion is

$$\sigma_x = \frac{\sigma_{Fx}}{B_x \cdot \omega_{0x}}$$

The surge damping B_x is obtained from an extinction curve. The numerical values are $B_x \cdot \omega_{0x} = 1.50$ ton/m, $\overline{\sin^2 \alpha} = 0.24$. The results compared with the experimental results are shown in Table II. The agreement is good.

TABLE II

$\tilde{\zeta}_{W1/3}$ in m	\tilde{T} in sec	σ_x in m calculated	σ_x in m measured
2.30	6.6	0.96	0.87
2.49	9.5	0.86	0.77
4.83	10.1	2.87	2.54

The reflection force on the fixed vessel in regular beam waves is

$$F_y = \frac{1}{2} \rho g a^2 L \gamma$$

where γ is a coefficient depending on the beam-wave length ratio. For the wave lengths under consideration ($\lambda/B \approx 5$) the mean value of γ is obtained from experimental data on Series 60 models is about 0.5. This value increases up to one for shorter waves and decreases for longer wave lengths.

Now the r.m.s. value of the low-frequency exciting force in irregular beam seas becomes

$$\sigma_{Fy} = \gamma \rho g \sigma_{E \text{ diff}} L$$

and the r.m.s. value of the low-frequency sway motion is

$$\sigma_y = \frac{\sigma_{Fy}}{B_y \omega_{oy}}$$

The sway damping is again obtained from an extinction curve. The numerical value is $B_y \omega_{oy} = 4 \text{ ton/m}$. The results compared with experimental results are shown in Table III.

TABLE III

$\tilde{\zeta}_{W1/3}$ in m	\tilde{T} in sec	σ_y in m calculated	σ_y in m measured
1.19	9.8	0.72	0.67
1.96	9.6	2.12	2.05
2.30	6.6	3.99	4.56

Taking in mind that in the last case the value of γ must be higher than 0.5, due to the shorter wave length, the agreement is very good again.

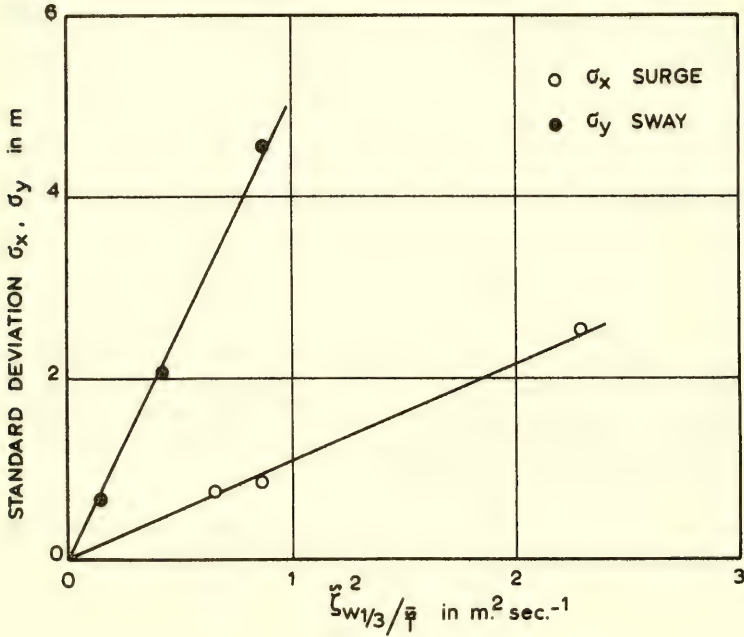


Fig. 17. Relation between surge, sway and wave characteristics

ACKNOWLEDGEMENT

The author would like to thank the staff of the Seakeeping Laboratory of the N.S.M.B. for the many fruitful discussions. He is indebted to Mr. Tan Seng Gie who carried out the experimental program.

REFERENCES

1. Maruo, H., "The excess resistance of a ship in rough seas," Int. Shipbuilding Progress, 1957.
2. Maruo, H., "The drift of a body floating on waves," Journal of Ship Research, 1960.
3. Newman, J. M., "The drift force and moment on ships in waves," Journal of Ship Research, 1967.
4. Verhagen, J. H. G. and van Sluijs, M. F., "The low-frequency drifting force on a floating body in waves," Int. Shipbuilding Progress, 1970.

DYNAMICS OF SUBMERGED TOWED CYLINDERS

M. P. Paidoussis
McGill University
Montreal, P.Q., Canada

I. INTRODUCTION

Interest in the dynamic stability of towed ships dates back to the halcyon-days when solutions to engineering problems could still be obtained by experience, without the aid of sophisticated analysis. Certainly, operators of horse-drawn barges in canals must have been aware of possible instabilities and remedial actions. Nevertheless, to the author's knowledge, the first substantive paper on the subject, by Strandhagen, Schoenherr and Kobayashi [1], did not appear until 1950. This is also surprising, if one considers that both the analytical techniques and physical concepts were understood long before that; indeed much earlier work does exist on the closely related topic of stability of airships moored to a mast and kite balloons, starting with the work of Bairstow, Relf and Jones [2] in 1915, and followed by the work of Munk [3], Glauert [4], and Bryant, Brown and Sweeting [5], for instance.

Strandhagen *et al.*, and the discussors of their paper, firmly established the following important criteria for stability of a towed ship: (i) the point of attachment of the tow-rope should be ahead of both the center of mass and the center of pressure of the (static) lateral hydrodynamic forces acting on the ship; (ii) the ship should be stable when moving untowed; (iii) in cases where (ii) is not satisfied, then the system could be rendered stable by either short enough or long enough tow-ropes. It is noteworthy that the criteria for stability, at least for the linearized theory of small departures from course, apply to all towing speeds, so that for a given configuration a (rigid) towed ship is either stable or unstable irrespective of how fast it is being towed. Instabilities were found to be of two distinct types: (a) yawing, i.e. a zero-frequency, amplified motion which in aeroelasticity would be referred to as 'divergence', and (b) oscillatory instability, where the system, when disturbed, oscillates about its position of rest with increasing amplitude.

More recently, interest in the instability of submerged towed bodies has arisen mainly in connection with sonar applications. Here

the body housing the sonar device is towed deeply submerged by surface craft, for the purpose of hydrographic survey, submarine detection, or location of schools of fish. We must refer to the work of Strandhagen and Thomas [6], Richardson [7], Laitinen [8], Patton and Schram [9], Jeffrey [10], Schram and Reyle [11], and Whicker [12]. The stability problem for the sonar-type towed bodies is of course quite similar to that of a towed glider [5]. The work referred to here deals with the dynamics of the towed body system as a whole; the geometry of the towed body for these applications tends to be fairly complex, and the analysis quite elaborate.

A considerable amount of work also exists on the equilibrium configuration and the dynamics of towing cables, starting with McLeod's [13] and Relf and Powell's [14] work, to more recent work by Landweber and Protter [15], Pode [16], [17], O'Hara [18], Kochin [19], Eames [20], and Albasiny and Day [21]; this represents a by no means exhaustive list of references.

The author's interest in this field comes from work associated with yet another application: that of the Dracone flexible barge, which is a flexible sausage-like container towed behind a small craft, and used for the transportation of oil and other lighter-than-water cargoes, including the sea transport of fresh water to arid lands (e.g. to some of the Aegean islands from the mainland). The new element that enters the problem in this case is that of elastic forces, making this a problem in the general area of fluidelasticity (cf. [22]). The first analysis of stability of the Dracone was by Hawthorne [23]. Later, the author studied systematically the dynamics of flexible slender cylindrical bodies immersed in axial flow, for various conditions of end-constraint [24], [25], including the case of a towed slender cylinder [26]. In the latter case, both rigid-body type instabilities and flexural instabilities were shown to exist; stability was highly dependent on the towing speed.

It was suggested [27] that cylindrical or quasi-cylindrical containers towed underwater by a small submarine could be used to transport liquid cargoes to and from arctic ports, avoiding the hazards of surface transportation in ice-covered seas. The containers could be either flexible or, more likely, rigid; there could of course be a string of such containers towed by the same submarine. This idea has taken added poignancy since the oil discoveries in the Arctic.

In this paper we shall re-examine the problem of stability of a submerged cylindrical body, both flexible and rigid, towed by a submarine craft.

II. THE EQUATION OF SMALL LATERAL MOTIONS OF A FLEXIBLE SLENDER BODY IN AXIAL FLOW

We shall derive the equation of small lateral motions of a slender body of revolution of the type shown in Fig. 1(a); the body is supposed to be supported somehow so that it is not washed away downstream. The fluid is incompressible and of density ρ ; it is flowing with velocity U parallel to the x -axis, which coincides with the undisturbed longitudinal axis of symmetry of the body. The body is of mass per unit length $m(x)$, cross-sectional area $S(x)$, and flexural rigidity $EI(x)$.

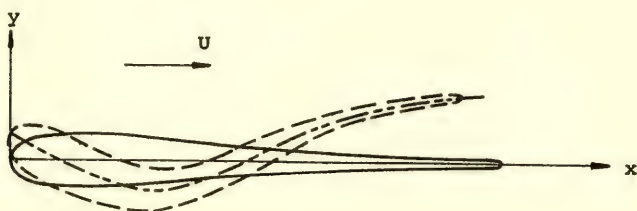


Fig. 1(a) Diagram of a flexible, slender body of revolution in axial flow

We consider small motions $y(x,t)$ and assume that y , $\partial y/\partial x$, $\partial^2 y/\partial x^2$ to be all small, so that no separation occurs in cross-flow. Moreover, we assume that dS/dx is small everywhere, except perhaps at the ends of the body, so that no separation occurs in the axial flow (except perhaps at the rear end), and so that slender-body theory may be used. Also $d(EI)/dx$ is assumed to be small, which, together with the restrictions on the displacement function, allows us to use the simple Euler-beam approximation to describe the flexural forces. The body is further assumed to be of null buoyancy and uniform density, so that no constraining force in the y -direction nor a moment is necessary to keep it lying along the x -axis, at least at zero flow velocity. Furthermore, the motions are considered to take place within the (x,y) -plane, which for the sake of simplicity is assumed to be horizontal. Finally, we neglect internal dissipation in the material of the body.

We now consider an element δx of the body. The forces and moments acting on it are shown in Fig. 1(b). Q is the transverse shear force, M is the bending moment, T is the axial tension, F_N and F_L are the normal and longitudinal components of frictional forces per unit length, and F_A is the lateral inviscid force per unit length.

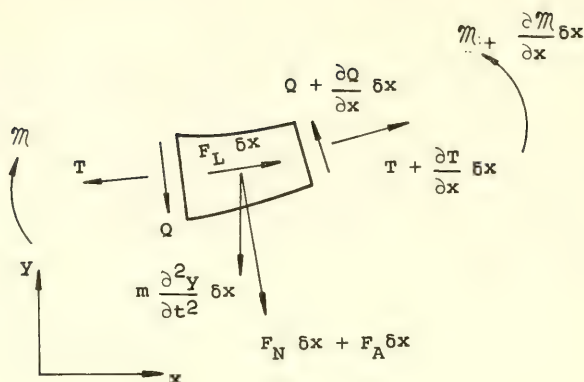


Fig. 1(b) Forces and moments acting on an element $\sigma(x)$ of the body

Taking force balances in the x - and y -directions and a moment balance we obtain

$$\frac{\partial T}{\partial x} + F_L + F_N \frac{\partial y}{\partial x} = 0, \quad (1)$$

$$\frac{\partial Q}{\partial x} - F_N + \frac{\partial}{\partial x} (T \frac{\partial y}{\partial x}) + F_L \frac{\partial y}{\partial x} - F_A - m \frac{\partial^2 y}{\partial t^2} = 0, \quad (2)$$

$$Q = - \frac{\partial m}{\partial x}, \quad (3)$$

where the inertia forces in the x -direction have been neglected.

We next consider the functional form of the forces. The lateral inviscid force $F_A \delta x$ represents the reaction on the body of the force required to accelerate the fluid around it, and may be written as

$$F_A = [(\partial/\partial t) + U(\partial/\partial x)] (Mv), \quad (4)$$

as discussed by Lighthill [28], [29], where v is the lateral relative velocity between the body and the fluid flowing past it, and M is the virtual mass of the fluid. Here the effects of sideslip have been neglected, effectively assuming that each cross section of the body is

part of an infinite cylinder; boundary layer effects have also been neglected. The virtual mass $M(x) = \rho S(x)$, and $v(x, t) = [(\partial/\partial t) + U(\partial/\partial x)] [y(x, t)]$, which substituted into (4) yield

$$F_A = \rho S [(\partial/\partial t) + U(\partial/\partial x)]^2 y + \rho U [(\partial y/\partial t) + U(\partial y/\partial x)] (dS/dx). \quad (5)$$

The frictional forces, as proposed by Taylor [30], and elaborated by Paidoussis [24], [25] are taken to be

$$F_N = \frac{1}{2} c_N (\rho S/D) U^2 \sin i \quad \text{and} \quad F_L = \frac{1}{2} c_T (\rho S/D) U^2 \cos i,$$

where i is the instantaneous angle of incidence on the cross-section and is given by $i = \sin^{-1} (v/U)$, and $D \equiv D(x)$ is the diameter. Accordingly, F_N and F_L are given by

$$F_N = \frac{1}{2} c_N (\rho S/D) U [(\partial y/\partial t) + U(\partial y/\partial x)] \quad \text{and} \quad F_L = \frac{1}{2} c_T (\rho S/D) U^2. \quad (6)$$

Finally, we note that the bending moment is related to the flexural rigidity by

$$\mathcal{M} = EI(\partial^2 y/\partial x^2). \quad (7)$$

Now, substituting (6) into (1), neglecting terms of second order of magnitude, and integrating from x to L , we obtain

$$T(x) = T(L) + \frac{1}{2} c_T \rho U^2 \int_x^L [S(x)/D(x)] dx,$$

where $T(L)$ is the value of T at the downstream end. We consider that $T(L)$ is non-zero and that it arises from possible form drag at the end. We accordingly write

$$T(x) = \frac{1}{2} c_2 \rho S(L) U^2 + \frac{1}{2} c_T \rho U^2 \int_x^L [S(x)/D(x)] dx, \quad (8)$$

where c_2 is the form-drag coefficient.

Substituting now (3), (5), (6), (7) and (8) into (2), making use of (1), and neglecting terms of second order of magnitude, we obtain

$$\begin{aligned} \frac{\partial^2}{\partial x^2} \left(EI \frac{\partial^2 y}{\partial x^2} \right) + \rho S \left(\frac{\partial}{\partial t} + U \frac{\partial}{\partial x} \right)^2 y + \rho U \left(\frac{\partial y}{\partial t} + U \frac{\partial y}{\partial x} \right) \frac{dS}{dx} \\ + \frac{1}{2} c_N U \left(\frac{\rho S}{D} \right) \left(\frac{\partial y}{\partial t} + U \frac{\partial y}{\partial x} \right) \\ - \frac{1}{2} \rho U^2 \left[c_2 S(L) + c_T \int_x^L \frac{S(x)}{D(x)} dx \right] \frac{\partial^2 y}{\partial x^2} + m \frac{\partial^2 y}{\partial t^2} = 0, \end{aligned} \quad (9)$$

which is the equation of small lateral motions. For a uniform cylinder this equation becomes

$$\begin{aligned} EI \frac{\partial^4 y}{\partial x^4} + M \left(\frac{\partial}{\partial t} + U \frac{\partial}{\partial x} \right)^2 y + \frac{1}{2} c_N \left(\frac{MU}{D} \right) \left(\frac{\partial y}{\partial t} + U \frac{\partial y}{\partial x} \right) \\ - \frac{1}{2} MU^2 \left[c_2 + c_T \frac{L-x}{D} \right] \frac{\partial^2 y}{\partial x^2} + m \frac{\partial^2 y}{\partial t^2} = 0, \end{aligned} \quad (10)$$

where the diameter, D , and $M = \rho S$ are now constant.

We note that in the absence of frictional forces, (10) becomes the governing equation for small motions of a cylindrical beam containing flowing fluid [31], where we interpret M as the mass of the contained fluid per unit length. The physical similarity between the internal and external flow cases is striking, albeit that in the former case fluid friction does not enter the problem. We shall refer to this later.

We finally note that Eqs. (9) and (10) also hold to describe the motions of a towed flexible body, if we identify U as the towing speed, provided the tow-rope forces are taken into account as part of the boundary conditions.

III. BOUNDARY CONDITIONS

Clearly the boundary conditions will depend on the mode of end constraint. Let us consider the case of a towed flexible cylindrical body shown in Fig. 2. The body consists of a uniform cylinder terminated by a rounded 'nose' and a streamlined, tapering 'tail', incorporated to provide reasonable axial flow conditions over the body. We assume that the towing craft moves horizontally in a straight course with uniform velocity U , so that the tow-rope in its undisturbed state lies along the x -axis; we also consider the assumptions made at the beginning of §2 to hold.

We may use Eq. (9) to analyze the system, together with boundary conditions stating that (a) at the downstream end, $x = L$,

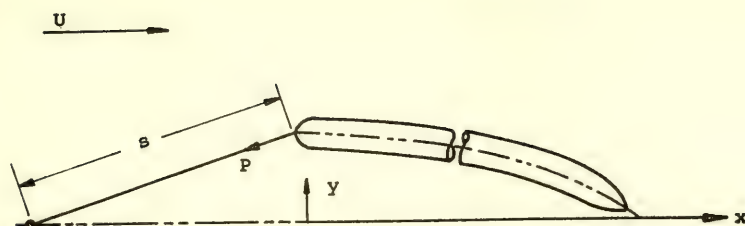


Fig. 2 Diagram of a towed flexible, slender cylinder with streamlined "nose" and "tail"

the bending moment and shear force are zero, and (b) at the upstream end, $x = 0$, the bending moment is zero, but the shear force is equal to the normal component of the tow-rope pull. It is obvious, however, that the very form of Eq. (9) will depend on the shape of the nose and the tail. As we are only looking for the general characteristics of the dynamical problem, this is not convenient. We shall instead proceed as follows: (i) we shall use Eq. (10) which satisfactorily applies over the uniform, cylindrical part of the body; (ii) the forces acting on the non-cylindrical ends will be lumped and incorporated in the boundary conditions. For this process to be meaningful we must have $l_1 \ll L$ and $l_2 \ll L$, where l_1 and l_2 are the lengths of the nose and tail, respectively; yet l_1 and l_2 are considered to remain great enough to permit the use of slender body approximations [23], [26]. Since l_1 and l_2 are small, compared to L , we may further simplify the problem by considering y and the lateral velocity v to be approximately constant over $0 \leq x \leq l_1$ and $L - l_2 \leq x \leq L$, and by neglecting the skin frictional forces over the same intervals. Hence, integrating Eq. (2) and using (4), and incorporating the forces arising from the tow-rope pull, P , we obtain

$$\int_0^{l_1} \frac{\partial Q}{\partial x} dx - f_1 \int_0^{l_1} \left(\frac{\partial}{\partial t} + U \frac{\partial}{\partial x} \right) (\rho S v) dx - P \left(\frac{y}{s} \right)_{x=0} - \int_0^{l_1} m \frac{\partial^2 y}{\partial t^2} dx = 0,$$

and

$$\int_{L-l_2}^L \frac{\partial Q}{\partial x} dx - f_2 \int_{L-l_2}^L \left(\frac{\partial}{\partial t} + U \frac{\partial}{\partial x} \right) (\rho S v) dx - \int_{L-l_2}^L m \frac{\partial^2 y}{\partial t^2} dx = 0;$$

the parameters f_1 and f_2 , which are equal to unity according to slender-body inviscid-flow theory, were introduced to account for the theoretical lateral force at the nose and the tail, respectively, not being fully realized because of (a) the lateral flow not being truly

two-dimensional, (b) boundary-layer effects, and (c) the use of fins. The tow-rope pull P is equal to the tension in the cylinder at $x = 0$, plus the form drag at the nose, i.e.

$$P = \frac{1}{2} MU^2(c_1 + c_2 + c_T L/D).$$

Substituting P into the above equations and assuming y and v to be constant over the intervals of integration, we obtain

$$\left[EI \frac{\partial^3 y}{\partial x^3} + f_1 MU \left(\frac{\partial y}{\partial t} + U \frac{\partial y}{\partial x} \right) + \frac{1}{2} MU^2 \left(c_T \frac{L}{D} + c_1 + c_2 \right) \frac{y}{S} + (m + f_1 M) x_1 \frac{\partial^2 y}{\partial t^2} \right]_{x=0} = 0, \quad (11)$$

$$\left[-EI \frac{\partial^3 y}{\partial x^3} - f_2 MU \left(\frac{\partial y}{\partial t} + U \frac{\partial y}{\partial x} \right) + (m + f_2 M) x_2 \frac{\partial^2 y}{\partial t^2} \right]_{x=L} = 0, \quad (12)$$

where

$$x_1 = \frac{1}{S} \int_0^{L_1} S(x) dx \quad \text{and} \quad x_2 = \frac{1}{S} \int_{L-L_2}^L S(x) dx.$$

Here $M = \rho S$, and S and D are quantities pertaining to the cylindrical part of the body.

In the above the forces arising from form drag were taken to be in the x -direction. If they are taken to be along the cylinder, then terms $\frac{1}{2} c_1 MU^2 (\partial y / \partial x)$ and $\frac{1}{2} c_2 MU^2 (\partial y / \partial x)$ should be added to Eqs. (11) and (12), respectively.

The other two boundary conditions are obtained by making the reasonable assumption that there are no bending moments at $x = 0$ and $x = L$, or

$$\left[\frac{\partial^2 y}{\partial x^2} \right]_{x=0} = \left[\frac{\partial^2 y}{\partial x^2} \right]_{x=L} = 0. \quad (13)$$

The advantages in this method of analysis, in which the shape characteristics of nose and tail were absorbed in the two parameters f_1 and f_2 , are obvious. The disadvantages are equally obvious: although we can estimate f_1 and f_2 , we cannot easily calculate them.

The range of f_1 and f_2 will be taken to be between zero and unity, the latter limit representing well-streamlined, gradually tapering nose or tail, and no flow separation; it is obviously much more likely for f_1 to approach unity than for f_2 . In the case of a blunt tail, on the other hand, $f_2 \rightarrow 0$.

IV. EQUATION OF MOTION AND BOUNDARY CONDITIONS OF [26]

The equation of motion given by Eq. (10) is not identical to that previously derived by Paidoussis [26]. The difference is in the frictional terms, because of the different manner in which frictional forces were resolved in [26]. The boundary conditions are identical.

As we shall make use of the results obtained in [26], we give the equation of motion below, for reference.

$$EI \frac{\partial^4 y}{\partial x^4} + M \left(\frac{\partial}{\partial t} + U \frac{\partial}{\partial x} \right)^2 y + \frac{1}{2} c_N \left(\frac{MU}{D} \right) \left(\frac{\partial y}{\partial t} + U \frac{\partial y}{\partial x} \right) + \frac{1}{2} c_T \left(\frac{MU^2}{D} \right) \frac{\partial y}{\partial x} - \frac{1}{2} MU^2 \left[c_2 + c_T \frac{L-x}{D} \right] \frac{\partial^2 y}{\partial x^2} + m \frac{\partial^2 y}{\partial t^2} = 0. \quad (10a)$$

The equation of motion and boundary conditions used in the 'new theory' presented in this paper are believed to be more self-consistent than those of the 'old theory' of [26].

V. DYNAMICS OF TOWED FLEXIBLE CYLINDERS

5.1 Method of Analysis

Upon expressing the equation of motion and the boundary conditions in dimensionless form, the dynamics of the system may be found to depend on the following dimensionless parameters:

- (i) f_1 and f_2 , which were defined in §3;
- (ii) ϵc_N , ϵc_T , c_1 and c_2 , where $\epsilon = L/D$;
- (iii) $\Lambda = s/L$; the ratio of tow-rope length to body length;
- (iv) $\chi_1 = x_1/L$ and $\chi_2 = x_2/L$, where x_1 and x_2 were defined in §3;
- (v) $u = (M/EI)^{1/2} UL$, the dimensionless towing speed.

It is noted that according to the assumptions made in the theory, $m = M$.

We shall not present the analysis here, as it is adequately documented elsewhere [26], [27]. Suffice it to say that solutions were obtained of the type

$$\frac{Y}{L} = Y\left(\frac{x}{L}\right) e^{i\omega\tau},$$

where Y is a function of x/L , τ is a dimensionless time and ω is the dimensionless frequency given by

$$\omega = \left(\frac{M+m}{EI}\right)^{1/2} \Omega L^2,$$

Ω being the circular frequency of motion. In general, ω will be complex. Clearly, we have an infinite set of frequencies, ω_i , as the system has an infinite number of degrees of freedom. If the imaginary components of the frequencies, $\text{Im}(\omega_i)$, are all positive, then the system will be stable. If, on the other hand, for the j th mode we have $\text{Im}(\omega_j) < 0$, then the system will be unstable in that mode; now if the corresponding real component of the frequency, $\text{Re}(\omega_j)$, is zero this will represent a divergent motion without oscillations, which we shall call yawing; if $\text{Re}(\omega_j) \neq 0$, then the instability will be oscillatory.

The calculation procedure was as follows: (a) a set of values of $f_1, f_2, \epsilon_{c_N}, \epsilon_{c_T}, c_1, c_2, \chi_1, \chi_2$ and Λ were selected; (b) the complex frequencies of a few of the lowest modes of the system were traced as functions of u , starting with $u = 0$.

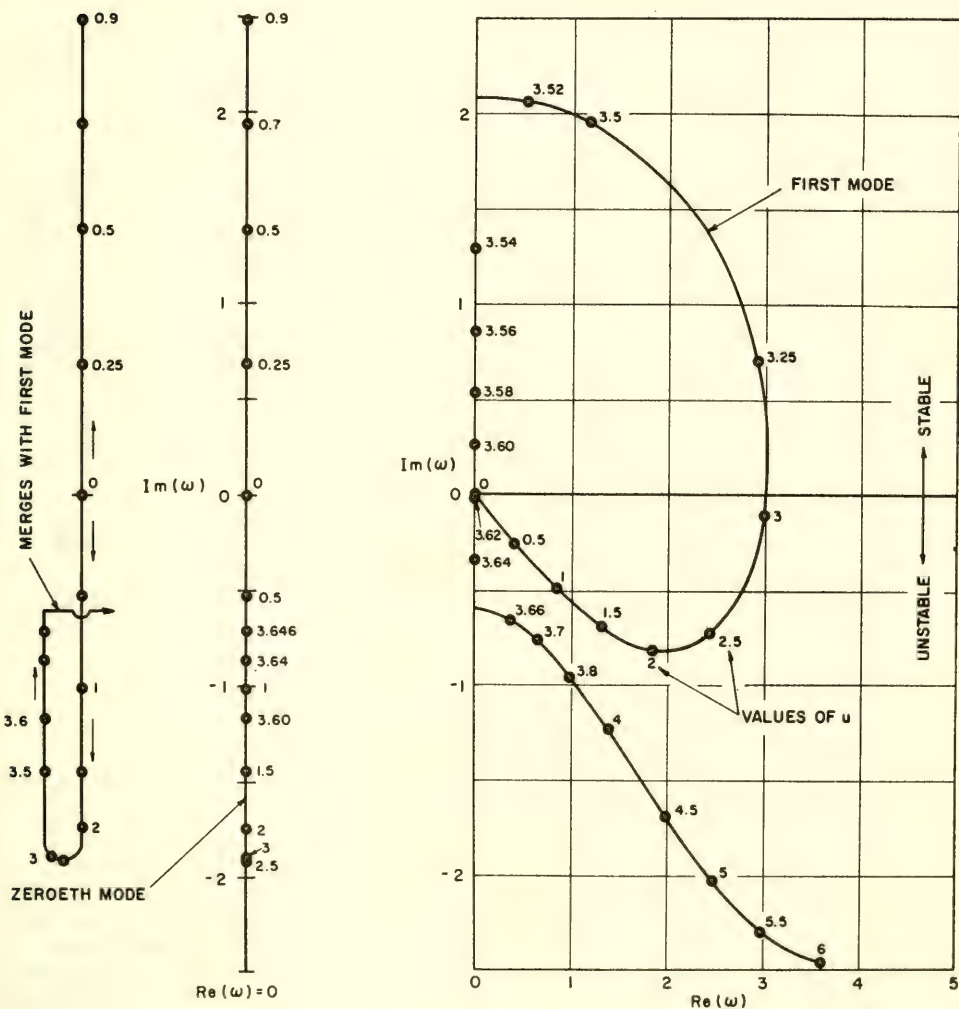


Fig. 3 The dimensionless complex frequencies of the zeroth and first modes of a flexible cylinder with $\epsilon_{c_N} = \epsilon_{c_T} = 1$, $f_1 = f_2 = 1$, $c_1 = c_2 = 0$, $\Lambda = 1$, $\chi_1 = \chi_2 = 0.01$, as a function of the dimensionless towing speed u . (Theory of [26]).

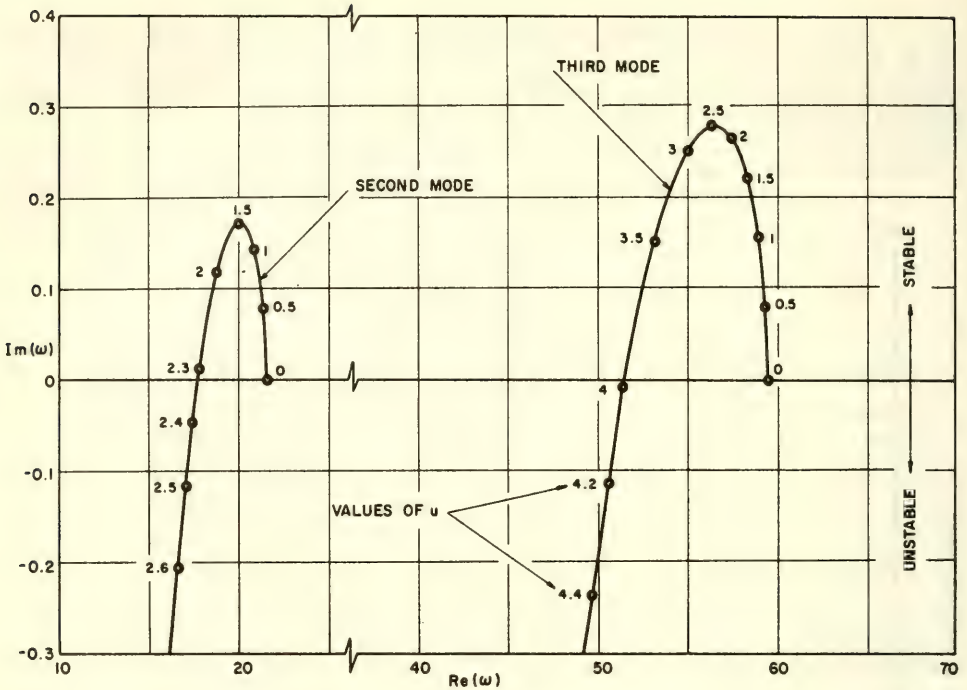


Fig. 4 The dimensionless complex frequencies of the second and third modes of a flexible cylinder with $\epsilon_N = \epsilon_T = 1$, $f_1 = f_2 = 1$, $c_1 = c_2 = 0$, $\Lambda = 1$, $\chi_1 = \chi_2 = 0.01$. (Theory of [26]).

5.2 Results Based on the Theory of [26]

Typical results are shown in Figs. 3, 4 and 5, obtained by using Eqs. (10a), (11), (12) and (13).

We first consider Figs. 3 and 4 applying to bodies with well streamlined nose and tail, and $\Lambda = 1$. Figure 3 shows the behavior (with increasing towing speed) of the two modes which at zero towing speed have frequencies $\omega_0 = \omega_1 = 0$; these are the so-called zeroth and first modes and, at low towing speeds, are associated with quasi-rigid body motions -- a matter to be further discussed in §6. Figure 4 shows the loci of the so-called second and third modes of the system as functions of towing speed. The frequencies of these modes at zero towing speed correspond to the second- and third-mode frequencies of the flexible body treated as a free-free beam; accordingly, these (and all higher modes) are flexural in character.

We observe in Fig. 3 that both the zeroth and first modes lead to instabilities for small, finite u . The instability associated with the zeroth mode is a yawing one, while that associated with the first mode is oscillatory. We see that for $u > 3.05$ the oscillatory instability ceases in the first mode, re-appearing at $u \approx 3.65$. However, at much lower towing speed ($u \approx 2.3$) the system loses stability in its second (flexural) mode, as shown in Fig. 4, and at $u \approx 4$ in its third mode. In short, this particular system is subject to several types of instabilities; at low towing speeds it is subject to quasi-rigid body instabilities, and at higher towing speeds to flexural oscillatory instabilities as well.

Figure 5 shows the zeroth and first mode of a system with a well streamlined nose and a very blunt tail. We see that it is not subject to yawing instability, and the first mode is only unstable in the range $0 < u < 0.9$. It is, however, subject to flexural oscillatory instability (not shown) in its second mode for $u > 5.29$. Accordingly, a blunt tail stabilizes the system considerably. Also shown in Fig. 5 is the first mode of a system with a less than perfectly streamlined nose; we see that the range of first-mode oscillatory instability in this case is larger, i.e. $0 < u < 1.75$.

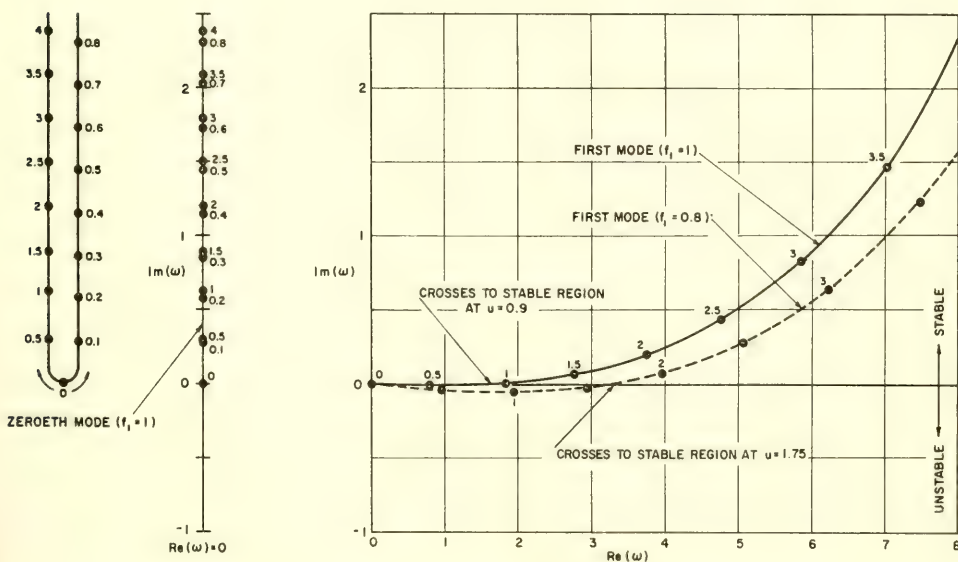


Fig. 5 The dimensionless complex frequencies of the zeroth and first modes of a flexible cylinder with $\epsilon c_N = \epsilon c_T = 1$, $f_1 = 1$, $c_1 = 0$, $f_2 = 0$, $c_2 = 1$, $\Lambda = 1$, $\chi_1 = \chi_2 = 0.01$. Also the first mode with $f_1 = 0.8$. (Theory of [26]).

Based on such complex-frequency calculations it was possible to construct stability diagrams illustrating the effect of various parameters on the stability of the system. Examples are given in Figs. 6 and 7 showing the effect of stability of f_2 and Λ , respectively. Other similar stability diagrams may be found in [26]. The following general conclusions may be drawn:

- (a) for optimal stability the tail should be blunt (f_2 small, c_2 large), the nose should be well-streamlined ($f_1 \rightarrow 1$), and the tow-rope length should be short (Λ small);
- (b) a system that is unstable by yawing, within a range of towing speeds, can be stabilized by blunting the tail, but not by manipulating the length of the tow-rope;
- (c) in some cases it is possible to stabilize a system which is unstable at low towing speeds, by towing it faster, within a specified range of towing speeds.

Conclusions (a) above are not contrary to reported experience with rigid bodies. On the other hand, (b) may sound surprising. The fact is that the onset of yawing is not a function of Λ , nor is its cessation (§6.2). This is also true with f_1 . Finally, conclusion (c) is characteristic of the dynamical behavior of towed flexible cylinders.

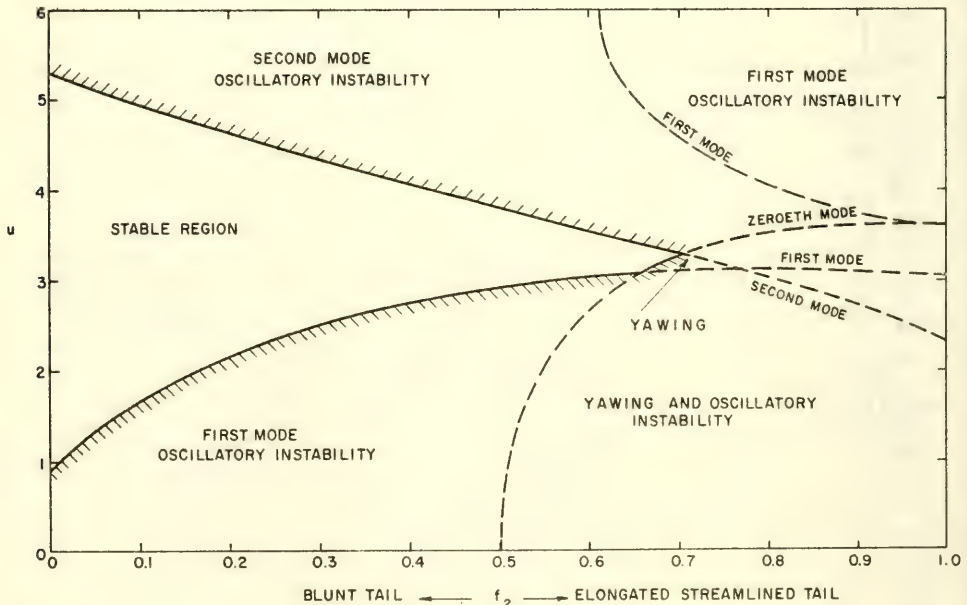


Fig. 6 Stability map showing the effect of the tail shape for a flexible cylinder with $\epsilon c_N = \epsilon c_T = 1$, $f_1 = 1$, $c_1 = 0$, $\Lambda = 1$, $\chi_1 = \chi_2 = 0.01$ and $c_2 = 1 - f_2$. (Theory of [26]).

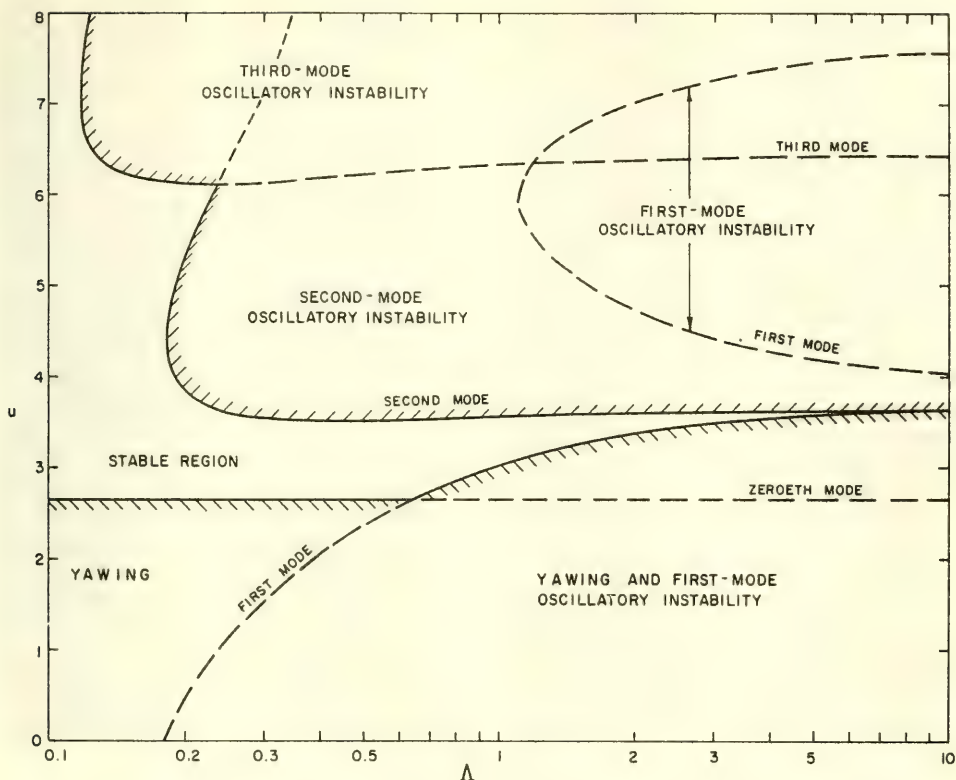


Fig. 7 Stability map showing the effect of Λ for a flexible cylinder with $\epsilon_{CN} = \epsilon_{CT} = 1$, $f_1 = 1$, $c_1 = 0$, $f_2 = 0.6$, $c_2 = 0.4$, $\chi_1 = \chi_2 = 0.01$. (Theory of [26]).

Some experiments were performed designed to test the theory [26]. Rubber cylinders of neutral buoyancy were held in vertical water flow by a nylon 'tow-rope'. Provided the tail was streamlined and the tow-rope not too short, 'criss-crossing', essentially non-flexural oscillations developed at very low flow; these were interpreted as corresponding to first-mode oscillatory instability. At higher flow velocities, flexural oscillations developed with a modal shape corresponding to that of the second mode; sometimes, at yet higher flow velocities, oscillations with a third-mode modal shape developed. These flexural oscillations were interpreted to correspond to second- and third-mode oscillatory instabilities. Sequences of ciné-film frames depicting these oscillations are shown in Figs. 8 and 9. Finally, it was observed that for sufficiently blunt tail and short tow-rope, the system was completely stable. Thus the experimental results were in generally good qualitative agreement with theory.

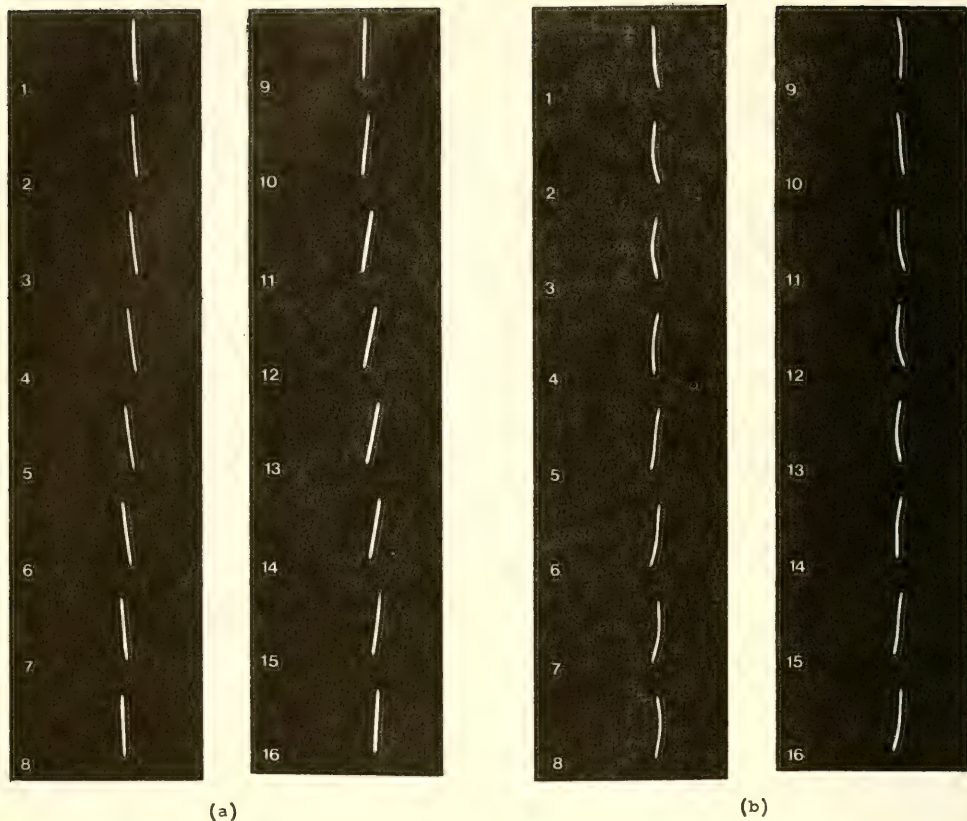


Fig. 8 Photographs in consecutive frames showing a cylinder 11.1 in. long and 0.54 in. diameter with streamlined nose and tail executing (a) criss-crossing, essentially rigid-body, oscillation (8 frames/sec), and (b) second-mode flexural oscillation (24 frames/sec)

Quantitative agreement in the various instability thresholds and stable zones, based on estimated values of some of the theoretical parameters, was also fairly good.

5.3 Results Based on the New Theory

Typical results based on the new theory and obtained by using Eqs. (10) - (13) are shown in Figs. 10 to 13.

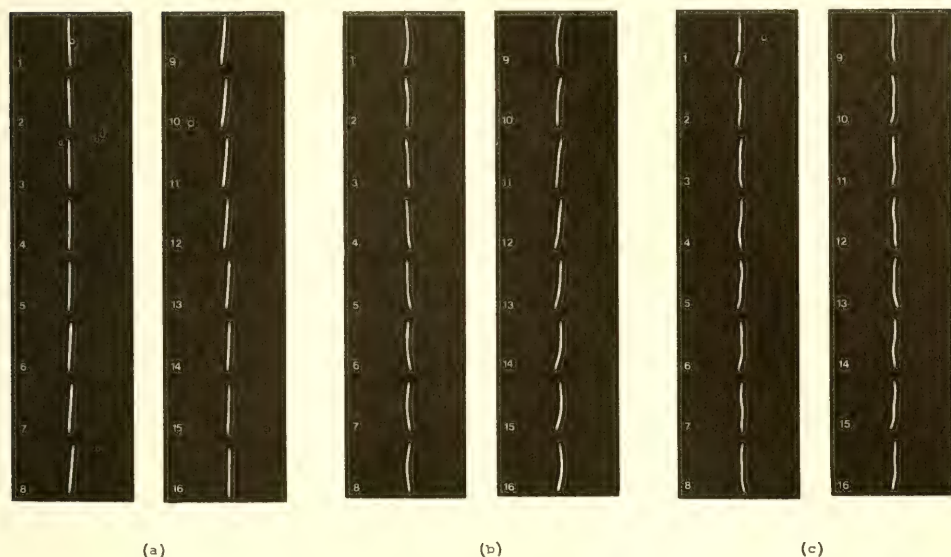


Fig. 9 Photographs in consecutive frames showing a cylinder 15.8 in. long and 0.68 in. diameter executing (a) criss-crossing, essentially rigid-body, oscillation (8 frames/sec), (b) second-mode flexural oscillation (24 frames/sec), and (c) third-mode flexural oscillation (24 frames/sec)

Figures 10 and 11 show the dynamical behavior, with increasing towing speed, of the zeroth, first, second and third modes of a system with well streamlined nose and tail and $\Lambda = 1$; this is the identical system, the dynamical behavior of which, according to the 'old' theory, is shown in Figs. 3 and 4. We observe that, according to the new theory, the system is considerably more stable than predicted by the old theory. Thus, the first mode is unstable only for $u < 0.74$ (not discernible in the scale of Fig. 10); moreover, the unstable locus originating from merging of branches of the zeroth and first modes regains stability at $u = 6.3$. Similarly, the system loses stability in its second and third modes at respectively higher towing speeds than predicted by the old theory.

Further calculations were conducted for the same system as above but with other values of f_2 , always taking $c_2 = 1 - f_2$. It was found that the first mode is not uniformly stabilized with decreasing f_2 as was the case with the old theory (cf. Fig. 6). The ranges of instability of the first mode, for various values of f_2 , were found to be as follows: $0 < u < 0.74$ for $f_2 = 1$; $0 < u < 1.66$ for $f_2 = 0.8$; $0 < u < 1.65$ for $f_2 = 0.6$; and $0 < u < 0.70$ for $f_2 = 0.4$. Thus the

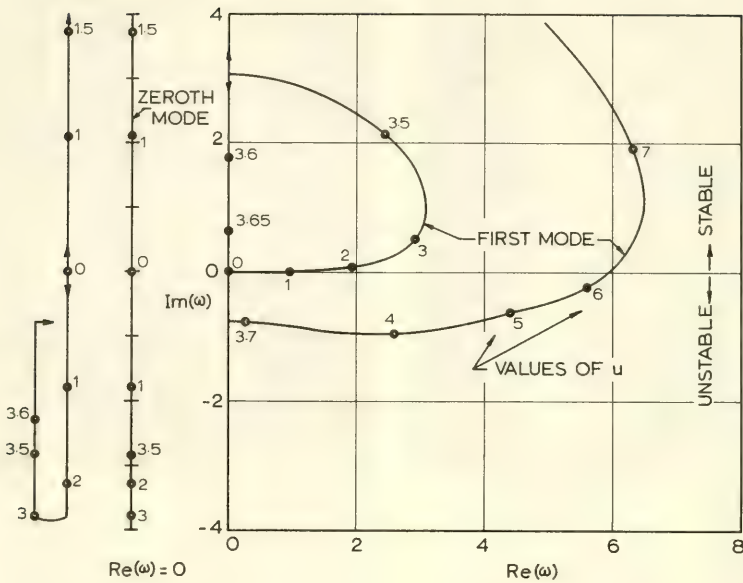


Fig. 10 The dimensionless complex frequencies of the zeroth and first modes of a flexible cylinder with $f_1 = 1 - c_1 = 1$, $f_2 = 1 - c_2 = 1$, $\epsilon c_N = \epsilon c_T = 1$, $\Lambda = 1$, $\chi_1 = \chi_2 = 0.01$, as a function of the dimensionless towing speed u . (New theory).

curve corresponding to that relating to the first mode in Fig. 6 will now exhibit a maximum at $f_2 < 1$; i.e. the system is least stable in its first mode, not for a perfectly streamlined tail as predicted by the old theory, but for a somewhat less perfectly streamlined tail. The second and third modes, on the other hand, are both unconditionally stabilized as the tail is made blunter; thus, the threshold of instability of the second mode is at $u = 2.83$ for $f_2 = 1$, at $u = 3.85$ for $f_2 = 0.6$, and at $u = 4.38$ for $f_2 = 0.4$.

Figures 12 and 13 show the dynamical behavior of a system with $\epsilon c_N = \epsilon c_T = 1$, $\Lambda = 1$, $\chi_1 = \chi_2 = 0.01$, $f_1 = 0.7$, $c_1 = 0$ and $f_2 = 1 - c_2 = 0.7$. We note that the effect of a less than perfectly streamlined nose is to destabilize the system in all its oscillatory modes. Thus the first mode is unstable for $0 < u < 2.80$, and the second and third modes lose stability at, respectively $u = 3.21$ and $u = 5.40$ (cf. values given above).

Also shown in Figs. 12 and 13 (dashed line) is the behavior of a system with $\epsilon c_N = \epsilon c_T = 0.5$ and all other parameters the same.

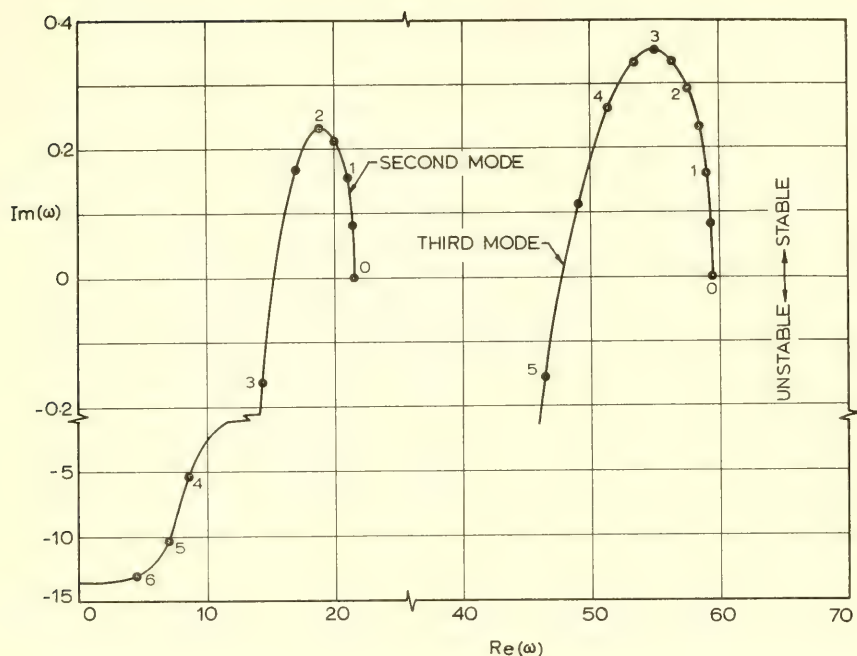


Fig. 11 The dimensionless complex frequencies of the second and third modes of a flexible cylinder with $f_1 = 1 - c_1 = 1$, $f_2 = 1 - c_2 = 1$, $\epsilon c_N = \epsilon c_T = 1$, $\Lambda = 1$, $\chi_1 = \chi_2 = 0.01$. (New theory).

This system is unstable in its first mode for $0 < u < 3.43$ and loses stability in its second and third modes at $u = 3.04$ and $u = 5.14$, respectively. As we may regard the smaller values of ϵc_N and ϵc_T to represent a smaller $\epsilon \equiv L/D$, we may conclude that reducing the slenderness of the system renders it less stable.

Other similar complex frequency calculations establish that the general conclusions regarding optimal stability are essentially identical to those given by the old theory, in spite of quantitative differences in the thresholds of instability. The main difference appears to be that the first-mode instability is less extensive, in terms of the range of parameters over which it is possible, than predicted by the old theory. (Here it should be mentioned that these calculations are still in progress and that stability maps of the type of Figs. 6 and 7 are not yet available.)

The question now remains on how well this theory is capable of predicting the experimentally observed dynamical behavior of the

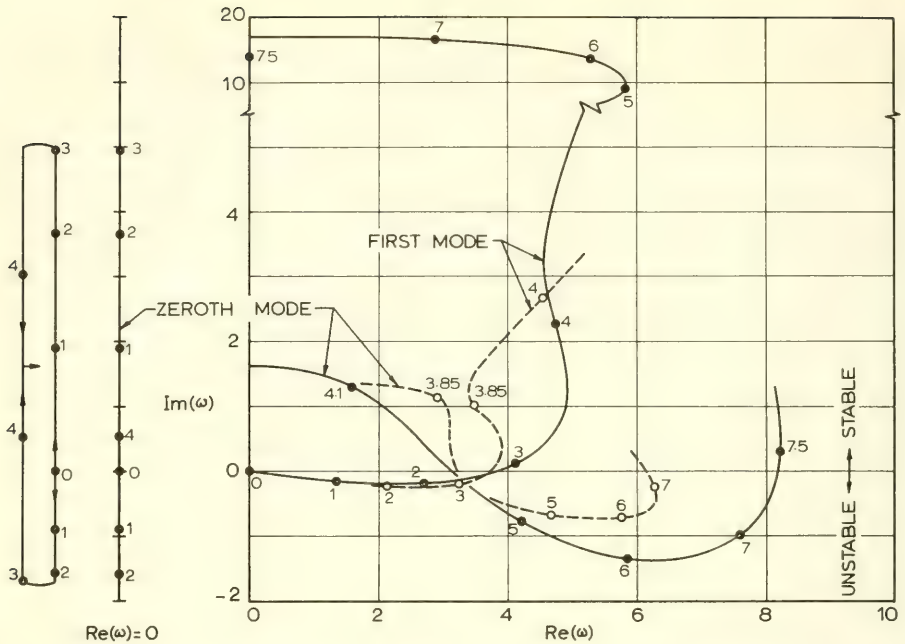


Fig. 12 The dimensionless complex frequencies of the zeroth and first modes of a flexible cylinder with $f_1 = 0.7$, $c_1 = 0$, $f_2 = 1 - c_2 = 0.7$, $\Lambda = 1$, $\epsilon_N = \epsilon_T = 1$, $\chi_1 = \chi_2 = 0.01$ (—). Also shown (---), portions of the zeroth and first modes with $\epsilon_N = \epsilon_T = 0.5$. (New theory).

system. The observed behavior of flexible cylinders with increasing towing speed [26] can be summarized as follows: (a) at low towing speeds a 'criss-crossing' oscillation developed in which the cylinder inclination was of opposite sign to that of the tow-rope; (b) at slightly higher towing speed, sometimes a narrow region of stability, or a region of stationary buckling, was observed; (c) at higher towing speeds, second-mode, and at yet higher towing speeds, third-mode flexural oscillation developed. The above are typical observations provided that the tail is not blunt and the tow-rope not too short; if they are, then the system remains stable for apparently all towing speeds.

We first note that, in terms of qualitative agreement, the results depicted in Figs. 12 and 13, for instance, agree with the experimental observations. Thus, at very low towing speeds the system is subject to first-mode oscillatory instability and yawing, the former ceasing at slightly higher towing speeds, while yawing persists (presumably corresponding to the observed buckling). At yet higher towing speeds, the second mode loses stability, followed by the third mode at even higher towing speeds.

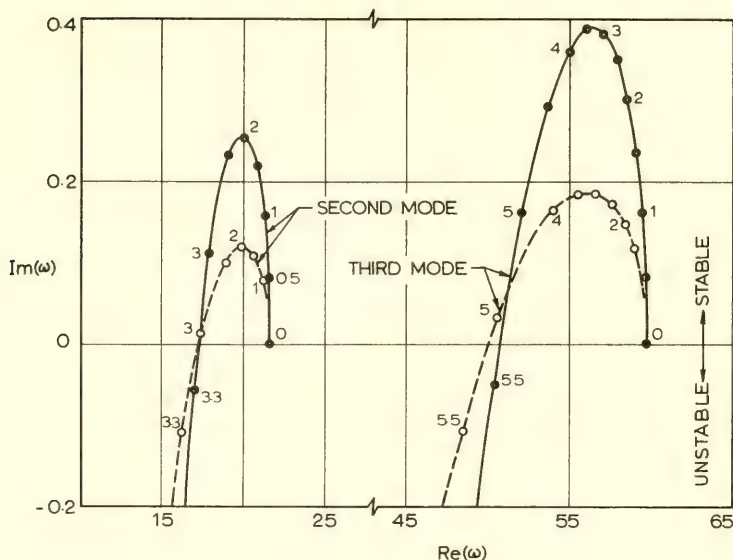


Fig. 13 The dimensionless complex frequencies of the second and third modes of a flexible cylinder with $f_1 = 0.7$, $c_1 = 0$, $f_2 = 1 - c_2 = 0.7$, $\Lambda = 1$, $\chi_1 = \chi_2 = 0.01$; — $\epsilon c_N = \epsilon c_T = 1$; --- $\epsilon c_N = \epsilon c_T = 0.5$. (New theory).

We next consider quantitative agreement for one specific case, the details of which are given in [26]: a cylinder with quite well streamlined nose and tail, $\epsilon = 20.4$ and $\Lambda = 1$ (cf. Table 2 of [26]). Theory is compared with experiment in Table 1. The rationale for the choice of parameters used to obtain the theoretical values has been discussed in [26] and will not be unduly elaborated here. The parameters used are $\epsilon c_N = \epsilon c_T = 1$, $\Lambda = 1$, $f_1 = 0.8$, $c_1 = 0$, $f_2 = 1 - c_2 = 0.7$, $\chi_1 = \chi_2 = 0.01$. It is noted that, although the tail is quite well streamlined, $f_2 < 1$ and $c_2 \neq 0$ were taken (cf. [26]), as the tail cannot be considered to be perfect in the sense described in §3, i.e. with regard to two-dimensionality of the lateral flow and lack of separation in the axial flow. On the other hand, the nose, although of identical shape to the tail, must have a value of f_1 nearer unity, as no separation takes place over the nose. Accordingly, $f_1 = 0.8$ and $c_1 = 0$ were taken in the new theory; (the calculated values of the old theory, also given in Table 1, were obtained with $f_1 = 1$, which is considered to be unrealistic, as the lateral flow over the nose is no more truly two-dimensional than over the tail).

TABLE 1
THEORY COMPARED WITH EXPERIMENT

Description		Old theory [26]*	New theory [†]	Exper. [26]
Criss-crossing oscillation (first-mode osc. instability)	u	0-3.1	0-2.5 (0-3.1) [‡]	0.8-3.3
	ω	0-4.2	0-3.3 (0-3.0) [‡]	2-4
Stationary yawing (zeroth-mode instability alone)	u	3.1-3.3	2.5-3.5	3.3-3.8
Second-mode oscillation threshold	u	3.3	3.5	3.8
	ω	15.5	15.5	17
Second-mode with first-mode oscillation superposed	u	4.6-6.9	4.4-7.2	4.4-6.8
Third-mode oscillation threshold	u	5.8	6.1	7.0
	ω	47	47	~49

* $\epsilon c_N = \epsilon c_T = 1$, $f_1 = 1 - c_1 = 1$, $f_2 = 1 - c_2 = 0.7$, $\Lambda = 1$, $\chi_1 = \chi_2 = 0.01$.

[†] same as above, but $f_1 = 0.8$, $c_1 = 0$.

[‡] same as for [†], but $f_2 = 1 - c_2 = 0.8$.

We see that agreement between the new theory and experiment is comparable to that between the old theory and experiment. No more can be said at this stage, until a more extensive comparison of the new theory with experiment has been undertaken, and also because of the several incompletely tested assumptions involved in the determination of the values of the system parameters. Agreement between the new theory and experiment is least satisfactory in predicting the

point of cessation of criss-crossing oscillation. Here it might be argued that $f_2 = 0.7$, $c_2 = 0.3$ may be too severe for low towing speeds; comparison with theoretical values calculated with $f_2 = 1 - c_2 = 0.8$ (shown in parentheses in Table 1) yields better agreement, as anticipated.

VI. DYNAMICS OF TOWED RIGID CYLINDERS

6.1 The Equations of Motion

We consider exactly the same configuration as in Fig. 2, but impose the restriction that the body be rigid. In this case the system is reduced to one of two degrees of freedom. The generalized coordinates may be taken to be the lateral displacement of the center of mass, y_c , and the angle that the body makes with the x-axis, ϕ . Accordingly, the displacement at any point is given by

$$y = y_c + x\phi. \quad (14)$$

For the sake of simplicity, we assume that the center of mass coincides with the geometric center of the body, x_1 and x_2 being small. For convenience we now measure x from the center of mass, so that the body extends from $x = -L/2$ to $x = L/2$.

Instead of deriving the equations of force and moment balance independently of the previous work, we shall proceed as follows. We shall integrate Eq. (10) or (10a) formally to obtain an equation of force balance, and similarly integrate the product of the forces in (10) or (10a) by x , to obtain the equation of moment balance. The boundary conditions are incorporated through the integral of the first term of these equations; alternatively, the shear forces at the ends may be viewed as forces replacing the effect of nose and tail on the main part of the body.

Thus using Eqs. (10) to (14) in the manner described above, we obtain the following two equations:

$$\begin{aligned} & [M(L + x_1 f_1 + x_2 f_2) + m(L + x_1 + x_2)] \ddot{y}_c \\ & + \left[\frac{1}{2} c_N M U L / D + f_1 - f_2 \right] \dot{y}_c + \frac{1}{2S} M U^2 c_{TP} y_c \\ & - \frac{1}{2} [m(x_1 - x_2) + M(x_1 f_1 - x_2 f_2)] L \ddot{\phi} + M U L \left[2 - \frac{f_1 + f_2}{2} \right] \dot{\phi} \\ & + M U^2 \left[\frac{1}{2} c_N \frac{L}{D} + f_1 - f_2 - \frac{1}{4} \frac{L}{S} c_{TP} \right] \phi = 0, \end{aligned} \quad (15)$$

and

$$\begin{aligned}
 & -\frac{1}{2} [ML(x_1 f_1 - x_2 f_2) + mL(x_1 - x_2)] \ddot{y}_c - \frac{1}{2} MUL(f_1 + f_2) \dot{y}_c \\
 & - \frac{L}{4s} MU^2 c_{TP} y_c + \left[ML^2 \left(\frac{L}{12} + \frac{x_1 f_1 + x_2 f_2}{4} \right) + mL^2 \left(\frac{L}{12} + \frac{x_1 + x_2}{4} \right) \right] \ddot{\phi} \\
 & + MUL^2 \left[\frac{f_1 - f_2}{4} + \frac{1}{24} c_N \frac{L}{D} \right] \dot{\phi} \\
 & + MU^2 L \left[\frac{1}{8} \frac{L}{s} c_{TP} - \frac{f_1 + f_2}{2} \right] \phi = 0,
 \end{aligned} \tag{16}$$

where $c_{TP} = c_T L/D + c_1 + c_2$. The same equations could have been obtained from first principles. It is noted that here L is the length of the cylindrical portion of the body which is smaller than the over-all length, as used in §5, by $\ell_1 + \ell_2$, the difference never exceeding a few per cent.

We non-dimensionalize these equations by introducing $\eta = y_c/L$, $\Lambda = s/L$, $\epsilon = L/D$, $\chi_1 = x_1/L$, $\chi_2 = x_2/L$ and $\tau = Ut/L$, and consider solutions of the form

$$\eta = He^{i\omega\tau} \quad \text{and} \quad \phi = \Phi e^{i\omega\tau}$$

where ω is a dimensionless frequency defined as $\omega = \Omega L/U$, Ω being the complex circular frequency of oscillation. Substituting η and ϕ into the non-dimensionalized equations, and noting that our assumptions require $m = M$, we obtain

$$\begin{aligned}
 & \left\{ [2 + \chi_1(1 + f_1) + \chi_2(1 + f_2)](-\omega^2) + \left[\frac{1}{2} \epsilon c_N + f_1 - f_2 \right](\omega i) + \left[\frac{1}{2} c_{TP}/\Lambda \right] \right\} H \\
 & + \left\{ -\frac{1}{2} [\chi_1(1 + f_1) - \chi_2(1 + f_2)](-\omega^2) + \left[2 - \frac{1}{2} (f_1 + f_2) \right](\omega i) \right. \\
 & \left. + \left[\frac{1}{2} \epsilon c_N + f_1 - f_2 - \frac{1}{4} (1/\Lambda) c_{TP} \right] \right\} \Phi = 0,
 \end{aligned} \tag{17}$$

and

$$\begin{aligned}
 & \left\{ -\left[\frac{1}{2} \chi_1(1 + f_1) - \frac{1}{2} \chi_2(1 + f_2) \right](-\omega^2) - \left[\frac{1}{2} (f_1 + f_2) \right](\omega i) - \left[\frac{1}{4} c_{TP}/\Lambda \right] \right\} H \\
 & + \left\{ \left[\frac{1}{6} + \frac{1}{4} \chi_1(1 + f_1) + \frac{1}{4} \chi_2(1 + f_2) \right](-\omega^2) + \left[\frac{1}{4} (f_1 - f_2) + \frac{1}{24} \epsilon c_N \right](\omega i) \right. \\
 & \left. + \left[\frac{1}{8} (1/\Lambda) c_{TP} - \frac{1}{2} (f_1 + f_2) \right] \right\} \Phi = 0.
 \end{aligned} \tag{18}$$

Similar equations were obtained when using the theory of [26], i.e. Eqs. (10a), (11), (12) and (13), namely

$$\begin{aligned} & \left\{ [2 + \chi_1(1 + f_1) + \chi_2(1 + f_2)](-\omega^2) + \left[\frac{1}{2} \epsilon c_N + f_1 - f_2\right](\omega i) + \left[\frac{1}{2} c_{TP}/\Lambda\right] \right\} H \\ & + \left\{ -\frac{1}{2} [\chi_1(1 + f_1) - \chi_2(1 + f_2)](-\omega^2) + \left[2 - \frac{1}{2}(f_1 + f_2)\right](\omega i) \right. \\ & \left. + \left[\frac{1}{2} \epsilon(c_N + c_T) + f_1 - f_2 - \frac{1}{4} c_{TP}/\Lambda\right] \right\} \Phi = 0, \end{aligned} \quad (17a)$$

$$\begin{aligned} & \left\{ -\left[\frac{1}{2} \chi_1(1 + f_1) - \frac{1}{2} \chi_2(1 + f_2)\right](-\omega^2) - \left[\frac{1}{2}(f_1 + f_2)\right](\omega i) - \left[\frac{1}{4} c_{TP}/\Lambda\right] \right\} H \\ & + \left\{ \left[\frac{1}{6} + \frac{1}{4} \chi_1(1 + f_1) + \frac{1}{4} \chi_2(1 + f_2)\right](-\omega^2) + \left[\frac{1}{4}(f_1 - f_2) + \frac{1}{24} \epsilon c_N\right](\omega i) \right. \\ & \left. + \left[\frac{1}{8} c_{TP}/\Lambda - \frac{1}{2}(f_1 + f_2)\right] \right\} \Phi = 0. \end{aligned} \quad (18a)$$

For non-trivial solution, the determinant of the coefficients of H and Φ in (17) and (18), or in (17a) and (18a), must vanish, yielding a quartic in ω ,

$$\omega^4 + A\omega^3 + B\omega^2 + C\omega + E = 0. \quad (19)$$

6.2 Calculations Based on the Theory of [26]

The aim here was to compare the dynamical behavior of the rigid body to that of a flexible body; as the rigid body may be regarded as a flexible one of very large flexural rigidity, it would be reasonable to expect correspondence of the dynamical behavior of the rigid body to the 'rigid-body' modes of the flexural one, i.e. the zeroth and first modes. Recalling that the dimensionless flow velocity in the case of a flexible body was defined as $u = (M/EI)^{1/2} UL$, the dynamical behavior of the rigid body should approach that of the flexible one as $u \rightarrow 0$. Two sets of calculations were conducted, as described below.

The four rigid-body frequencies, given by (19), were computed for a number of cases and the values compared with the existing complex frequencies of the flexible body. As an example, let us compare the case corresponding to Fig. 3. The four frequencies are $\omega_1 = 1.956$, $\omega_2 = -0.761$, $\omega_{3,4} = \pm 0.582 - 0.357i$. These compare well with the four frequencies associated with the flexible body for $u = 0.7$, namely $\omega_1 = 1.934$, $\omega_2 = -0.734$, $\omega_{3,4} = \pm 0.580 - 0.350i$; the first

two are associated with the zeroth mode, and the other two with the first mode and its mirror image about the $[\operatorname{Im}(\omega)]$ -axis.

Surprisingly, the correspondence of the rigid-body frequencies to those of the flexible body, for the apparently arbitrary value of $u = 0.7$ persists for other values of f_2 , as shown in Table 2. This value of $u = 0.7$ can be explained as follows. We have defined the dimensionless frequency of the rigid body by $\omega_{rb} = \Omega L/U$. On the other hand, the dimensionless frequency of the flexible body was defined as $\omega_{fb} = [(M+m)/EI]^{1/2} \Omega L^2/U$, which may be rewritten as $\omega_{fb} = [(M+m)/M]^{1/2} u \Omega L/U$, where u is the dimensionless flow velocity (§5.1). The assumptions made in the theory require that $m = M$, so that $\omega_{fb} = \sqrt{2} u \Omega L/U$. Now, if the dimensional frequency, Ω , of the rigid body and of the flexible body are identical, we may rewrite this as $\omega_{fb} = \sqrt{2} u \omega_{rb}$, and we can see that identity of the dimensionless frequencies will occur when $u = 1/\sqrt{2} \approx 0.707$.

Calculations were also conducted to pin-point the thresholds of yawing and oscillatory instability in terms of f_2 , Λ etc., and to compare with the existing stability diagrams, e.g. Figs. 6 and 7.

TABLE 2
RIGID-BODY AND FLEXIBLE-BODY FREQUENCIES COMPARED
Other parameters: $\Lambda = 1$, $\epsilon_{c_N} = \epsilon_{c_T} = 1$, $f_1 = 1 - c_1 = 1$, $c_2 = 1 - f_2$,
 $\chi_1 = \chi_2 = 0.01$

f_2	Rigid body			Flexible body ($u = 0.7$)		
	ω_1	ω_2	ω_3	ω_1	ω_2	ω_3
1.0	1.95	-0.76	0.58-0.36i	1.93	-0.73	0.58-0.35i
0.8	1.95	-0.30	0.84-0.39i	1.93*	-0.29	0.83-0.38i
0.4	1.96	-0.08	1.15-0.20i	1.95	-0.09	1.14-0.19i
0	2.03	0.42	1.28-0.01i	2.02	0.42	1.28-0.004i

In the case of a rigid body with parameters corresponding to those of Fig. 6, it was found that oscillatory instability exists for $0 \leq f_2 \leq 1$ and that yawing occurs for $f_2 > 0.5$. Correspondingly, for the case of Fig. 7 it was found that yawing persists throughout, and

* Upon examination, the stable branch of the zeroth mode as given in [26] was found to be in error; the locus moves away from the $[\operatorname{Re}(\omega)]$ -axis much faster than shown in Fig. 3, [26]. The corrected value for $u = 0.7$ is given here.

that oscillatory instability occurs for $\Lambda > 0.20$. Once again agreement in behavior of the rigid body and the flexible body (for $u = 1/\sqrt{2}$) is good. Similar calculations confirmed agreement with the other stability maps of [26].

Two stability diagrams were constructed (Figs. 14 and 15) showing the effect of ϵc_N , ϵc_T , f_2 and Λ on stability, for comparison with those to be obtained using the new theory.

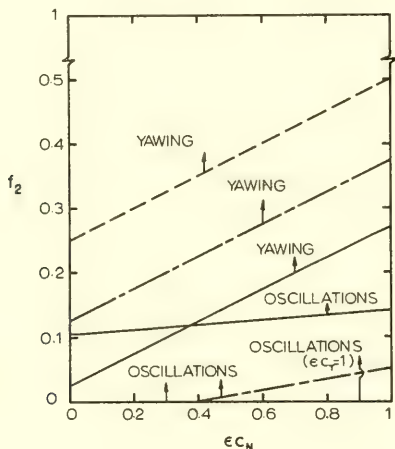


Fig. 14. The effect of ϵc_N , ϵc_T and f_2 on stability of a rigid cylinder with $\Lambda = 1$, $f_1 = 1 - c_1 = 1$, $c_2 = 1 - f_2$ and $\chi_1 = \chi_2 = 0.01$. — $\epsilon c_T = 0.1$; --- $\epsilon c_T = 0.5$; - - - $\epsilon c_T = 1$. (Theory of [26]).

In Fig. 14 we observe that unless ϵc_T is considerably less than ϵc_N , the region of oscillations practically covers the whole plane; moreover, oscillations persist to lower values of f_2 than yawing does.

In Fig. 15 we see that a sufficiently short tow-rope has a very definite stabilizing effect on the system, as far as oscillatory instability is concerned. Very long tow-ropes, on the other hand, evidently have a very weak stabilizing effect.

The foregoing clearly establish that the dynamical behavior of the rigid body is represented by the behavior of the zeroth and first modes of the flexible body at small u .

One noteworthy aspect of the analysis is that the existence of yawing instability cannot be affected by varying Λ , i.e. by altering

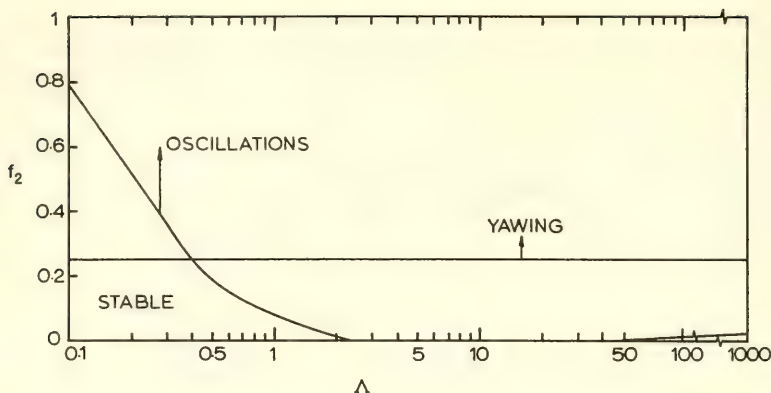


Fig. 15. The effect of Λ on stability of a rigid cylinder with $f_1 = 1 - c_1 = 1$, $\epsilon c_N = \epsilon c_T = 0.5$, $c_2 = 1 - f_2$ and $\chi_1 = \chi_2 = 0.01$. (Theory of [26]).

the tow-rope length. In the case of the rigid body this becomes obvious upon considering equation (19). Since the threshold for yawing instability implies $\omega = 0$, this threshold is established by the equation $E = 0$. Now E is found to be

$$E = (c_{TP}/2\Lambda) \left[\frac{1}{2} \epsilon (c_N + c_T) - 2f_2 \right].$$

Clearly we see that the threshold is not dependent on Λ . This seems to be in contradiction with Strandhagen's et al. [1] criterion (iii) for the stability of towed ships (as given in §1); on closer examination of their own work, however, we see that the equivalent of term E , in their case also, contains Λ as a common factor. Accordingly, we must conclude that the only form of instability the existence or non-existence of which may be controlled by the tow-rope length is oscillatory.

6.3 Calculations Based on the New Theory

Calculations were also conducted with the new theory. It was found that, in this case also, the dynamical behavior of the rigid body corresponds to that of the zeroth and first modes of the flexible one at low towing speeds -- quantitative correspondence of frequencies occurring at $u = 1/\sqrt{2}$ as before.

Stability plots were also constructed (Figs. 16 and 17). These are markedly different to those given by the old theory (Figs. 14 and 15), the main difference being in that oscillatory instability according

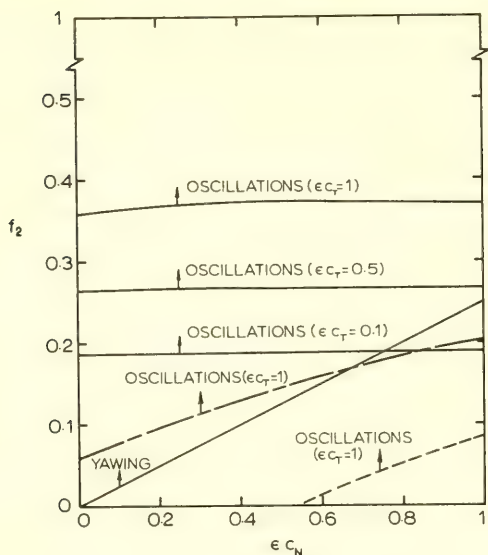


Fig. 16 The effect of ϵc_N , ϵc_T and f_2 on stability of rigid cylinders with $\Lambda = 1$, $c_2 = 1 - f_2$, $c_1 = 0$ and $\chi_1 = \chi_2 = 0.01$; — $f_1 = 1$; --- $f_1 = 0.8$; ... $f_1 = 0.7$. (New theory).

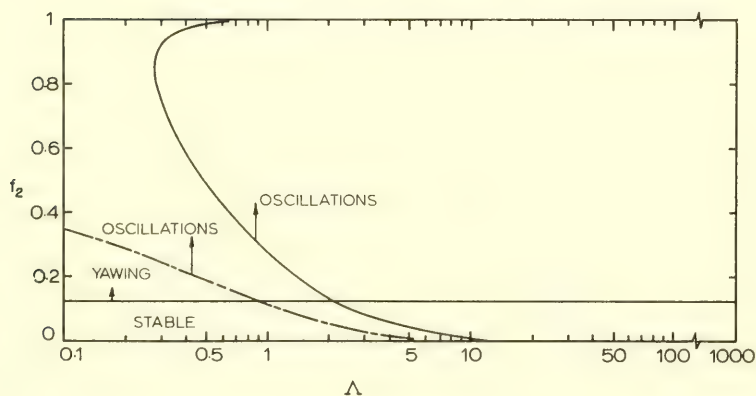


Fig. 17 The effect of Λ on stability of a rigid cylinder; $c_2 = 1 - f_2$, $\epsilon c_N = \epsilon c_T = 0.5$, $\chi_1 = \chi_2 = 0.01$; — $f_1 = 1 - c_1 = 1$; --- $f_1 = 0.8$, $c_1 = 0$. (New theory).

to the new theory occurs over a much more limited range of system parameters, while yawing is more prevalent.

Comparing Fig. 16 to Fig. 14 we note the following essential differences: (i) yawing, being independent of c_T according to the new theory, is represented by a single line; (ii) according to the new theory oscillations persist to progressively lower values of f_2 as ϵc_T is reduced, while the opposite trend was predicted by the old theory; (iii) according to the new theory, for $f_1 = 1$, there are large regions in the $(\epsilon c_N, f_2)$ parameter space where yawing occurs alone, but not where oscillations occur alone; on the other hand, according to the old theory the opposite is true. However, this last point applies only for $f_1 = 1$. It may be seen that for $f_1 = 0.8$ and 0.7 , the results of the new theory become much more like those of Fig. 14 in this respect.

We note that the onset of yawing is independent of f_1 as well as c_T , so that the line shown in Fig. 16 applies to all cases examined therein. Once again considering term E of Eq. (19), which in this case is given by $E = (c_{TP}/2\Lambda)(\frac{1}{2}\epsilon c_N - 2f_2)$, we see that f_1 , c_1 , c_2 , c_T and Λ are all parameters that cannot affect the onset of yawing.

We next compare Fig. 17 to Fig. 15. The results are quite similar, except that (when $f_1 = 1$) oscillatory instability occurs over a more limited range according to the new theory than predicted by the old theory. However, the results of the new theory for $f_1 = 0.8$ when compared with those of the old one for $f_1 = 1$ are quite similar. The results for $f_1 = 0.7$, not shown in Fig. 17, are of interest in that oscillatory instability, in that case, occurs practically over the whole plane, i.e. for $f_2 > 0.013$ for $\Lambda = 0.1$ and for $f_2 > 0.008$ for $\Lambda = 0.2$.

VII. CONCLUSION

In this paper we have reviewed an existing theory for the dynamics of flexible cylindrical bodies towed underwater, and developed a parallel theory for rigid cylinders. It was shown that, whereas the dynamical problem in the case of rigid cylinders is independent of towing speed, in the case of flexible cylinders the dynamical behavior (and stability) of the system is highly dependent upon towing speed. It was found that, in general, flexible towed cylinders are subject to both flexural and 'rigid-body' instabilities, the latter occurring at relatively low towing speeds. It was also established that at low towing speeds, the dynamical behavior of the flexible cylinders in their two lowest modes (the so-called zeroth and first) correspond to that of rigid cylinders, which of course have but two degrees of freedom. Thus the study of the dynamics of towed flexible cylinders yields sufficient information to establish the dynamical behavior of the corresponding rigid bodies.

A new theory was also presented (for both flexible and rigid cylinders) which, it is believed, represents the physical system more closely. The main difference in the results obtained by the old and new theories are associated with the behavior of the rigid-body modes of the system; specifically, the new theory predicts the system to be more stable in its first (oscillatory) mode and less stable in its zeroth (yawing) mode than does the old theory.

The new theory is in general qualitative agreement with experiment. Quantitative agreement cannot be assessed definitively until a means is found for accurately determining the values of some of the dimensionless system parameters, particularly f_1 and f_2 . Nevertheless, it is possible to make intelligent estimates of these parameters based on experience from other experiments [25]. On that basis quantitative agreement between theory and experiment, for one particular experiment (Table 1), is seen to be fair, although clearly leaving a good deal to be desired.

In all the above discussion, as in [26], the observed criss-crossing instability was identified with the theoretically predicted first-mode oscillatory instability, despite the fact that in most cases theory predicts that the system is also subject to yawing instability over the same range of towing speeds. This is supported by the observed frequency characteristics of the oscillation and the observed effect of varying Λ , for instance, being essentially as theoretically indicated for the behavior of the first mode. It has thus been presumed that oscillatory instability is the prevalent form of instability. There is, however, an alternative interpretation of the observed behavior, namely that criss-crossing oscillation is a nonlinear manifestation of yawing. This may be postulated, but cannot be proven by the present linear theory.

In fact a number of questions remain. More careful and extensive experiments, including experiments with rigid cylinders, and more extensive theoretical calculations are necessary to resolve these questions.

We next consider briefly the mechanism underlying the onset of instabilities, to the extent of identifying the physical forces at work.

We first consider the mechanism involved in yawing. The first thing to recognize is that yawing must involve angular motion as opposed to pure translation. This is evident upon considering the cylinder momentarily displaced parallel to the x -axis; in this case the forces acting on the cylinder are exactly as in the equilibrium configuration, except that the tow-rope exerts a restoring force on the body. We next imagine the cylinder momentarily displaced such that the y -displacement of the nose is positive and that of the tail negative. Then, considering boundary conditions (11) and (12), we note that the inviscid hydrodynamic force at the nose is $f_1 \mu U^2 \{\partial y / \partial x\}$

while at the tail it is $-f_2 MU^2 (\partial y / \partial x)$, producing a moment tending to exaggerate the original inclination. However, there are Coriolis forces proportional to $MU (\partial^2 y / \partial x \partial t)$ which always oppose rotation [cf. Eq. (10)].

To understand this action of the Coriolis forces we consider the related physical system of a hinged-free tube containing flowing fluid (as mentioned in §2), depicted in Fig. 18(a), which was first considered by Benjamin [32]. We see that if the system rotates about A without bending, the fluid suffers a Coriolis acceleration which has a reaction on the tube always opposing the motion. This is clearly a stabilizing effect, as energy has to be expended by the tube to keep the motion going; as further elaborated by Benjamin, this represents the action of a pump from the energy-transfer point of view.

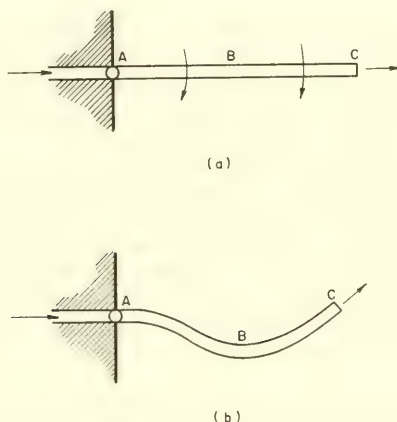


Fig. 18 Rudimentary representation of a pump and a radial-flow turbine

We next consider flexural instabilities. Clearly everything mentioned so far applies here also. But we also have another force coming into play. Once again we consider the hinged-free tube containing flowing fluid, as shown in Fig. 18(b), where the tube is momentarily 'frozen' in the bent shape shown. The centrifugal force of the fluid acts to increase the curvature further. This is clearly a destabilizing force, energy flowing from the fluid to the tube; it is the action of a radial-flow turbine. In flexural oscillations we have a play between these 'centrifugal' forces and the Coriolis forces; when the former prevail, then instabilities may develop.

More formally, we may consider the work done, ΔW , on the cylinder over one period of oscillation, t_1 , in much the same way as was done in [24]. We find that

$$\Delta W = (1 - f_1)MU \int_0^{t_1} [\dot{y}^2 + U\dot{y}y']_{x=0} dt - (1 - f_2)MU \int_0^{t_1} [\dot{y}^2 + U\dot{y}y']_{x=L} dt - \frac{1}{2} c_N \int_0^{t_1} \int_0^L \left(\frac{MU}{D} \right) (\dot{y}^2 + U\dot{y}y') dx dt. \quad (20)$$

If $\Delta W < 0$, oscillations will be damped, while if $\Delta W > 0$ oscillations will be amplified, i.e. the system will be unstable. We first note that if $f_1 = f_2 = 1$, then instability can only arise from viscous effects (cf. [24]). We next consider the first two terms of (20). We note that for arbitrarily small U stability will be governed by whether $(1 - f_1) \int_0^{t_1} \dot{y}_0^2 dt - (1 - f_2) \int_0^{t_1} \dot{y}_L^2 dt$ is positive or negative; it is clear, therefore, that a well streamlined nose ($f_1 \approx 1$) and a blunt tail ($f_2 < 1$), both tending to make $\Delta W < 0$, will promote stability. For higher U , however, the situation becomes more complex, as $U|\dot{y}y'| > \dot{y}^2$ may now obtain, and $\dot{y}y'$ may be either positive or negative, the bar representing the mean value over one period of oscillation. (It is noted that from Figs. 8 and 9 it may be found that for oscillatory instabilities we generally have $(\dot{y}y')_0$ being strongly negative, and $(\dot{y}y')_L$ also negative but with smaller absolute value.) Stability will depend on the magnitude of f_1 , f_2 , \dot{y}_0^2 , \dot{y}_L^2 etc., and no simple general rules can be formulated beyond the statement of Eq. (20).

It was found that the most effective way of stabilizing a towed system is by making it blunt at the tail, which has the disadvantage of increasing the towing drag. Clearly, what is needed is a blunt tail without separated flow! The present work and that of [26] indicate that small f_2 and large c_2 (both associated with a blunt tail) have individually stabilizing effects on the system. Clearly then what we need is a sufficiently small f_2 for stability, and a small c_2 for moderate form drag. From the boundary conditions we note that a small f_2 has the effect of reducing the lateral shear exerted by the tail on the cylinder. Accordingly, if the tail is made very flexible with the rest of the body essentially rigid, the full shear force might not be transmitted to the cylinder, simulating the effect of a small f_2 ; yet insofar as axial flow conditions are concerned, they would be fairly good. Of course, this particular solution might give rise to other problems, e.g. whiplash-type behavior of the tail may be envisaged.

Another point of possible practical interest hinges on the fact that a towed flexible body, which is unstable at low towing speeds, may be stable at an intermediate range of towing speeds. (On the other hand, a rigid towed body of the same shape would be unstable

at all towing speeds.) Accordingly, in the case of a flexible towed system this suggests the possibility of removable stabilizers; these would be operative only at low towing speeds, and would be removed at the operating speed to reduce drag. Incidentally, the above would generally also apply to articulated towed systems, made up of a number of rigid tubular sections flexibly connected [32], [33].

ACKNOWLEDGMENTS

The author is grateful to his student, Mr. Jean J. Baribeau for assistance in the preparation of this paper during the summer of 1970. The author wishes to thank the National Research Council (Grant No. A4366) and the Defense Research Board (Grant No. 9550-47) for financial support making this research program possible.

REFERENCES

- [1] A. G. Strandhagen, K. E. Schoenherr, P. M. Fobayashi, "The Dynamic Stability on Course of Towed Ships," Trans. Soc. Naval Arch. and Marine Eng., Vol. 58, pp. 32-66, 1950.
- [2] L. Bairstow, E. F. Relf, R. Jones, "The Stability of Kite-Balloons: Mathematical Investigation," A.R.C. R & M 208, 1915.
- [3] M. M. Munk, "The Aerodynamic Forces on Airship Hulls," NACA Rept. No. 184, 1924.
- [4] H. Glauert, "The Stability of a Body Towed by a Light Wire," A.R.C. R & M 1312, 1930.
- [5] L. W. Bryant, W. S. Brown, N. E. Sweeting, "Collected Research on Stability of Kites and Towed Gliders," A.R.C. R & M 2303, 1942.
- [6] A. G. Strandhagen, C. F. Thomas, "Dynamics of Towed Underwater Vehicles," Rept. No. 219, U.S. Navy Mine Defense Lab, Panama City, Florida, 1963.
- [7] J. R. Richardson, "The Dynamics of Towed Underwater Systems," Eng. Res. Associates Rept. No. 56-1, Toronto, Canada, 1965.
- [8] P. O. Laitinen, "Cable-towed Underwater Body Design," Rept. No. 1452, U. S. Navy Electronics Lab., San Diego, California, 1967.

- [9] K. T. Patton, J. W. Schram, "Equations of Motion of a Towed Body Moving in a Vertical Plane," Rept. No. 736, U.S. Navy Underwater Sound Lab., Fort Turnbull, Conn., 1966.
- [10] N. E. Jeffrey, "Influence of Design Features on Underwater Towed System Stability," J. Hydronautics, Vol. 2, pp. 205-13, 1968.
- [11] J. W. Schram, S. P. Reyle, "A Three-dimensional Dynamic Analysis of a Towed System," J. Hydronautics, Vol. 2, pp. 213-20, 1968.
- [12] L. F. Whicker, "Oscillatory Motion of Cable-Towed Bodies," Ph.D. Thesis, Univ. of Calif., Berkeley, California, 1957.
- [13] A. R. McLeod, "On the Action of Wind on Flexible Cables with Application to Cables below Aeroplanes and Balloon Cables," A.R.C. R & M 554, 1918.
- [14] E. F. Relf, C. H. Powell, "Tests on Smooth and Stranded Wires Inclined to the Wind Direction and a Comparison of Results on Stranded Wires in Air and Water," Adv. Comm. Aero., R & M 307, 1917.
- [15] L. Landweber, M. H. Protter, "The Shape and Tension of a Light Flexible Cable in a Uniform Current," Rept. No. 533, David Taylor Model Basin, Navy Department, Washington, D. C., 1944.
- [16] L. Pode, "An Experimental Investigation of the Hydrodynamic Forces on Stranded Cables," Rept. No. 713, David Taylor Model Basin, Navy Department, Washington, D. C., 1950.
- [17] L. Pode, "Tables for Computing the Equilibrium Configuration of a Flexible Cable in a Uniform Stream," Rept. No. 687, David Taylor Model Basin, Navy Department, Washington, D.C., 1951.
- [18] F. O'Hara, "Extension of Cylinder Tow Cable Theory to Elastic Cables Subject to Air Forces of a Generalized Form," A.R.C. R & M 2334, 1945.
- [19] N. E. Kochin, "Form Taken by the Cable of a Fixed Barrage Balloon under the Action of Wind," Appl. Math. Mech. Vol. 10, pp. 152-64, 1946.
- [20] M. C. Eames, "Steady-state Theory of Towing Cables," Quart. Trans. Roy. Instn. Naval Arch., Vol. 110, pp. 185-206, 1968.

- [21] E. L. Albasny, W. A. Day, "The Forced Motion of an Extensible Mooring Cable," J. Inst. Maths. Applics, Vol. 5, pp. 55-71, 1969.
- [22] G. H. Toebes, "Flow-induced Structural Vibrations," J. Eng. Mech. Div., Proc. ASCE, Vol. 91, No. EM6, pp. 39-66, 1965.
- [23] W. R. Hawthorne, "The Early Development of the Dracone Flexible Barge," Proc. Instn. Mech. Engrs., Vol. 175, pp. 52-83, 1961.
- [24] M. P. Païdoussis, "Dynamics of Flexible Slender Cylinders in Axial Flow -- Part 1. Theory," J. Fluid Mech., Vol. 26, pp. 717-36, 1966.
- [25] M. P. Païdoussis, "Dynamics of Flexible Slender Cylinders in Axial Flow -- Part 2. Experiments," J. Fluid Mech., Vol. 26, pp. 737-51, 1966.
- [26] M. P. Païdoussis, "Stability of Towed, Totally Submerged Flexible Cylinders," J. Fluid Mech., Vol. 34, pp. 273-97, 1968.
- [27] M. P. Païdoussis, "Stability of Towed, Totally Submerged Flexible Cylinders," Rept. Eng. R-5, Atomic Energy of Canada, Chalk River, Ontario, 1967.
- [28] M. J. Lighthill, "Mathematics and Aeronautics," J. Roy. Aero. Soc., Vol. 64, pp. 375-94, 1960.
- [29] M. J. Lighthill, "Note on the Swimming of Slender Fish," J. Fluid Mech., Vol. 9, pp. 305-17, 1960.
- [30] G. I. Taylor, "Analysis of the Swimming of Long and Narrow Animals," Proc. Roy. Soc. (A), Vol. 214, pp. 158-83, 1952.
- [31] R. W. Gregory, M. P. Païdoussis, "Unstable Oscillation of Tubular Cantilevers Conveying Fluid -- I. Theory," Proc. Roy. Soc. (A), Vol. 293, pp. 512-27, 1966.
- [32] T. B. Benjamin, "Dynamics of a System of Articulated Pipes Conveying Fluid -- I. Theory," Proc. Roy. Soc. (A), Vol. 261, pp. 457-86, 1961.
- [33] M. P. Païdoussis and E. B. Deksnis, "Articulated Models of Cantilevers Conveying Fluid: The Study of a Paradox," J. Mech. Eng. Sc., Vol. 12, pp. 288-300, 1970.

HYDRODYNAMIC ANALYSES APPLIED TO A MOORING AND POSITIONING OF VEHICLES AND SYSTEMS IN A SEAWAY

Paul Kaplan
Oceanics, Inc.
Plainview, New York

I. INTRODUCTION

At present, increasing interest is being devoted to the problems of deep sea operations of vessels that must remain on station for an extended period of time in order to accomplish their intended mission. This concern was given its initial impetus by the successfully conducted preliminary operation of drilling through the ocean bottom from a surface ship in the operation known as the "Mohole Project," as well as the increase in oil exploration in deeper water depths. On the other hand, from the point of view of military operations, there is need for placing instrumentation packages and other military systems on the ocean floor for various purposes of National Defense. These operations require a definite degree of precision, safety during the course of the operation, and the capability of returning to a particular locale and retrieving information and/or the equipment itself for further study of data or for emplacement in another location.

As a result of this emphasis on deep-sea operations, it is necessary to determine the response of representative moored ships in the open sea, and also to determine the characteristics of the important parameters associated with lowering loads from such a vessel to the ocean floor and returning them to the ship. The parameters that are of interest to the personnel aboard the ship are the forces in the mooring cables, the displacements and tensions in the lowering lines, the degree of precision in placing the loads, the accelerations acting on the loads, and the magnitudes of impact on the ocean bottom. In order to arrive at some appropriate engineering estimates of the capabilities of carrying out such operations, application of available theoretical hydrodynamic studies can be made to deal with problems of this nature.

The study of motions of ships at sea is a general problem of

naval concern, and has received increasing emphasis during the last fifteen years or so by virtue of the advance of statistical methods which describe the effects with greater realism than in previous studies based on simplified wave representations. Major concern has been devoted primarily to the problems of an advancing ship in head seas, with the prime variables of concern being the heave and pitch motions. Recent studies, however, have been concerned with motions in oblique waves, wherein lateral motions (sway, yaw, and roll) are also important. All of these studies involved large ships advancing in waves, and only limited theoretical studies have been developed to predict adequately the motions in all six degrees of freedom under these operating conditions. A treatment of the motion of a free ship with six degrees of freedom in waves is a formidable problem that has not achieved a complete solution at the present time, and when the influences of moorings are also included, the problem is further compounded. Nevertheless, there exists a need for some means of preliminary estimation of the expected motions of a moored vessel, and there is sufficient hydrodynamic information available to allow a study that will indicate the expected range of amplitudes of motion so that the results obtained can be used as guide-lines for operating personnel.

Another related problem that is assuming more significance recently is that of a moored buoy system. These smaller payloads are planned for use over large ocean regions to provide a network of environmental reporting stations that will yield continuous data on the important properties of the ocean and atmosphere for use in weather forecasting and other technologies dependent on air-ocean interaction. The effective design and engineering development of such systems requires an ability to predict the buoy (and hence the transmitting antenna) oscillatory motions and structural acceleration loadings in various seaways; the determination of the tensions along the cable under various operating conditions; etc. Knowledge of such results will greatly enhance the design of handling equipment for both launching and retrieving of buoys at sea, and will also provide basic information on system survivability under extreme environmental conditions.

A tool that can provide engineering estimates of such information is a mathematical model that describes the essential mechanical-dynamic characteristics of a moored buoy system. This mathematical model will be a system of equations and relationships that allows the calculation of the spatial configuration, dynamic motion and internal tensions of a specified moored buoy in a given excitation environment. The hydrodynamic force acting on the buoy hull and the forces acting on the cable system (hydrodynamic, inertial and elastic) are coupled so that each affects the other, especially when considering dynamic effects and rapidly varying motions. Certain similarities exist between this problem and that of a moored ship, together with definite differences as well. The applicability of basic techniques of analysis from one problem to another provides useful

insight and extends the utility of basic "tools" used in hydrodynamic and dynamic investigations.

When considering the problem of maintaining a ship on station for a long time period, various concepts for achieving a minimum deviation from a derired operating point are possible, with the two main methods being that of fixed mooring or by use of a dynamic positioning system. In certain situations where mobility is required, as well as due to the high capital cost of a mooring system for very deep water operations, the associated high cost of emplacement and the dangers of damage due to large storm conditions, a mooring system does not appear to be attractive. Dynamic positioning is a more recent development, which has only received limited applicability to date.

In order to provide the information necessary to determine the possibility of an application of dynamic positioning, it is necessary to carry out particular analyses to determine the environmental conditions appropriate to possible operating areas; the resulting forces and moments acting on the ship; the arrangement and type of control effectors; the possible signal systems that provide the error and command signals for actuation of controls; possible control system concept designs; etc.

The important quantities that must be determined for proper design of the positioning system are the disturbing forces that act on the ship. The major forces and moments that affect the ship stationkeeping ability in this case are the more-or-less steady type of "drifting" forces imposed by the environment, and these quantities are amenable to computation by means of hydrodynamic analyses using available theory.

In all of the foregoing situations the importance of hydrodynamic force evaluation and its applicability to obtain desired engineering performance data is paramount. Many publications are available in the literature on ship motion theoretical studies that can be applied to the above problem areas, with reasonable expectation of validity for the results. The central theme of this Symposium, "Hydrodynamics in the Ocean Environment," is certainly appropriate to the present International Decade of Ocean Exploration which will emphasize the technology that will yield benefits to Mankind. The application of the basic developments in hydrodynamics of ship motion to the applied engineering problems associate with maintaining vessel operations at fixed positions in the ocean, which will be required as part of this extensive international effort, is a vital element in achieving improved system performance. It is also a good illustration of the direct application of many years of basic research toward the solution of problems that are anticipated as further and deeper ventures into the sea are made. The present paper is aimed at providing a limited description of the use of hydrodynamic analysis when applied to some of these problem areas.

II. SCOPE OF INVESTIGATION

It is easily seen that there are a host of problems associated with the subjects considered in this paper. As a result, some limitations are imposed so that only certain aspects are considered in detail. The region of application of the results in this paper is in deep water, so that no shallow water effects are considered. This limitation thereby excludes problems of ship oscillation when moored at docks in harbors, which is an important problem that can be treated in a similar fashion to those herein by proper inclusion of shallow water effects. The main emphasis within this paper is on the seaway and its effects, and in some cases the influence of a current will not be considered. However it is known that currents are often present together with sea waves, and their combined effect is often very important. In addition the presence of a current is often necessary to establish certain static equilibrium conditions for a vehicle about which the seaway disturbances are imposed, and in that case certain assumptions are made as to the existence of such initial conditions for purposes of simplifying the analysis. Similarly, the presence of any wind effects is also not considered in detail within this paper.

When considering the problem of the motions of moored systems, it is known that the effects of drift forces are also present and that they produce an important influence on the resulting motions and cable forces. However, in an effort to obtain tractable solutions and to provide information on the characteristics due to different force mechanisms, these effects will be considered separately. Illustrations of the different influences that act on vehicles and systems in a seaway will be presented separately, with some discussion given to the expectations with combined effects in a realistic situation when more than one mechanism is acting on a system. The discussions of results are devoted to the more important phenomena influencing performance of a system in the sea, and they will be given throughout the paper for each case treated.

III. TECHNIQUES USED FOR MOORED SHIP ANALYSIS

In order to determine the motions of a moored ship in irregular waves, it is necessary to determine the response in regular sinusoidal waves. The aim is to predict these motions, and the technique to be utilized is that of spectral analysis [1] wherein the statistical definition of the seaway in the form of its energy spectrum is used as the initial data. The energy spectrum of the time history of each motion of the vessel in response to irregular waves is evaluated for the corresponding degrees of freedom to the energy spectrum of the seaway. These operators are obtained from the solutions for the motions in sinusoidal waves, and in accordance with the basic premise of this technique of analysis, a linear theory of ship motions is a prerequisite.

The equations of motion in regular waves, for six degrees of freedom, are formulated according to linear theory by the balance of inertial, damping, restoring, exciting, and coupling forces and moments. Both hydrodynamic and hydrostatic effects due to the body-fluid interaction are included in the analysis, together with the influences of the mooring system. The longitudinal motions (heave, pitch, and surge) are coupled to each other, and similarly, the lateral motions (sway, yaw, and roll) are also coupled. There is no coupling between the two planes of motions, in accordance with linear theory.

The hydrodynamic forces and moments such as damping, exciting effects due to waves, etc., are determined by application of the methods of slender-body theory. Essentially, this theory makes the assumption that, for an elongated body where a transverse dimension is small compared to its length, the flow at any cross section is independent of the flow at any other section; therefore, the flow problem is reduced to a two-dimensional problem in the transverse plane. The forces at each section are found by this method, and the total force is found by integrating over the length of the body. A description of the application of slender-body theory to calculate the forces acting on submerged bodies and surface ships in waves is presented in [2], where simplified interpretations of force evaluation in terms of fluid momentum are also given. The hydrostatic and mooring forces and moments are combined with the hydrodynamic terms, resulting in linear combinations of terms that are proportional to acceleration, velocity and displacement in the various degrees of freedom. All of these expressions, when related to the appropriate ship inertial reactions by Newton's law, lead to the set of six linear coupled differential equations of motion.

Solutions of the equations are found for regular sinusoidal seas with varying wave length and heading relative to the barge. The response amplitude operators are found from these solutions together with the phases of the motions relative to the system of regular waves. Assuming a knowledge of the oncoming irregular sea conditions (e.g. in terms of sea state, as specified by an associated surface-elevation energy spectrum from information in [3]), the set of energy spectra for the ship motions are determined. Information on average values and probabilities of relatively high values of the amplitudes of oscillations in the ship-motion time histories for the different degrees of freedom are found from the ship-motion energy spectra in accordance with the methods of [1]. Cross-spectra are also used to determine the energy spectra and hence the various average values and the probabilities for the remaining quantities of interest, such as load-displacement time histories and other quantities which are linear combinations of the ship motions and their time rates of change (the presence of lowering lines for placing loads on the ocean floor is considered in this analysis). These energy spectra may also be obtained from the solutions of the differential equations by linear superposition, and explicit use of cross-spectra here is necessary

only for obtaining phase information.

The ship is assumed to be placed in a currentless seaway, with no wind effects being considered. This may be somewhat unrealistic from the practical point of view, but since concern here is devoted only to the motions induced by the seaway, this neglect is reasonable (as discussed previously). The ship is assumed to be moored with bow and stern moorings of conventional line and anchor type. The line and anchor mooring system utilized for this study is a particular system especially suited to deep-sea operations [4], and utilizes a taut line. Other types of mooring lines can be considered as well, but separate analyses to determine the static orientation, restoring force variations, etc. must be carried out. The extent of linearity for these different mooring arrangements must be determined for use in the present type of analysis. The effects of the moorings will be to provide restoring effects in the particular displacements of surge, sway and yaw, thereby providing "spring-like" terms in the equations for these degrees of freedom. As a result, there are certain natural frequencies associated with these motions, which do not ordinarily occur in case of free (unmoored) ships. The moorings are assumed to have a negligible influence on the motions of heave, pitch, and roll, which have large hydrostatic restoring effects.

Following the evaluation of the various motions of the moored ship, equations are formulated to determine the forces in the mooring cables, and the displacement of and tension in the lowering line, as a function of the different degrees of freedom of the oscillating platform moored in the seaway. The lowering line displacement and tension, which are functions of the ship motions are then related to the seaway and all of the resulting spectra determined. Operations on these quantities provide information on expected amplitudes for particular sea states, and in addition the vertical accelerations of the loads are determined and similarly expressed, where this information is useful for study of impact of the loads on the ocean bottom.

IV. EQUATIONS OF SHIP MOTION

The equations of motion of the moored ship are derived on the basis of linear theory, with the body allowed to have six degrees of freedom. A right-hand cartesian coordinate system is chosen with the axes fixed in the body, and with the origin at the center of gravity of the body. The x-axis is chosen positive toward the bow, the y-axis is positive to port, and the z-axis is positive upward. These axes are defined to have a fixed orientation, i.e. they do not rotate with the body, but they can translate with the body. The body angular motions can be considered to be small oscillations about a mean position given by the axes. The dynamic variables are the linear displacements x , y , and z along the respective axes, and the angular displacements ϕ , θ and ψ which are defined as positive in

a direction of positive rotation about the x , y , and z axes, respectively, (i.e. port upward, bow downward and bow portward). The positive directions of the forces and moments acting on the body are similarly defined.

The force (or moment) acting on the body is composed of the inertial force due to dynamic body motions (denoted as F_i), the force due to damping (denoted as F_d), the force due to hydrostatic restoring action (denoted as F_h), the force due to the moorings (denoted as F_m), and the force due to waves (denoted as F_w). The equations of motion are then established as

$$m\ddot{s} = F = F_i + F_d + F_h + F_m + F_w \quad (1)$$

for rectilinear motions (with s representing any rectilinear displacement, and m the mass of the ship), with similar representations for the angular motions. A discussion of these different types of forces is given below, together with some results obtained, for purposes of illustration.

The hydrodynamic forces and moments due to dynamic body motions are of inertial nature, and do not contain any terms of dissipative nature. The effect of the free surface is accounted for by different frequency-dependent factors that modify the added masses of each section. All couplings of inertial nature are exhibited in the results of the analysis. In the case of dynamic body motions, the simplified results of slender-body theory states that the local force on any section is equal to the negative time rate of change of fluid momentum [2]. For the vertical force (z -force), this is expressed by

$$\frac{dZ_i}{d\xi} = - \frac{D}{dt} |A'_{33}w_b|, \quad (2)$$

where A'_{33} is the added mass of the cross-section and w_b is the body vertical velocity, given by

$$w_b = \frac{D}{Dt} (z - \xi\theta) = \dot{z} - \xi\dot{\theta}. \quad (3)$$

In the above equations, the coordinate ξ is a "dummy" variable along the longitudinal coordinate x (and coincident with it), and the time derivative D/Dt is just the partial derivative $\partial/\partial t$, since there is no forward speed. The quantity A'_{33} is the added mass of the cross section, including free-surface effects, which is obtained from the work of Grim [5] for the class of sections known as Lewis forms. The total vertical inertial force is then found to be

$$Z_i = - \int_{\xi_s}^{\xi_b} A'_{33} d\xi \cdot \ddot{z} + \int_{\xi_s}^{\xi_b} A'_{33} \xi d\xi \cdot \ddot{\theta} \quad (4)$$

where ξ_b and ξ_s are the bow and stern ξ -coordinates respectively.

In a similar manner, the lateral force (along y -direction) may also be expressed by use of this same procedure, but certain additional factors enter in that case. These factors are the necessity of including roll effects which influence the lateral velocity, and also the fact that the representation of the lateral force is based upon added mass terms that are evaluated for motions relative to the free surface level, rather than the body center of gravity position. Corrections to refer the final forces to the center of gravity position are made after finding the forces referred to the free-surface position. The detailed procedures for determining these inertial force (and moment) results, as well as all other forces of hydrodynamic, hydrostatic, etc. nature are described in [6], which is the basic report on which the present section of this paper is based. In view of this, only limited discussion of the remaining forces and moments will be presented.

The damping forces and moments are dissipative in nature, and are primarily due to the generation of waves by the ship motions on the surface, which continually transfer energy by propagating outward to infinity. In accordance with the two-dimensional treatment used for the analysis of inertial forces due to body motions, the same concept is used in evaluating the local forces at a section of the ship due to wave generation. With the ratio of the amplitude of the heave-generated two-dimensional waves to the amplitude of heaving motion of the ship section denoted by \overline{A}_z , the vertical damping force per unit vertical velocity of the ship section is expressed as

$$N'_{zz} = \frac{\rho g^2 \overline{A}_z^2}{\omega^3} = \rho \omega \left(\frac{\lambda}{2\pi} \right)^2 \overline{A}_z^2 \quad (5)$$

where \overline{A}_z for Lewis-form sections are available as a function of $\omega^2 B^*/2g = \pi B^*/\lambda$, for different beam-draft ratios and section coefficients, where B^* is the local beam and λ the wave length.

The vertical damping force at each section is

$$\frac{dZ_d}{d\xi} = - N'_{zz} (\dot{z} - \xi \dot{\theta}), \quad (6)$$

and this is integrated over the ship length to determine the total vertical damping force, given by

$$Z_d = - N_z \dot{z} + N_{z\theta} \dot{\theta} , \quad (7)$$

where

$$N_z = \rho \omega \left(\frac{\lambda}{2\pi} \right)^2 \int_{\xi_s}^{\xi_b} \overline{A_z}^2 d\xi , \quad (8)$$

and

$$N_{z\theta} = \rho \omega \left(\frac{\lambda}{2\pi} \right)^2 \int_{\xi_s}^{\xi_b} \overline{A_z}^2 \xi d\xi . \quad (9)$$

Similar treatments yield the lateral damping force, pitch damping moment, etc.

In the initial discussion of damping, emphasis was placed upon energy dissipation due to wave generation. Actually, viscous effects also manifest themselves and contribute to damping. The contribution of the viscous damping term is quite negligible for most motions, with the possible exception of roll. Roll damping due to wave generation is often small for most normal ships and viscous effects (or other drag mechanisms, such as eddy-making) assume greater importance, especially if the ship is fitted with bilge keels. In that case, the roll damping is often of nonlinear form, and an approximation is used to determine some equivalent linear representation. Knowledge obtained from model experiments [7] was used to determine the value of roll damping used in treating the illustrative ship case in this paper.

The hydrostatic restoring forces and moments are, as the name implies, due to buoyancy effects arising from static displacements. The only displacements that will result in hydrostatic restoring effects are heave, pitch and roll. On the basis of linear theory, the local hydrostatic vertical force change due to vertical displacements is

$$\frac{dZ_h}{d\xi} = - \rho g B^* (z - \xi \theta) , \quad (10)$$

where the ship is assumed to be almost wall-sided near the intersection with the free surface, and the effective buoyancy change comes from the total immersion. Similarly, the hydrostatic restoring pitch moment is

$$\frac{dM_h}{d\xi} = - \xi \frac{dZ_h}{d\xi} , \quad (11)$$

leading to total hydrostatic restoring vertical force and pitch moment given by

$$Z_h = - \rho g \int_{\xi_s}^{\xi_b} B^* d\xi \cdot z + \rho g \int_{\xi_s}^{\xi_b} B^* \xi d\xi \cdot \theta, \quad (12)$$

and

$$M_h = \rho g \int_{\xi_s}^{\xi_b} B^* \xi d\xi \cdot z - \rho g \int_{\xi_s}^{\xi_b} B^* \xi^2 d\xi \cdot \theta. \quad (13)$$

In the case of roll motion, the hydrostatic restoring effect is given by

$$K_h = - \rho g \nabla |GM| \phi = - W |GM| \phi, \quad (14)$$

where ∇ is the displaced volume, $|GM|$ is the metacentric height, and $W = \rho g \nabla$ is the ship displacement.

The exciting forces and moments due to waves are obtained as the sum of terms due to buoyancy alterations as the waves progress past the ship hull, together with hydrodynamic terms of inertial and damping. The buoyancy effect for the vertical force is represented by

$$\rho g B^* \eta(\xi, t) \quad (15)$$

at each section, and these contributions are combined to determine the total forces and moments due to waves. The analysis includes an allowance for the waves to be propagating at an oblique heading with respect to the ship, and a further allowance for the influence of the non-slenderness of the ship is also included. A correction factor, relating the beam to the wave length and the heading, is included for this purpose since the shipforms considered for mooring application are often not very slender. Details of the evaluation of wave forces and moments by these methods are presented in [6].

Before discussing the mooring forces and moments, information on the characteristics of the vessel studied in this investigation is given below. The particular vessel for which the equations are formulated and solutions carried out is the CUSS I, which was the vessel used in the preliminary Mohole drilling operation. This ship is considered representative of the class of construction type barges which will be utilized for deep-sea construction operations. A diagram of the barge, together with its mooring and load-lowering lines, is shown in Fig. 1. A summary of the numerical values of the parameters characterizing the moored-barge system is presented in Table 1.

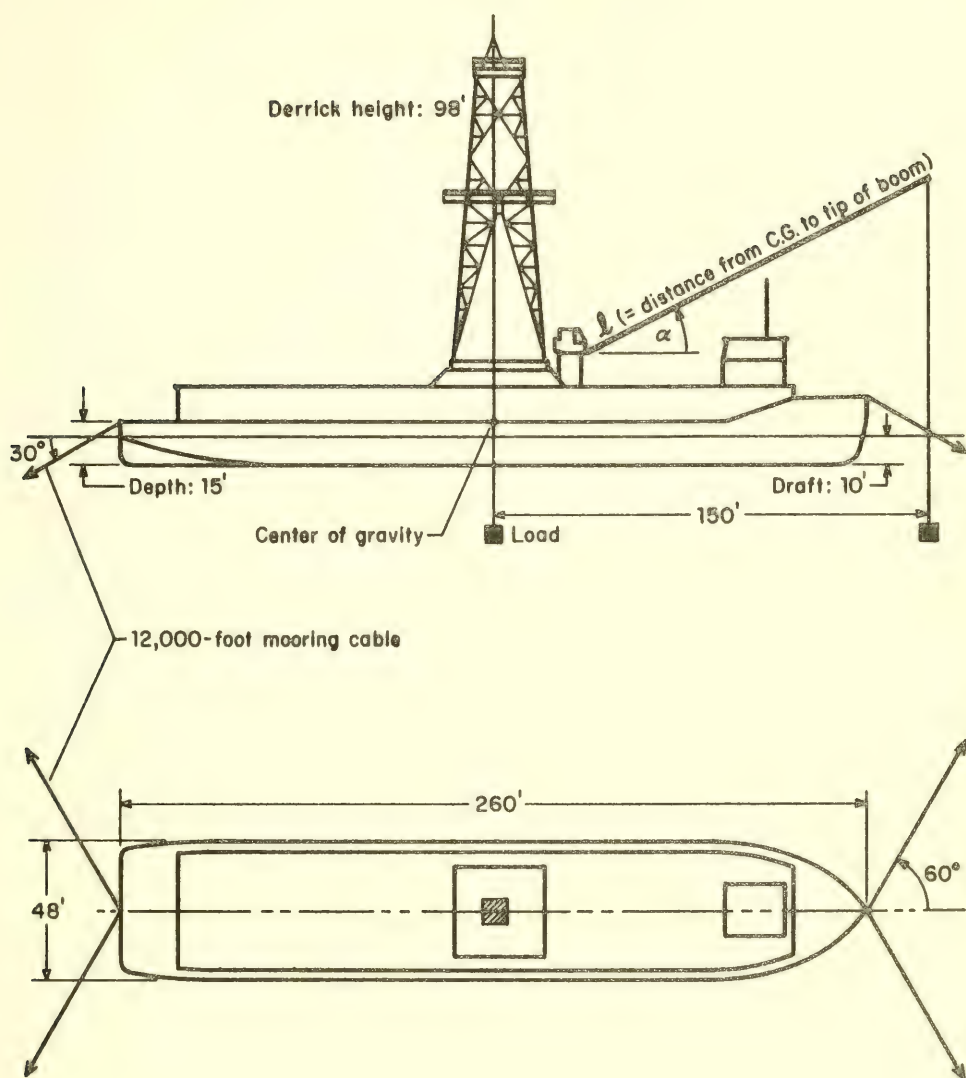


Fig. 1. Schematic diagram of moored barge
(Profile and plan views)

Table 1
Numerical Values of Moored-Barge System

Length	= L	= 260 ft
Beam	= B	= 48 ft
Draft		= 10 ft
Vertical distance from CB to CG	= BG	= 9.8 ft
Vertical distance from free surface to CG	= (\overline{OG})	= 5.1 ft
Vertical distance from CG to keel	= KG	= 15.1 ft
Metacentric height	= GM	= 8.16 ft
Displacement		= 2823.2 long tons
Weight	= W	= 6.324×10^6 lbs
Mass	= m	= 197.624×10^3 slugs
Pitch moment of inertia ¹	= I_{y_0}	= 706.7×10^6 slug-ft ²
Yaw moment of inertia ¹	= I_{z_0}	= 706.7×10^6 slug-ft ²
Roll moment of inertia ²	= I_{x_0}	= 49×10^6 slug-ft ²
Total roll moment of inertia (including added inertia due to fluid)	= I_{x_t}	= 78.69×10^6 slug-ft ²
Surge period ³	= T_{surge}	= 79 seconds
Sway period	= T_{sway}	= 64.5 seconds
Heave period	= T_{heave}	= 4.6 seconds
Pitch period	= T_{pitch}	= 4 seconds
Roll period	= T_{roll}	= 7.75 seconds
Effective spring constant for mooring cable ⁵	= C	= 1250 lbs/ft
Effective mooring system spring constants:		
Surge	= k_x	= 1250 lbs/ft
Sway	= k_y	= 3750 lbs/ft
Yaw	= k_ψ	= 633.75×10^5 lb-ft/rad
Depth of barge		= 15 ft

¹Assuming longitudinal gyradius = 0.25 L.

²Without added fluid inertia; it is assumed that transverse gyradius = B/3.

³For all motions these are uncoupled periods determined in terms of effective spring constants and values of total masses or inertias. The effects of coupling will change these somewhat, but for first approximations and interpretation of critical conditions, this will suffice.

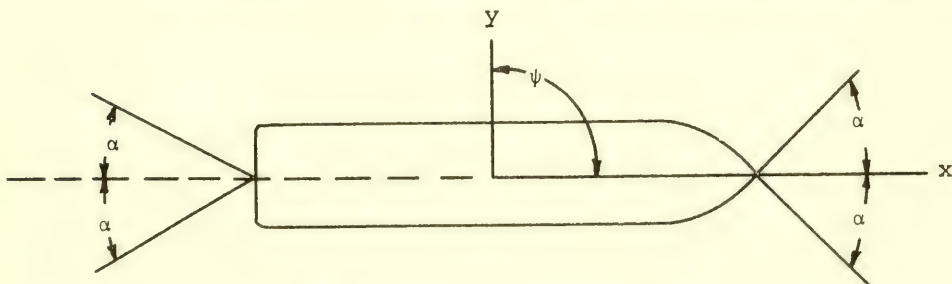
⁴From model tests [7].

⁵Bridge strand wire rope, of cross section 0.595 in².

In analyzing the mooring forces and moments, the barge is assumed to be moored by a conventional line and anchor system, with both bow and stern moorings. However, for application to deep-sea conditions with depths of the order of 1000 fathoms, a certain particular mooring scheme is utilized. This scheme utilized a long-wire rope for each mooring leg assembly (12,000 ft in length), which is supported in the water by a series of submerged spherical buoys. The buoyancy of these buoys keeps the rope taut along its entire length, thereby not allowing it to assume the usual catenary shape. With this arrangement, an initial tension is applied along each mooring leg, and any changes in mooring forces on the ship (and therefore also in the cables) occur as a result of elastic forces resulting from ship displacements. A layout drawing of such a system is shown in [4], which has direct applicability to ships of the same general displacement as the construction barge presently studied.

The displacements having greatest influence on the moorings are in the horizontal plane, and these are surge, sway and yaw. Since the mooring lines are fairly taut and are under an initial tension, the elastic restoring effects may be taken to be fairly linear, i.e. the restoring force is proportional to the displacement. The proportionality factor for an effective displacement along a single mooring cable is found from a knowledge of the modulus of elasticity of the cable material. For the present case of 1-inch diameter bridge strand wire rope, which is 12,000 ft long, has a cross section area of 0.595 in^2 , and an assumed modulus of $25 \times 10^6 \text{ lb/in}^2$, the effective spring constant for a single wire rope is found to be $C = 1250 \text{ lb/ft}$. This linear result only holds below the yield point of 60,000 lb of static force (in a single cable), but it is anticipated that the maximum deflection necessary for attaining this force (viz. 48 ft) will not be experienced in the present case.

For the purposes of analysis, the barge is assumed to be moored in an arrangement similar to that shown in the following sketch of the mooring plan. A longitudinal displacement of the barge



along x , denoted as Δx , leads to an effective displacement along a single cable given by $\Delta x \cos \alpha$, where α is defined in the sketch above. The force in a single cable is then $C \Delta x \cos \alpha$. The longi-

tudinal force component at one end of the ship is represented by

$$(C\Delta x \cos \alpha) \cos \alpha + (C\Delta x \cos \alpha) \cos \alpha = 2C\Delta x \cos^2 \alpha,$$

and since an extension of the cable at one end of the ship requires a contraction at the other end, a similar force occurs. These forces are restoring forces and the net result is a longitudinal force in the barge due to the moorings, given by

$$X_m = 4C \cos^2 \alpha \cdot x = -k_x x, \quad (16)$$

where x is the surge displacement variable.

In the case of sway displacement, the effective displacement along the cable is $y \sin \alpha$, and combining components for net Y -force on the barge, accounting for all the cables, leads to a net mooring lateral force given by

$$X_m = -4C \sin^2 \alpha \cdot y = -k_y y. \quad (17)$$

For yaw displacements, $Y \approx L/2$ where L is the ship length. The lateral force at one end of the ship is then

$$2C \sin^2 \alpha \cdot \frac{L}{2} \psi = CL \sin^2 \alpha \cdot \psi, \quad (18)$$

and the contribution to the yaw moment is

$$CL \sin^2 \alpha \cdot \psi \left(\frac{L}{2} \right) = \frac{1}{2} CL^2 \sin^2 \alpha \cdot \psi \quad (19)$$

at each end. Since the forces at each end are equal and opposite (approximately, since the origin is not exactly at the ship center), the net yawing moment acting on the barge is given by

$$N_m = -CL^2 \sin^2 \alpha \cdot \psi = -k_\psi \psi \quad (20)$$

The variations in the force in the mooring cables due to the motions of the barge can easily be found, since they are related kinematically to the motions. It is seen that the longitudinal displacement, x , and the net lateral displacements, $y + (L/2)\psi$ at the bow and $y - (L/2)\psi$ at the stern, can be combined to determine the net variation in elongation of each mooring cable. The cable displacements due to surging motion on the barge are $x \cos \alpha$, while the cable displacement due to the motions of sway and yaw are $[y \pm (L/2)\psi] \sin \alpha$, according as the cable is at the bow or the stern.

Different effects as to the cable displacement directions occur for the cables, at either the bow or the stern, for the influence of the lateral motions, while the same direction of displacement (at either bow or stern) occurs for the surge motion. The general expression for the fluctuating cable force may be written as

$$F_c = C \left[x \cos \alpha \pm \left(y \pm \frac{L}{2} \psi \right) \sin \alpha \right]$$

where C is the effective spring constant for a single wire rope, and particular values for each of the four cables are given in the following, where a positive cable force is defined as that which pulls on the restraining anchor support on the ocean floor.

The expressions for the individual cable forces (c.f. sketch of mooring-line system) are listed below:

Bow

$$\begin{aligned} F_1 &= - C \left[x \cos \alpha + \left(y + \frac{L}{2} \psi \right) \sin \alpha \right] \text{ port} \\ F_2 &= - C \left[x \cos \alpha - \left(y + \frac{L}{2} \psi \right) \sin \alpha \right] \text{ starboard} \end{aligned} \tag{21}$$

Stern

$$\begin{aligned} F_3 &= C \left[x \cos \alpha - \left(y - \frac{L}{2} \psi \right) \sin \alpha \right] \text{ port} \\ F_4 &= C \left[x \cos \alpha + \left(y - \frac{L}{2} \psi \right) \sin \alpha \right] \text{ starboard} \end{aligned} \tag{22}$$

For the present case where the barge is moored with $\alpha = 60^\circ$, $L = 260$ ft, the mooring system restoring constants are

$$\begin{aligned} k_x &= 1250 \text{ lb/ft} \\ k_y &= 3750 \text{ lb/ft} \\ k_\psi &= 633.75 \times 10^5 \text{ lb-ft/rad} \end{aligned} \tag{23}$$

These values are the effective spring constants for surge, sway and yaw, and as a result there also exist natural periods for these motions in the case of moored ships. There still exist natural periods of heave, pitch and roll, as in the case of free ships, and these natural periods are relatively unaffected in the present case. The introduction of the existence of natural periods in surge, sway and yaw (with possible large motions associated with resonances in

these degrees of freedom) is the main characteristic of moorings applied to ships that distinguishes the resulting motions from those of free ships in waves.

V. SOLUTION OF EQUATIONS

The equations of motion result from combining all of the constituent terms discussed above, and solutions can be obtained by converting them to a simpler form for sinusoidal waves. Since the exciting forces and moments are sinusoidal functions, the motions will also be sinusoidal with the same frequency. Defining

$$x = \bar{x}e^{i\omega t}, \quad y = \bar{y}e^{i\omega t}, \quad z = \bar{z}e^{i\omega t}, \quad X_w = \bar{X}e^{i\omega t}, \quad Y_w = \bar{Y}e^{i\omega t}, \quad \text{etc.}$$

the equations of motion are then converted to (complex) algebraic linear equations. In matrix form the equations may be represented by

$$\begin{bmatrix} a_{11} & 0 & a_{13} \\ 0 & a_{22} & a_{23} \\ a_{31} & a_{32} & a_{33} \end{bmatrix} \begin{bmatrix} \bar{x} \\ \bar{z} \\ \bar{\theta} \end{bmatrix} = \begin{bmatrix} \bar{X} \\ \bar{Z} \\ \bar{M} \end{bmatrix} \quad (24)$$

for the longitudinal motions, where the coefficient matrix is symmetric, i.e. $a_{13} = a_{31}$, $a_{23} = a_{32}$. The matrix elements are defined by:

$$a_{11} = (-m\omega^2 + i\omega N_x + k_x) \quad (25)$$

$$a_{13} = a_{31} = m |BG| \omega^2 \quad (26)$$

$$a_{22} = - \left(m + \int_{\xi_s}^{\xi_b} A'_{33} d\xi \right) \omega^2 + i\omega C_z N_z + \rho g \int_{\xi_s}^{\xi_b} B^* d\xi \quad (27)$$

$$a_{23} = a_{32} = \omega^2 \int_{\xi_s}^{\xi_b} A'_{33} \xi d\xi - i\omega N_z \theta - \rho g \int_{\xi_s}^{\xi_b} B^* \xi d\xi \quad (28)$$

$$a_{33} = - \left(I_y + \int_{\xi_s}^{\xi_b} A'_{33} \xi^2 d\xi \right) \omega^2 + i\omega C_\theta N_\theta + \rho g \int_{\xi_s}^{\xi_b} B^* \xi^2 d\xi \quad (29)$$

The lateral equations are represented by

$$\begin{bmatrix} b_{11} & b_{12} & b_{13} \\ b_{21} & b_{22} & b_{23} \\ b_{31} & b_{32} & b_{33} \end{bmatrix} \begin{bmatrix} \bar{y} \\ \bar{\psi} \\ \bar{\theta} \end{bmatrix} = \begin{bmatrix} \bar{Y} \\ \bar{N} \\ \bar{K} + (\overline{OG})\bar{Y} \end{bmatrix} \quad (30)$$

where the matrix here is also symmetric, i.e. $b_{12} = b_{21}$, $b_{13} = b_{31}$, $b_{23} = b_{32}$. The elements are defined by

$$b_{11} = - \left(m + \int_{\xi_s}^{\xi_b} A_{22}' d\xi \right) \omega^2 + i\omega C_y N_y + k_y \quad (31)$$

$$b_{12} = b_{21} = - \omega^2 \int_{\xi_s}^{\xi_b} A_{22}' \xi d\xi + i\omega N_y \psi \quad (32)$$

$$b_{13} = b_{31} = - \omega^2 \int_{\xi_s}^{\xi_b} (A_{42}' + (\overline{OG})A_{22}') d\xi + i\omega C_y N_y |BG| \quad (33)$$

$$b_{22} = - \left(I_z + \int_{\xi_s}^{\xi_b} A_{22}' \xi^2 d\xi \right) \omega^2 + i\omega C_\psi N_\psi + k_\psi \quad (34)$$

$$b_{23} = b_{32} = - \omega^2 \int_{\xi_s}^{\xi_b} (A_{42}' + (OG)A_{22}') \xi d\xi + i\omega N_y \psi |BG| \quad (35)$$

$$b_{33} = - \omega^2 I_{x_T} + i\omega N_\phi + W |GM| \quad (36)$$

The presence of symmetric matrices helps in effecting an easier solution of the equations, obtained by matrix inversion on a large digital computer. The solutions are then available for each degree of freedom and also for any linear combination of degrees of freedom. The real form of the final solutions is obtained by taking the real part of the complex function, which was the original definition implied in the complex representation of the solution variables.

The lowering line displacements are related kinematically to the body motions, and hence they are relatively simple to determine once the different methods of lowering loads are specified in this study, viz. center-lowered loads and boom-lowered loads. Center-lowered loads, as the name indicates, are lowered through some sort of opening through the ship's keel, and it is assumed that this is done at just about amidships. The instantaneous displacement vector components of the load and lowering line are s_x , s_y and s_z and are then given by simple geometry as

$$s_x = x$$

$$s_y = y + |KG|\phi \quad (37)$$

$$s_z = z$$

where x , y , z and ϕ are the instantaneous ship motions of surge, sway, heave, and roll, respectively, and KG is the vertical distance between the center of gravity and the keel.

The tension, T , in the lowering line is given by the relation

$$T - W_l = \frac{W_l}{g} \ddot{s} = \frac{W_l}{g} \ddot{z} \quad , \quad (38)$$

where W_l is the weight of the load, and only vertical effects are considered to affect the tension. At rest,

$$T = T_0 = W_l \quad ,$$

so that upon representing the tension as

$$T = T_0 + T' = W_l + T'$$

where T' is the tension change due to dynamic effects, one obtains

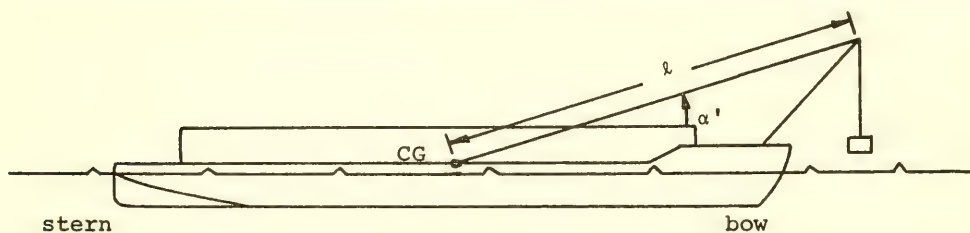
$$\frac{T'}{W_l} = \frac{\ddot{z}}{g} \quad . \quad (39)$$

Thus the tension variation due to the dynamics of the ship motion is directly related to the vertical acceleration of the load, and it is also proportional to the weight of the load.

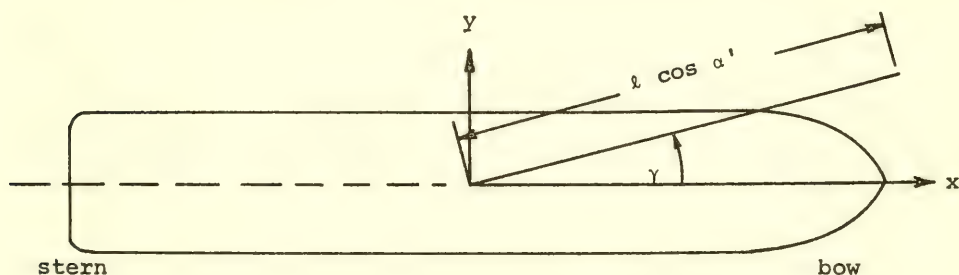
In the derivation of the formulas given above, it is assumed that the trajectory of the load attached to the line is such that at each instant it is on the vertical line through the point of attachment of the lowering line to the barge. It is also assumed that the elastic effects of the lowering lines may be neglected; the only dynamic influences considered being those due to the ship motions. The neglect of elastic effects in the lowering line appears to be a fairly safe assumption, since the major influence would occur only if the wave frequencies excited the natural frequency of wave propagation in the lowering line. In view of the lack of specification of the line's physical characteristics, as well as the expectation of wave-propa-

gation frequencies out of the range of interest in the present problem, the tensions and accelerations are considered adequately represented by Eq. (39).

For boom-lowered loads, the situation may be visualized by reference to the accompanying sketch, where the boom length l is



elevated at an angle α' . An appropriate value for the relevant horizontal projection of the boom length ($l \cos \alpha'$) is considered, for computational purposes in the present case of a 260 ft length barge, to be 150 ft. As shown below, the boom is also oriented horizontally at an azimuth angle γ , measured from the bow, positive in the counterclockwise sense, viewed from above. The load and



lowering-line displacements about their respective equilibrium positions are given by

$$s_x^\gamma = x - (l \cos \alpha') \sin \gamma \cdot \psi$$

$$s_y^\gamma = y + (l \cos \alpha') \cos \gamma \cdot \psi \quad (40)$$

$$s_z^\gamma = z - (l \cos \alpha') \cos \gamma \cdot \theta + (l \cos \alpha') \sin \gamma \cdot \phi$$

and the line tension (fluctuating part), T_1^γ and vertical acceleration are represented by

$$\frac{T^{\gamma}}{W_{\ell}} = \frac{\ddot{s}_z^{\gamma}}{g} = \frac{1}{g} [\ddot{z} + \ell \cos \alpha' (\sin \gamma \cdot \ddot{\phi} - \cos \gamma \cdot \ddot{\theta})] \quad (41)$$

where ϕ , θ , and ψ are the rotational barge motions, roll, pitch and yaw, respectively, and the superscript γ denotes the boom azimuth angle. These quantities are derived on the same basis as those for center-lowered loads, it being assumed that the boom pivots about the ship CG. The instantaneous magnitudes of these quantities thus appear as linear combinations of the instantaneous ship-motion solutions.

Each motion of the barge in response to a regular sinusoidal wave having a given frequency and propagating in a given direction will also be sinusoidal, of the same frequency, but will, in general, possess a different phase. In addition, the amplitude of each motion will, in general, differ from that of the wave, the ratio of the former to the latter being a function of the wave frequency and the heading of the wave relative to the heading of the barge, and this amplitude-ratio function is known as the response amplitude operator for the particular motion of interest. In order to arrive at an effective characterization of the barge motions in a random sea, in which case these motions themselves have a random nature, the function known as the spectral energy density, or the energy spectrum, of each motion must be found. This spectrum is a measure of the variation of the squares of the amplitudes of the sinusoidal components of the motion, as a function of frequency and wave direction. The total area under the spectral-energy density curve contains much of the statistical information on average amplitudes, near-maximum amplitudes, etc., for the particular motion considered. For an arbitrary motion, represented by the i -subscript, the energy spectrum of that motion, due to the effects of irregular waves, is given by

$$\Phi^{(i,i)}(\omega) = |T_{i\eta}(\omega)|^2 A^2(\omega) \quad (42)$$

for a particular fixed barge heading in a unidirectional irregular sea, where $A^2(\omega)$ is the wave spectrum and $|T_{i\eta}|$ is the response amplitude operator for that heading.

For computational purposes in the present study, the Neumann Pierson spectral-energy description of the seaway has been adopted, and calculations made for these particular sea states, corresponding to three particular wind speeds. The following table illustrates the conditions.

Table 2

Sea State	Wind Speed v_w (knots)	Sig. Wave Ht. $H_{1/3}$ (ft)	Surface Elevation (Time History and Energy Spectrum)		
			r.m.s. value, σ , (ft)	Ttl. energy, σ^2 , (ft) ²	$2\sigma^2 = E$
3	14	3.3	0.81	0.66	1.32
4	19	6.9	1.75	3.05	6.10
5	22	10.0	2.50	6.23	12.46

The Newmann wave spectrum for a unidirectional fully-developed sea represented by

$$A^2(\omega) = C\omega^{-6}e^{-2g^2/(\omega v_w)^2} \quad (43)$$

where C is an empirical constant having the value $51.5 \text{ ft}^2/\text{sec}^5$, v_w is the wind speed in units of ft/sec , and $A^2(\omega)$ has the units $\text{ft}^2\text{-sec}$. The wave spectrum for a non-unidirectional sea, allowing for angular variation (a two-dimensional spectrum), is represented by

$$A^2(\omega, \beta_w) = \frac{2}{\pi} C\omega^{-6}e^{-2g^2/(\omega v_w)^2} \cos^2 \beta_w, \quad \text{for } -\frac{\pi}{2} < \beta_w < +\frac{\pi}{2}, \quad 0 < \omega < +\infty$$

$$0, \quad \text{otherwise,} \quad (44)$$

where β_w is an angle measured from the direction toward which the wind is blowing (the predominant wave direction). In this case, the motion spectrum occurring for a particular barge heading β_B , measured relative to the wind direction is

$$\Phi^{(i,i)}(\omega) = A^2(\omega) \frac{2}{\pi} \int_{-\pi/2}^{+\pi/2} d\beta_w \cos^2 \beta_w |T_{i\eta}(\omega, \beta)|^2 \quad (45)$$

where $\beta = \beta_w - \beta_B$, and this energy spectrum will depend upon the angle β_B .

From the spectral density function, $\Phi^{(i,i)}(\omega)$, for a particular motion, there may be obtained, in principle, all the statistical or probabilistic properties possessed by the random process. The total area, E_i , under the spectral density function curve, as defined above,

$$E_i = \int_0^{\infty} d\omega \Phi^{(i,i)}(\omega) \quad (46)$$

is equal to $2\sigma_i^2$, i.e. twice the variance of the ordinates on the corresponding time-history curve. Under the assumption that the seaway is a Gaussian or normal stochastic process which is exciting a linear system (in this case, the barge), the set of responses of the system will in turn represent a Gaussian stochastic process. The probability of an ordinate of a particular response lying between two values is given by the definite integral of the Gaussian probability density between those two limits, and will be a function of the variance σ_i . Thus, E_i or σ_i may be used to estimate the probability of the occurrence of instantaneous values in any range of interest, for any given barge motion, including infrequently-occurring large or near-maximum values. Characteristics of the motion time history may be obtained in terms of the quantity E_i by relating the behavior of the envelope of the record (interpreted as the instantaneous amplitude of the time history curve) to this quantity. Such relations are based on assumed narrow-band behavior of the energy spectrum, and yield expressions for the mean amplitude of oscillation (half the distance between the trough and crest of an oscillation), the mean of the highest 1/3 of such amplitudes (known as the significant amplitude), and other related statistical parameters of interest for a specified sea condition. In particular the relations for average pitch amplitude and significant pitch amplitude are

$$\begin{aligned} \theta_{av} &= 0.88 \sqrt{E_\theta} \\ \theta_{sig} &= 1.41 \sqrt{E_\theta} \end{aligned} \quad (47)$$

VI. DISCUSSION OF RESULTS

Computations of the amplitudes and phases of the six separate motions of the moored barge for the complete range of possible headings were carried out for wave lengths varying from 100 feet to 800 feet, which covers the range of periods significant for ship motion in an operational environment up to Sea State 5. Solutions to the equations were obtained for the complex response operators (both amplitude and phase) of the various motions relative to the wave. Representative solutions for a particular wave length, for both the longitudinal and lateral motion amplitudes, as functions of the heading angle β are shown in Figs. 2 and 3. From this data the response amplitude operators, as functions of frequency (since $\omega = \sqrt{2\pi g/\lambda}$), are obtained and representative curves are presented in Figs. 4 and 5. Application of the techniques of spectral superposition theory [1] results in spectral energy density values for particular barge motions in Sea State 5 (as an example), and these values are indicated in Figs. 6 and 7, as illustrations of some of the results.

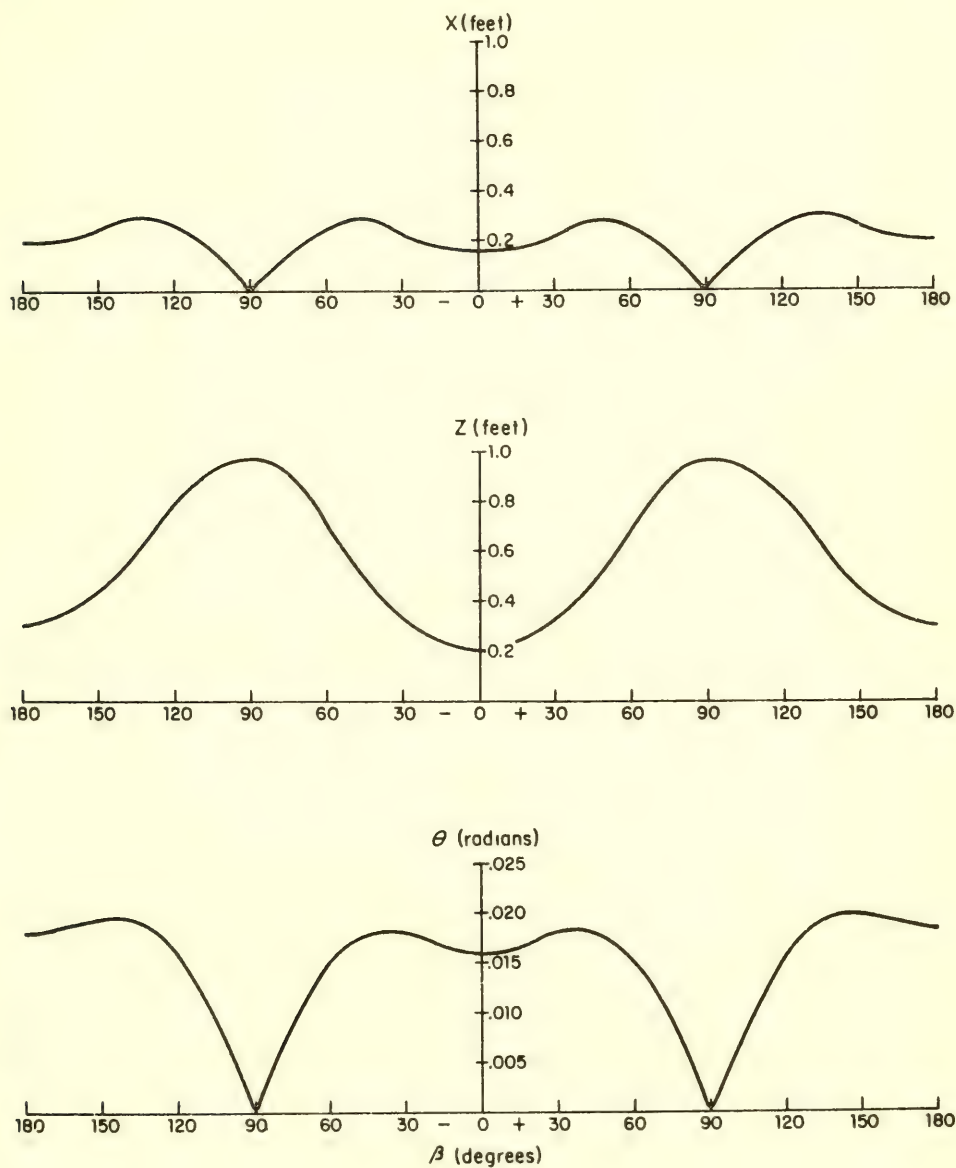


Fig. 2. Amplitude of response for unit-amplitude wave as a function of direction of wave relative to barge. Longitudinal motion; $\lambda = 300'$.

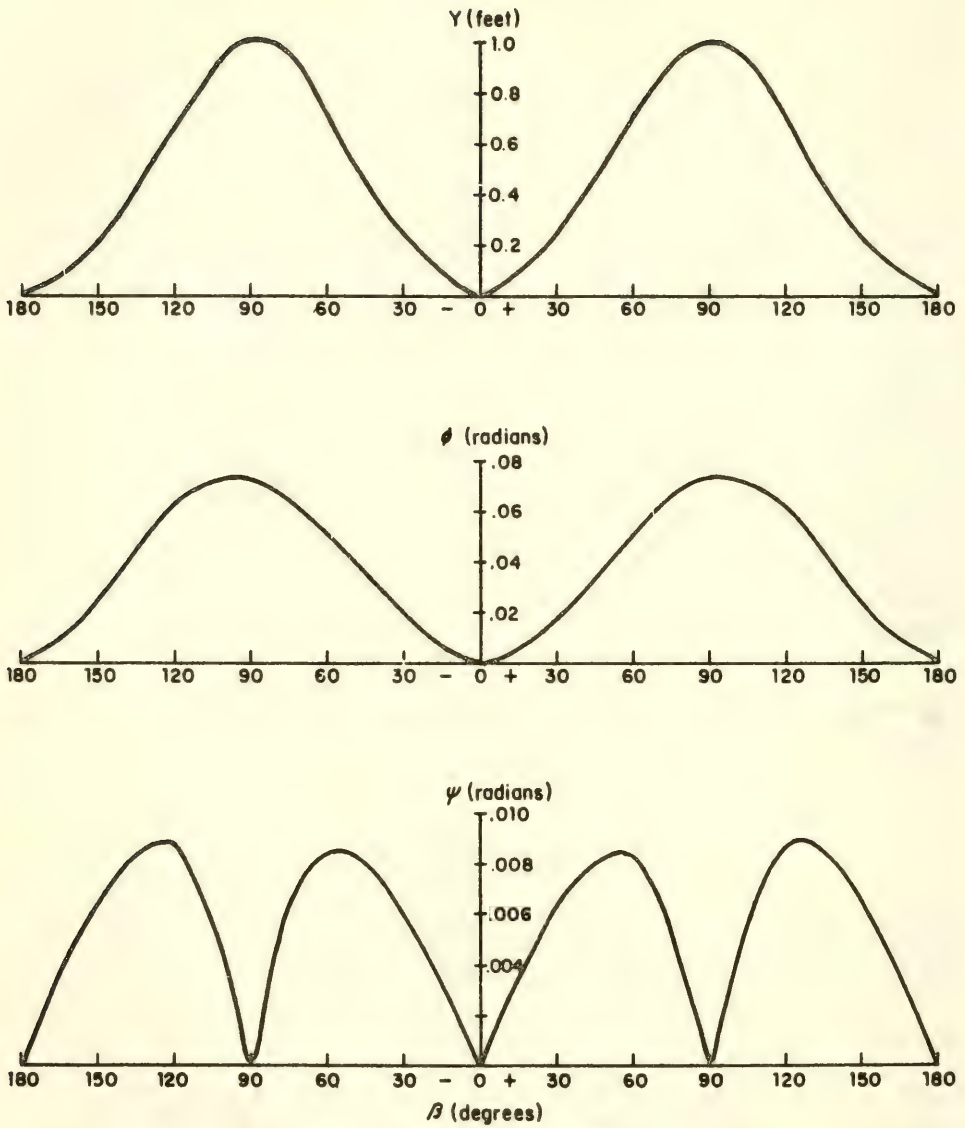
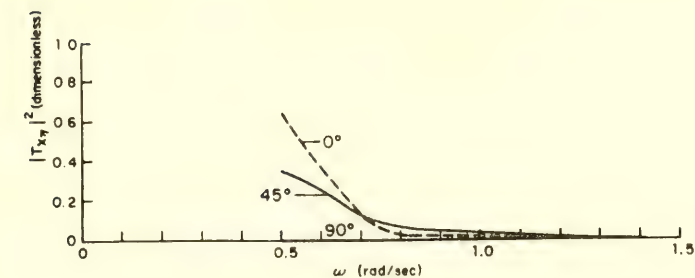
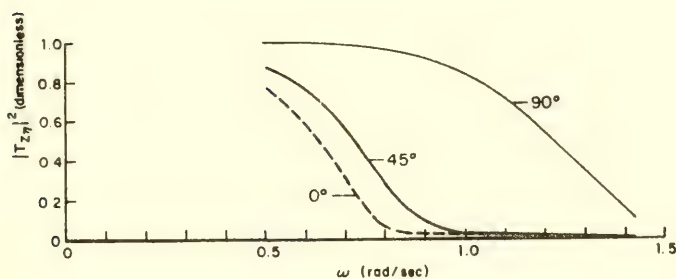


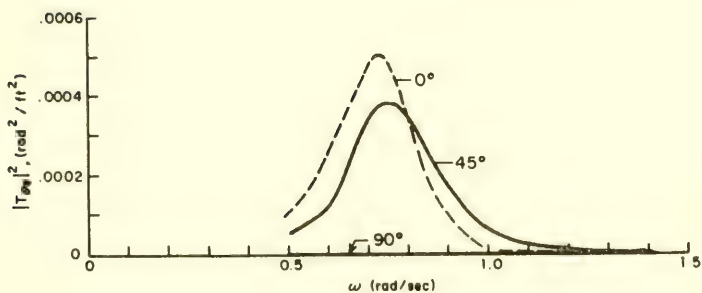
Fig. 3. Amplitude of response for unit-amplitude wave as a function of direction of wave relative to barge. Lateral motion; $\lambda = 300'$.



(Response amplitude operator)² for surge, $|T_{x\eta}|^2$

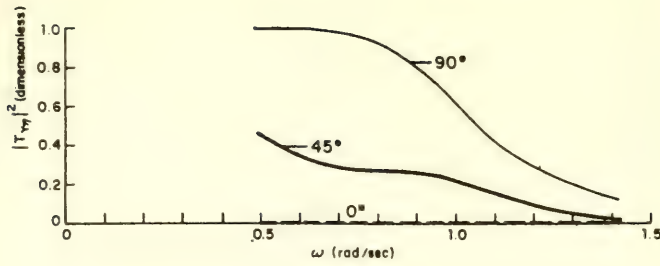


(Response amplitude operator)² for heave, $|T_{z\eta}|^2$

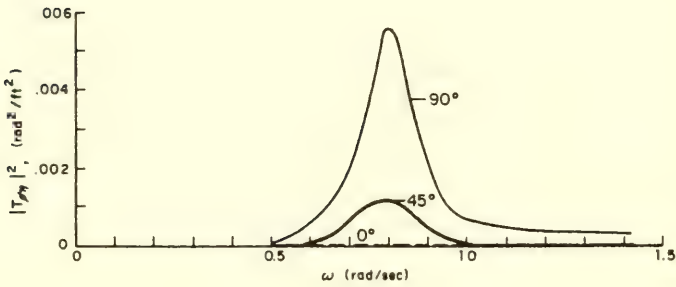


(Response amplitude operator)² for pitch, $|T_{\theta\eta}|^2$

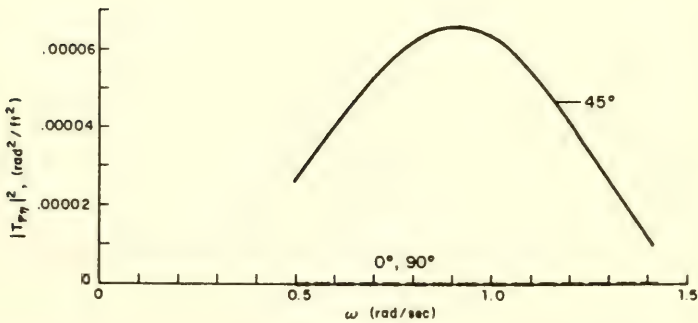
Fig. 4. Response amplitude operators for longitudinal motions.



(Response amplitude operator)² for sway, $|T_{\gamma\eta}|^2$



(Response amplitude operator)² for roll, $|T_{\phi\eta}|^2$



(Response amplitude operator)² for yaw, $|T_{\psi\eta}|^2$

Fig. 5. Response amplitude operators for lateral motions.

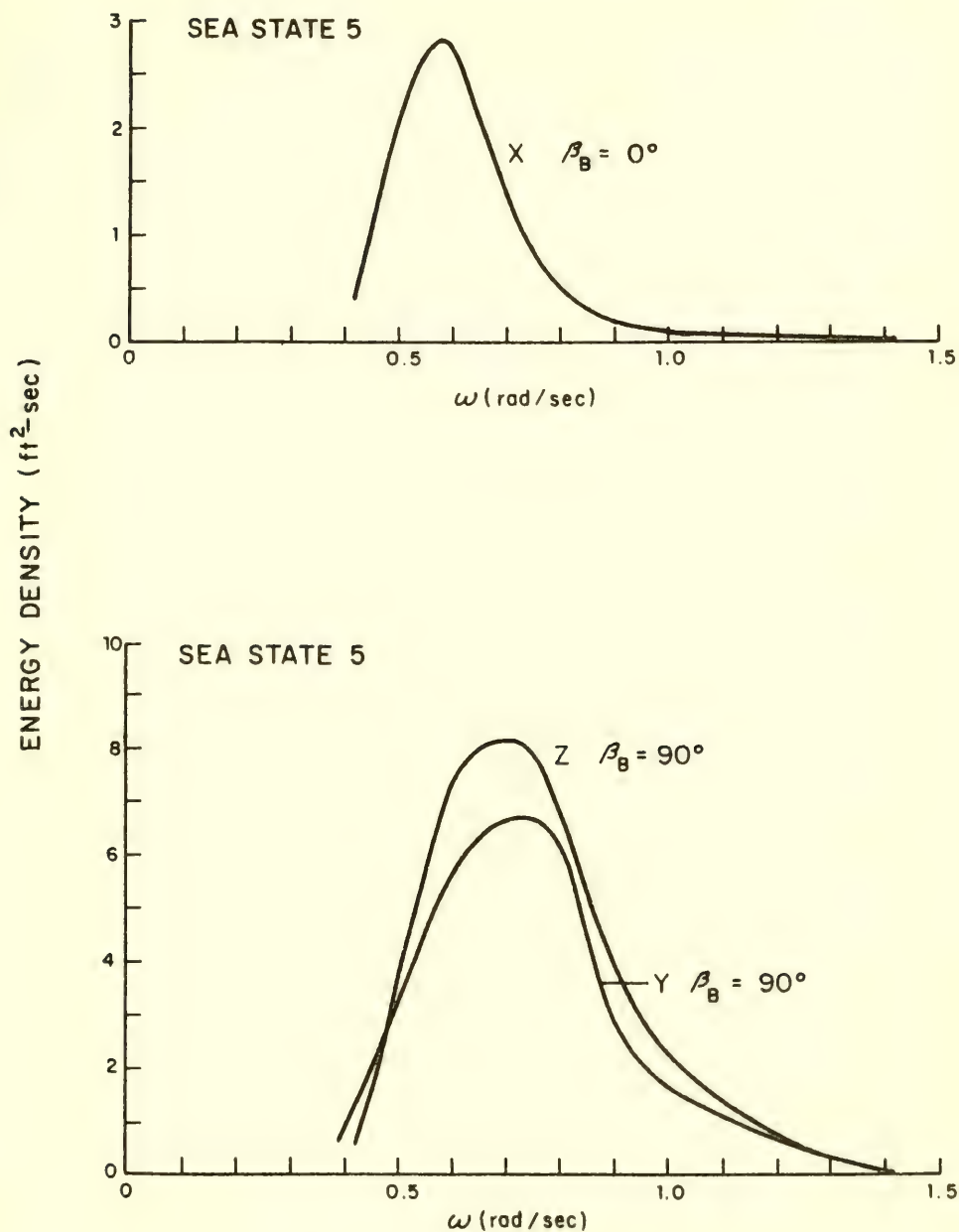


Fig. 6. Spectral energy density for translational barge motions for indicated barge heading β_B

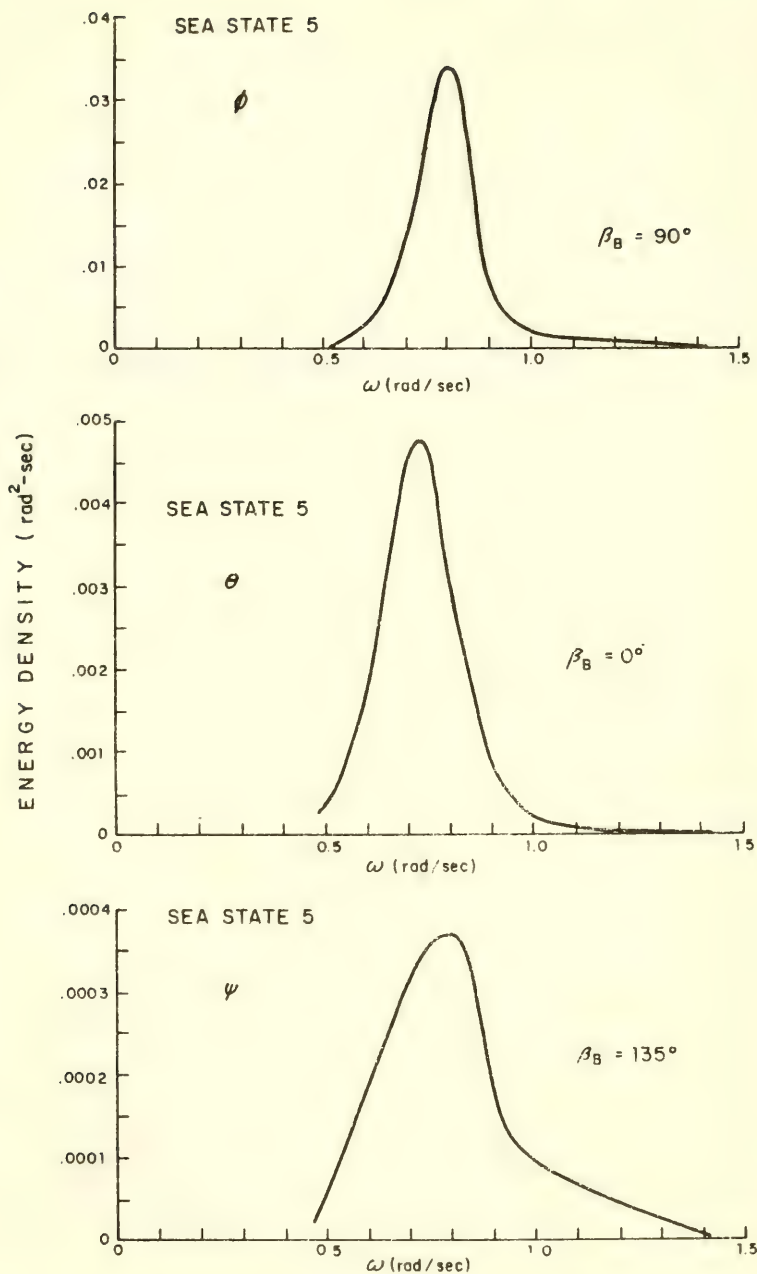


Fig. 7. Spectral energy density for rotational barge motions for indicated barge heading β_B

In the present study the angle for the predominant wind direction was taken to be $\beta_0 = 0$, and a variable barge heading angle, β_B , introduced to allow for the relative heading of barge to wind. The relationships of the wind direction, the wave heading, and the barge heading are shown in Fig. 8, together with the difference angle $\beta_w - \beta_B$ representing the wave heading relative to the barge heading. Also shown in this figure are the conventions made use of later for the designation of the forces in the mooring cables and the azimuth angle for the boom used to lower loads from the barge.

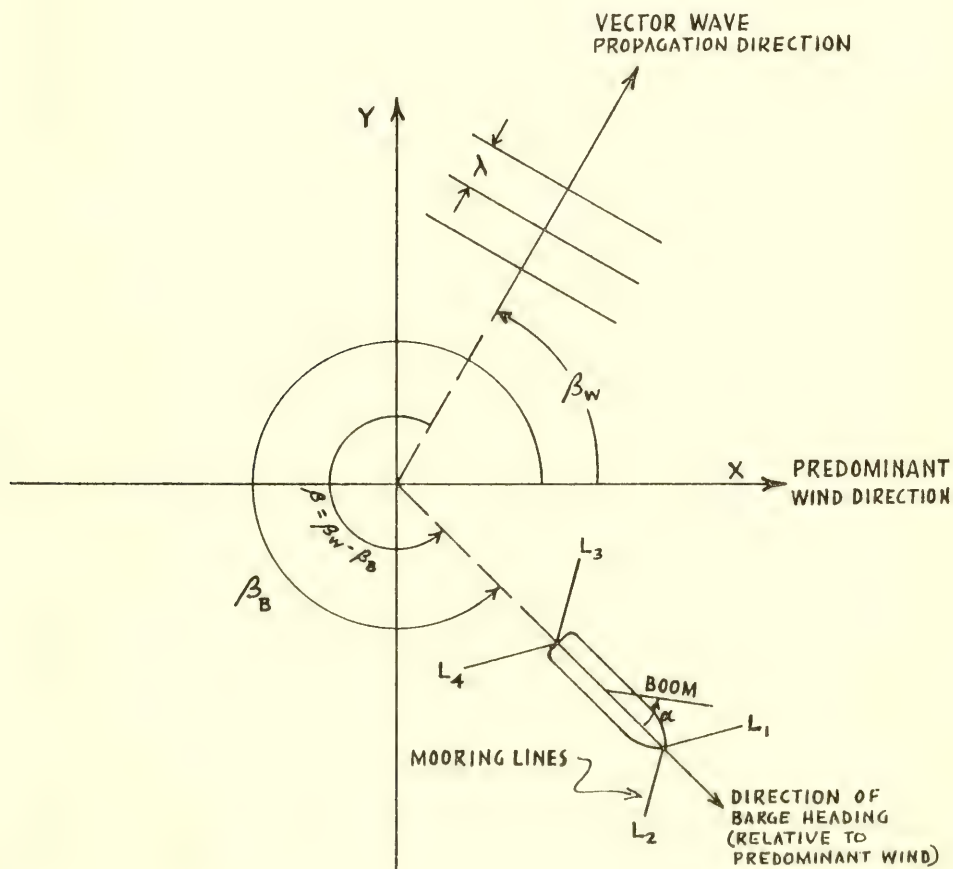


Fig. 8. Orientation and relations between barge, wind and waves

Figures 9 and 10 show, for each of the six barge motions, the variation of total spectral energy with barge heading, for each of the three sea states considered. The ordinate plotted for each of the curves is the r.m.s. value, σ_i , for the time history of the barge motion represented, and it will be convenient to refer to the variance σ_i^2 of the function as the total energy. The r.m.s. value of any time-history function is therefore the square root of its total energy (assuming, here, as always, the mean value of any time-history function to be zero).

Representative examples of calculated spectral energy density functions for the case of the center-lowered load are presented for two sea states and two barge headings relative to the predominant wind direction in Fig. 11. The spectral energy density functions shown for the load were calculated from those of the fundamental set of cross-spectral energy density functions, i.e. those of the six barge motions. Since the time histories of the load and amplitude operators for the former may be obtained by forming appropriate linear combinations of the complex response operators, $T_{i\eta}$, for the barge motions, and calculating their squared absolute values.

The r.m.s. values (as defined here) were obtained for all quantities of interest for the load lowering operation such as displacements, accelerations, tensions, etc. as well as the forces in the mooring cables, for each sea state and barge heading relative to the waves. Similarly variations of these quantities as a function of the boom azimuth angle were found, from which an optimum boom angle (which minimizes the r.m.s. values of any one of the time histories of interest) may be determined. As an example of results obtained for a 200 ton load lowered in a State 5 sea with a crosswind barge heading and with the optimum boom azimuth angle (here 180° , i.e. boom over the stern), the r.m.s. value of the added-dynamic line tension given by Fig. 12 is $(2.38)(200)/32.2 = 14.8$ tons. From data on the normal probability curve for this r.m.s. value, it can be shown that the downward force of impact on the bottom would exceed 25 tons approximately 2.3% of the time, if the instant of impact were allowed to occur at random. For a center-lowered load under the same conditions, the r.m.s. value of its acceleration is $1.17(200)/32.2 = 7.27$ tons, and the downward impact force on the bottom would exceed 14.3 tons approximately 2.3% of the time.

The r.m.s. value of the fluctuating component of the force in each of the four mooring cables is shown in Fig. 13 as a function of barge heading for each sea state. The four are seen to have nearly the same r.m.s. value for any particular barge heading in a Sea State 3, with the actual values varying between 300 and 600 lb. For a Sea State 4 the range is from 1100 to 1750 lb, with the differences between r.m.s. values for the four fluctuating cable forces being as much as 150 lb. For Sea State 5, the range is from 1800 to 2700 lbs with differences in r.m.s. values between cables of 250 lb. In all

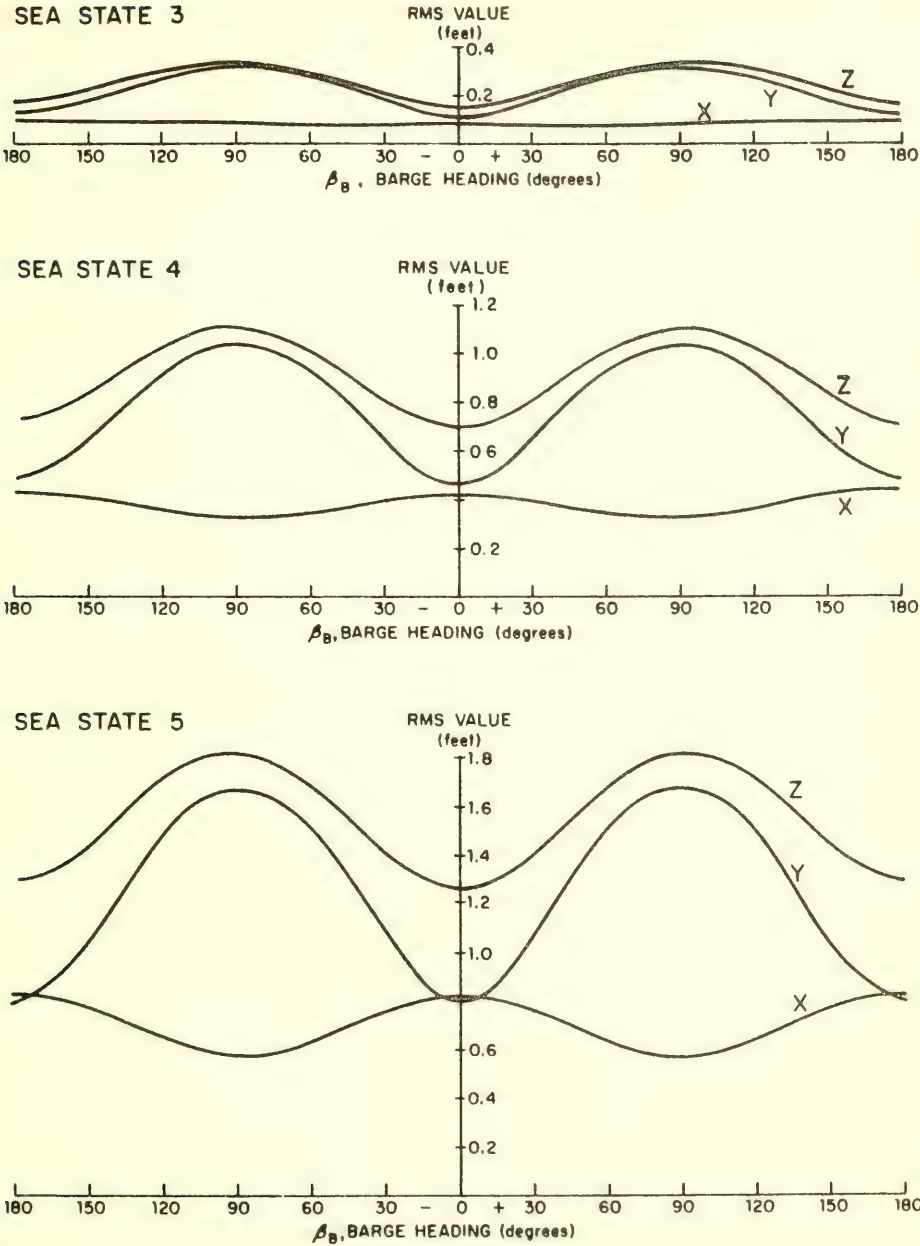


Fig. 9. RMS values of the translational barge motions as a function of barge heading at indicated sea state.

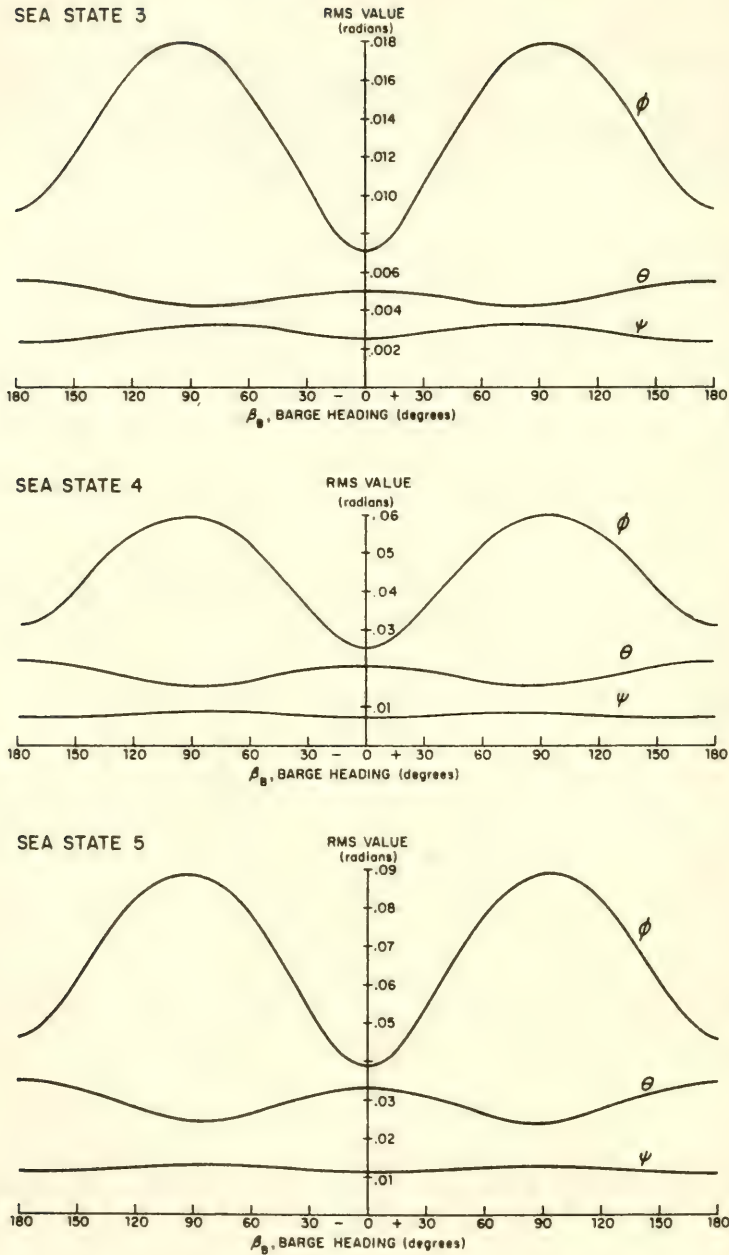


Fig. 10. RMS values of the rotational barge motions as a function of barge heading at indicated sea state.

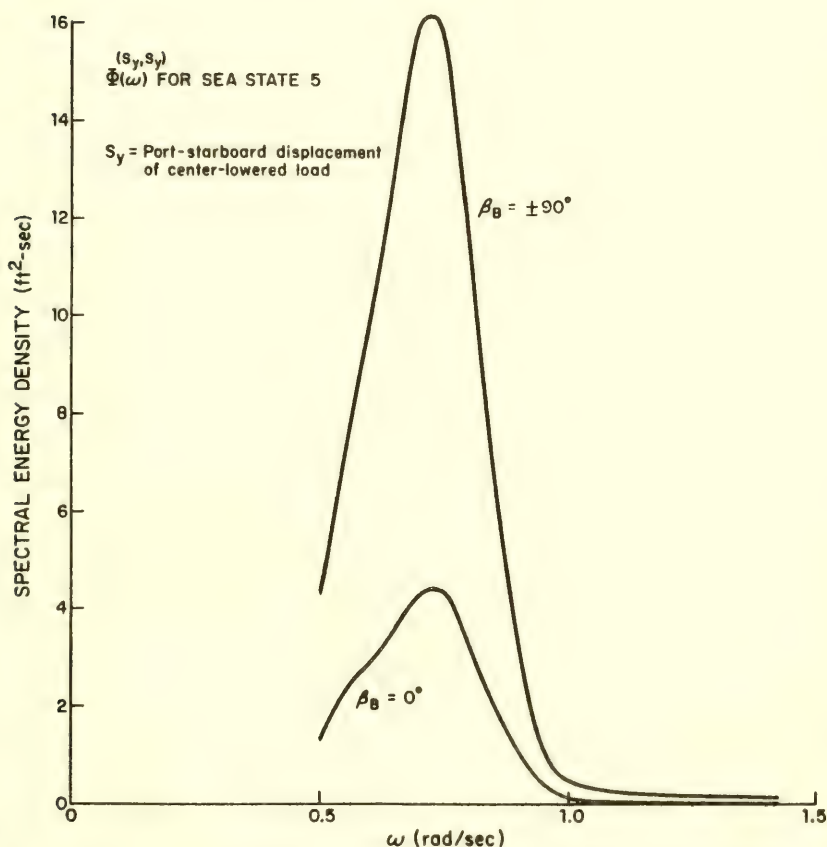
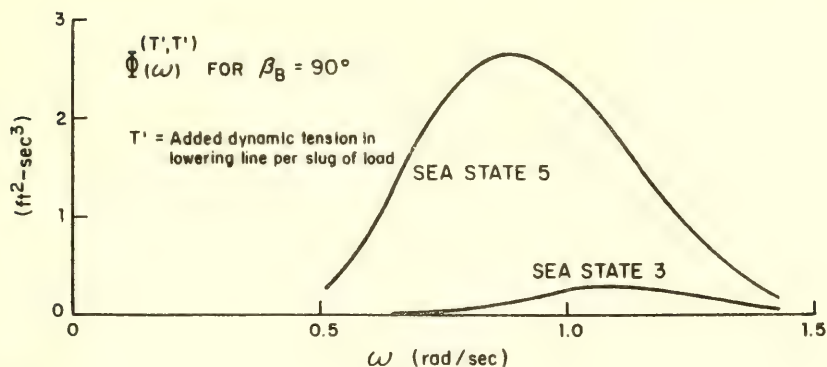


Fig. 11. Spectral energy density functions for added-dynamic tension in lowering line and lateral displacement for center-lowered load, for indicated barge heading and sea state.

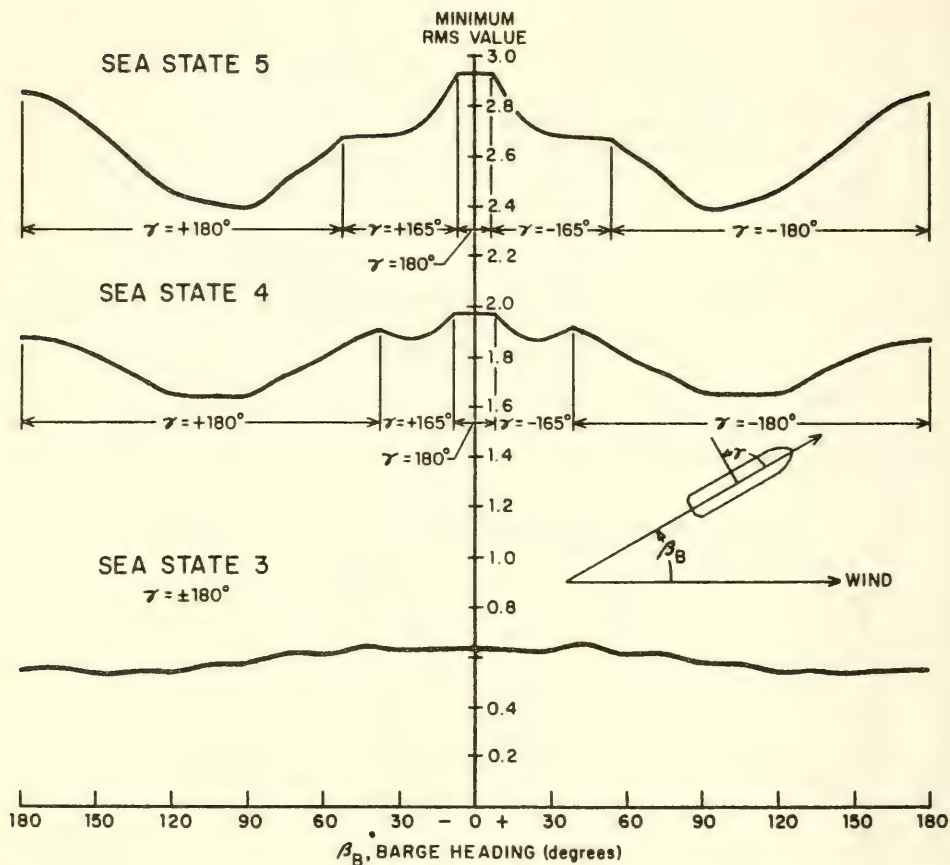


Fig. 12. Minimum r.m.s. values of added-dynamic line tension (pounds/slug) and vertical load acceleration (feet/second) for boom-lowered load, as a function of barge heading at indicated sea state

cases the cable force r.m.s. values are greatest near crosswind, and least for upwind and downwind barge headings.

All of the results obtained in this study provide useful information for application to many operations that can be performed at sea, using a moored ship as the base. The major questions concerning these results are their degree of validity, as well as the capability of extending the results of related situations such as shallow water operation, different mooring systems, the effects of nonlinearity, etc. Some extensions and/or applications of the present theory have

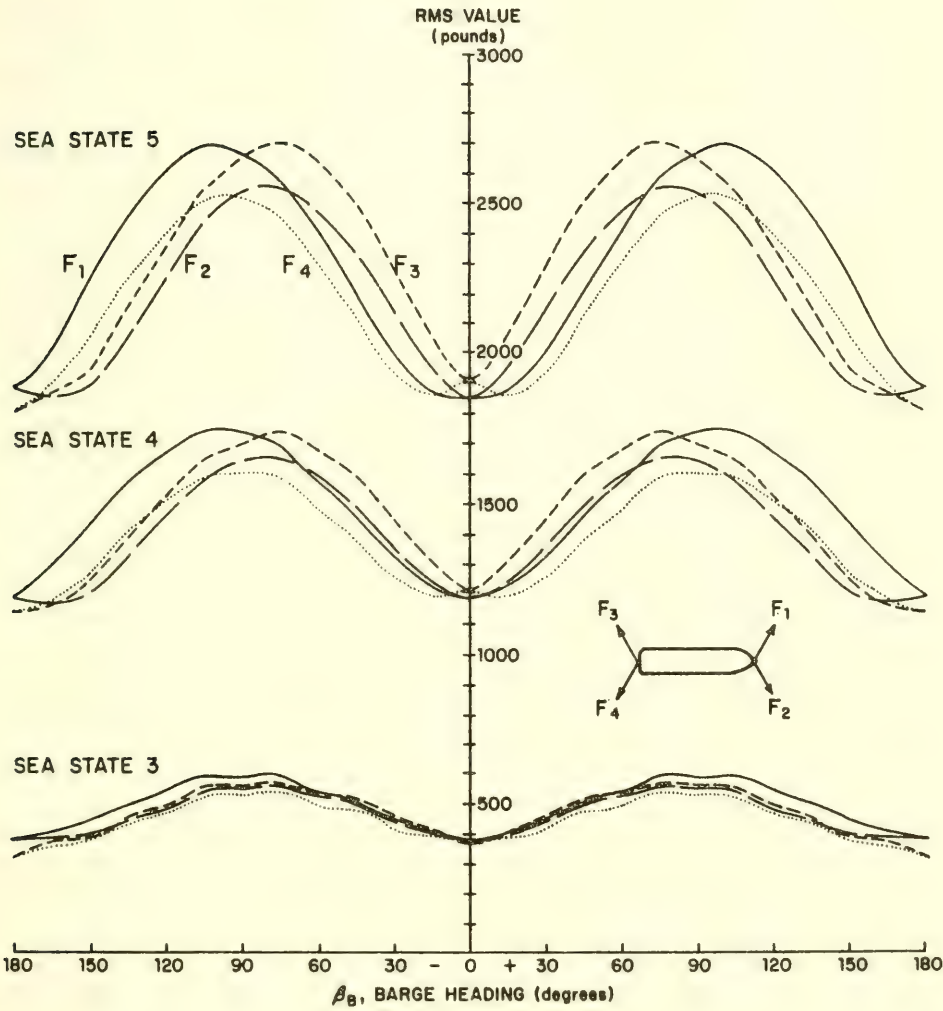


Fig. 13. RMS values of mooring cable forces as a function of barge heading at indicated sea state.

been carried out, where comparisons between theory, model experiment, and (in some cases) prototype behavior were made (see [8], [9]). The conclusions of those studies were that linear theory produced good predictions of motion response operators; shallow water effects may be easily incorporated; the effects of other mooring arrangements (such as the usual catenary form of weighted chain cables) can be represented in linear form and produce results agreeing with theory, within the range of lower sea states.

While agreement between theory and experiment was generally obtained for almost all conditions, some degrees of freedom of the vessels considered in [8] and [9] were not properly predicted for irregular sea conditions. The motions of surge, sway, and yaw exhibited large spectral response characteristics at very low frequencies where little (if any) wave energy was present, but close to the natural frequencies of those motions (due to the mooring "spring" forces). Since these motions are very lightly damped, a very small amount of input excitation can still produce relatively large motions at these low frequencies. There are a number of possible explanations for this behavior, but the most plausible one is related to the influence of the nonlinear "drift" forces and moments, which will be discussed in a later section when considering dynamic positioning.

The theory described here supplements what may be known qualitatively for moored vessel behavior by furnishing quantitative estimates for the motions and their inter-relationships. While the validity of these analytical results for any particular vessel is subject to test, the results for other moored vessels using this same analytical procedure give support to the reliability of the predictions. Thus, it is feasible to treat all six degrees of freedom of a moored ship in a realistic seaway and obtain results for response characteristics of various motions of the ship and any associated load.

Considering the results and examples concerning the load-lowering operation, there are two main conclusions. First, motions having amplitudes of oscillation or giving rise to forces and accelerations sufficiently high to influence construction operations may occur under certain of the environmental conditions considered in this study, particularly when loads are lowered by means of a boom in a high sea state. Secondly, the violence of these motions, forces, or accelerations may be significantly reduced by the proper choice of vessel heading relative to the wind, and boom azimuth angle. The latter factor regardless of the sea state, has by far the greater effect in minimizing the energy of the fluctuating tension in the lowering line, the vertical acceleration of the load, and its three displacement components. These results provide useful information for conducting operations from a moored ship platform, and hence the capability of obtaining guidelines for operating vessels and performing engineering work at sea is available with the tools of theoretical hydrodynamic analysis presented here.

VII. MOORED BUOY ANALYSIS

A moored buoy system is similar in many respects to the moored ship case, and simplifications are made in order to treat a representative problem. The buoy system is assumed to be a single point mooring, with a surface floating buoy hull connected by a flexible line to the ocean bottom. Both slack and taut types of moorings are included in the analysis, and the surface buoy form can be either a ship-like form, a spar shape, or an axisymmetric disc shape. The analysis is restricted to motion in a single plane and the current direction and wave direction thereby lie in this plane, making a two-dimensional problem. Allowance for current magnitude variation with depth is considered, with its main influence being in the static equilibrium problem (which will not be treated in detail here).

Considering the static equilibrium problem, a free-body diagram of a differential element of the cable in the plane of interest is shown in Fig. 14. The cable bends and the tension varies along its length so as to keep all the indicated forces in equilibrium. The cable weight acts vertically and the tension forces are directed along the cable axis. The hydrodynamic forces due to the current are resolved into components normal and tangential to the cable direction. These unit forces are represented as follows:

$$F(\phi) = C_N \cdot \frac{1}{2} \rho c (V_c \sin \phi)^2 \quad (48)$$

$$G(\phi) = C_T \cdot \frac{1}{2} \rho c (V_c \cos \phi)^2 \quad (49)$$

where

ρ = mass density of fluid

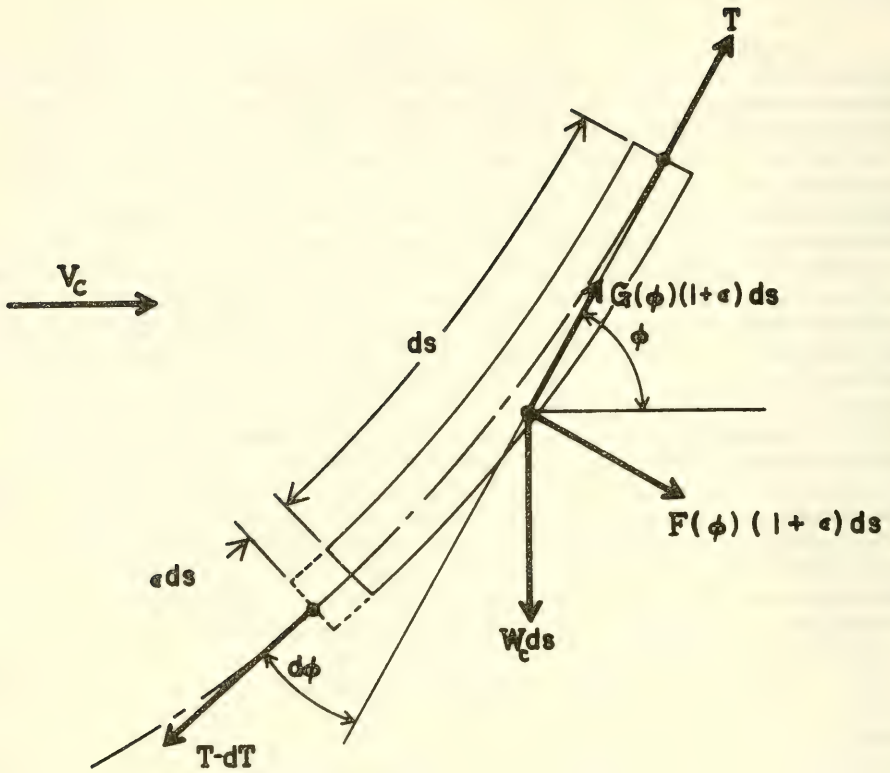
c = cable chord length (in current direction)

and C_N , C_T are appropriate drag coefficients. These coefficients depend on the cable cross section and surface geometry.

The summation of forces along the direction of the cable axis yields:

$$T + G(\phi)(1 + \epsilon) ds - W_c ds \sin \phi - (T - dT) \cos (d\phi) = 0$$

For a differential element, $d\phi \rightarrow 0$, so that $\cos (d\phi) \rightarrow 1.0$. This gives the differential equation for cable tension in terms of the independent variable s , as follows:



V_c = current velocity

T = cable tension

s = distance along relaxed cable

ϵ = cable strain

ϕ = angle of cable from horizontal

W_c = unit submerged weight of cable

$G(\phi)$ = tangential unit force component due to current

$F(\phi)$ = normal unit force component due to current

Fig. 14. Cable Free-Body Diagram

$$dT = [-G(\phi)(1 + \epsilon) + W_c \sin \phi] ds. \quad (50)$$

The summation of forces normal to the cable axis yields:

$$F(\phi)(1 + \epsilon) ds + W_c ds \cos \phi - (T - dT) \sin (d\phi) = 0$$

and with $d\phi \rightarrow 0$, we can approximate $\sin (d\phi)$ by $d\phi$. Neglecting higher order terms involving products of differentials, results in an equation for the differential angle:

$$d\phi = \frac{1}{T} [F(\phi)(1 + \epsilon) + W_c \cos \phi] ds. \quad (51)$$

The strain, or cable elongation, is obtained from the following simple relationship for an elastic cable material:

$$\epsilon = \frac{T}{A_c E_c} \quad (52)$$

where

A_c = cable (load-bearing) cross section area

E_c = effective static elastic modulus of cable material.

Associated with these equations is the representation of the forces and moments acting on the buoy due to the wind and the current (not considered here, but discussed in [10] from which the present analysis is abstracted). All of these effects are considered to be in equilibrium with the weight, buoyancy, and cable forces.

All the forces and moments acting on the buoy due to current and wind are considered to be in equilibrium with the weight, buoyancy and cable forces. At the surface buoy we then have:

$$\begin{aligned} D_a + D_c &= T \cos \phi \\ L_c + B(\theta, h) &= W + T \sin \phi \\ M_a + M_c &= T(\ell_c^2 + z_c^2)^{1/2} \sin (\phi + \theta - \tan^{-1} \frac{z_c}{\ell_c}) + B(\theta, h) \overline{GZ}(\theta, h) \end{aligned} \quad (53)$$

where

D_0 = drag due to wind acting on a buoy

D_c, L_c, M_c = current-induced drag, lift, and moment acting on buoy

T = cable tension (at buoy attachment point)

ϕ = cable angle from horizontal (at same point)

$B(\theta, h)$ = buoyancy force

W = total weight of buoy

l_c, z_c = horizontal and vertical distances respectively from cable attachment to CG

$\overline{GZ}(\theta, h)$ = hydrostatic righting arm

Thus, for a given buoy configuration in a particular condition of submergence in a given current, Eq. (53) can be solved for θ , T and ϕ ; that is, the buoy trim equilibrium and the cable tension and angle at the buoy. This result then becomes the initial condition for the static equilibrium cable geometry calculation.

When considering the problem of the dynamics of the complete moored buoy system, separate considerations in the analysis are given initially to the buoy and to the mooring system, with ultimate combination (i.e. coupling) exhibited later. The motion of a buoy in waves considers the buoy to be equivalent to some type of hull form, and the restriction to planar motion results in analyzing only three degrees of freedom which may be considered to be surge, heave and pitch. The equations of motion of the buoy are formulated in the same general way as for a surface ship, described previously. The only possible additional influence in the present case of the buoy is to allow for the effect of a uniform surface current, which can be included in the equations by interpreting the current as an equivalent forward speed of the buoy hull through the water. However, for simplicity here, this effect is deleted when analyzing the buoy wave responses.

For the case of a ship-form buoy hull the hydrodynamic force derivation is similar to that shown previously for the moored ship. The general equations of motion in the vertical plane for the coupled motions of surge, heave and pitch can be represented in a more specific form as

$$a_{11}\ddot{x} + a_{12}\dot{x} + a_{17}\ddot{\theta} = X_m + X_w \quad (54)$$

$$a_{24}\ddot{z} + a_{25}\dot{z} + a_{26}z + a_{27}\ddot{\theta} + a_{28}\dot{\theta} + a_{29}\theta = Z_m + Z_w \quad (55)$$

$$a_{31}\ddot{x} + a_{34}\ddot{z} + a_{35}\dot{z} + a_{36}z + a_{37}\ddot{\theta} + a_{38}\dot{\theta} + a_{39}\theta = M_m + M_w \quad (56)$$

where the mooring forces are represented in general form and the wave forces can be represented as sinusoidal functions of time for different wave frequencies. The mooring forces will depend upon the mooring arrangement (i.e. number of cables, attachment point, etc.), whereas the functional form and degrees of freedom in the force representation depend upon the geometric arrangement.

For the surge degree of freedom, the coupling with the pitch equation, and vice versa, occurs as a result of hydrodynamic inertial coupling (potential flow theory) and hence the symmetry relation $a_{17} = a_{31}$ is attained. This result is due to the equivalence of the off-diagonal terms of the added mass tensor representation of inertial forces. With the longitudinal force $m\ddot{x}$ assumed to act through the center of buoyancy (CB) of the hull, a pitch moment $m|BG|\ddot{x}$ occurs, i.e. $a_{31} = m|BG| = a_{17}$ where $|BG|$ is the vertical distance between the CB and the CG (center of gravity). The remaining terms in the surge equation are $a_{11} = m$ and some estimate for surge damping a_{12} .

The surge damping can be represented in a number of ways, either linearly with allowance for the current by means of perturbation theory, or in a nonlinear form as a drag coefficient representation, etc. (see [10] for more details). Ordinarily, this surge damping term is not very important in its influence on the resulting ship or buoy motions since there is no natural resonant response in surge. However, in the present case of a moored buoy there is a restraining surge force from the mooring cable and there may be some resonant surge motion. Thus, the proper inclusion of the surge damping force on the buoy hull can be important for dynamic behavior calculations.

The mooring cable forces acting on the buoy hull are considered separately further ahead in this study. They are important since such forces affect the buoy motions, and the buoy motions in turn determine the boundary conditions as well as the input excitation for the cable dynamics. The techniques for inclusion of these effects in the overall mathematical model are considered later in this investigation.

A spar buoy hull form is axisymmetric about the vertical axis and hence motion analysis can be carried out for the three degrees of freedom with slender body theory techniques used in the analysis of the hydrodynamic action on a long slender spar form.

$$m\ddot{z} = -\rho g S_0 \cdot z + z_d + z_w + z_m \quad (57)$$

where S_0 is the spar cross section area at the waterline intersection. The mooring force will depend upon the mooring arrangement and geometry, and is deleted temporarily from consideration. The wave exciting force can be evaluated and the wave generation damping is determined from work in [11].

The velocity potential and the pressure on a slender axisymmetric body in waves are found using the results of [12] for the case of a vertically rising body in waves, at zero forward speed and evaluated for the condition where only the submerged portion from the waterline down is of interest. The fluid pressure on the body in regular sinusoidal waves is (from [12])

$$p = \rho g a e^{2\pi\xi/\lambda} \left(\frac{4\pi R}{\lambda} \cos \theta' \cos \omega t - \sin \omega t \right) \quad (58)$$

where ξ and θ' are the longitudinal and angular coordinates of the spar hull and R is the local hull radius. The local vertical force on a section of the spar buoy is then

$$\frac{dZ_w}{d\xi} = -2R \tan \alpha \int_0^\pi p \, d\theta' \quad (59)$$

with $\tan \alpha = dR/d\xi$ (the slope of the body contour), the local vertical force is

$$\frac{dZ_w}{d\xi} = \rho g a \sin \omega t \cdot e^{2\pi\xi/\lambda} \frac{dS'}{d\xi} \quad (60)$$

where S' is the local hull cross section area, leading to

$$Z_w = \rho g a \sin \omega t \int_{-L}^0 e^{k\xi} \frac{dS'}{d\xi} \, d\xi \quad (61)$$

where $k = 2\pi/\lambda = \omega^2/g$, which can be simplified further by integration by parts (with $S'(L) = 0$).

The surge equation for the spar hull form is represented as

$$m\ddot{x} = -\rho \int_{-L}^0 S'(\xi) [\ddot{x} + (\xi - \xi_g)\ddot{\theta}] \, d\xi + X_d + X_w + X_m \quad (62)$$

where ξ_g is the C.G. location along the ξ -axis, and the wave force is obtained as

$$X_w = \int_{-L}^0 \int_0^{2\pi} p \cos \theta' R \, d\theta \, d\xi = 2\rho a \omega^2 \int_{-L}^0 e^{k\xi} S'(\xi) \, d\xi \cdot \cos \omega t \quad (63)$$

The surge damping force expression due to wave generation (proportional to \dot{x}) in [11] and to this should be added the surge damping due to real fluid drag effects, which is nonlinear. This drag term is represented in the form

$$\frac{\rho}{2} \frac{C_D}{L} A_p \int_{-L}^0 [\dot{x} + (\xi - \xi_g) \dot{\theta}] |\dot{x} + (\xi - \xi_g) \dot{\theta}| \, d\xi \quad (64)$$

where A_p is the lateral projected submerged area of the buoy and C_D is a drag coefficient whose value is ≈ 1.2 , the value for long slender bodies and sections in an oncoming normal flow.

The pitch equation for the spar hull form is represented by

$$\begin{aligned} I_y \ddot{\theta} = & -\rho \int_{-L}^0 S'(\xi) [\ddot{x} + (\xi - \xi_g) \ddot{\theta}] (\xi - \xi_g) \, d\xi \\ & - \rho g \int_{-L}^0 (\xi - \xi_g) S'(\xi) \, d\xi \cdot \theta + M_d + M_w + M_m \end{aligned} \quad (65)$$

and the wave induced exciting moment is given by

$$\begin{aligned} M_w = & \int_{-L}^0 (\xi - \xi_g) \frac{dX_w}{d\xi} \, d\xi \\ = & 2\rho a \omega^2 \int_{-L}^0 (\xi - \xi_g) e^{k\xi} S'(\xi) \, d\xi \cdot \cos \omega t \end{aligned} \quad (66)$$

The pitch damping moment coefficient due to wave generation is given by [11], and as with the surge damping above, the pitch moment equation has additional nonlinear damping given by

$$\frac{\rho}{2} \frac{C_D}{L} A_p \int_{-L}^0 [\dot{x} + (\xi - \xi_g) \dot{\theta}] |\dot{x} + (\xi - \xi_g) \dot{\theta}| (\xi - \xi_g) \, d\xi \quad (67)$$

which must also be induced. By considerations of symmetry, a cross-coupling damping term due to pitch angular velocity, $\dot{\theta}$, will appear in the surge equation, which is given by

$$X_c = -\frac{\rho \omega^2}{g^3} \int_{-L}^0 e^{k\xi} S'(\xi) \, d\xi \cdot \int_{-L}^0 (\xi - \xi_g) e^{k\xi} S'(\xi) \, d\xi \cdot \dot{\theta} \quad (68)$$

and a similar term will occur in the pitch equation, proportional to x , given by

$$M_c = - \frac{\rho \omega^7}{g^3} \int_{-L}^0 e^{k\xi} S'(\xi) d\xi \cdot \int_{-L}^0 (\xi - \xi_g) e^{k\xi} S'(\xi) d\xi \cdot \dot{x}. \quad (69)$$

All of the above expressions can be combined to produce the coupled surge and pitch motion equations of the spar buoy, together with the heave motion equation. The effects of the mooring are included in terms of the appropriate degrees of freedom to allow computation of the complete system response, which will be the end product of the program.

The disc-shaped buoy hull is analyzed as a case of a shallow draft vessel. The section in the water is a circular cylinder with a small draft compared to the cylinder diameter, and the form is axisymmetric. The hydrodynamic and hydrostatic forces are found using the shallow draft approximation, as in [13], together with other simplified representations for the wave-induced forces. Because of symmetry relations, where the disc-shaped buoy is assumed to be circular shape, some of the coefficients in the basic equations of motion, Eqs. (54) - (56), are immediately evident:

$$\begin{aligned} a_{27} &= a_{34} = 0 \\ a_{29} &= a_{36} = 0. \end{aligned} \quad (70)$$

Specific values of certain other coefficients are readily evaluated for a circular discus shape, and they are given below. Assuming that the discus buoy is a cylinder of radius R , and draft d' , the following heave restoration coefficient value is found:

$$a_{26} = \rho g \pi R^2. \quad (71)$$

For the case of the pitch restoring moment, the basic term (corresponding to the hydrostatic portion) of the coefficient a_{39} is obtained from the expression

$$M_h = - W |GM| \theta \quad (72)$$

where

W = weight of buoy

$|GM|$ = metacentric height

$|GM|$ is the difference between the distance between the CG and the CB of the submerged portion of the buoy, and the metacentric radius between the CB and the intersection of the displaced buoyancy vector with the vertical axis.

The metacentric radius is determined from the value of the lateral displacement of the CB of the submerged section of the disc cylinder. This is determined as the ratio of the moment of inertia of the waterplane area about the buoy vertical centerline plane, to the displaced volume. With this moment of inertia found to be $\pi R^4/4$, and with the value of the buoy volume given by $\pi R^2 d'$, the metacentric radius is $R^2/4d'$, leading to a metacentric height $|GM|$ given by

$$|GM| = \frac{R^2}{4d'} - |BG| \quad (73)$$

where $|BG|$ is the vertical distance between the CB and CG of the buoy.

Similarly, values for added mass and added inertia for the disc-shaped buoy can be found from the work of [13], based on considering this hull as a shallow draft vessel. In that case the total added mass in the vertical direction is given by

$$\int A'_{33} dx = \rho R^3 M_y \quad (74)$$

where the value of M_y is given in [13]. Similarly, the added pitch inertia term is represented by

$$\int A'_{33} x^2 dx = \rho R^5 I'_z \quad (75)$$

where the value of I'_z is given in [13]. These values are weakly frequency dependent for the range of significant wave lengths of concern in the buoy problem, and an appropriate approximate constant value can be used. The damping coefficients for heave and pitch are represented, respectively, by

$$a_{25} = \int N'_z dx = \rho R^3 \omega N_y \quad (76)$$

and

$$a_{38} = \int N'_z x^2 dx = \rho R^5 \omega H_z \quad (77)$$

where the quantities N_y and H_z are indicated as frequency-dependent parameters in (77).

For the surge degree of freedom the same expressions as for the ship hull form for the coupling terms with pitch, and vice versa for pitch with surge, are valid for the case of the disc-shaped buoy. The damping due to surge also has the same expression, and can be carried over to the present case of a disc-shaped buoy, with appropriate values of drag coefficient and reference area for the disc.

The wave forces acting on the disc-shaped buoy are primarily due to hydrostatic action and are evaluated on that basis. The vertical wave force is expressed as

$$Z_w = 2\rho g \int_{-R}^R f(x)\eta(x,t) dx \quad (78)$$

where

$$f(x) = \sqrt{R^2 - x^2} \quad (79)$$

is the lateral offset of the buoy circular section and $\eta(x,t)$ is the wave height representation, as follows:

$$\begin{aligned} \eta(x,t) &= a \sin \frac{2\pi}{\lambda} (x \cos \beta - c_w t) \\ &= a \sin \left(\frac{2\pi x}{\lambda} - \omega t \right) \end{aligned} \quad (80)$$

where the dependence on the heading angle β is deleted due to symmetry. The resulting expression for the vertical wave force is

$$Z_w = -4\rho g R^2 a \sin \omega t \int_0^1 (1 - \sigma^2 \cos \gamma \sigma) d\sigma \quad (81)$$

where $\sigma = x/R$ and $\gamma = 2\pi R/\lambda$, leading to

$$Z_w = -2\pi\rho g R^2 a \cdot \frac{J_1(\gamma)}{\gamma} \sin \omega t \quad (82)$$

where $J_n(\)$ is a Bessel function. The pitch moment term due to waves is given by

$$M_w = -2\rho g \int_{-R}^R x f(x) \eta(x,t) dt \quad (83)$$

leading to

$$M_w = \frac{\pi}{2} \rho g R^3 a |J_1(\gamma) - J_3(\gamma)| \cos \omega t. \quad (84)$$

For the surge force due to waves the pressure component in the axial direction is required, and this is found in terms of the axial gradient of the wave amplitude record along the disc. For a hull of draft d' , the surge force due to waves is given by

$$X_w = -2\rho g d' \int_{-R}^R f(x) \frac{\partial}{\partial x} \eta(x, t) dx \quad (85)$$

which leads to

$$X_w = -2\rho g \pi d' R a J_1(\gamma) \cos \omega t. \quad (86)$$

Thus the above expressions complete the representation of the terms required for treating the motion of a disc-shaped buoy in regular waves.

VIII. MOORING DYNAMICS

The initial treatment of mooring cable dynamics will be based upon a complete formulation of equations of motion for a continuous line that is assumed to be completely flexible and extensible. The analysis is restricted to two-dimensional motion in a single plane, which is coplanar with the oncoming current, and the velocities, etc. are converted from directions along x - and y -axes (fixed in space) to those along the normal to the cable, which leads to consideration of the velocities U (normal) and V (tangential) relative to the cable as basic variables.

The basic equations of motion in the x - and y -directions are

$$\mu \frac{\partial u}{\partial t} = \frac{\partial}{\partial s} \left(T \frac{\partial x}{\partial s(1+\epsilon)} \right) + G(1+\epsilon) \cos \phi + F(1+\epsilon) \sin \phi \quad (87)$$

$$\mu \frac{\partial v}{\partial t} = \frac{\partial}{\partial s} \left(T \frac{\partial y}{\partial s(1+\epsilon)} \right) + G(1+\epsilon) \sin \phi - F(1+\epsilon) \cos \phi - W_c \quad (88)$$

where μ is the sum of the cable mass and added fluid mass per unit length, when considering an elongated element of the cable, of length $(1+\epsilon) ds$. From geometric considerations

$$\frac{\partial x}{\partial s} = (1+\epsilon) \cos \phi, \quad \frac{\partial y}{\partial s} = (1+\epsilon) \sin \phi \quad (89)$$

and with the definitions

$$u = \frac{\partial x}{\partial t}, \quad v = \frac{\partial y}{\partial t} \quad (90)$$

$$U = u \sin \phi - v \cos \phi \quad (91)$$

$$V = u \cos \phi + v \sin \phi \quad (92)$$

it can be shown that

$$U_s - V\phi_s = - (1+\epsilon)\phi_t \quad (93)$$

and

$$V_s + U\phi_s = \epsilon_t \quad (94)$$

where the s and t subscripts represent partial derivative operations.

By considering effects normal and tangential to the cable, the basic dynamic equations can be expressed in the form

$$\mu[U_t - V\phi_t] = -T\phi_s + F(1+\epsilon) + W_c \cos \phi \quad (95)$$

$$\mu[V_t + U\phi_t] = T_s + G(1+\epsilon) - W_c \sin \phi. \quad (96)$$

In addition the relation

$$\epsilon = \frac{T}{A_c E_c} \quad (97)$$

is also necessary, so that the basic equations governing the cable dynamics are Eqs. (93) - (97), where the first two relations are basically kinematic. For the steady state case, i.e. neglecting time derivatives, Eqs. (95) and (96) reduce to the same expressions as given in the static equilibrium case, i.e. Eqs. (50) and (51).

To solve the quasilinear partial differential equations given in Eqs. (93) and (97), a linearization procedure can be applied. Defining the expressions

$$U = U_0(s) + U'(s, t) \quad (98)$$

$$V = V_0(s) + V'(s, t) \quad (99)$$

$$T = T_0(s) + T'(s, t) \quad (100)$$

$$\phi = \phi_0(s) + \phi'(s, t) \quad (101)$$

$$\epsilon = \epsilon_0(s) + \epsilon'(s, t) \quad (102)$$

where the ' -symbol quantities are perturbations about the equilibrium positions (o-subscript terms), and expanding various constituent terms up to first order terms alone, leads to

$$\sin \phi = \sin (\phi_0 + \phi') \simeq \sin \phi_0 + \phi' \cos \phi_0 \quad (103)$$

$$\cos \phi = \cos (\phi_0 + \phi') \simeq \cos \phi_0 - \phi' \sin \phi_0 \quad (104)$$

The hydrodynamic loading terms are expanded in the form

$$F = F_0 + F_U U' + F_V V' + F_\phi \phi' \quad (105)$$

$$G = G_0 + G_U U' + G_V V' + G_\phi \phi' \quad (106)$$

where the partial derivatives of the loading functions with respect to particular velocities are indicated. This can be accomplished when considering the steady state velocity solutions (from Eqs. (93) and (94) when time derivatives equal zero) which, when combined with Eqs. (114), are

$$U_0 = 0 \quad (107)$$

$$V_0 = 0 \quad (108)$$

The linear perturbation equations are then given by

$$-\mu U' = T_0 \phi'_s + T' \phi_{0s} - (1 + \epsilon_0) [F_U U' + F_V V' + F_\phi \phi'] + F_0 \epsilon' + W_c \phi' \sin \phi_0 \quad (109)$$

$$-\mu V' = T'_s + (1 + \epsilon_0) [G_U U' + G_V V' + G_\phi \phi'] + G_0 \epsilon' - W_c \phi' \cos \phi_0 \quad (110)$$

$$(1 + \epsilon_0) \phi'_1 = V' \phi_{0s} + V_0 \phi'_s - U_s \quad (111)$$

$$\epsilon'_1 = V'_s + U' \phi_{0s} \quad (112)$$

$$\epsilon = \frac{T'}{A_c E_c} \quad (113)$$

which are a set of first order linear partial differential equations. The boundary conditions for this set of equations is the next task of importance. For a moored buoy in a combined current and seaway, the current is felt acting on the buoy and also on the cable. However, the wave effects attenuate rapidly with depth, and hence the wave forces act on the buoy along with no influence assumed on the cable. In that case the buoy motions due to a regular sinusoidal seaway (assumed for analytical simplification) are transmitted to the cable at its attachment point, and the cable motions are then sinusoidal in time at that point.

The boundary conditions at the anchor point at the sea bottom are given by

$$U = V = 0, \quad s = 0 \quad (114)$$

and at the buoy attachment point for the cable, $s = l$, the boundary conditions are much more complicated. The velocities at the buoy attachment point are given by

$$u = \dot{x} - z_c \dot{\theta} \quad (115)$$

$$v = \dot{z} - l_c \dot{\theta} \quad (116)$$

where \dot{x} , \dot{z} and $\dot{\theta}$ are the wave-induced surge velocity, heave velocity, and pitch angular velocity, respectively, and z_c and l_c are the vertical and horizontal distances from the buoy CG to the cable attachment point. The normal and tangential velocities are defined by Eqs. (91) and (92), and considering the wave-induced motions to be of the same order as linearized perturbation terms, the boundary condition relations for the perturbations are

$$U' = (\dot{x} - z_c \dot{\theta}) \sin \phi_0 - (\dot{z} - l_c \dot{\theta}) \cos \phi_0 \quad (117)$$

$$V' = (\dot{x} - z_c \dot{\theta}) \cos \phi_0 + (\dot{z} - l_c \dot{\theta}) \sin \phi_0 \quad (118)$$

at $s = l$, where \dot{x} , \dot{z} and $\dot{\theta}$ can be represented in the $e^{i\omega t}$ form for a sinusoidal wave input. The boundary conditions at $s = 0$ are

$$U' = V' = 0 \quad (119)$$

where only four boundary conditions are necessary since ϵ' can be eliminated as a variable by use of Eq. (113).

The representation of the boundary conditions at the upper end of the cable ($s = \ell$), at the attachment with the buoy, shows how the cable motions are influenced by the buoy motions. However, the buoy motion is also influenced by the cable system dynamics since a mooring force acts on the buoy as well. The mooring force that affects the buoy motion is due to the component of tension at the attachment point, which leads to

$$X_m = -T'(\ell) \cos \phi_0(\ell) + T_0(\ell) \sin \phi_0(\ell) \phi'(\ell) \quad (120)$$

$$Z_m = -T'(\ell) \sin \phi_0(\ell) - T_0(\ell) \cos \phi_0(\ell) \phi'(\ell) \quad (121)$$

$$M_m = -z_c X_m - \ell_c Z_m \quad (122)$$

where these expressions are component terms on the right-hand sides of the respective equations, e.g. Eqs. (54) - (56). With $T'(\ell, t)$ and $\phi'(\ell, t)$ represented as $f(s)e^{i\omega t}$ forms the total system of buoy and cable can be solved using linear equations of motion for sinusoidal wave inputs at different frequencies (assuming the non-linear damping terms in the buoy motion equations are linearized). The "feedback" nature of the equations governing the buoy motion and the cable motion is illustrated by the above discussion, where the cable tension force influences the buoy motion directly and the buoy motions determine the cable upper point boundary condition.

As mentioned earlier, the study of a moored buoy system is closely related to other mechanical cable system problem areas. The case of a moored ship is, of course, very similar to a moored buoy but the distinguishing difference is the relative masses that are involved. For a moored ship case, the ship is so large (relatively) that it can be realistically assumed that only the quasi-static forces applied to it by the mooring cable are significant, and that the cable dynamics do not influence the ship's response; that is, mooring cable dynamic forces can be assumed small with respect to other excitation forces. Thus, the dynamic problem of the ship and the cable can be treated separately. Similar reasoning applies to the surface condition of a cable-towed body system. However, the analysis of the component forces involved in such systems is applicable to the present case of a moored buoy system, keeping in mind the required coupling in the mathematical model, as shown above.

The equations developed here for a moored buoy system have to be solved in order to determine the necessary information on

system performance. The methods to be applied should recognize the problem as involving complicated two-point boundary value problems, or alternatively another technique that replaces the equations by a set of difference equations or differential-difference equations similar to the case of a beam vibration problem can be applied (see [10] for a discussion of different computational techniques for this problem). The solution of the class of partial differential equations given above is a specialized simulation problem that is the subject of presently on-going research so no further detailed discussions can be given. The development of these equations is another illustration of the application of knowledge of hydrodynamics of ship motion toward other related problems of engineering significance.

IX. DRIFT FORCES DUE TO WAVES

When a floating vessel is acted upon by waves it experiences forces and moments that are predominantly oscillatory-like in nature, with the frequency characteristics similar to that in the spectrum of the oncoming wave system. These forces are also linear with regard to wave amplitude. In addition there are also nonlinear force contributions that arise from the presence of the vessel hull modifying the incident waves by virtue of its function as an obstruction, as well as the effect of interaction between the vessel motion and the incident waves. These nonlinear forces are much smaller than the linear wave forces, but nevertheless exert a significant effect on certain degrees of freedom of the vessel.

The major nonlinear drift forces of importance to the problem of maintaining a desired position in a seaway are in the longitudinal and lateral directions relative to the vessel, as well as the yawing moment that tends to rotate the vessel in heading. Some theoretical studies of these quantities have been made, but only for determining average values in regular waves, with the work of Havelock [14], Maruo [15], Hu and Eng [16] and Newman [17] serving as typical examples.

Havelock [14] treats only the drift force in head seas. His formula is based on the heave and pitch motions and their relative phase to the incident wave. The theoretical approach of Hu and Eng [16], which follows that of Maruo [15], yields expressions only for the lateral drift force and draft yaw moment in waves. (Maruo's results only considered the lateral drift force.) While their results are quite general, they have only been reduced to workable formulas under the restrictive assumptions of a thin ship, with small draft, in long waves. These results indicate infinite (practically unrealistic) forces and moment as the wave length goes to zero. The maximum lateral drift force occurs in beam seas (varying as $\sin^3 \beta$), and the maximum moment occurs at an angle of 45° (varying as $\sin^2 \beta$).

Newman's method [17] , based on slender body theory, does show some comparison with very limited experimental work for lateral drift force and yaw moment which indicates rough agreement. His results for longitudinal force, for which no experimental comparison is given, indicate that this force in head seas generally exceeds the lateral forces for a given wave length condition. Furthermore, these results indicate that the maximum lateral force occurs in bow waves ($\beta \approx 45^\circ$), with the force going to zero in both head and beam waves.

The results of Hu and Eng [16] include the effects of sway, yaw and roll motions, with no influence of heave and pitch included (as to be expected for thin ship analysis) while Newman [17] only accounts for heave and pitch motion effects without any influence of the three lateral degrees of freedom. Thus there is a question as to the proper representation of the drift forces that would reflect the influence of the important dynamic motions that produce these forces. The analysis by Maruo [15] presents a final expression for the average lateral drift force in beam seas that depends upon the reflected wave amplitude, which in turn is defined in terms of the relative motion between the incident wave and the resulting heave motion. The presence of sway motion has no effect on the lateral drift force since the body acts like a wave particle in beam seas and no relative motion occurs (to that order). A similar result is indicated for submerged cylinders in the work of Ogilvie [18] , where the average lateral force identically vanishes.

In all of these hydrodynamic studies, the force is found to be proportional to the square of the incident wave amplitude, since the nonlinear pressures are represented in terms of squares of generated wave amplitudes, squares of fluid velocities, and products of first order oscillatory displacements with derivatives of fluid velocities. While the previous hydrodynamic analyses have been concerned with the average drift force for a regular sinusoidal wave, it is important also to determine the actual time histories of these forces, especially for the case of an irregular incident wave system. In that case it is expected that the drift force will be a slowly varying function, in terms of the frequencies contained in the defining incident wave bandwidth, and it is of interest to determine the basic representation of the forces, the response of floating vessels to such forces, the statistical properties, etc.

In order to illustrate the basic characteristics of these forces, particular attention will be given to the case of the lateral drift force acting on a vessel in beam seas. Using the results of Maruo [15] , the lateral drift force acting on a cylinder (in the two-dimensional case) is given by

$$\frac{\overline{F}_y}{L} = \frac{1}{2} \rho g \overline{A_z^2} |z - \eta|^2 = \frac{1}{2} \rho g a^2 \overline{A_z^2} \left| \frac{z}{a} - 1 \right|^2 \quad (123)$$

where \overline{A}_z is the ratio of the amplitude of the heave-generated two-dimensional wave to the amplitude of heaving motion of the ship section, and $|z - \eta|$ is the absolute value of the relative heave motion. It is seen that this expression is thus proportional to the square of the incident wave amplitude, with the force only occurring due to the relative motion between the heave and the incident wave. It can be shown that the mean value of this force in an irregular sea characterized by a wave spectrum such as the Neumann spectrum is given by

$$\overline{F}_y = \int_0^\infty \frac{\overline{F}_y}{a^2} A^2(\omega) d\omega \quad (124)$$

where $A^2(\omega)$ is the Neumann spectrum representation given in Eq. (43).

The results obtained in the basic derivations for determination of the drift force have been carried out for the case of a single sine wave at a fixed frequency. In the real case, the waves are composed of many frequencies in a band, and for the purposes of simplification of the following analysis it will be assumed that this bandwidth is relatively narrow. If a combination of two different frequencies is present in a wave, and hence in the relative heave motion represented by

$$z - \eta = b_1 \sin \omega_1 t + b_2 \sin (\omega_2 t + \phi) \quad (125)$$

the square of this term is given by

$$\begin{aligned} (z - \eta)^2 &= b_1^2 \sin^2 \omega_1 t + b_2^2 \sin^2 (\omega_2 t + \phi) + 2b_1 b_2 \sin \omega_1 t \sin (\omega_2 t + \phi) \\ &= \frac{1}{2} \left\{ b_1^2 + b_2^2 + 2b_1 b_2 \cos [(\omega_2 - \omega_1)t + \phi] \right\} \\ &\quad - \frac{1}{2} \left\{ b_1^2 \cos 2\omega_1 t + b_2^2 \cos 2(\omega_2 t + \phi) - 2b_1 b_2 \cos [(\omega_2 + \omega_1)t + \phi] \right\}. \end{aligned} \quad (126)$$

It can be seen that this expression is made up of a group of terms that are essentially constants and slowly varying terms (due to the narrow band assumption), and another group of terms representing higher frequency oscillations, i.e. at higher frequencies than the wave terms. If a time average of this quantity is made, it will be seen that the combination of the constants and the slowly varying term remains and the higher frequency terms drop out, and that this first grouping of terms can be represented as the square of the envelope of the combined signal given in Eq. (125) (see [19]).

If the wave system, and the resulting relative heave motion, are represented by the sum of a larger number of terms of different frequencies, with these frequencies having only small increments relative to a single reference frequency (as a result of the narrow band assumption), the contribution to the drift force value in that case can be shown to be given by an expression that is also identified as the square of the envelope of the total signal. This identification and interpretation of this type of expression for the drift force can generally be extended to the case of an arbitrary input, including a random input which is assumed to be made up of a combination of different frequencies within a narrow band. Thus a simulation technique in the time domain for this term requires determination of the envelope of the input signal (relative heave motion), squaring this quantity, and applying the appropriate constants to produce the required time history signal.

The drift force has been shown to be a nonlinear function of the wave amplitude, and in a random sea it is a slowly varying function of time, where this slow variation is considered relative to the wave frequencies and the linear wave-induced forces. Since the wave surface elevation and all linear terms derived from it are assumed to be Gaussian random processes, the drift force is known to be non-Gaussian in regard to its probability density. In order to obtain further characterization of the properties of the suction force, it would be useful to determine the probability distribution and spectral properties of this force. The accomplishment of this task will be aided by the simplified interpretation of the drift force that was presented above.

Considering the drift force as the square of the envelope of a Gaussian random process, certain information is available concerning the probability density of this type of function. A square-law detector produces an output proportional to the square of the envelope of the input, if the input is a narrow band Gaussian random process [20] which is the assumption used in the present analysis. For a particular input into such a square-law detector, the probability density function of the output (denoted as w) is given by

$$p(w) = \frac{1}{E(w)} e^{-w/E(w)}, \quad w \geq 0 \quad (127)$$

where $E(w)$ is the mean value of the square-law detector output. On that basis, the probability density for the drift force in a random sea can be represented by

$$p(F_y) = \frac{1}{\bar{F}_y} e^{-F_y/\bar{F}_y}, \quad F_y > 0 \quad (128)$$

where \bar{F}_y is the mean drift force, and hence the probability distri-

bution is given by

$$P\left(\frac{F}{\bar{F}} < x\right) = 1 - e^{-x} \quad (129)$$

In addition to information on the probability density, additional statistical properties of the drift force are provided in terms of the autocorrelation and power spectral density functions for that force. The relationship between the statistical characteristics of an input to the nonlinear form of drift force representation, to the output characteristics, as defined by the autocorrelation and spectral density, is a useful description which can be applied in further analyses and for simulation studies. The problem of a square-law detector has been treated in the available literature, e.g. [20] and the results can be applied to the present case. If a general narrow band Gaussian random process, represented by the variable $x(t)$, is the input to a square-law device, and the output is defined as r^2 , the autocorrelation function $R_{r^2}(\tau)$ is given by

$$\begin{aligned} R_{r^2}(\tau) &= 4\sigma_x^4 + 4R_x^2(\tau) \\ &= (\overline{r^2})^2 + 4R_x^2(\tau) \end{aligned} \quad (130)$$

where

$$\overline{r^2} = 2\sigma_x^2 \quad (131)$$

is the mean value of the square of the envelope, with σ_x^2 the mean square value of the input function $x(t)$. The relations between the autocorrelation and power spectral densities of the input function are given by

$$S_x(\omega) = \frac{2}{\pi} \int_{-\infty}^{\infty} R_x(\tau) e^{-i\omega\tau} d\tau, \quad R_x(\tau) = \frac{1}{4} \int_{-\infty}^{\infty} S_x(\omega) e^{i\omega\tau} d\omega \quad (132)$$

where

$$R_x(0) = \sigma_x^2 = \frac{1}{2} \int_0^{\infty} S_x(\omega) d\omega \quad (133)$$

thus being in conformity with the relations described by the Neumann wave spectrum and all linear functions derived from that spectral formulation.

The power spectral density of the square-law device output is then

$$\begin{aligned} S_{r^2}(\omega) &= \frac{2}{\pi} \int_{-\infty}^{\infty} R_r^2(\tau) e^{-i\omega\tau} d\tau \\ &= 4(\overline{r^2})^2 \delta(\omega) + \frac{8}{\pi} R_x^2(\tau) e^{-i\omega\tau} d\tau \end{aligned} \quad (134)$$

where $\delta(\omega)$ is the delta function. The last term on the right in Eq. (134) can be evaluated by using the definitions in Eq. (132), so that

$$\begin{aligned} \frac{8}{\pi} \int_{-\infty}^{\infty} R_x^2(\tau) e^{-i\omega\tau} d\tau &= \frac{2}{\pi} \int_{-\infty}^{\infty} S_x(\omega') d\omega' \int_{-\infty}^{\infty} R_x(\tau) e^{-i(\omega-\omega')\tau} d\tau \\ &= \int_{-\infty}^{\infty} S_x(\omega') S_x(\omega - \omega') d\omega' \end{aligned} \quad (135)$$

which leads to the final result

$$S_{r^2}(\omega) = 4(\overline{r^2})^2 \delta(\omega) + \int_{-\infty}^{\infty} S_x(\omega') S_x(\omega - \omega') d\omega'. \quad (136)$$

The power spectral density of the square-law device output, which is proportional to the drift force, contains the delta function term (that represents the non-zero mean value of the force) and a convolution integral of the input spectral density whose value will depend on the nature of the particular input. The square law detector output is obtained by operating on the output of the square law device with an ideal low pass zonal filter that filters out completely the high frequency part of its input, thereby leaving only the low frequency part representing the envelope.

A particular application to illustrate the results of applying this analysis is given for the case of a vessel moored in a seaway such that an irregular beam sea is present. The vessel chosen for this illustration is the same CUSS I moored barge treated previously, and the sea condition is represented by a Newmann spectrum corresponding to a 24 kt. wind (upper Sea State 5). A mathematical representation of a filter circuit whose amplitude characteristics are approximately the same as the square root of the Newmann spectrum formula (Eq. (43)) was derived, programmed on an analog computer with a white noise generator input, and produced an output that represented a continuous time history of the surface waves with that desired spectrum, r.m.s. value etc. A simplified constant coefficient second order differential equation for ship heave

motion in beam seas was set up on the analog computer, with the input wave force excitation assumed to be proportional to the wave record, and solutions obtained for $z(t)$, the heave motion as a function of time, and also for $[z(t) - \eta(t)]$, the relative heave motion.

At the same time another equation was programmed on this analog computer representing the uncoupled sway motion of the moored barge, viz.

$$(m + A_{22})\ddot{y} + N_y\dot{y} + k_y y = Y_{ex}(t) \quad (137)$$

where $Y_{ex}(t)$ is the wave exciting force. This exciting force was simulated to represent the linear wave-induced force and then the nonlinear drift force, with separate solutions obtained for each excitation above in order to illustrate the different output results. The linear wave excitation force was represented as proportional to $\dot{\eta}(t)$, after a 90° phase shift over the pertinent wave bandwidth, which is an adequate approximation. The nonlinear drift force was represented by

$$Y_{drift} = \rho g L \bar{A}_z^2 \{z - \eta\}^2, \quad (138)$$

where the $\{ \}$ symbol represents the envelope operation, and a constant value is assumed for \bar{A}_z . The envelope of a time-varying function is obtained by rectifying the signal (i.e. an absolute value circuit), followed by a low pass filter.

The results of this simulation study are shown in Fig. 15 for the case of linear wave force excitation and in Fig. 16 for the drift force input. The time histories of the surface wave motion, sway motion output, and input exciting force are shown in each figure. The linear wave force response is seen in Fig. 15 to be generally oscillatory, of the same general frequency content as the wave input, and with an amplitude of the same order as the wave. The input excitation force has somewhat higher frequency content (since it is proportional to $\dot{\eta}$) and it reaches amplitudes of 4×10^6 lb.

The sway motion in Fig. 16, due to the nonlinear drift force input, has an entirely different character than the surface wave motion or the wave-induced sway motion shown in Fig. 15. It is a long period, almost regular response at the natural period of sway for the moored ship, viz. 64 sec. (see Table 1). The input force that caused this response is also shown in Fig. 16, as derived according to Eq. (138) and it can be seen to be a slowly varying function of time, reaching a maximum value of about 50,000 lb and causing a response reading up to 15 ft in amplitude. Thus the characteristics of the slowly varying nonlinear force, of much

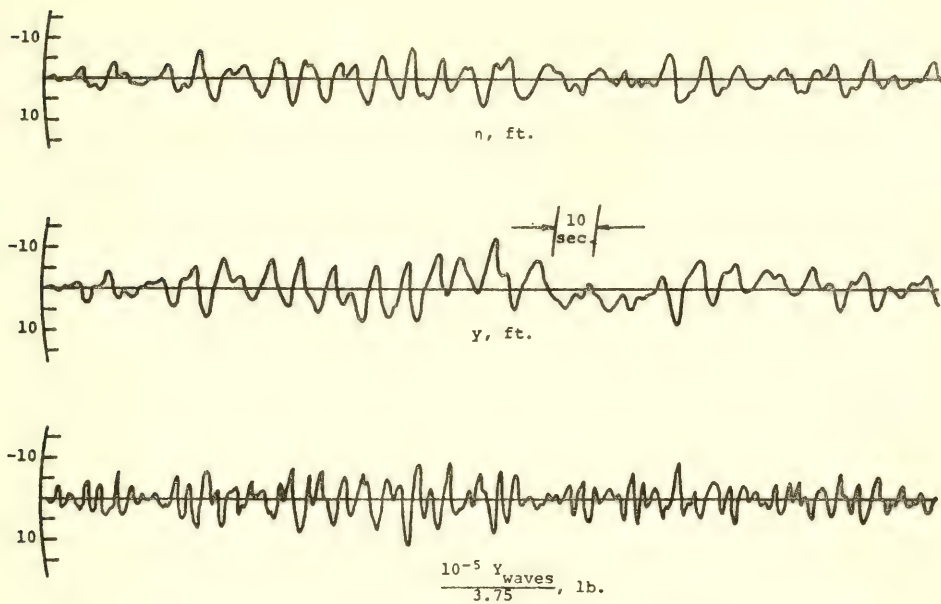


Fig. 15. Sway motion response to linear wave force in irregular beam seas.

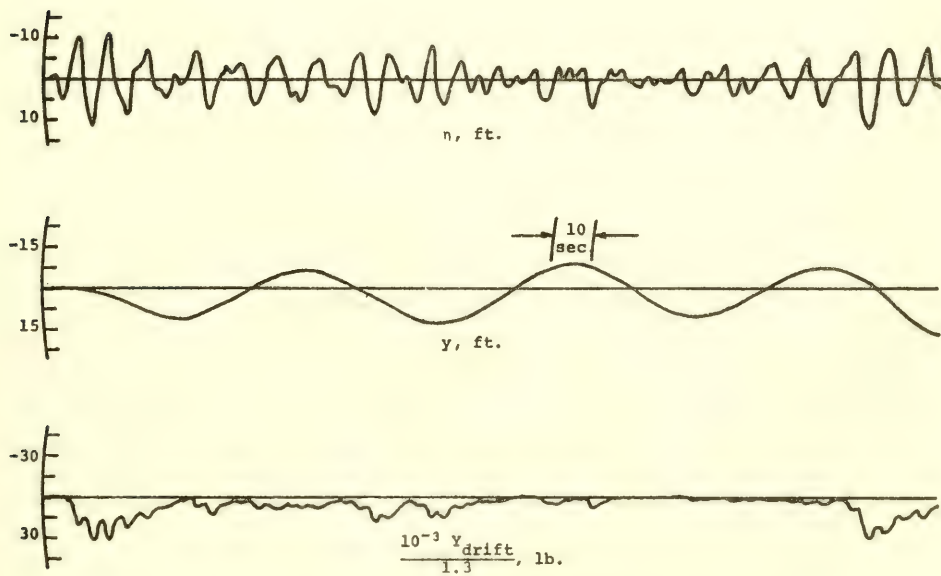


Fig. 16. Sway motion response to nonlinear drift force in irregular beam seas.

smaller magnitude than the linear wave force, produce large motions of moored vessels by causing resonant responses with the low frequency modes introduced by the moorings.

If the two responses given in Fig. 15 and 16 were linearly combined, as in the realistic case at sea when both forces are generated simultaneously, the total output would represent the actual motion of the moored vessel. The resulting large motions would cause significant stretching of the mooring cables, leading to larger forces in the cables than indicated by the linear wave effects above (e.g. as shown in Fig. 13). Thus proper consideration of the non-linear wave forces and their influence must be included in any analytical estimation of expected motions and forces of moored vessels, thereby requiring further effort at understanding and simulating these effects.

As an aid in obtaining further insight into the characteristics of the lateral drift force in this case, an evaluation was made of the power spectrum of this force using the expressions given in Eq. (136) for the part that represents the random variations of this force about its mean value (the convolution integral term). The result of this evaluation is shown in Fig. 17, and when considering the effect of the low pass filter, all values for $\omega > 1.0$ will be eliminated. Thus it can be seen that the drift force itself is concentrated at low frequencies, and that the response of a dynamic system with a very low natural frequency (i.e. the ship sway motion) will result in a response spectrum concentrated at an even smaller low frequency band. This is what is usually found in the results of model tests and full-scale experience, and thus an explanation is provided by the preceding analysis.

X. APPLICATION TO DYNAMIC POSITIONING

When considering the case of dynamic positioning, various forces act on a free vessel in the open sea that cause it to move from its required position. These forces are the relatively steady forces due to wind and due to current, the oscillatory-type forces due to waves and the drift forces. The wind generates forces and moments because of its impingement upon the abovewater surfaces of the hull and superstructure, while the current forces act on the underwater hull (and any submerged drilling equipment, if that is the purpose for the vessel). These steady forces can be overcome by the generation of steady forces by some type of thruster mechanism that will act to maintain the ship more-or-less in its desired location.

The oscillatory-type forces due to waves are very large, and no force-generating system installed on a vessel is expected to be able to overcome such effects. The ship will therefore oscillate "back-and-forth" in response to these large wave forces with essentially no net deviation of significance from its average position.

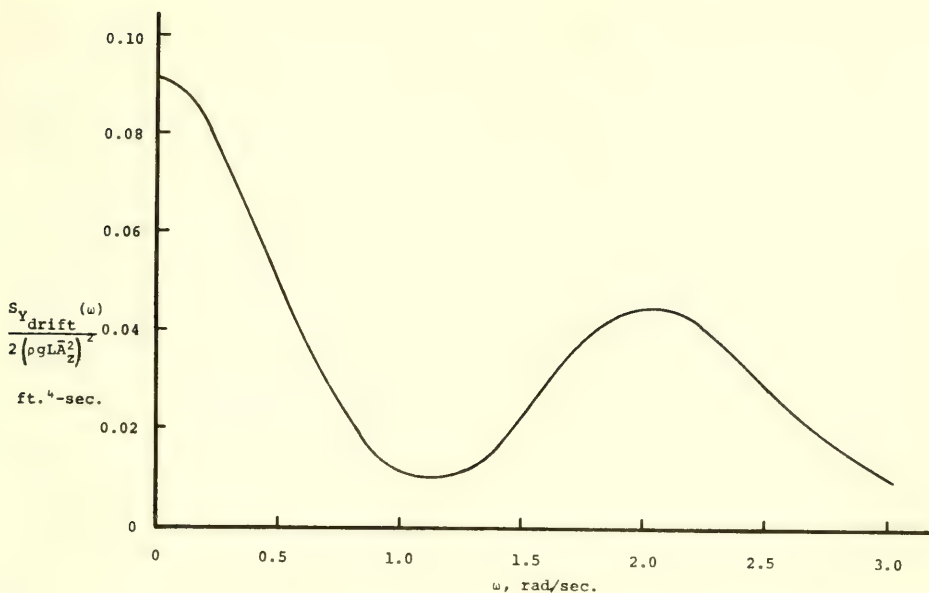


Fig. 17. Representative power spectrum of lateral drift force.

It is the drift forces and moments whose mean values tend to move and/or rotate the ship off position, with their level of fluctuation causing dynamic responses that produce ship motion. Thus some means of control must be applied to "modulate" the forces developed by the thruster system in order to minimize the ship's average motion relative to its desired position.

The ship will experience drift-like forces in the lateral and longitudinal directions, as well as a yaw moment, and the philosophy of applying control forces to the ship will be aimed at countering these forces by orienting the ship in the proper direction so that the resultant force is acting along the ship's longitudinal axis and there will be no significant moment. It would then be possible to use the main propulsive thrust of the ship, assuming controllable pitch propellers, to counter this resultant force. Lateral forces that are developed by particular thrusters, or other force systems, will be used to overcome any tendency of the ship to rotate out of its preferred direction due to any resulting yaw moments. The force magnitudes in regard to average values can be estimated from the results of some of the cited references given in this paper, and some idea of the time history variations and maximum magnitudes expected relative to the average values can also be inferred from the work presented here.

In a complete simulation study of the resultant motion of a ship in which a dynamic positioning system is to be installed, all three degrees of freedom (surge, sway and yaw) will be coupled and the forces and moments will be dependent upon the relative orientation with respect to the incident wave system. This will be a somewhat complicated analysis, but the tools are generally available for determining the various hydrodynamic parameters entering into such a study. It will also be necessary to consider the type of signal system that would incite the position errors of the ship, together with a signal processing operation (i.e. control system design) that will be necessary in order to achieve the desired type of operation. Similarly, some estimate of the response time of the thruster force development must be included in determining ship response so that a measure of positioning accuracy can be obtained as a result of the analysis.

In view of the complexity of this problem, a discussion of a simple application will be given for the case of sway motion alone in beam seas. In that case the equation of motion will be similar to that given in Eq. (137), without the presence of the linear spring term (that was due to the mooring in the previous case). The response due to the linear wave forces will be generally the same for this case as in the case of the moored ship, as shown in Fig. 15. However, the effect of the drift forces will cause the ship to continually deviate in position within a very short time. The deviation will be almost a quadratic growth with time since the response is similar to that of a constant force acting on a system primarily represented as a pure second derivative dynamic response. Thus a control force is necessary, and the control rule should include terms proportional to sway displacement and velocity, i.e. the control force will be of the form

$$Y_c = -C_1(y - y_0) - C_2\dot{y} \quad (139)$$

where y represents the lateral error displacement relative to the desired position, y_0 , and this control force is included in the basic equation

$$(m + A_{22})\ddot{y} + N_y\dot{y} = Y_{\text{waves}} + Y_{\text{drift}} + Y_c. \quad (140)$$

The lateral position error, which can be obtained from an acoustic reference system placed on the ocean bottom, will contain the influence of the higher frequency response due to the linear wave forces and in addition the control signal that includes the lateral velocity error will contain more "noise" in the resulting control signal. This can be overcome by the inclusion of appropriate filter circuits associated with the control signal processing, which involves the use of standard servomechanism techniques within the state-of-the-art of control design. A closed loop feedback system using the

appropriate measured inputs can then be evaluated in detail by computer system simulation to determine the optimum gains to be used in the control rule in Eq. (139). The only guidance that can be given for this selection, based on simple dynamic principles, is to select the value of the gain C_1 that will produce a resultant frequency that lies between the frequency associated with the maximum spectral energy of the predominant wave system and the very low (near zero) frequency for large responses to drift forces. The value of the gain C_2 should be such that, when added to the normal ship damping, the resulting response of the system will be relatively "flat" throughout the major band of disturbing frequencies for the drift force. All of these characteristics can be refined in the course of control system analysis and design, as well as from the simulation results, and further discussion lies beyond the scope of the present paper.

XI. CONCLUDING REMARKS

All of the preceding problem areas discussed in this paper have illustrated the application of a specific area of Naval Hydrodynamics, viz. hydrodynamics of ship motion in waves. The utility of presently existing techniques of analysis for solution of practical problems in ocean engineering, with emphasis on mooring and positioning of vessels and other systems in a seaway, has been shown within the limits of the present state of development of this field. Greater emphasis toward consideration of certain nonlinear hydrodynamic forces for application to these problems has been indicated, especially in view of their predominant effect in certain modes of motion. Possible directions for future research and development activities in this field will involve consideration of better techniques of representing the form of these forces in terms of body geometric parameters, more concentration of basic model measurements for comparison with theory, and techniques of simulation in dynamic analyses of motion behavior. This information will be fundamental in establishing computer models for determining many aspects of system performance at sea prior to actual construction, thereby providing insight as to expected problem areas and methods of solution. The methods of applied hydrodynamics for these purposes are generally available now, and it remains for the ocean engineering profession to determine the utility or applicability of these tools to the particular practical problems that they face in their own operations.

REFERENCES

1. St. Denis, M. and Pierson, W. J.: "On the Motions of Ships in Confused Seas," Trans. SNAME, 1953.
2. Kaplan, P.: "Application of Slender Body Theory to the Forces Acting on Submerged Bodies and Surface Ships in Regular Waves," Journal of Ship Research, November 1957.
3. Pierson, W. J., Neumann, G. and James, R. W.: "Practical Methods for Observing and Forecasting Ocean Waves by Means of Wave Spectra and Statistics," U.S. Navy Hydrographic Office Pub. No. 603, 1954.
4. Deep sea mooring plan and typical mooring legs, and deep sea mooring details, U.S. Navy, Bureau of Yards and Docks, Dwgs. Nos. 896131, 896132, June 1961.
5. Grim, O.: "Die Schwingungen von schwimmenden, zweidimensionalen Korpern," Hamburgische Schiffbau-Versuchsanstalt Gessellschaft Rpt. No. 1172, September 1959.
6. Kaplan, P. and Putz, R. R.: "The Motions of a Moored Construction Type Barge in Irregular Waves and Their Influence on Construction Operation," Report for U.S. Naval Civil Engr. Lab. under Contract NBy-32206, August 1962.
7. Technical Memorandum containing information concerning "CUSS I," supplied by U. S. Naval Civil Eng. Lab., Port Hueneme, California, August 1961.
8. Muga, B. J.: "Experimental and Theoretical Study of Motion of a Barge as Moored in Ocean Waves," Hydraulic Engineering Series No. 13 of the U. of Illinois, January 1967.
9. Hsieh, T., Hsu, C. C., Roseman, D. P. and Webster, W. C.: "Rough Water Mating of Roll-On/Roll-Off Ships with Beach Discharge Lighters," Hydronautics, Inc., Tech. Rpt. 631-1, July 1967.
10. Kaplan, P. and Raff, Alfred I.: "Development of a Mathematical Model for a Moored Buoy System," Oceanics, Inc. Rpt. No. 69-61, April 1969.
11. Newman, J. N.: "The Motions of a Spar Buoy in Regular Waves," DTMB Report 1499, May 1963.

12. Breslin, John P. and Kaplan, P.: "Theoretical Analysis of Hydrodynamic Effects on Missiles Approaching the Free Surface, Including the Influence of Waves," Proceedings BOHAC Hydroballistics Symposium, September 1957.
13. Kim, W. D.: "On the Forced Oscillations of Shallow-Draft Ships," Journal of Ship Research, Vol. 7, No. 2, October 1963.
14. Havelock, T. H.: "The Drifting Force on a Ship Among Waves," Philo. Mag., Vol. 33, 1942.
15. Maruo, Hajime: "The Drift of a Body Floating on Waves," Journal of Ship Research, Vol. 4, December 1960.
16. Hu, Pung Nien, and Eng, King: "Drifting Force and Moment on Ships in Oblique Waves," Journal of Ship Research, Vol. 10, March 1966.
17. Newman, J. N.: "The Drift Force and Moment on Ships in Waves," Journal of Ship Research, Vol. 11, March 1967.
18. Ogilvie, T. Francis: "First- and Second-Order Forces on a Cylinder Submerged Under a Free Surface," Journal of Fluid Mechanics, Vol. 16, 1963.
19. Terman, Frederick E.: Radio Engineering, McGraw-Hill Book Co., Inc., Second Ed., 1937.
20. Davenport, Wilbur B., Jr., and Root, William L.: An Introduction to the Theory of Random Signals and Noise, McGraw-Hill Book Co., Inc., 1958.

WAVE INDUCED FORCES AND MOTIONS OF TUBULAR STRUCTURES

J. R. Paulling

*University of California
Berkeley, California*

ABSTRACT

Many types of stable ocean platforms consist of space-frame assemblages of tubular structural and buoyancy members. An approximate method of predicting the hydrodynamic forces and resulting motions of such structures is described. In this procedure, the force on each member is computed by assuming that the member is long and slender and all other members are absent. Such forces for all members are summed and introduced into the linear equations of motion of the entire structure, which may then be solved for the resulting platform motions. Reasonably good agreement is obtained between the results of such analysis and model experiments with several different platform configurations.

I. INTRODUCTION

Many of the stable floating platforms which have been proposed or constructed for deep water drilling, mining, or emplacement and recovery of heavy objects can be described as space-frame assemblages of tubular members. R. H. Macy [1969] describes and illustrates several oil-drilling platforms of this type. One of them, BLUE WATER II, consists of a square base configuration approximately 200 feet square, made up of cylindrical members 14.5 feet in diameter, with four vertical corner caissons 24.7 feet in diameter supporting the main deck. This platform normally operates at a draft of about 40 feet. A second platform, the SEDCO 135, consists of three main vertical caissons located approximately at the vertices of an equilateral triangle, several diagonal tubular truss members, and, at the bottom of the main caissons, elongated pontoons of oval planform. These platforms are moored by a spread array of anchors, and operate in water depths of up to 600-1,000 feet.

McClure [1965] described a platform which was designed for the MOHOLE deep sea drilling project. This platform was to consist of two submerged main horizontal pontoons 35 feet in diameter, and 390 feet long, with a centerline separation of 215 feet. Three vertical caissons extended from each horizontal pontoon through the free water surface to support the main working deck. This platform was intended to operate in a water depth of 14,000 feet, and was to be dynamically positioned by means of trainable propulsion units controlled through a central computer system. The foregoing types of platforms are referred to as "column stabilized," which implies that pitch and roll static stability are obtained primarily from the waterplane moment of inertia of the surface piercing vertical column.

A third type of platform for which a tubular space frame configuration has been proposed is the tension leg platform, an example of which is shown by Macy [1969] and described by Paulling and Horton [1970]. This is a moored stable platform for which the buoyancy exceeds the platform weight, and the net equilibrating vertical force is supplied by vertical tension mooring cables secured by deadweight or drilled-in anchors. As a final example of tubular stable platform structure, we mention the spar-type platforms, the prime example of which is FLIP, described by Fisher and Spiess [1963]. The platform consists of a single cylindrical member of tapering cross section arranged to float vertically, with a small portion of its length projecting above the surface of the sea.

All of these platforms share a common characteristic in that their configuration consists of a space frame assemblage of relatively long, slender, cylindrical members, with the addition in some cases of small buoyancy chambers or pontoons. All share a common objective of producing a working platform having minimum wave-induced motions, even under relatively severe sea conditions, i.e., a platform which is "transparent" to the waves. The positioning methods used differ greatly in each case, ranging from essentially no positioning, in the case of FLIP, dynamic positioning with no physical connection to the sea bottom, in the case of the MOHOLE platform, to various types of anchoring systems exemplified by the tension leg and the column stabilized platforms. The sea environment and resultant platform responses are similar in each case, i.e., all are intended to operate in relatively deep water under severe environmental conditions, with platform motions which are small compared to the overall dimensions of the platform and to the length of waves involved. Our objective here is to describe a procedure for analyzing the forces and motions which can be applied equally to all of these platforms if suitable account is taken of the type of anchoring or positioning restraint involved.

Such an analysis of wave-induced forces and motions forms an essential part of the process of designing a platform to perform a specific mission. At least three such functions are envisioned. First, for a platform of given geometry, a range of sea conditions may be investigated to determine what limitations may be imposed

on the platform's performance by the resulting wave motions. Second, given a set of sea conditions and platform requirements, we may investigate a family of platform configurations to determine those members of the family which will be able to perform the specified mission under the stated sea conditions. This kind of analysis, in turn, might form a part of a more extensive system study aimed at determining the most cost effective platform system. As a third function, the force distributions on structural members which are obtained during the force and motion analysis may be used in connection with the detailed structural design of the platform.

The general procedure followed in analyzing the dynamic behavior of such a platform is to assume that it behaves as a rigid body having six degrees of freedom. The external forces which excite the motion of the structure are associated with the fluid motion relative to the structure, and with the structure's mooring or positioning system. Two alternative methods are available for the computation of the fluid forces. In the first, the fluid is assumed inviscid and its motion irrotational, and we proceed on the basis of classical hydrodynamic theory to seek a solution to Laplace's equation in the fluid region subject to certain boundary conditions. These include kinematic boundary conditions on the free water surface and on the wetted surface of the structure itself, a constant pressure dynamic boundary condition on the free surface, a dynamic boundary condition on the wetted surface of the body, which is derived from the rigid body equations of motion, and other conditions far from the body which are necessary for uniqueness of the solution. This approach yields great insight into the fundamental nature of the fluid phenomena, and is exact within the limits of the necessary fluid idealization and motion linearization. Its implementation, however, is beset with almost insurmountable difficulties unless the geometry of the body is extremely simple.

The second method is less exact in principle, but provides approximate means of including real fluid effects and of dealing with geometrically complex, realistic configurations. This procedure, which is employed in the present analysis, is termed "hydrodynamic synthesis." Here we consider the complex structure to be assembled from a group of simpler bodies whose individual hydrodynamic properties are known, perhaps as a result of an analysis of the first type above. A fundamental assumption is then made that the hydrodynamic force on the assembled structure may be computed by taking the sum of the forces of all of the component members. In the simplest case, these forces are computed as though each member were completely remote and independent of the rest of the structure, but subject to the same pattern of body and fluid motions. The forces computed in this way might be refined by introducing modifications to the fluid flow to account for the hydrodynamic interaction between adjacent members.

The result of this hydrodynamic synthesis is a system of hydrodynamic forces acting upon the assembled structure, containing terms dependent upon the incident wave system and upon the motion

of the structure itself. Additional restraint forces are introduced to account for the effects of the mooring or dynamic position system. This total system of external forces is then equated to the mass times acceleration of the body by Newton's second law, yielding a system of coupled differential equations of motion. These equations are then solved to obtain the time-dependent motion of the structure.

In the present analysis, a linear relationship will be assumed to exist between all forces and the appropriate motion parameters. Two important consequences follow as a result of such an assumption: (1) The hydrodynamic forces acting on the structure may be divided into two independent parts, one depending only on the incident wave motion, and the second depending only on the platform motion. (2) A prediction of the platform response to a realistic random seaway may be obtained by superimposing the responses to the seaway's regular wave components.

The validity of such a linearization may be tested either empirically or by comparing its results with results of an "exact" analysis. An exact analysis is normally possible only for such a simplified class of geometries that the validity of the comparison for the realistic case is subject to question. We are, therefore, forced to an experimental test. For the present, we have considerable evidence on the usefulness of linear techniques in predicting ship motions as in Gerritsma [1960], and motions of platforms of the present type, Burke [1969], Paulling and Horton [1970]. Some further experimental comparisons are given in the present paper.

II. THE EQUATIONS OF MOTION

The motion of the platform will be expressed as a small deviation from a mean position, and for this purpose it is convenient to define two coordinate systems. The first, OXYZ, is fixed relative to the structure such that O is located at the structure's center of gravity, Y is directed vertically upward, and OXZ is parallel to the mean waterplane. In many cases, we may take advantage of symmetry to arrange these axes so that one or more of them is a principal axis of inertia. Also, in some cases, a designer's coordinate system may be used for drafting or other design purposes, which is parallel to OXYZ but whose origin is located elsewhere. Quantities defined in this latter system may always be transformed to the OXYZ system by simple coordinate transforms, and it is assumed that this is done.

A second coordinate system, *oxyz*, is fixed in space such that it occupies the mean position of OXYZ as the platform moves in waves. In general, it is found most convenient to express the inertial properties and the forces acting on the structure in OXYZ since the geometry of the structure is fixed in this system. On the other hand, it is more convenient to express the equations of linear motion in the space system, *oxyz*, since this is an inertial system, and because we ultimately wish to obtain the motion of the platform

in terms of time dependent deviations from this mean position. The linear displacements of the center of gravity of the platform from its mean position may then be expressed by the small quantities $x(t)$, $y(t)$, $z(t)$, measured in the $oxyz$ system. We next express the rotational motion of the platform in terms of the Eulerian angles $\alpha(t)$, $\beta(t)$, $\gamma(t)$. These angles are so defined that the angular displacement between the two coordinate systems, $oxyz$ and $OXYZ$, may be created by imagining the platform as first oriented such that the two coordinate systems coincide. It is then rotated about OX through the angle α , then about the new position of OY through the angle β , and finally about the new position of OZ through the angle γ to bring the platform to the final position of angular displacement. For small values of α , β , γ , the two coordinate systems will now be related by:

$$\begin{Bmatrix} x \\ y \\ z \end{Bmatrix} = \begin{bmatrix} 1 & -\gamma & \beta \\ \gamma & 1 & -\alpha \\ -\beta & \alpha & 1 \end{bmatrix} \cdot \begin{Bmatrix} X \\ Y \\ Z \end{Bmatrix}. \quad (1)$$

The equations of motion may now be written. It is convenient to first write the equation for translatory motion in $oxyz$, thus it is assumed that all forces acting on the body have been expressed* in this system, giving

$$f_i = m\ddot{x}_i, \quad i = 1, 2, 3, \quad (2)$$

where the $x_i = x(t)$, $y(t)$, and $z(t)$, respectively.

The equations of angular motion may be most easily written in the body coordinates, $OXYZ$, since the moments and products of inertia of the structure are constant in this system. If the external moments are also expressed in $OXYZ$, the Euler equations for rotational motion in rotating coordinates are obtained:

$$M_i = \sum_{j=1}^3 I_{ij} \dot{\Omega}_j + O(\Omega_i \Omega_j), \quad i = 1, 2, 3. \quad (3)$$

Here,

Ω_j = components of the angular velocity vector in $OXYZ$,

I_{ij} = moment of inertia about i -axis if $i = j$,

I_{ij} = (-) product of inertia if $i \neq j$.

* Note that the transformation expressed by Eq. (1) can be applied to forces and velocities as well as to coordinates.

Now, M_i may be transformed by (1) into components, m_i , expressed in the space coordinate system. We note, further, that if the angular velocities, Ω_i , are small quantities, the moments, m_i , causing the motions must be small of the same order. The transformation of moments, therefore, after dropping products of small quantities, yields

$$m_i = M_i. \quad (4)$$

Similarly, the components of angular velocity, Ω_i , in OXYZ may be transformed into the space coordinate system. For small angular velocities, this results, approximately, in

$$\ddot{\alpha}_i = \dot{\Omega}_i. \quad (5)$$

Here, the α_i are the components in oxyz of a small rotation of the structure about an instantaneously fixed axis in space. In other words, for the small angular motions to which we limit the present analysis, the Euler angles are approximately equal to the components of the body rotation during a small time interval about the fixed space axes.

We may now write the translational and rotational equations of motion, in the fixed coordinate system, in the combined form

$$f_i = \sum_{j=1}^6 m_{ij} \ddot{x}_j \quad i = 1, 2, \dots, 6. \quad (6)$$

Here $f_i, x_i; i = 1, 2, 3$, are the forces and displacements in the x, y, z -directions, $f_i, x_i; i = 4, 5, 6$, are the moments and rotations about the x, y, z -axes,

$m_{11}, m_{22}, m_{33} = m = \text{mass of structure},$

$m_{44}, m_{55}, m_{66} = \text{moments of inertia about XYZ-axes},$

respectively.

$$\left. \begin{aligned} m_{45} = m_{54} &= - \iiint XY \, dm \\ m_{56} = m_{65} &= - \iiint YZ \, dm \\ m_{46} = m_{64} &= - \iiint XZ \, dm \end{aligned} \right\} \begin{array}{l} \text{Products of inertia about} \\ \text{the OXYZ-axes.} \end{array}$$

The force system acting on the structure comprises hydrodynamic forces resulting from wave and platform motion, hydrostatic forces from the changes in displaced volume associated with static displacements of the platform and the restraining forces exerted by the positioning or anchoring system.

III. COMPUTATION OF THE FORCES

The total hydrodynamic force exerted on the body is assumed to be composed of three parts:

- (1) The force resultant of the pressure exerted by the undisturbed incident wave train on the stationary body in its mean position.
- (2) The force resulting from the disturbance of the incident waves by the body occupying its mean position.
- (3) The force resulting from the motion of the body computed as though it undergoes the same motion in calm water.

In a formalized linear analysis, these terms would be associated with velocity potentials representing the incident wave train, a diffracted wave train, and the waves generated by the motion of the body. The force represented by (1) above, i.e., that part obtained by neglecting the effect of diffracted waves and body motions, is termed the Froude-Krylov force.

Procedures based on assumptions similar to these have, as previously noted, proven successful in predicting the motions of ships in waves. The present situation is somewhat simpler than the ship case because the structure has no forward speed.

As noted in the Introduction, we shall obtain the total force on the structure by computing the force separately on each member of which the structure is composed. Two principal assumptions will be made in computing these forces. First, each member is assumed to be either a cylinder whose cross sectional dimensions are small compared to the lengths of both the cylinder and the incident waves, or the member is a small pontoon (point volume) all of whose dimensions are small compared to the incident wave lengths. Second, all hydrodynamic interaction effects between adjacent members will be neglected, thus the force on an individual member will be computed as though the member occupies its mean position in the field with all other members absent.

In Fig. 1, we show a cylindrical member located in the flow field corresponding to a train of waves and undergoing motions corresponding to the rigid-body motions of the entire structure. The force per unit length at a given point along the length of the member

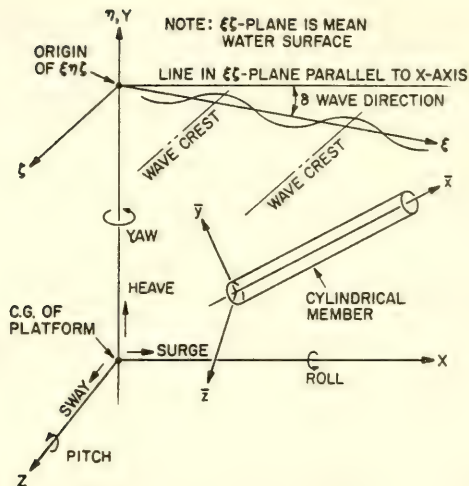


Fig. 1. Coordinate systems and nomenclature for member

is assumed to be expressed as

$$\vec{F} = - \iint p \vec{n} \, ds + C_D (\vec{u}_{nw} - \vec{u}_{nb}) + C_m (\vec{a}_{nw} - \vec{a}_{nb}). \quad (7)$$

The first term is the resultant force obtained by integrating over the surface of the body the pressure, p , which would exist at that location if the body were not present and is seen to be the Froude-Krylov force. Note that \vec{n} is the unit normal vector directed out of the body into the fluid.

The second term is called the drag force and is assumed proportional to the relative normal velocity between the member and the fluid. The third term is called the added mass force and is assumed proportional to the relative normal acceleration between the member and the fluid.

The first term and the first parts of the second and third terms are seen to be dependent on the wave motion while the remaining parts of the last two terms depend on the structure's rigid-body motions. In order to evaluate these forces for the cylinder, we must define two additional coordinate systems. The first, $O\bar{x}\bar{y}\bar{z}$, is associated with the member such that the \bar{x} -axis lies along the centerline of the member, the \bar{y} -axis is directed generally upwards, the \bar{z} is defined to form a right-handed system. The second coordinate system, $O\xi\eta\zeta$, is used to express the waves, and is so defined that the ξ -axis lies in the mean water surface and is positive

in the direction of propagation of the waves, η is directed upward, and ζ is defined so as to form a right-handed coordinate system.

Wave Forces

In order to be consistent with our assumption of small platform motions, an assumption of small incident waves must also be made. The velocity potential for regular infinitesimal gravity waves moving in the direction of the positive ξ -axis is

$$\varphi(\xi, \eta, \zeta, t) = \frac{ga}{\omega} \frac{\cosh k(\eta+d)}{\cosh kd} \sin(k\xi - \omega t). \quad (8)$$

The pressure is given by

$$p = -\rho g\eta - \rho \frac{\partial \varphi}{\partial t}, \quad (9)$$

and the linearized velocities and accelerations in the ξ - and η -directions by

$$\begin{aligned} u &= \frac{\partial \varphi}{\partial \xi} & v &= \frac{\partial \varphi}{\partial \eta} \\ \dot{u} &= \frac{\partial u}{\partial t} & \dot{v} &= \frac{\partial v}{\partial t}. \end{aligned} \quad (10)$$

We shall first compute the Froude-Krylov force which is given by the first term in (7). This integral, which is to be evaluated over the entire immersed surface of the body in order to obtain the total force, may be replaced by the following volume integral through the application of Gauss' theorem

$$-\iint p \vec{n} \, ds = -\iiint \left(\frac{\partial p}{\partial \xi}, \frac{\partial p}{\partial \eta}, \frac{\partial p}{\partial \zeta} \right) dv. \quad (11a)$$

The corresponding integral expressed for the moment referred to the $\xi\eta\zeta$ -axes is

$$\begin{aligned} \vec{m} &= -\iint p(\vec{r} \times \vec{n}) \, ds \\ &= \iiint \left(\zeta \frac{\partial p}{\partial \eta} - \eta \frac{\partial p}{\partial \zeta}, \xi \frac{\partial p}{\partial \zeta} - \zeta \frac{\partial p}{\partial \xi}, \eta \frac{\partial p}{\partial \xi} - \xi \frac{\partial p}{\partial \eta} \right) dv. \end{aligned} \quad (11b)$$

Note that in defining these integrals for a member which projects

through the free water surface, the pressure and its derivatives vanish for that part of the member's surface or volume above the free surface.

The evaluation of both of these integrals is a straightforward but rather tedious process, yielding the components of force in the $\xi\eta\zeta$ -directions, and the moments about these axes. We first perform the indicated differentiation of the two terms in the pressure equation with respect to ξ , η , and ζ , then substitute for ξ , η , and ζ , their values transformed to the \overline{oxyz} -coordinates. The element of volume is given in \overline{oxyz} by $A \, d\overline{x}$ where A is the constant cross sectional area of the cylinder. Since the cross sectional dimensions are assumed small compared to the wave length, the integrand may be assumed constant over A and, consequently, the volume integrals are reduced to one-dimensional integrals in \overline{x} to be evaluated over the length of the cylindrical member.

If the member is completely immersed, the evaluation of this integral yields two terms corresponding to the two terms in Eq. (9) for the pressure. The first term is the static buoyancy force or moment and the second is a time-dependent "variable buoyancy" corresponding to the variation in effective weight density of the fluid as a result of the wave motion.

If the member projects through the free surface, the region of integration must be dealt with in two parts. The first part is the constant volume of the member below the mean water surface, and the second is the time varying part of the volume of the member lying between this mean waterline and the instantaneous water surface. Evaluation of the integrals over the first part of the volume, i.e., that part below the mean waterline, yields a result identical with that for a completely submerged member. In evaluating the integral over the second part of the volume, we note that this volume is of the same small order of magnitude as the wave amplitude. Since the velocity potential, (8), and therefore the second term in the pressure, (9), is of this same small order of magnitude, only the first term in the pressure, i.e., the hydrostatic part, has a linear contribution to this part of the integral.

In evaluating these integrals, (11), for the pontoon or point volume, we note that the assumed small dimensions of the pontoon imply that the integrands are constant over its volume. Therefore, the integration reduces to taking the product of this volume with the appropriate derivatives of the pressure expression.

The first parts of the last two terms in (7), i.e., the drag and added mass forces associated with wave induced water motion, are each computed in a similar manner. Let u_i and \dot{u}_i represent the components of fluid velocity and acceleration in $\overline{o\xi\eta\zeta}$, with \overline{u}_i and $\dot{\overline{u}}_i$ the corresponding components in \overline{oxyz} . A coordinate

rotation may be expressed by α_{ij} such that

$$\begin{aligned}\bar{u}_i &= \alpha_{ij} u_j \\ \dot{\bar{u}}_i &= \alpha_{ij} \dot{u}_j\end{aligned}\quad (12)$$

The components of force on an element of length, $d\bar{x}$, in the $\bar{o}\bar{x}\bar{y}\bar{z}$ -directions are given by

$$d\bar{F}_i = (\bar{\mu}_{ij} \dot{\bar{u}}_j + \bar{\lambda}_{ij} \bar{u}_j) d\bar{x}, \quad j = 1, 2, 3 \quad (13)$$

where $\bar{\mu}_j$ and $\bar{\lambda}_j$ are added mass and linear drag coefficients. For the cylindrical member, only $\bar{\mu}_{22}$, $\bar{\mu}_{33}$, $\bar{\lambda}_{22}$, and $\bar{\lambda}_{33}$ are non-zero, while for the point volume all of the diagonal terms in $\bar{\mu}$ and $\bar{\lambda}$ are nonzero.

The forces may now be expressed in $o\xi\eta\zeta$ by the inverse of the above transformation

$$\begin{aligned}dF_i &= \alpha_{ji} d\bar{F}_j \\ &= (\mu_{ij} \dot{u}_j + \lambda_{ij} u_j) d\bar{x}.\end{aligned}\quad (14)$$

Here, the added mass and drag coefficients in $o\xi\eta\zeta$ are seen to be related to those in $\bar{o}\bar{x}\bar{y}\bar{z}$ by the following expressions.

$$\begin{aligned}\mu_{ij} &= \alpha_{ji} \bar{\mu}_{ij} \alpha_{ij} \\ \lambda_{ij} &= \alpha_{ji} \bar{\lambda}_{ij} \alpha_{ij}.\end{aligned}\quad (15)$$

Corresponding expressions for the elementary moments about $\bar{o}\bar{x}\bar{y}\bar{z}$ and $o\xi\eta\zeta$ may be written. The total forces and moment may be obtained by integrating these expressions over the length of the member, noting that u_i and \dot{u}_i contain terms with the same trigonometric functions of time which appear in the Froude-Krylov buoyancy integrals, (11), and may, in fact, be combined with them in carrying out the integration over the member length.

Evaluation of these integrals yields a set of forces and moments in $o\xi\eta\zeta$. A coordinate translation and rotation may now be applied to express these forces and moments in the space coordinate system $oxyz$.

Motion-Dependent Hydrodynamic Forces

We now consider a velocity vector, \vec{U} , whose components are the velocities of the center of gravity of the structure in $oxyz$ and are given by $\dot{x}_1, \dot{x}_2, \dot{x}_3$ in Eq. (6). We may similarly define an angular velocity vector, $\vec{\Omega}$, whose components are the three rotations about $oxyz$, and were denoted $\dot{x}_4, \dot{x}_5, \dot{x}_6$ in (6). The resultant velocity of a point $P(x, y, z)$ is given by

$$\vec{u}_p = \vec{U} + \vec{\Omega} \times \vec{r},$$

where \vec{r} is the radius vector drawn from the origin of $oxyz$ to the point P . Similarly, the resultant acceleration is given by

$$\vec{a}_p = \vec{u} + \vec{\Omega} \times \vec{r}.$$

(Note that this neglects the radial or "centripetal" acceleration which is of the order of the square of the (small) angular velocity.) Point P may be thought of as lying on the \bar{x} -axis of a member of the structure. We therefore may obtain the velocity and acceleration vectors u_{nb} and a_{nb} appearing in Eq. (7) by a transformation similar to (12). The α_{ij} , however, relate the member coordinates \bar{oxyz} to the space coordinates $oxyz$ in this case. Also note that the velocities and accelerations are now unknown quantities.

Applying these transformations, we obtain expressions similar to (12) where the u_j, \dot{u}_j are replaced by the components of u_p and a_p . The elementary forces are given by an expression which is the negative of (13) but containing the same μ 's and λ 's. These are then transformed back to the $oxyz$ -directions by the inverse of the above transformation. Integration of these elementary forces and their moments over the length of the member is somewhat simpler now since the velocities and accelerations vary in a somewhat simpler manner than in the case of the wave-induced velocities and accelerations.

The Added Mass and Drag Coefficients

The idealization made in arriving at the subdivision of forces illustrated in Eq. (7) is a computational expedient at best. In reality, the total force experienced by a member of the structure will be the resultant of distributed normal pressure forces and tangential shearing forces arising from viscosity. The subdivision into a Froude-Krylov force, a force proportional to relative fluid velocity, and a force proportional to relative fluid acceleration, is done partly on an intuitive basis and partly on the basis of our knowledge of simpler problems. Such a subdivision has the great advantage of leading to solutions in which there is a linear relationship between platform motion and the exciting wave motion. Let us review some of the

justification for this simplification.

Maruo [1954] and Havelock [1954] have discussed the forces on submerged bodies which are caused by waves of small amplitude in an ideal fluid. Maruo deals with the two-dimensional problem of a horizontal cylinder completely submerged below the surface of an inviscid fluid, and gives some results which can be compared directly with Eq. (7). In particular, he shows that, for the case of a deeply submerged cylinder, the "exact" total force is equal to twice the Froude-Krylov force, Eq. (7), and that this corresponds to a value of the added mass coefficient equal to that of the cylinder in an infinite fluid combined with the wave motion at the centerline of the cylinder. If the cylinder is near the free surface, the force differs from this deeply submerged value by an amount dependent upon the depth of submergence and the wave length. The error, however, is small if both the depth of submergence and the wave length are greater than several cylinder diameters. Similarly, C. M. Lee [1970] has analyzed the problem of an oscillating cylinder submerged beneath the free surface, and has shown that the added mass coefficient for forced motion approaches the infinite fluid value within a small error if the depth of submergence is more than two times the cylinder diameter and the length of generated waves is more than about five times the cylinder diameter. For our present purposes, these results imply that we may assume a constant value of the added mass coefficient in Eq. (7), since in the majority of practical situations the cylindrical members will be sufficiently deeply submerged and of sufficiently small diameter compared to wave lengths of interest to fulfill the above conditions. Thus the first and last terms in Eq. (7) can be expected to give a good approximation to the non-dissipative parts of the force on the individual member considered here.

The drag or velocity dependent force acting on an oscillating body under a train of waves is associated with two phenomena: (1) the dissipation of energy in surface waves which are generated as a result of motion of the body, and (2) the viscous effects which are felt both as tangential forces on the surface of the body, and as a deviation of the pressure distribution from its ideal fluid value. This latter effect, which is associated with the formation of a wake and vortices downstream of the body, will cause the added mass coefficient to differ from its ideal fluid value as well. The drag force associated with free surface wave effects decays to zero with increasing depth of submergence at the same rate that the added mass coefficient approaches the infinite fluid value. Therefore wave damping is of little significance to the configurations being considered here. The drag forces associated with viscosity are generally of much greater importance, and also less clearly defined. The usual method of approximating these forces, Wiegel [1964], is to assume that they behave in a manner similar to the drag on a body immersed in a flow of constant velocity. In such case, the drag force is expressed as a quadratic function of velocity and the drag coefficient is found to be a

function of Reynolds number. In applying this concept to the present situation in which we have a periodic fluid motion resulting from the superposition of wave and body motions, we might compute a Reynolds number using the mean absolute velocity, and choose the drag coefficient accordingly. The drag term in Eq. (7) should then be a quadratic function of velocity. This, however, destroys the linearity of our analysis, and in view of the crude approximation involved, it is not worth the added complication. In order to preserve linearity, an equivalent linear drag coefficient is therefore defined, as described in Blagoveshchensky [1962], such that the linear drag force dissipates the same energy per cycle of periodic motion as the nonlinear drag force which is being approximated.

The derivation of the equivalent linear drag coefficient is as follows. Assume a sinusoidal variation of the relative fluid velocity given by

$$v = v_0 \sin \omega t. \quad (16)$$

The linear drag force is given by

$$D_l = C_{Dl} v,$$

and the nonlinear drag by

$$D_n = C_{Dn} v^n.$$

The energy dissipated per quarter cycle of motion is given in the linear case by

$$C_{Dl} \int_0^{\pi/2\omega} v^2 dt,$$

and in the nonlinear case by

$$C_{Dn} \int_0^{\pi/2\omega} v^{n+1} dt.$$

Equating the two energies enables us to solve for the equivalent linear drag coefficient in terms of the assumed nonlinear coefficient. In the case of $n = 2$ (quadratic drag) the result is

$$C_{Dl} = \frac{8v_0}{3\pi} C_{D2}. \quad (17)$$

Thus, it is seen that the use of such equivalent linearization requires a prior knowledge of the amplitude of the motion. No difficulty is introduced by this in the case of the wave force on a stationary member. However, the amplitude is unknown for the absolute motion of the member. This leads to the necessity for an iterative solution in which we first assume an amplitude of motion, compute the equivalent linear coefficient, and then solve the equations of motion using this value. This solution then is used to compute a refined value of the linear drag coefficient, which is used for the second solution of the equations of motion, and so on. It is questionable whether the approximations involved warrant more than two iterations, as noted by Burke [1969].

Hydrostatic Forces

A floating body which is displaced in heave, pitch, or roll from its equilibrium position experiences hydrostatic forces proportional to these displacements as a result of the changes induced in the immersed volume. There will be no forces in surge, sway, or yaw since these displacements, which are parallel to the free surface, cause no change in the immersed volume.

These forces, including coupling terms, are computed by standard naval architectural formulas. Thus, the vertical force resulting from a small heave displacement, x_2 , is given by

$$F_y = - \rho g A_w x_2, \quad (18)$$

where A_w is the waterplane area.

Similarly, the moments of this force about the x - and z -axes (static coupling terms) are given by

$$M_x = \rho g A_w z_w x_2 \quad (19)$$

$$M_z = - \rho g A_w x_w x_2.$$

The roll and pitch moments resulting from small angular displacements are given by

$$M = - \rho g \nabla GM \alpha, \quad (20)$$

where GM is the appropriate metacentric height, ∇ is the volume displaced by the structure, and α is the small roll or pitch angle, either x_4 or x_6 in the notation of Eq. (6).

Finally, the force in the y -direction resulting from a small

roll displacement, x_4 , is

$$F_y = \rho g A_w z_w x_4, \quad (21)$$

and for a small pitch displacement, x_6

$$F_y = - \rho g A_w x_w x_6. \quad (22)$$

x_w, z_w are the coordinates of the center of gravity of A_w . These forces are included in the equations of motion as static restoring or coupling force terms.

The Restoring Forces

Three types of restraints have been described in the Introduction, dynamic positioning, spread array mooring, and vertical tension leg mooring.

A dynamic positioning system incorporates two principal components: sensors for detecting deviations from the desired position, and thrusters which may be activated automatically or manually to exert a force tending to restore the structure to the desired position. In the simplest system, the thrusters are actuated without time lag to exert a force proportional to the displacement. This would be termed a pure proportional controller. Real systems seldom operate this simply but incorporate time lags, back lash, and other non-ideal characteristics. Increased sensitivity and response may be built into the system by having it sense velocity (rate control) and acceleration. If the system can be approximated by linear features, i. e., if the applied thrust can be linearly related to displacements, velocity, and acceleration of the structure, then the control system constants may merely be introduced in the force terms of the equations of motion, (6), as additions to the already defined hydrodynamic and hydrostatic terms.

In a spread mooring system, several pretensioned anchor lines are arrayed around the structure to hold it in the desired location. If the structure moves from its mean position, the tensions in the anchor lines change and these changes may be related to the geometry (catenary), elasticity, and hydrodynamic properties of the anchor lines. It is usually permissible to neglect the hydrodynamic forces on the anchor lines and to approximate the force by a linear relationship between force and displacements in the plane of the anchor line. The displacements at the point of attachment of the anchor line may be determined in terms of the coordinates of this point for given displacements of the structure. These are resolved into horizontal and vertical displacements, x_l, y_l , in the plane of the anchor line by a transformation similar to (12). The horizontal and vertical forces exerted by the anchor line may then be expressed

as

$$F_{lx} = k_{xx}x_l + k_{xy}y_l \quad (23)$$

$$F_{ly} = k_{yx}x_l + k_{yy}y_l.$$

These forces may then be transformed back to the $oxyz$ coordinates for inclusion in the equations of motion. The anchor spring constants, $k_{xx} \dots k_{yy}$ are computed from a knowledge of the aforementioned elasticity and weight-shape characteristics of the anchor line.

In a tension leg mooring, the mooring lines are vertical and provide essentially total restraint against vertical movement of their upper ends. Figure 2 illustrates the horizontal force which results when the upper end of such a mooring line is displaced horizontally as a result of surge, sway, and yaw. The restoring force in the direction opposite the displacement, x_n , of the end of mooring line n is given by

$$F_n = \frac{T_n}{L_n} x_n. \quad (24)$$

The displacement, x_n , may be expressed in terms of its components in the x - and z -directions, in which case the corresponding components of F_n in these directions will be given by (24).

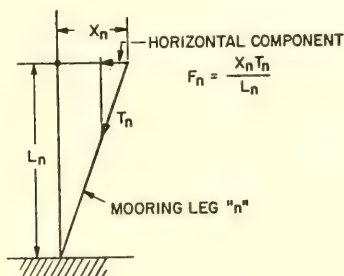


Fig. 2. Restoring force in tension mooring legs

IV. SOLUTION OF THE EQUATIONS OF MOTION

The total system of forces described in the preceding sections are now introduced into the equations of motion, Eq. (6). Our linearization of the problem has resulted in the subdivision of these forces into two categories: those forces resulting from the wave motion in the presence of the stationary structure, and those resulting from the motion of the structure in a stationary fluid. The former category contains the first term and the first parts of the second and third term on the RHS of Eq. (7). The platform motion dependent forces are contained in the second parts of terms two and three of the RHS of Eq. (7), plus the hydrostatic and restraint forces. The wave motion depending forces are seen, as a result of the velocity potential assumed to represent the wave motion, Eq. (8), to be sinusoidal functions of time. If we rearrange the equations of motion into the standard form, placing the motion-dependent terms on the left-hand side and the time dependent forcing terms on the right-hand side the result is a set of six simultaneous second-order differential equations of the form

$$\sum_{j=1}^6 [(m_{ij} + a_{ij}) \ddot{x}_j + b_{ij} \dot{x}_j + c_{ij} x_j] = F_{0i} \sin(\omega t + \epsilon_i), \quad (25)$$

where the exciting force amplitude, F_{0i} , is proportional to the wave amplitude, a . The solution of these equations may be expressed in the form

$$x_i = x_{0i} \sin(\omega t + \delta_i),$$

where x_{0i} is proportional to F_{0i} , therefore to the wave amplitude. The quantity x_{0i}/a , or the amplitude of response to unit waves varies with wave frequency, since the exciting force F_{0i} is a function of frequency and because the coefficients a, b, c the LHS of (25) may also vary with frequency. The square of this unit response is then the response amplitude operator, which may be combined with the wave spectral density function to obtain the platform response to a random seaway.

V. MODEL EXPERIMENTS

A number of model experiments have been conducted in the University of California Towing Tank in order to test several parts of the procedures described in the previous sections. The initial objective of the study was to evaluate the tension leg platform, and all experiments deal with this configuration. Initial experiments were made on single cylinder members to test some of the hydrodynamic force predictions and the linearity of the resultant motions in regular waves. Next, experiments were conducted in regular

waves using a platform model of triangular plan form to investigate the predictability and linearity of motions and mooring tensions of a composite structure consisting of a number of cylindrical members. Finally, experiments were made in random seas to test the applicability of linear superposition.

The arrangement of the model and experimental apparatus is shown in Fig. 3. The model configuration shown is typical of a number of those tested, consisting of three base cylinders arranged to form an equilateral triangle with three or more vertical legs supporting the deck. An important geometrical parameter studied in these tests was the relative proportion of buoyant volume contained in the vertical and horizontal legs.

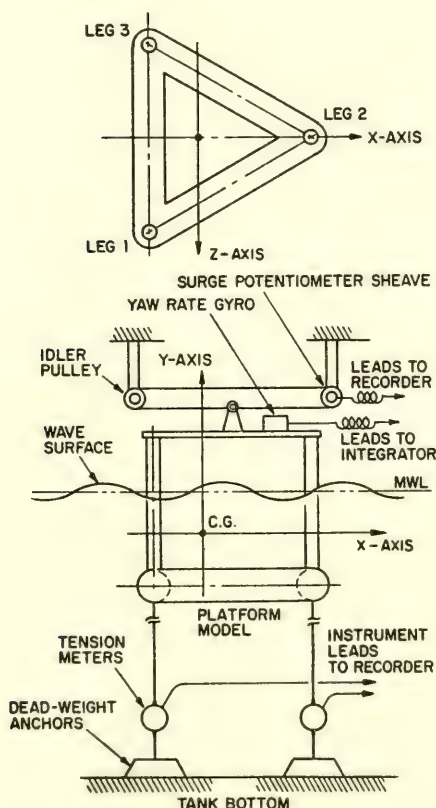


Fig. 3. Arrangement of experimental apparatus

From Fig. 3 it is seen that instrumentation was provided for measuring model motions, tension variations in the mooring legs, and incident wave amplitude. The surge motion was sensed and converted to an electrical signal by a miniature low torque potentiometer driven by the model through a string and pulley arrangement. Yaw was sensed by a rate gyroscope mounted on the model, the output of which was integrated electronically to give the yaw displacement. Tension meters were installed in each mooring leg. These consisted of small proving rings fabricated from seamless stainless steel tubing and mounted with etched foil strain gages. Four gages on each ring were connected to form a four-arm Wheatstone bridge, the output of which is proportional to the applied force. The bridge was balanced initially to bias out the initial static tension. Therefore only the time dependent variations are recorded.

The outputs of these force and motion transducers, as well as the output of a resistance wire wave meter, were recorded, using a multichannel oscillograph. During experiments in random waves, a simultaneous recording was made of the same quantities in digital form on magnetic tape for processing by electronic computer.

Single Cylinder Experiments

The first group of experiments were conducted using a single circular cylindrical model having hemispherical ends and moored by two legs, one at each end. Only the incident regular waves and tension variations were recorded. The model dimensions and test conditions were:

Length	3.44 ft
Diameter	0.282 ft
Depth of model	$0.792 \text{ ft} = 2.8 \times \text{dia.}$
Weight	6.5 lbs
Water depth	4.17 ft

For this configuration, the computed tension variations in the mooring legs will be equal to the hydrodynamic forces expressed in Eq. (7), i.e., there will be no linear coupling between the tension variations and the motions of the model. These results, for regular waves of 1.45 second period, and several different amplitudes striking the model at 0, 45, and 90 degrees, are shown in Fig. 4. Experimental points show the amplitudes of force variations which were measured in the two mooring legs. The theoretical lines have been determined by the method described here and by Havelock [1954]. Havelock's procedure gives the wave force and moment on a spheroid having its long axis horizontal, moving beneath a train of regular waves. For the present computation the approximating spheroid was assumed to have the same length and diameter as the cylinder model. The dashed curve labelled "present work" was computed by Eq. (7) assuming the infinite fluid value of unity for the added mass coefficient

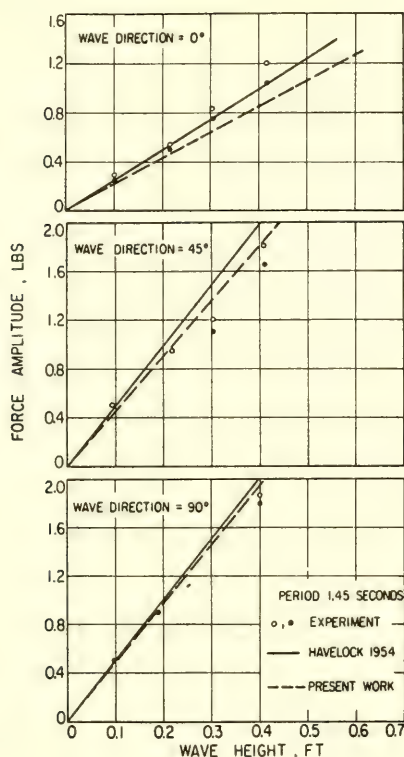


Fig. 4. Tension leg single cylinder

of the circular cylinder and a quadratic drag coefficient of unity.

Within the limits of experimental accuracy, the forces are seen to vary linearly with wave height for a range of heights tested. The two theoretical procedures are seen to give results of about equal degree of conformity with experiments.

Triangular Platform 1 in Regular Waves

Experiments similar to those with a single cylinder were next conducted with a complete platform model. This model was similar to the one shown schematically in Fig. 3 except that the main horizontal pontoons were of oval cross section and the above-water deck was supported by a space frame arrangement of very small vertical and inclined tubes. The dimensions of this model, referred to as Model 1, are given below:

Weight	40.13 lbs
Buoyancy	56.40 lbs
Length of side of equilateral triangle	3.92 ft
Main pontoon cross section, vertical and horizontal semi-axes	0.175 X 0.109 ft
Vertical member - radius	0.031 ft
Draft to centerline of main pontoon	0.77 ft
Water depth	4.18 ft

This model was subjected to a large number of tests in regular and irregular waves. Only a few of the regular wave tests are reported here.

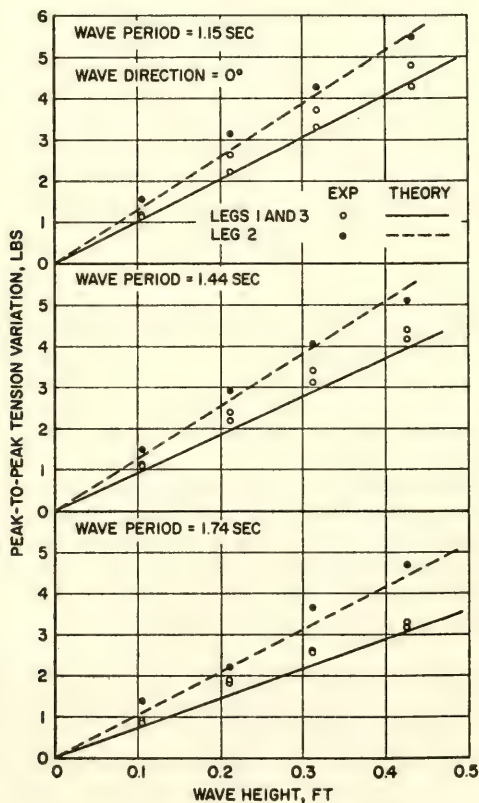


Fig. 5. Tension variations in legs -- Model 1

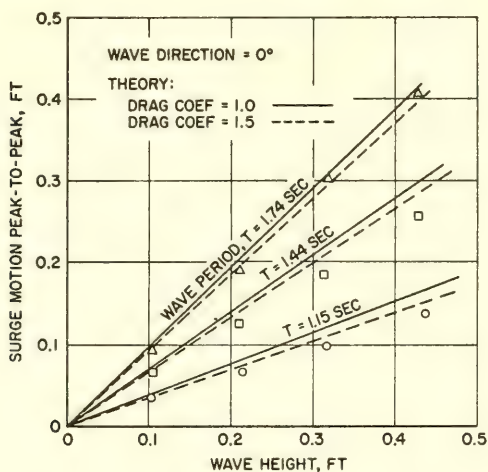


Fig. 6. Surge motion -- Model 1

Figure 5 contains a comparison of measured and computed tension variations in the mooring legs for three different wave periods and Fig. 6 contains the platform surge motion. Again, the agreement between computed and measured values is about as good as in the case of the single cylinder. Two features should be noted here. First, a mean curve drawn through the experimental tension variations appears to curve slightly concave downward with increasing wave height, thus indicating a measurable nonlinearity in this quantity. Second, better agreement between the computed and measured values is obtained for motions than for forces. Note that the motions are shown for two different values of the assumed quadratic drag coefficient. The effect of a substantial change in this quantity is seen to be slight.

Triangular Platform 2 in Random Waves

A second triangular platform was tested in both regular and irregular waves. This platform, designated Model 2; was similar in arrangement to the platform depicted in Fig. 3 and had the following characteristics:

Weight	28.49 lbs
Buoyancy	32.30 lbs
Length of side	3.12 ft
Main horizontal pontoon dia.	0.187 ft
Vertical cylinder dia.	0.381 ft

Draft to centerline, horizontal pontoon	0.78 ft
Water depth	4.70 ft

This model was tested in six different random sea conditions, representing two families of wave spectra. The first family of spectra, designated "A," have their peak ordinate at a wave period of about 0.9 second. The second family, or "B" spectra, have their peak at about 1.55 seconds. Both families for several different significant wave heights are shown in Fig. 7. These two spectra were used in order to adequately excite the model over the range of wave periods of interest.

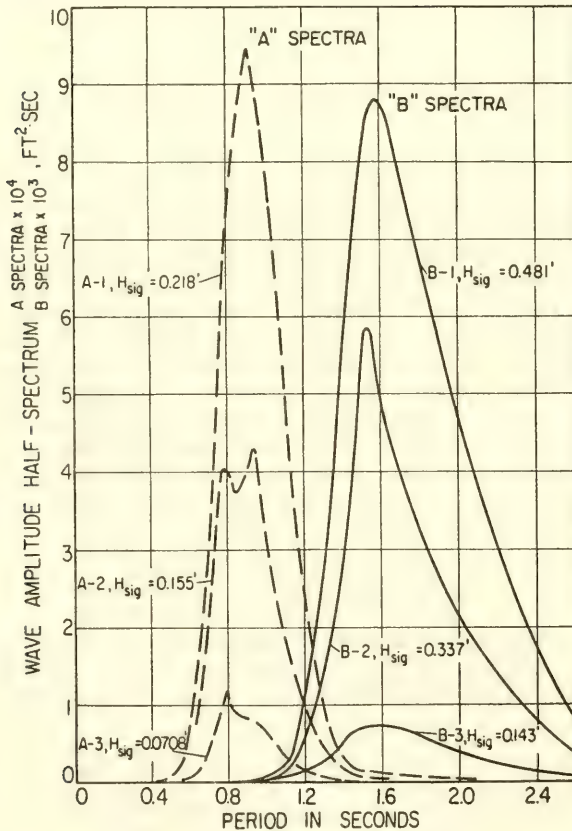


Fig. 7. Experimental tank wave spectra

The model response is shown in Figs. 8 - 10 for waves moving parallel to the X-axis. The first two of these figures show the mooring tension variations, and the last shows the surge motion versus wave period. In each case the ordinate is the double amplitude of the force or motion in question divided by wave double amplitude, thus the amplitude of the transfer function obtained from a time series analysis of the random wave tests. Points on the figures display these random wave results for three significant wave heights within the applicable range of periods for the "A" and "B" spectra. Also shown on these figures are results from experiments in regular waves, and theoretical predictions.

It is interesting to note that the random sea tension variation results display an apparent amplitude dependence in the range of longer periods. This is the range in which drag forces would be most strongly felt and no doubt points to a possible deficiency in the process of linearizing the drag force.

As before, the surge motion shows very good agreement between experiment and theory.

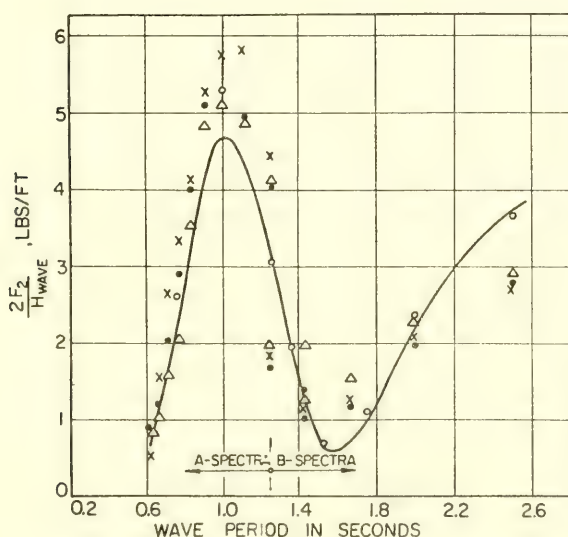


Fig. 8. Tension variations in anchor leg 2

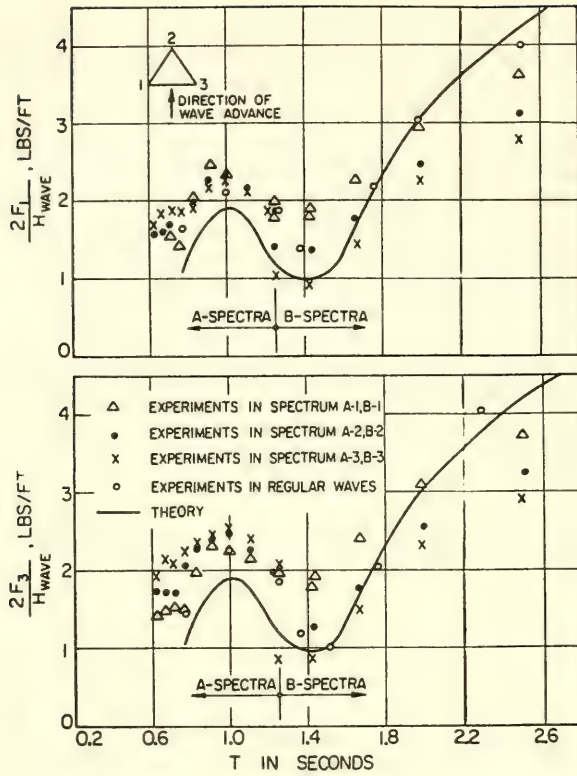


Fig. 9. Tension variations in anchor legs 1, 3

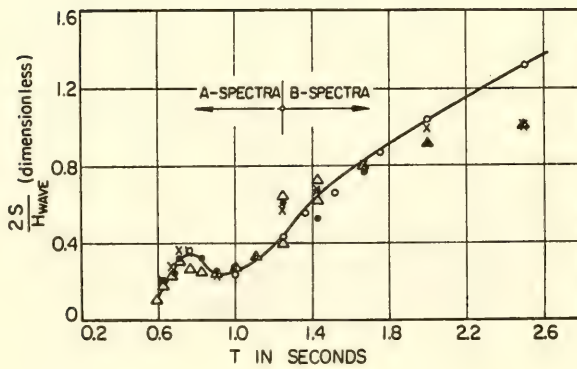


Fig. 10. Surge motion

VI. CONCLUSIONS

In the previous section, a comparison is shown of experimental measurements and theoretical predictions of platform motions and mooring leg tensions, using the procedure developed here. The theoretical results were obtained by the simplest form of the procedure in which constant infinite fluid values were assumed for added mass coefficients. Constant linear drag coefficients were used, and no attempt was made to account for the hydrodynamic interference between members of the structure. The first two groups of experimental results show that the observed performance of single members and assemblages does, indeed, follow a nearly linear pattern in regular waves, and this pattern is well predicted by the present procedure. The last group of experimental results show nearly equally good results in both regular and irregular waves. There is, however, some consistent nonlinear amplitude variation in longer waves, as may be seen in Fig. 9.

It is probable that the good agreement is obtained because the structures tested consisted of assemblages which satisfied the initial assumption reasonably well, i.e.,

- (1) All members were long, slender cylinders relatively sparsely distributed throughout the structure.
- (2) The bulk of the members were submerged sufficiently deeply below the free surface.
- (3) The cross sectional dimensions of all members were small compared to the waves used in the experiments.
- (4) The motions of the models were small compared to the model dimensions and to the wave lengths.

The aforementioned nonlinear behavior probably illustrates the failure of a single value of the linear drag coefficient to adequately represent this component of the hydrodynamic force over the entire range of frequencies.

ACKNOWLEDGMENTS

This work was conducted under the sponsorship of Deep Oil Technology, Inc. and the author expresses his appreciation for their permission to publish the foregoing results. The assistance of a number of individuals in conducting experiments and performing calculations is also acknowledged. Special thanks in this respect are due to Mr. O. J. Sibul, and graduate students Kwang June Bai and Nabil Daoud of the University of California, Department of Architecture, and Mr. Paul Gillon of Deep Oil Technology.

REFERENCES

- Blagoveshchensky, S. N., Theory of Ship Motions, Dover, 1962, p. 142.
- Burke, Ben G., "The Analysis of Motions of Semisubmersible Drilling Vessels in Waves," Paper No. OTC 1024, Offshore Technology Conference, Houston, 1969.
- Fisher, F. D. and Spiess, F. N., "FLIP -- Floating Instrumental Platform," J. Acoust. Soc. Am., v. 35, no. 10, 1963, pp. 1633-44.
- Gerritsma, J., "Ship Motions in Longitudinal Waves," Netherlands Research Center, TNO Report 35S, Feb. 1960.
- Havelock, T. H., "The Forces on a Submerged Body Moving Under Waves, Trans., RINA, 1954, pp. 1-7. Also "Collected Papers of ...," pub. by ONR, Dept. of the Navy, ONR/ACR-103.
- Lee, C. M., private communication, 1970.
- Macy, R. H., "Drilling Rigs," Ch. XVI of "Ship Design and Construction," A. M. D'Archangelo, Ed., SNAME, 1969.
- Maruo, H., "Force of Waves on an Obstacle," J. Soc. Naval Arch. Japan, v. 95, 1954, pp. 11-16.
- McClure, Alan C., "Development of the Project Mohole Drilling Platform," Trans. SNAME, v. 73, 1965, pp. 50-99.
- McClure, Alan C., "Delos: An Application of Oil Field Marine Technology to Space Programs," Marine Technology, v. 6, no. 2, 1969, pp. 156-170.
- McDermott, J. Ray, Inc., "Feasibility Study of a Floating Ocean Research and Development Station (FORDS)," Final Report to Dept. of the Navy, Bureau of Yards and Docks, under Contract NBy-37640, April 1966.
- Paulling, J. R. and Horton, Edward E., "Analysis of the Tension Leg Stable Platform," Paper No. OTC 1263, Offshore Technology Conference, Houston, 1970.
- Wiegel, R. L., Oceanographical Engineering, Prentice-Hall, 1964, p. 248ff.

SIMULATION OF THE ENVIRONMENT AND OF THE VEHICLE DYNAMICS ASSOCIATED WITH SUBMARINE RESCUE

H. G. Schreiber, Jr., J. Bentkowsky, and K. P. Kerr
Lockheed Missiles and Space Company
Sunnyvale, California

I. INTRODUCTION

The U.S. Navy's first Deep Submergence Rescue Vehicle (DSRV) was launched at San Diego, California on January 24, 1970. This vehicle was designed and built by Lockheed Missiles & Space Company (LMSC) under contract to the U.S. Navy's Deep Submergence System Program Office (DSSPO) to provide the capability to rescue the crew of a submarine immobilized on the ocean floor. The DSRV is 50 feet long, 8 feet in diameter, has a fiberglass external hull and an inner (pressure) hull made of three interconnected HY140 steel spheres. Propulsion and control of the vehicle are provided by a stern propeller in a movable shroud, horizontal and vertical ducted thrusters located in pairs fore and aft, and a mercury trim and list system. An Integrated Control And Display (ICAD) system developed at the Massachusetts Institute of Technology Instrumentation Laboratory enables the DSRV operators to correlate information from sonars, closed circuit television, and advanced navigation devices, in order to perform this intricate rescue mission. The mission scenario of the DSRV is as follows. Word and position of a distressed submarine is received and the DSRV and its support equipment are flown by three C141 aircraft to a nearby port. The DSRV is then loaded on to a mother submarine, by being attached to the after escape trunk, and transported to the area of the downed submarine. The DSRV then detaches itself from the mother submarine and descends to the disabled submarine, and mates to one of the escape trunks of the distressed vessel as shown in Fig. 1. The rescues are then transferred into the aft two spheres of the DSRV and returned to the mother submarine, 24 at a time. Because of the possibility that the distressed submarine may be at an unusual attitude, and there may be bottom currents, the DSRV must be able to perform this hovering and mating maneuver in a one knot current and at attitudes up to 45 degrees in pitch and roll.

RESCUEE TRANSFER

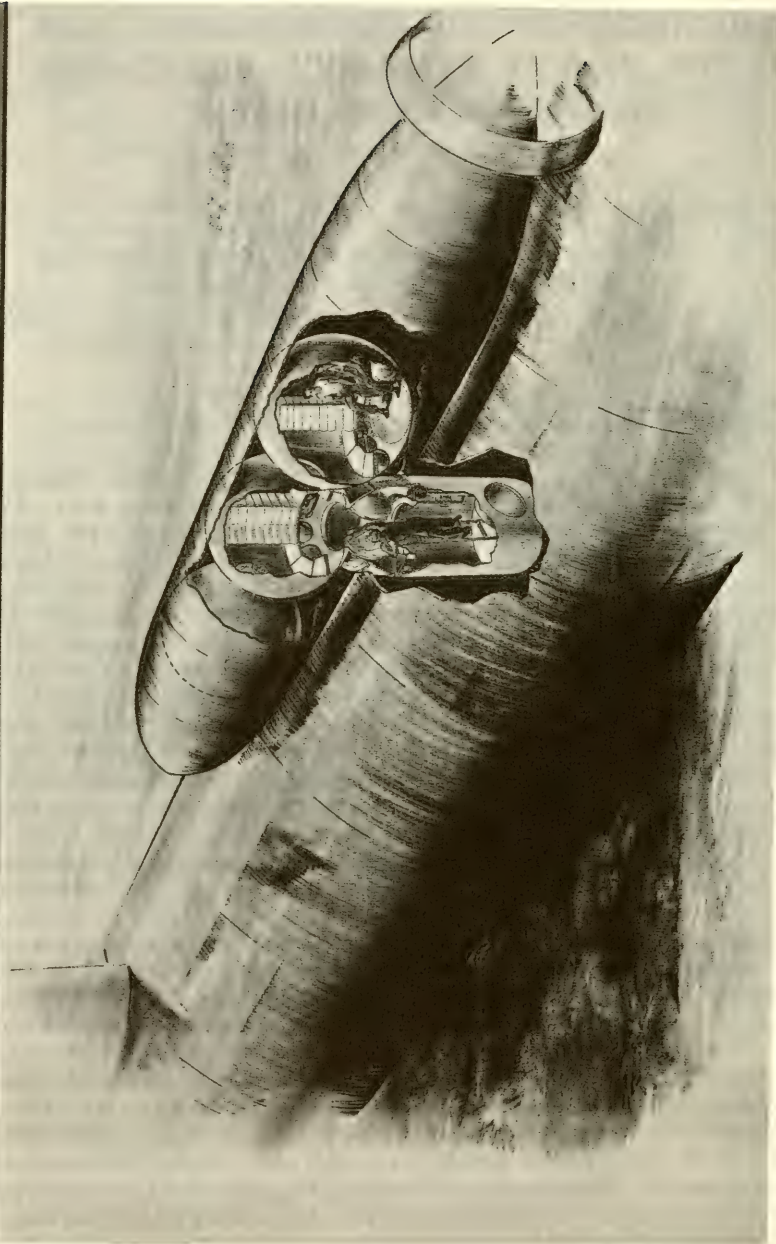


Fig. 1. Rescuee Transfer

This hovering and mating operation puts the DSRV in a new and growing class of submersibles which because of their missions, are required to hover, work, search, and otherwise maneuver at low speeds. This requirement for low speed, high angle of attack maneuverability is far outside the range of operation of the conventional fleet type submarine and consequently analysis designed to predict the dynamic behavior of conventional submarines is not completely applicable to the prediction of motions of the DSRV and other submersibles of the same class. The adequate prediction of the DSRV dynamics requires six degrees of freedom and a simulation capable of predicting the forces and moments at high angles of attack wherein the vehicle will experience lateral forces equal in magnitude to the axial forces. To be useful, the simulation must be precise enough for use in the design of the automatic control system. The operational environment is also quite different from that normally simulated in that the vehicle must hover and maneuver in currents at near zero forward speed and in the presence of the disabled submarine which causes considerable disturbances to the flow field. This paper, which is divided into three general parts, presents one approach to the simulation of the dynamics of a highly maneuverable submersible. The first part describes the simulation of the free-stream vehicle dynamics or the dynamics outside the influence of the distressed submarine. The second section deals with the interaction forces and moments caused by the presence of the distressed submarine and includes a discussion of a test program conducted to measure these forces and moments. The third section describes the application of the resulting equations of motion in conducting a man-in-the-loop simulation of the DSRV motions during the mating maneuver.

The equations of motion were developed at LMSC and programmed on a Remington Rand 1103A computer. They were used to determine the performance characteristics of the vehicle to be used in design studies and to provide equations of motion for use in the control system development. The interaction forces were measured in the 12-foot variable pressure wind tunnel at the Ames Research Center in Mountain View, California. Tests of this nature were necessary due to the lack of data on interaction forces and the possibility that these forces would provide a significant influence on the vehicle and control system design. The manned simulation was performed at the Marine Systems Division of the Sperry Rand Corporation to provide demonstration of the ability to manually control the DSRV within the limits necessary for mating and to determine operational limits for this mode of operation.

II. FREE STREAM DSRV DYNAMICS SIMULATION

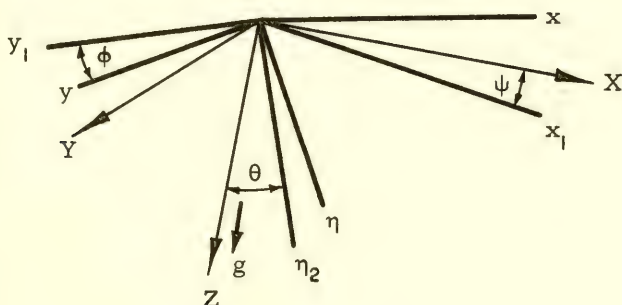
EQUATIONS OF MOTION

The development of a dynamic simulation of the Deep Submergence Rescue Vehicle (DSRV) follows a different approach than the methods used in most submarine studies. This deviation from the standard approach is necessary because of the basic differences in the mode of operation of the DSRV compared to that of conventional submarines. While the analysis of a submarine is generally confined to prediction of the vehicle dynamics at speed in an infinite fluid, the DSRV dynamics must also be simulated while hovering and docking in the presence of a downed submarine. The conventional method used to simulate the dynamics of a submarine is to calculate the position of the center of gravity of the vehicle using linear force and moment coefficients for the complete vehicle which are referenced to its center of gravity. The basic equations of motion for the DSRV differ in two ways from this conventional method, first in the choice of an axis system and secondly in the manner of handling the forces on the vehicles and appendages.

Axis System

Since the DSRV is required to assume angles of 45° to the horizontal in pitch and roll (very unrealistic for a conventional submarine) a mercury trim and list system is incorporated which moves the vehicle's center of gravity (c.g.) to accomplish these attitudes. The fact that the vehicle's c.g. moves with respect to the vehicle during maneuvers makes it a poor choice as a reference point for describing force and moment coefficients since they would have to be changed as a function of c.g. position. Using the c.g. as a reference axis system would also lead to complications in describing the vehicle's motion with respect to the distressed submarine since the motion of the axis system with respect to the vehicle would be included in the velocity of the axis system. Therefore, an axis system fixed to the body was used as a reference point. Since the axis system is not always at the center of gravity and terms to account for this shift must be included in the equations of motion there is no advantage in choosing the nominal vehicle c.g. as the center of the axis system. There are, however, advantages to having the x-axis lie along the vehicle centerline since the basic DSRV shape is a body of revolution. This axial symmetry provided by having one axis of the system lie along the vehicle centerline greatly reduces the number of cross coupling coefficients required to describe the forces and moments on the body. The positive direction of this axis is forward so that positive vehicle velocities are associated with vehicle forward motion. Similarly with the z-axis through the centerline of the transfer skirt (280.8 inches aft of the forward perpendicular) the number of cross coupling coefficients are reduced and the direct reference to the centerline of the transfer skirt simplifies the description of relationships between transfer skirt and the hatch during mating

maneuvers. The positive direction of this axis is downward commensurate with standard submarine dynamics analysis. The y-axis is through the x-axis z-axis intersection with positive direction to the starboard to provide a right handed orthogonal system. This x, y, z body axis frame is related to an inertial axis system, X, Y, Z , through the ordered rotations Ψ, θ , and Φ about the z, y and x axis. The origin of inertial axis system is located at the origin of the vehicle axis system at the start of a computation and the $X Y$ plane is parallel to the water surface with the vehicle axis in the $X Z$ plane.



The Euler angles are formed in the following manner. With the two systems initially coincident, a first rotation, $(Z\Psi)$, is performed giving the system (x_1, y_1, Z) . Next a rotation, $(y_1\theta)$, is performed about the y_1 axis resulting in the system (x, y_1, z_2) . A third rotation, $(x\phi)$, about the x axis brings the body axis system, (x, y, z) to the final position. The transformation matrix relating the (X, Y, Z) system to the (x, y, z) system through the above ordered rotations is then

$$\begin{bmatrix} x \\ y \\ z \end{bmatrix} = \begin{bmatrix} \cos\theta \cos\psi & \cos\theta \sin\psi & \sin\phi \\ \sin\theta \sin\phi \cos\psi - \cos\theta \cos\psi & \sin\theta \sin\phi \sin\psi + \cos\phi \cos\psi & \sin\phi \cos\theta \\ \sin\theta \cos\phi \cos\psi + \sin\psi \sin\phi & \sin\theta \cos\phi \sin\psi - \sin\phi \cos\psi & \cos\phi \cos\theta \end{bmatrix} \begin{bmatrix} X \\ Y \\ Z \end{bmatrix}$$

It remains to relate the Euler angle rates to the roll, pitch and yaw rates, (p, q, r) respectively. The relation is

$$\begin{bmatrix} \dot{\phi} \\ \dot{\theta} \\ \dot{\psi} \end{bmatrix} = \begin{bmatrix} p + \tan \theta (q \sin \phi + r \cos \phi) \\ q \cos \phi - r \sin \phi \\ (r \cos \phi + q \sin \phi) / \cos \theta \end{bmatrix}$$

High Angle of Attack Considerations

The second major difference between the DSRV simulation and the conventional method is required because of the high angles of attack experienced during the hovering and docking maneuvers. This high angle of attack problem becomes accentuated by the vehicle which, by using its thrusters, is capable of turning without forward way, a maneuver entirely outside the scope of those covered by conventional analysis. These shortcomings of the conventional analysis were overcome by a technique used during development of LMSC's DEEP QUEST research submersible where the hydrodynamic forces on the body and appendages (in this case the shroud ring) are considered separately. This allows for adequate representation of stall characteristics of the shroud ring as a function of the local angle of attack at the shroud ring which is essentially impossible to account for when a total coefficient for the body-ring combination is used in the simulation. The coefficients of the body itself are handled through addition of a normal drag components to the standard small angle of attack representation of forces. These high angle of attack considerations will be discussed further in the following sections.

The equations of linear motion are derived from the fundamental equation

$$\overline{\mathbf{F}}_{\text{external}} = \frac{d}{dt} (\overline{\mathbf{mV}}_G) \quad (1)$$

stating that the sum of the external forces acting on a rigid body of mass m , equals the time rate of change of the momentum of the body. The momentum, $\overline{\mathbf{mV}}_G$, is a vector quantity and $\overline{\mathbf{V}}_G$ is the inertial velocity of the center of mass. Expressing $\overline{\mathbf{V}}_G$ in terms of the velocities and rates about the vehicle fixed axis system described earlier

$$\overline{\mathbf{V}}_G = \begin{bmatrix} u + qZ_G - rY_G + \dot{X}_G \\ v + rX_G - pZ_G + \dot{Y}_G \\ w + pY_G - qX_G + \dot{Z}_G \end{bmatrix}$$

where X_G, Y_G, Z_G are the coordinates of the vehicle center in the body axis system. Neglecting the velocity and acceleration of the c.g. with respect to the body ($\dot{X}_G, \dot{Y}_G, \dot{Z}_G = 0$) because they are small and performing the operations

$$\overline{F}_{\text{external}} = \frac{d}{dt}(m\overline{V}_G) = m\dot{\overline{V}}_G + \omega \times m\overline{V}_G$$

we obtain

$$\overline{F}_{\text{external}} = m \begin{bmatrix} \dot{u} + qw - rv - X_G(q^2 + r^2) + X_G(pq - \dot{r}) + Z_G(pr + \dot{q}) \\ u + ru - pw - Y_G(r^2 + p^2) + Z_G(qr - \dot{p}) + X_G(qp + \dot{r}) \\ \dot{w} + pv - qu - Z_G(p^2 + q^2) + X_G(rp - \dot{q}) + Y_G(rq + \dot{p}) \end{bmatrix}$$

The equations of angular motion are derived from

$$\overline{M}_{\text{external}} = \frac{d}{dt}(\overline{I}\omega) \quad (2)$$

which states that the sum of the external moments acting on a body equals the time rate of change of the angular momentum of the body with both the moments and angular momentum expressed about the same point. Since the hydrodynamic moments are described about an off c.g. axis system the development of the right-hand side of the equations consists of expressing the time rate of change of the angular momentum of the body about the center of the axis system with the rotational vector expressed in the directions of the body axis. The results of this operation [1] yield:

$$\overline{M}_{\text{external}} = \begin{bmatrix} I_x \dot{p} + (I_z - I_y)qr + m \{ Y_G(\dot{w} + pv - qu) - Z_G(\dot{v} + ru - pw) \} \\ I_y \dot{q} + (I_x - I_z)rp + m \{ Z_G(\dot{u} + qw - rv) - X_G(\dot{w} + pv - qu) \} \\ I_z \dot{r} + (I_y - I_x)pq + m \{ X_G(\dot{v} + ru - pw) - Y_G(\dot{u} + qw - rv) \} \end{bmatrix}$$

The moments of inertia I_x, I_y and I_z are the moments of inertia about the center of the body axis system and not about the vehicle center of gravity. Since there is near symmetry in weight distribution about this body axis system, cross products of inertia have been dropped from the equations of motion.

The external forces and moments, $\overline{F}_{\text{external}}$ and $\overline{M}_{\text{external}}$, on the vehicle during free stream operations come from three

sources; the body, the shroud ring, and the thrusters.

$$F_{\text{external}} = F_{\text{body}} + F_{\text{shroud}} + F_{\text{thruster}} .$$

The following sections will discuss the simulation of these three classes of forces.

BODY FORCES

The forces on the body can be divided into several types: the static forces, $F_{\text{body, static}}$, associated with buoyancy and weight and the dynamic forces, $F_{\text{body, dynamic}}$, which depend on vehicle motions with respect to the water.

Static Forces

The weight or gravitational force (W) acts in the Z direction and the buoyancy, Δ , acts in the $-Z$ direction. The total vehicle weight, W , can be best expressed as the vehicle weight when in neutral trim $W_0 = \Delta$ plus the change in variable ballast from initial conditions. The resulting static forces on the body are:

$$\overline{F}_{\text{body, static}} = (W_0 + \sum W_{ti} - \Delta) \begin{bmatrix} -\sin \theta \\ \sin \phi \cos \theta \\ \cos \phi \cos \theta \end{bmatrix}$$

The DSRV contains the following ballast and trim systems which will affect the static forces on the vehicle:

- Main Ballast
- Variable Ballast
- Transfer Ballast
- Rescuee Ballast
- Mercury Trim
- Mercury List and BG Control

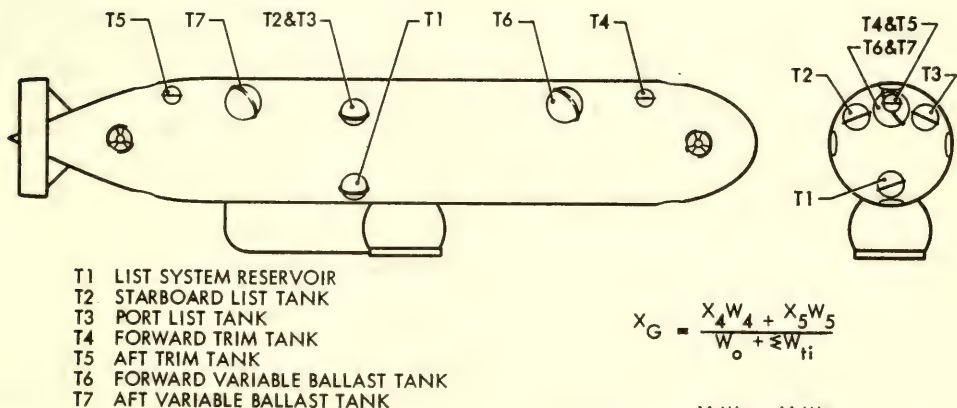
In operation, the main ballast tanks are full when submerged. The Transfer Ballast tanks are empty except when they are being used in the dewatering process, and rescuee ballast is exchanged for rescuees providing a constant value during submerged operations. These systems do not vary during normal submerged operations and therefore are not included in the simulation.

The tanks whose contents vary during submerged, unmated operation are the variable ballast (T_6 and T_7), trim (T_4 and T_5),

and list (T_1 , T_2 , and T_3) system tanks, Fig. 2.

The variable ballast tanks (6, 7) are hard tanks each with a capacity of 500 pounds of seawater. Water can be transferred to and from the sea from either or both tanks at a rate of 2 gallons per minute.

The mercury trim system is a set of two tanks (4,5) containing 225 pounds of mercury and 15 pounds of oil. A pumping rate of 3 gallons per minute provides a net weight change of 5.3 pounds per second between the two tanks. With the list system reservoir full (Z_G maximum) a 23 degree trim angle is attainable.



$$X_G = \frac{X_4 W_4 + X_5 W_5}{W_o + \sum W_{ti}}$$

$$Y_G = \frac{Y_2 W_2 + Y_3 W_3}{W_o + \sum W_{ti}}$$

$$Z_G = Z_{G0} + \frac{Z_n (W_n - W_{no})}{W_o + \sum W_{ti}}$$

Fig. 2. DSRV Trim and List System Tanks

The list system consists of three spherical tanks each with a capacity of 2780 pounds of mercury. The two list tanks (2, 3) are located 2.2 feet above the vehicle centerline and are separated by 4.4 feet. The reservoir (1) is located 3 feet below the centerline. The configuration of the list system piping and valving is shown in Fig. 3. It is noted that transfer can be effected between list tanks, between each list tank and reservoir and between the two list tanks tied together and the reservoir. Pumping rate can be varied between

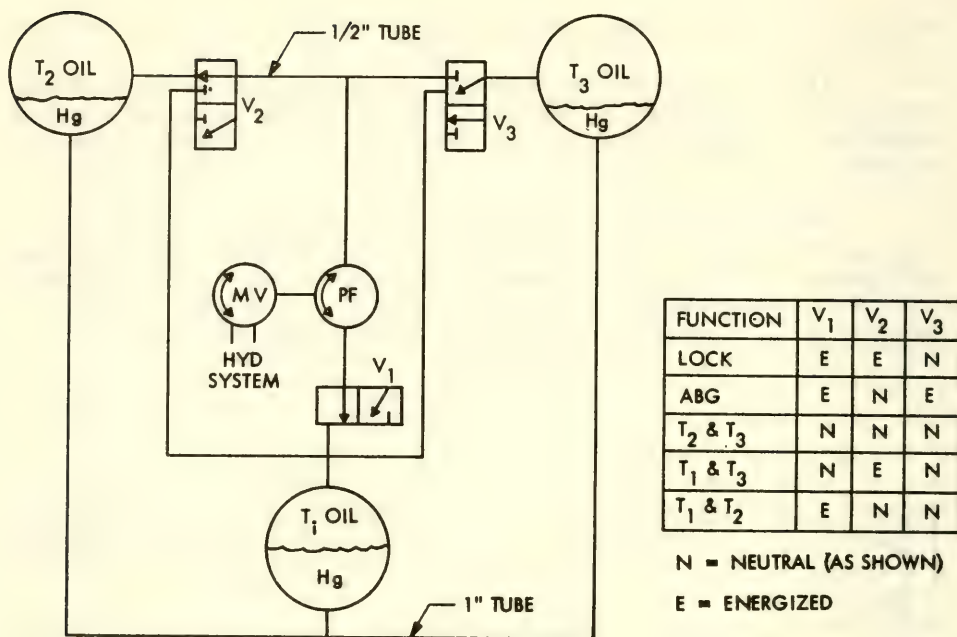


Fig. 3. List System Schematic

0 and 28 GPM (51.3 pounds per second net change). During roll damping operation the rate is controlled proportionally. In all other modes of operation, maximum rate is used.

Variation of BG is accomplished by transferring from the reservoir to the two list tanks. Roll damping is accomplished by transferring between list tanks for list angles less than 22.5 degrees, and between reservoir and the appropriate list tank for list angles greater than 22.5 degrees.

W_n = net weight in tank n - pounds

\dot{W}_n = rate of change of weight in tank n - pounds/second

\dot{W}_{nc} = commanded rate of change

W_{n0} = net weight in tank n for vertical buoyancy, neutral trim and maximum z_G - DSRV on surface

D = Depth, feet

Baseline operation is represented by 200 pounds plus a correction for depth in each of the variable ballast tanks, 93 pounds in each list tank, 2404 pounds in the list system reservoir, and equal

distribution of mercury between the two trim tanks. Note that all mercury system weights listed represent the difference in weight between mercury and an equal volume of oil.

Table 1 summarizes the location of all tanks and the value of W_{n_0} .

TABLE 1

Physical Parameters of Ballast and Trim Systems

Tank	x (ft)	y (ft)	z (ft)	W_0 (initial weight)	W_{max} (capacity)
1	-3.37	0	3.08	2404	2590
2	-3.37	2.21	-2.21	93.	2590
3	-3.37	-2.21	-2.21	93.	2590
4	18.9	0	-2.84	210	420
5	-18.4	0	-2.50	210	420
6	12.75	0	-2.46	200	500
7	-12.3	0	-2.28	200	500

$$W_0 = 140,369 \text{ pounds}$$

$$z_{G_0} = 0.1335 \text{ feet}$$

The effects of variations in the weight of water in the variable ballast tank on z_G have been included in the basic vehicle equations and the z_G variations computed in this section are due only to variations in the list and trim systems.

Changes in depth effect both the density of the water and the compressibility of the hull. The net effect on buoyancy, using temperatures and salinities corresponding to sub-tropical waters corresponds to a gradient of 0.1 pounds per foot of depth. Under normal conditions the required ballast change is divided equally between the two variable ballast tanks. Thus, for neutral conditions

$$W_6 = W_{60} + 0.05D$$

$$W_7 = W_{70} + 0.05D$$

All operations are written with $t = 0$ corresponding to neutral

buoyancy at the initial operating depth of the problem.

Thus

$$W_n = W_{n_0} + \int_0^t \dot{W}_n dt \quad n = 1, 2, 3, 4, 5$$

$$W_n = W_{n_0} + 0.05D + \int_0^t \dot{W}_n dt \quad n = 6, 7$$

The term $\sum W_{ti}$ which is used in the vehicle equations matrix is given by

$$W_{ti} = W_6 + W_7 - W_{60} - W_{70}.$$

Location of the center of gravity is given by

$$x_G = \frac{x_4 W_4 + x_5 W_5}{W_0 + \sum W_{ti}}$$

$$y_G = \frac{y_2 W_2 + y_3 W_3}{W_0 + \sum W_{ti}}$$

$$z_G = z_{G_0} + \frac{\sum z_n (W_n - W_{n_0})}{W_0 + \sum W_{ti}} ; \quad n = 1, 2, 3, 4, 5$$

Dynamic Forces

The hydrodynamic forces arise because of the motion of the body with respect to the water and are defined in terms of hydrodynamic force coefficients. The hydrodynamic force and moment coefficients used in this report are not the standard non-dimensional coefficients used in most studies. It has been found that a set of dimensional coefficients provides a much easier nomenclature. The force and moment coefficients are represented by subscripted capital letters of the form $X_{abc\dots}$. The letter denotes the direction of the force (X for forces along the x-body axis, Y along the y-body axis, and Z along the z-body axis) or the axis about which the moment results (L, M and N for moment coefficients describing the moments about the x, y, and z body axes respectively).

The subscripts vary in number and form and denote the variable quantities that the coefficient must be multiplied by to obtain a force or moment on the body. For example, $X_{u|u|}$ is the dimensional axial drag coefficient since when multiplied by $u|u|$ the square of the axial velocity, u , it results in an axial force

$X_{ulul}u|u| = F_{x \text{ drag}}$. Similarly, $M_{ulul}w|u|$ is the pitching moment used by the normal velocity, w . The use of absolute values in these coefficients provide for the proper signs on the force and moments, and because of most of the near fore-aft symmetry of the DSRV less the shroud, the coefficients are independent of the direction of various velocity components. The direction of the normal force $Z_{wlul}w|u|$ is dependent only on the direction of the normal velocity regardless of whether the vehicle is going forward ($u > 0$) or backward ($u < 0$). Since the sign of Z_{wlul} is negative the normal force due to normal velocity is always in the opposite direction of the normal velocity. A brief description of the development of the representation of hydrodynamic forces on the body follows. First consider the forces on the axisymmetric bare body of the DSRV and then add forces resulting from asymmetries, such as the transfer skirt and splitter plate. The representation of lift, acceleration and axial drag forces on an axisymmetric bare body is relatively well known and can be obtained from slender body theory, Ref. 2, other potential flow analysis, Ref. 3, or test data and is of the form

$$F_{\text{EXT lift, acceleration, axial drag}} = \begin{bmatrix} X_{\dot{u}}\dot{u} + X_{ulul}u|u| \\ Y_{\dot{v}}\dot{v} + Y_{\dot{r}}\dot{r} + Y_{rlul}r|u| + Y_{vlul}v|u| \\ Z_{\dot{w}}\dot{w} + Z_{\dot{q}}\dot{q} + Z_{qlul}q|u| + Z_{wlul}w|u| \end{bmatrix}$$

These lift, accelerating and axial drag forces are those normally used to simulate the dynamics of submarines and provide a very adequate representation of the forces and moments at low angles-of-attack ($\alpha < 15^\circ$). At high angles-of-attack, however, they become inadequate. For example $Z_{wlul}w|u|$, the only force resulting from normal velocity, w , goes to 0 as u goes to 0, while a vehicle normal to the flow experiences a significant normal force. This normal force is due primarily to flow separation and is, excluding Reynolds number effects proportional to the normal velocity squared w^2 . Wind tunnel and water tunnel tests on the Polaris, Poseidon, DEEP QUEST, and other vehicles have shown that a reasonably good representation of the forces and moments due to normal velocity can be obtained by using the two terms $Z_{wlul}w|u| + Z_{wlwl}w|w|$ where Z_{wlwl} is measured force at $u = 0$ ($\varphi = 90^\circ$) divided by the normal velocity squared and Z_{wlul} is the slope of the force versus angle of attack curve. Pitching (yawing) of the vessel will cause a variation in normal velocity along the vessel and therefore a variation in this normal drag over the body. It remains then to develop a method to account for the distribution of this local normal drag caused by pitching and yawing. The use of a strip theory method provides that the normal force due to normal drag can be expressed as $Z_{\text{normal drag}} = \int Z'_{wlwl}w'|w'|dx$ where Z'_{wlwl} is the local value of the normal force coefficient and w' is the local normal velocity and can be expressed as $w' = w + qX$ where X is the distance between

the point in question and the center of the axis (- forward). This integral can be evaluated at each step in the integration of a simulation when the distribution of $Z'_{w|w|}$ is known but it proves both cumbersome and time consuming. On the other hand, for a nearly cylindrical body such as a missile or the DSRV, test data has shown that a fair representation of both the force and moment are obtained when a constant value is used for $Z'_{w|w|}$ from the nose of the vehicle to the forward edge of the shroud, a distance L_s from the nose. This then allows the value $Z'_{w|w|}$ to be removed from the integral and sets the equality $Z'_{w|w|} = Z'_{w|w|}/L_s$. Replacing the local normal velocity w' by its equivalent $w + qX$, the integration $Z'_{w|w|} \int_{\text{body}} (w + qX) \cdot |(w - qX)| dX$ still poses some problems because of the absolute value signs. To accommodate these two integrals are formed depending whether the center of rotation, the point where $w' = 0$, is on or off of the body. Expressing the ratio of the distance the center of the axis system is off of the nose, L_1 , and the length L_s as $K_s = L_1/L_s$ the center of rotation is forward of the nose when $w/qL_s < K_s$ and aft of the body when $w/qL_s > K_s - 1$ and the value $w'|w'|$ can be replaced by $(|w|/w)(w')^2 = (|w|/w)(w^2 + 2wxq + x^2q^2)$ and the integration

$$Z'_{w|w|} \int_{-L_1}^{L_s-L_1} w'|w'| dx = Z'_{w|w|} \frac{|w|}{w} \int_{-L_1}^{L_s-L_1} (w^2 + 2wxq + x^2q^2) dx$$

results in three terms

$$C_{1w} w|w| + C_{2w} q|w| + C_{3w} \frac{|w|}{w} q^2$$

where

$$C_1 = L_s^2 Z'_{w|w|}$$

$$C_2 = L_s^3 (1 - 2K_s) Z'_{w|w|}$$

$$C_3 = L_s^4 / 4 (1 - 3K_s + 3K_s^2) Z'_{w|w|}$$

When the center of rotation is on the body $K_s \geq w/qL_s \geq K_s - 1$ the integral must be divided into two parts to account for the sign change in $w'|w'|$ at the center of rotation and

$$Z'_{w|w|} \int_{-L_1}^{L_s-L_1} w'|w'| dX = - Z'_{w|w|} \frac{|q|}{q} \left[\int_{-L_1}^{-w/q} w'^2 dX - \int_{-w/q}^{L_s-L_1} w'^2 dX \right]$$

where the $|q|/q$ is used to denote the direction of force since the local normal velocity forward of the center of rotation depends only

on q . This when expanded to

$$- Z_{wlwl} \frac{|q|}{q} \left[\int_{-L_1}^{-w/q} (w^2 + 2qxw + (qx)^2) dX - \int_{-w/q}^{L_s - L_1} (w^2 + 2qxw + (qx)^2) dX \right]$$

and integrated yields a four term expression for the normal drag with the center of rotation on the body

$$C_{4w}q/|q| w^3/q + C_{5w}q/|q| w^2 + C_{6w}w|q| + C_{7w}q|q|$$

where

$$C_{4w} = 2L_s/3 Z'_{wlwl}$$

$$C_{5w} = L_s^2 (1 - 2K_s) Z'_{wlwl}$$

$$C_{6w} = L_s^3 [(1 - K_s)^2 + K_s^2] Z'_{wlwl}$$

$$C_{7w} = L_s^4 /3 [(1 - K_s + K_s^2)(1 - 2K_s)] Z'_{wlwl}$$

In a similar manner the lateral drag terms for the sway or \dot{V} equation are developed and result in $C_{1v}v|v| + C_{2v}r|v| + C_{3v}v/|v| r^2$ for the center of rotation off of the body $v/-rL_s > K_s$ or $v/-rL_s < K_s - 1$ and $C_{4vr}/|r| v^3/r + C_{5vr}/|r| V^2 - C_{6v}v|r| + C_{7vr}|r|$ for the center of rotation on the body $K_s \geq v/-rL_s \geq K_s - 1$ with

$$C_{1v} = L_s^2 Y'_{vlvl}$$

$$C_{2v} = L_s^3 (2K_s - 1) Y'_{vlvl}$$

$$C_{3v} = L_s^4 /3 (1 - 3K_s + 3K_s^2) Y'_{vlvl}$$

$$C_{4v} = 2L_s/3 Y'_{vlvl}$$

$$C_{5v} = L_s^2 (2K_s - 1) Y'_{vlvl}$$

$$C_{6v} = L_s^3 [(1 - K_s)^2 + K_s^2] Y'_{vlvl}$$

$$C_{7v} = L_s^4 /3 (1 - K_s + K_s^2) (2K_s - 1) Y'_{vlvl}$$

This then completes the simulation of forces on the axisymmetric bare body of the DSRV. This representation has been developed

keeping in mind the fact that it will be programmed on a digital and/or analog computer and several simplifying assumptions were made to allow for mechanization of the resultant equations. As in any simulation a trade-off must be made between the accuracy of representation of forces and moments, the ability to mechanize certain types of expressions, and the availability of data.

The presences of the transfer skirt and splitter plate add additional coefficients to the body because of the asymmetries they provide. A complete set of these terms due to asymmetries were developed, their numerical values determined, and their relative importance established, with the reduction in the number of terms in the simulation as an end goal. It was determined that additional terms of the form $X_{qw}qw$, $X_{rv}rv$, $X_{rr}r^2$, $X_{qq}q^2$, $X_{rp}rp$, Y_{pp} , $Y_{pw}pw$, $Y_{qp}qp$, $Y_{v|w|}v|w|$, $Z_{pp}p^2$, $Z_{pr}pr$, $Z_{uu}u^2$, $Z_{rv}rv$, $Z_{rr}r^2$, and $Z_{u|u|}u|u|$ would be required for adequate simulation of the dynamics of the DSRV during the hovering maneuvers.

The addition of forces due to the shroud, \overline{F}_{shroud} , propeller, \overline{F}_{prop} , thrusters, \overline{F}_{thr} , and the interaction forces during mating, \overline{F}_{dist} , complete the force equations.

A similar line of development was used for determination of a set of moment equations. Values for most of the coefficients were obtained from model tests conducted at NSRDC (Ref. 4) and Hydro-nautics (Ref. 5), and theoretical values were computed for the remaining coefficients. A complete set of equations of motion used for the DSRV Model for Analysis (Ref. 6) follow along with numerical values of the hydrodynamic coefficients, Table 2.

Surge:

$$\begin{aligned} m[\dot{u} + qw - rv - x_G(q^2 + r^2) + y_G(pq - \dot{r}) + z_G(pr + \dot{q})] \\ = X_{\dot{u}}\dot{u} + X_{qw}qw + X_{rv}rv + X_{u|u|}u|u| + X_{rr}r^2 + X_{qq}q^2 + X_{rp}rp \\ - (W_0 + \sum W_{ti} - \Delta) \sin \theta + X_{shroud} + X_{prop} + X_{thr} + X_{dist} \end{aligned}$$

Sway:

$$\begin{aligned} m[\dot{v} + ru - pw - y_G(r^2 + p^2) + z_G(qr - \dot{p}) + x_G(qp + \dot{r})] \\ = Y_{\dot{v}}\dot{v} + Y_{\dot{r}}\dot{r} + Y_{\dot{p}}\dot{p} + Y_{r|u|}r|u| + Y_{pw}pw + Y_{qp}qp \\ + Y_{v|w|}v|w| + Y_{p|u|}p|u| + Y_{v|u|}v|u| + \end{aligned}$$

$$\begin{aligned}
 & + [C_{1v} v |v| + C_{2v} r |v| + C_{3v} \frac{|v|}{v} r^2]^{**} \\
 & + [C_{4v} \frac{r}{|r|} \frac{v^3}{r} + C_{5v} \frac{r}{|r|} v^2 + C_{6v} v |r| + C_{7v} r |r|]^{*} \\
 & + (W_0 + \sum W_{ti} - \Delta) \cos \theta \sin \phi + Y_{shroud} + Y_{prop} + Y_{thr} + Y_{dist}
 \end{aligned}$$

*Terms are cancelled when $\frac{v}{-rL_s} > K_s$ or $\frac{v}{-rL_s} < K_s - 1$

**Terms are cancelled when $K_s \geq \frac{v}{-rL_s} \geq K_s - 1$

$$C_{1v} = \frac{1}{2} \rho L_s^2 Y'_{v|v|}$$

$$C_{2v} = \frac{1}{2} \rho L_s^3 (2K_s - 1) Y'_{v|v|}$$

$$C_{3v} = \frac{1}{2} \rho L_s^4 / 3 (1 - 3K_s + 3K_s^2) Y'_{v|v|}$$

$$C_{4v} = \frac{1}{2} \rho \frac{2L_s}{3} Y'_{v|v|}$$

$$C_{5v} = \frac{1}{2} \rho L_s^2 (2K_s - 1) Y'_{v|v|}$$

$$C_{6v} = \frac{1}{2} \rho L_s [(1 - K_s)^2 + K_s^2] Y'_{v|v|}$$

$$C_{7v} = \frac{1}{2} \rho L_s^4 / 3 (1 - K_s + K_s^2) (2K_s - 1) Y'_{v|v|}$$

Heave:

$$\begin{aligned}
 & m[\dot{w} + pv - qu - z_G(p^2 + q^2) + x_G(rp - \dot{q}) + y_G(rq + \dot{p})] \\
 & = Z_{\dot{w}\dot{w}} + Z_{\dot{q}\dot{q}} + Z_{pp}p^2 + Z_{pv}pv + Z_{pr}pr + Z_{vv}v^2 + Z_{rv}rv + Z_{rr}r^2 \\
 & + Z_{u|u|}u|u| + Z_{w|u|}w|u| + Z_{q|u|}q|u| \\
 & + (W_0 + \sum W_{ti} - \Delta) \cos \theta \cos \phi +
 \end{aligned}$$

$$\begin{aligned}
& + [C_{1w} w |w| + C_{2w} q |w| + C_{3w} \frac{|w|}{w} q]^{**} \\
& + [C_{4w} \frac{q}{|q|} \frac{w^3}{q} + C_{5w} \frac{q}{|q|} w^2 + C_{6w} w |q| + C_{7w} q |q|]^* \\
& + Z_{\text{shroud}} + Z_{\text{prop}} + Z_{\text{thr}} + Z_{\text{dist}}
\end{aligned}$$

* Terms are cancelled when $w/qL_s > K_s$ or $w/qL_s < K_s - 1$

** Terms are cancelled when $K_s \geq w/qL_s \geq K_s - 1$

$$\begin{aligned}
C_{1w} &= \frac{1}{2} \rho L_s Z'_{w|w|} \\
C_{2w} &= \frac{1}{2} \rho L_s^3 (1 - 2K_s) Z'_{w|w|} \\
C_{3w} &= \frac{1}{2} \rho L_s^4 / 3 (1 - 3K_s + 3K_s^2) Z'_{w|w|} \\
C_{4w} &= \frac{1}{2} \rho 2L_s / 3 Z'_{w|w|} \\
C_{5w} &= \frac{1}{2} \rho L_s^2 (1 - 2K_s) Z'_{w|w|} \\
C_{6w} &= \frac{1}{2} \rho L_s^3 [(1 - K_s)^2 + K_s^2] Z'_{w|w|} \\
C_{7w} &= \frac{1}{2} \rho L_s^4 / 3 (1 - K_s + K_s^2) (1 - 2K_s) Z'_{w|w|}
\end{aligned}$$

Yaw:

$$\begin{aligned}
& I_z \dot{r} + (I_y - I_x) q p + m [x_G (\dot{v} + ru - pv) - y_G (\dot{u} + qw - rv)] \\
& = N_f \dot{r} + N_v \dot{v} + N_{pq} p q + N_{u|v|} |u| v + N_{r|u|} r |u| + N_{wp} w p \\
& + N_{vq} v q + N_{p|u|} |u| + N_{|w|v} |w| v \\
& + (W_0 x_G + \sum W_{t_i} x_{t_i}) \cos \theta \sin \phi + W_0 y_G \sin \theta \\
& + Y_{\text{shroud}} x_{\text{shrd}} + N_{\text{thr}} + N_{\text{prop}} + N_{\text{dist}} \\
& + [C_{1r} r |r| + C_{2r} \frac{r}{|r|} v^2 + C_{3r} \frac{r}{|r|} \frac{v^4}{r^2} + C_{4r} |r| v]^*
\end{aligned}$$

$$C_{5r}|v|r + C_{6r}v|v| + C_{7r}\frac{|v|}{v}r^2]**$$

*Terms are cancelled when $-\frac{v}{rL_s} > K_s$ or $-\frac{v}{rL_s} < K_s - 1$

**Terms are cancelled when $K_s \geq -\frac{v}{rL_s} \geq K_s - 1$

$$C_{1r} = \frac{1}{2} \rho L_s^5 / 4 [K_s^4 + (1 - K_s)^4] Y'_{v|v|}$$

$$C_{2r} = \frac{1}{2} \rho L_s^3 / 2 [K_s^2 + (1 - K_s)^2] Y'_{v|v|}$$

$$C_{3r} = -\frac{1}{2} \rho L_s / 6 Y'_{v|v|}$$

$$C_{4r} = \frac{1}{2} \rho 2L_s^4 / 3 [K_s^3 - (1 - K_s)^3] Y'_{v|v|}$$

$$C_{5r} = \frac{1}{2} \rho 2L_s^4 / 3 [K_s^3 + (1 - K_s)^3] Y'_{v|v|}$$

$$C_{6r} = \frac{1}{2} \rho L_s^3 / 2 [K_s^2 - (1 - K_s)^2] Y'_{v|v|}$$

$$C_{7r} = \frac{1}{2} \rho L_s^5 / 4 [K_s^4 - (1 - K_s)^4] Y'_{v|v|}$$

Roll:

$$I_x \dot{p} + (I_z - I_y)qr + m[y_G(\dot{w} + pv - qu) - z_G(\dot{v} + ru - pw)]$$

$$= K_p \dot{p} + K_v \dot{v} + K_{qr}qr + K_{v|w|}v|w| + K_{rw}rw + K_{vq}vq + K_{pw}pw$$

$$+ K_{v|u|}v|u| + K_{v|v|}v|v| + K_{p|u|}p|u| + K_{r|u|}r|u| + K_{p|p|}p|p|$$

$$+ W_0 y_G \cos \theta \cos \phi - (W_0 z_G + \sum W_{ti} z_{ti}) \cos \theta \sin \phi$$

$$+ K_{prop} + K_{dist}$$

Pitch:

$$\begin{aligned}
& I_y \dot{q} + (I_x - I_z) p r + m [z_G (\dot{u} + q w - r v) - x_G (\dot{w} + p v - q u)] \\
& = M_{\dot{q}} \dot{q} + M_{\dot{w}} \dot{w} + M_{pr} p r + M_{ulwl} |u| w + M_{qlul} q |u| + M_{vp} v p \\
& + M_{ulul} u |u| + M_{vv} v^2 + M_{rv} r v + M_{rr} r^2 - (W_0 z_G + \sum W_{ti} z_{ti}) \sin \theta \\
& - (W_0 G_G + \sum W_{ti} x_{ti}) \cos \theta \cos \phi - Z_{shroud} x_{shroud} + M_{prop} + M_{thr} \\
& + M_{dist} + [C_{1q} q |q| + C_{2q} \frac{q}{|q|} w^2 + C_{3q} \frac{q}{|q|} \frac{w^4}{q} + C_{4q} |q| w]^* \\
& + [C_{5q} |w| q + C_{6q} w |w| + C_{7q} \frac{|w|}{w} q^2]^{**}
\end{aligned}$$

* Terms are cancelled when $w/qL_s > K_s$ or $w/qL_s < K_s - 1$

** Terms are cancelled when $K_s \geq w/qL_s \geq K_s - 1$

$$\begin{aligned}
C_{1q} &= \frac{1}{2} \rho L_s^5 / 4 [K_s^4 + (1 - K_s)^4] Z'_{wlwl} \\
C_{2q} &= \frac{1}{2} \rho L_s^3 / 2 [K_s^2 + (1 - K_s)^2] Z'_{wlwl} \\
C_{3q} &= -\frac{1}{2} \rho L_s / 6 Z'_{wlwl} \\
C_{4q} &= \frac{1}{2} \rho 2/3 L_s^4 [-K_s^3 + (1 - K_s)^3] Z'_{wlwl} \\
C_{5q} &= \frac{1}{2} \rho 2/3 L_s^4 [K_s^3 + (1 - K_s)^3] Z'_{wlwl} \\
C_{6q} &= \frac{1}{2} \rho L_s^3 / 2 [-K_s^2 + (1 - K_s)^2] Z'_{wlwl} \\
C_{7q} &= \frac{1}{2} \rho L_s^5 / 4 [-K_s^4 + (1 - K_s)^4] Z'_{wlwl}
\end{aligned}$$

TABLE 2

DSRV (ML-493-03) Parameters and Coefficients

w (1)	4363 slugs	I _x	3.78×10^4 slug-ft ²
z _G	0.1335 feet	I _y	4.52×10^5 slug-ft ²
L	49.33 feet	I _z	4.50×10^5 slug-ft ²
L ₁	23.4 feet		
L _s	46.95 feet		

FORWARD MODE

Coefficient	Non-Dimensional	Factor	Dimensional
X ¹ _{ulul}	-6.87×10^{-3}	$\rho/2L^2 =$	-1.67×10^1
Y ¹ _{vlul}	-5.1×10^{-2}	2.433×10^3	-1.24×10^2
*Y ¹ _{vlwl}	-4.6×10^{-2}		-1.12×10^2
Z ¹ _{ulul}	1.0×10^{-3}		2.43
**Z ¹ _{vlvl}	-8.0×10^{-2}		-1.95×10^2
Z ¹ _{wlul}	-2.3×10^{-2}		-5.59×10^1
Y ¹ _{vlvl}	-1.42×10^{-1}	$\rho/2L^2 =$	-3.36×10^2
Z ¹ _{wlwl}	-9.41×10^{-2}	2.198×10^3	-2.07×10^2

NOTE * Indicates coefficient value is zero when w is negative.
 ** Indicates coefficient value is zero when $|\frac{v}{u}| > 0.173$.

(1) Under following conditions:
 200# in each variable ballast tank,
 93# in each mercury list tank,
 remainder in reservoir.

TABLE 2 (Cont'd.)

Coefficient	Non-Dimensional	Factor	Dimensional
$X_{\dot{u}}^i$	-1.2×10^{-3}	$\rho/2L^3 =$	-1.44×10^2
X_{rv}^i	3.1×10^{-2}	1.20×10^5	3.72×10^3
X_{qw}	-3.0×10^{-2}		-3.60×10^3
$Y_{\dot{v}}^i$	-3.6×10^{-2}		-4.32×10^3
Y_{rlul}^i	8.7×10^{-3}		1.04×10^3
Y_{plul}^i	2.2×10^{-3}		2.64×10^2
Y_{pw}^i	3.0×10^{-2}		3.60×10^3
$Z_{\dot{w}}^i$	-3.0×10^{-2}		-3.60×10^3
Z_{qlul}^i	-3.7×10^{-3}		-4.44×10^2
Z_{pv}^i	-3.1×10^{-2}		-3.72×10^3
* $K_{v wl}^i$	5.32×10^{-3}	$\rho/2L^3 =$	6.32×10^2
M_{ulul}^i	-5.5×10^{-4}	1.20×10^5	-6.6×10^1
M_{wlul}^i	2.3×10^{-2}		2.76×10^3
** $M_{v vl}^i$	-2.8×10^{-2}		-3.36×10^3
N_{vlul}^i	-3.0×10^{-2}		-3.6×10^3
* $N_{v wl}^i$	4.98×10^{-3}		5.98×10^2
X_{rr}^i	-1.4×10^{-4}	$\rho/2L^4 =$	-8.3×10^2
X_{qq}^i	-1.3×10^{-4}	5.92×10^6	-7.7×10^2
X_{pr}^i	-1.34×10^{-4}		-7.93×10^2
$Y_{\dot{r}}^i$	1.4×10^{-4}		8.3×10^2
$Y_{\dot{p}}^i$	1.34×10^{-4}		7.93×10^2
Y_{pq}^i	1.3×10^{-4}		7.7×10^2
$Z_{\dot{q}}^i$	-1.3×10^{-4}		-7.7×10^2

TABLE 2 (Cont'd.)

Coefficient	Non-Dimensional	Factor	Dimensional
Z'_{rr}	0	5.92×10^6	0
Z'_{pr}	1.4×10^{-4}		8.3×10^2
Z'_{pp}	1.34×10^{-4}		7.93×10^2
K'_{rw}	-1.0×10^{-4}		-5.92×10^2
K'_{vq}	1.0×10^{-5}		5.92×10^1
Z'_{rv}	0		0
K'_{vlul}	2.2×10^{-3}		2.64×10^2
$K'_{v vl}$	1.18×10^{-3}		1.42×10^2
K'_{plul}	-3.16×10^{-4}	$\rho/2L^4 =$	-1.87×10^3
K'_y	1.55×10^{-4}	5.92×10^6	9.17×10^2
K'_{rlul}	-2.34×10^{-4}		-1.39×10^3
M'_{qlul}	-4.5×10^{-3}		-2.66×10^4
M'_{rv}	1.34×10^{-4}		7.93×10^2
M'_w	-1.3×10^{-4}		-7.7×10^2
M'_{pv}	-1.4×10^{-4}		-8.3×10^2
N'_y	1.4×10^{-4}		8.3×10^2
N'_{plul}	-1.58×10^{-4}		-9.35×10^2
N'_{rlul}	-5.4×10^{-3}		-3.2×10^4
N'_{vq}	-1.34×10^{-4}		-7.93×10^2
N'_{pw}	-1.3×10^{-5}		-7.7×10^2
K'_{pw}	-1.34×10^{-4}		-7.93×10^2
K'_p	-1.55×10^{-5}	$\rho/2L^3 =$	-4.53×10^3
K'_{qr}	0	2.92×10^8	0

TABLE 2 (Cont'd.)

Coefficient	Non-Dimensional	Factor	Dimensional
$K_{p p }^I$	-1.13×10^{-4}	2.92×10^8	-3.3×10^4
M_q^I	-1.4×10^{-3}		-4.1×10^5
M_{pr}^I	1.39×10^{-3}		4.06×10^5
M_{rr}^I	0		0
N_r^I	-1.4×10^{-3}		-4.1×10^5
N_{pq}^I	-1.39×10^{-3}		-4.06×10^5
REVERSE MODE			
X_{ulul}^I	-8.05×10^{-3}	$\rho/2L^2 =$	-1.96×10^1
Y_{vlul}^I	-9.9×10^{-2}	2.433×10^3	-2.41×10^2
Z_{ulul}^I	-1.0×10^{-3}	$\rho/2L^3 =$	-2.43
Z_{wlul}^I	-6.5×10^{-2}		-1.58×10^2
Y_{rlul}^I	7.7×10^{-2}		9.24×10^3
Y_{plul}^I	5.35×10^{-3}		6.42×10^2
Z_{qlul}^I	-8.7×10^{-2}		-1.04×10^4
K_{vlul}^I	5.35×10^{-3}		6.42×10^2
M_{ulul}^I	-5.5×10^{-4}	$\rho/2L^4 =$	-6.6×10^1
M_{wlul}^I	-2.5×10^{-2}		-3.0×10^3
N_{vlul}^I	2.4×10^{-2}		2.88×10^3
K_{plul}^I	-6.2×10^{-4}		-3.67×10^3
K_{rlul}^I	-7.25×10^{-4}		-4.29×10^3
M_{qlul}^I	-5.4×10^{-3}		-3.2×10^4
N_{plul}^I	-7.25×10^{-4}	5.92×10^6	-4.29×10^3
N_{rlul}^I	-8.4×10^{-3}		-4.97×10^4
NOTE: All other coefficient values are identical with those listed for the forward mode.			

SHROUD RING FORCES

The control shroud is a circular movable wing located at the aft end of the vehicle, supported by four struts space 90° apart, Fig. 4. The force and moments on the shroud ring are obtained from curves of lift and drag on the shroud as a function of total angle of attack of the shroud, Figs. 4 and 5. Resolving the resultant force, \bar{F} , into the directions of the vehicle's axis system provides the components used in the equations of motion, X_{shroud} , Y_{shroud} , and Z_{shroud} . The relative velocity of the shroud with respect to the water in the directions of body axis system is

$$\bar{V}_{SB} = \begin{bmatrix} u_s \\ v_s \\ w_s \end{bmatrix} = \begin{bmatrix} u \\ v - X_s r \\ w + X_s q \end{bmatrix}$$

The ordered deflection of the shroud, δp , a deflection in the vehicle pitch plane followed by δy a deflection about the pitched shroud yaw axis results in the relationship

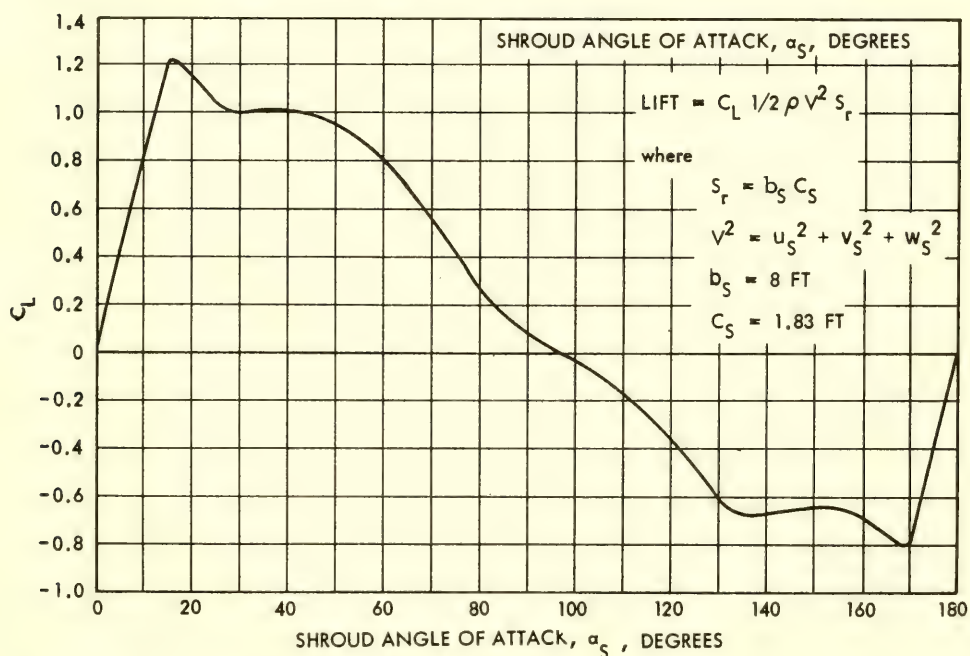


Fig. 4. Shroud Lift Coefficient, C_L , vs. Shroud Angle-of-Attack, α_S

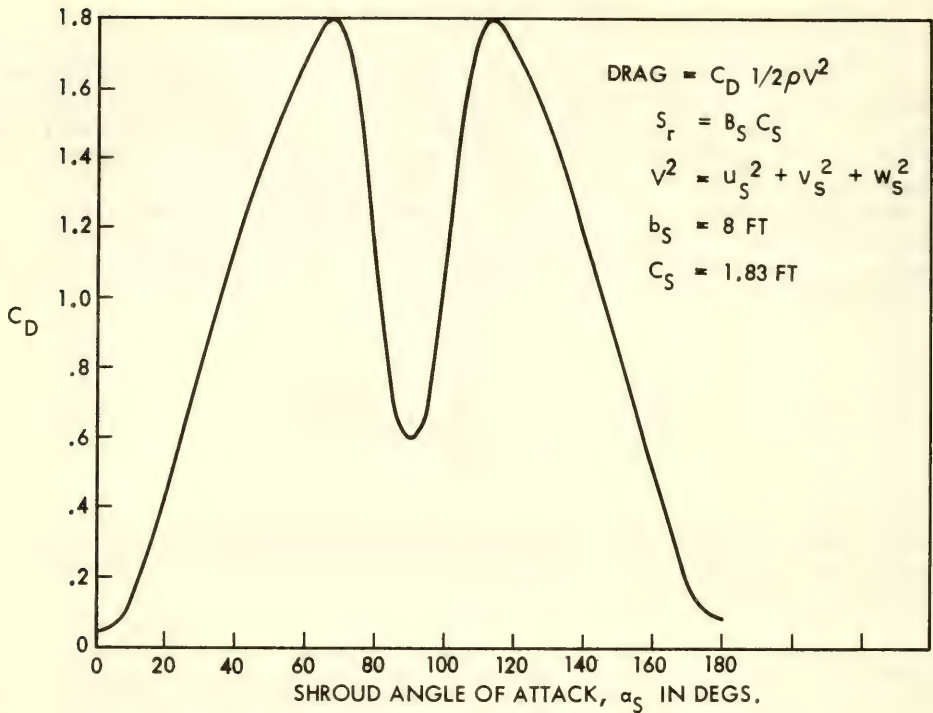
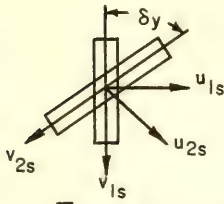


Fig. 5. Shroud Drag Coefficient vs. Shroud Angle of Attack

$$\bar{V}_{ss} = \begin{bmatrix} u_{2s} \\ v_{2s} \\ w_{2s} \end{bmatrix} = T_{s22s} \begin{bmatrix} u_s \\ v_s \\ w_s \end{bmatrix} = T_{s22s} \bar{V}_{SB}$$

between the velocity of the shroud relative to the water expressed in the direction of the body axis system \bar{V}_{SB} and the same velocity expressed in the direction of the deflected shroud axis system \bar{V}_{ss} .

$$\begin{bmatrix} u_{ls} \\ v_{ls} \\ w_{ls} \end{bmatrix} = \begin{bmatrix} \cos \delta_p & 0 & -\sin \delta_p \\ 0 & 1 & 0 \\ \sin \delta_p & 0 & \cos \delta_p \end{bmatrix} \begin{bmatrix} u_s \\ v_s \\ w_s \end{bmatrix}$$



$$\bar{V}_{ss} = \begin{bmatrix} u_{2s} \\ v_{2s} \\ w_{2s} \end{bmatrix}$$

$$= \begin{bmatrix} \cos \delta_y & \sin \delta_y & 0 \\ -\sin \delta_y & \cos \delta_y & 0 \\ 0 & 0 & 1 \end{bmatrix} \begin{bmatrix} \cos \delta_p & 0 & -\sin \delta_p \\ 0 & 1 & 0 \\ \sin \delta_p & 0 & \cos \delta_p \end{bmatrix} \begin{bmatrix} u_s \\ v_s \\ w_s \end{bmatrix}$$

$$= T_{s22s} \begin{bmatrix} u_s \\ v_s \\ w_s \end{bmatrix} = \begin{bmatrix} \cos \delta_y \cos \delta_p & \sin \delta_y & -\cos \delta_y \sin \delta_p \\ -\sin \delta_y \cos \delta_p & \cos \delta_y & \sin \delta_y \sin \delta_p \\ \sin \delta_p & 0 & \cos \delta_p \end{bmatrix} \begin{bmatrix} u_s \\ v_s \\ w_s \end{bmatrix} = T_{s22s} \bar{V}_{SB}$$

The total angle of attack at the shroud can then be expressed as

$$\alpha_{shroud} = \tan^{-1} \left[\frac{(v_{2s} + w_{2s})^{1/2}}{u_{2s}} \right] = \tan^{-1} \left[v_{ns}/u_{2s} \right]$$

or performing the indicated operation

$$\alpha_{shroud} = \left\{ \frac{[(-\sin \delta_y \cos \delta_p u_s + \cos \delta_y v_s + \sin \delta_y \sin \delta_p w_s)^2 + (\sin \delta_p u_s + \cos \delta_p w_s)^2]^{1/2}}{(\cos \delta_y \cos \delta_p u_s + \sin \delta_y v_s - \cos \delta_y \sin \delta_p w_s)} \right\}$$

are then looked up on Figs. 4 and 5 and values of lift, L_s , and drag, D_s , on the shroud are calculated from

$$L_s = \rho / 2 S_r C_L V^2 \quad \text{and} \quad D_s = \rho / 2 S_r C_D V^2$$

with

$$S_r = b_s C_s$$

$$V = u_s^2 + v_s^2 + w_s^2$$

$$b_s = 8 \text{ feet}$$

$$C_s = 1.83 \text{ feet}$$

The lift and drag on the shroud are then resolved into forces on the shroud \bar{F}_{SB} and transformed into the body axis system, \bar{F}_{shroud} .

$$N_F = C_L \cos \alpha_s + C_D \sin \alpha_s$$

$$\overline{F}_{SB} = \begin{bmatrix} C_L \sin \alpha_s - C_D \cos \alpha_s \\ -v_{2s}/v_{ns} N_F \\ -w_{2s}/v_{ns} N_F \end{bmatrix}$$

and

$$\overline{F}_{shroud} = T_{s22s} \overline{F}_{SB}$$

The moments on the shroud are the product of the shroud force and the distance of the shroud center from the center of the axis system as shown in the moment equations.

THRUSTER FORCES

The propulsion system of the DSRV consists of a single conventional screw propeller for axial thrust and four ducted screw propellers arranged in forward and aft pairs for lateral and normal thrust. This system provides the vehicle with five degrees of maneuvering freedom (heave, sway, surge, pitch and yaw) and provides forces and moments sufficient to meet hovering requirements in currents of the order of one knot. The control of the sixth degree of freedom, roll, is provided by the trim and list system. A complete treatment of the development of the maneuvering system is contained in Ref. 7. The following treatment will present the data used in the simulation with a little explanation of its development.

Main Propeller

The main propeller is a 6-foot diameter, wake adapted, three-bladed propeller with a blade area ratio of 0.24 and a maximum speed of 1.64 revolutions per second.

For estimates of the vehicle maneuvering performance the propeller thrust and torque characteristics are required for ahead and astern motion of the vehicle and for positive as well as negative propeller rpm. "Behind-the-ship" tests of the DSRV propeller were performed for all four operating modes at the Naval Ship Research and Development Center (Ref. 8).

The curves of the thrust and torque coefficients, Fig. 6, are typical for ahead and astern operation of a propeller and can be expressed in the form

$$K = a + bJ + cJ^2$$

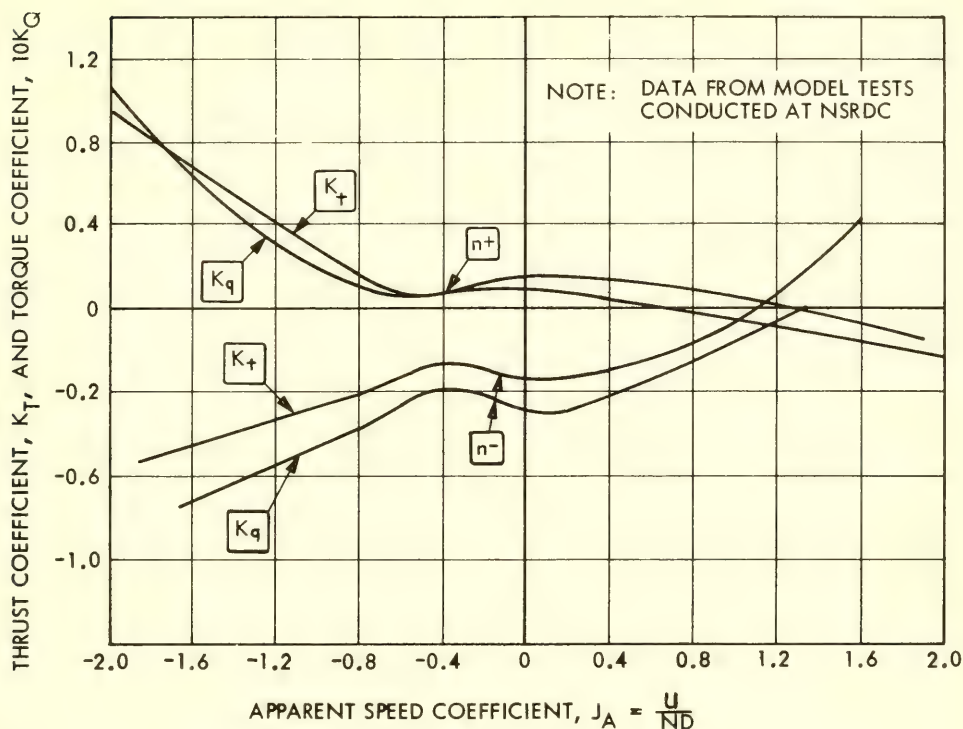


Fig. 6. Characteristics Curves for DSRV Propeller
(Note: Data from model tests conducted at
NSRDC (Ref. 8))

The coefficients a , b , c have been evaluated separately for each quadrant of the propeller curves, and the resulting thrust and torque coefficients are used as an expression of the steady and transient characteristics of the propeller forces and moments. During maneuvering the propeller may also experience velocities normal to its axis. The resulting effect on the propeller thrust in the axial direction and torque about the roll axis have been estimated and the form of the coefficients can be rewritten including this effect as follows:

$$K = a + bJ_u + cJ_u^2 + d(J_v^2 + J_w^2)^{1/2}$$

where

$$J_u = \frac{u}{nd}$$

$$J_v = \frac{v - \ell r}{nd}$$

$$J_w = \frac{w + \ell q}{nd}$$

$u, v, w = x, y, z$ components of vehicle velocity

r, q = components of vehicle angular velocity relative to yaw and pitch axis

ℓ = distance of propeller from coordinate system origin

The coefficients of the y and z components of the propeller force and the corresponding moment coefficients can be similarly estimated and are proportional to J_v and J_w respectively. For the computations of the vehicle responses, all six force and moment components have been considered. The resulting propeller force and moment equations are:

$$X_{\text{prop}} = 755 n |n| - 58 un - 3.8 u^2 + 26 n (v_p^2 + w_p^2)^{1/2} \quad ; \quad u \geq 0; \quad \frac{n}{u} \geq -0.21$$

$$= -365 n^2 - 172 un - 45 u^2 + 26 n (v_p^2 + w_p^2)^{1/2} \quad ; \quad u \geq 0, \quad \frac{n}{u} \leq -0.21$$

$$= 755 n^2 + 60 un + 22 n^2 + 26 n (v_p^2 + w_p^2)^{1/2} \quad ; \quad u < 0, \quad n \geq 0$$

$$= -365 n^2 - 13 un + 22 n^2 + 26 n (v_p^2 + w_p^2)^{1/2} \quad ; \quad u < 0, \quad n < 0$$

$$Y_{\text{prop}} = -30 n v_p \quad ; \quad n \geq 0$$

$$= -12 n v_p \quad ; \quad n < 0$$

$$Z_{\text{prop}} = -30 w_p \quad ; \quad n \geq 0$$

$$= -12 n w_p \quad ; \quad n < 0$$

$$P_{\text{prop}} = 530 n |n| - 6.5 un - 4.05 u^2 + 22 n (v_p^2 + w_p^2)^{1/2} + 131 \dot{n} \quad ;$$

$$u \geq 0, \quad \frac{n}{u} \geq -0.21$$

$$= -468 n^2 - 155 un - 38 u^2 + 22 (v_p^2 + w_p^2)^{1/2} + 131 \dot{n} \quad ;$$

$$u \geq 0, \quad \frac{n}{u} \leq -0.21$$

$$= 530 \dot{n}^2 + 80 \dot{u} \dot{n} + 35.2 \dot{u}^2 + 22(\dot{v}_p^2 + \dot{w}_p^2)^{1/2} + 131 \dot{n} \quad ;$$

$$u < 0, \dot{n} \geq 0$$

$$= -468 \dot{n}^2 - 8 \dot{u} \dot{n} + 15.2 \dot{u}^2 + 22(\dot{v}_p^2 + \dot{w}_p^2)^{1/2} + 131 \dot{n} \quad ;$$

$$u < 0, \dot{n} < 0$$

$$M_{prop} = -765 \dot{n} \dot{w}_p \quad ; \quad \dot{n} \geq 0$$

$$= -306 \dot{n} \dot{w}_p \quad ; \quad \dot{n} < 0$$

$$N_{prop} = 765 \dot{n} \dot{v}_p \quad ; \quad \dot{n} \geq 0$$

$$= 306 \dot{n} \dot{v}_p \quad ; \quad \dot{n} < 0$$

where

$$\dot{v}_p = \dot{v} - 25.5 \dot{r}$$

$$\dot{w}_p = \dot{w} + 25.5 \dot{q}$$

Ducted Thrusters

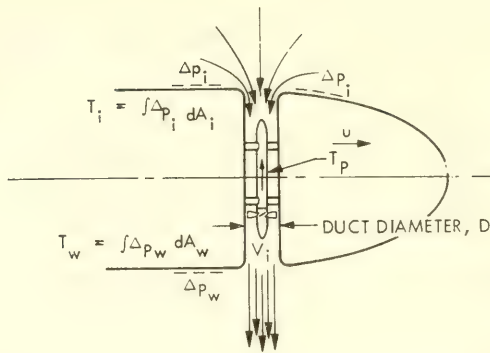
There are two pairs of ducted thrusters used for maneuvering in the pitch and yaw planes, as shown in Fig. 2. The four-bladed propellers are 18 inches in diameter and have a maximum speed of 9.8 revolutions per second and produce side force through a combination of impeller thrust and a change in the pressure distribution on the hull (Fig. 7 and Ref. 7). The thrust due to variation in pressure distribution is very dependent on forward speed and the total thrust coefficient for the steady state $\dot{n} = 0$ condition was measured at NSRDC as a function of forward speed (Ref. 9). Force coefficients derived from this test are shown in Figs. 5 and 6 as a function of $u/|n|$ where n is the propeller RPS. The steady state force is obtained from the relationships

$$X_{thr\ mf} = \dot{n}_{mf}^2 T_3^*$$

$$X_{thr\ ma} = \dot{n}_{ma}^2 T_4^*$$

$$Y_{thr\ yf} = \dot{n}_{yf} |n_{yf}| T^*$$

$$Y_{thr\ ya} = \dot{n}_{ya} |n_{ya}| T_2^*$$



$$T_b = T_i + T_w$$

Fig. 7. Ducted Thruster Schematic

$$Z_{thr\ zf} = n_{zf} |n_{zf}| T_1^*$$

$$Z_{thr\ za} = n_{za} |n_{za}| T_2^*$$

$$M_{thr\ zf} = 1.06 n_{zf} |n_{zf}| M_1^*$$

$$M_{thr\ za} = 1.13 n_{za} |n_{za}| M_2^*$$

$$M_{thr\ yn} = -0.686 n_{yn} |n_{yn}|$$

$$N_{thr\ yf} = 0.98 n_{yf} |n_{yf}| M_1^*$$

$$N_{thr\ ya} = 1.04 n_{ya} |n_{ya}| M_2^*$$

$$N_{thr\ zn} = -0.686 n_{zn} |n_{zn}|$$

where

$$X_{thr\ mn} = \text{X force due to thruster } mn$$

$$Y_{thr\ mn} = \text{Y force due to thruster } mn$$

$Z_{thr\ mn}$ = Z force due to thruster mn

$M_{thr\ mn}$ = Pitch moment due to thruster mn

$N_{thr\ mn}$ = Yaw moment due to thruster mn

M = Direction in which force acts

n = f for forward-thruster, a for aft-thruster

with the force $(T_1^*, T_2^*, T_3^*, T_4^*)$ and moment coefficients $(M_1^*, M_2^*, M_3^*, M_4^*)$ shown in Figs. 8 and 9.

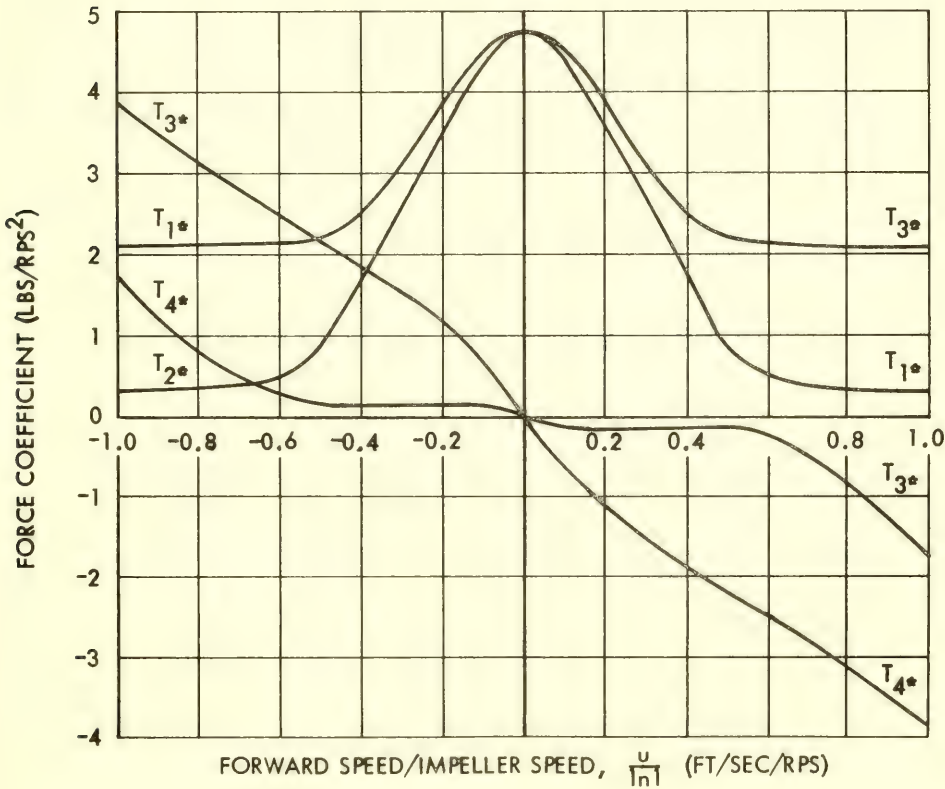


Fig. 8. Effect of Forward Speed on Duct Forces

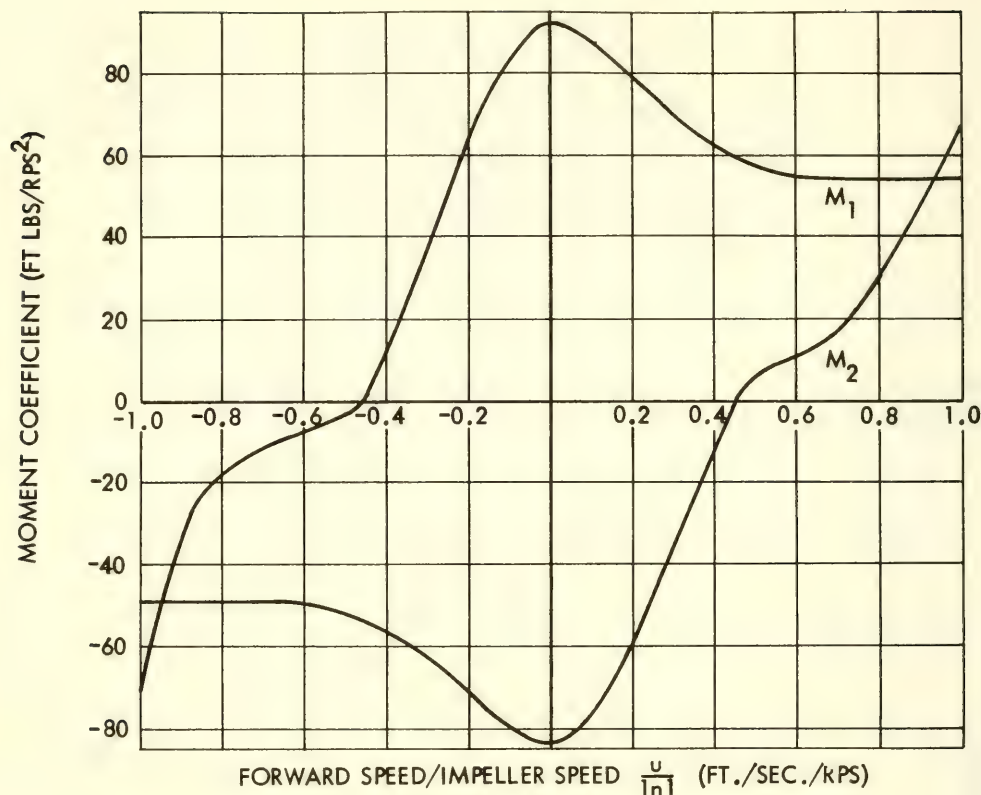


Fig. 9. Effect of Forward Speed on Duct Movements

When the propeller in the duct is accelerating, the thrust component due to the propeller is a function of the ratio of jet velocity, V_j , to propeller speed, n . The thrust coefficient for a propeller of this type was estimated from data taken from Ref. 10 and fit with a second order curve resulting in

$$T_{p_{mn}} = 10.63 n_{mn} |n_{mn}| - 5.04 V_{jmn} |V_{jmn}| ; \quad \frac{V_{jmn}}{n_{mn}} \geq 0$$

$$= 10.63 n_{mn} |n_{mn}| + 6.0 n_{mn} |V_{jmn}| - 5.04 V_{jmn} |V_{jmn}| ;$$

$$\frac{V_{jmn}}{n_{mn}} < 0$$

where the jet velocity is obtained by integration of the expression

$$\frac{dV_{jmn}}{dt} = 0.035 (T_{pmn} - 1.91 V_{jmn} |V_{jmn}|)$$

The forces on the body due to pressure distribution changes are a function of the jet velocity alone and are expressed as

$$T_{bm f} = 0.655 V_{jmf} |V_{jmf}| (T_1^* - 2.93)$$

$$T_{bma} = 0.655 V_{jmf} |V_{jmf}| (T_2^* - 2.93)$$

The resulting forces and moments on the body are then expressed as

$$X_{thr mf} = 0.655 V_{jmf}^2 T_3^*$$

$$X_{thr ma} = 0.655 V_{jmf}^2 T_4^*$$

$$Y_{thr yn} = T_{pyn} + T_{byn}$$

$$Z_{thr zn} = T_{pzn} + T_{bzn}$$

$$M_{thr zf} = 1.06 \frac{M_{10}^*}{T_{10}^*} T_{pzf} + 1.31 \frac{2M_1^*}{T_1^*} - \frac{M_{10}^*}{T_{10}^*} T_{bz f}$$

$$M_{thr za} = 1.13 \frac{M_{20}^*}{T_{20}^*} T_{pza} + 1.31 \frac{2M_2^*}{T_2^*} - \frac{M_{20}^*}{T_{20}^*} T_{bza}$$

$$M_{thr yn} = 0.238 T_{iyn} + 0.73 \dot{n}_{yn}$$

$$N_{thr yf} = 0.98 \frac{M_{10}^*}{T_{10}^*} T_{pyf} + 1.31 \frac{2M_1^*}{T_2^*} - \frac{M_{20}^*}{T_{20}^*} T_{bz f}$$

$$N_{thr ya} = 1.04 \frac{M_{20}^*}{T_{20}^*} T_{pya} + 1.31 \frac{2M_2^*}{T_2^*} - \frac{M_{20}^*}{T_{20}^*} T_{bya}$$

$$N_{thr zn} = -0.238 T_{izn} - 0.73 \dot{n}_{zn}$$

with T_{10}^* , T_{20}^* , M_{10}^* , M_{20}^* being the values of T_1^* , T_2^* , M_1^* and M_2^* for 0 forward way ($u = 0$).

III. SIMULATION OF DSRV/SUBMARINE INTERACTION FORCES

There are two forms of DSRV/submarine interaction forces. The first is a mechanical type of force produced when the shock mitigation system touches on the deck and transmits a force to the DSRV. The second type of force is caused by changes in the flow field caused by the bottom and the downed submarine and will be called flow interaction forces.

SHOCK MITIGATION SYSTEM

The shock mitigation system is primarily designed to protect the transfer skirt and absorb shocks in the event of obstacle collision. A secondary purpose is to act as a retractable base from which the transfer skirt may be slowly lowered to contact the hatch mating surface.

The shock system consists of a bumper ring concentric about the transfer skirt (see Fig. 10). The ring is attached to eight struts extending from four points on the outer hull. Each strut has a hydraulic piston/cylinder arrangement designed to attenuate impacts, as well as extend and retract upon command.

A simplified model of the shock mitigation system is presented for purposes of simulating near normal impacts during the controlled docking event. Figure 11 illustrates the DSRV with four vertical legs extending down from the four hardpoints on the outer

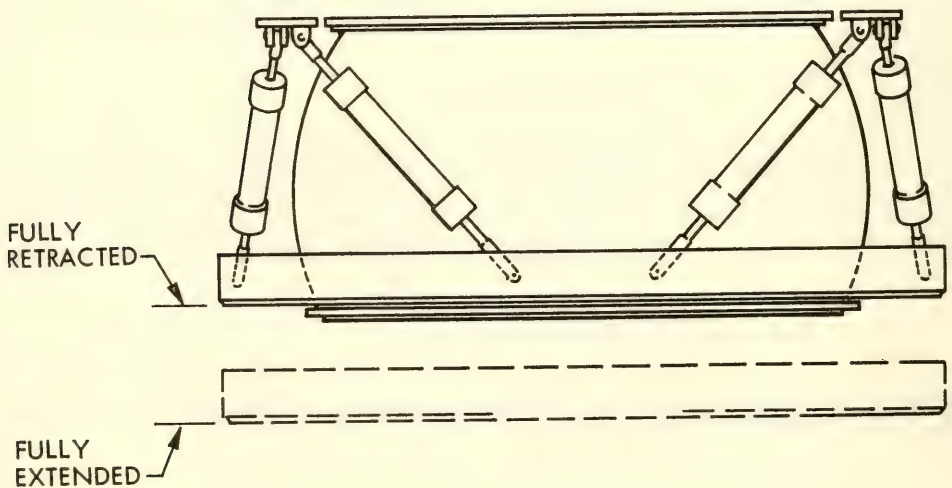


Fig. 10. Shock Mitigation System

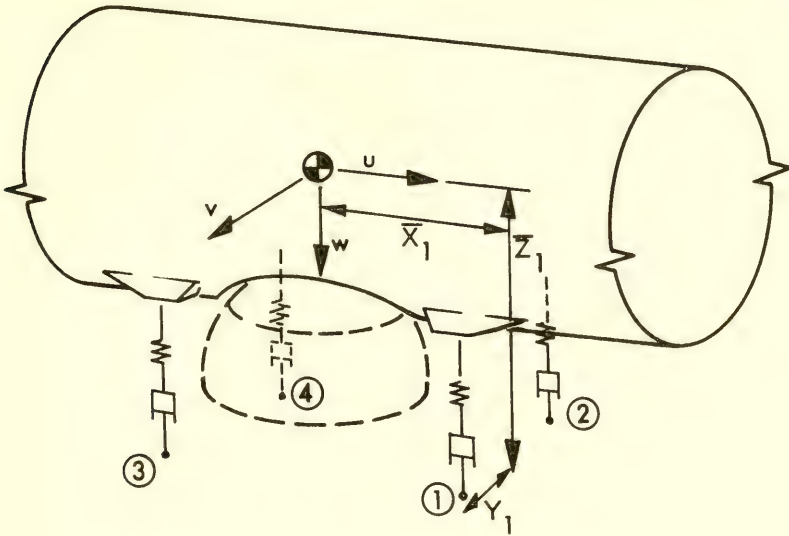


Fig. 11. Simplified Shock Mitigation System for Simulation

hull. Each leg acts independently of the other three and is limited to axial deflections only. The force elements in each leg consist of a spring in series with either a damper or a constant force element depending on both deflection magnitude and rate. Other forces applied to the leg ends are due to lateral friction at the contact surface. The equations that follow, approximate the force effects on the vehicle due to near normal impact during docking. The approximation is good if the deviation of the transfer skirt mating flange plane from the plane of impact at instant of contact is less than 10 degrees. Also, the vehicle velocity parallel to the impact plane should be less than 0.5 fps at time of contact.

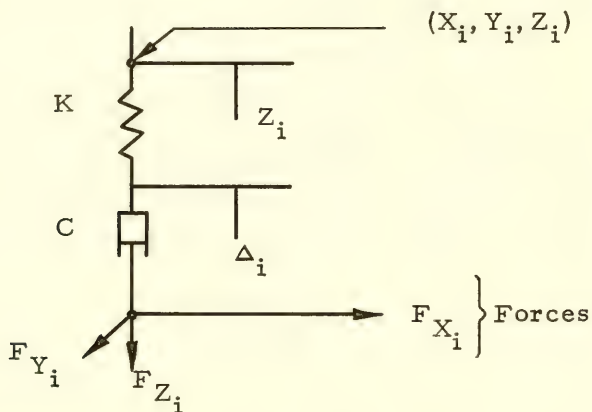
The resulting equations will give a disturbing force and moment expression, X_{DIST} , Y_{DIST} , Z_{DIST} , K_{DIST} , M_{DIST} , and N_{DIST} for application to the vehicle model equations of motion.

Using the direction cosine matrix

$$[D] = \begin{bmatrix} \cos\psi\cos\theta & \cos\psi\sin\theta\sin\phi - \sin\psi\cos\phi & \sin\psi\sin\phi + \cos\psi\sin\theta\cos\phi \\ \sin\psi\cos\theta & \cos\psi\cos\phi + \sin\psi\sin\theta\sin\phi & \sin\psi\sin\theta\cos\phi - \cos\psi\sin\phi \\ \sin\theta & \cos\theta\sin\phi & \cos\theta\cos\phi \end{bmatrix}$$

$$[D]^{-1} = [D]^T$$

The forces on the i^{th} leg can be calculated:



$$\begin{Bmatrix} X_v \\ Y_v \\ Z_v \end{Bmatrix} = [D]^{-1} \begin{Bmatrix} X_o \\ Y_o \\ Z_o \end{Bmatrix}$$

Subscript V refers to vehicle axis systems.

$$X_{vi} = X_v + \overline{X}_i$$

$$Y_{vi} = Y_v + \overline{Y}_i$$

$$Z_{vi} = Z_v + \overline{Z}_i$$

Also,

$$\dot{X}_{vi} = u + q\overline{Z}_i - r\overline{Y}_i$$

$$\dot{Y}_{vi} = v - p\overline{Z}_i + r\overline{X}_i$$

$$\dot{Z}_{vi} = w + p\overline{Y}_i - q\overline{X}_i$$

$$\begin{Bmatrix} X_i \\ Y_i \\ Z_i \end{Bmatrix} = [D] \begin{Bmatrix} X_{vi} \\ Y_{vi} \\ Z_{vi} \end{Bmatrix} = \begin{Bmatrix} X_o \\ Y_o \\ Z_o \end{Bmatrix} + [D] \begin{Bmatrix} \bar{X}_i \\ \bar{Y}_i \\ \bar{Z}_i \end{Bmatrix}$$

$$\begin{Bmatrix} \dot{X}_i \\ \dot{Y}_i \\ \dot{Z}_i \end{Bmatrix} = [D] \begin{Bmatrix} \dot{X}_{vi} \\ \dot{Y}_{vi} \\ \dot{Z}_{vi} \end{Bmatrix}$$

$$\left. \begin{array}{l} F_{xi} = F_{yi} = F_{si} = 0 \\ \dot{\Delta}_i = 0 \end{array} \right\} \text{ if } Z_i - \Delta_i \leq 0$$

$$\left. \begin{array}{l} \dot{\Delta}_i = \{K/C(Z_i - \Delta_i)^{1/2}\} \\ F_{si} = -C\dot{\Delta}_i^2 \end{array} \right\} \text{ if } \begin{cases} Z_i - \Delta_i > 0 \\ \Delta_i < 0.58 \text{ ft} \\ \dot{\Delta}_i < 0.5 \text{ ft/sec} \end{cases}$$

$$\left. \begin{array}{l} \dot{\Delta}_i = 0 \\ F_{si} = -K(Z_i - \Delta_i) \end{array} \right\} \text{ if } \begin{cases} Z_i - \Delta_i > 0 \\ \Delta_i \geq 0.58 \text{ ft} \\ K(Z_i - \Delta_i) < 11,000 \text{ lbs} \end{cases}$$

$$\left. \begin{array}{l} F_{si} = -11,000 \text{ lbs} \\ \Delta_i = Z_i - 11,000/K \\ \dot{\Delta}_i = d\Delta_i/dt \end{array} \right\} \text{ if } \begin{cases} Z_i - \Delta_i > 0 \\ \Delta_i \geq 0.58 \\ K(Z_i - \Delta_i) > 11,000 \text{ lbs} \end{cases}$$

$$\left. \begin{array}{l} F_{si} = -11,000 \text{ lbs} \\ \Delta_i = Z_i - 11,000/K \\ \dot{\Delta}_i = d\Delta_i/dt \end{array} \right\} \text{ if } \begin{cases} Z_i - \Delta_i > 0 \\ \Delta_i < 0.58 \text{ ft} \\ \dot{\Delta}_i > 0.5 \text{ ft/sec} \end{cases}$$

In all cases,

$$\Delta_i = \int_0^t \dot{\Delta}_i dt$$

$$F_{xi} = \mu F_{si} \{ \dot{X}_i / (\dot{X}_i^2 + \dot{Y}_i^2)^{1/2} \}$$

$$F_{yi} = \mu F_{si} / \{ \dot{Y}_i / (\dot{X}_i^2 + \dot{Y}_i^2)^{1/2} \}$$

Once F_{xi} , F_{yi} and F_{zi} have been calculated, they are transferred back into the vehicle frame of reference and summed:

$$\begin{aligned} \begin{Bmatrix} F_{x_{vi}} \\ F_{y_{vi}} \\ F_{z_{vi}} \end{Bmatrix} &= [D]^{-1} \begin{Bmatrix} F_{xi} \\ F_{yi} \\ F_{zi} \end{Bmatrix} \\ X_{DIST} &= \sum_{i=1}^4 F_{x_{vi}} \\ Y_{DIST} &= \sum_{i=1}^4 F_{y_{vi}} \\ Z_{DIST} &= \sum_{i=1}^4 F_{z_{vi}} \\ K_{DIST} &= \sum_{i=1}^4 (-F_{y_{vi}} \bar{Z}_i + F_{z_{vi}} \bar{Y}_i) \\ M_{DIST} &= \sum_{i=1}^4 (F_{x_{vi}} \bar{Z}_i - F_{z_{vi}} \bar{X}_i) \\ N_{DIST} &= \sum_{i=1}^4 (-F_{x_{vi}} \bar{Y}_i + F_{y_{vi}} \bar{X}_i) \end{aligned}$$

The physical and geometric properties of the system are shown below.

i th Leg	\bar{X}_i (ft)	\bar{Y}_i (ft)	\bar{Z}_i (ft)
1	2.8	2.8	8.2
2	2.8	-2.8	8.2
3	-2.8	2.8	8.2
4	-2.8	-2.8	8.2

$$K = 310,000 \text{ lbs/ft}$$

$$C = 44,000 \text{ lbs-sec}^2/\text{ft}^2$$

$$\mu = 0.1 \text{ lbs/lb for wet rubber on steel}$$

TESTS TO MEASURE FLOW INTERACTION FORCES

Because of the complex flow phenomena, tests were required to obtain measurements of the forces applied to the DSRV during the mating sequence with probable currents of 0 to 1.5 knots, wherein the flow forces are dependent on the approach attitude of the rescue vehicle, the orientation of the bottomed submarine, and the proximity of the two bodies.

In order to obtain meaningful experimental data, the following test requirements had to be satisfied:

- (1) The tests had to be performed at full scale Reynolds number, and
- (2) The environmental conditions had to be known.

Test Facility

The operating characteristics of existing hydromechanic test facilities were investigated to determine the facility most suited to conduct the test program. Because of the stringent combination of test conditions, i. e., (1) test operating Reynolds number range of $2 \text{ to } 6 \times 10^6$ per foot, (2) rescue vehicle angles-of-attack up to 45° , and (3) varying proximity of two bodies in the test channel, it was determined that the test requirements extended beyond the operating characteristics of all hydromechanics laboratories. However, the National Aeronautics and Space Administration (Ames) 12-foot variable pressure low turbulence wind tunnel was capable of meeting all the test requirements. The Ames Research Center is located at the Moffett Field Naval Air Station at Mountain View, California. The DSRV test program was conducted at this facility, which operates at subsonic speeds up to approximately Mach 1.0. The facility was

operated by the Arnold Research Organization under contract with NASA. The operating Reynolds number per foot versus Mach-number range of the tunnel is presented in Fig. 12. With a 1/30 scale model of the bottomed submarine, Reynolds numbers up to 6×10^6 based on the model diameter could be achieved at a Mach number of 0.2. This corresponded to the full-scale Reynolds number in a 1.5 knot current. Compressibility effects at a Mach number of 0.2 are known to be insignificant. Because of the large size of the test channel and the available equipment and instrumentation this facility afforded a unique capability for the DSRV program.

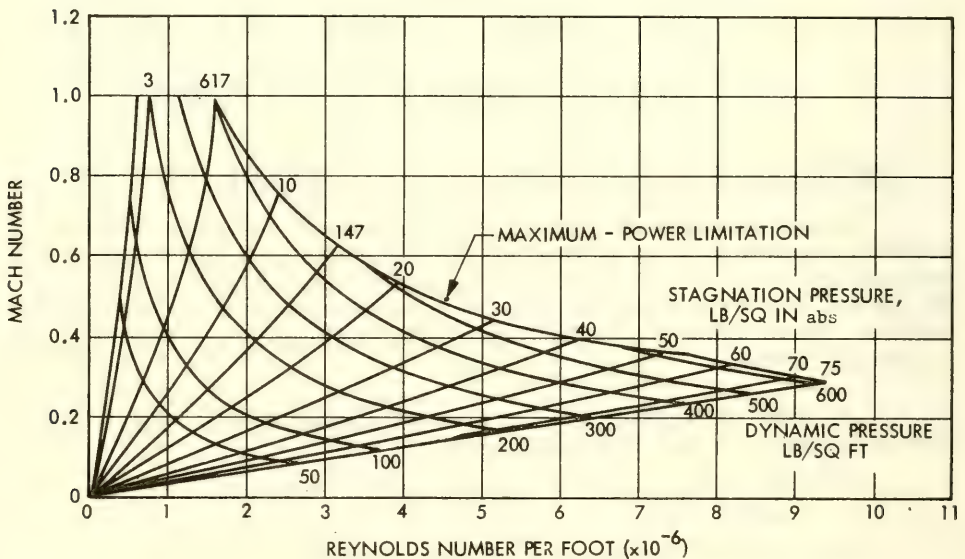


Fig. 12. Operating Characteristics of the Ames 12-Foot Pressure Wing Tunnel

Test Section and Model Support System

The test section is circular in cross section except for flat fairings. Figure 13 presents a schematic sketch of the general arrangement of the test section and the DSRV model support system. As illustrated, the sting-type model support consists of a fixed strut mounted vertically in the wind tunnel to which is attached a movable body of revolution carrying the sting and, in turn, the DSRV model. The strut functions as a support and guide for the body of revolution which can be pitched in the vertical plane by means of motor-driven lead screws. The range of pitch angles is 10 to 20 degrees; however,

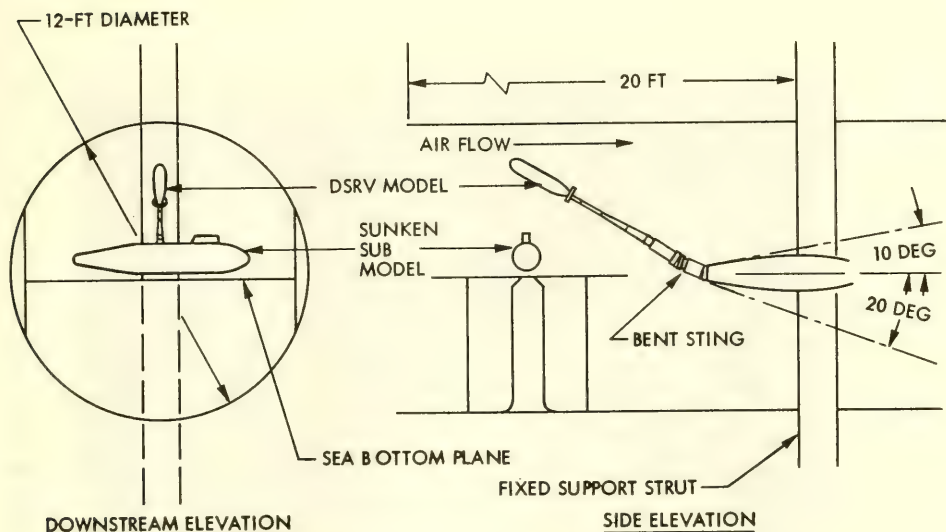


Fig. 13. Arrangement of the Test Section and Support System

pitch angles of 45 degrees were obtained using a bent sting.

The 1/30th scale submarine model was situated on a ground plane installed to simulate the ocean floor, and was oriented both into and normal to the current at 0, ± 22.5 , and ± 45 degree roll positions. For these mating positions, the DSRV model was set at various attitudes when approaching the submarine model along its longitudinal axis and from the side (athwartships). Photographs of the actual model installation for various mating conditions on the forward and aft hatches are shown in Figs. 14 and 15.

The displacement between the two bodies was regulated by vertical movement of the sting mount which supports the DSRV.

Models

The 1/30-scale model of the bottomed submarine, shown in Fig. 16, was constructed of poplar wood. The diameter of the model was 1.07 feet and its overall length was 8.2 feet. The model was constructed with a removable aft section in order to position the DSRV sting-support, which is located vertically along the centerline of the tunnel, over the area of the forward hatch. The model was also provided with a small and a large sail in order to simulate Permit (594) and Skipjack (588) class submarines. The forward hatch locations with the small and large sails was as shown in Fig. 5. Only one location of the aft hatch was considered.

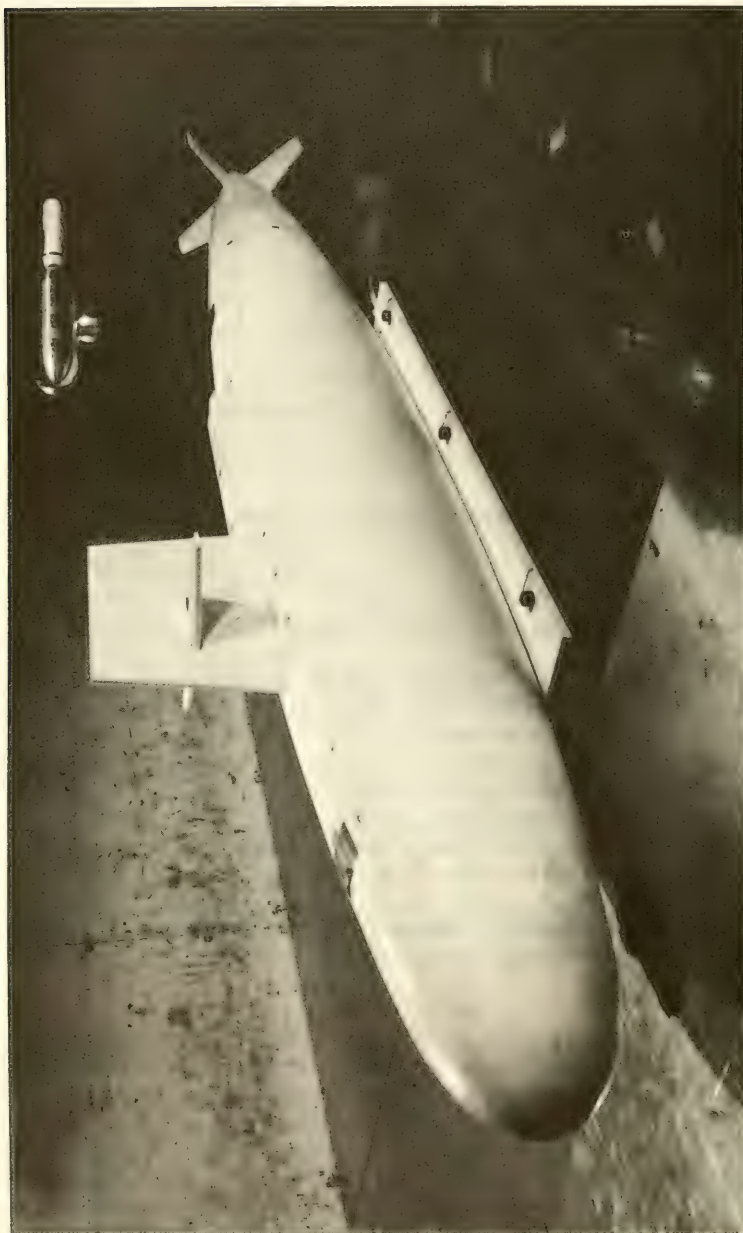


Fig. 14. Model Installation-Mating on the Aft Hatch with a Submarine Heading of 0 Degrees

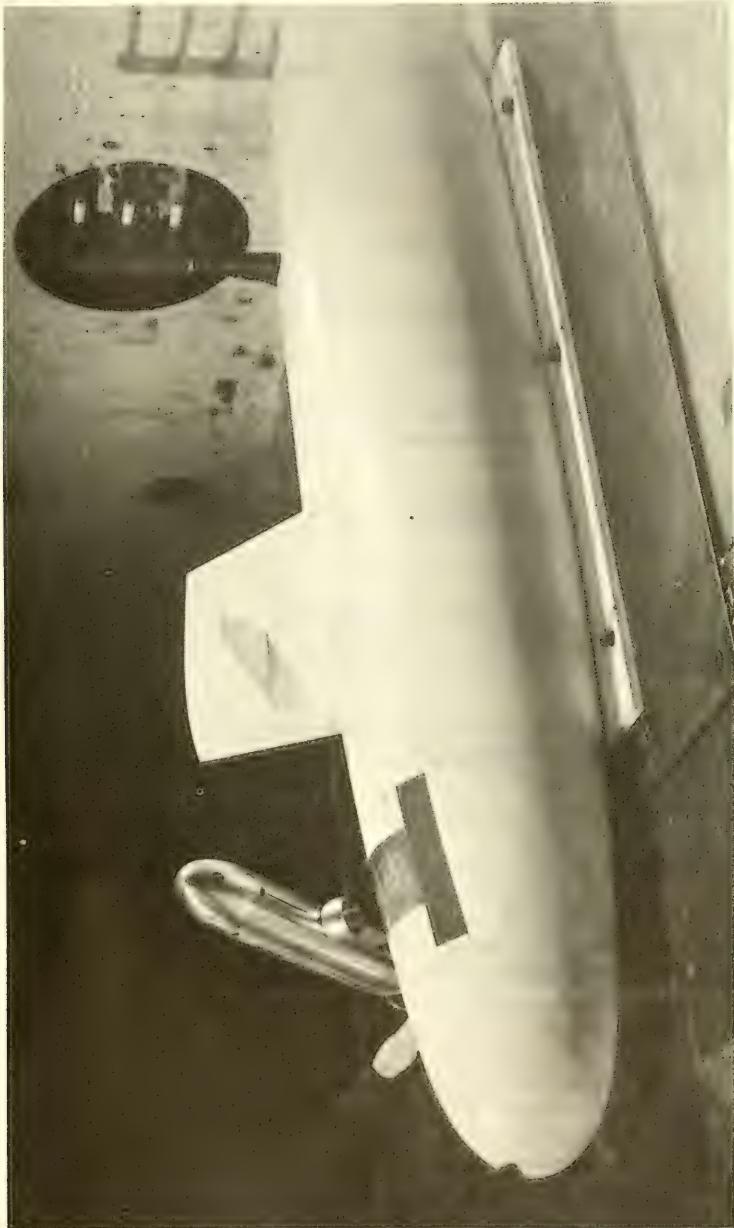


Fig. 15. Model Installation-Mating on the Forward Hatch with a Submarine Heading of 90 Degrees

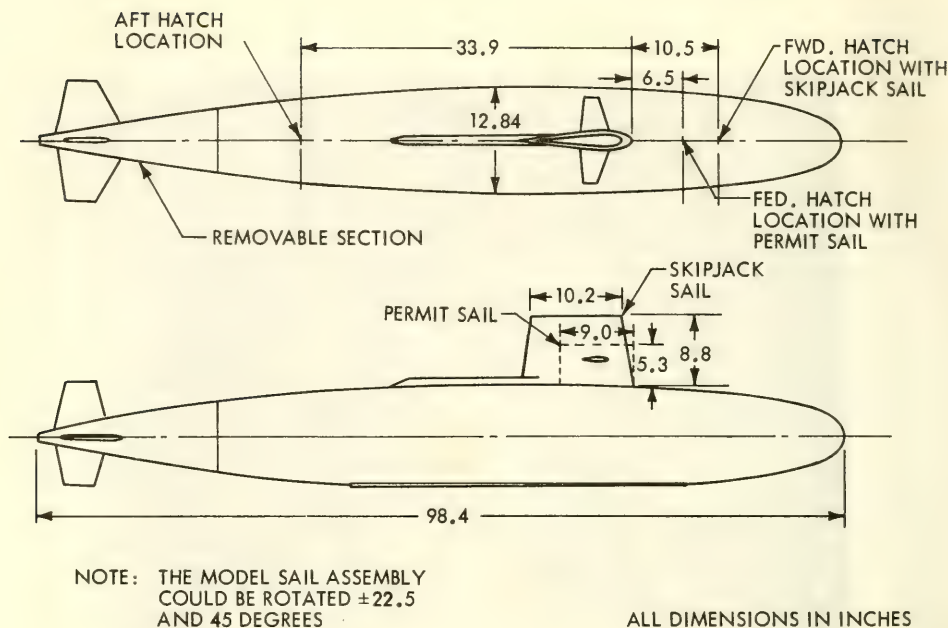


Fig. 16. 1/30 Scale Submarine Model

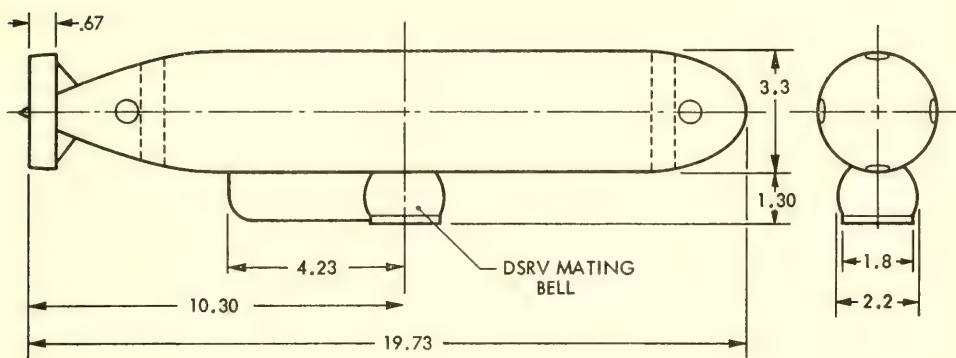
The submarine model was mounted on a flat rectangular plate, $1/2" \times 40" \times 45"$, to distribute the load on the ground plane. The roll positions of the planes and sail were adjustable to simulate submarine roll angles of $0, \pm 22.5$, and 45 degrees.

The DSRV model (1/30 scale), shown in Fig. 17, was constructed principally of aluminum. The diameter of the model was 3.3 inches and its overall length, 19.73 inches corresponding to a full-scale length of 49.33 feet. The transfer bell extended 1.3 inches below the baseline of the DSRV hull.

Instrumentation

The overall steady-state forces and moments acting on the DSRV model were measured by a strain-gauge balance mounted on the end of the supporting sting within the model. A type T-0.75 (i.e., 3.4 inch diameter) six-component internal strain gauge was used for the test program.

A seven-track FM tape recorder was used to record the balance outputs and to provide a time code in order to locate specific data for later analysis. Additionally, a switching network was pro-



ALL DIMENSIONS IN INCHES

Fig. 17. 1/30-Scale Model of the DSRV

vided for each data input to provide direct data entry to an oscillograph as well as the conventional "Record onto tape/Play-back from tape to graph" and for quick-look at model oscillation frequencies where they occurred.

Test Conditions

The test program (Ref. 11) consisted of 258 runs, at Reynolds numbers up to 6.0×10^6 per foot, and the DSRV positioned at 6 or more locations (distances from the submarine model). The data were recorded for about five minutes for each set of test conditions.

The vertical distance from the mating surface of the DSRV rescue bell to the mating surface (hatch) of the submarine, Z_d , was varied from 0 to at least 12 inches, which corresponds to 30 feet, or about one submarine diameter, in full scale.

As shown in Fig. 13, an angle adapter was used to obtain different pitch angles, θ_{rv} , of the DSRV. For these test conditions, the angle of attach, α_{rv} , of the DSRV was the same as θ_{rv} . Angle adapters of 0, 15, 30 and 45 degrees were used. When the submarine model was removed from the tunnel to obtain DSRV free stream conditions, the vehicle's angles of attack (pitch angles) were obtained by a combination of adapter arrangements and pitch of the strut mechanism.

REDUCTION AND PRESENTATION OF DATA

The proximity effects are described by a time independent term and a time varying term in each of the six equations of motion. These components are functionally dependent on the proximity to the distressed submarine, Z_d , the DSRV attitude angle, θ_{rv} ; and the orientation of the distressed submarine relative to the current. By means of the tests conducted in the Ames facility, these effects were determined primarily for two orientations of the submarine to the current: head-on and athwartships. The tests were conducted with the DSRV mating at both the forward and aft hatches with various attitude angles of the DSRV and roll angles of the distressed submarine. The DSRV yaw angle was zero for all test conditions.

Time Independent Interaction Forces

At the Ames facility the balance data were recorded by printing devices, punched onto paper tape by a Beckman 210 computer, and carried to the laboratory's computing center. The resultant steady-state force and moment coefficients were computed at the Ames center in the body-axis system. The force coefficients were non-dimensionalized by the DSRV's maximum cross sectional area; the moment reference arm for moment coefficients was the maximum diameter of the DSRV.

In order to determine the DSRV characteristics in free stream, the submarine model was removed from the tunnel, and the forces on the DSRV were determined through an angle of attack (pitch angles) range from - 12.5 to + 35.0 degrees. The resulting normal force, pitching moment, and axial force coefficients versus angle of attack are shown in Fig. 18. These results are shown to correlate well with previous free stream tests conducted at Hydro-nautics, Inc. (Ref. 5).

Interaction coefficients were determined by plotting the measured data and extrapolating the curves to the free stream conditions.

The interaction coefficients are:

$$C_{X_i} (-C_{A_i}), C_{Y_i}, C_{Z_i} (-C_{N_i}) \quad \text{Force Coefficients}$$

$$C_{Z_i}, C_{M_i}, C_{N_i} \quad \text{Moment Coefficients}$$

where

$$C_{X_i} = C_{X_{\theta_m}} + K \frac{\theta_{rv} - \theta_m}{15}, \text{ etc.}$$

$$C_{Z_i} = C_{Z_{\theta_m}} + K \frac{\theta_{rv} - \theta_m}{15}, \text{ etc.}$$

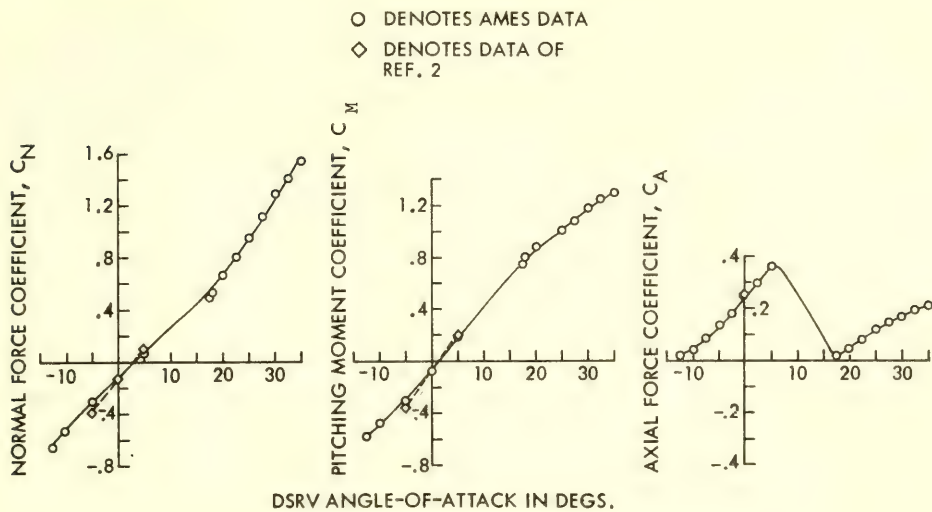


Fig. 18. DSRV Free Stream Characteristics

where $C_{x\theta_m}$ and K are functions of the vertical distance between the bottom of the transfer bell and the hatch, Z_d .

θ_{rv} is the pitch angle of the DSRV (in degrees). θ_m denotes the mean DSRV attitude angle (the angle to which the data is referenced) in degrees and can be converted to disturbing forces and moments as follows:

$$X_{dist} \text{ (lbs)} = C_{x_i} \frac{\pi d_{max}^2}{4} \frac{1}{2} \rho V_c^2, \text{ etc.}$$

$$L_{dist} \text{ (ft-lbs)} = C_{L_i} \frac{\pi d_{max}^2}{4} d_{max} \frac{1}{2} \rho V_c^2, \text{ etc.}$$

It was determined early in the experimental program that the flow forces encountered during mating on the forward hatch with the Skipjack sail configuration were more severe than those with the Permit sail geometry, and flow forces encountered during mating on the aft hatch are less severe than those encountered on the forward hatch. Hence, almost the entire test program was conducted with the Skipjack sail, and the data presented herein are representative of the most severe flow forces that the DSRV will experience during mating with a downed submarine.

When the DSRV is approaching the distressed submarine along its centerline and headed into the current, a suction force is applied to the DSRV when it is within a one submarine diameter of the hatch, Fig. 19, because of the accelerated flow and the associated reduced pressures between the DSRV and the hull. This suction force increases as the displacement between the bodies, Z_D , is decreased. The maximum value of the suction force, F_{suction} , for a 1 knot current is 45.5 lbs. This result correlates well with the theory presented in Ref. 12.

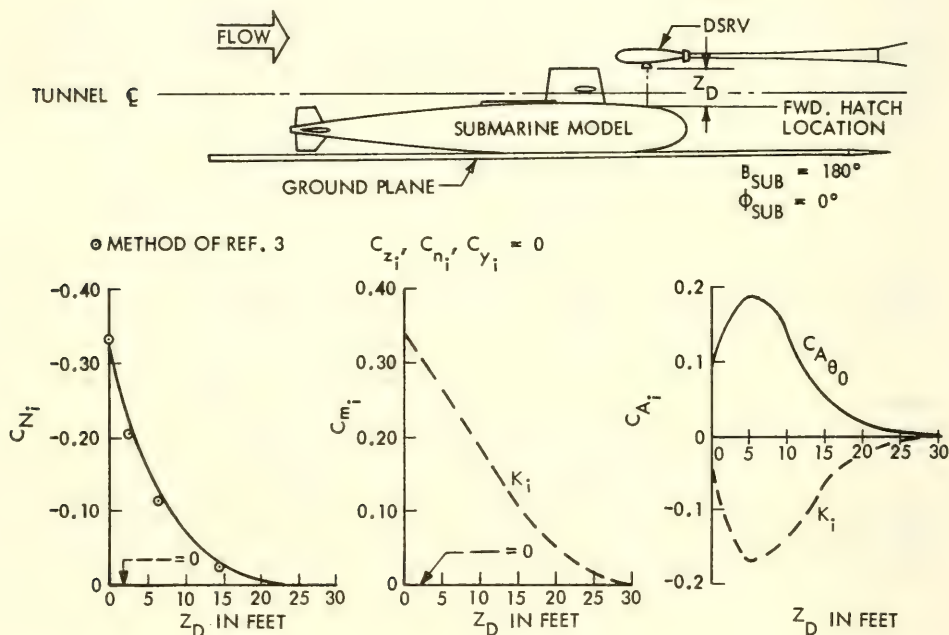


Fig. 19. Time Independent Flow Interaction Forces -- DSRV Mating Parallel to Submarine Centerline

In contrast, when the DSRV is approaching the distressed submarine athwartships and headed into the current, interaction forces are applied to the DSRV when it is within 2-1/2 submarine diameters (75 feet) of the hatch. Referring to the solid $C_{N_{\theta_0}}$ curve of Fig. 20, it is apparent that the maximum suction force is also 45.5 lbs, for this orientation in a 1 knot current.

* Note: The subscript θ_0 denotes that the attitude angle of the DSRV is zero.

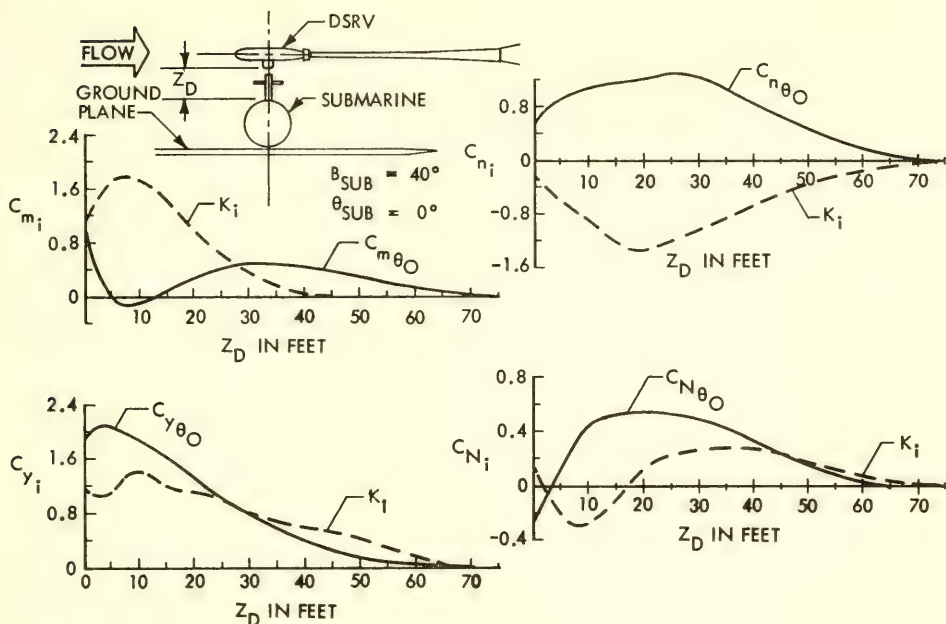


Fig. 20. Time Independent Flow Interaction Forces -- DSRV Mating Normal to Submarine Centerline

Although the DSRV was heading athwartships directly into the current for this series, it is shown in Fig. 20 that lateral forces were applied to the vehicle, i.e., C_{y_i} , C_{n_i} , and C_{l_i} were not equal to zero. This result is due to the fact that a cross flow results when the current is deflected off the sail and the DSRV is therefore not heading directly into the resultant flow. The magnitude of the side force, F_{side} , in a 1 knot current is 300 lbs.

Time Dependent Forces

During the test program, the outputs of the six-component balance (i.e., normal and lateral forward and aft gauges and the roll and axial-force channels) were recorded over a five minute interval. The long recording time was established to provide a high confidence level during analysis of the unsteady effects (Ref. 13).

The information was digitized by data conversion and input to an IBM 7094 force and moment conversion program. The output of the 7094 program was then used as input for an existing LMSC Power-Spectral Density Computer Program.

Plots of typical power-spectral energy versus frequency in model scale are shown in Figs. 21 and 22 for the unsteady normal force and pitching moments acting on the DSRV. These conditions were for the DSRV mated ($Z_D = 0$) athwartships on the forward hatch of a downed submarine with no roll.

The full-scale natural pitch period of the DSRV can range from 41.5 to 72 seconds, corresponding to a BG value of 1 to 3 inches and a weight of 75,000 lbs. This information shown in terms of model data for a 1 knot current in Fig. 22 indicates that there is no significant concentration of energy near the DSRV natural frequency; therefore, motion excitation at resonant conditions will not be significant.

The standard deviation of forces and moments in model scale were determined as the square root of the spectral energy, which

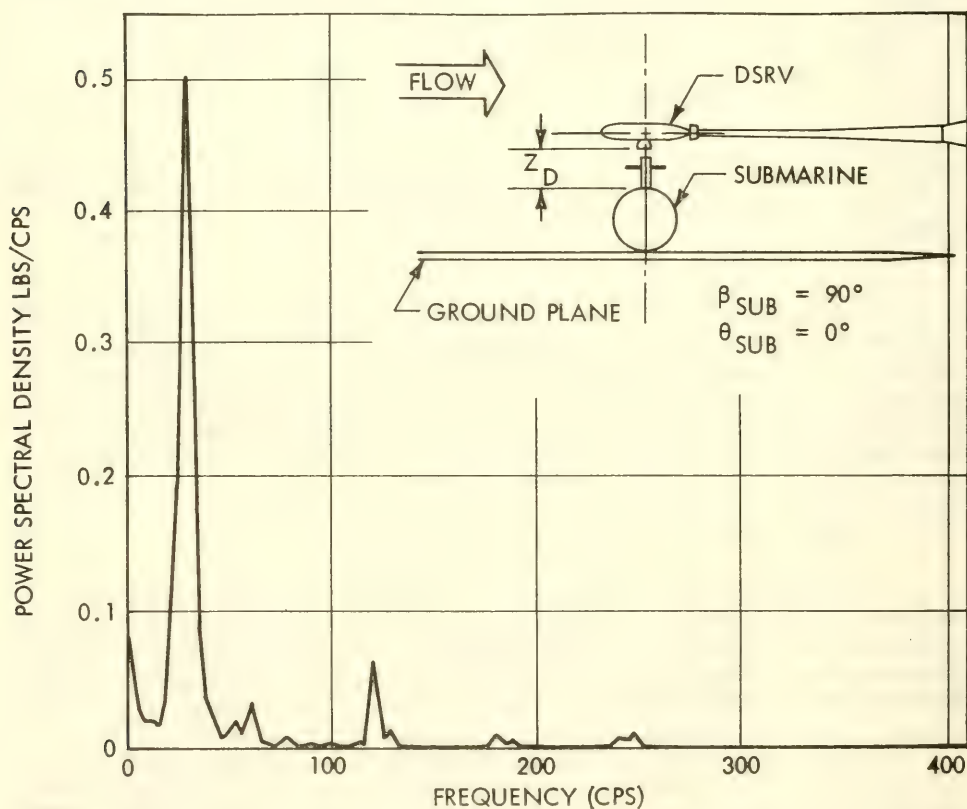


Fig. 21. Normal Force Power Spectral Density vs. Frequency (Model Scale Values Shown)

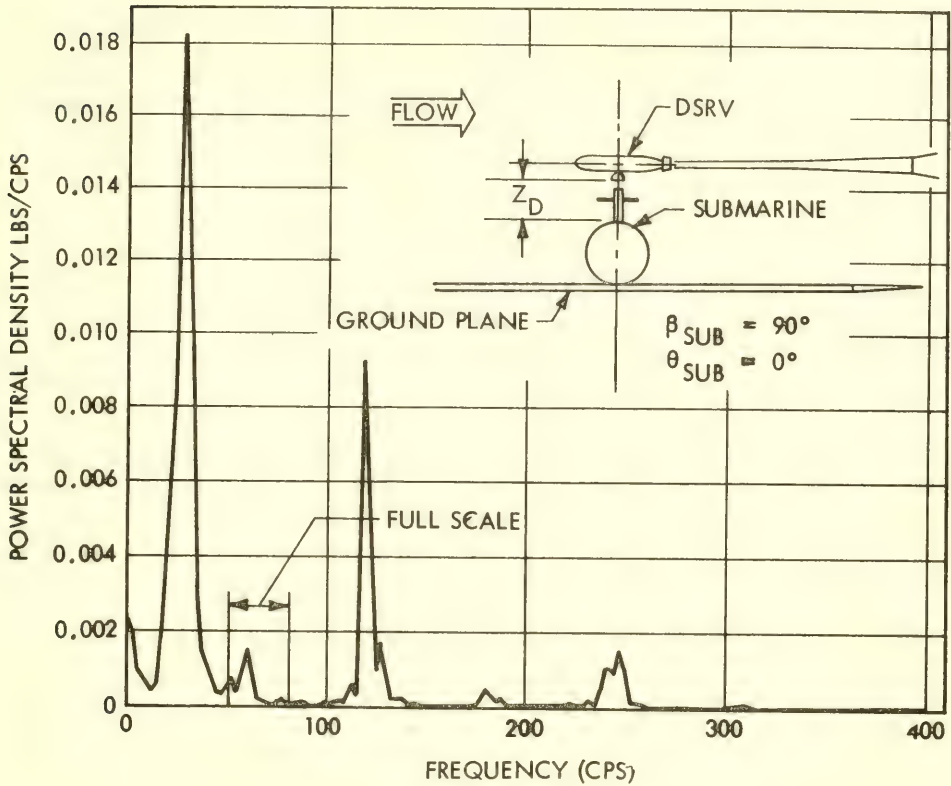


Fig. 22. Pitching Moment Power Spectral Density vs. Frequency (Model Scale Values Shown)

was obtained from the integrated power density spectrum. Then using Strouhal number and Reynolds number scaling, the full-scale unsteady (a.c.) component standard deviation of forces and moments were computed. For the corresponding test conditions, the interaction data were used to compute the full-scale magnitude of the steady components. In the simulation the unsteady forces were approximated by a white noise perturbation on the current used to generate the steady forces. Based on the standard deviation of the test data a ratio of unsteady (a.c.) to steady (d.c.) forces of 0.15 was selected in the frequency range from 0 to $0.082 V_c$ Hertz.

The ducted thrusters of the DSRV are presently designed to provide 830 lbs of normal and lateral force and are required to maintain vehicle heading in a 1 knot current. The worst side force condition, obtained during tests with the sail rolled 22.5 degrees

into a 1 knot current and mating on the forward hatch, was 690 lbs well within the thruster forces available. Furthermore, during mating, the operational procedure will be to head the DSRV, within practical limits, into the actual flow (the resultant of the current and the cross-flow due to deflected flow off the sail). This operation will result in a reduction to the side force to a much lower force level.

INCLUSION IN THE MATHEMATICAL MODEL

Attempts to mathematically simulate the interaction forces by using the potential solution of flow around a cylinder on a plane to generate the flow field were unsuccessful in the time available. In addition, not enough submarine-current configurations were tested to verify superposition techniques.

The parameters $C_{x\theta_m}$ and K of the previously mentioned interaction terms were approximated in the simulation by two-slope nonlinearities. Figure 23 shows the two slope approximations of the

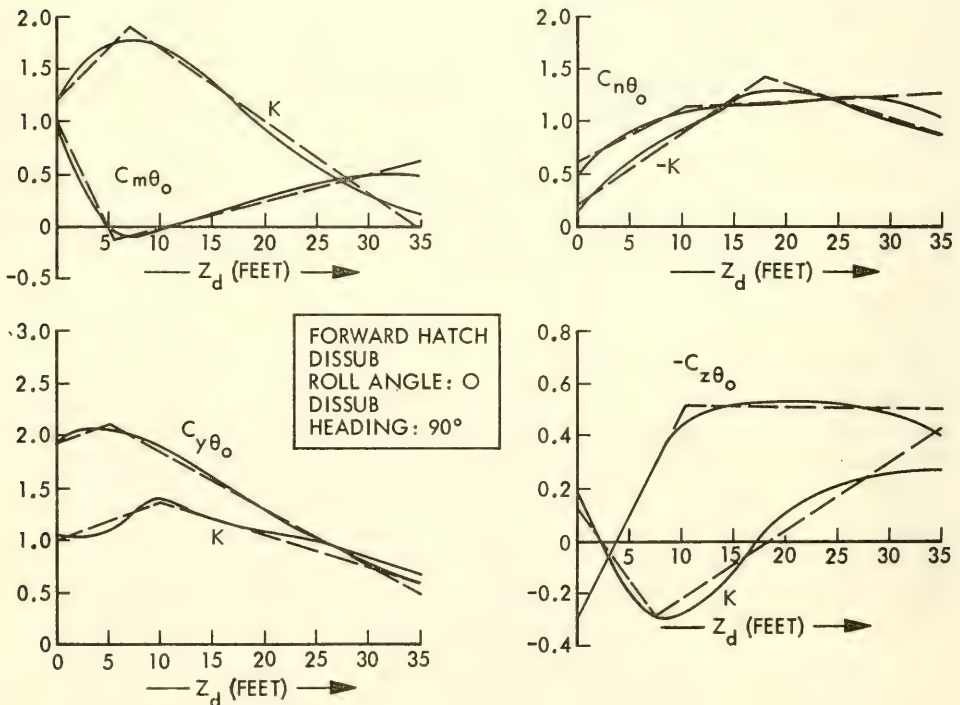


Fig. 23. Interaction Force Parameters

experimental data equivalent to Fig. 20 with the initial conditions starting with the DSRV 35 feet above the submarine hatch.

The method of simulating the steady and unsteady interaction effects is shown in Fig. 24.

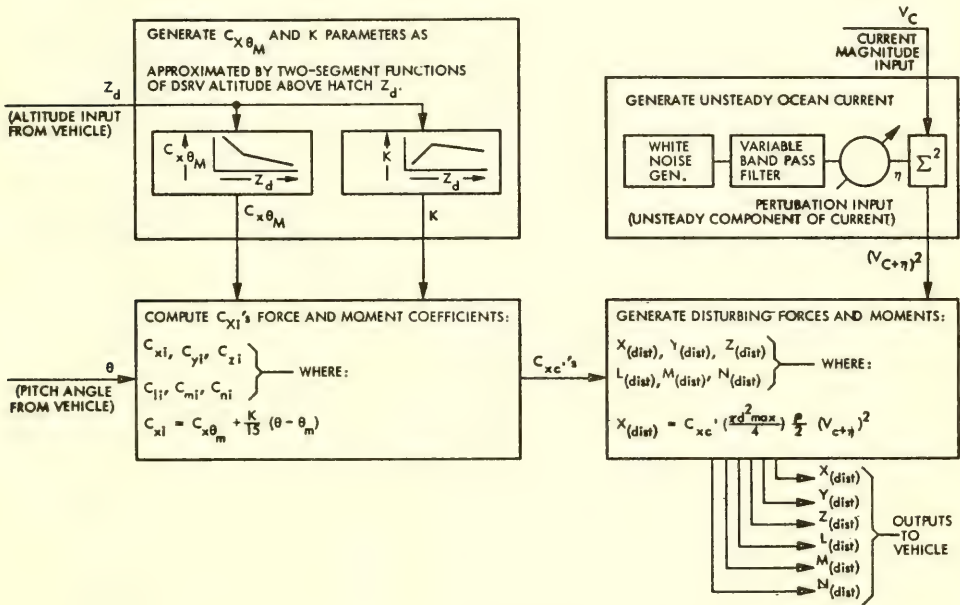


Fig. 24. Simulation of Interaction

IV. MANNED SIMULATION

Early in the DSRV program it was decided to initiate a manned simulation study, whose primary objective would be the investigation of the operation of DSRV under manual control conditions, using minimum backup displays. The control system aboard DSRV is relatively sophisticated, providing substantial pilot assistance in the form of augmented stabilization, decoupling of degrees of freedom, and automated control loops. Although the primary operating modes of the DSRV were not to be manual, it was believed that a manual control capability was essential for backup in the event of failure or damage of the primary control system.

The simulation program was confined to the most severe segment of the rescue mission, the mating of the DSRV to the hatch of the distressed submarine (DISSUB). This segment starts when the

DSRV is approximately 20 feet above the deck of the DISSUB, and ends when the DSRV is sitting on the deck and has positioned itself to the accuracy required to assure a satisfactory seal. This simulation would be used to determine the limits of current magnitude and direction and distressed submarine attitude for which manual control is feasible. Mating aids would be used as required.

The manned simulation program was undertaken sufficiently early in the design program to permit some design investigation of the parameters of various control elements. Several significant design changes were made as a result of these investigations.

This computerized simulation program complemented the simulations undertaken with the LASS (Lighter than Air Submarine Simulator) vehicle. LASS operations (Ref. 14) had established the feasibility of manual control. However, they did not permit controlled variation of the environment.

The facility used for the manned simulation program was located at the Sperry Marine Systems Division in Charlottesville, Virginia. This facility had previously been used for simulation studies of the NR-1 research submersible, and many of the programs developed for the NR-1 were available for the DSRV studies. Ron Rau, one of Lockheed's DSRV test pilots, served as test pilot for the simulation study.

FACILITY DESCRIPTION

The computer facility utilized in the simulation combined an Ambilog 200 hybrid computer with an EAI-231R analog computer. The Ambilog 200 has a basic 4,096-30 bit word memory with a memory cycle of 2 μ sec. The analog portion, used for multiplication and division, has a 50 μ sec cycle. The Ambilog 200 was used to simulate the vehicle, coordinate transformations, actuators and effectors, current interaction effects and the mating aids. The EAI-231R was used for display generation and for simulating the ballast and trim systems.

In addition to the computer, the simulation facility included a cab driven in two degrees of freedom (roll and pitch). The cab contained a control station consisting of control sticks and other system inputs, various meter type displays, and a TV display. Figures 25 and 26 show the cab and its interior display arrangement, respectively.



Fig. 25. Simulation Cab

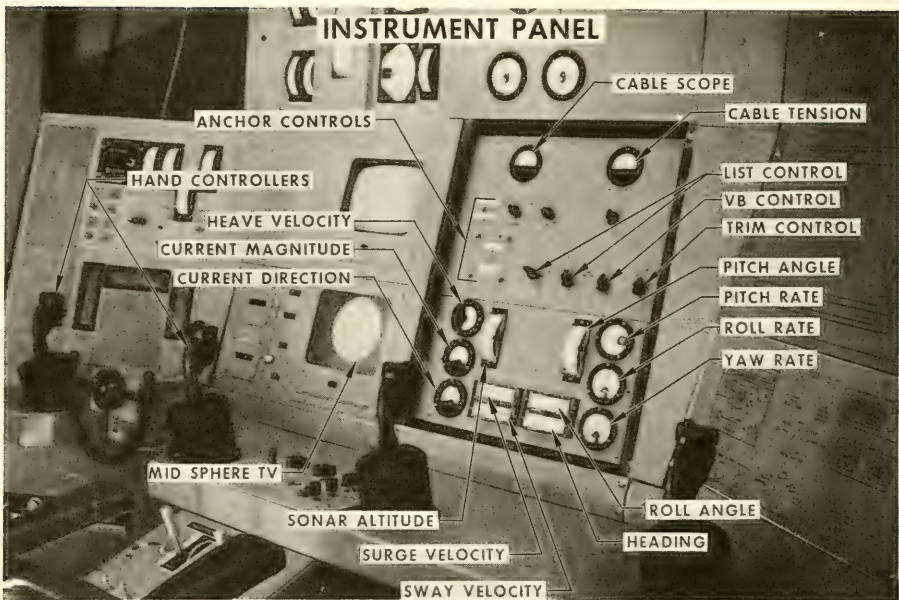


Fig. 26. Instrument Panel

ELEMENTS OF SIMULATION

Vehicle

Because the mating operation is confined to low current velocities, vehicle control is obtained by means of the main propulsion and thrusters; the shroud remaining locked amidships. The relatively limited capability of the Ambilog computer necessitated some approximations of the equations of motion to assure fitting the entire problem to the computer. The major approximation used ignored the stalling effect of the shroud.

The effect of this approximation is shown in the comparison of the heave versus angle of attack curves of the analysis and simulation models of Fig. 27. At high angles of attack the simulation model provides higher heave forces than the analysis model, an effect which tends to make the results of the simulation conservative.

The iteration interval used in the computation was 125 milliseconds. Since some of the degrees of freedom, particularly the mating aids, require a higher frequency response, selected portions of the simulation utilized a 62.5 millisecond interval. A relatively simple integration routine was employed, as shown in Fig. 28.

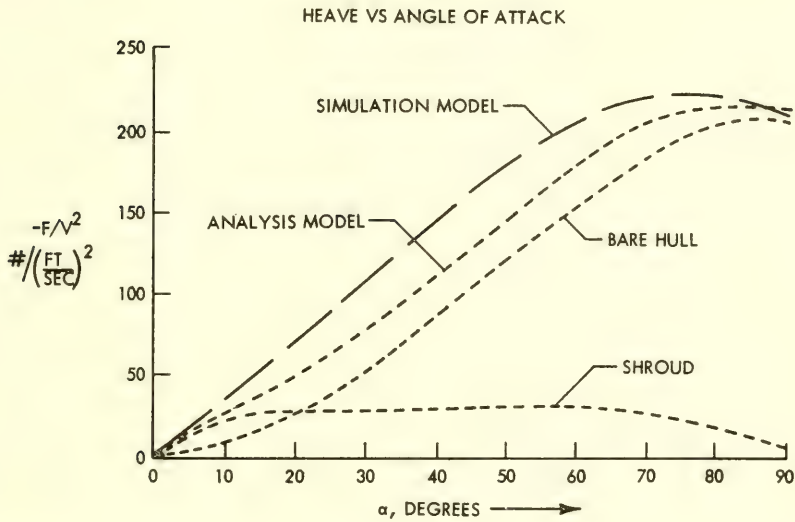
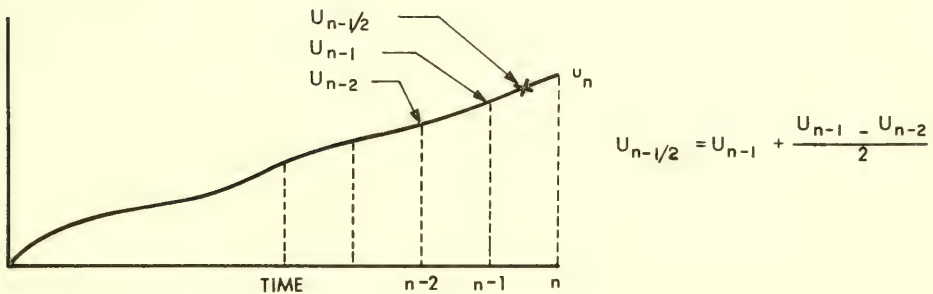


Fig. 27. Comparison of Simulation and Analysis Models



EQUATIONS OF MOTION

$$\dot{u} = f(u, v, w, p, q, r)$$

SOLUTION

$$\dot{u}_n = f(u_{n-1/2}, v_{n-1/2}, \text{ETG})$$

$$\text{AND } u_n = u_{n-1} + \dot{u}_n \Delta t$$

ITERATION INTERVAL 62.5 OR 125 MILLISECONDS

Fig. 28. Computation of Vehicle Motions

Throughout the course of the program, vehicle responses using the simulation model were compared to responses computed from the more complete analysis model, which had been programmed with a more sophisticated integration routine.

Vehicle Control System

The control effectors available are main propulsion for surge, a pair of horizontal thrusters for yaw and sway, a pair of vertical thrusters for pitch and heave, and mercury ballast control for list and trim. Experience with DEEP QUEST and other submersibles had shown that independent control of the thrusters was not effective, since each horizontal thruster, for example, affected both yaw and sway. To achieve effective control it is desirable to separate the commands to each degree of freedom. Thus, a sway command would be applied equally to both fore and aft thrusters, while a yaw command would be applied differentially to the two thrusters.

Vehicle control (except for trim and list) is obtained from two hand controllers. The block diagram of the system, including the actuators and effectors, is shown in Fig. 29. The output of

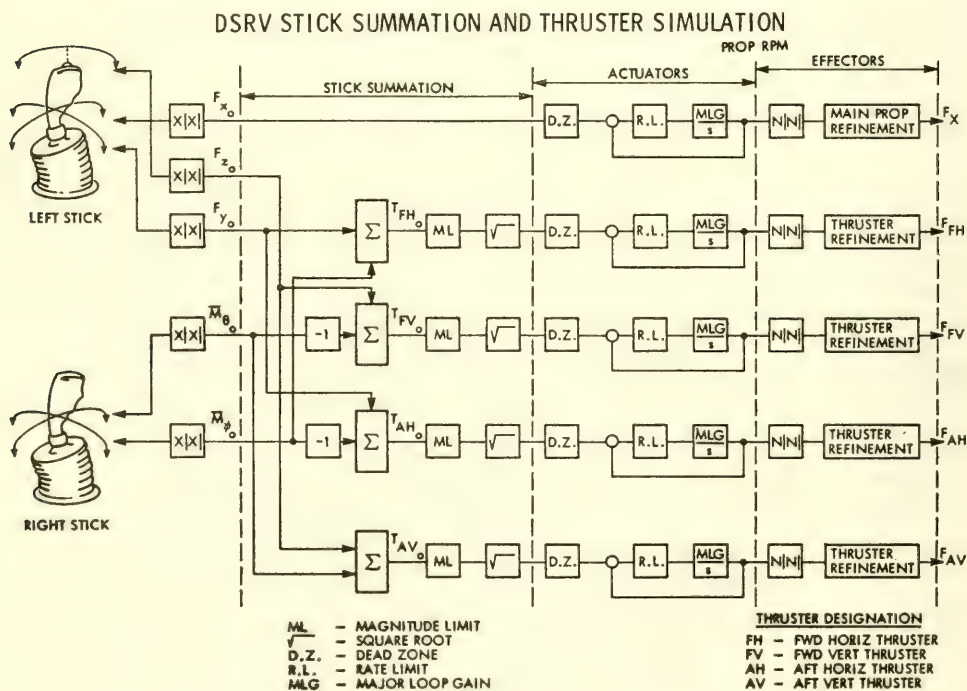


Fig. 29. DSRV Stick Summation and Thruster Simulation

each command axis is fed into a "signed square" circuit, so that the commands represent forces rather than propeller RPM. After mixing the signals appropriately, they are fed into square root circuits so that the commands to the actuators represent RPM. Each actuator is represented by a delay network which includes a maximum motor acceleration limit. The effectors are represented by an $(\text{RPM})^2$ network (to convert RPM to thrust) and a "thrust refinement" circuit. The latter accounts for the variations of thrust with the forward speed of the vehicle. The approximations used in the thrust refinement are shown in Fig. 30.

The actuator/effector simulation shown in Fig. 29 ignores the lead-lag thrust effect of the thrusters which results from the delay in accelerating the water in the thruster duct. Exploratory experiments showed that, in manual control, the thrusters are used in a bang-bang fashion, and the effects of ignoring the lead-lag response of the thrusters are minimal.

In the more sophisticated control modes used aboard the DSRV, the mercury list system control is integrated into the right-hand stick, and the pitch control motion of the right-hand stick affects both thrusters and mercury trim control.

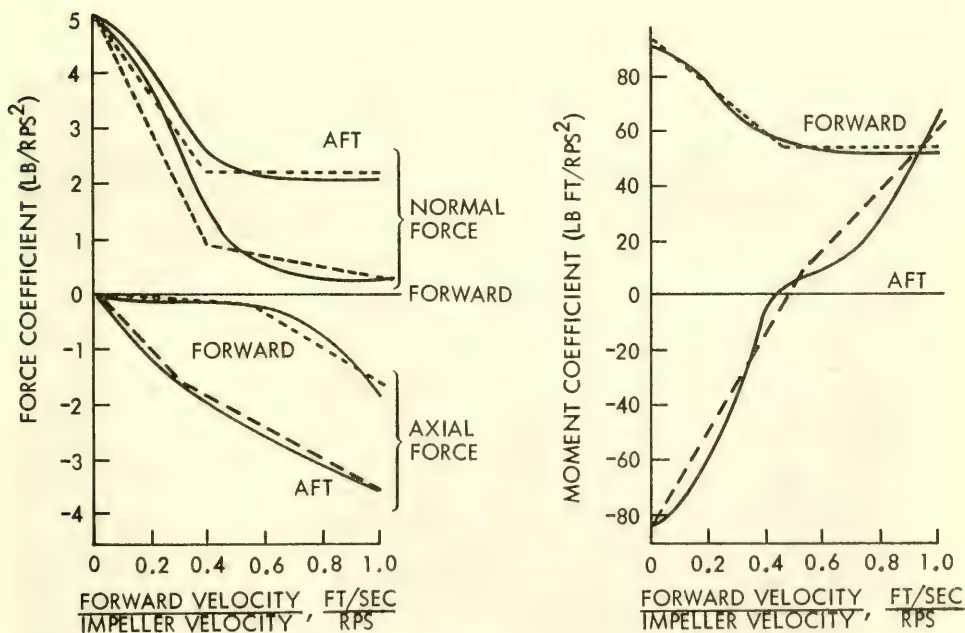


Fig. 30. Effect of Forward Speed on Thruster Forces and Moments

Displays

Two sensors are available aboard the DSRV for assistance in performing the final mating maneuvers. These are a TV camera which looks through a viewport in the midsphere lower hatch, and a high resolution short range sonar (SRS) mounted to a retractable boom in the transfer skirt. Only the TV was simulated. Details of the performance of the SRS were not available at the time the simulation study was performed. Also, with good visibility, the TV is a much more informative sensor than the SRS.

The midsphere TV display was simulated by photographing a model of a submarine. The photograph was then scanned by a CRT, using a flying spot scanner. The size of the area scanned is a function of the distance from the camera to the hatch. The displacement of the center of the hatch from the center of the screen is proportional to the distance between the hatch center and the intersection of the camera axis with the hatch plane. Because of the relatively small angles between the DSRV and DISSUB planes, no attempt was made to provide foreshortening effects. Reproductions of the TV display are shown in Fig. 31. The four radial line segments at the extremity of the picture represent the staples on the submarine deck surface to which a McCann Rescue Chamber can be attached. These staples provide precise centering information for the pilot.

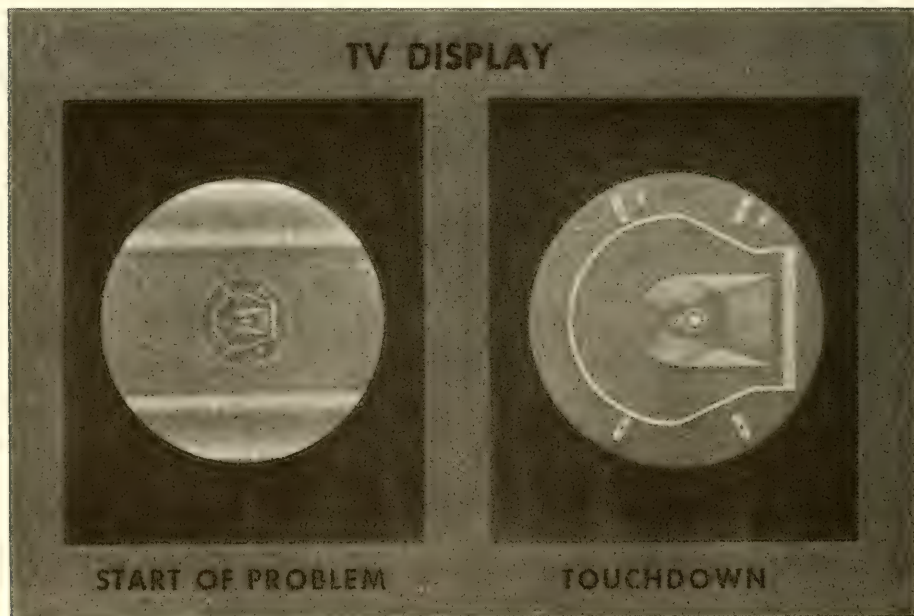


Fig. 31. TV Display

The most significant meter displays are those of doppler velocity, attitude rates. The doppler sonar, located 8.9 feet aft of the C.G. and 3.3 feet below the centerline, provides 3 axis ground velocity data. Since the doppler sonar is offset from the center of gravity, angular motions couple into the doppler signals, and in some situations were interpreted by the pilot as translation velocities.

Displays were also provided for roll, pitch and heading angles, and for sonar altitude above the DISSUB. Current magnitude and direction indicators were available, but were not used in the simulation, since the corresponding sensors were not installed in the vehicle. The additional displays shown in Fig. 26 are associated with the anchors and haul down winch control systems.

Shock Mitigation System

The shock mitigation system serves a dual purpose in the mating operation. The primary one is that of dissipating the kinetic energy of the DSRV when it lands on the DISSUB. The second function was realized only after the simulation study was started. Prior to dewatering, the DSRV is connected to the DISSUB primarily by vertical thrust forces from the DSRV and coulomb friction. Because of the existence of the shock mitigation system it is not necessary for the DSRV to land precisely on target. As long as the shock mitigation ring encloses all the staples, the DSRV can slide on the DISSUB deck until precise alignment is reached.

As described previously the shock mitigation system has been simulated as four independent damped springs. The natural frequency of the DSRV-shock mitigation system is approximately 11 radians per second, which is too high to simulate with a 62.5 millisecond iteration interval. Accordingly, the spring constant was reduced, with a reduction in the natural frequency to 1.7 radians per second. The damping constant was also reduced to maintain essentially the same percentage damping.

Anchor and Hauldown

Exploratory runs were made using both the anchors and haul-down as mating aids. No help was obtained with the anchors, and very limited assistance was obtained from the hauldown. Schedule and budget limitations did not permit an intensive evaluation of this problem at the time. Some digital simulation was performed at a later date with the hauldown system, which indicated that it should provide substantial assistance, particularly when the DSRV is required to mate bow up to the current. These results were confirmed on simulated tests made with LASS.

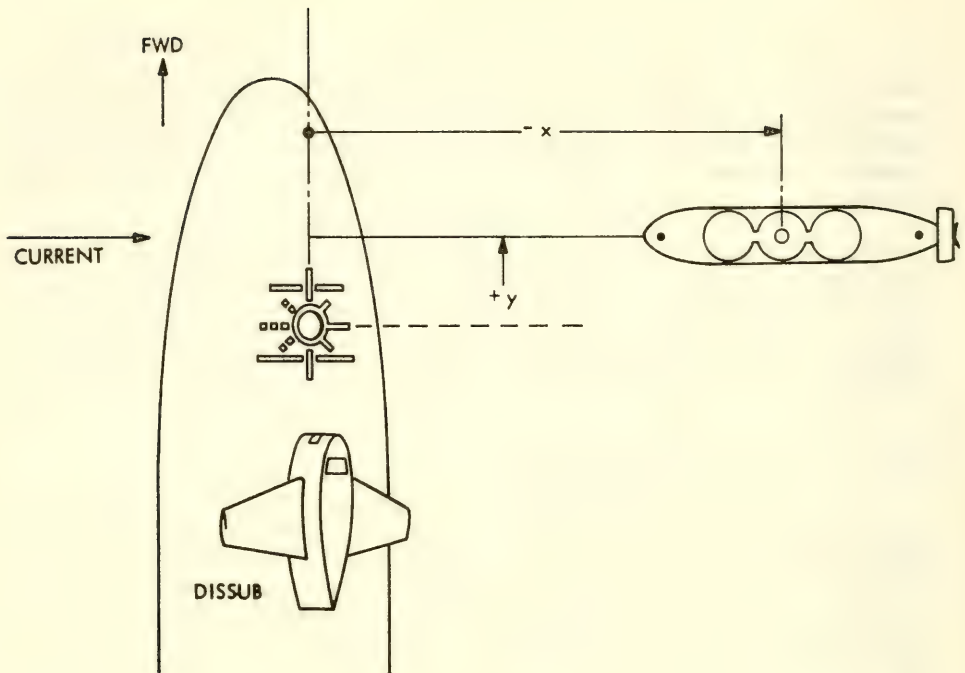


Fig. 32. Mating Geometry

A TYPICAL SIMULATION RUN

The mating situation to be described is depicted schematically in Fig. 32. The DISSUB is rolled 225 degrees in an athwartship current, so that the DSRV is required to mate bow up. With the DSRV heading into the free stream, the interaction forces and moments are as depicted in Fig. 33. Deflection of current off the sail of the DISSUB causes a starboard sway force on the DSRV. The corresponding yaw moment is counterclockwise at large separations, but becomes clockwise as the DSRV approaches the DISSUB. The normal force provides a suction effect at relatively large displacements, but becomes destabilizing as the DSRV approaches the DISSUB. Thus the normal force, due to interaction, adds to the force due to the free stream and tends to push the DSRV away from the hatch. Pitch moments remain rather constant over the distance included in the run.

In performing the mating operation the pilot attempts to head into the local stream rather than into the free stream. He sees and "feels" the DSRV sway and adjusts his heading to minimize the sway motions. Thus, the relative heading is not into the free stream but

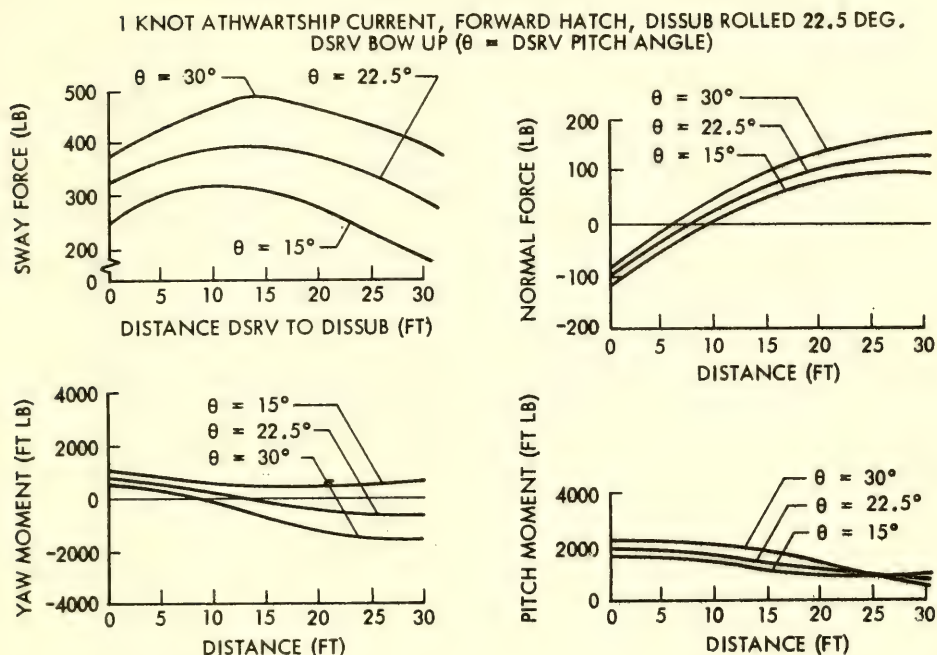


Fig. 33. Interaction Forces and Moments

rather is in a relatively arbitrary direction. The effects of heading changes on the interaction problem are illustrated in Fig. 34.

First of all, as the DSRV heading is changed, Euler angle variations occur (Fig. 34a). Where initially the DSRV was not required to list at all, it must now both list and trim, and can no longer make precise list and trim adjustments prior to landing. Concurrent with these changes, the free stream current components change with heading (Fig. 34b) which must be compensated appropriately.

Assuming that the ideal heading corresponds to zero sway force, the variation of optimum heading with distance to hatch is shown in Fig. 34c. The optimum relative heading is approximately 30 degrees, with a significant heading change required as the separation is decreased. It will be noted from Fig. 34d that the zero heading yaw angle does not correspond to the zero yaw moment angle. This is due to the horizontal gradients in fluid velocity along the length of the DSRV. Thus, there is no yaw plane equilibrium condition, and yaw plane control becomes a more severe problem than

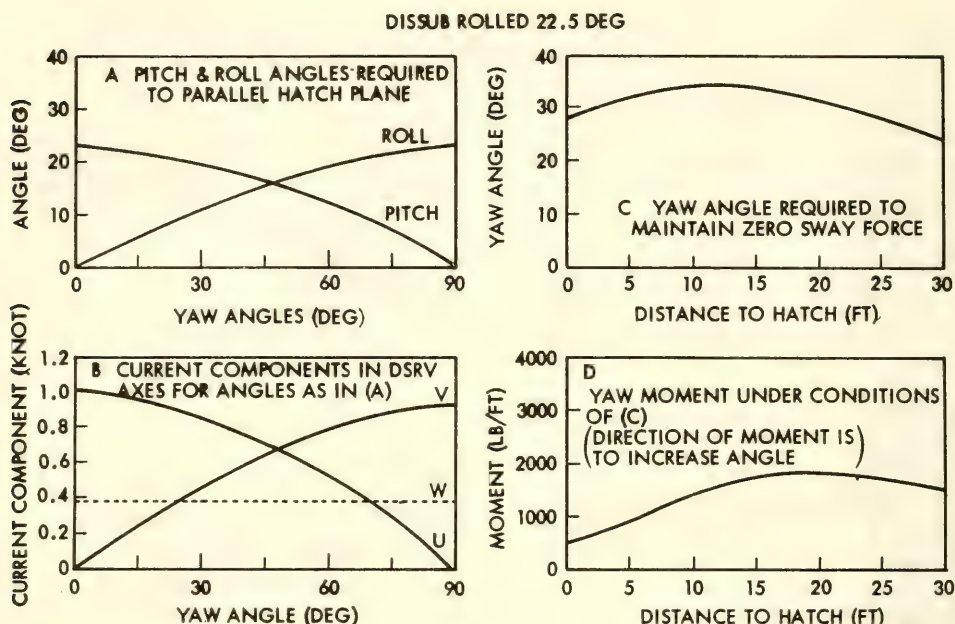


Fig. 34. Counteracting Interaction Forces by Heading Changes

pitch plane control.

A six channel recording of the simulation test run under these conditions is shown in Fig. 35. The variables plotted are the displacements x , y and z of the camera of the DSRV from the center of the hatch in the coordinate frame of the DSRV as shown in Fig. 32. Also plotted are the roll, pitch and heading angles of the DSRV, zero heading being into the free stream. For a one minute interval during the run the roll, pitch and yaw angle traces are replaced with RPM traces from the forward vertical, forward horizontal and main propeller, respectively.

The run begins with the DSRV aligned with the free stream, in a level attitude, and at a camera elevation of 20 feet (corresponding to 15 foot distance between the DSRV seal and the DISSUB hatch). This initial condition results in a more severe transient than would occur on a mission, so that the advantages of the relative proximity in distance is overcome by the necessity to restore dynamic equilibrium. At the start the pilot turned to port about 20 degrees to try to maintain equilibrium. Simultaneously, the roll and pitch angles are adjusted to try to maintain the DSRV sealing surface parallel to the hatch plane. After about two minutes, the pilot descends about

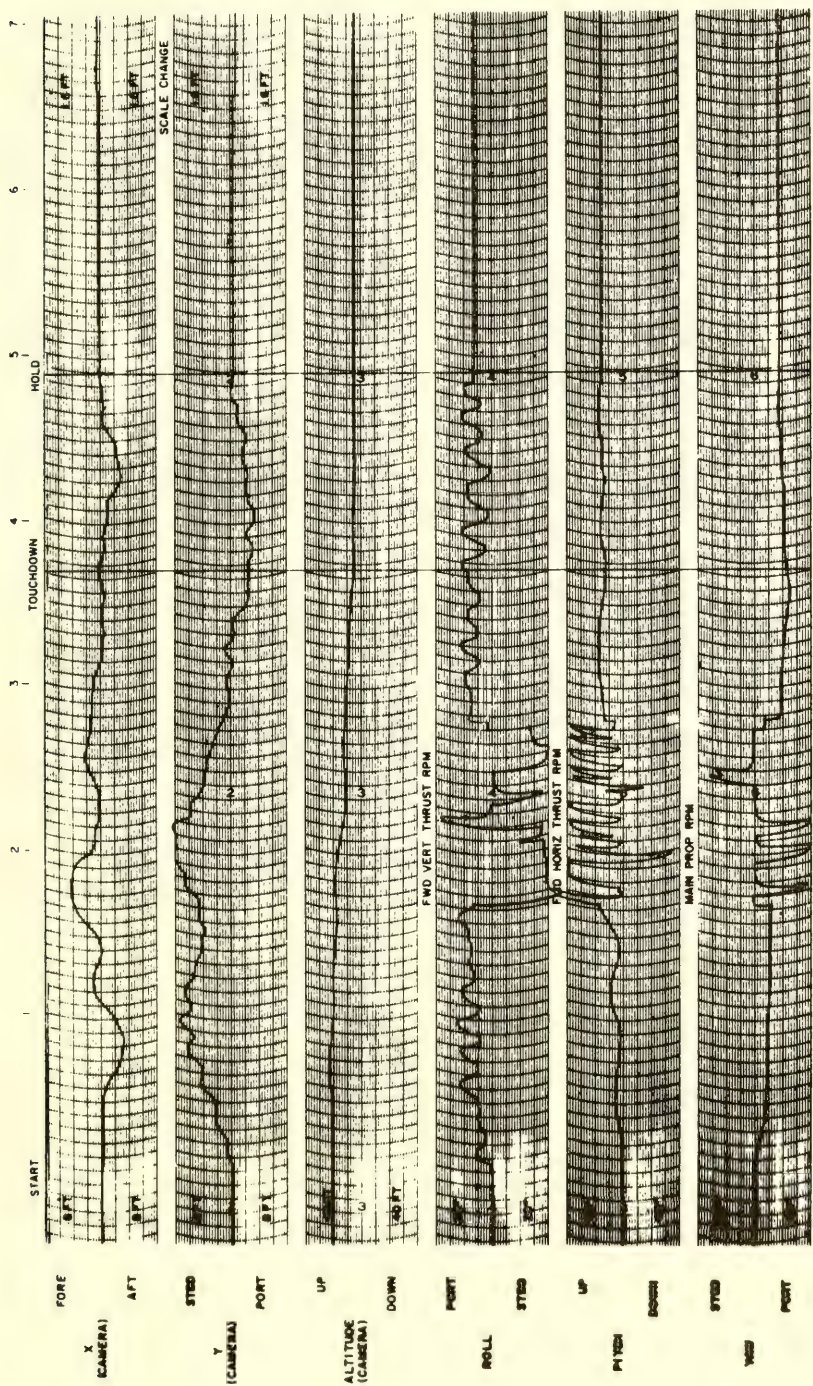


Fig. 35. Simulation Run -- Forward Hatch, Athwartship 1 Knot Current DISSUB Rolled 20 Degrees

half the distance to the hatch, then attempts to maintain altitude while adjusting his x and y coordinates. In the process the yaw angle has been increased to about 35 degrees. The final descent is made, the DSRV touching the deck somewhat in excess of 3.5 minutes after the start of the problem. At touchdown the DSRV was almost perfectly aligned in the x direction but was nearly 2.5 feet off center in the y direction. On the deck, vertical thrust was applied (trace not shown) in an attempt to keep from being lifted off by the current. Roll and pitch angles were adjusted to try to position all four legs in contact with the deck. Note that during this time the DSRV continues to roll and pitch. The transients at impact caused the DSRV to slip aft about 2.5 feet. This was corrected, as was the misalignment in the y axis. After nearly 5 minutes the pilot had the DSRV under control and could commence the final retraction of the shock mitigation ring and start up the dewatering pump. At this time the computer was placed into HOLD. The final misalignments were 0.10 feet in the x direction and 0.16 feet in the y direction, within the required tolerances. The final yaw pitch and roll angles were 36, 6 and 16 degrees, respectively.

Unfortunately, this would not have been a completely successful landing. At the time the pilot terminated the run, the DSRV seal plane and the deck hatch plane were misaligned about 7 degrees in roll and 2 degrees in pitch so that all four shock mitigation legs were not in contact with the deck and a satisfactory seal could not be made. No instrumentation exists on the DSRV to provide this relative attitude data which could result in a serious operational limitation. The problem can be alleviated in part by use of the hauldown system which provides a larger stabilizing moment, reducing the offset angles.

A major assistance was obtained by installing, in the simulation, a set of 4 indicators which measured the stroke of the shock mitigation hydraulic cylinders. Roll and pitch alignment could be achieved with this system, while maintaining the horizontal plane alignment.

A review of the thruster activity leads to two interesting observations. First, the thrusters are operated in a bang-bang fashion, that is, either maximum thrust or zero thrust is commanded. This, despite the fact that an accurate proportional control system is available. Second, the activity of the horizontal thrusters is much greater than either the vertical thruster or the main propeller. This was somewhat predictable from the environmental curves of Fig. 9. The frequency of the horizontal thruster activity has implications in the thermal design of the thruster motors.

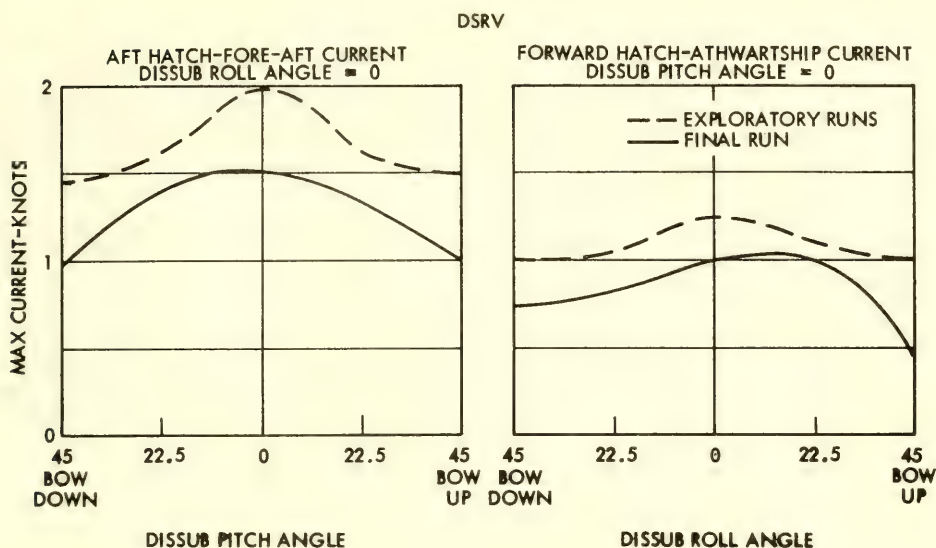


Fig. 36. Experimental Results

RESULTS OF MANNED SIMULATION PROGRAM

The experimental results of the simulation study are summarized in Fig. 36. Two sets of curves are shown, those for the final runs, of which Fig. 35 was an example, and those of earlier, exploratory runs which were made prior to the inclusion of the shock mitigation system in the simulation. Performance of the final runs did not meet those of the exploratory runs. Schedule constraints did not permit much training with the use of the shock mitigation system. The pilot believes that with such training the results of the two sets of runs would match more closely.

On the basis of these results, we have tentatively arrived at the following performance predictions.

- a) Mating on the aft hatch is feasible for currents in excess of one knot at all attitudes of the DISSUB (up to 45 degrees) and headings of the DISSUB with respect to the local current.
- b) On the forward hatch, we have to distinguish between longitudinal and athwartship currents. In athwartships currents the goal of mating in a one knot current can be achieved except possibly for very high DISSUB roll angles which require the DSRV to mate bow up to the current. With respect to longitudinal currents, on those submarine

classes which have sufficient clearance between the sail and the forward hatch to permit the alignment of the axes of the two vehicles, mating is possible in currents well in excess of one knot. For those submarine classes which do not have sufficient clearance, mating is limited to about $3/4$ of a knot.

The manned simulation program yielded some important by-product results which impacted on the vehicle design. The most significant ones are as follows:

- a) The splitter plate behind the transfer skirt was originally incorporated to reduce flow separation behind the skirt and minimize axial drag. Model testing unfortunately did not verify this drag reduction. However, the splitter plate was found in the simulation to provide sufficient roll damping to permit mating without automatic roll stabilization (automatic roll stabilization is, however, provided even in the manual mode).
- b) The shock mitigation system had originally been designed to dissipate energy only for impact velocities in excess of 0.25 feet per second. Below 0.25 ft/sec, the system acted as a spring. However, because the DSRV is neutrally buoyant, it will bounce off any spring unless the impact energy is absorbed. As a result of observing this phenomenon in the manned simulation study, the shock mitigation system was redesigned to provide damping for all impact velocities.
- c) The relative attitude indicators required to assure angular alignment have not yet been incorporated in the design.

The results of the Ames tunnel tests have been invaluable in gaining an understanding of the problems involved in submarine mating. In the early phases of the simulation program, before the Ames results were available, mating runs were made under free stream conditions. Although there had been apprehension about the ability of the pilot to perform the 6 degree of freedom control function manually, we found that experienced aircraft pilots, with nominal DSRV simulator training, could control the DSRV with ease. Successful mating to currents up to two knots were anticipated for virtually all orientations and in excess of two knots for the most favorable conditions.

The inclusion of the interaction effects, particularly on the forward hatch, dampened our optimism. The performance goals could be met, but at considerably reduced current magnitudes, and requiring considerably more pilot training.

Prior to the start of the Ames test program, it was believed that the most serious interaction effects would be in the pitch plane, due to Bernoulli or "suction" effects. The experimental program was organized primarily to determine those forces. As we have seen, yaw plane interactions are more critical than those in the pitch plane. It would be desirable to have additional data, particularly with respect to interactions as a function of yaw angle and (for the longitudinal current) as a function of lateral separation of the longitudinal axes of the two vehicles.

Recognizing the above limitations in the test conditions, no attempt has been made to use the Ames data quantitatively in the control system design. The data has been useful in the following areas:

- a) It has provided an appreciation of the yaw plane problems associated with mating.
- b) The force and moment gradients observed have been used to select and verify the static gain requirements of the automatic control system.
- c) The non-steady interactions have provided an input which could be used to establish the dynamic requirement of the actuators and effectors, in particular the pumping rate requirements of the list system.

The DSRV is completing preliminary sea trials and will soon be conducting mating trials. Before too long we will have some full scale verification of the usefulness of the Ames test results.

IV. CONCLUDING REMARKS

This paper has presented an approach to the problems of simulation of the dynamics of highly maneuverable submersibles. All elements of the simulation are covered in considerable detail to provide an adequate base to build on for others with similar problems. No such comprehensive reference was available for our use.

Although the model test data are not presented in their entirety, a reasonably complete description of the test procedure and results should allow determination of the usefulness of the data. Several references are given for more complete test results.

It is hoped that this paper illustrates where Naval Hydrodynamics is a continually expanding field and must take into consideration aspects of control system design, man-in-the-loop analysis, and numerous other fields not normally considered as relevant to the theoretician.

Finally a note about the methods used during the development of the simulation. The work was not done in a theoretically rigorous manner but rather the simulation was built upon the background of the personnel involved in its development and their ability to apply existing theories to the problem. A number of the elements in the complete simulation of the vehicle dynamics reflect engineering judgment and experience. The major output of the study was required on a tight schedule and relatively little new theoretical analysis were initiated. Since the DSRV is presently preparing for sea trials the validity of the simulation should soon be checked and correlation between the sea trials data and the results of the simulation should provide valuable insight for further simulations.

REFERENCES

1. Johnstone, R. S., "A Mathematical Model for a Three Degree-of-Freedom Simulation of the Underwater Launch of a Rigid Missile," Lockheed Missiles and Space Company, TM5774-69-21, May 1969.
2. Kerr, K. P., "Determining Hydrodynamic Coefficients by Means of Slender Body Theory," Lockheed Missiles and Space Company, IAD/790, 21 July 1959.
3. Hess, John L., "Calculation of Potential Flow about Bodies of Revolution Having Axes Perpendicular to the Free Stream Direction," Douglas Aircraft Company, Report No. ES29812, October 1, 1960.
4. Feldman, Jerome P., "Model Investigation of Stability and Control Characteristics of a Preliminary Design for the DSRV," David Taylor Model Basin Report 2249, June 1966.
5. Goodman, H. and Ettis, P., "Experimental Determination of the Stability and Control Characteristics of a Proposed Rescue Submarine (DSRV) Using the Hydronautics High Speed Channel," Hydronautics Inc. Technical Report 511-4, November 1966.
6. Bentskowsky, J., et al., "DSRV Model for Analysis ML 493-03 Vehicle," Lockheed Missiles and Space Company Report No. RV-R-0037A, May 1968.
7. Reichart, G., "A Propulsion and Maneuvering System for Deep Submergence Vehicles," presentation at ALAA meeting in Seattle, Washington, June 1969.

8. Beveridge, J. L. and Paryear, F. W., "Performance of a DSRV Propeller on Four Modes of Vehicle Operation (NSRDC Model 5128)," Naval Ship Research and Development Center T & E Report 099-H-05, August 1967.
9. Beveridge, J. L., "Static Performance of a DSRV Ducted Propeller Thruster at Discrete Pitch Ratios," David Taylor Model Basin Hydromechanics Test Lab Report 099-H-03, July 1966.
10. Chislett, M. S. and Bjorheden, O., "Influence of Ship Speed on the Effectiveness of a Lateral Thrust Unit," April 1966.
11. Kerr, K. P., "Experimental Determination of DSRV/Submarine Mating Forces Using the Ames Variable Pressure Wind Tunnel," Lockheed Missiles and Space Company, TMOS-H-67-62, June 1967.
12. Ogilvie, A., "Force on an Ellipsoid Moving Near a Wall," David Taylor Model Basin Report, 1967.
13. Moody, R. C., "Statistical Considerations in Power Spectral Density Analysis," Technical Products Company, 1966.
14. Turpen, F. J. and Goodman, A., "Experimental Determination of the Performance Characteristics of the DSRV Based on a 1.25-Scale Lighter-Than-Air Submarine Simulator (LASSI)," Hydronautics, Inc., Technical Report No. 705-3, August 1968.

AUTHORS INDEX

- Bentkowsky, J., 1111
 Bessho, M., 547
 Brennen, C., 117
 Carrier, G. F., 3
 Chan, R. K. C., 149
 Coantic, M., 37
 Dagan, G., 607, 625
 Doctors, L. J., 601
 Favre, A., 37
 Fromm, J. E., 149
 Hasselman, K., 361
 Hogben, N., 446, 473, 540
 Holmquist, C. O., xi
 Hsu, E. Y., 11
 James, E. C., 951
 Kaplan, P., 1017
 Kerr, K. P., 1111
 Krishnamurti, R., 289
 Lackenby, H., 474
 Landweber, L., 449, 475
 Lee, C. M., 905, 951
 Le Méhauté, B., 71
 Linden, T. L. J., 477
 Maestrello, L., 477
 Maruo, H., 624, 658
 Miles, J. W., 95
 Munk, W. H., 217
 Neal, E., 239
 Newman, J. N., 519
 Norrbin, N. H., 807
 Ogilvie, T. F., 663
 Païdoussis, M. P., 981
 Paulling, J. R., 1083
 Savitsky, D., 389, 447
 Sawatzki, O., 275
 Schooley, A. H., 311
 Schieler, M., 361
 Schreiber, H. G. Jr., 1111
 Sharma, S. D., 601
 Shwartz, J., 321
 Street, R. L., 149
 Taylor, P. J., 627, 659
 Tuck, E. O., 627, 659
 Tulin, M. P., 321, 607, 626
 Van Mater, P. R. Jr., 239
 van Wijngaarden, L., 235, 287, 622
 Verhagen, J. H. G., 955
 Wang, D. P., 189
 Waters, O. D. Jr., xiv
 Weinblum, G. B., 599
 Whitney, A. K., 117
 Yih, C. S., 219, 236
 Yim, B., 573, 604
 Yu, H. Y., 11
 Zierep, J., 275, 288

